

Preston, Robert Jeremy (1996) *The petrogenesis of the Loch Scridain xenolithic sill complex, Isle of Mull*. PhD thesis.

<http://theses.gla.ac.uk/2089/>

Copyright and moral rights for this thesis are retained by the author

A copy can be downloaded for personal non-commercial research or study, without prior permission or charge

This thesis cannot be reproduced or quoted extensively from without first obtaining permission in writing from the Author

The content must not be changed in any way or sold commercially in any format or medium without the formal permission of the Author

When referring to this work, full bibliographic details including the author, title, awarding institution and date of the thesis must be given

The Petrogenesis of the Loch Scridain Xenolithic Sill Complex, Isle of Mull

A Thesis Submitted for the Degree of Doctor of Philosophy

by

Robert Jeremy Preston
BSc (Keele), MSc (Leeds)

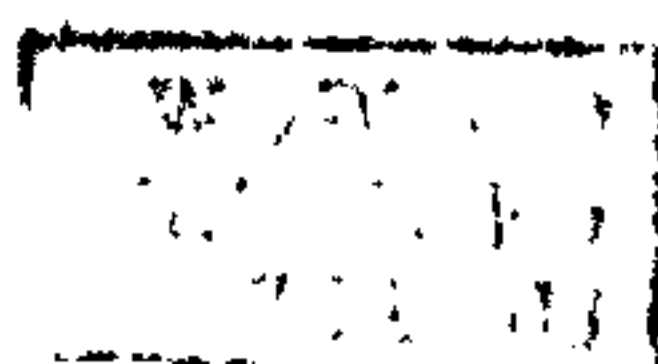
Department of Geology & Applied Geology

Faculty of Science

University of Glasgow

January, 1996

© Jeremy Preston, 1996



ABSTRACT

Intruded into the Palaeogene lava field and underlying Moine (Neoproterozoic) crystalline basement rocks around Loch Scridain, Isle of Mull, Scotland, is a suite of high-level, inclined, xenolithic sheets, ranging in composition from basalt, through andesite and dacite, to rhyolite. These sheets, associated with the Mull central volcano, were emplaced at approximately 58Ma. Three distinct (magma) groups are recognised. Group I consists of fine-grained, aphyric basalts and basaltic andesites, the most primitive of which has MORB-like chemical affinities. Group II predominantly comprises aphyric two-pyroxene andesites, and glassy plagioclase- and pyroxene-phyric dacites (pitchstones). Group III consists solely of fine-grained rhyolites. Many of the sheets are composite. The phase relationships and major-element geochemistry suggest that many of the Group I specimens evolved via fractional crystallization of olivine + plagioclase + augite, followed by plagioclase + augite + low-Ca pyroxene, from the more primitive samples. Evidence for this fractionation scheme is supported by the occurrence of gabbroic cumulate xenoliths in many of the Group I and Group II sheets. Group II evolved via the mixing between basic magmas and crustally derived silicic melts, followed by the fractionation of plagioclase + pigeonite. However, Sr-Nd isotope analyses and trace-element characteristics, in particular the LREE enrichment and Nb depletion of all but the least evolved samples, suggest that both Groups I and II contain significant amounts of crustally derived material. Strontium initial ratios correlate positively with degree of fractionation throughout Groups I and II, with the least evolved members of Group I ($Mg\# \sim 0.3$) having $(^{87}Sr/^{86}Sr)_{58}$ of around 0.7037. More evolved members of Group I and the dacites of Group II have $(^{87}Sr/^{86}Sr)_{58}$ in excess of 0.7167. Phenocryst population evidence and phase relationships suggest that some Group I samples are the result of mixing between evolved and more basic magmas, implying that the magma-storage reservoir for the Loch Scridain Sill Complex (LSSC) was continually being replenished with fresh batches of basic magma. This process would also maintain a high heat flow within the magmatic plumbing system, facilitating the assimilation of crustal material. The rhyolites of Group III are considered to be near

minimum granitic melts segregated from the Moine basement rocks, with strontium initial ratios varying between 0.7171 and 0.7203. Direct evidence of assimilation is preserved in many of the sheets in the form of a variety of crustal xenoliths. The crustal xenoliths have mainly been derived from the Moine basement rocks, although xenoliths from the Mesozoic sedimentary succession are also locally found. The most common xenolith types consist of almost pure quartzites and high-temperature mullite-bearing aluminous buchites, the latter generally having refractory selvages of plagioclase, corundum and aluminous spinel. The textural characteristics, mineral chemistry and isotope geochemistry of these rims suggest that they have crystallized from a hybrid liquid formed by the complex interaction of liquids produced by melting more refractory crust with basic magmas. The plagioclase is highly calcic (up to An₈₇), and crystals are often oscillatory zoned, implying crystallization from a melt. The spinel (pleonaste) compositions vary from the contact between the xenolith and the host sheet rock (e.g. Al₂O₃ = 60 Wt%), to the buchitic core of the xenolith (Al₂O₃ = 65 Wt%). Trapped between plagioclase crystals in the rims of the buchites are pockets of quenched contaminated melt. These contain skeletal plagioclase and clinopyroxene crystals. The 'average' composition of these melts changes from pigeonite-bearing andesite close to the xenolith core, to augite-bearing basalt nearer the contact with the host intrusion. Sr and Nd isotope values of the buchitic cores (⁸⁷Sr/⁸⁶Sr_i = 0.7098-0.7115; ¹⁴³Nd/¹⁴⁴Nd_i = 0.51188), plagioclase selvages (⁸⁷Sr/⁸⁶Sr_i = 0.7137- 0.7148; ¹⁴³Nd/¹⁴⁴Nd_i = 0.51187-0.51193) and associated trapped melts (⁸⁷Sr/⁸⁶Sr_i = 0.7126; ¹⁴³Nd/¹⁴⁴Nd_i = 0.51187-0.51192), document a complex series of magma-xenolith interactions, which have a bearing on the geochemical evolution of the LSSC as a whole.

The tectonic environment of the LSSC is not unusual, in that it involved basic magmas passing through old continental crust. The LSSC basic magmas are also not unusual, except for their very high initial Sr isotope ratios. What is exceptional about the suite, however, is the excellent preservation of a suite of crustal xenoliths showing evidence of extensive interaction and reaction with basic magmas. These features suggest that the magmatic processes which occurred in the LSSC are potentially very common, and that it was the mode of magma storage and sheet emplacement which controlled the excellent

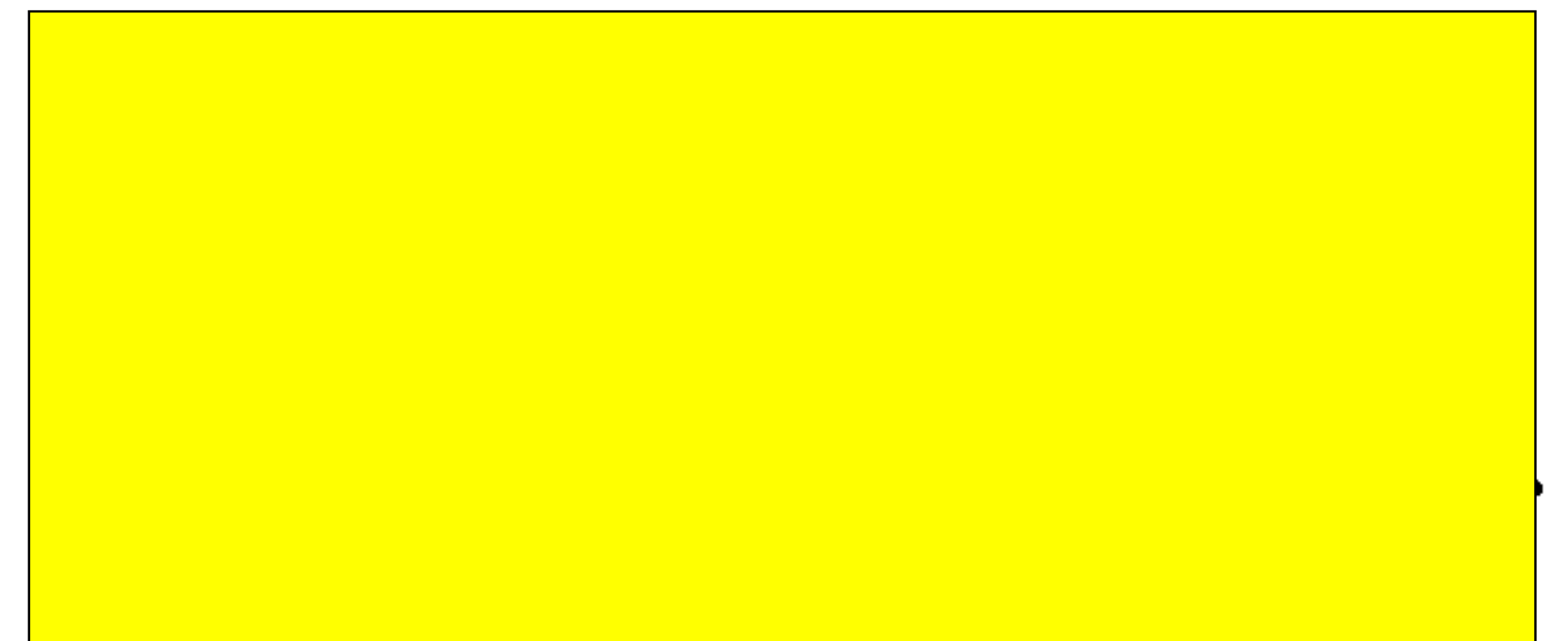
preservation of the xenoliths and the geochemical evidence for the magmatic history of the suite.

It is suggested that depleted so-called Preshal More type basic magmas (akin to present-day MORB-type magmas from Iceland) rose and ponded at high levels within the crust, probably within the Moine basement rocks. The magma storage reservoirs are unlikely to have been large magma chambers in the strict sense, but most likely consisted of a large number of small, poorly connected sheet-like bodies. Once ponded, the basic magmas underwent combined assimilation and fractional crystallization. Turbulent flow through the magma conduits connecting the sheet complexes, and during sheet emplacement most likely contributed to the extreme contamination of the basic magmas. Upper crustal sheet complexes of this type were most likely continually replenished with fresh pulses of basic magma. Such an *active* system provides the ideal scenario for the production of the crustal xenoliths, and their extensive interaction with the basic magmas, resulting in extreme trace-element and isotopic contamination of relatively basic magmas.

DECLARATION

The material presented in this thesis is the result of research carried out between October 1992 and January 1996 in the Department of Geology & Applied Geology, University of Glasgow, under the supervision of Dr T.J. Dempster and Dr B.R. Bell.

This thesis is based on my own independent research and any published or unpublished material used by me has been given full acknowledgement in the text.



Jeremy Preston

January, 1996

ACKNOWLEDGEMENTS

I would like to acknowledge the following people for all their help and encouragement throughout my period of study at Glasgow.

This project was sponsored by the NERC, to whom I am grateful for the opportunity to continue my studies. Funding for the final four months work from the DHSS is gratefully acknowledged

To my supervisors Tim Dempster and Brian Bell, many hearty thanks (and a large bottle of whiskey!!) for all their patient discussions, suggestions and support over the last three years. Thanks also for help with the field work logistics - the Fourth Year trip to Mull was a God send!! But most of all, thank you for reading this thesis, and making sure that it is up to scratch...its a job I do not envy!!

The project would not have run if it were not for the support of the Technical Staff in the Dept. of Geology. Many thanks to John for preparing probe slides, and to the "lads downstairs" for thin-section preparation. The probe work would have come unstuck but for the patient efforts of Robert...the random number generator downstairs really worked a treat, cheers mate! To Bill, Jim and Murdo for help with geochemical preparations, XRF and XRD work, to Douglas for focussing the photomicrographs, to Pete for assistance with the SEM, to Jim for computer logistics, and to "Big" John for being so friendly...I think I owe you all a pint or two.

Many thanks must go to the staff of the Rb/Sr labs at the SURRC, East Kilbride. This very important part of my work would not have been possible without the support of Anne in the preparation lab, and Vinny for actually running the samples for me. Thanks for putting up with me on those cold winter days!! Thanks also to Graeme, their boss and my third supervisor, for your suggestions, and thank you also for taking the time to read my thesis, it really was appreciated.

Outwith Glasgow, I must thank Nick Walsh and crew at Royal Holloway University for allowing me to use their ICP facility, and Godfrey Fitton and Dodie James at Edinburgh University for running my XRF analyses. This "without whom" section would not be complete without mentioning (by name) the numerous fellow postgraduate sufferers at the Dept. Geology. The following people are thanked for the numerous beer sessions which helped keep me sane throughout my studies, and just for being all round good eggs: Richard, Andy, Lynda, John, Robbie, Tim, Gary, Carolyn, Vojta, John, Simon, Alison, Chris, Dave, Clinton, and Paula. Some of you have now moved on to better things, lets hope I'll soon be joining you!! Also, a mention for Thomas, Ken and Gavin, with whom the beers have often flowed.

Particular thanks must go to Rose for a years supply of good times. Thanks for all the help with my thesis preparation, I'll return the favour when you write yours.

To my "non-geological" friends for your constant support, encouragement, and entertaining evenings, in particular, Sarah, Ems, Alison, and Chris. And to "the folks" from home, Mark, Annabel, Dev and Cathy for your continued friendship.

Finally, to Mum, Dad, Kathy (and family!) for putting up with my continuous studies over the last seven years....I'll get a job now, promise!!

TABLE OF CONTENTS

ABSTRACT

DECLARATION

ACKNOWLEDGEMENTS

LIST OF FIGURES

LIST OF TABLES

LIST OF ABBREVIATIONS

	<i>Page</i>
Chapter 1 : INTRODUCTION	
1.1 Background.	1
1.2 The British Tertiary Volcanic Province (BTVP) : Magma types and crustal contamination.	4
1.3 Geological Setting : Regional geology, and distribution, size and field relationships of the Loch Scridain Sheets.	8
Chapter 2 : SHEET PETROGRAPHY	
2.1 Introduction.	12
2.2 Detailed petrography and mineral chemistry.	14
<i>Group I : Tholeiitic basalts and basaltic andesites</i>	14
Plagioclase	14
Clinopyroxene	18
Elemental Variations in Al, Ti, Cr, Mn, and Na	19
Fe-Ti Oxides	20
<i>Group II : Augite andesites and porphyritic dacites.</i>	23
Non-porphyritic rocks	23
Plagioclase	23
Pyroxene	25
Fe-Ti oxides	28
Porphyritic rocks	29
Plagioclase	29
Clinopyroxene	30
Fe-Ti oxides, apatite and zircon	30
<i>Group III : Rhyolites</i>	31
Chapter 3 : WHOLE-ROCK MAJOR-ELEMENT GEOCHEMISTRY	
3.1 Normative mineralogy and phase relationships.	35
3.2 Whole-rock major-element data.	46
3.3 Major-element evolution of the Group I basalts and basaltic andesites.	50
<i>Fractional crystallization</i>	50
Modelling the crystal fractionation process	
(a) Closed system crystal fractionation	55
(b) Open-system processes : Fractional crystallization and assimilation	59
<i>Differential Partial Melting</i>	61
<i>Magma mixing</i>	63
3.4 Major-element evolution of the Group II andesites. and dacites.	67
3.5 Major-element evolution of the Group III rhyolites.	70
3.6 Conclusions.	72

	<i>Page</i>
Chapter 4 : WHOLE-ROCK TRACE-ELEMENT GEOCHEMISTRY	
4.1 Compatible trace-elements.	73
4.2 Incompatible trace-elements.	77
<i>Multi-element diagrams</i>	82
<i>Rare-earth elements</i>	84
REE profiles for the LSSC	85
4.3 Trace-elements and petrogenetic models.	86
<i>Closed-system fractional crystallization</i>	86
<i>Combined assimilation and fractional crystallization - AFC</i>	90
<i>Dynamic Models : The RTF magma chamber</i>	94
4.4 Trace-element evidence and the petrogenesis of Group II and Group III magmas.	97
<i>Magma mixing in the Group II andesites and porphyritic dacites</i>	97
<i>Crustal anatexis as a source for the Group III rhyolites</i>	99
4.5 The LSSC and Hebridean magma types : Trace-element evidence.	100
4.6 Conclusions.	103
Chapter 5 : WHOLE-ROCK ISOTOPE GEOCHEMISTRY	
5.1 Introduction : Isotope geology of Sr and Nd in igneous rocks.	104
5.2 The Epsilon (ε) Notation.	107
5.3 The Sr and Nd Isotope Geochemistry of the LSSC.	109
<i>Group I</i>	110
<i>Group II</i>	112
<i>Group III</i>	114
5.4 Extreme Sr and Nd isotopic systematics : Crustal Contamination or Source Enrichment ?	116
5.5 Conclusions.	119
Chapter 6 : CHEMICAL VARIATIONS WITHIN INDIVIDUAL SHEETS	
6.1 Port Mor.	120
6.2 Rudh' a' Chromain.	123
<i>Petrography</i>	123
(a) Upper & Lower Tholeiites	123
(b) Central Rhyolite	124
(c) Hybrid Rhyolite	124
(d) Separate Tholeiite Sheet	125
<i>Geochemistry and Petrogenesis</i>	125
6.3 Traigh Bhan na Sgurra.	129

	Page
Chapter 7 : THE GABBROIC XENOLITHS	
7.1 Occurrence.	133
7.2 Mineralogy.	134
<i>Olivine-plagioclase cumulate (feldspathic peridotite)</i>	135
<i>Clinopyroxene cumulate (pyroxenite)</i>	137
<i>Plagioclase-clinopyroxene cumulate (gabbro)</i>	137
<i>Plagioclase cumulate (anorthosite)</i>	137
<i>Plagioclase-orthopyroxene-magnetite crystal clusters</i>	138
7.3 Mineral chemistry.	139
<i>Olivine</i>	139
<i>Clinopyroxene</i>	141
<i>Plagioclase</i>	145
<i>Spinel</i>	148
7.4 Whole-rock geochemistry.	152
7.5 Origin and Significance of the Gabbroic Xenoliths.	155
Chapter 8 : THE PETROGENESIS OF THE LSSC	
8.1 The Magmatic History of the BTVP.	157
8.2 A Petrogenetic Model for the LSSC.	160
8.3 The LSSC and its Magmatic Plumbing System.	161
8.4 A Few Conclusions.	164
Chapter 9 : THE CRUSTAL XENOLITHS	
9.1 Introduction.	166
9.2 Mineralogy and Mineral Chemistry.	167
<i>Siliceous Xenoliths</i>	167
(a) Sandstones and conglomerates	167
(b) Quartzites	168
(c) Quartzo-feldspathic schists	169
(d) Possible granite xenoliths	170
<i>Aluminous Xenoliths</i>	174
(a) Mullite-buchites	174
(b) Cordierite (mullite) buchites	176
(c) Plagioclase-corundum-spinel assemblages	181
Corundum	181
Spinel	184
Mullite	188
Melt pockets	188
Plagioclase	190
9.3 Concluding Remarks.	197

	<i>Page</i>
Chapter 10 : THE INTERACTION OF CRUSTAL XENOLITHS AND BASIC MAGMA	
10.1 Introduction	199
10.2 Origins of the crustal xenoliths	200
<i>Partial melt extraction processes</i>	202
10.3 Magma-xenolith interactions within the LSSC	204
(a) <i>The initial stages of pyrometamorphism</i>	205
(b) <i>Production of the mullite buchites</i>	210
(c) <i>The crystallization of the plagioclase-spinel-corundum rims</i>	212
(d) <i>Geochemical evidence for complex magma/xenolith interactions</i>	214
(e) <i>Post-crystallization magma-xenolith interactions</i>	218
Chapter 11 : FINAL CONCLUSIONS : THE SIGNIFICANCE OF MAGMA-XENOLITH INTERACTION TO THE CONTAMINATION OF CONTINENTAL BASALTIC MAGMAS	220-224
REFERENCES	225-243
APPENDIX I	A1-A12
APPENDIX II	A13-A28
APPENDIX III	A29-A35
APPENDIX IV	A36-A90

LIST OF FIGURES

Chapter One	Preceding Page
1.1 System di-ol-hy-ne-Q for Hebridean magma types.	4
1.2 Ross of Mull geological sketch map.	8
1.3 General geological sketch map of the Isle of Mull.	8
1.4 Geological sketch map showing the distribution of the Palaeocene lava fields, central igneous complexes and dyke swarms in the BTVP.	8
1.5 Field photograph of the sill at Traigh Bhàn na Sgurra.	10
1.6 Field photograph of the chilled margin of the Rudh' a' Chromain composite sheet.	10
1.7 Field photograph of a composite Group I - Group II sheet.	10
Chapter Two	
2.1 Plot of TiO ₂ vs. Mg# showing LSSC magma groupings.	13
2.2 Plot of Total alkalis vs. SiO ₂ for classification of volcanic rocks (LeBas <i>et al.</i> , 1986).	13
2.3 Photomicrographs of crystal textures in Group I basalts. (a) Sub-ophitic texture. (b) Dendritic texture.	14
2.4 System An-Ab-Or for Group I plagioclase phenocryst compositions.	15
2.5 Photomicrographs of Group I plagioclase phenocryst and xenocryst. (a) Euhedral phenocryst. (b) Resorbed xenocryst.	15
2.6 Zoning profiles in Group I plagioclase xenocrysts.	15
2.7 Compositions of Group I and Group II pyroxenes plotted in the Di-He-En-Fs pyroxene quadrilateral.	18
2.8 Cation variations in Group I and Group II pyroxenes.	20
2.9 Photomicrographs of glassy, non-porphyritic Group II andesite.	25
2.10 Plot of Fe vs. Mg# for Group I and Group II pyroxenes.	25
2.11 Field photograph of "sheath and core" structure in Group II porphyritic dacite.	29

	Preceding Page
2.12 Photomicrographs of Group II porphyritic dacites.	29
(a) Plagioclase & pigeonite phenocrysts in glassy matrix.	
(b) Plagioclase & pigeonite phenocrysts in devitrified matrix.	
2.13 Photomicrograph of Group III rhyolite.	33
 Chapter Three	
3.1 Plot of H_2O^+ vs. Silica saturation for the LSSC.	40
3.2 System di-ol-hy-ne-Q for the LSSC.	40
3.3 System forsterite-diopside-silica for the LSSC (after Campbell, 1985).	41
3.4 (a) System Cpx-Ol-Qtz (after Grove <i>et al.</i> , 1984).	45
(b) Schematic diagram of the system Cpx-Ol-Qtz showing crystallization, assimilation and AFC trends.	
(c) System Cpx-Ol-Qtz for the LSSC data.	
3.5 Major-element variation diagrams for the LSSC.	46
(a)-(i) Wt% oxide vs. Wt% SiO_2 .	
(j)-(r) Wt% oxide vs. Mg#.	
3.6 Plot of Wt% K_2O vs. SiO_2 for the LSSC, showing tholeiitic and alkaline magma trends.	46
3.7 (a) AFM diagram for the LSSC.	47
(b) Plot of Wt% $Fe_2O_3^*$ vs. MgO.	
3.8 Plot of Wt% CaO/Al_2O_3 vs. SiO_2 for the LSSC showing importance of pyroxene fractionation.	51
3.9 (a) System diopside-olivine-silica (after Walker <i>et al.</i> , 1979).	52
(b) System diopside-olivine-silica for the LSSC.	
3.10 Major-element AFC models.	61
3.11 (a) Plot of K_2O vs. $Fe_2O_3^*$.	62
(b) Plot of TiO_2 vs. $Fe_2O_3^*$.	
(c) Plot of Al_2O_3 vs. $Fe_2O_3^*$.	
(d) Plot of SiO_2 vs. $Fe_2O_3^*$.	
3.12 (a) Plot of Na_8 vs. Si_8 .	62
(b) Plot of Na_8 vs. Fe_8 .	
3.13 Major-element mixing tests.	65
3.14 Major-element mixing tests.	65
3.15 System albite-anorthite for Group II glasses and plagioclase phenocrysts.	69

	<i>Preceding Page</i>
3.16 Major-element mixing tests.	69
3.17 System Ab-Or-Qtz for Group III rhyolites, and experimental granitic melts.	70
 Chapter Four	
4.1 Compatible trace-element variations with Wt% SiO ₂ .	75
4.2 Incompatible trace-element variations with Wt% SiO ₂ .	78
4.3 Incompatible trace-element covariations.	79
(a) Ce vs. Zr (b) Ce vs. Nb	
(c) Zr vs. Nb (d) Ce vs. La	
4.4 Incompatible trace-element ratio variations with Wt% SiO ₂ .	79
(a) Zr/Y (b) Ti/Zr	
(c) Y/Nb (d) Ce/Y	
4.5 Incompatible trace-element ratio variations with Wt% Fe ₂ O ₃ *.	80
(a) Zr/Y (b) Ce/Y	
4.6 Plot of Cr vs. Zr showing partial melting and crystal fractionation curves.	80
4.7 Covariance of incompatible trace-element ratios.	80
(a) Zr/Y vs. Ce/Y (b) Ti/Zr vs. Y/Nd	
4.8 Incompatible trace-element ratio variations with Wt% SiO ₂ , showing importance of crustal contamination.	81
(a) Nb/TiO ₂ (b) K/Zr	
(c) Ba/Nb (d) (Ce/Yb) _n	
4.9 Mantle normalized Spider diagrams for the LSSC.	83
4.10 MORB normalized Spider diagrams for the LSSC.	83
4.11 REE profiles for the LSSC.	83
4.12 Log-log incompatible trace-element covariance plots showing calculated AFC trends.	91
4.13 Covariance of REE ratios.	97
(a) (Nd/Sm) _n vs. (La/Ce) _n	
(b) (La/Nd) _n vs. (Sm/Yb) _n	
4.14 Trace-element characteristics of the SMLS, Preshal More, Fairy Bridge magma types compared to the LSSC.	100
4.15 REE profiles of the SMLS, Preshal More, and Fairy Bridge magma types.	101

Chapter Five

5.1	ESr-ENd correlation diagram for MORB, OIB, CFB and crustal rocks.	106
5.2	ESr-ENd correlation diagram for the LSSC. 109	
5.3	(a) ESr vs. SiO ₂ (b) ENd vs. SiO ₂	110
5.4	Covariance of ESr with incompatible trace-elements. (a) Ce (b) Zr (c) La (d) Nb	110
5.5	Covariance of ENd with incompatible trace-elements. (a) Ce (b) Zr (c) La (d) Nb	110
5.6	ESr-ENd correlation diagram for Group I magmas with calculated AFC trend.	111
5.7	(a) ESr vs. Fe ₂ O ₃ * (b) ENd vs. Fe ₂ O ₃ *	111
5.8	Isotope mixing plot for Group II magmas.	113
5.9	ESr-ENd correlation diagram for Lewisian granulite and amphibolite facies rocks, and Moine metasediments.	114
5.10	Plot of ENd vs. Ti/Yb showing importance of crustal contamination compared to source contamination.	118

Chapter Six

6.1	Geological sketch map of the Group I sheet at Port Mor.	120
6.2	Variation of major- and trace-elements through the Port Mor sheet.	120
6.3	Photomicrographs of specimens from the top, middle and base of the Port Mor sheet.	120
6.4	REE profiles for the Port Mor sheet.	122
6.5	Geological sketch map of the composite basalt-rhyolite sheet at Rudh' a' Chromain.	123
6.6	Variation of major- and trace-elements through the Rudh' a' Chromain sheet.	126
6.7	REE profiles for the separate facies of the Rudh' a' Chromain composite sheet.	127
6.8	Major and trace-element mixing tests for the Rudh' a' Chromain composite sheet.	129

	<i>Preceding Page</i>
6.9 Geological sketch map of the area around the Group I sheet at Traigh Bhàn na Sgurra.	129
6.10 Field photograph of xenolith-rich lenses in the sheet at Traigh Bhàn na Sgurra.	130
6.11 Field photographs of the Moine metasedimentary succession at Traigh Bhàn na Sgurra.	130
6.12 Selected major- and trace-element variations through the Traigh Bhàn na Sgurra Group I sheet.	130
 Chapter Seven	
7.1 Field photographs of gabbroic cumulate xenoliths.	133
7.2 Photomicrographs of feldspathic peridotite xenolith.	135
7.3 Photomicrograph of pyroxenite xenolith.	137
7.4 Photomicrograph of cumulus plagioclase in a gabbroic xenolith showing overgrowth texture.	137
7.5a-b Photomicrograph of poikilitic and cumulus clinopyroxene in a gabbroic xenolith.	137
7.6 Photomicrograph of cumulus plagioclase in an anorthosite xenolith.	137
7.7 Photomicrograph of fibrous zeolite in an anorthosite xenolith.	137
7.8 Pyroxene compositions from the cumulate xenoliths plotted in the Di-Hd-En-Fs pyroxene quadrilateral.	141
7.9 Cation variations in pyroxenes from the cumulate xenoliths.	141
7.10 Plagioclase compositions for the cumulate xenoliths, plotted in the system Ab-An-Or.	145
7.11 Photomicrograph of cumulus plagioclase showing overgrowth textures.	145
7.12 Photomicrograph of oscillatory zoned cumulus plagioclase.	145
7.13 Photomicrograph of cumulus plagioclase showing complex, patchy zoning.	145
7.14 Zoning profiles for cumulus plagioclase.	145

	Preceding Page
7.15 (a) Cr-spinel compositions plotted in the spinel prism - Fe/(Fe+Mg) vs. Cr/(Cr+Al).	148
(b) Cr-spinel compositions plotted in the spinel prism - Fe/(Fe+Mg) vs. Fe ³⁺ /(Fe ³⁺ +Cr+Al).	
(c) Cr-spinel compositions plotted in the Al ³⁺ - Fe ³⁺ - Cr ³⁺ triangle.	
(d) Cr-spinel cation variations.	149
7.16 Chondrite-normalized REE plot for the gabbroic xenoliths.	152
7.17 ¹⁴³ Nd/ ¹⁴⁴ Nd _i vs. ⁸⁷ Sr/ ⁸⁶ Sr _i correlation diagram for the gabbroic xenoliths compared to the Group I magmas.	152
 Chapter Eight	
8.1 (a) β factors and geotherms for mantle T _p = 1280°C.	157
(b) β factors and geotherms for mantle T _p = 1480°C.	
(c) Cumulative % of melt with changing β factor.	158
(d) Average depth of melting as a function of β factor.	
8.2 Schematic diagram of the proposed magmatic plumbing system for the LSSC.	164
 Chapter Nine	
9.1 (a) Unmetamorphosed Carsaig sandstone.	167
(b) Thermally metamorphosed Carsaig sandstone.	
9.2 Field photograph of quartzite xenolith.	169
9.3 Field photograph of schistose xenolith.	169
9.4 Photomicrograph of partially melted Moine pelite.	169
9.5 System Ab-Or-Qtz for siliceous glasses from xenoliths.	171
9.6 Field photograph of mullite buchite.	174
9.7 Photomicrograph of residual plagioclase in mullite buchite.	176
9.8 Photomicrograph of cordierite buchite.	176
9.9 Field photograph of plagioclase-rimmed mullite buchite.	181
9.10 Field photograph of euhedral plagioclase in mullite buchite.	181
9.11 Schematic scale diagram of a plagioclase-rimmed mullite buchite showing major textural features examined.	181

	<i>Preceding Page</i>
9.12 Photomicrograph of euhedral corundum in plagioclase.	182
9.13 Photomicrograph of skeletal corundum.	182
9.14 (a) Photomicrograph of euhedral spinel in plagioclase. (b) SEM back scattered image of alteration of spinels.	184
9.15 Photomicrographs of spinels showing variation in colour.	184
9.16 Photomicrograph of corundum altering to spinel.	184
9.17 (a) Modified (Cr-free) spinel prism showing limited compositional range of spinels from aluminous xenoliths. (b) Spinel compositions plotted on to prism base. (c) Spinel compositions plotted on to Fe-rich prism side.	184
9.18 Variations in spinel chemistry with distance to basalt contact.	185
9.19 Covariation of $\text{Al}_2\text{O}_3\text{-Fe}_2\text{O}_3$ and FeO-MgO for spinels from aluminous xenoliths.	186
9.20 (a) Mullite inclusions in plagioclase. (b) Mullite-free zones in mullite-bearing plagioclase.	188
9.21 Photomicrograph of basaltic melt pocket in aluminous xenolith.	188
9.22 (a) Composition of plagioclase from melt pockets. (b) Composition of pyroxenes from melt pockets.	189
9.23 Major-element variations for basaltic melt pockets, as a function of distance to the host basalt contact.	189
9.24 Photomicrograph of large euhedral plagioclase from aluminous xenoliths.	190
9.25 Photomicrograph of finer-grained plagioclase from aluminous xenoliths.	190
9.26 Plagioclase compositions from aluminous xenoliths.	190
9.27 Photomicrograph of oscillatory zoned plagioclase from aluminous xenolith.	190
9.28 Examples of zoning profiles in plagioclase from aluminous xenoliths.	190
9.29 SEM back scattered image of basaltic melt pockets, showing sodic rims on plagioclase adjacent to melt pocket.	191
9.30 SEM back scattered image of fine-grained, recrystallized plagioclase in the centre of large plagioclase lath.	191

	<i>Preceding Page</i>
9.31 Photomicrograph of fine-grained plagioclase "armour" around resorbed spinel.	191
9.32 Photomicrograph and SEM back scattered images of "fingerprint" texture in xenolithic plagioclase.	192
 <i>Chapter Ten</i>	
10.1 Schematic diagram showing the proposed mechanism for the formation of xenolith-rich pods and lenses.	202
10.2 (a) Photomicrograph of a typical Moine pelite. (b) Photomicrograph of a partially melted Moine pelite.	206
10.3 System FeO-SiO ₂ -Al ₂ O ₃ .	211
10.4 (a) System CaO-SiO ₂ -Al ₂ O ₃ . (b) System CaO-SiO ₂ -Al ₂ O ₃ showing proposed crystallization path for the plagioclase-rimmed mullite buchites.	211
10.5 System MgO-SiO ₂ -Al ₂ O ₃ .	211
10.6 System forsterite-diopside-anorthite-silica. (a) System forsterite-anorthite-silica. (b) System forsterite-anorthite-diopside.	213
10.7 REE profiles for plagioclases and mullite buchites from a aluminous xenolith.	214
10.8 Schematic scale diagram of a plagioclase-rimmed mullite buchite showing sample positions and Sr-Nd isotope analysis results.	215
10.9 Selected major-element variations with Wt% SiO ₂ for basaltic melt pockets from aluminous xenolith.	218
10.10 Schematic diagram showing alternative explanations for the variations in spinel chemistry.	219
 <i>Chapter Eleven</i>	
11.1 Schematic diagram showing the proposed evolution of a plagioclase-rimmed mullite buchite xenolith.	220

LIST OF TABLES

	<i>Page</i>
 Chapter Two	
2.1 Plagioclase compositions in Group I basaltic sheets.	16-17
2.2 Pyroxene compositions in Group I basaltic sheets.	21
2.3 Fe-Ti oxide compositions in Group I basaltic sheets.	22
2.4 Plagioclase compositions in non-porphyritic Group II andesitic sheets.	24
2.5 Pyroxene compositions in non-porphyritic Group II andesitic sheets.	27
2.6 Fe-Ti oxide compositions in non-porphyritic Group II andesitic sheets.	28
2.7 Feldspar compositions in porphyritic Group II dacitic sheets.	31
2.8 Pyroxene compositions in porphyritic Group II dacitic sheets.	32
2.9 Feldspar compositions in Group III rhyolitic sheets.	34
 Chapter Three	
3.1 Representative whole-rock compositions of sheets from the LSSC, including major-elements, trace-elements, Sr and Nd isotope ratios, and CIPW norms.	36-39
3.2 Results from a computer simulation of cotectic crystallization (Nathan & Van Kirk, 1978), for Group I sheets.	42
3.3 Criteria for projection of compositions into the Normative basalt tetrahedron.	43
3.4 (a) Mineral compositions used in least-squares modelling of crystal fractionation.	56
(b) Results of least-squares modelling.	57
3.5 Compositions of possible contaminants for the use in major-element modelling of AFC processes.	60
3.6 Effects of differential partial melting, and of pressure of melting, on major-element concentrations in mantle melts.	62
3.7 Glass analyses from a Group II porphyritic dacite.	68
3.8 Experimental partial melts from pelitic rocks.	71

	<i>Page</i>
Chapter Four	
4.1 Trace-element distribution coefficients used in crystal fractionation and AFC modelling.	88
4.2 Summary of results from closed system fractionation modelling for Group I magmas.	89
4.3 Summary of results from AFC modelling for Group I magmas.	93
4.4 Trace-element characteristics of the various Hebridean magma types, compared to the LSSC.	101
Chapter Five	
5.1 Summary of the Sr and Nd isotope analyses for the LSSC, Group I, Group II and Group III rocks.	109
5.2 Sr and Nd isotope ratios from Moine rocks.	115
Chapter Six	
6.1 Mineral modes in the Port Mor basaltic sheet.	121
6.2 Whole-rock compositions of the various rocks from the composite basalt-rhyolite sheet at Rudh' a' Chromain.	126
6.3 Sr and Nd analyses of the various rocks from the composite basalt-rhyolite sheet at Rudh' a' Chromain.	127
6.4 Sr and Nd analyses from the basaltic sheet at Traigh Bhàn na Sgurra.	132
Chapter Seven	
7.1 Mineral modes in the various types of cumulate xenoliths.	135
7.2 Olivine analyses from a feldspathic peridotite xenolith.	140
7.3 Clinopyroxene analyses from various cumulate xenoliths.	144
7.4 Plagioclase analyses from various cumulate xenoliths.	147
7.5 Cr-spinel analyses from a feldspathic peridotite xenolith.	151
7.6 Whole-rock compositions of four cumulate xenoliths.	154

	Page
Chapter Nine	
9.1 Compositions of glasses in siliceous xenoliths.	172
9.2 Mullite analyses from aluminous xenoliths.	175
9.3 Glass and whole-rock compositions from a mullite buchite.	178
9.4 Cordierite analyses from aluminous xenoliths.	179
9.5 Glass and whole-rock compositions from a cordierite buchite.	180
9.6 Corundum analyses from a plagioclase-rimmed mullite buchite.	183
9.7 Spinel analyses from a plagioclase-rimmed mullite buchite.	186
9.8 Plagioclase analyses from a plagioclase-rimmed mullite buchite.	193-196
Chapter Ten	
10.1 (a) Primary mineral compositions in a typical Moine pelitic schist.	208
(b) Restite mineral compositions in a partially melted Moine pelitic schist.	209
10.2 Sr and Nd isotope ratios from various mullite buchites.	216
Chapter Eleven	
11.1 Geochemical fingerprints during the interaction of basic magmas with pelitic crustal rocks.	222

ABBREVIATIONS USED THROUGHOUT THE TEXT

SMLS	-	Skye Main Lava Series
FB	-	Fairy Bridge
PM	-	Preshal More
NPC	-	Non Porphyritic Central
BTVP	-	British Tertiary Volcanic Province
NATIP	-	North Atlantic Tertiary Igneous Province
LSSC	-	Loch Scridain Sheet Complex
MOR	-	Mid Ocean Ridge
MORB	-	Mid Ocean Ridge Basalt
OIB	-	Ocean Island Basalt
CFB	-	Continental Flood Basalt
HPT	-	High phosphorus and titanium
LPT	-	Low phosphorus and titanium
CPFU	-	Cations per formula unit
REE	-	Rare-earth element
LREE	-	Light Rare-earth element
HREE	-	Heavy Rare-earth element
PPL	-	Plain Polarised Light
XPL	-	Cross Polarised Light
SEM	-	Scanning Electron Microscope

**THE PETROGENESIS OF THE LOCH SCRIDAIN XENOLITHIC
SHEETS, ISLE OF MULL.**



Frontpiece

Aluminous xenoliths in a basaltic sheet on the shore of Loch Scridain

"The subterranean magmas act powerfully on their containing walls, and transform highly argillaceous sediments into crystalline rocks composed of cordierite, sillimanite, biotite, quartz, and sometimes spinelle and corundum. The rocks of the inner contact-zone become shattered, and the igneous magma insinuates itself between the cracks, or may even permeate the mass. Portions of the metamorphic rock float off into the molten material, and travel with it through dykes and other channels to the surface."

Sir Jethro Teal

"The Natural History of Cordierite & its Associates"
Proceedings of the Geological Association, Vol 16 (1899)

CHAPTER 1

INTRODUCTION

1.1 Background

Assimilation of continental crust by basic magmas is a widely invoked process for explaining compositional and isotopic characteristics of associated intermediate and silicic igneous rocks. The importance of crustal contamination has provided petrologists with debate since Fournet (1846) suggested that digestion of country-rock may produce changes in magma chemistry. Bowen (1922, 1928) provided the first rigorous studies on possible mechanisms for, and the consequences of, crustal contamination. Addressing the question in the context of crystal-liquid equilibria, Bowen showed that the limiting factors in the process of crustal assimilation were the difference between the heat capacity and heat of fusion of the materials involved, and that magmas at or near the Earth's surface are unlikely to contain substantial superheat. As a result, he concluded that the heat required to raise the temperature of the country-rock to that of the magma is provided by the crystallization of the phases with which the liquid is currently saturated; the compositional trend of the liquid follows the liquidus just as it would without assimilation, and only the proportions of the crystalline end-products differ.

Since then, many crustal assimilation mechanisms have been suggested, and used to explain the petrogenesis of both tholeiitic and calc-alkaline magmas from many different tectonic environments.

Within the 'classic' magma chamber environment, the walls, roof and floor of the chamber may begin to melt when the solidus temperature of the country-rock is exceeded. However, experimental studies (*e.g.* Campbell & Turner, 1987) have shown that the resident magma and the crustal melt will possibly remain unmixed due to density and viscosity differences, and that mass transfer will be limited unless vigorous convective overturn is initiated. The stoping of wall-rock blocks into the magma body provides a more efficient mechanism for bringing country-rock into contact with hot magma.

When magma flows in dyke-like conduits the extent of wall-rock assimilation may be controlled by the nature of the flow (Huppert &

Sparks, 1985). If the flow is laminar, the magma is likely to solidify against the walls, preventing significant contamination. However, during turbulent flow, heat transfer is more efficient and the products of partial melting of the wall-rocks will be continuously swept away, allowing further assimilation to occur. The mechanical break-up of country-rocks and their entrainment as xenoliths will also bring more fusible material into contact with the magma. Huppert & Sparks (1985) indicate that flow of high-temperature primitive magma will be fully turbulent if the conduit width exceeds 3m.

Recent studies of continental basalt provinces have revealed the occurrence of two contrasting styles of crustal contamination (cf. Thompson *et al.*, 1982; Mantovani *et al.*, 1985; Fodor *et al.*, 1985a, 1985b; Devey & Cox, 1987) :

- (a) Contamination is accompanied by concurrent fractional crystallization within magma chambers or dyke complexes, where the heat released by crystallization allows fusion of the country-rocks. This process has been termed AFC (Assimilation and Fractional Crystallization) by DePaolo (1981), and has been widely used to interpret trace-element and radiogenic isotope variations within suites of volcanic rocks. In such AFC processes, positive correlations should develop between indices of fractionation (*e.g.* wt% SiO₂) and incompatible trace-element ratios or Sr-Nd-Pb isotopic ratios.
- (b) In those provinces where deep magma chambers develop at the base of the crust, fractional crystallization may occur without significant crustal contamination because of the refractory nature of the wall-rocks. When magmas from these chambers subsequently ascend to higher levels in the crust, it will be the hotter, more primitive magmas that will be capable of assimilating the easily fusible upper crustal rocks (Wilson, 1989).

Many studies which call upon substantial crustal contamination to explain compositional variations in a suite of co-magmatic rocks have had to make assumptions over the nature of the contaminant due to the lack of exposure of suitable basement rocks, or the lack of preserved xenoliths.

The Loch Scridain Sill Complex (LSSC) on the Isle of Mull, NW Scotland, provides perhaps a unique opportunity to study the interaction of basic magmas with crustal material. The LSSC is a suite of high level, inclined, basic to silicic sheets that are intruded into a variety of country-rocks. Many of the sheets preserve numerous crustal xenoliths in all stages of partial fusion (see Chapter 9), as well as ultrabasic xenoliths of cumulate origin (see Chapter 7). The aim of the present study is to examine the petrography and geochemistry of the LSSC in order to fingerprint the petrogenetic processes which occurred to produce the large range of compositions seen within the suite, and also to investigate the small-scale mechanisms by which basic magmas assimilate crustal material.

The petrogenesis of the suite as a whole is constrained using petrography, mineral chemistry, phase relationships, and whole-rock major- and trace-element and isotope geochemistry data. The mechanisms behind the process of crustal contamination have been elucidated by examining the mineralogy and textural relationships preserved within the crustal xenoliths, and by the analysis of small-scale trace-element and radiogenic isotope ratio variations in xenoliths and the enclosing host-rock (*i.e.* magma).

1.2 The British Tertiary Volcanic Province (BTVP) : Magma types and crustal contamination.

The concept of magma types was introduced by Bailey *et al.* (1924) when the original mapping of Mull was carried out. These workers proposed a considerable number of basic, intermediate and acid (*i.e.* silicic) magma types. Today, however, the usage of the term 'magma type' has restricted the concept to various groups of basaltic liquids, and their derivatives.

Thompson *et al.* (1972, 1980) recognised two distinct basic magma types during extensive mineralogical and geochemical studies of the lavas of north Skye. A third, much rarer magma type was also added (Mattey *et al.*, 1977) :-

- (a) The majority of the plateau lavas of the BTVP, together with dykes away from the central axis of the Skye Main Swarm (and most likely the other major swarms : Mull etc.) are identified as transitional basalts and their fractionates. *Figure 1.1* shows that the most primitive specimens straddle the *di-ol* join in the system normative *di-ol-hy-ne-Q*. These comprise the Skye Main Lava Series (SMLS) magma type. Two discrete fractionation trends are recognised:

- (i) basalt - hawaiite - mugearite - benmoreite
- (ii) basalt - low-Fe intermediates - trachyte

The SMLS magma type has characteristic light REE enrichment, with $(\text{Ce}/\text{Yb})_N \sim 2-5$ (Mattey *et al.*, 1977; Thompson *et al.*, 1980).

- (b) The so-called Preshal More (PM) Basalt magma type is of a distinctly tholeiitic nature. It is recognised as a single flow in the Skye lava field, the Giant's Causeway flow in Antrim (Lyle & Preston, 1993), together with a significant proportion of the dyke swarm from Skye and Mull, and a number of small and large intrusions associated with the Cuillin Igneous Complex and the Mull Central Complex (*e.g.* Bell *et al.*, 1994). The PM type is characterized by distinctive values of the ratios Ti/Zr ($\sim 110-120$) and Y/Zr (~ 0.4) and light REE depletion with $(\text{Ce}/\text{Yb})_N < 1$ (Mattey *et al.*, 1977).

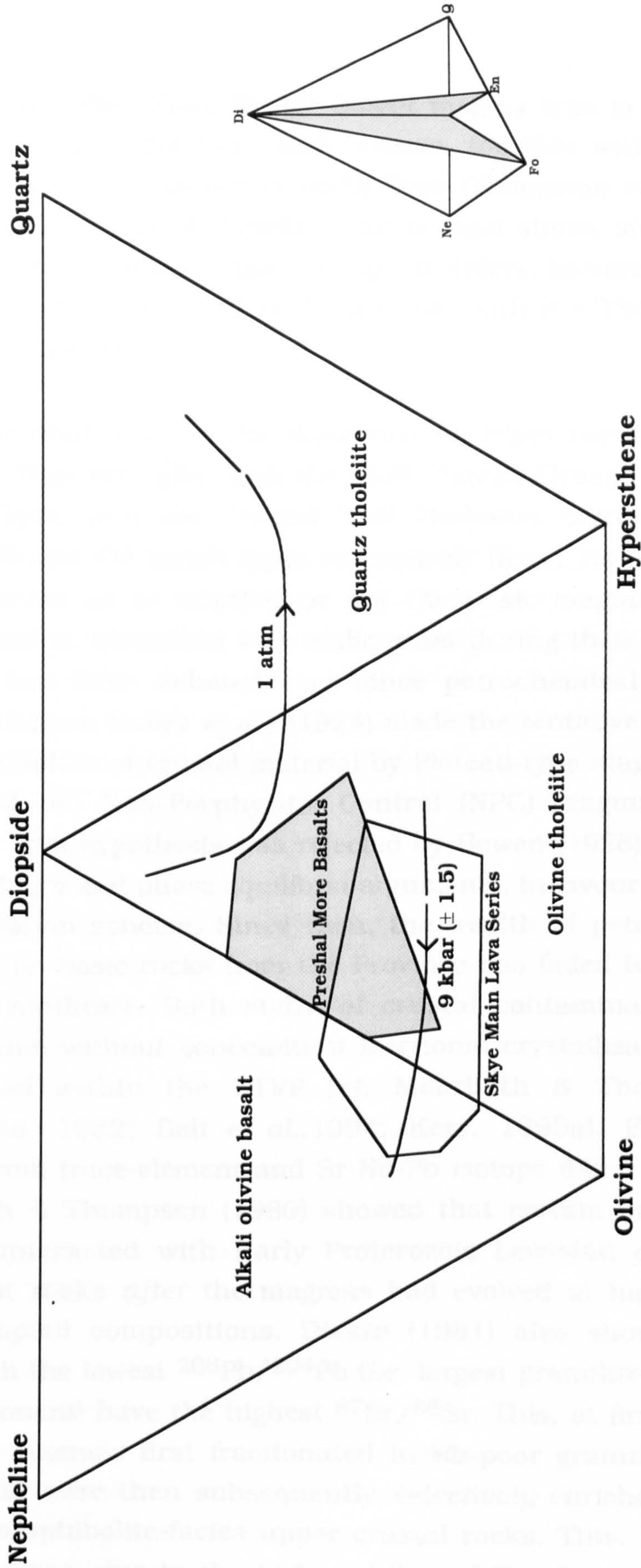


FIGURE 1.1 CIPW normative di, hy, ol, ne and q for Hebridean magma types. Shown are fields occupied by the Skye Main Lava Series and the Preshal More Basalt magma type, together with anhydrous cotectic curves at 1 atm and 9 kbars for olivine + plagioclase + clinopyroxene + basaltic liquid (Thompson, 1982). Inset shows the relationship of the diagram to the surfaces in the Yoder-Tilley basalt tetrahedron (Yoder & Tilley 1962).

- (c) The so-called Fairy Bridge Basalt magma type is found as dykes belonging to the Skye Main swarm, together with one lava from the plateau sequence of north Skye (Thompson *et al.*, 1980). This magma type is of tholeiitic nature, and shows similar Ti/Zr and Y/Zr ratio values to the PM type. It differs, however, in having flat chondrite-normalized REE patterns, with $(\text{Ce/Yb})_N \sim 1\text{-}2$ (Mattey *et al.*, 1977).

These are equivalent to the three magma types recently re-evaluated from the Mull lava pile, with the Mull Plateau Group, the Coire Gorm Magma Type, and the Central Mull Tholeiites corresponding to the SMLS, FB and PM basalt types respectively (Kerr, 1995b).

The question as to whether or not the basic magmas of the BTVP assimilated or interacted with sialic crust during their uprise from the mantle, has been debated ever since petrochemical studies of the Province began. Bailey *et al.*, (1924) made the tentative suggestion that the assimilation of crustal material by Plateau-type magmas (*i.e.* SMLS) generated the Non-Porphyrific Central (NPC) magma type (*i.e.* PM basalts). This hypothesis was rejected by Bowen (1928) on the basis of mass-balance and phase equilibria arguments, in favour of his fractional crystallization scheme. Since then, the wealth of petrochemical data gathered on basic rocks from the Province has failed to illuminate one *single* hypothesis. Both styles of crustal contamination, AFC, and assimilation without concomitant fractional crystallization, have been recognised within the BTVP (*cf.* Moorbath & Thompson, 1980; Thompson, 1982; Bell *et al.*, 1994; Kerr, 1995a). Evidence comes mainly from trace-element and Sr-Nd-Pb isotope data.

Moorbath & Thompson (1980) showed that certain batches of SMLS magma interacted with Early Proterozoic Lewisian *granulite-facies* basement rocks *after* the magmas had evolved at high pressures to their erupted compositions. Dickin (1981) also showed that those lavas with the lowest $^{206}\text{Pb}/^{204}\text{Pb}$ (*i.e.* largest granulite-facies Lewisian Pb component) have the highest $^{87}\text{Sr}/^{86}\text{Sr}$. This, at first sight, implies that the magmas first fractionated in Rb-poor granulite-facies lower crust, and were then subsequently *selectively* enriched in ^{87}Sr from Rb-rich amphibolite-facies upper crustal rocks. This, however, seems unlikely since, due to the high mobility of Pb, the magmas would be expected to take-on upper crustal Pb isotopic signatures (Thompson,

1982). This paradox can be overcome in three ways if it is assumed that only granulite-facies rocks are involved :-

- (a) The ^{87}Sr enrichment resulted from the selective breakdown of a minor Rb-rich phase, such as biotite, in the granulites (Thompson, 1982)
- (b) The superheated SMLS magmas assimilated distinctive rock types with unradiogenic Pb and comparatively radiogenic Sr isotope signatures. Such Lewisian granulites are reported to crop out on Skye (Dickin, 1981)
- (c) The magmas extracted K-rich minimum melts from the sheets and lenses of potassic pegmatites which occur sparsely but are wide spread within the Lewisian Gneiss. These have been shown to have high present-day $^{87}\text{Sr}/^{86}\text{Sr}$ (Lyon *et al.*, 1975) The Pb isotope signature would have been derived through equilibration with the more dominant granulite lithologies.

Thirlwall & Jones (1983) presented Sr and Nd isotopic evidence from the SMLS which suggests that the contamination of many of the basalts and hawaiites, was achieved by the incorporation of melts derived from the Lewisian basement, into a range of magma compositions produced by high pressure fractional crystallization and by variable degrees of partial melting. Such melts are likely to be highly siliceous (Dickin, 1981), and therefore contamination should therefore be accompanied by increasing SiO_2 in the basalts. There appears to be no correlation between SiO_2 and $^{87}\text{Sr}/^{86}\text{Sr}$ within the SMLS (Moorbath & Thompson, 1980), and as such contamination with crustal melts would therefore appear unlikely (Dickin, 1981). However, by recalculating SMLS analyses on a volatile-free basis, and using $^{143}\text{Nd}/^{144}\text{Nd}$ as an index of contamination, Thirlwall & Jones (1983) found clear correlations between $^{143}\text{Nd}/^{144}\text{Nd}$ and SiO_2 , silica saturation and K/Zr, thus lending weight to their crustal melt hypothesis.

Kerr (1993) showed that certain flows at the base of the lava pile on Mull are relatively enriched in the full range of incompatible elements when compared with 'typical' Mull Plateau Type basalts. He concluded that these magma batches had been contaminated by 5-10% of an

enriched, fusible, small-fraction-melt from the lithospheric mantle. The source for this relatively enriched contaminant was suggested as being Permo-Carboniferous lamprophyric dykes (cf. Morrison *et al.*, 1980).

In contrast, many studies on PM type suites have tended to show AFC style contamination. The PM basalts are thought to have originated from the limited partial fusion of the lherzolitic residuum after the SMLS magma genesis, leaving a final harzburgitic residue (Thompson *et al.*, 1980).

Bell *et al.*, (1994) demonstrated that the cone-sheets from the Cuillin Igneous Complex originated from PM type magmas, and evolved via combined fractional crystallization of olivine, plagioclase and augite, and assimilation of Lewisian *amphibolite-facies* crustal rocks at relatively low pressures. Holland & Brown (1972) tentatively suggested a similar mode of origin for the Ardnamurchan cone-sheet complex. Unlike 'typical' PM basalts, the Ardnamurchan cone-sheet magmas are dominantly *quartz-tholeiites*, and follow the 1atm cotectic in the system normative *di-ol-hy-ne-Q* (Figure 1.1). Although this work was carried out before the recent concept of magma types was significantly developed, these authors concluded that the suite had an *olivine-normative* NPC type parent magma, and evolved to quartz-normative derivatives via low-pressure crystal fractionation, possibly coupled with the assimilation of siliceous country-rock.

AFC-style contamination was also reported from the picrites and picrodolerites of the Trotternish sills, northern Skye (Gibson, 1990). This extensive suite of ultramafic sills evolved via the fractionation of olivine and clinopyroxene, coupled with the assimilation of up to 22% amphibolite-facies Lewisian gneiss.

The evolution of the Mull lava sequence has been recently re-evaluated by Kerr (1993, 1994, 1995a), and by Kerr *et al.* (1995). This work is extensively discussed in later chapters.

1.3 Geological Setting : Regional geology, and distribution, size and field relationships of the Loch Scridain Sheets.

The LSSC is restricted to a relatively small area on the Ross of Mull, between Carsaig and Pennyghael to the east, and Bunessan on the west. Also, sheets from the same suite can be found, in less profusion, to the north of Loch Scridain around Tiroran on the peninsula of Ardmeanach (*Figure 1.2*). The suite is mainly hosted by the extensive lava field which is of Palaeocene age (Musset, 1986). The plateau lavas overlie the Precambrian Moine Complex of metasedimentary rocks, which is itself overlain by a thin sequence of Mesozoic (Triassic - Cretaceous) clastic and carbonate lithologies. Sheets from the LSSC intrude all of the pre-Palaeocene lithologies (*Figure 1.3*). However, the crustal structure of the Ross of Mull area has been shown to be very complex (Potts, *et al.*, 1995). The Moine of Mull is likely to be a very thin crustal slice, brought into position along major faults (Moine Thrust?). The Great Glen Fault also passes through the southern-most part of Mull, and therefore Dalradian rocks are likely to occur just to the south of the island. All of these rocks are likely to be underlain, ultimately, by rocks of the Lewisian gneiss complex. Rocks of Lewisian age, and possibly of Torridonian age, crop out of the Isle of Iona, just to the south of Mull, separated from Mull by the Sound of Iona Fault (*Figure 1.3*) (Potts, *et al.*, 1995). The whole structure has been further complicated by the intrusion of a late Caledonian Granite on the tip of the Ross of Mull. Such a complex crustal structure in a small geographical area has obvious ramifications when attempting to assess the effects of crustal contamination on a suite of basaltic rocks.

The activity which produced the LSSC clearly post-dates the extrusion of the plateau lavas, and is thought to be related to the activity of the Mull central volcano, and the production of the Central Igneous Complex. The Mull Central Igneous Complex is one of a number of intrusive centres in the BTVP, which extends from Skye, south along the west coast of Scotland, into Ireland (*Figure 1.4*). The Mull Central Igneous Complex is broadly circular in plan, having a diameter of approximately 15km. The evolution of the complex can be traced in terms of three successive centres, each defined by arcuate ring-fractures with associated intrusions, and interspersed with silicic to basic cone-sheets, the focus of activity in each case shifting with time

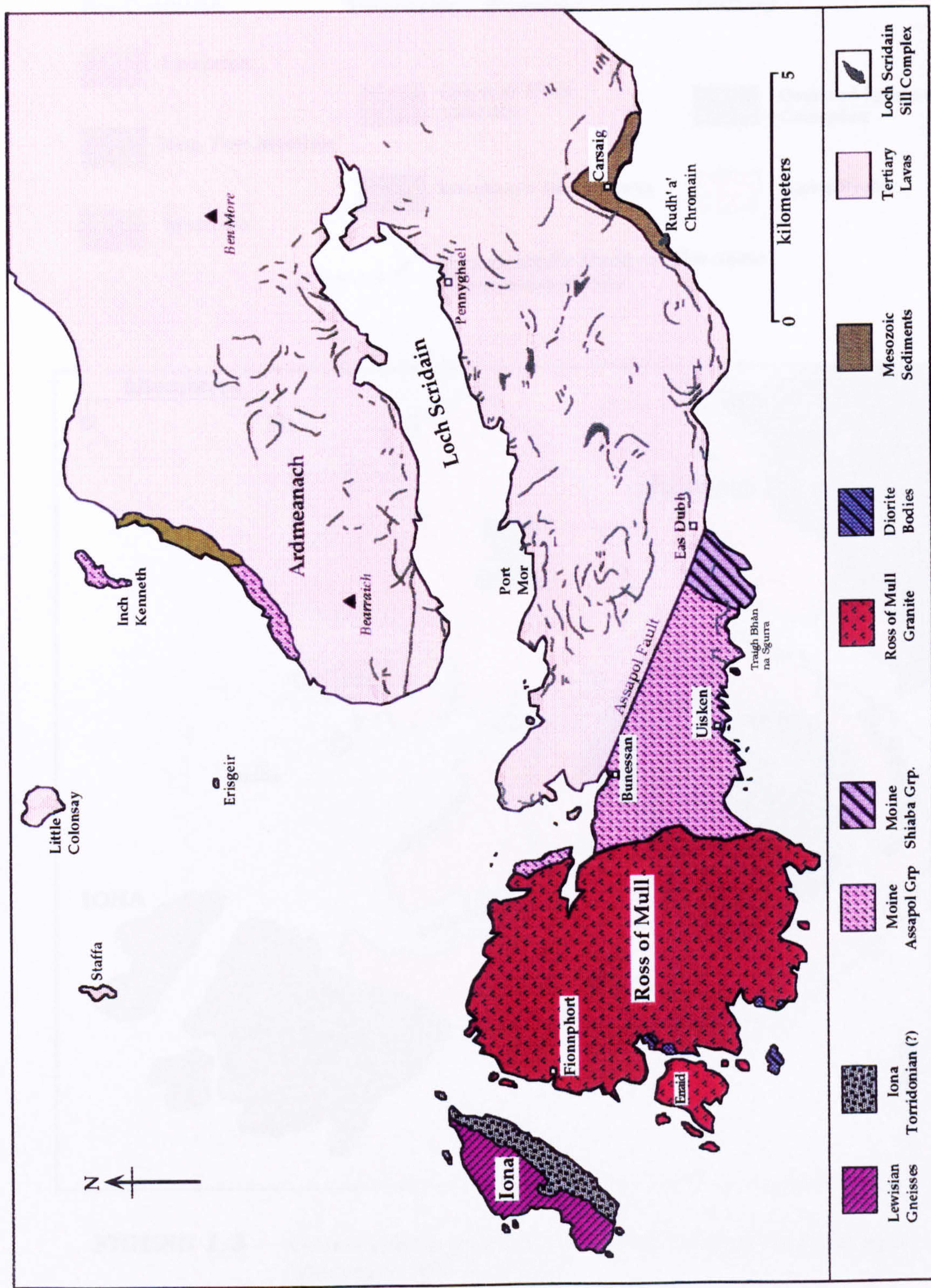


FIGURE 1.2 Geology of the Ross of Mull, showing the major lithological divisions in the area studied. Number of the LSSC shown is greatly reduced for clarity. Modified from Bailey *et al.* (1922) and Kille (1987).

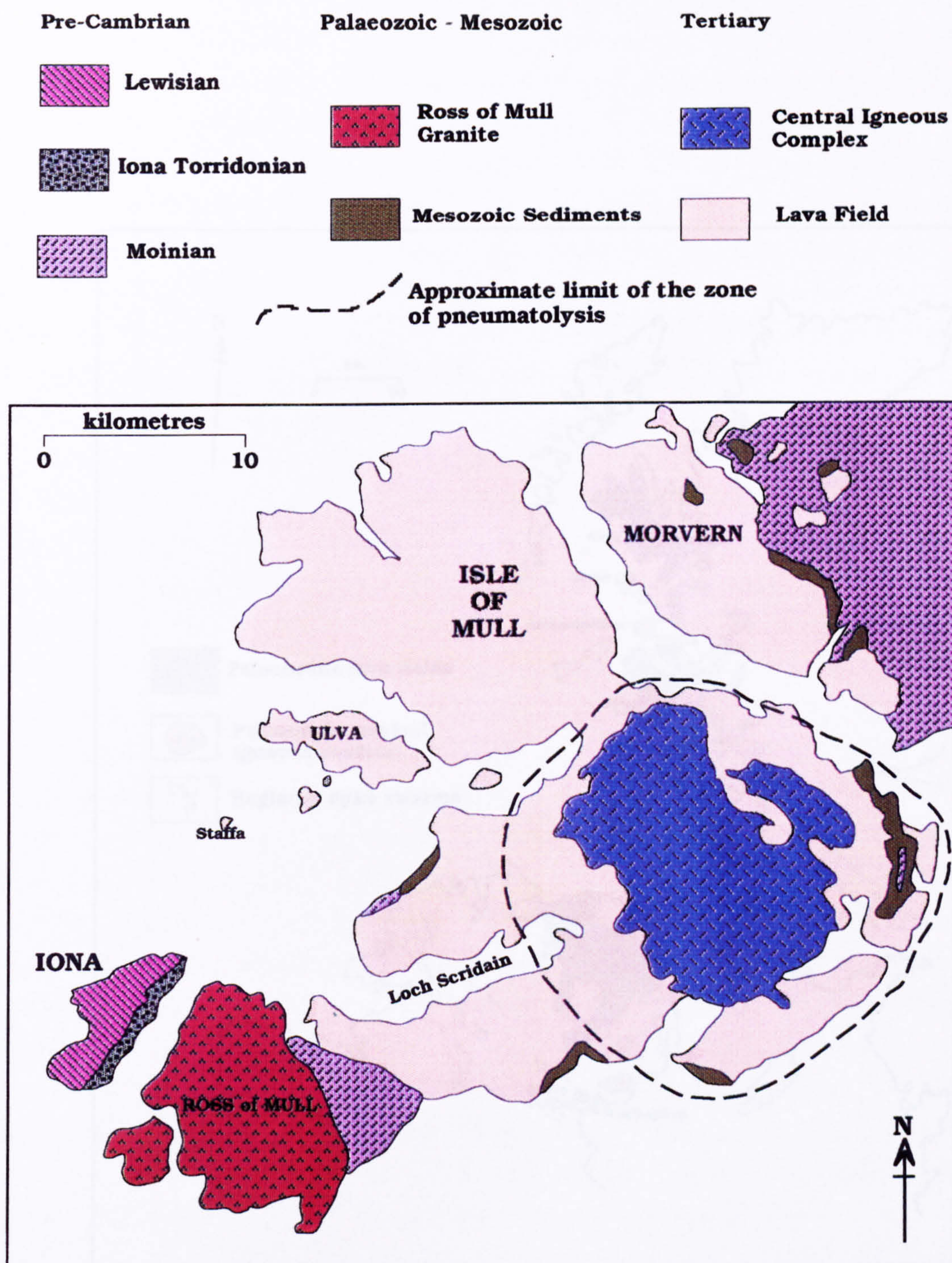


FIGURE 1.3 Generalised geological map of the Isle of Mull and Morvern, NW Scotland.

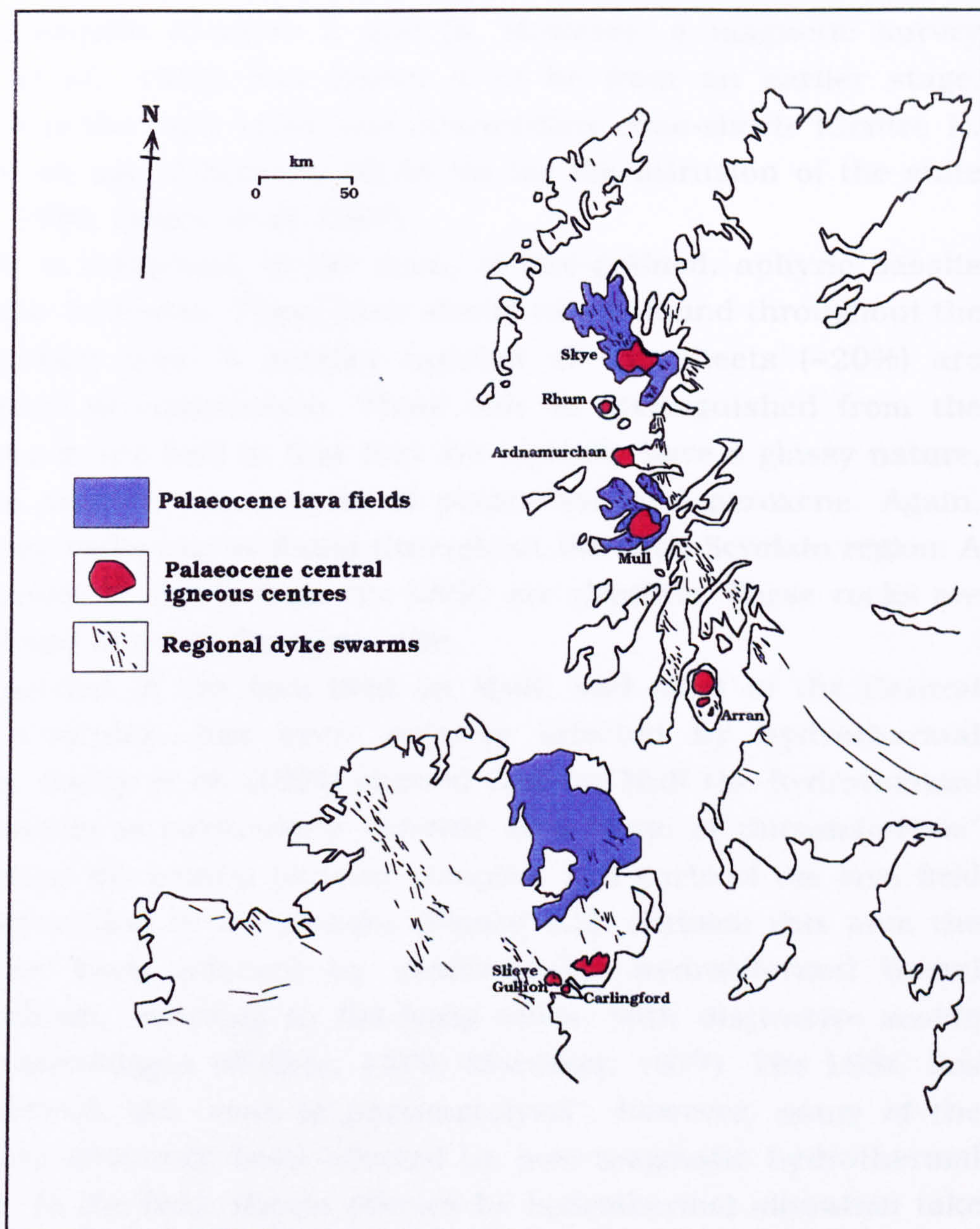


FIGURE 1.4 Map of the Palaeocene lava fields, central igneous complexes and associated dyke swarms of the British Tertiary Volcanic Province. (Modified from Sutherland, 1976)

in a north-westerly direction. As in Skye, a large mass of basic material is inferred from gravity and magnetic surveys to underlie the Mull Central Igneous Complex. The volume of these gabbroic and ultrabasic rocks may be of the order of 3500km³ (Bott & Tantrigoda, 1987).

Bailey *et al.* (1924) suggested that the LSSC was intruded contemporaneously with the late basic cone-sheets of Allt Molach-Beinn Chàisgidle (Centres 2 and 3). However, a magnetic survey (Dagley *et al.*, 1987) has shown it to be from an earlier stage, equivalent to the early silicic and intermediate cone-sheets (Centre 1). This puts an age of between 60-58 Ma for the intrusion of the suite (Musset, 1986; Dagley *et al.*, 1987).

The LSSC is composed, in the main, of fine-grained, aphyric basalts and basaltic andesites. These basic sheets can be found throughout the Loch Scridain area. A smaller number of the sheets (~20%) are intermediate in composition. These can be distinguished from the basic rocks in the field in that they are typically have a glassy nature, and often contain phenocrysts of plagioclase and pyroxene. Again, these glassy rocks can be found throughout the Loch Scridain region. A small number of sheets from the LSSC are rhyolitic. These rocks are light-grey and of a very fine grain size.

A large portion of the lava field on Mull, and most of the Central Igneous Complex, has been severely affected by hydrothermal alteration. Bailey *et al.* (1924) showed that on Mull the hydrothermal metamorphism is particularly extreme in a "zone of pneumatolysis" incorporating the central plutonic complex, and parts of the lava field within about 5km of the plutons (*Figure 1.3*). Outside this area the lavas have been affected by zeolite-facies hydrothermal burial metamorphism, resulting in flat-lying zones, with distinctive zeolite mineral assemblages (Walker, 1970; Morrison, 1977). The LSSC lies mainly outwith the "zone of pneumatolysis", however, many of the sheets have obviously been affected by post-magmatic hydrothermal alteration. In the field, sheets affected by hydrothermal alteration take on a distinctive green colour due to the growth of secondary chlorite. Such sheets are obviously of no use when trying to examine the magmatic history of a suite of rocks, and consequently have not been included in the sampling.

Members of the LSSC show great variation in thickness, from mere centimetres, up to about 14m; however, most sheets vary between 0.5m and 6m (*Figure 1.5*). There were several phases of intrusion,

with cross-cutting relationships between two or more sheets being relatively common (*e.g.* Sgeir an Fhéidh [NM 504262])

Most sheets are gently inclined and discordant to the bedding of the lava field. Unlike the cone-sheets, however, they show no tendency to dip towards a central focal-point, indeed dip directions and degree of dip are highly variable (5-60°). Kille (1987) provided evidence for flow direction within a small number of the sheets, suggesting that the magma source for the LSSC was the Central Igneous Complex at the centre of the island. Bott & Tandrigoda (1987) have shown that a large body of concealed basic igneous rock is located beneath the Mull Central Igneous Complex.

The large majority of the sheets have well developed chilled margins of several cm thickness (*Figure 1.6*). However, some individual sheets exhibit a local tendency not to chill at one or both margins. This may be attributed to turbulent flow within the conduit (Huppert & Sparks, 1989). Where the magma has failed to chill, contact metamorphic effects are occasionally evident, particularly in those sheets which invade the Moine metasedimentary, and Mesozoic sedimentary sequences (see Chapter 10).

A small number of sheets are composite in nature. That at Rudh' a' Chromain (NM 523202) consists of a central portion of rhyolite some 10m thick. The upper and lower portions are both of tholeiitic basalt, approximately 1m thick, and are markedly xenolithic. The dolerite is chilled against an earlier monzonite intrusion (bostonite; Bailey *et al.*, 1924), and Jurassic sandstones. The contacts between the rhyolite and the basaltic portions are unchilled, there being broad zones of hybridization. This implies the earlier intrusion of the basic magma was followed by the rhyolitic magma while the basalt was still reasonably hot (see Chapter 6 for further discussion). In places the intermediate sheets have margins of holocrystalline dolerite, the boundaries generally being very sharp (*Figure 1.7*). Composite sheets of this nature can be found throughout the region. Basaltic sheets also contain lenses and unmixed 'strings' of dacite (*e.g.* Killunaig [NM 495258]).

Early workers (Thomas, 1922; Bailey *et al.*, 1924) were struck by the number of sheets in the Loch Scridain district which carried abundant crustal xenoliths. It was this characteristic which partly contributed to the sheets being recognised as one co-magmatic suite, and was the main criteria used when sampling. The xenoliths occur dominantly in



FIGURE 1.5

A thick basaltic sheet at Traigh Bhàn na Sgurra [NM 423185]. Sheet is some 8m thick, and is intruded into Moinian metasediments. Moine lithologies consist of bands of pelitic schist and quartzite. At the top of the sheet are two lenses which contain numerous crustal xenoliths derived from the local lithologies.



FIGURE 1.6

Chilled margin of the basaltic facies of the composite basalt-rhyolite sheet at Rudh' a' Chromain [NM 521202], against the Jurassic Carsaig sandstone (bottom). Hand lens approx. 5cm long.



FIGURE 1.7

Composite sheet at Kilfinichen Bay [NM 484280]. Sheet consists of a basaltic portion (B) and a glassy centre of dacite (D). Basaltic facies contains numerous xenoliths of crustal origin, along with cumulate gabbroic xenoliths. Hammer shaft is approximately 1m long.

the holocrystalline basaltic and basaltic andesite members of the suite, although a few of the glassy intermediate sheets do contain a few small inclusions. The crustal xenoliths fall into two broad categories, which can be further subdivided on the basis of mineralogy:-

(a) Quartz-rich xenoliths

- (i) Sandstones.
- (ii) Conglomerate.
- (iii) Pure quartzites.
- (iv) Schistose rocks.
- (v) Granite-like rocks.

(b) Aluminous xenoliths

- (i) Mullite buchites.
- (ii) Cordierite buchites.
- (iii) Mullite buchite-plagioclase-spinel-corundum rocks

These xenoliths occur in sheets throughout the whole region. They occur as isolated blocks, or in xenolith-rich pods and lenses, always at the top of the sheets. Quartz-rich and aluminous xenoliths occur together, and generally in equal proportions. Individual xenoliths are typically no more than a few tens of centimetres across, although large rafts of aluminous material several metres in length have been found. Bailey *et al.* (1924) also described a limited number of sheets which contained small xenoliths of graphite. However, this study did not find specimens of graphite xenoliths. The occurrence of graphite however, may potentially have an important control over the oxidation state of the magmas (*cf.* Pedersen, 1978, 1979, 1981). A comprehensive mineralogical and geochemical study of the crustal xenoliths and how they may have interacted with the basic magmas of the LSSC is presented in Chapters 9 and 10. The LSSC also contains xenoliths of coarse grained gabbroic rocks. These are described in detail in Chapter 7.

Although the LSSC has been studied before (Bailey *et al.*, 1924; Kille, 1987), this study provides new geochemical data (major-element, trace-element and Sr-Nd isotope data) from both the sheets and their crustal and gabbroic xenoliths, which sheds some light on the importance of magma/crust interactions in this tectonically and magmatically complex region.

CHAPTER 2

PETROGRAPHY AND MINERAL CHEMISTRY

2.1 Introduction

During the initial mapping of the island, Bailey *et al.* (1924) coined numerous terms to sub-divide the basic, intermediate and silicic rocks, mainly on the basis of field and thin-section characteristics. The LSSC was no exception, with no less than six subdivisions being erected. The tholeiitic basic rocks found as dykes and sills within the area were split into 3 groups on the basis of petrography:-

Talaidh Type - Olivine scarce or absent, often with elongate, feathery augite crystals.

Brunton Type - Olivine-free, with sub-ophitic relationship between augite and plagioclase. Often has abundant mesostasis.

Salen Type - Essential olivine, with sub-ophitic relationship between augite and plagioclase. Amount of mesostasis is reduced.

The intermediate rocks of the LSSC were split into two groups :-

Leidleites - Olivine-free, plagioclase-augite rocks, often with greatly elongate augite crystals, similar to the Talaidh Type. Glassy mesostasis is often abundant.

Inninmorite - Finely-crystalline or completely glassy rocks, containing numerous phenocrysts of basic plagioclase and pigeonite ("uniaxial augite"; Hallimond, 1914).

The siliceous rocks were all grouped together, and mainly described as felsites.

In the field, it is very often difficult to tell the basic types apart due to their very fine-grain, and almost impossible to separate the basic rocks, from the non-glassy, aphyric intermediate rocks (leidleites). In thin-section, the different types suggested by Bailey *et al.*, (1924) also tend to grade into each other, with a variety of textures being present within individual samples, on the thin-section scale. In the field there

is no spatial distribution of the various rock types, with sheets of all types being found throughout the area.

For the purpose of clarifying the terminology used in this report it is necessary to subdivide the members of the LSSC into three major rock groups. This has been done on the basis of whole-rock geochemistry rather than petrography:-

- | | | |
|-----------|---|--|
| Group I | - | Tholeiitic basalts and basaltic andesites |
| Group II | - | Tholeiitic andesites and porphyritic dacites |
| Group III | - | Rhyolites |

This sub-division is based on the plot of Wt% TiO_2 *vs.* Mg\# ($=\text{MgO}/(\text{MgO} + \text{Fe}_2\text{O}_3^*)$) which shows three distinct lineages (*Figure 2.1*). This division also corresponds broadly to that used by Cox *et al.* (1979) and Le Bas *et al.* (1986) which utilises the total-alkalis *vs.* silica diagram to classify volcanic rocks (see *Figure 2.2*).

Rocks of Group I are all holocrystalline and generally phenocryst poor (< 1 vol.%), although most thin-sections will yield at least a few small phenocrysts of plagioclase. Group I is dominated by basaltic andesites. Group II can be split into rocks similar in degree of crystallinity to the basalts and basaltic andesites of Group I but with a more continuous glassy groundmass, and rocks which are both wholly glassy and contain phenocrysts of plagioclase and pyroxene. Rocks of dacitic composition make up the bulk of Group II. Group III rocks (rhyolites) are very distinctive fine-grained, grey rocks which contain the occasional phenocryst of plagioclase.

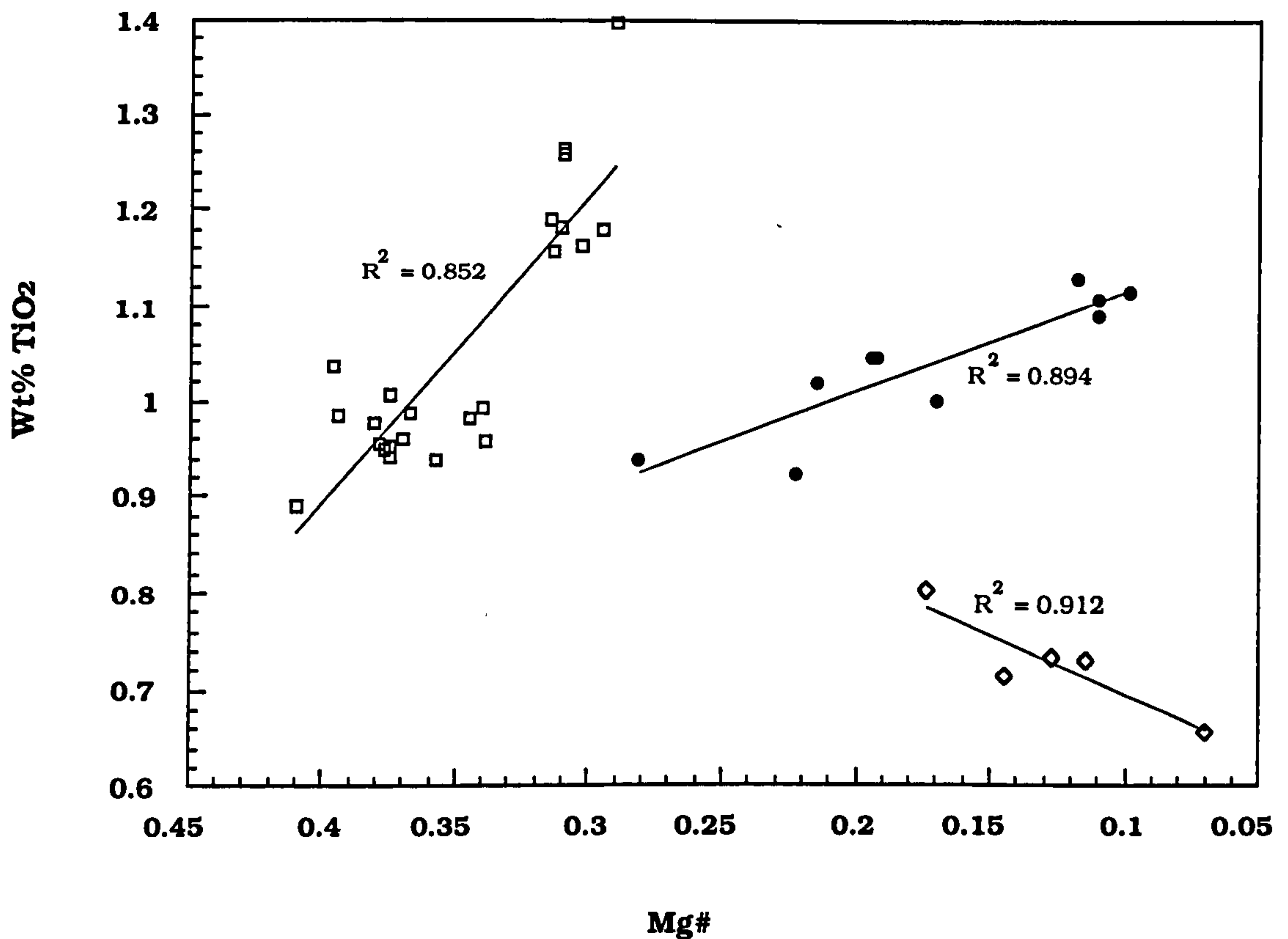


FIGURE 2.1 Plot of Wt% TiO₂ vs. Mg# (defined as Wt% MgO/(MgO+Fe₂O₃*)) for all LSSC magmas. Diagram divides the magmas into three definite groups, which correspond approximately to petrographic differences, and their classification in the Total alkalis - silica diagram (LeBas *et al.*, 1986).

The groups are defined as follows :-

Group I = Aphyric basalts and basaltic andesites (□)

Group II = Aphyric andesites, and porphyritic dacites (●)

Group III = Aphyric and porphyritic rhyolites (◇)

All variation diagrams will use this grouping and the symbols defined here.

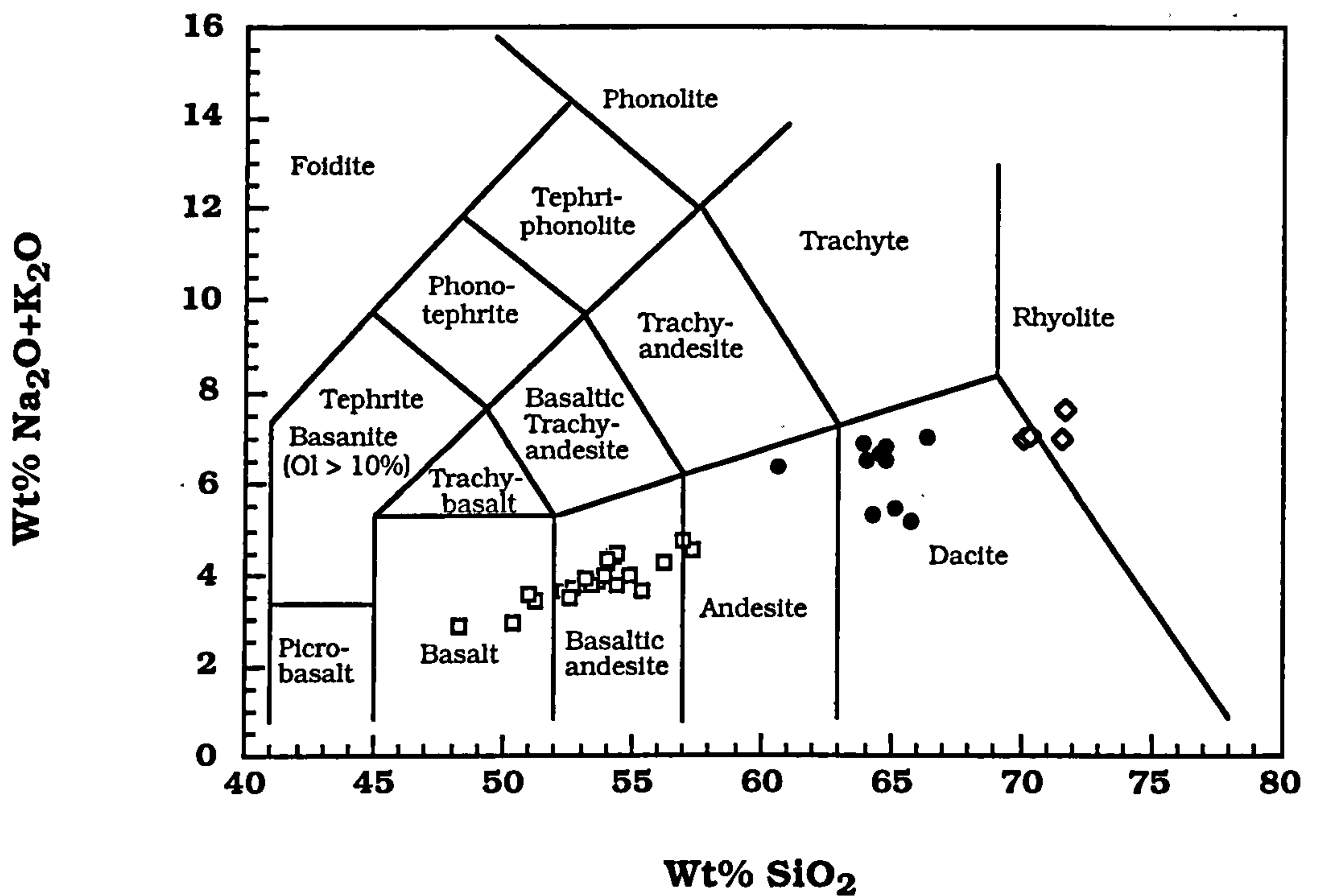


FIGURE 2.2 Total alkalis (Wt% Na₂O + K₂O) vs. Wt% SiO₂ for the classification of volcanic rocks (after LeBas *et al.*, 1986). The Loch Scridain magmas fall into three distinct groups, as defined below :-

- Group I - Basalts and Basaltic andesites
- Group II - Porphyritic dacites and aphyric andesite/dacite
- ◇ Group III - Rhyolites

2.2 Detailed Petrography and Mineral Chemistry

Group I : Tholeiitic basalts and basaltic andesites

Rocks of Group I make up the bulk of the LSSC. The tholeiites of the LSSC are olivine-poor or olivine-free, plagioclase-augite rocks, and are generally devoid of phenocrysts (< 1 vol.%). There are two distinct textural varieties:

- (i) Sub-ophitic to ophitic texture
- (ii) Dendritic and variolitic textures, sometimes with weak flow alignment

Within individual thin sections both crystal textures can be present, which would suggest very uneven cooling of the magma on a small scale. Minor interstitial glass is common in rocks of Group I. It is occasionally very fresh, but, as a rule, it is highly altered to a fine-grained chloritic material. Typical crystal structures of Group I rocks are shown in *Figures 2.3a-b*.

Plagioclase

In thin section, plagioclase forms narrow, acicular crystals up to about 1mm in length, often with sharp or 'swallow tail' terminations. It also builds short stubby laths within ophitic-textured rocks. In rocks of a more glassy nature with predominant dendritic and variolitic textures, the plagioclase forms narrow laths and needles with ill-defined edges and ends. Skeletal growth forms are common. The groundmass crystals invariably show a slight normal zoning and are generally simply twinned. These rocks also contain the occasional microphenocryst of plagioclase up to 2mm in length. Where present, they are either euhedral, or show highly irregular, resorbed crystal outlines. Euhedral crystals are more common than the resorbed type. Both types display polysynthetic twinning and often show well-developed oscillatory zoning. These crystals also occur in glomeroporphyritic clots. Representative analyses of groundmass and phenocryst plagioclase are presented in *Table 2.1*. The groundmass crystals show a typical compositional range from core to rim of An₆₆ to An₅₆.

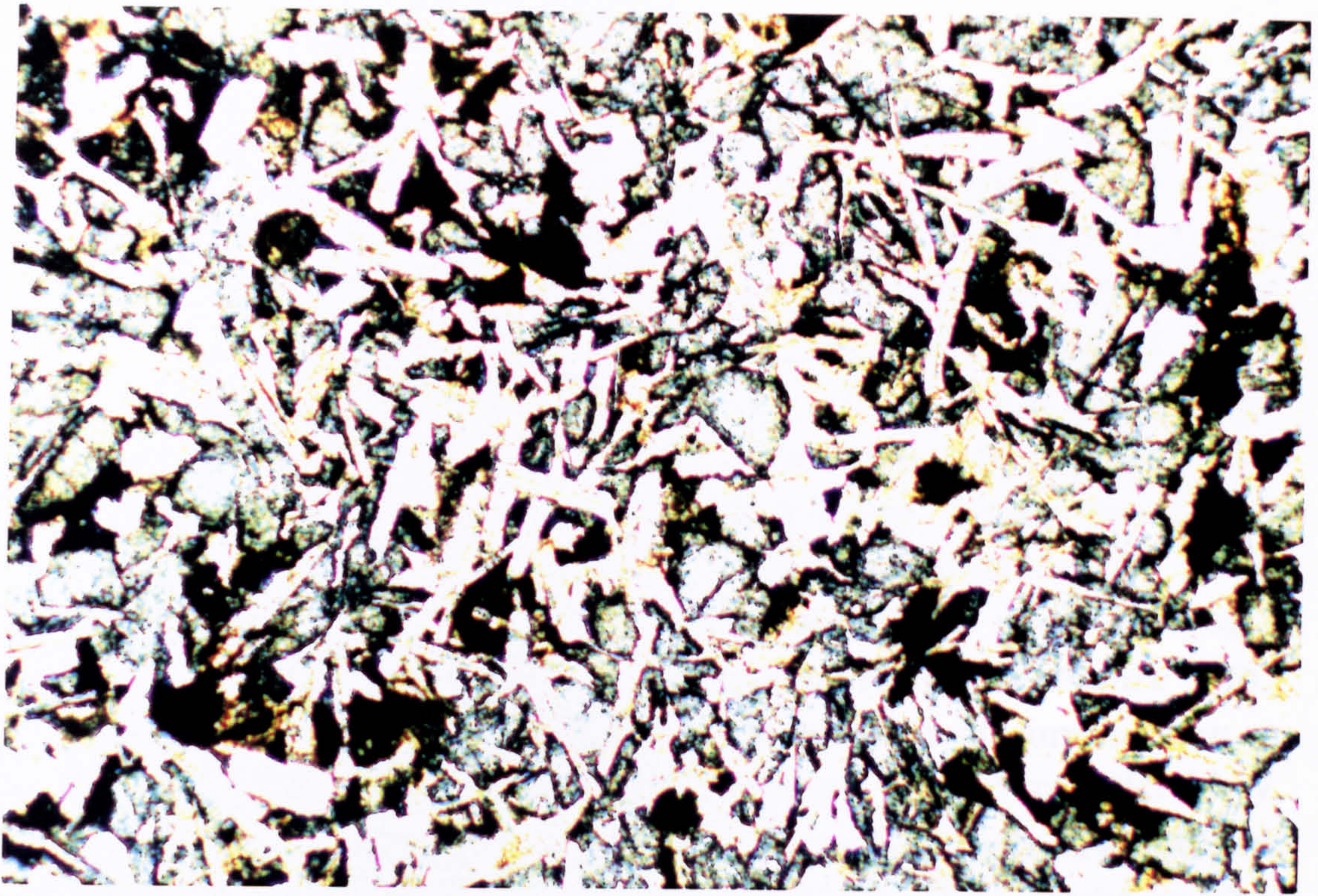


FIGURE 2.3a

Sub-ophitic texture in a Group I basalt, between plagioclase laths and clinopyroxene. Magnetite forms ragged octahedra evenly distributed through the rock. (ppl; Field of view 2x3mm; Sample KBHXY4)

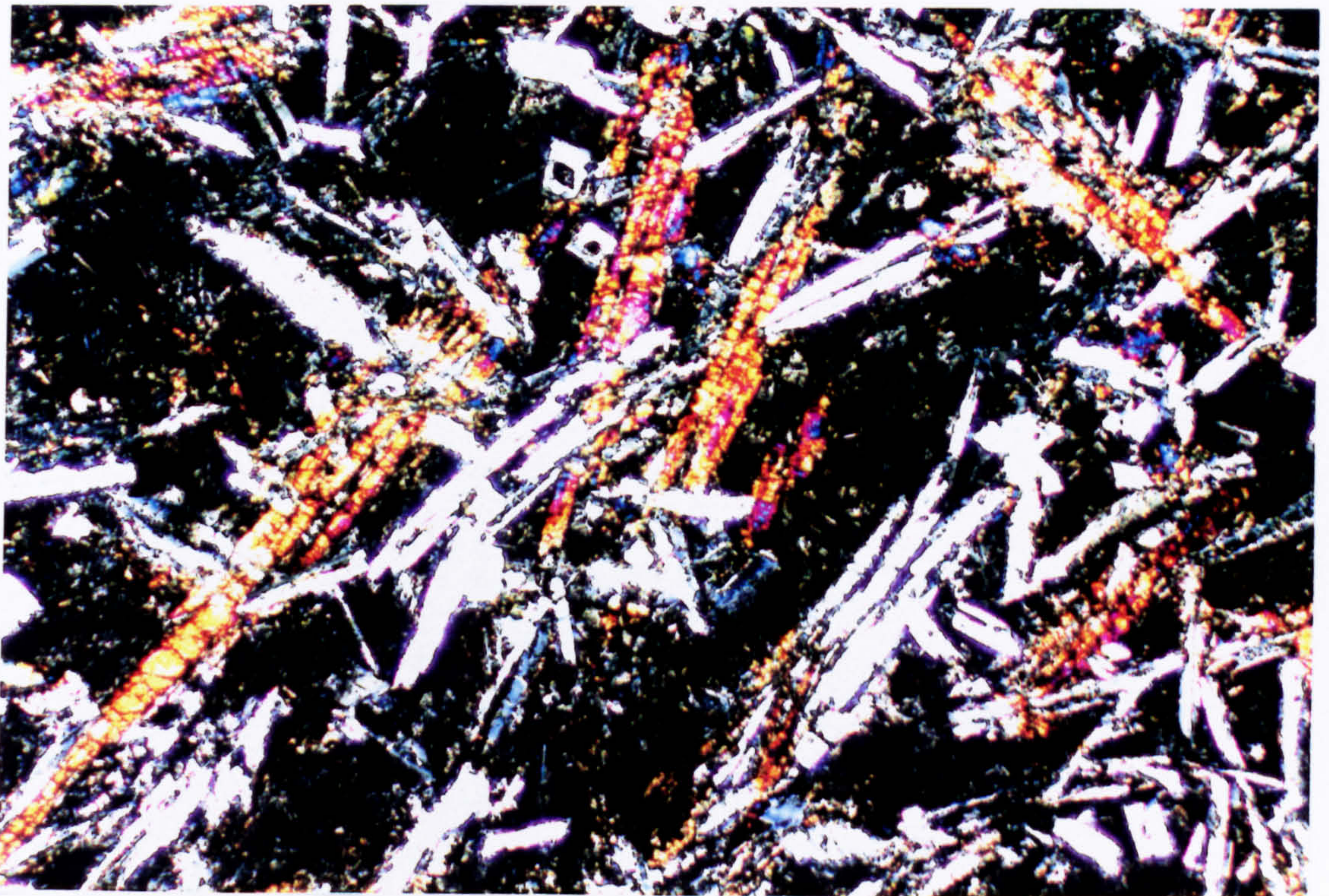


FIGURE 2.3b

Group I basaltic andesite displaying dendritic growth of clinopyroxene. Plagioclase forms narrow needles and hollow "hopper" crystals. Interstitial glass has devitrified to give an intergrowth of K-feldspar and quartz. Structure is indicative of rapid crystallization histories. (xpl; Field of view 2x3mm; Sample ARB1).

Microphenocryst compositions are strongly bimodal (see *Figure 2.4*). The most common microphenocryst composition is similar to that of the groundmass crystals. These display euhedral, lath-shaped crystals (see *Figure 2.5a*), and although they display oscillatory zoning, the compositional range is not large. These crystals are considered to be 'phenocrysts' in the strict sense of the term. The second population show more strongly resorbed crystal edges and cloudy interiors (*Figure 2.5b*). They are more calcic, and have better developed oscillatory zoning. Crystal cores generally have a composition of $\sim \text{An}_{80}$ - An_{82} , which then ranges down to $\sim \text{An}_{70}$ towards the rims, although calcic 'spikes' are common towards the crystal rims (see *Figure 2.6*). These crystals often have an equilibrium overgrowth of composition $\sim \text{An}_{50}$ - An_{60} . These calcic crystals may therefore be xenocrystic. They may be 'cognate' in that they represent crystals which crystallized earlier in the host magma's history. Alternatively, they could be the phenocrysts from a more basic, but unrelated, magma that was involved in some form of mixing event.

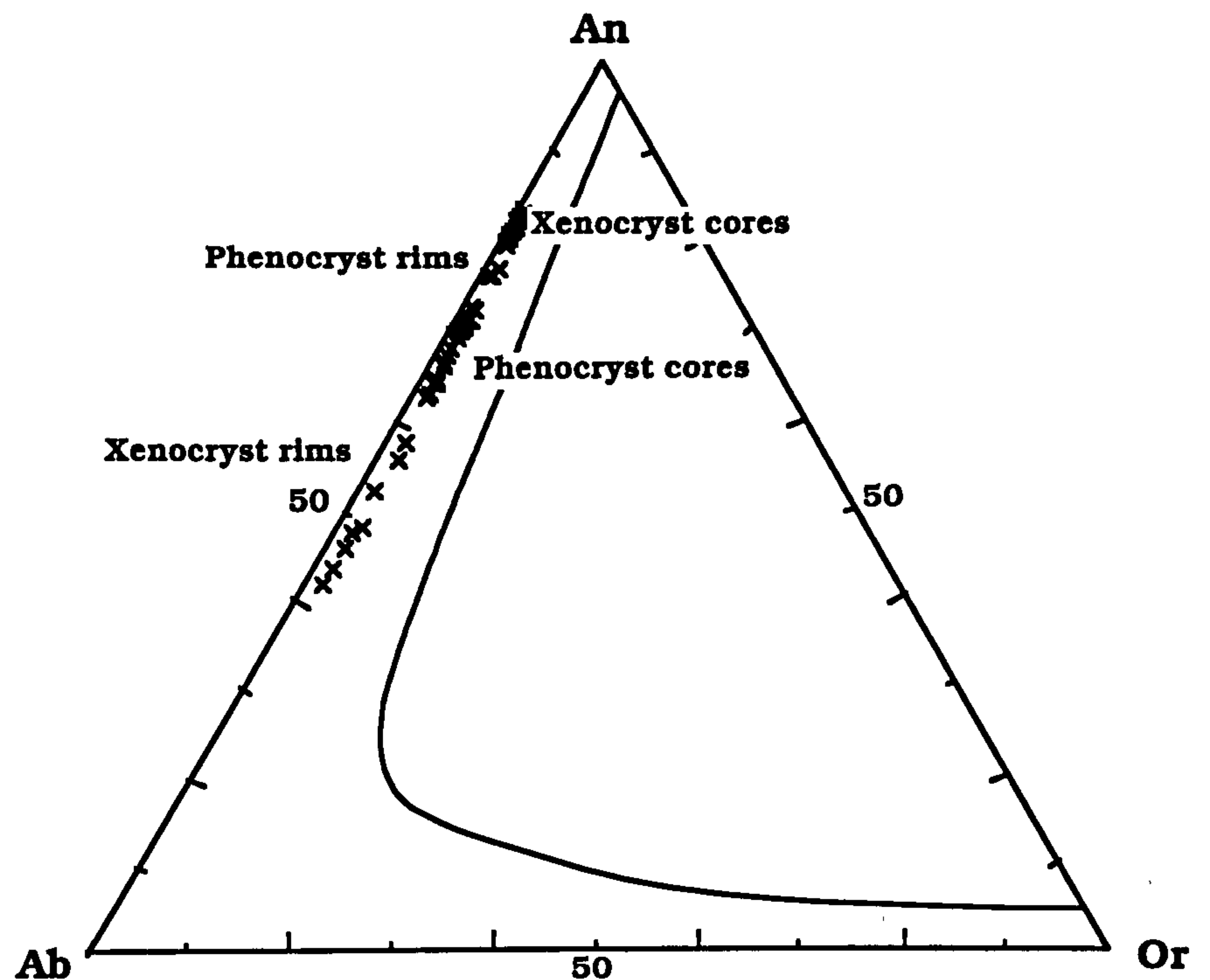


FIGURE 2.4 Plagioclase phenocryst and xenocryst compositions in the ternary Anorthite-Albite-Orthoclase projection at 2kbar water pressure (after Tuttle & Bowen, 1958). Core compositions are strongly bi-modal, suggesting that mixing between evolved and less-evolved Group I magmas occurred. Part of the spread in the core composition data is due to normal and oscillatory zoning within the plagioclase crystals. Rim compositions were taken from obvious overgrowths.



FIGURE 2.5a

Euhedral plagioclase phenocryst (An₆₀) in a Group I basalt. Groundmass consists of plagioclase laths with sub-ophitic augite. Augite is altered to chlorite in places. (xpl, Field of view 0.8x1.2mm; Sample PMBASE).

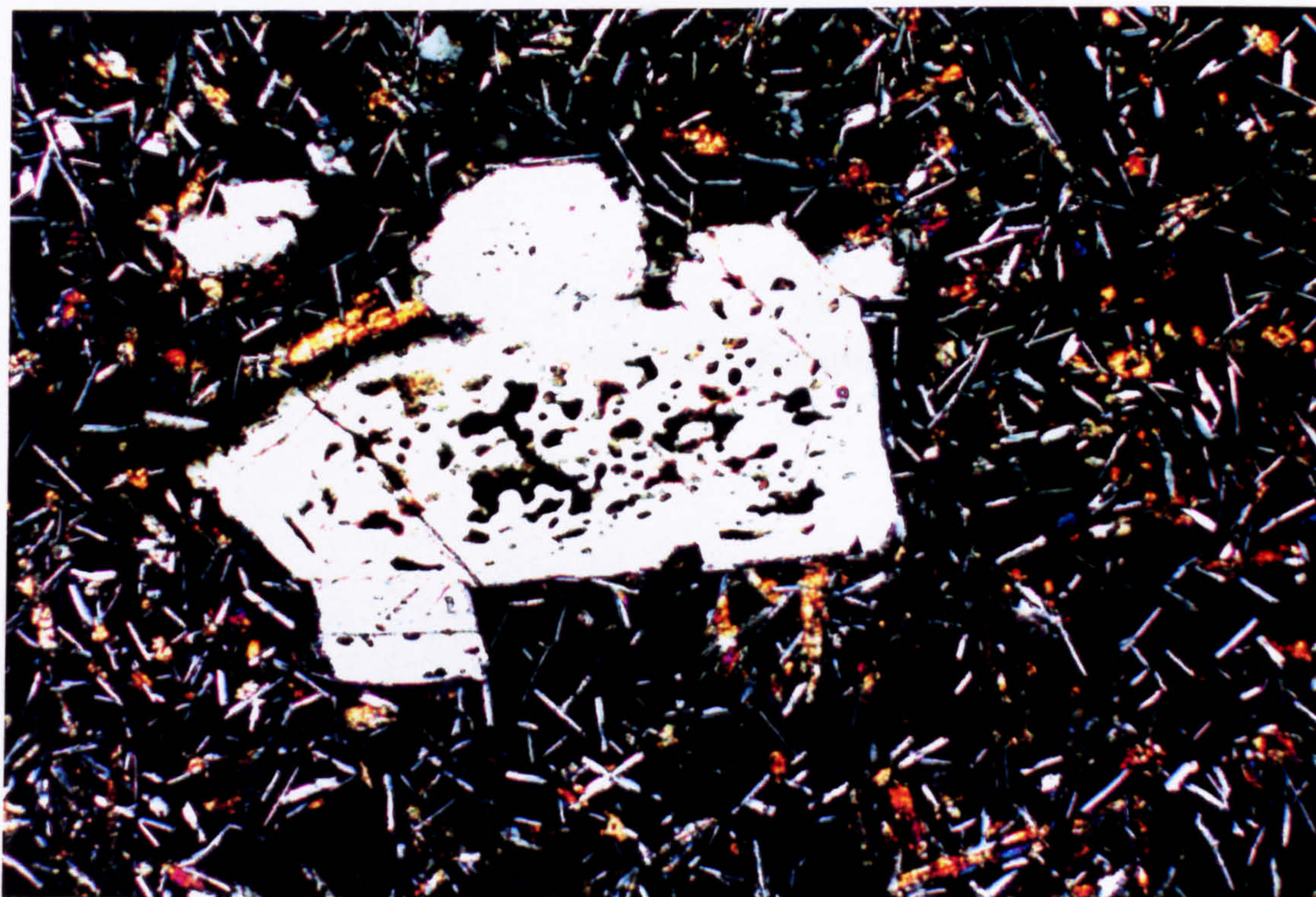


FIGURE 2.5b

Plagioclase xenocryst (An₈₀) in Group I basaltic andesite. Xenocrysts are typically highly resorbed and full of glass inclusions. Matrix consists of needles of plagioclase and grains of augite set in fresh glass(xpl; Field of view 2x3mm; Sample SFB2).

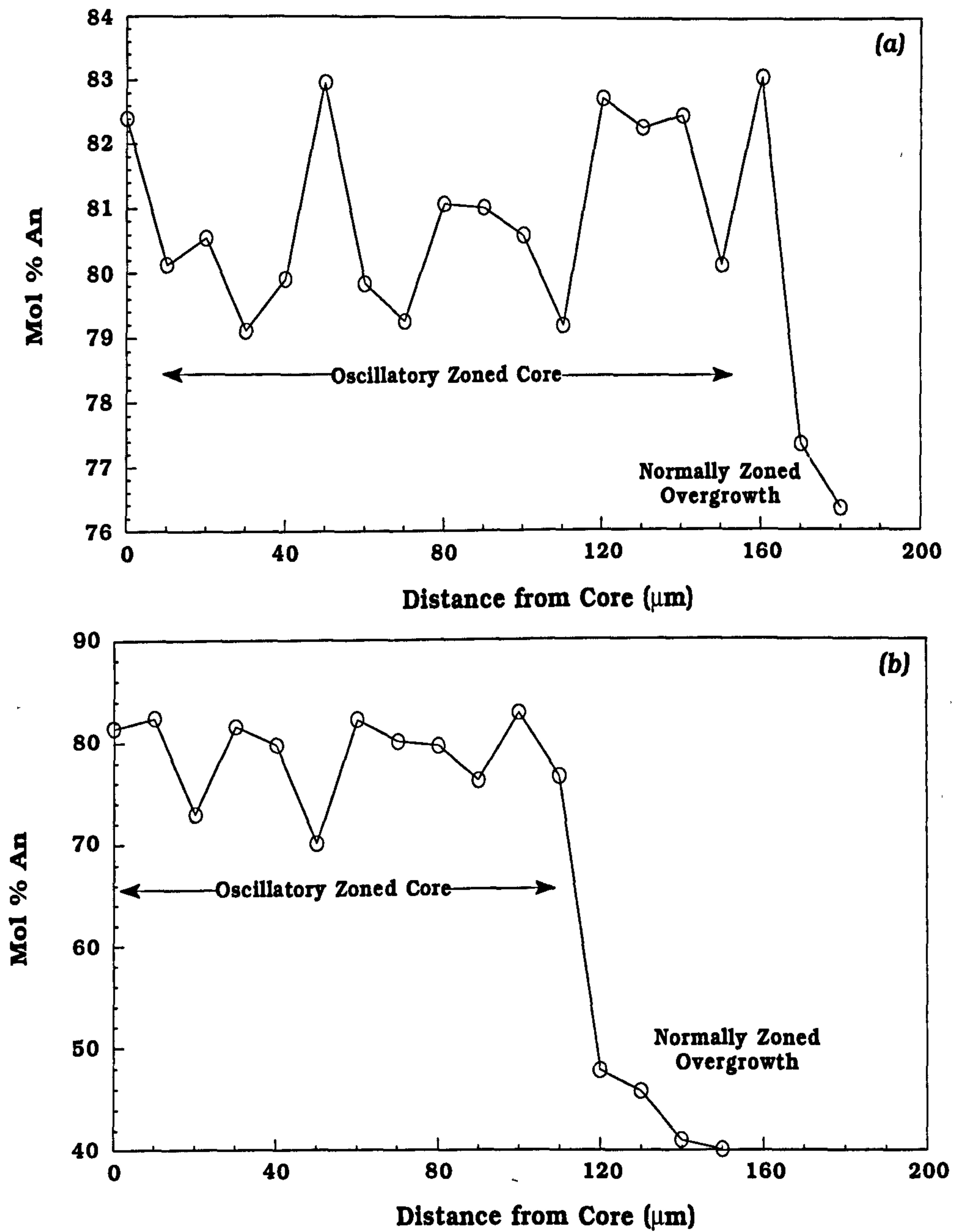


FIGURE 2.6 Zoning profiles in plagioclase xenocrysts from Group I rocks. Profile (a) is from specimen TILE1 and Profile (b) is from PMBASE. Profiles show well defined complex oscillatory zoning at the crystal cores, with a normally zoned overgrowth.

SAMPLE	PGB9		KIB1				ARB1		PM +200
TYPE	G	G	G core	G rim	P core	P rim	G core	G rim	G
SiO ₂	49.39	49.49	49.44	52.26	49.23	49.98	50.61	53.20	50.26
TiO ₂	0.00	0.05	0.03	0.14	0.01	0.08	0.08	0.06	0.00
Al ₂ O ₃	32.02	31.73	31.18	29.44	32.51	31.33	31.29	29.64	30.34
FeO*	0.80	1.18	0.90	1.17	0.62	0.95	0.73	0.95	2.17
CaO	13.54	13.12	13.14	10.66	13.97	12.91	12.86	10.37	12.67
Na ₂ O	3.69	3.69	3.85	5.13	3.32	4.05	4.01	5.06	3.69
K ₂ O	0.19	0.28	0.19	0.37	0.17	0.25	0.39	0.55	0.24
TOTAL	99.64	99.53	98.73	99.15	99.82	99.55	99.96	99.83	99.37
FORMULA ON BASIS OF 32 OXYGENS									
Si	9.07	9.11	9.16	9.59	9.02	9.18	9.25	9.67	9.28
Ti	0.00	0.01	0.00	0.02	0.00	0.01	0.01	0.01	0.00
Al	6.93	6.88	6.81	6.37	7.02	6.78	6.74	6.35	6.60
Fe (ii)	0.12	0.18	0.14	0.18	0.10	0.15	0.11	0.14	0.34
Ca	2.66	2.59	2.61	2.10	2.74	2.54	2.52	2.02	2.51
Na	1.32	1.32	1.38	1.83	1.18	1.44	1.42	1.78	1.32
K	0.04	0.07	0.05	0.09	0.04	0.06	0.09	0.13	0.06
TOTAL	20.14	20.14	20.15	20.16	20.09	20.17	20.13	20.10	20.11
ENDMEMBER %									
Ab	32.69	33.19	34.23	45.57	29.77	35.66	35.24	45.34	34.02
Or	1.08	1.64	1.12	2.13	1.02	1.46	2.27	3.27	1.45
An	66.23	65.17	64.65	52.30	69.20	62.89	62.50	51.39	64.53

Table 2.1 Representative analyses of plagioclases from Group I sheets. G=Groundmass; P=Phenocryst; X=xenocryst. All analyses crystal cores unless otherwise stated. Sample Numbers defined in Appendix II.

SAMPLE					TILE1				
PMBASE									
TYPE	P core	P rim	G core	G rim	P core	P rim	X core	X rim	G
SiO ₂	51.96	51.97	52.62	52.23	48.05	51.88	46.06	49.38	49.38
TiO ₂	0.06	0.01	0.03	0.00	0.09	0.02	0.00	0.06	0.13
Al ₂ O ₃	30.61	29.96	29.59	29.92	33.44	30.01	34.84	31.49	31.72
FeO*	0.43	1.01	1.20	0.88	0.45	1.17	0.43	0.83	1.13
CaO	11.42	11.40	10.99	11.30	14.48	11.34	16.41	13.48	13.57
Na ₂ O	4.43	4.52	4.88	4.72	3.09	4.74	2.16	3.68	3.67
K ₂ O	0.41	0.31	0.42	0.30	0.23	0.36	0.04	0.19	0.14
TOTAL	99.33	99.17	99.72	99.35	99.83	99.51	99.94	99.11	99.74
FORMULA ON BASIS OF 32 OXYGENS									
Si	9.49	9.53	9.60	9.56	8.82	9.50	8.48	9.12	9.07
Ti	0.01	0.00	0.00	0.00	0.01	0.00	0.00	0.01	0.02
Al	6.59	6.47	6.36	6.44	7.23	6.48	7.56	6.85	6.87
Fe (ii)	0.07	0.16	0.18	0.13	0.07	0.18	0.07	0.13	0.17
Ca	2.23	2.24	2.15	2.21	2.85	2.22	3.24	2.67	2.67
Na	1.57	1.61	1.73	1.67	1.10	1.68	0.77	1.32	1.31
K	0.10	0.07	0.10	0.07	0.05	0.08	0.01	0.04	0.03
TOTAL	20.05	20.07	20.12	20.09	20.13	20.14	20.13	20.13	20.25
ENDMEMBER %									
Ab	40.23	41.01	43.45	42.29	27.51	42.16	19.22	32.72	32.59
Or	2.50	1.83	2.46	1.76	1.34	2.09	0.23	1.09	0.80
An	57.27	57.17	54.09	55.95	71.16	55.75	80.55	66.19	66.61

Table 2.1cont. Representative analyses of plagioclases from Group I sheets. G=Groundmass; P=Phenocryst; X=xenocryst. All analyses crystal cores unless otherwise stated. Sample Numbers defined in Appendix II.

Clinopyroxene

The clinopyroxene (augite) is a colourless to pale yellow, non-pleochroic variety and occurs either as ophitic plates surrounding the plagioclase, isolated grains, or greatly elongated feathery crystals up to 3mm in length. Plagioclase and pyroxene needles are sometimes arranged in radiating clusters or sheath-like aggregates producing a variolitic structure. Pyroxene has not been identified as a phenocryst phase in Group I. The pyroxene is typically very fresh, but is occasionally altered to chlorite, or possesses a haematite staining.

Electron-probe micro-analyses of groundmass clinopyroxenes from Group I are presented in *Table 2.2*. From these data it is evident that there is not only a wide range in composition between the basic and more evolved members of Group I, but also within individual crystals. Most groundmass crystals have a compositional gradient from core to rim. This zoning normally involves an enrichment in total iron, and a depletion in magnesium, a change typical of fractionating tholeiitic magmas. For example, one crystal analysed from sample PMFX1 shows a 100% increase in the ferrosilite component from core to rim ($\text{Wo}_{38}\text{En}_{50}\text{Fs}_{12}$ - $\text{Wo}_{34}\text{En}_{42}\text{Fs}_{24}$). However, most zoning ranges are generally not so extreme. The compositions of all Group I pyroxenes are illustrated on diagrams such as *Figure 2.7a*, the pyroxene quadrilateral, which plots compositions in terms of the three end-member pyroxenes wollastonite, enstatite and ferrosilite. Data for Group II rocks are also presented for comparison, and will be discussed later. Also shown on these diagrams are: the fractionation trends from a typical tholeiitic magma body (the Skaergaard Intrusion, east Greenland; Wager & Brown, 1968); the alkalic fractionation trend of the Shiant Isles Sill, Inner Hebrides (Gibb, 1973), and the fields occupied by pyroxenes from the Skye Main Lava series (*Figure 2.7a*), and the Preshal More basalt magma types (Bell *et al.*, 1994) (*Figure 2.7b*). As *Figure 2.7b* shows, the pyroxenes from the Group I rocks occupy a similar region in the quadrilateral to those of the other BTVP magma types. However, there is a tendency towards more Mg-rich compositions. The Group I groundmass augites comprise an ill-defined scatter within the pyroxene quadrilateral rather than a regular trend. This may be due either to local small-scale variations in melt composition, or to disequilibrium crystal-liquid partitioning (Smith & Lindsley, 1971.) Similar 'quench' variations in groundmass

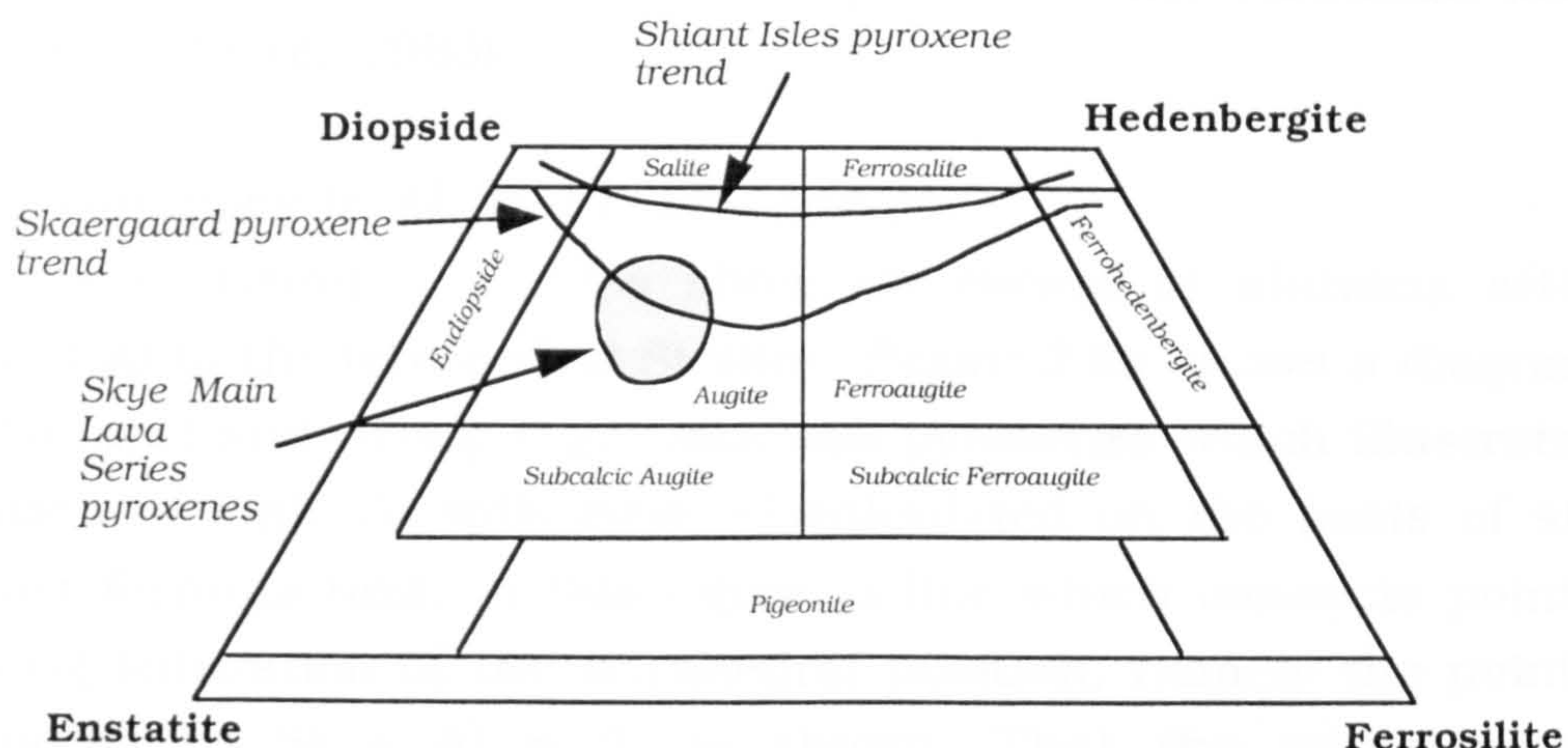


FIGURE 2.7a Pyroxene nomenclature in the pyroxene quadrilateral (After Brown, 1967). Shiant Isles pyroxene trend after Gibb, 1973; Skaergaard pyroxene trend after Wager & Brown, 1968; field for SMLS pyroxenes after Bell et al, 1994.

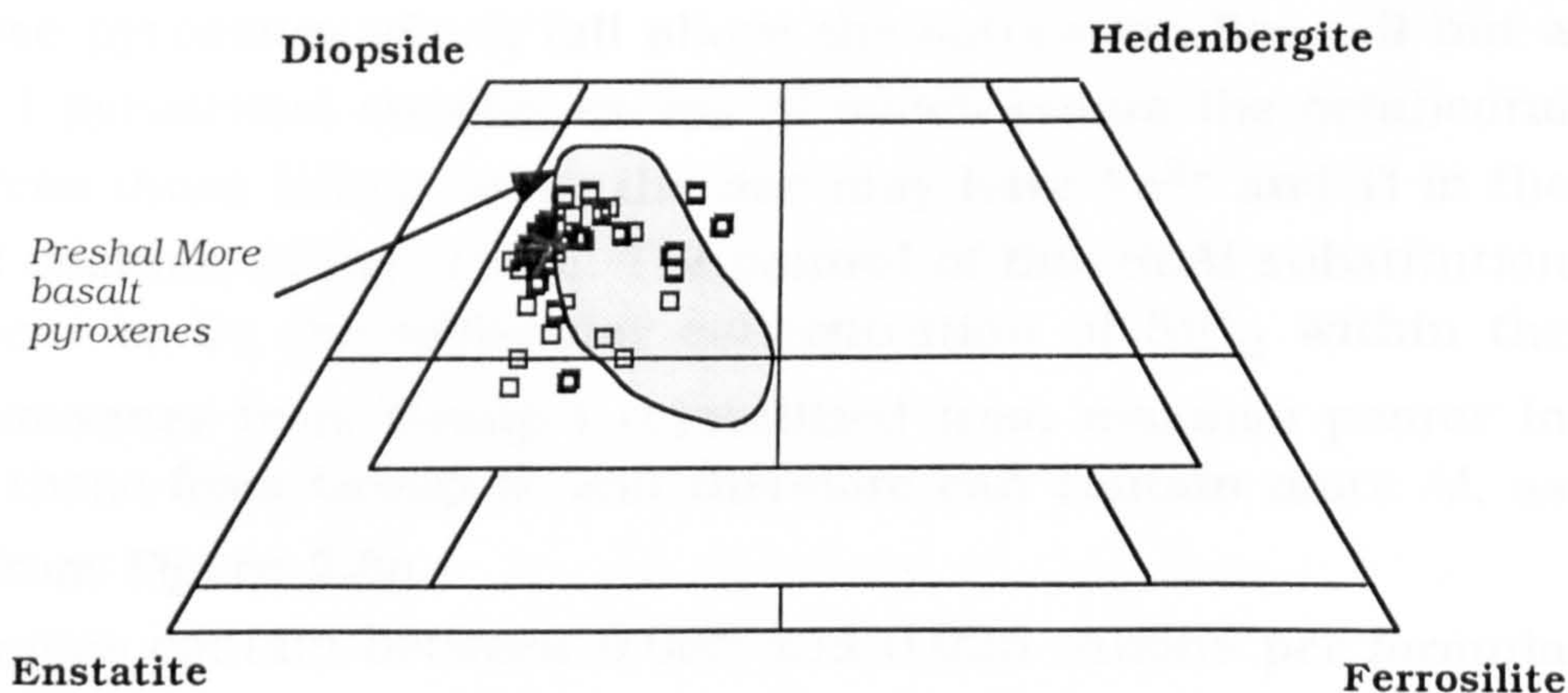


FIGURE 2.7b Groundmass pyroxene compositions from Group I magmas. Shown is the field occupied by pyroxenes from the Preshal More magma type (after Bell et al., 1994)

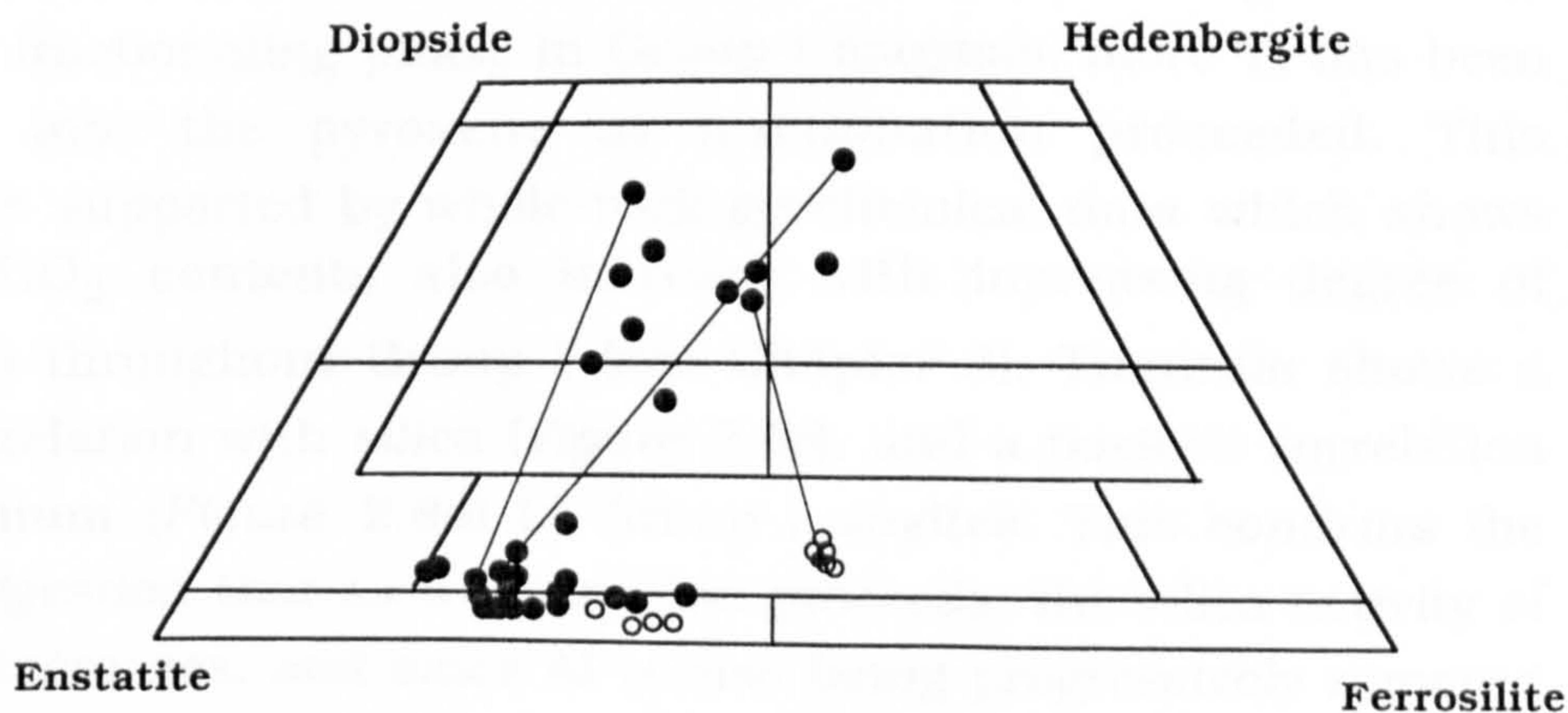


FIGURE 2.7c Groundmass and phenocryst pyroxene compositions of Group II magmas. Tie lines join coexisting groundmass-groundmass, and groundmass-phenocryst pairs. Phenocryst compositions are denoted by open circles.

clinopyroxenes have been noted in samples from the Hawaiian lava lake (Evans & Moore, 1968).

Elemental Variations in Al, Ti, Cr, Mn, and Na

All analyses of Group I augites show an excess of alumina after allocation of Al to the tetrahedral Si sites. *Figure 2.8a* shows a diagram for both Group I and Group II groundmass pyroxenes which illustrates the variation of ionic Si with ionic Al calculated on the basis of six oxygens per formula unit. In this figure, a line which connects points representing saturation of the tetrahedral position, namely the points corresponding to $\text{Si} + \text{Al} = 2$, is shown. That the groundmass pyroxenes from both groups fall around this line, indicates that Al in these pyroxenes is mainly in the tetrahedral position. The Al ions in the tetrahedral position are electronically compensated for by the entrance of Ti, Al and Fe^{3+} ions into the octahedral position (Kushiro, 1960.) Those pyroxenes which fall above the saturation line (all but a few Group I pyroxenes) contain excess Al which enters the octahedral sites, whereas those falling below the line may have Fe^{3+} and Ti in the tetrahedral position (Kuno, 1955). The control of this Si:Al substitution would appear to be the molecular concentration of SiO_2 within the magma; pyroxenes from Group I crystallized from magmas poorer in SiO_2 than those from Group II, and therefore can contain more Al, as is evident from *Figure 2.8a*

Group I augites contain between 0.005 and 0.025 cations per formula unit (CPFU) of titanium. Titanium contents show a slight tendency to increase with degree of fractionation (decreasing $\text{Mg}/(\text{Mg}+\text{Fe})$) as shown in *Figure 2.8b*. As discussed above, Ti enters the pyroxene structure to maintain electrical neutrality. Since titanomagnetite was not a major fractionating phase in Group I magmas, more Ti has been partitioned into the pyroxene as fractionation proceeded. This conclusion is supported by whole-rock geochemical data which shows that total TiO_2 contents also increase with increasing degree of fractionation throughout Group I (see Chapter 3). Titanium shows a negative correlation with silica (*Figure 2.8c*), and a positive correlation with aluminium (*Figure 2.8d*) in Group I augites. This confirms the previous suggestion that as fractionation proceeds, the silica activity of the magma increases, and since Al is also being progressively removed from the melt in plagioclase, less Al will be available for pyroxene. This enables a greater proportion of Ti and Fe^{3+} to be taken up in the

pyroxene lattice.

Chromium shows a very distinctive correlation with degree of fractionation (*Figure 2.8e*). Between $\text{Mg}/(\text{Mg}+\text{Fe}) = 0.82$ and 0.7 , Cr contents drop rapidly from 0.022 CPFU to 0.001 CPFU. At higher degrees of fractionation ($\text{Mg}/(\text{Mg}+\text{Fe}) < 0.7$), Cr contents are at constantly low values and very often at zero. Identical relationships can be seen in the groundmass clinopyroxenes of the Shiant Isles sill (Gibb, 1973.) This concentration of Cr in the early, Mg-rich pyroxenes is undoubtedly due to the strong partitioning of Cr into pyroxene rather than the liquid, and it appears that by the stage at which a pyroxene with $\text{Mg}/(\text{Mg}+\text{Fe}) = 0.7$ crystallized, the liquid was highly depleted in Cr. Chromium is also partitioned into chrome-spinel during the early stages of crystallization of basaltic magmas (Irvine, 1967). The Group I magmas do not contain a spinel phase, other than magnetite. However, Cr-spinel is present in small quantities in the cognate gabbroic xenoliths. These represent early-formed cumulate rocks (see Chapter 7), and will have undoubtedly contributed to the early depletion of Cr from the magma. It is considered likely, therefore, that Cr contents in the intruded magmas were controlled solely by the later removal of diopside and augite.

The Mn contents of the pyroxenes shows a steady increase with degree of fractionation from ~ 0.004 to 0.01 CPFU (*Figure 2.8f*).

Gibb (1973) suggested that the Na contents of the Shiant Isles sill pyroxenes were controlled by the Fe^{3+} activity of the magma, and hence its oxygen fugacity. Although Na contents of the Group I pyroxenes are very low (between 0.01 and 0.02 CPFU), the positive correlation between Na and Fe^{3+} confirms a similar relationship (*Figure 2.8g*).

Fe-Ti oxides

Fe-Ti oxides form irregular masses or single small octahedra, always in association with the pyroxene. Representative electron-probe analyses are shown in *Table 2.3*. As can be seen, the oxide phase is typically a highly titaniferous magnetite. No separate ilmenite has been found. However, in certain samples (*e.g.* ORB1) exsolution textures have been identified in a few grains. The association is titanomagnetite with sphene. It is suggested that the sphene resulted from the alteration of exsolved ilmenite (*e.g.* Morrison, 1978)

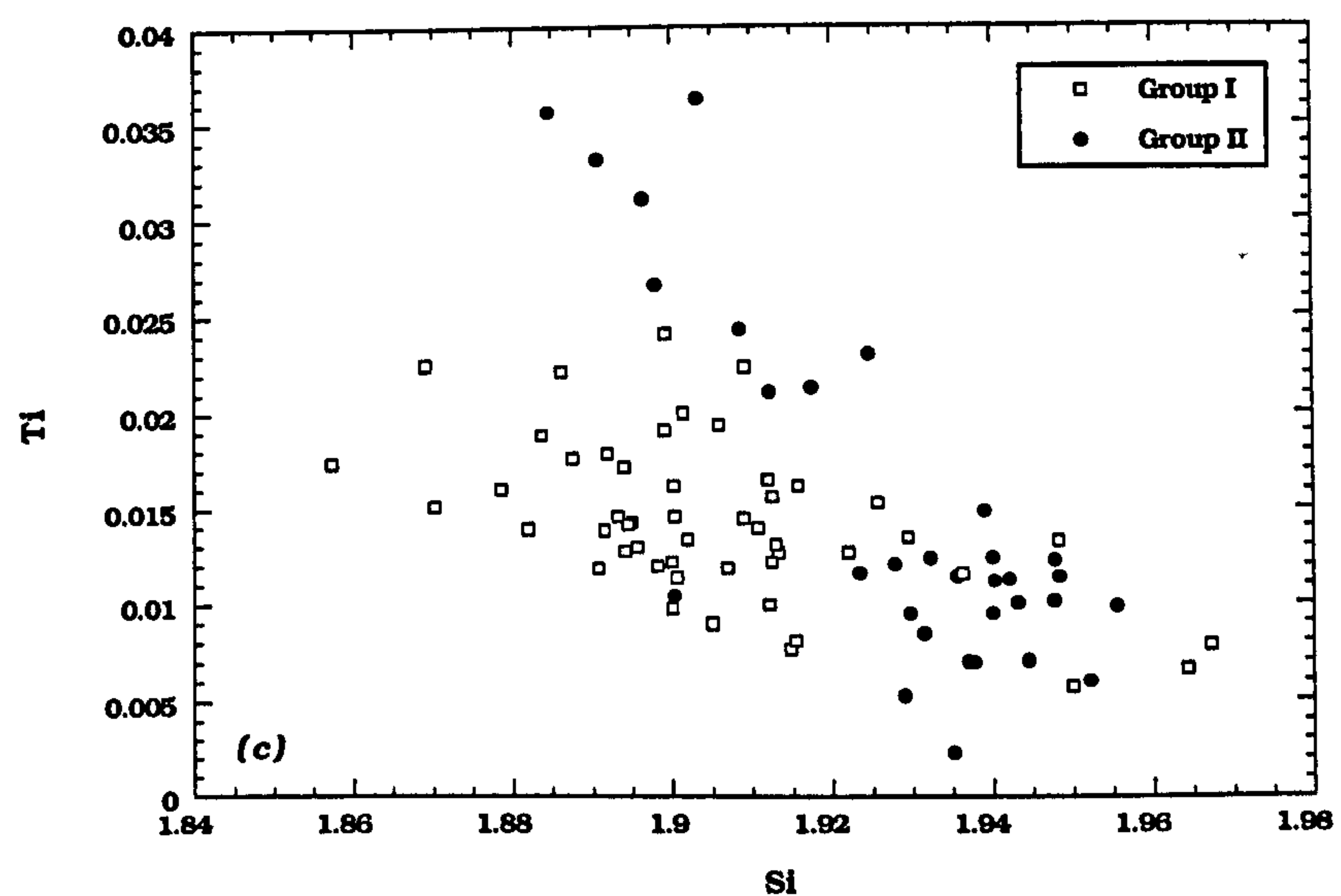
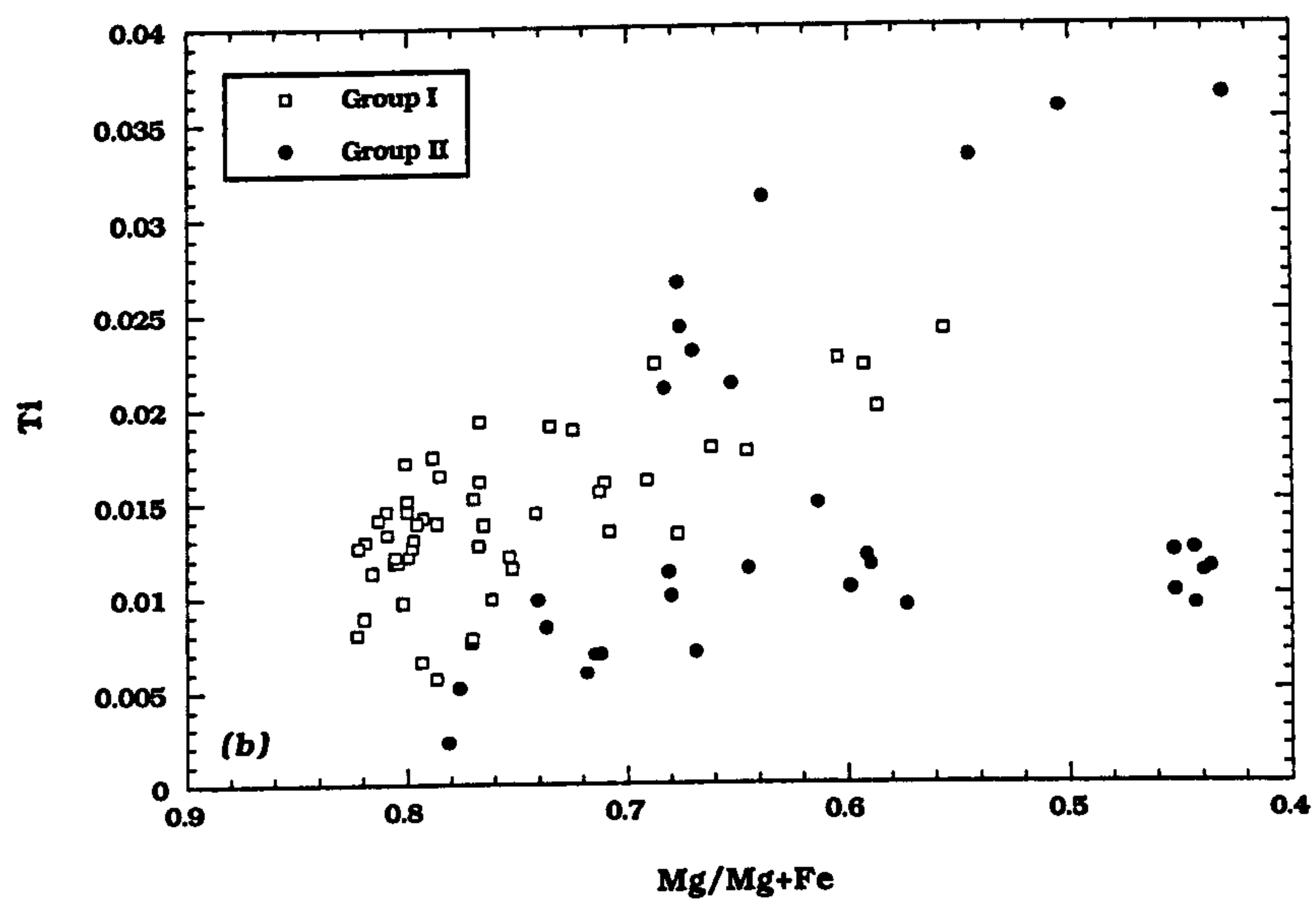
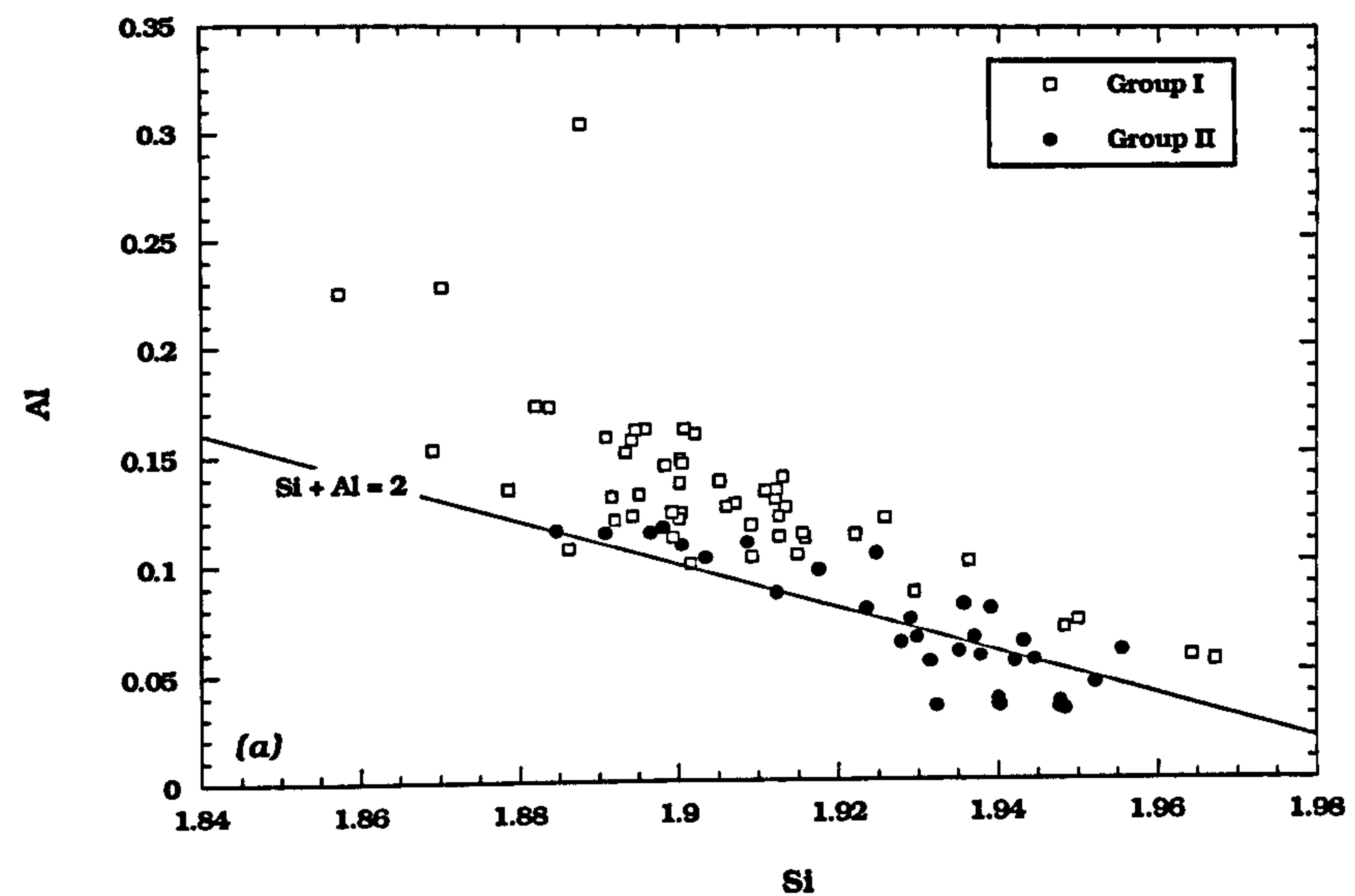


FIGURE 2.8 Cation variations in Group I and Group II clinopyroxenes. Cations calculated on the basis of 6 oxygens per formula unit.

(a) Si vs. Al

(b) Ti vs. Mg#

(c) Ti vs. Si

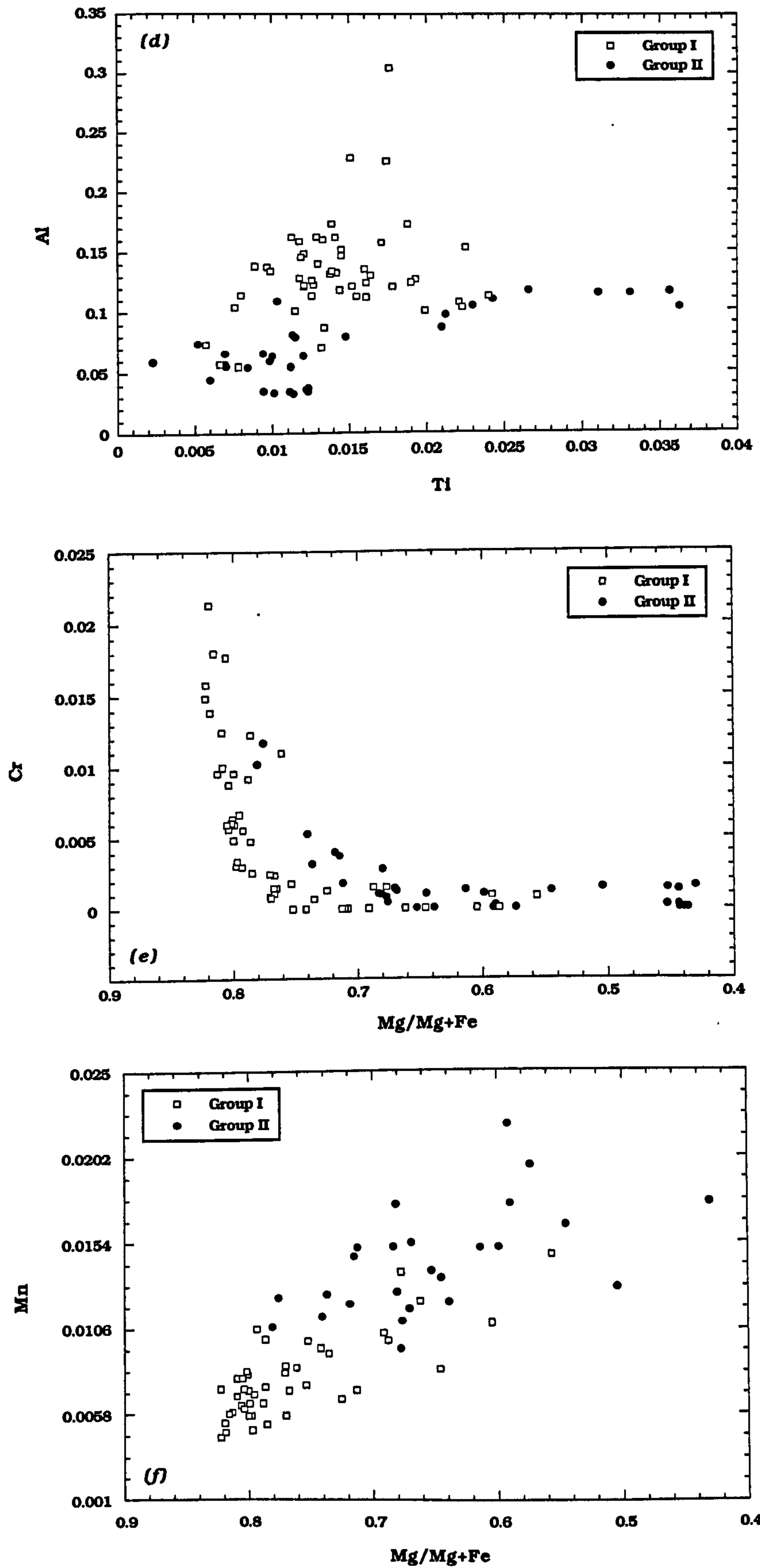


FIGURE 2.8 Cation variations in Group I and Group II clinopyroxenes. Cations calculated on the basis of 6 oxygens per formula unit.

(d) Ti vs. Al

(e) Cr vs. Mg#

(f) Mn vs. Si

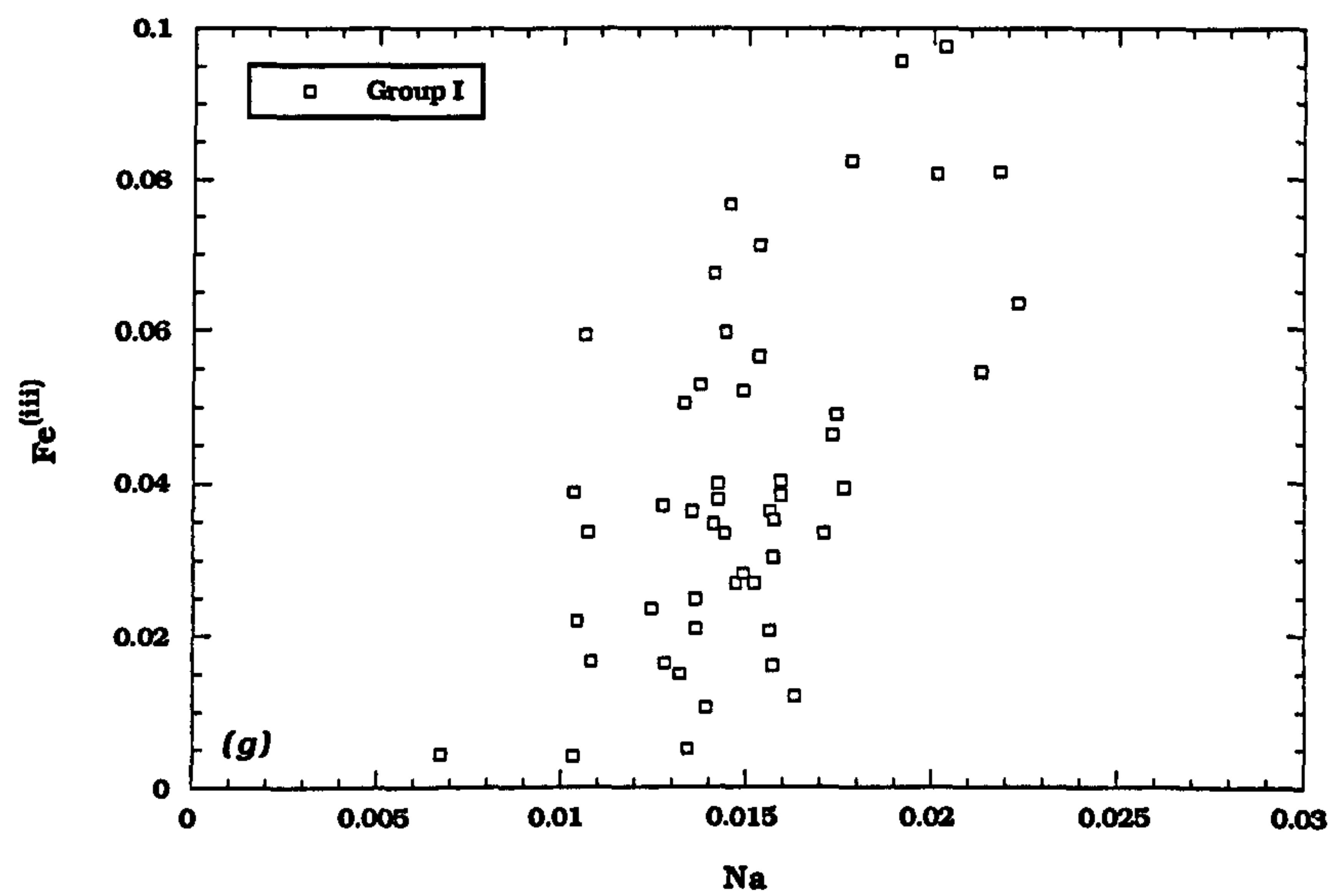


FIGURE 2.8 Cation variations in Group I clinopyroxenes. Cations calculated on the basis of 6 oxygens per formula unit.

(g) Na vs. Fe^(III)

SAMPLE ARB1				PMBASE				TILE1	
TYPE	G	G	G	G	G	G core	G rim	G	G
SiO ₂	53.30	53.15	53.46	51.74	51.20	51.26	51.90	48.82	49.95
TiO ₂	0.18	0.14	0.27	0.47	0.62	0.43	0.35	0.71	0.63
Al ₂ O ₃	1.77	1.84	1.82	3.76	3.60	3.64	3.18	4.79	4.69
Cr ₂ O ₃	0.35	0.38	0.59	0.48	0.22	0.61	0.21	0.08	0.29
Fe ₂ O ₃	1.54	2.60	1.42	0.76	1.09	1.31	1.83	2.72	1.66
MgO	26.50	26.39	26.74	18.68	17.31	18.01	18.16	14.25	16.91
CaO	3.26	3.30	3.00	16.58	17.92	16.96	17.57	19.60	17.41
MnO	0.37	0.36	0.37	0.16	0.26	0.20	0.26	0.26	0.26
FeO	11.92	11.75	11.98	6.67	6.68	6.54	6.35	7.02	6.41
Na ₂ O	0.04	0.06	0.07	0.19	0.22	0.22	0.19	0.25	0.24
K ₂ O	0.00	0.02	0.00	0.01	0.00	0.00	0.00	0.02	0.03
TOTAL	99.23	99.99	99.72	99.49	99.10	99.17	100.00	98.52	98.47
FORMULA ON THE BASIS OF 6 OXYGENS									
Si	1.93	1.92	1.93	1.90	1.89	1.89	1.90	1.84	1.86
Al	0.07	0.08	0.07	0.10	0.11	0.11	0.10	0.16	0.14
Al	0.01	0.00	0.01	0.06	0.05	0.05	0.04	0.06	0.07
Fe(III)	0.04	0.07	0.04	0.02	0.03	0.04	0.05	0.08	0.05
Fe(II)	0.36	0.35	0.36	0.20	0.21	0.20	0.19	0.22	0.20
Ti	0.01	0.00	0.01	0.01	0.02	0.01	0.01	0.02	0.02
Mn	0.01	0.01	0.01	0.01	0.01	0.01	0.01	0.01	0.01
Ca	0.13	0.13	0.12	0.65	0.71	0.67	0.69	0.79	0.70
Mg	1.43	1.42	1.44	1.02	0.96	0.99	0.99	0.80	0.94
Cr	0.01	0.01	0.02	0.01	0.01	0.02	0.01	0.00	0.01
Na	0.00	0.00	0.01	0.01	0.02	0.02	0.01	0.02	0.02
K	0.00	0.00	0.00	0.00	0.00	0.00	0.00	0.00	0.00
TOTAL	4.00	4.00	4.00	4.00	4.00	4.00	4.00	4.00	4.00
ENDMEMBER %									
Wo	6.55	6.67	6.02	34.61	37.8	35.88	36.6	43.45	37.73
En	74.14	74.23	74.63	54.26	50.78	52.99	52.64	43.94	50.98
Fs	19.31	19.11	19.35	11.13	11.43	11.13	10.76	12.61	11.29

Table 2.2 Representative analyses of pyroxene from Group I sheets. G=Groundmass; P=Phenocryst; X=xenocryst. All analyses crystal cores unless otherwise stated. Aluminium partitioned between tetrahedral and octahedral sites assuming tetrahedral site only filled with Si and Al. All Fe measured as FeO. Fe^{II} and Fe^{III} calculated assuming stoichiometry. Sample Numbers defined in Appendix II.

SAMPLE	ORB1		RCB1		PGB9	PM+200	PMBASE
SiO ₂	0.14	0.19	0.18	0.74	n.d.	n.d.	n.d.
TiO ₂	24.33	24.24	21.97	21.34	17.25	18.00	16.82
Al ₂ O ₃	1.89	1.94	1.94	1.90	n.d.	n.d.	n.d.
Cr ₂ O ₃	0.01	0.06	0.07	0.08	0.23	0.08	0.00
Fe ₂ O ₃	42.97	42.84	44.68	44.03	34.10	31.68	33.19
MgO	0.03	0.00	0.01	0.07	n.d.	n.d.	n.d.
MnO	1.65	1.48	1.00	0.84	1.95	1.24	2.17
FeO	29.70	29.99	30.01	29.86	44.49	45.41	42.99
ZnO	0.10	0.16	0.19	0.35	n.d.	n.d.	n.d.
TOTAL	100.81	100.90	100.05	99.21	98.02	96.41	95.16
FORMULA BASED ON 32 OXYGENS							
Si	0.04	0.05	0.05	0.21	-	-	-
Ti	5.08	5.06	4.65	4.55	4.01	4.25	4.03
Al	0.62	0.64	0.64	0.64	-	-	-
Cr	0.00	0.01	0.02	0.02	0.06	0.02	0.00
Fe(iii)	8.98	8.95	9.47	9.40	7.93	7.48	7.95
Mg	0.01	0.00	0.01	0.03	-	-	-
Mn	0.39	0.35	0.24	0.20	0.51	0.33	0.58
Fe(ii)	6.90	6.97	7.07	7.08	11.50	11.92	11.44
Zn	0.02	0.03	0.04	0.07	-	-	-
TOTAL	22.04	22.07	22.17	22.19	24.00	24.00	24.00
Fe/Fe+Mg	99.85	100.00	99.93	99.61	-	-	-
Cr/Cr+Al	0.26	2.16	2.37	2.79	-	-	-

Table 2.3 Representative analyses (partial and full) of groundmass Ti-rich magnetite from Group I sheets. All Fe measured as FeO. Feⁱⁱ and Feⁱⁱⁱ calculated assuming stoichiometry. n.d. = not determined

Group II : Augite andesites and porphyritic dacites.

Rocks of Group II can be split into those which are similar in mineralogy and texture to the basaltic andesites of Group I and which are not porphyritic, and those which are porphyritic in nature. Although most rocks contain at least a few phenocrysts of plagioclase, the term porphyritic, as used here, relates to rocks with >5% by volume of phenocrysts, *which are visible in hand specimen.*

Non-porphyritic rocks

The rocks of Group II are more typically hypocrystalline, with small needles of plagioclase and grains of pyroxene set in a more-or-less continuous glassy groundmass. *Figure 2.9a* shows a photomicrograph of a typical glassy Group II rock. They differ from the basaltic andesites in having abundant pigeonite and occasional orthopyroxene in the groundmass, along with occasional phenocrysts of plagioclase and orthopyroxene. Compositions of the plagioclase, pyroxene and Fe-Ti oxides are given in *Tables 2.4, 2.5 and 2.6.*

Plagioclase

The plagioclase forms small needles (<1mm) which have sharp terminations and are simple twinned. Compositions of these small quench crystals are between An₅₈ and An₆₂. Larger, slightly zoned laths are also present, and have compositions which lie within the same range as the quench crystals. Rare phenocrysts and xenocrysts of plagioclase are found within these rocks. The phenocrysts are oscillatory zoned within the range An₆₅-An₅₀ and with the rims being generally more sodic. Crystals which are thought to be xenocrystic show strongly resorbed crystal faces and dusty-looking interiors with glassy inclusions. Compositions of these oscillatory zoned feldspars range from An₆₄ to An₇₀, with the rims being more calcic. Representative analyses of groundmass and phenocryst plagioclases are given in *Table 2.4.*

SAMPLE	KBB8		KBB3				KBB5		
TYPE	G	G	G	G	P core	P rim	P core	P rim	G
SiO ₂	52.27	51.71	52.03	50.57	49.27	48.32	52.55	52.29	52.38
TiO ₂	0.02	0.03	0.05	0.09	0.05	0.03	0.09	0.00	0.11
Al ₂ O ₃	30.35	30.67	29.97	31.06	32.25	32.83	30.44	30.46	30.12
FeO*	0.83	0.55	1.10	0.75	0.66	0.72	0.61	0.42	0.85
CaO	11.11	11.61	11.16	12.71	13.21	13.86	11.29	11.39	11.38
Na ₂ O	4.79	4.29	4.91	4.01	3.72	3.23	4.49	4.46	4.62
K ₂ O	0.48	0.45	0.41	0.33	0.37	0.24	0.47	0.41	0.45
TOTAL	99.84	99.31	99.63	99.53	99.52	99.23	99.95	99.42	99.90
FORMULA ON BASIS OF 32 OXYGENS									
Si	9.52	9.46	9.51	9.27	9.05	8.91	9.54	9.53	9.53
Ti	0.00	0.00	0.01	0.01	0.01	0.00	0.01	0.00	0.02
Al	6.51	6.61	6.46	6.71	6.98	7.14	6.51	6.54	6.46
Fe (ii)	0.13	0.08	0.17	0.12	0.10	0.11	0.09	0.06	0.13
Ca	2.17	2.27	2.19	2.50	2.60	2.74	2.20	2.22	2.22
Na	1.69	1.52	1.74	1.43	1.32	1.16	1.58	1.58	1.63
K	0.11	0.11	0.10	0.08	0.09	0.06	0.11	0.10	0.10
TOTAL	20.12	20.05	20.17	20.11	20.15	20.12	20.04	20.32	20.09
ENDMEMBER %									
Ab	42.57	38.97	43.27	35.64	33.00	29.26	40.68	40.45	41.24
Or	2.79	2.71	2.40	1.94	2.16	1.44	2.82	2.44	2.63
An	54.63	58.32	54.33	62.41	64.84	69.30	56.50	57.12	56.13

Table 2.4 Representative analyses of plagioclases from Group II non-porphyritic sheets. G=Groundmass; P=Phenocryst. All analyses crystal cores unless otherwise stated. Sample Numbers defined in Appendix II.

Pyroxene

The pyroxenes of the Group II hypocrystalline rocks form very similar textures to the basalts and basaltic andesites of Group I, with subophitic relationships with plagioclase being widespread. However, skeletal forms of the pyroxenes are also common, indicating rapid growth histories. A typical specimen is depicted in the photomicrograph of *Figure 2.9b*.

The groundmass pyroxenes show a very large compositional range (*Table 2.5*). End-member compositions are presented in *Figure 2.7c*, which shows that augite, sub-calcic augite, ferroaugite, pigeonite, and enstatite compositions all occur. Indeed, some samples contain the entire compositional spectrum as groundmass crystals. Under ordinary conditions of crystallization of magmas, subcalcic-augite does not form; an immiscibility gap exists between augite and pigeonite. However, sub-calcic augite does form when some of the Si^{4+} is replaced by Fe^{3+} in the tetrahedral sites, enabling Ca^{2+} , Mg^{2+} and Fe^{2+} to enter the pyroxene structure in all proportions. The $\text{Si}^{4+}/\text{Fe}^{3+}$ substitution is favoured by rapid cooling at relatively high temperatures (Kuno, 1955). Most crystals show compositional zoning, with low-Ca pyroxene 'mantling' augite, and augite occasionally forming the rims to pigeonite and enstatite crystals. Again, this great variation within individual crystals may be due to small-scale, local inhomogeneities in magma composition during rapid crystallization.

Augite compositions are essentially similar to those of Group I; however, they tend to be enriched in iron. This is demonstrated in *Figure 2.10* which plots ionic Fe against $\text{Mg}/\text{Mg}+\text{Fe}$ for pyroxenes of Groups I and II. The augites of Group I show a steady increase in Fe content with degree of fractionation, and this trend is 'continued' by the Group II groundmass augites. It must be stressed, however, that Groups I and II are *not* related via fractional crystallization processes (see Chapter 3). The trend at higher total-Fe contents is defined by the pigeonite and enstatite groundmass crystals found in Group II rocks. Group II groundmass pyroxenes contain similar but slightly lower Al contents to those of Group I (*Figure 2.8a*). The Ti contents of the Group II groundmass augites are typically slightly higher than the augites from Group I (0.02-0.035 CPFU). However, the groundmass pigeonite and enstatite from Group II has lower Ti contents at around 0.005-0.015 CPFU. Since it is probable that the groundmass pyroxenes

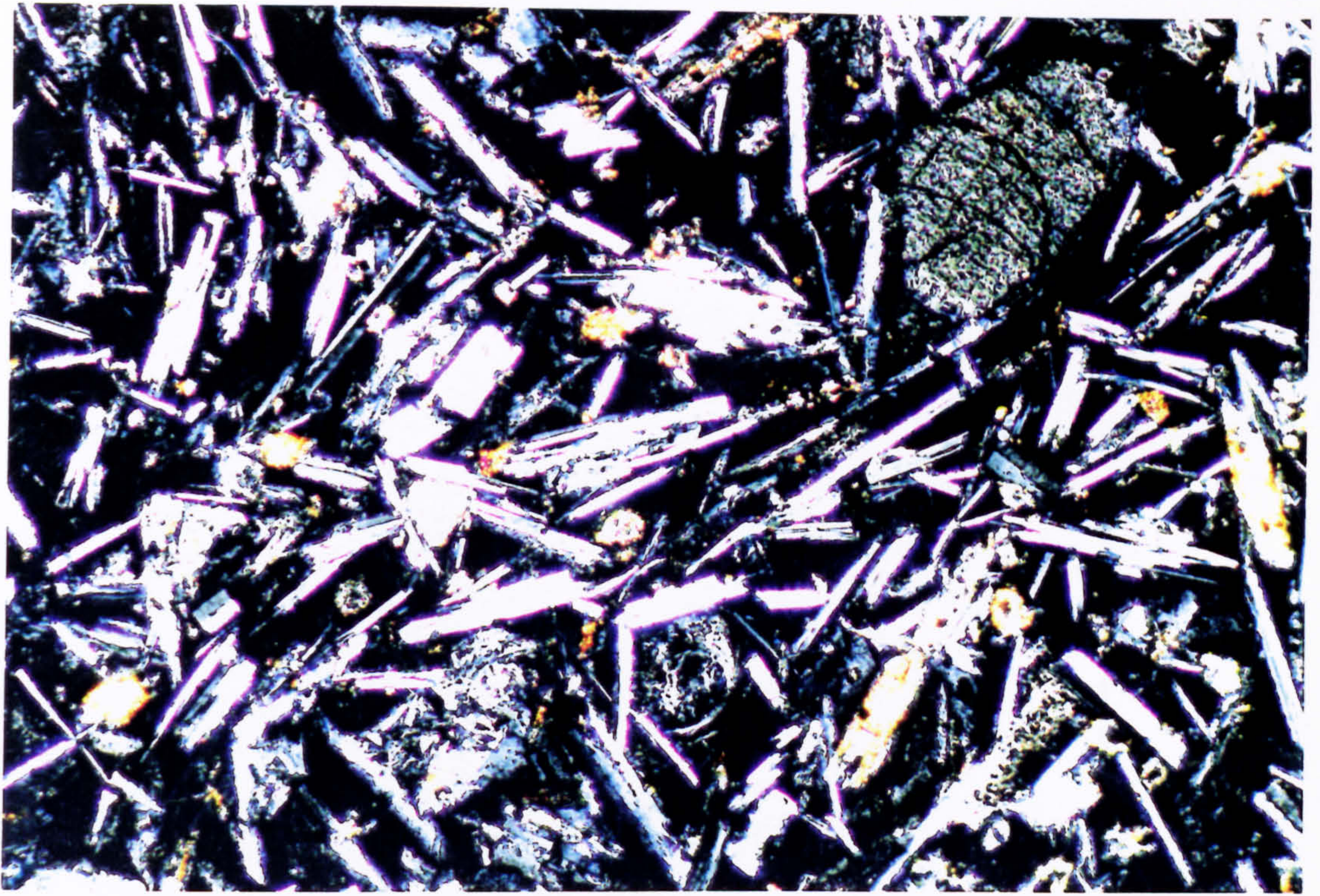


FIGURE 2.9a Plagioclase needles and dendritic clinopyroxene in a glassy Group II andesite. Alteration of the interstitial glass to chlorite is common. (xpl; Field of view 0.8x1.2mm; Sample KBB3).

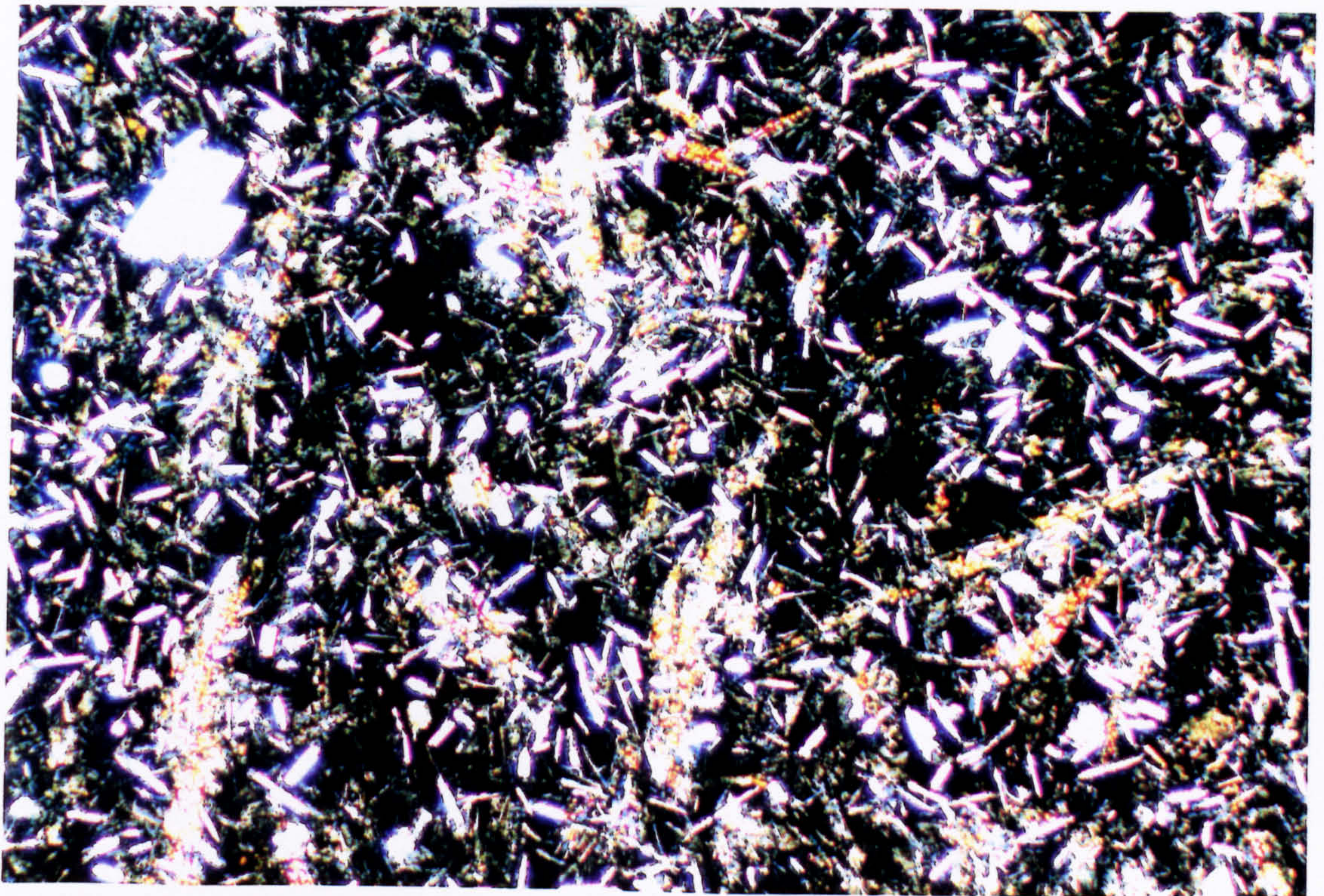


FIGURE 2.9b Highly elongate, feathery clinopyroxene in a glassy Group II andesite. (xpl; Field of view 2x3mm; Sample TIPI1).

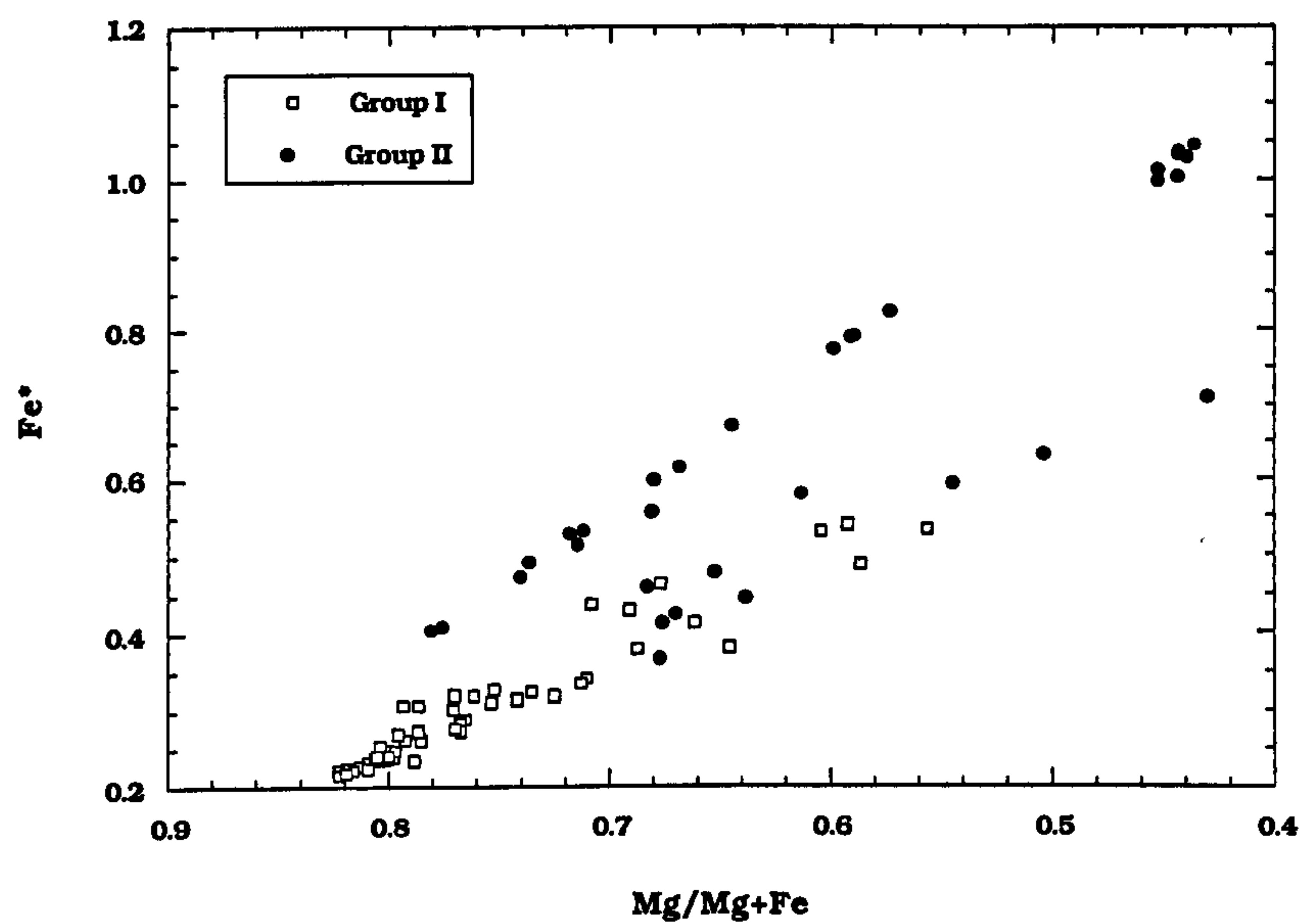


FIGURE 2.10 Variation of $Fe\#$ with $Mg\#$ in Group I and Group II clinopyroxenes. Cations calculated on the basis of 6 oxygens per formula unit.

crystallized under metastable conditions, the high Ti concentrations in the augites are therefore likely to be a consequence of this rapid cooling. Work by Coish & Taylor (1979) and Gamble & Taylor (1980), suggests that the minor-element concentrations of pyroxenes are partly controlled by the cooling rate of the magma. They found that at a given degree of fractionation, the Al and Ti contents of pyroxenes increased with increasing cooling rate, suggesting that under rapid cooling conditions, growth of crystals in preferred directions is faster than the diffusion of impurities (*e.g.* Ti) away from the growth surfaces. Under slower, near-equilibrium, cooling conditions, these impurities can be expelled from the pyroxene structure (Coish & Taylor, 1979.) The low-Ca clinopyroxene (pigeonite) and orthopyroxene (enstatite) forms groundmass crystals of slightly larger size and are more euhedral than the coexisting augites, with the latter being generally interstitial to the plagioclase laths. This suggests two stages of pyroxene growth, with the low-Ca pyroxenes growing at a slightly slower rate, and therefore being able to expel impurities such as Ti (Coish & Taylor, 1979). Enstatite ($\text{Wo}_{1.7}\text{En}_{60.6}\text{Fs}_{37.7}$) also occurs as phenocrysts, and also in association with clots of plagioclase. These are discussed in Chapter 7 along with the gabbroic xenoliths.

SAMPLE	KBB5			KBB3				PGB8	
TYPE	G	G	G	G	G	G	P	G	G
SiO ₂	48.46	52.21	53.32	52.64	53.59	53.12	50.09	52.07	50.90
TiO ₂	1.23	0.40	0.36	0.36	0.08	0.19	0.36	0.30	0.37
Al ₂ O ₃	2.22	1.25	1.38	1.46	1.40	1.73	2.44	1.81	2.12
Cr ₂ O ₃	0.05	0.04	0.18	0.10	0.36	0.41	0.03	0.20	0.34
Fe ₂ O ₃	1.36	1.48	0.26	1.06	2.21	1.87	2.51	1.78	2.09
MgO	9.16	21.49	24.81	23.21	26.88	26.26	20.42	21.97	22.21
CaO	15.91	5.54	3.18	2.23	3.24	3.37	0.81	6.16	1.52
MnO	0.53	0.56	0.36	0.40	0.35	0.40	0.47	0.37	0.54
FeO	20.40	16.59	15.24	18.49	11.44	11.82	22.16	14.22	18.98
Na ₂ O	0.28	0.05	0.03	0.03	0.07	0.07	0.02	0.19	0.03
K ₂ O	0.04	0.00	0.01	0.00	0.01	0.01	0.02	0.00	0.00
TOTAL	99.63	99.60	99.13	99.98	99.62	99.25	99.34	99.06	99.09
FORMULA ON THE BASIS OF 6 OXYGENS									
Si	1.90	1.94	1.96	1.94	1.94	1.93	1.90	1.93	1.91
Al	0.10	0.06	0.05	0.06	0.06	0.07	0.10	0.07	0.09
Al	0.01	0.00	0.02	0.01	0.00	0.00	0.01	0.01	0.00
Fe(iii)	0.04	0.04	0.01	0.03	0.06	0.05	0.07	0.05	0.06
Fe(ii)	0.67	0.52	0.47	0.57	0.35	0.36	0.70	0.44	0.60
Ti	0.04	0.01	0.01	0.01	0.00	0.01	0.01	0.01	0.01
Mn	0.02	0.02	0.01	0.01	0.01	0.01	0.02	0.01	0.02
Ca	0.67	0.22	0.13	0.09	0.13	0.13	0.03	0.25	0.06
Mg	0.54	1.19	1.36	1.28	1.45	1.42	1.16	1.22	1.24
Cr	0.00	0.00	0.01	0.00	0.01	0.01	0.00	0.01	0.01
Na	0.02	0.00	0.00	0.00	0.01	0.01	0.00	0.01	0.00
K	0.01	0.00	0.00	0.00	0.00	0.00	0.00	0.00	0.00
TOTAL	4.00	4.00	4.00	4.00	4.00	4.00	4.00	4.00	4.00
ENDMEMBER %									
Wo	35.35	11.35	6.37	4.53	6.50	6.82	1.73	12.81	3.18
En	28.33	61.22	69.20	65.53	75.04	73.88	60.62	63.52	64.84
Fs	36.32	27.42	24.43	29.94	18.46	19.30	37.65	23.67	31.99

Table 2.5 Representative analyses of pyroxene from Group II non-porphyritic sheets. G=Groundmass; P=Phenocryst. All analyses crystal cores unless otherwise stated. Aluminium partitioned between tetrahedral and octahedral sites assuming tetrahedral site only filled with Si and Al. All Fe measured as FeO. Feⁱⁱ and Feⁱⁱⁱ calculated assuming stoichiometry. Sample Numbers defined in Appendix II.

Fe-Ti oxides

Oxide phases occur in the groundmass, and are also associated with the plagioclase-orthopyroxene glomerocrysts. The groundmass oxides, where present, form small, isolated grains which show no evidence of exsolution. They are evenly distributed throughout the rock, but sometimes cluster around pyroxene grains. They are all titanomagnetite in composition (*Table 2.6*). Those which occur in the glomerocrysts tend to be of a larger size, but have a similar composition.

SAMPLE	KBB3				KBB5	PCRPI1
TYPE	MP	MP	MP	G	G	MP
TiO ₂	14.69	15.19	15.27	17.46	21.09	17.25
Cr ₂ O ₃	0.00	0.08	0.00	0.03	0.02	0.22
Fe ₂ O ₃	38.90	36.73	37.36	34.28	22.13	48.41
MnO	0.38	0.37	0.42	0.40	0.78	0.36
FeO	43.54	43.50	43.84	46.42	47.10	29.28
TOTAL	97.51	95.87	96.89	98.60	91.11	95.53
FORMULA BASED ON 32 OXYGENS						
Ti	3.44	3.62	3.60	4.03	5.25	3.93
Cr	0.00	0.02	0.00	0.01	0.01	0.05
Fe(iii)	9.12	8.76	8.81	7.92	5.51	11.03
Mn	0.10	0.10	0.11	0.11	0.22	0.09
Fe(ii)	11.34	11.52	11.48	11.93	13.02	7.42
TOTAL	24.00	24.00	24.00	24.00	24.00	22.53

Table 2.6 Representative partial analyses of groundmass (G) and microphenocrysts (MP) of Ti-magnetite from Group II non-porphyritic andesite and porphyritic dacite sheets. All Fe measured as FeO. Fe^{II} and Fe^{III} calculated assuming stoichiometry. Sample numbers defined in Appendix II. Samples KBB3 and KBB5 are non-porphyritic dacites, PCRPI1 is porphyritic

Porphyritic rocks

The porphyritic dacites (inninmorite in the classification of Anderson *et al.*, 1916) have completely glassy, heterogeneous groundmasses (pitchstones), with patches and streaks of darker glass being intermingled with paler glass. However, within the larger sheets, the interior portions, which most likely cooled more slowly, have crystallized to a fine-grained intergrowth of plagioclase, K-feldspar and quartz. The phenocryst assemblage consists predominantly of intermediate plagioclase with subordinate Ca-poor clinopyroxene (pigeonite) (see *Tables 2.7 and 2.8*). Microphenocrysts of titanomagnetite, apatite and zircon also occur within the porphyritic rocks. Many of the phenocrysts have a mantle of dark glass. The porphyritic dacites also display the unusual 'sheath and core' structure. In the field this is appears as central 'cores' of glassy rock surrounded by a network or 'sheaths' of more crystalline material. This structure is thought to result from the secondary hydration and devitrification initiated at relatively high temperatures during cooling of the sheets. This devitrification is controlled by the original columnar jointing and other small-scale fracturing of the cooling rock (Drysdale, 1979). This structure is depicted in *Figure 2.11*.

Plagioclase

The plagioclase forms stumpy prisms up to 3 or 4mm in length. It normally shows complex Carlsbad or pericline twins. Most of the plagioclase phenocrysts show complex zoning patterns. Many crystals preserve evidence of earlier resorption surfaces, with later oscillatory growth (*Figure 2.12a*). The phenocrysts occasionally have rims which are slightly more calcic than the cores. The plagioclase often has a resorbed appearance, with fritted crystal edges. As in the basalts and basaltic andesites of Group I, cumulate clots of plagioclase, here joined by pigeonite, also occur. Some of these are of much finer grain size than the phenocrysts. Where the original glassy groundmass has devitrified, the plagioclase takes on the form of minute needles enclosed in K-feldspar with interstitial quartz as illustrated in *Figure 2.12b*. Representative analyses of phenocryst and groundmass feldspars are presented in *Table 2.7*.

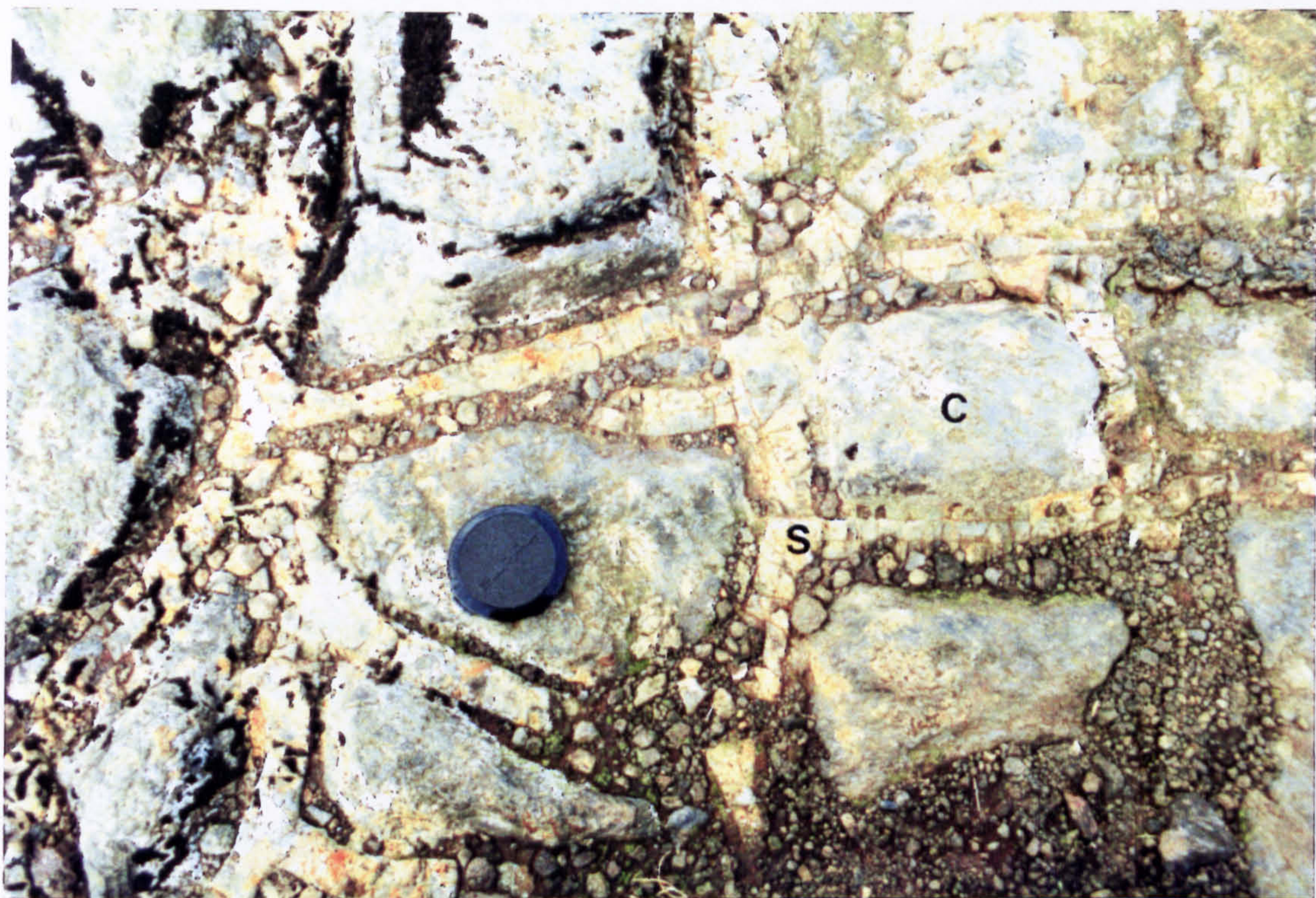


FIGURE 2.11

"Sheath and core" in Group II porphyritic dacite. Cores (C) consist of massive dacite. Sheaths (S) consist of devitrified dacite. Structure is thought to be due to the late-stage movement of water through the cooling dacite sheets. Lens cap approx. 5cm across.



FIGURE 2.12a Plagioclase phenocrysts ($\sim\text{An}_{50}$) showing oscillatory zoning, and pigeonite phenocrysts ($\sim\text{Wo}_{10}\text{En}_{41}\text{Fs}_{49}$) in a glassy porphyritic dacite of Group II. (xpl; Field of view 2x3mm; Sample PGB11).

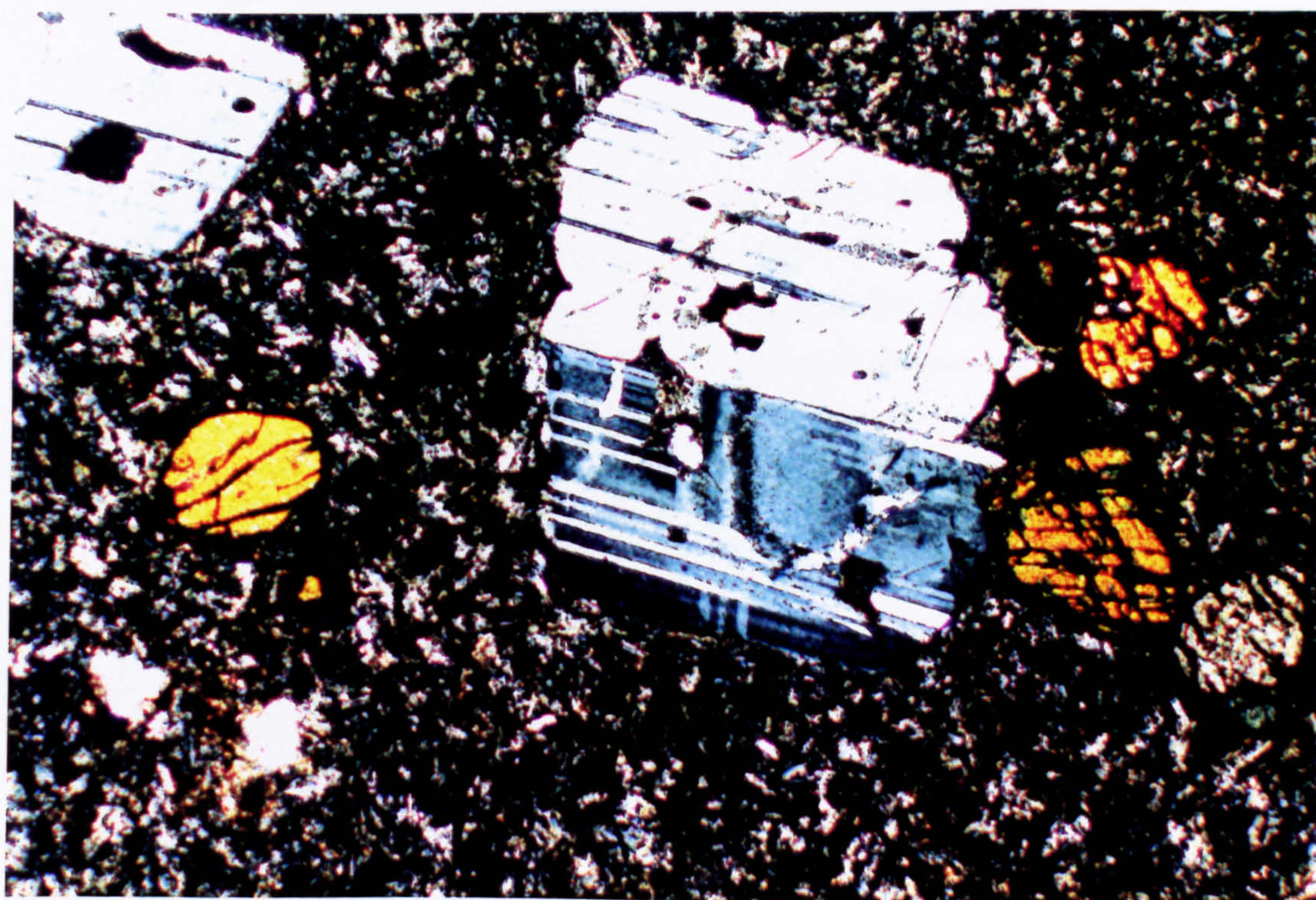


FIGURE 2.12b Plagioclase ($\sim\text{An}_{50}$), and pigeonite phenocrysts ($\sim\text{Wo}_{10}\text{En}_{41}\text{Fs}_{49}$) in a matrix of K-feldspar (Or_{60}), plagioclase (An_{39}), and quartz. From the centre of a large porphyritic dacite sheet of Group II. (xpl; Field of view 2x3mm; Sample CUP11).

Clinopyroxene

The pyroxene is a low-Ca pigeonite, and comprises rounded crystals, generally less than 2mm in diameter. The pigeonite is generally fresh, but is occasionally pseudomorphed by chlorite and serpentine masses, with alteration rims of haematite also being common. Electron-probe micro-analyses of pigeonite phenocrysts are given in *Table 2.8*. Compositions are generally similar within any one specimen ($\text{Wo}_{7.5}\text{En}_{42.5}\text{Fs}_{50}$), and individual crystals show no zoning. Within the finely crystalline centres of the larger dacite sheets, groundmass clinopyroxene forms small grains of composition ($\text{Wo}_{32}\text{En}_{36}\text{Fs}_{32}$) in association with plagioclase, K-feldspar and quartz.

Titanomagnetite, apatite and zircon

Titanomagnetite forms small, euhedral octahedra, often completely enclosed in pigeonite phenocrysts. It has a TiO_2 contents of around 15 wt% (see final analysis in *Table 2.6*). The inclusion of titanomagnetite within the pyroxene suggests that this phase was first to crystallize (cf. Carmichael, 1963).

Microphenocrysts of apatite, and rare zircon occur as inclusions within phenocrysts of plagioclase, and occasionally within the groundmass. The apatite is either needle-like, with dimensions in the order of $50 \times 15 \mu\text{m}$, or more rounded, larger crystals ($100\text{--}200 \mu\text{m}$), which often occur in embayments in the plagioclase crystals. Zircon occurs as irregularly shaped microphenocrysts approximately $80 \mu\text{m}$ across. The apatite and zircon may be xenocrystic. The presence of apatite and zircon microphenocrysts will obviously have very important implications for certain trace-element characteristics of these rocks. Apatite and zircon can contain high concentrations of the rare-earth elements (REE), and care must therefore be exercised when interpreting the petrogenesis of the Group II rocks on the basis of whole-rock, trace-element geochemistry.

SAMPLE	PCRPI1		PCRPI2				TIPI1		
TYPE	<i>P core</i>	<i>P rim</i>	<i>P core</i>	<i>P rim</i>	<i>G</i>	<i>G</i>	<i>P core</i>	<i>P rim</i>	<i>G</i>
SiO ₂	56.39	57.01	56.03	54.90	57.08	63.88	51.58	57.61	50.57
TiO ₂	0.13	0.14	0.06	0.14	0.02	0.05	0.06	0.34	0.00
Al ₂ O ₃	27.37	25.98	27.77	28.07	26.83	19.82	31.51	26.70	31.36
FeO*	0.65	0.94	0.46	1.44	0.61	0.29	0.30	1.02	0.67
CaO	9.15	8.05	9.46	9.97	8.09	0.33	12.14	7.54	12.46
Na ₂ O	5.46	6.07	5.69	4.99	6.44	4.15	4.18	5.71	4.26
K ₂ O	0.71	0.76	0.65	0.53	0.70	10.21	0.49	0.89	0.46
TOTAL	99.86	98.95	100.12	100.04	99.76	98.71	100.27	99.80	99.78
FORMULA ON BASIS OF 32 OXYGENS									
Si	10.17	10.37	10.09	9.94	10.29	11.75	9.35	10.36	9.25
Ti	0.02	0.02	0.01	0.02	0.00	0.01	0.01	0.05	0.00
Al	5.82	5.57	5.89	5.99	5.70	4.30	6.73	5.66	6.76
Fe (II)	0.10	0.14	0.07	0.22	0.09	0.04	0.05	0.15	0.10
Ca	1.77	1.57	1.82	1.93	1.56	0.07	2.36	1.45	2.44
Na	1.91	2.14	1.99	1.75	2.25	1.48	1.47	1.99	1.51
K	0.16	0.18	0.15	0.12	0.16	2.39	0.11	0.20	0.11
TOTAL	19.94	19.99	20.02	19.98	20.06	20.03	20.07	19.86	20.18
ENDMEMBER %									
Ab	49.74	55.11	50.16	46.03	56.61	37.56	37.30	54.60	37.18
Or	4.22	4.53	3.76	3.21	4.08	60.77	2.88	5.57	2.65
An	46.03	40.36	46.07	50.79	39.31	1.66	59.82	39.83	60.17

Table 2.7 Representative analyses of plagioclases and K-feldspar from Group II porphyritic dacite sheets. G=Groundmass; P=Phenocryst. All analyses crystal cores unless otherwise stated. Sample Numbers defined in Appendix II.

SAMPLE	PCRPI1			PCRPI1				TIPI1	
TYPE	P	P	P	P	P	P	G	G	G
SiO ₂	48.76	49.02	48.71	49.76	49.86	49.83	44.89	50.79	51.07
TiO ₂	0.41	0.34	0.41	0.32	0.39	0.38	0.96	0.27	0.41
Al ₂ O ₃	0.80	0.72	0.74	0.76	0.72	0.76	5.27	1.35	1.36
Cr ₂ O ₃	0.04	0.04	0.01	0.00	0.00	0.00	0.00	0.08	0.05
Fe ₂ O ₃	2.12	1.74	2.74	2.25	1.70	2.26	13.69	2.37	2.46
MgO	13.51	14.13	13.93	14.19	13.95	13.90	8.28	20.22	20.88
CaO	4.62	3.65	3.76	3.49	3.50	4.18	10.13	1.84	2.11
MnO	n.d.	n.d.	n.d.	n.d.	n.d.	n.d.	n.d.	0.59	0.55
FeO	28.25	28.90	28.66	29.74	30.46	29.57	13.08	21.77	20.76
Na ₂ O	0.09	0.03	0.06	0.07	0.03	0.05	2.25	0.04	0.04
K ₂ O	0.00	0.01	0.01	0.00	0.00	0.00	1.09	0.01	0.01
TOTAL	98.62	98.58	99.02	100.58	100.62	100.92	99.63	99.32	99.69
FORMULA ON THE BASIS OF 6 OXYGENS									
Si	1.94	1.95	1.93	1.94	1.95	1.94	1.77	1.93	1.92
Al	0.04	0.03	0.03	0.04	0.03	0.04	0.23	0.06	0.06
Al	0.00	0.00	0.00	0.00	0.00	0.00	0.01	0.00	0.00
Fe(iii)	0.06	0.05	0.08	0.07	0.05	0.07	0.41	0.07	0.07
Fe(ii)	0.94	0.96	0.95	0.97	1.00	0.96	0.43	0.69	0.65
Ti	0.01	0.01	0.01	0.01	0.01	0.01	0.03	0.01	0.01
Mn	-	-	-	-	-	-	-	0.02	0.02
Ca	0.20	0.16	0.16	0.15	0.15	0.17	0.43	0.08	0.09
Mg	0.80	0.84	0.82	0.83	0.81	0.81	0.49	1.14	1.17
Cr	0.00	0.00	0.00	0.00	0.00	0.00	0.00	0.00	0.00
Na	0.01	0.00	0.01	0.01	0.00	0.00	0.17	0.00	0.00
K	0.00	0.00	0.00	0.00	0.00	0.00	0.16	0.00	0.00
TOTAL	4.00	4.00	4.00	4.00	4.00	4.00	4.13	4.00	4.00
ENDMEMBER %									
Wo	10.16	7.96	8.25	7.51	7.50	8.97	31.80	3.88	4.41
En	41.34	42.85	42.58	42.50	41.57	41.50	36.16	59.31	60.78
Fs	48.50	49.19	49.16	49.99	50.92	49.53	32.05	36.81	34.81

Table 2.8 Representative analyses of pyroxene from Group II porphyritic andesite and dacite sheets. G=Groundmass; P=Phenocryst. All analyses crystal cores unless otherwise stated. All Fe measured as FeO. Fe^{II} and Fe^{III} calculated assuming stoichiometry. Sample Numbers defined in Appendix II.

Group III : Rhyolites

Rocks of rhyolitic composition make up a very small proportion of the LSSC (about 3%). The rhyolites are generally compact, light grey rocks often showing rusty-weathered surfaces. They are generally aphyric, but one of the larger sheets (that which forms the central portion of the composite sheet at Rudh' a' Chromain) does have porphyritic facies. In thin section the rhyolites are composed, in the main, of an intergrowth of oligoclase (~An₂₅), orthoclase, and quartz. Alteration to chlorite and sericite is common. Narrow, acicular pyroxene occurs, but it is generally completely pseudomorphed by chlorite. Sporadic phenocrysts of oligoclase occur throughout the rock, and form laths up to 2mm long showing Carlsbad twinning. Alteration of these phenocrysts to sericite, calcite and epidote is characteristic (*Figure 2.13*). The occasional microphenocryst of apatite and zircon can also be found. Analyses of groundmass and phenocryst feldspars are presented in *Table 2.9*. The porphyritic rhyolite consists of oligoclase phenocrysts 3-4mm in length. Phenocrysts of pyroxene (pigeonite; Buist, 1961) also occur; these however, are generally pseudomorphed by chlorite and calcite. Aggregates of magnetite occur in association with the pyroxene. The rhyolites are locally vitreous in nature, and similar to the porphyritic dacites (Group II) of the area, a distinct "sheath and core" structure has been developed.

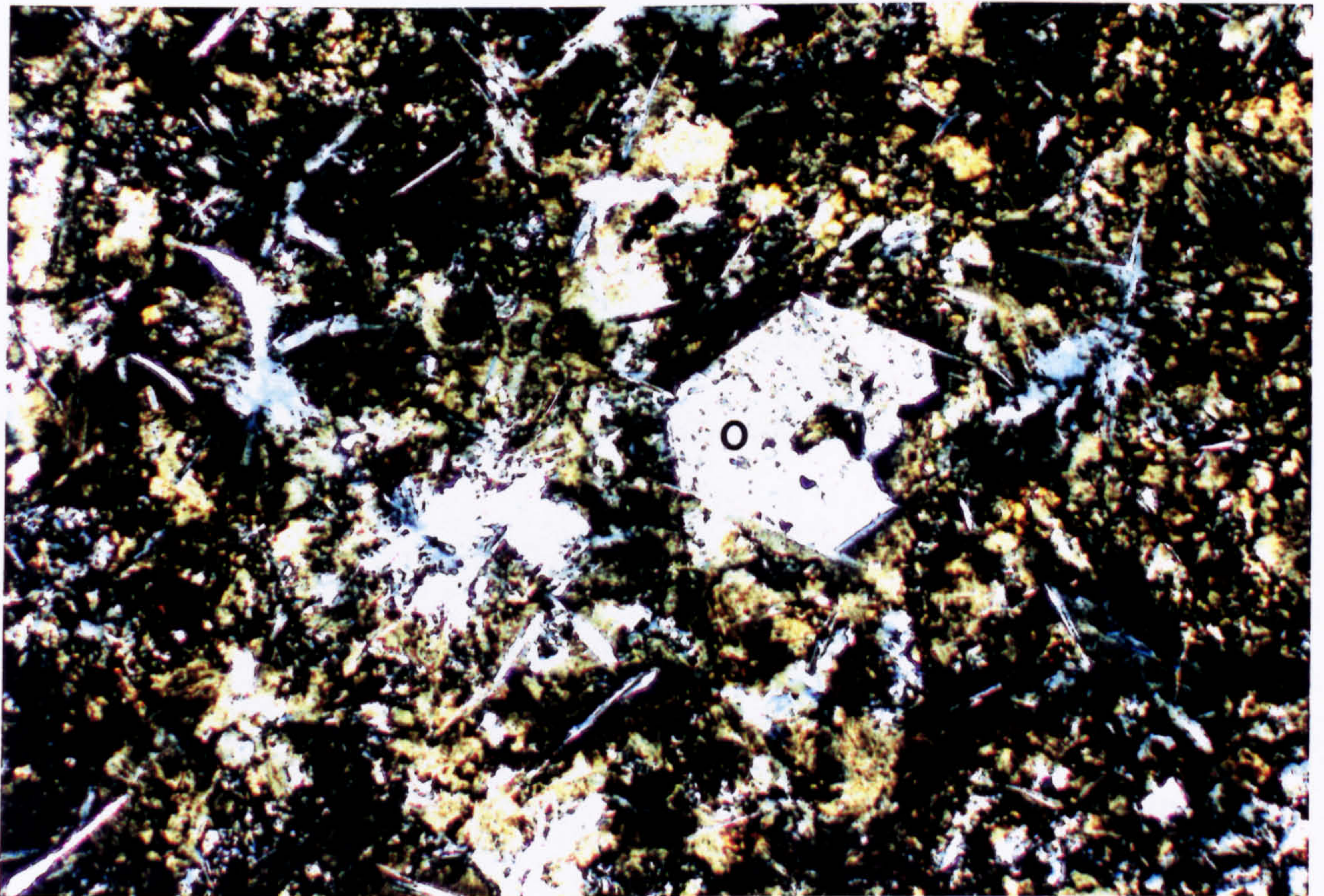


FIGURE 2.13

Group III rhyolite. Consists of an felsitic intergrowth of plagioclase (An₁₂), K-feldspar (Or₇₅) and quartz. Occasional phenocryst of oligoclase can be found (O). Rocks are highly altered, with feldspar commonly being replaced by calcite, epidote and sericite. (xpl; Field of view 0.8x1.2mm; Sample PGF1).

SAMPLE		PGF1				
TYPE	G	G	P	P	P	P
SiO ₂	65.10	65.50	65.62	66.05	65.94	65.08
TiO ₂	0.00	0.00	0.02	0.00	0.00	0.00
Al ₂ O ₃	21.53	21.84	21.62	21.58	21.66	22.16
FeO*	0.02	0.02	0.06	0.04	0.02	0.00
CaO	1.81	1.88	1.62	1.73	1.64	2.26
Na ₂ O	6.86	6.35	7.20	7.13	6.30	7.04
K ₂ O	0.06	0.07	0.14	0.11	0.05	0.09
TOTAL	95.37	95.66	96.27	96.64	95.60	96.63
FORMULA ON BASIS OF 32 OXYGENS						
Si	11.78	11.79	11.78	11.80	11.85	11.66
Ti	0.00	0.00	0.00	0.00	0.00	0.00
Al	4.59	4.63	4.57	4.54	4.59	4.68
Fe (ii)	0.00	0.00	0.01	0.01	0.00	0.00
Ca	0.35	0.36	0.31	0.33	0.32	0.44
Na	2.41	2.22	2.50	2.47	2.19	2.44
K	0.01	0.02	0.03	0.03	0.01	0.02
TOTAL	19.14	19.01	19.20	19.18	18.96	19.24
ENDMEMBER %						
Ab	86.84	85.41	87.97	87.38	87.04	84.30
Or	0.47	0.63	1.09	0.92	0.46	0.71
An	12.68	13.95	10.93	11.69	12.50	14.99

Table 2.9 Representative analyses of plagioclase from a Group III porphyritic rhyolite sheet. G=Groundmass; P=Phenocryst. All analyses crystal cores unless otherwise stated. Poor wt% and cation totals due to the pervasive alteration of the feldspar to sericite and calcite. Sample Numbers defined in Appendix II.

CHAPTER 3

WHOLE-ROCK MAJOR-ELEMENT GEOCHEMISTRY

3.1 Normative mineralogy and phase relationships

Representative whole-rock major- and trace-element data and Sr/Nd isotope analyses for the entire compositional range displayed by the LSSC are presented in *Table 3.1*. A complete listing of all the whole-rock major- and trace-element, and Sr/Nd isotope analyses for the LSSC are given in Appendix II. Discussion in this chapter is restricted to the major-element characteristics. In terms of their normative mineralogy, all rocks are hypersthene (hy) normative (4 - 28%), with most being oversaturated with respect to silica (quartz in the norm) (0 - 34%), and five samples (*i.e.* all Group I Basalts) being silica saturated (olivine normative) (3 - 10%).

It is important when evaluating the validity of petrologic conclusions based on normative mineralogy to eliminate the possibility that the trends seen are the result of hydrothermal alteration. Tilley and Muir (1962) suggested that with progressive alteration and leaching due to hydrothermal activity, the contents of H_2O^+ and Fe_2O_3 in basaltic rocks will increase, thus increasing the apparent silica saturation as a result of the excessive production of magnetite, releasing silica to produce other phases. They concluded that the Hebridean plateau magma types were all originally ne-normative, and that the hy-normative character of much of the published data was due to the analysis of hydrothermally-altered samples. However, later work by Thompson *et al.* (1972), and Ridley (1973) showed that fresh basalts from the BTVP range in silica-saturation from ne- to hy-normative,

SAMPLE:	ORB2	PGB9	PMBASE	TMB2	TILE1	TMB3	PM2B1
SiO ₂	48.29	50.31	50.93	51.27	52.38	52.63	53.06
TiO ₂	1.40	0.89	1.04	1.01	0.99	0.99	0.95
Al ₂ O ₃	13.75	14.96	15.16	14.53	14.77	15.05	14.43
Fe ₂ O ₃ *	15.37	11.15	10.82	11.67	11.19	11.06	10.90
MnO	0.25	0.18	0.21	0.18	0.18	0.21	0.17
MgO	6.29	7.75	7.10	7.01	7.30	6.43	6.54
CaO	11.53	11.80	11.40	10.92	10.66	9.60	10.05
Na ₂ O	2.76	2.59	2.98	2.77	2.92	2.64	2.78
K ₂ O	0.15	0.33	0.57	0.67	0.73	1.06	0.98
P ₂ O ₅	0.11	0.07	0.11	0.11	0.11	0.12	0.11
LOI	0.53	0.33	0.31	0.26	0.15	0.61	0.23
TOTAL	99.89	100.04	100.31	100.14	101.23	99.79	99.97
Mg#	0.29	0.41	0.40	0.38	0.40	0.37	0.38
Nb	2.0	2.3	3.9	3.8	4.5	7.6	5.4
Zr	84.6	65.8	89.4	94.0	96.2	133.1	114.3
Y	43.3	24.9	28.6	27.9	27.4	32.5	28.3
Sr	120.8	205.4	226.1	226.1	224.3	223.9	225.0
Rb	3.9	6.2	12.2	12.7	18.1	18.3	26.8
Th	3.5	2.6	3.4	3.5	2.3	6.2	3.2
Pb	1.4	2.6	2.6	3.2	4.8	6.8	5.1
Zn	117.9	90.8	83.7	103.4	144.0	111.8	121.8
Cu	179.7	105.4	77.1	73.7	71.6	27.7	65.1
Ni	49.0	76.0	58.9	52.3	52.8	11.9	48.7
Cr	73.1	351.8	242.9	224.0	232.6	41.2	206.7
V	364.0	295.8	321.0	297.7	295.5	273.8	270.5
Ba	151.6	183.1	270.7	280.1	288.8	297.2	356.6
Sc	51.3	51.2	49.1	45.2	47.9	47.6	44.8
La	2.77	5.97	8.72		10.96		
Ce	8.63	13.92	21.01		25.10		
Pr	1.36	1.71	2.58		2.92		
Nd	8.66	8.36	11.44		14.49		
Sm	3.22	2.20	2.78		2.99		
Eu	1.37	0.95	1.11		1.11		
Gd	5.33	3.19	3.80		3.83		
Dy	6.03	3.53	3.89		3.97		
Ho	1.44	0.82	0.90		0.91		
Er	3.98	2.31	2.50		2.52		
Yb	3.91	2.30	2.44		2.54		
Lu	0.63	0.37	0.39		0.41		
(⁸⁷ Sr/ ⁸⁶ Sr) _i	0.703756	0.707690	0.708464		0.709445		
(¹⁴³ Nd/ ¹⁴⁴ Nd) _i	0.512916	0.512167	0.511979		0.511932		
CIPW NORMS							
Ap	0.25	0.17	0.25	0.25	0.25	0.28	0.26
Il	2.66	1.70	1.98	1.92	1.88	1.88	1.81
Mt	2.92	2.12	2.36	2.22	2.13	2.11	2.08
Or	0.86	1.97	3.39	3.97	4.33	6.28	5.76
Ab	23.34	21.90	25.20	23.43	24.70	22.33	23.52
An	24.68	28.19	26.28	25.22	25.02	26.07	24.01
Di	26.48	24.46	24.22	23.24	22.29	17.12	20.68
Hy	6.89	11.92	8.54	15.27	16.52	21.01	19.32
Ol	10.47	6.63	7.23	3.60	3.14	0.00	0.00
C	0.00	0.00	0.00	0.00	0.00	0.00	0.00
Qtz	0.00	0.00	0.00	0.00	0.00	1.75	1.60
TOTAL	98.55	99.07	99.45	99.12	100.25	98.83	99.02

Table 3.1 Representative whole-rock major-, trace-element and isotope compositions of Group I basalts and basaltic andesites. Major-elements in wt%, trace-elements in ppm. All iron measured as Fe₂O₃. CIPW Norms calculated assuming Fe²⁺/Fe³⁺ ratio of 0.15 (after Brookes, 1976).
Mg# = MgO/(MgO + Fe₂O₃*). Sr and Nd isotope ratios age corrected to 58Ma.

SAMPLE:	KIB1	SFB2	RCB1	ORB1	SOB1	SFB3	PGB10
SiO ₂	53.28	54.02	54.06	54.28	54.86	55.32	56.18
TiO ₂	0.94	0.99	1.16	0.97	0.98	1.16	1.19
Al ₂ O ₃	14.64	14.66	14.29	14.71	14.78	14.60	14.46
Fe ₂ O ₃ *	11.29	11.21	11.62	10.84	10.60	10.08	9.83
MnO	0.18	0.20	0.18	0.18	0.18	0.16	0.14
MgO	6.30	5.78	5.06	5.50	5.59	4.62	4.52
CaO	9.36	8.74	8.39	9.16	8.76	8.37	8.06
Na ₂ O	2.98	2.94	2.91	2.58	2.73	2.82	2.70
K ₂ O	0.83	1.40	1.35	1.35	1.25	0.85	1.59
P ₂ O ₅	0.10	0.12	0.14	0.12	0.12	0.20	0.14
LOI	0.43	0.47	0.75	0.77	0.43	2.04	1.22
TOTAL	99.90	100.06	99.16	99.68	99.85	98.17	98.82
Mg#	0.36	0.34	0.30	0.34	0.35	0.31	0.32
Nb	4.1	7.3	7.4	7.3	7.0	9.0	8.4
Zr	105.1	132.9	145.4	134.5	136.9	148.7	156.2
Y	25.7	32.0	35.1	31.4	31.5	29.2	27.9
Sr	276.3	201.6	222.4	212.1	214.1	410.9	278.5
Rb	22.6	31.2	42.6	42.5	44.1	49.4	44.8
Th	4.6	6.1	7.4	6.7	7.0	6.0	6.1
Pb	5.3	7.6	8.1	7.0	7.7	9.9	9.5
Zn	103.5	99.6	104.0	109.0	95.5	110.0	162.7
Cu	42.6	29.9	32.3	23.3	25.8	31.5	38.2
Ni	23.1	11.2	14.3	12.1	11.5	18.1	22.1
Cr	68.0	34.6	42.8	39.3	39.2	77.0	89.7
V	298.6	274.4	209.0	256.4	258.4	276.7	261.2
Ba	312.6	425.2	455.0	783.9	362.7	504.2	458.2
Sc	43.0	44.4	43.2	41.1	44.8	32.5	35.6
La			19.32			21.05	
Ce			44.04			47.78	
Pr			5.01			5.41	
Nd			19.30			20.58	
Sm			4.31			4.29	
Eu			1.28			1.29	
Gd			4.96			4.58	
Dy			4.95			4.22	
Ho			1.15			0.95	
Er			3.12			2.55	
Yb			3.13			2.58	
Lu			0.50			0.42	
(⁸⁷ Sr/ ⁸⁶ Sr) _i			0.712282				
(¹⁴³ Nd/ ¹⁴⁴ Nd) _i			0.511986				
CIPW NORMS							
Ap	0.23	0.28	0.33	0.27	0.28	0.47	0.33
Il	1.79	1.89	2.21	1.85	1.87	2.20	2.27
Mt	2.15	2.13	2.21	2.06	2.02	1.92	1.87
Or	4.91	8.27	7.98	7.95	7.39	5.00	9.40
Ab	25.21	24.87	24.62	21.82	23.09	23.85	22.84
An	24.11	22.67	21.93	24.58	24.37	24.67	22.63
Di	17.89	16.46	15.58	16.63	15.11	12.87	13.61
Hy	20.64	19.86	18.69	18.58	19.23	16.88	15.86
Ol	0.00	0.00	0.00	0.00	0.00	0.00	0.00
C	0.00	0.00	0.00	0.00	0.00	0.00	0.00
Qtz	2.00	2.66	4.60	4.99	5.56	9.43	9.16
TOTAL	98.92	99.09	98.15	98.74	98.93	97.29	97.96

Table 3.1cont.

Representative whole-rock major-, trace-element and isotope compositions of Group I basaltic andesites. Major-elements in wt%, trace-elements in ppm. All iron measured as Fe₂O₃. CIPW Norms calculated assuming Fe²⁺/Fe³⁺ ratio of 0.15 (after Brookes, 1976). Mg#=MgO/(MgO+Fe₂O₃*). Sr and Nd isotope ratios age corrected to 58Ma.

SAMPLE:	KBB3	KBB5	KMB1	CUPI1	PCRPI1	PCRPI2	TVPI1
SiO ₂	61.88	63.97	66.43	64.84	64.84	64.34	64.63
TiO ₂	1.02	1.02	1.00	1.11	1.13	1.09	1.11
Al ₂ O ₃	14.09	14.31	13.38	13.21	13.29	13.10	13.33
Fe ₂ O ₃ *	8.15	7.61	6.48	8.05	8.42	8.17	8.35
MnO	0.13	0.15	0.09	0.13	0.14	0.13	0.11
MgO	2.64	2.08	1.37	1.01	1.12	1.03	0.91
CaO	4.79	3.53	2.49	3.27	2.92	3.15	2.91
Na ₂ O	3.70	3.15	3.16	3.96	3.23	3.32	3.23
K ₂ O	1.61	3.33	3.83	2.62	3.57	3.47	3.52
P ₂ O ₅	0.17	0.18	0.21	0.30	0.30	0.30	0.30
LOI	2.11	0.74	1.56	1.46	1.08	1.53	1.09
TOTAL	100.28	100.06	100.01	99.97	100.05	99.63	99.49
Mg#	0.24	0.21	0.17	0.11	0.12	0.11	0.10
Nb	13.9	15.9	16.5	18.3	18.3	17.5	18.2
Zr	254.3	277.4	303.9	366.7	368.0	358.6	365.8
Y	37.6	29.1	41.8	56.9	69.8	54.9	57.1
Sr	278.6	234.1	156.2	218.9	207.3	210.0	207.7
Rb	82.5	108.0	100.8	108.8	108.9	106.4	106.3
Th	9.1	10.5	10.2	10.7	10.4	10.9	10.6
Pb	17.2	17.4	17.6	19.4	17.7	16.8	17.8
Zn	116.8	118.4	103.2	111.2	137.8	128.4	132.3
Cu	21.3	13.5	14.4	12.1	16.3	12.2	13.6
Ni	12.2	6.0	6.0	6.5	8.0	5.7	4.9
Cr	49.5	27.9	23.0	2.2	2.2	6.4	5.2
V	211.6	192.3	103.1	45.0	47.1	47.9	49.3
Ba	689.7	751.1	934.0	999.2	935.2	933.1	929.3
Sc	24.1	22.3	20.4	20.2	19.4	20.5	26.7
La			41.45	48.16	54.55		48.66
Ce			94.03	108.75	121.26		108.81
Pr			10.40	12.44	13.63		12.13
Nd			36.78	45.79	50.58		44.70
Sm			7.32	9.19	10.26		9.07
Eu			1.54	2.18	2.26		2.16
Gd			7.08	9.35	10.91		9.12
Dy			6.11	8.46	9.81		8.32
Ho			1.39	1.93	2.26		1.89
Er			3.61	5.07	5.96		4.98
Yb			3.71	5.11	5.98		5.01
Lu			0.61	0.83	0.99		0.81
(⁸⁷ Sr/ ⁸⁶ Sr) _i			0.714106	0.715742	0.71573		0.715803
(¹⁴³ Nd/ ¹⁴⁴ Nd) _i			0.511846	0.511839	0.51183		0.511807
CIPW NORMS							
Ap	0.39	0.41	0.49	0.71	0.71	0.70	0.71
Il	1.94	1.94	1.90	2.10	2.15	2.07	2.12
Mt	1.55	1.45	1.23	1.53	1.60	1.56	1.59
Or	9.48	19.69	22.64	15.50	21.09	20.46	20.76
Ab	31.30	26.65	26.73	33.49	27.32	28.08	27.32
An	17.09	15.06	10.99	10.52	11.21	10.61	11.49
Di	4.68	1.09	0.00	3.20	1.10	2.64	0.84
Hy	13.59	13.32	10.54	9.97	11.81	10.51	11.29
Ol	0.00	0.00	0.00	0.00	0.00	0.00	0.00
C	0.00	0.00	0.00	0.00	0.00	0.00	0.00
Qz	17.44	19.06	23.37	20.78	21.24	20.77	21.57
TOTAL	97.46	98.66	97.88	97.80	98.23	97.39	97.67

Table 3.1cont. Representative whole-rock major-, trace-element and isotope compositions of Group II rocks. First three analyses are of non-porphyrritic andesites, and final four analyses are of porphyritic dacites. Major-elements in wt%, trace-elements in ppm. All iron measured as Fe₂O₃. CIPW Norms calculated assuming Fe²⁺/Fe³⁺ ratio of 0.15 (after Brookes, 1976). Mg# = MgO/(MgO+Fe₂O₃*). Sr and Nd isotope ratios age corrected to 58Ma.

SAMPLE:	PGF1	RCF1	RCF2	RCF3	RCF4
SiO ₂	71.80	70.13	70.38	71.61	65.95
TiO ₂	0.66	0.73	0.73	0.71	0.80
Al ₂ O ₃	12.23	12.17	12.19	12.24	12.34
Fe ₂ O ₃ *	4.91	5.26	5.52	5.04	6.63
MnO	0.08	0.09	0.05	0.03	0.09
MgO	0.39	0.68	0.80	0.85	1.39
CaO	1.47	1.97	1.48	1.14	2.87
Na ₂ O	3.23	2.76	2.89	2.72	2.48
K ₂ O	4.31	4.15	4.08	4.20	3.53
P ₂ O ₅	0.17	0.19	0.19	0.19	0.18
LOI	0.65	1.58	1.70	1.16	2.80
TOTAL	99.90	99.71	100.01	99.89	99.06
Mg#	0.07	0.11	0.13	0.14	0.17
Nb	17.9	17.9	17.9	17.8	16.3
Zr	364.2	355.5	351.6	357.5	318.3
Y	49.2	48.4	47.5	46.1	45.4
Sr	122.1	132.3	98.2	90.7	140.2
Rb	154.4	136.4	131.1	137.0	117.4
Th	12.0	11.4	12.6	11.5	10.3
Pb	24.0	22.2	21.8	23.2	20.6
Zn	133.4	89.2	88.0	97.6	139.3
Cu	9.1	10.7	11.1	10.6	17.5
Ni	4.2	3.6	4.0	4.1	7.7
Cr	0.0	0.0	1.1	0.0	11.7
V	14.6	23.4	28.6	23.3	67.4
Ba	914.1	866.8	876.7	816.2	822.3
Sc	14.6	17.7	17.1	19.1	17.9
La	47.55	48.05		46.03	41.94
Ce	108.25	109.90		104.83	94.92
Pr	12.23	12.33		11.78	10.25
Nd	43.28	43.58		41.38	35.28
Sm	8.31	8.53		8.16	7.39
Eu	1.34	1.41		1.40	1.36
Gd	7.86	8.17		7.87	7.45
Dy	7.04	7.04		7.00	6.25
Ho	1.59	1.58		1.59	1.45
Er	4.18	4.13		4.19	3.79
Yb	4.24	4.19		4.30	4.00
Lu	0.68	0.68		0.70	0.68
(⁸⁷ Sr/ ⁸⁶ Sr) _i	0.720319	0.717169		0.719059	0.717622
(¹⁴³ Nd/ ¹⁴⁴ Nd) _i	0.511853	0.511886		0.511862	0.511862
CIPW NORMS					
Ap	0.40	0.45	0.44	0.44	0.41
Il	1.25	1.39	1.41	1.38	1.52
Mt	0.93	1.00	1.06	0.98	1.31
Or	25.45	24.50	24.30	25.22	20.84
Ab	27.32	23.35	24.64	23.38	20.98
An	6.14	8.51	6.17	4.51	12.11
Di	0.04	0.00	0.00	0.00	0.82
Hy	6.54	7.64	8.26	7.81	11.67
Ol	0.00	0.00	0.00	0.00	0.00
C	0.00	0.00	0.02	0.03	0.00
Qtz	30.77	30.83	31.55	34.57	26.60
TOTAL	98.84	97.67	97.84	98.32	96.26

Table 3.1cont. Representative whole-rock major-, trace-element and isotope compositions of Group III rhyolites. Major-elements in wt%, trace-elements in ppm. All iron measured as Fe₂O₃. CIPW Norms calculated assuming Fe²⁺/Fe³⁺ ratio of 0.15 (after Brookes, 1976). Mg# = MgO/(MgO+Fe₂O₃*). Sr and Nd isotope ratios age corrected to 58Ma.

whilst preserving petrographic features of alkali olivine basalts, such as groundmass olivine. Thompson *et al.* (1972, 1980) also showed that the chemical diversity was not a result of variable hydrothermal metamorphism, by demonstrating a strong correlation between silica-saturation and elements known to be essentially immobile during this type of alteration, such as Ti, P and Zr. *Figure 3.1* is a plot of H_2O^+ (measured as loss-on-ignition) against silica-saturation for the LSSC. Although a small number of the Group I basaltic andesites have high H_2O^+ values (>1.5), and therefore may be slightly affected by hydrothermal alteration, this diagram reveals that there is no well-constrained correlation between these two parameters, and it is therefore concluded that the normative mineralogy of the LSSC can be used to formulate valid petrologic conclusions. Moreover, analyses of lavas from the Loch Scridain area (Beckinsale *et al.*, 1978; Kerr, 1994) report H_2O^+ values in excess of 3.7. This suggests that the LSSC has not been as pervasively hydrothermally altered compared to the plateau lavas, a fact which is very often evident in the field.

Figure 3.2 shows the normative nepheline-olivine-diopside-hypersthene-quartz projection (after Thompson, 1982) derived from the basalt tetrahedron (inset) (Yoder & Tilley, 1962). The low pressure (1 atm). and high pressure (9 kbar), anhydrous cotectics for olivine + plagioclase + Ca-pyroxene in equilibrium with basaltic liquid are shown. The LSSC data for Group I rocks define a trend which falls just below, but generally parallels, the 1 atm. cotectic. However, several samples fall well below the 1 atm. cotectic in *Figure 3.2*. This equilibrium migrates away from the diopside apex with rising pressure (Morrison *et al.*, 1985) and, judging from experimental data (Thompson, 1982), such samples were probably in pre-emplacement cotectic equilibrium at about 2-3 kbar, equivalent to a depth of about one-third of the thickness of the continental crust. The low pressure cotectic terminates with the crystallization of Ca-poor clinopyroxene (\pm Fe-Ti oxides) from a tholeiitic basaltic andesite magma (Morrison *et al.*, 1985).

Campbell (1985) provides compelling evidence that the appearance of a Ca-poor pyroxene (pigeonite or orthopyroxene) before Ca-clinopyroxene (diopside or augite) on the liquidus of many continental tholeiitic suites is due to primitive magmas assimilating sialic crust or derived partial melts en route to the surface. This is the opposite case to the majority of oceanic tholeiitic suites, where augite crystallizes

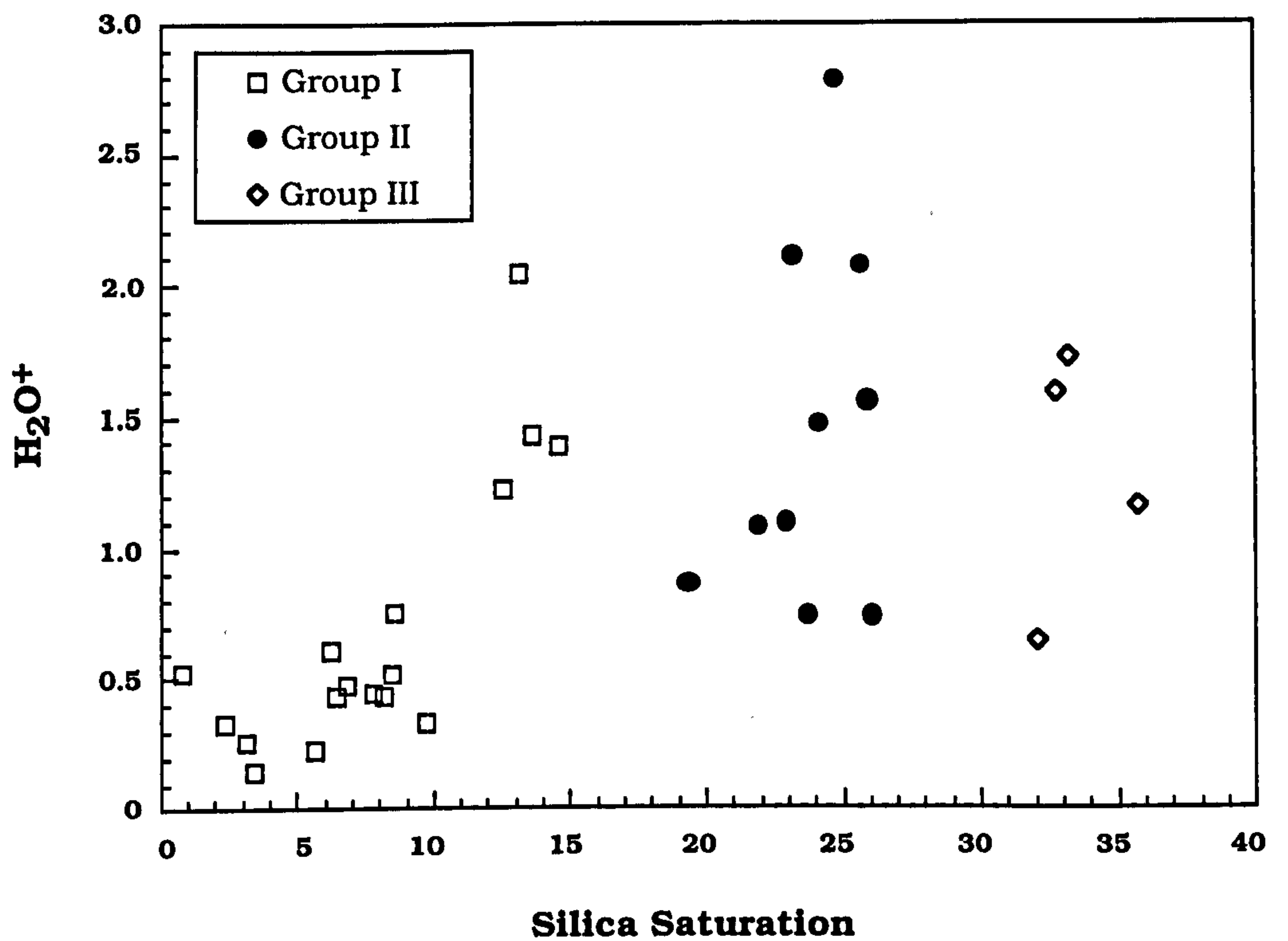


FIGURE 3.1 Plot of H_2O^+ (measured as loss-on-ignition) vs. Silica Saturation (Normative quartz plus that recast from hypersthene). The lack of coherent trends throughout the suite suggests that the whole-rock geochemistry of the sheets has not been greatly influenced by late-stage hydrothermal alteration.

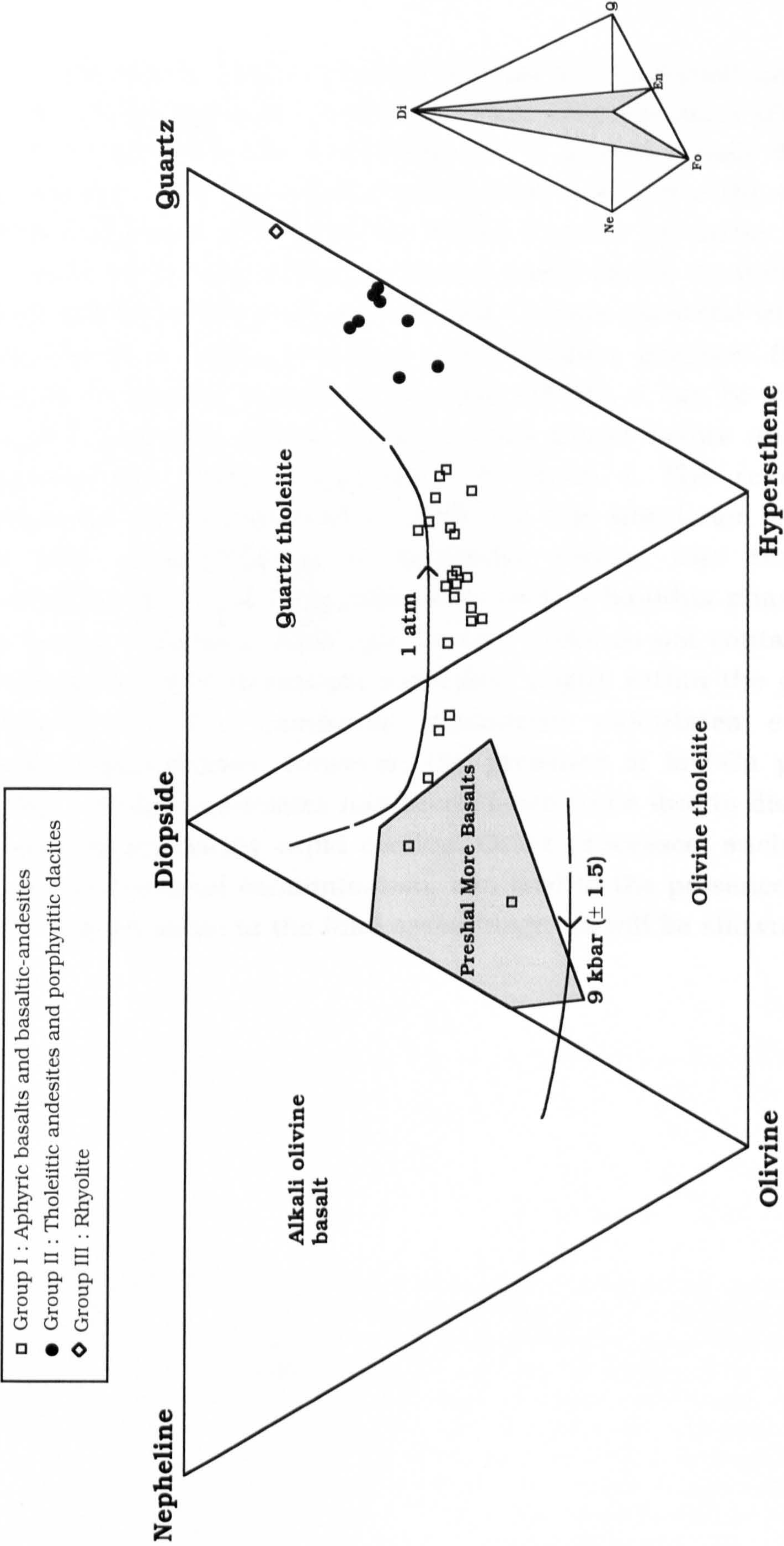


FIGURE 3.2 CIPW normative di, hy, ol, ne and q for members of the LSSC. The field occupied by the Preshal More Basalt magma type, together with anhydrous cotectic curves at 1 atm and 9 kbars for olivine + plagioclase + clinopyroxene + basaltic liquid (Thompson, 1982) are shown. Inset shows the relationship of the diagram to the surfaces in the Yoder-Tilley basalt tetrahedron (Yoder & Tilley, 1962).

before pigeonite. The mechanism behind the Campbell argument can be illustrated using the system forsterite-diopside-silica (*Figure 3.3*). If point A represents the composition of a primitive melt derived from the mantle, pure fractional crystallization will follow the path ABCD. Ca-rich pyroxene will crystallize before Ca-poor pyroxene. If, however, the melt assimilates siliceous crustal melts before crystallization, the liquid will follow the path AEFCD, and Ca-poor pyroxene will crystallize first. Using a computer-based crystallization program (based on a method devised by Nathan & Van Kirk (1978)), it can be shown that a Ca-poor pyroxene should be a liquidus phase before augite for the more-evolved basaltic andesites of Group I. The results of the simulation are summarised in *Table 3.2*. The simulation was only run for 30% crystallization to minimise errors, and through this crystallization period, magnetite was never a liquidus phase in any of the Group I samples. Although Group I rocks do not contain pigeonite or enstatite, they do contain sub-calcic augite within the groundmass (*Chapter 2*). The computer simulation calculates *equilibrium* fractionating phases. However, the presence of low-Ca pyroxene in Group I basaltic andesites has been shown to be due to disequilibrium crystallization during rapid cooling. Other processes, such as magma mixing and crustal contamination, can lead to the presence or absence of low-Ca pyroxene in the final assemblage, as will be shown later.

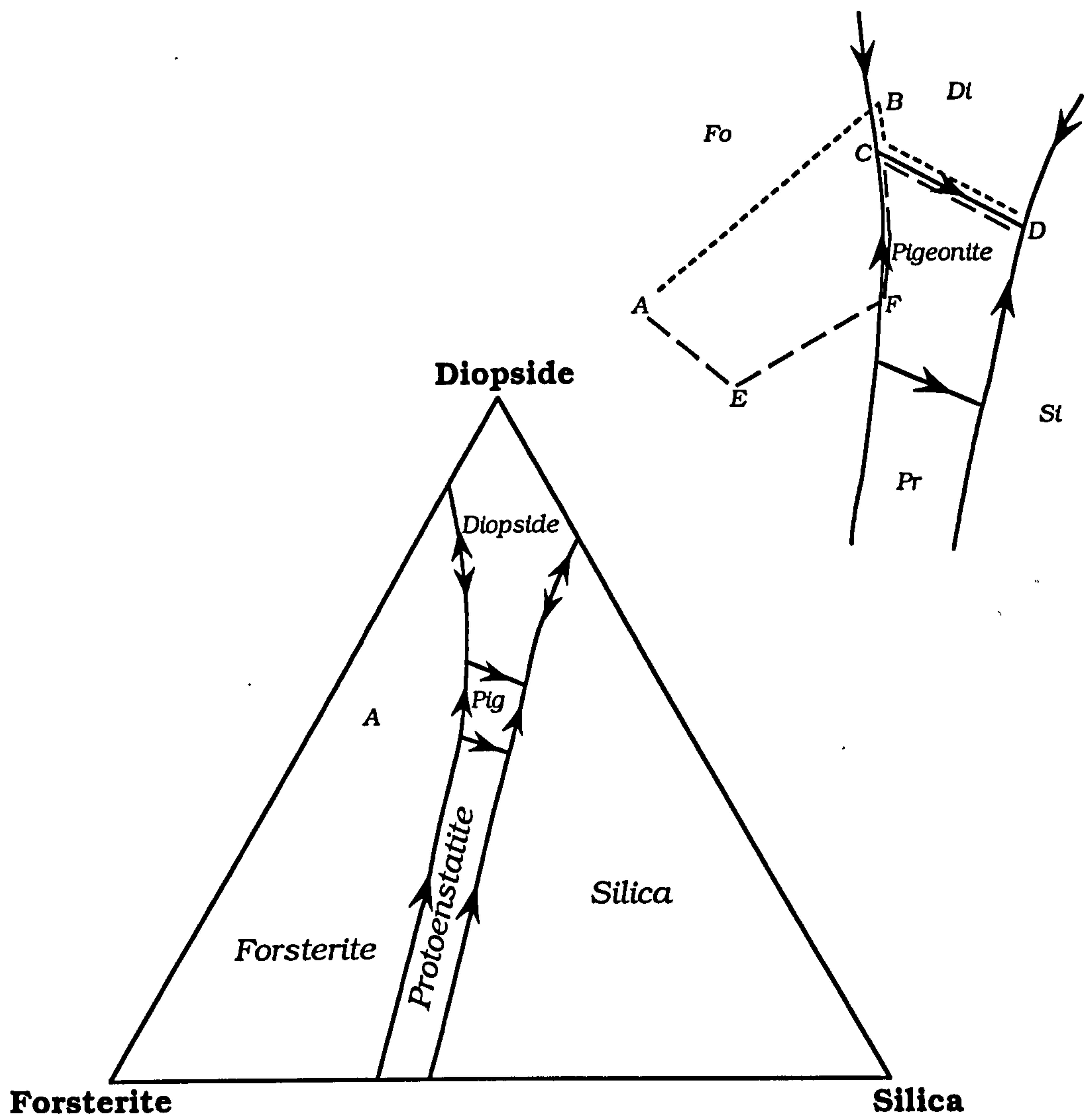


FIGURE 3.3 Equilibrium 1atm. phase diagram of the system diopside-forsterite-silica showing only the fields in which various minerals appear as primary phases. Point A represents a primary mantle melt which fractionates away from the forsterite apex under normal conditions. A melt contaminated with siliceous country-rock will move towards the silica apex prior to fractionation. The two crystallization paths are shown diagrammatically in the enlargement. Contaminated melts will precipitate pigeonite before diopside, whereas, uncontaminated melts will crystallize diopside before pigeonite. (modified from Campbell, 1985)

	Liquidus Temperatures			
SAMPLE	Olivine	Plagioclase	Augite	Ca-poor PX
PGB9	1193.7°C Fo79	1196.1°C An 76-73	1197.2°C Di 85-84	1194.3°C En 85-82
TMB2	1181.6°C Fo 65	1180.3°C An 72-65	1182.2°C Di 83-75	1180.2°C En83-74
RCB2	1123.0°C Fo 60	1153.8°C An 63-54	1132.6°C Di 74-69	1152.0°C En 77-65
PGB10	- -	1160.0°C An 65-52	1143.7°C Di 78-71	1139.8°C En 75-67

Table 3.2 Computer simulation of 1atm. closed-system fractional crystallization (after Nathan & Van Kirk, 1978). The model takes a whole-rock major-element composition and calculates equilibrium liquidus phases. These phases are then removed from the parent composition in small % steps. The new liquid composition is calculated, and the process iterates until a chosen finishing point. The model used was run up to 30% crystallization to minimize cumulative errors. The liquidus temperatures, and the composition of calculated equilibrium phases are shown.

In order to examine the phase relationships displayed by a suite of fine-grained basaltic rocks, many workers have used diagrams based on normative projections in the basalt tetrahedron. For example, one of the most widely used projections is the olivine-clinopyroxene-plagioclase diagram of Cox and Bell (1972). One of the disadvantages of using such normative projections is that evolved compositions cannot be adequately represented within the basalt tetrahedron. Using the criteria suggested by Cox and Bell (1972) for the screening of samples before projection in their diagram (presented below in *Table 3.3*), not one of the LSSC samples would satisfy all of the requirements, and many would fail on all counts.

(a)	Normative plagioclase to be at least as calcic as An ₅₀
(b)	The ratio $\text{FeO} + \text{Fe}_2\text{O}_3 / \text{MgO} + \text{FeO} + \text{Fe}_2\text{O}_3 < 0.7$
(c)	Wt% K ₂ O contents to be less than 1%
(d)	Normative quartz > 10 to be avoided

Table 3.3 Criteria for screening specimens before plotting within the normative projection olivine-clinopyroxene-plagioclase; Cox & Bell (1972).

Grove *et al.* (1982) provide a phase diagram based on low-pressure melting experiments on a basalt-andesite-dacite-rhyolite suite of volcanics from Medicine Lake, California. This diagram has the advantage over most normative projections in that both parental basic compositions and residual silicic liquids can be plotted on the same diagram, and the entire fractionation history of a suite of volcanic rocks can be examined. Although the diagram was designed mainly for use with calc-alkaline suites, Grove & Baker (1984) have also utilised it to explain the difference between tholeiitic and calc-alkaline differentiation trends. The plagioclase-saturated phase diagram with low-pressure cotectics and reaction curves is presented in *Figure 3.4a*. It is essentially a modification of O'Hara's (1968) CMAS projection. Whole-rock analyses in wt% are converted to molecular proportions, and the mineral components calculated as shown in *Figure 3.4a*. Three of the curves in the diagram are reaction curves and are denoted by a double arrow. The projected phase diagram also has two reaction points (A and B) where olivine reacts with the liquid to form augite + pigeonite + plagioclase and orthopyroxene + pigeonite + plagioclase, respectively. These two reaction points require that the olivine-pigeonite-plagioclase reaction curve has a thermal divide (TD).

As a first example, consider the crystallization of an olivine-normative tholeiitic liquid whose bulk composition lies at OT in the pseudoternary projection. Under equilibrium conditions, OT precipitates olivine + plagioclase as liquidus phases and the residual liquid composition moves away from the olivine apex until it reaches the augite-olivine-plagioclase cotectic. Here, augite starts to crystallize and the liquid follows the cotectic to point A, at which point olivine reacts with the liquid to form augite + pigeonite + plagioclase.

Composition OT would crystallize completely at point A under equilibrium conditions. However, during fractional crystallization, where all phases are continually removed from contact with the liquid, derivative liquids can move away from point A down the pigeonite-augite-plagioclase cotectic. Further fractional crystallization drives residual liquids towards the pigeonite-augite-plagioclase-quartz point, C.

As a second example, composition CA, a quartz-normative andesite, would crystallize olivine and plagioclase under equilibrium conditions and derivative liquids would move towards the olivine-orthopyroxene-plagioclase reaction curve. Here, olivine reacts with the liquid to form orthopyroxene, and liquids move down the curve towards reaction point B. At this point, olivine reacts to produce pigeonite + orthopyroxene + plagioclase, until all olivine is removed from the solid assemblage. The liquid composition then follows the orthopyroxene-pigeonite-plagioclase reaction curve, orthopyroxene reacts with the liquid and pigeonite and plagioclase precipitate until all the orthopyroxene is removed. The liquid then moves through the pigeonite + plagioclase primary phase volume to the pigeonite + augite + plagioclase cotectic, and moves along this curve towards silicic derivatives.

During fractional crystallization, the liquid line of descent again begins with olivine + plagioclase crystallization. When the liquid reaches the olivine-orthopyroxene-plagioclase reaction curve, since all the olivine has been removed from reaction with liquid, continued fractional crystallization drives the liquid away from orthopyroxene through the orthopyroxene + plagioclase primary phase volume to the orthopyroxene-pigeonite-plagioclase reaction curve. Orthopyroxene is removed during fractionation, and compositions move off the curve away from pigeonite into the pigeonite + plagioclase primary phase volume. Finally, the pigeonite-augite-plagioclase boundary is reached and the liquid moves to silica-enriched residual compositions.

Processes such as magma-mixing, assimilation of crustal material and combined assimilation and fractional crystallization (AFC) will have dramatic effects on the course of crystallization of parental magmas. A parent basic magma (e.g. PM basalt) magma injected into the crust will produce partial melts of rhyolitic composition from metapelitic material. Thus, assimilation of this melt will drive liquids towards the silica-rich cotectic, as shown by the schematic vector in *Figure 3.4b*.

Crystallization of the parent magma must accompany assimilation to provide the heat necessary to melt the surrounding country-rock. The result is a combined assimilation and fractional crystallization vector. At reaction point A, AFC moves bulk compositions into the pigeonite + plagioclase primary phase volume. Mixing of more primitive liquids lying on the olivine-augite-plagioclase cotectic with more evolved liquids lying below reaction point A, will produce intermediate compositions which lie in the augite + plagioclase primary phase volume (Walker *et al.*, 1979). This is shown by the mixing vectors in Figure 3.4b.

Figure 3.4c shows the data from the LSSC Groups I and II projected into the plagioclase-saturated phase diagram olivine-clinopyroxene-silica (Grove *et al.*, 1982). It has previously been stated that it is believed that the LSSC basic magmas may have last equilibrated at between 2-3kbar (Page 46). The effect of increasing pressure under anhydrous conditions in the system forsterite-diopside-silica and in natural basalts, is to decrease to size of the olivine primary phase volume and to expand the orthopyroxene and augite volumes. The opposite effect is seen under conditions of H₂O saturation (Grove & Baker, 1984). However, from data presented by Grove & Baker (1984) for the positions of the cotectics at 5kbar, it is evident that at a pressure of 2-3kbar the shifting of the cotectics will be minimal when compared to the 1atm cotectics.

None of the projected samples approach compositions which may represent parental basic liquids. However, those samples which lie near the olivine-augite join could represent liquids derived via the fractional crystallization of olivine + plagioclase from a parent magma; this possibility is further investigated when the fractional crystallization hypothesis for Group I specimens is tested using least-squares modelling techniques. Many Group I samples fall on the augite-pigeonite-plagioclase cotectic, and therefore could be derived via fractional crystallization of the less-evolved liquids. Those samples which fall well within the augite + plagioclase primary phase volume could be produced by the mixing of less-evolved and evolved liquids from Group I. Those samples which fall within the pigeonite + plagioclase primary phase volume (many Group I samples and all of Group II) are possibly derived from mixing of basaltic melts and silicic liquids, *i.e.* the rhyolites of Group III.

FIGURE 3.4 (a) Plagioclase saturated Olivine-Clinopyroxene-Quartz projection at 1atm; after Grove *et al.* (1982). Single arrows on liquidus surfaces represent simple cotectic relationships. Double arrows define reaction curves. Thermal divide on Olivine-Pigeonite surface denoted by (o). Compositions OT = Olivine tholeiite, CA = Calc-alkaline andesite discussed in text.

The projection scheme is calculated by converting Wt% oxides into mole%. Alkalis and alumina are converted to $\text{KO}_{0.5}$, $\text{NaO}_{0.5}$ and $\text{AlO}_{1.5}$. Mineral components are calculated as follows :

$$\text{SUM} = \text{SiO}_2 - \text{CaO} - 2(\text{KO}_{0.5} + \text{NaO}_{0.5}) + \text{Cr}_2\text{O}_3 + \text{TiO}_2$$

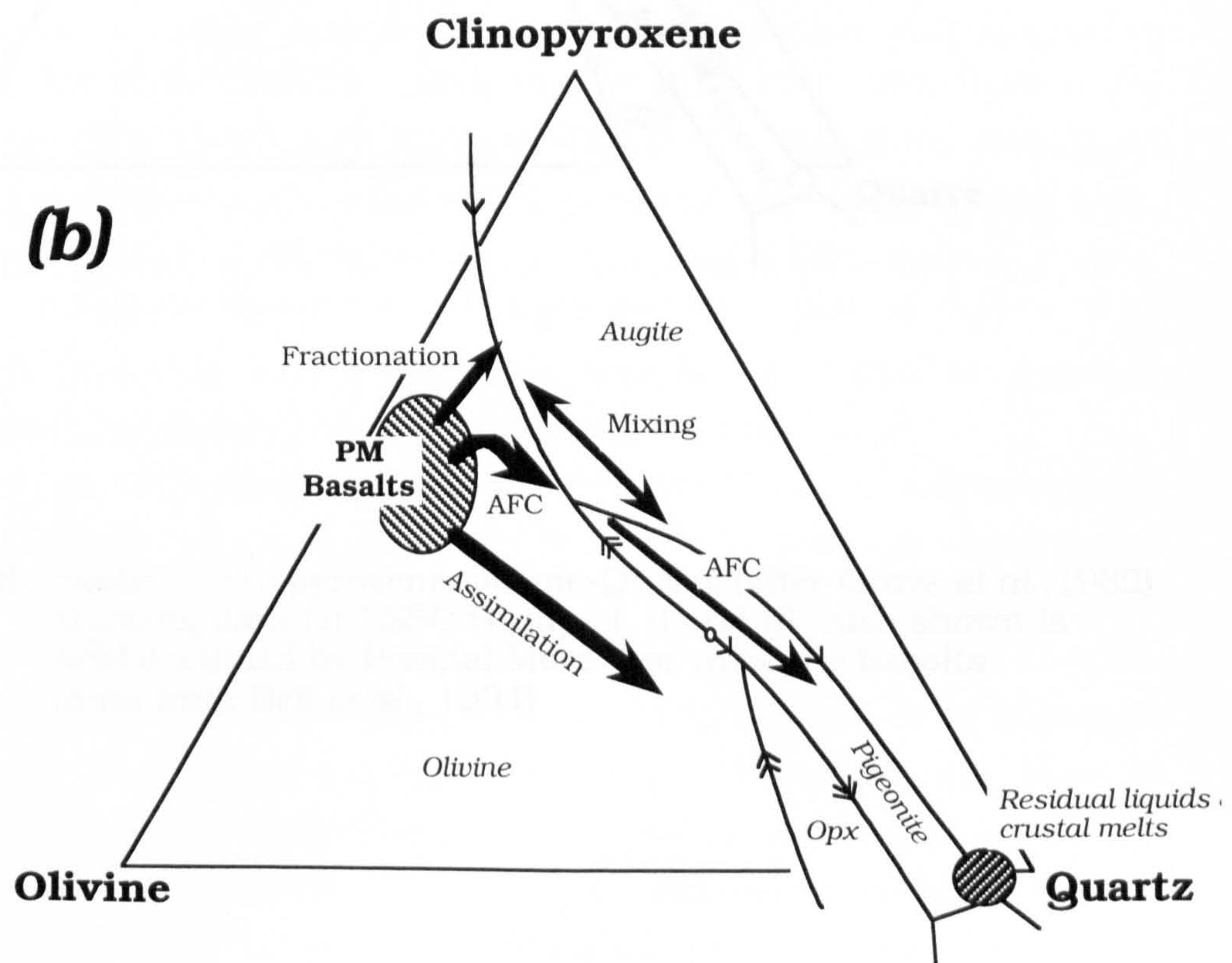
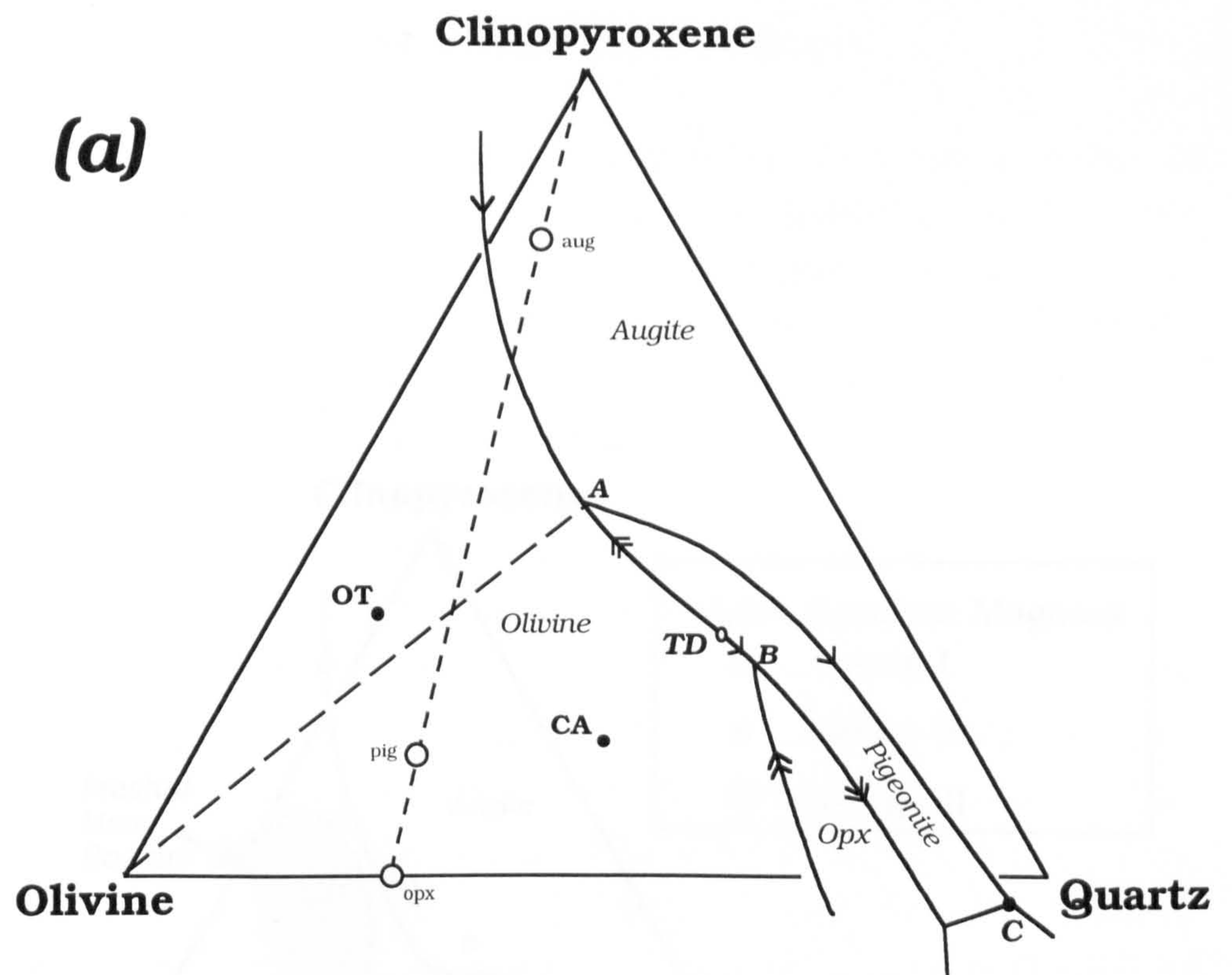
$$\begin{aligned} \text{Qtz} = & (\text{SiO}_2 - 0.5 (\text{FeO} + \text{MgO}) - 1.5 \text{CaO} - 1.25 \text{AlO}_{1.5} \\ & - 2.75 (\text{NaO}_{0.5} + \text{KO}_{0.5}) + \text{Cr}_2\text{O}_3 + 0.5 \text{TiO}_2) / \text{SUM} \end{aligned}$$

$$\text{Plag} = 1/2 (\text{AlO}_{1.5} + \text{NaO}_{0.5} - \text{KO}_{0.5}) / \text{SUM}$$

$$\begin{aligned} \text{Oliv} = & 1/2 (\text{FeO} + \text{MgO} + 1/2 (\text{AlO}_{1.5} - \text{KO}_{0.5} - \text{NaO}_{0.5}) \\ & - \text{CaO} - 2 \text{TiO}_2 - \text{Cr}_2\text{O}_3) / \text{SUM} \end{aligned}$$

$$\text{Cpx} = \text{CaO} - 1/2 \text{AlO}_{1.5} + 1/2 (\text{KO}_{0.5} + \text{NaO}_{0.5}) / \text{SUM}$$

FIGURE 3.4(b) System Cpx-Ol-Qtz (Grove *et al.*, 1984) with schematic fractionation, AFC, assimilation and mixing vectors.



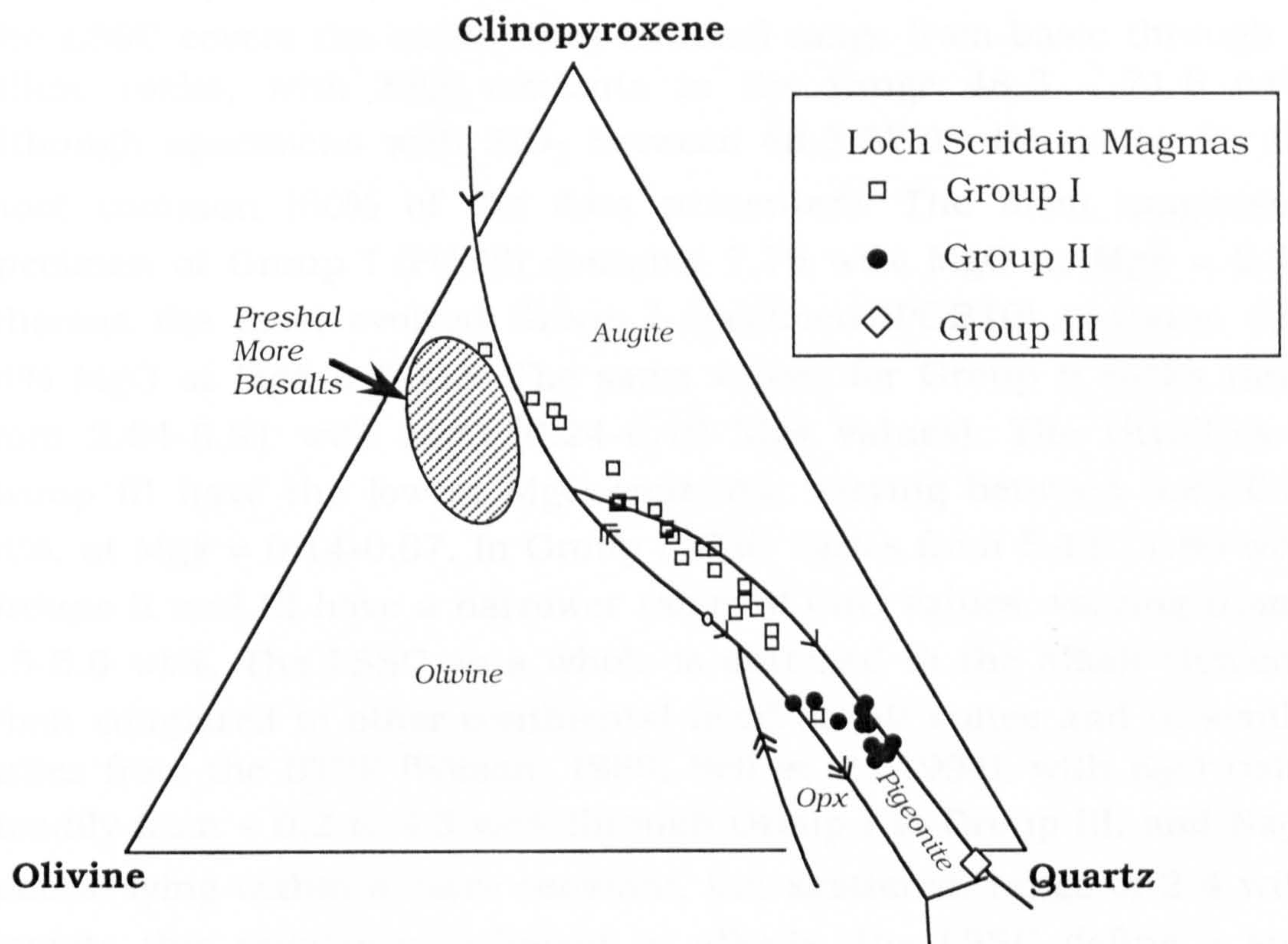


FIGURE 3.4 (c) System Clinopyroxene-Olivine-Quartz (after Grove *et al.*, 1982) showing data for LSSC Groups I, II and III. Also shown is field occupied by Preshal More type tholeiitic basalts (data from Bell *et al.*, 1994)

3.2 Whole-rock major-element data.

The variations in major-element geochemistry through a suite of related rocks are best displayed on diagrams involving each of the major-element oxides plotted against an index of fractionation, such as wt% SiO₂ or Mg# ($\text{Mg\#} = \text{MgO} / \text{MgO} + \text{FeO} + \text{Fe}_2\text{O}_3$). These diagrams are presented in *Figures 3.5a* through to *3.5r*, with rocks from Groups I, II, and III plotted with different symbols.

The LSSC covers the entire compositional range from basic through to silicic rocks, with SiO₂ contents in the range 48.3 - 71.6 wt%, although specimens with SiO₂ between 48.3-57.0 wt% are by far the most common (60% of the data presented). The most magnesian specimen of Group I (PGB9) contains 7.75 wt% MgO at Mg# = 0.41, whereas the most evolved Group I specimen (PGB10) contains 4.52 wt% MgO at Mg# = 0.315. The same values for Group II rocks range from 2.64-0.91 wt% MgO (0.24-0.10 Mg# values). The rhyolites of Group III have the lowest MgO contents, varying between 0.85-0.39 wt%, at Mg# = 0.14-0.07. In Group I, CaO varies from 5.49-11.80 wt%; Groups II and III have a narrower range of CaO values, varying from ~ 1.5-5.0 wt%. The LSSC as a whole is enriched in the alkali elements when compared to other continental flood basalt suites and to similar suites from the BTVP (Wilson, 1989; Bell *et al.*, 1994), with K₂O rising steadily from ~ 0.2 to 4.3 wt% through Group I to Group III, and Na₂O generally lying within a more constant, but scattered, range of 2-4 wt%. Despite this relative enrichment in alkalis, the LSSC define a sub-alkaline or tholeiitic trend on the K₂O *vs.* SiO₂ plot of *Figure 3.6*. However, in terms of iron-enrichment trends the LSSC is perhaps atypical when compared with other tholeiitic suites.

On a Fe₂O₃* *vs.* SiO₂ diagram (*Figure 3.5c*), the Group I magmas show relatively constant iron contents until SiO₂ = ~ 54 wt%, at which point iron depletion indicates a change in the fractionating assemblage. One sample (ORB2) has an anomalously high Fe₂O₃* content at 15.37 wt%, as well as having the lowest SiO₂ content (48.29 wt%). It is however, not the most magnesian at 6.29 wt% MgO. Although the rock is petrographically reasonably fresh, with little or no alteration of the feldspars and clinopyroxene. However, the clinopyroxene is in places, haematite stained. This alteration is small in total amount, but is disseminated throughout the specimen. This may explain the

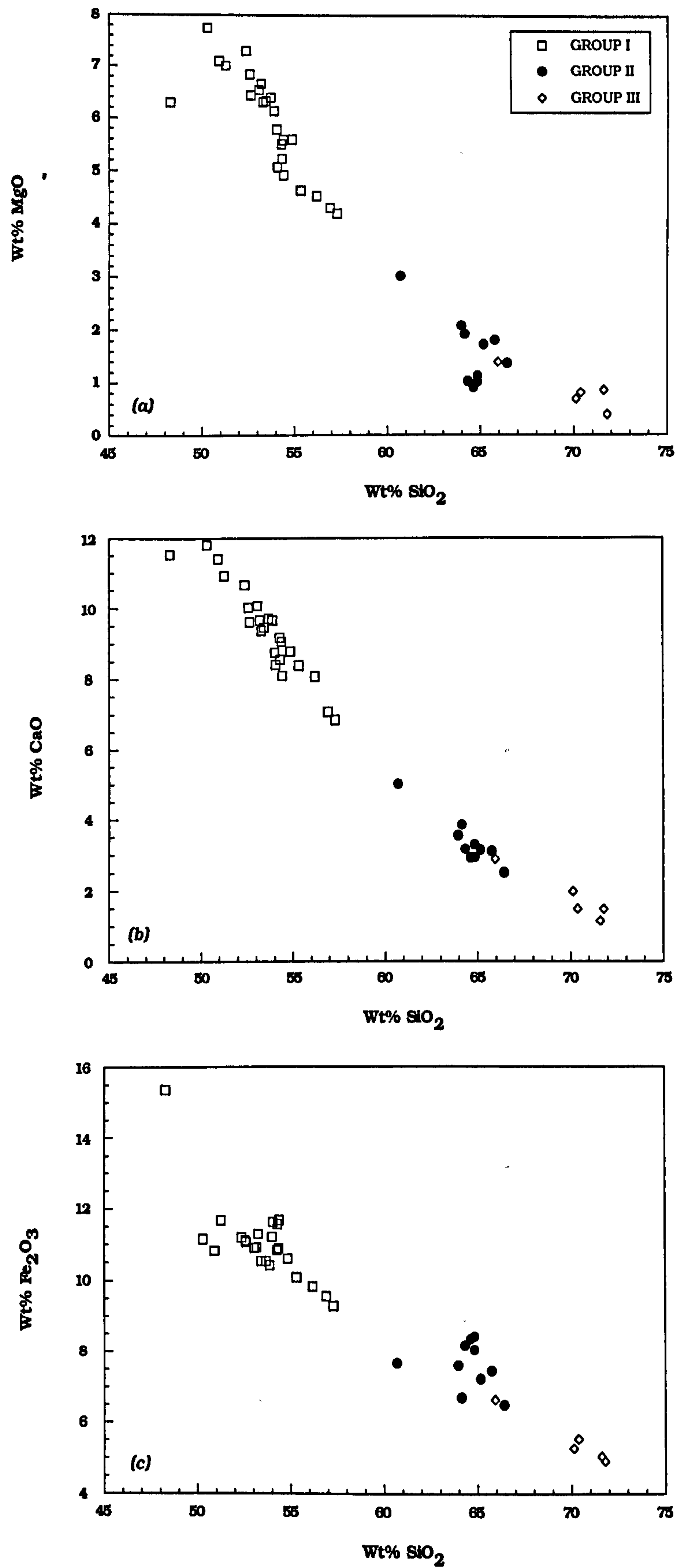


FIGURE 3.5 Variation of the major-elements within the LSSC.

(a) MgO vs. SiO_2

(b) CaO vs. SiO_2

(c) Fe_2O_3^* vs. SiO_2

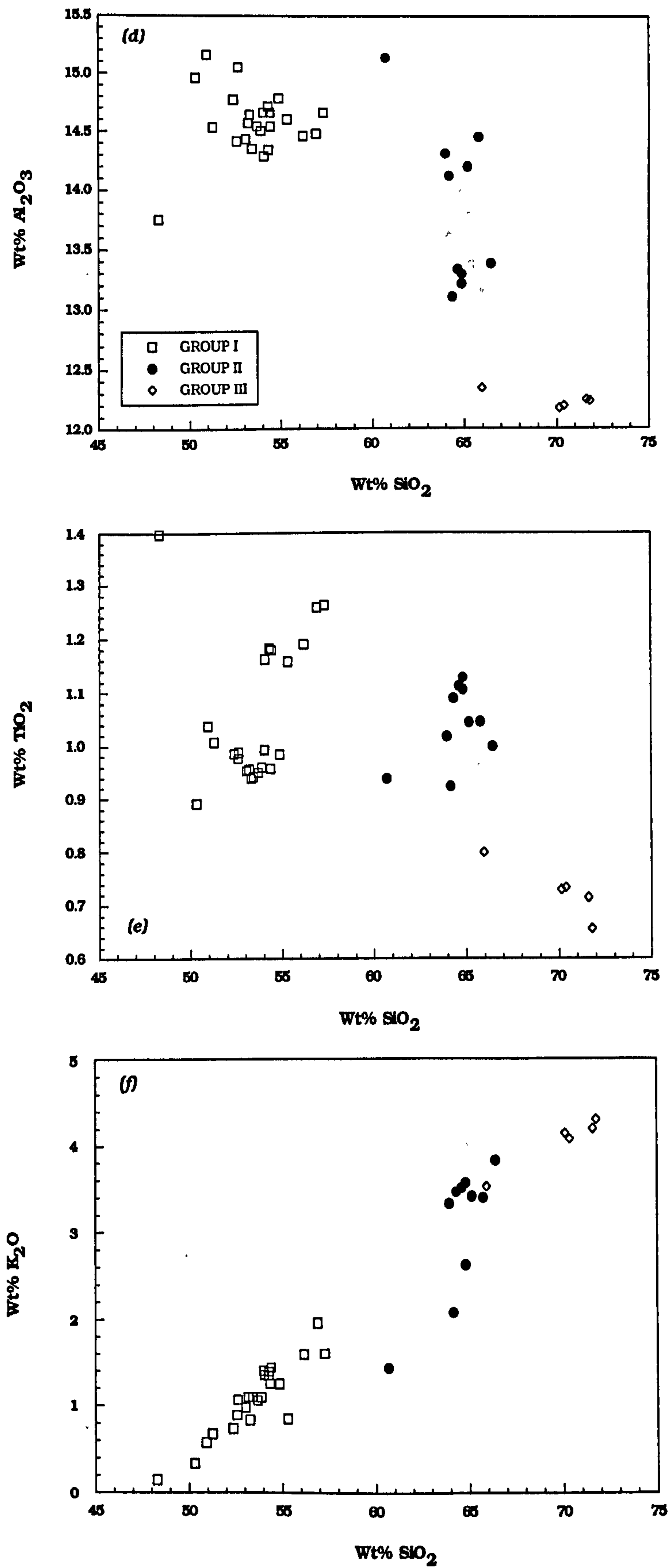


FIGURE 3.5 Variation of the major-elements within the LSSC.

(d) Al_2O_3 vs. SiO_2

(e) TiO_2 vs. SiO_2

(f) K_2O vs. SiO_2

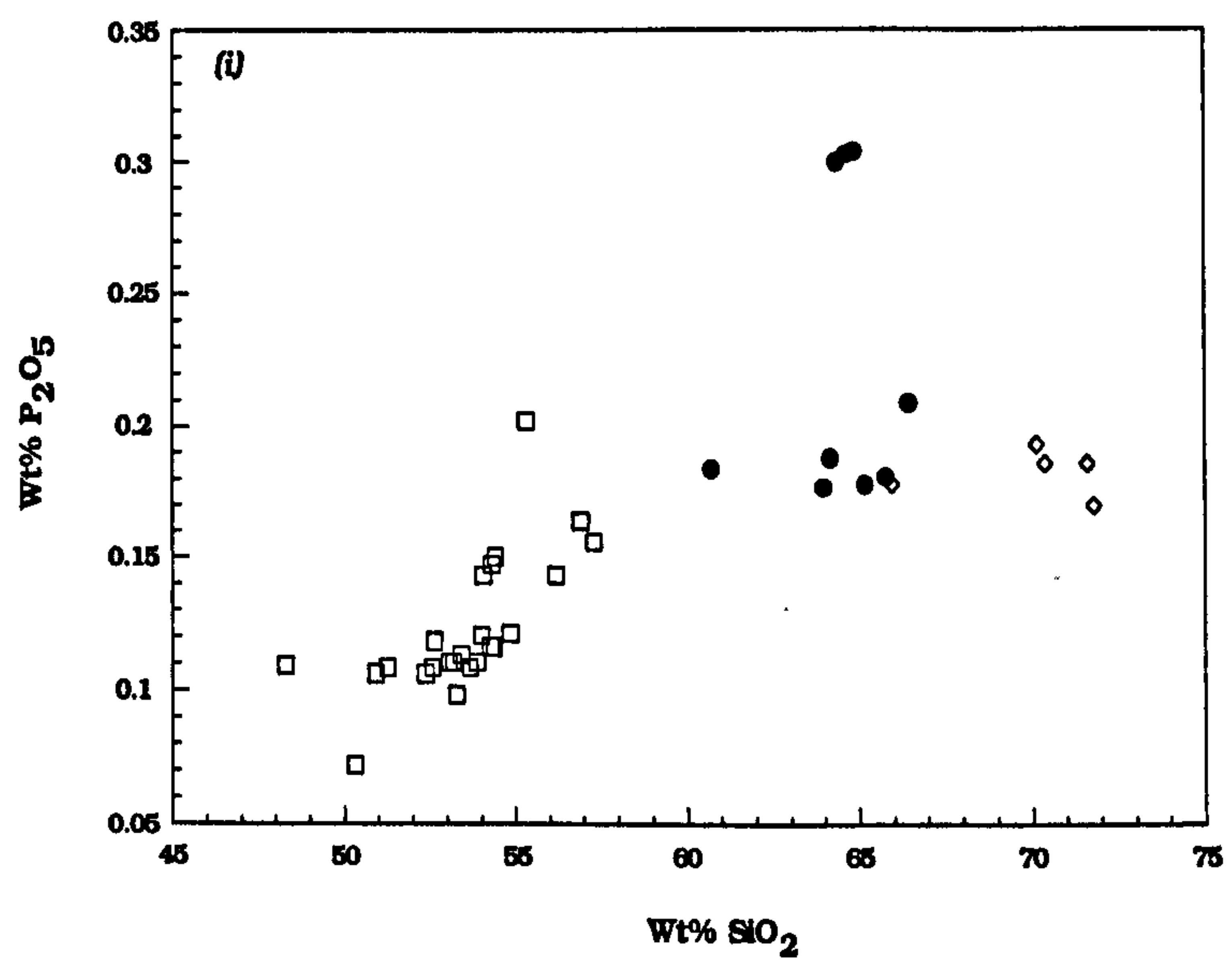
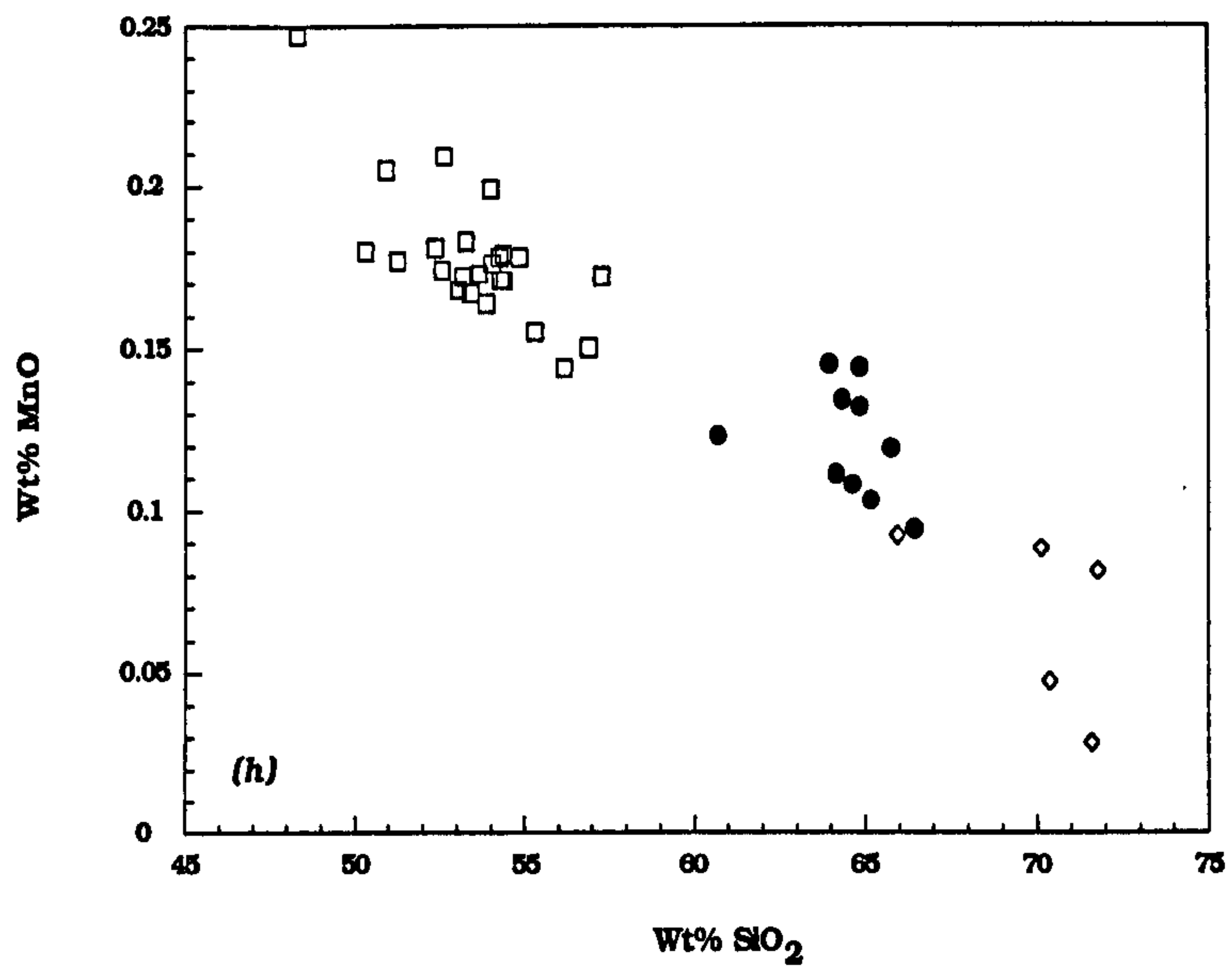
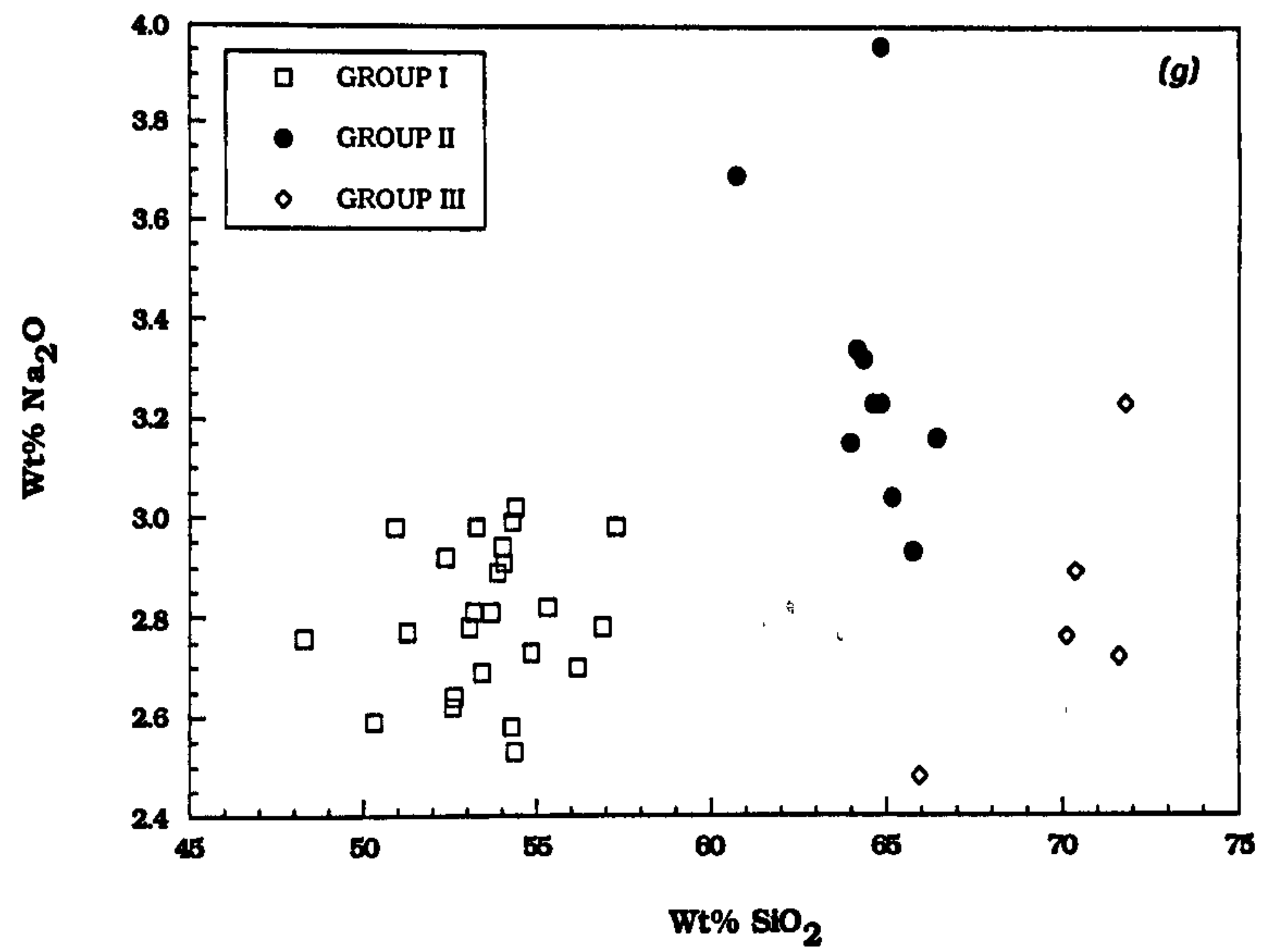


FIGURE 3.5 Variation of the major-elements within the LSSC.

(g) Na₂O vs. SiO₂

(h) MnO vs. SiO₂

(i) P₂O₅ vs. SiO₂

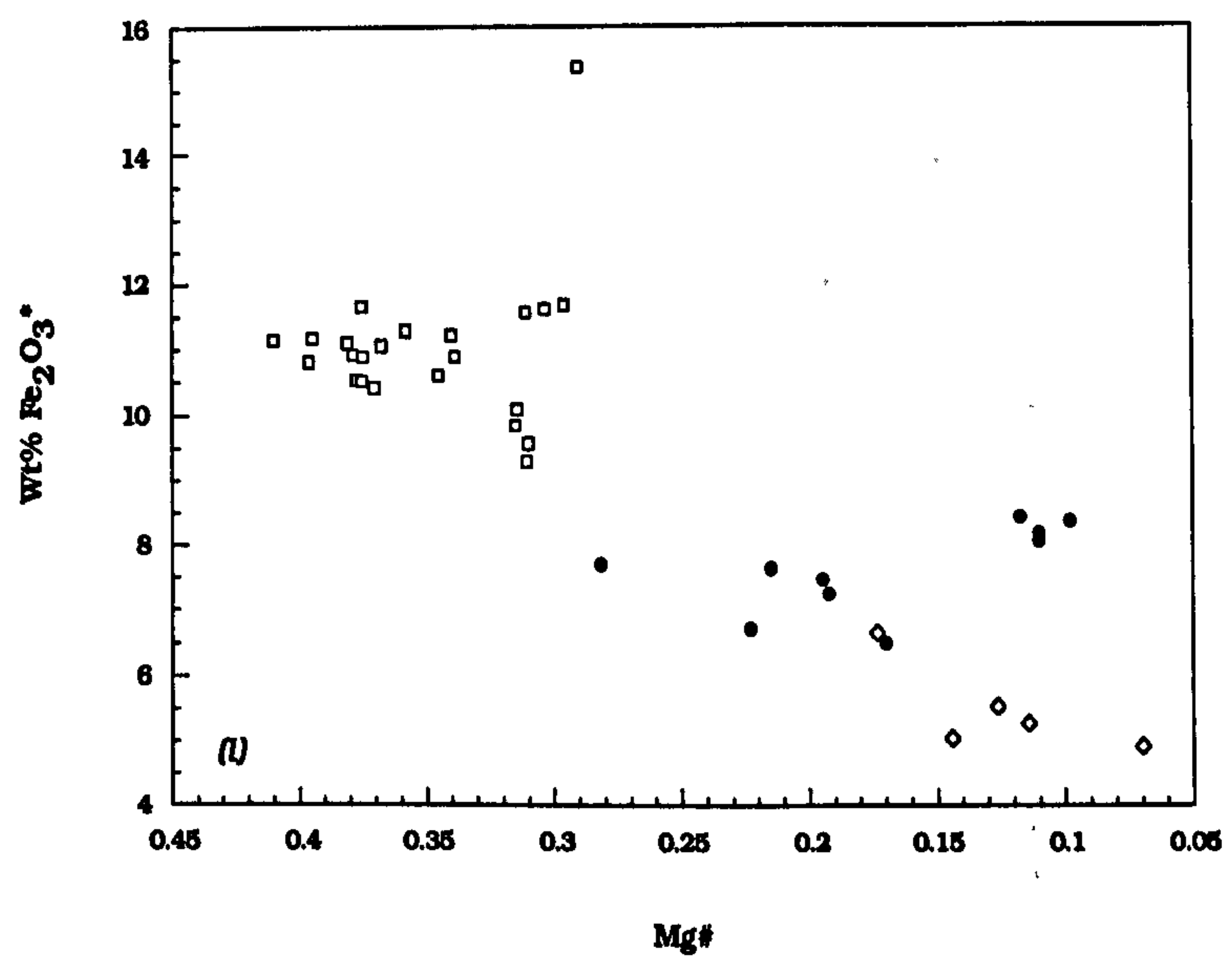
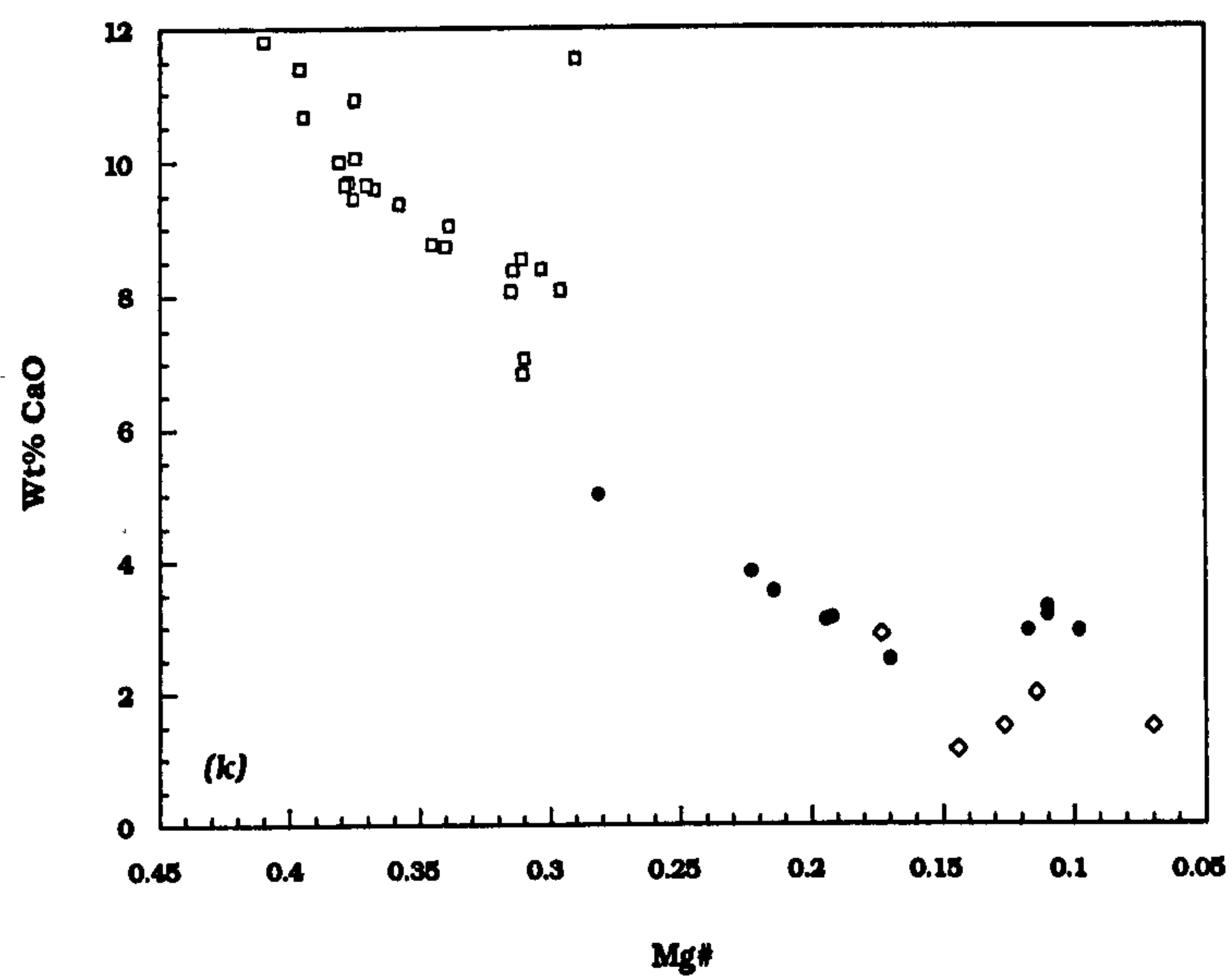
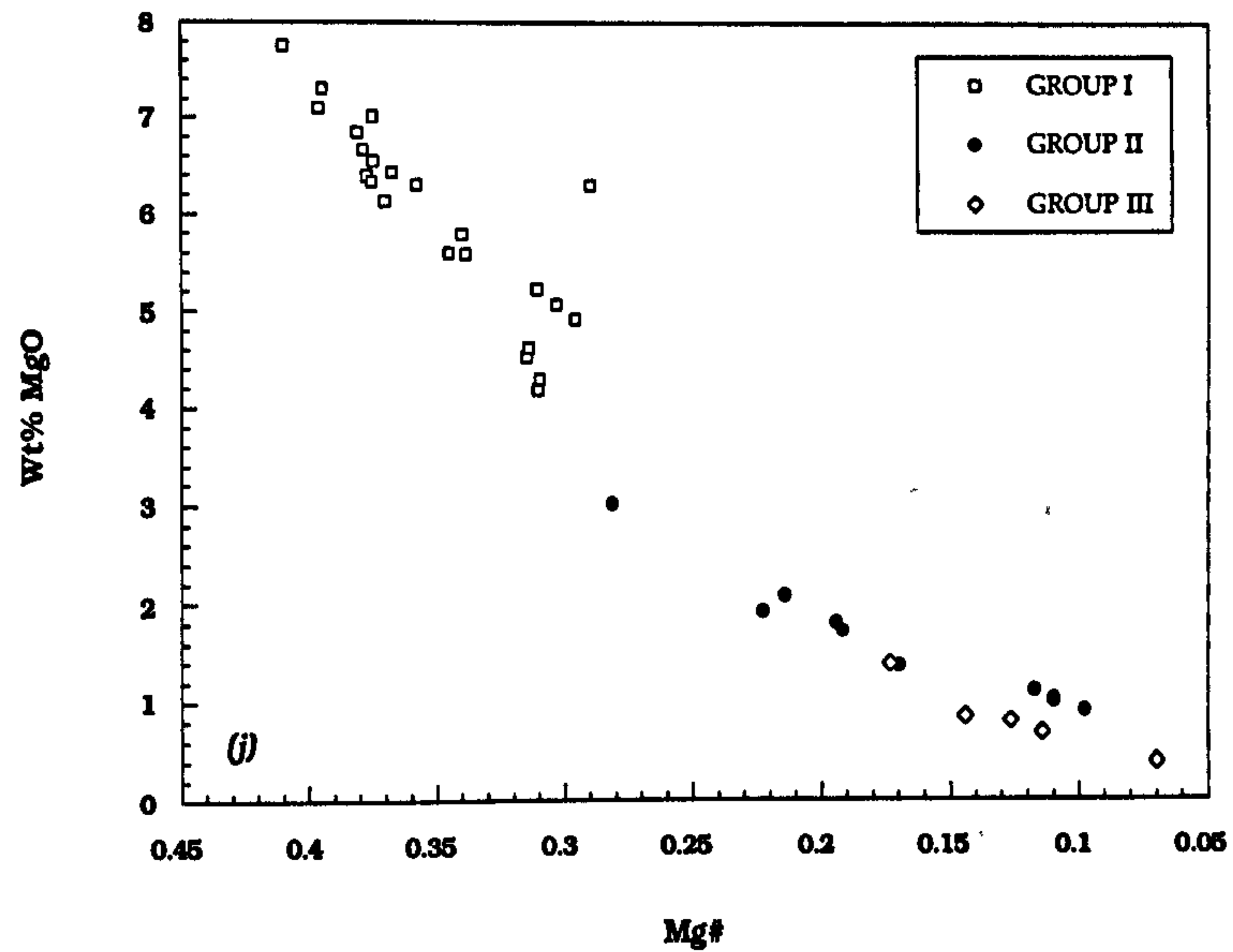


FIGURE 3.5 Variation of the major-elements within the LSSC.

(j) MgO vs. Mg#
(k) CaO vs. Mg#
(l) Fe₂O₃ vs. Mg#

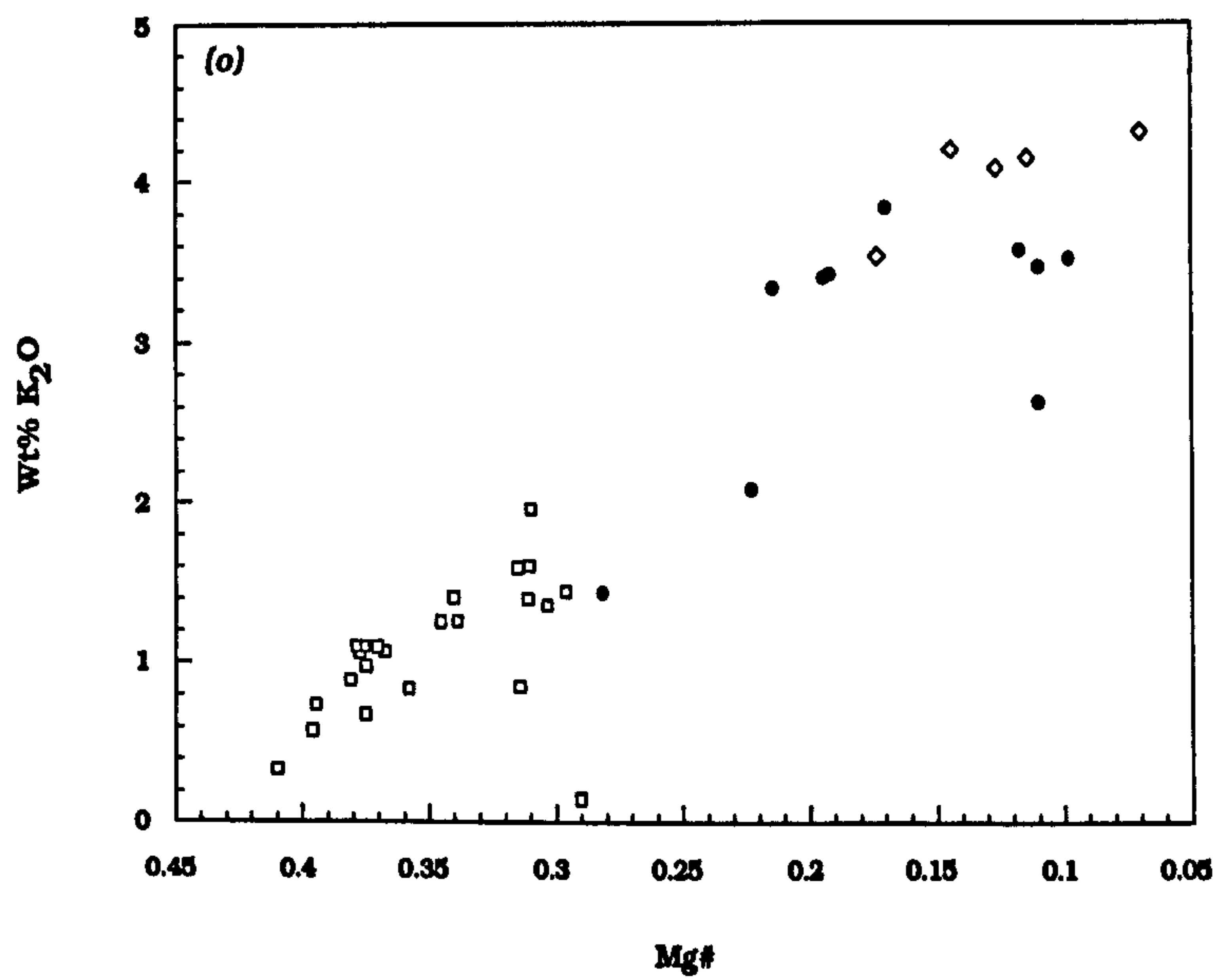
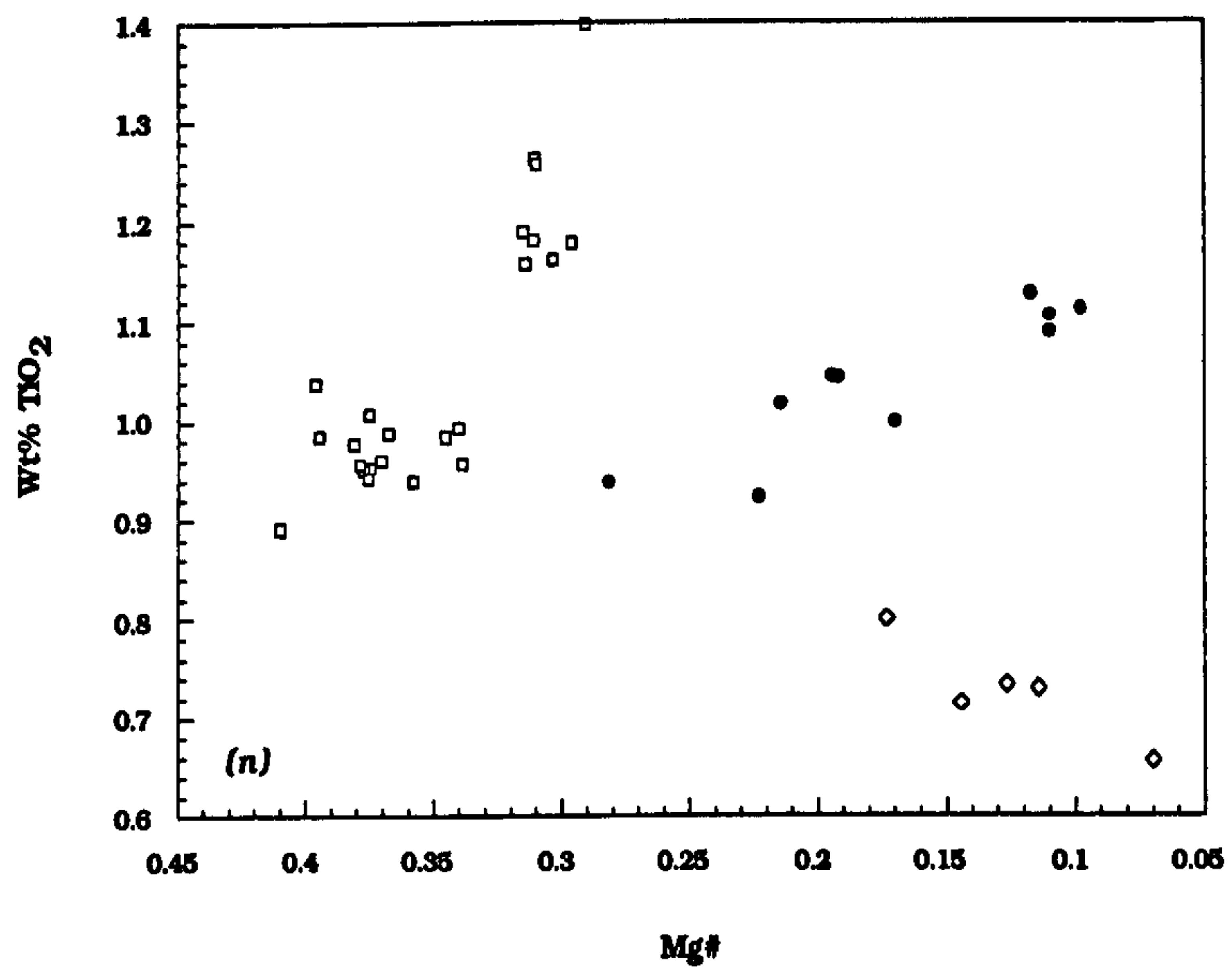
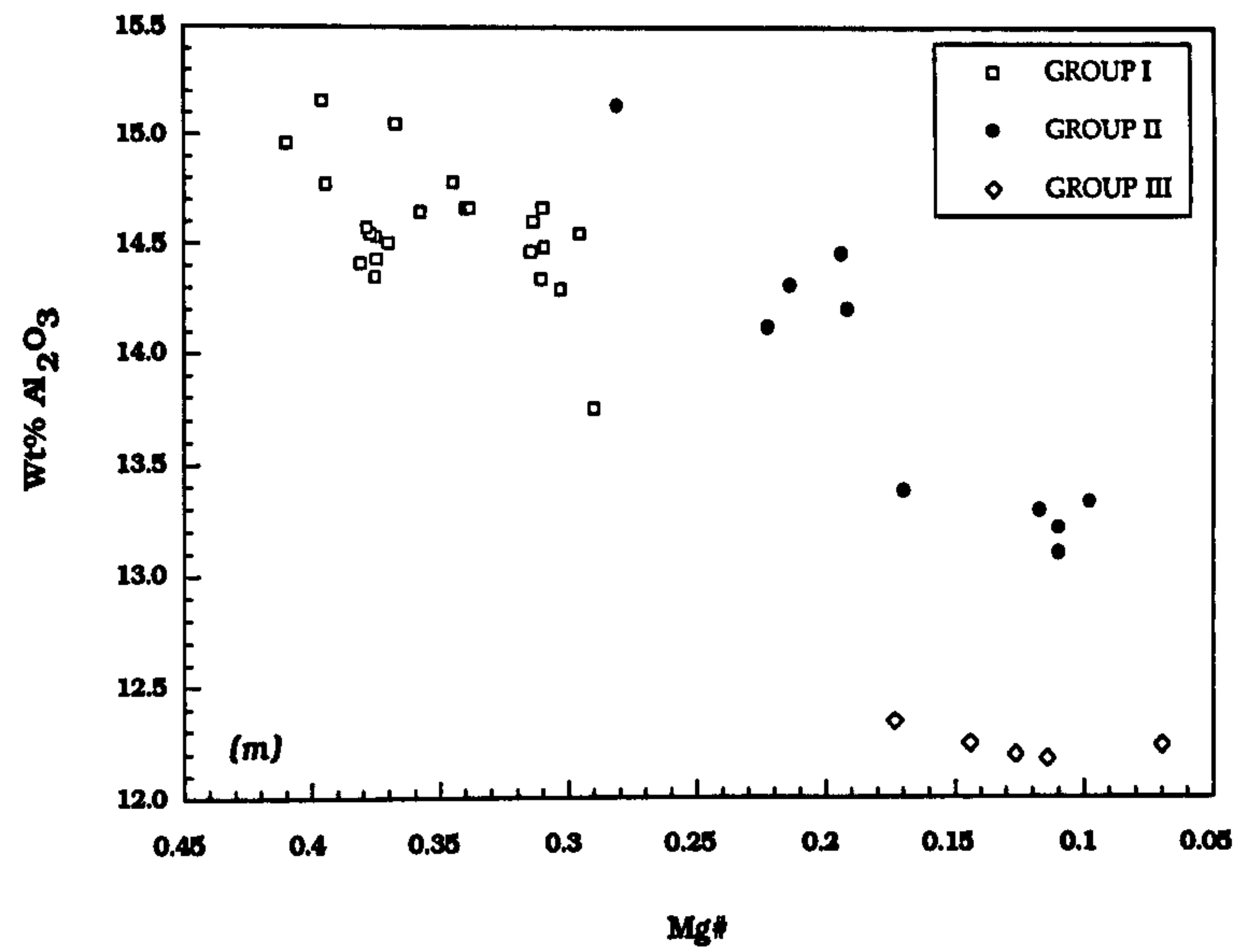


FIGURE 3.5 Variation of the major-elements within the LSSC.

(m) Al_2O_3 vs. Mg\#

(n) TiO_2 vs. Mg\#

(o) K_2O vs. Mg\#

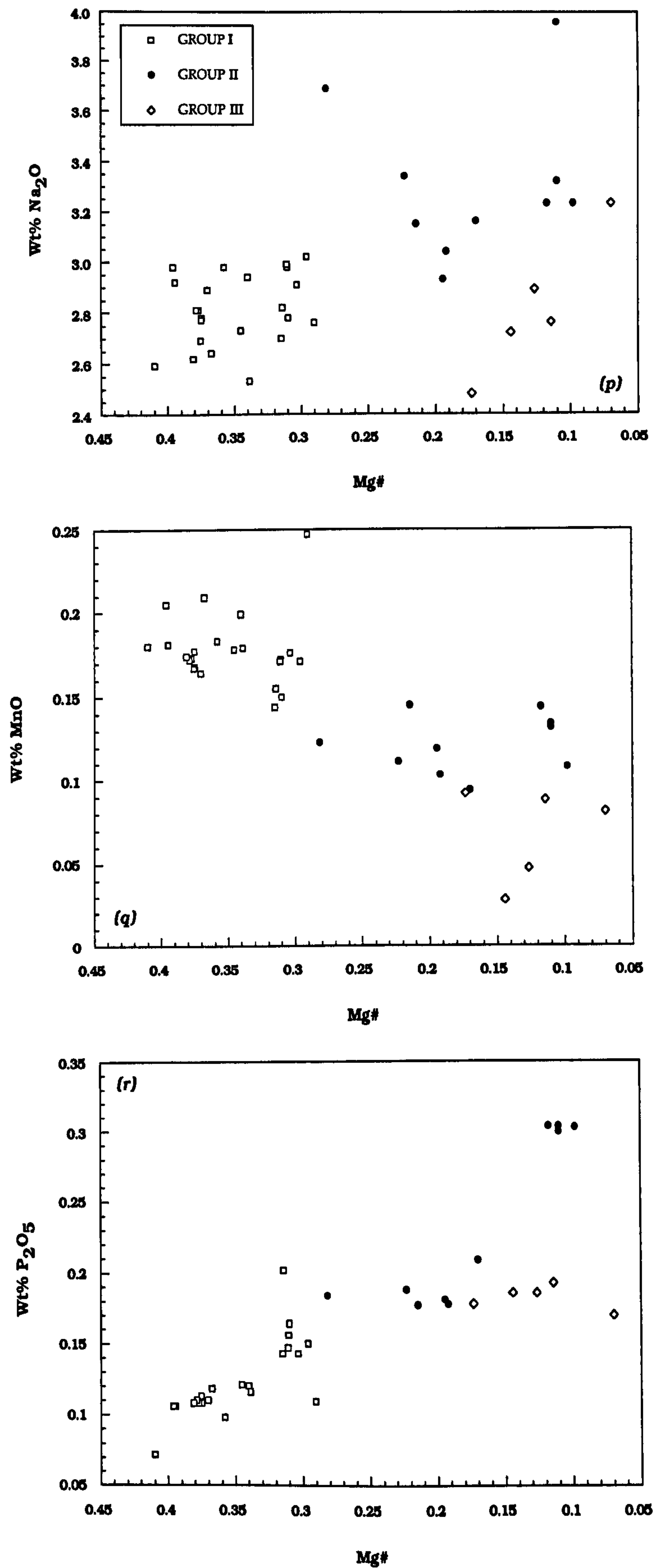


FIGURE 3.5 Variation of the major-elements within the LSSC.

(p) Na₂O vs. Mg#

(q) MnO vs. Mg#

(r) P₂O₅ vs. Mg#

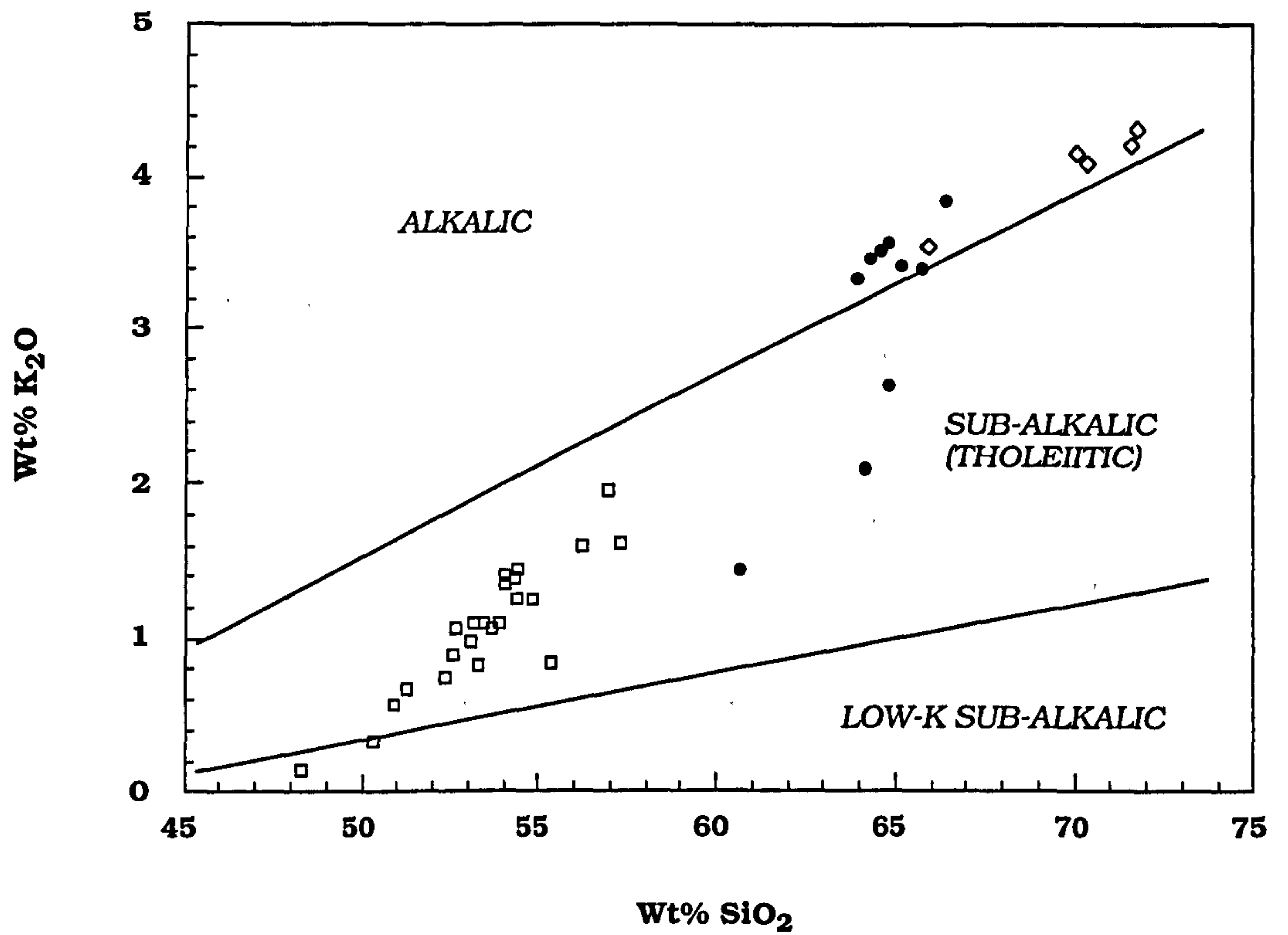


FIGURE 3.6 Plot of wt% K₂O vs. SiO₂ for the LSSC. Fields dividing Alkalic from Tholeiitic suites from Middlemost (1975).

anomalously high Fe contents of the rock. However, as will become evident in Chapters 4 and 5, this sample is the least-contaminated, and as such would be the obvious choice as a 'parental' magma for major-element, trace-element, and radiogenic isotope modelling of magmatic processes. However, its "extreme" major-element composition has prohibited its effective use as a parent magma for major-element modelling. As such, it has also not been used in trace-element or Sr-Nd isotopic modelling. Instead, the most magnesian sample (PGB9) has been used. Sample ORB2 has been used for magma mixing tests because it represents a relatively unfractionated sample. However, the very fact that sample ORB2 is from a xenolithic sheet, suggests that the parent magmas to the LSSC may have been of similar type.

Shown in *Figures 3.7a* and *3.7b*, respectively, are an AFM ternary variation diagram, and the variation of wt% MgO vs. Fe₂O₃* for the LSSC. *Figure 3.7a* shows the trends defined by tholeiitic lavas from Thingmuli volcano, Iceland (Carmichael, 1964), the iron-enrichment trend of the Skaergaard intrusion, Greenland (Wager & Brown, 1968), and a calc-alkaline trend from the Cascades Province (Yoder & Tilley, 1962). In addition, *Figure 3.7b* shows the trend of the Pigeonite series from the Hakone volcano, Japan (Kuno, 1950).

In the Skaergaard intrusion, the highly reduced state of the initial liquids are thought to have caused a delay in the appearance of magnetite as a fractionating phase, thus contributing to the extreme iron-enrichment in the early stages of magma evolution (Wager & Brown, 1968; cf. Hunter & Sparks, 1987). A similar explanation was put forward for the iron-enrichment trend of the Thingmuli volcano (Carmichael, 1964). The calc-alkaline trends of iron-depletion are thought to result from the early removal of magnetite from these more oxidised magmas. However, Grove & Baker (1984) have shown that the difference between the two trends is controlled mainly by the proportions of olivine, plagioclase and pyroxene that crystallize from the parental basaltic melt. The tholeiitic trend is produced by fractional crystallization of a basaltic magma at low pressures. The typical crystallization sequence is olivine, followed by plagioclase, followed by augite. Plagioclase dominates the assemblage (up to 75%) and the three-phase crystallization continues until a reaction point is reached, where olivine plus liquid react to give augite, plagioclase and pigeonite. Total iron in the liquid increases throughout this

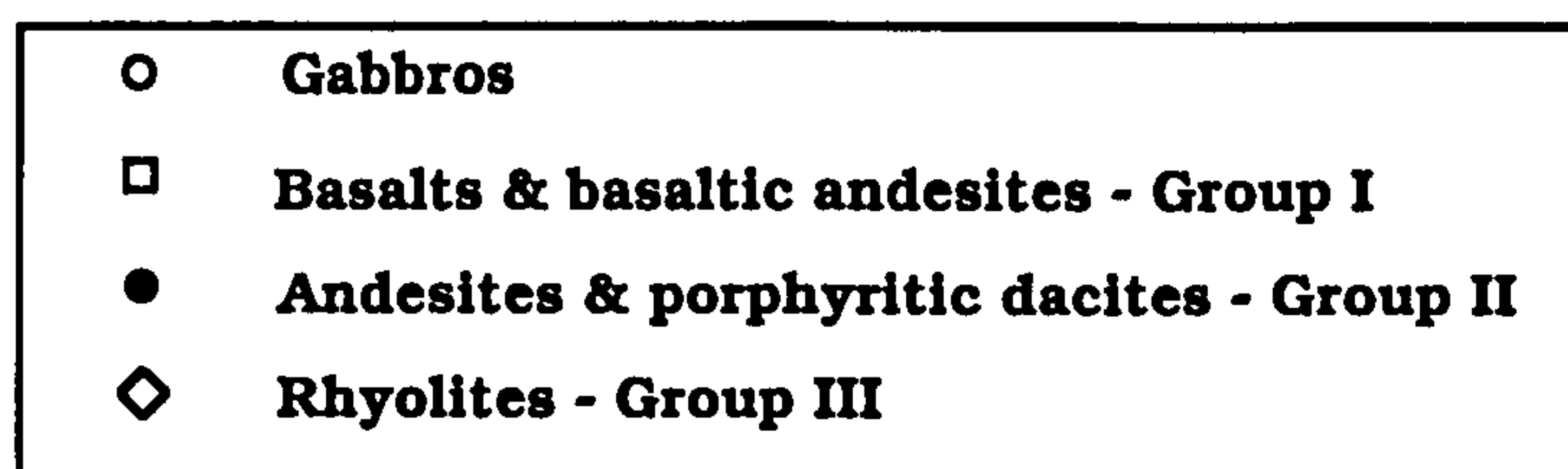
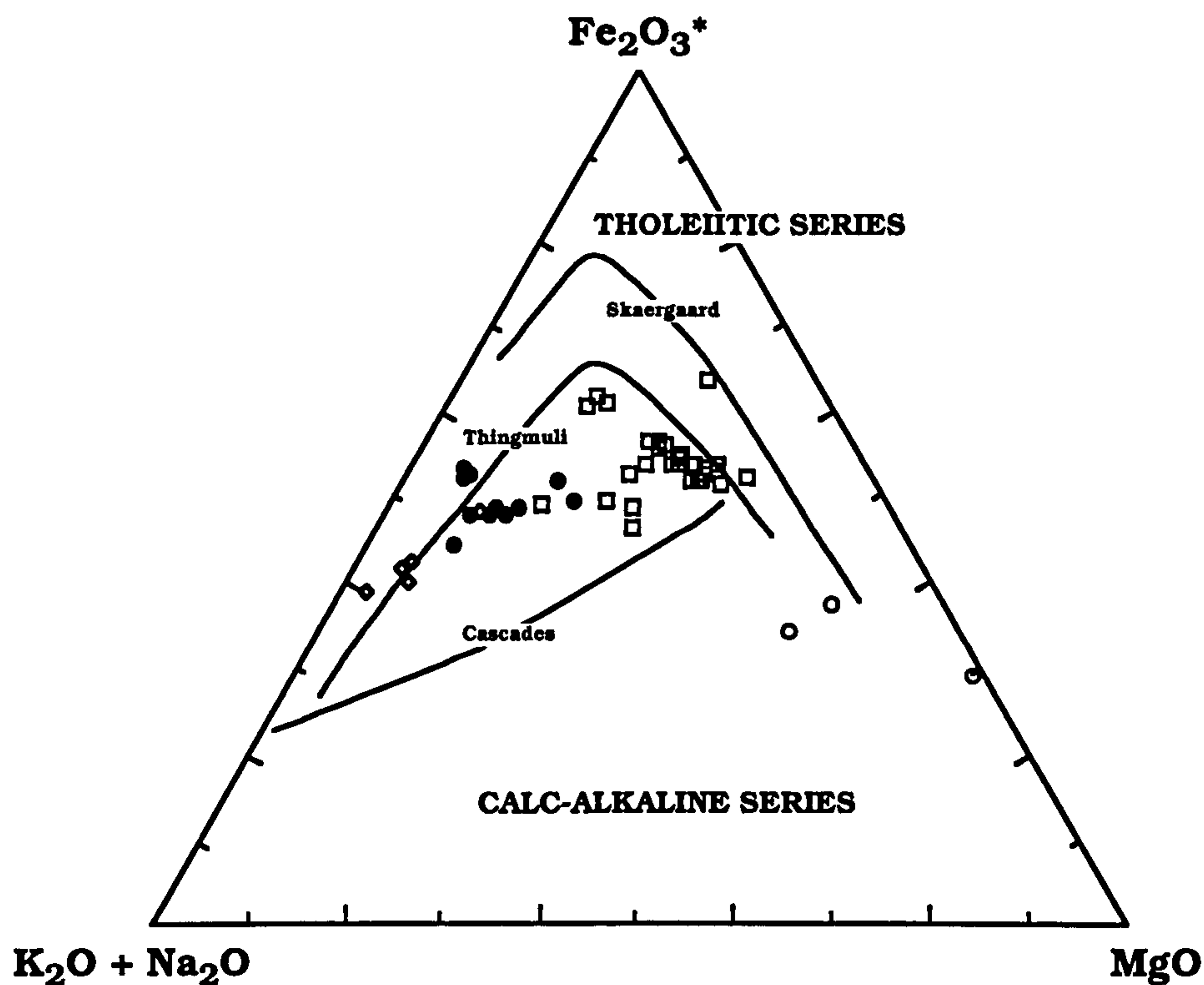


FIGURE 3.7a AFM diagram for members of the LSSC. Also shown are the differentiation trends for the Skaergaard calculated liquids (Wager & Brown, 1968), the Thingmuli Volcano Iceland (Carmichael, 1964), and Cascades lavas (Carmichael, 1964).

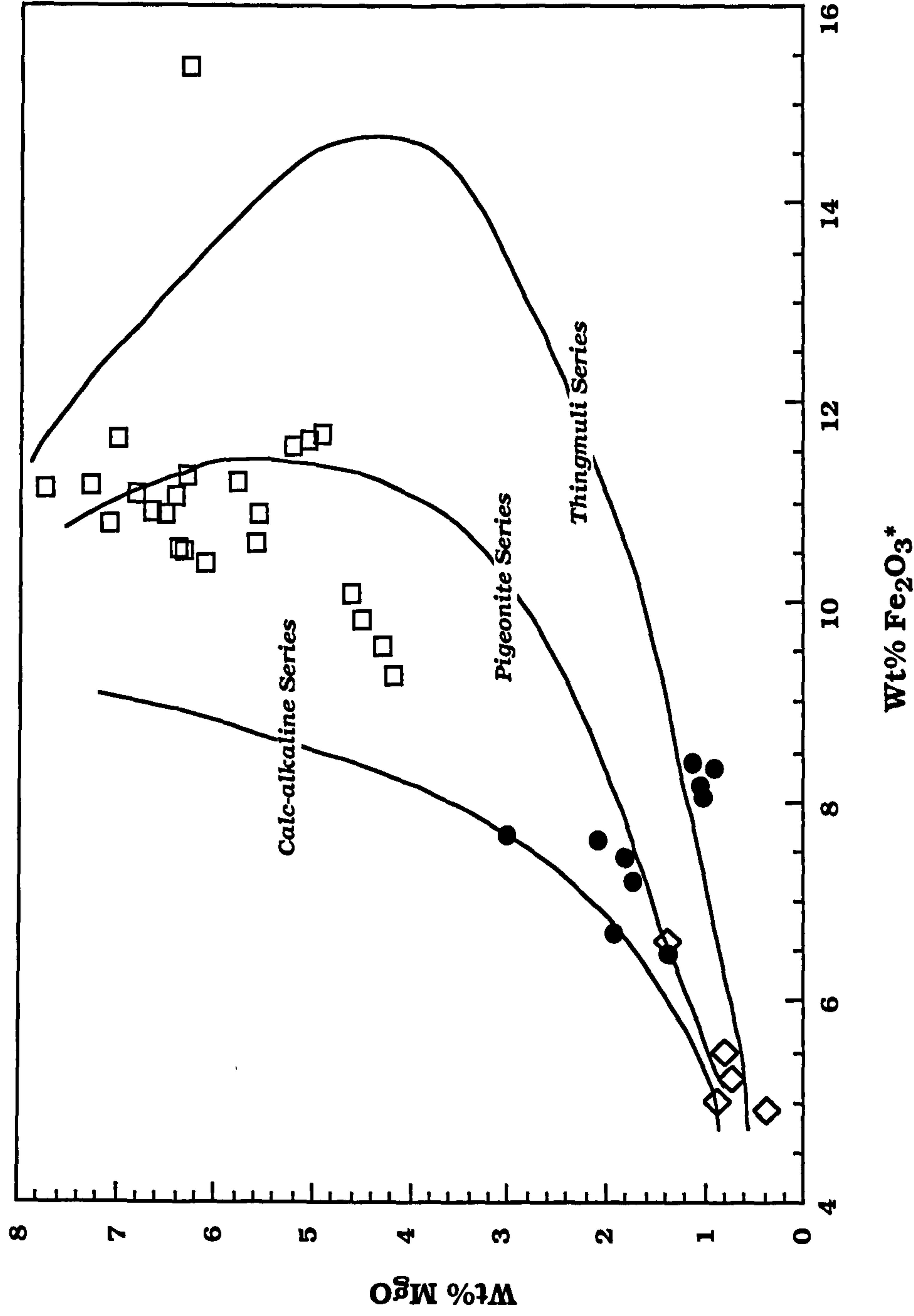


FIGURE 3.7 (b) Plot of wt% MgO vs. Fe₂O₃* for the LSSC. Diagram shows that the LSSC data do not define a typical tholeiitic trend of iron-enrichment as shown by the products of Thingmuli Volcano, Iceland (Carmichael, 1964). Also shown are the calc-alkaline trend of the Cascades Province Lavas (Yoder & Tilley, 1962), and the Pigeonite Series of the Hakone Volcano, Japan (Kuno, 1950).

crystallization process, and a dramatic increase in iron and a mild decrease in silica occur at the reaction point. Once olivine is completely consumed, the crystallization of plagioclase, augite and pigeonite causes silica enrichment, and the eventual appearance of magnetite causes iron depletion. In contrast, the calc-alkaline trend is produced at moderate to high pressures where olivine and augite precipitate in slightly greater proportions than plagioclase. The assimilation of silicic crustal material can also assist in the production of the calc-alkaline trend (Grove & Baker, 1984). From the data plotted in *Figures 3.7a* and *3.7b* it is evident that the LSSC falls between the extremes of tholeiitic and calc-alkaline differentiation trends. From the previous discussion on the normative mineralogy and phase relationships of the LSSC, it was concluded that the magmas equilibrated at upper-crustal levels (2-3 kbar), and that mixing of basic magmas with silicic melts, combined with fractional crystallization, contributed to the formation of some of the intermediate liquids. This combination of magmatic processes at slightly elevated pressures probably contributed to the Loch Scridain sills defining neither a strictly tholeiitic nor a calc-alkaline fractionation trend in terms of iron-enrichment.

Coherent trends on Harker type diagrams for related volcanic rocks can be produced through the processes of fractional crystallization, differential partial melting, magma mixing and crustal assimilation, or any combination of the four. Chayes (1964) has argued that at least some negative correlations with SiO_2 are to be expected as a consequence of the so-called constant sum effect, *i.e.* as silica varies between 40 and 75%, the sum of all the other constituent oxides must decrease from 60 to 25%. However, this is considered by some workers to be generally insignificant in most cases (*e.g.* Cox *et al.*, 1979; Wilson, 1989). The compositional trends for MgO , CaO and K_2O *vs.* SiO_2 are generally well-correlated (R^2 , the correlation coefficient, for Groups I and II is typically > 0.8). Fe_2O_3^* and MnO are well-correlated with SiO_2 (*Figures 3.5c,h*), taking the suite as a whole, although there is marked inter-group scatter. P_2O_5 (*Figure 3.5i*) shows a relative enrichment with increasing SiO_2 content through Group I (0.07-0.20 wt%), although the correlation coefficient is less than 0.8. For the majority of Group II and Group III, P_2O_5 has a relatively constant value of around 0.2 wt% with increasing SiO_2 content. However, several samples of Group II fall well off this general trend at

slightly elevated P_2O_5 values (0.32 wt%). These are the porphyritic dacites and, as discussed in Chapter 2, they contain occasional microphenocrysts of apatite. Na_2O , TiO_2 , and Al_2O_3 do not correlate well with SiO_2 . The possible reasons behind these trends are discussed further in the following sections.

It is not possible to resolve the petrogenesis of a suite of cogenetic rocks on the basis of major-element geochemistry alone. Combined studies utilising major-elements along with trace-element and isotope geochemistry are the only way to determine which processes have occurred. However, the following discussion presents the conclusions that can be drawn from the major-element data in terms of the competing magmatic processes, for each group in turn.

3.3 Major-element evolution of the Group I basalts and basaltic andesites

The Group I magmas provide perhaps the greatest opportunity to assess the relative contributions of the processes of fractional crystallization, crustal assimilation, differential partial melting, and magma mixing to the evolution of the LSSC. This is due to the relatively continuous differentiation trend from basalt through to basaltic andesite defined by the group. The presence of possible "parent" magmas within the suite also enables the modelling of these competing magmatic processes to be carried out. Although the major-element evolution of each magma group will essentially be discussed separately, differences between the groups, and possible inter-group links will also be highlighted throughout.

Fractional crystallization.

It is evident from the major-element data that the observed compositional trends of the LSSC (*Figures 3.5a-i*) require the fractionation of a Mg-rich phase throughout Group I. Olivine fractionation is one possibility. However, olivine is generally absent as a phenocryst (and groundmass) phase in Group I (one specimen (SFB2) does contain possible olivine phenocrysts, now completely pseudomorphed by serpentine and iddingsite). Minor olivine fractionation is required for the basalts of Group I to enable the SiO₂ contents of the liquids to stay at a relatively constant 54wt%. Clinopyroxene fractionation alone would be able to produce the same reduction in MgO contents, but with a concomitant early reduction in SiO₂. The Group I compositional trends also calls for a calcic phase to be fractionating. Since Group I rocks contain occasional microphenocrystic and glomeroporphyritic plagioclase, this phase would seem an obvious candidate. The marked scatter in the Al₂O₃ data (*Figure 3.5d*) does not negate this possibility since between 40%-50% plagioclase must be in the fractionate to enable Al₂O₃ to diminish noticeably (Albarède, 1992). Whereas plagioclase phenocryst accumulation may be the cause of some of the scatter about the Group I trend (*e.g. Figure 3.5d*), olivine + plagioclase removal alone cannot explain the displayed lineages. The role of a third phase during the

evolution of the Group I magmas is confirmed when the $\text{CaO}/\text{Al}_2\text{O}_3$ data is examined. From a consideration of the data displayed in *Figure 3.8*, it is evident that the fractionation of a phase with $\text{CaO} > \text{Al}_2\text{O}_3$ is required.

Combining these observations and those obtained from the low-pressure phase relationships, a calcium-rich clinopyroxene (diopside or augite) would be the obvious choice. However, diopside and augite, like olivine, do not occur as a phenocryst phase in Group I. Furthermore, gabbroic fractionation would cause iron enrichment. As pointed out previously, Fe_2O_3^* stays at relatively constant values of around 11 wt% until $\text{SiO}_2 = \sim 54$ wt%, at which point iron depletion sets in. Fractionation of titanomagnetite has not occurred, as the wt% of TiO_2 rises steadily through Group I (*Figure 3.5n*). It is considered most likely that the fractionation of an iron-rich pyroxene (pigeonite or orthopyroxene) has caused the iron depletion in specimens with $\text{SiO}_2 > 55$ wt%. The continued fractionation of plagioclase and augite would ensure that CaO and MgO were also simultaneously depleted. This fractionation scheme for Group I magmas is supported by the phase relationship data presented above, and also by the presence of olivine-bearing, and hypersthene-bearing cumulate xenoliths in a number of the Group I sheets (see Chapter 7).

The need to suggest the role of the three-phase mineral assemblage olivine + clinopyroxene + plagioclase during the evolution of basaltic magmas, even though the members of a suite are devoid of one or more of these minerals (especially clinopyroxene) within the phenocryst assemblage, has provided a paradoxical problem for many studies of tholeiitic basalt suites—from both the continental and oceanic environments. Within the BTVP, the cone sheet complex of Skye (Bell *et al.*, 1994) and Ardnamurchan (Holland & Brown, 1972) highlight the so-called pyroxene paradox. The work of Cox & Mitchell (1988) on plagioclase-phyric and aphyric basalts from the Deccan Traps, India, suggests that only the denser liquids (Fe-rich tholeiites) are capable of transporting suspended crystals to the site of emplacement, thus discriminating strongly in favour of less dense plagioclase over denser olivine and clinopyroxene. The aphyric rocks, which are generally more primitive (Fe-poor), were therefore considered to have lost all the fractionating phases via a process of crystal settling. This is identical to the case of the Skye tholeiitic cone-sheets, where the least evolved specimens ($\text{Mg\#} \sim 0.425$) are the most Fe-poor ($\text{wt\% Fe}_2\text{O}_3^* =$

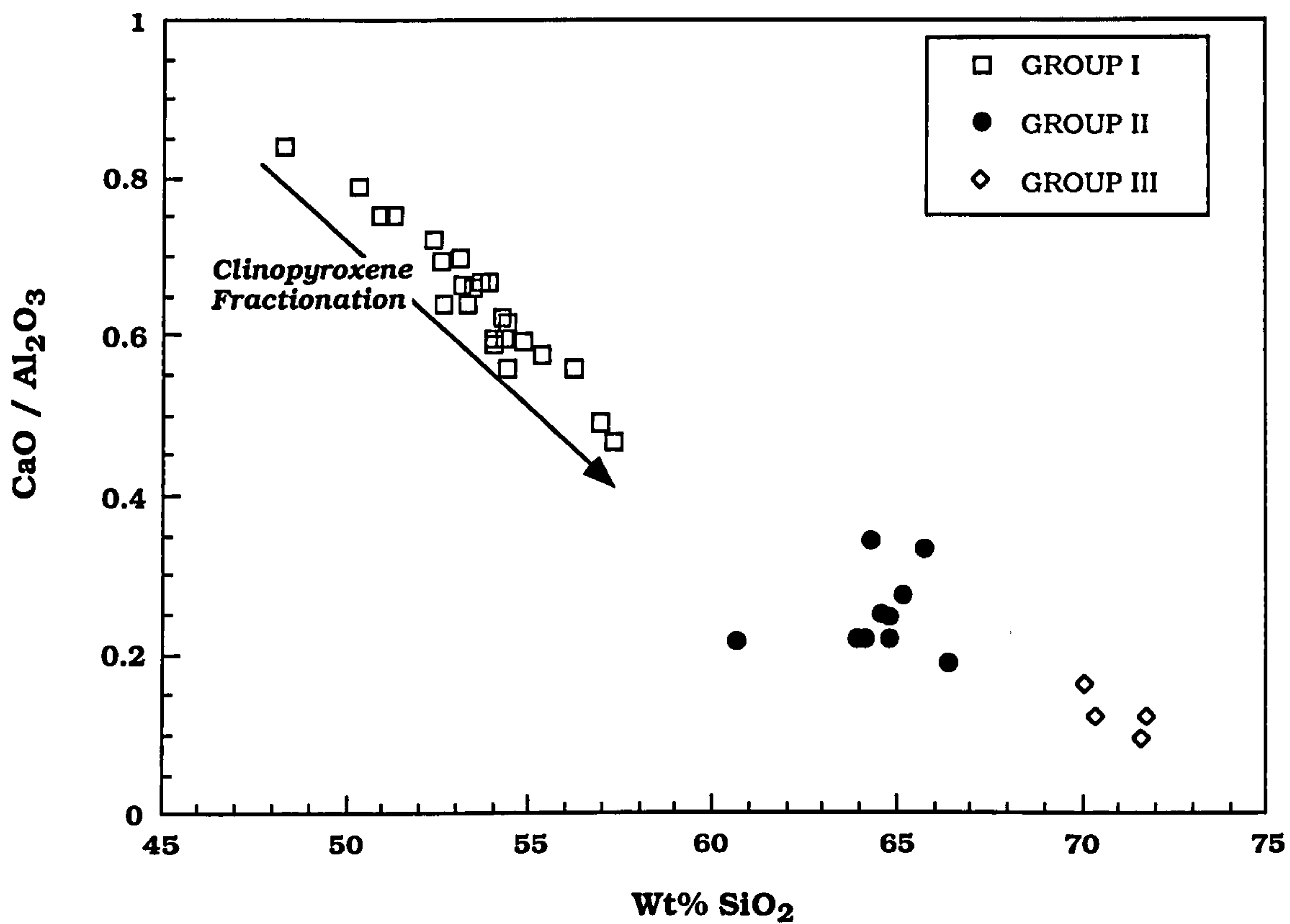


FIGURE 3.8 Wt% CaO/Al₂O₃ vs. SiO₂ for members of the LSSC. A phase with CaO > Al₂O₃ must be partly responsible for the trend seen. Clinopyroxene fractionation is therefore considered important through Group I.

11.42) there being a steady increase in Fe_2O_3^* with progressive crystal fractionation (Bell *et al.*, 1994). Although the majority of the Loch Scridain Group I rocks are not as Fe-enriched as those studied by Cox & Mitchell, the least evolved specimen does have Fe_2O_3^* at a comparable 16 wt%. A similar process may have been in operation in the Loch Scridain magma chamber(s), with the cognate xenoliths being testament to the efficient separation of liquids and crystals. Francis (1986) argued that the pyroxene paradox may actually be illusory. His work on Mid Ocean Ridge (MOR) picrites from the Baffin Bay volcanic province, Greenland, suggests that the compositional variation that is responsible for the problem of occult pyroxene fractionation may be attributed to the dispersion of olivine fractionation trends between the limits of equilibrium and fractional crystallization. However, the evolved nature of the Loch Scridain magmas suggests that olivine fractionation played only a minor role in the production of the intra-suite variation recorded here. This problem was also addressed by Walker *et al.* (1979), who explained it in terms of mixing processes between unevolved and fractionated compositions on a common curved cotectic so that the resultant liquids plot within the high-Ca pyroxene saturated field on relevant phase diagrams. This is illustrated by the hypothetical compositions plotted in the plagioclase-saturated projection diopside-olivine-silica (Walker *et al.*, 1979) shown in *Figure 3.9a*. During equilibrium crystallization the primitive liquid, *P*, would evolve to the three phase cotectic, crystallizing olivine and plagioclase. It would then follow the cotectic crystallizing olivine + plagioclase + diopside, until it reaches the reaction point, *R*. The liquid would crystallize completely at this point. During fractional crystallization the same primitive liquid could evolve further down the pigeonite + diopside + plagioclase curve. In both cases the residual liquids never approach more evolved compositions such as liquid *E*. If however, a basic liquid which lies on the olivine + diopside + plagioclase cotectic is mixed with a more evolved liquid which lies nearer the reaction point *R*, a liquid composition such as *E* within the diopside primary phase field can result. This scenario is shown in *Figure 3.9a* with the thick mixing arrows. It is the strong curvature of the cotectic which enables this paradox to occur. *Figure 3.9b* shows the Loch Scridain data projected on to the diopside-olivine-silica diagram of Walker *et al.* (1979). Only one sample (ORB2) plots within the olivine primary phase volume.

FIGURE 3.9 (a)

Plagioclase-saturated diopside-olivine-silica projection at 1atm pressure, showing schematic fractionation and mixing vectors. Cotectic after Walker *et al.*, (1979).

R = Reaction point

P = Primitive mantle derived melt

E = More evolved composition produced by magma mixing (SEE TEXT)

FIGURE 3.9 (b)

Loch Scridain magmas projected on to plagioclase-saturated diopside-olivine-silica diagram (after Walker *et al.*, 1979). Many Group I samples project in the diopside primary phase volume, indicating that they may be the products of a mixing process between evolved and less-evolved basic magmas which lie on the strongly curved cotectic.

Plotting procedure is as follows:

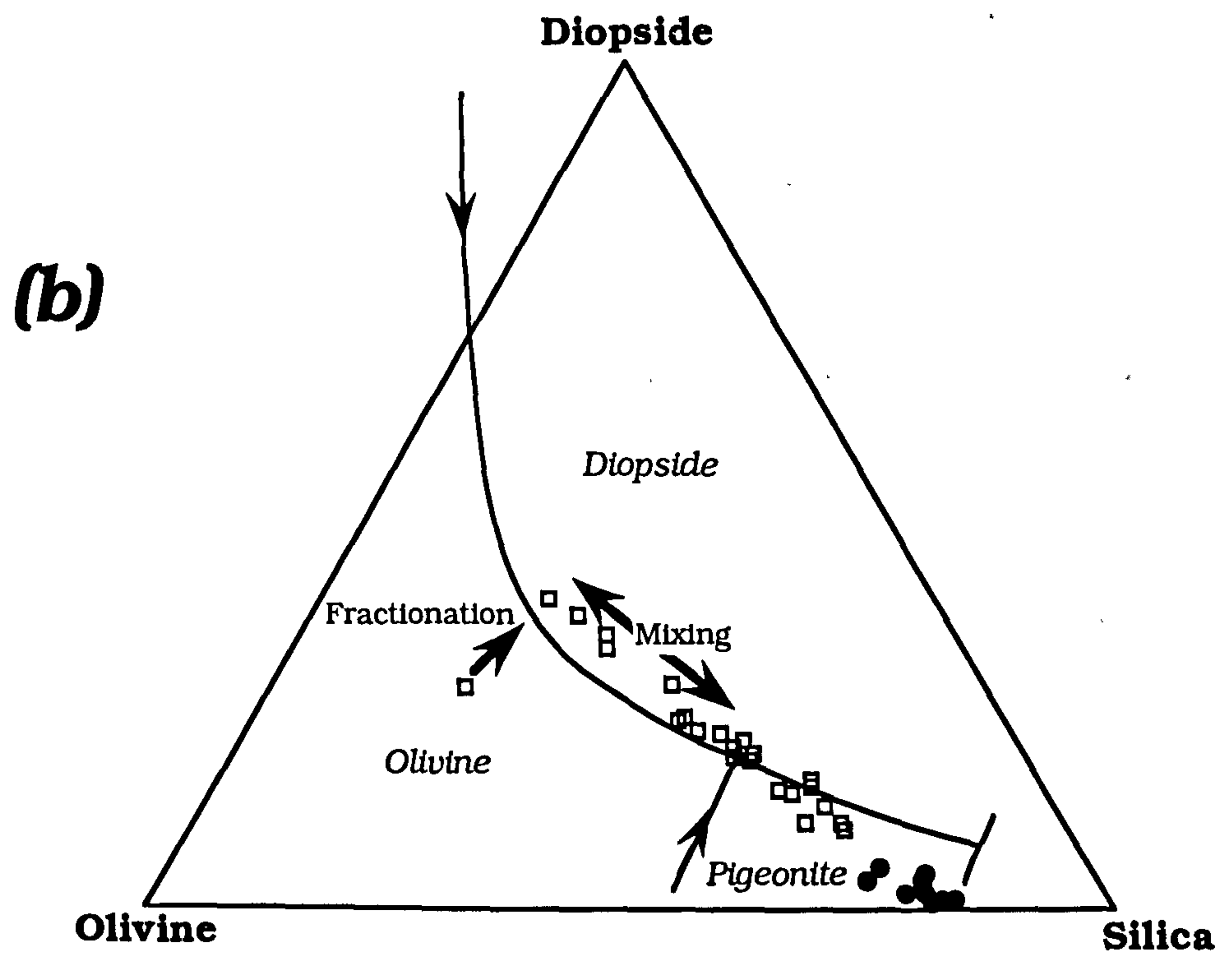
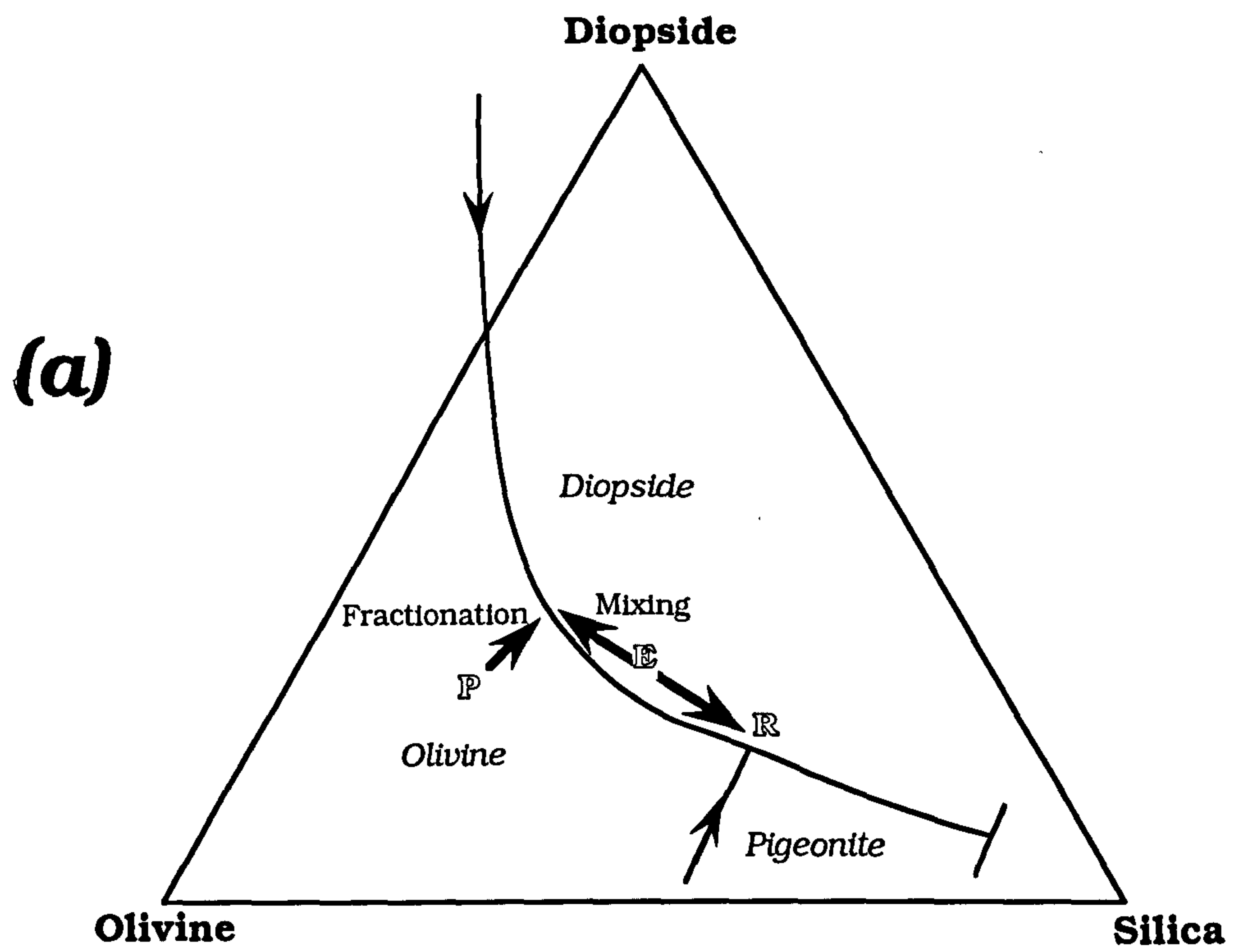
DIOPSIDE = $\text{CaO} - \text{Al}_2\text{O}_3 + \text{Na}_2\text{O} + \text{K}_2\text{O}$

OLIVINE = $(\text{FeO} + \text{MgO} + \text{MnO} + 2\text{Fe}_2\text{O}_3 + \text{Al}_2\text{O}_3 - \text{CaO} - \text{Na}_2\text{O} - \text{K}_2\text{O}) / 2$

SILICA = $\text{SiO}_2 - (\text{Al}_2\text{O}_3 + \text{FeO} + \text{MgO} + \text{MnO} + 3\text{CaO} + 11\text{Na}_2\text{O} + 11\text{K}_2\text{O} + 2\text{Fe}_2\text{O}_3) / 2$

All weight % converted to molecular proportions prior to calculation.

- Group I - Aphyric basalts and basaltic andesites
 - Group II -Tholeiitic andesites and porphyritic dacites



This liquid composition will crystallize olivine + plagioclase during fractional crystallization, and derivative liquids will move towards the three phase cotectic curve. Many Group I samples cluster around the four phase reaction point, *R*, whereas some of the Group I samples and all from Group II plot either along the pigeonite-diopside-plagioclase cotectic, or within the pigeonite-plagioclase primary phase volume. However, between the reaction point, *R*, and the least evolved samples which lie on the olivine-augite-plagioclase cotectic, a linear array of Group I samples occurs within the augite primary phase volume, and suggests that mixing between more primitive and more evolved liquids has occurred within Group I.

Examination of the variation diagrams for rocks of Group II suggests that it is possible to draw similar conclusions. Certain compositional trends for Group II rocks suggest that the fractionation process was continuous through Group I and Group II (*e.g.* CaO and MgO vs. SiO₂; *Figures 3.5a,b*). However, the separation of the trends in the TiO₂ vs. Mg# diagram (*Figure 3.5n*) appears to negate this possibility.

A geochemical grouping of continental tholeiites involving low- and high-TiO₂ varieties has been noted from several flood basalt provinces. In the Paraná flood-basalt province, Brazil, low-P₂O₅-TiO₂ (LPT) basalts dominate the southern part of the province, whereas high-P₂O₅-TiO₂ (HPT) basalts are found in the north (Bellieni *et al.*, 1986; Fodor, 1987). Similar provinciality has been found in the Karoo (Cox *et al.*, 1967), and in the Etendeka province of Namibia (Duncan, 1987). Similarly, the Kirkpatrick Basalts and Ferrar Group Tholeiites of Antarctica also contain high-TiO₂ and low-TiO₂ types (Siders & Elliot, 1985; Morrison & Reay, 1995). Within the Paraná, Fodor (1987) favours a model in which the low-TiO₂ lavas are generated via larger degrees of partial melting than the high-TiO₂ lavas from a homogeneous mantle source. The low-TiO₂ magmas are also thought to have suffered more crustal contamination, as indicated by their higher initial strontium isotope ratios (Fodor, 1987). However, other workers (Mantovani *et al.*, 1985; Petrini *et al.*, 1987) prefer a model involving substantial mantle heterogeneity coupled with crustal contamination. Likewise, the Antarctic suites are thought to have suffered little in the way of crustal contamination, despite the elevated initial strontium isotope ratios (Hergt *et al.*, 1991; Morrison & Reay, 1995). Hergt *et al.*, (1991) demonstrated that crustal contamination of the Ferrar Group Tholeiites is not a viable mechanism. They concluded that the

very low abundance of certain elements (*e.g.* Ti) would require an unusually depleted parent magma, coupled with 25-30% assimilation of crustal material with unusually high Rb/Ba, Rb/Sr, SiO₂ and ⁸⁷Sr/⁸⁶Sr. Work by Morrison & Reay (1995) on the Ferrar Group Tholeiites confirms this contention, and suggests that the geochemistry of these tholeiites can be explained by the combined influence of the mantle source region, RTF magma chamber processes (periodically replenished and tapped, continuously fractionating magma chamber; O'Hara, 1977; O'Hara & Mathews, 1981; Cox, 1988), and via sub-solidus hydrothermal alteration. In the Paraná province, the LPT and HPT basaltic lavas are associated with rhyolitic lavas which have similar low- and high-TiO₂ characteristics. These silicic lavas can be accounted for through the fractional crystallization of the associated basalts. However, there is a relative absence of intermediate rock types (a 'silica gap' exists between SiO₂ = 54-65 wt%) (Bellieni *et al.*, 1986). Consequently, Bellieni *et al.* (1986) favour an origin of the silicic magmas by partial melting of underplated basic rocks in the base of the crust during the lithospheric thinning associated with the opening of the South Atlantic Ocean.

It is difficult to relate the LSSC magmas to these hypotheses since the HPT and LPT groupings relate to magmas at the same stage of evolution. The LSSC magmas display divergent TiO₂ trends at different stages of evolution. None of the LSSC magmas could be described as having high TiO₂ contents; some of the Paraná basalts (SiO₂ ~ 50 Wt%) have TiO₂ contents at 4 Wt% (Wilson, 1989). As a result, it is envisaged that the divergent nature of the TiO₂ trends in the LSSC basic and intermediate magmas is a result of the two groups being derived either from different sources, or from the same source, but having suffered variable amounts of fractional crystallization with different fractionating assemblages, and/or crustal contamination prior to emplacement.

Modelling the crystal fractionation process.

Since Group I comprises the most continuous fractionation trend, the following sections investigate the possible mechanisms by which these magmas may have evolved. The petrogenesis of Group II is more problematical since no basic end-member is evident. This will be returned to in a later section.

a) Closed-system crystal fractionation

Using the phase relationships determined in Section 3.1 as a guide, those samples which appear to be cotectic with respect to plagioclase, augite and pigeonite on the olivine-clinopyroxene-silica phase diagram (Figure 3.4c), were tested using a least-squares fitting model in order to determine whether the most evolved samples could be generated from the least evolved samples via fractional crystallization. The model takes analysed mineral compositions, and 'parental' and 'daughter' rock analyses as input and, using a matrix inversion technique, calculates the best fit solution by minimising the sum of the squares of the residuals (R^2 i.e. the difference between the calculated and observed derivative compositions). Output from the model consists of the calculated daughter composition, and the proportion of each fractionating phase removed from, or added to, the parent magma to derive the best possible fit. Each element can be weighted prior to calculation to take into account the mineral phases being used. For example, if apatite were considered an important fractionating phase, then P_2O_5 would be given a higher weighting factor than if apatite were not involved. Values for $R^2 < 1$ are considered reasonable, whereas < 0.3 suggests a good fit, and < 0.1 an excellent fit. Table 3.4a presents the mineral compositions used in the calculations; all mineral compositions are actual analyses determined on phenocryst phases, or phases from the coarse-grained gabbroic cumulate xenoliths. The results of the model for selected Group I members of the LSSC are presented in Table 3.4. Only samples which are considered to have been cotectic with respect to plagioclase, augite and pigeonite have been modelled with any success ($R^2 < 1.0$). In order to minimise spurious correlations, the smallest possible steps down the cotectic path have been modelled, with a daughter composition used in one calculation being used as the parent composition in the subsequent

calculation. It is evident from the low residuals shown by the calculations in *Table 3.4b* that the fractional crystallization of the cotectic phases of plagioclase plus one or two pyroxenes, is a viable model for a few members of Group I. The proportions of the phases required appear to be reasonable in all but one of the steps (RCB2-RCB3) where augite dominates over plagioclase. However, the large amounts of crystallization required for each step (between 66 and 93%) would appear to argue against fractional crystallization being the sole process responsible for the compositional spectrum seen in the Group I magmas.

	Plagioclase	Augite	Pigeonite
SiO₂	53.08	49.27	49.76
TiO₂	0.07	0.79	0.32
Al₂O₃	29.30	3.42	0.76
FeO	0.56	14.14	29.74
Fe₂O₃	n.d.	2.89	2.25
MnO	n.d.	0.34	n.d.
MgO	n.d.	14.35	14.19
CaO	11.75	14.37	3.49
Na₂O	4.39	0.24	0.07
K₂O	0.44	0.01	0.01
TOTAL	99.59	99.82	100.59

Table 3.4a Mineral compositions used in *least-squared* major-element crystal fractionation models. All compositions are analyses of phenocryst phases or phases from coarse-grained cumulate gabbroic xenoliths. n.d. = not determined.

TMB3		SFB2		SFB2	RCB2	
Parent		Daughter		Parent	Daughter	
	obs.	obs.	calc.	obs	obs	calc
SiO ₂	52.63	54.02	54.22	54.02	54.31	54.91
TiO ₂	0.99	0.99	1.27	0.99	1.18	1.06
Al ₂ O ₃	15.05	14.66	14.92	14.66	14.34	14.64
FeO	8.65	8.77	8.75	8.77	9.05	9.01
Fe ₂ O ₃	1.45	1.47	1.49	1.47	1.52	1.49
MnO	0.21	0.20	0.24	0.20	0.17	0.20
MgO	6.43	5.78	6.17	5.78	5.22	5.71
CaO	9.60	8.74	8.63	8.74	8.54	8.40
Na ₂ O	2.64	2.94	2.85	2.94	2.99	3.03
K ₂ O	1.06	1.40	1.46	1.40	1.39	1.53
P ₂ O ₅	0.12	0.12	0.12	0.12	0.15	1.15
R Squared			0.399			0.325
% Phase	Plag		49.1			50.5
	Augite		42.3			49.2
	Pig		8.6			0.3
% Crystallized			69.1			90.8
RCB2		RCB3		RCB3	PGB1	
Parent		Daughter		Parent	Daughter	
	obs.	obs.	calc.	obs	obs	calc.
SiO ₂	54.31	54.41	55.36	54.41	56.03	57.38
TiO ₂	1.18	1.18	1.25	1.18	1.53	1.61
Al ₂ O ₃	14.34	14.54	14.68	14.54	13.56	14.03
FeO	9.05	9.13	9.15	9.13	9.96	9.96
Fe ₂ O ₃	1.52	1.53	1.51	1.53	1.67	1.62
MnO	0.17	0.17	0.17	0.17	0.18	0.18
MgO	5.22	4.91	4.97	4.91	3.16	3.80
CaO	8.54	8.08	8.27	8.08	6.08	5.84
Na ₂ O	2.99	3.02	3.13	3.02	3.50	3.48
K ₂ O	1.39	1.44	1.51	1.44	2.02	2.11
P ₂ O ₅	0.15	0.15	0.15	0.15	0.20	0.20
R Squared			0.046			0.568
% Phase	Plag		35.1			49.4
	Augite		64.9			46.9
	Pig		0.0			3.7
% Crystallized			92.7			65.5

Table 3.4b Results from least-squared modelling. R Squared = Weighted squares of the residuals from daughter observed (obs.) - daughter calculated (calc.)

The presence of linear trends on Harker plots for members of Group I enables mass-balance modelling of the fractionation process to be carried out. In order to model closed system fractionation processes, first a bulk mineral extract is calculated from the proportions and compositions of the minerals being removed. The proportions of each phase were estimated generally using trial and error. However, it was assumed that plagioclase dominated the fractionating assemblage at all points (see least-squares modelling), and that Ca-clinopyroxene was the next dominant phase, followed by olivine or pigeonite, depending upon whether the early or later crystallization sequences were being examined. The bulk assemblage composition is then extracted from the parent rock analysis in a small amounts over a number of steps (5% removed at each step); at each stage the new analysis being recalculated to 100%. This new analysis then becomes the parent liquid for the next step, and so on. Various models have been considered for Group I rocks :-

- (a) Continuous fractionation of olivine, plagioclase and Ca-clinopyroxene in their low-pressure cotectic proportions 10:55:35 (gabbroic fractionation).
- (b) Gabbroic fractionation until $\text{SiO}_2 = \sim 54 \text{ wt\%}$, followed by removal of plagioclase, Ca-clinopyroxene, low-Ca pyroxene, and magnetite in various proportions.
- (c) Gabbroic fractionation until $\text{SiO}_2 = \sim 54 \text{ wt\%}$, followed by removal of plagioclase, Ca-clinopyroxene and low-Ca pyroxene in various proportions.

Model (a) is clearly inappropriate, since phase relationships show that the majority of Group I magmas would have been cotectic with respect to plagioclase plus two pyroxenes (*Figure 3.4c*), and that only the low- SiO_2 basalt magmas would be saturated with respect to olivine. Simple gabbroic fractionation cannot account for the SiO_2 enrichment seen in Group I, and also causes excessive iron enrichment.

Magnetite fractionation (model (b)) would deplete the liquid in iron as seen in Group I magmas. However, all magnetite analysed within the suite is highly titaniferous, and very few samples contain significant

amounts of magnetite phenocrysts. As a result, the TiO_2 (Figure 3.5n) enrichment indicates that the liquids never became saturated with titanomagnetite or ilmenite.

Model (c) appears to be the most applicable, given the phase relationships and major-element variations in Group I. Although this model can account for the abundances of MgO , CaO , Fe_2O_3^* , K_2O , Al_2O_3 , MnO , and Na_2O , it is incapable of producing the associated enrichment in SiO_2 and TiO_2 . This suggests that *closed-system* processes, alone, did not operate in the processing magma chamber(s).

(b) Open-system processes : Fractional crystallization and assimilation

The effects of crustal contamination on fractionating basaltic magmas have already been discussed (Chapter 1). That the Loch Scridain magmas interacted with crustal lithologies of various sorts is not in question. However, what is difficult to ascertain is the *exact* nature of the contaminant, and how best to model the process. Major-elements are generally insensitive indicators of crustal contamination, their abundances being controlled by crystal-liquid equilibria. In general, however, tholeiitic magmas contaminated with upper-crustal material, tend to be enriched in SiO_2 and K_2O , relative to uncontaminated continental basic magmas, at any given stage of fractionation (as shown by the Mg#) (Thompson *et al.*, 1986).

Simple, linear, two-component mixing models are considered in a following section. Here, a similar model to that used to model closed-system fractional crystallization can be applied to combined fractional crystallization and assimilation. At each step in the model, the bulk crystal extract is removed from the parent, a proportion of the selected contaminant is added and, as before, the resulting compositions are recalculated to 100%. Again, it was found that the fractionating assemblages of olivine + plagioclase + Ca-pyroxene, followed by plagioclase + Ca-pyroxene + low Ca-pyroxene produced the best fitting models. The contaminants considered included: bulk Moine pelite compositions; a Group III rhyolite; theoretical/experimental minimum granitic melts; and aluminous buchites of the type found as xenoliths in the Group I magmas. These compositions are presented in Table 3.5.

	Group III Rhyolite (PGF1)	Moine Pelite (SOM2)	Aluminous Buchite (PMAX2)	Experimental Melt (JE6)
SiO₂	70.13	67.9	54.68	70.42
TiO₂	0.73	0.77	2.73	0.14
Al₂O₃	12.17	14.85	30.75	13.63
Fe₂O₃*	5.26	5.04	1.11	0.83*
MnO	0.09	0.08	0.007	n.d.
MgO	0.68	1.56	0.50	0.38
CaO	1.97	2.23	0.49	1.41
Na₂O	2.76	4.67	2.21	4.12
K₂O	4.15	1.89	1.61	3.42
P₂O₅	0.19	0.13	0.04	n.d.
TOTAL	98.13	99.12	94.13	94.41

Table 3.5 Compositions of possible contaminants used in major-element modelling process. Experimental melt (JE6) from Thompson (1981). n.d. = not determined. * = all Fe as FeO

Models which used a Group III rhyolite or an experimental granitic minimum melt (*e.g.* Thompson, 1981) are able to account for the abundances of SiO₂, MgO, CaO, Fe₂O₃*, K₂O, Al₂O₃, MnO and Na₂O in the more evolved rocks of Group I. They cannot, however, account for the enrichment in TiO₂. A model involving a bulk Moine pelite as the contaminant can resolve this problem, but at the expense of poor fits in the abundances of MnO and Na₂O. The aluminous buchite xenoliths within many of the sills, which possibly represent the restite after the extraction of more than one melt from a pelitic rock (see Chapters 9 and 10), are highly enriched in TiO₂ (2.7 wt%). Although the assimilation of small amounts (<1%) of such material can account for the TiO₂ enrichment trend of Group I, the highly aluminous nature (30 wt% Al₂O₃) and silica deficiency (53 wt% SiO₂) of these rocks means that these two elements in particular cannot be modelled adequately. This problem can be addressed by the addition of two contaminants: melts with compositions similar to the Group III rhyolites and the aluminous buchites, in the ratio of approximately 4:1. This solution almost equates to the addition of bulk Moine pelite as a contaminant. It

is unlikely, however, that the aluminous buchites represent the restite after only *one* melt has been extracted from a Moine pelite. *Figures 3.10a-i* show the trends for the Group I magmas with the best fit model superimposed. As can be seen, the fit of the data is reasonable. This however, does not prove that the Group I magmas definitely evolved via a process of combined fractional crystallization and assimilation. This can only be assessed with more certainty by the consideration of the trace-element and isotope geochemistry characteristics of the group (Chapters 4 and 5).

Differential partial melting

As discussed in above, it has proved impossible to model the evolution of many members of the LSSC using simple closed-system fractional crystallization processes. The possibility remains, therefore, that the variation in the major-element chemistry of the Group I sheets is a consequence of varying degrees of partial melting within the mantle source. Melting experiments on a variety of natural and synthetic mantle materials (*e.g.* Jaques & Green, 1980) have shown that a wide range of silicate liquids can be generated by melting of the mantle. Variations in the bulk composition and mineralogy of the source, and in the depth and degree of melting, can combine to generate magmas ranging from kimberlite to alkali basalt, to tholeiitic basalt, and perhaps even andesite under hydrous melting conditions. In general, tholeiitic basalt magmas can be produced by moderate degrees of partial melting (20-30%) of both depleted and enriched lherzolite sources, at pressures below 15-20 kbar. At higher pressures picritic liquids are generated at similar degrees of partial melting. Alkali basalts appear to be generated by smaller degrees of melting (<20%) of enriched sources at pressures greater than 10 kbar (Jaques & Green, 1980).

Table 3.6 summarises the effects of degree of partial melting and pressure on the major-element concentrations of any given mantle-derived melt.

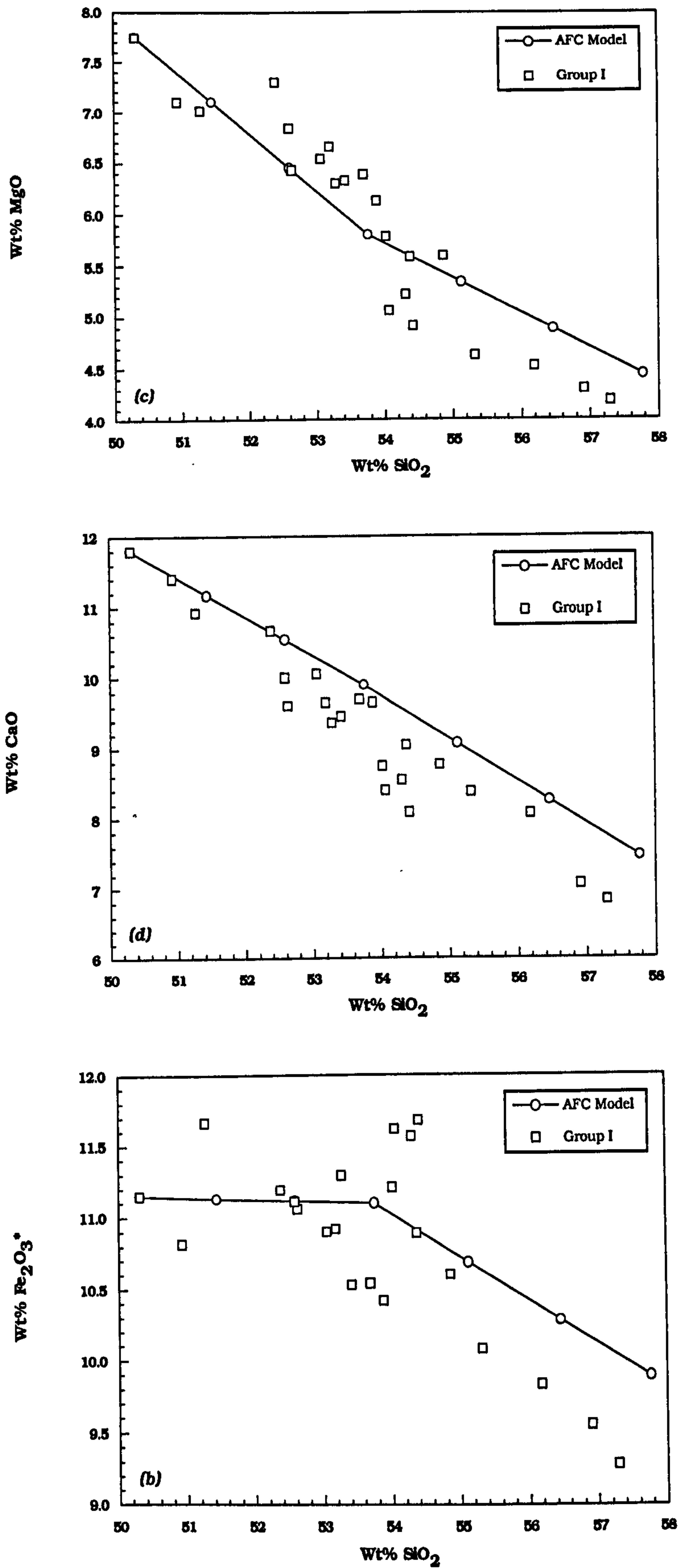


FIGURE 3.10 Major-element AFC modelling of the evolution of the Group I magmas. Starting composition was PGB9 (see Appendix II). Stage One = Removal of olivine, plagioclase and augite. Stage Two = Removal of plagioclase, augite and pigeonite. Assimilant = Group III rhyolite + aluminous buchite in ratio ~ 4:1 (See text for details).

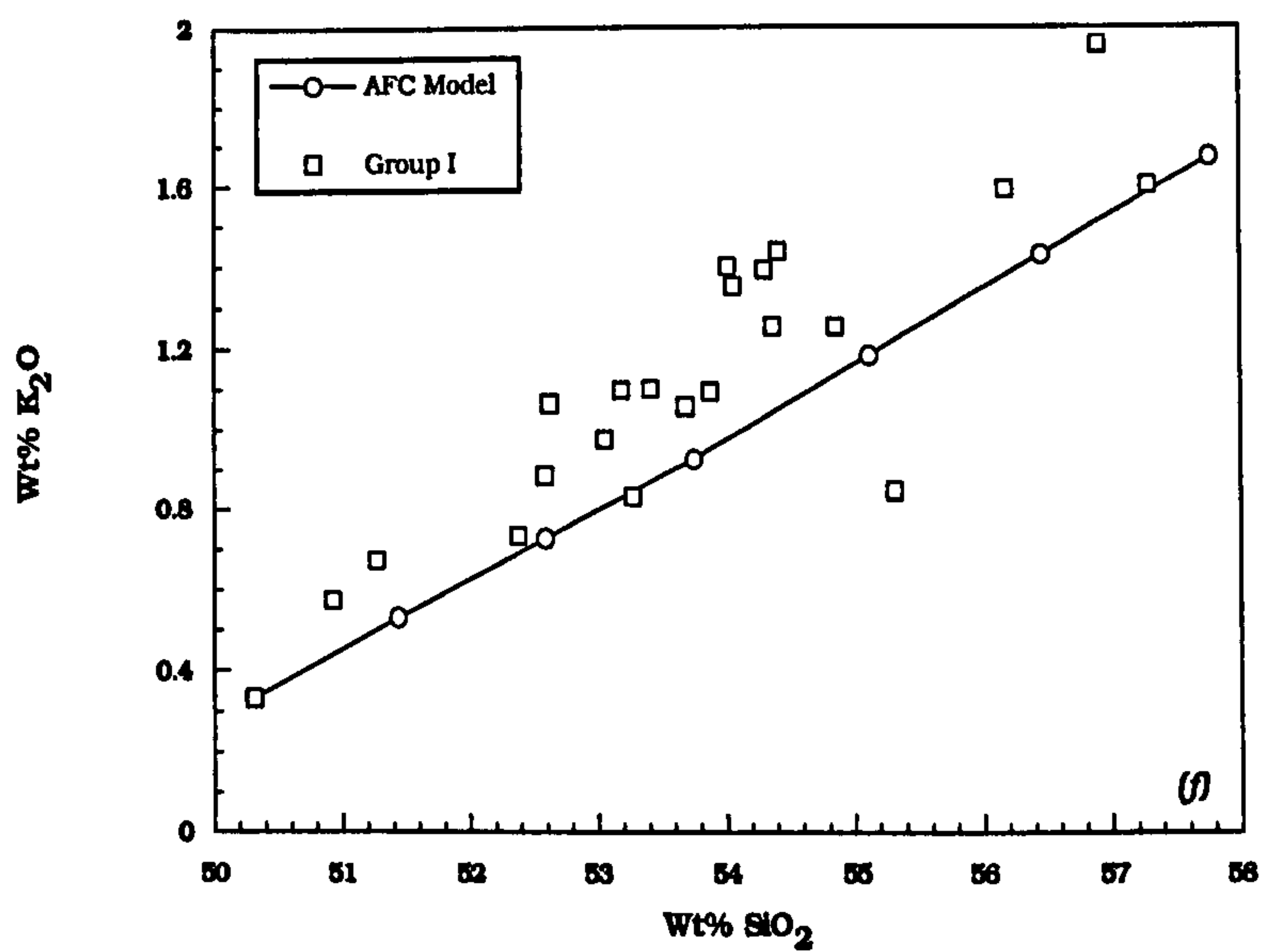
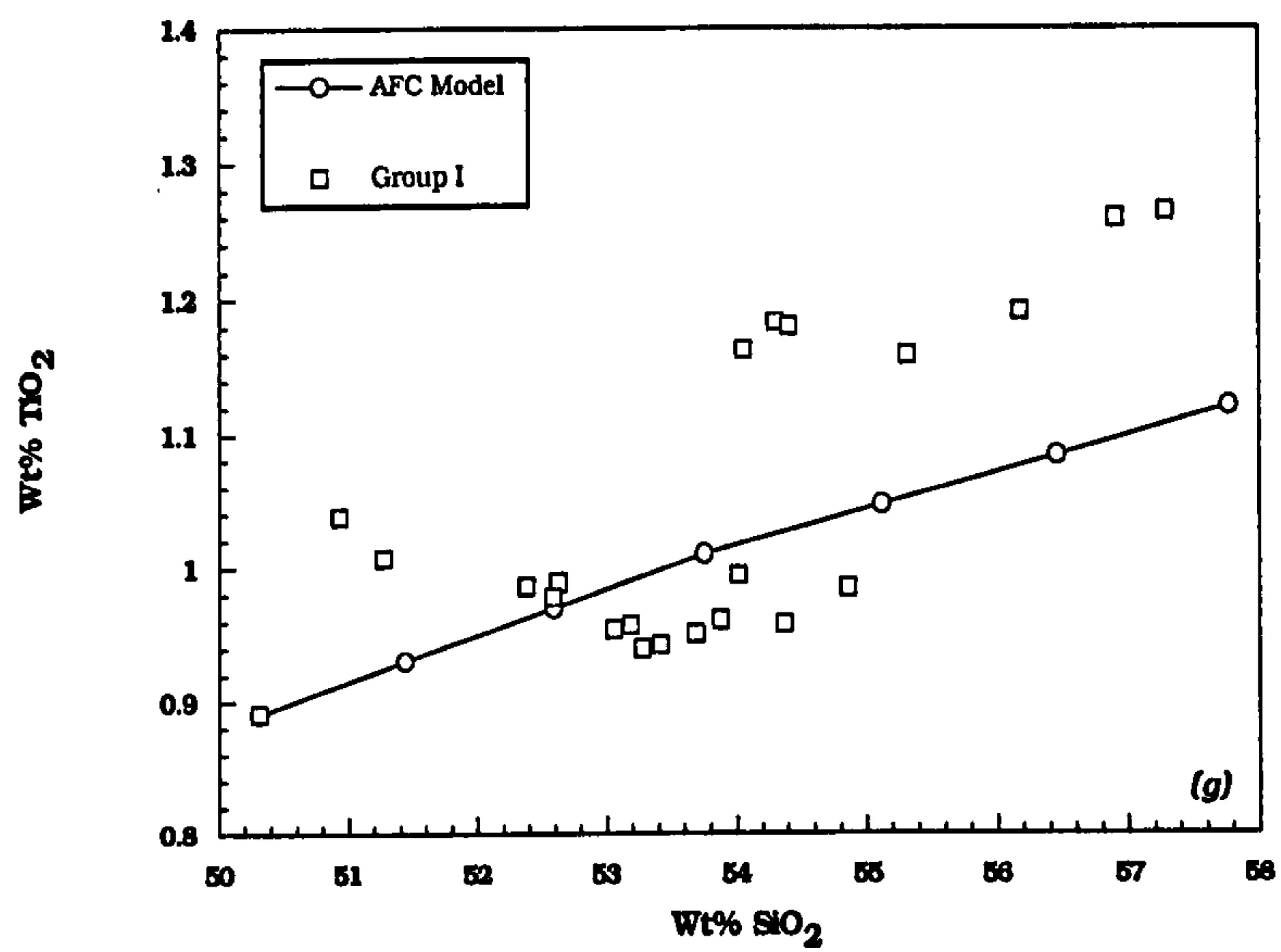
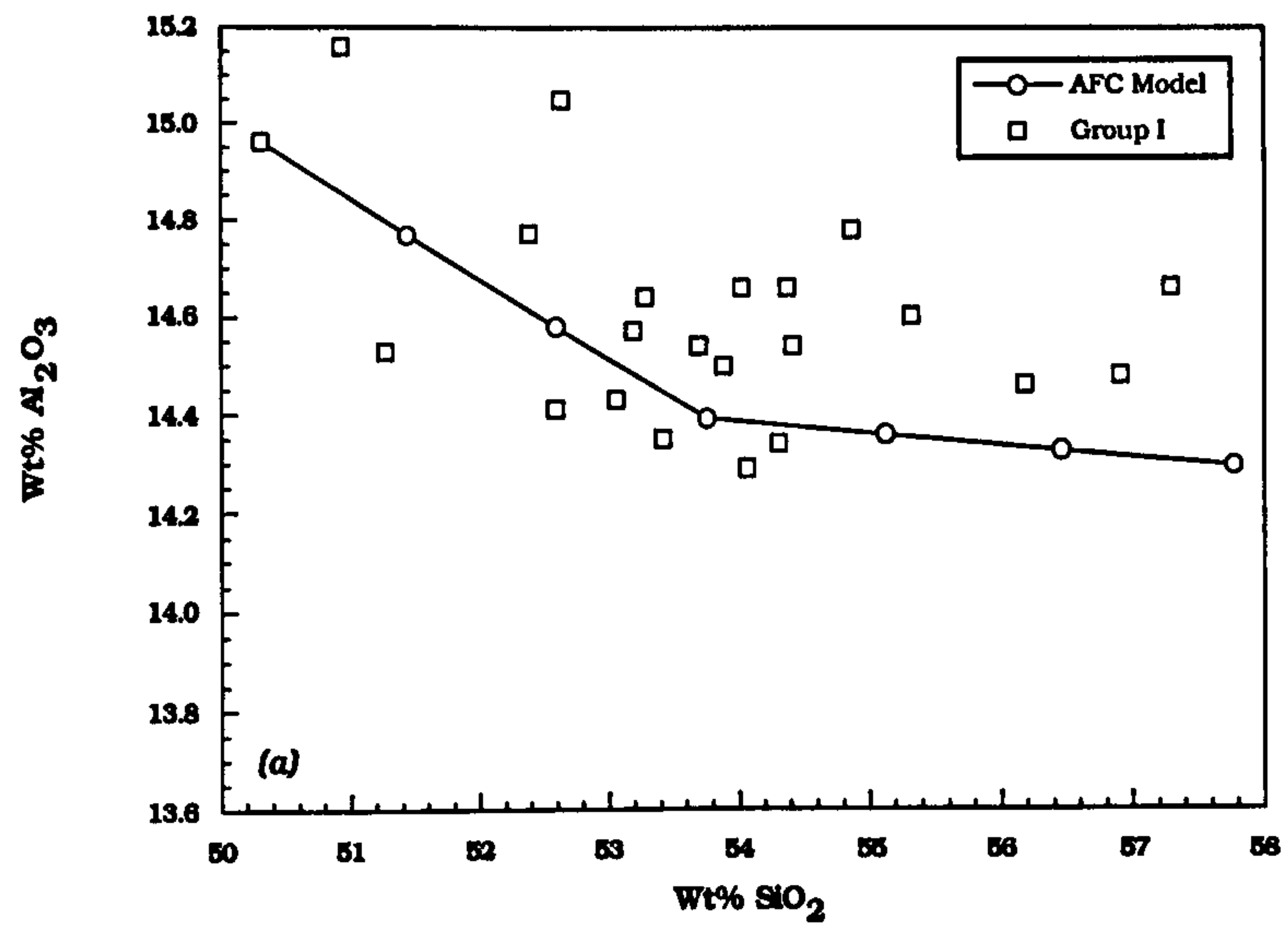


FIGURE 3.10 cont. Major-element AFC modelling of the evolution of the Group I magmas. Starting composition was PGB9 (see Appendix II). Stage One = Removal of olivine, plagioclase and augite. Stage Two = Removal of plagioclase, augite and pigeonite. Assimilant = Group III rhyolite + aluminous buchite in ratio ~ 4:1 (See text for details).

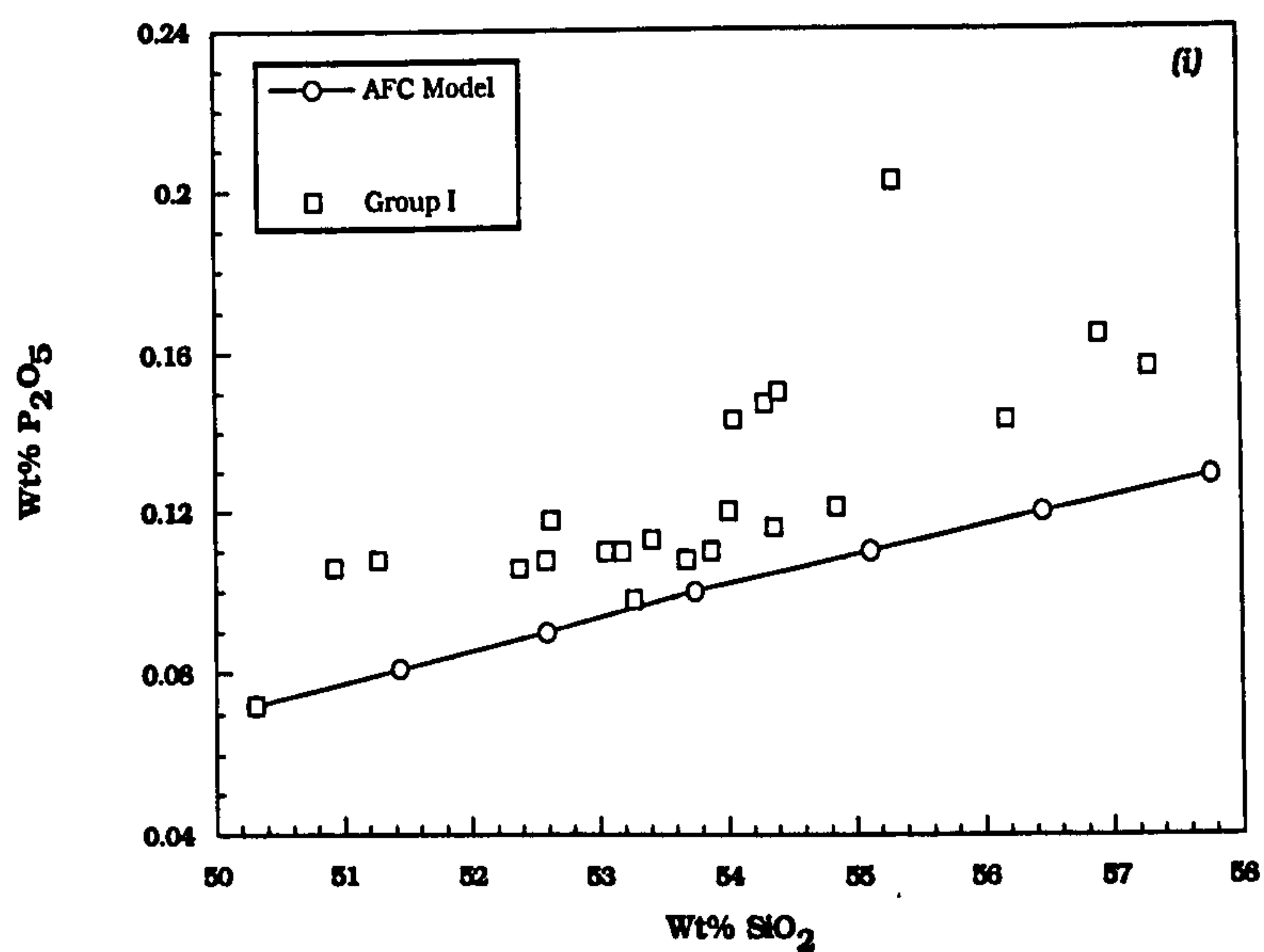
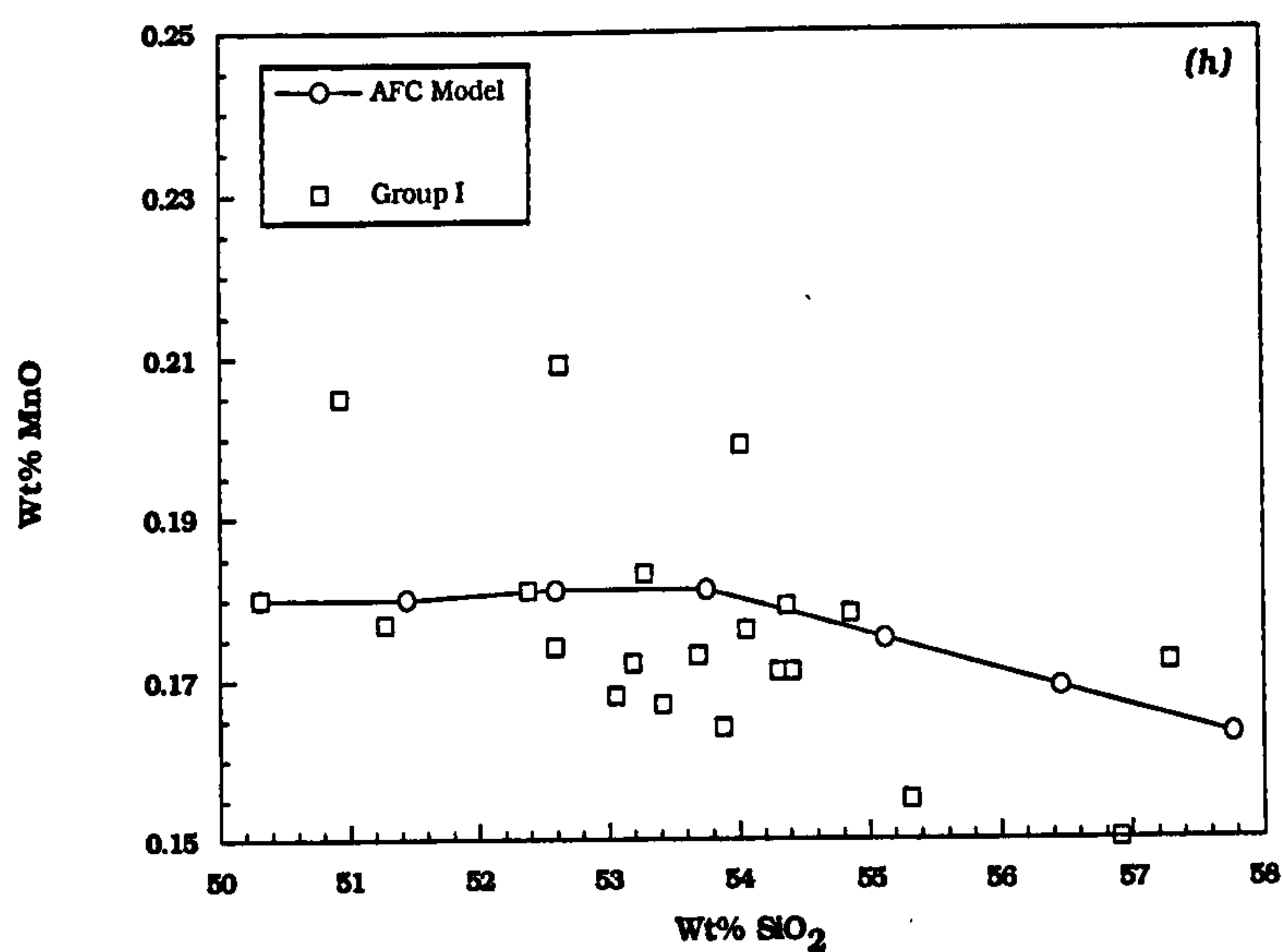
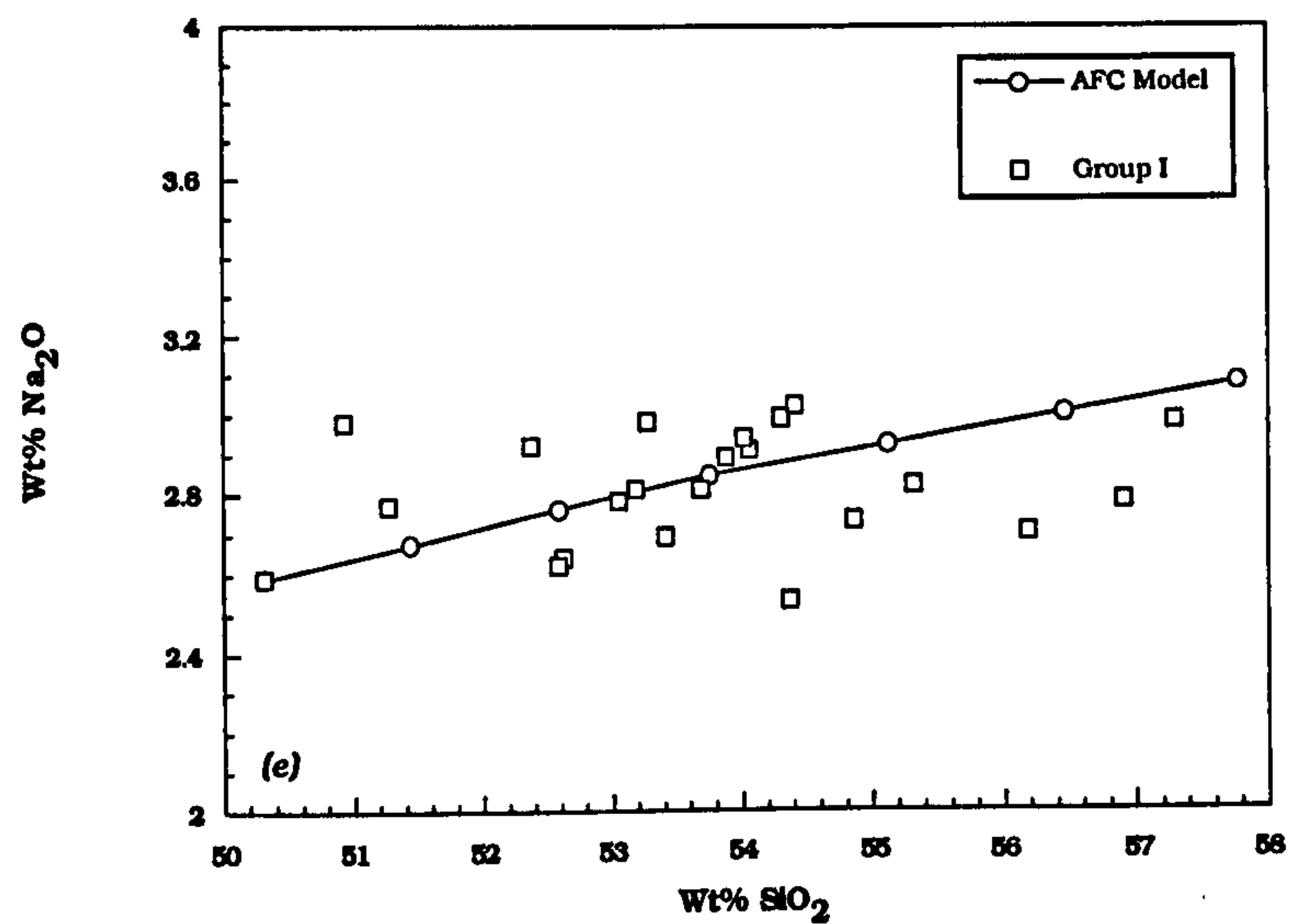


FIGURE 3.10 cont. Major-element AFC modelling of the evolution of the Group I magmas. Starting composition was PGB9 (see Appendix II). Stage One = Removal of olivine, plagioclase and augite. Stage Two = Removal of plagioclase, augite and pigeonite. Assimilant = Group III rhyolite + aluminous buchite in ratio ~ 4:1 (See text for details).

ELEMENT	EFFECT INCREASING DEGREE OF PARTIAL MELTING (F)	EFFECT OF PRESSURE
SiO ₂	For constant MgO, increases with F	Decreases with increasing pressure
Al ₂ O ₃	Decreases with F	Decreases with increasing pressure
MgO	Increases with F at constant pressure	Increases with increasing pressure
FeO	Constant with F at constant pressure	Increases with increasing pressure
Fe ₂ O ₃	Decreases with F	Increases with increasing pressure
Na ₂ O	Decreases with F, incompatible element	
CaO	Increases with F while CPX is residual, then decreases with increasing F	
K ₂ O	Decreases with F	
TiO ₂	Decreases with F	Increases with increasing pressure

Table 3.6 The effects of degree of partial melting and pressure on the major-element composition of mantle-derived melts. (Klein & Langmuir, 1987). F = degree of partial melting.

A consequence of these relationships is that if variation in the degree of partial melting is to be considered as a viable cause for the *major-element* trends seen in the Group I magmas, assuming these to represent primary mantle melts, positive correlations should exist between the element pairs K₂O-Fe₂O₃^{*}, TiO₂-Fe₂O₃^{*}, and Al₂O₃-Fe₂O₃^{*} and a negative correlation between the element pair SiO₂-Fe₂O₃^{*}. As can be seen from *Figure 3.11a-d*, despite the obvious scatter in these plots, all but one of these relationships does not exist within the LSSC. Klein & Langmuir (1987) make extensive use of major-element compositional trends to assess the effects of pressure and the extent of mantle-melting on basalt geochemistry. To achieve this, they first minimise the effects of fractional crystallization, by re-calculating FeO, SiO₂ and Na₂O values after the MgO content of the basalt data set has been normalized to 8 wt% (the so-called Fe_{8.0}, Si_{8.0} and Na_{8.0} values). These have been calculated for the Group I magmas of the LSSC. *Figures 3.12a-b* show the variation of Na_{8.0} vs. Si_{8.0}, and Na_{8.0} vs. Fe_{8.0}. The trends show a fair degree of scatter, possibly due to the effects of contamination and alteration (Kerr, 1995). However, the overall pattern is identical to what would be expected from a suite of basalts related via varying degrees of partial melting, or melting at varying

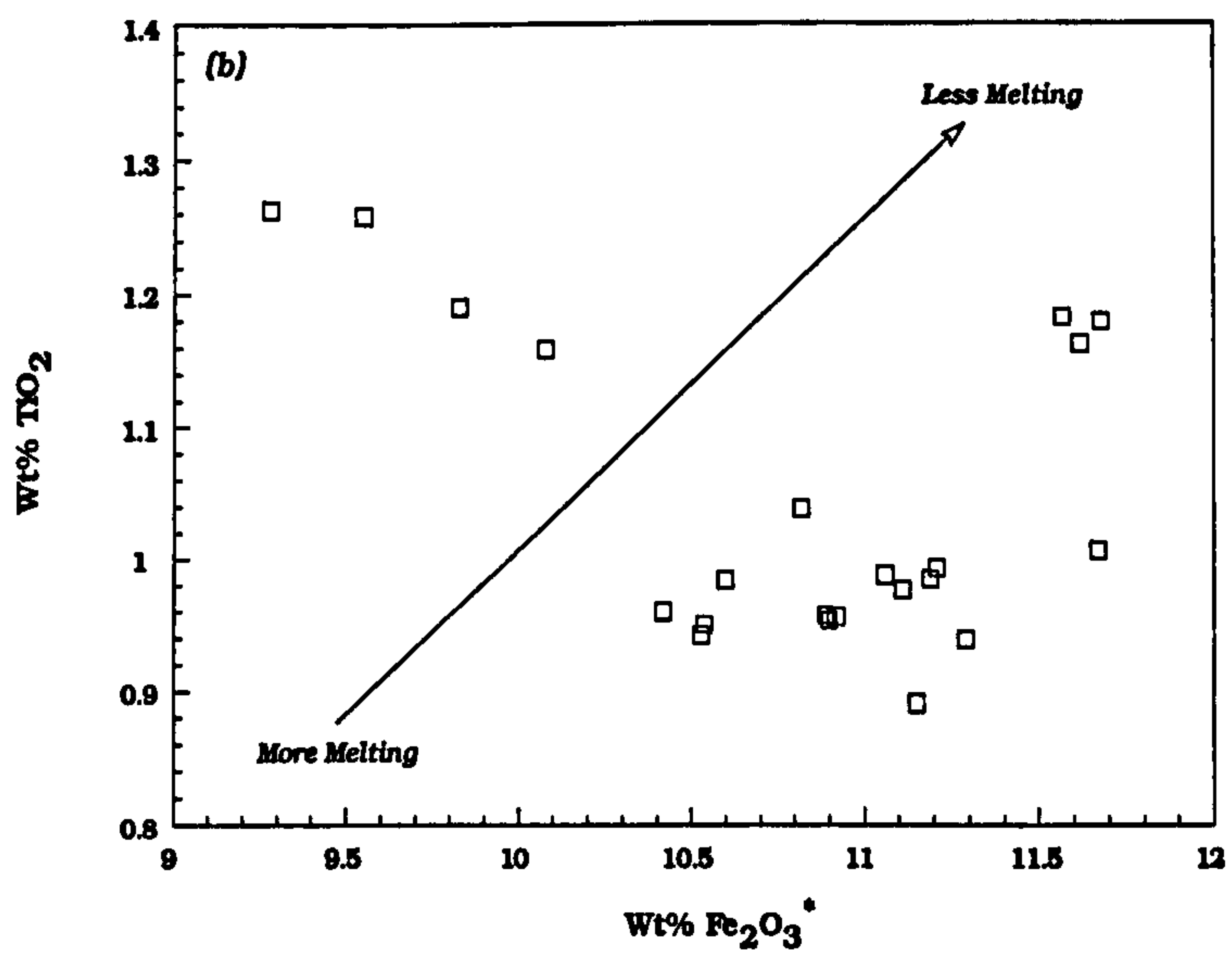
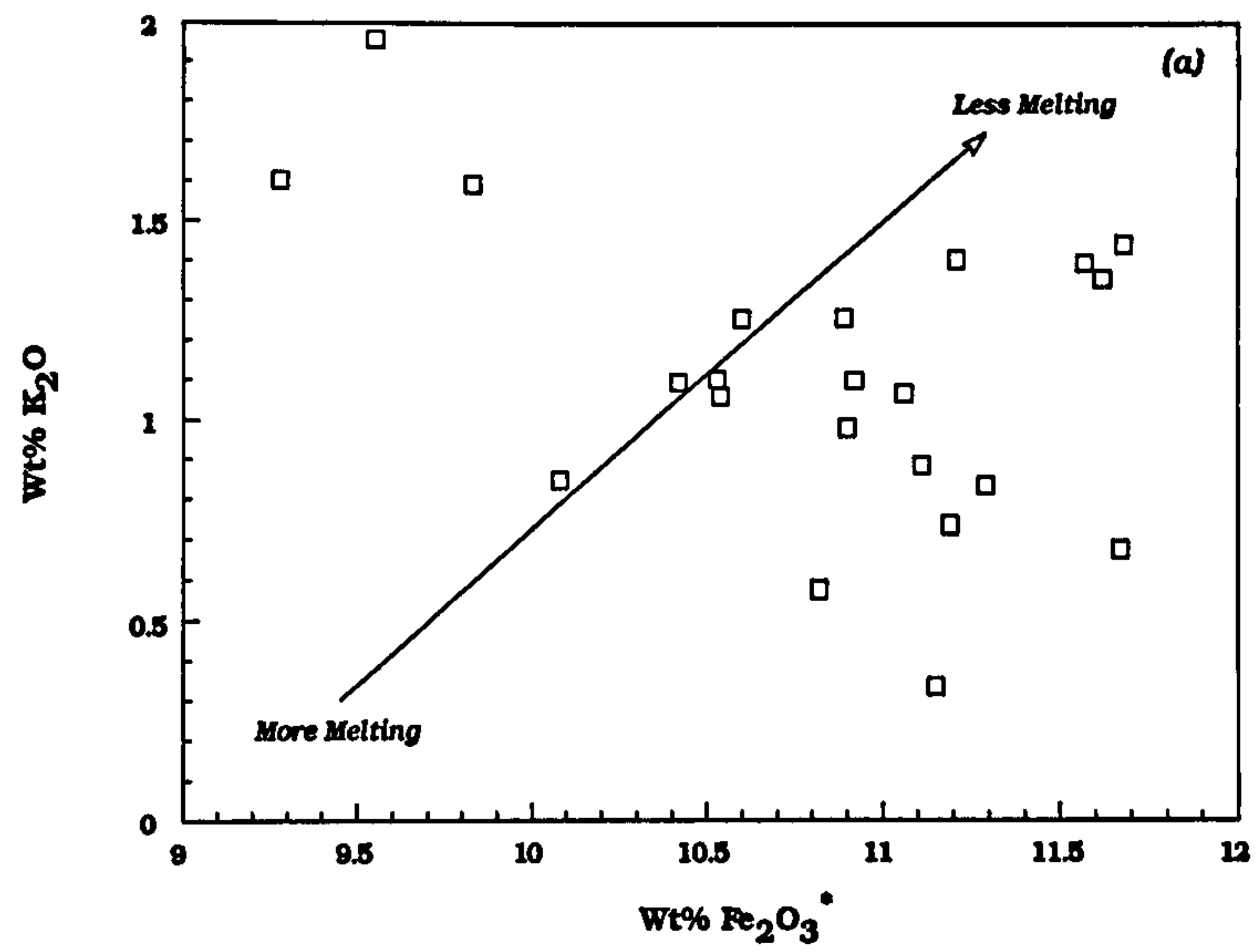


FIGURE 3.11 Variation of (a) $\text{wt\% K}_2\text{O}$, and (b) wt\% TiO_2 with $\text{wt\% Fe}_2\text{O}_3^*$ for Group I magmas. Diagrams show that the variation within the group cannot be the result of differential partial melting. Arrow shows trend that would be expected if suite were related via differential partial melting. See text for details.

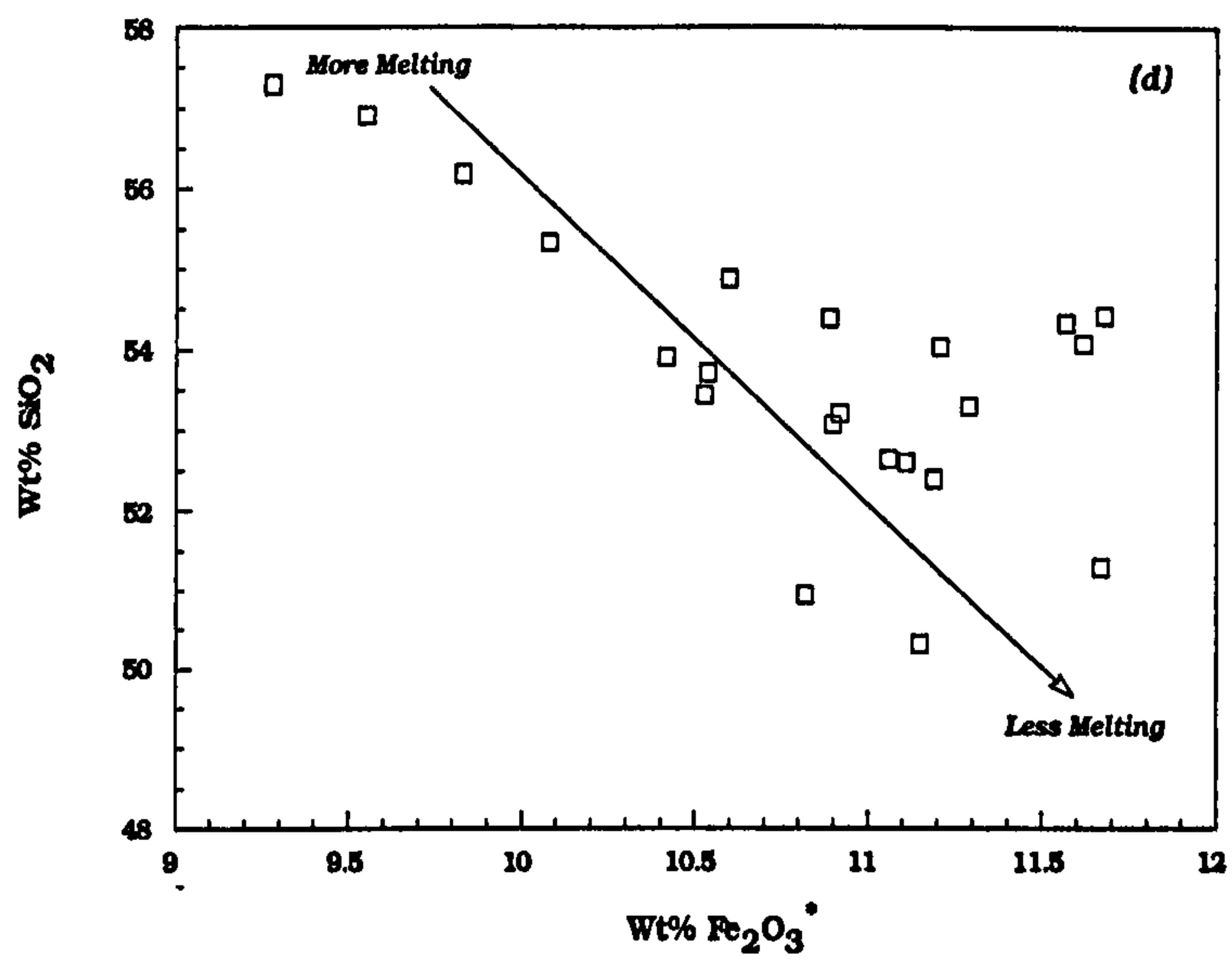
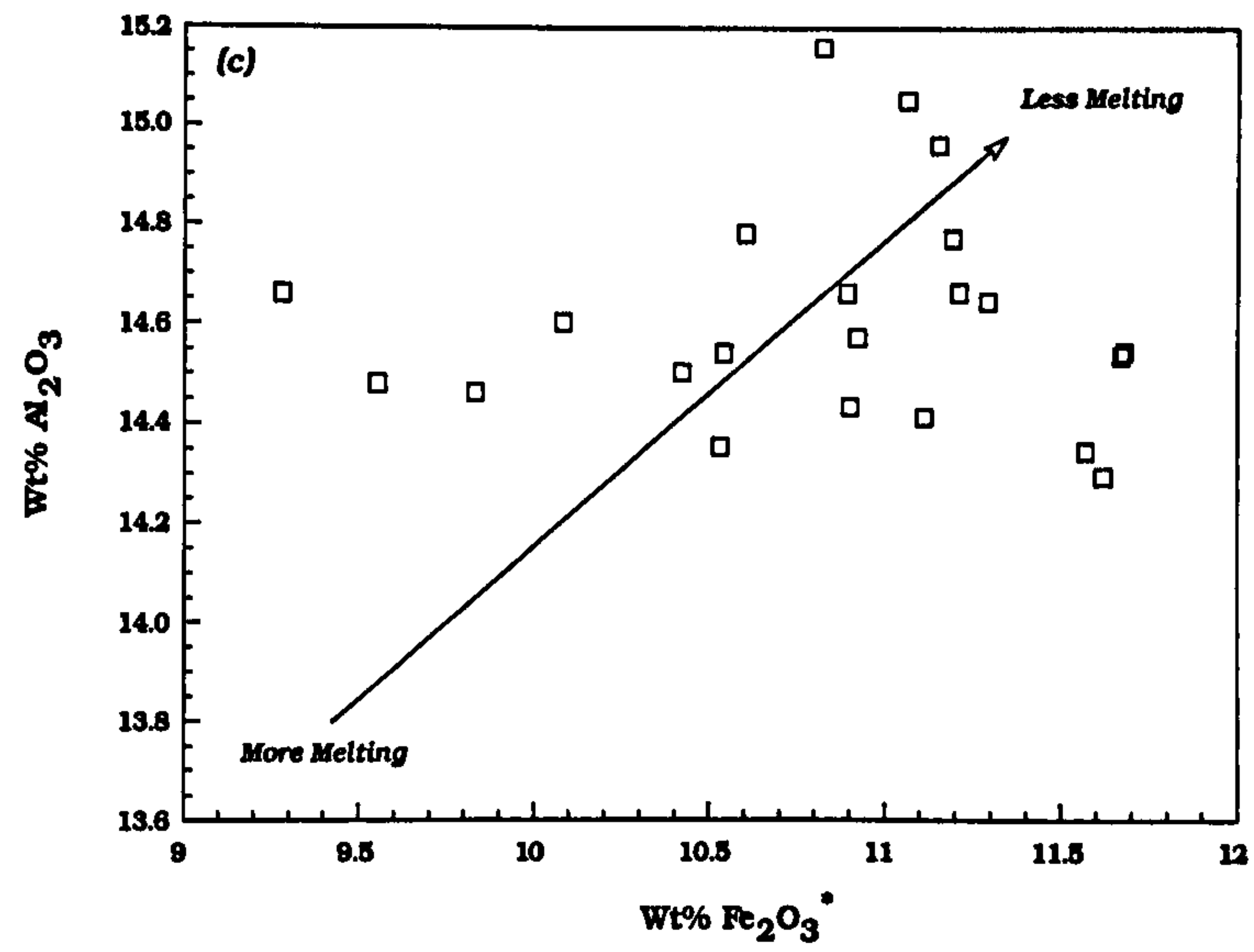


FIGURE 3.11 cont. Variation of (c) wt% Al_2O_3 , and (d) wt% SiO_2 with wt% Fe_2O_3^* for Group I magmas. Arrows show the trend expected if the suite were related via differential partial melting. Only SiO_2 - Fe_2O_3^* plot agrees with predicted behaviour of mantle melting (Klein & Langmuir, 1987, 1989).

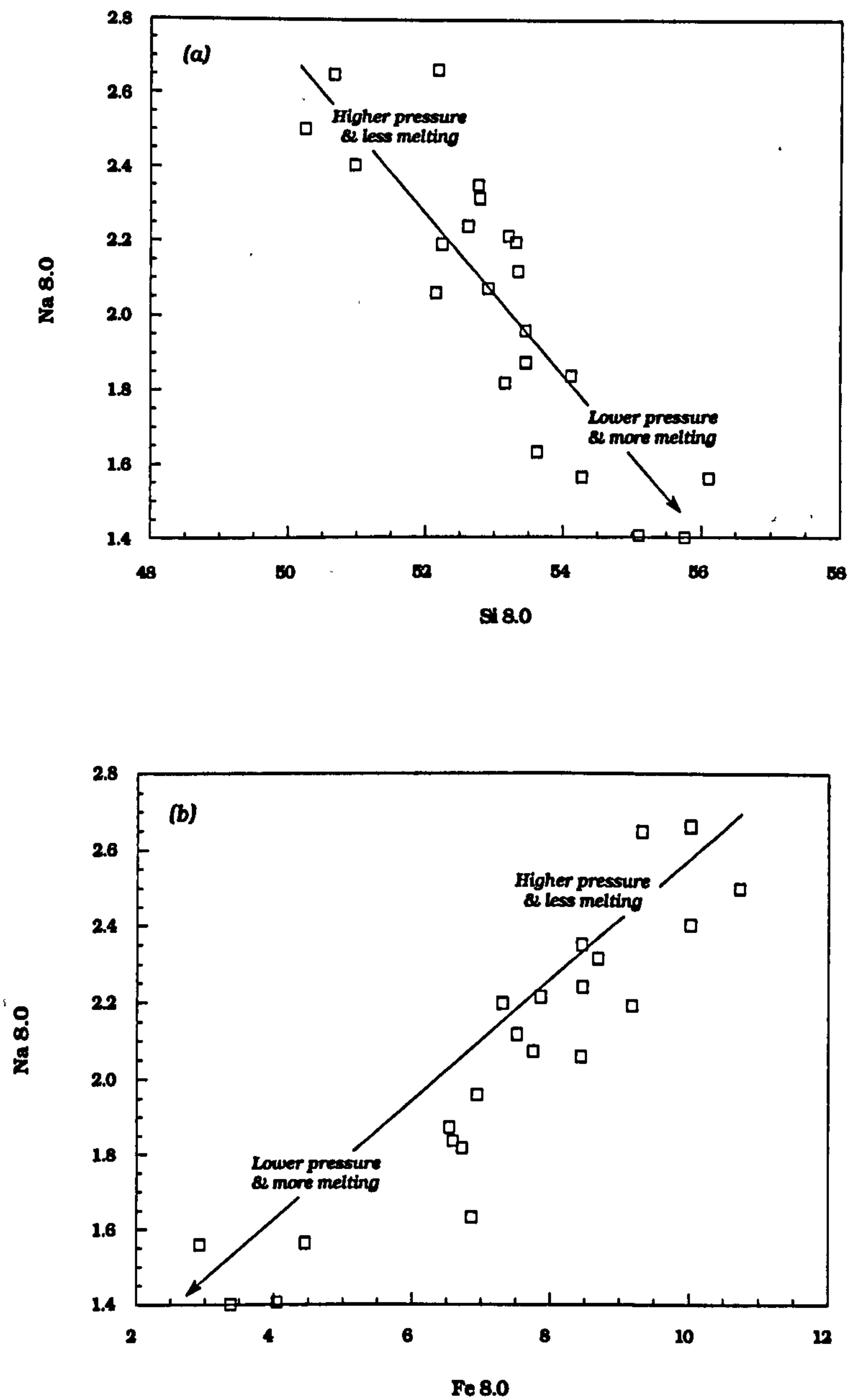


FIGURE 3.12 Plots of (a) Na₈ vs. Sl₈, and (b) Na₈ vs. Fe₈ for Group I magmas. After Klein & Langmuir (1987, 1989).

$$\text{Na}_8 = \text{Na}_2\text{O} + (0.373 * \text{MgO}) - 2.98$$

$$\text{Fe}_8 = \text{FeO}^* + (1.664 * \text{MgO}) - 13.313$$

$$\text{Sl}_8 = \text{SiO}_2 + (0.31 * \text{MgO}) - 2.48$$

pressures (Klein & Langmuir, 1987; Kerr, 1995).

Similar results have been found from work on the SMLS, where Scarrow & Cox (1995) show that once the effect of olivine (\pm Cr-spinel) fractionation has been removed from samples having MgO > 7%, the compositional spread observed can be accounted for by a process of decompressive adiabatic melting. Kerr (1995) also found that the compositional spread of the early Plateau Group lavas from the Mull succession could be explained in a similar manner.

The evidence from the major-element geochemistry of the LSSC Group I magmas is therefore highly ambiguous, with the uncorrected major-element (*e.g.* K₂O *vs.* Fe₂O₃^{*}) data conflicting with the fractionation-corrected parameters (*e.g.* Na_{8.0} *vs.* Fe_{8.0}). To confirm that the major-element signatures are a result of differential partial melting within the mantle, similar systematics *must* be found within the trace-element geochemistry of the suite. These are discussed in Chapter 4. However, since the majority of the major-elements are highly compatible within the phases crystallizing from the Loch Scridain magmas, and that the Group I magmas are relatively evolved quartz tholeiites, it is considered more likely that the spread in compositions seen within the suite is a consequence of magmatic processes that occurred subsequent to the melting event (fractional crystallization, magma mixing, crustal contamination).

Magma mixing

It has been suggested that the andesites and dacites of the LSSC are the products of assimilation of crustal melts (Hall, 1987). Rocks of intermediate tholeiitic composition are rare on Mull, and it seems an unlikely coincidence that where they do occur in relative abundance happens to be within a suite of highly xenolithic sheets.

The exact composition of country-rock melts will obviously be controlled by factors such as the compositions of the crustal lithologies involved, the temperature and pressure at which melting occurred, the volatile content of the rocks, and the length of time over which melts were extracted. However, in general, the first melts to be formed from pelitic or metapelitic source materials will be granitic in composition, and melting should commence in the deeper regions of the continental crust at about 700°C (Thompson, 1981; Gardien *et al.*,

1995). Melting will leave restites enriched in Al, and refractory elements such as Mg, Ti and Ca (MacRae & Nesbitt, 1980; Gardien *et al.*, 1995), corresponding to assemblages including plagioclase, spinel, corundum and aluminosilicates. The melting process may be summarised by the following reaction :



It will be these first partial melts that are most likely to mix with basic magmas to produce hybrids of intermediate composition. Trace-element and Sr/Nd isotope data for the Group III rhyolites (Chapters 4 and 5) show that these silicic magmas have been derived predominantly from melting of crustal sources. In the case of the LSSC therefore, enough silicic magma was segregated to allow the emplacement of a number of rhyolite sheets, rather than all the silicic melts being incorporated into the basic magmas as contaminant.

If it is assumed that the most basic and the most silicic compositions from a single suite approximate the composition of the two end-member magmas involved in the mixing process, then a simple test of the mixing hypothesis may be carried out (Langmuir *et al.*, 1978).

Since the perfect mixing of two components (A and B) is a simple linear procedure, then the amount of each element, *i*, in any hybrid, *h*, must satisfy the relation :

$$C_h^i = a C_A^i + (1 - a) C_B^i \quad \{3.2\}$$

or

$$C_h^i - C_B^i = a(C_A^i - C_B^i) \quad \{3.3\}$$

Relation {3.3} is the equation of a straight line, where *a* is the proportion of magma A in the hybrid, *h*, with $0 < a < 1$. Using this relationship a simple graphical test of the mixing hypothesis may be carried out. The slope of the best fit curve through the individual elements, *a*, gives the proportion of the silicic end-member involved in the mixing, and the correlation coefficient, *R*², describes the fit of

the data as a whole. Elements which fall outside the limits of $\alpha = 1.0$ and $\alpha = 0$ do not satisfy the mixing relation. Again, using the phase relationships as a guide (Section 3.1), those members of the LSSC which may possibly have interacted with crustal melts (potentially many of Group I, and all of Group II samples) were tested using the simple graphical method described above. Two basic end-members were used in the test (ORB2 and TMB3), each mixed with the same acid end-member (RCF1). ORB2 is the most basic member of Group I, with TMB3 being slightly more evolved. ORB2 is an olivine-normative tholeiite, similar in composition to the MORB-like PM basalts. This composition possibly represents the parental magma-type to the entire LSSC (see Chapter 4). TMB3 lies near to the reaction point, A, on the clinopyroxene-olivine-silica projection (*Figure 3.4a*) discussed in Section 3.1, and experiments suggest that mixing of such liquids with crustal melts will drive derivative liquids into the pigeonite primary phase volume on this diagram (Grove *et al.*, 1982). The silicic end-member (RCF1) is the most silicic member of Group III. All samples tested for possible magma-mixing processes lie within the pigeonite primary phase volume. The results of these mixing tests for Group I magmas are shown as a series of graphs in *Figure 3.13a-f*. As indicated on *Figure 3.13a-f*, all the tests which use the most basic member of Group I (ORB2) have correlation coefficients in excess of 0.95, which describes an excellent fit of the data. The compositions of these intermediate liquids would involve mixing between 28% and 52% of the silicic end-member, as described by the slope of the best fit line. If these tests are compared with those which use a more evolved member of Group I (TMB3), it can be seen that the fit of many of the data are more or less indistinguishable from those which use the more basic end-member. To resolve which basic end-member is the more likely to have been involved in the mixing process, similar tests must be carried out using trace-element concentrations. These are presented in Chapter 4.

The phase relationships also predict that mixing between more- and less-evolved basic magmas may also have occurred, resulting in liquids which plot within the augite primary phase volume in the diopside-olivine-silica phase diagram (*Figure 3.9b*). The mixing tests presented in *Figure 3.14a-b* show that such processes are chemically viable. This suggests that the magma storage reservoir for the LSSC was continually being replenished with batches of fresh basic magma. The theoretical

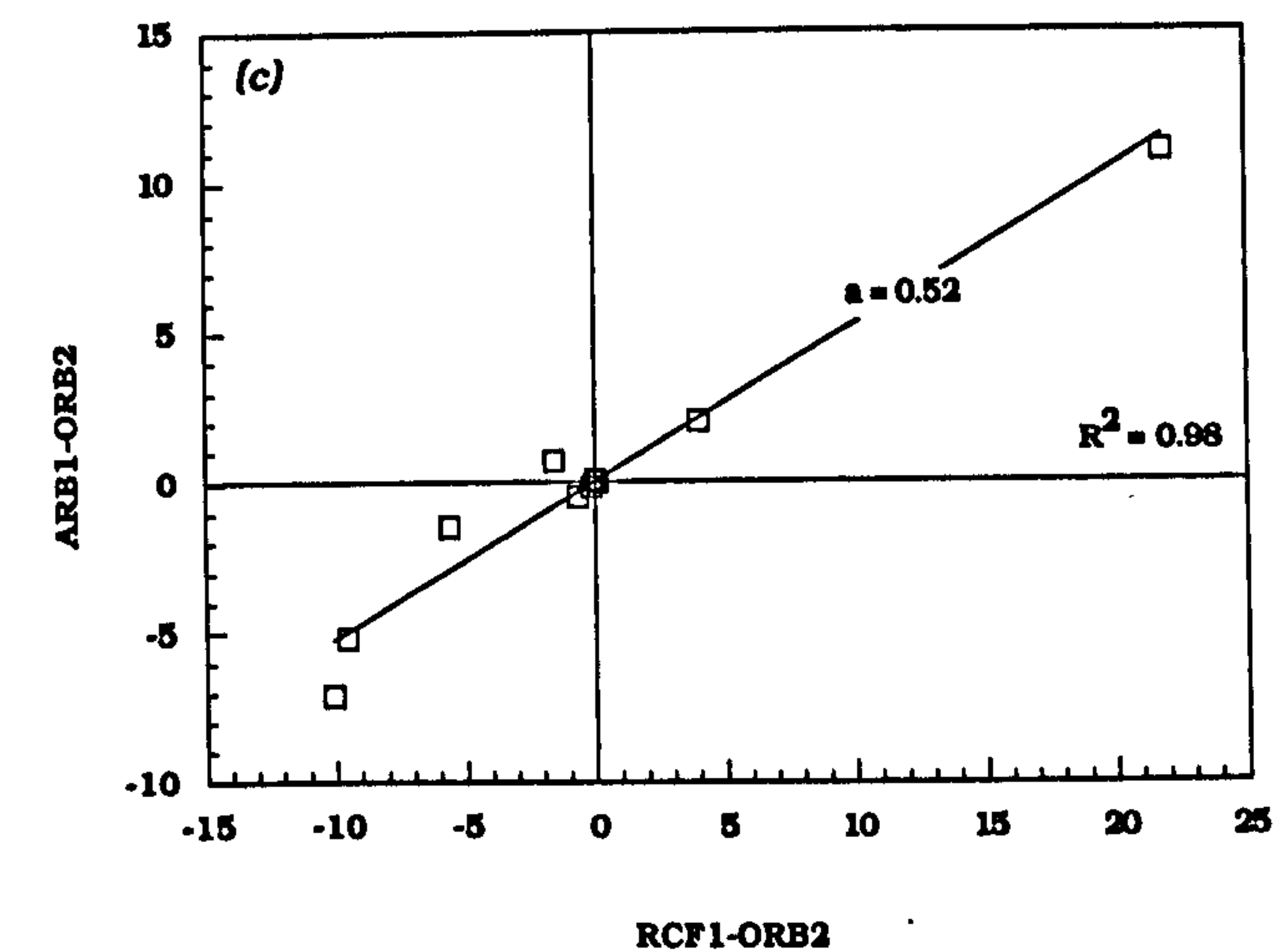
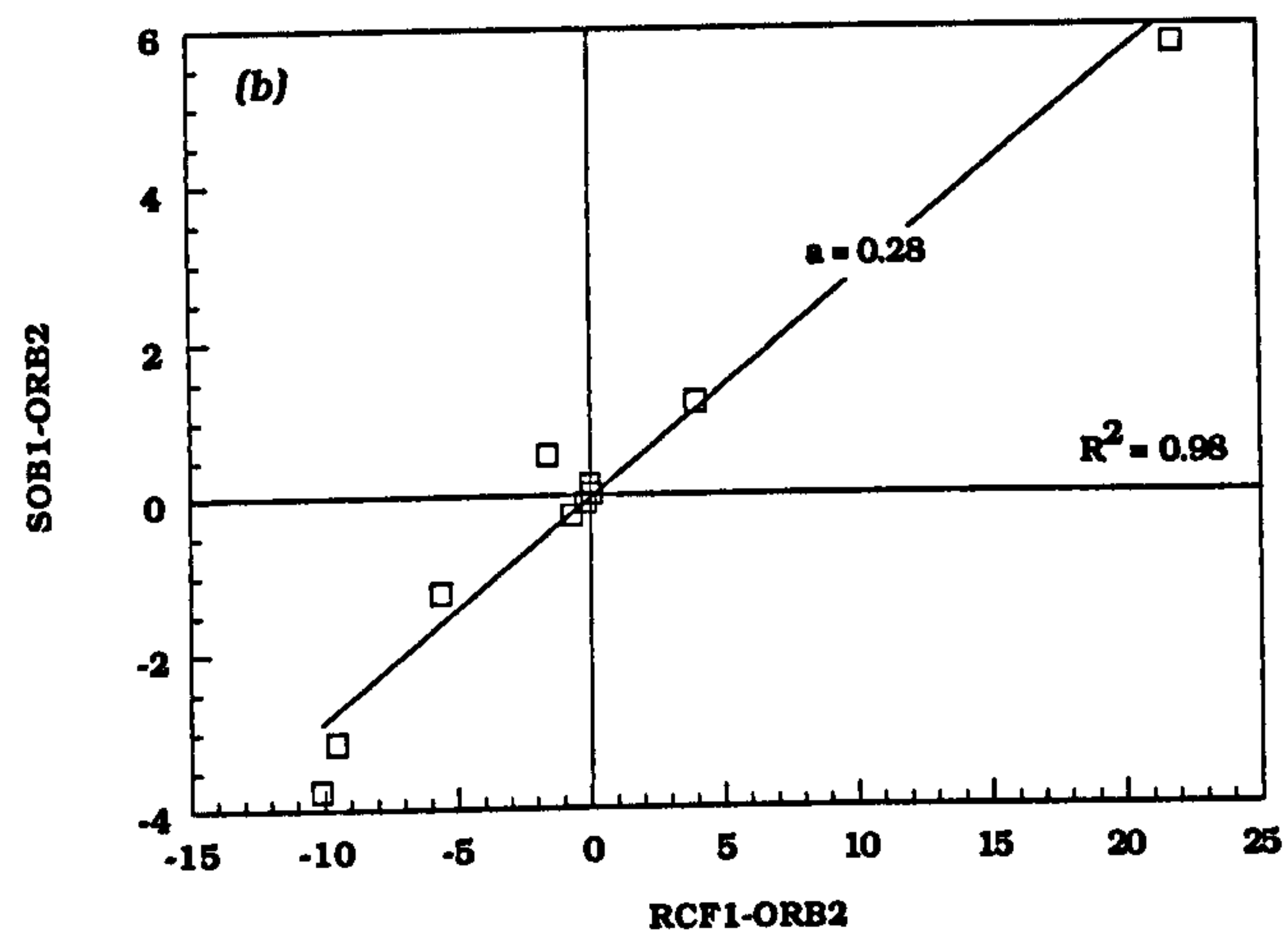
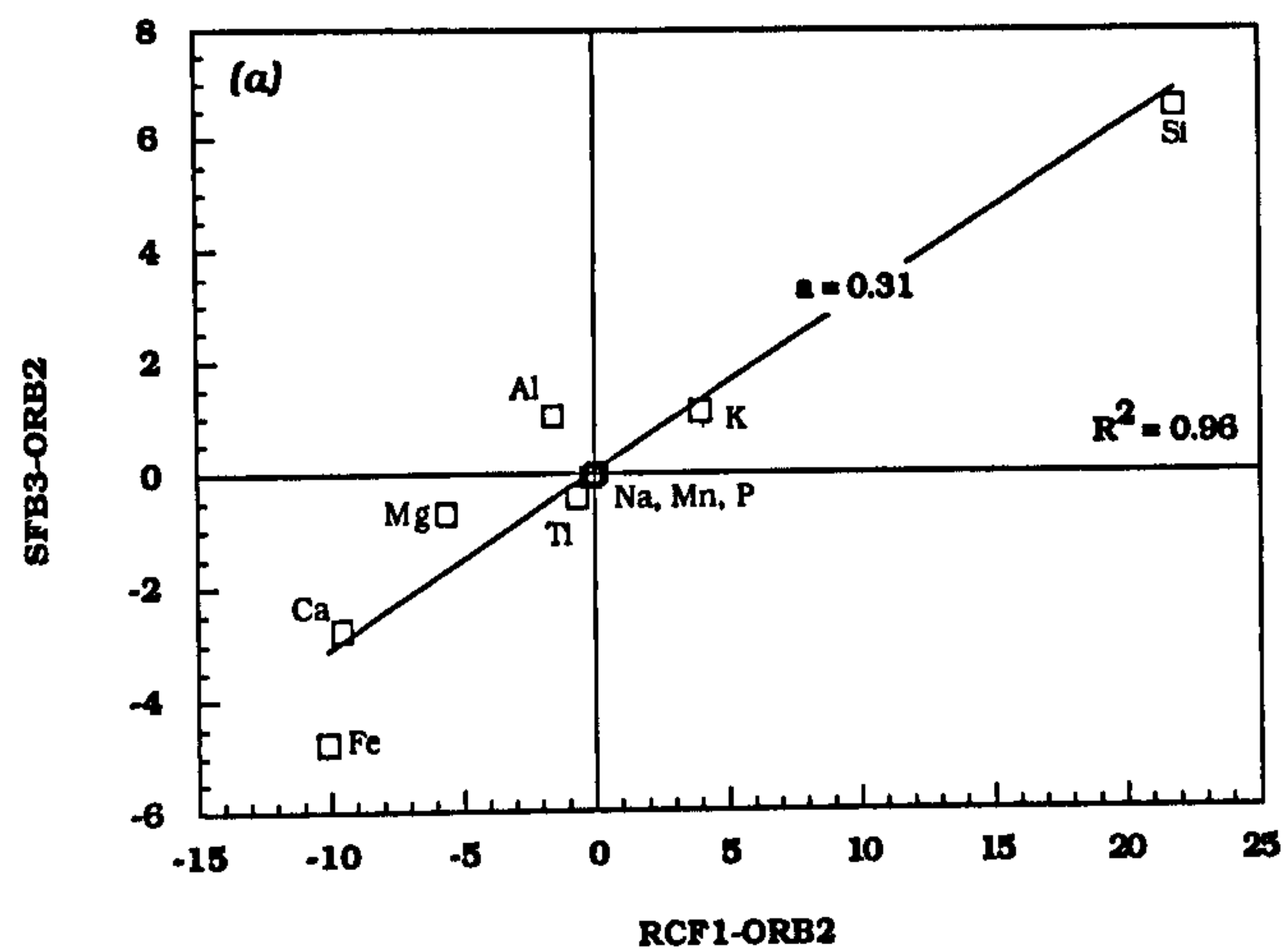


FIGURE 3.13 Mixing plots for possible hybrid Group I magmas. ORB2 and RCF1 are basic and silicic endmembers respectively. 'a' is amount of silicic endmember involved in the mixture. R^2 = Correlation coefficient.

After Langmuir et al. (1978)

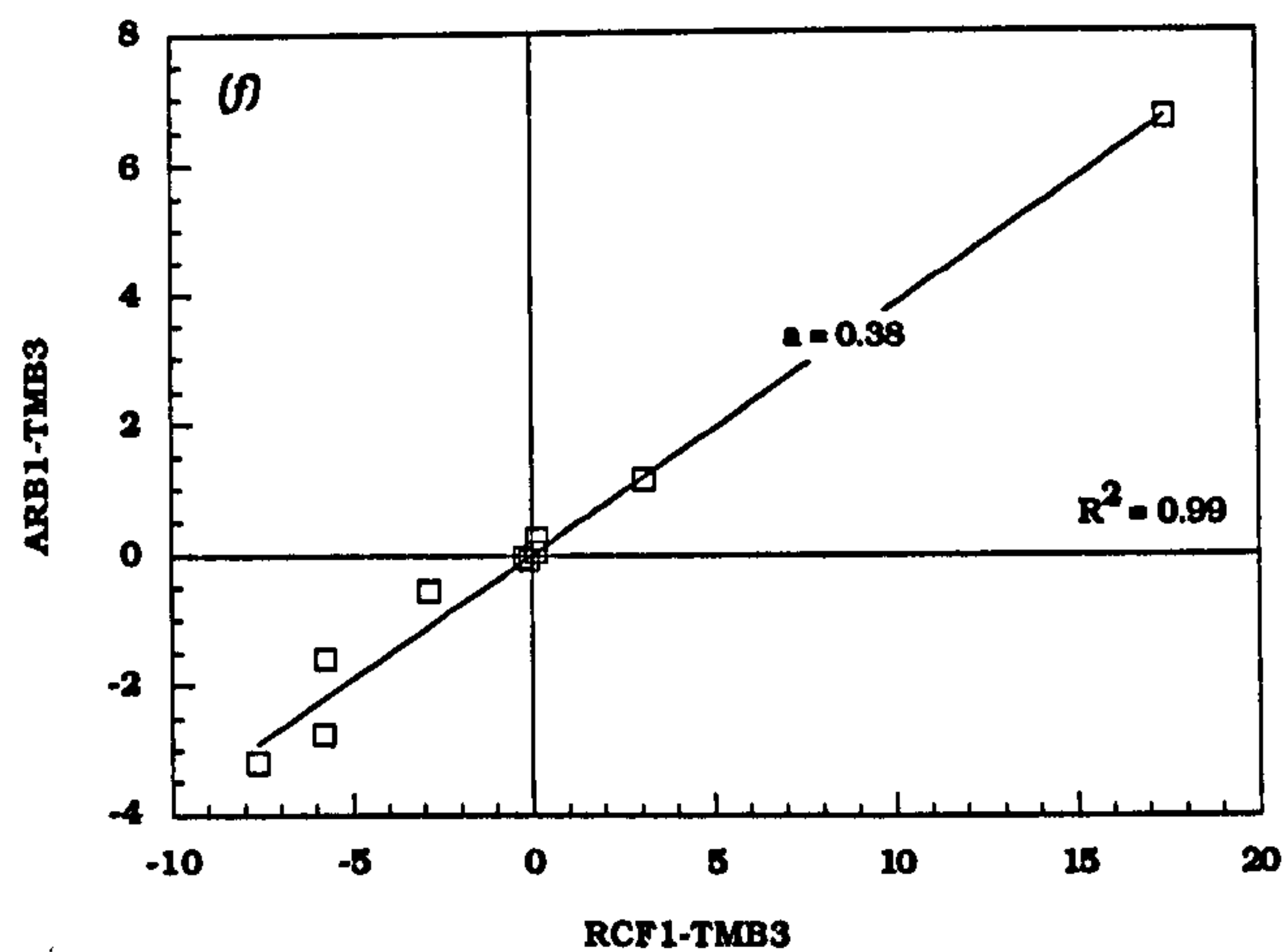
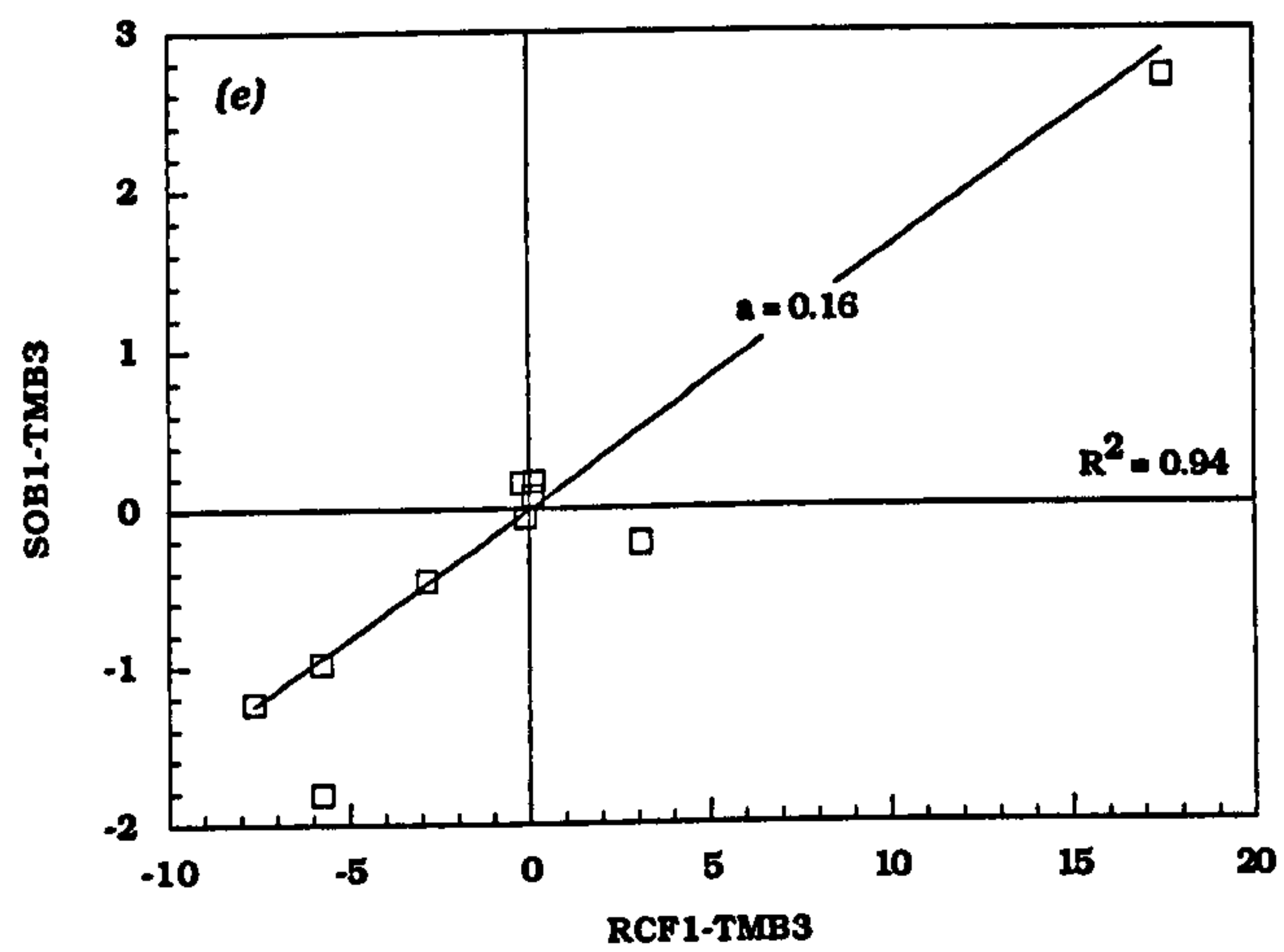
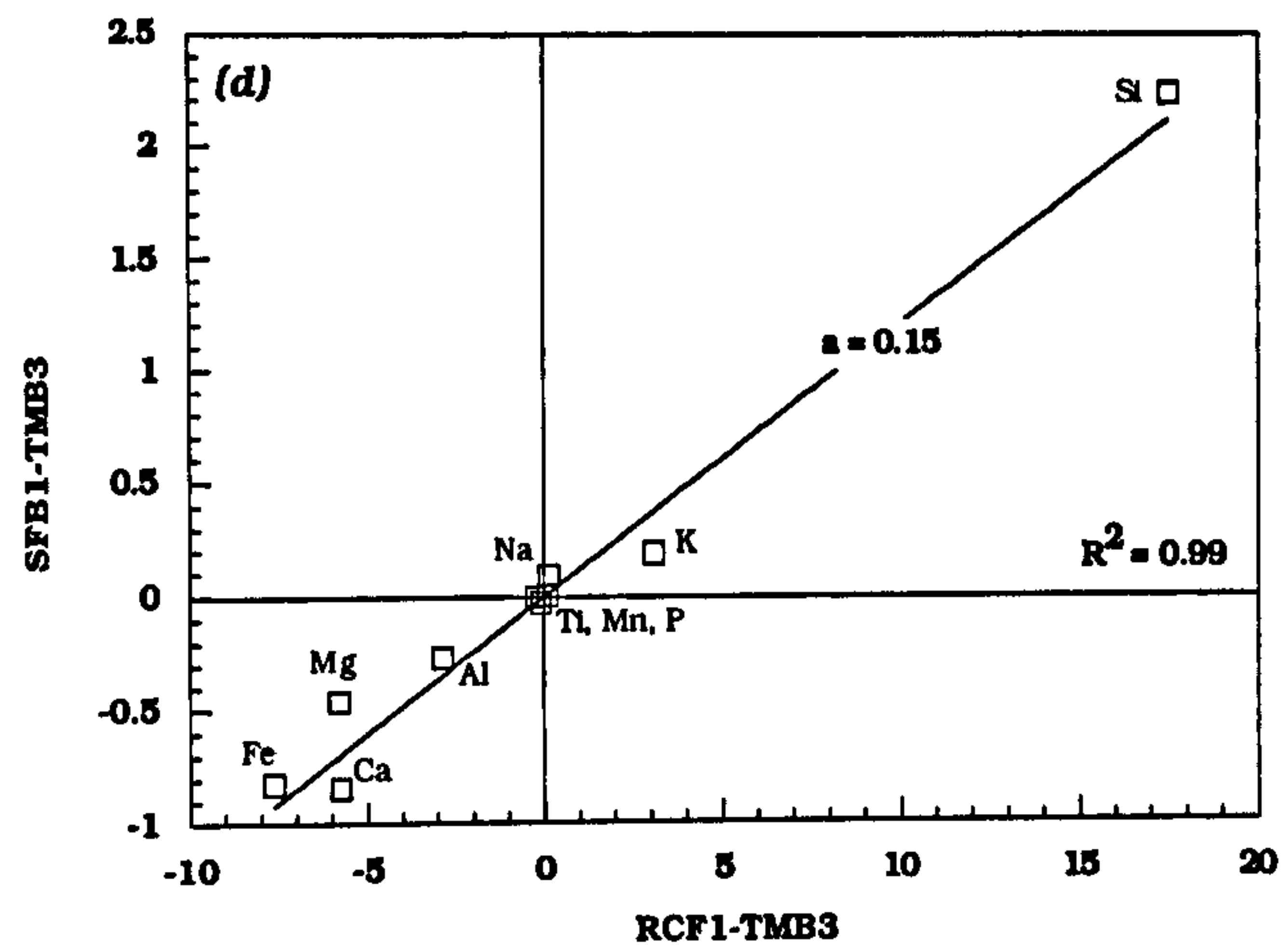


FIGURE 3.13 cont. Mixing plots for possible hybrid Group I magmas. TMB3 and RCF1 are basic and silicic endmembers respectively. 'a' is amount of silicic endmember involved in the mixture. R^2 = Correlation coefficient.

After Langmuir et al. (1978)

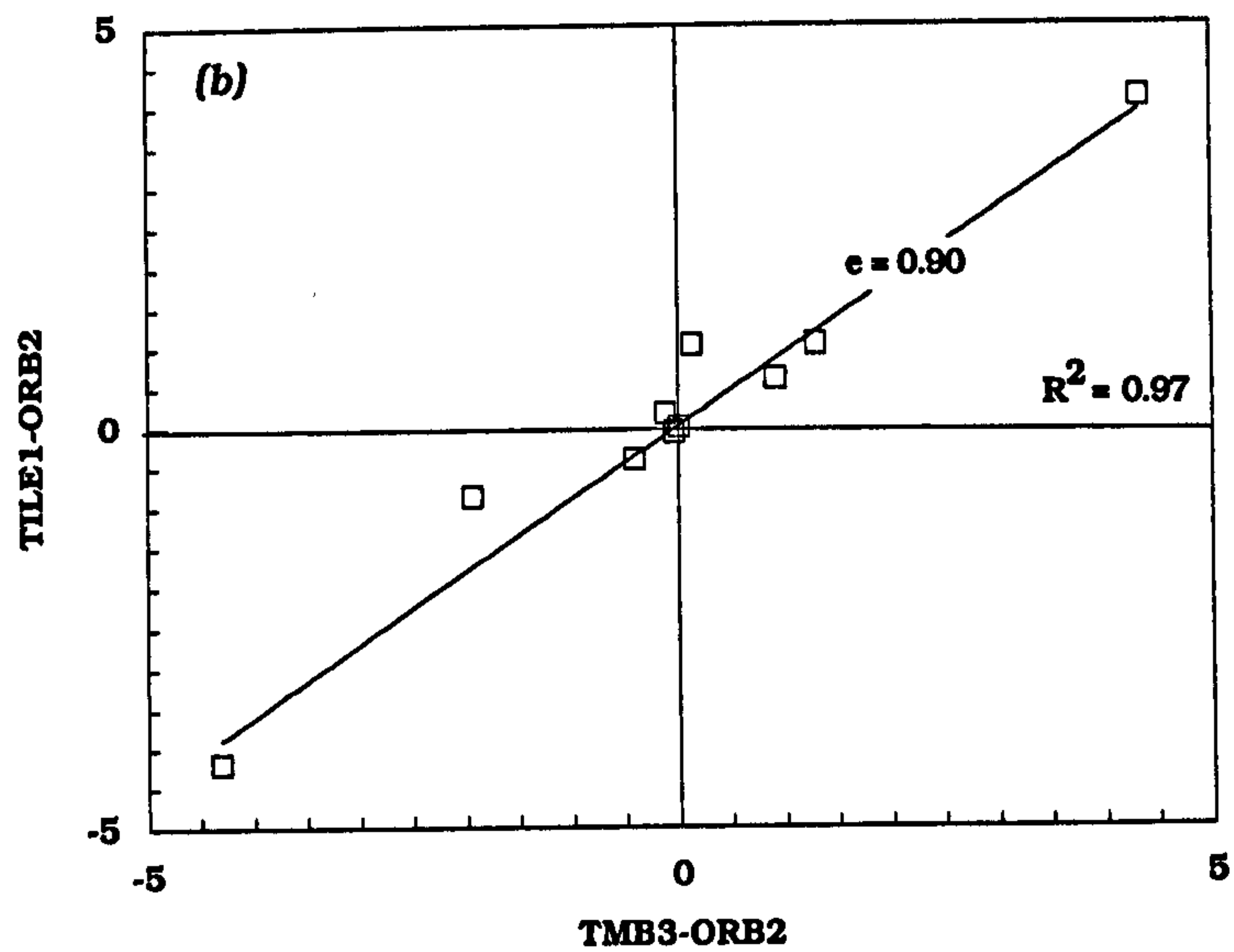
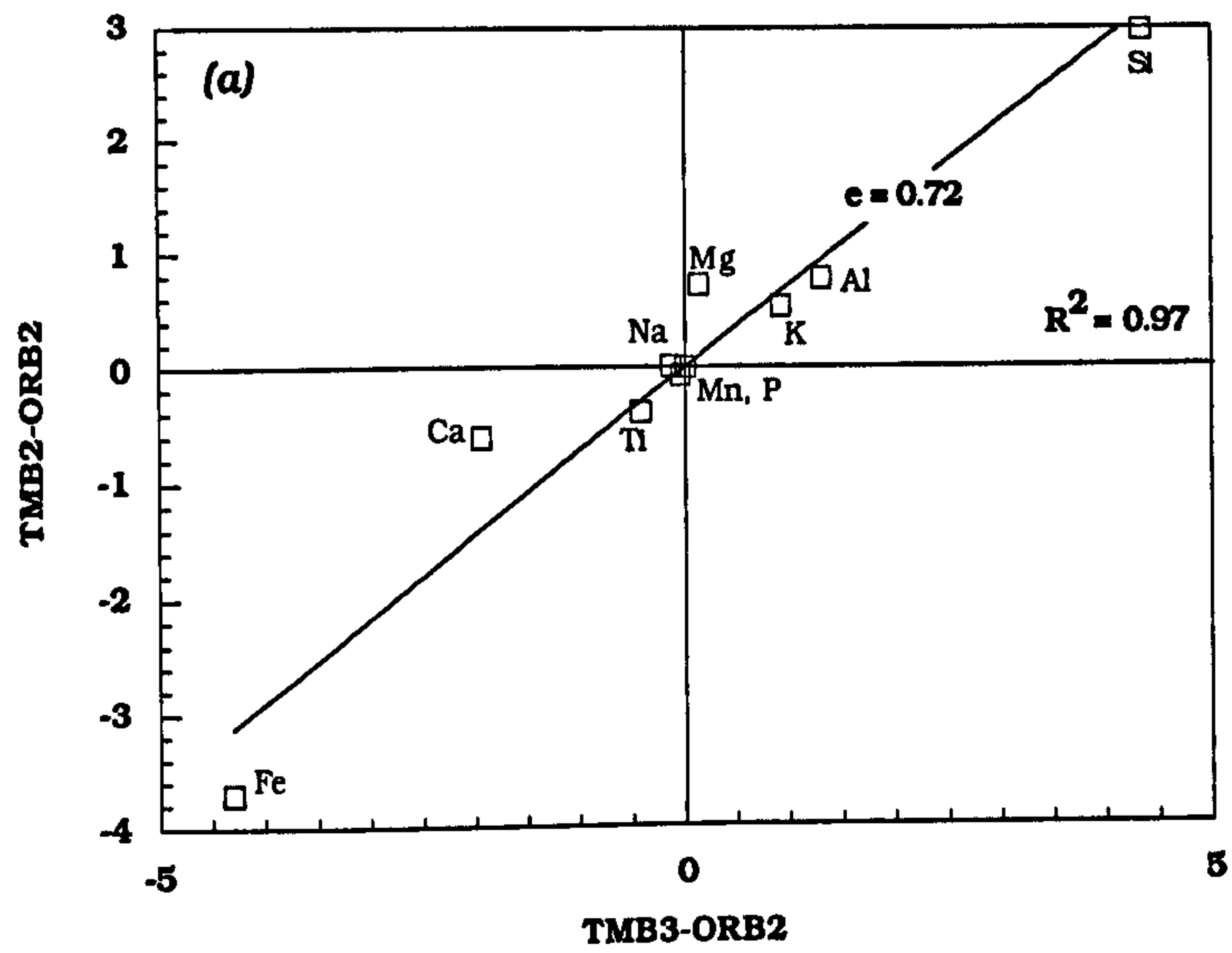


FIGURE 3.14 Mixing plots for least evolved / more evolved basic magma mixing in Group I. ORB2 and TMB3 are least evolved and evolved endmembers respectively. R^2 = Correlation coefficient.

"e" = amount of evolved endmember in mixture

After Langmuir et al. (1978)

geochemical evolution of magmas in a chamber undergoing periodic replenishment, tapping and fractionation (RTF), introduced by O'Hara (1977), can be used to explain the decoupling of major- and trace-elements during crystal-liquid fractionation (Cox, 1988; Bell *et al.*, 1994). This process will be discussed further in Chapter 4.

The extent of mixing between one magma and another depends upon the flow rate and on the relative densities and viscosities of the two magmas involved. Passively emplaced, dense magma inputs may mix very little with a resident magma of comparable viscosity. However, a similar magma injected with high upward momentum will produce turbulent overturn which is a very efficient magma mixing process (Campbell & Turner, 1986). Direct, physical evidence for magma mixing is rarely preserved within derivative liquids. However, features suggestive of magma mixing and mingling include (McBirney, 1979):

- a) Disequilibrium phenocryst assemblages;
- b) Unusual zoning profiles in phenocrysts;
- c) Highly corroded and embayed phenocrysts suggesting resorption and reaction with the magma;
- d) Physically unmixed blebs of basic material in silicic rocks, or vica versa (magma mingling).

These features can all be found within members of the LSSC. Disequilibrium plagioclase phenocryst assemblages have already been described in Chapter 2.2, and the mixing of basic and silicic magmas at the site of emplacement will be discussed in Chapter 6.2. The wholesale mixing of large volumes of basic and silicic magmas is strongly inhibited by large viscosity differences, as exemplified by the Rudh' a' Chromain composite sheet [NM 521202], where mixing has in places, been incomplete, with blebs of basic material being preserved in the rhyolitic portion of the sheet. Therefore, if the compositional spectrum seen within the LSSC is considered to be the result of mixing between basic magmas and silicic (possibly crustal) melts, then the mixing process probably involved very small volumes of granitic melts introduced over considerable periods of time. Such a process would require a constant high heat flow within the magma storage reservoir, again, suggesting that fresh batches of basic magma were continually available, or that the magma was continuously fractionating to provide the necessary heat for melting.

3.4 Major-element evolution of the Group II andesites and dacites

The Group II magmas, in particular the porphyritic dacites, are more problematical than the Group I magmas. The petrogenesis of the group cannot be completely separated from the evolution of the Group I magmas, since the two are found together as composite sheets. Group II magmas are also found as xenoliths within Group I.

The drop-off in the slope of the MgO *vs.* SiO₂ (*Figure 3.5a*) trend for Group II magmas indicates that olivine, at this stage, is no longer a fractionating phase. The slopes on the CaO and CaO/Al₂O₃ *vs.* SiO₂ (*Figure 3.8*) also diminish, indicating either the increased importance of plagioclase fractionation, or the incoming of a Ca-poor clinopyroxene. The most reasonable conclusion is that both occurred, since the dacites of Group II contain both plagioclase and pigeonite phenocrysts.

Similar phenocryst assemblages to that found in the Group II magmas can be found in dacitic and rhyolitic intrusions throughout the North Atlantic Tertiary Igneous Province (NATIP). On Mull, the Loch Ba ring dyke, dominantly a banded rhyolitic welded tuff, contains dark glasses with phenocrysts of plagioclase (An₆₅₋₃₀), high-Ca pyroxene (Wo₄₅En₄₅Fs₁₀-Wo₄₃En₁₁Fs₄₆), pigeonite (Wo₉En₅₆Fs₃₅-Wo₉En₃₃Fs₅₆), and Fe-Ti oxides (Sparks, 1988). The rhyolitic portion of the intrusion contains phenocrysts of plagioclase (An₃₁₋₁₇), alkali-feldspar, ferroaugite (~Wo₄₀En₂₇Fs₃₃), orthopyroxene (~Wo₄En₆₃Fs₃₃), fayalite (~Fa₈₆) and quartz (Sparks, 1988). This latter assemblage is almost identical to that found in minor silicic intrusions associated with the Thingmuli central volcano, Iceland (Carmichael, 1960a, 1960b). Elsewhere in the BTVP, porphyritic dacites, with alkali-feldspar, plagioclase, augite and quartz phenocrysts, can be found on the Isle of Eigg, and the Isle of Arran (Carmichael, 1960a, 1960b, 1963; Dickin *et al.*, 1981).

The mineralogical and textural relationships between the different rocks types within the Loch Ba ring dyke point to it being produced by the intimate mixing of magmas during emplacement (Sparks, 1988). However, Carmichael (1960a, 1960b, 1963) demonstrates that the phenocryst assemblage of the Icelandic and other Hebridean silicic minor intrusions is in equilibrium with the residual glasses.

The porphyritic dacites of the LSSC contain glasses of two distinct

compositions, with the glassy portion of the sheets being visibly heterogeneous (see Chapter 2). One glass is more basic, with SiO₂ at ~ 57 wt%, the other is silicic, with SiO₂ at ~ 71 wt%. Table 3.7 gives the compositions of these glasses.

	Basic Glass	Silicic Glass
SiO₂	56.66	71.17
TiO₂	1.53	0.72
Al₂O₃	13.59	14.30
FeO*	11.75	1.76
MnO	0.16	0.00
MgO	0.63	0.02
CaO	4.98	2.19
Na₂O	3.49	3.46
K₂O	3.85	4.56
P₂O₅	0.14	0.19

Table 3.7 Average basic and silicic glass compositions in porphyritic dacites of Group II.

The plagioclase phenocrysts, as discussed in Chapter 2, have resorbed cores of composition An₄₅, with overgrowth plagioclase generally being more calcic at An₅₀.

Figure 3.15 shows the system albite-anorthite (after Bowen, 1913). On this diagram are plotted the phenocryst core and overgrowth compositions from a Group II dacite, along with the normative anorthite content of the two co-existing glasses. It is clear that the plagioclase phenocryst cores, at An₄₅, will be in equilibrium with the silicic glass, whereas the more calcic overgrowths will be in equilibrium with the more basic glass. These features suggest that silicic magma had fractionated plagioclase before the introduction of the basic magma, and that after an initial period of resorption of the phenocrysts (coinciding with the mixing of hot basic magma), crystal fractionation resumed. The new plagioclase which grew (An₅₁) were in equilibrium with the *hybrid*, basic magma. The basic glass, as analysed, does not therefore represent the basic magma involved in the mixing process, but is rather the product of mixing between the silicic magma and a more basic magma.

Since the textural and chemical features of the Group II dacites indicate that they resulted from the intimate mixing of separately generated basic and silicic magmas, two-component linear mixing tests, as described in Section 3.3, were carried out for selected Group II magmas. Figure 3.16a-c show the results of these mixing tests. All these diagrams show an excellent fit of the data ($R^2 > 0.98$), with the dacitic rocks of Group II possibly being generated by mixing between 70 and 80% of the rhyolitic end-member with 30 to 20% of the basic magma.

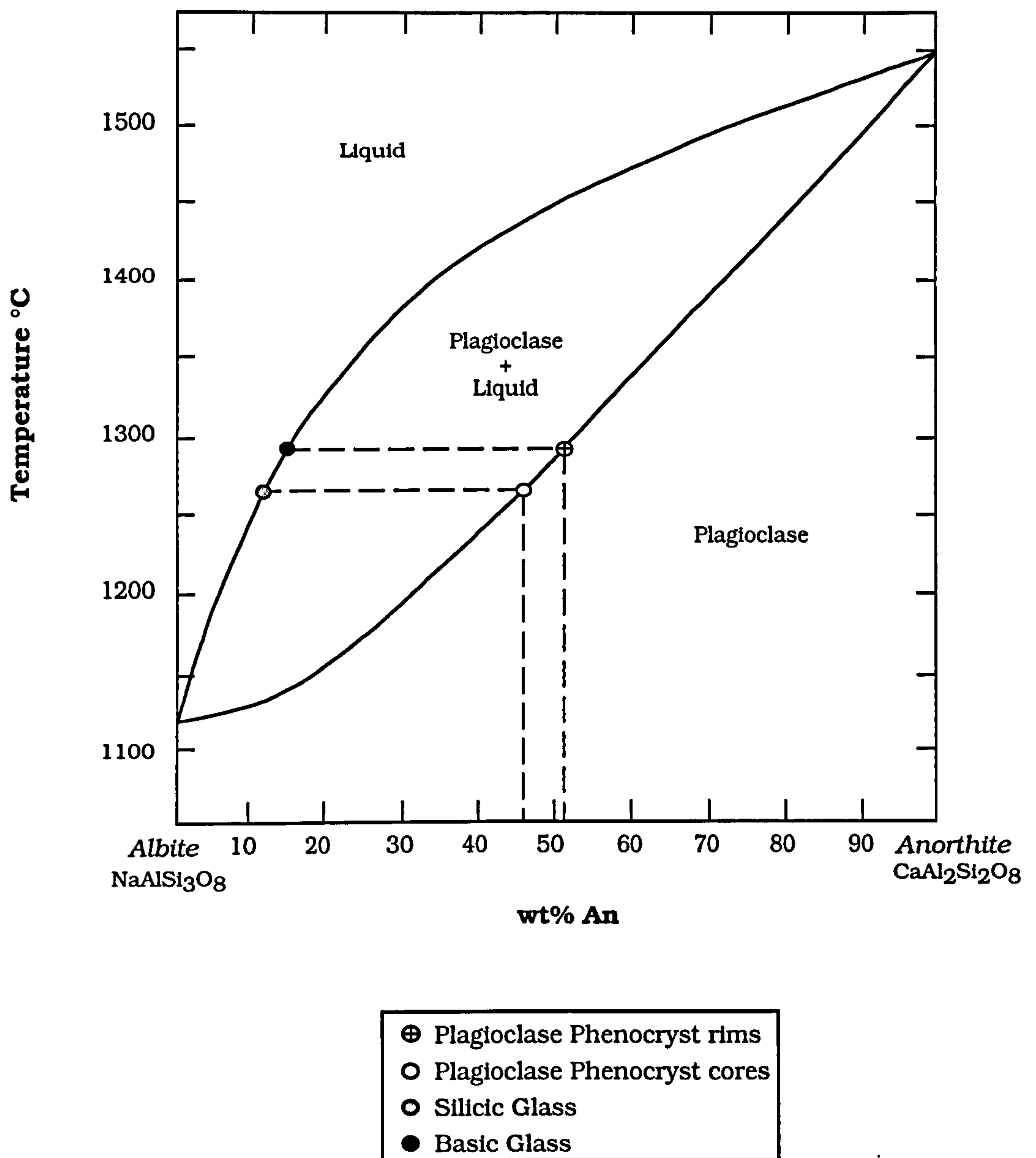


FIGURE 3.15 System albite-anorthite (after Bowen, 1913) at 1atm pressure, showing the composition of plagioclase phenocryst cores, and overgrowths from porphyritic dacites of Group II. Also shown are the plagioclase component compositions of the coexisting basic and silicic glasses from these rocks. It is evident that the crystal cores would have been in equilibrium with the silicic glass, and the phenocryst rims with the more basic glass (which is considered to be a hybrid). This implies that growth of the plagioclase continued after the mixing event. The resorption surfaces present in many of the plagioclase phenocrysts would have developed after hot basic magma was mixed with the silicic liquids.

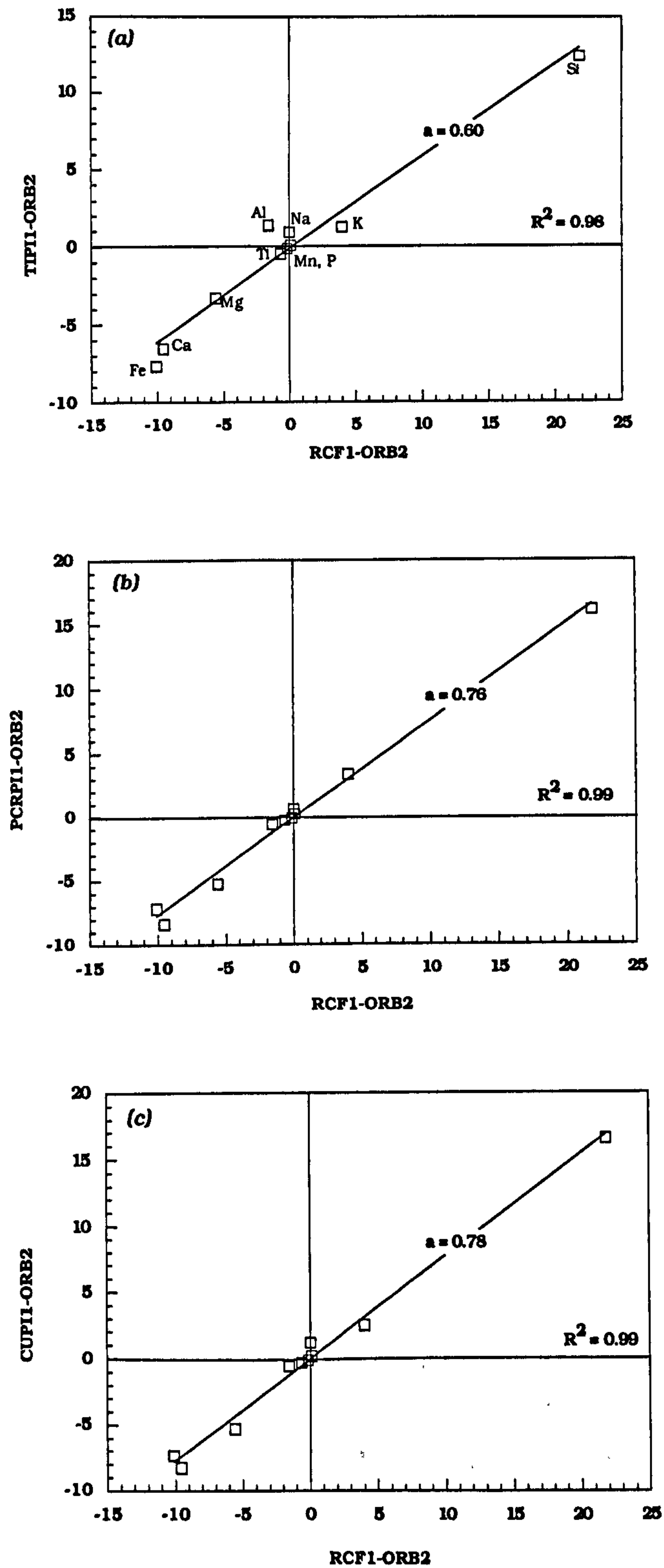


FIGURE 3.16 Mixing plots for possible hybrid Group II magmas. ORB2 and RCF1 are basic and silicic endmembers respectively. 'a' is amount of silicic endmember involved in the mixture. R^2 = Correlation coefficient.

After Langmuir et al. (1978)

3.5 Major-element evolution of Group III rhyolites

The rocks of rhyolitic composition (Group III) sit at the end of the fractionation trend defined by Groups I and II, (*Figures 3.5a-j*). Consequently, the rhyolites could be interpreted as the final-stage products of crystal fractionation of a basaltic magma. However, to produce even minor amounts of silicic magma by fractional crystallization requires a large volume of basaltic liquid. For example, it is possible that basaltic magma will produce between 5 and 15% of silicic residual liquids through protracted crystal fractionation (King, 1982). This model may be applicable to the LSSC, as rhyolites make up a very small percentage of the total number of sheets within the suite (1-2%).

However, it is hard to reconcile the low TiO_2 characteristics (*Figure 3.5n*) of the silicic rocks with a model of prolonged crystal fractionation. If the LSSC comprises one fractionation trend from basalt to rhyolite, provided magnetite is not a major fractionating phase, the silicic rocks would be expected to have high TiO_2 contents. Since the rhyolites have low TiO_2 contents (~ 0.7 wt%) it must be concluded that either the magmas have fractionated substantial amounts of titanomagnetite, for which there is little evidence, or that the rhyolites have a different source to the basic and intermediate rocks. It is therefore proposed that the rhyolites represent partial melts extracted from the continental crust, which in this case is most likely to be the Moine metasedimentary basement. Partial melts extracted from pelitic metasediments will be peraluminous (cationic $\text{Al} > (\text{K} + \text{Na} + 2\text{Ca})$), resulting in normative corundum (e.g. Douce, 1995; Gardien *et al.*, 1995). They will also have high K/Na ratios (Whitney, 1988). Partial melting experiments on common, natural metasedimentary rocks (MacRae & Nesbitt, 1980; Thompson, 1981; Vielzeuf & Holloway, 1988) show that liquid compositions similar to the rhyolitic rocks of the LSSC, can be produced at temperatures of between 700 and 950°C. The first melts produced will have compositions which lie close to the minimum in the system Ab-Or-Qtz. *Figure 3.17* illustrates these compositional relationships for the rhyolites and for Moine metasedimentary compositions. Point *m* marks the minimum on the cotectic. Also shown for comparison are the liquids produced during melting experiments on Lewisian

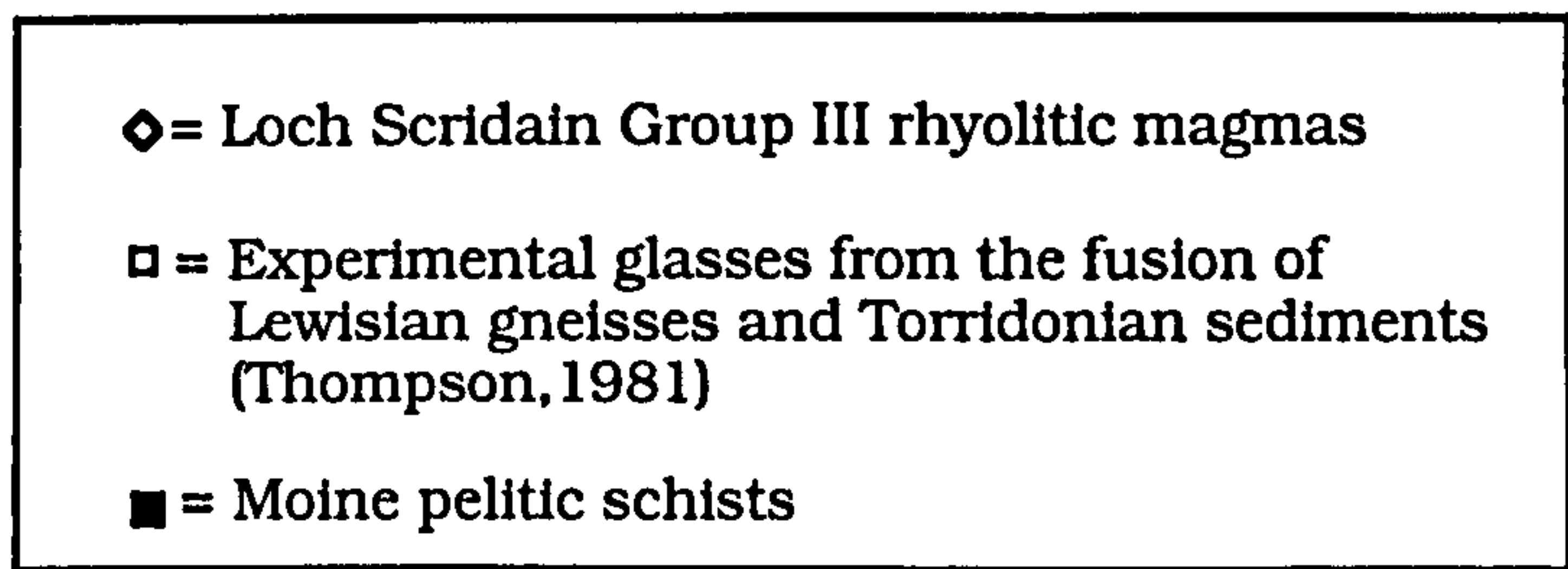
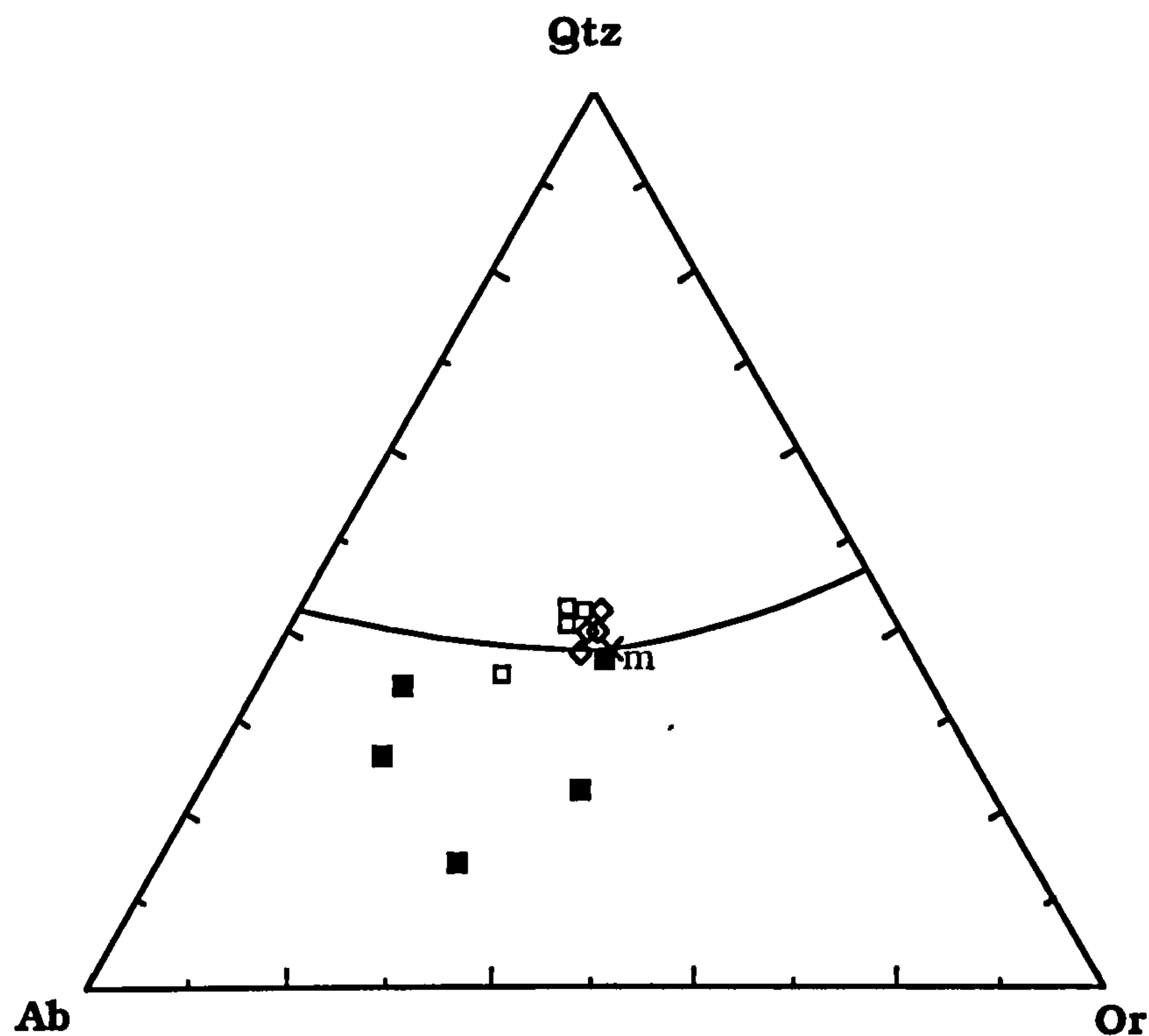


FIGURE 3.17 Normative Qtz-Ab-Or for the Group III rhyolitic magmas, experimental melts (Thompson, 1981) and Moine pelites. 1 kbar liquidus surface and ternary minimum (m) after Tuttle & Bowen (1958).

quartzofeldspathic gneisses and Torridonian sediments (Thompson, 1981). As can be seen, the rhyolites plot almost directly at the minimum melt point. They are, however, slightly enriched in CaO, Fe₂O₃, TiO₂ and in some cases MgO, when compared with the experimental melts (Table 3.8). This suggests that the silicic magmas may have been hybridized with small amounts of basic magma.

	JE6 (780°C)	JE6 (815°C)	JE6 (893°C)	LMS14	PGF1
SiO ₂	72.07	74.57	70.42	74.61	71.80
TiO ₂	0.04	0.06	0.14	0.01	0.66
Al ₂ O ₃	12.13	11.86	13.63	10.25	12.23
FeO*	0.77	0.79	0.83	1.03	4.91*
MnO	n.d.	n.d.	n.d.	0.31	0.08
MgO	0.20	0.25	0.38	0.41	0.39
CaO	0.59	0.87	1.41	0.20	1.47
Na ₂ O	3.06	3.24	4.12	1.77	3.23
K ₂ O	4.25	4.10	3.48	4.39	4.31
P ₂ O ₅	n.d.	0.01	n.d.	n.d.	0.17
TOTAL	93.11	95.75	94.41	92.98	99.25

Table 3.8 Composition of experimental melts from partial melting experiments on Lewisian leucogneiss (JE6), and Torridonian arkose (LMS14) (Thompson, 1981) compared with rhyolite of Group III (PGF1) of LSSC. n.d. = not determined. * = all Fe as Fe₂O₃.

The partial melting of common pelitic sedimentary and metasedimentary rocks will leave a *restite* which is enriched in refractory phases rich in CaO, Al₂O₃ and MgO, such as calcic-plagioclase, corundum and spinel. As a result the derived liquids are likely to be poor in these elements. It is envisaged that the rhyolitic magmas were produced when hot basic magma ponded within crustal magma reservoirs, causing partial melting of the wall rocks (cf. Bell, 1983; Bell & Pankhurst, 1993). Convective mixing within the magma chamber will produce a spectrum of hybrid rock compositions. As a result, the slightly elevated concentrations of refractory elements, over the experimental compositions, shown by the Group III rhyolites suggests that they may represent rhyolite mixed with small amounts of basalt

3.6 Conclusions

Previous work (Bailey *et al.*, 1924; Thompson *et al.*, 1986; Kille, 1987) coupled with the preceding discussion on the major-element geochemistry of the LSSC has given the first clues as to how the suite may have evolved. At this stage it is suggested that:

- (a) Group I magmas evolved by a combined process of fractional crystallization and crustal assimilation.
- (b) Group II magmas are a result of mixing between separately generated basic and silicic magmas, perhaps followed by limited crystal fractionation involving plagioclase and pigeonite.
- (c) Group III magmas were generated by a process of crustal anatexis, possibly involving Moine metasedimentary basement rocks.

The following discussion on the trace-element and isotope geochemistry of the LSSC will be used to test the above hypotheses. A final synthesis of the petrogenesis of the suite will be presented in Chapter 8.

CHAPTER 4

WHOLE-ROCK TRACE-ELEMENT GEOCHEMISTRY

All specimens were analysed for the trace-elements Ba, Ce, Cr, Cu, La, Nb, Nd, Pb, Rb, Th, Sc, Sr, V, Y, Zn and Zr using standard XRF techniques, and selected samples for the full range of the rare-earth-elements (REE) using ICP-MS and ICP-AES analysis. Representative trace-element analyses are presented in *Table 3.1*. The complete listing of trace-element analyses is presented in Appendix II. As with the major-element data, the trace-element variation within the suite is displayed on Harker diagrams using SiO₂ and/or Mg# as indices of fractionation.

4.1 Compatible trace-elements

Elements such as Cr, Ni, Sc, V and Sr are all strongly partitioned into the mineral phases that fractionate from basaltic magmas; Ni is taken-up by olivine, Cr, Sc and to a lesser extent V, into clinopyroxene, and Sr is partitioned predominantly into plagioclase (Drake & Weill, 1975; Colson *et al.* 1988). Chromium is also strongly partitioned into Cr-spinel, which crystallizes at an early stage from basaltic magmas (Irvine, 1967). As a result, these elements may be used as an independent test on the extent of fractional crystallization that has occurred.

Nickel shows a strongly bi-modal distribution for Group I magmas in the LSSC (*Figure 4.1a*). Members of subgroup (a) contain between 78 and 42ppm Ni which decreases with SiO₂ content (50-54 wt%), and subgroup (b) samples contain between 10 and 22ppm Ni, which shows no correlation with SiO₂. The trend seen in subgroup (a) is, at first sight, compatible with these slightly more basic magmas fractionating olivine. However, none of the magmas contain phenocryst or groundmass olivine. Subgroup (a) samples are the same as those which plot within the diopside primary phase volume of the olivine-diopside-silica projection of Walker *et al.* (1979) (See *Figure 3.9b*). These samples have already been interpreted as evolved magmas which have mixed with fresh batches of less-evolved magma. Shibata *et al.* (1979) found that such magmas often contained significantly greater

abundances of trace-elements (particularly Ni) than would be expected from fractionation calculations. The Ni concentrations of subgroup (b) are consistent with highly evolved tholeiitic magmas which have *already* fractionated olivine, a fact which reinforces the hypothesis that the Group I rocks are not primary mantle melts (see Chapter 3.2). Concentrations of Ni are generally low in Group II and Group III (<10ppm).

Chromium shows a similar behaviour to Ni within Group I, with a strong bi-modal distribution (*Figure 4.1b*). Again, the same samples form a high Cr trend (350-180ppm), with the remainder scattering around 30-100ppm. However, the sample with the lowest SiO₂ content, ORB2, has a low Cr content at ~ 70ppm; the Ni content of ORB2 is also lower than would be expected for such an un-evolved specimen (~48ppm). The low Cr and Ni contents of this particular sample could be due to relatively large amounts of olivine, clinopyroxene and/or Cr-spinel fractionation from the parental liquids. Alternatively, these anomalously low values may be due to hydrothermal alteration, since Ni and Cr are held in minerals (olivine and clinopyroxene) which are readily altered. The general trend of Cr depletion with fractionation within Group I may be attributed to the removal of either Cr-spinel or clinopyroxene. Cr-spinel has been identified in the cumulate xenoliths found in many of the Group I and Group II sheets (Chapter 7). However, since Cr-spinel appears very early on the liquidus during cooling of basaltic magmas (Irvine, 1967), the higher concentrations of Cr in the more basic liquids (Mg# 0.45-0.35) would suggest that the Cr depletion through Group I is not a consequence of Cr-spinel crystallization, but was controlled primarily by the removal of clinopyroxene (Bell *et al.*, 1994). Chromium contents within Groups II and III, are again low (0 - 69 ppm)

Although the overall depletion of Ni and Cr with fractionation through Group I can be explained by the removal of olivine and clinopyroxene respectively, the strong bi-modal distributions of these elements, coupled with the phase relationships, suggest that mixing between differentiated magmas and fresh less-evolved liquids did in fact occur. This process has been discussed and modelled in detail by O'Hara (1977). He concluded that periodically replenished, tapped and fractionating (RTF) magma chambers can reach steady-state provided the process is continuous. The generation of liquids with abnormally high trace-element concentrations can also be a consequence of RTF

processes (O'Hara, 1977; O'Hara & Matthews, 1981; Cox, 1988). RTF processes are discussed further in Section 3.4. It will suffice to say at this point that it is interesting that the Group I fractionation trend gets no further than basaltic-andesite, a feature that may be an artefact of the sampling procedure, or further evidence that RTF processes operated within the Loch Scridain magma reservoir(s).

Scandium shows a very well-constrained trend with SiO₂ (*Figure 4.1c*). Scandium is compatible in clinopyroxene (K_D values range from 1.7-3.2; Rollinson, 1993), and shows a two-fold depletion through Group I and similarly through Group II, suggesting that clinopyroxene fractionation may have been important.

The decrease in vanadium with decreasing SiO₂ contents (*Figure 4.1d*) may be consistent with pyroxene fractionation; the mineral/melt partition coefficients (K_D) in basaltic liquids for V in clinopyroxene is just over unity, whereas, as noted above, for Sc it ranges up to 3.2 (Rollinson, 1993). Vanadium is however, highly compatible in magnetite, with a mineral/melt partition coefficient in basic magmas ranging between 26 and 30 (Rollinson, 1993). As such, the depletion of V through Group I could be explained by the removal of magnetite (*Figure 4.1d*). However, as shown in Chapter 3, this is not a viable explanation, since Ti *increases* through Group I. The V depletion through Group I can therefore be best accounted for by clinopyroxene fractionation. Vanadium shows a marked scattered distribution within Group II, and is at relatively constant low values within Group III (~25ppm).

However, given the range of possible K_D values for V and Sc, simple closed-system crystal fractionation is *not* able to account for the sympathetic decrease in the concentration of these elements. As magnetite fractionation has been discounted, another magmatic process must be controlling the trends seen. One possibility is combined assimilation and crystal fractionation, which will be discussed in a subsequent section.

Strontium, which is highly compatible in plagioclase, shows a scattered, but positive correlation with SiO₂ increasing from ~ 120 to 430 ppm through Group I (*Figure 4.1e*). However, the majority of Group I rocks have Sr concentrations between 170 and 280 ppm. K_D values for Sr in plagioclase range up to 1.8 in basaltic and basaltic andesite liquids (Rollinson, 1993). However, the *bulk distribution coefficient* for Sr may only be greater than unity if plagioclase

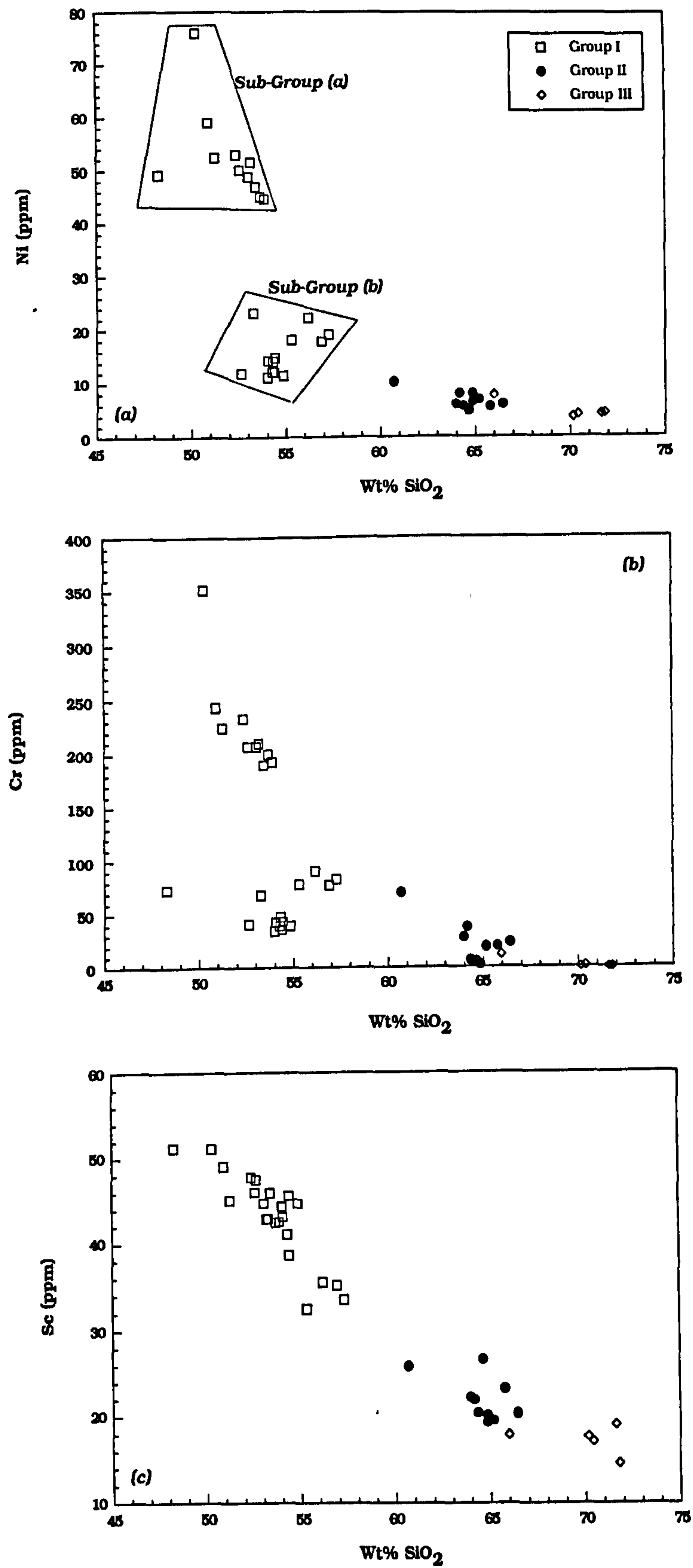


FIGURE 4.1 (a) Variation of Ni with SiO₂
 (b) Variation of Cr with SiO₂
 (c) Variation of Sc with SiO₂

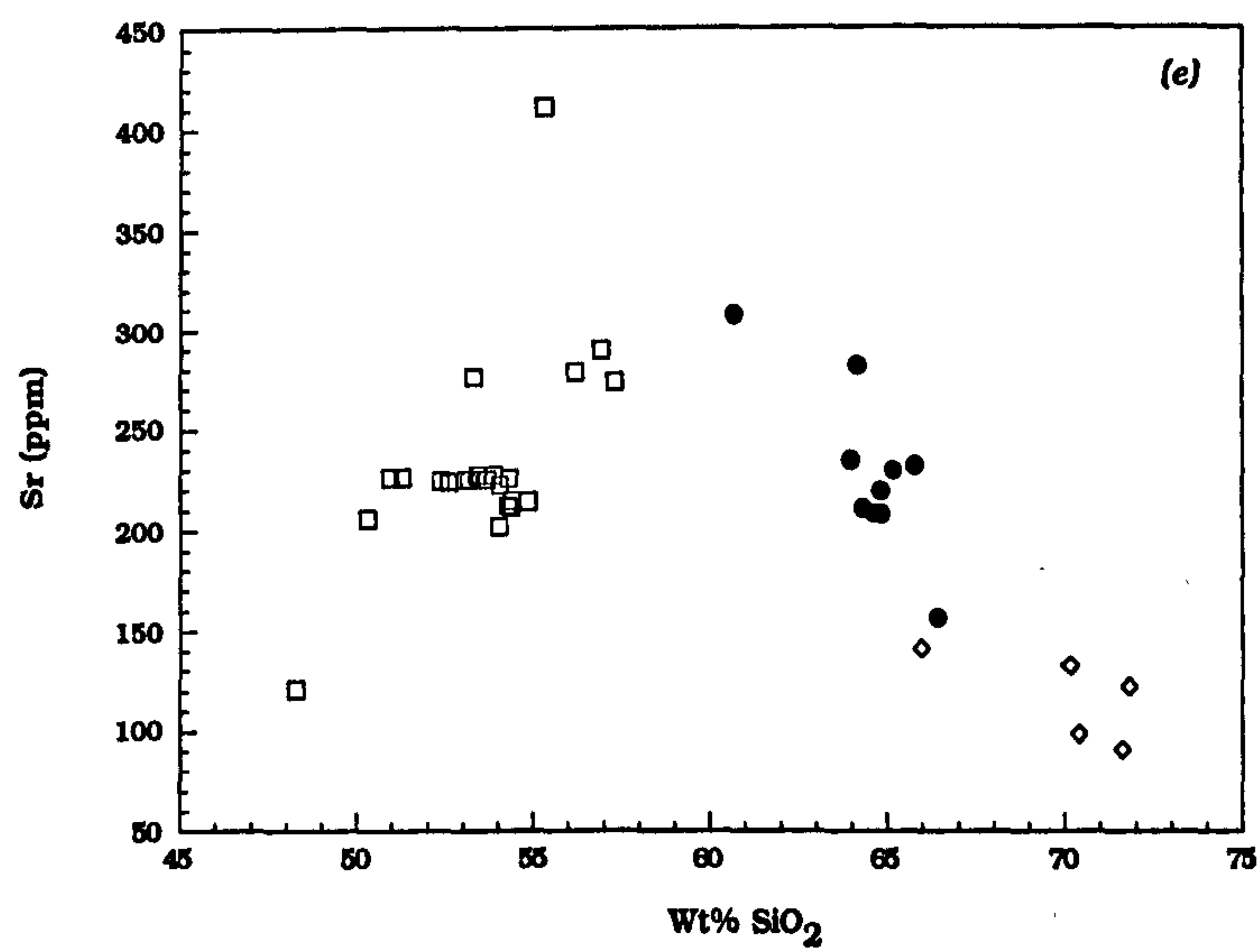
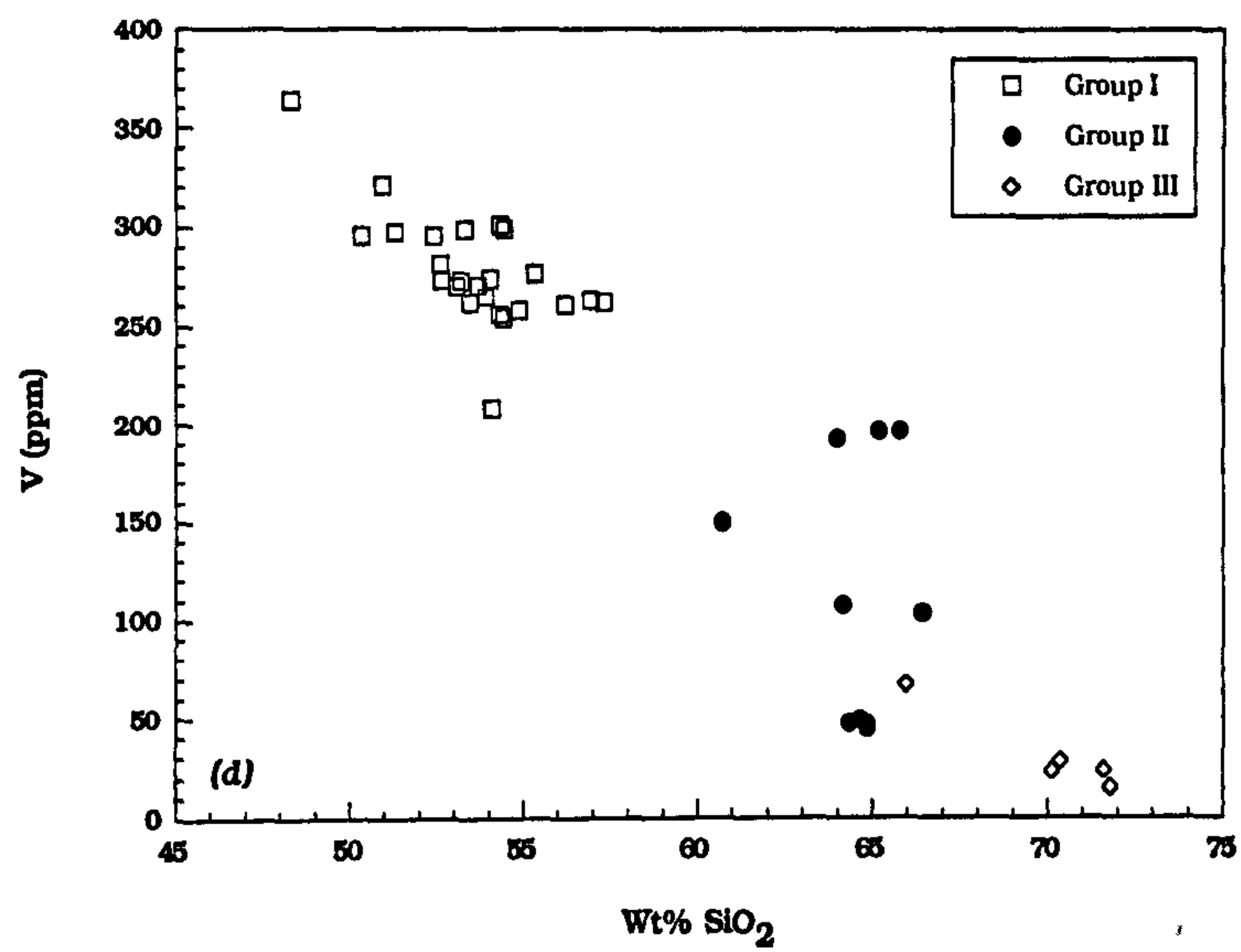


FIGURE 4.1 (d) Variation of V with SiO₂
(e) Variation of Sr with SiO₂

approaches being 60% of the fractionating assemblage. K_D values for Sr in augite and pigeonite in basic magmas range from 0.02-0.06 (Rollinson, 1993). Plagioclase fractionation may have played an important role in the petrogenesis of Group I rocks as discussed in Chapter 3, but the marked scatter in the Sr data would confirm that plagioclase did not exceed being 60% of the fractionating assemblage, or that magma-mixing processes involving basic-silicic, and basic-basic mixing also occurred. A similar explanation was forwarded by Grove *et al.* (1982) for the complex behaviour of Sr in the calc-alkaline series lavas of Medicine Lake, California. However, it was also pointed out that there is some bulk-compositional dependence on the distribution coefficient for Sr in plagioclase (Grove *et al.*, 1982). For example, K_D values for Sr in plagioclase in andesitic liquids range from 1.8-2.8, and in silicic melts from 2.8-15.6. Consequently, as the liquid evolves, Sr is likely to become more compatible in plagioclase, thus requiring less plagioclase to fractionate in order to deplete the liquid in Sr.

Many workers have shown that Sr can be a highly mobile element, especially in hydrothermal fluids. Dickin & Jones (1983a) found that total Sr contents can be strongly depleted in hydrothermally altered basaltic rocks, and that a concomitant transferral of radiogenic Sr into the 'fresh' material can occur. Morrison (1978) also found that Sr was mobilised in tholeiites (but not in transitional basalts) during the regional zeolitization in the BTVP, and that it was mobilised in both basalt types during local greenschist-facies hydrothermal alteration. The marked scatter in the Sr data for some of the Group I rocks may therefore be due to a local re-distribution of this element.

In contrast, the Sr data for the Group II specimens show a relatively coherent depletion with increasing SiO_2 content (300-150 ppm.) This reinforces the conclusion drawn from the major-element data which suggests that plagioclase fractionation played an important role in the evolution of Group II magmas.

The Sr contents in the Group III rhyolites are low (<150 ppm). These data supports the suggestion that the Group III rocks represent partial-melts extracted from the Moine metasedimentary basement rocks. Partial-melting of pelitic schists will leave a restite dominated by plagioclase, and therefore produce a liquid depleted in Sr (Chappell & White, 1992).

4.2 Incompatible trace-elements

Those elements which are strongly partitioned into the melt during fractional crystallization or partial melting, are termed incompatible elements. The 'compatibility' of any given element is obviously controlled by the mineral assemblage precipitating from a melt, or by those left as residue after a melting event, and thus by the bulk composition of the system. Incompatible elements have crystal/ liquid partition coefficients (K_D) $\ll 1$.

The trace-elements Ba, Ce, Cu, La, Nb, Nd, Pb, Rb, Th, Y, Zn and Zr exhibit incompatible behaviour with respect to the fractionating phases of olivine, plagioclase and pyroxene. Most show strong positive correlations with SiO_2 (Figures 4.2a-l). These elements show between four (e.g. Nb) and twenty times (e.g. Rb) enrichment with progressive fractionation through Group I, a trend seemingly continued by Groups II and III. Yttrium shows a more scattered relationship with SiO_2 (Figure 4.2i), although abundances generally increase with advancing fractionation (25-70 ppm.) The large ion lithophile elements (LIL) Ba and Rb are considered relatively mobile during hydrothermal alteration (Morrison, 1978; Dickin & Jones, 1983a). However, the generally tight trends of these elements with progressive fractionation through Group I (Figures 4.2a and 4.2b) helps confirm previous inferences that the LSSC has been little affected by hydrothermal alteration.

The chalcophile elements Zn and Cu show very contrasting distributions throughout the suite. Zinc shows no correlation with either SiO_2 or (Mg#) (Figure 4.2c). Zinc is thought to be mobile in hydrothermal fluids in basalts, particularly at high temperatures ($\sim 300^\circ\text{C}$) (Seewald & Seyfried, 1990), which may explain the scatter seen in the LSSC.

Copper appears to have behaved as a compatible element through Group I (Figure 4.2d), with abundances decreasing from ~ 180 ppm to a relatively constant value of ~ 20 ppm. Unlike other transition metals (e.g. V, Zn, Ti), copper is incompatible with respect to 'gabbroic' fractionation. The other transition metals can all be accommodated to some extent into olivine and pyroxene, and particularly into magnetite. Copper is, however, readily taken up by sulphide phases such as pyrite and chalcopyrite. These phases are common accessory minerals in basic igneous rocks, and are thought to result from either

sulphide/silicate melt immiscibility, or from late-stage hydrothermal precipitation. Certain members of Group I contain rounded and irregularly shaped globules of pyrite. These globules are about 1mm in diameter and are full of inclusions of quenched plagioclase and pyroxene. Similar sulphide globules have been found in MOR basalts from the FAMOUS area (Czamanske & Moore, 1977). These authors suggest that the sulphide globules either persisted in the basaltic melt from its place of formation in the mantle, or that they may have exsolved from the melt as it became sulphur-saturated in high-level magma chambers. The occurrence of plagioclase and pyroxene inclusions in the pyrite globules of the Group I magmas, would favour the second mode of origin for these rocks.

The incompatible element concentrations of Group II magmas are more extreme than those of Group I. They generally form a tight cluster on variation diagrams using SiO_2 as the index of fractionation (*e.g.* Rb- SiO_2 , Pb- SiO_2 - Figures 4.2b and 4.2k). However, in certain diagrams (*e.g.* Figures 4.2g,h), a few samples define an enrichment trend which continues that made by the Group I magmas, whereas four samples consistently plot off this trend, and form a coherent cluster at higher element concentrations. This is clearly demonstrated in the diagram of Zr vs. SiO_2 (Figure 4.2l). These samples are the porphyritic dacites, and they are enriched in P_2O_5 , Zr, Nb, La, Ce, Nd, and Y, over and above other Group II magmas. However, trace-element *ratios* of these samples are consistent with Group II magmas as a whole. The enrichment of these samples in Zr, Y and the REE can be accounted for by the occurrence of microphenocrysts of apatite and zircon that are included within the plagioclase and pigeonite phenocrysts, and within the groundmass. These minerals both preferentially take up the rare-earth elements. The rhyolites of Group III contain similar microphenocrysts of zircon and apatite, which could both be equilibrium phases in such silicic magmas. It is believed that *some* of the apatite and zircon within the Group II magmas may be inherited from a mixing event between basic and silicic magmas. It was demonstrated in Chapter 3 that the plagioclase phenocrysts in the porphyritic dacites grew initially in equilibrium with a silicic liquid, and then, after a period of resorption, grew an overgrowth in equilibrium with a more basic liquid. This suggests that basic magma was mixed with silicic magma to produce some of the Group II intermediate rocks. Apatite and zircon crystals included within the

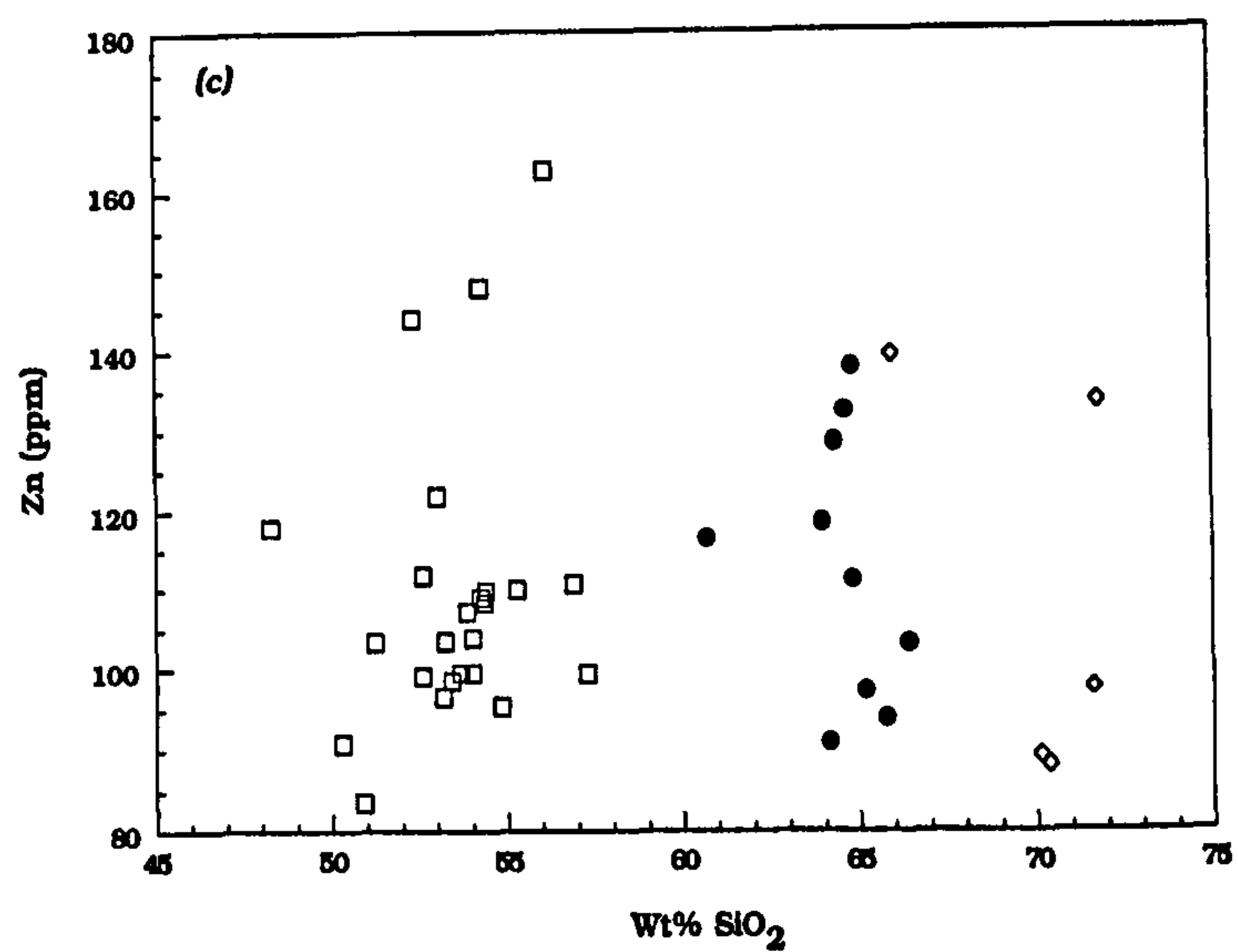
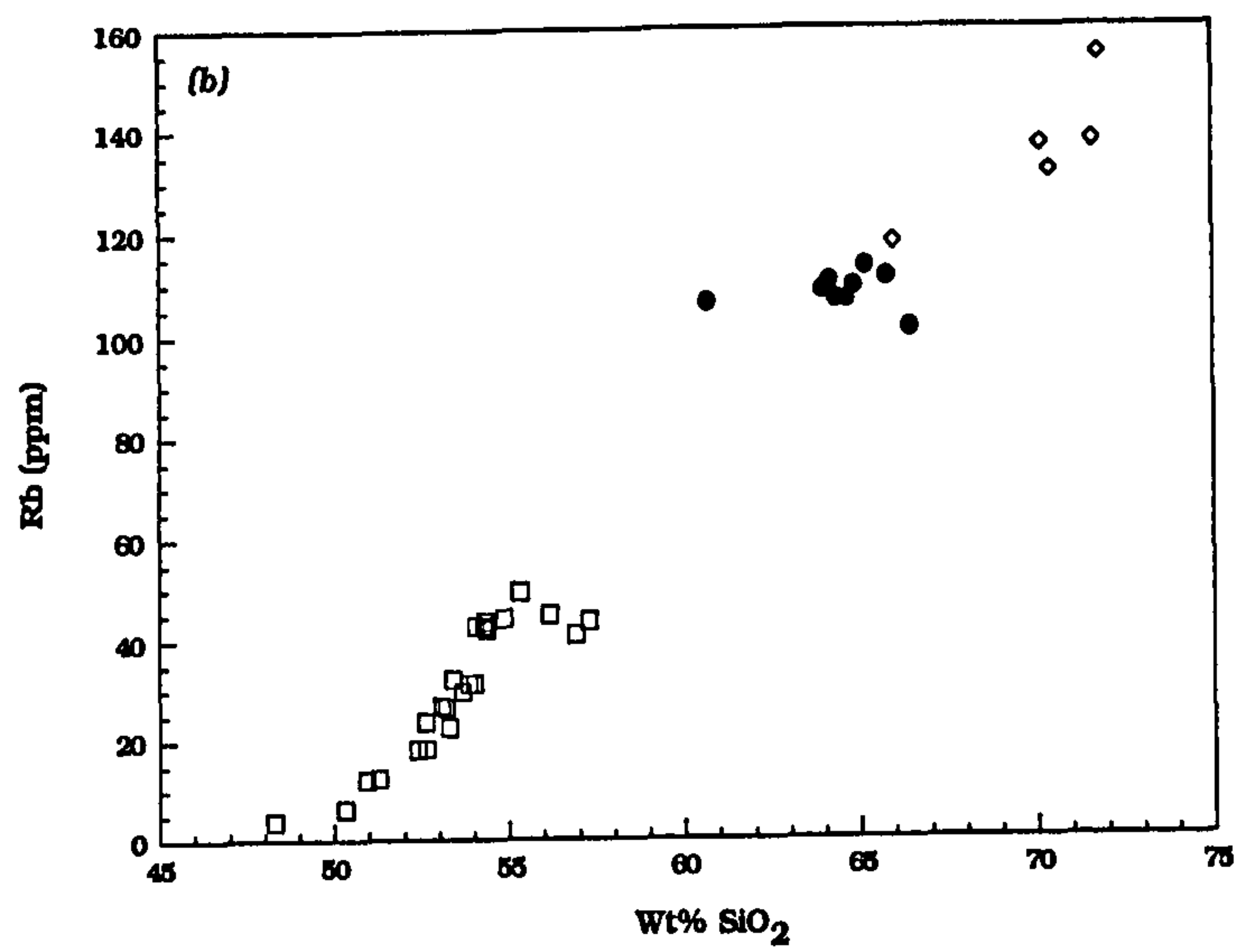
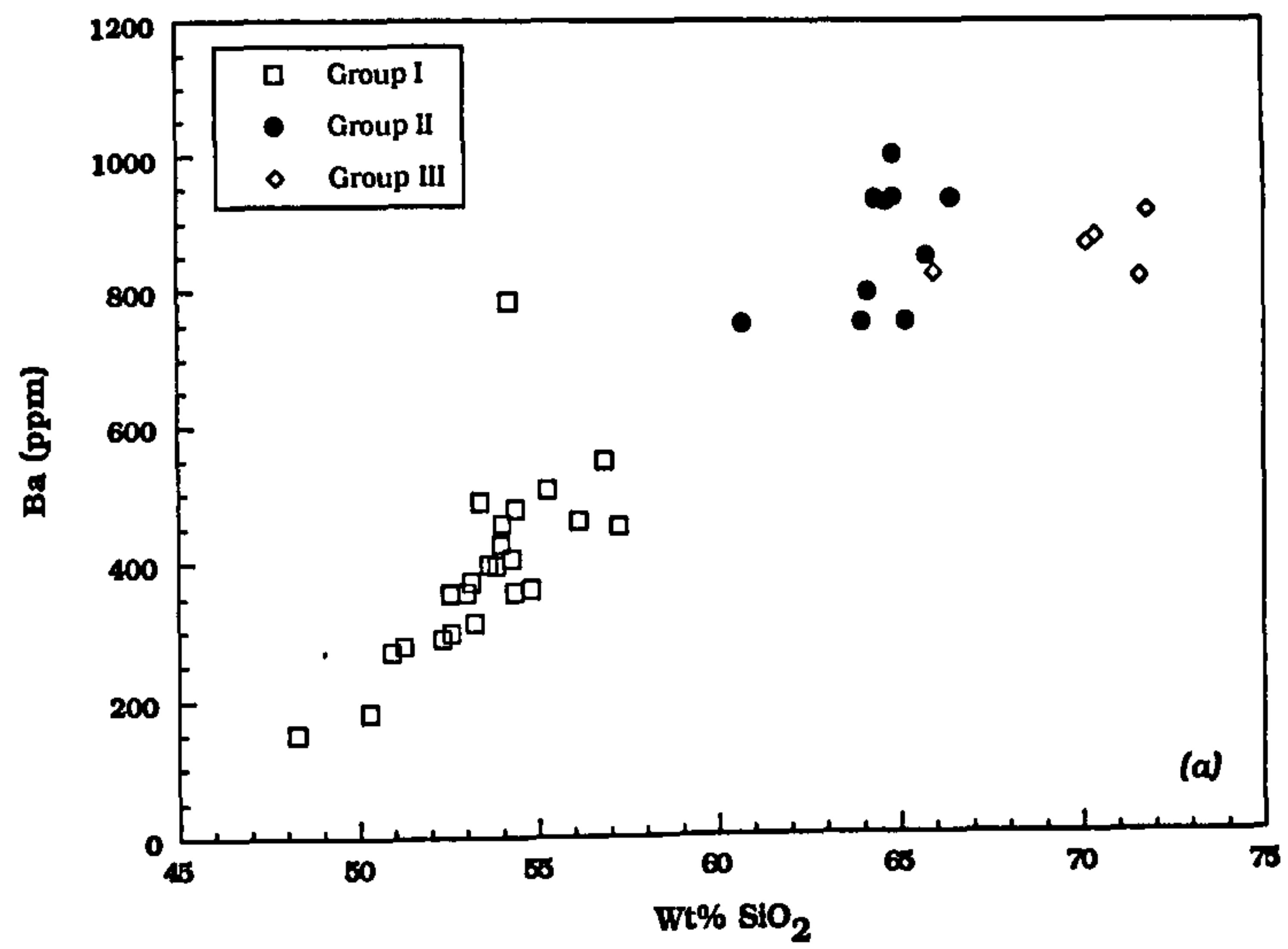


FIGURE 4.2 (a) Variation of Ba with SiO₂

(b) Variation of Rb with SiO₂

(c) Variation of Zn with SiO₂

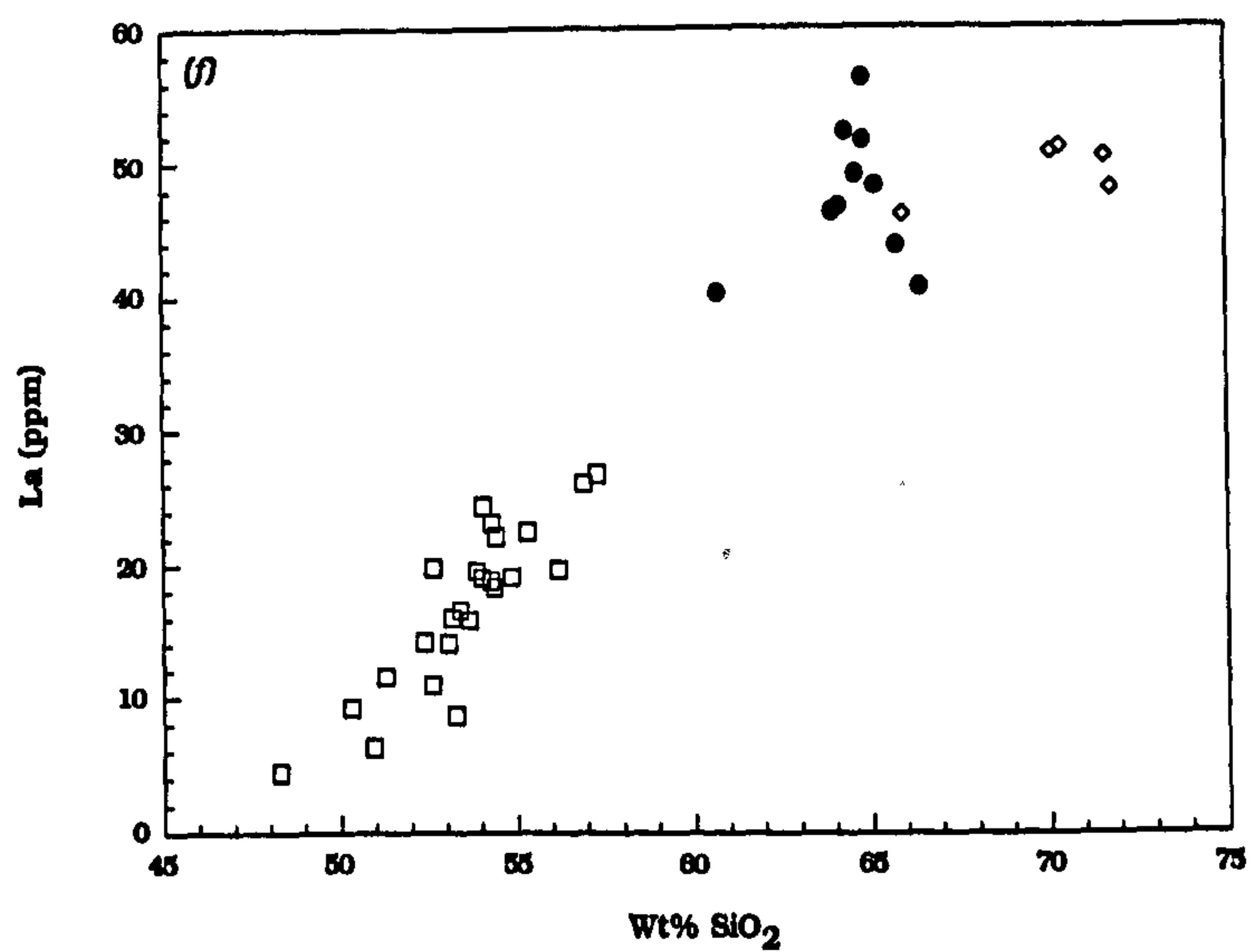
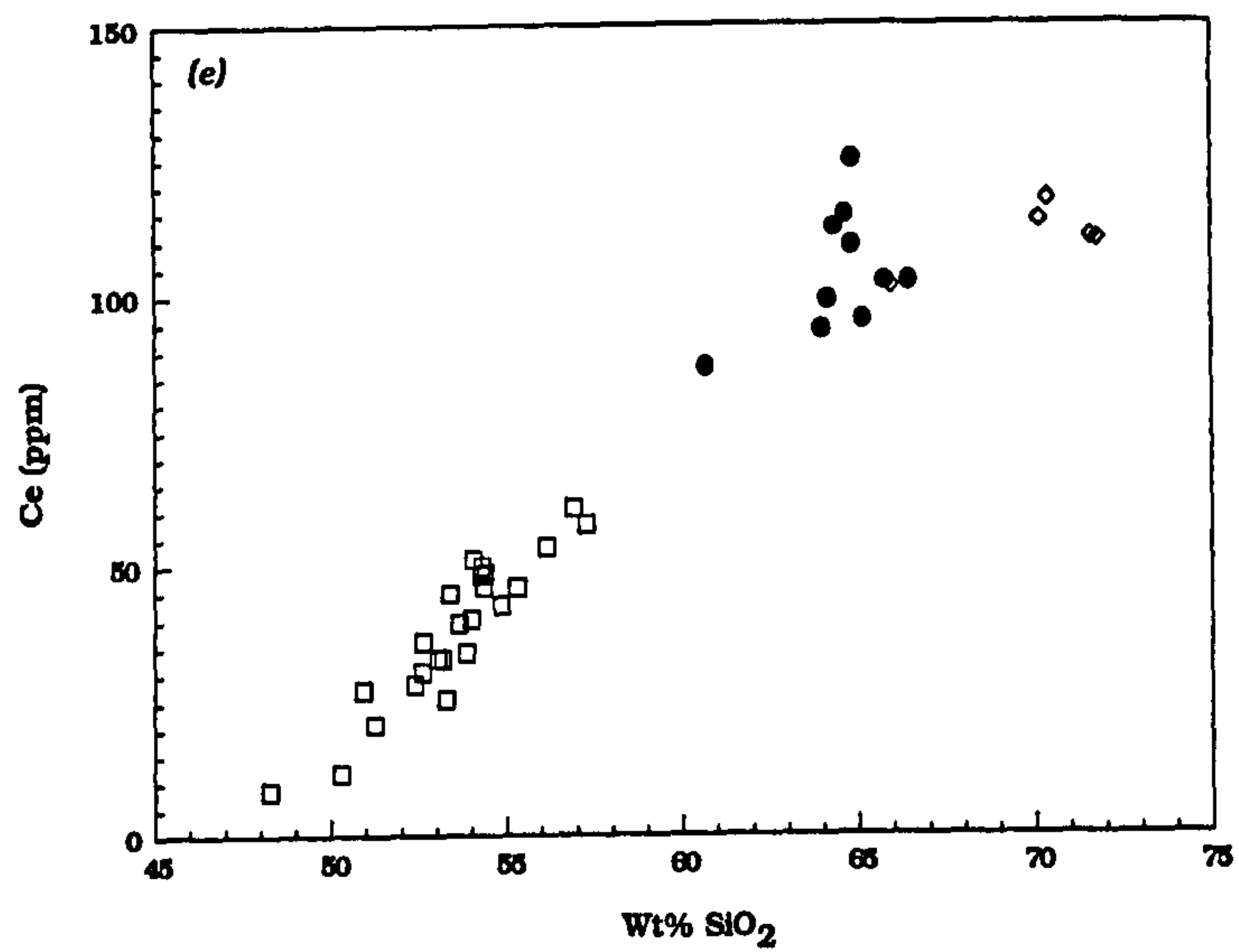
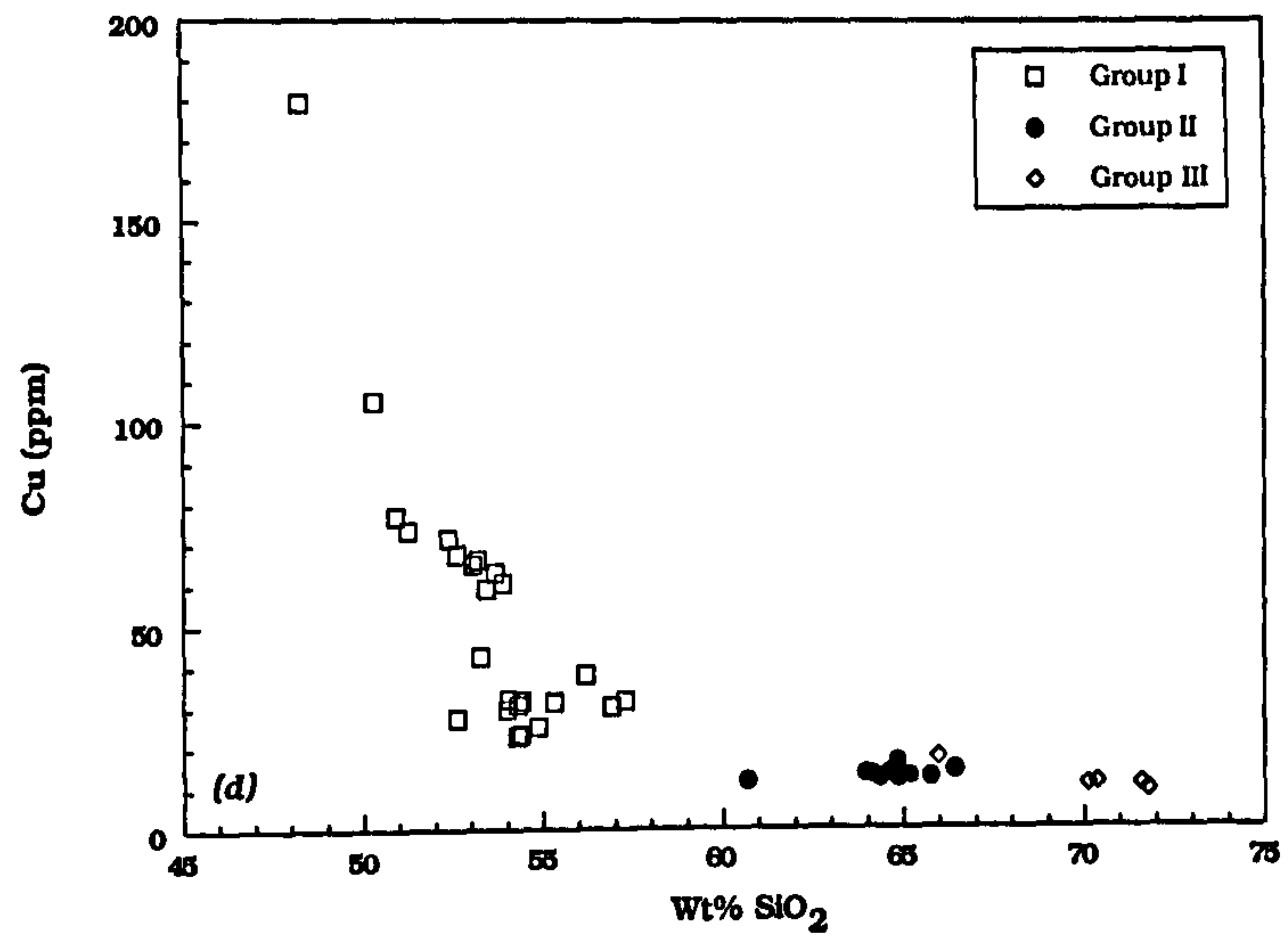


FIGURE 4.2 (d) Variation of Cu with SiO₂

(e) Variation of Ce with SiO₂

(f) Variation of La with SiO₂

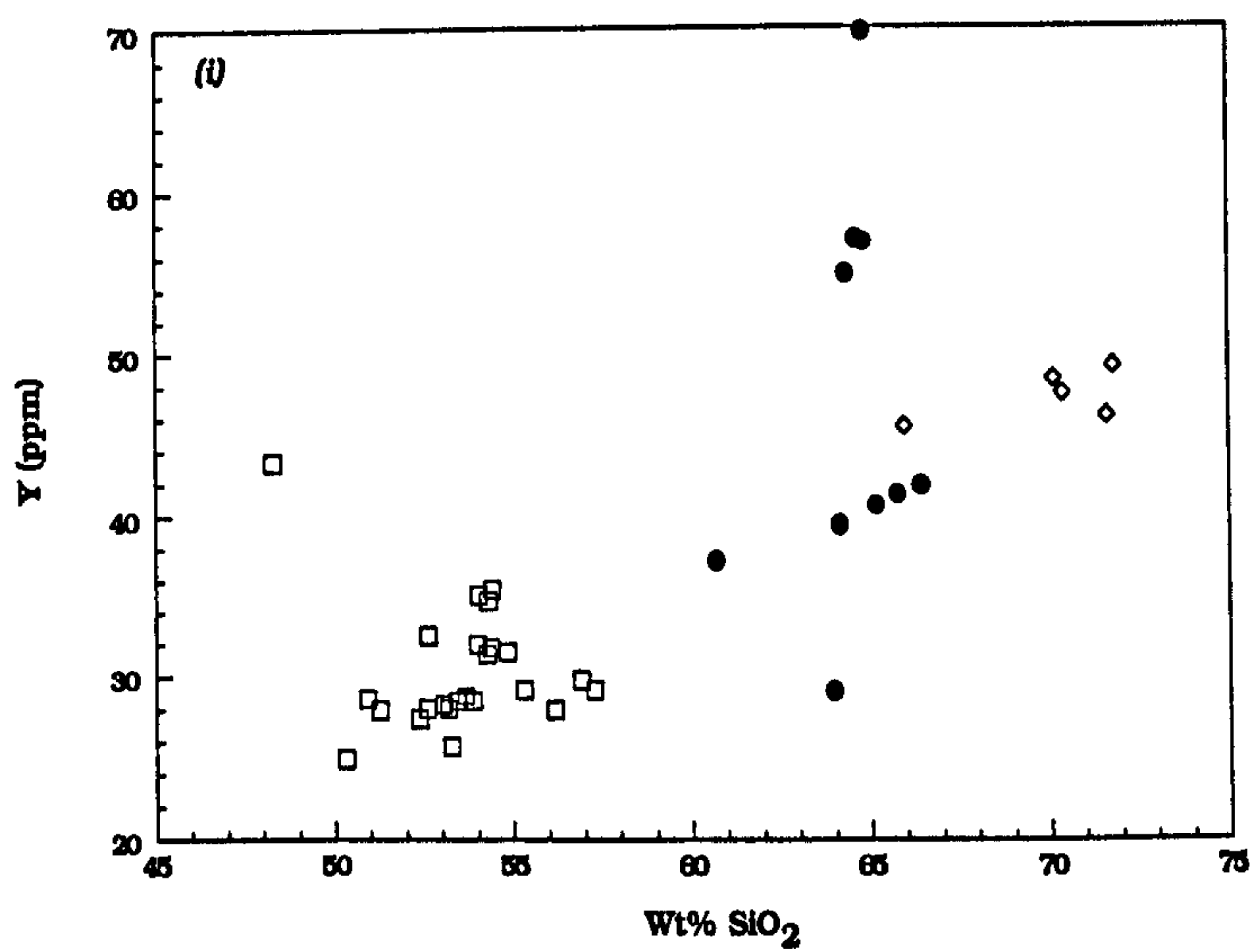
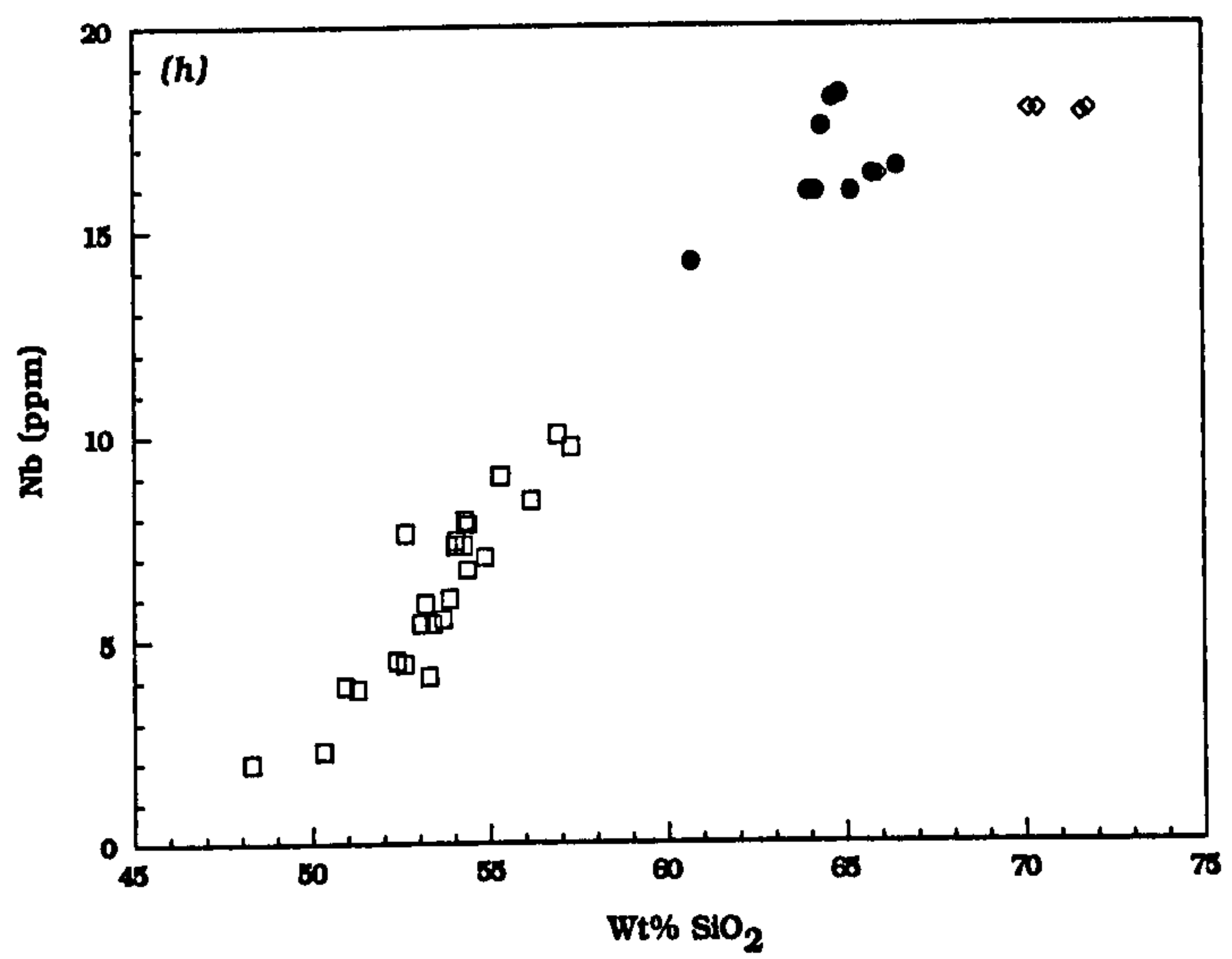
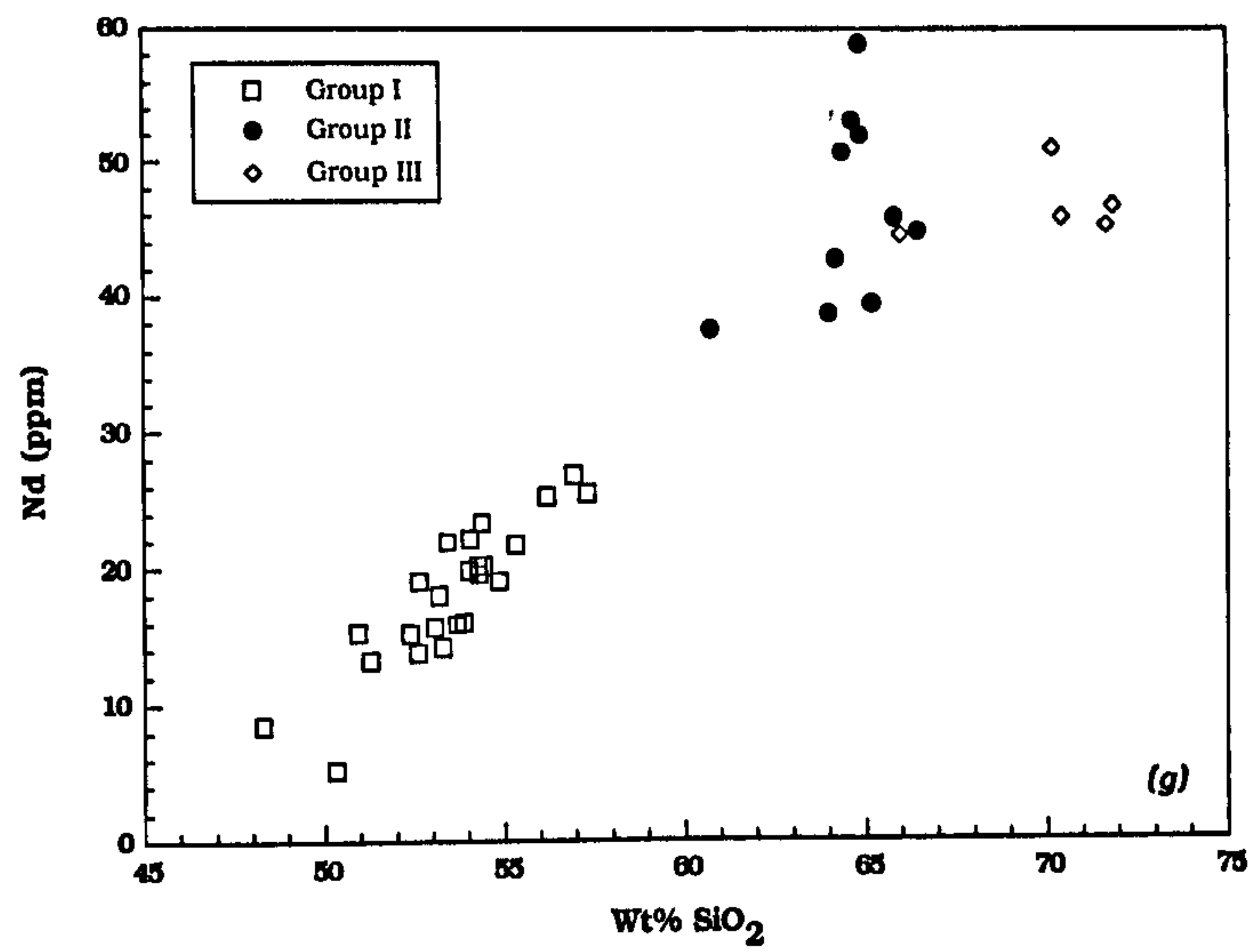


FIGURE 4.2 (g) Variation of Nd with SiO_2

(h) Variation of Nb with SiO_2

(i) Variation of Y with SiO_2

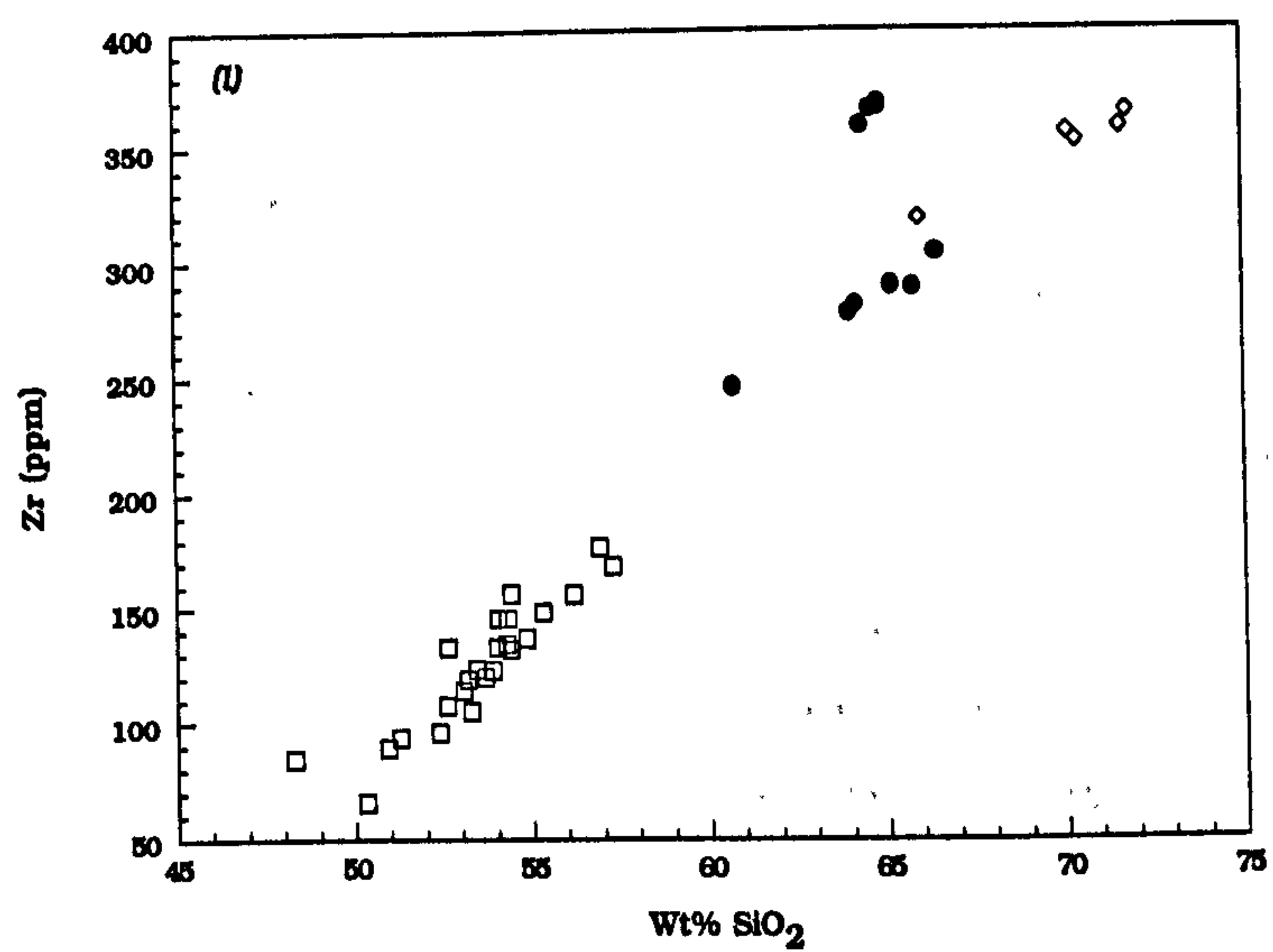
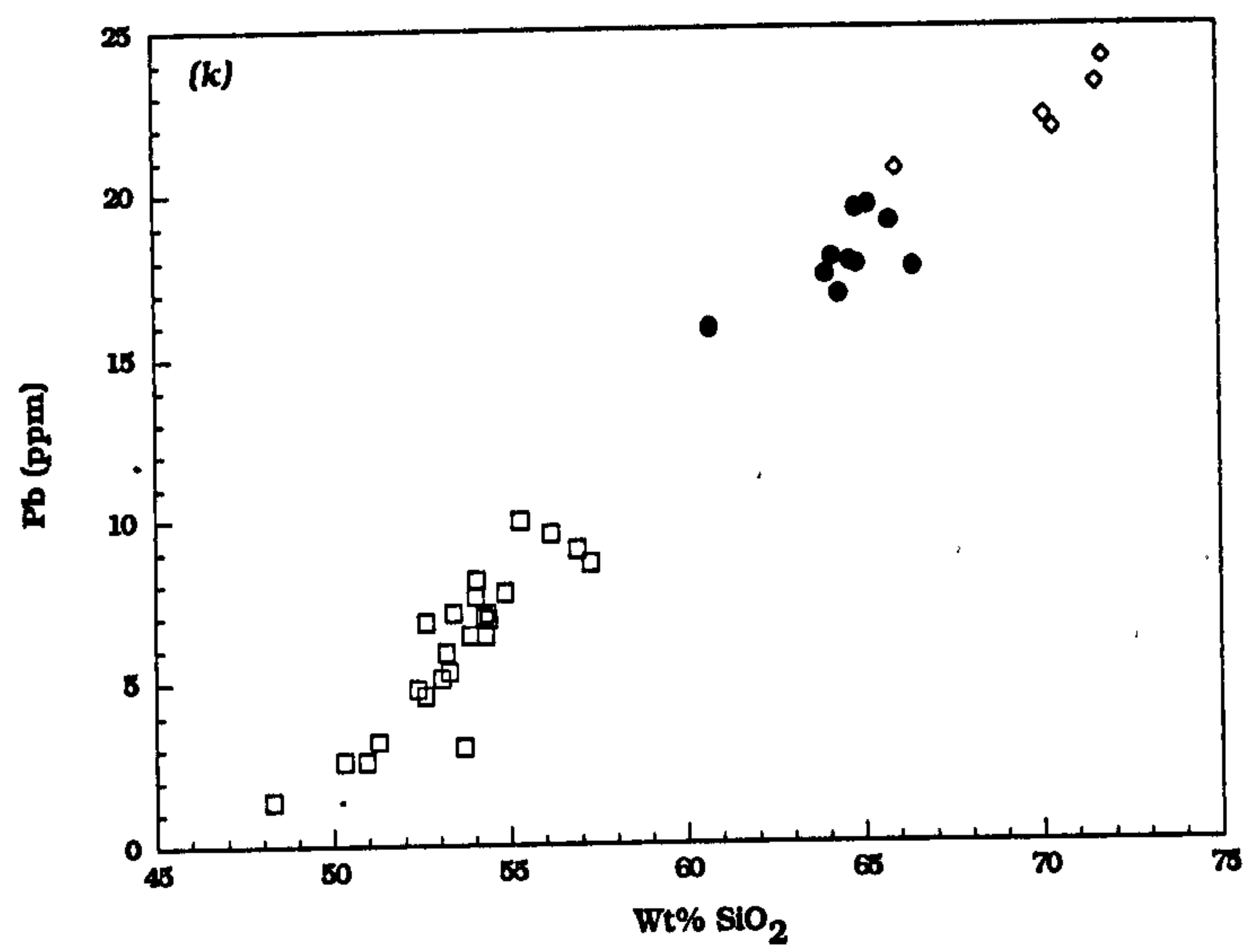
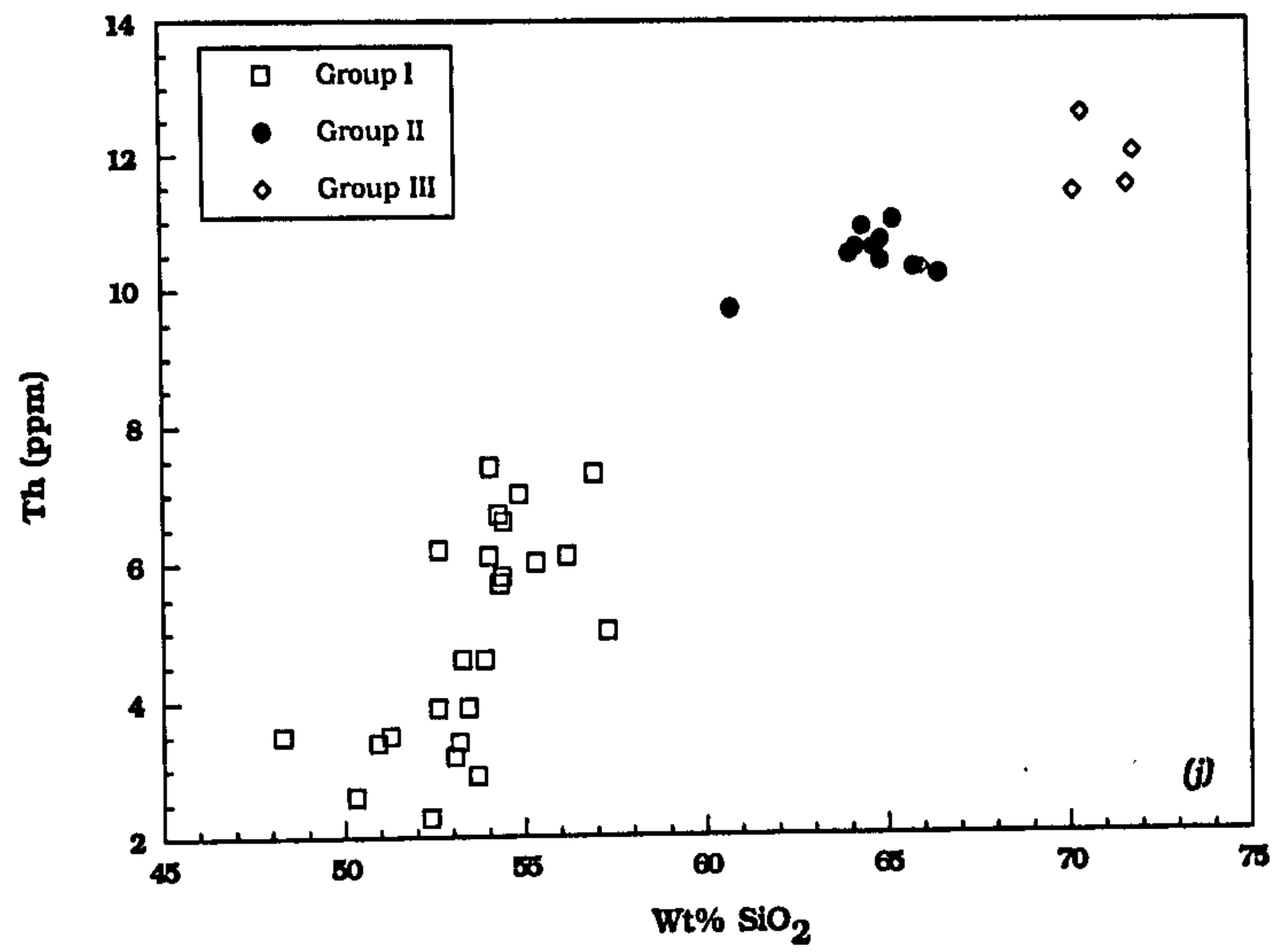


FIGURE 4.2 (j) Variation of Th with SiO₂

(k) Variation of Pb with SiO₂

(l) Variation of Zr with SiO₂

cores of plagioclase crystals could therefore be interpreted as being xenocrysts.

Figures 4.3a-d show the covariance of the highly incompatible elements Ce-Zr, Ce-Nb, Zr-Nb and La-Ce respectively. Both Groups I and II show relatively well-constrained positive correlations ($R^2 > 0.92$) for each of these pairs of elements. However, it is also evident that the element ratios are slightly different for Group I compared with Group II. Since closed-system fractional crystallization is likely to preserve a constant ratio between pairs of highly incompatible elements, the within group consistency of these elemental ratios suggests that crystal fractionation did indeed play an important role in the genesis of both magma Groups, but that the two Groups cannot be simply related via fractional crystallization of a single fractionating assemblage. A change in fractionating assemblage could possibly cause a change in gradient on such diagrams. For example, if orthopyroxene became a fractionating phase, elements such as Zr may become enriched at a "slower" rate (K_D values for Zr in orthopyroxene in basic liquids are ~ 0.18 , compared to ~ 0.1 in clinopyroxene; Rollinson, 1993). However, if orthopyroxene constituted a small % of a fractionating assemblage dominated by plagioclase, as in the case for the LSSC, the effect on the bulk distribution coefficient is likely to be negligible. Also, there is considerable overlap between Group I and Group II specimens on *Figures 4.3a-d*, which also argues against a simple fractionation relationship between the two groups.

Varying degrees of partial melting is also likely to preserve constant ratios between pairs of similarly incompatible trace-elements. However, where the degree of partial melting is small, significant changes in the ratio of two incompatible elements where one has a bulk partition coefficient of, say, 0.1 and the other 0.01, can occur. However, varying degrees of partial melting is not believed to be a viable mechanism to control the distribution of the incompatible elements in the LSSC magmas, as will be shown below.

However, when many of the trace-element *ratios* are examined in detail, there is often a significant variation displayed in members of Group I. *Figure 4.4a-d* show the trace-element ratios Zr/Y, Ti/Zr, Y/Nb and Ce/Y plotted against SiO_2 . The trends seen within Group I are either markedly curved or linear, and either increasing or decreasing with degree of fractionation. Such variations in trace-element ratios have been attributed to variable degrees of melting within the mantle

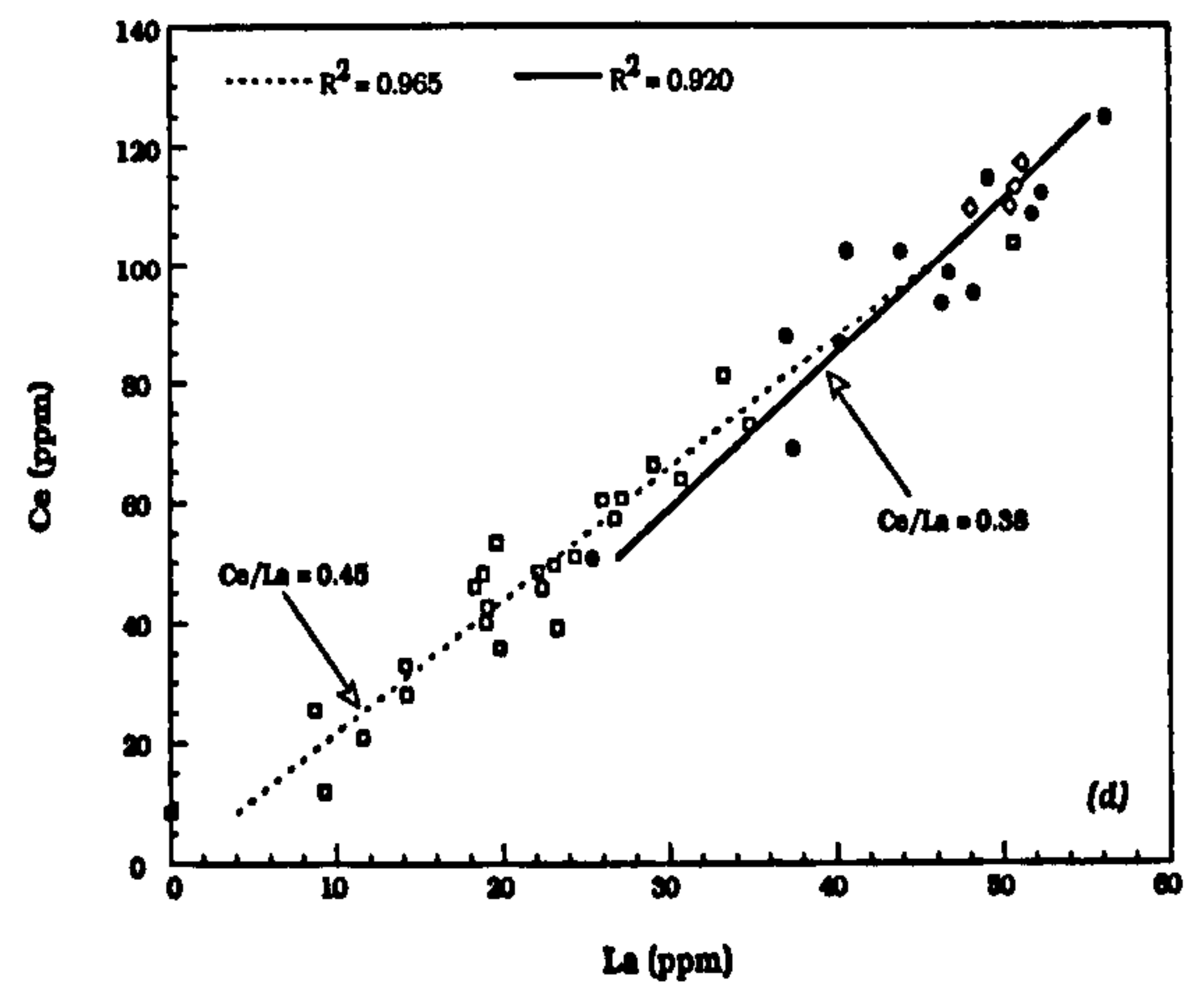
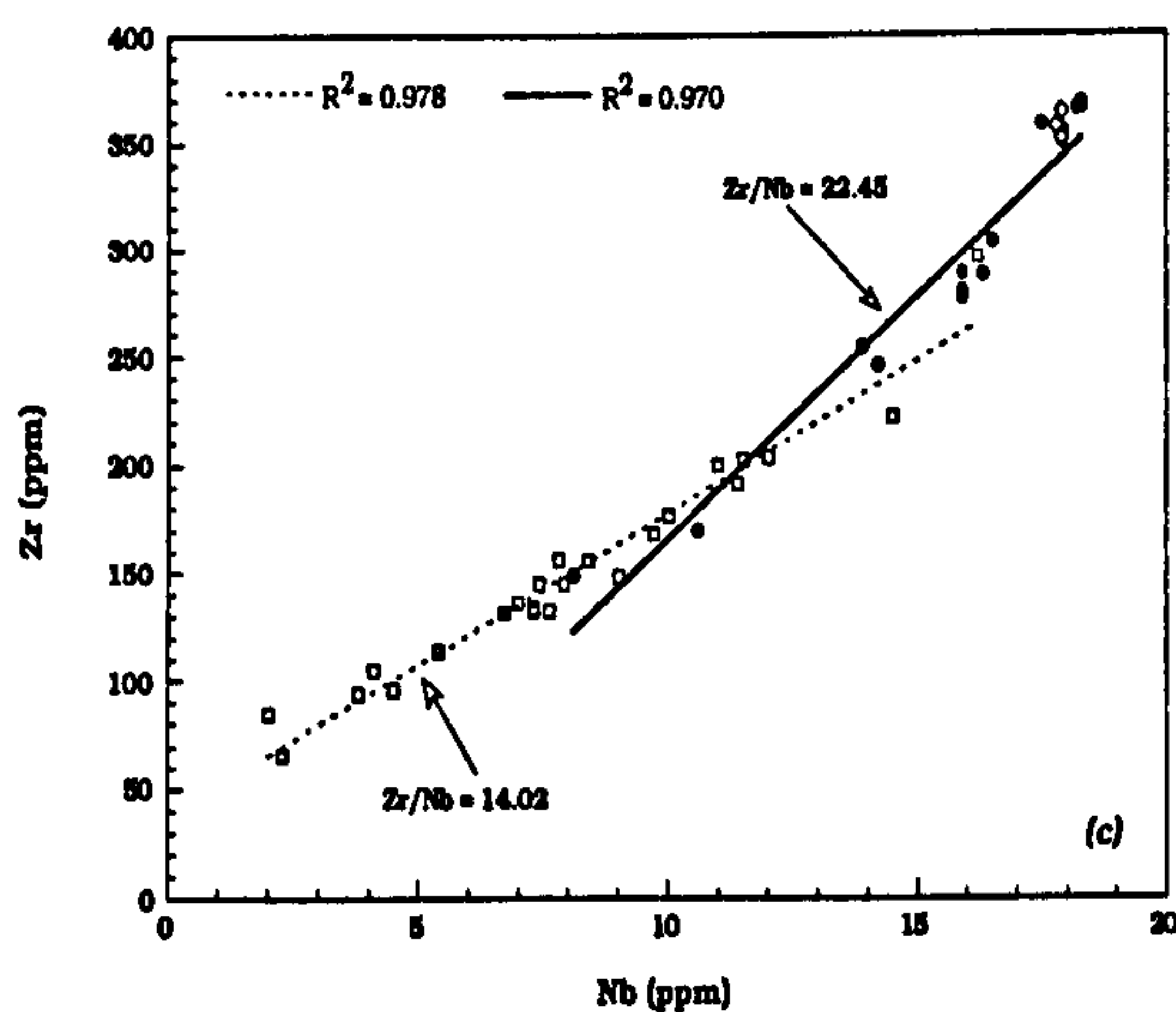
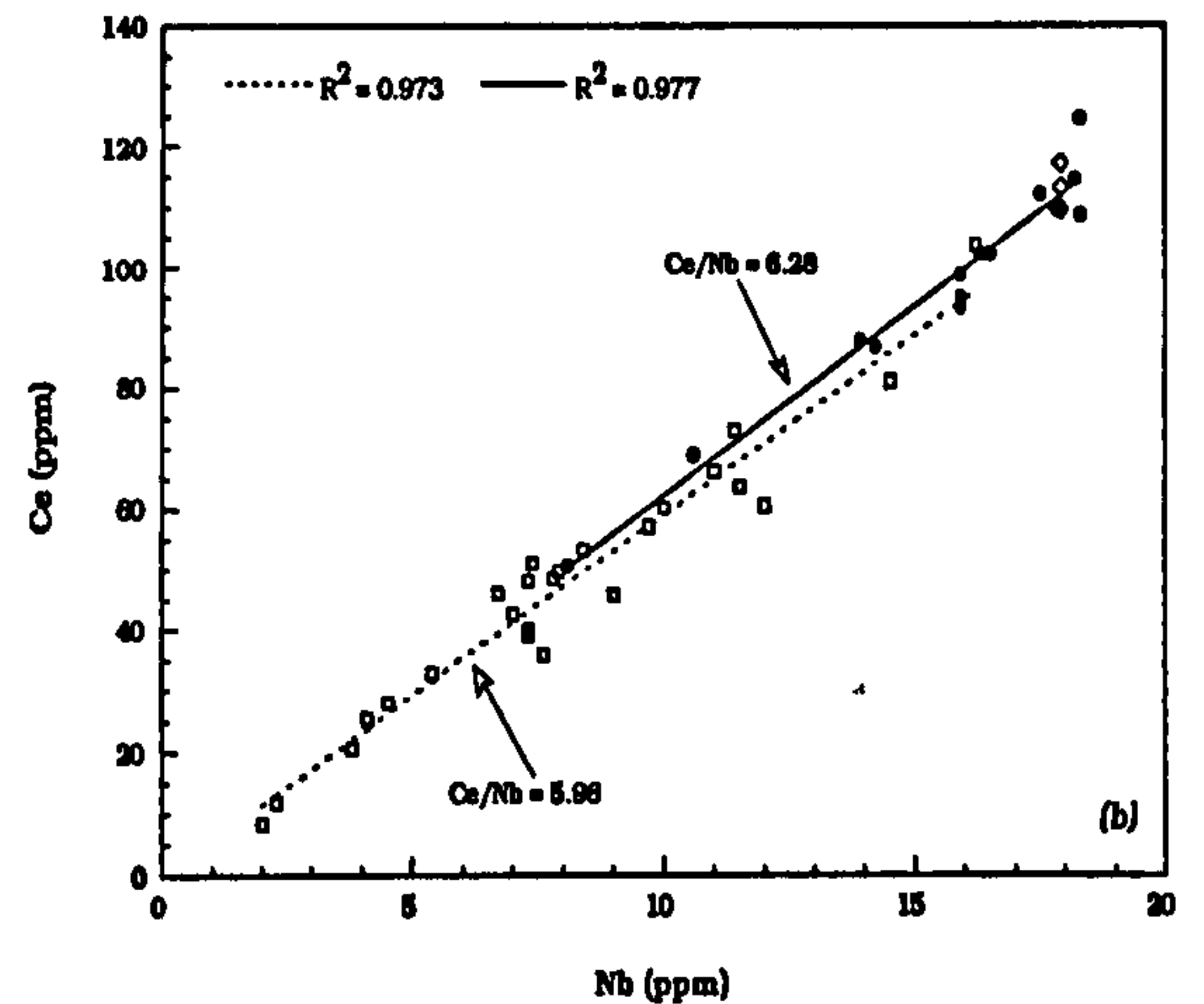
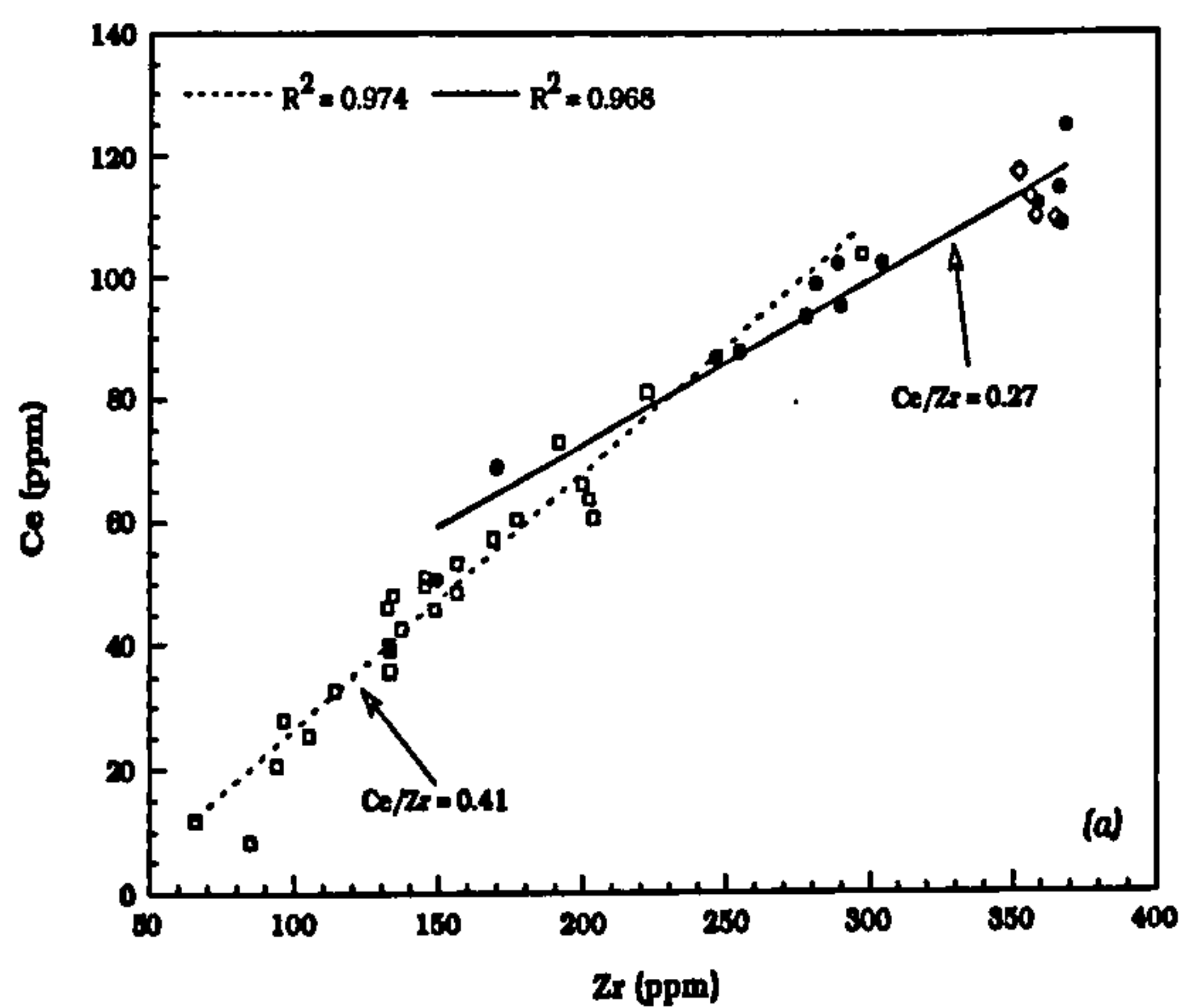


FIGURE 4.3 Covariance of certain highly incompatible elements. Showing strong correlations for Group I and Group II magmas.

(a) Variation of Ce with Zr

(b) Variation of Ce with Nb

(c) Variation of Zr with Nb

(d) Variation of Ce with La

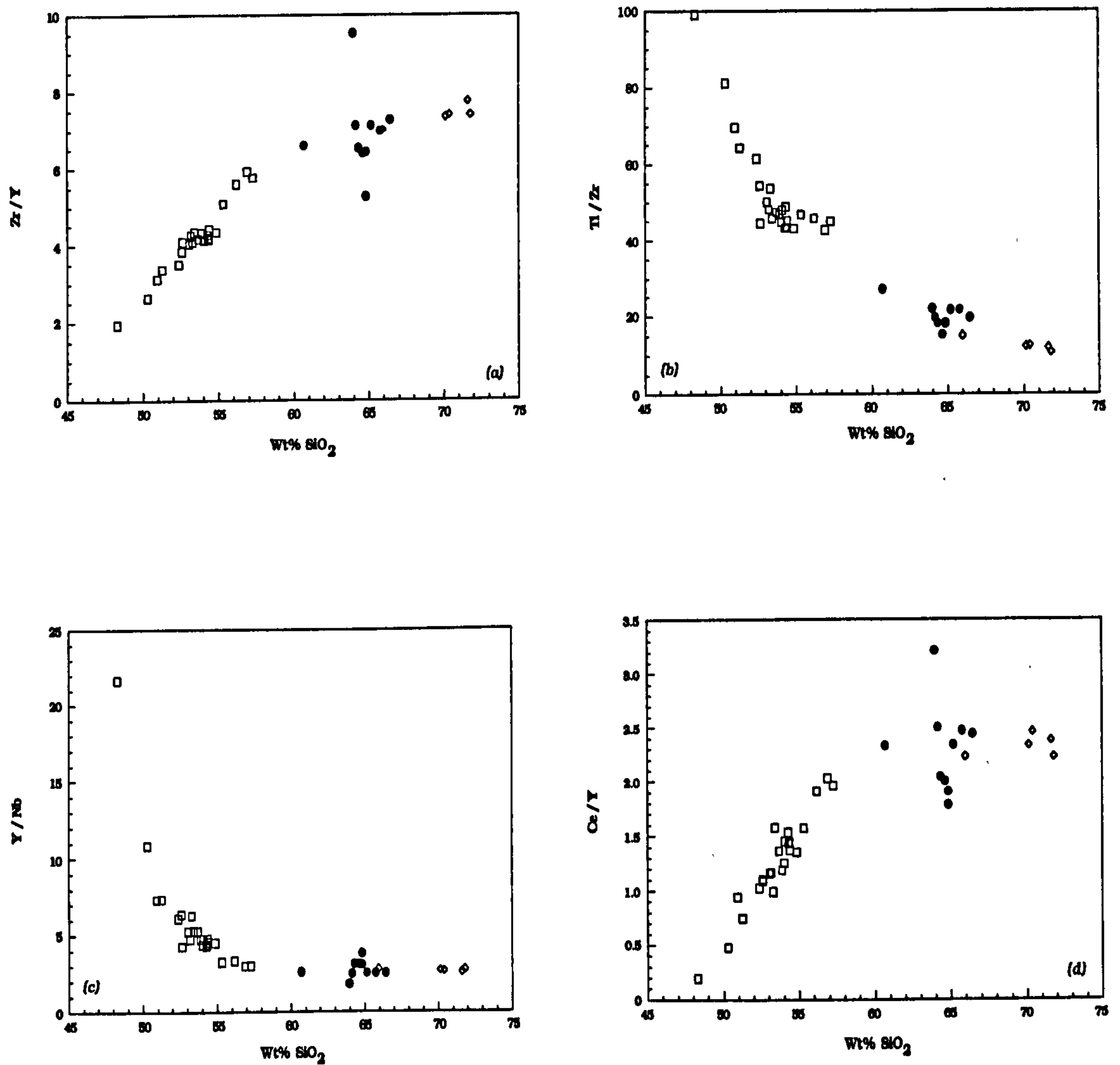


FIGURE 4.4 Covariance of certain highly incompatible element ratios with degree of fractionation. Showing strong correlations for Group I magmas.

- (a) Variation of Zr/Y with SiO_2
- (b) Variation of Ti/Zr with SiO_2
- (c) Variation of Y/Nb with SiO_2
- (d) Variation of Ce/Y with SiO_2

(e.g. Nicholson & Latin, 1992). For example, both Zr and Y are incompatible during gabbro fractionation, and so the ratio between these two elements is unlikely to be disturbed by fractional crystallization. They do, however, behave differently during mantle melting. As Zr is more incompatible in mantle phases than Y, the value of Zr/Y will tend to be greatest when the degree of melting is small. The same holds for the ratios of La/Y and Ce/Y. As a result, there should be positive correlations between these ratios and Fe_2O_3^* , which decreases with increasing degree of partial melting (McKenzie & Bickle, 1988).

Figures 4.5a-b show the relationship between Fe_2O_3^* and Zr/Y and Ce/Y for the LSSC. It is clear that a negative correlation exists between these element ratios and Fe_2O_3^* , suggesting that variable degrees of partial melting were not responsible for the variations seen within the suite.

Figure 4.6 shows the covariance of Cr with Zr. During mantle melting, Cr is initially held back in residual chrome-diopside, and spinel. As the degree of partial melting increases, these phases are consumed and the Cr content of the liquid will rise. Zr, being an highly incompatible element in mantle phases, will decrease in concentration in the melt, as the degree of partial melting increases. This is shown by the partial melting vector in Figure 4.6. During fractional crystallization of basaltic magmas, Cr will decrease with increasing degrees of fractionation as Cr-spinel or clinopyroxene is removed, and Zr will increase in concentration. These combined compatible and incompatible trace-element systematics show that the variation in the trace-element geochemistry of the LSSC magmas cannot be as a result of differential partial melting in the mantle.

The trace-element correlations which exist may, therefore, be due to binary magma mixing, or to combined assimilation and fractional crystallization. Binary mixing should lead to linear trends on incompatible element-element plots, and hyperbolic distributions on incompatible element ratio-ratio diagrams where the denominators of both ratios are different (e.g. Zr/Yb vs. Ce/Y), and linear trends on diagrams where the denominator of the two ratios is the same (e.g. Zr/Yb vs. Nb/Yb), which point directly towards the two end-members involved (Langmuir et al., 1978). Figures 4.7a-b show that reasonably good linear (e.g. Zr/Y vs. Ce/Y; Figure 4.7a), or hyperbolic (e.g. Ti/Zr vs. Y/Nb; Figure 4.7b) relationships exist for certain incompatible-element

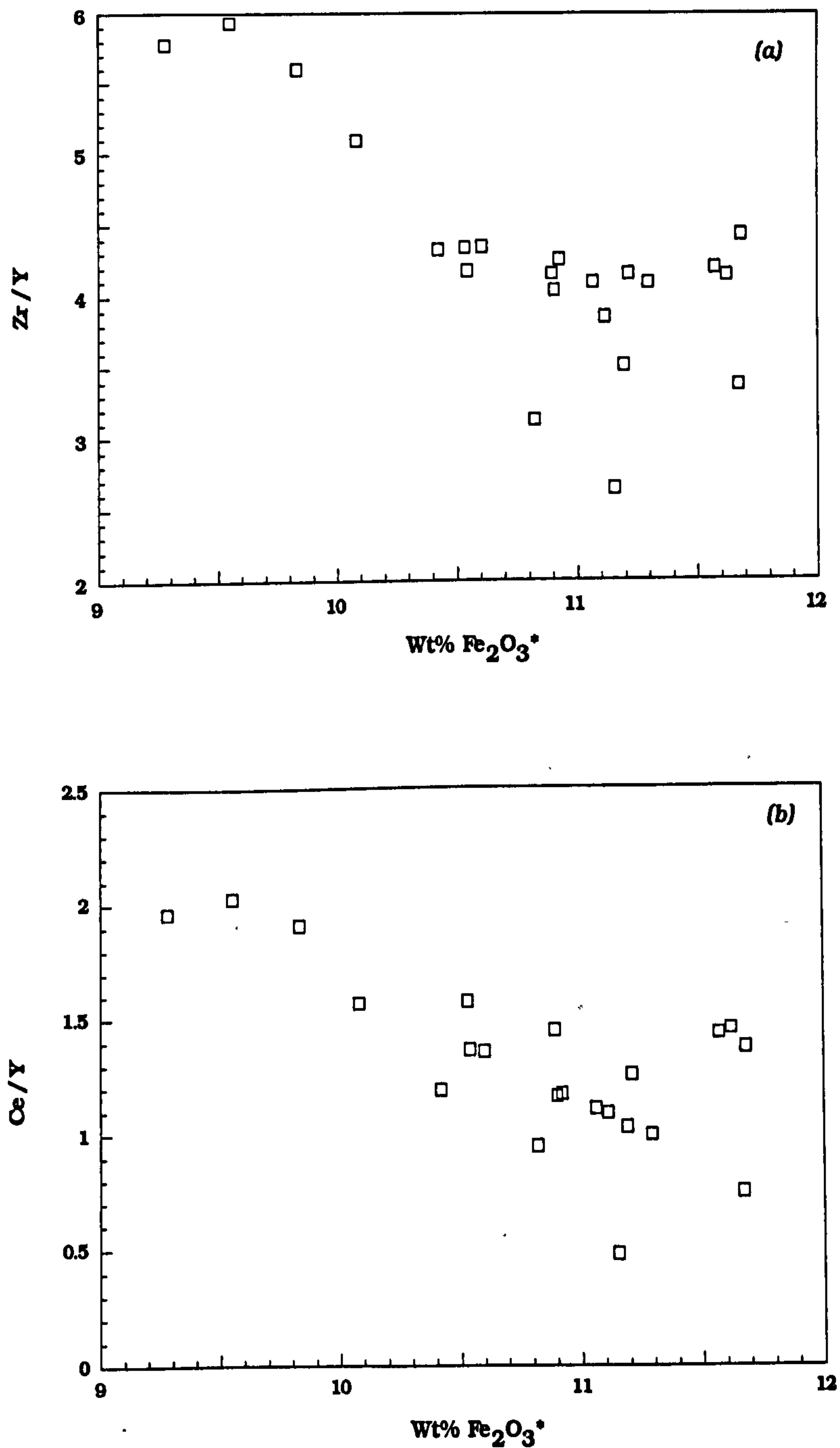


FIGURE 4.5 Covariance of certain highly incompatible element ratios with Fe_2O_3^* . Trends show that variation within Group I magmas cannot be due to differential partial melting within the source.

(a) Variation of Zr/Y with Fe_2O_3^*

(b) Variation of Ce/Y with Fe_2O_3^*

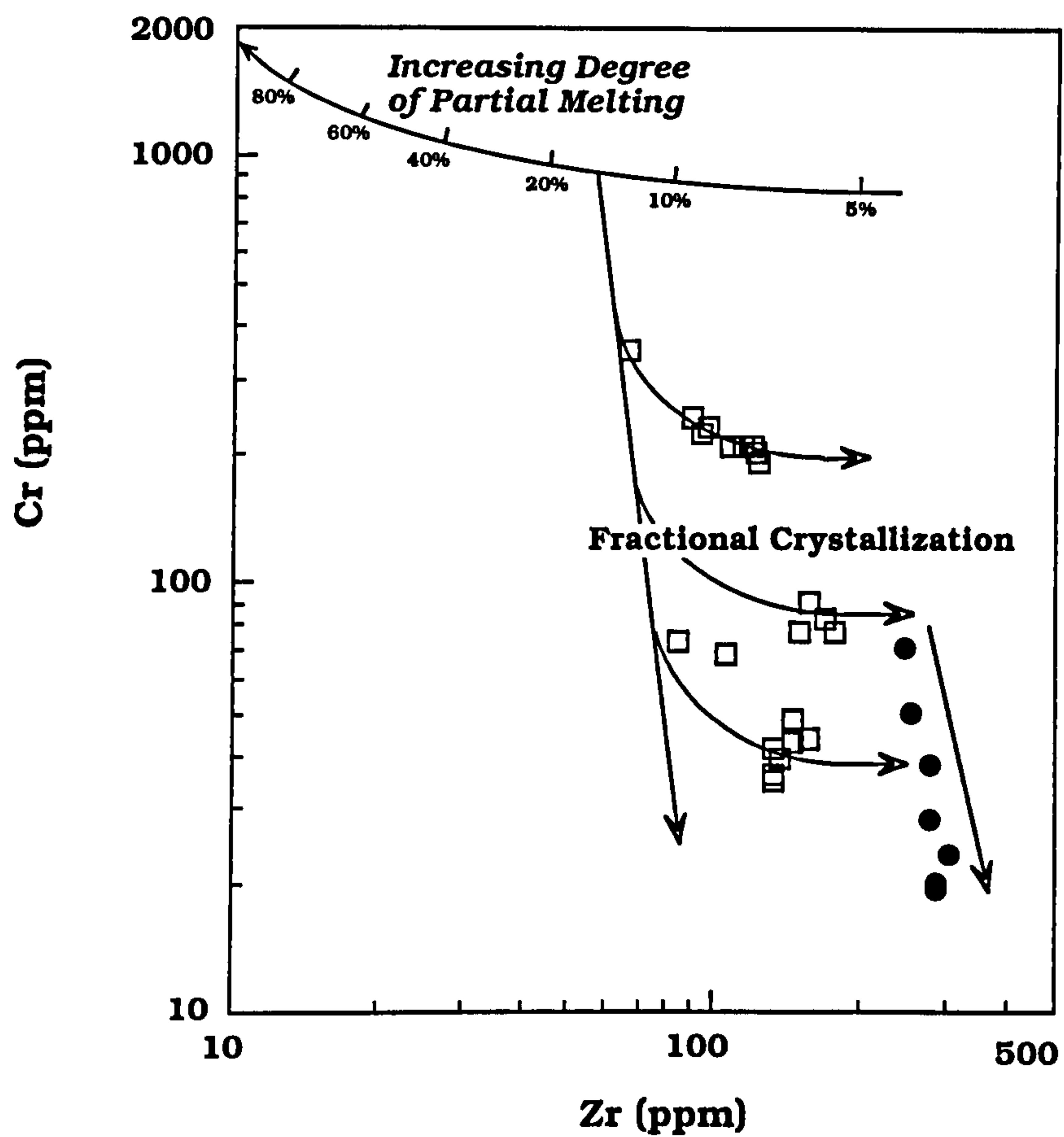


FIGURE 4.6 Plot of Cr vs. Zr for the LSSC Groups I and II, showing path for mantle derived melts with increasing degree of melting, and schematic fractionation paths from these primary magmas.

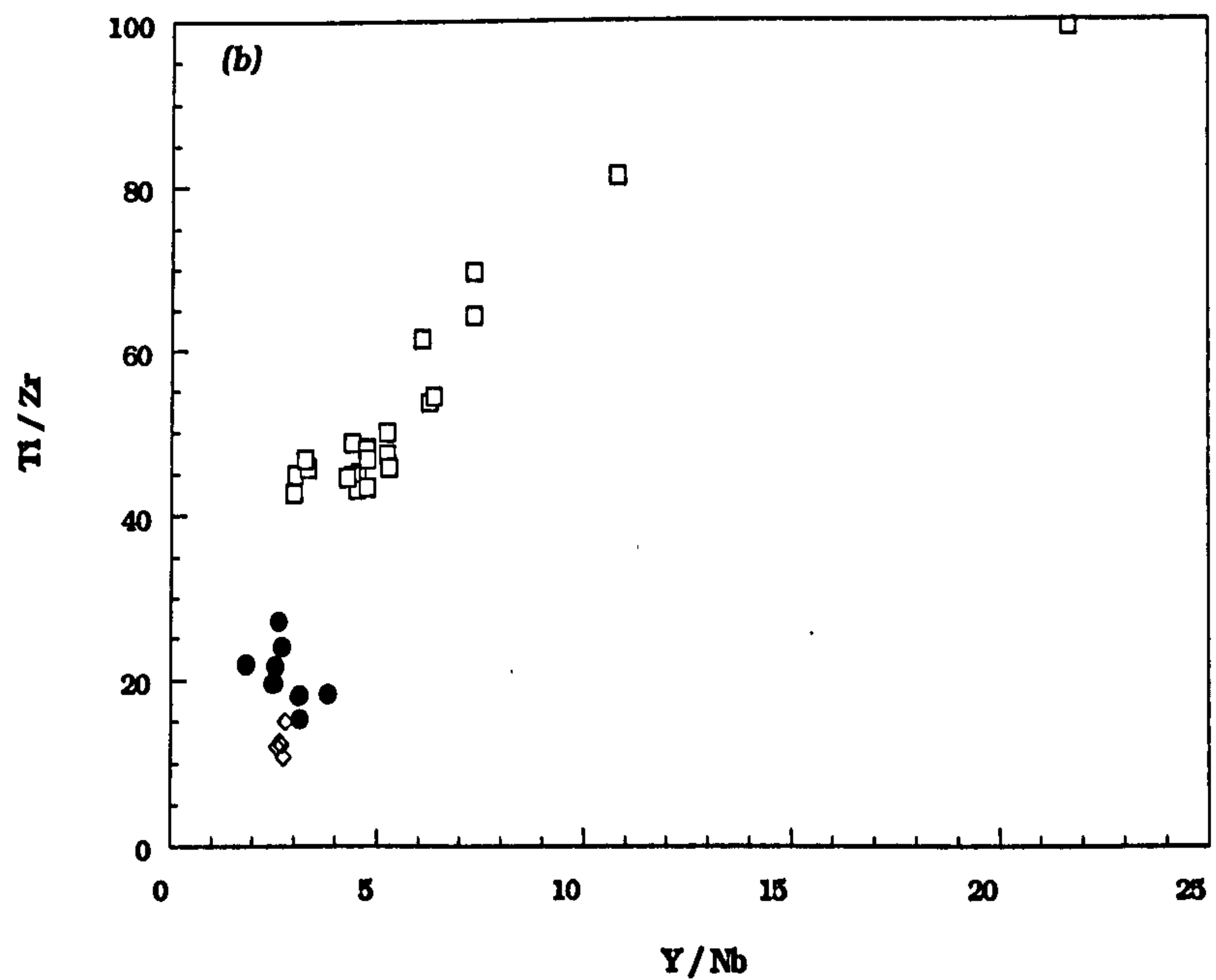
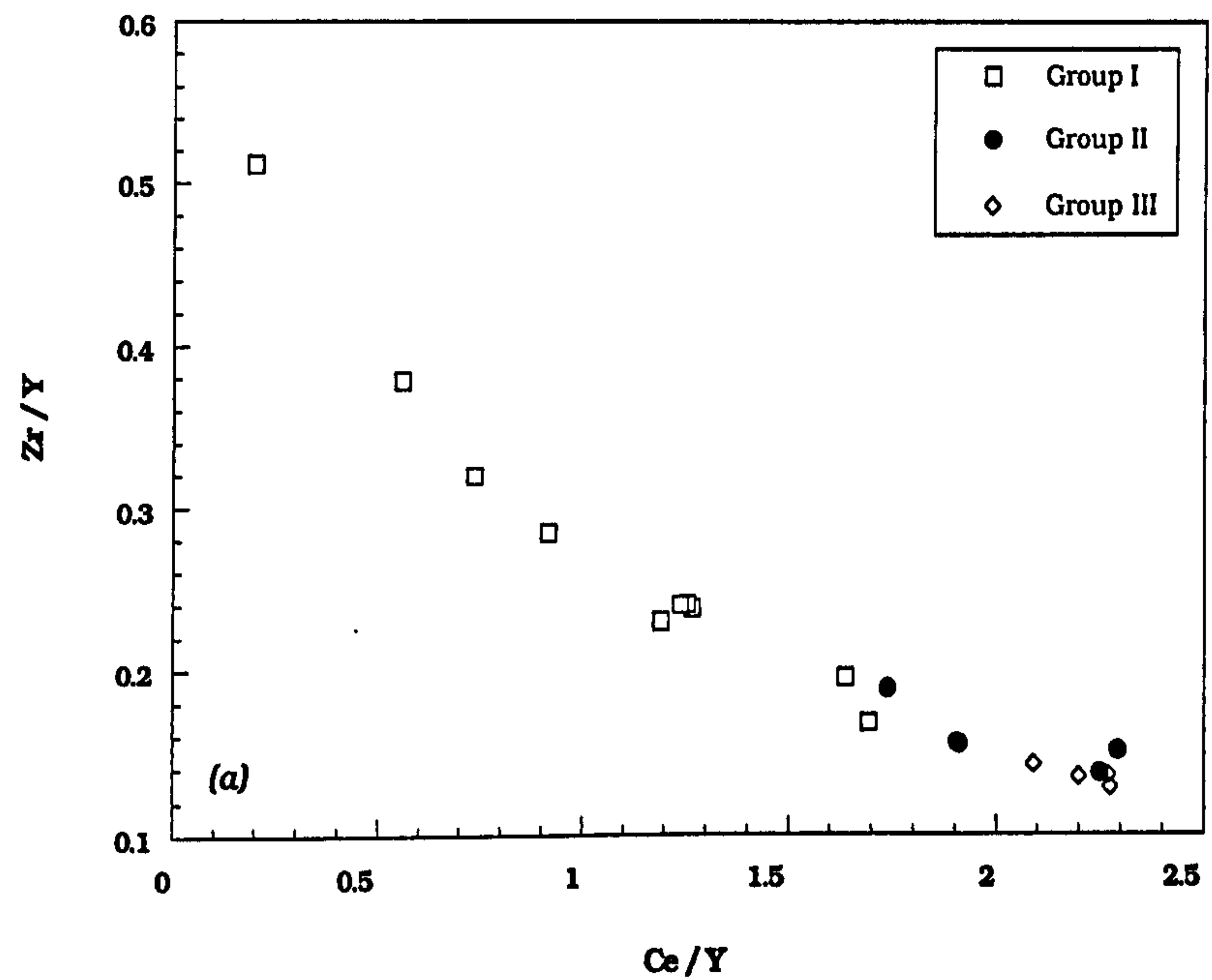


FIGURE 4.7 Covariance of certain highly incompatible element ratios pairs. Trends show that variation within Group I and Group II could be the result of magma mixing (Langmuir et al., 1978)

(a) Variation of Zr/Y with Ce/Y

(b) Variation of Ti/Zr with Y/Nb

ratio-ratio pairs. Consequently, simple, binary mixing between a basic liquid and a silicic liquid, cannot be ruled out for the evolution of Group I magmas. In contrast, simple mixing should lead to straight line relationships on incompatible-element ratio *vs.* element plots (Langmuir *et al.*, 1978; St. Seymour & Vlassopoulos, 1992). For magma-mixing to be proved as the only cause of intra-suite variation, *all plots must show the same systematics* (St. Seymour & Vlassopoulos, 1992). As a result, the curved trends seen in *Figure 4.4a-d* suggest that other processes were involved in the petrogenesis of the LSSC basic magmas, most likely dominated by fractional crystallization.

As stated previously, *closed-system* crystal fractionation will also produce linear trends on incompatible element-element diagrams. If crustal contamination is combined with fractional crystallization (AFC), incompatible element ratios may vary with degree of fractionation.

To test this hypothesis, diagrams which incorporate an 'index of contamination' can be used. Those which are most useful are ratios of elements, one of which is enriched in the crust, and one which is enriched in the mantle source (*e.g.* Nb/Ti), or in the case of contamination with a crustal melt, one which is concentrated in the melt, compared to one remaining in the residue (*e.g.* K/Zr). As such, *Figures 4.8a-d* show the variation of four of these ratios with degree of fractionation (SiO₂). In the case of bulk-assimilation, these diagrams should show simple linear or hyperbolic mixing relations that point directly at the end-members (Langmuir *et al.*, 1978; Thirlwall & Jones, 1983). However, when fractional crystallization is also an important process, such relationships may no longer hold (DePaolo, 1981). The two possible crustal contaminants of the LSSC basic magmas (*i.e.* silicic melts such as the Group III rhyolites, or bulk Moine pelite) are shown in *Figures 4.8a-d*. It is evident from the data presented in *Figures 4.8a-d*, that many of the relationships are simple linear or hyperbolic curves, which point towards the Group III rhyolites, suggesting that the assimilation process may have been one of bulk addition of a silicic melt derived from the crust. However, the trends do not point directly at a bulk Moine pelite, which suggests that AFC-type processes involving bulk Moine, may also explain the trends seen. To test the hypothesis further, combined trace-element and Sr-Nd isotope data are required. This is presented in Chapter 5.

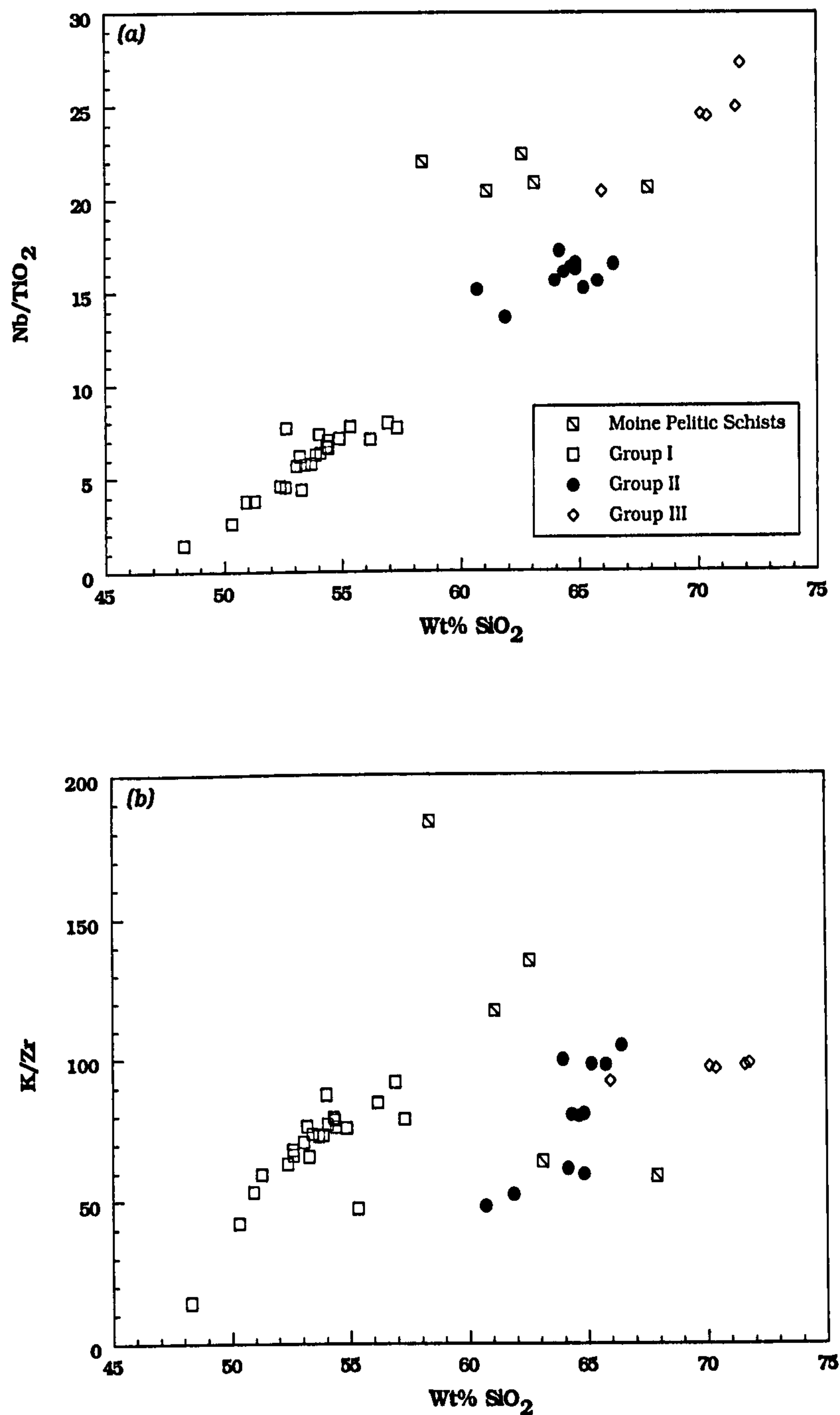


FIGURE 4.8 Covariance of certain highly incompatible elements which can act as an "index of contamination" with degree of fractionation. Trends show that contamination increases with fractionation, indicating AFC type processes.

(a) Variation of Nb/TiO₂ with SiO₂

(b) Variation of K/Zr with SiO₂

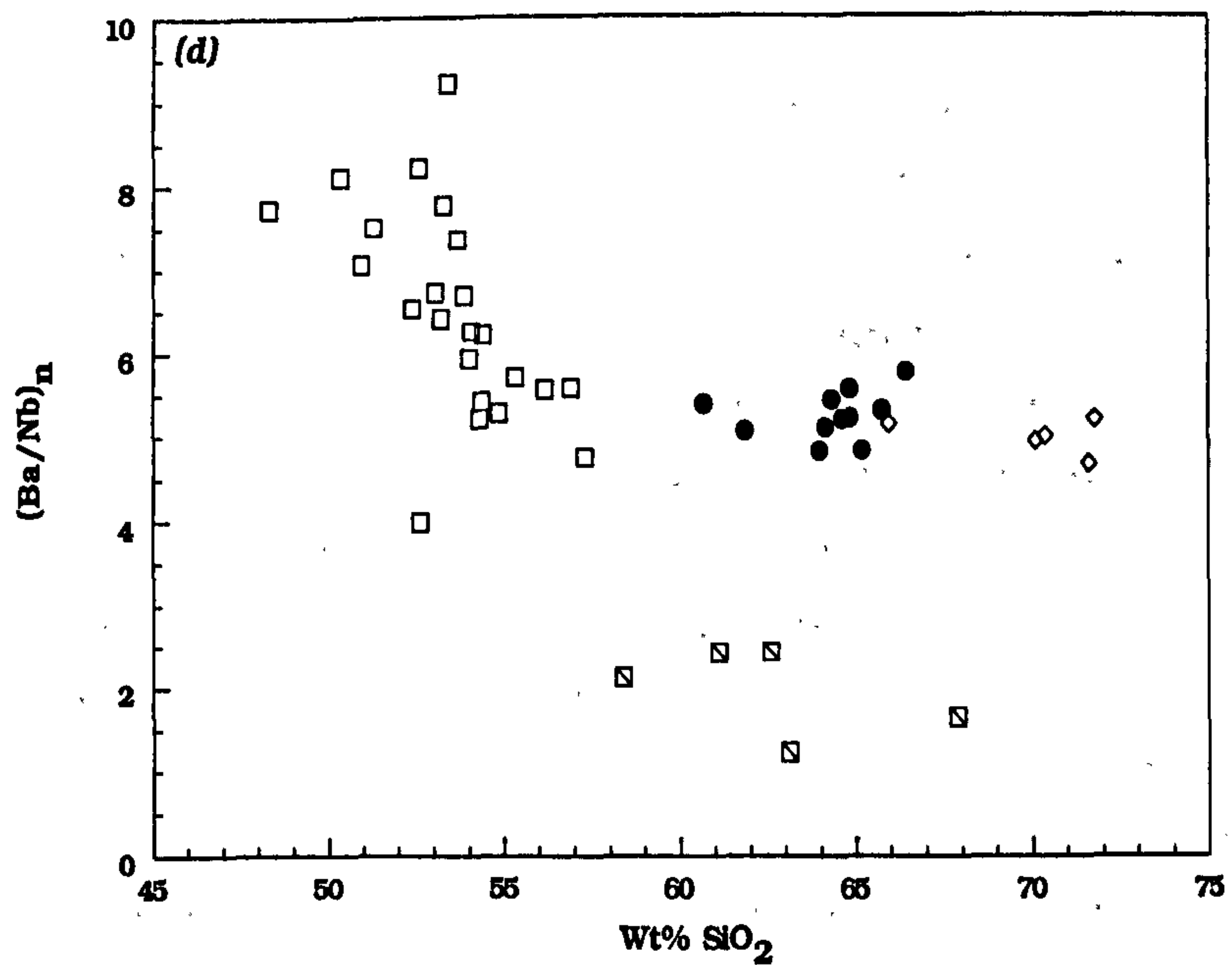
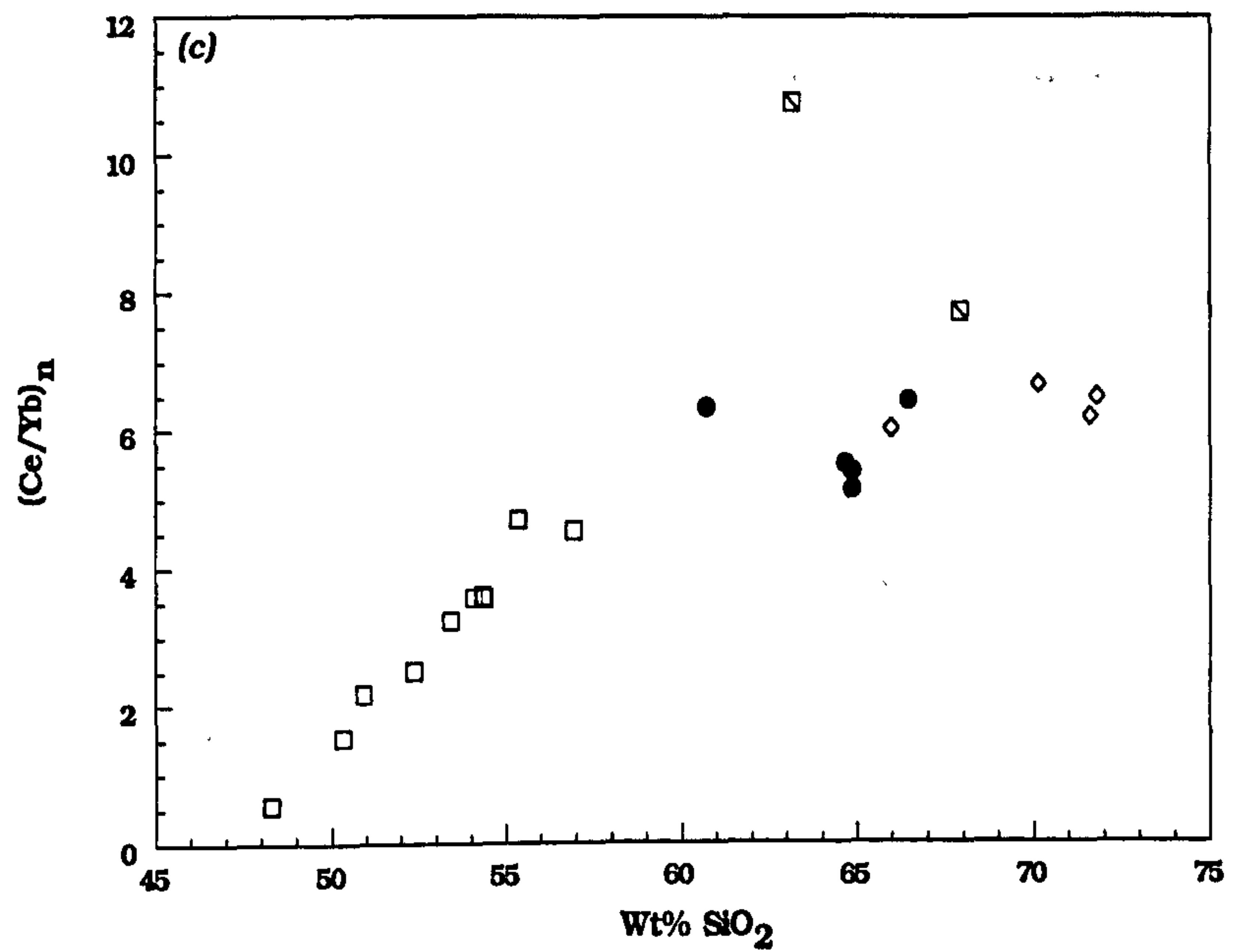


FIGURE 4.8 cont.

Covariance of certain highly incompatible elements which can act as an "index of contamination" with degree of fractionation. Trends show that contamination increases with fractionation, indicating AFC type processes.

(c) Variation of $(Ba/Nb)_n$ with SiO_2

(d) Variation of $(Ce/Yb)_n$ with SiO_2

Chondrite normalizing values after Sun & McDonough (1989) and McDonough (1991)

Multi-element diagrams

Multi-element 'spider diagrams' provide a useful reference frame in which the elemental abundances in suites of volcanic rocks can be compared (*e.g.* Thompson *et al.*, 1983). They are essentially an extension to the plotting of chondrite-normalized REE patterns and, as in REE diagrams, the elemental abundances are normalized. Three normalizing systems have been adopted:- primitive mantle, chondritic and MORB normalization. This study utilises primitive mantle normalization with the elemental order and normalizing data of Sun & McDonough (1989) and McDonough *et al.* (1991), and MORB normalization after Pearce (1983). Analytical error may be the source of many apparently spurious peaks and troughs in 'spider diagram' patterns. However, once these effects have been taken into account, the patterns displayed may provide invaluable petrogenetic information concerning crystal-liquid equilibria. For example, troughs at Sr probably result from the fractional crystallization of plagioclase from many basalts. In contrast, a peak at Th, Rb and a trough at Nb, may suggest contamination of the magma with continental crustal rocks.

The mantle-normalized spider diagrams for samples from Group I are shown in *Figure 4.9a-c*, with the plots being arranged from the most basic magmas (*Figure 4.9a*) through to the more evolved specimens (*Figure 4.9c*). All members of the group are strongly enriched in the full range of trace-elements when compared to primitive-mantle abundances. However, the most magnesian basalts (ORB2 and PGB9) do not show the same degree of enrichment as the rest of the group. The individual patterns throughout the group show many similarities, with each displaying a very prominent trough at Nb, with others at P and Ti. A broad peak is invariably present between Ba and K, possibly suggesting that the magmas have been contaminated with continental crust (Thompson *et al.*, 1983; Wilson, 1989). The least-evolved members of Group I have no Sr anomaly. As fractionation proceeds, some members of the group have developed a negative Sr anomaly, suggestive of low pressure plagioclase fractionation. The numerous 'cross overs' between individual members of Group I precludes there being a simple fractional crystallization relationship between the basic and more evolved members. The trough at P is thought to be controlled by source characteristics, with minor apatite probably

remaining in the source after partial melting. Apatite fractionation is not a viable mechanism for the production of the P trough since P_2O_5 increases with increasing SiO_2 content (*Figure 3.5i*). Indeed, the P anomaly increases through the sequence of diagrams for Group I magmas. The trough at Ti would suggest that minor titanomagnetite fractionation. However, this has been negated since total TiO_2 increases with fractionation through Group I. Members of Group II show similar patterns to those of Group I (*Figure 4.9d-f*). However, there is much more variability in the profiles, with many samples displaying highly 'spiked' patterns, a feature commonly attributed to variable degrees of crustal contamination (Wilson, 1989). Many of the Group II porphyritic dacites (*e.g.* TVPI1) have very prominent peaks at Zr, P and Y. This is consistent with the presence of apatite and zircon microphenocrysts within these rocks. Other members of this group have very prominent troughs at P and Ti, indicating that these siliceous rocks may have *fractionated* apatite and titanomagnetite.

The Group III rhyolites show similar spiked patterns, a fact consistent with their possible derivation from the partial melting of crustal rocks (*Figure 4.9g*). Again, the following discussion of the Sr and Nd isotope geochemistry of the LSSC will allow a firm conclusion to be made.

When compared to MORB (*Figure 4.10a-e*) it is obvious that the majority of the Loch Scridain magmas are enriched in a wide range of incompatible elements, especially K, Rb, Ba and Th. However, the more basic members of Group I (*e.g.* ORB2, PGB9, TILE1) have abundances of the elements Nb - Y that are similar, if not depleted, compared to N-type MORB. (Pearce, 1983; Wilson, 1989). This general enrichment in incompatible elements of the Loch Scridain magmas when compared to MORB, would suggest that they cannot have been generated in a depleted MORB source mantle. They may however, have fractionated from a MORB-like parent basic magma. However, the strong enrichment in LIL elements is difficult to explain in this simple fashion. The LSSC, and other CFB tholeiitic suites (*e.g.* Deccan, Paraná) have similar spider diagram patterns to those of oceanic-island tholeiites (Sun & McDonough, 1989; Wilson, 1993b). Thompson *et al.* (1983) suggested that CFB tholeiites are simply magmas geochemically similar to oceanic tholeiites that have been variably contaminated by the continental crust. Fusible crustal rock-types are generally much richer in Ba, Rb, Th, K and the light REE than ocean island basalts (OIB), but have similar or lower contents of Nb, P, Zr, Y and the middle

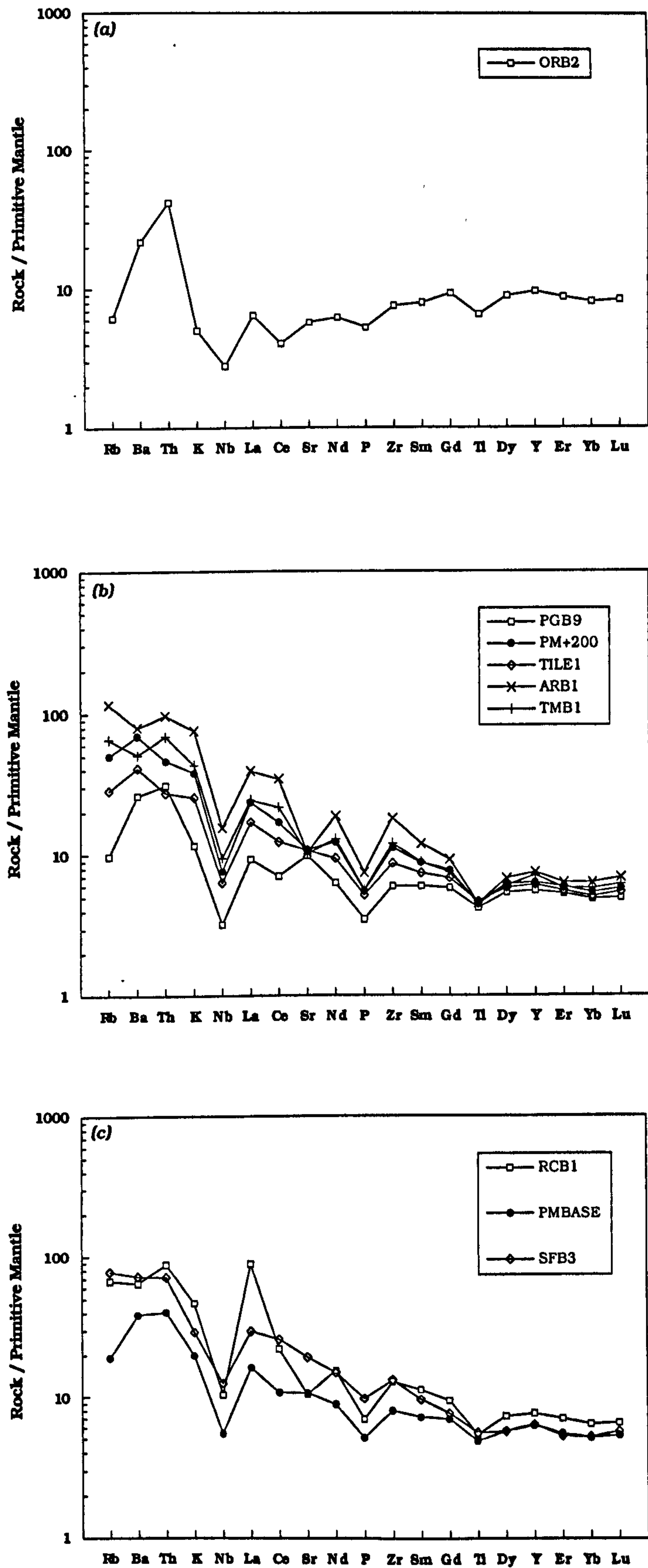


FIGURE 4.9 (a) - (c) Primitive mantle normalized multi-element diagrams for Group I magmas (after Thompson et al, 1983). Normalizing data from Sun & McDonough (1989) and McDonough (1991).

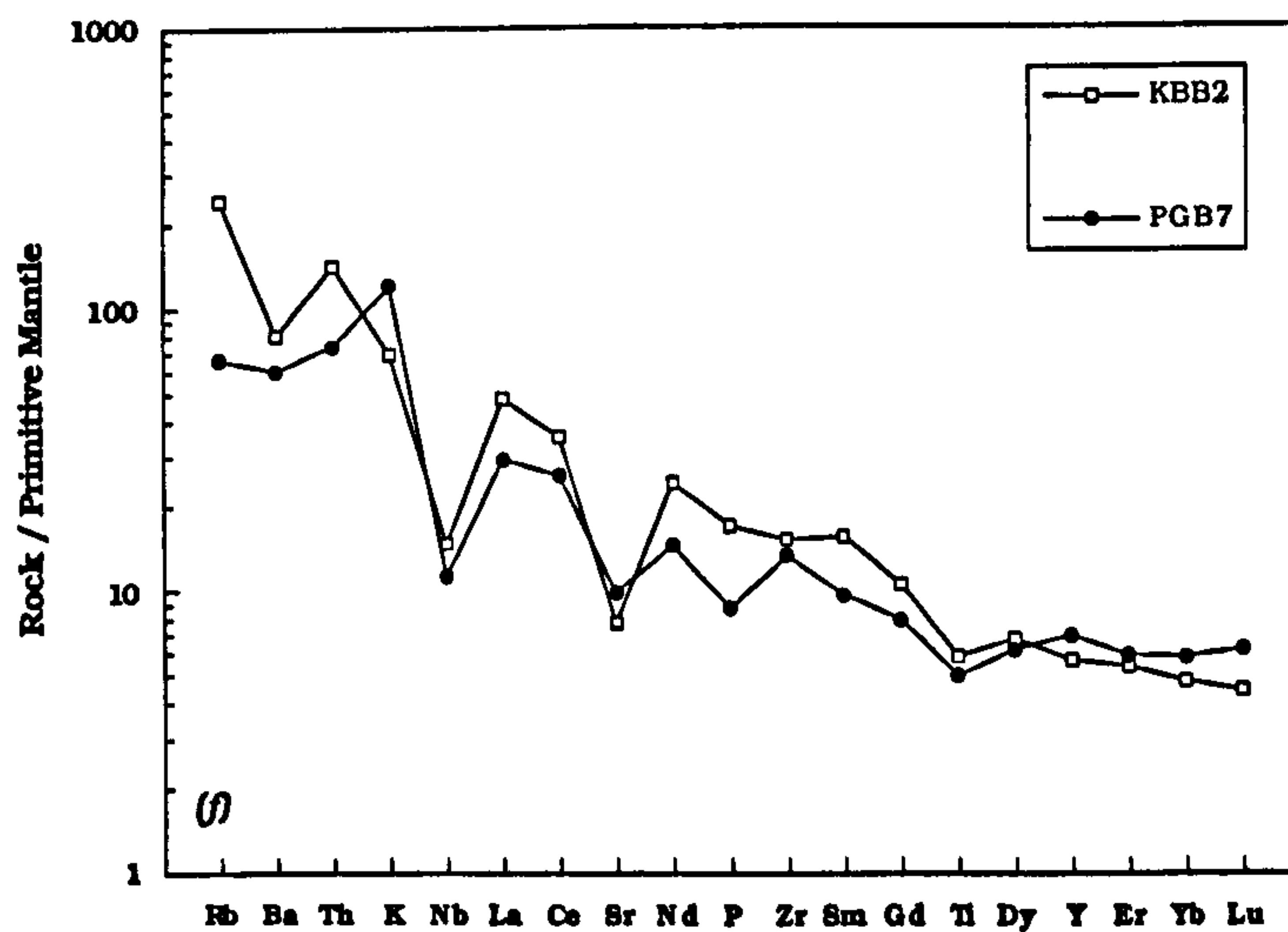
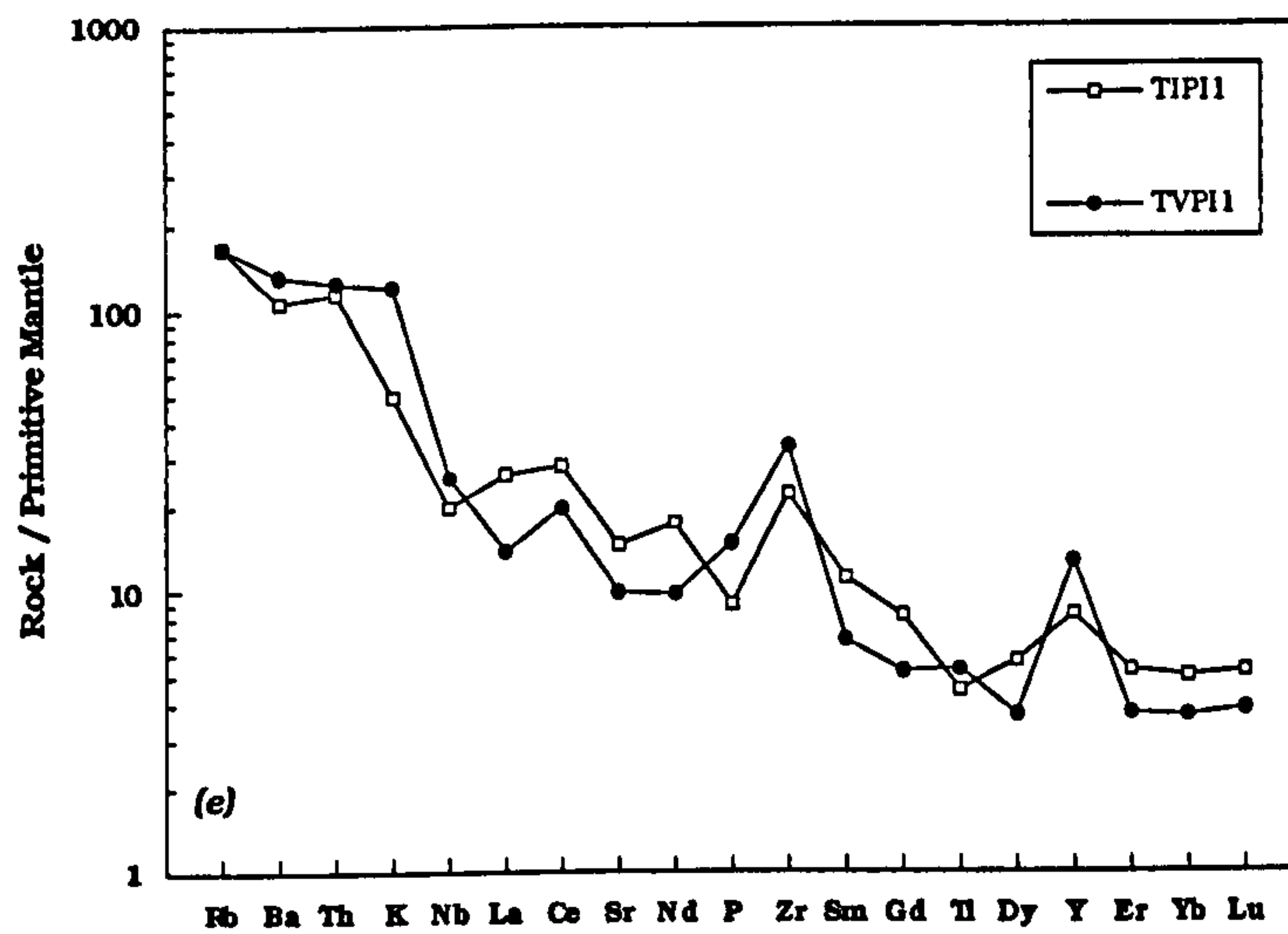
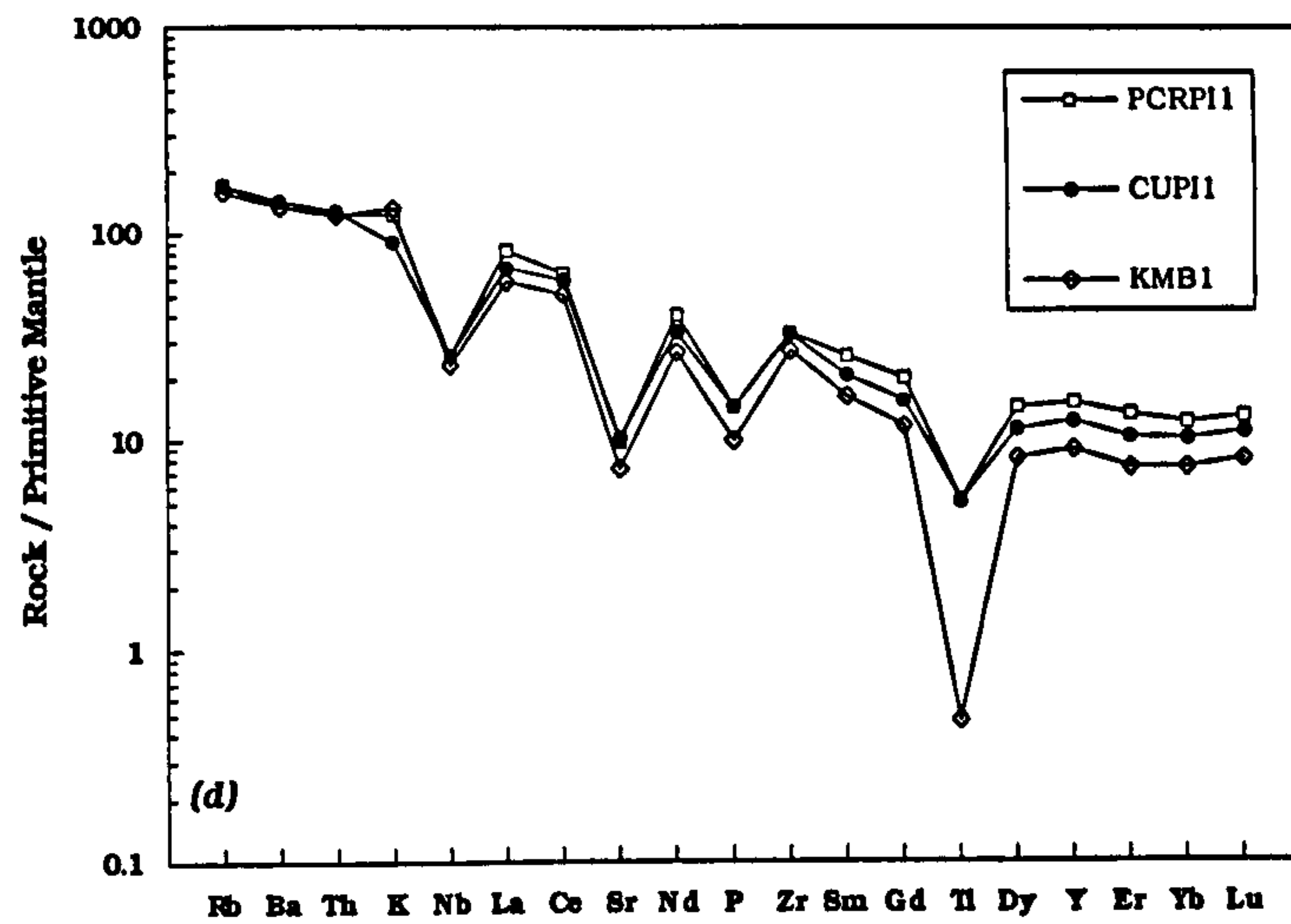


FIGURE 4.9 (d) - (f)

Primitive mantle normalized multi-element diagrams for Group II magmas (after Thompson et al, 1983). Normalizing data from Sun & McDonough (1989) and McDonough (1991).

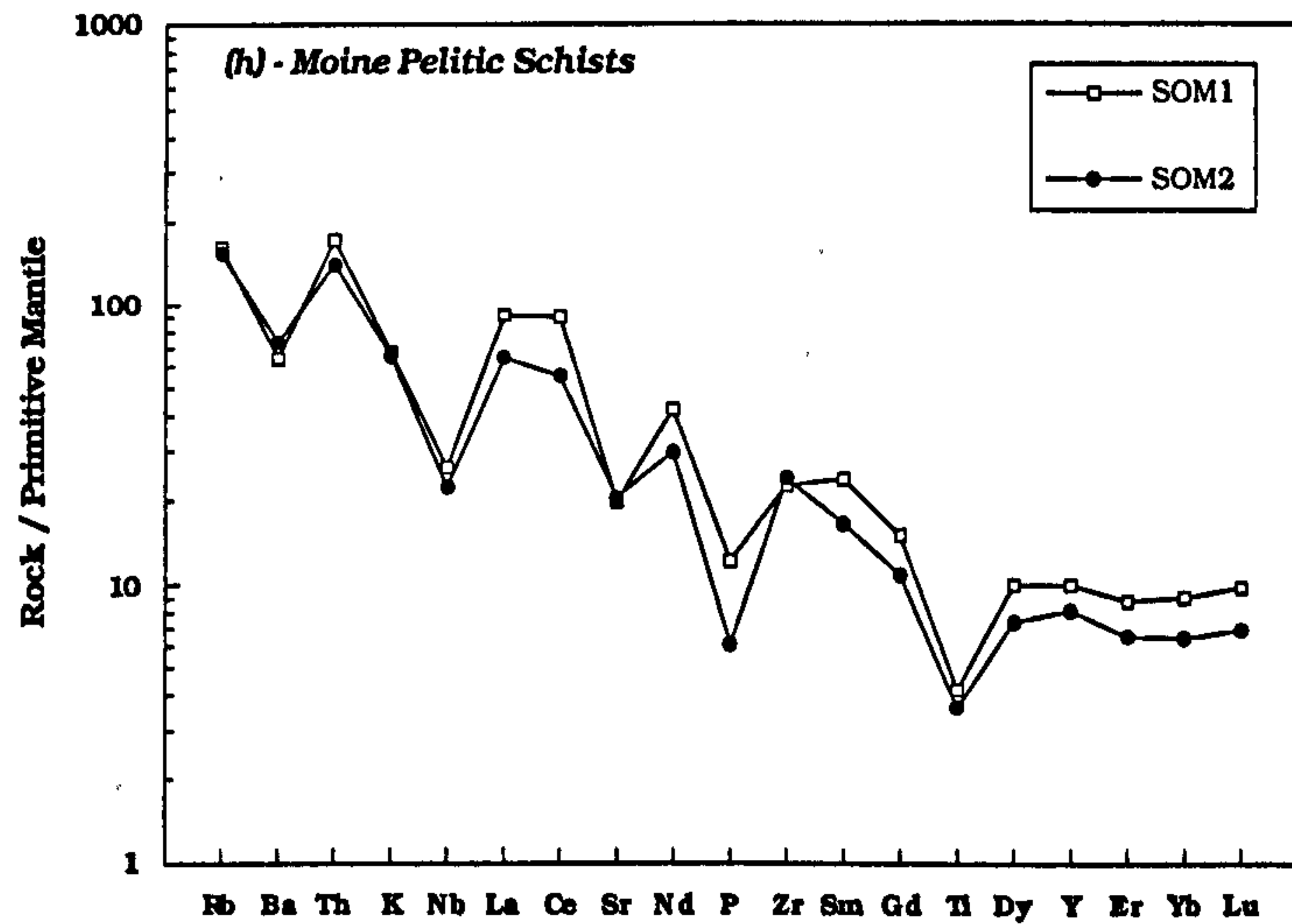
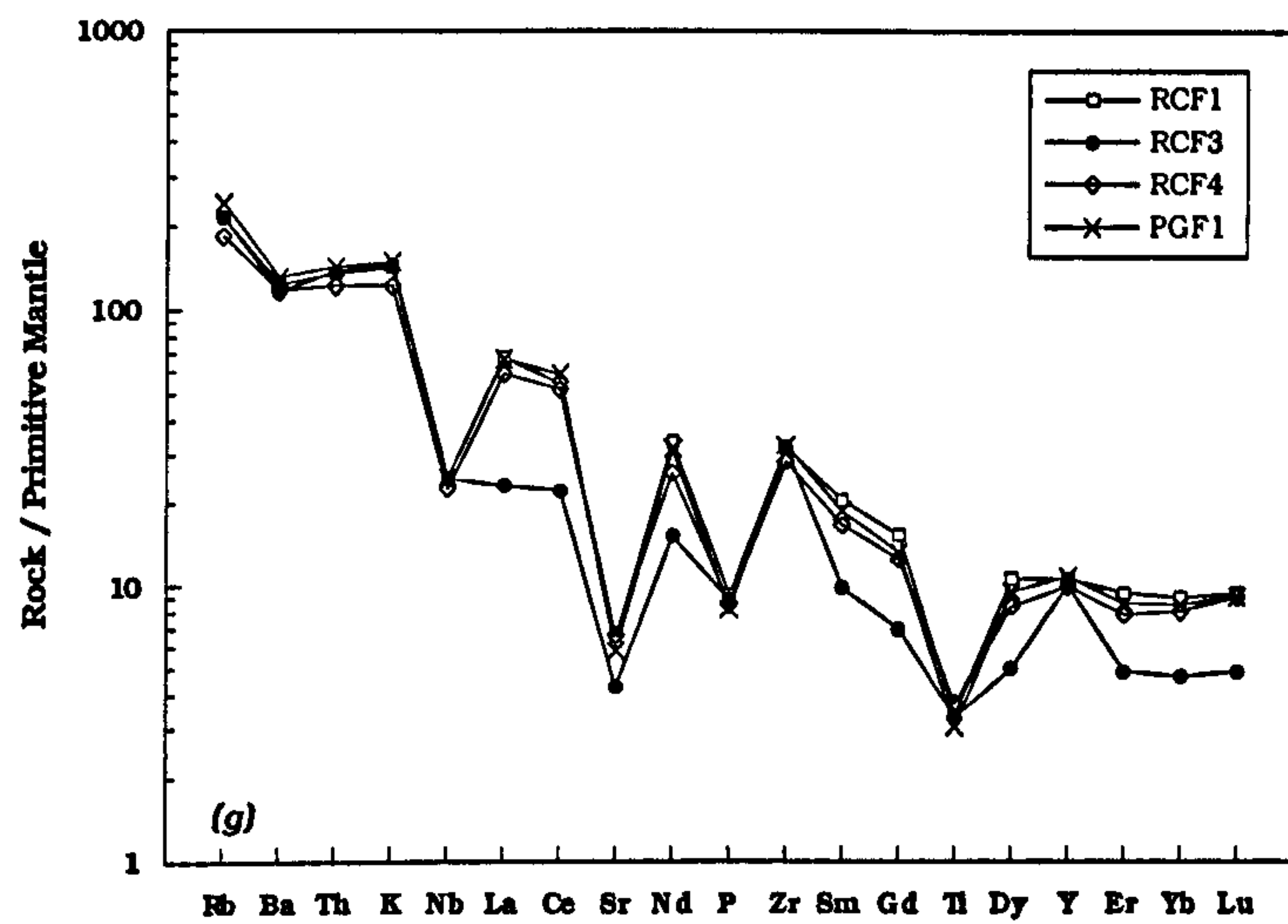


FIGURE 4.9 (g) - (h) Primitive mantle normalized multi-element diagram for Group III magmas, and for comparison, Moine pelitic schists (after Thompson et al, 1983). Normalizing data Sun & McDonough (1989) and McDonough (1991).

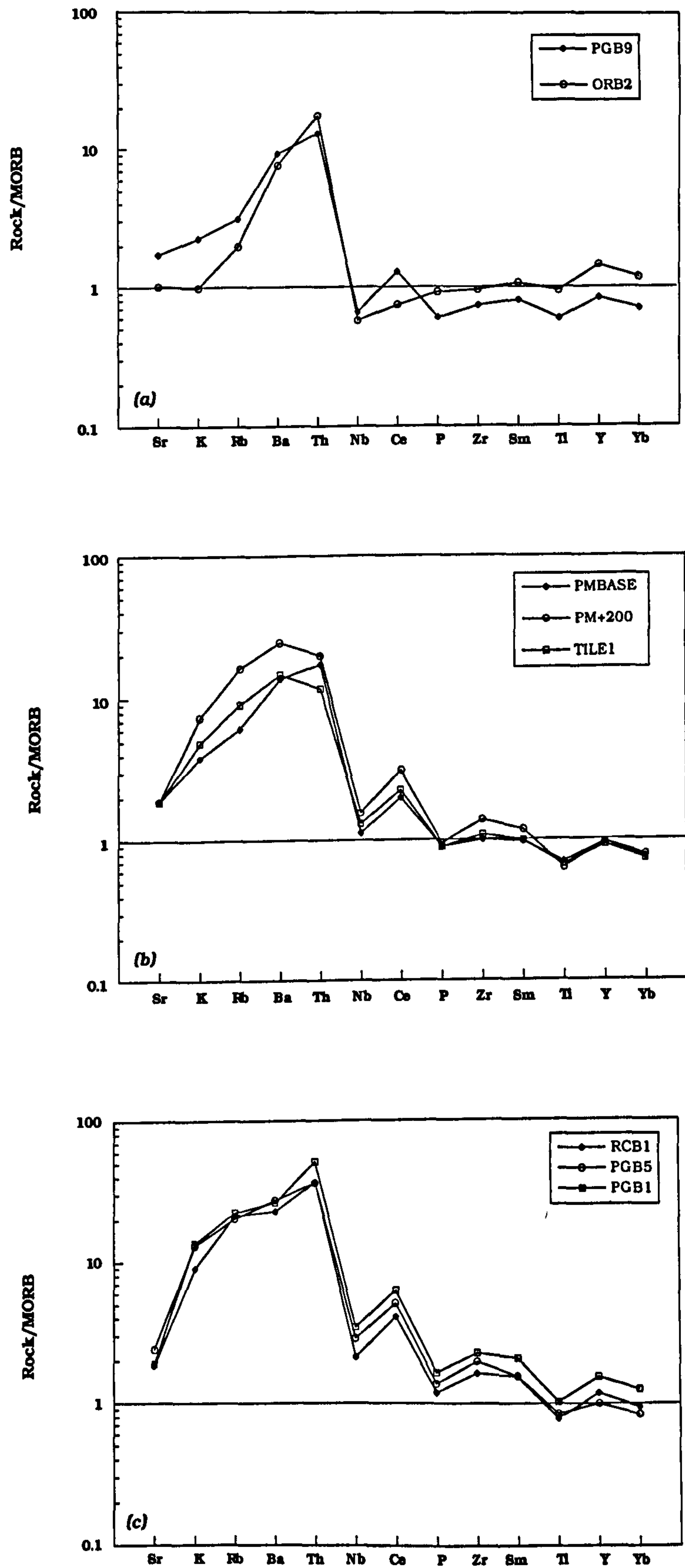


FIGURE 4.10 (a) - (c) MORB normalized multi-element diagrams for Group I magmas (after Pearce, 1983). Normalizing data from Pearce (1983).

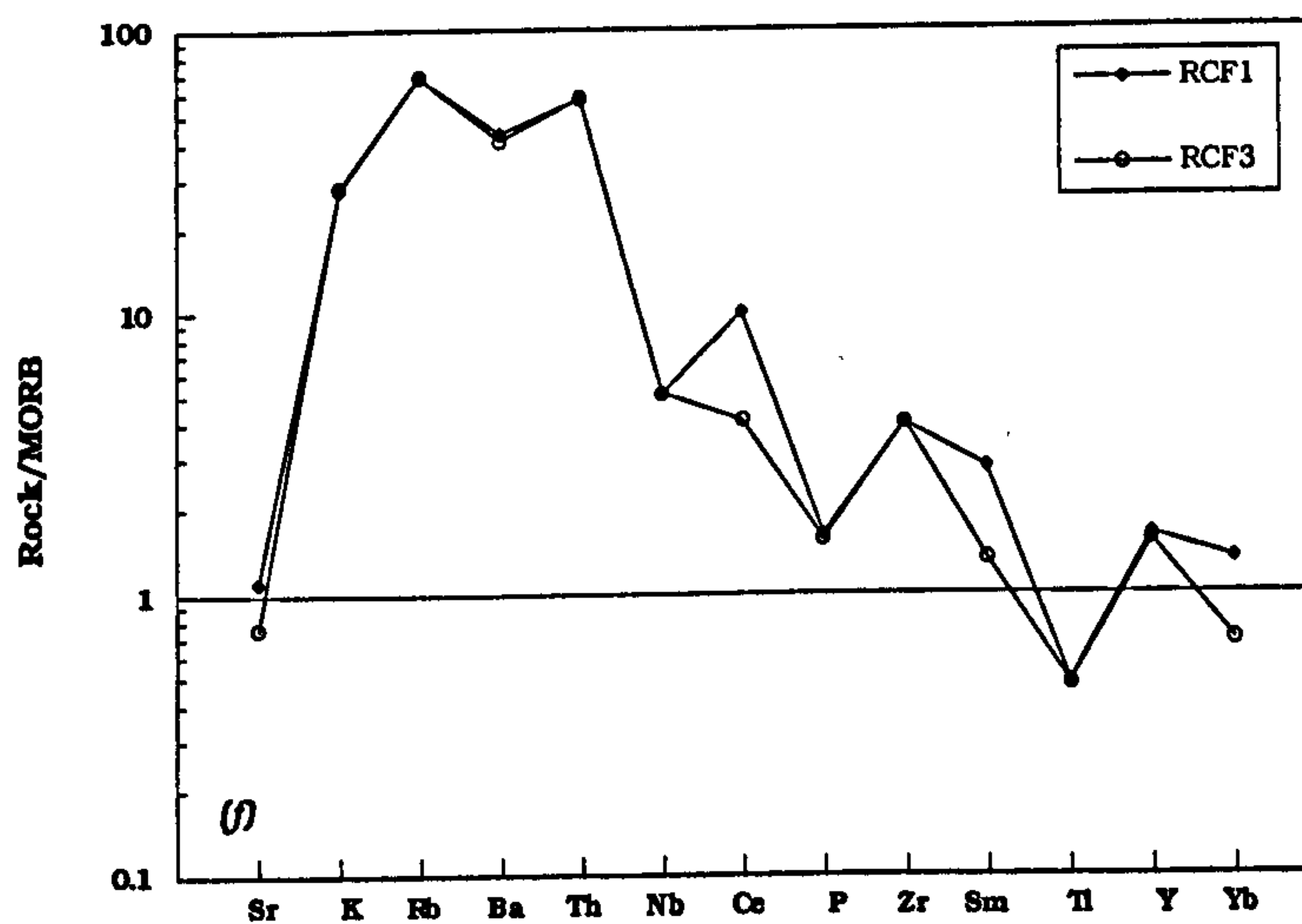
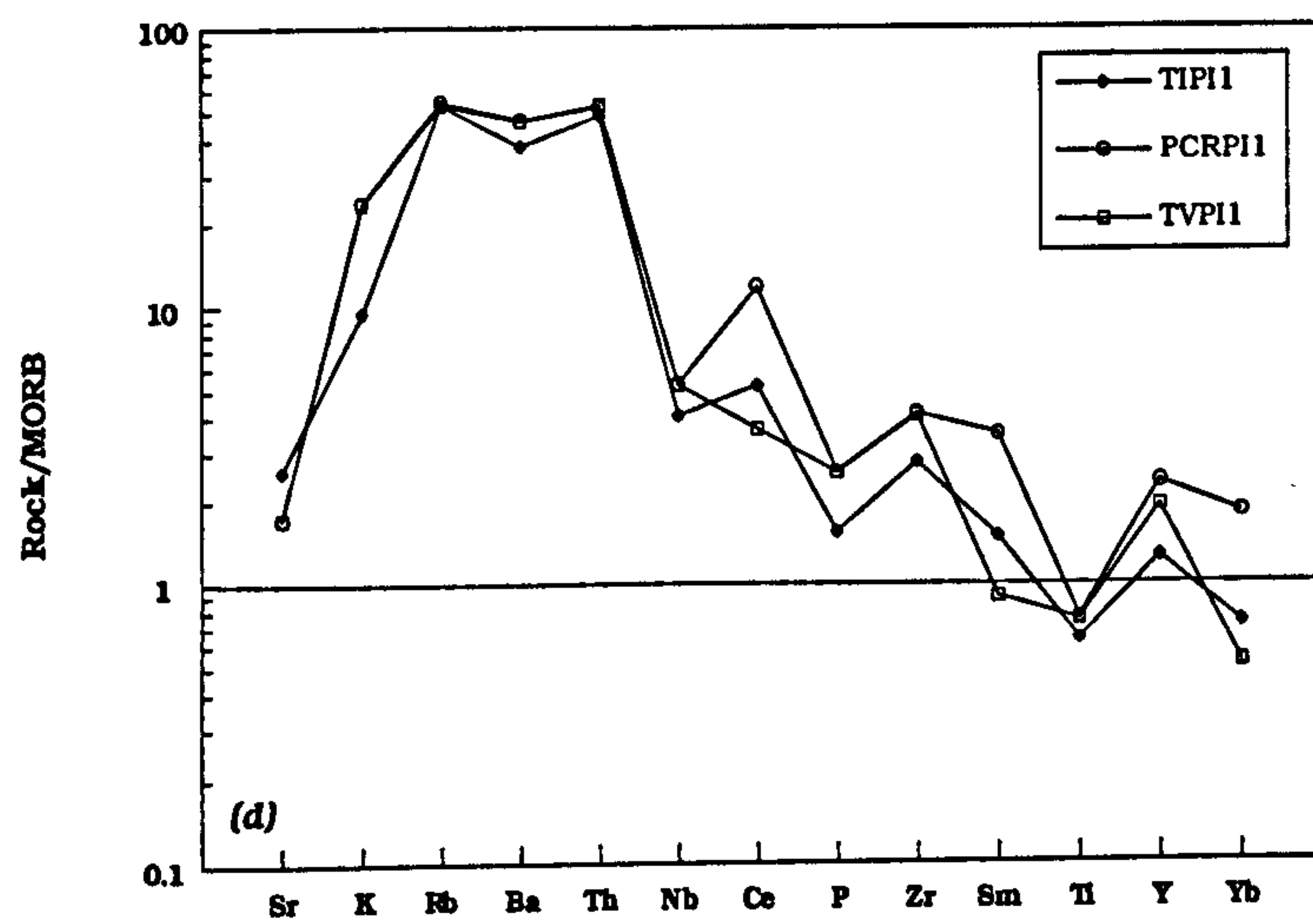


FIGURE 4.10 (d) - (e) MORB normalized multi-element diagrams for (d) Group II magmas; (e) Group III magmas. Normalizing data from Pearce (1983).

REE (Thompson *et al.*, 1983). Therefore, the contamination of a magma with an OIB-like trace-element chemistry will produce the spiked patterns very often seen in CFB provinces.

The most basic magmas of the LSSC, are however, more MORB-like in character (*e.g.* ORB2). If it is assumed that these samples most closely reflect the parental liquid compositions for the suite, and that these magmas may have fractionated from their parental liquid (as MgO contents would suggest), it is still necessary to suggest a depleted, lherzolitic mantle source for these magmas, and that the progressive enrichment in incompatible elements in more evolved magmas is due to any fractional crystallization that occurred, coupled with the effects of crustal contamination. Similar, depleted magmas occur elsewhere in the BTVP, mainly in the dyke swarms of Mull and Skye, and within the central plutonic complexes. These are of the so called Preshal More magma type (*cf.* Bell *et al.*, 1994).

Rare-earth elements

Selected samples from the three magma groups have been analysed for the rare-earth-elements (REE), using ICP-MS and ICP-AES techniques (See Appendix I). Selected results from this analysis are presented in *Table 3.1*. Full analyses of all the LSSC specimens are presented in Appendix II.

The REE are considered to be immobile elements and resistant to late-stage hydrothermal alteration (Morrison, 1978; Dickin & Jones, 1983a). The REE content of basaltic and andesitic rocks is strongly controlled by accessory phases such as apatite and zircon. Clinopyroxene to some extent favours the middle-heavy rare-earth-elements (HREE) over the light rare-earth-elements (LREE), with partition coefficients between clinopyroxene and melt for the HREE approaching unity (Rollinson, 1993). As a result, the ratio of LREE/HREE in the melt may increase with pyroxene fractionation. However, REE partitioning into accessory phases and residual glass is greatly enhanced. Apatite and zircon have not been identified within Group I samples, which suggests that the REE were mainly concentrated in the often abundant residual glass. Apatite and zircon have, however, been identified as microphenocrysts in Group II and Group III magmas. The one exception to this is europium (Eu), which is preferentially partitioned into plagioclase. Europium can exist in either the divalent or trivalent state depending upon oxygen fugacity.

Most silicate melts will therefore develop an appreciable $\text{Eu}^{2+}/\text{Eu}^{3+}$ ratio, and if plagioclase is precipitating, it will incorporate Eu^{2+} due to its similar ionic size and charge to Ca. Consequently, Eu data may be used as an indicator of plagioclase fractionation/accumulation.

Ludden & Thompson (1978) demonstrated REE mobilization within basalts during submarine weathering, with significant uptake of the LREE (La-Sm), particularly at low temperatures. However, most other studies, for example, Menzies *et al.* (1979) and Humphris *et al.* (1978), have found little evidence for such mobility. Assuming REE immobility, the degree of enrichment for a particular REE, relative to chondritic abundances, is a function of the initial concentration of that element in the source, the degree of partial melting, and the amount of subsequent fractional crystallization and/or crustal contamination.

REE profiles for the LSSC

Chondrite-normalized (Nakamura, 1974) REE profiles for the LSSC are presented in *Figure 4.11a-d*. The profiles range from being LREE-depleted ($(\text{Ce}/\text{Yb})_N = 0.61$), with the most basic member of Group I (ORB2) having LREE concentrations between 10 and 20 times chondritic values, to LREE-enriched profiles ($(\text{Ce}/\text{Yb})_N = 5.65$), with values reaching 200 times chondritic values in the more evolved members of Groups I and II. The HREE profile (Gd-Lu) is generally flat in both Groups I and II. More evolved members of Groups I and II have developed negative Eu anomalies ($\text{Eu}/\text{Eu}^* = 0.72$), indicative of plagioclase fractionation. The profiles for the rhyolites of Group III (*Figure 4.11c*) are strongly LREE-enriched ($(\text{Ce}/\text{Yb})_N = 6.29$), with deep negative Eu anomalies ($\text{Eu}/\text{Eu}^* = 0.51$). This would be consistent with a derivation of the silicic magmas as partial melts from pelitic crustal lithologies, leaving a plagioclase-rich restite.

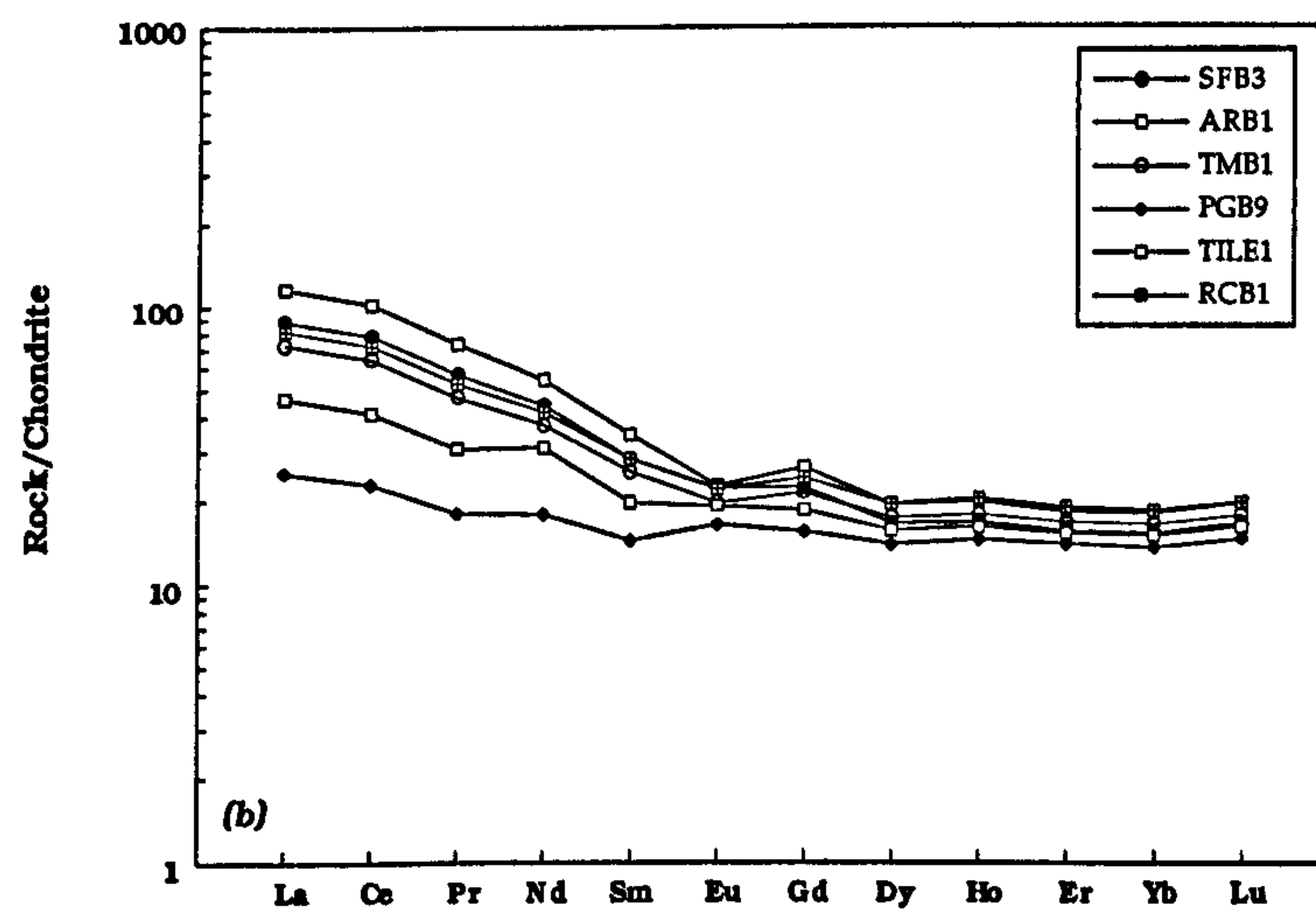
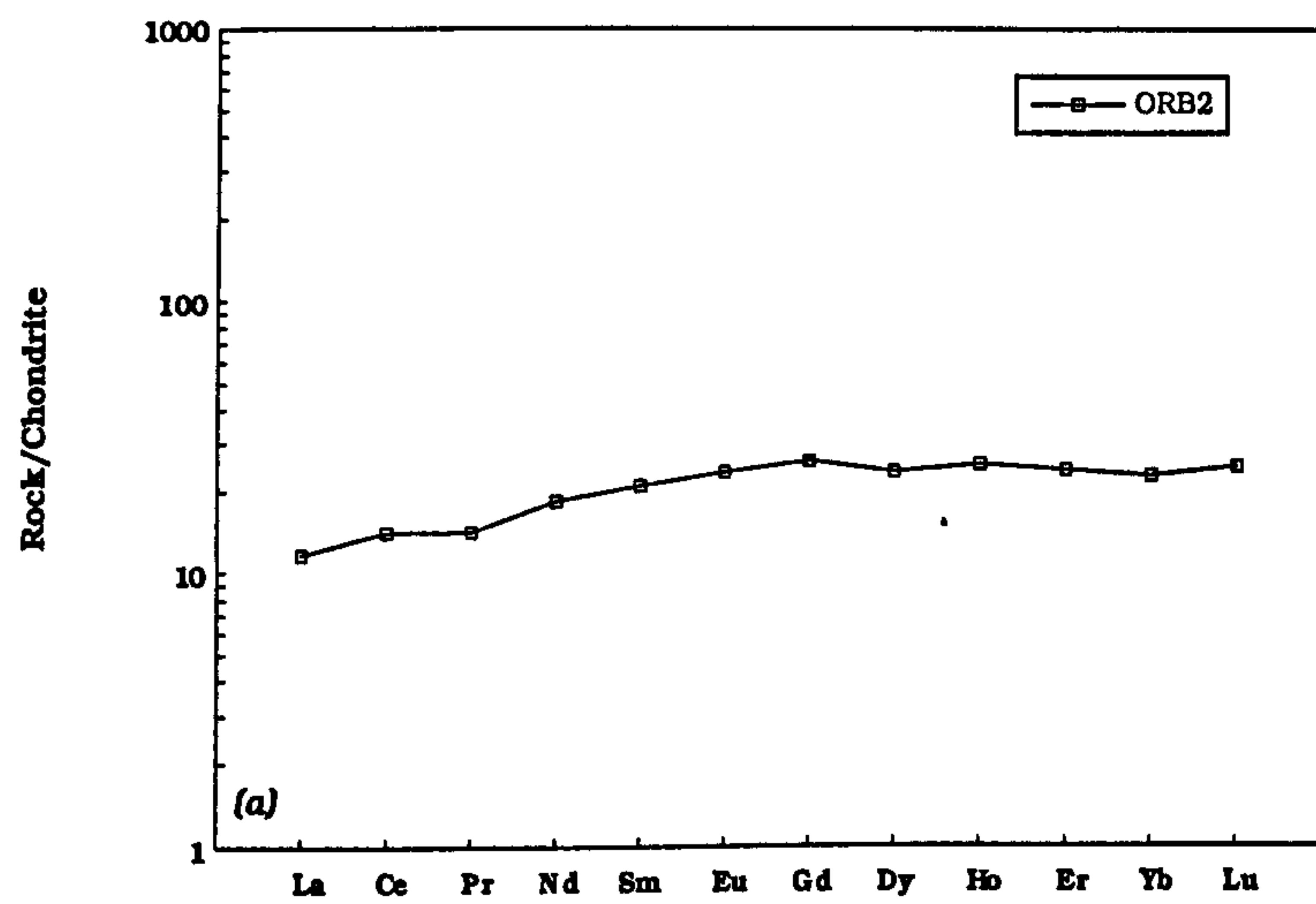


FIGURE 4.11 (a) Chondrite normalized (Nakamura, 1974) profile for the least-evolved member of Group I

(b) REE profiles for the remainder of Group I

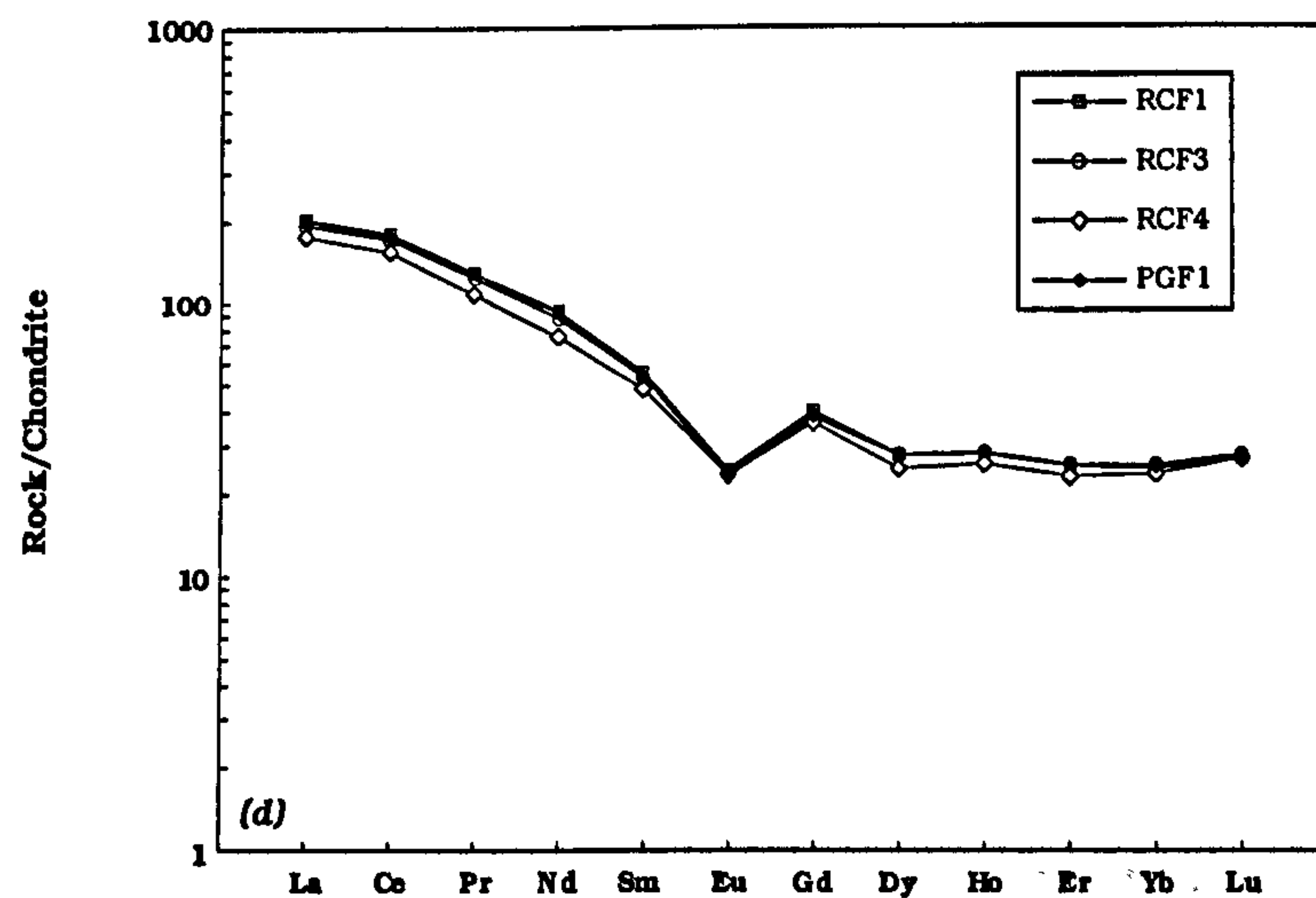
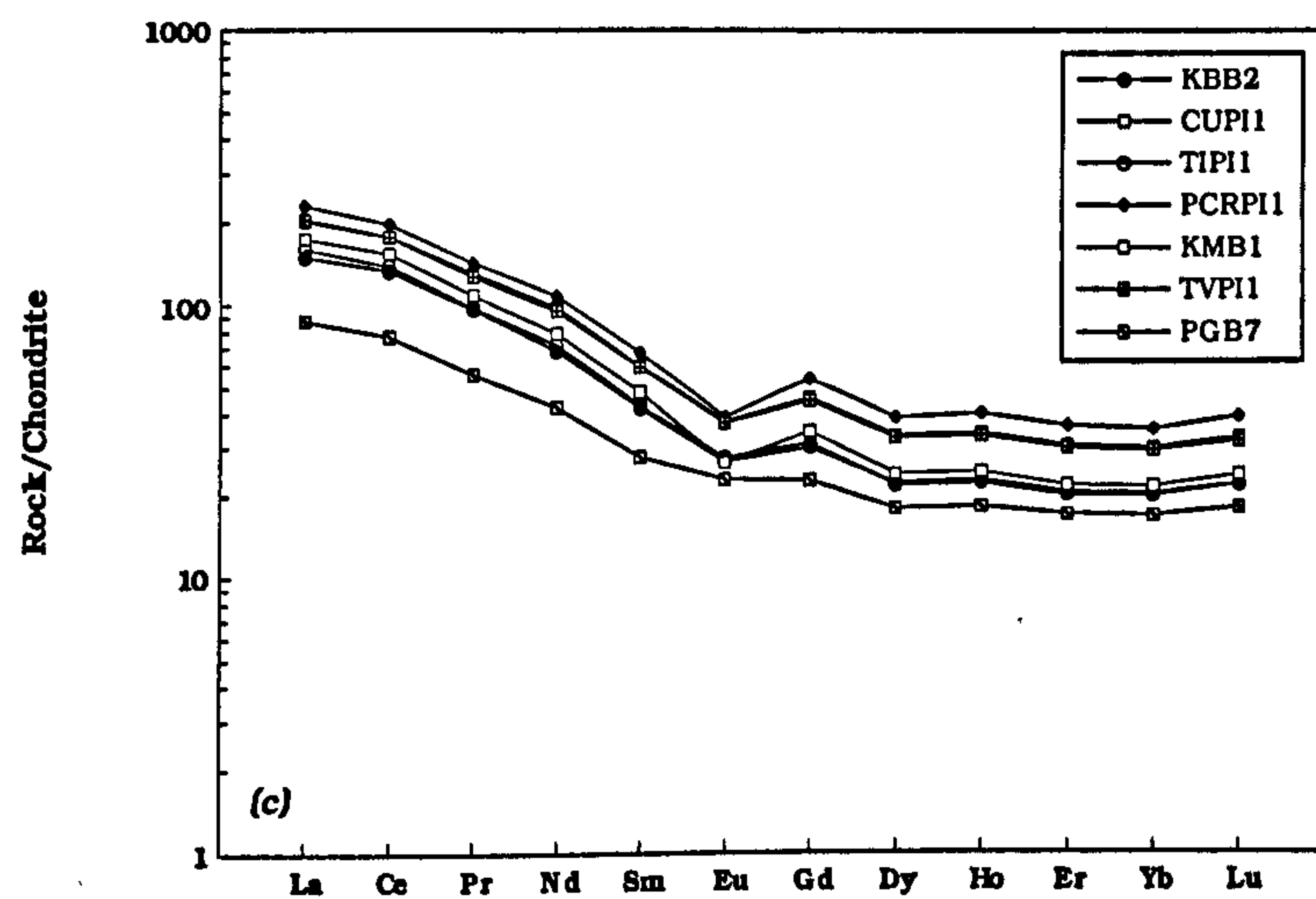


FIGURE 4.11 (c) Chondrite normalized (Nakamura, 1974) profile for Group II magmas.

(d) REE profiles for Group III magmas.

4.3 Trace-elements and petrogenetic models.

Having used major-element geochemistry and phase relationships to shed some light on the petrogenesis of the LSSC, trace-element variations can be used as an independent test of individual models. As with the major-element modelling, since Group I has the most complete fractionation history, the following models will concentrate on this group. The petrogenesis of Group II and Group III will be dealt with separately.

Closed-system fractional crystallization

Fractional crystallization involves the removal of crystals from the site of formation after crystallization, and the distribution of trace-elements is not an equilibrium process. This process is best described by the Rayleigh Law. Rayleigh fractionation describes the extreme case where crystals are effectively removed from contact with the melt the instant they have formed. Although it is difficult to envisage how such a process might actually physically occur, calculations based on Rayleigh fractionation equations do at least give some measure as to whether closed-system processes could produce the variations in trace-element concentrations seen in a suite of volcanic rocks.

The equation for Rayleigh fractionation is :-

$$\frac{C_L}{C_0} = F^{(D-1)} \quad \{4.1\}$$

Where,

C_L = Weight concentration of a trace-element in the liquid

C_0 = Weight concentration of a trace-element in the parental liquid

F = Fraction of melt remaining

D = Bulk distribution coefficient of a trace-element in the fractionating assemblage

Calculations based on this equation were carried out for Group I magmas. The fractionating assemblages used were olivine + plagioclase + augite (15:50:35), followed by plagioclase + augite + pigeonite/orthopyroxene (45:40:15), which were extracted in 5%

steps. Distribution coefficients for olivine, plagioclase, clinopyroxene and orthopyroxene were taken from the compilation in Rollinson (1993) and are given in *Table 4.1*.

A summary of the results from the closed-system fractionation modelling is presented in *Table 4.2*. This table shows that these calculations can not account for the enrichment in the majority of the incompatible elements seen within Group I, even after a hypothetical 100% crystallization. Certain other elements (*e.g.* V and Sc) behave as incompatible elements with this fractionation scheme, whereas the actual trends (*e.g. Figures 4.1c,d*) seen suggest compatible behaviour. This confirms the conclusions drawn from the major-element modelling that closed-system fractional crystallization was not the only process involved in the petrogenesis of the Loch Scridain magmas.

	Olivine	Augite	Orthopyroxene	Pigeonite	Plagioclase
Nb	0.01	0.005	0.15		0.01
Zr	0.012	0.1	0.18	0.08	0.048
Y	0.01	0.9	0.18	0.15	0.03
Sr	0.04	0.06	0.04	0.02	1.83
Rb	0.0098	0.031	0.022	0.03	0.071
Th		0.03		0.08	
Ni	12	1.5	5	6	
Cr	0.7	34	10	10	
K	0.0068	0.038	0.014		0.17
Ti	0.02	0.4	0.1		0.04
V	0.06	1.35	0.6		
Ba	0.0099	0.026	0.013	0.02	0.23
Sc	0.17	1.7	1.2		
La	0.0067	0.056	0.02	0.00678	0.1477
Ce	0.006	0.092	0.02	0.009	0.0815
Pr	0.006	0.1	0.2	0.0119	0.06
Nd	0.0059	0.23	0.03	0.0151	0.0551
Sm	0.007	0.445	0.05	0.02	0.0394
Eu	0.0074	0.474	0.05	0.02	1.1255
Gd	0.01	0.556	0.09	0.04	0.031
Dy	0.013	0.582	0.15	0.0479	0.0228
Ho	0.015	0.5	0.2	0.0732	0.02
Er	0.0256	0.583	0.23	0.114	0.0202
Yb	0.0491	0.542	0.34	0.18	0.0232
Lu	0.0454	0.506	0.42	0.2	0.0187

Table 4.1 Mineral/melt distribution coefficients, for basaltic and basaltic andesite compositions, used in trace-element fractionation modelling. Data from Colson *et al.* (1988), and compilation in Rollinson (1993).

ELEMENT	STARTING COMPOSITION	MOST EVOLVED GRP I	MODELLED COMPOSITION	% CRYSTALLIZED
Nb	2.3	10.0	6.3	100
Zr	65.8	176.8	169.3	100
Y	24.9	29.8	29.5	25
Sr	205.4	289.5	218.0	100
Rb	6.2	40.7	16.5	100
Th	2.6	7.3	6.5	100
Ni	90.8	17.8	46.2	100
Cr	351.8	76.4	36.8	20
V	295.8	263.1	329.0	20
Ba	183.1	546.9	449.9	100
Sc	51.2	35.2	55.3	20
La	5.9	37.4	15.9	100
Ce	13.9	50.4	36.0	100
Pr	1.7	6.1	4.4	100
Nd	8.4	24.7	20.7	100
Sm	2.2	5.1	5.0	100
Eu	0.9	1.5	1.3	100
Gd	3.2	5.6	6.9	100
Dy	3.5	5.0	7.6	100
Ho	0.8	0.9	1.8	100
Er	2.3	3.0	4.9	100
Yb	2.3	2.8	4.9	100
Lu	0.4	0.4	0.8	100

Table 4.2 Summary of results from closed-system fractionation trace-element model for the Group I LSSC magmas. Starting composition is most magnesian basalt (PGB9). Observed, most evolved member of Group I is PGB5. Modelled values are maximum enrichment/depletion possible after % crystallization shown in final column.

Combined assimilation and fractional crystallization - AFC

It was Bowen (1928) who first postulated that crustal contamination of magmas could be driven by the latent heat of crystallization during fractional crystallization. DePaolo (1981) derived equations which describe the concentration of a trace-element in a melt relative to the original magma composition in terms of AFC processes. Powell (1984) pointed out that although AFC processes are likely to be the norm, they only leave recognisable trace-element and isotopic signatures in volcanic rocks when there are marked differences in trace-element concentrations between the parent magma and the wall-rocks. DePaolo's equation for AFC processes is :-

$$\frac{C_L}{C_0} = f + \frac{r}{(r - 1 + D)} \cdot \frac{C_A}{C_0} (1 - f) \quad \{4.2\}$$

Where,

C_L = Weight concentration of a trace-element in the liquid

C_0 = Weight concentration of a trace-element in the parental liquid

C_A = Weight concentration of a trace-element in the assimilant

r = Ratio of the assimilation rate to the fractionation rate

D = Bulk distribution coefficient of the fractionating assemblage

and $f = F \cdot (r+D)/(r-1)$

Where,

F = Fraction of melt remaining

Where the rate of assimilation to fractionation is small ($r=0.2$), incompatible elements behave in a similar way to Rayleigh fractionation. Compatible elements are not depleted as quickly, particularly when the concentration of the trace-element in the assimilant is higher than in the parental magma. Very compatible element concentrations level off after a small degree of fractionation (Rollinson, 1993).

When the rate of assimilation is high ($r=0.8$), and the concentration of the trace-element in the assimilant relative to the parental magma is small, incompatible elements are enriched, and there is some separation between incompatible and highly incompatible elements.

Compatible elements are rapidly depleted. As the trace-element concentration in the contaminant increases relative to the parental liquid, enrichment increases, and compatible element concentrations may also increase (Rollinson, 1993).

Such equations are obviously limited by the ability to identify all the components of the system. The nature of the assimilant is often poorly constrained, although inversion techniques can often resolve this problem (Powell, 1984). The bulk distribution coefficients will obviously change as the nature of the fractionating assemblage changes, and the rate of assimilation need not necessarily be constant. However, taking all this into consideration, simple calculations can illustrate the feasibility of AFC processes operating within a suite of volcanic rocks, providing sensible assumptions are made.

Two stage calculations were carried out for the Group I compositions. As in the major-element modelling (see Section 3.2), the first mineral assemblage removed was olivine + plagioclase + augite in their approximate cotectic proportions 15:50:35. This assemblage was removed until Ni reached steady, sub- 15ppm levels, indicating that perhaps olivine was no longer fractionating, at which point plagioclase + augite + pigeonite (or orthopyroxene) was removed in the proportions 45:40:15. These assemblages were removed in 5% steps. The assimilant was chosen to be either bulk Moine metasediment, or a rhyolite from Group III.

Results from a few of these calculations are summarised in *Table 4.3*, and are shown graphically in *Figures 4.12a-d*, and These are log-log plots, and show the actual data for Groups I and II magmas, and the predicted AFC model lines. As can be seen, the fit between the actual data and the model lines is, in many cases, very good. The models which used a bulk Moine pelite as the contaminant proved most successful, and those which had reasonable high rates of assimilation ($r=0.4$). As can be seen from *Table 4.3*, most elements can be modelled very successfully. However, what is most evident, is that different elements require different amounts of crystallization to achieve the desired enrichment or depletion. For example incompatible elements such as Zr, Nb, Ba and LREE require between 40% and 60% crystallization, whereas highly incompatible elements such as Y and HREE require between 5% and 35% crystallization. Compatible elements such as Ni and Sc provide the only major problem. Ni would require at least 70% crystallization involving olivine, and Sc cannot be

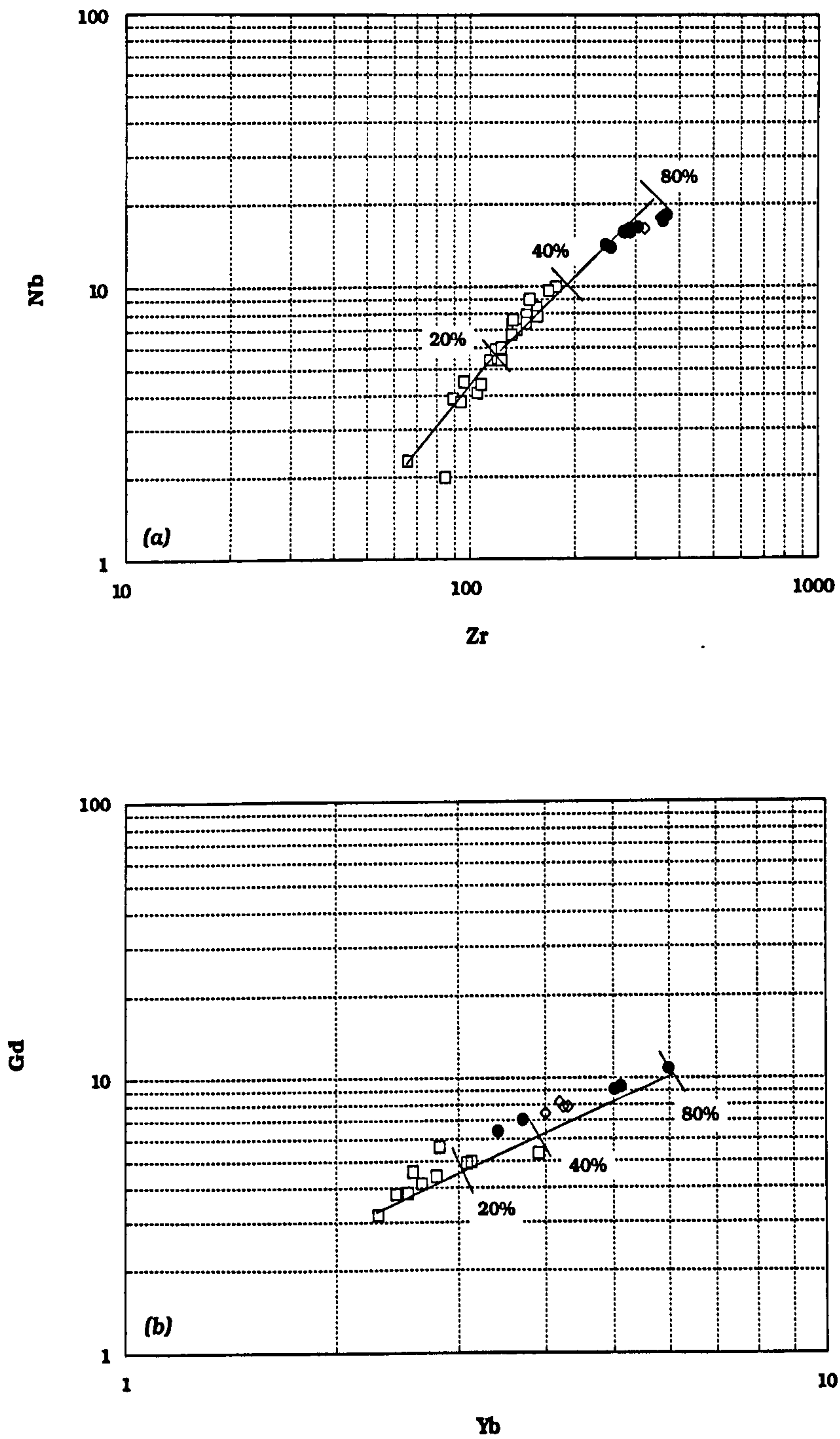


FIGURE 4.12 (a) - (b) Log-Log diagrams of incompatible elements for the LSSC. Shown are the calculated two-stage AFC trends as described in the text, with %fractionation marked.

STAGE ONE = Olivine + Ca-clinopyroxene + plagioclase (15:35:50)
 STAGE TWO = Plagioclase + Ca-clinopyroxene + low Ca pyroxene (45:40:15)
 ASSIMILANT = Bulk Moine Pelite
 r value = 0.4

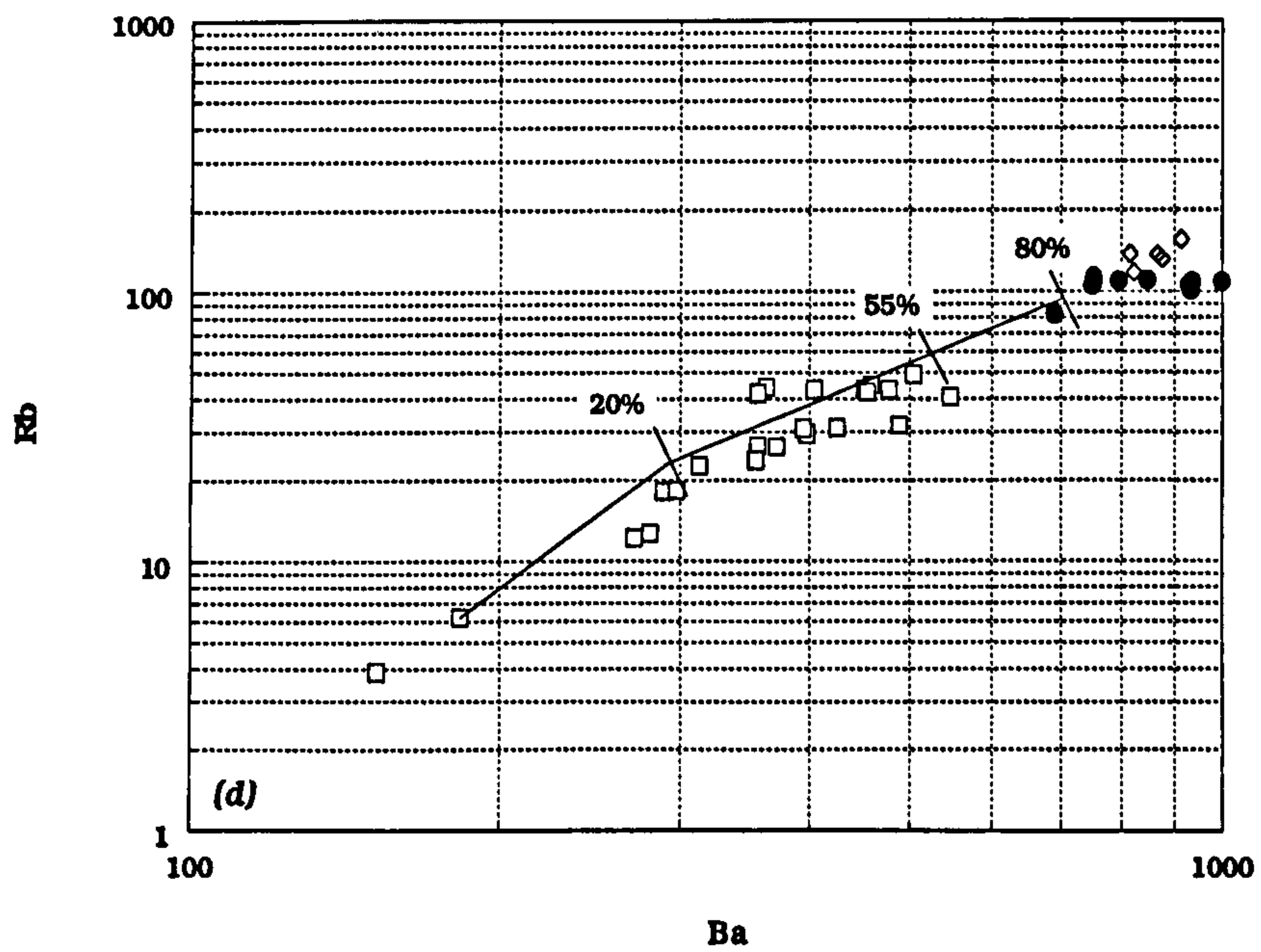
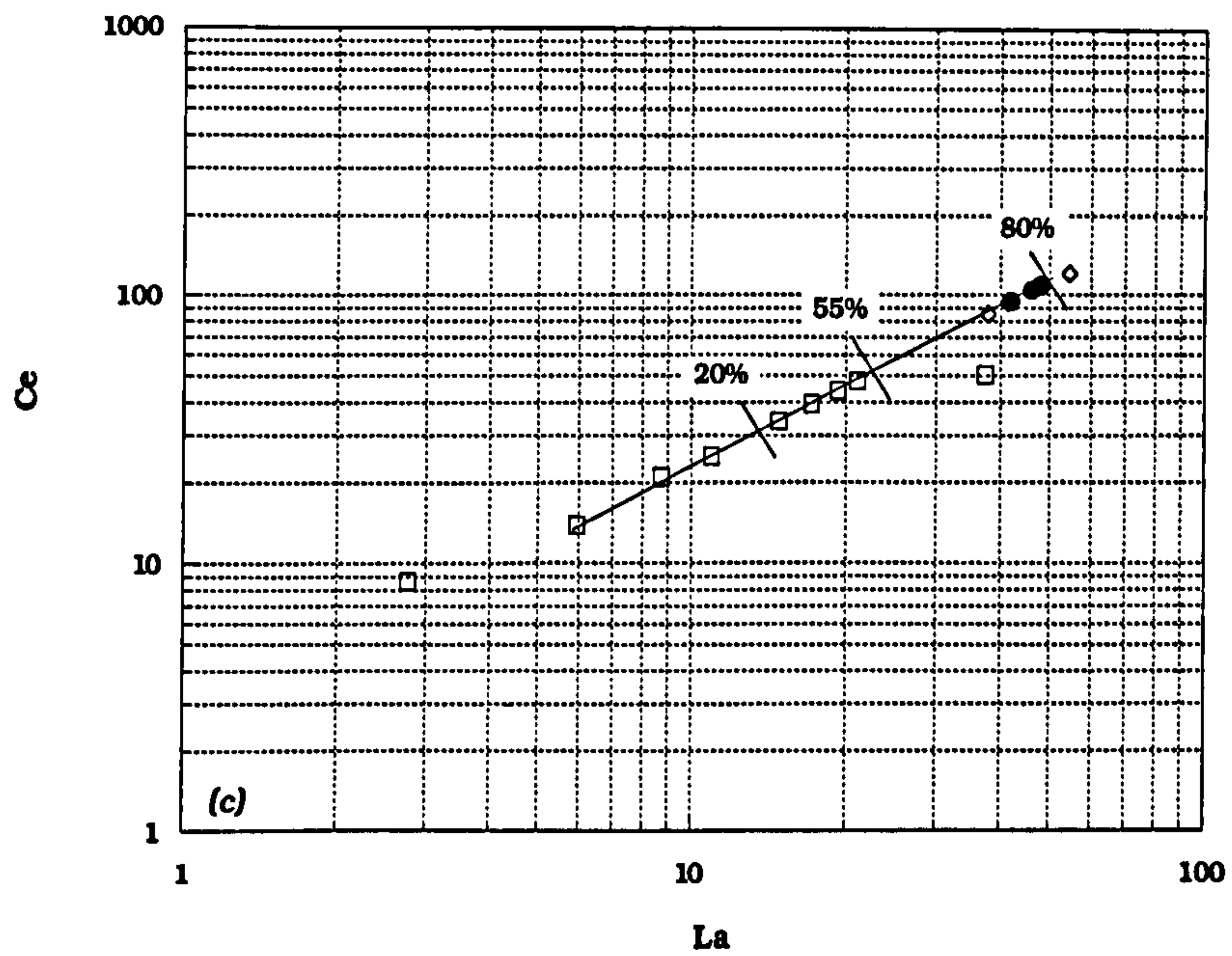


FIGURE 4.12 (c) - (d) Log-Log diagrams of incompatible elements for the LSSC. Shown are the calculated two-stage AFC trends as described in the text, with %fractionation marked.

STAGE ONE = Olivine + Ca-clinopyroxene + plagioclase (15:35:50)

STAGE TWO = Plagioclase + Ca-clinopyroxene + low Ca pyroxene (45:40:15)

ASSIMILANT = Bulk Moine Pelite

r value = 0.4

modelled successfully unless clinopyroxene dominates the fractionating assemblage (>60%). Such problems seem difficult to overcome. However, the presence of near monomineralic cumulate xenoliths within the LSSC Group I sheets (peridotites and clinopyroxenites), suggests that the fractionation process was not as simple as such AFC models suggest. Although such calculations do not prove that AFC processes were operating within the magma reservoir, they do, however, lend some weight to the conclusion that crustal contamination most likely played a very important role in the genesis of the Loch Scridain magmas. To elucidate further as to the probable nature of the contamination process, the whole-rock Sr-Nd isotope geochemistry of the suite is examined in Chapter 5.

ELEMENT	STARTING COMP'N	MOST EVOLVED GRP I	ASSIMILANT (PELITE)	MODELLED COMP'N	% CRYSTAL'D
Nb	2.3	10.0	15.9	12.0	50
Zr	65.8	176.8	267.6	178.4	40
Y	24.9	29.8	36.7	29.23	10
Sr	205.4	289.5	429.1	288.3	55
Rb	6.2	40.7	97.6	40.9	35
Th	2.6	7.3	11.8	6.99	30
Ni	90.8	17.8	21.4	23.6	100
Cr	351.8	76.4	35.4	51.57	10
V	295.8	263.1	86.1	344.3	35
Ba	183.1	546.9	514.5	536.1	60
Sc	51.2	35.2	15.6	51.5	100
La	5.9	37.4	45.5	37.7	65
Ce	13.9	50.4	101.5	101.5	75
Pr	1.7	6.1	11.5	6.2	40
Nd	8.4	24.7	40.3	24.8	40
Sm	2.2	5.1	7.3	5.2	40
Eu	0.9	1.5	1.5	1.48	65
Gd	3.2	5.6	6.4	5.8	35
Dy	3.5	5.0	5.4	5.2	25
Ho	0.8	0.9	1.2	0.9	5
Er	2.3	3.0	3.1	2.5	5
Yb	2.3	2.8	3.2	2.9	15
Lu	0.4	0.4	0.5	0.4	5

Table 4.3 Summary of results from open-system fractionation and assimilation (AFC) trace-element model for the Group I LSSC magmas. Starting composition is most magnesian basalt (PGB9). Observed, most evolved member of Group I is PGB5. Assimilant is a bulk Moine pelitic schist (SOM2). Modelled values are maximum enrichment/depletion possible after % crystallization shown in final column. r-value and fractionation assemblage as discussed in the text.

Dynamic Models : The RTF magma chamber

From an examination of the major- and trace-element models, it is clear that the various elements are behaving differently during fractionation. Major-element models suggest that between 45 and 60% crystallization, coupled with 10-15% assimilation, is necessary to explain their distribution. In contrast, compatible trace-elements (*e.g.* Cr) require less than 45% crystallization. There is also great variation within the incompatible elements, with elements such as Rb, Ba and the LREE requiring at least 65% crystallization, and others such as Zr, Th and the HREE requiring 40% crystallization to explain their abundances (*Table 4.3*).

This decoupled behaviour between major- and trace-elements during crystal-liquid fractionation can be explained in terms of the magma evolving in a chamber undergoing periodic replenishment, tapping, and fractionation (*i.e.* RTF processes) (O'Hara, 1977; O'Hara & Mathews, 1981; Cox, 1988). The model suggests that the life of a magma chamber after its initial formation, comprises a number of cycles, each of which has three components - fractional crystallization, magma eruption and replenishment. These processes have the ability to decouple trace-elements on the basis of their distribution coefficients. O'Hara & Mathews (1981) concluded that the composition of the magma in a RTF chamber would approach steady-state provided that the amount and composition of the parental magma in each cycle was held constant, as was the ratio of the magma crystallizing to that erupting from the chamber. The concentration of an element in the steady-state liquid is given by the equation (O'Hara & Mathews, 1981):

$$C_B^{ss} = C_0 \cdot \frac{(x + y)(1 - x)^{D-1}}{1 - (1 - x - y)(1 - x)} \quad \{4.3\}$$

Where,

C_B^{ss} = Weight concentration of a trace-element in a steady state liquid after a large number of RTF cycles.

C_0 = Weight concentration of a trace-element in the parental liquid

x = Mass fraction of the liquid crystallizing in each RTF cycle

y = Mass fraction of the liquid escaping in each RTF cycle

D = Bulk distribution coefficient of the fractionating assemblage

One cycle represents the eruption and replenishment of a mass of magma from the chamber. The chamber is refilled with new parental magma, which subsequently mixes with any residual liquid. The number of cycles required to produce a steady-state composition is dependent upon the bulk distribution coefficients of the elements under consideration, and the parameters x and y . Cox (1988) explored numerical models of RTF processes which randomized the parameters within certain bounds, in an attempt to simulate the natural world more closely. He found that there are many problems associated with comparing such models with CFB sequences such as the Deccan, and concluded that it was impossible to *prove* whether RTF processes actually occurred in natural systems. However, if it is assumed that RTF magma chambers do operate, we have a mechanism by which there can be strong decoupling between compatible and incompatible elements, leading to poor correlations on plots of elements with differing bulk distribution coefficients, and to the possibility of changing the ratios between incompatible elements through fractional crystallization (Cox, 1988). This, however, leads to problems in assigning parent-daughter status on the liquid line of descent. The assignment of parental liquids is very often obvious on major-element plots, but the decoupling effect on trace-elements in RTF magma chambers may lead to such allocations being meaningless. The modelling of fractional crystallization then becomes fraught with difficulties. Due to the

complexities of the RTF system, no modelling for the LSSC Group I magmas has been attempted. However, the strong decoupling between major-elements and incompatible trace-elements, and even between different highly incompatible elements (*e.g.* between LREE and HREE) during fractional crystallization, highlighted by the AFC model, strongly suggests that RTF processes were operating within the LSSC. RTF processes may also explain the high concentrations of certain compatible elements (*e.g.* Ni, Cr, Sc and V) as discussed in Section 4.1 (Shibata *et al.*, 1979), and therefore would provide a solution to the inability of AFC modelling to reproduce the trends seen for such elements.

4.4 Trace-element evidence and the petrogenesis of Group II and Group III magmas.

Magma mixing in the Group II andesites and porphyritic dacites

In Chapter 3 it was suggested that the andesites and porphyritic dacites of Group II are the products of magma mixing between separately generated basic and silicic magmas. It was also stated that the silicic magmas involved in the mixing had undergone fractional crystallization of plagioclase prior to the mixing event, and that the resulting hybrid magmas had fractionated further. However, major-elements are most strongly influenced by fractional crystallization, and are not well-suited to assessing the importance of processes such as crustal assimilation and magma mixing (St. Seymour & Vlassopoulos, 1992). Consequently, this hypothesis can best be tested by looking at the trace-element geochemistry of these rocks. However, since the process is not one of simple magma mixing, in that the magmas have fractionated at various stages of the process, the most commonly used graphical methods for confirming magma mixing, will generally show some departure from the simple mixing case.

Incompatible trace-element systematics will show linear trends for incompatible element-element plots for cases of fractional crystallization and binary magma mixing, and hyperbolic distributions on incompatible element ratio-ratio plots if the denominators of the two ratios are different, and linear trends if the denominators of the two ratios are the same, indicating mixing of magmas, or mixing in the source region (Langmuir *et al.*, 1978; St. Seymour & Vlassopoulos, 1992). However, such relations may no longer hold if the magmas undergo subsequent fractional crystallization.

Figures 4.13a and 4.13b show the covariance between $(\text{Nd}/\text{Sm})_n$ and $(\text{La}/\text{Ce})_n$, and between $(\text{La}/\text{Nd})_n$ and $(\text{Sm}/\text{Yb})_n$, respectively, for the LSSC. These plots show that the majority of the Group II magmas sit on a possible mixing line between the least-evolved member of Group I and a rhyolite of Group III (analyses can be found in Appendix II). The porphyritic dacites of Group II fall off the trend in Figure 4.13a. and this is most likely due the subsequent fractionation that these magmas experienced. Judging from the mineral/melt distribution coefficients

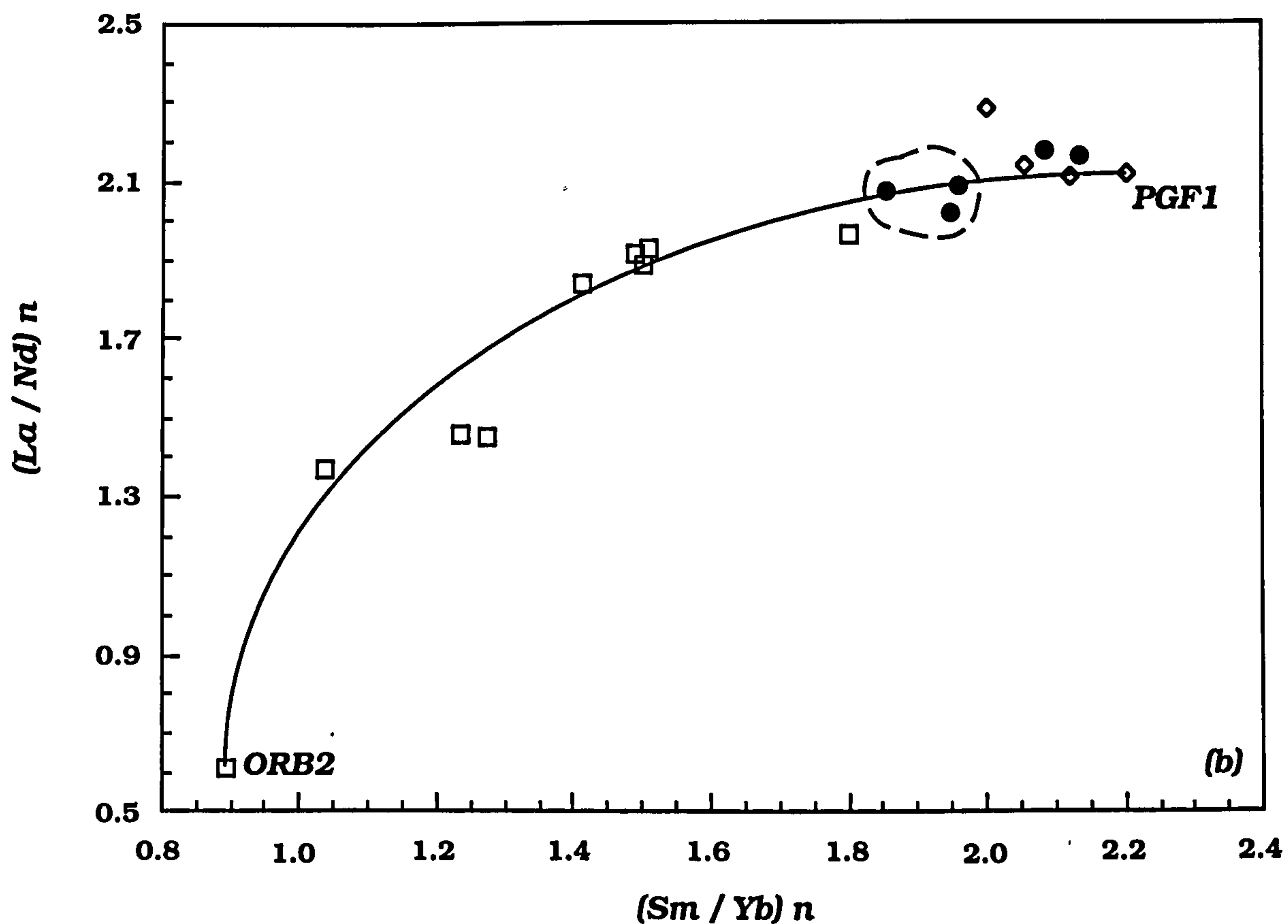
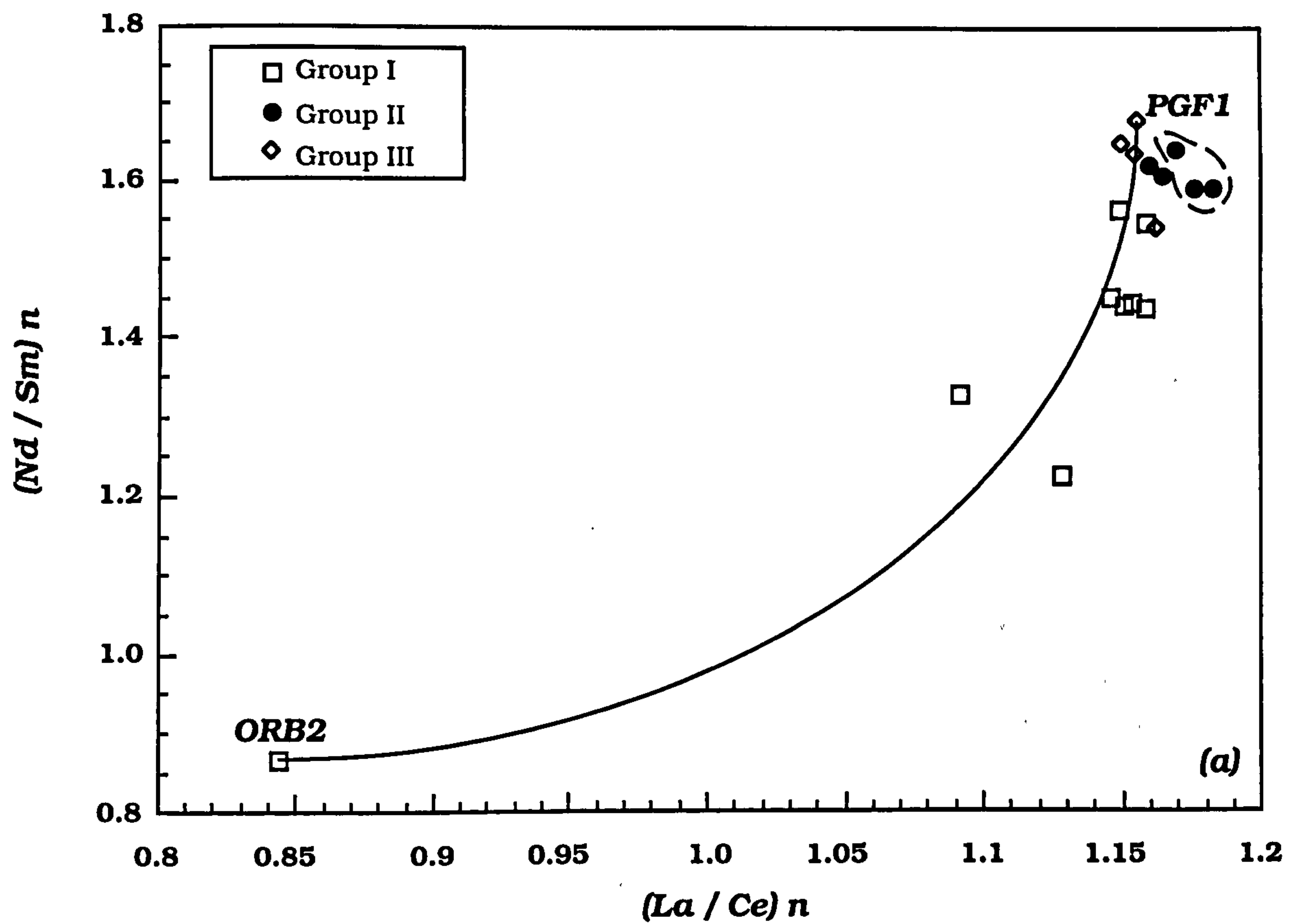


FIGURE 4.13 Covariance in rare-earth element pairs showing possible mixing curves between the least evolved member of Group I (ORB2), and a Group III rhyolite (PGF1). Dashed line encloses porphyritic dacites. Normalization data after Nakamura (1974)

(a) $(Nd/Sm)_n$ vs. $(La/Ce)_n$

(b) $(La/Nd)_n$ vs. $(Sm/Yb)_n$

shown in *Table 4.1*, a fractionating assemblage consisting of almost equal proportions of plagioclase and pigeonite (as the porphyritic dacites contain) could not drastically change any of the incompatible element ratios depicted in *Figure 4.13*. However, it was suggested previously, that the porphyritic dacites may have fractionated minor apatite. Apatite has the "ability" to fractionate the REE, and apatite fractionation should increase the La/Ce ratio and decrease the Sm/Yb ratio of the liquid, without drastically altering the Nd/Sm and La/Nd ratios (from mineral/melt distribution coefficients in Rollinson, 1993). This is well shown in *Figure 4.13*, where the porphyritic dacites have the highest (La/Ce)_n values and the lowest (Sm/Yb)_n values.

These diagrams can also be used to constrain the *exact* nature of the end-members involved in the mixing. Although the trends shown are reasonable, the choice of the least-evolved member of Group I (ORB2), and the most siliceous member of Group III (PGF1), is probably in error. The end-members involved were probably the parent basic magma to Group I (ORB2 has experienced fractional crystallization), and a 'uncontaminated' silicic melt from the country-rock; although the rhyolites of Group III may represent such melts, the rocks as they are seen now, have possibly mixed with small amounts of basic magma, therefore removing them from their initial compositions.

Crustal anatexis as a source for the Group III rhyolites

The phase relationships and major-element geochemistry of the Group III rhyolites are consistent with their having been derived via crustal anatexis of basement rocks. Chappell & White (1974) proposed a scheme whereby granitic rocks could be sub-divided into two main groups. Their "I-type" granites were thought to be derived from igneous sources which had not gone through a stage of sedimentary recycling. These granites have primary geochemical features such as high CaO, Na₂O and Sr, coupled with low K₂O values and low initial ⁸⁷Sr/⁸⁶Sr ratios. "S-type" granites are thought to result from the partial melting of crustal rocks which had seen a stage of sedimentary recycling. Such granites are peraluminous, and have lower CaO, Na₂O and Sr, higher K₂O, and higher initial ⁸⁷Sr/⁸⁶Sr ratios. S-type granites also generally contain higher concentrations of certain trace-elements such as Rb, Ba, and P₂O₅ (Chappell & White, 1992). However, no formal classification of granites has been suggested and accepted on the basis of trace-element geochemistry.

The trace-element geochemistry of silicic melts derived from crustal sources will be controlled by the phases involved in the melting process. For example, if muscovite and biotite are consumed in the melting process, the melt is likely to be enriched in trace-elements such as Rb, Ba and Li. It is therefore highly likely that major local variations in melt trace-element geochemistry will occur due to the typically inhomogeneous nature of the crustal rock sources, and due to the local physical conditions (pressure and temperature) of melting.

However, given these obvious limitations, it is believed that the trace-element characteristics of the Group III rhyolites are consistent with their derivation from crustal sources. The rhyolites are characterized by high K₂O contents (> 4 wt%), low Na₂O (< 3 wt%), low Sr (< 132 ppm), high Ba (> 816 ppm) and high Rb (> 130 ppm). Two of the rhyolites are also peraluminous (normative corundum). These values are typical for S-type granites as defined by Chappell & White (1992). All the Group III rhyolites are LREE-enriched, with (Ce/Yb)_n in excess of 7, and they all have negative Eu anomalies, consistent with crustal melting leaving a plagioclase-rich restite.

4.5 The LSSC and Hebridean magma types : Trace-element evidence.

The existence of at least three distinct basic magma types within the BTVP has already been introduced (Chapter One). Matthey *et al.* (1977) showed that each type has characteristic trace-element ratios (*e.g.* Ti/Zr) and chondrite-normalized REE profiles. Because the highly incompatible trace-elements are excluded from the crystallization of olivine, plagioclase and pyroxene, the *ratios* of certain trace-elements in more evolved magmas will be inherited from the parental magmas. *Table 4.4* lists some of the characteristic trace-element ratios of the LSSC, together with data for the SMLS, Preshal More and Fairy Bridge magma types. The range of these trace-element ratios in the Group I magmas of the LSSC is sometimes quite large (*e.g.* Ce/Y and La/Nb). Ranges are typically smaller in the Group II magmas. It is evident from *Table 4.4* that there is considerable overlap between the LSSC magmas and the three Hebridean magma types. However, the Group I magmas appear to share more similarities with the Preshal More magma type, than either the SMLS or the Fairy Bridge magma types. The SMLS, Preshal More and Group I data are also shown in *Figures 4.14a-d*. Group I magmas are clearly distinguishable from the SMLS in all these diagrams. They do share some similarities with the Preshal More magma type, but trends are distinctly different in most cases. However, in a suite which has suffered extensive crustal contamination, the application of such comparisons is obviously limited.

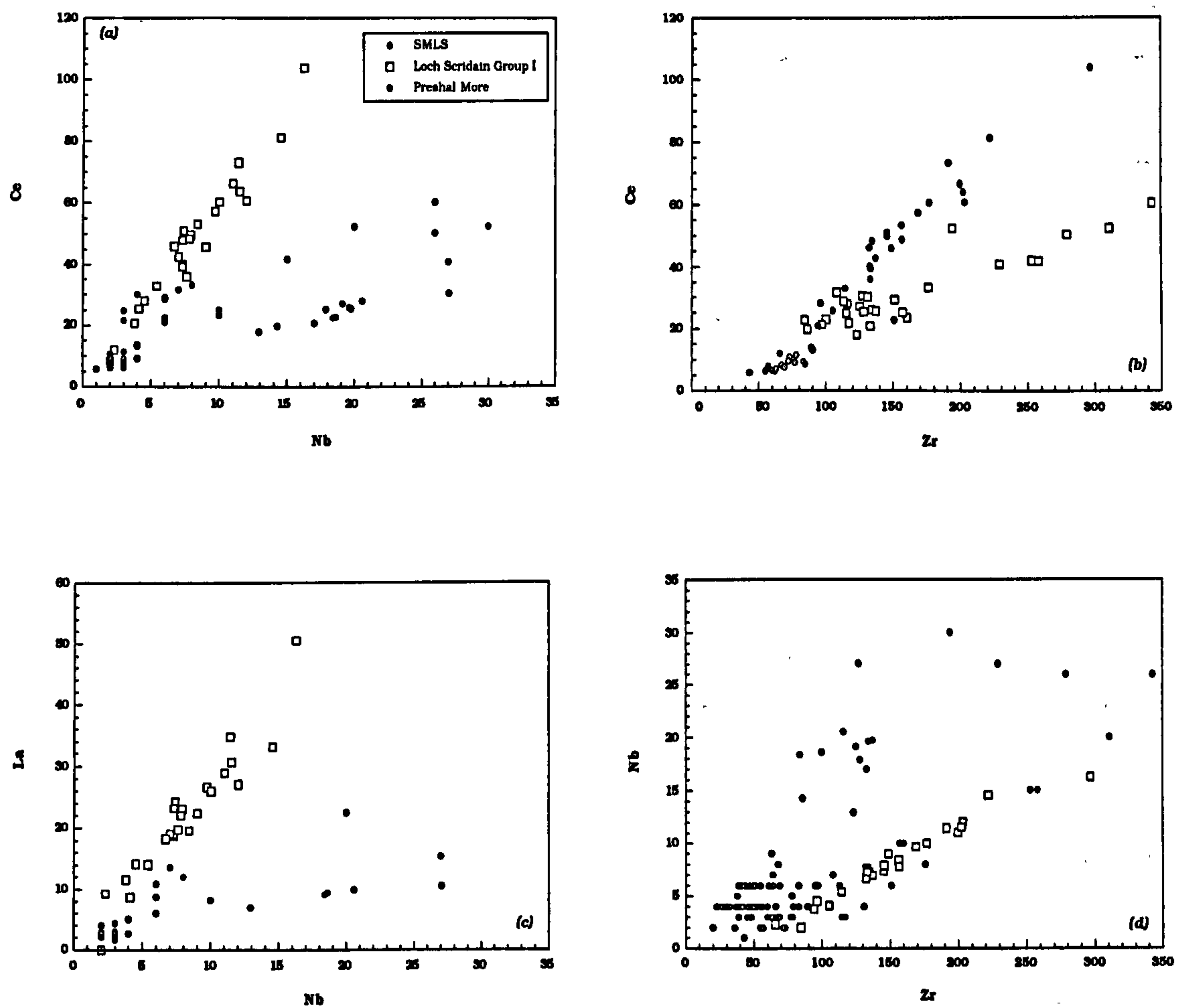


FIGURE 4.14 Comparison of incompatible elements variations for the SMLS, Preshal More magma types of Skye and the LSSC Group I magmas. Data from Matthey et al, 1977; Bell et al, 1994

(a) Ce - Nb

(b) Ce - Zr

(c) La - Nb

(d) Nb - Zr

	Average SMLS	Average Preshal More	Average Fairy Bridge	Loch Scridain Group I	Loch Scridain Group II
Nb/Zr	0.10	0.09	0.09	0.02-0.06	0.05-0.06
Ce/Zr	0.20	0.13	0.23	0.10-0.32	0.30-0.35
La/Nb	0.40	1.14	1.14	1.39-3.74	2.51-2.67
Y/Zr	0.19	0.47	0.36	0.14-0.51	0.10-0.21
Ce/Nb	2.85	3.39	2.66	4.32-6.29	5.70-6.63
Ce/Y	1.11	0.34	0.59	0.20-1.69	1.50-2.29

Table 4.4 Trace-element ratios of samples from Groups I and II compared to the Skye Main Lava Series, Preshal More and Fairy Bridge magma types. Data from Esson *et al.*, (1975); Matthey *et al.*, (1977); Morrison, (1978).

Figures 4.15a-c show the ranges of chondrite-normalized REE concentrations for the three Hebridean magma types, compared to the range show by the LSSC Group I and Group II magmas. The SMLS shows strongly LREE-enriched profiles, with the Fairy Bridge magma type having slight LREE-enriched patterns. Within the Preshal More magma type, Matthey *et al.* (1977) identified two magma sub-types on the basis of REE profiles. Both are LREE-depleted, with relatively flat HREE profiles. However, sub-type I shows a slight positive Eu anomaly, a feature not found in sub-type II. Sub-type II also shows a greater degree of LREE depletion. These two sub-types can be equated to those found in MORB. Sun *et al.* (1979) showed that MORB can be subdivided into two major groups. Normal-MORB (N-type) is the most common, and typically shows highly depleted trace-element geochemistry (*e.g.* LREE depletion). P-type MORB is related to the presence of mantle plumes under the ridge segments (*e.g.* Iceland), and these basalts have more enriched trace-element signatures (*e.g.* LREE enrichment). Transitional MORB (T-type) is thought to be the result of mixing between these two other MORB types (Sun *et al.*, 1979; Wilson, 1989). The sub-types found in Preshal More magmas probably relate to the N-type MORB (Preshal More sub-type II), and the mixing of this with more enriched magmas (Preshal More sub-type I). This could be consistent with the operation of RTF magma chambers

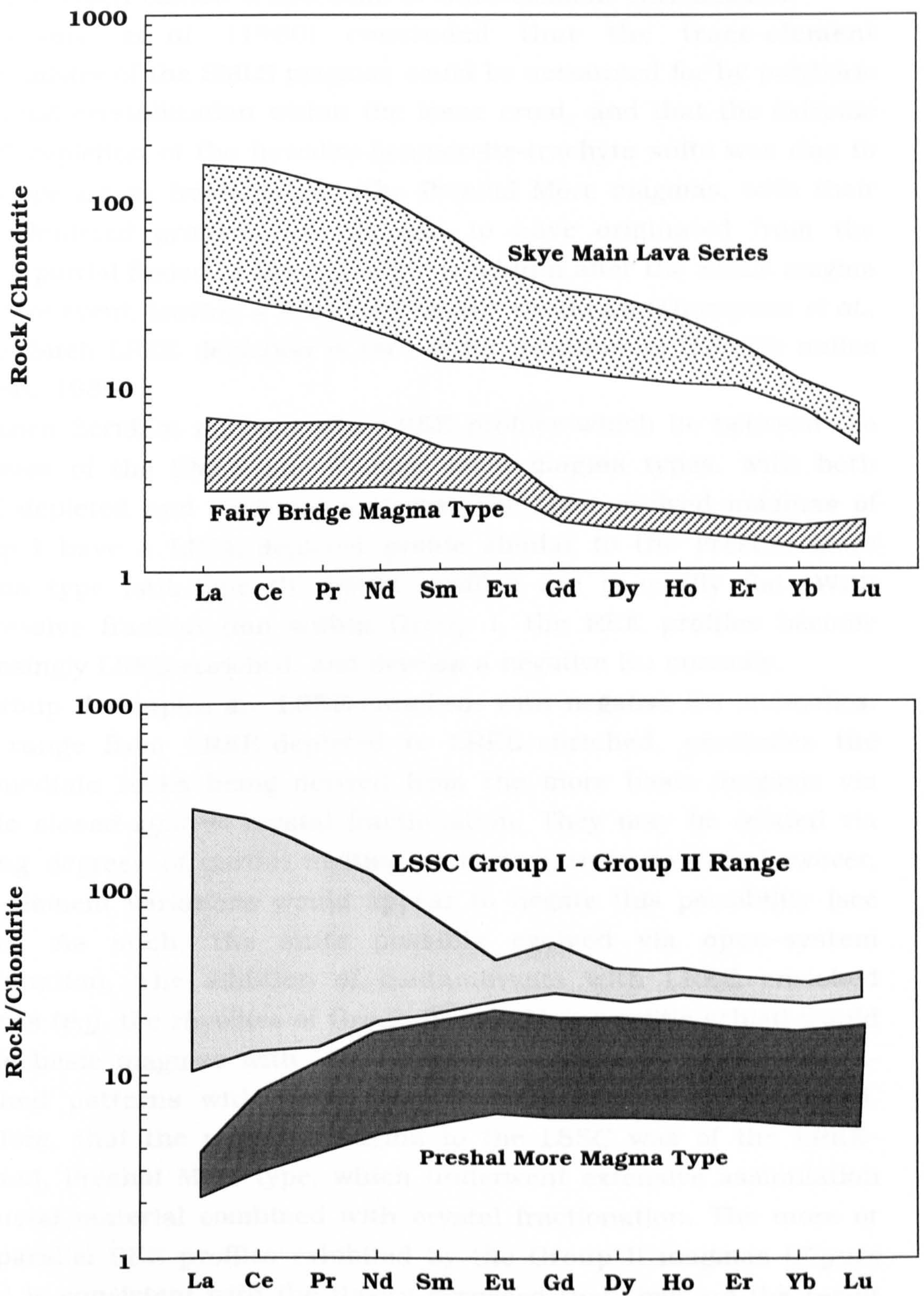


FIGURE 4.15 Chondrite-normalized REE profiles for the three Hebridean magma types, compared to the LSSC Group I and Group II magmas. Data from Matthey *et al.* (1977); Bell *et al.* (1994).

within the Hebridean magmatic plumbing system, since the mixing of depleted basic magmas with more evolved magmas will produce magmas which exhibit a spectrum of trace-element enrichments.

Thompson *et al.* (1980) concluded that the trace-element geochemistry of the SMLS magmas could be accounted for by polybaric fractional crystallization within the lower crust, and that the extreme HREE depletion of the hawaiite-benmoreite-trachyte suite was due to late-stage zircon fractionation. The Preshal More magmas, with their LREE-depleted profiles, are thought to have originated from the limited partial fusion of the lherzolithic residuum after the SMLS magma extrusive event, leaving a final harzburgitic residuum (Thompson *et al.*, 1980). Such LREE depletion is rare within continental tholeiite suites (Wilson, 1989).

The Loch Scridain magmas show REE profiles which lie between the extremes of the SMLS and Preshal More magma types, with both LREE-depleted and enriched patterns. The least evolved magmas of Group I have a LREE-depleted profile similar to the Preshal More magma type (sub-type II). HREE profiles are generally flat. With progressive fractionation within Group I, the REE profiles become increasingly LREE-enriched, and develop a negative Eu anomaly.

All Group II samples are LREE-enriched, with negative Eu anomalies. This range from LREE-depleted to LREE-enriched, precludes the intermediate rocks being derived from the more basic magmas via simple *closed-system* crystal fractionation. They may be related via varying degrees of partial melting of their mantle source; however, trace-element variations would appear to negate this possibility (see above). As such, the suite possibly evolved via open-system fractionation. The addition of contaminants with LREE enriched patterns (*e.g.* the rhyolites of Group III or a Moine pelitic schist) would enable basic magmas with LREE-depleted profiles to develop LREE-enriched patterns with progressive fractionation. It is suggested, therefore, that the parental magma to the LSSC was of the LREE-depleted, Preshal More type, which underwent extensive assimilation of crustal material combined with crystal fractionation. The more or less parallel REE profiles exhibited by the Group II magmas (*Figure 4.11c*) is consistent with the theory proposed that they are the result of mixing between silicic magmas derived through partial melting of the crust, with small amount of basic magma

4.6 Conclusions

The trace-element characteristics of the LSSC support the conclusions drawn from the phase relationships and major-element geochemistry in Chapter 3. It is suggested that depleted, Preshal More type parental magmas underwent combined fractional crystallization and assimilation in crustal reservoirs. The decoupling of certain trace-elements during fractionation also suggests that the magma reservoirs experience periodic replenishment (RTF processes; O'Hara, 1977; O'Hara & Mathews, 1981; Cox, 1988). These combined processes are necessary to explain the extreme trace-element enrichment seen with progressive fractionation in Group I.

The trace-element data also supports the suggestion that the Group III rhyolites are the products of crustal anatexis, and that the Group II andesites and dacites resulted in the mixing between these silicic melts and more basic magmas. Both Group II and Group III magmas suffered subsequent fractional crystallization.

CHAPTER 5

WHOLE-ROCK ISOTOPE GEOCHEMISTRY

5.1 Introduction : Isotope Geology of Sr & Nd in Igneous Rocks

The isotopic compositions of Sr and Nd in volcanic, hypabyssal and plutonic rocks provide information about the sources from which the magmas originated, and about the processes by which their chemical and isotopic compositions are modified.

Work by Richard *et al.* (1976) and by DePaolo & Wasserburg (1976a,b) demonstrated that the $^{87}\text{Sr}/^{86}\text{Sr}$ and $^{143}\text{Nd}/^{144}\text{Nd}$ ratios of young oceanic basaltic volcanic rocks varied widely, and that they formed a strongly correlated array, the so-called "Mantle Array". This correlation between $^{87}\text{Sr}/^{86}\text{Sr}$ and $^{143}\text{Nd}/^{144}\text{Nd}$ ratios indicates that oceanic basalts and their derivatives were formed from rocks whose Rb/Sr ratios were lowered but whose Sm/Nd ratios were elevated relative to chondritic values, sometime in the past. Consequently, uncontaminated magmas derived from a mantle source will generally have low $^{87}\text{Sr}/^{86}\text{Sr}$ and high $^{143}\text{Nd}/^{144}\text{Nd}$.

Studies of the isotopic composition of MORBs (*e.g.* Engel *et al.*, 1965; Richard *et al.*, 1976; Sun *et al.*, 1979) have shown that these basalts originated from sources that had *higher* Sm/Nd than the chondritic reservoir (the primordial composition to which isotope data is often normalized; CHUR), and lower Rb/Sr ratios than the uniform reservoir (UR), whose Sr isotopic composition is determined from the intersection of the mantle array with the chondritic Nd isotopic composition. Such source regions are said to be "depleted", since they appear to have lost Rb and other large ion lithophile (LIL) elements. In contrast, the Sr and Nd isotope systematics of many basalts from ocean islands suggest that the mantle also has "enriched" regions with lower Sm/Nd and higher Rb/Sr than the bulk earth reservoir. The "Mantle Array" could possibly be due to the blending of magmas derived from both these mantle sources (DePaolo & Wasserburg, 1976a).

Zindler *et al.* (1979) suggested that the mantle was heterogeneous on a small scale due to the introduction of partial melts which infiltrated the originally homogeneous mantle in the form of veinlets and "blobs". Over time the mantle therefore developed very distinctive isotopic variations.

The isotopic composition and trace-element geochemistry of certain ocean island basalt suites (*e.g.* St Helena, Tristan da Cunha, Samoa) are very distinctive (Hart, 1988; Weaver, 1991; Wilson, 1993b). It has been suggested that the introduction of subducted oceanic crust and pelagic sediment into the mantle has contributed to the characteristic geochemical signatures of these basalts (Hart, 1988; Weaver, 1991).

The initial Sr and Nd isotopic compositions of continental basalts world-wide show a very wide range. Certain members of continental flood basalt suites have initial Sr and Nd isotope signatures which overlap with MORB and OIB (*e.g.* Columbia River Basalt, Deccan, Paraná) (Cox & Hawkesworth, 1985; Hawkesworth *et al.*, 1992; Saunders *et al.*, 1992; Hooper & Hawkesworth, 1993). In contrast, other members of these and other suites have initial Sr and Nd isotope ratios which extend to extreme values (*e.g.* Columbia River Basalt, Italian Province, Antarctica) (Carter *et al.*, 1978; Carlson *et al.*, 1981; Hergt *et al.*, 1989; Elliot, 1992).

These extreme Sr and Nd isotope signatures require the introduction of crustal material, whether it be as a subduction-related input direct into the mantle source (*e.g.* Hergt *et al.*, 1989), or as a contaminant as the basalts pass through the continental crust (*e.g.* Bellieni *et al.*, 1984; Cox & Hawkesworth, 1985).

The majority of igneous and metamorphic rocks of the upper continental crust have higher Rb/Sr and lower Sm/Nd compared to mantle sources because they represent the final products of geochemical differentiation of the mantle (Faure, 1986). High Rb/Sr ratios are generated through the slight fractionation of Rb and Sr during mantle melting (Hawkesworth & Ellam, 1989), and by their large fractionation during crystal fractionation in the crust and during sedimentary processes. Sm and Nd are only really fractionated during mantle melting. As such, upper crustal rocks typically have high $^{87}\text{Sr}/^{86}\text{Sr}$ and low $^{143}\text{Nd}/^{144}\text{Nd}$ values. The extremity of these values depends upon the age of the rocks involved. As a result, basaltic magmas which interact with such lithologies, and silicic magmas formed by partial melting of crustal rocks, will have similarly high $^{86}\text{Sr}/^{86}\text{Sr}$ and low $^{143}\text{Nd}/^{144}\text{Nd}$ isotope signatures.

In contrast, the lower continental crust is characterized by granulite facies metamorphism and is often strongly depleted in Rb. As a result, such rocks have low $^{87}\text{Sr}/^{86}\text{Sr}$ signatures, often comparable to mantle derived basalts. They also have low $^{143}\text{Nd}/^{144}\text{Nd}$ values due to their low

Sm/Nd ratios, and in the case of Archean granulites (*e.g.* the Lewisian of Scotland) due to their extreme age. These type of rocks therefore represent another distinct contaminant of basic magmas which pass through the continental crust.

Figure 5.1 shows the areas occupied by MORB, various OIB and CFB suites on the Sr-Nd isotopic correlation diagram, as well as those occupied by upper and lower crustal rocks.

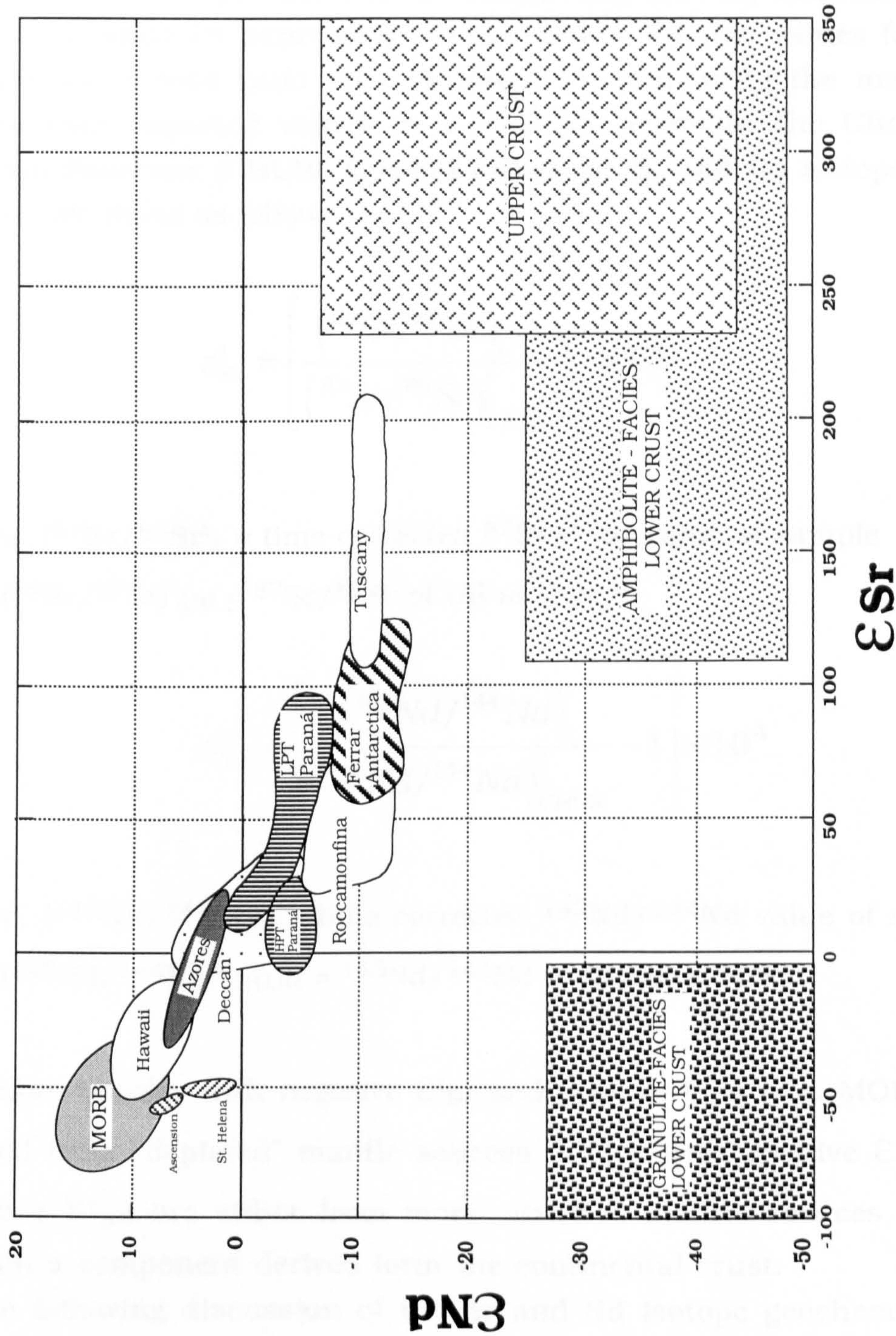


FIGURE 5.1 ϵ_{Sr} - ϵ_{Nd} correlation diagram for various oceanic and continental volcanic suites. Also shown are approximate areas covered by upper and lower crustal rocks. Data from Carter *et al.* (1978, Roman Province); Cox & Hawkesworth (1985, Deccan); Hart (1988, MORB and OIB); Petrini *et al.* (1987, Paraná); Brewer *et al.* (1992, Antarctica); DePaolo & Wasserburg (1979; Crust).

5.2 The Epsilon (ϵ) Notation

Since isotope ratios are only strictly comparable if the samples plotted are of the same age, DePaolo & Wasserburg (1976a) introduced the epsilon notation for expressing isotope ratios. Epsilon values for both Sr and Nd isotope ratio are calculated by comparing the measured values with expected values in a uniform reservoir, the Chondritic Uniform Reservoir (CHUR). Epsilon values for Sr and Nd isotope ratios can be calculated as follows :

$$\epsilon_{\text{Sr}}^t = \left[\frac{(^{87}\text{Sr}/^{86}\text{Sr})_t}{(^{87}\text{Sr}/^{86}\text{Sr})_{\text{UR}}^t} - 1 \right] \times 10^4 \quad \{5.1\}$$

Where, $(^{87}\text{Sr}/^{86}\text{Sr})_t$ = time corrected $^{87}\text{Sr}/^{86}\text{Sr}$ value of sample
and, $(^{87}\text{Sr}/^{86}\text{Sr})_{\text{UR}}^t$ = $^{87}\text{Sr}/^{86}\text{Sr}$ of UR at time t .

$$\epsilon_{\text{Nd}}^t = \left[\frac{(^{143}\text{Nd}/^{144}\text{Nd})_t}{(^{143}\text{Nd}/^{144}\text{Nd})_{\text{CHUR}}^t} - 1 \right] \times 10^4 \quad \{5.2\}$$

Where, $(^{143}\text{Nd}/^{144}\text{Nd})_t$ = time corrected $^{143}\text{Nd}/^{144}\text{Nd}$ value of sample,
and, $(^{143}\text{Nd}/^{144}\text{Nd})_{\text{CHUR}}^t$ = $^{143}\text{Nd}/^{144}\text{Nd}$ of CHUR at time t .

Therefore basalts with negative ϵ_{Sr}^t and positive ϵ_{Nd}^t (*e.g.* MORB) are derived from "depleted" mantle sources. Those with positive ϵ_{Sr}^t and negative ϵ_{Nd}^t are either from more enriched mantle sources and/or contain a component derived from the continental crust.

In the following discussion of the Sr and Nd isotope geochemistry of the LSSC, both initial isotope ratios and the ϵ values are reported. Most diagrams however use only the ϵ notation. Initial isotope values are used in those diagrams which plot calculated models (*e.g.* AFC and mixing models), since the calculations use isotope ratios rather than

epsilon values. ϵ values have been calculated using the following present day parameters :

$$(^{147}\text{Sm}/^{144}\text{Nd})_{\text{CHUR}} = 0.1966$$

$$(^{143}\text{Nd}/^{144}\text{Nd})_{\text{CHUR}} = 0.512638$$

$$(^{87}\text{Rb}/^{86}\text{Sr})_{\text{UR}} = 0.0847$$

$$(^{87}\text{Sr}/^{86}\text{Sr})_{\text{UR}} = 0.7047$$

Therefore at 58Ma,

$$(^{143}\text{Nd}/^{144}\text{Nd})^t_{\text{CHUR}} = 0.512563$$

$$(^{87}\text{Sr}/^{86}\text{Sr})^t_{\text{UR}} = 0.7044$$

5.3 The Sr and Nd Isotope Geochemistry of the LSSC

Whole-rock Sr and Nd isotope data have been determined for 13 samples from Group I, 6 samples from Group II, and 4 samples from Group III of the LSSC. These were determined on the freshest samples, and cover the entire compositional spectrum of the suite. These data are presented in Table 3.1 and have been age corrected to 58Ma (Musset, 1986; Dagley *et al.*, 1987). A full listing of the Rb/Sr and Sm/Nd isotopic data can be found in Appendix II. The LSSC magmas cover a very large range of Sr and Nd isotope compositions. Table 5.1 summarises the variation in compositions seen in each group.

	GROUP I	GROUP II	GROUP III
$(^{86}\text{Sr}/^{86}\text{Sr})_i$	0.703756 - 0.715405	0.714106 - 0.716794	0.717169 - 0.720319
$\epsilon^{58}\text{Sr}$	-9.6 - +155.76	+142.0 - +175.5	+180.8 - +225.5
$(^{143}\text{Nd}/^{144}\text{Nd})_i$	0.512926 - 0.511872	0.511877 - 0.511807	0.511886 - 0.511853
$\epsilon^{58}\text{Nd}$	+7.07 - -13.48	-13.4 - -14.75	-13.69 - -13.86

Table 5.1 Sr and Nd isotope compositional ranges of the LSSC magma groups

Figure 5.2 is an the $\epsilon^{58}\text{Sr}$ - $\epsilon^{58}\text{Nd}$ correlation diagram for the LSSC data. The data defines a well correlated parabolic curve. The least-evolved member of Group I (ORB2) plot close to the "Mantle Array", whereas the more-evolved members of Group I , and all of Groups II and III plot towards the regions occupied by upper crustal lithologies. Since the processes of differential partial melting and fractional crystallization cannot fractionate the isotopes of Sr and Nd, the spread in data seen within the LSSC cannot therefore be due to these processes. Such variation can only be due, therefore, to either the mixing of magmas with different isotopic signatures, the contamination of basic magma with crustal material, or the derivation of each magma batch from isotopically distinct sources.

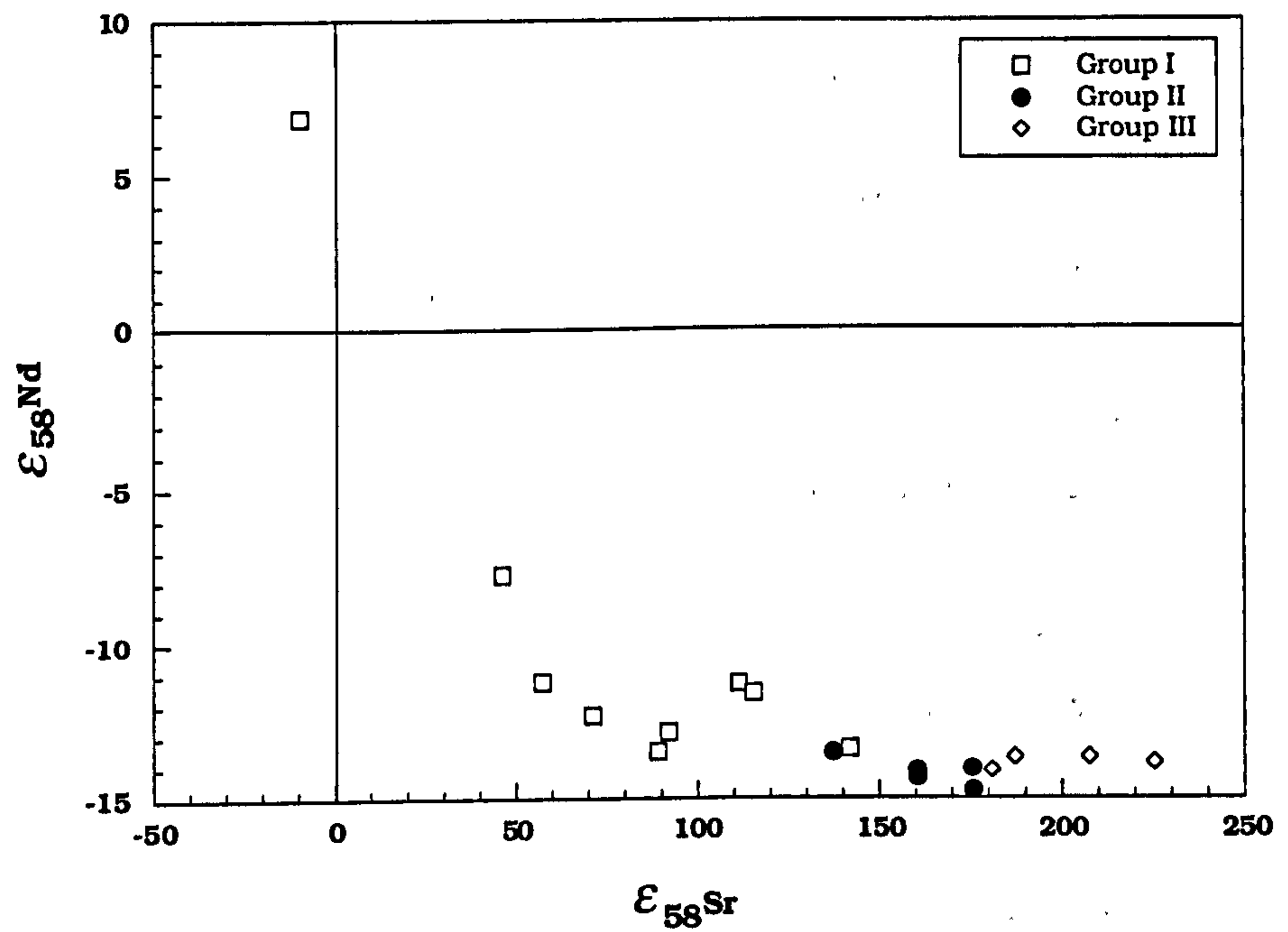


FIGURE 5.2 $\epsilon_{58}\text{Sr}$ - $\epsilon_{58}\text{Nd}$ correlation diagram for the LSSC.
 Only one sample (ORB2) falls within the Mantle Array. All other samples show high Sr_{58} and low Nd_{58} isotope ratios, indicative of crustal involvement.

Group I

The initial isotope signatures of Group I magmas correlate well with degree of fractionation. This is clearly shown in *Figures 5.3a* and *5.3b* which plot $\epsilon^{58}\text{Sr}$ and $\epsilon^{58}\text{Nd}$ against wt% SiO_2 . $\epsilon^{58}\text{Sr}$ and $\epsilon^{58}\text{Nd}$ are also well correlated with certain trace-elements such as Ce, Zr, La and Nb (see *Figures 5.4a-d* and *5.5a-d*). The trend for Group I magmas is distinctly curved on all of these diagrams, as it is on the $\epsilon^{58}\text{Sr}$ - $\epsilon^{58}\text{Nd}$ correlation diagram (*Figure 5.2*).

DePaolo (1981) has shown that assimilation with concomitant fractional crystallization (AFC) may shift compositions on a $\epsilon^{58}\text{Sr}$ - $\epsilon^{58}\text{Nd}$ correlation diagram far from what might be expected on the basis of simple mixing. Simple mixtures define straight or curved trends between the magma and the contaminant on the $\epsilon^{58}\text{Sr}$ - $\epsilon^{58}\text{Nd}$ diagram, whereas in AFC processes, when there is a marked difference in the bulk solid/liquid distribution coefficients for Sr and Nd, the trends produced can depart significantly from the simple mixing line. The trends are generally curved and may not necessarily point at the two end-members involved (DePaolo, 1981).

The trends displayed on the $\epsilon^{58}\text{Sr}$ - $\epsilon^{58}\text{Nd}$ diagram provide perhaps the best constraints on the nature of magmatic processes which are responsible for the compositional spectrum of the LSSC. The isotope data for Group I magmas lends very strong support to the inferences made from the major- and trace-element geochemistry that AFC-type processes controlled the evolution of the group.

Figure 5.6 shows the $(^{87}\text{Sr}/^{86}\text{Sr})_i$ - $(^{143}\text{Nd}/^{144}\text{Nd})_i$ correlation diagram for the LSSC, along with the modelled AFC trend (DePaolo, 1981). The parameters used in the model are those determined to give the best fit for the trace-element AFC model (Chapter 4) (i.e. a two stage fractionating history involving olivine + augite + plagioclase, followed by augite + pigeonite/orthopyroxene + plagioclase, using a Moine pelitic schist as a contaminant; K_D values as in *Table 4.1*; r value = 0.4). It was necessary to use a Moine pelite in this case, instead of a Group III rhyolite/mullite buchite mix, because as will be shown in Chapter 10, the initial Sr isotope ratios of the mullite buchites has been reset to low values due to isotopic exchange with basic magma. It would

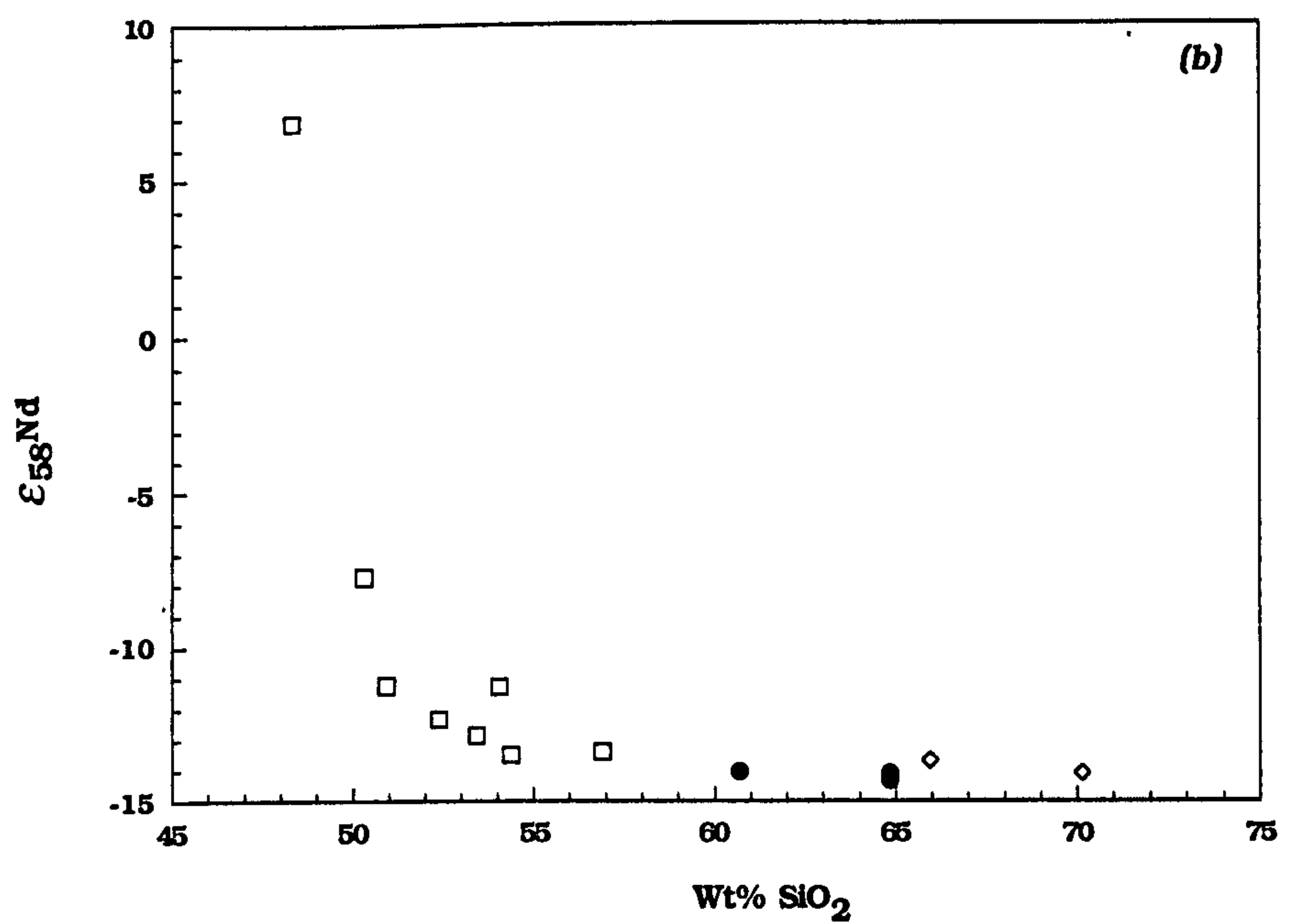
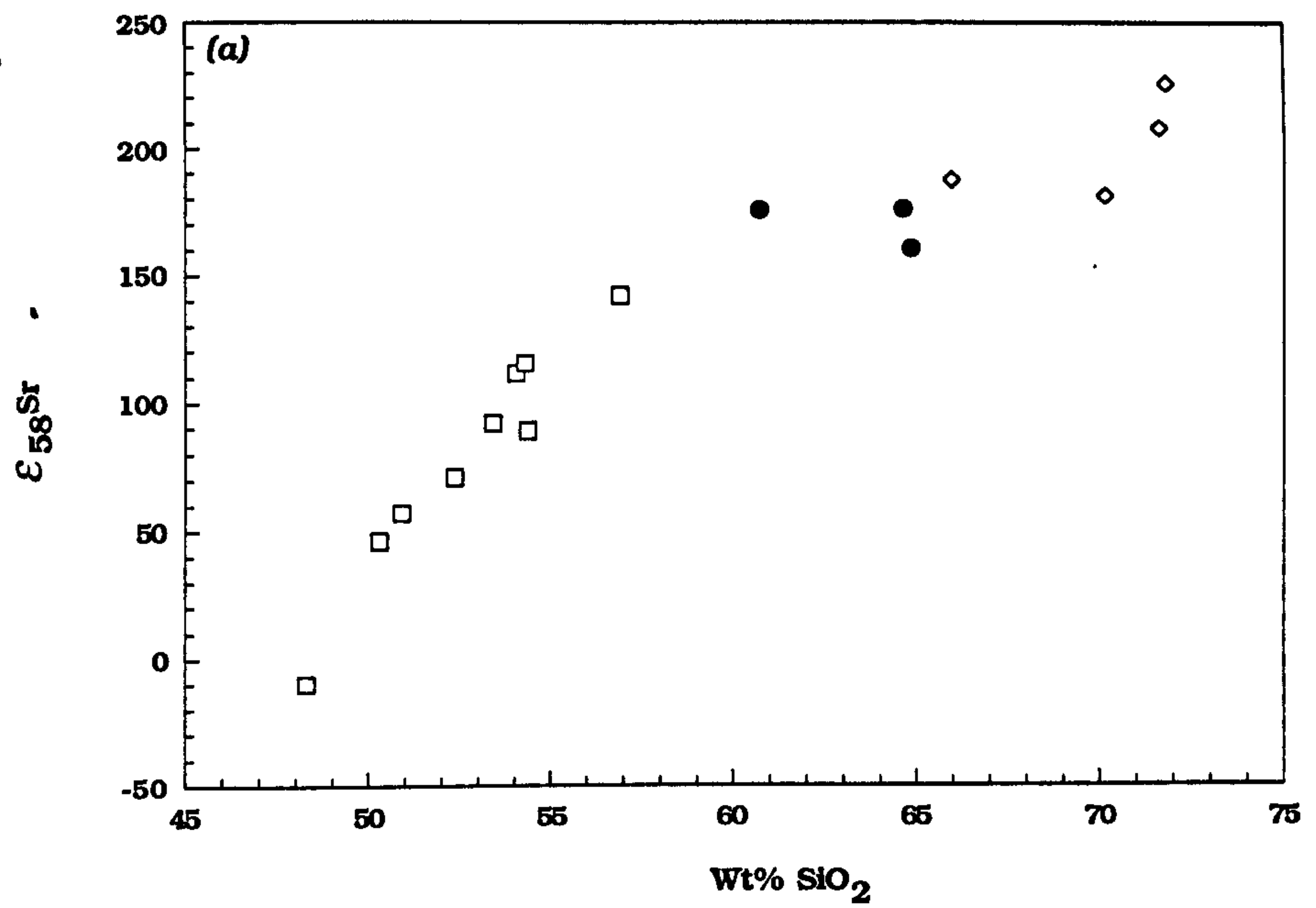


FIGURE 5.3 Variation of (a) $\epsilon_{58}\text{Sr}$ and (b) $\epsilon_{58}\text{Nd}$ with degree of fractionation as shown by Wt% SiO_2 . The curved trend of Group I samples is indicative of AFC type processes (DePaolo, 1981).

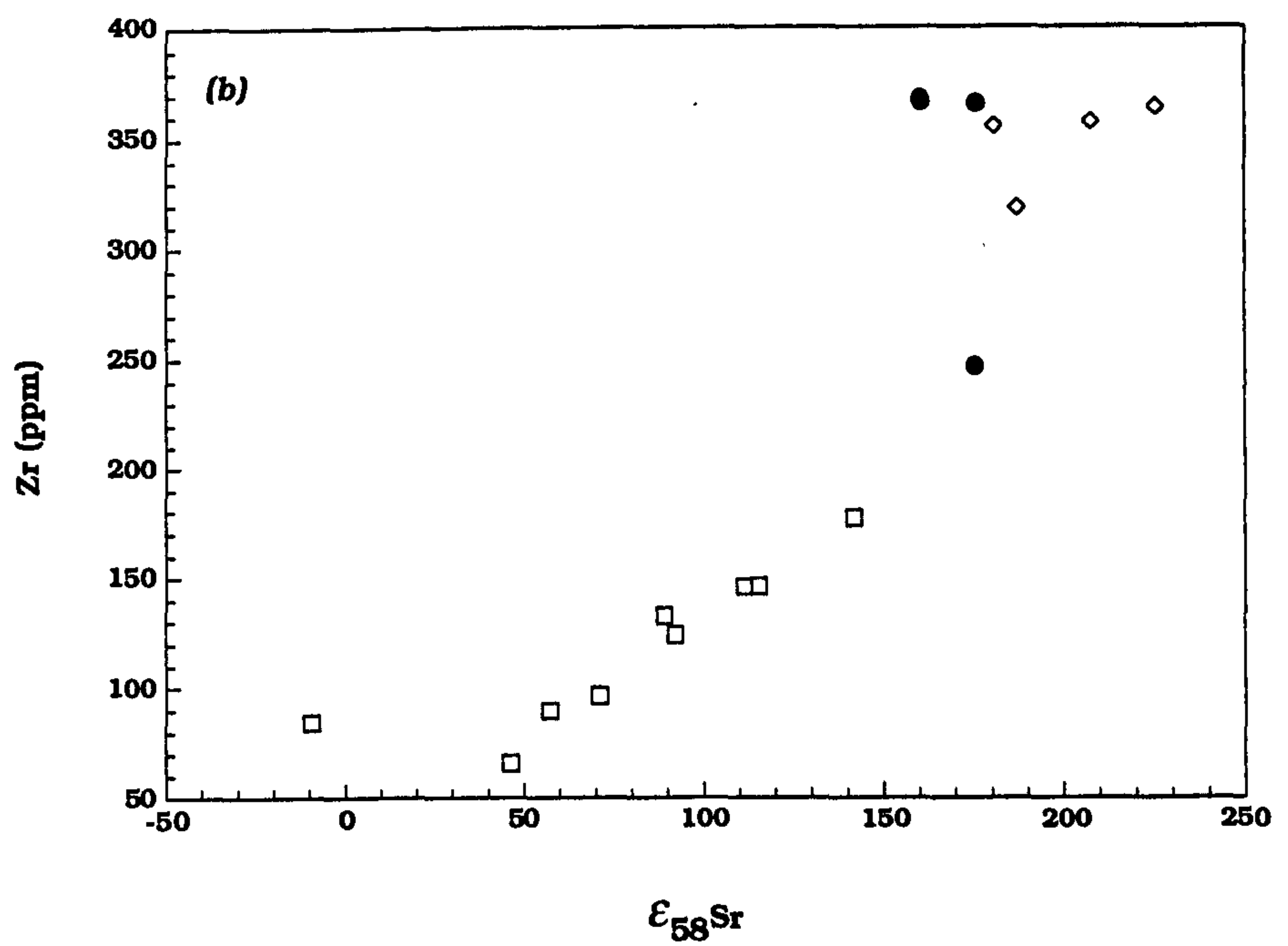
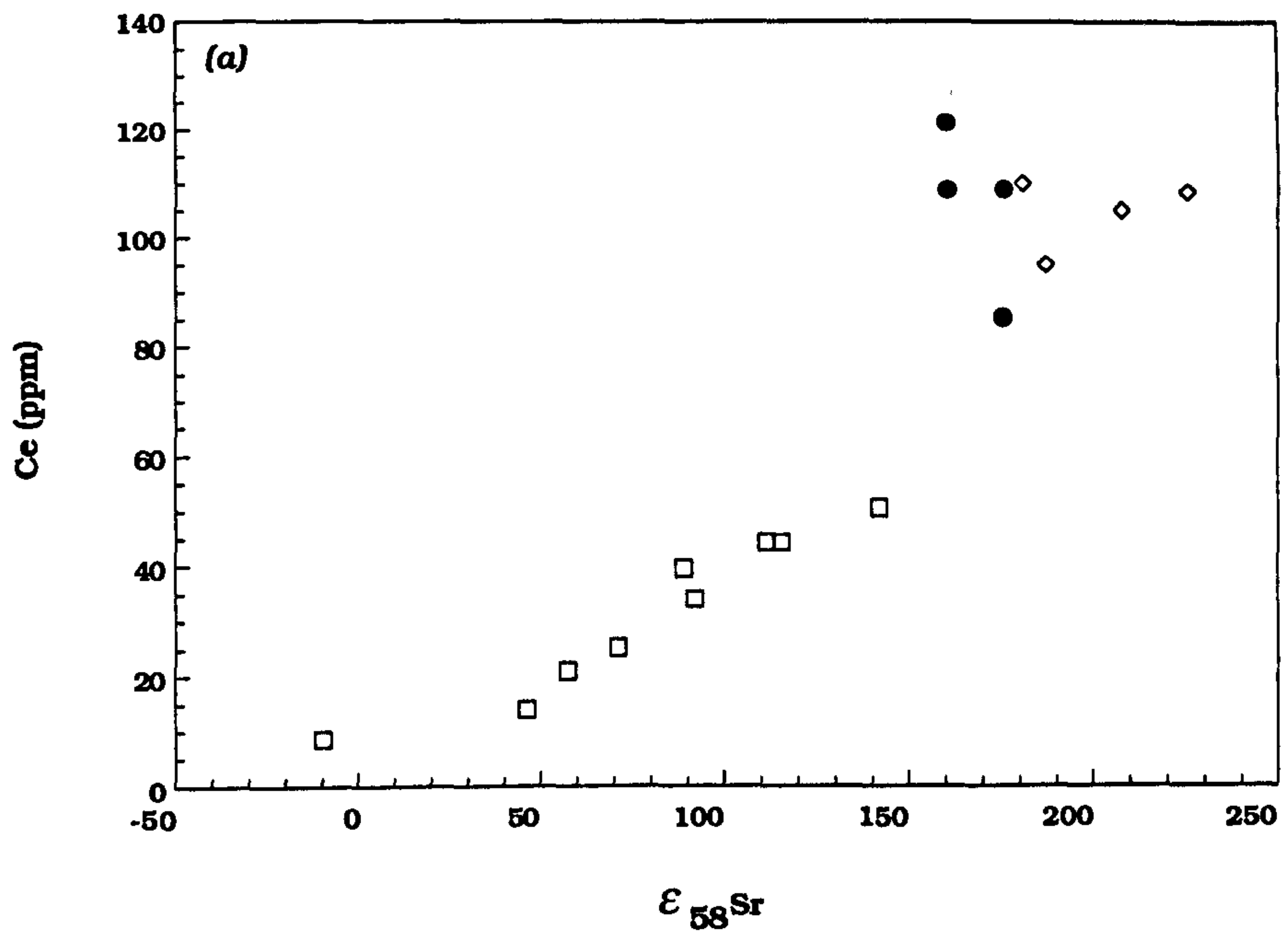


FIGURE 5.4 Variation of incompatible-elements with $\epsilon_{58}\text{Sr}$

(a) Ce- $\epsilon_{58}\text{Sr}$

(b) Zr- $\epsilon_{58}\text{Sr}$

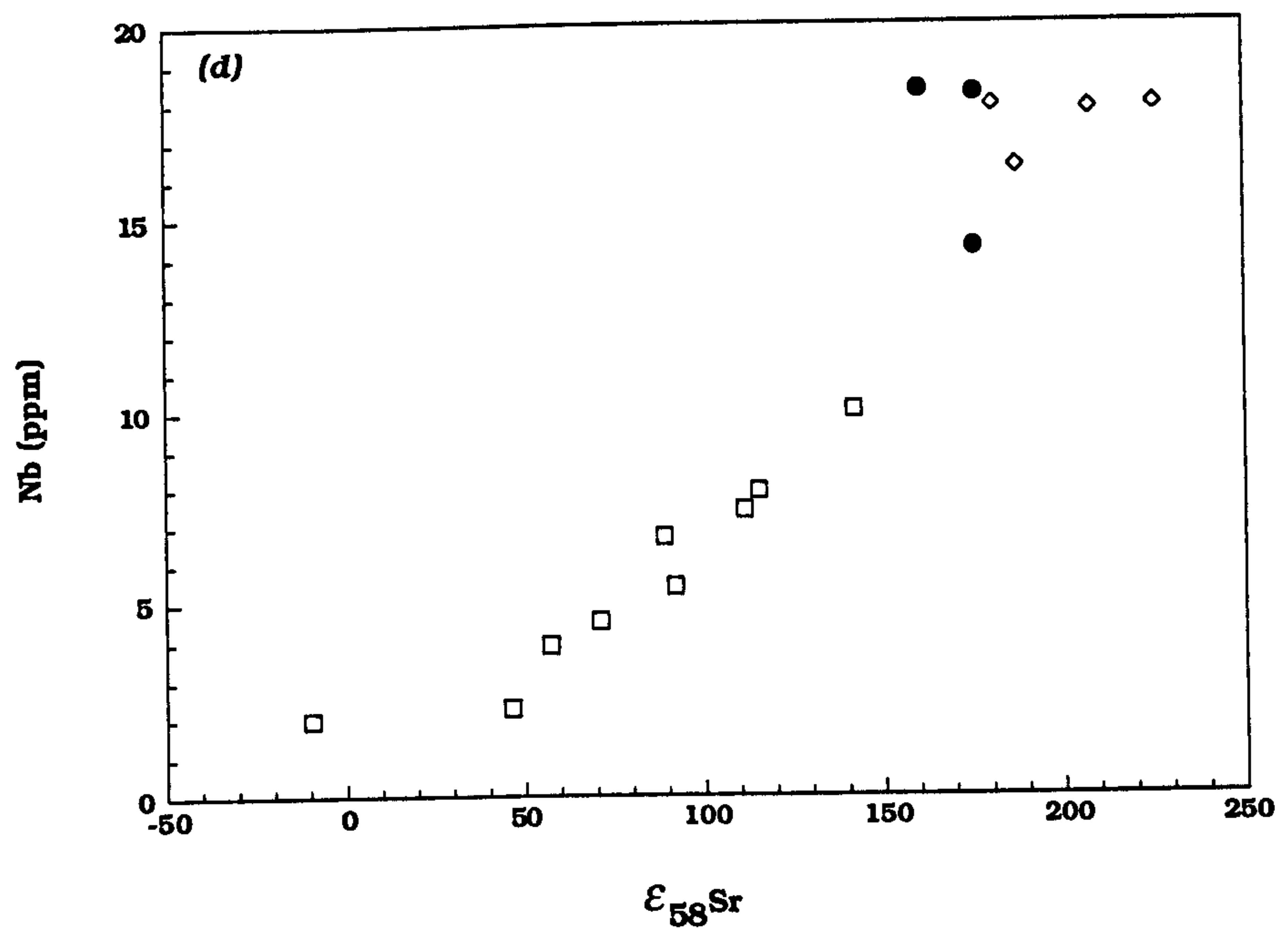
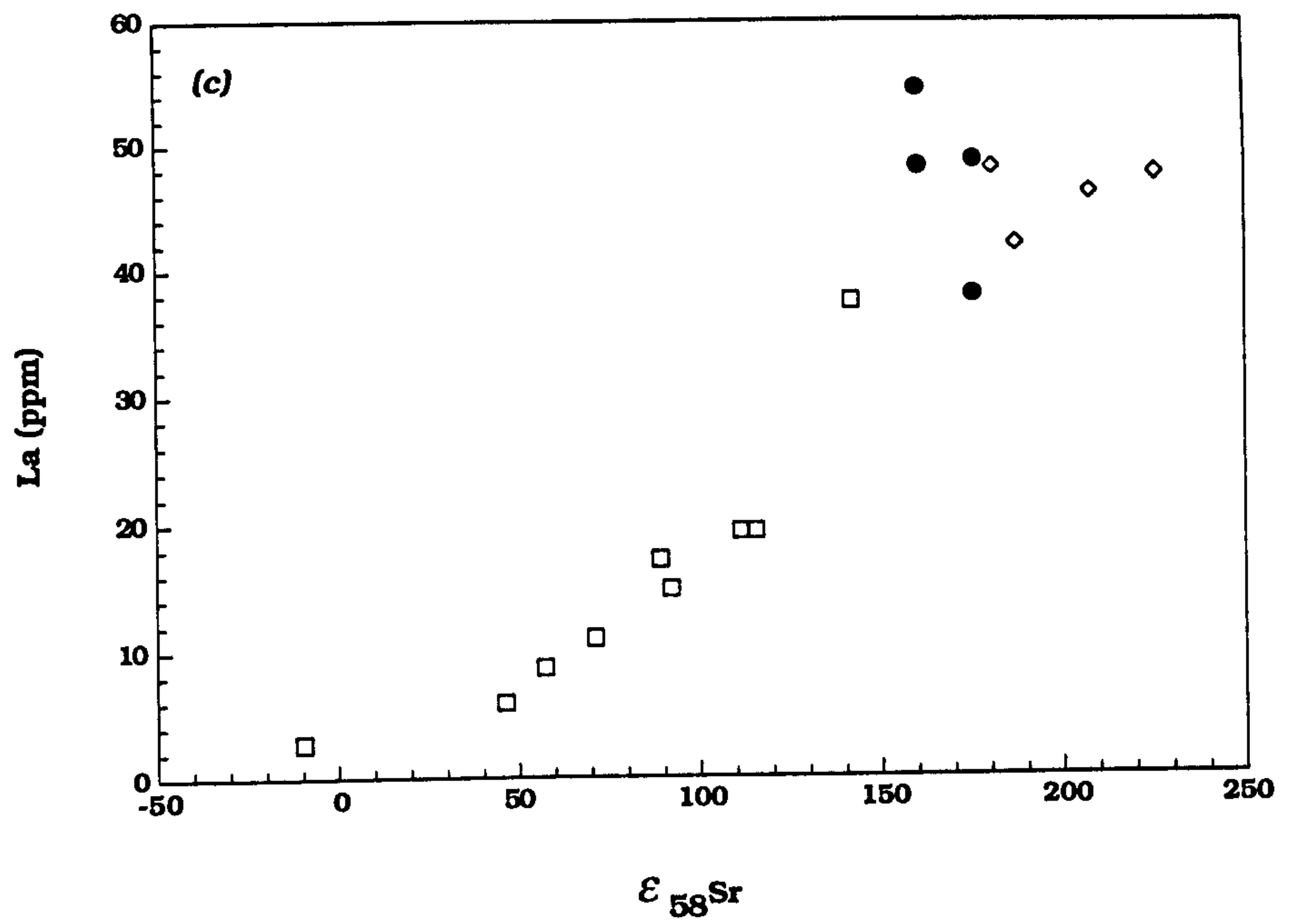


FIGURE 5.4 Variation of incompatible-elements with $\epsilon_{58}\text{Sr}$

(c) La- $\epsilon_{58}\text{Sr}$

(d) Nb- $\epsilon_{58}\text{Sr}$

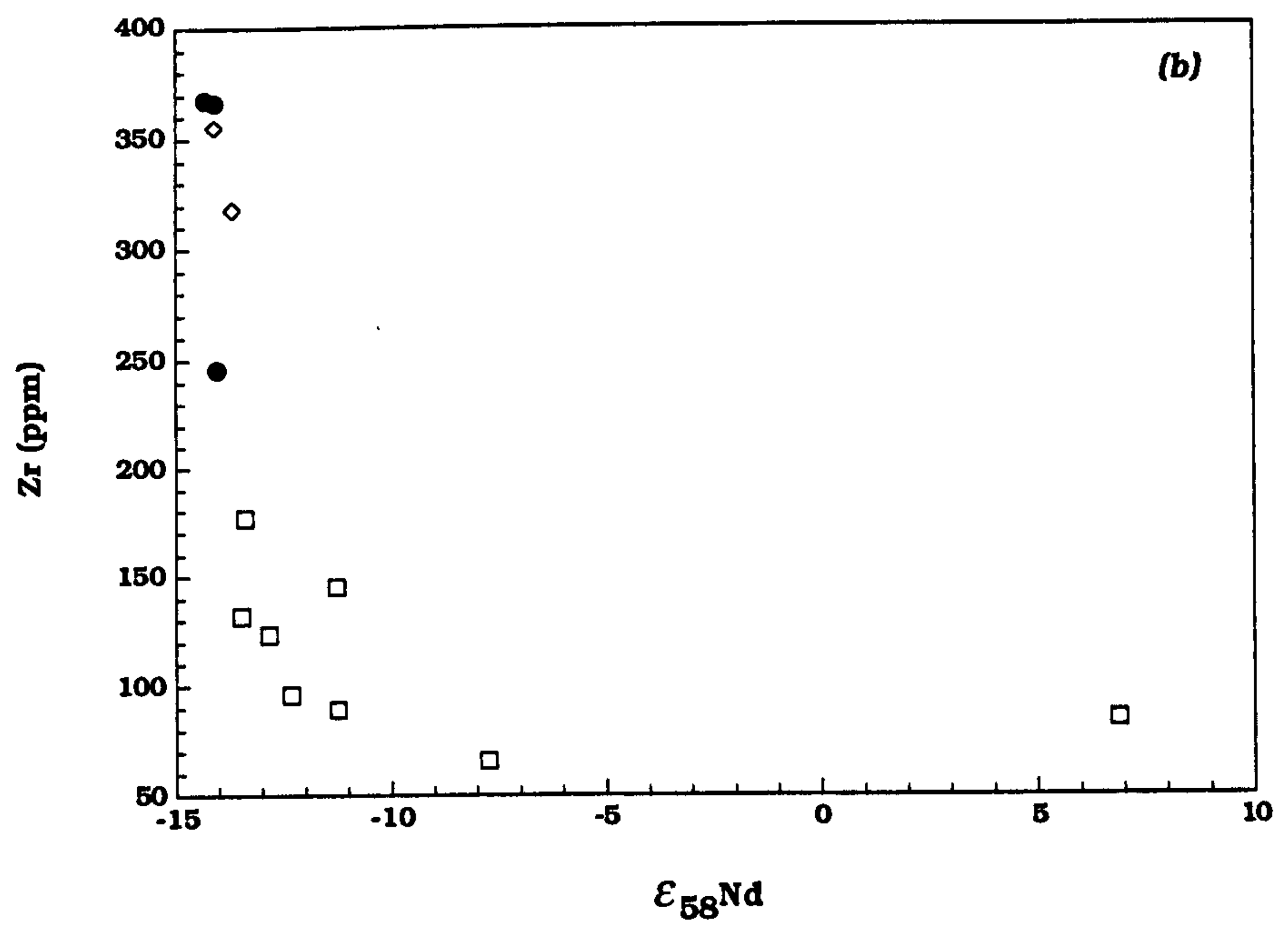
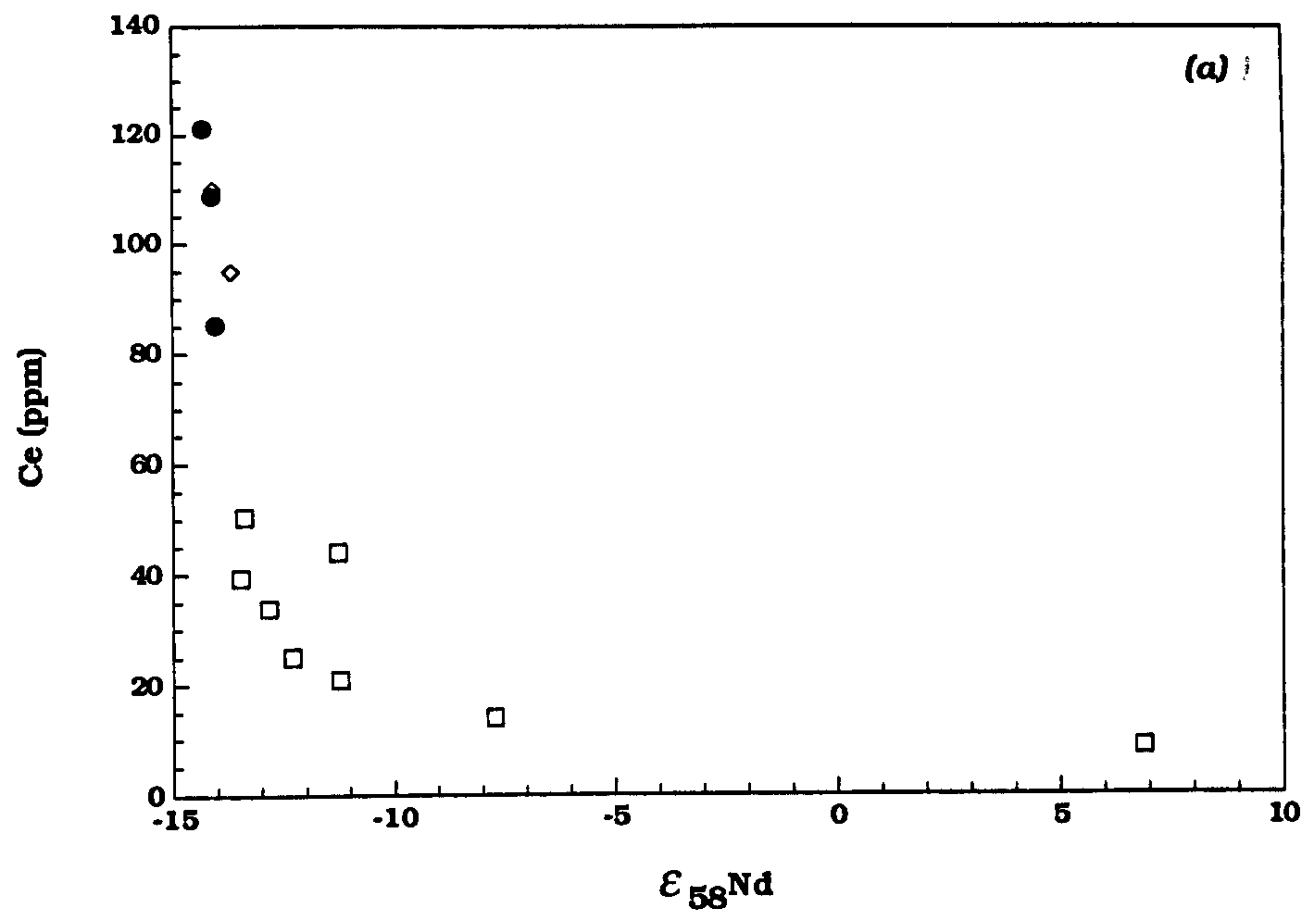


FIGURE 5.5 Variation of incompatible-elements with $\epsilon_{58}\text{Nd}$
 (a) Ce- $\epsilon_{58}\text{Nd}$
 (b) Zr- $\epsilon_{58}\text{Nd}$

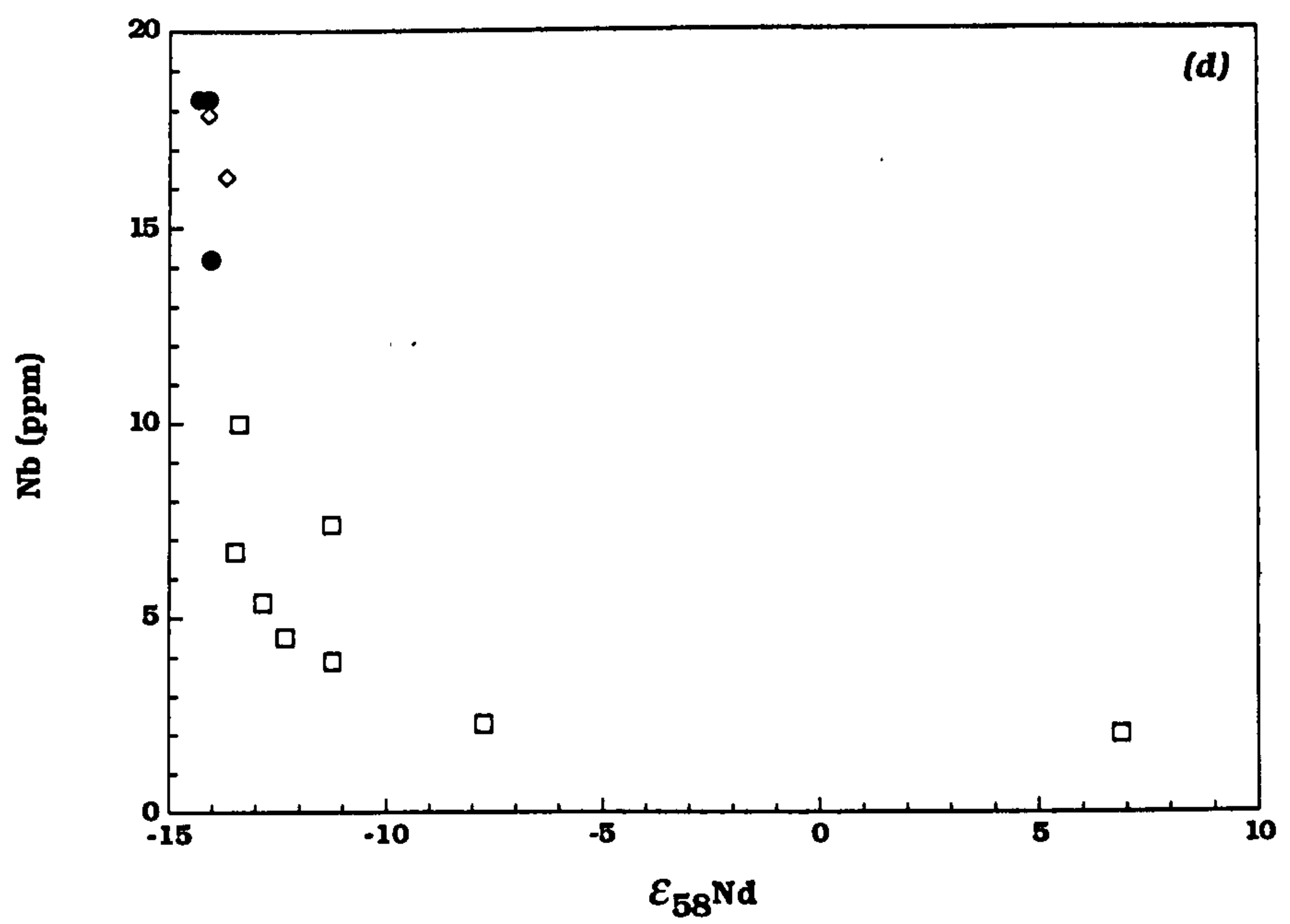
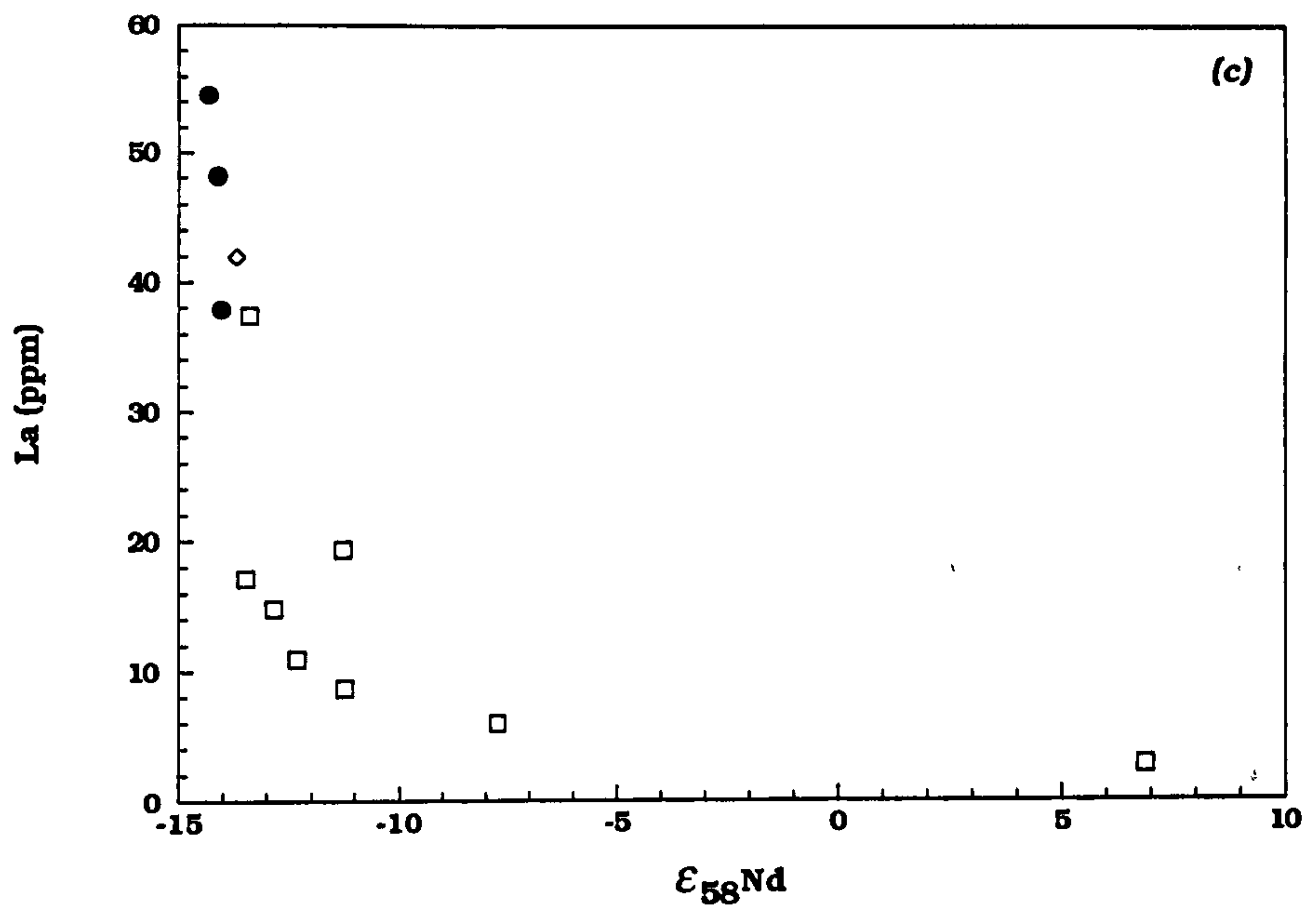


FIGURE 5.5 Variation of incompatible-elements with $\epsilon_{58}\text{Nd}$
 (c) La- $\epsilon_{58}\text{Nd}$
 (d) Nb- $\epsilon_{58}\text{Nd}$

therefore be difficult to calculate the initial Sr isotope ratio of a rhyolite/mullite buchite mix with any degree of certainty. This diagram shows that the model fits the data reasonably well. The amount of crystallization required (~40%) is consistent with the amounts of crystallization required to model the elemental abundances of Sr and Nd (55% and 40% respectively). However, it must be stressed that these simple models have numerous limiting assumptions attached to them. For example, Reiners *et al.* (1995) have shown that during the initial stages of AFC, assimilation can significantly exceed crystallization ($r = 2.0 - 2.7$), and that during this stage, large changes in the trace-element and isotopic characteristics of the magma may occur with little accompanying differentiation. During the second stage of AFC, after plagioclase and clinopyroxene become significant crystallizing phases, the rate of assimilation declines ($r = 0.5 - 1.0$) and the magma evolves more rapidly. This two stage process with its change of fractionating assemblage, also implies that bulk-distribution coefficients are variable.

Bell *et al.* (1994) suggested that the cone-sheets from the Cuillin Igneous Complex of the Isle of Skye, evolved via AFC processes. They concluded that a Preshal More parent magma type assimilated small amounts of amphibolite facies gneiss of the Lewisian Gneiss Complex. The fractionating assemblage involved olivine, plagioclase and clinopyroxene in their cotectic proportions of 10:55:35 (gabbroic fractionation) (Bell *et al.*, 1994). They were also able to distinguish between AFC processes and bulk assimilation on the basis that there will be positive correlations on plots involving $\epsilon^{58}\text{Sr}$ and Fe_2O_3^* and TiO_2 for AFC, and negative correlations for bulk assimilation, the opposite being the case for $\epsilon^{58}\text{Nd}$ versus Fe_2O_3^* and TiO_2 . Figures 5.7a-b show the correlation diagrams for $\epsilon^{58}\text{Sr}$ - Fe_2O_3^* and $\epsilon^{58}\text{Nd}$ - Fe_2O_3^* respectively, for the LSSC data. From these it could be concluded that the LSSC magmas evolved via the bulk assimilation of crustal material. However, the evolution of the LSSC Group I magmas is not dominated by gabbroic fractionation, but involves significant amounts of clinopyroxene and plagioclase, plus minor low-Ca pyroxene (pigeonite or orthopyroxene). As a result, AFC and bulk assimilation processes will lead to very similar trends on these diagrams. Sr and Nd isotope work on the SMLS (Dickin, 1981; Thirlwall & Jones, 1983), and the Plateau Group lavas of Mull (Kerr, 1995) require that the basic magmas were

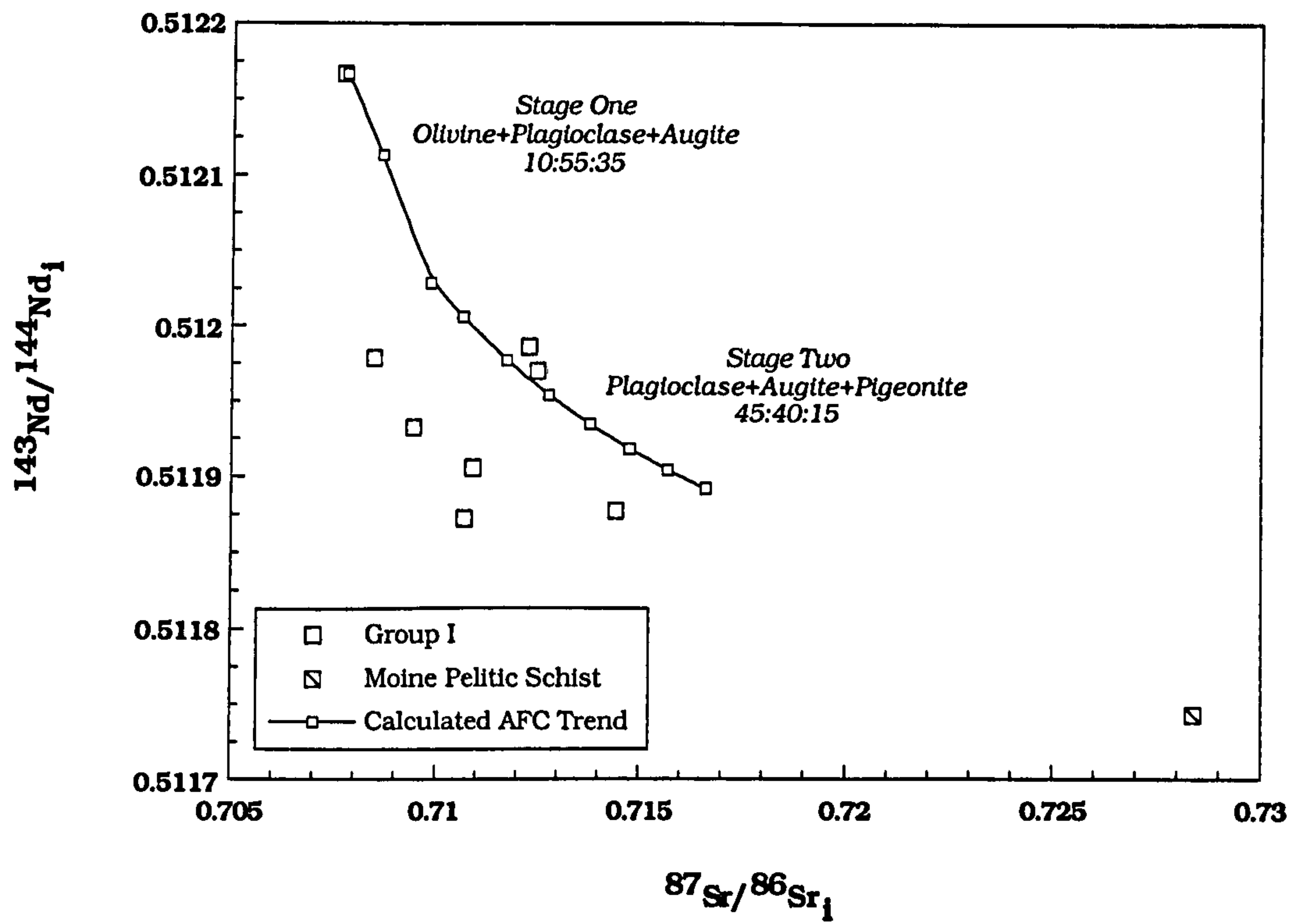


FIGURE 5.6 Variation of Sr and Nd initial isotope ratios for the Group I magmas. Also shown is the calculated AFC model. Model uses the equations of DePaolo (1981). Model contaminant is bulk Moine pelite as shown. Model shown is in 5% crystallization steps. r value = 0.4 for both stages.

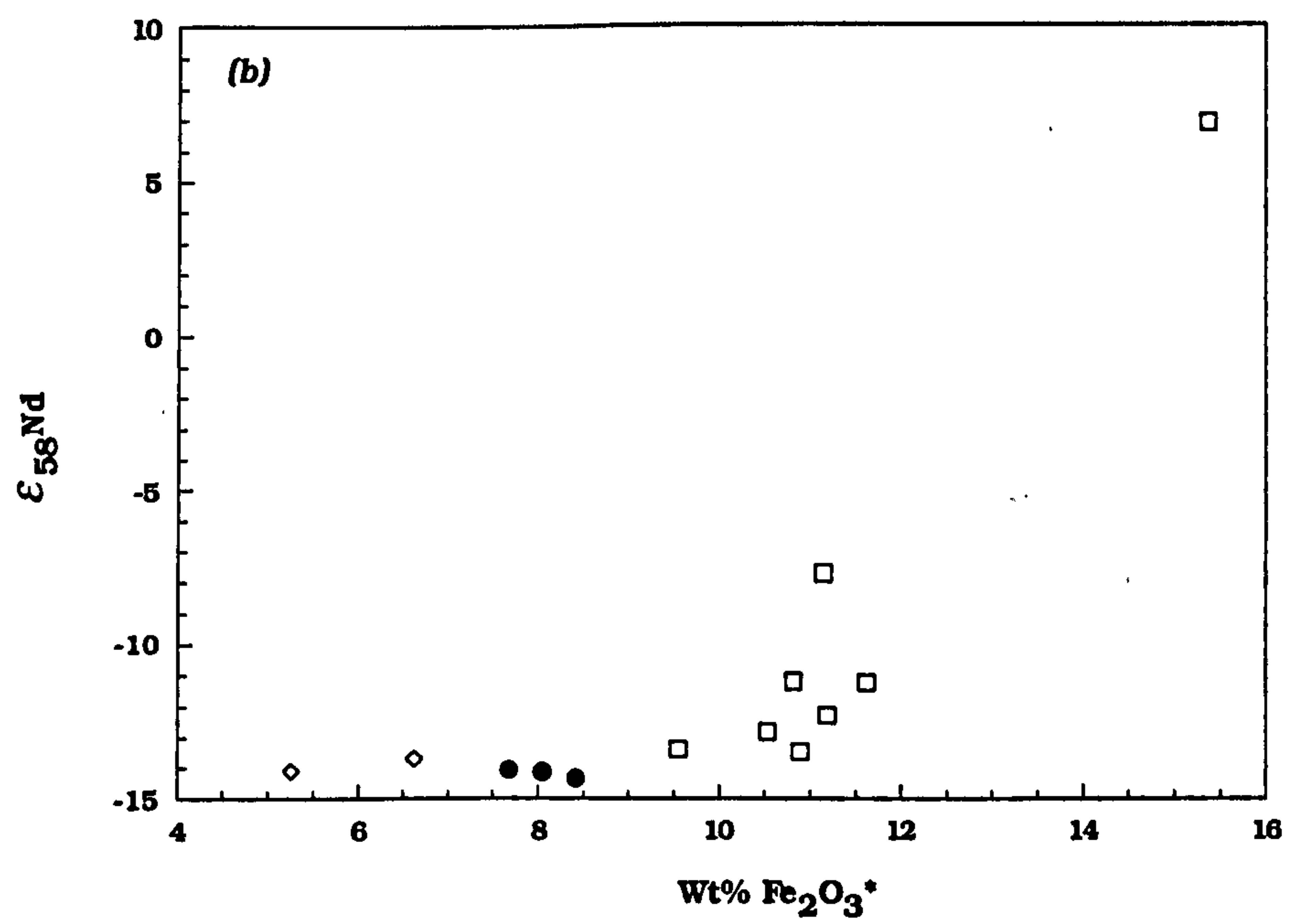
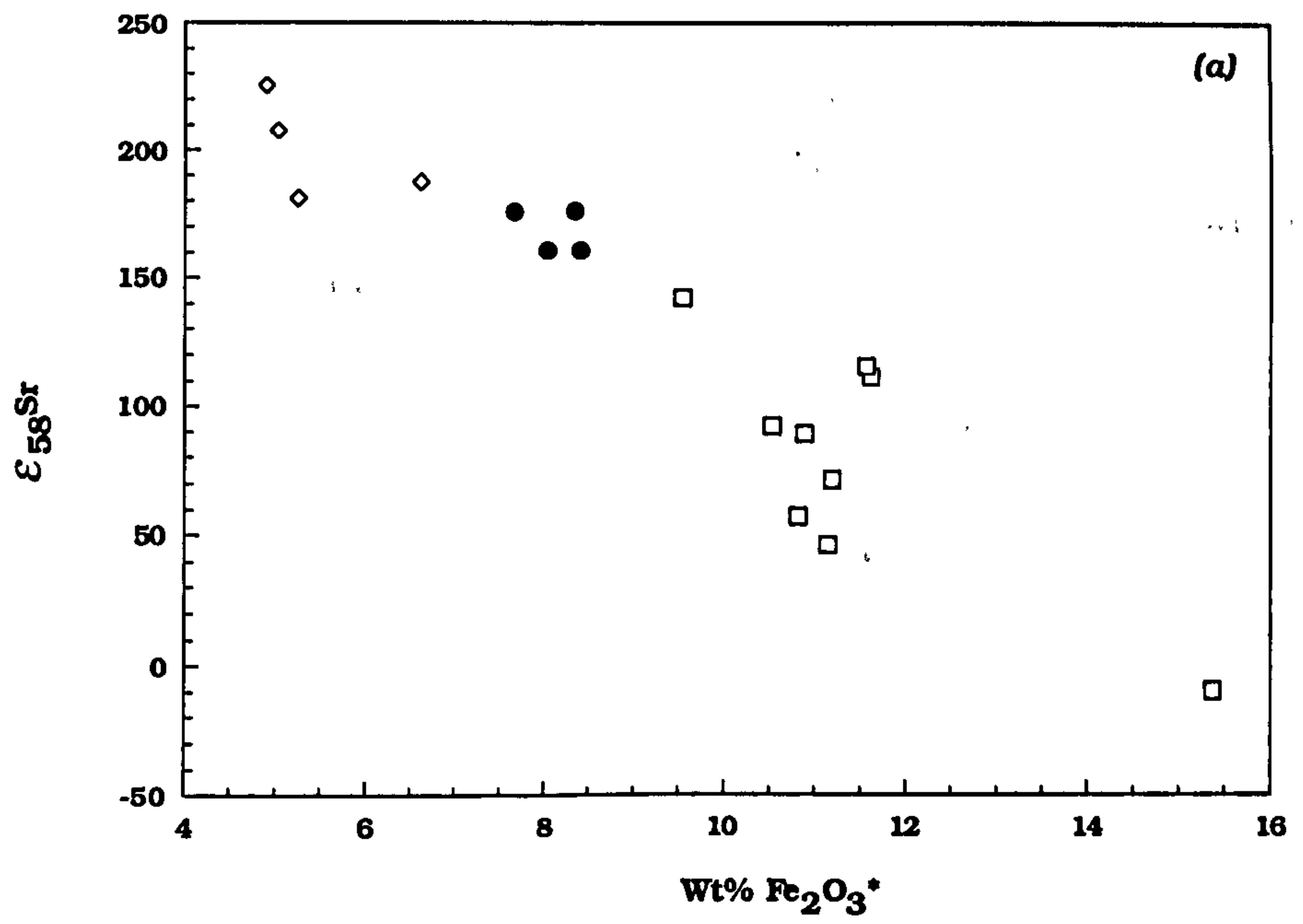


FIGURE 5.7 Variation of (a) $\epsilon_{58\text{Sr}}$ and (b) $\epsilon_{58\text{Nd}}$ with $\text{wt\% Fe}_2\text{O}_3^*$.

contaminated with Lewisian granulite facies material. There is no strong correlation between $(^{87}\text{Sr}/^{86}\text{Sr})_i$ and degree of fractionation (as shown by their SiO_2 contents) for either of these magma groups, unlike the LSSC and the Skye cone-sheet magmas (Bell *et al.*, 1994). This suggests that the contamination mechanism was not one of combined assimilation and fractional crystallization (AFC), but one whereby partial melts extracted from the Lewisian basement rocks, either during their ponding at the base of the crust (Thirlwall & Jones, 1983), or during their turbulent ascent through crustal conduits (Kerr *et al.*, 1995).

Group II

The physical characteristics of the Group II andesites and porphyritic dacites suggests that they are the products of mixing between coexisting basic and silicic magmas (Chapter 2). The major-element data are consistent with this mixing hypothesis (Chapter 3). The trace-element data, are partly consistent with the simple mixing theory, but generally shows that prior and subsequent fractional crystallization of plagioclase and pigeonite has modified the composition of many of the Group II magmas (Chapter 4). The porphyritic dacites often "fall-off" mixing and fractionation arrays in major- and trace-element diagrams due to the presence of zircon and apatite phenocrysts/xenocrysts.

The $\epsilon^{58}\text{Sr}$ and ϵ_{Nd} data for Group II magmas form a very coherent grouping, with elevated $\epsilon^{58}\text{Sr}$ (+142 to +175) and low $\epsilon^{58}\text{Nd}$ at a relatively constant -14 (Figure 5.2). This suggests that these rocks contain a substantial crustal component.

The isotope data can be used to substantiate the simple two component mixing model proposed in Chapters 2, 3 and 4. Since any fractional crystallization after the mixing event will not alter the Sr or Nd isotopic characteristics of the magmas, the isotopic signatures will be solely due to the amounts of the two end-members involved. Using the general mixing equation for isotopic data defined by DePaolo and Wasserburg (1979), it can be shown that the major-element mixing model involving between 70 and 80% of the rhyolitic end-member, and between 30 and 20% of the basic end-member, is entirely consistent with the observed isotopic data. The mixing equation has the following form:

$$\left(\frac{^{87}\text{Sr}}{^{86}\text{Sr}}\right)_M = \frac{\left(\frac{^{87}\text{Sr}}{^{86}\text{Sr}}\right)_A \times \text{Sr}_A \times f + \left(\frac{^{87}\text{Sr}}{^{86}\text{Sr}}\right)_B \times \text{Sr}_B \times (1-f)}{\text{Sr}_A \times f + \text{Sr}_B \times (1-f)} \quad \{5.3\}$$

Where $(^{87}\text{Sr}/^{86}\text{Sr})_M$ = the Sr isotope ratio of a mixture M of two components A and B.

and, f = weight fraction of component A in the mixture.

Figure 5.8 shows the $(^{87}\text{Sr}/^{86}\text{Sr})_i$ - $(^{143}\text{Nd}/^{144}\text{Nd})_i$ correlation diagram for the Group II magmas. Also shown are the basic and silicic end-members used in the mixing model, and the calculated mixing line between the two, graduated in 10% steps. The mixing hypothesis is therefore considered the most likely to explain the evolution of the Group II magmas.

Similar conclusions have been drawn about the evolution of certain other siliceous minor intrusions from elsewhere in the BTVP. Isotope data (Sr, Nd and Pb) for similar porphyritic dacites from the Isle of Arran, and from Eigge, suggest that they resulted from the contamination of basaltic differentiates with Dalradian schists in the case of the Arran rocks (Dickin *et al.*, 1981), and with granulite-facies Lewisian gneiss and Torridonian sandstone in the case of the Eigge dacitic sheets (Dickin & Jones, 1983b). Dickin & Exley (1981) also proposed a magma mixing hypothesis for the petrogenesis of the Coire Uaigneich Granophyre, Isle of Skye. The mixing involved a high $\epsilon^{58}\text{Sr}$ liquid formed from the anatexis of late Precambrian (Torridonian) clastic sedimentary rocks, and another silicic, incompatible-element-enriched liquid formed by the fractional crystallization of basaltic magma (Dickin & Exley, 1981).

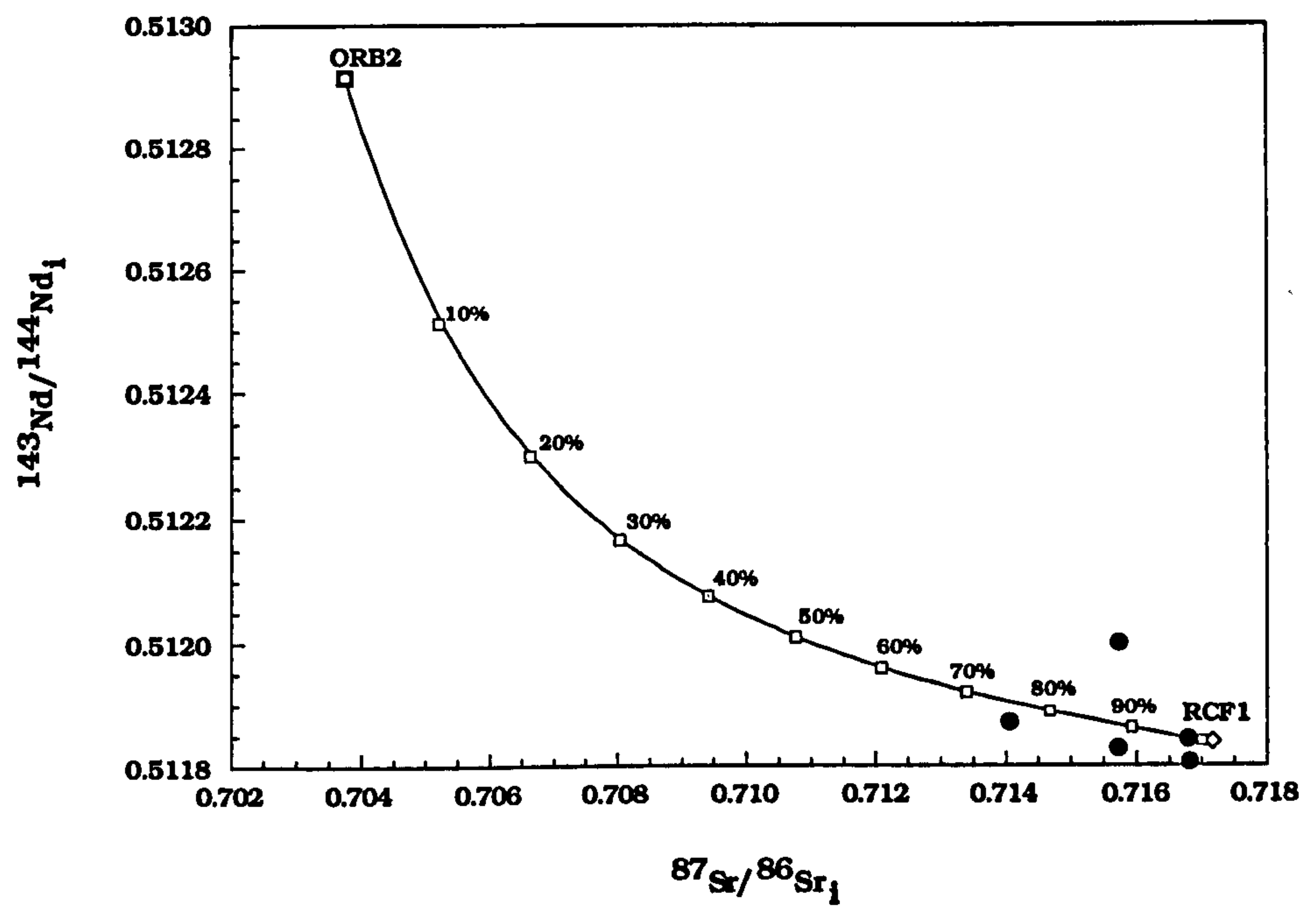


FIGURE 5.8 Sr-Nd isotope mixing model for Group II magmas. Endmembers involved are least-evolved member of Group I (ORB2), and a Group III rhyolite (RCF1).

Group III

The rhyolites of Group III have the most extreme $\epsilon^{58}\text{Sr}$ and $\epsilon^{58}\text{Nd}$ data of the LSSC. $\epsilon^{58}\text{Sr}$ values are very high (+180 to +225), and $\epsilon^{58}\text{Nd}$ values are low (~13) (*Figure 5.2*). These values indicate substantial crustal involvement in their petrogenesis, and are compatible with the derivation of the rhyolitic magmas via direct anatexis of crustal lithologies. This is consistent with the peraluminous nature of the rhyolites, and their low total Sr contents (~ 100ppm); in general, partial melting of common sedimentary or metasedimentary rocks will leave a restite rich in Ca-plagioclase, and therefore a melt poor in Sr. The bulk of the crust underlying the Mull Igneous Centre is assumed to be predominantly Lewisian in age (~2.7Ga), with amphibolite-facies rocks overlying granulite-facies lower crustal rocks (Bamford *et al.*, 1977). Torridonian rocks may also be present in the sequence since they crop out on the isle of Iona. These rocks are overlain by a thin slice of Moine metasedimentary rocks, and younger Mesozoic strata (Bailey *et al.*, 1924). The Great Glen Fault cuts the south part of the island, suggesting that part of the crust under Mull may consist of Dalradian rocks (Potts, *et al.*, 1995). Although it is possible to distinguish between amphibolite- and granulite-facies Lewisian gneisses on the basis of Sr and Nd isotopic data, Moine metasedimentary rocks occupy a very similar region to Lewisian amphibolite-facies rocks in $\epsilon^{58}\text{Sr}$ - $\epsilon^{58}\text{Nd}$ space (Thompson *et al.*, 1986); this is shown in *Figure 5.9*. Although three of the Group III samples have $\epsilon^{58}\text{Sr}$ which fall outside the range of Moine pelitic schists, one sample falls within the Moine field. The $\epsilon^{58}\text{Nd}$ data for the Group III rhyolites is more consistent with their derivation from Moine source rocks, which range up to more positive $\epsilon^{58}\text{Nd}$ values than typical Lewisian amphibolite-facies gneiss. Two analysed samples of Moine pelitic schist from Mull, have $\epsilon^{58}\text{Sr}$ and $\epsilon^{58}\text{Nd}$ values far removed from any of the Group III samples (*Table 5.2*). However, it has been shown that even on Mull and the Morvern Peninsula, the Moine has a very wide range of isotopic compositions (Pankhurst *et al.*, 1978; Thompson *et al.*, 1986).

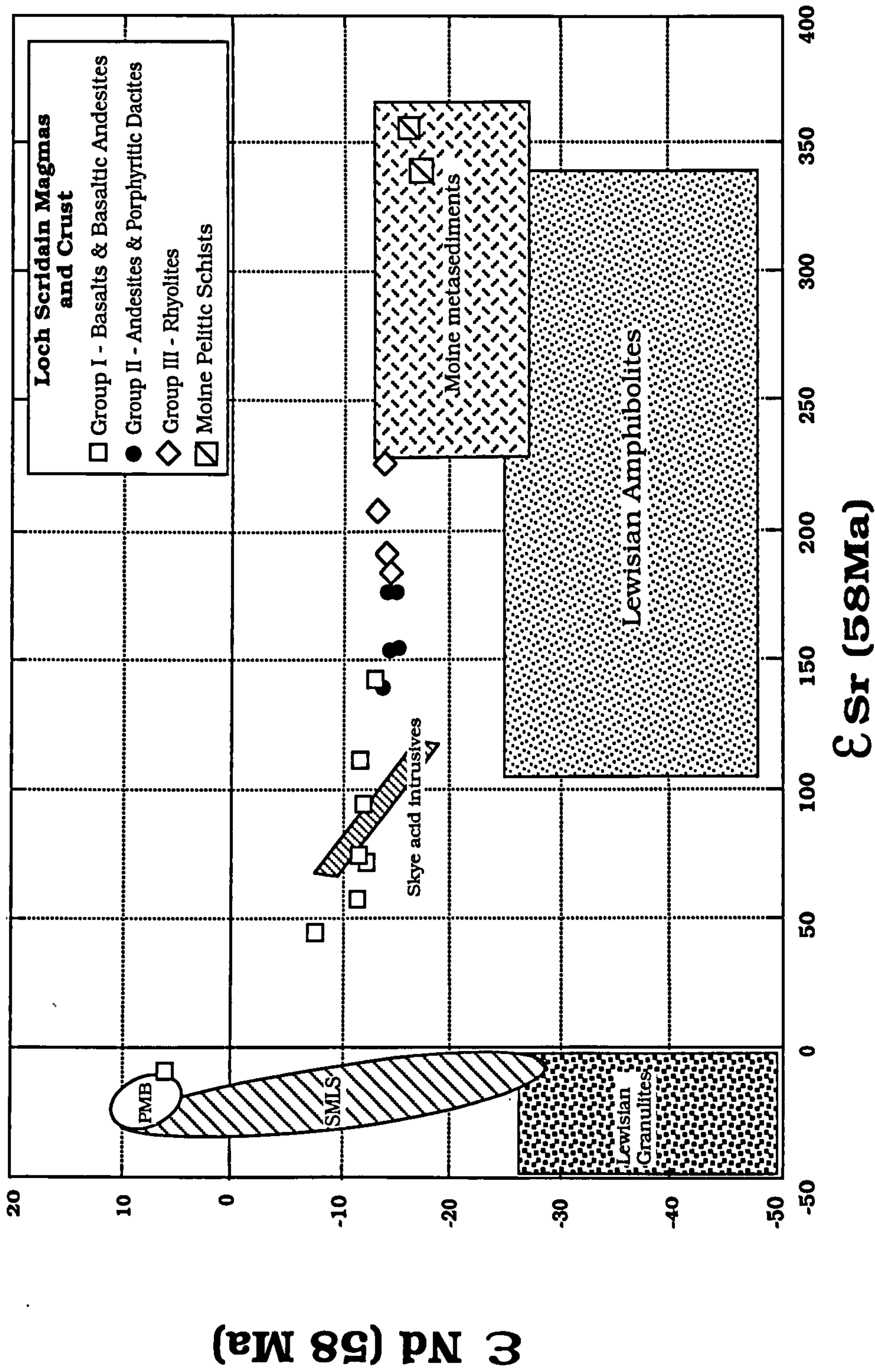


FIGURE 5.9 εSr-εNd correlation daigram for the LSSC, along with fields covered by SMLS, Preshal More basalt types, Skye granitic intrusives, Lewisian granulite and amphibolite facies gneisses, and Moine metasediments. Additional data from : Bell *et al.*, (1994); Clayburn, (1988); Holden *et al.*,(1987)

SAMPLE	$^{87}\text{Sr}/^{86}\text{Sr}$	$^{143}\text{Nd}/^{144}\text{Nd}$
SOM1 - Pelite	0.72897	0.51179
SOMBC - Pelite	0.72999	0.51180
MS324 - Pelite	0.75230	-
MS326 - Psammite	0.73259	-
73/4 - Pelite	0.73995	-
73/9 - Pelite	0.73995	-
73/15 - Psammite	0.71989	-
RC1445 - Pelite	-	0.51183
RC1447 - Pelite	-	0.51184
M121 - Pelite	0.76378	-
M153 - Semipelite	0.72080	-

Table 5.2 Isotopic characteristic of Moine metasediments from the Isle of Mull, the Morvern Peninsula, and the NW Highlands. Samples SOM1 and SOMBC this study; samples MS324 and 326 from the Ross of Mull (Thompson *et al.*, 1986); samples 73/4, 73/9, 73/15 from the Ross of Mull; samples RC1445 and 1447 from NW Highlands (van Breeman & Hawkesworth, 1980); and samples M121 and M153 from Morvern (Pankhurst *et al.*, 1978). All ratios are as measured.

Although the $\epsilon^{58}\text{Sr}$ - $\epsilon^{58}\text{Nd}$ isotope data is inconclusive on its own, coupled with the major- and trace-element geochemistry of the Group III rhyolites, it is suggested that they do indeed represent partial melts from Moine pelitic schists. Those Group III samples which fall out-with the field of Moine metasediments are those associated with the Rudh' a' Chromain composite sheet. The detailed petrogenesis of this sheet is discussed in Chapter 7. However, the basic-silicic composite nature of this sheet requires that these two magma types coexisted, possibly in a small magma chamber. As a result, there is a distinct possibility of isotopic exchange between the two magmas. Leshner (1990) has shown that when silicate magmas of different chemical and isotopic compositions are brought into contact, their equilibration is governed by the kinetics of diffusion, and that isotopic exchange

proceeds at a faster rate than chemical homogenization. It was also shown that Sr isotopes exhibit more rapid rates of equilibration than Nd isotopes (Leshner, 1990). Consequently, it should therefore be possible to contaminate a basic magma with radiogenic Sr, without concomitant elemental contamination or magmatic evolution (*i.e.* without increasing SiO₂ contents). In the case of the Rudh' a' Chromain composite sheet there has been some hybridization of the silicic and basaltic magmas. However, the high initial Sr isotope ratios of the basaltic facies (~0.7124), compared to ~0.720 within the central rhyolite, may be a consequence of Sr isotopic equilibrium between two coexisting magmas.

The possible derivation of partial melts from the Moine pelitic schists is in direct contrast to the genesis of many of the other granitic intrusions from the Mull Central Igneous Complex. Pankhurst *et al.* (1978) and Walsh *et al.* (1979) have demonstrated that the granitic intrusions associated with Centre 1 of the Mull Central Igneous Complex (*e.g.* Loch Uisg Granophyre, Early Acid Cone Sheets) resulted from the mixing between partial melts derived from the Lewisian amphibolite facies basement rocks, and magmas derived from the fractional crystallization of basalt. Similar explanations have been forwarded for the evolution of many of the major and minor silicic intrusions from the Skye Central Igneous Complex (*e.g.* Moorbath & Bell, 1965; Moorbath & Welke, 1969; Bell & Pankhurst, 1993).

5.4 Extreme Sr and Nd isotopic systematics : Crustal Contamination or Source Enrichment ?

The Sr and Nd isotopic compositions of MORB and OIB clearly demonstrate that the sub-oceanic mantle is isotopically heterogeneous (Section 5.1). This variation reflects its time-integrated evolution over the last 4.5 Ga in response to enrichment and depletion events. Such changes result from the migration of trace-element-enriched fluids and partial melts, and also to the re-cycling of crustal material at subduction zones (Bailey, 1982; Hart, 1988; Wilson, 1989; Weaver, 1991). As a result, it is to be expected that the sub-continental mantle is equally as heterogeneous. Direct evidence for this comes from the isotopic characteristics of mantle nodules brought to the surface in kimberlite diatremes (Menzies, 1983; Hawkesworth *et al.*, 1983, 1984).

Figure 5.1 shows that the isotopic data for many continental volcanic provinces overlaps considerably with MORB and OIB, whereas others extend well away from the Mantle Array. This has led to conflicting viewpoints concerning their origins, particularly for suites with radiogenic Sr and non-radiogenic Nd. Many studies have invoked crustal contamination processes to explain the high $^{87}\text{Sr}/^{86}\text{Sr}$ ratios (e.g. Thompson *et al.*, 1986; Petrini *et al.*, 1987). In contrast, Menzies (1983) and Hawkesworth *et al.* (1983, 1984) have argued that such ratios could develop over a comparatively short time scale in high Rb/Sr mantle xenoliths and, therefore, such ratios may be a characteristic of the mantle source region. It is therefore important to be able to distinguish between the production of high Sr and low Nd isotopic ratios in continental basalts via crustal contamination, and via partial melting of an enriched mantle source.

Petrini *et al.* (1987) have shown that the rare low- P_2O_5 - TiO_2 (LPT) basalts from the central and northern parts of the Paraná Flood Basalt Province have similar incompatible-element enriched characteristics and similar Sr-Nd isotope ratios to the dominant high- P_2O_5 - TiO_2 (HPT) basalts. In contrast, in the southern part of the region, where the LPT basalts dominate, they have less enriched trace-element signatures, and higher $^{87}\text{Sr}/^{86}\text{Sr}$, and lower $^{143}\text{Nd}/^{144}\text{Nd}$ ratios. If it is assumed that both LPT and HPT basalts with $^{87}\text{Sr}/^{86}\text{Sr}$ initial ratios of less than 0.706 are essentially uncontaminated (Petrini *et al.*, 1987; cf. Fodor, 1987), then the primary melts for the LPT and HPT basalts must have been derived from isotopically distinct sources. Additionally, this data suggests that it must have been possible to derive both the LPT and the HPT magmas from the same source (Wilson, 1989). It has therefore been suggested that the high $^{87}\text{Sr}/^{86}\text{Sr}$ ratios of the majority of the LPT magmas was derived through interaction with the continental crust (Petrini *et al.*, 1987).

From the above it is apparent that the TiO_2 content of continental basalts may therefore be a good indicator of crustal contamination. Crustal rocks and their partial melts are characterized by low TiO_2 contents, and therefore low TiO_2 in basalts may be an imprint of crustal contamination. However, it must be stressed that the precipitation of titanomagnetite can rapidly deplete magmas in TiO_2 . Taking this into consideration, the converse is that high- TiO_2 contents in basaltic magmas are unlikely to result from any form of crustal

contamination, and must therefore reflect derivation from enriched mantle sources.

Figure 5.10 shows a plot of $\epsilon^{58}\text{Nd}$ versus TiO_2/Yb for the LSSC magmas. Assuming that the fractionation of Fe-Ti oxides has not been important in the petrogenesis of a suite of basaltic rocks, the TiO_2/Yb ratio is likely to be a sensitive indicator of crustal contamination. During progressive upper crustal contamination, the Yb content of the basic magmas is likely to increase. The TiO_2 content of basalts contaminated with crustal material is likely to be low, as noted above. Therefore the lowest TiO_2/Yb ratios are likely to be linked with highly contaminated rocks. Source enrichment is more likely to produce rocks with high TiO_2 contents, therefore high TiO_2/Yb ratios. ϵ_{Nd} also decreases with progressive crustal contamination. The Group I data define a trend of decreasing $\epsilon^{58}\text{Nd}$ coupled with low TiO_2/Yb , consistent with a crustal contamination theory. The Group II and III magmas also have low TiO_2/Yb and low $\epsilon^{58}\text{Nd}$ which is also consistent with their derivation mainly via crustal anatexis.

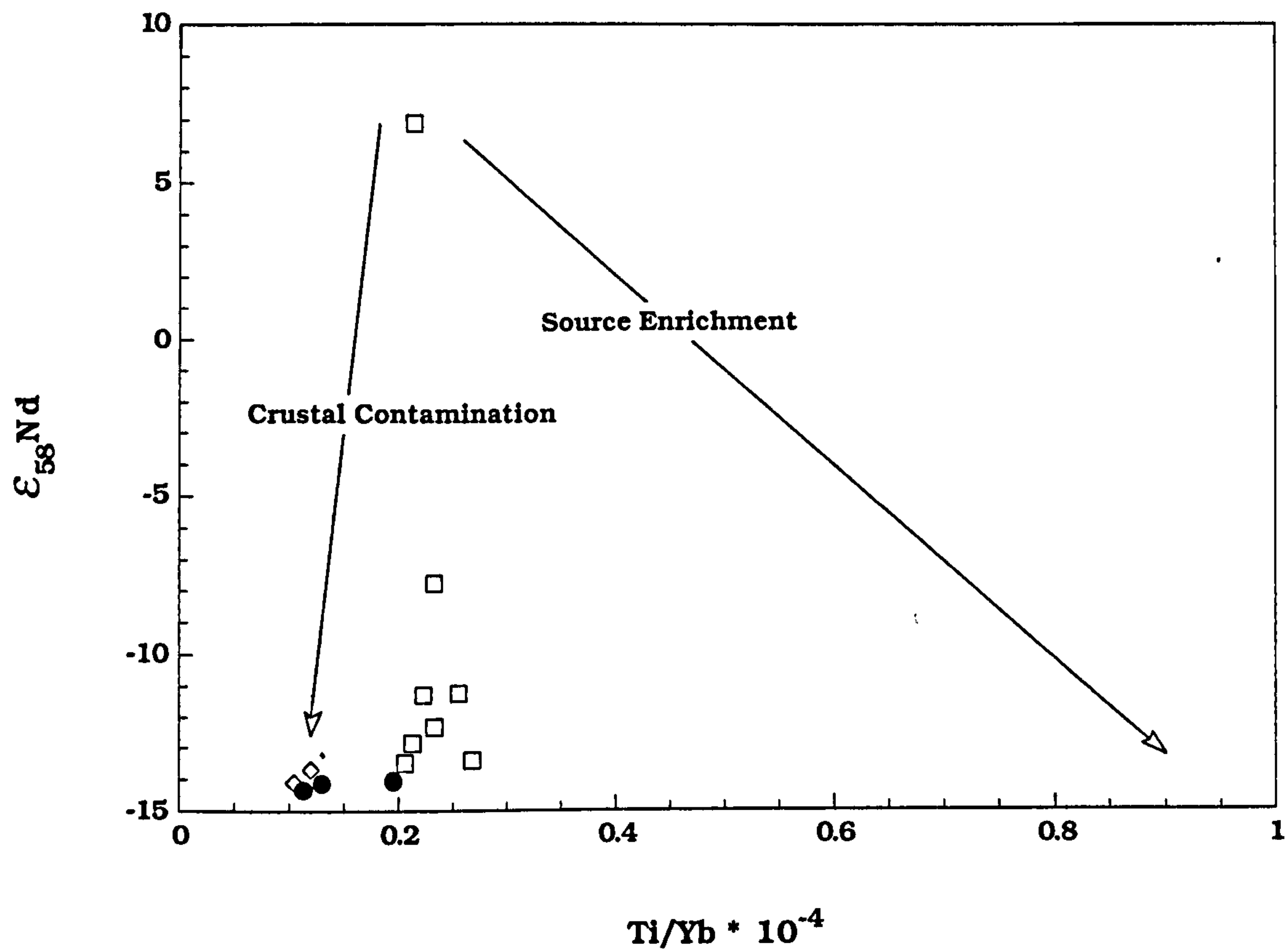


FIGURE 5.10 Variation of $\epsilon_{58}\text{Nd}$ with Ti/Yb for the LSSC. Graph shows that the variation seen in Group I magmas is more likely to be due to variable crustal contamination, rather than partial melting of a variably enriched mantle source.

5.5 Conclusions

The Sr and Nd isotope data for the LSSC provide perhaps the best constraints on the magmatic processes responsible for the intra-suite compositional variation. The relatively extreme ϵ_{Sr} and ϵ_{Nd} of the basic rocks suggests that crustal contamination played a very important role in their petrogenesis. The high ϵ_{Sr} especially, and low ϵ_{Nd} of the most contaminated Group I rocks suggests that the contaminant was upper crustal rocks. Since both ϵ_{Sr} and ϵ_{Nd} are correlated with degree of fractionation, it is considered likely that the basic magmas evolved via a combined process of crystal fractionation and crustal contamination. The isotope data also lend support to the theory that the Group III rhyolites are the direct result of crustal anatexis, and that these melts mixed with small amounts of basic magma (10-20%) to produce the Group II intermediate rocks. The high ϵ_{Sr} and low ϵ_{Nd} of the rhyolites is consistent with their derivation from *upper* crustal lithologies. This, coupled with their peraluminous nature (Chapter 3), and trace-element characteristics (Chapter 4), suggests that Moine pelitic schists represent a possible source for the silicic magmas.

CHAPTER 6

CHEMICAL VARIATIONS WITHIN INDIVIDUAL SHEETS

Several of the larger sheets, namely those at Port Mor, Traigh Bhàn na Sgurra, and the composite sheet at Rudh' a' Chromain (*Figure 1.2*), have been sampled in detail, with sample traverses being collected through the sheets from base to top. Sample traverses were collected away from any concentrations of xenoliths. These sheets were examined to assess the relative significance of processes such as *in situ* contamination, magma mixing, and *in situ* differentiation.

6.1 Port Mor

The sheet at Port Mor is intruded into amygdaloidal basalt lavas on the south shore of Loch Scridain [NM 435239]. The sheet is approximately 4m thick, and dips at a shallow angle to the south. The top surface is highly xenolithic, with concentrations of both quartzitic and aluminous xenoliths occurring along the entire length of the exposure (see map in *Figure 6.1*). Six bulk samples have been collected from the base to the 'top'. The top contact with the lavas is very poorly exposed and has not been sampled. The Port Mor sheet shows considerable chemical variation from base to top, in terms of major- and trace-elements and isotope geochemistry. *Figures 6.2a-h* illustrate the variation of the major- elements, and selected trace-elements as a function of distance from the base of the sheet. These plots display a marked asymmetry for many elements; the base and, to a lesser extent, the top, being significantly enriched in CaO, MgO, Cr, V and Ni. The less-evolved compositions at the margins of the sheet could be explained in terms of: (i) the presence of chilled margins preserving true liquid compositions; (ii) differences in the modal mineralogy from base to centre due to some sort of differentiation process; and/or (iii) a multiple intrusive event. *Figure 6.3* shows three photomicrographs of the two margins and the centre of the Port Mor sheet. These photomicrographs clearly show that there is both a increase in grain-size from the margins to the centre of the sheet, and a change in the modal mineralogy, the centre being richer in plagioclase, and the margins richer in clinopyroxene. They also show that the margins have a texture which indicates more rapid crystallization, shown in

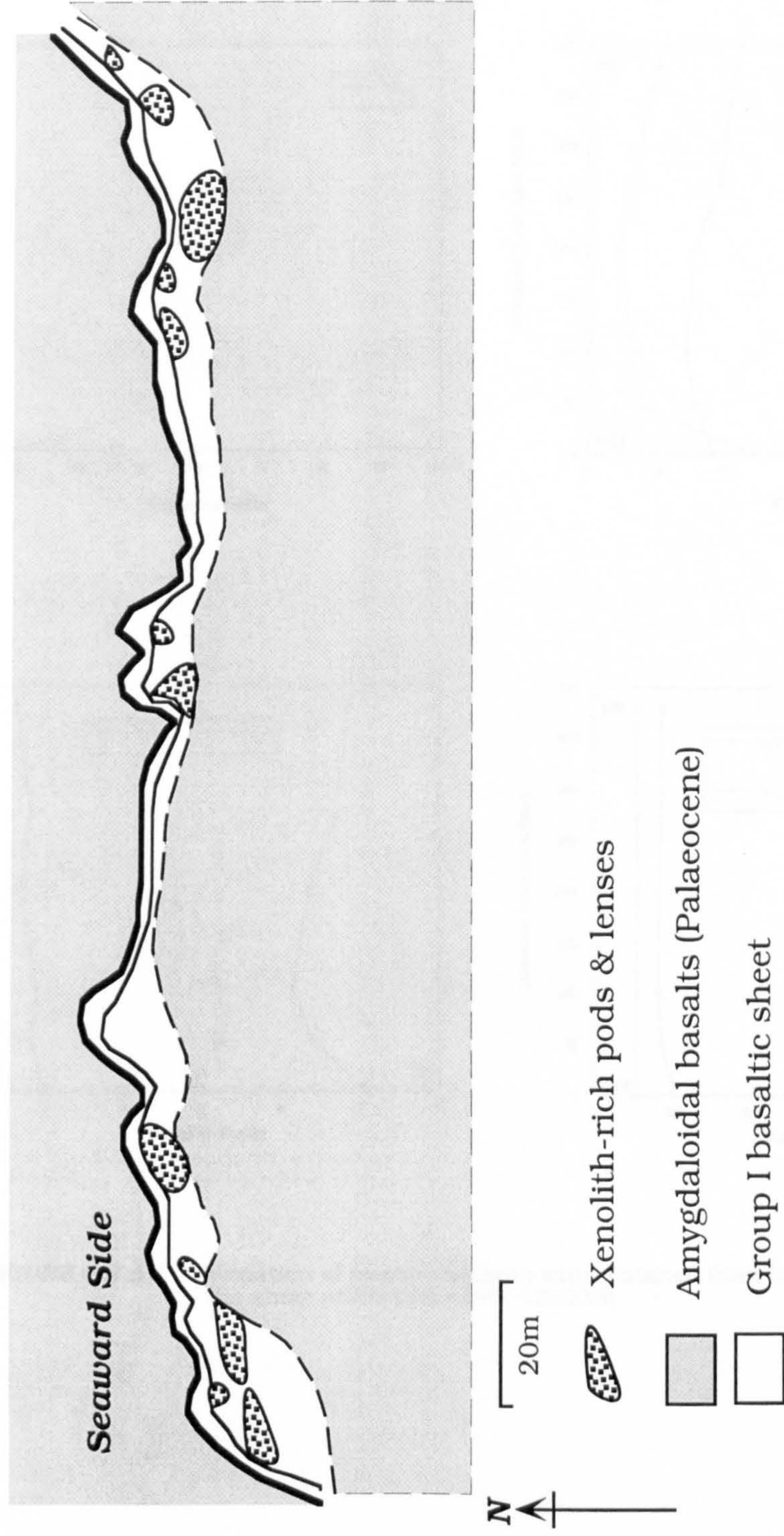


FIGURE 6.1 Geological sketch-map of the Group I basaltic sheet at Port Mor [NM435239]. Sheet is intruded into Palaeocene amygdaloidal basalts as shown, and contains numerous aluminous and siliceous crustal xenoliths, which occur in pods and lenses on the top surface of the sheet.

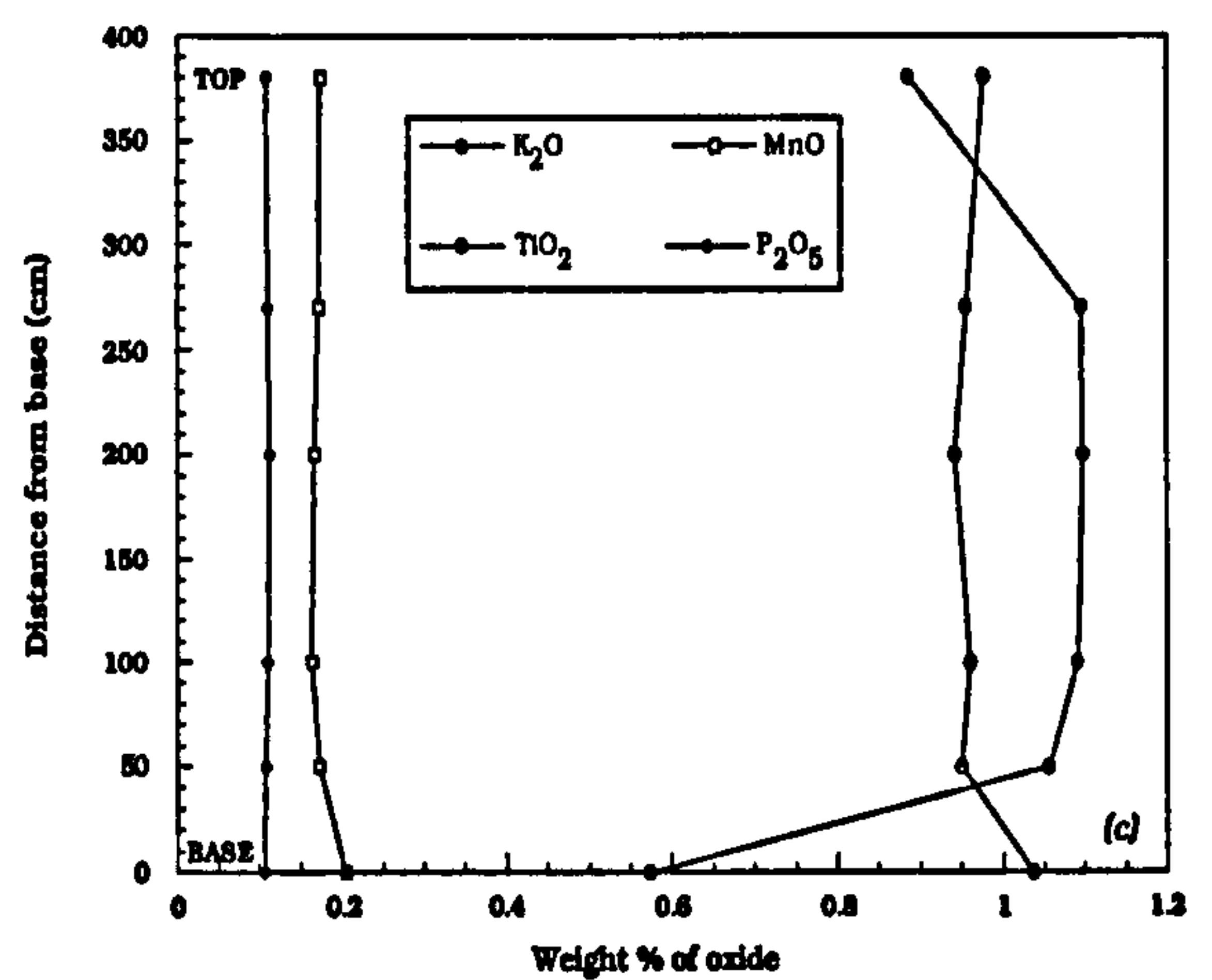
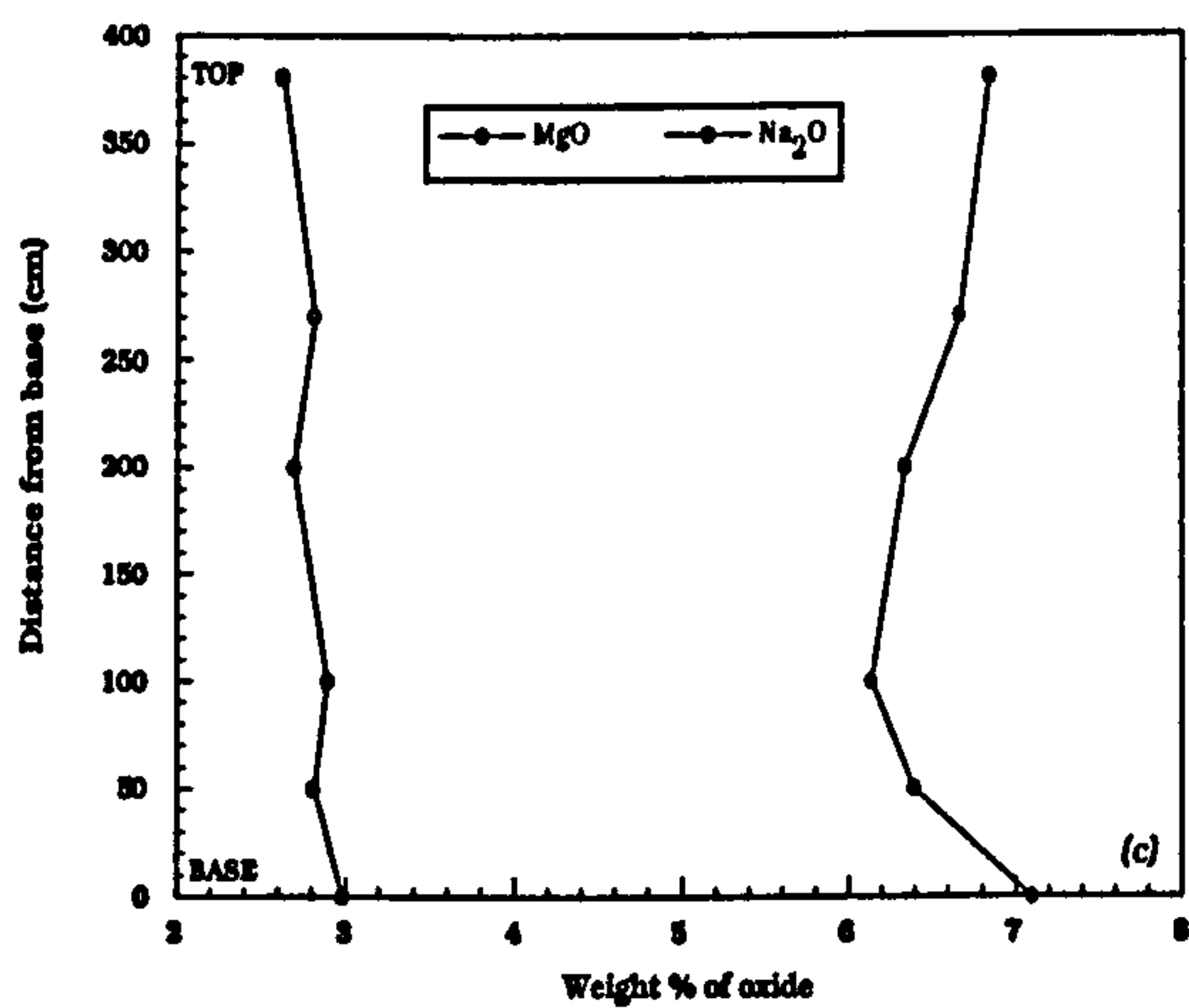
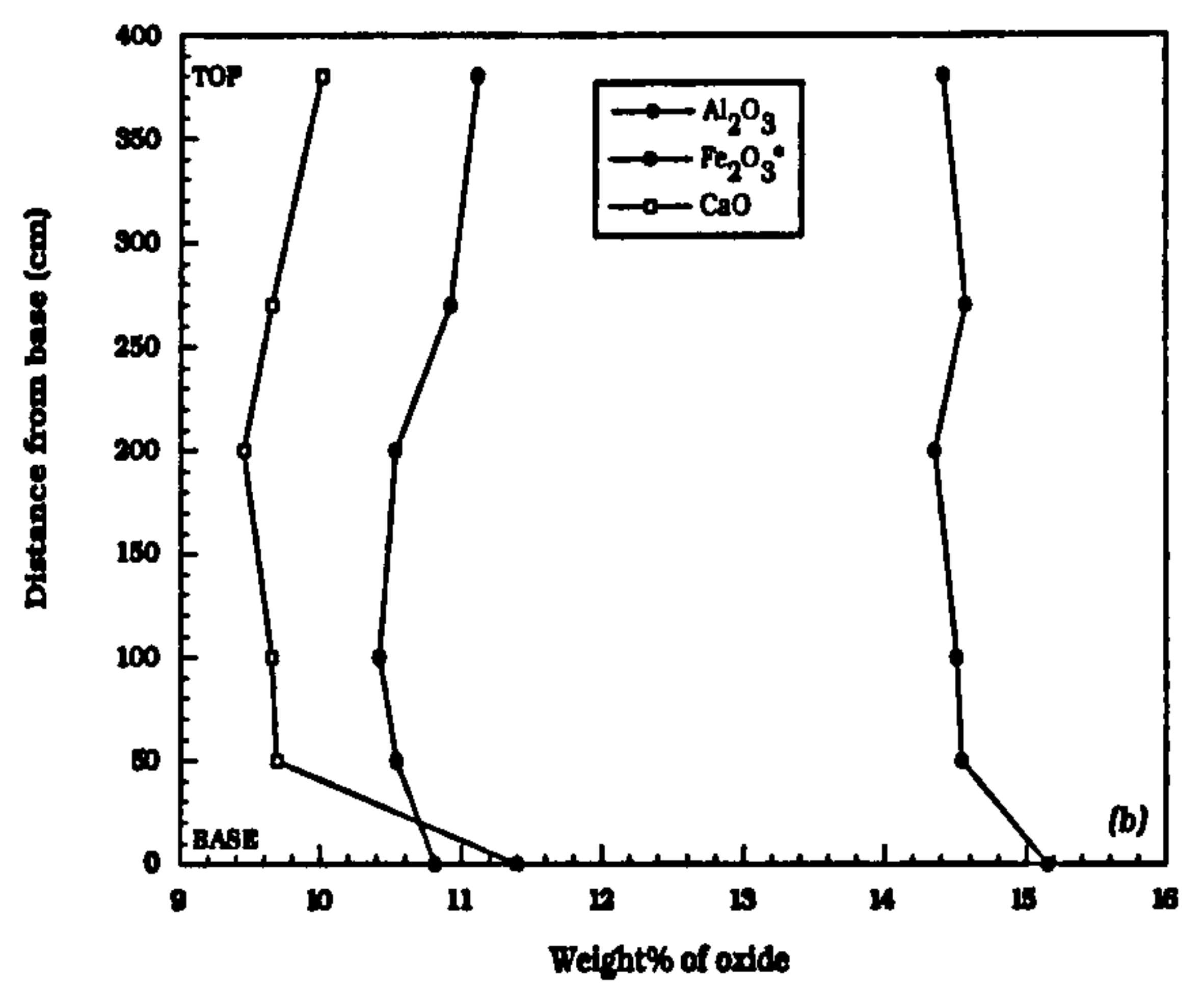
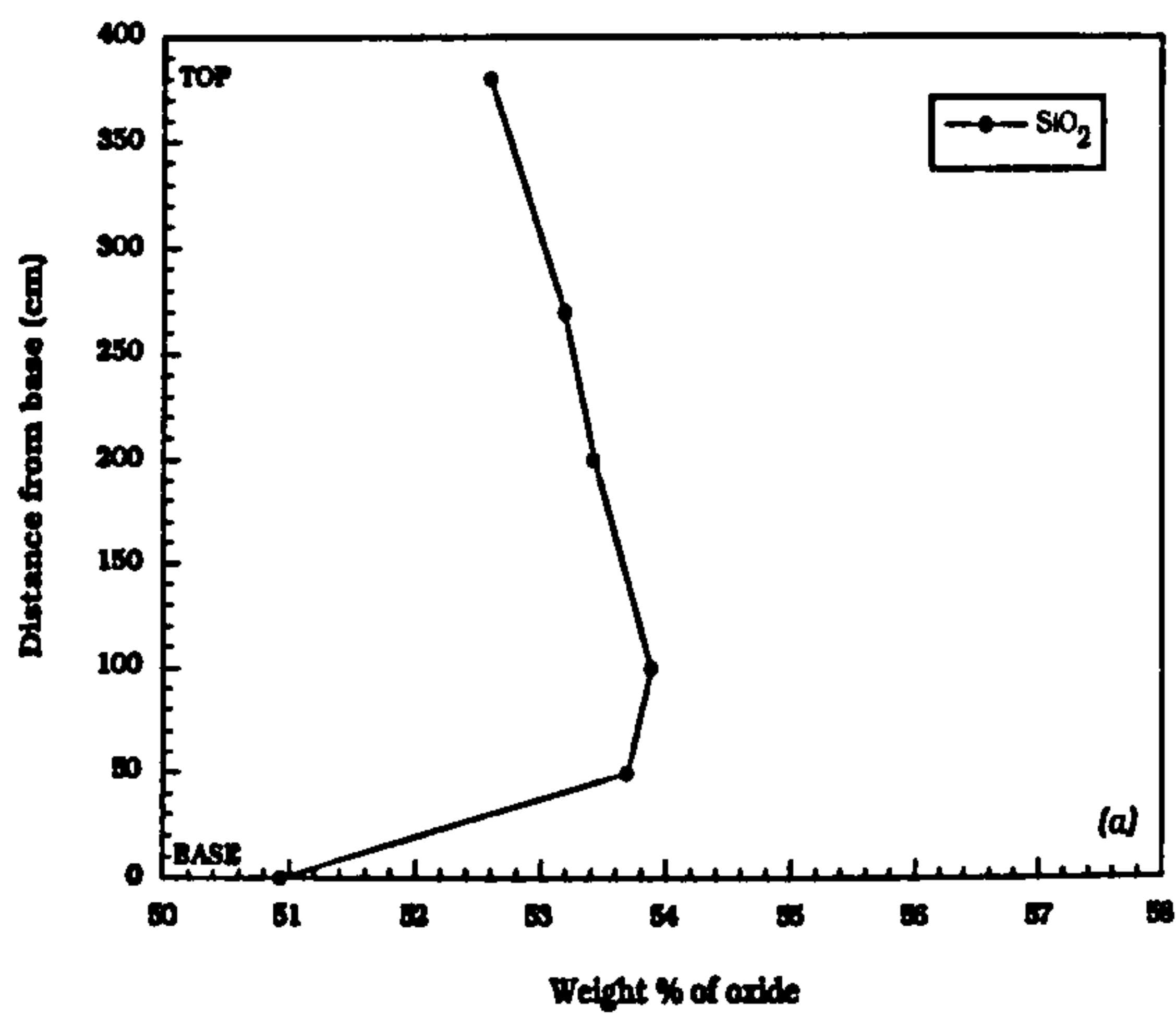


FIGURE 6.2 a-d Variation of major-elements with distance from the base of the sheet at Port Mor [NM 435239].

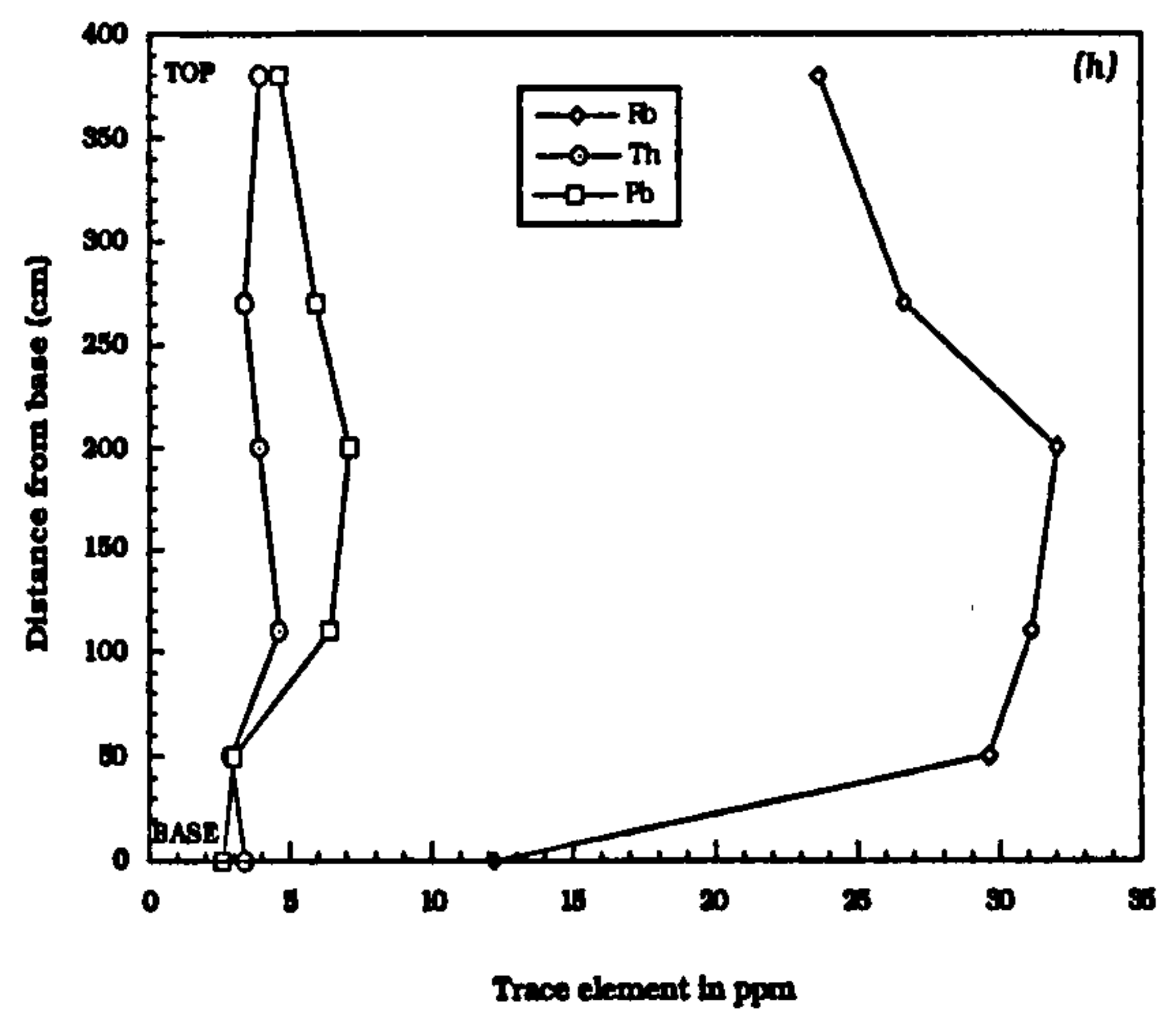
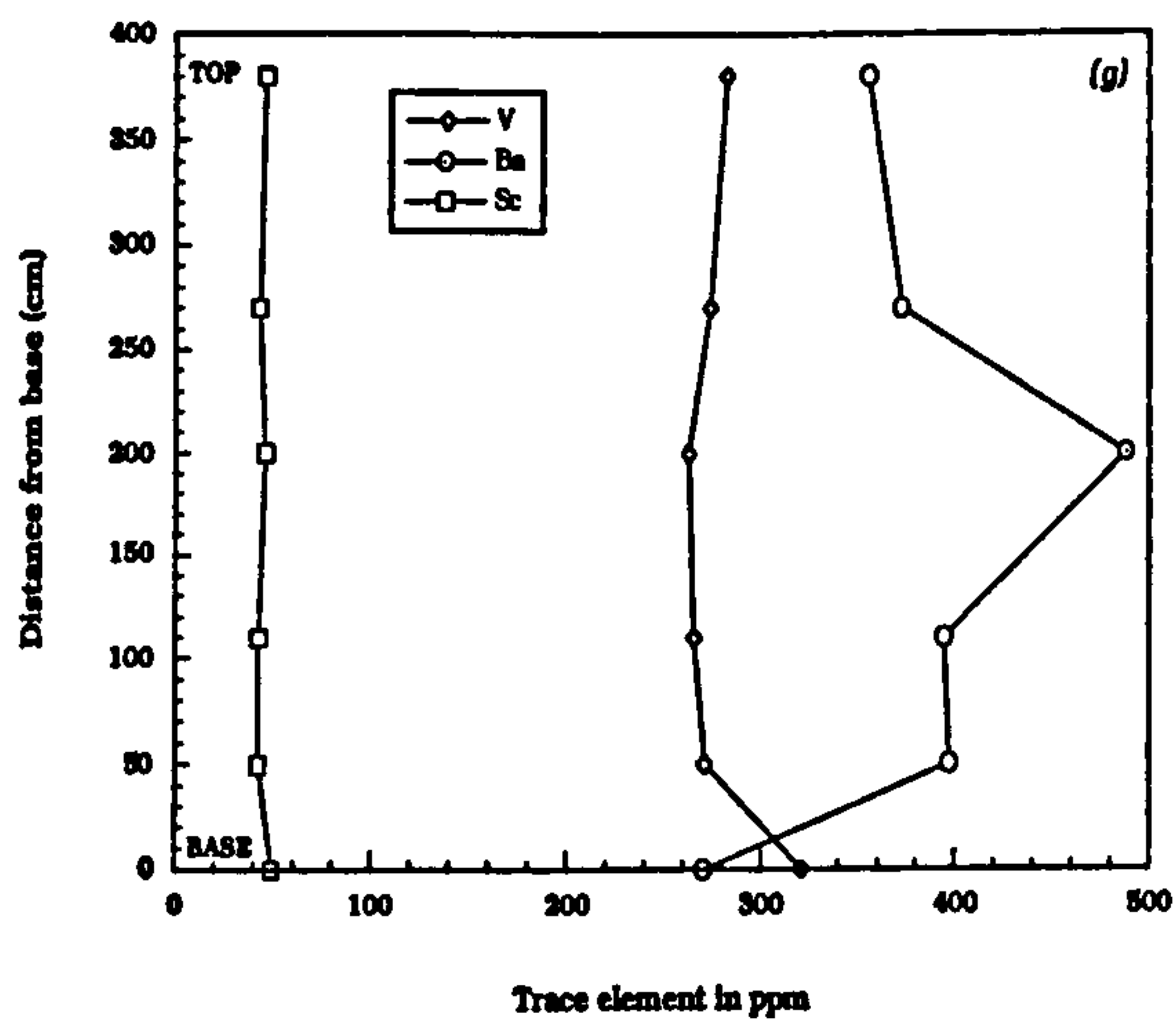
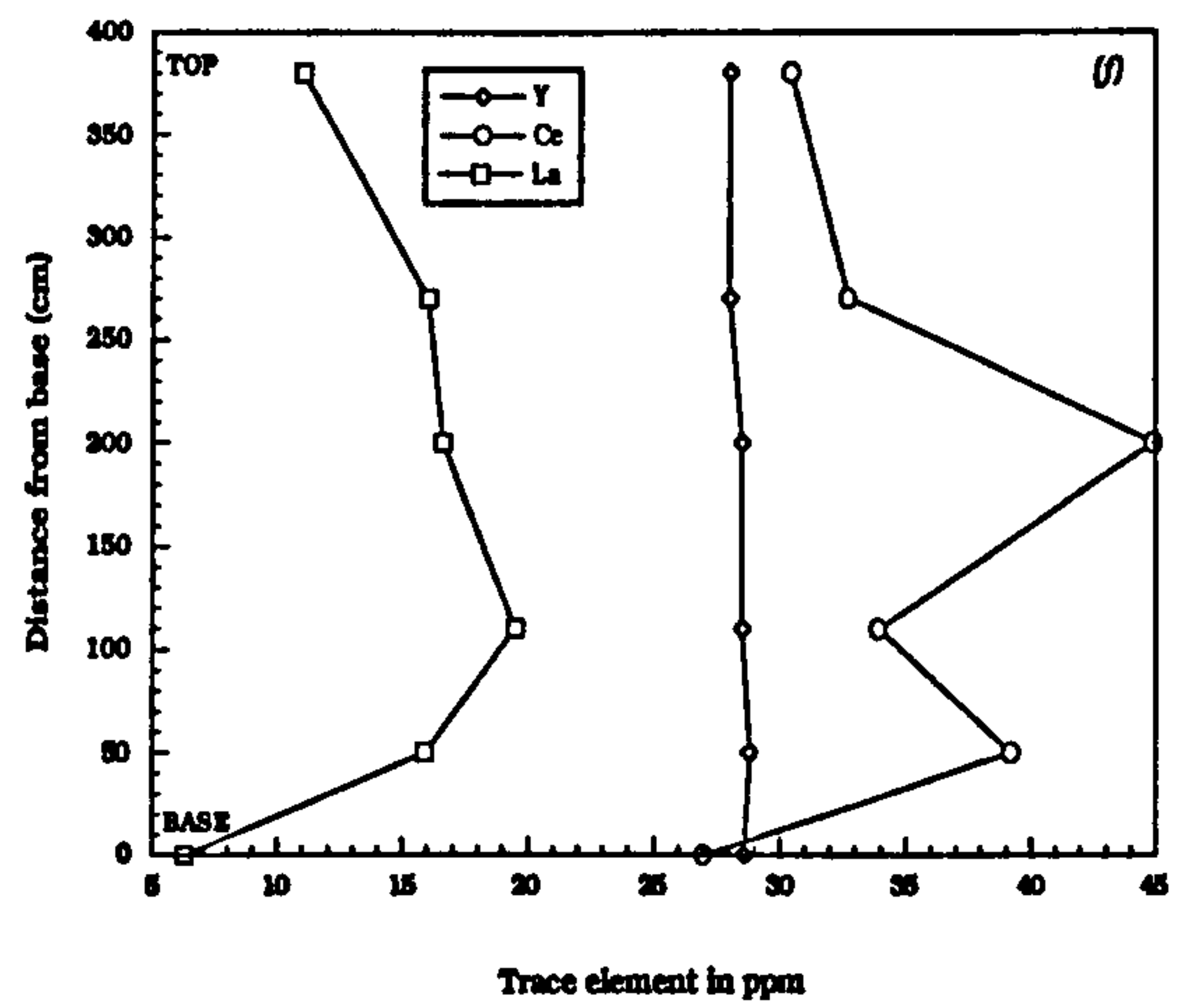
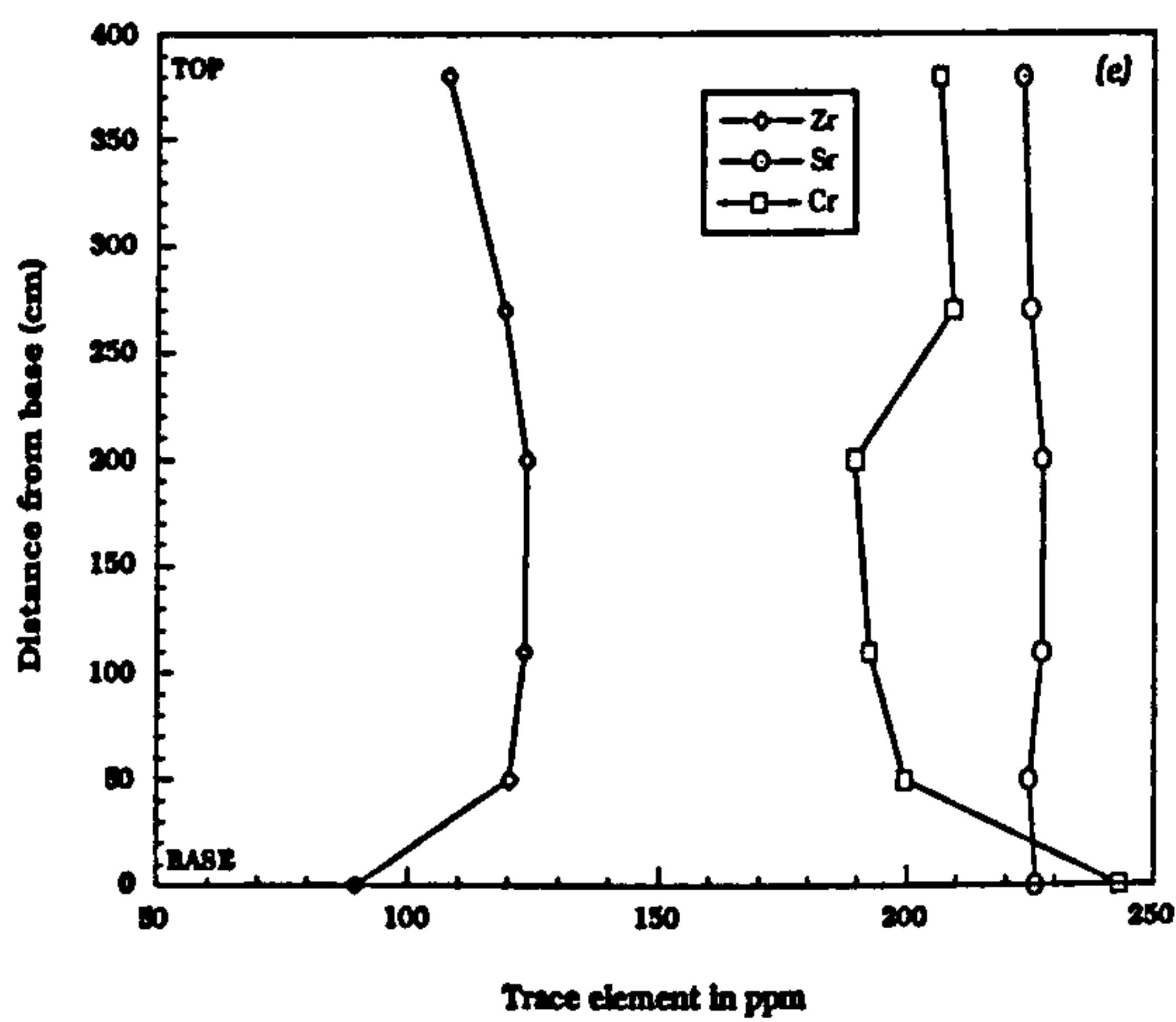


FIGURE 6.2 e-h Variation of trace-elements with distance from the base of the sheet at Port Mor [NM 435239].

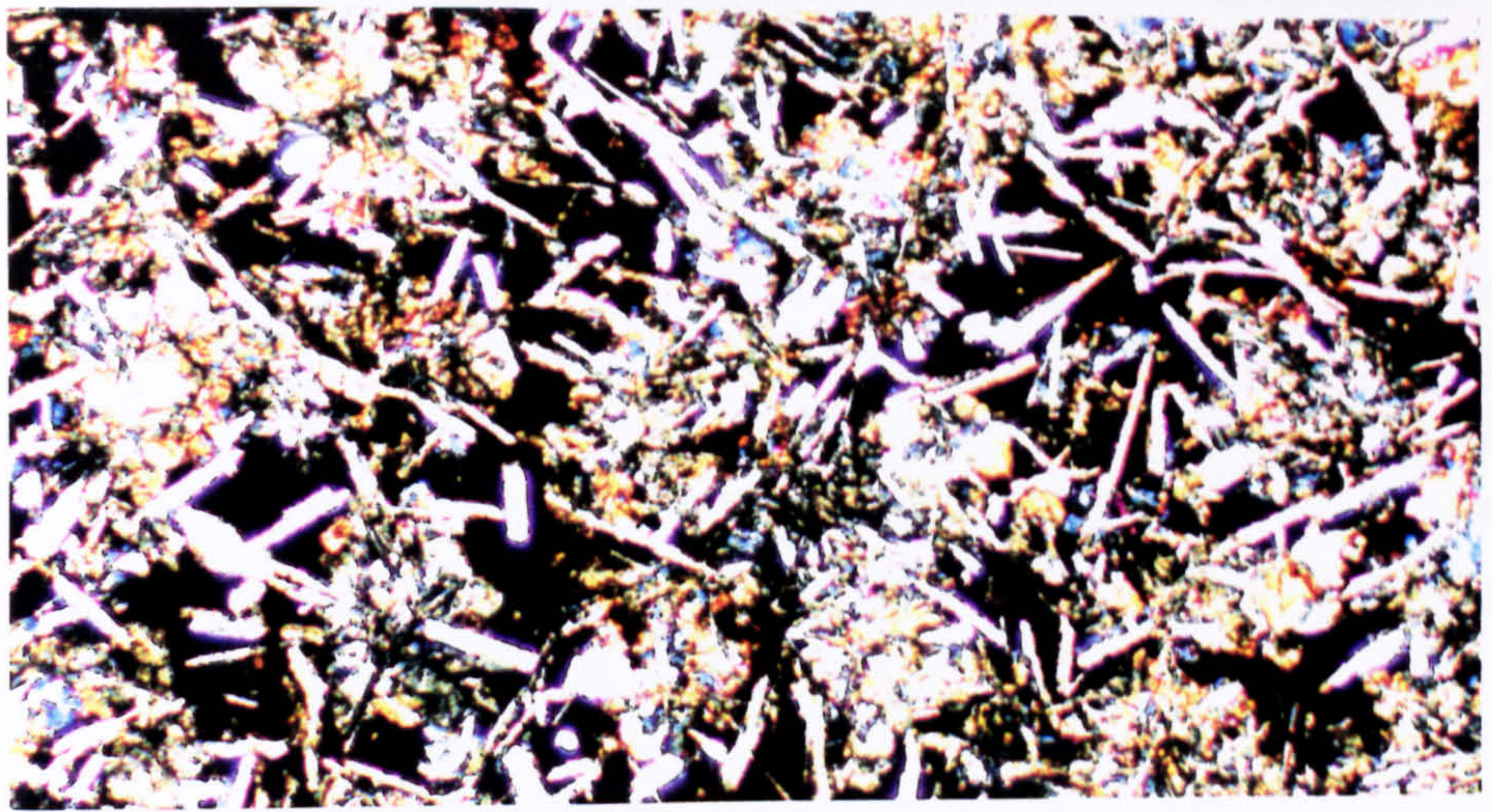


FIGURE 6.3a Sample PM+380 from the top of the Group I basaltic sheet at Port Mor [NM435239]. Fine grained plagioclase needles with poorly developed sub-ophitic clinopyroxene. Clinopyroxene is more typically granular in nature. Specimen has abundant mesostasis, which is occasionally altered to chlorite. (xpl; Field of view 2x3mm)

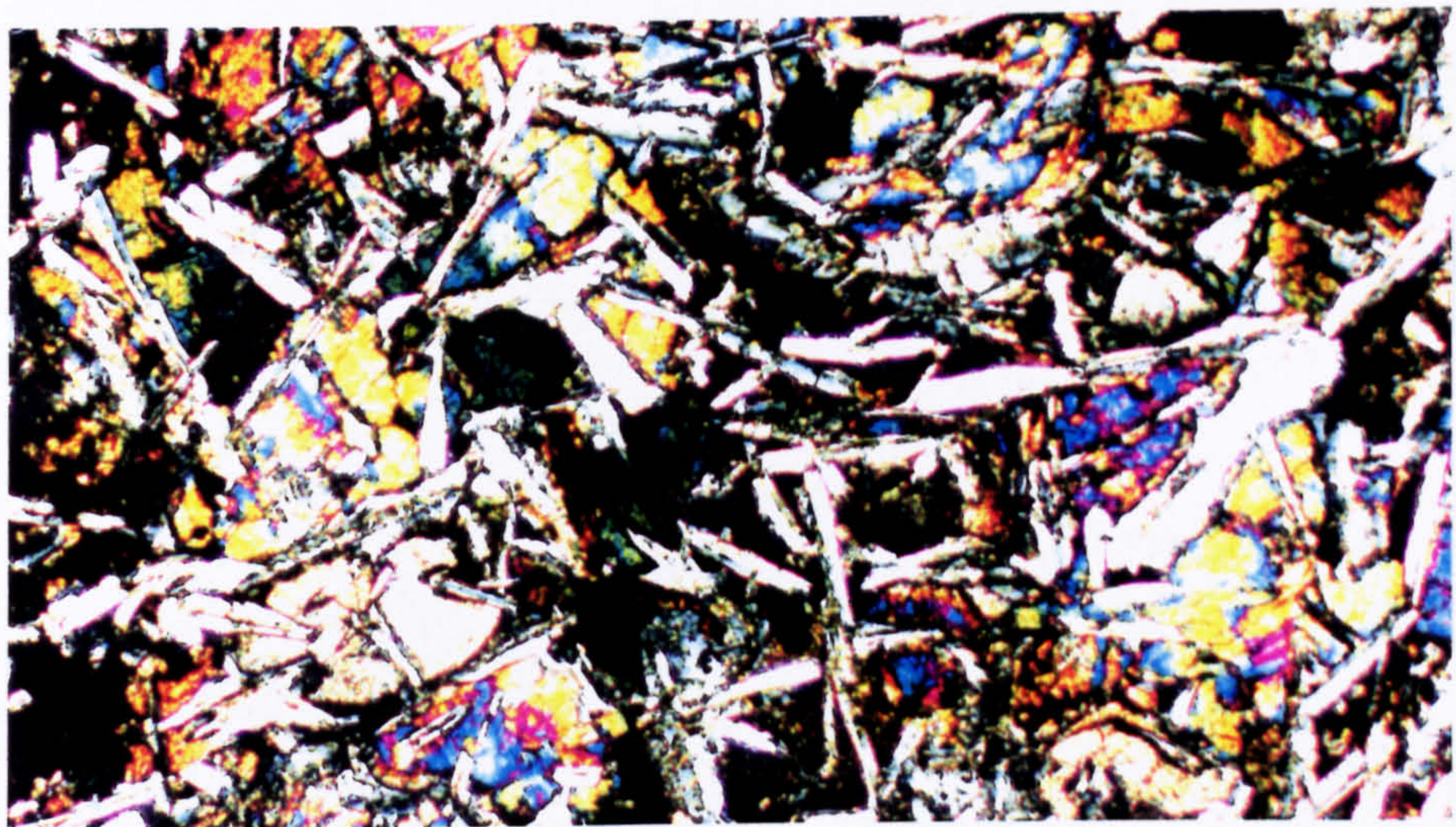


FIGURE 6.3b Sample PM+200 from the centre of the Port Mor sheet. Coarser grained plagioclase with well developed sub-ophitic clinopyroxene. (xpl; Field of view 2x3mm).

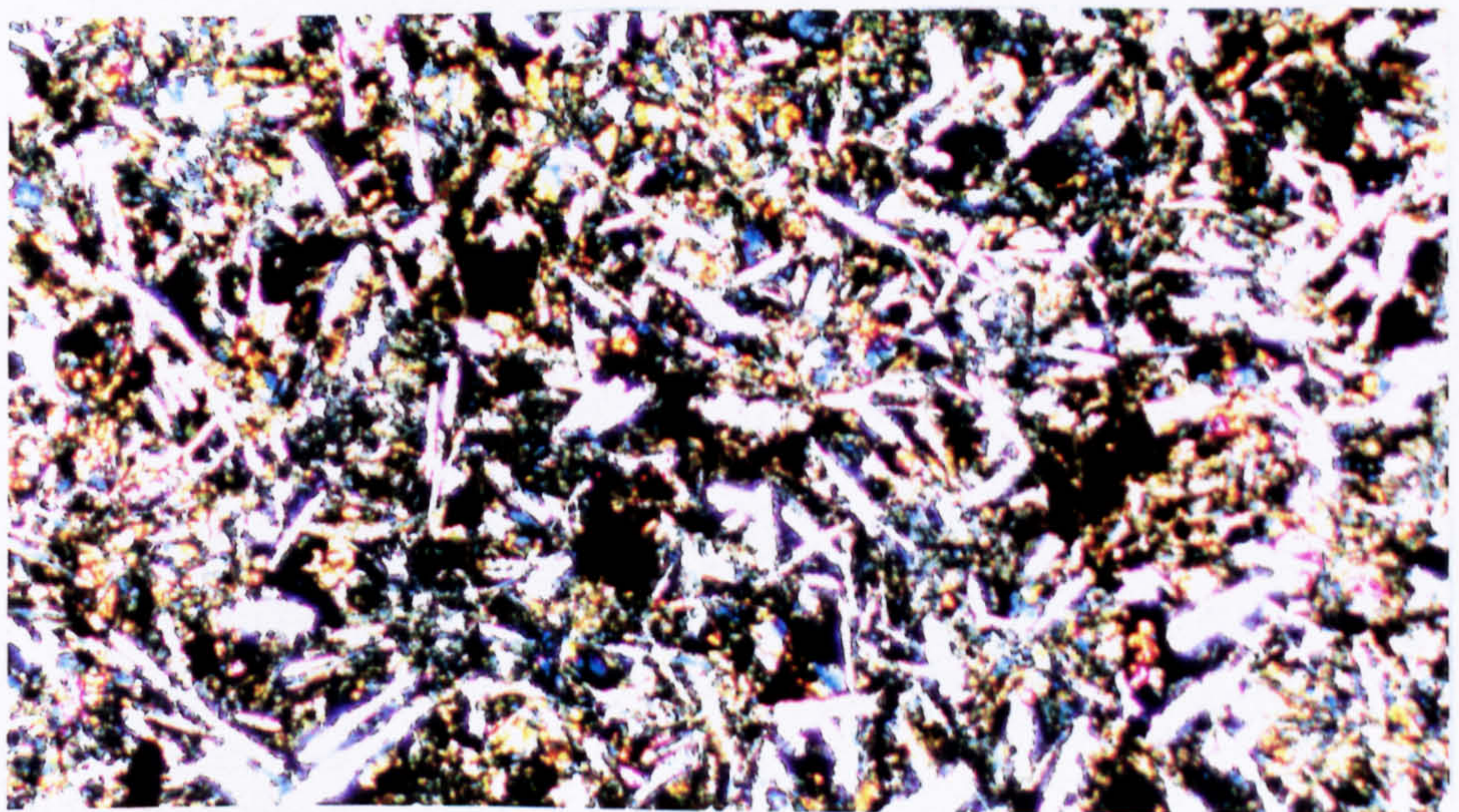


FIGURE 6.3c Sample PMBASE from the base of the Port Mor sheet. Very fine grained plagioclase and granular clinopyroxene. (xpl; Field of view 2x3mm)

particular by the dendritic crystals of clinopyroxene (*cf.* Lofgren, 1974). The centre of the sheet displays a sub-ophitic to ophitic relationship between plagioclase and clinopyroxene. *Table 6.1* details the modal percentages of plagioclase, clinopyroxene and Fe-Ti oxides as determined by image analysis on a scanning electron microscope (see Appendix I for details of the technique).

Sample	Plagioclase	Clinopyroxene	Fe-Ti Oxides	Mesostasis
PM+380	62.1	26.7	4.4	6.8
PM+200	69.1	24.4	4.0	2.5
PMBASE	63.4	27.8	4.1	4.4

Table 6.1. Modal mineralogy of three samples from the Port Mor sheet. Values are the means of five measurements taken on each slide. PMBASE = Base of sheet, PM+200 = 200cm from base, PM+380 = 380cm from base.

The centre of the sheet contains significantly more plagioclase, and less clinopyroxene and mesostasis than either of the margins, consistent with a more slowly cooled interior.

Electron probe micro-analyses indicate that no significant variation in the composition of either the plagioclase or the clinopyroxene occurs throughout the sheet (Mineral analyses of clinopyroxene and plagioclase from the Port Mor sheet can be found in Appendix IV). All thin sections reveal only one or two small phenocrysts/xenocrysts of plagioclase. This, coupled with the textures displayed by the various samples, implies that the plagioclase and pyroxene essentially crystallized *in situ*, after intrusion. It seems unlikely therefore, that the variation in bulk-rock geochemistry seen in the Port Mor sheet is due to a differentiation process, either *in situ*, or during emplacement (*i.e.* gravitational settling or flow differentiation; *cf.* Simkin, 1967; Gibb, 1968).

Initial Sr and Nd isotope compositions show considerable variation from the centre to the margin of the sheet. The centre of the sheet has a higher initial strontium isotope ratio of 0.710796, relative to a value of 0.708464 from the base (Data given in Appendix III). The initial

neodymium isotope ratios are not as variable, with the centre of the sheet having a $^{143}\text{Nd}/^{144}\text{Nd}_i$ value of 0.511906, compared with 0.511979 for the base of the sheet. The centre of the sheet is also significantly more LREE-enriched than the marginal facies, as shown in *Figure 6.4*. The centre of the sheet has a normalized Ce/Yb ratio of 3.54, compared with a value of 2.39 for the base of the sheet. These data preclude the chilled marginal rocks from simply representing true liquid compositions which crystallized to give the centre of the sheet, as if this was the case, the initial Sr/Nd isotope values and the REE profiles would be identical throughout the sheet.

Having previously discounted a differentiation process to explain the variation in composition seen through the sheet, it is suggested that the sheet, as it is now seen, was intruded over a period of time. Since no internal boundaries are present, and cooling joints run from the base to the top of the sheet, it is envisaged that the first magma intruded chilled against the country rocks and had the least radiogenic strontium isotope signature. Subsequently, magma which was somewhat more evolved and with a higher initial strontium isotopic ratio was emplaced whilst the initial magma was still relatively hot and fluid, thus explaining the lack of internal discontinuities within the sheet. The data is consistent with the theory that regionally available basaltic magma ponded within a magma chamber or sill complex, and evolved via a process of combined fractional crystallization and assimilation (AFC; DePaolo, 1981) prior to an extended period of intrusion (Buist, 1961). Since the crustal xenoliths in the Port Mor sheet are all concentrated within the top portion of the intrusion, it is suggested that the initial intrusion was forceful and turbulent resulting in wall-rock xenolith being carried to the site of emplacement. Later magma pulses may have passed through the conduits with a more laminar flow due to the lining of the conduit walls with semi-crystallized magma.

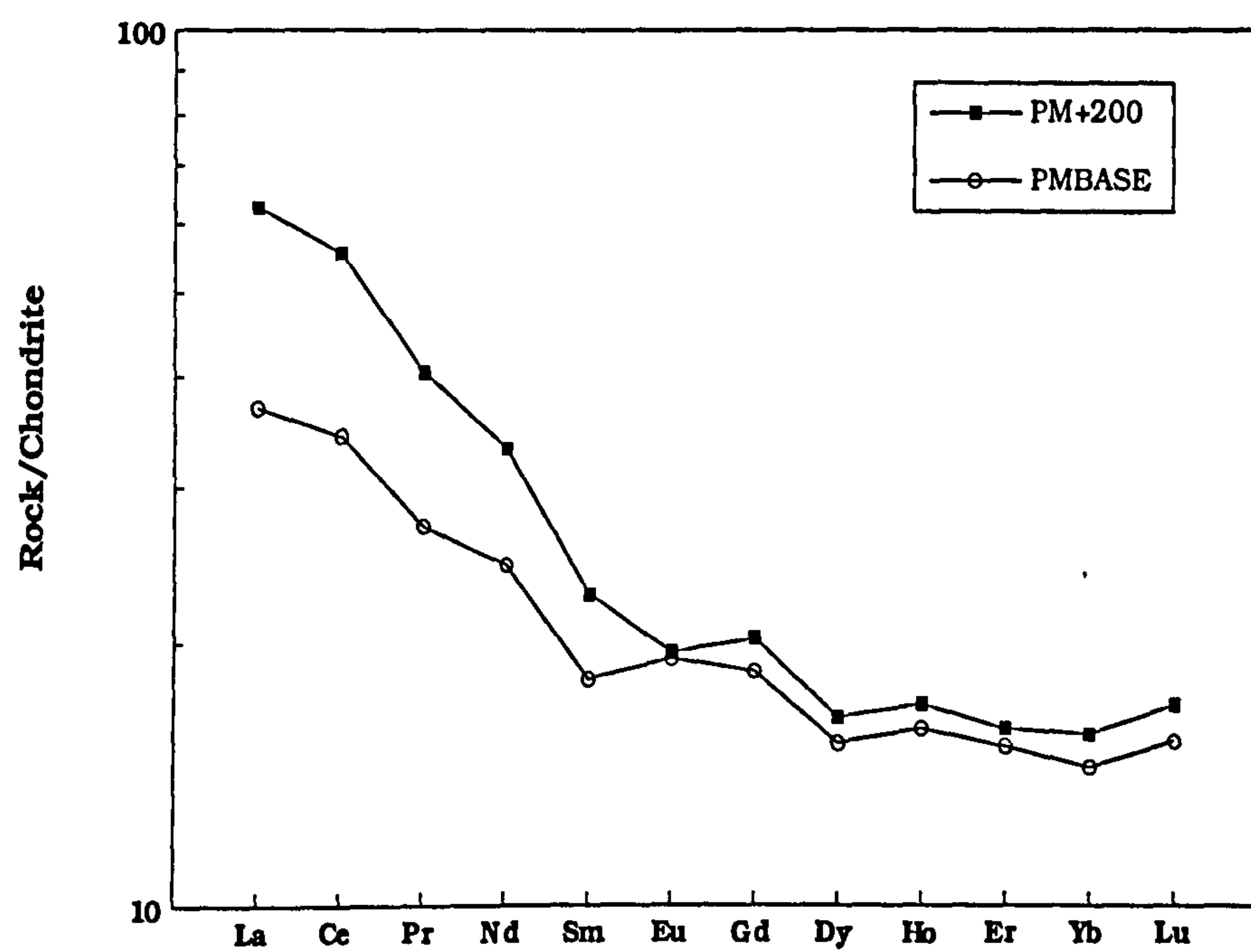


FIGURE 6.4 Chondrite normalized REE profiles for the base and centre of the Port Mor sheet.

6.2 Rudh' a' Chromain

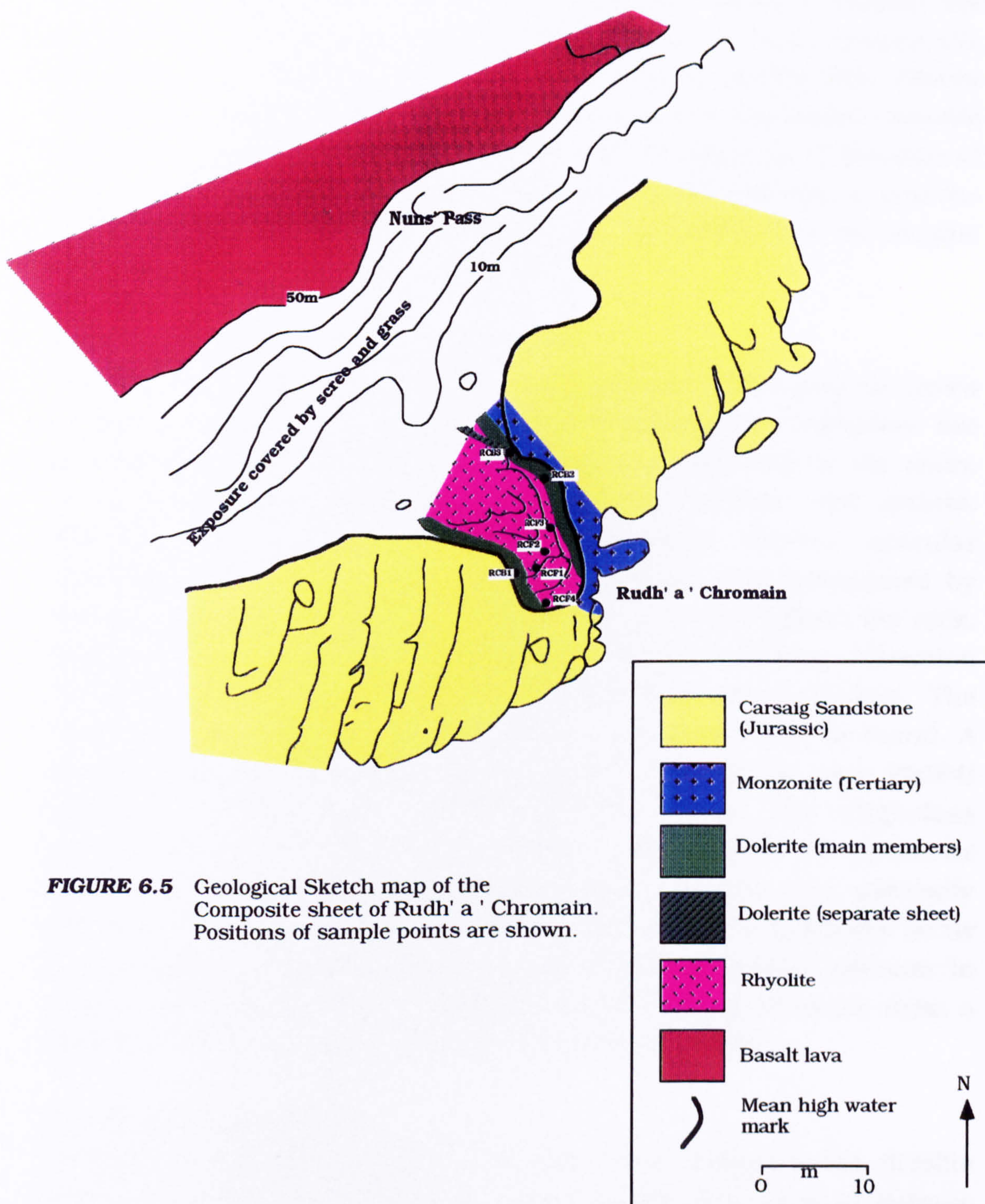
The sheet at Rudh' a' Chromain is situated about 2.5km south-west of Carsaig on the south coast of the Ross of Mull (*Figure 1.2*), and forms a low headland [NM 521202]. The sheet is intruded into the Carsaig Sandstone (Middle Lias) at its lower surface, with the upper surface being in contact with an earlier intrusion of monzonite, against which the sheet has chilled. The sheet is 14 metres thick and is composite in nature, comprising a central portion of grey rhyolite (~ 9m), bounded by tholeiitic basalt at each margin (Bailey *et al.*, 1924; Buist, 1961). There are no internal discontinuities, the basalt grading into rhyolite over a broad zone (3m) of hybridization. The sheet is highly xenolithic, containing both crustal xenoliths (quartzites, sandstones and mullite buchites), and gabbroic xenoliths. The field relationships and petrography of the separate units have been described by Thomas (1922), Bailey *et al.* (1924), and Buist (1961). Petrographic descriptions, a map, and seven new full chemical analyses are presented here.

Figure 6.5 is a geological sketch map of the Rudh' a' Chromain promontory showing the field relationships of the various components of the sheet, as well as the position of a separate tholeiite sheet described by Buist (1961). Also shown are the positions of the sample points, and of some of the xenoliths. The sheet dips at approximately 15° to the north-east, with the emplacement of the sheet probably being guided by the earlier monzonite intrusion (Buist, 1958, 1961).

Petrography

(a) Upper & Lower Tholeiites (RCB1, RCB2)

Mineral analyses of plagioclase, pyroxene and magnetite are presented in *Appendix IV*. The tholeiites are composed of laths of plagioclase (~An₆₀) of average length 0.08mm, together with grains of augite (~Wo₃₇En₄₈Fs₁₅), some of which have developed as elongate, feathery crystals up to 2mm in length. Magnetite forms small octahedra and ragged grains, and is found associated with the pyroxene. Interstitial glass is generally replaced by fine, brown chloritic material, and occasional calcite. Small phenocrysts of plagioclase (1.5cm) occur sporadically throughout the rock. Some plagioclase phenocrysts have a strongly resorbed, rounded outline and display good oscillatory zoning



(An₇₀-An₈₄) Other phenocrysts form well-defined laths and show little zoning (~An₆₄). This bi-modal distribution of plagioclase phenocrysts has been noted in other members of the LSSC Group I basalts; the resorbed, more calcic crystals are interpreted as being xenocrystic (see Chapter 2). The rock contains small vesicles, chiefly with chlorite or calcite. A section through the chilled margin of the upper tholeiite shows that the basalt has quenched to a brown glass for a distance of several cm. This glass now contains numerous tiny microlites, and the occasional microphenocryst of plagioclase, indicating that the magma contained crystals before emplacement.

(b) Central Rhyolite (RCF1, RCF2, RCF3)

The central portion of the sheet is composed of a pale grey to brown rhyolite. Analyses of groundmass and phenocryst feldspars are presented in Table 6.3. The central rhyolite is composed, in the main, of an intergrowth of oligoclase (~An₂₅), orthoclase, and quartz. Alteration to chlorite and sericite is common. Narrow, acicular pyroxene occurs, but it is generally completely pseudomorphed by chlorite. Sporadic phenocrysts of oligoclase occur throughout the rock, and form laths up to 2mm long showing Carlsbad twinning. Alteration of these phenocrysts to calcite and epidote is characteristic. The occasional microphenocryst of apatite and zircon can also be found. A distinctly porphyritic facies occurs next to the hybrid zone (RCF4) adjacent to the upper tholeiite (RCF3). Here, the oligoclase phenocrysts reach 3-4mm in length. Phenocrysts of pyroxene (pigeonite; Buist, 1961) also occur; these, however, are generally pseudomorphed by chlorite and calcite. Aggregates of magnetite occur in association with the pyroxene. The rhyolite is locally vitreous in nature, and, similar to the porphyritic dacites (Group II) of the area, a distinct "sheath and core" structure has been developed.

(c) Hybrid Rhyolite (RCF4)

Towards the margins with the upper and lower tholeiites, the rhyolite grades gradually over about 1m into a darker grey rock of definite hybrid character. It is essentially similar to the 'normal' rhyolite, but contains more in the way of acicular pyroxene (now pseudomorphed). The groundmass feldspar is also elongate, with sharp terminations. Interstitial material consists of orthoclase, quartz and calcite. Phenocrysts of oligoclase and pseudomorphed pyroxene are also

present. Blebs of unmixed basalt can be found throughout the hybrid zone, attesting to its mixed nature.

(d) Separate Tholeiite Sheet (RCB3)

The separate tholeiite sheet, which cuts the upper portion of the composite sheet, is of distinctly finer grain size than the tholeiites of the main sheet. It is composed of tiny laths and needles of plagioclase, along with granules and more elongate grains of colourless augite. There is less in the way of interstitial material, but where present, it is composed of chlorite and calcite. No phenocrysts are present.

Geochemistry and Petrogenesis

Table 6.2 contains the full major-, trace-element and REE data of the seven samples collected from the Rudh' a' Chromain sheet, and *Table 6.3* lists the initial Sr and Nd isotope data for the upper and lower tholeiites, two samples of the central rhyolite, and a hybrid rock. The tholeiites (RCB1, RCB2 and RCB3) are all basaltic andesites of Group I type, and are essentially geochemically inseparable. They are all LREE-enriched, with normalized Ce/Yb ratios of the order of 3.9, and have high initial strontium isotope values at 0.7123-0.7126. The rhyolite does, however, show some compositional variation, both in terms of major- and trace-elements, and in initial Sr and Nd isotope values. Initial strontium isotope ratios for the central rhyolite vary from 0.7176 to 0.7191. The hybrid rock grades compositionally between the tholeiite and the rhyolite. *Figures 6.6a-h* show the major- and trace-element profiles through the sheet. The plots have obvious C- and D-shaped profiles; however, it is considered likely that with a more comprehensive sampling program, the profiles would be smoother through the hybrid zone.

SAMPLE	-----THOLEIITES-----			-----RHYOLITES-----			HYBRID
	Upper RCB1	Lower RCB2	Separate RCB3	RCF1	RCF2	RCF3	RCF4
SiO ₂	54.06	54.31	54.41	70.13	70.38	71.61	65.95
TiO ₂	1.16	1.18	1.18	0.73	0.73	0.71	0.80
Al ₂ O ₃	14.29	14.34	14.54	12.17	12.19	12.24	12.34
Fe ₂ O ₃ *	11.62	11.57	11.68	5.26	5.52	5.04	6.63
MnO	0.18	0.17	0.17	0.09	0.05	0.03	0.09
MgO	5.06	5.22	4.91	0.68	0.80	0.85	1.39
CaO	8.39	8.54	8.08	1.97	1.48	1.14	2.87
Na ₂ O	2.91	2.99	3.02	2.76	2.89	2.72	2.48
K ₂ O	1.35	1.39	1.44	4.15	4.08	4.20	3.53
P ₂ O ₅	0.14	0.15	0.15	0.19	0.19	0.19	0.18
LOI	0.75	0.44	0.52	1.58	1.70	1.16	2.80
TOTAL	99.91	100.30	100.10	99.71	100.01	99.89	99.06
Mg#	0.30	0.31	0.30	0.11	0.13	0.14	0.17
Nb	7.4	7.9	7.8	17.9	17.9	17.8	16.3
Zr	145.4	145.5	156.6	355.5	351.6	357.5	318.3
Y	35.1	34.7	35.4	48.4	47.5	46.1	45.4
Sr	222.4	225.7	214.3	132.3	98.2	90.7	140.2
Rb	42.6	43.4	43.4	136.4	131.1	137.0	117.4
Th	7.4	5.7	6.6	11.4	12.6	11.5	10.3
Pb	8.1	6.4	6.9	22.2	21.8	23.2	20.6
Zn	104.0	147.9	109.9	89.2	88.0	97.6	139.3
Cu	32.3	31.0	31.9	10.7	11.1	10.6	17.5
Ni	14.3	14.1	14.8	3.6	4.0	4.1	7.7
Cr	42.8	47.6	43.3	0.0	1.1	0.0	11.7
V	209.0	301.2	299.1	23.4	28.6	23.3	67.4
Ba	455.0	403.8	477.3	866.8	876.7	816.2	822.3
Sc	43.2	41.1	45.7	17.7	17.1	19.1	17.9
La	19.32	19.34		48.05		46.03	41.94
Ce	44.04	43.89		109.90		104.83	94.92
Pr	5.01	4.99		12.33		11.78	10.25
Nd	19.30	19.20		43.58		41.38	35.28
Sm	4.31	4.31		8.53		8.16	7.39
Eu	1.28	1.28		1.41		1.40	1.36
Gd	4.96	4.91		8.17		7.87	7.45
Dy	4.95	4.90		7.04		7.00	6.25
Ho	1.15	1.13		1.58		1.59	1.45
Er	3.12	3.06		4.13		4.19	3.79
Yb	3.13	3.09		4.19		4.30	4.00
Lu	0.50	0.50		0.68		0.70	0.68

Table 6.2 Major- and trace-element geochemistry of the Rudh' a' Chromain rocks. Major and trace-elements determined by XRF analysis, REE by ICP-AES analysis. Major elements in Wt%, trace-elements in ppm.

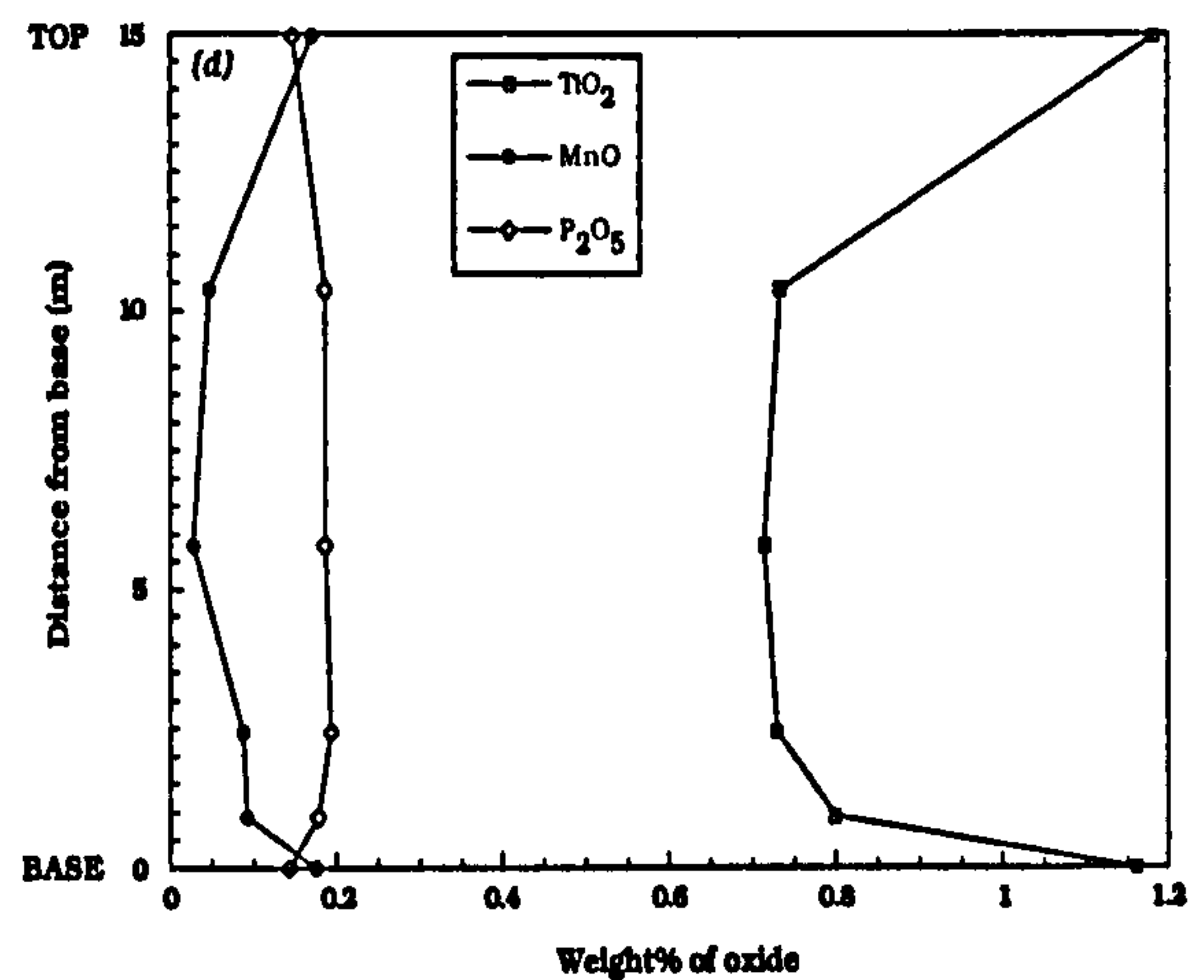
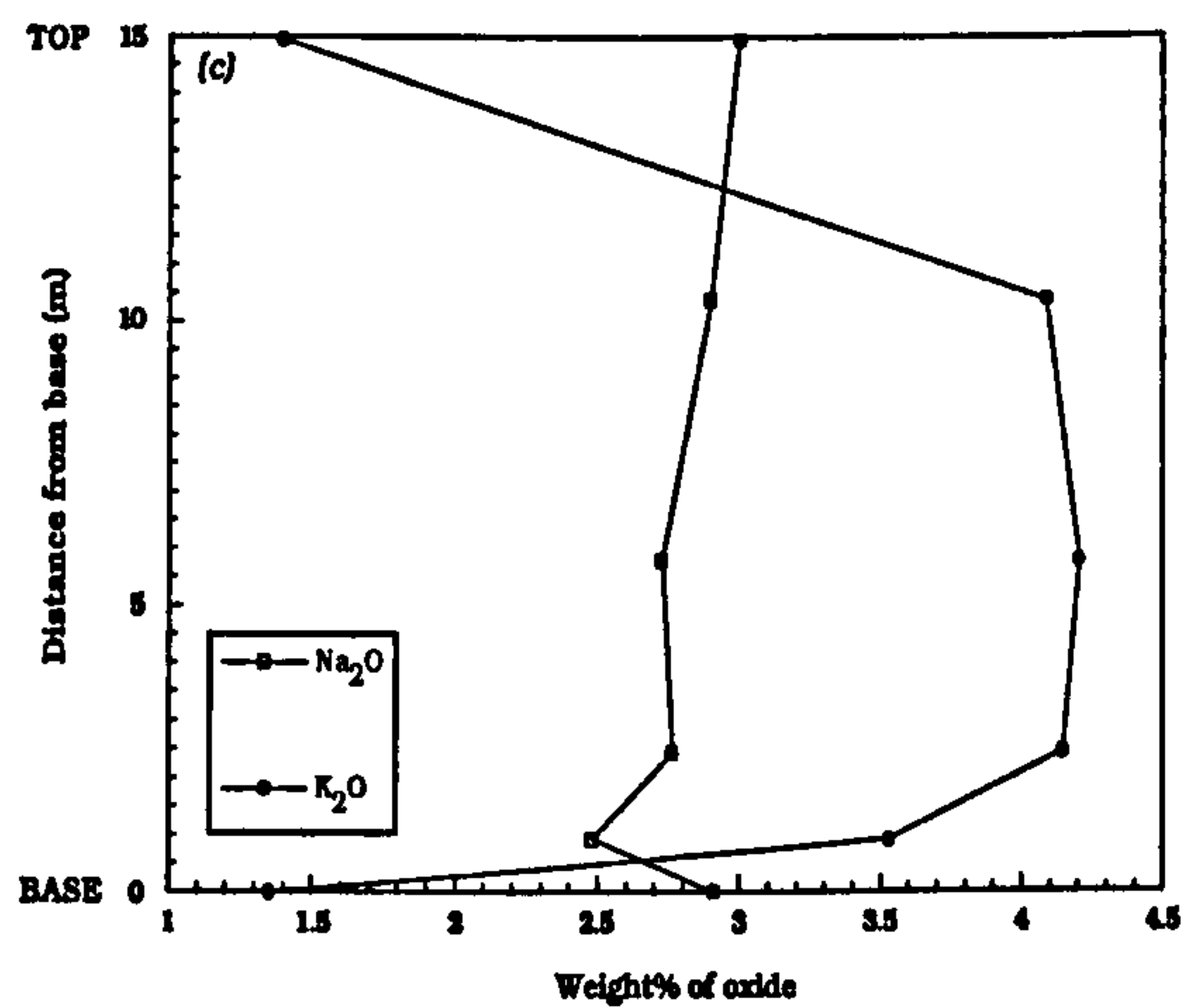
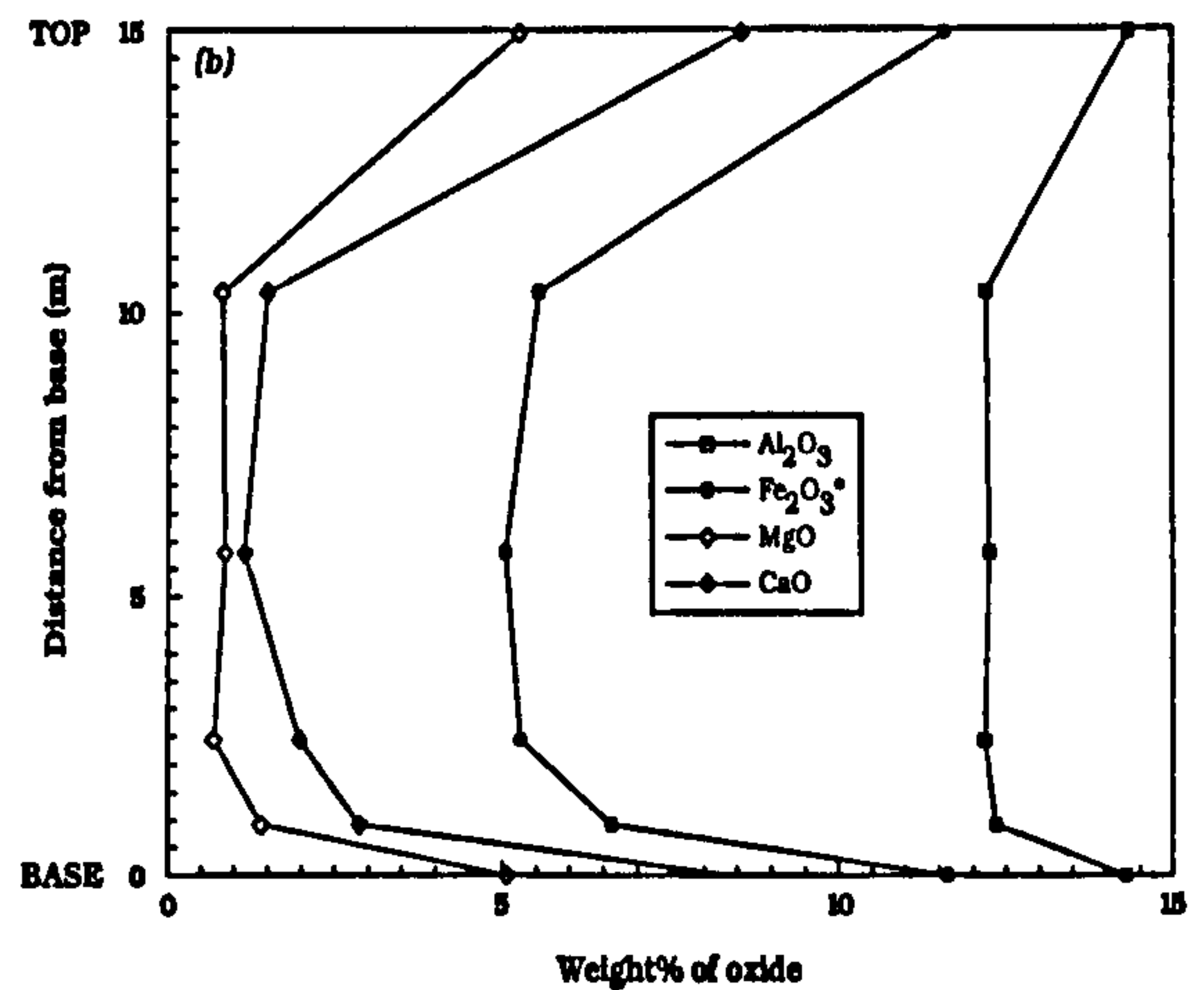
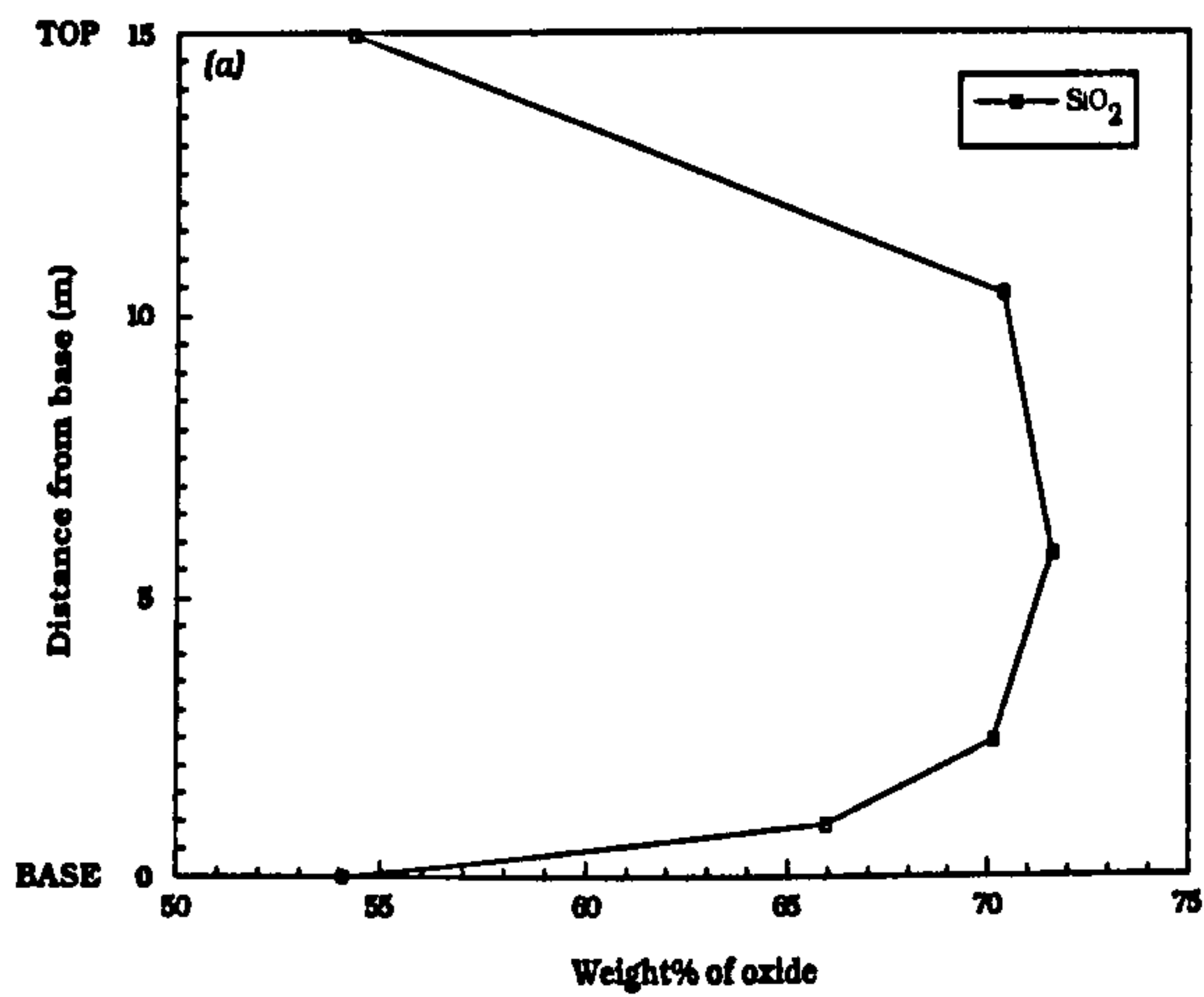


FIGURE 6.6a-d Variation in major-elements with distance from the base of the composite basalt-rhyolite sheet at Rudh' a' Chromain [NM 521202].

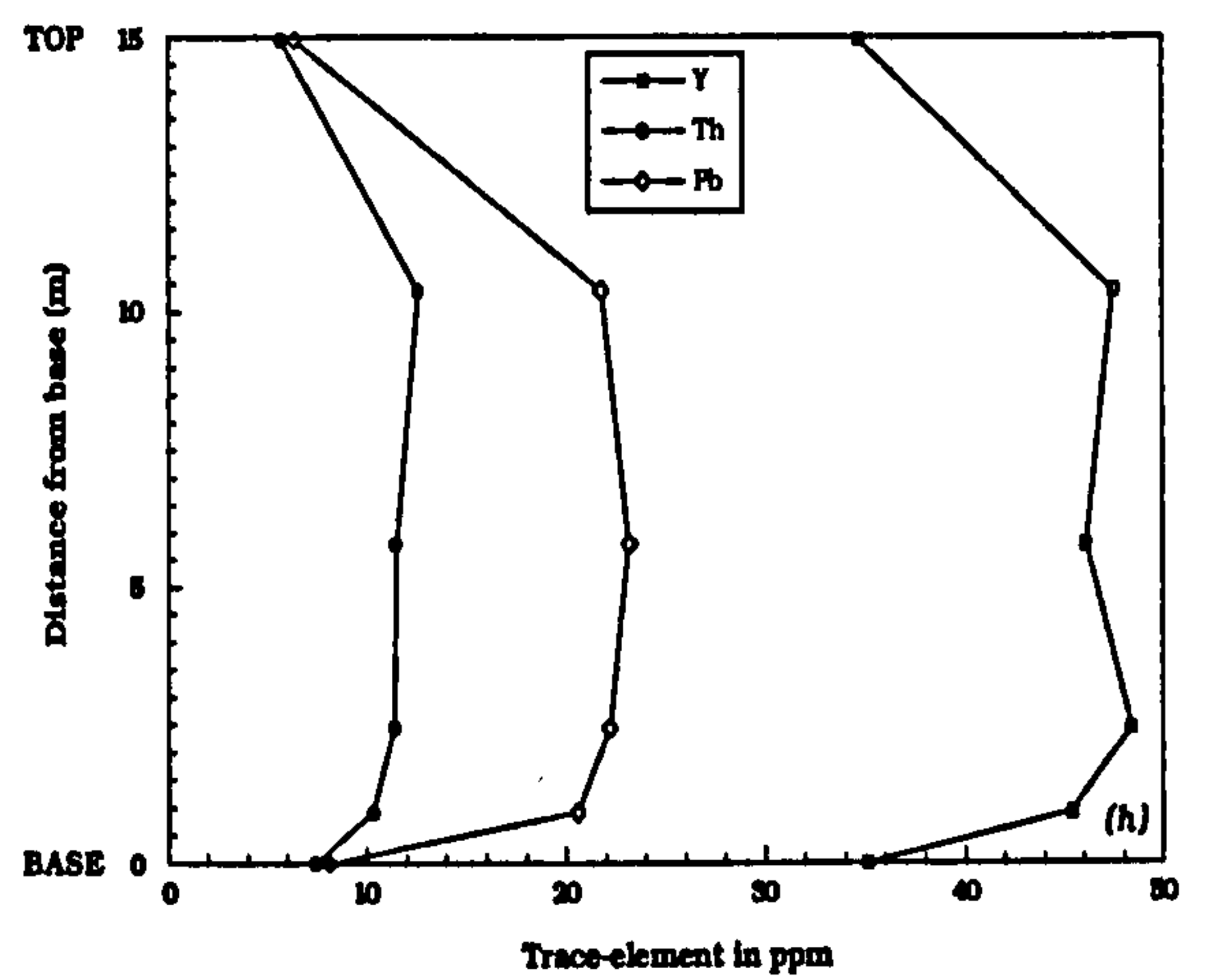
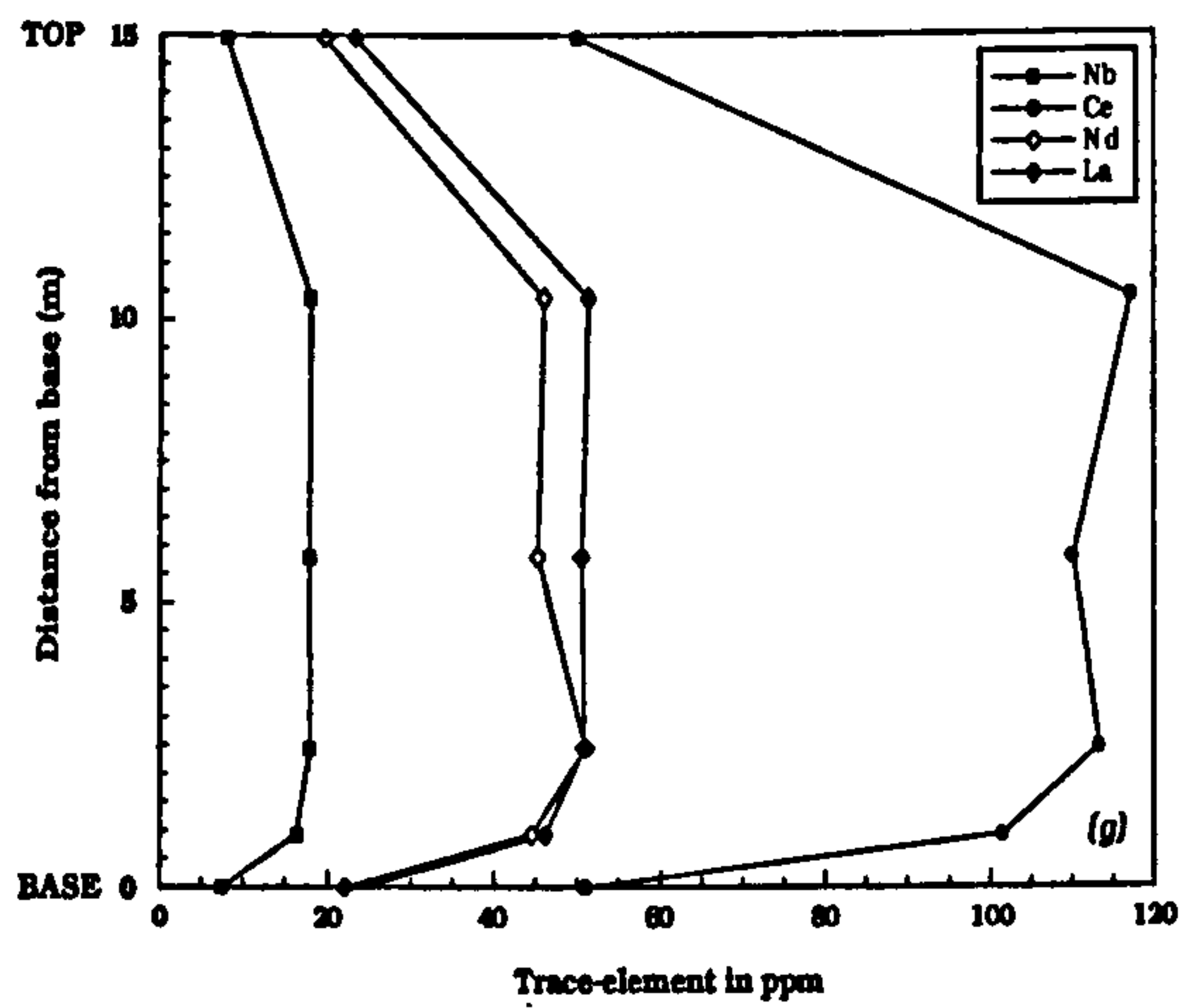
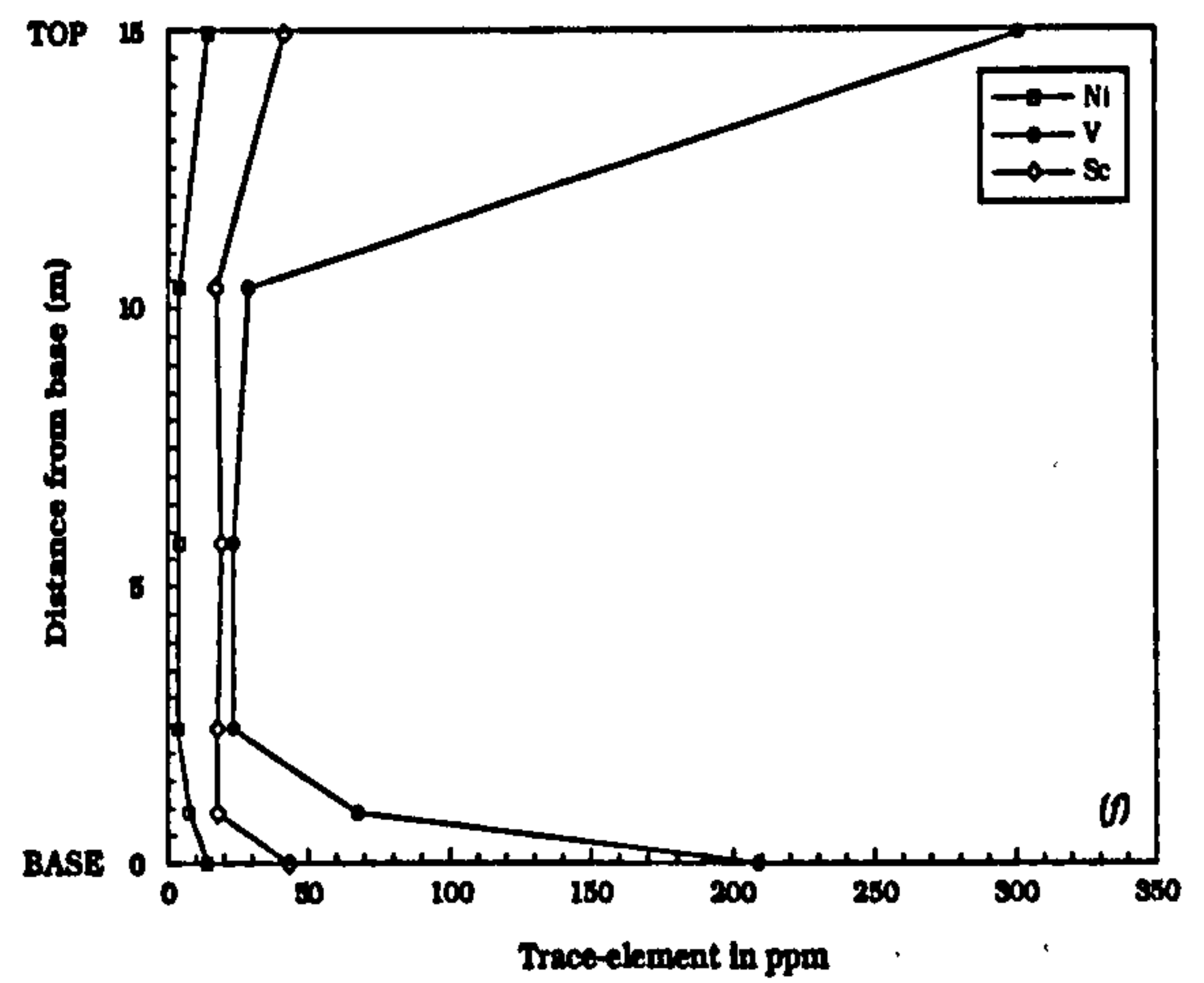
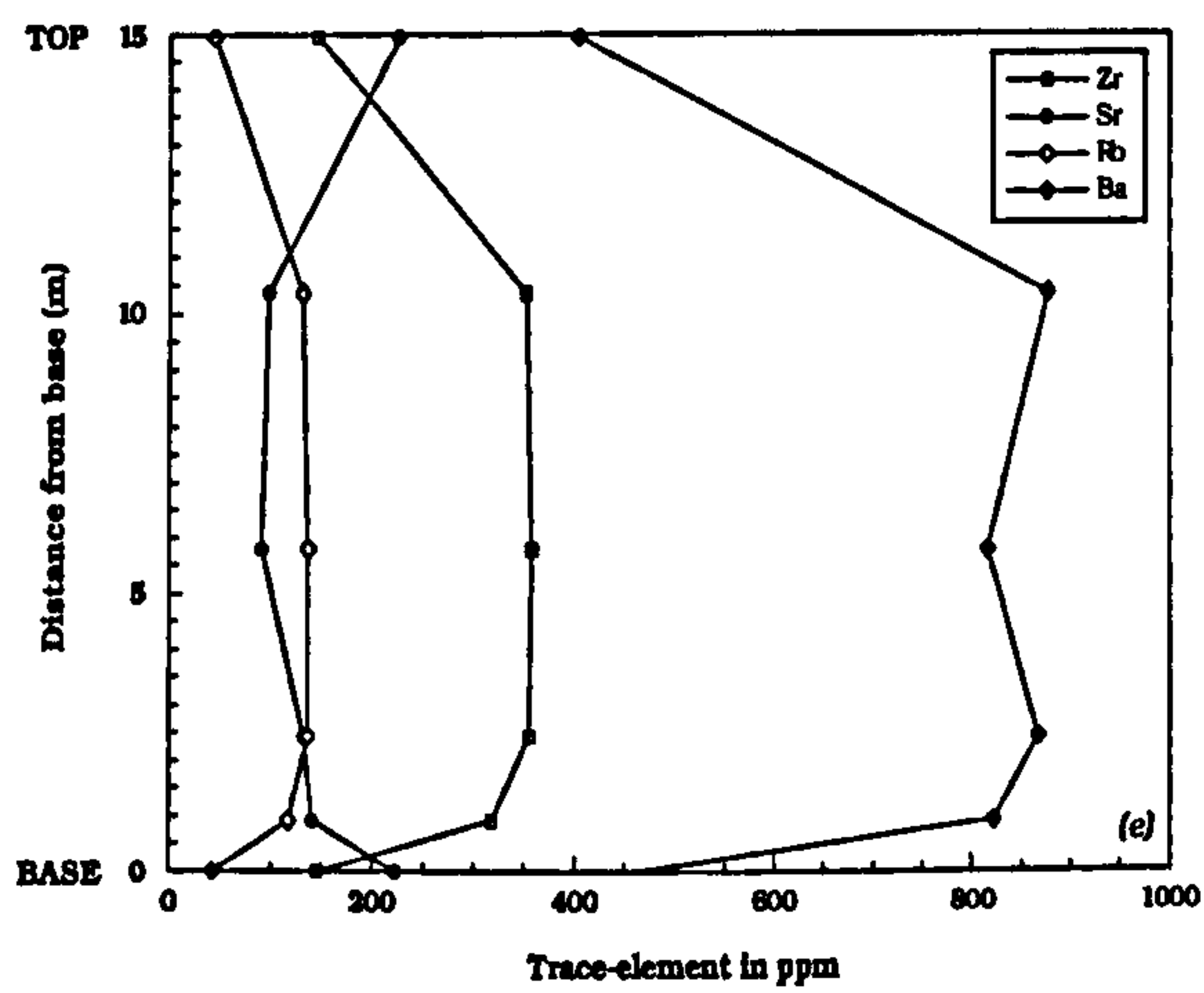


FIGURE 6.6e-h Variation in trace-elements with distance from the base of the composite basalt-rhyolite sheet at Rudh' a' Chromain [NM 521202].

Bailey *et al.*, (1924) considered that the silicic and basic portions of the sheet were related by a process of gravitational differentiation, stating that the concentration of gabbroic and crustal xenoliths mainly within the basic portions of the sheet was evidence in favour of this hypothesis. Buist (1961) rejected this theory in favour of a multiple intrusion by separately generated magmas. A large basic sheet (approx. 3m) was emplaced, being guided by the pre-existing monzonite sheet. The silicic interior was intruded later, before the basic magma had cooled to any great extent, allowing the two liquids to mix in a zone of hybridization. The new data supports, in part, this theory. The REE data, and Sr-Nd isotope data confirm that the two magmas are not related by a process of differentiation, but that the range in chemistry seen is a result of mixing between coexisting basic and silicic liquids. *Figure 6.7* shows the chondrite-normalized REE profiles for the basic and silicic portions of the sheet. The converging REE profiles precludes the basic and silicic end-members being related via the fractionation of plagioclase and pyroxene. The large negative Eu anomalies in the rhyolites are consistent with these magmas having either been generated by the partial melting of pelitic crustal rocks leaving a plagioclase-rich restite, and/or by them fractionating plagioclase.

SAMPLE	(⁸⁷ Sr/ ⁸⁶ Sr) _i	(¹⁴³ Nd/ ¹⁴⁴ Nd) _i
Lower Tholeiite RCB1	0.712282	0.511986
Hybrid RCF4	0.717622	0.511862
Central Rhyolite RCF1	0.717169	0.511840
Central Rhyolite RCF3	0.719059	0.511862
Upper Tholeiite RCB2	0.712560	0.511970

Table 6.3 Sr and Nd isotope data for the basic and silicic members of the Rudh' a' Chromain sheet. Measured Sr and Nd isotope ratios were age corrected to 58Ma. Full isotopic data is given in Appendix III.

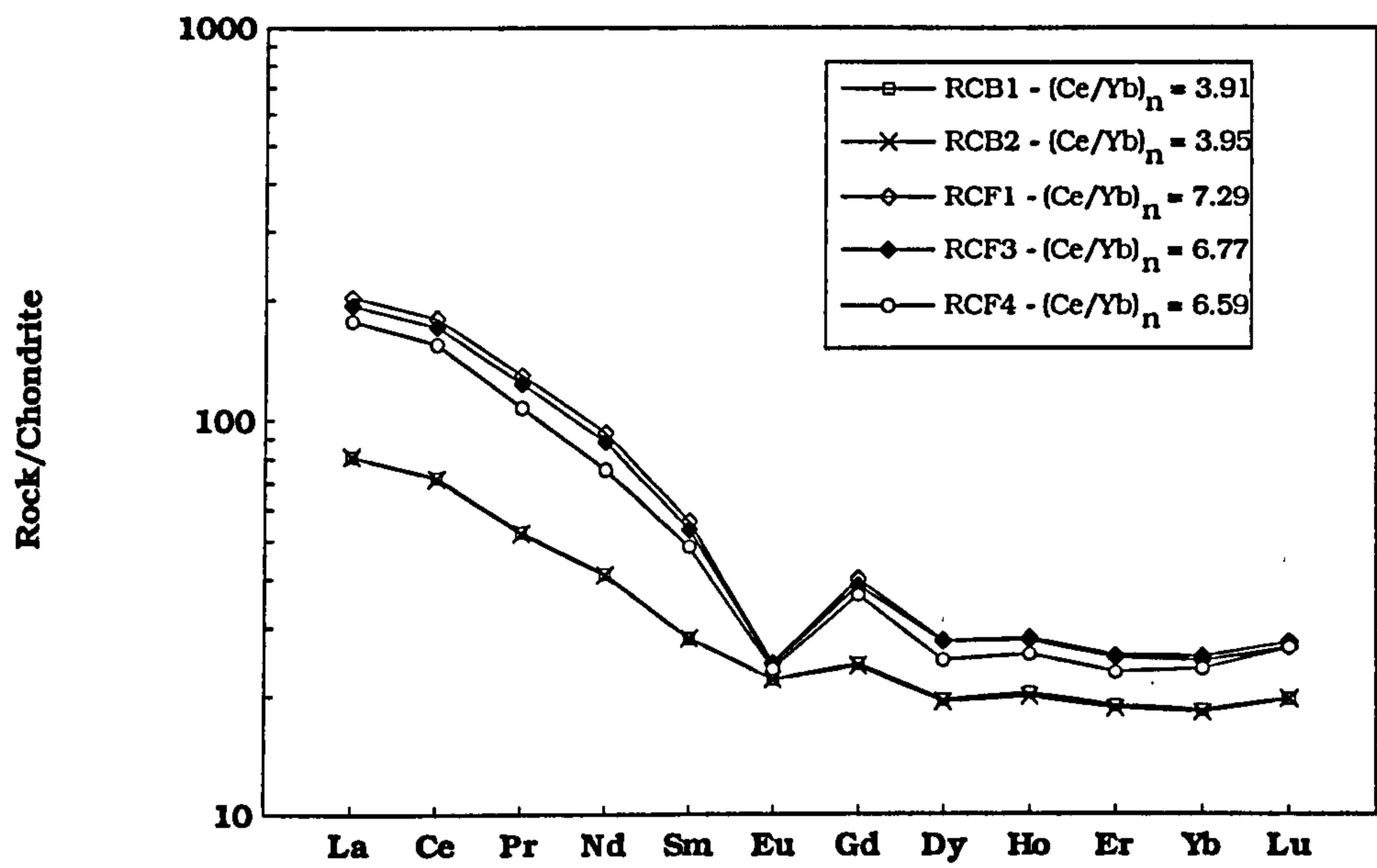


FIGURE 6.7 Chondrite normalised REE profiles for the base and centre of the Rudh' a' Chromain composite basalt-rhyolite sheet.

The basaltic members are essentially identical in terms of their initial Sr and Nd isotope ratios, attesting to them being the "same" magma. Values for $^{87}\text{Sr}/^{86}\text{Sr}_i$ are, however, elevated at around 0.712, suggesting that the basalt has been contaminated with upper crustal material. The rhyolites, with such high $^{87}\text{Sr}/^{86}\text{Sr}_i$ (> 0.719) and low $^{143}\text{Nd}/^{144}\text{Nd}_i$ (0.511840) values, are considered to be silicic melts extracted from lithologies such as the basement Moine pelitic schists (*cf.* Walsh *et al.*, 1979; Pankhurst *et al.*, 1978; Chappell & White, 1992). The occurrence of oligoclase phenocrysts also suggests that the magma has undergone some fractional crystallization. However, due to the highly altered nature of the central rhyolites, some perturbation of certain trace-elements (*e.g.* Rb, Ba), and the Sr isotope ratios may be expected due to hydrothermal alteration.

These Sr-Nd isotope values are similar to those found in other composite sills of the BTVP. One, examined by Harker (1904), Buist (1959), Bell (1983), and Bell & Pankhurst (1993), intrudes the shales of the Lower Jurassic Broadford Beds on the promontory of Rubh'an Eireannaich on the west side of Broadford Bay, Isle of Skye. The sheet is some 5m thick, and is composed of margins of ferrobasaltic andesite, with a central portion of rhyolite. Like the Rudh' a' Chromain sheet, there is a complete gradation between the two facies in terms of their mineralogy, texture and chemical composition (Bell, 1983). The work by Bell (1983), and Bell & Pankhurst (1993), suggests that two distinct magmas were involved in the formation of the sill. The ferrobasaltic andesite was generated by contamination and fractional crystallization of regionally available basaltic magma. The silicic magma was generated from the partial fusion of crustal lithologies. The model of Bell (1983) suggests that there was stable stratification of rhyolitic magma above the ferrobasaltic andesite magma, with a gradational intervening layer of hybrid composition. The chamber was most likely tapped in the order: ferrobasaltic andesite, followed by the hybrid magma, after which the rhyolite was injected along the central portion of the conduit. This must have been completed in a short period of time since the complete absence of internal boundaries suggests that each magma was still largely fluid before the next arrived.

A similar model can be forwarded for the sheet at Rudh' a' Chromain. The basic end-member in this sheet is slightly less-evolved when compared to the sheet at Rubh'an Eireannaich ($\text{Mg\#} = 0.311$ compared

to $Mg\# = 0.327$), and the rhyolite slightly more siliceous ($wt\% SiO_2 = 71.8$ compared to $wt\% SiO_2 = 69.7$) (Bell, 1983). Both members of the Rudh' a' Chromain sheet also contain more radiogenic strontium ($^{87}Sr/^{86}Sr_1$ for the Rubh'an Eireannaich sheet range from 0.70749 to 0.71248) (Bell & Pankhurst, 1993). The favoured model involves a small upper crustal magma reservoir, perhaps taking the form of a sill-like body, in which tholeiitic basic magma is undergoing combined assimilation and fractional crystallization. Silicic melts will form and pond at the top of the reservoir and, provided the lower basic magma is turbulently mixed, a zone of hybridization can develop. This will result in a strongly zoned magma reservoir similar, but smaller, to those envisaged for the Skaergaard intrusion and the Loch Ba ring-dyke (Sparks, 1988). The order and mode of emplacement of the various magmas will be the same as for the Rubh'an Eireannaich sheet. Emplacement was probably induced by the forceful and turbulent emplacement from below of a new pulse of basic magma. This turbulent ascent of magma may account for the sheet being highly xenolithic. As an independent chemical test for this theory, linear mixing equations have been applied to the Rudh' a' Chromain data (Langmuir *et al.*, 1978). Figures 6.8a and 6.8b show the graphical results for this mixing test for the major- and trace-elements, respectively. These plots show that the hybrid rock (RCF4) could indeed be the result of simple mixing between a basic (RCB1) and silicic (RCF3) end-member. The fit of the data is excellent ($R^2 > 0.98$ in both cases), and the hybrid consists of between 75 and 90% of the silicic end-member. Any elements which do not fit on the trend may be due, in part, to post mixing fractionation of any of the magmas.

6.3 Traigh Bhàn na Sgurra

The sheet at Traigh Bhàn na Sgurra [NM 423185] is a Group I basaltic andesite. It, along with other sheets, crops out along the shore on the South coast of the island (Figure 1.2), and on adjacent crags, within the Moine metasedimentary succession. Figure 6.9 shows a sketch map of the local geology. The largest sheet is some 6m thick; the others are generally 1.5-4m thick. The sheets contain xenoliths of the local lithologies, which occur both singly and in lens-shaped patches at the top of the sheets. These are up to 1m wide and 10m long and contain up to an estimated 50% by volume of xenoliths set in a glassy or

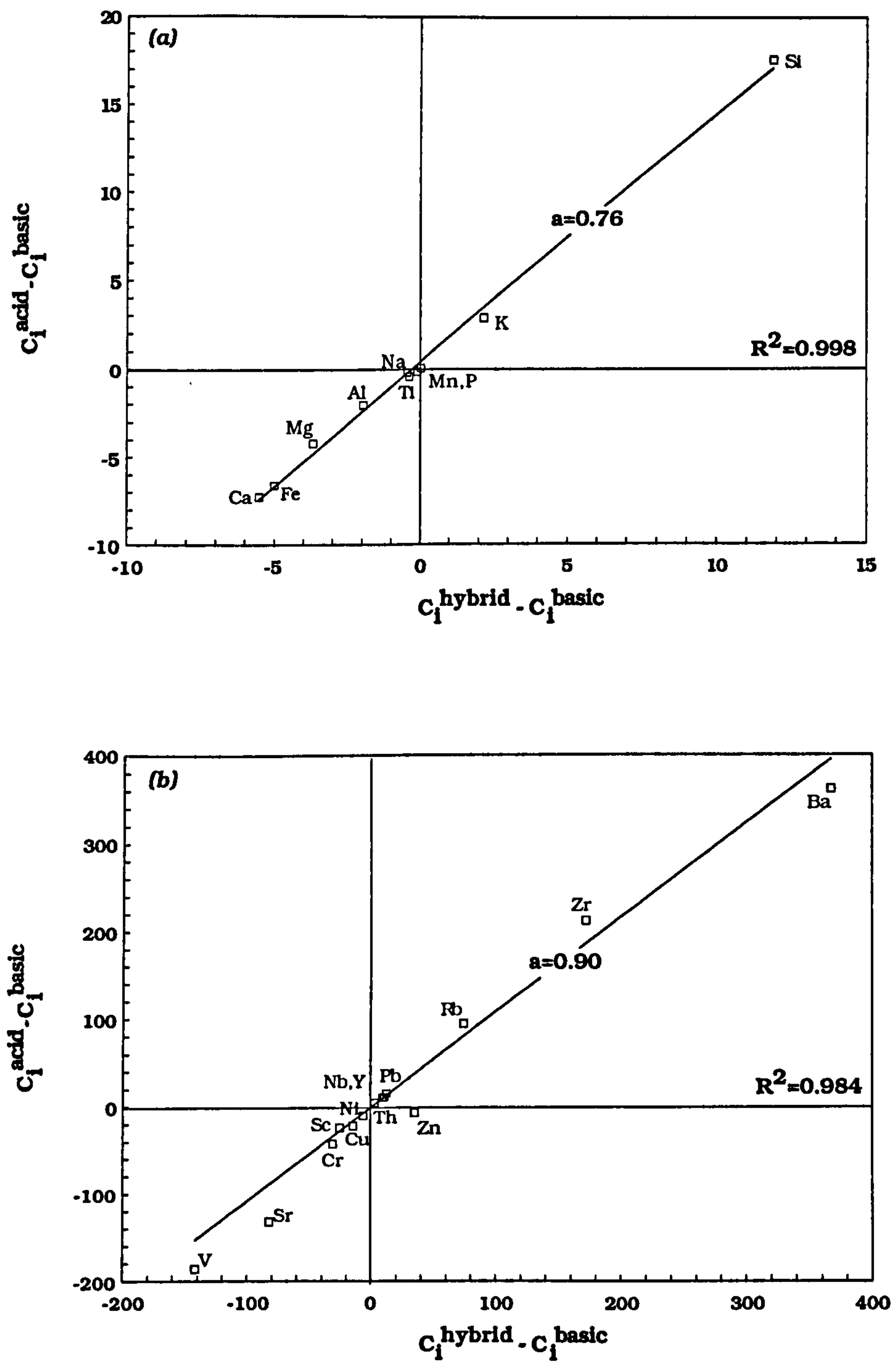


FIGURE 6.8 Mixing test for hybrid rocks of Rudh' a' Chromain.
 Basic End-member = RCB1
 Silicic End-member = RCF3
 Hybrid = RCF4
 C_1 = Concentration of Element 1

(a) Major-elements : % silicic magma = 76

(b) Trace-elements : % silicic magma = 90

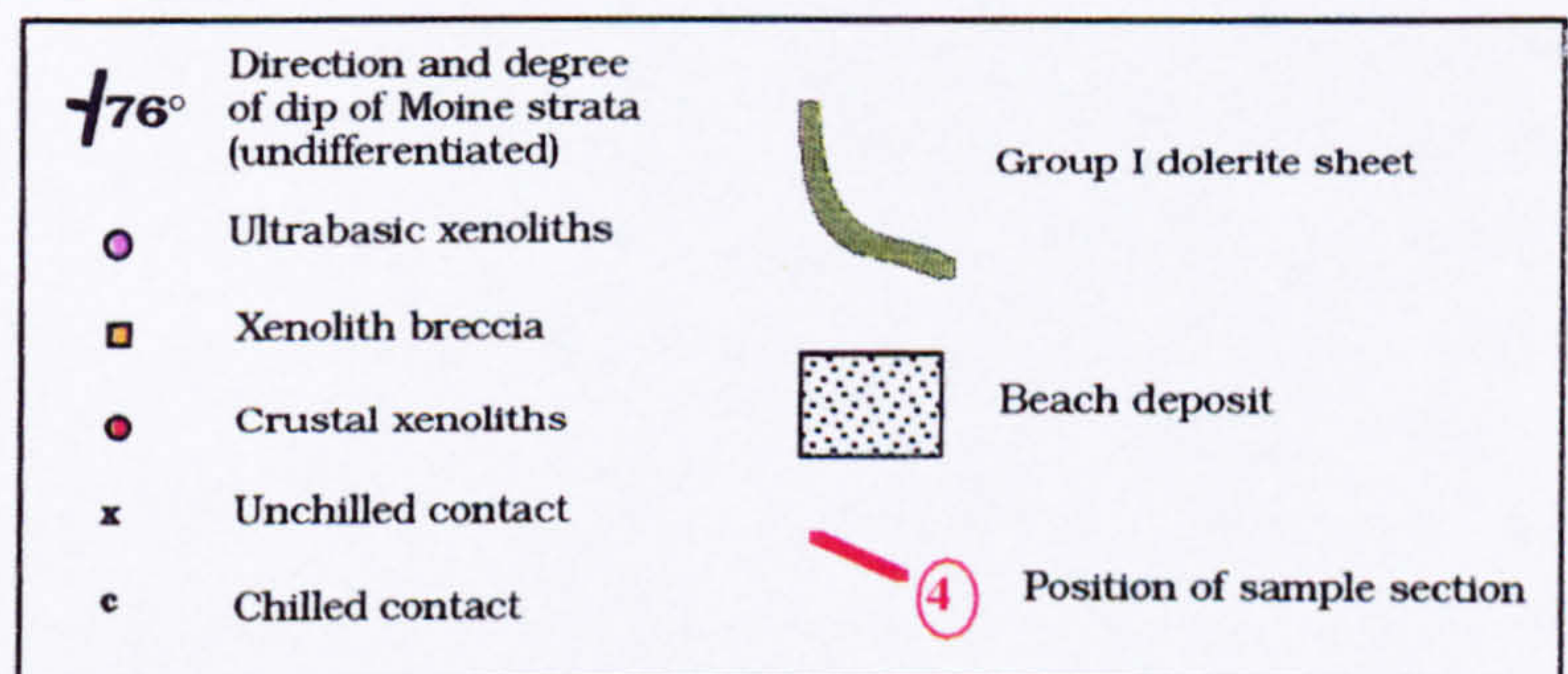
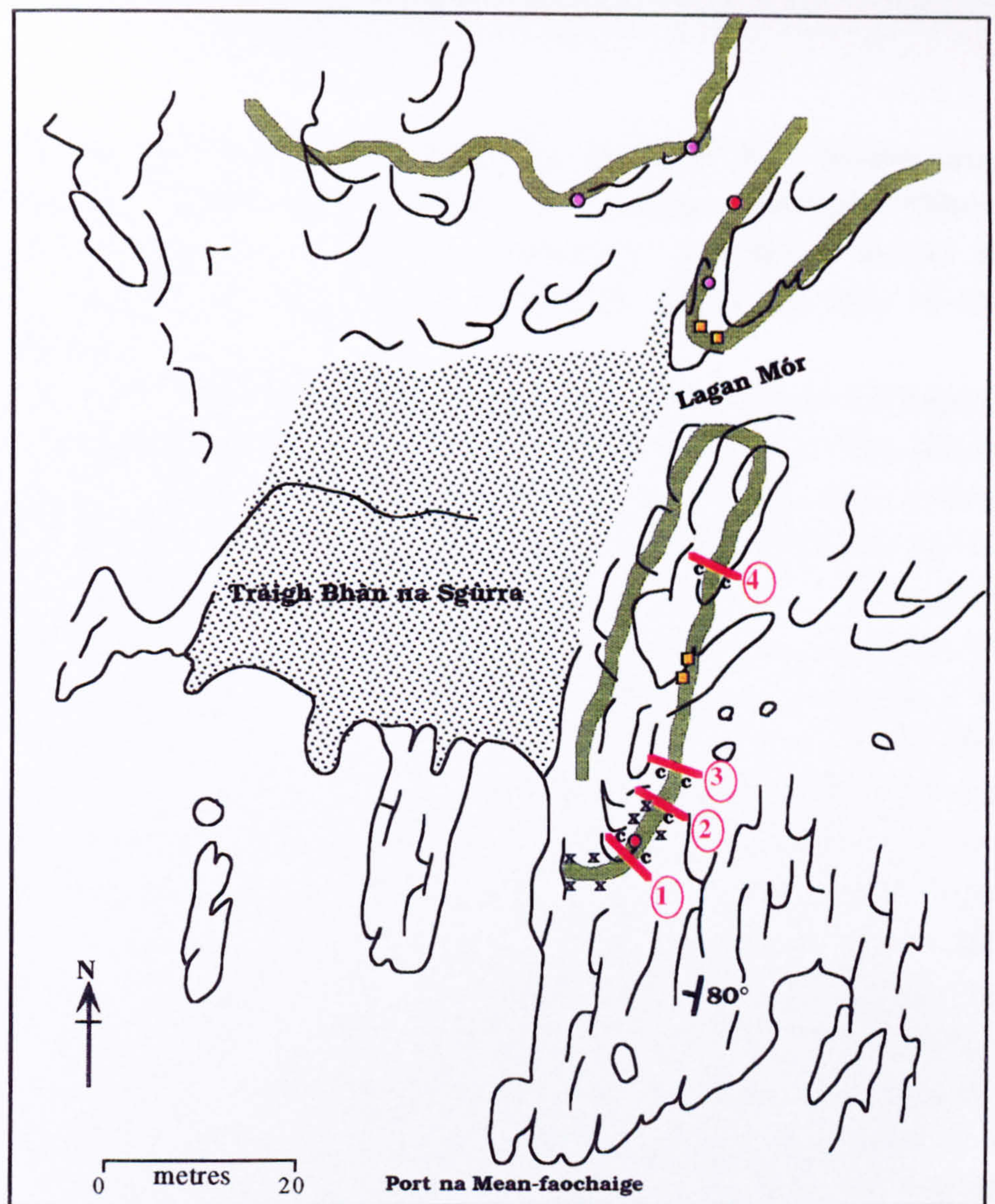


FIGURE 6.9 The Group I sheets of Tràigh Bhàn na Sgùrra [NM 423185]. Shown are the positions of crustal and cumulate xenoliths, and sections sampled through the sheet.

microcrystalline matrix (*Figure 6.10*). The xenolith-rich lenses may have developed in "quiet spots" within the magma conduit. Where magma flow was rapid or turbulent, entrained xenoliths would be continuously "moved on", only being deposited where the flow of the magma slackened.

The sheet which has been sampled in detail at Traigh Bhàn na Sgurra occupies the headland between two small bays (*Figure 6.9*). The Moine metasedimentary rocks are predominantly garnet-bearing pelitic schists in the western (sandy) bay, and thick-bedded quartzites in the eastern bay. A prominent transition between these two lithologies occurs on the headland, where schists and quartzites alternate on scales between 1cm and 1m. The zone also contains large lenses (up to 1m) of polycrystalline quartz (*Figures 6.11a and 6.11b*) This transition zone, the so-called Lagan Mor Formation, marks the boundary between the predominantly psammitic Shiaba Group and the predominantly pelitic Assapol Group (Holdsworth *et al.*, 1987). This zone is cut by a 2-4m thick dolerite sheet, as shown in *Figure 6.9*. The sheet cross-cuts the bedding of the pelites and quartzites, although the level of intrusion is highly variable (see *Figure 6.11*). The sheet shows a *very localized tendency* to chill against the country rocks. The majority of the boundary is unchilled, the pelitic rocks having been baked in a zone up to 5cm from the contact. The dip of the sheet is highly variable, and the contact with the metasediments extremely irregular. Kille *et al.* (1986) present field evidence for turbulent flow within the sheets at this locality. In places, pelitic bands appear to have been selectively assimilated and eroded in preference to the more refractory quartzites (see *Figure 6.11*). Kille *et al.* (1986) suggest that where magma flow in the conduit was turbulent, the magma failed to chill and was therefore capable of melting the more readily fusible pelitic bands. Where the magma flow was laminar, a chilled margin formed, preventing assimilation. It is suggested that the variable dip of the sheet contributed to the magma flow being only locally turbulent, and as a consequence a *highly variable chilled contact developed*. The localized chilling of the basalt sheet, and the presence of xenolith-rich pods and lenses may also suggest that the temperature gradients within the magma may have been very irregular, and that "turbulent" convection currents were operative. If convection currents were established within the magma, the wall rocks would have been thermally eroded, thus contributing to the formation of the lens-



FIGURE 6.10a

Xenolith-rich lens at the top of a thick Group I basaltic andesite sheet at Traigh Bhàn na Sgurra [NM 423185]. Xenoliths consist of quartzites and aluminous mullite-buchites thought to be derived from the local Moine metasediments. Lens is believed to result from the thermal erosion of the wall rocks through turbulent and convective flow of the basaltic magma.



FIGURE 6.10b

Close-up of a xenolith pod at Traigh Bhàn na Sgurra [NM 423185]. Quartzite and aluminous xenoliths are set in a highly weathered basaltic matrix. Hammer shaft is approx. 60cm long.



FIGURE 6.11a

The Moine metasedimentary sequence at Traigh Bhàn na Sgurra [NM 423185]. Sequence consists of pelitic schists (PS) which contain garnet, and locally kyanite and staurolite, along with bands of relatively pure quartzite (QZ). Hammer shaft 60cm long.



FIGURE 6.11b

Moine metasedimentary succession at Traigh Bhàn na Sgurra contains numerous pods and lenses of polycrystalline quartz, which furnish the LSSC with numerous xenoliths. Hammer shaft approx. 60cm long.

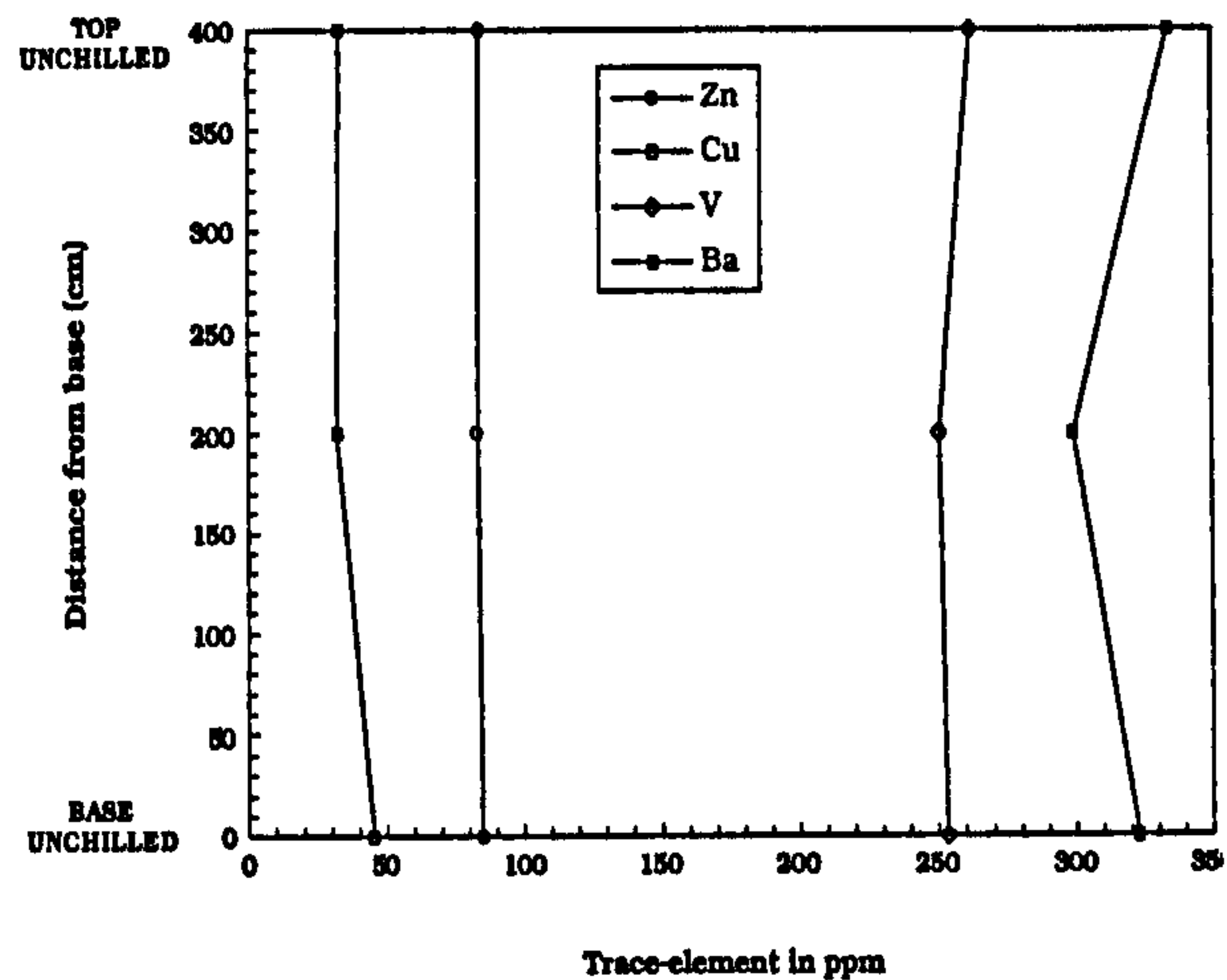
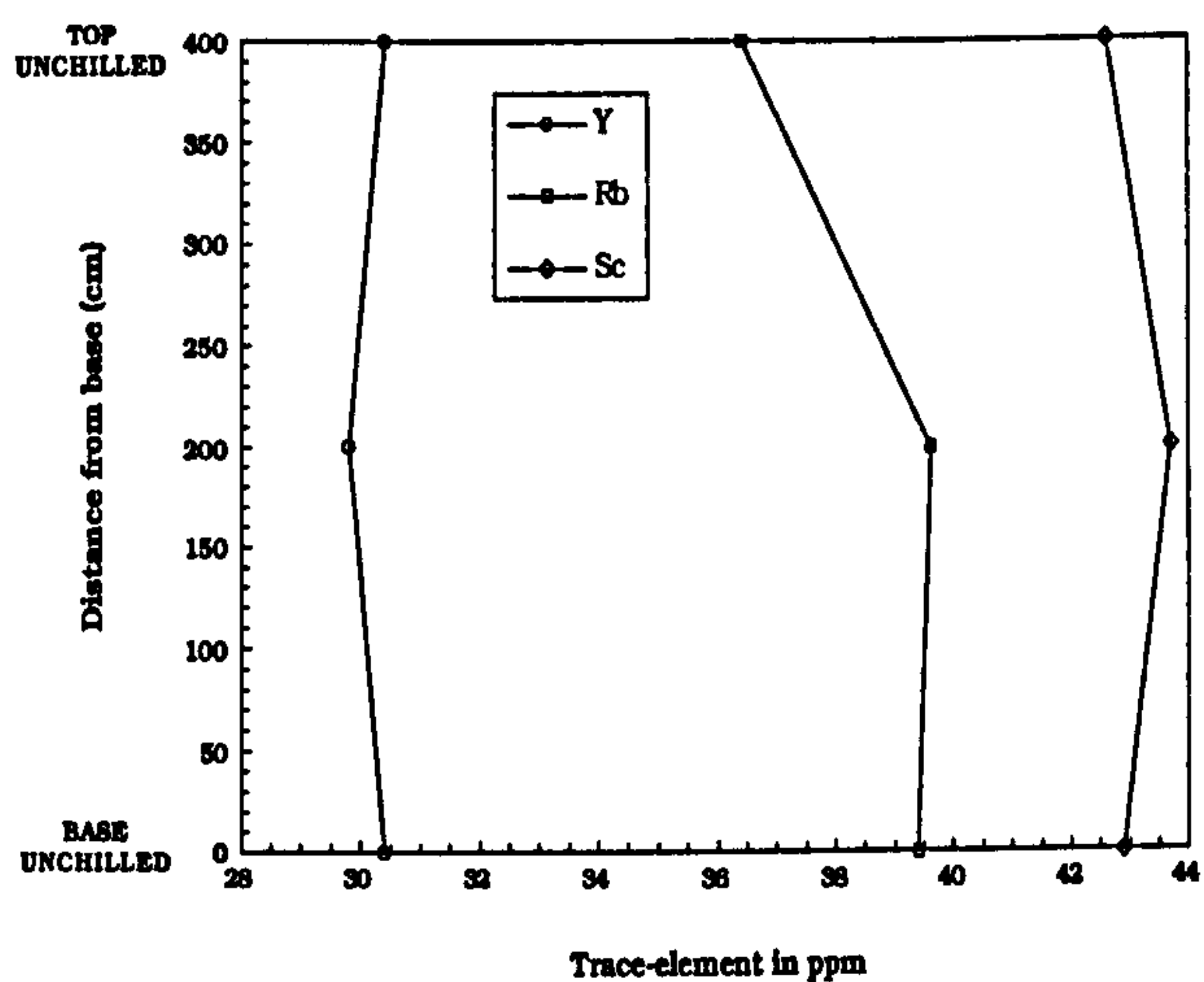
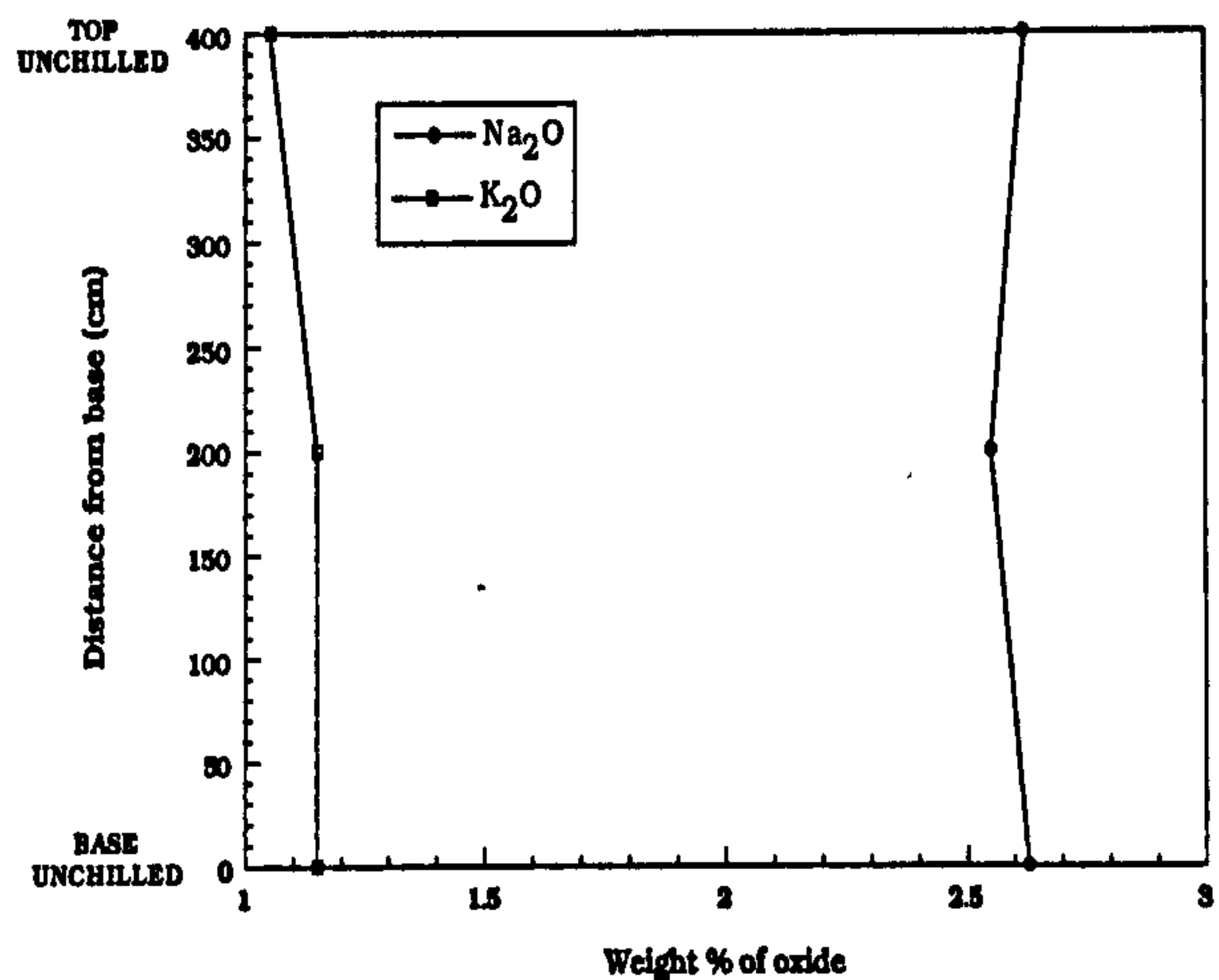
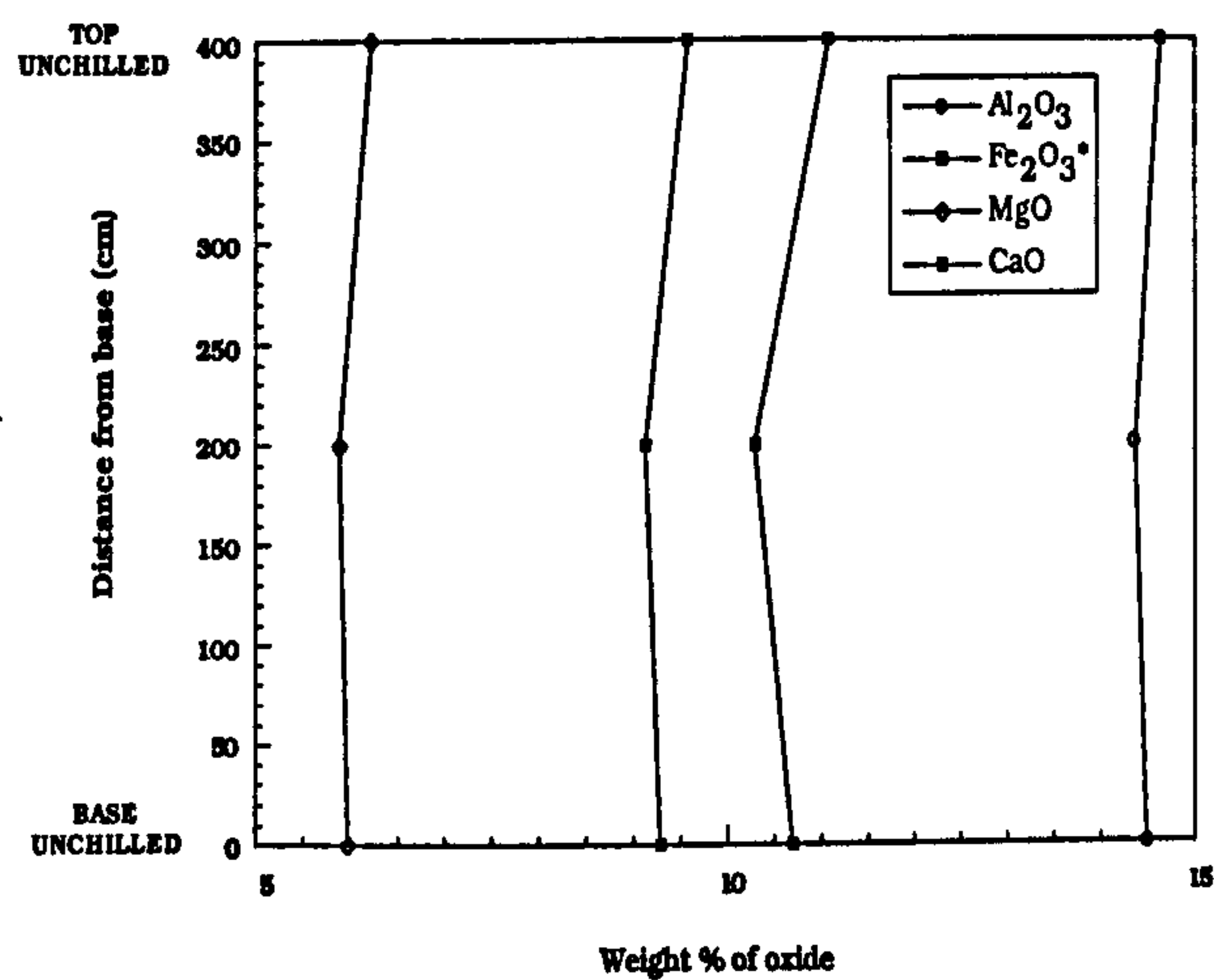


FIGURE 6.12a Variation of selected major- and trace-elements with distance from the base of the basaltic sheet at Traigh Bhan na Sgurra. SECTION 1 = Neither contact chilled.

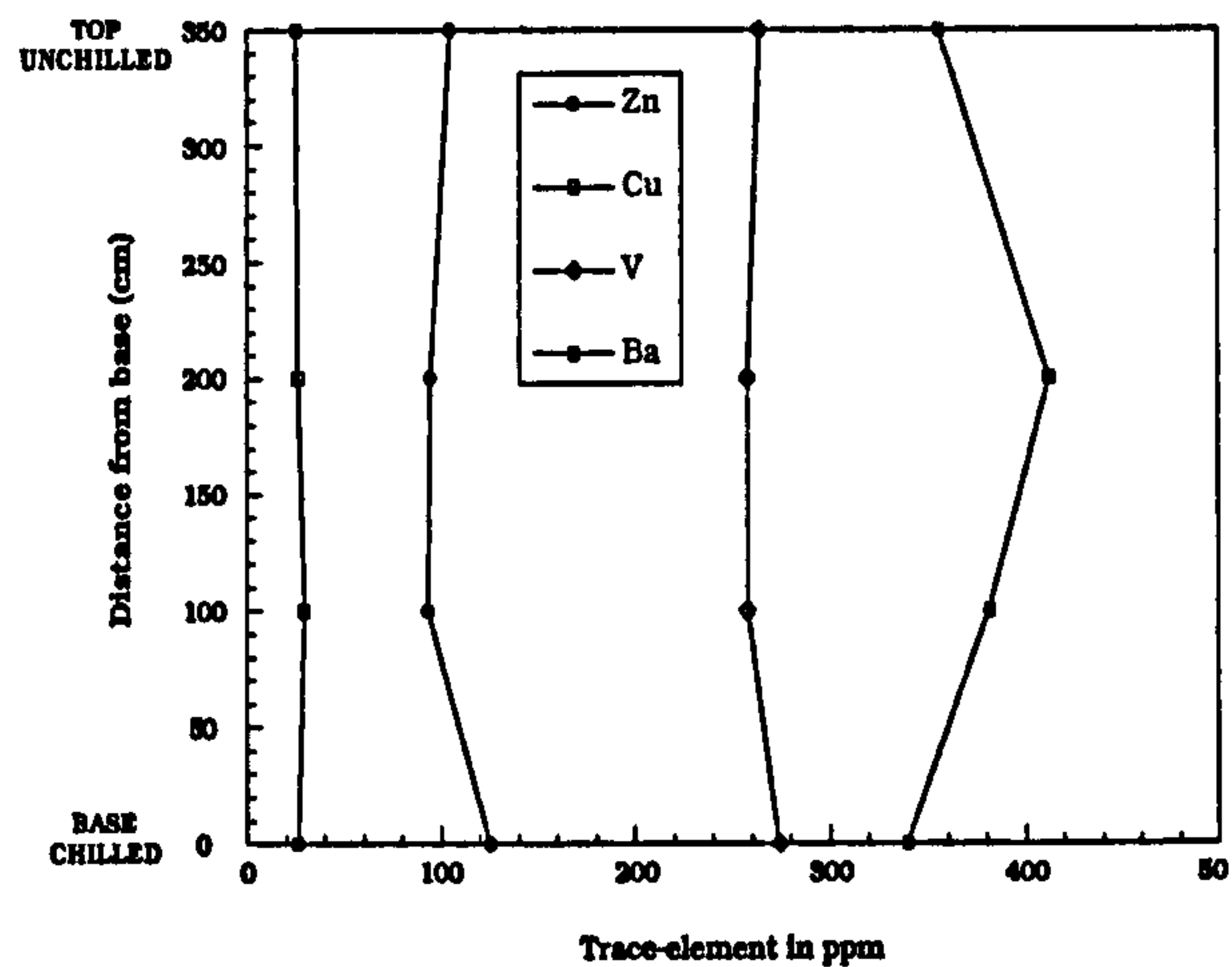
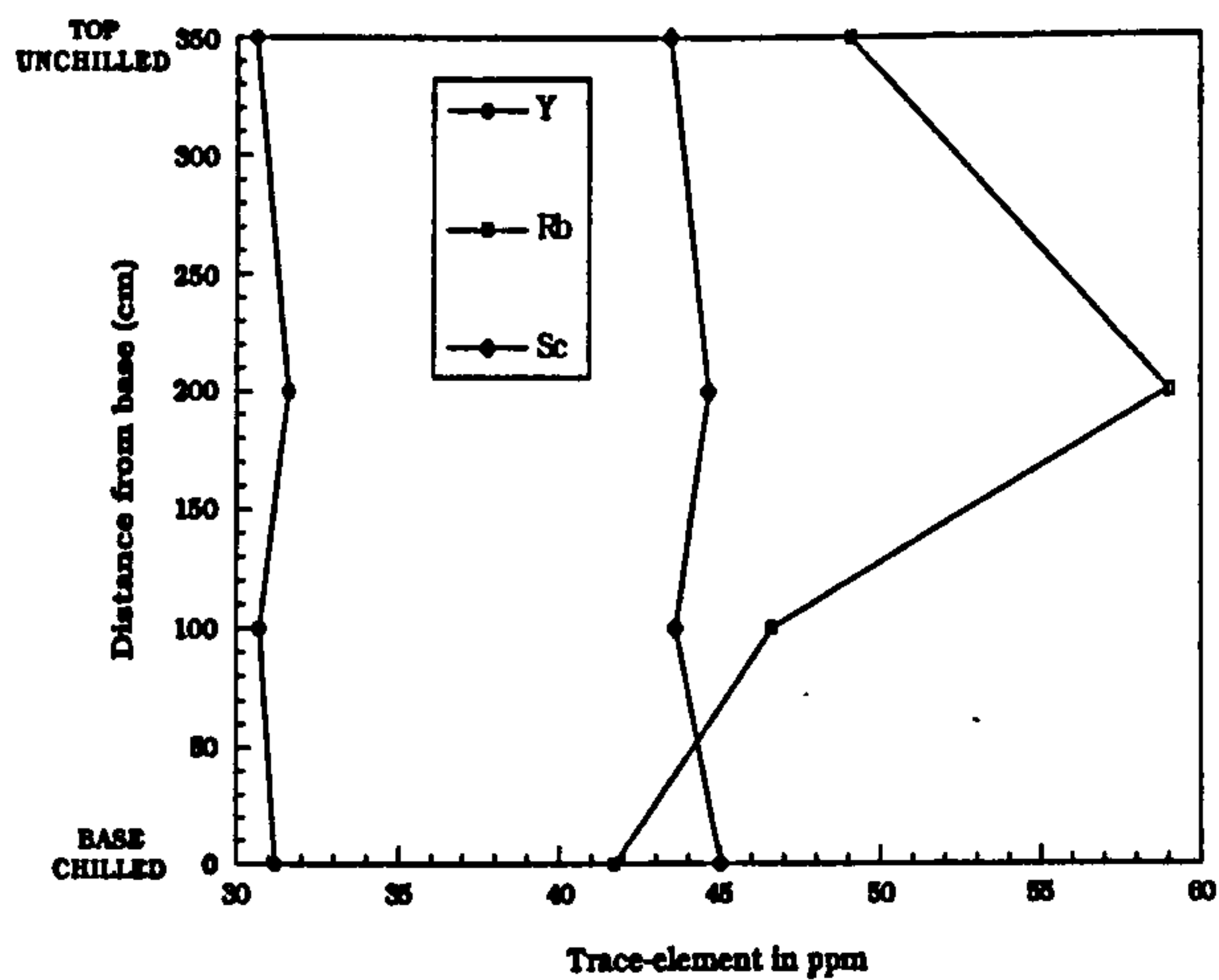
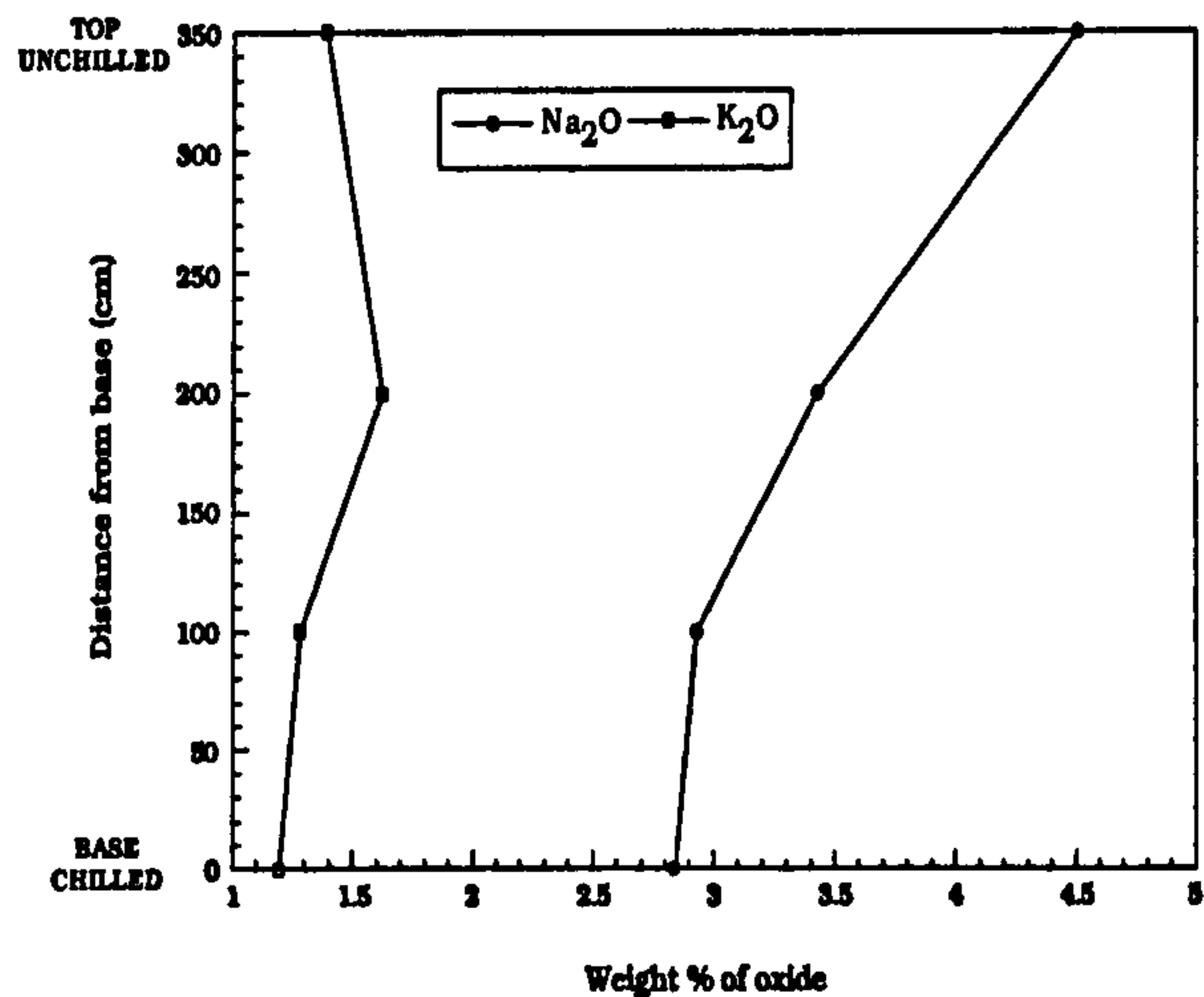
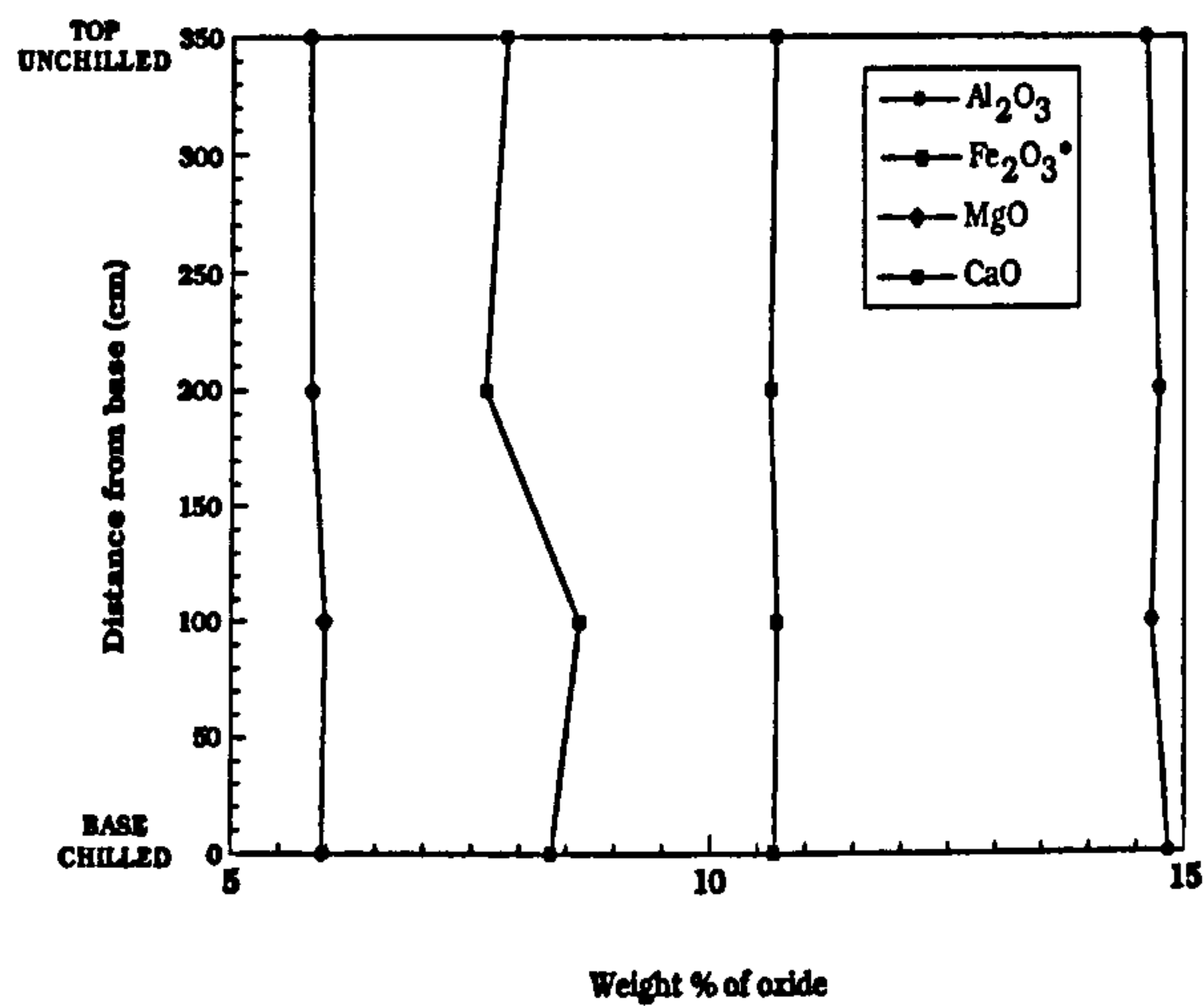


FIGURE 6.12b Variation of selected major- and trace-elements with distance from the base of the basaltic sheet at Traigh Bhan na Sgurra. SECTION2 = Bottom contact chilled.

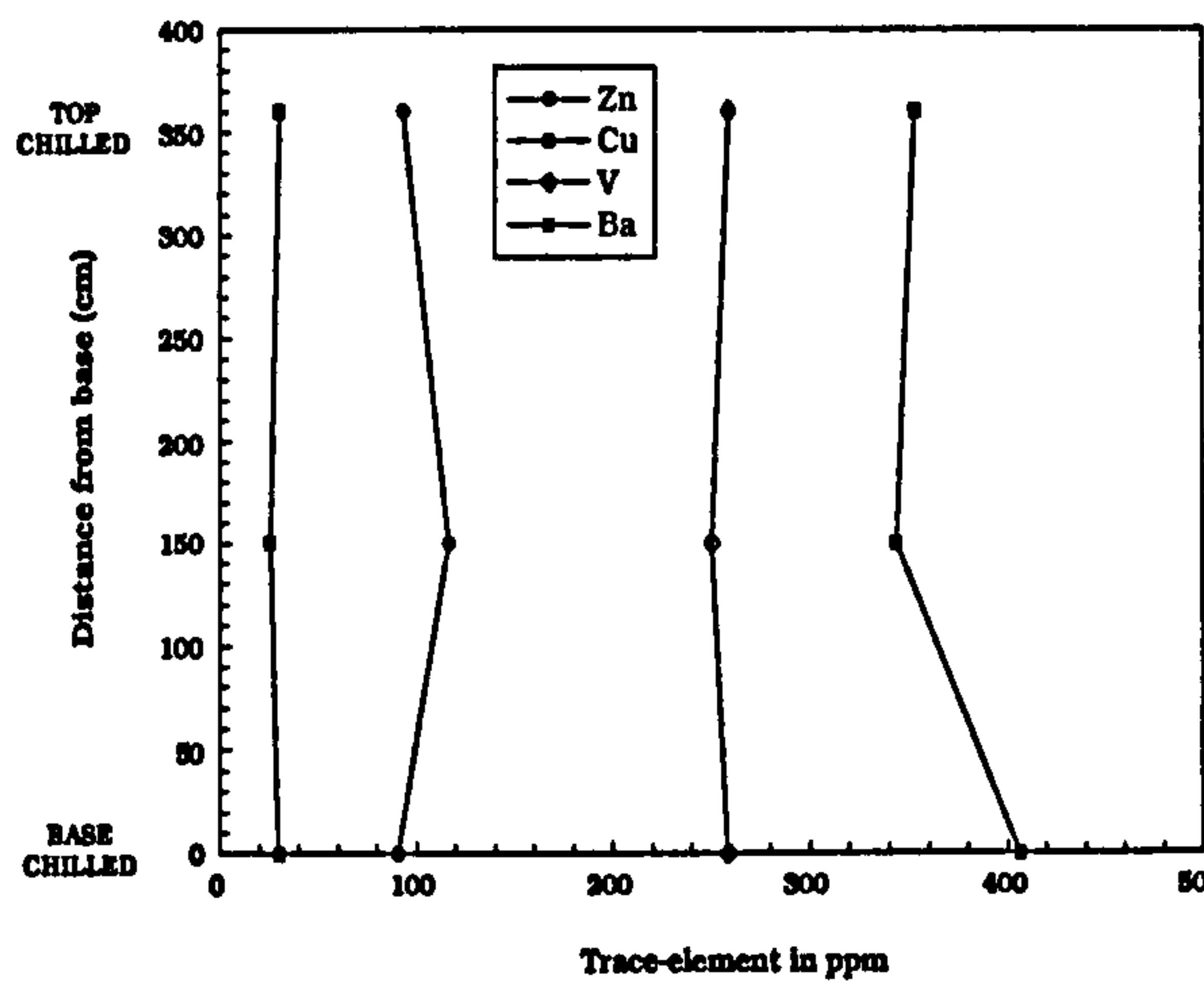
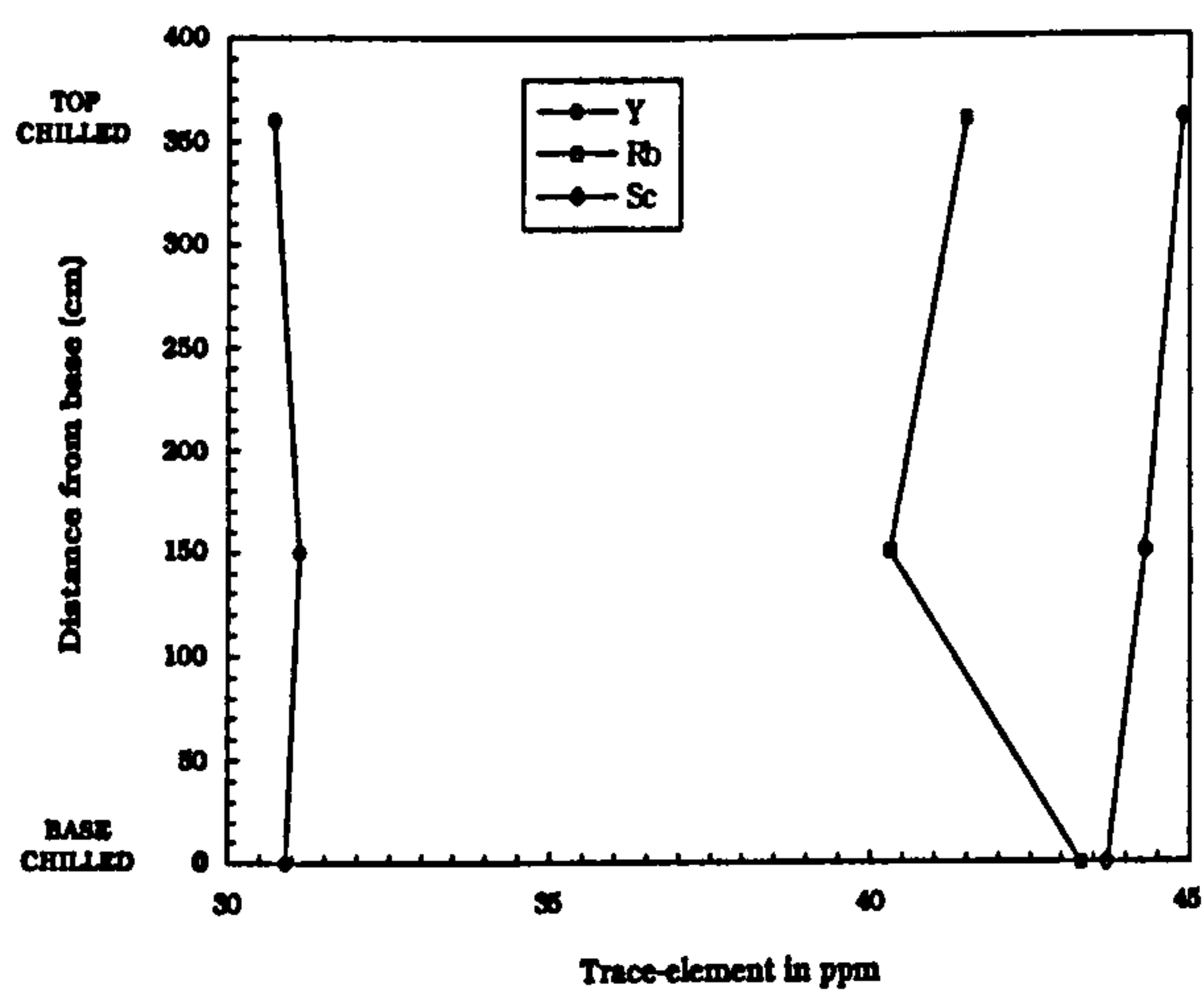
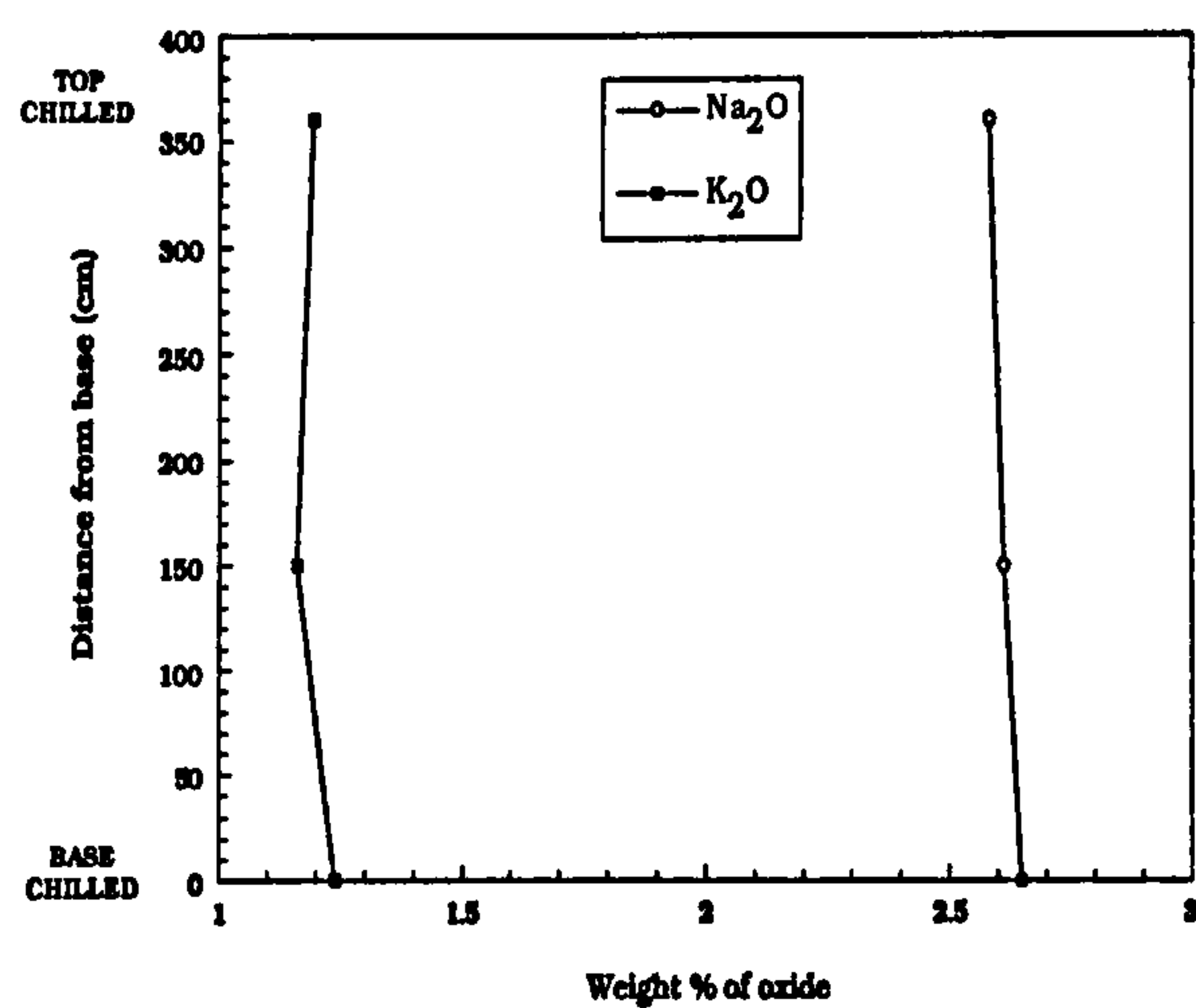
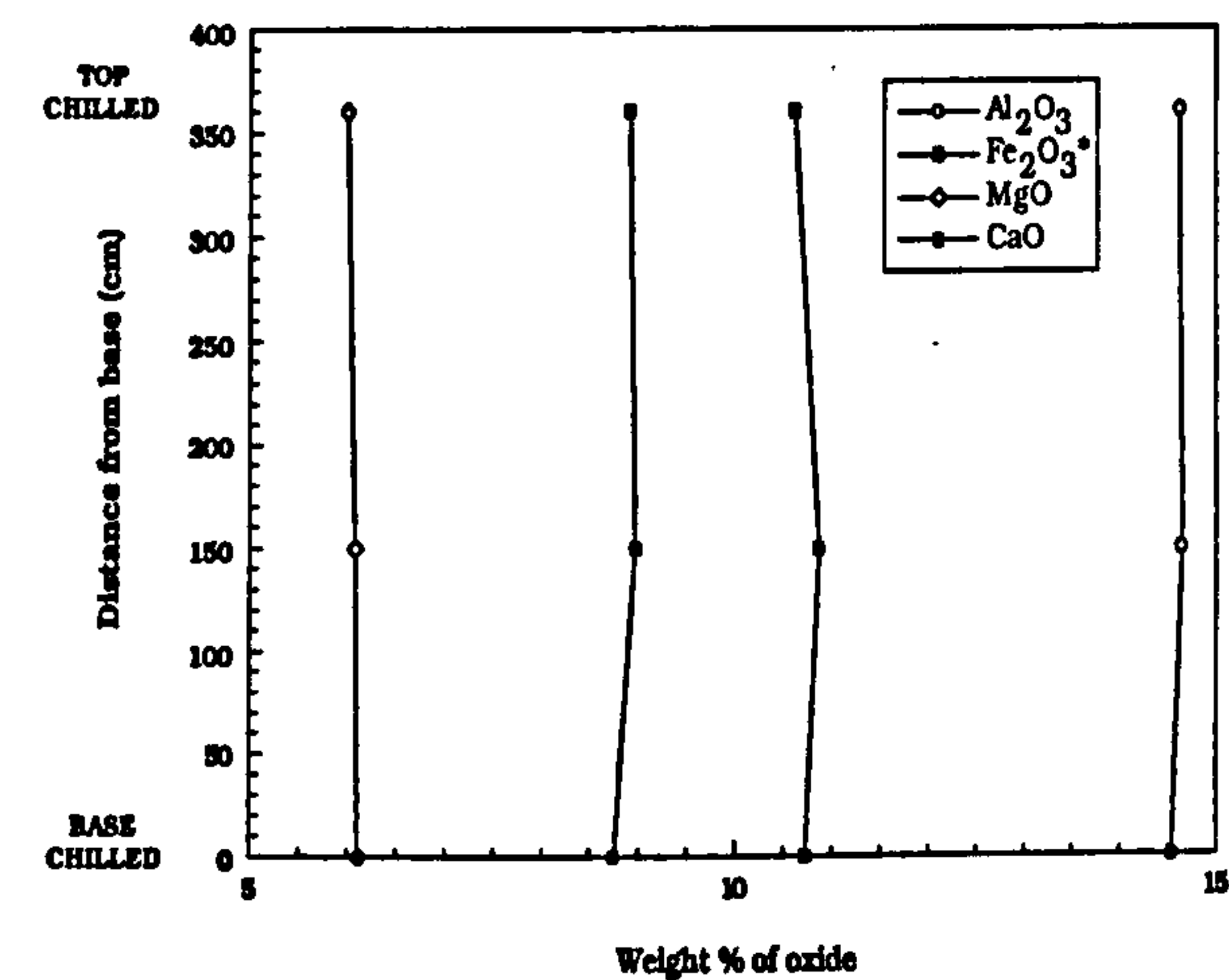


FIGURE 6.12c Variation of selected major- and trace-elements with distance from the base of the basaltic sheet at Traigh Bhàn na Sgurra. SECTION4 = Top & Bottom contact chilled.

shaped channels in the roof of the magma conduit.

In the present study this sheet has been sampled in four sections across variably chilled contacts in order to examine whether or not the chilling process has had an influence on *in situ* contamination. Whole-rock major- and trace-element analyses of all the specimens taken from the sheet are presented in Appendix II. *Figure 6.12a-c* shows the variation in selected major- and trace-elements as a function of distance from the base for three of the sections. These include one section with both margins chilled, one section with one chilled contact, and one section without chilled margins. These data reveal that there are generally no *significant* differences in the major-element composition which, in this case, can be attributed to magma chilling controlling the *in situ* contamination of the magma. All analyses are essentially identical. Major-elements are, however, relatively insensitive indicators of contamination. Trace-element concentrations, however, are more variable through the sheet. It might be expected that the trace-elements which are enriched in the crust (*e.g.* Rb, Ba) would be enriched in the intruding magma at, or close to, unchilled contacts. Unchilled contacts are thought to develop where the flow of the magma in the conduit is turbulent (Kille *et al.*, 1986). If the profiles for Section 1 (no chilled contact) are examined (*Figure 6.12a*), it can be seen that Ba is indeed enriched at both margins. Rubidium, however, shows a maximum at the centre of the sheet. In Section 2 (chilled base), Ba and Rb are all enriched towards the top of the sheet. Variations in most other trace-elements are very small (a few ppm). Barium and Rb can both be highly mobile under conditions of hydrothermal alteration (Dickin & Jones, 1983a; Dickin *et al.*, 1984b; Morrison, 1978). It is considered likely that the perturbations observed in the trace-element concentrations of the sheet could equally be explained by a process of minor late-stage hydrothermal alteration (the rocks are generally very fresh, with only minor alteration of the plagioclase and pyroxene), as by a process of *in situ* incorporation of crustal material. The variable chilled margin of the sheet would obviously exert some control on fluid flow through the rock, with a fine-grained chill acting as a barrier to the passage of hydrothermal fluids.

Sr and Nd isotopes are a more sensitive indicator of crustal contamination. Three samples were therefore analysed for whole-rock Sr-Nd ratios, one next to a chilled contact, one next to an unchilled

contact, and one from the centre of the sheet. The Sr and Nd data are presented in *Table 6.4*. Full isotopic data is presented in Appendix III.

Type of Margin	(⁸⁷ Sr/ ⁸⁶ Sr) _i	(¹⁴³ Nd/ ¹⁴⁴ Nd) _i
UNCHILLED (Section 1, Top)	0.715125	0.512031
CHILLED (Section 3, Top)	0.714512	0.512031
CENTRE (Section 2)	0.714838	0.512025

Table 6.4 Sr/Nd isotope ratios for the Traigh Bhàn na Sgurra sheet.

These results show that the magma in the Traigh Bhàn na Sgurra sheet has indeed been contaminated with upper-crustal material (high ⁸⁷Sr/⁸⁶Sr_i and low ¹⁴³Nd/¹⁴⁴Nd_i). It also shows that there is *some* evidence for *in situ* contamination preserved in the Sr isotopic ratios of the sheet. Samples taken from an unchilled section would be expected to have higher ⁸⁷Sr/⁸⁶Sr_i, due to the incorporation of radiogenic Sr from the country-rocks. As *Table 6.4* documents, the unchilled contact rocks do have the highest ⁸⁷Sr/⁸⁶Sr_i. However, as with the case of mobile trace-elements, Sr isotope signatures can be elevated through hydrothermal processes. For example, ⁸⁷Sr/⁸⁶Sr_i values of the Dippin Sill, Isle of Arran, were raised from magmatic values of 0.7032 to a maximum of 0.7091 due to the passage of ⁸⁷Sr-enriched hydrothermal fluids, although contamination at the magmatic stage also occurred (Dickin *et al.*, 1984b).

Within error, there is no variation in the ¹⁴³Nd/¹⁴⁴Nd_i values for the Traigh Bhàn na Sgurra sheet. Nd isotope values are generally not disturbed by hydrothermal activity (Dickin & Jones, 1983a). This, at first sight, lends support to the theory that the limited elemental and isotopic variation seen in the Traigh Bhàn na Sgurra sheet is a consequence of limited hydrothermal activity, rather than *in situ* crustal contamination. However, since at high degrees of crustal contamination the initial Nd isotopic composition of the magma tends to be buffered close to the values of the crustal contaminant (both for binary mixing and AFC processes), a lack of variation within the Nd isotope data doe not necessarily preclude the possibility of *in situ* contamination.

CHAPTER 7

THE GABBROIC XENOLITHS

The presence of 'non-mantle'-derived ultramafic and mafic xenoliths in suites of volcanic and hypabyssal rocks is widely reported (*e.g.* Arculus & Wills, 1980; Harris, 1983; Munha *et al.*, 1990). They appear to be common in island-arc calc-alkaline/alkaline suites (*e.g.* DeLong *et al.*, 1975; Cigolini & Kudo, 1987), and in continental and oceanic alkaline rocks (*e.g.* Binns *et al.*, 1970). Certain occurrences are thought to be related to the host lava via a process of earlier high-pressure crystal fractionation (*e.g.* Binns, 1969). Such xenoliths are reported less frequently from continental tholeiitic suites. However, examples have been reported from the BTVP. Donaldson (1977) described olivine-anorthite, augite-anorthite, olivine-labradorite, and anorthite cumulate xenoliths from gabbroic anorthosite dykes, of Preshal More affinity, from north-west Skye, and Gibb (1969) described dunitic and peridotitic xenoliths from ultrabasic dykes in central Skye. These occurrences are considered to represent fragments of early-formed cognate cumulates (Gibb, 1969; Donaldson, 1977).

7.1 Occurrence

Several of the sheets from Groups I and II contain ultramafic xenoliths of varying size and mineralogy. They were briefly described by Bailey *et al.* (1924), and were considered to be cognate in origin, although no reasoning was put forward. The xenoliths are generally found near the base of the sheets, suggesting that they were denser than the host magma and the associated aluminous xenoliths, the latter tending to be found near to the top surfaces of the sheets. The xenoliths vary in size from single crystals (xenocrysts) and crystal aggregates a few cm across, to large rounded blocks up to a metre in diameter. Two examples are shown in *Figures 7.1a* and *7.1b*. Mineralogically, they consist of a combination of olivine, pyroxene and plagioclase, together with minor chrome spinel and magnetite.



FIGURE 7.1a

Cognate gabbroic xenolith in a Group I basaltic andesite sheet from Kilfinichen Bay [NM 484280]. Xenoliths are found mainly toward the base of the sheets, and also consist of feldspathic peridotites, pyroxenites and anorthosites. Xenoliths are typically friable, indicating an advanced state of alteration. Hammer shaft 60cm long.



FIGURE 7.1b

Small gabbroic xenoliths in the basaltic facies of the composite sheet at Rudh' a' Chromain [NM 521202]. Xenoliths consist of plagioclase (~An65) and clinopyroxene (~Wo45En47Fs8). Hand lens approx. 5cm in length.

7.2 Mineralogy

Four distinct ultramafic-mafic xenolith types have been found within the LSSC:

- a) Olivine-plagioclase cumulate (feldspathic peridotite);
- b) Clinopyroxene cumulate (pyroxenite);
- c) Plagioclase-clinopyroxene cumulate (gabbro);
- d) Plagioclase cumulate (anorthosite).

Also present are plagioclase-orthopyroxene-magnetite crystal clusters, which will be considered along with the xenoliths.

Approximate primary mineral modes for each rock-type are given in *Table 7.1*. Modes were calculated by averaging 500 point counts from at least two thin sections of each specimen, ignoring those counts which included secondary minerals. Most xenoliths contain interstitial patches of very fine-grained material, consisting of plagioclase, augite and magnetite. This suggest that the xenolith still contained interstitial liquid which was quenched upon emplacement (Arculus & Wills, 1980). The gabbroic xenoliths are also reasonably altered, especially those which contain abundant olivine. Alteration of the olivine to serpentine and iddingsite along cracks and around the crystal margins is ubiquitous. Plagioclase is often very fresh, although alteration to sericite does occur. Clinopyroxene is typically very fresh.

	OLIVINE PLAGIOCLASE CUMULATE	CLINOPYROXENE CUMULATE	PLAGIOCLASE CLINOPYROXENE CUMULATE	PLAGIOCLASE CUMULATE
CUMULUS OLIVINE	60.2%	-	-	-
CUMULUS PLAGIOCLASE	22.2%	-	51.2%	> 98%
INTERSTITIAL PLAGIOCLASE	-	39.6%	-	-
CUMULUS PYROXENE	-	58.2%	36.6%	-
INTERSTITIAL PYROXENE	9.6%	-	-	-
Fe-Ti OXIDES	-	2.4%	-	-
INTERSTITIAL SCORIA	8.0%	-	12.2%	~ 1%

Table 7.1 Mineral modes for the various cognate xenolith types from the LSSC. Modes were calculated by averaging 500 point counts from at least two thin sections. Points which included secondary minerals were ignored.

All xenolith types are medium- to coarse-grained plutonic rocks, comprising orthocumulates, adcumulates and mesocumulates (Wager *et al.*, 1960; McBirney & Hunter, 1995). None of those examined exhibit igneous layering or possess a tectonic fabric.

Olivine-plagioclase cumulate (feldspathic peridotite)

These are the most common gabbroic xenoliths found. They are generally the largest type, and consist of dark green or black, rounded blocks up to 1 metre in diameter. The blocks are often highly friable, presumably due to pervasive alteration (see below). In thin-section they consist of cumulus olivine (mode > 80%), which forms rounded to subhedral grains up to 5mm in diameter (*Figure 7.2*). Alteration to serpentine and red-brown iddingsite is ubiquitous along cracks and around crystal margins. Some crystals are completely pseudomorphed by serpentine, together with, in places, aggregates of tiny magnetite crystals. However, much of the olivine is fresh, and compositions range from Fo₈₀ to Fo₈₃. Some olivines contain inclusions of chrome-spinel,

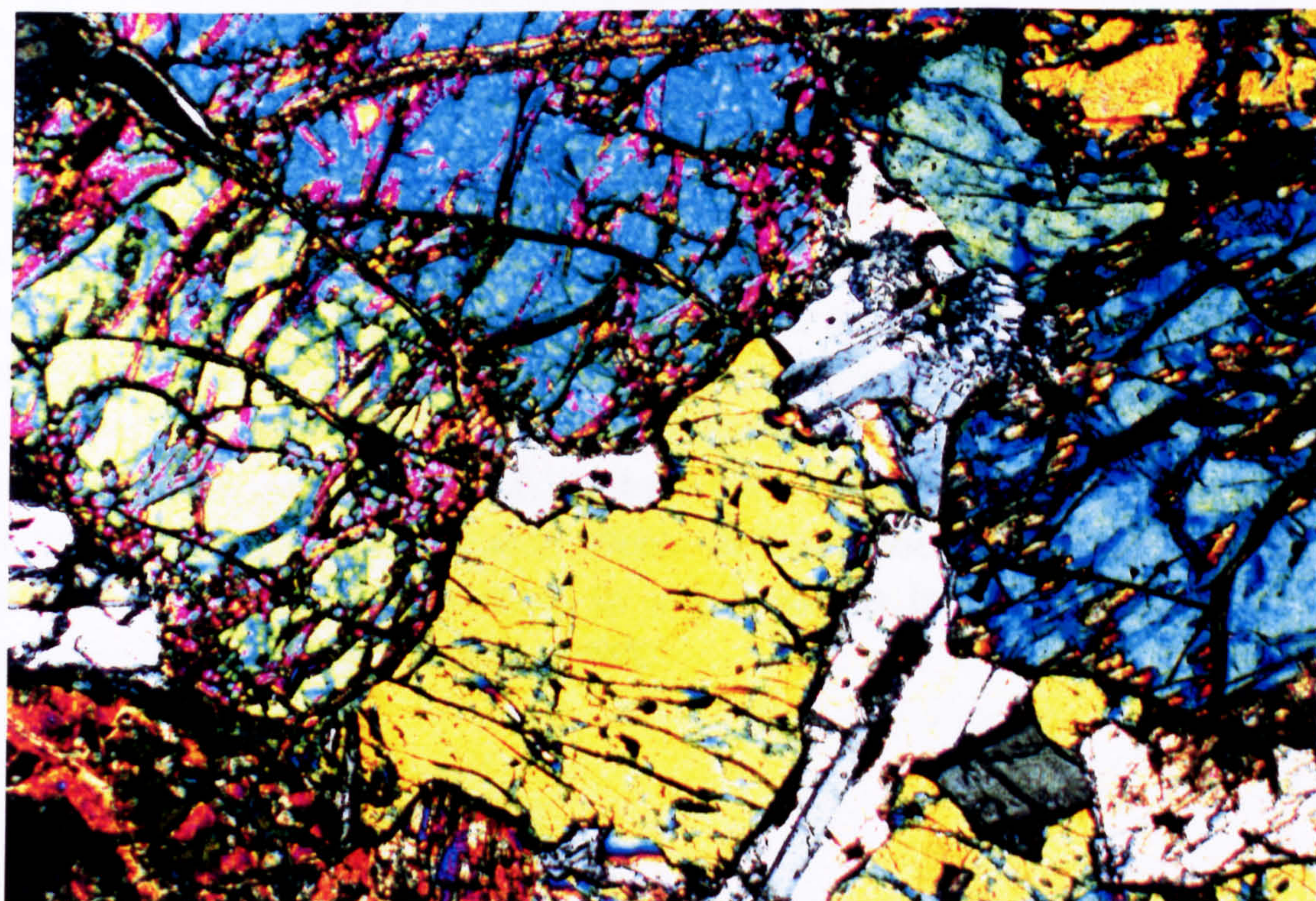
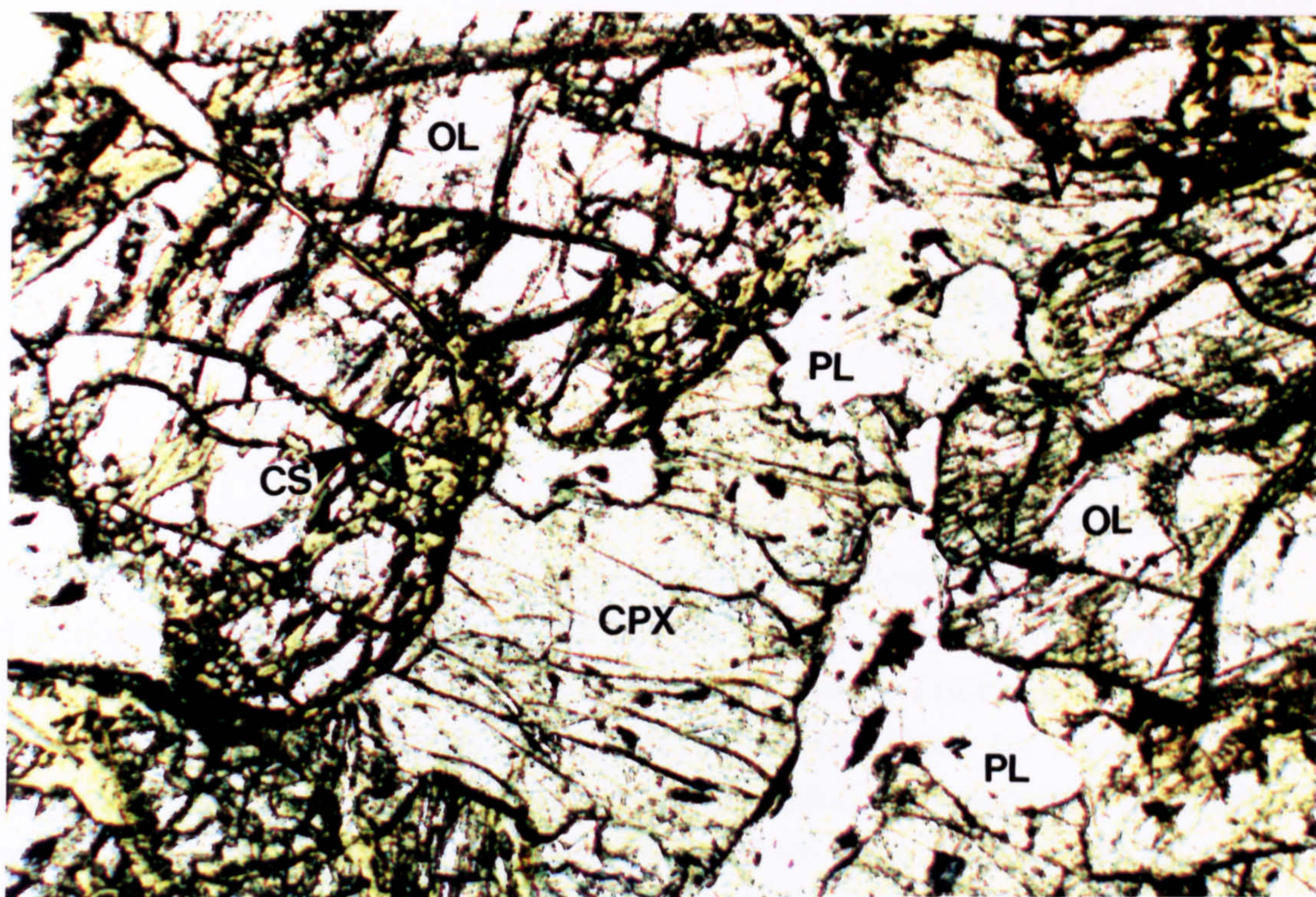


FIGURE 7.2

Feldspathic peridotite cognate xenolith. Rock contains cumulus olivine (Fo₈₄) (OL) with small inclusions of Cr-spinel (CS), with intercumulus plagioclase (An₈₇) (PL), and clinopyroxene (Wo₄₂En₄₈Fs₁₀) (CPX). Olivine is extensively altered to serpentine, iddingsite and magnetite along cracks and around the crystal margins. Intercumulus plagioclase and clinopyroxene are generally much fresher. (ppl upper, xpl lower; Field of view 2x3mm; Sample KBGX1)

which forms euhedral crystals a few μm across, and which are homogeneous in composition. Cr-spinel also occurs in embayments within individual olivine crystals, and also disseminated through the interstitial clinopyroxene and cumulus plagioclase. There is, however, some inter-sample variation in Cr-spinel composition: $(\text{Mg}_{0.58-0.54}\text{Fe}^{2+}_{0.42-0.46})(\text{Cr}_{0.85-1.10}\text{Al}_{0.90-0.65}\text{Fe}^{3+}_{0.25-0.25})\text{O}_4$ (see Table 7.5). This variation appears to be related to the nature of the individual crystal's immediate environment. Those Cr-spinels trapped in cumulus olivine tend to be the most Mg and Al-rich, whereas those contained within plagioclase or clinopyroxene are the most Cr-rich. The chrome-spinel is considered to be an early cumulus phase. There is also minor cumulus plagioclase, which forms laths up to 3mm in length. The plagioclase generally has complex twinning and is invariably strongly zoned ($\text{An}_{87} - \text{An}_{67}$), core to rim. There does not appear to be any adcumulate growth of either the olivine or the plagioclase, although the zoned nature of the plagioclase crystals might warrant these rocks being described as mesocumulates (*cf.* Conrad & Kay, 1984).

Clinopyroxene occurs as interstitial crystals. It is generally fresh, and is a pale-brown, non-pleochroic variety. Individual crystals show no zoning, but there is slight compositional variation within each sample, from: $\text{Wo}_{41}\text{En}_{49}\text{Fs}_{10}$ to $\text{Wo}_{45}\text{En}_{45}\text{Fs}_{10}$. Intercumulus plagioclase is also present and has the same composition as the cumulus feldspar. Some interstitial liquid has quenched to a fine-grained, mixture of plagioclase (An_{45}), diopsidic-augite ($\text{Wo}_{45}\text{En}_{45}\text{Fs}_{10}$) and magnetite. Those cumulus crystals which project into these fine-grained areas tend to have well-formed crystal edges, and plagioclase crystals often have an overgrowth rim similar in composition to the fine-grained plagioclase (*cf.* Arculus & Wills, 1980).

Clinopyroxene cumulate (pyroxenite)

This uncommon variety of xenolith (only one specimen has been found), is pale brown and generally appears fresher than the olivine-plagioclase cumulates. It is dominated by fresh clinopyroxene in thin-section (*Figure 7.3*), which forms large, euhedral grains up to 4mm across, elongate grains 5mm long, and, more commonly, rounded and anhedral grains a few mm in diameter. The cumulus pyroxene is generally strongly zoned, showing marked Fe-enrichment from core to rim ($\text{Wo}_{50}\text{En}_{41}\text{Fs}_9$ - $\text{Wo}_{36}\text{En}_{32}\text{Fs}_{32}$). A few crystals show this zoning optically, although this is not the rule. In places there is evidence for a small amount of adcumulate growth. Plagioclase is interstitial to the clinopyroxene, forms small (1-2mm), well-shaped laths, and typically shows continuous normal zoning (An_{63} - An_{47}).

Plagioclase-clinopyroxene cumulate (gabbro)

These xenoliths are light-coloured, feldspar-rich rocks, which also contain bright green crystals of pyroxene visible in hand-specimen. In thin-section, the main cumulus phase can be seen to be plagioclase, which forms elongate laths up to 3mm in length. These crystals are zoned from An_{86} to An_{80} , core to rim, although most show a narrow adcumulate overgrowth at $\sim \text{An}_{63}$ (*Figure 7.4*). Clinopyroxene has crystallized as a cumulus phase, forming large (3-4mm) euhedral crystals, and, interstitially, often forming large poikilitic plates which enclose the cumulus plagioclase (*Figure 7.5*). The clinopyroxene is a diopsidic augite ($\text{Wo}_{45}\text{En}_{47}\text{Fs}_8$), and shows no compositional zoning. As with the other varieties of gabbroic xenolith, some of the interstitial liquid has quenched to a fine-grained mixture of plagioclase (An_{57}), augite ($\text{Wo}_{45}\text{En}_{45}\text{Fs}_{10}$), and titanomagnetite.

Plagioclase cumulate (anorthosite)

One specimen of an extreme plagioclase adcumulate (Wager *et al.*, 1960; McBirney & Hunter, 1995) has been found. It is pale grey, and consists entirely of feldspar in hand-specimen. In thin-section the rock consists of coarse-grained plagioclase (up to 10mm) which forms euhedral laths and irregularly-shaped grains (*Figure 7.6*). All the grains are interlocking, and there is very little interstitial material. Unlike

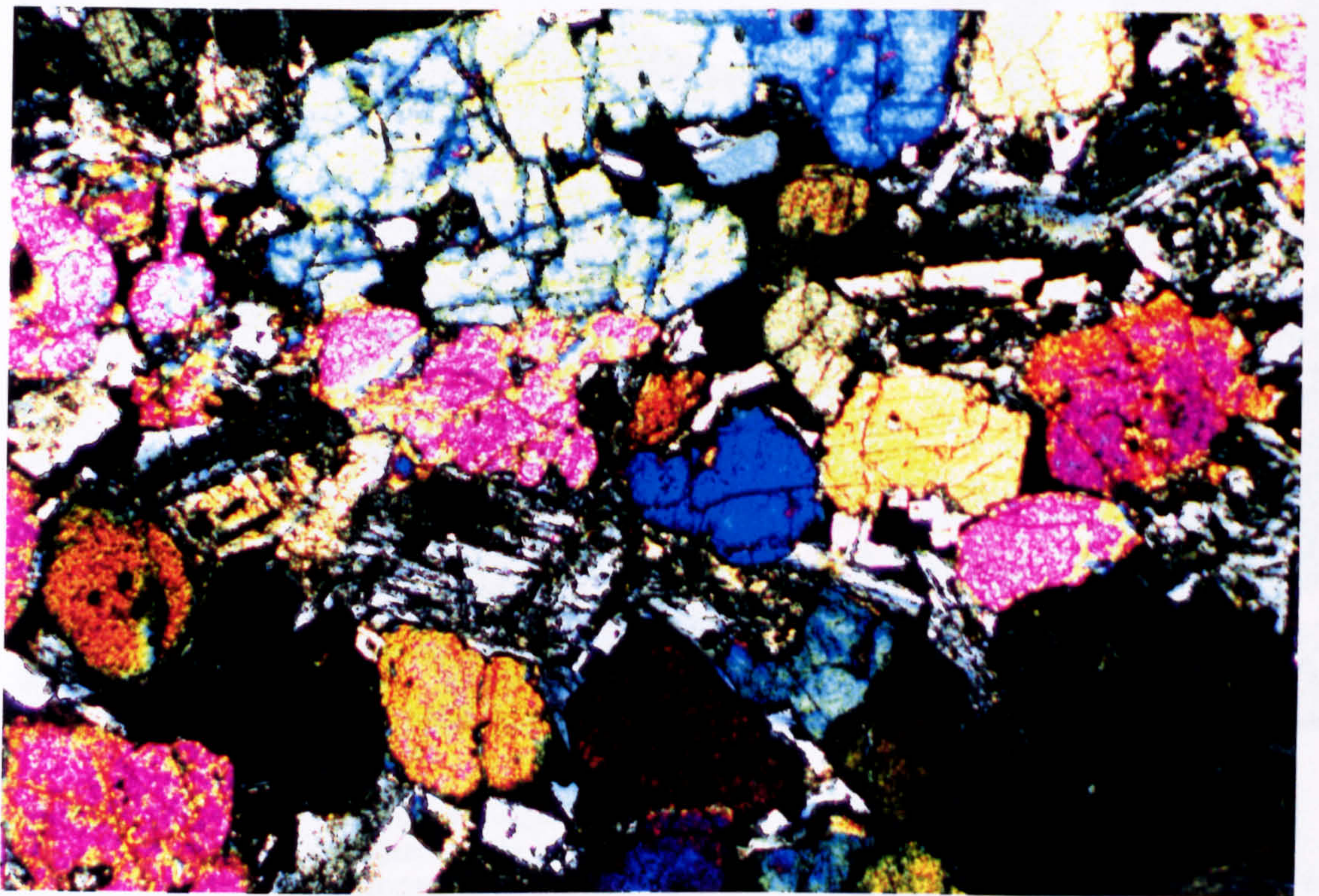


FIGURE 7.3

Cumulus clinopyroxene in a pyroxenite cognate xenolith. Pyroxene crystals are often strongly zoned (Wo₅₀En₄₁Fs₉ to Wo₃₆En₃₂Fs₃₂) core to rim. Rock also contains intercumulus plagioclase (~An₆₅), which shows alteration to sericite. (xpl; Field of view 2x3mm; Sample KBGX2).

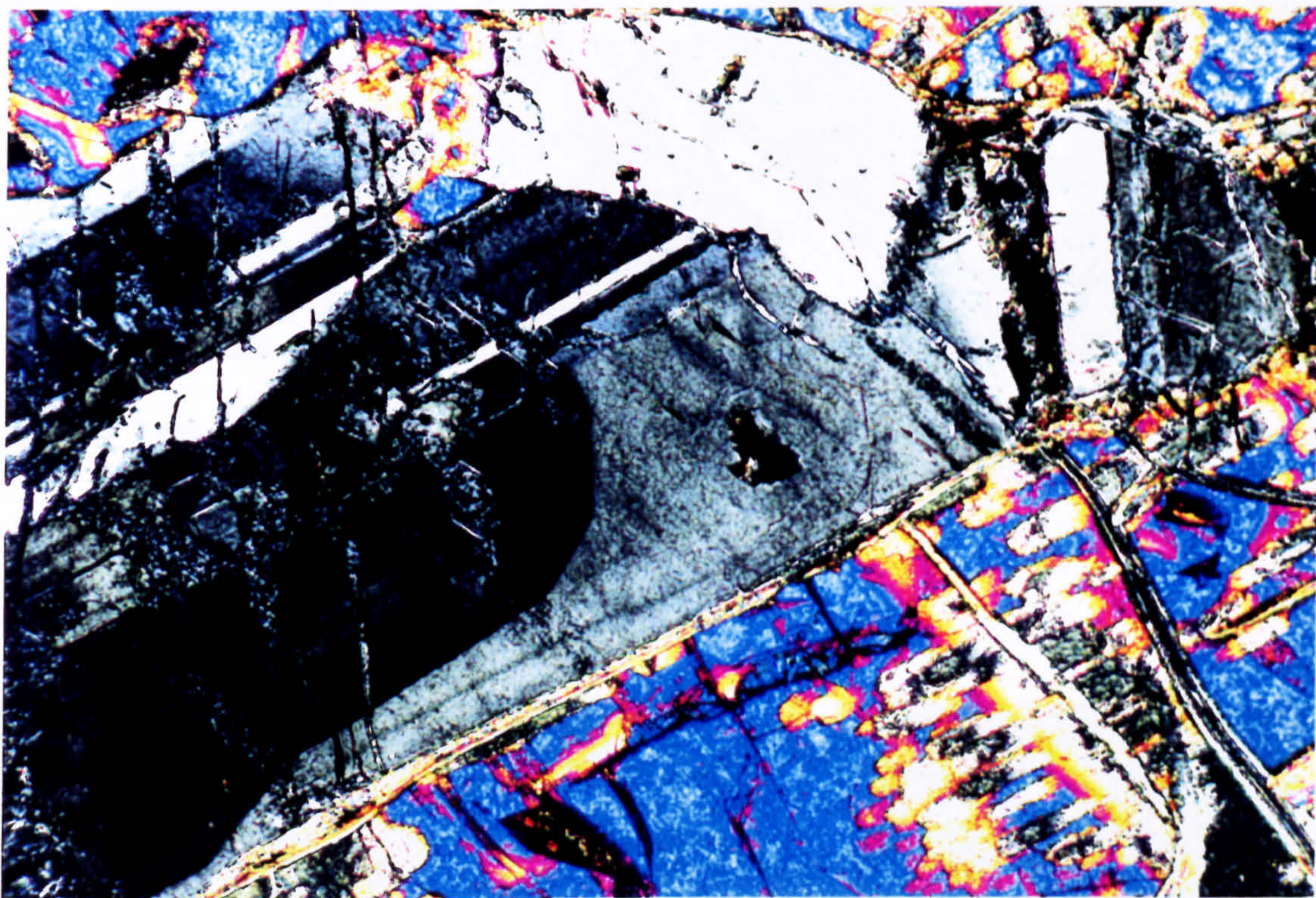


FIGURE 7.4

Cumulus plagioclase showing resorbed core and overgrowth. Plagioclase is altered to sericite. Also shown is poikilitic clinopyroxene, showing minor alteration to chlorite. (xpl; Field of view 0.8x1.2mm; Sample KGHYX3).

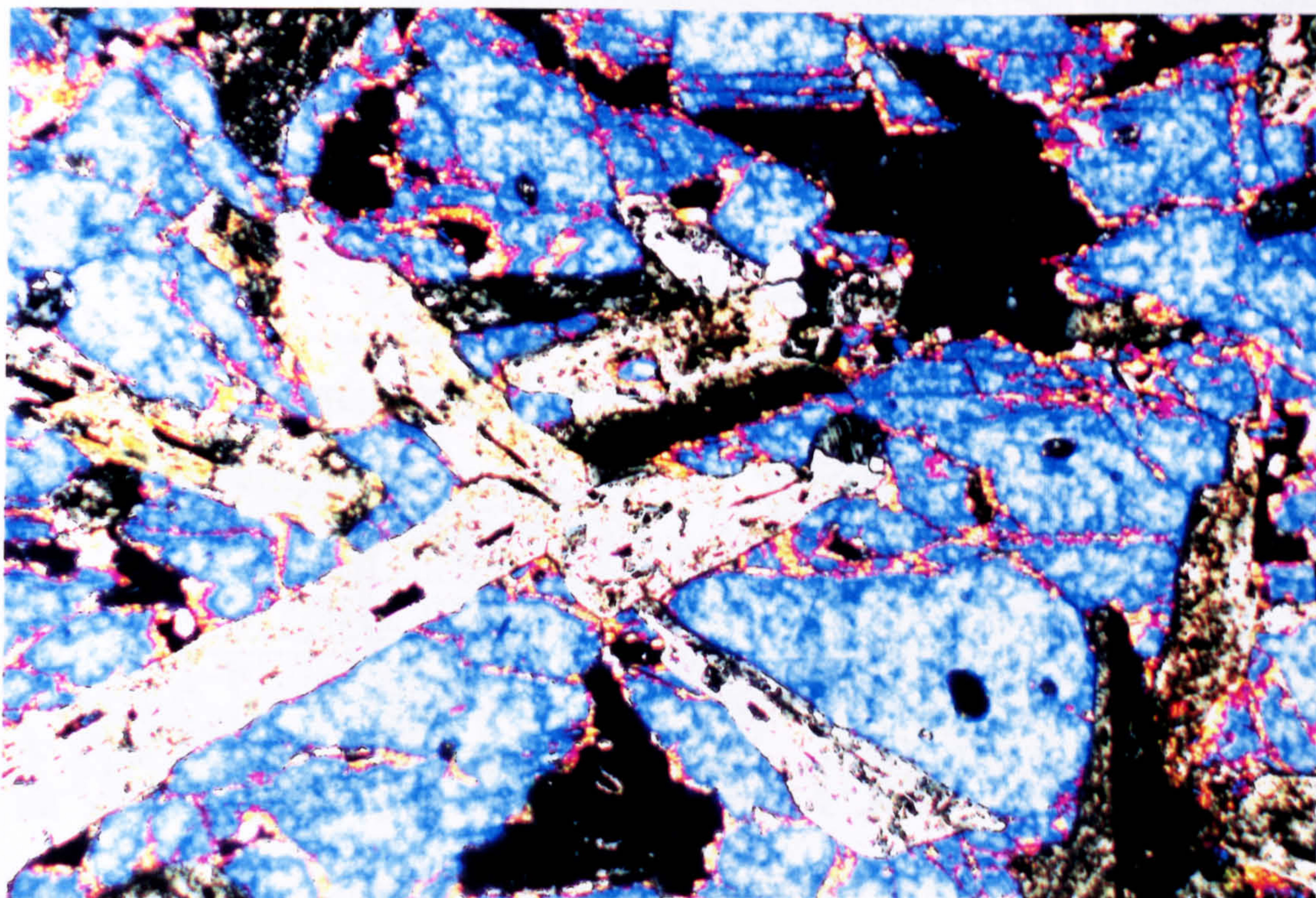


FIGURE 7.5a Large poikilitic plates of clinopyroxene (Wo₄₅En₄₇Fs₈) in gabbroic cognate xenolith, surrounding cumulus plagioclase (An₈₀). (xpl; Field of view 2x3mm; Sample KBHYX3).

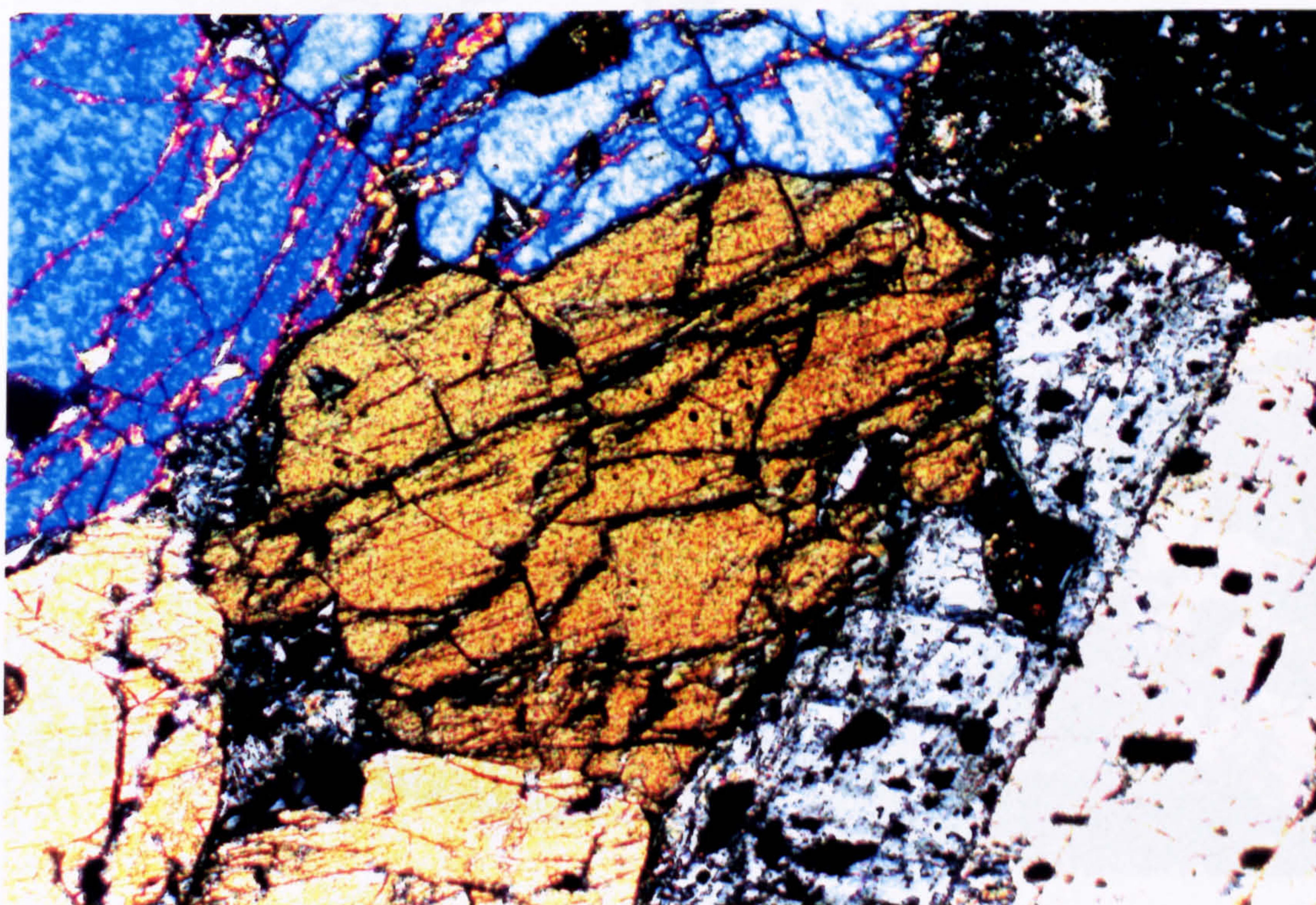


FIGURE 7.5b Fresh, cumulus clinopyroxene (Wo₄₅En₄₇Fs₈) in a gabbroic cognate xenolith. Cumulus plagioclase is also present (An₈₅). (xpl; Field of view 2x3mm; Sample KBHYX1).

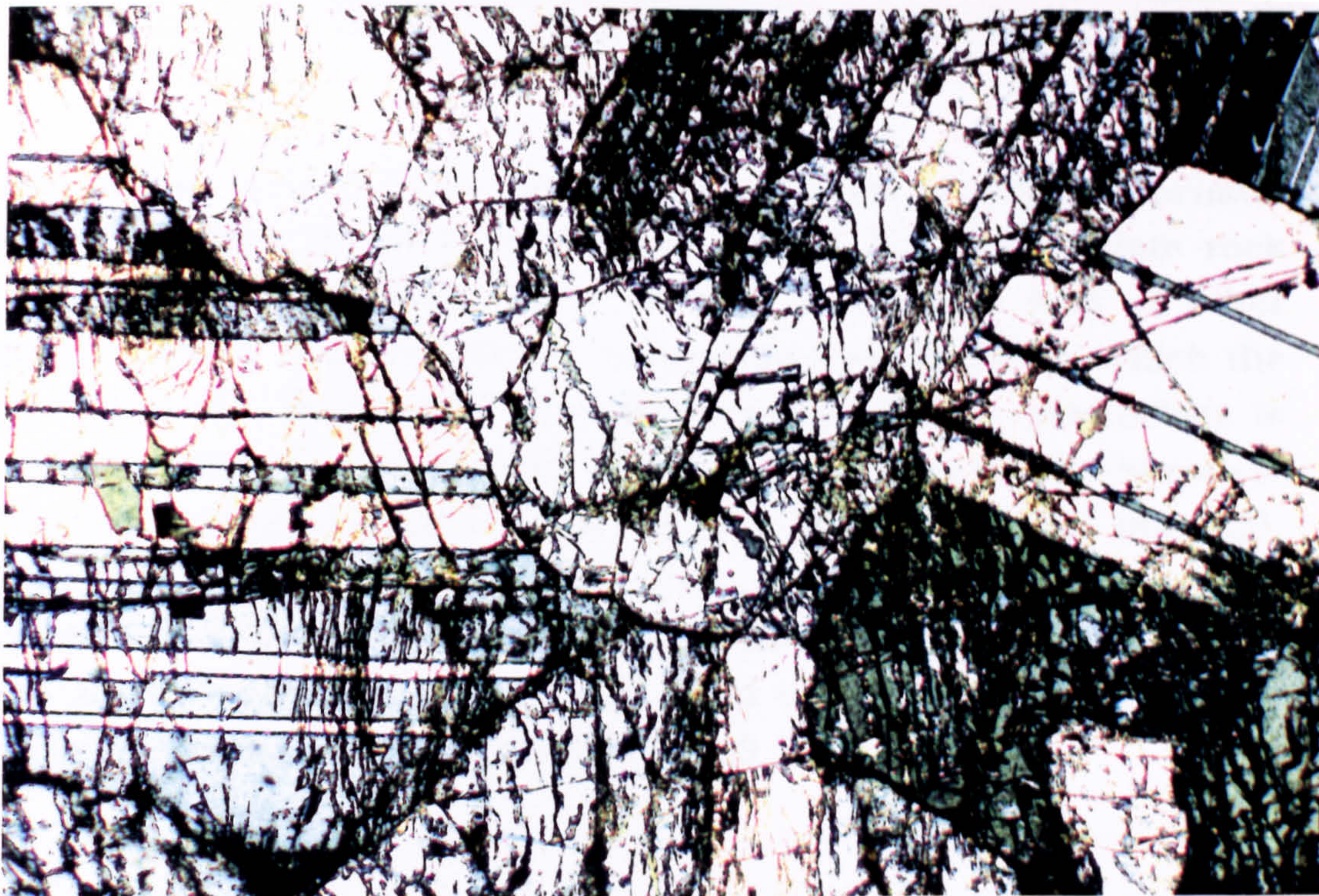


FIGURE 7.6

Cumulus plagioclase in anorthosite xenolith. Plagioclase shows normal zoning (An₈₄ to An₈₀) core to rim. Extensive alteration has occurred, with growth of zeolite along crystal edges and down cracks. (xpl; Field of view 2x3mm; Sample KIFX1).

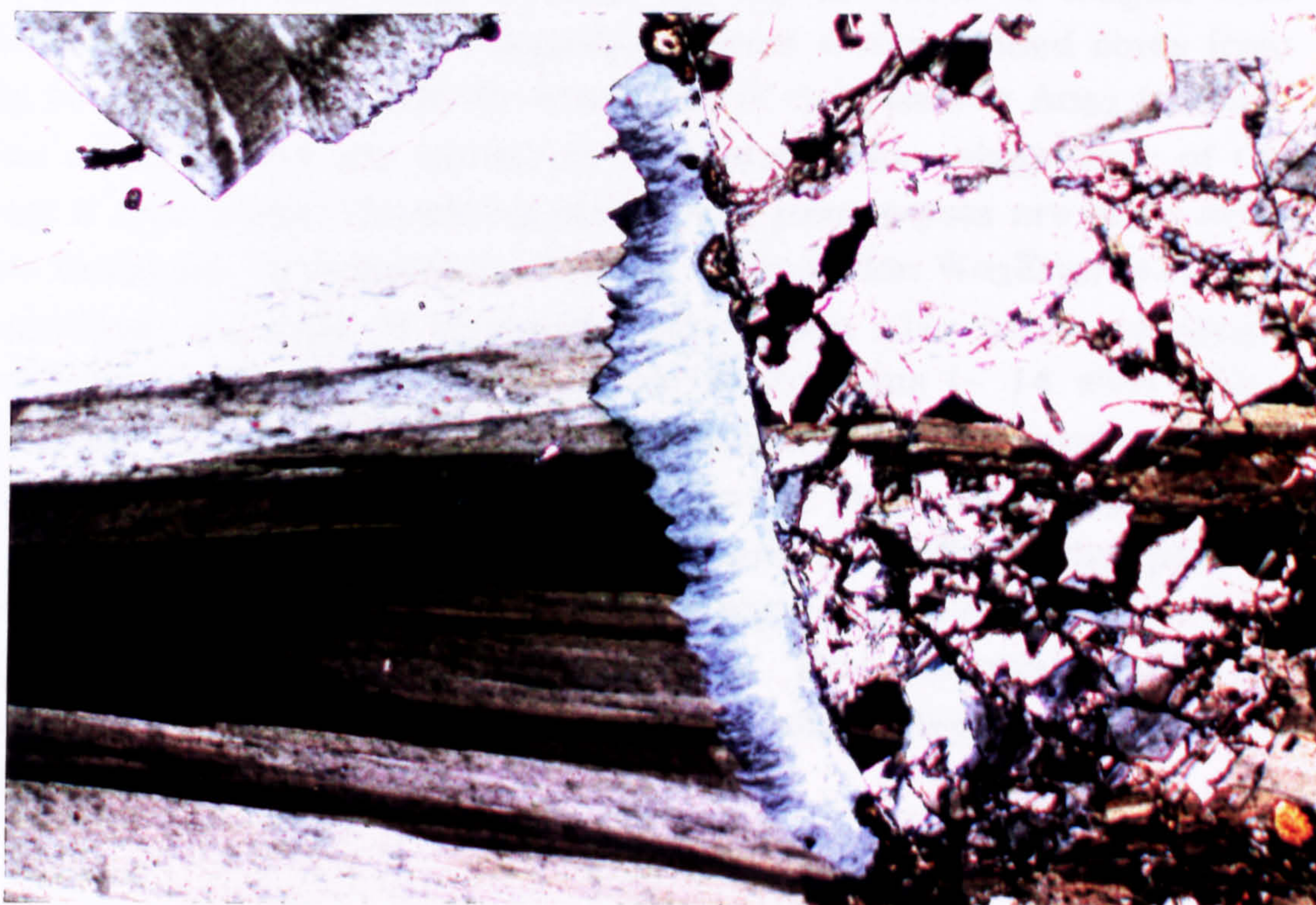


FIGURE 7.7

Fibrous zeolite filling cavities in an anorthosite cognate xenolith. Zeolite shows radial growth, and has also altered the plagioclase along fractures. (xpl; Field of view 2x3mm; Sample KIFX1).

the plagioclase which forms the rims to certain aluminous crustal xenoliths (Chapter 9), each plagioclase crystal in the cumulate rock has distinct normal zoning. There is also a complete lack of other aluminous phases such as mullite, corundum and pleonaste, which the crustal xenoliths ubiquitously contain (Chapter 9). The plagioclase is extensively fractured, presumably due to compaction of the cumulate pile, an interpretation reinforced by the lack of intercumulus material. The fracturing of the feldspar has facilitated infiltration of hydrothermal fluids, as many of the crystals display alteration to zeolite, and some of the cavities are filled with radiating clusters of zeolite (most likely thomsonite) (Figure 7.7).

Plagioclase-orthopyroxene-magnetite crystal clusters

The more evolved members of the LSSC occasionally contain crystal clusters comprising plagioclase, orthopyroxene and magnetite. These are considered here along with the gabbroic xenoliths since the presence of orthopyroxene phenocrysts is relatively rare in the host rocks (although orthopyroxene occurs as a groundmass pyroxene in several sheets). Individual crystals are up to 1mm in length, and clusters up to 1cm across. Plagioclase shows reverse-zoned cores from An₅₈ to An₆₃, with a normally-zoned rim of composition An₆₂ to An₆₁. These compositions are similar to the groundmass plagioclase of the Group II host rocks. Coexisting plagioclase primocrysts are often more calcic (An₆₅₋₇₀). Orthopyroxene has the composition Wo₂En₅₇Fs₄₁, and is unzoned. Crystals of identical composition also occur as single 'phenocrysts'. The magnetite is highly titaniferous (~ 14 wt% TiO₂), and shows no exsolution features. The coarse grain-size and euhedral habit of all three phases, and the zoning in the plagioclase, suggest that the plagioclase, magnetite and orthopyroxene were all liquidus phases. As such, the crystal clusters most likely represent cognate precipitates from a relatively evolved basic magma. This contrasts with the predominantly ultramafic nature of the other types of cumulate xenolith.

7.3 Mineral Chemistry

Mineral compositions of cumulus, interstitial and quench phases were investigated using electron-probe micro-analysis. The aim was to document inter sample variations, and to discover the nature of the compositional zonation evident in many of the phases. Representative analyses of each phase from each xenolith type are presented in *Tables 7.2-7.5*. A complete listing of mineral analyses from the gabbroic xenoliths is given in Appendix IV.

Olivine

Olivine compositions cover a limited range within the xenoliths examined, varying from Fo₈₃ to Fo₈₅. Representative analyses are presented in *Table 7.2*. Individual crystals show no zoning from core to rim, with compositions generally varying by less than 0.5% Fo. Nickel concentrations are highly variable within any one specimen, and range from 690ppm to 1980ppm. There is no correlation between Ni content and olivine composition (*cf.* Donaldson, 1977; Conrad & Kay, 1984; Claydon, 1990). Calcium contents are also variable, ranging from ~1500ppm to 2100ppm. These are generally higher than the calcium contents of olivines from the Rum Intrusion (Donaldson, 1977) and are more typical of the olivine phenocrysts from the Skye Preshal More olivine tholeiites (Esson *et al.*, 1975). Again, there is no correlation between Ca content and olivine composition (*cf.* Donaldson, 1977). The lack of correlations between the forsterite content and Ni or Ca within the olivines may suggest that they have suffered extensive post crystallization re-equilibration (*e.g.* Evans & Moore, 1968).

SAMPLE : Cognate Xenolith - KBGX1 (Feldspathic Peridotite) - Cumulus Olivine							
ANALYSIS No.	Olivine 1	Olivine 2	Olivine 3 Core	Olivine 3 Rim	Olivine 4	Olivine 5	Olivine 6
SiO ₂	39.43	39.61	39.35	39.35	39.35	39.22	39.58
TiO ₂	0.03	0.08	0.05	0.00	0.00	0.12	0.00
Al ₂ O ₃	0.05	0.02	0.05	0.02	0.04	0.05	0.05
Cr ₂ O ₃	0.04	0.04	0.03	0.03	0.05	0.01	0.03
MgO	44.40	44.38	44.57	44.38	44.12	44.90	44.68
CaO	0.26	0.26	0.29	0.29	0.28	0.27	0.22
MnO	0.18	0.24	0.23	0.24	0.23	0.21	0.26
FeO	15.71	15.70	14.82	14.71	14.29	14.48	14.62
NiO	0.09	0.25	0.18	0.19	0.17	0.17	0.07
TOTAL	100.18	100.58	99.58	99.20	98.53	99.43	99.50
FORMULA BASED ON 4 OXYGENS							
Si	0.99	0.99	0.99	1.00	1.00	0.99	1.00
Ti	0.00	0.00	0.00	0.00	0.00	0.00	0.00
Al	0.00	0.00	0.00	0.00	0.00	0.00	0.00
Cr	0.00	0.00	0.00	0.00	0.00	0.00	0.00
Mg	1.67	1.66	1.68	1.68	1.67	1.69	1.68
Ca	0.01	0.01	0.01	0.01	0.01	0.01	0.01
Mn	0.00	0.01	0.01	0.01	0.01	0.01	0.01
Fe(ii)	0.33	0.33	0.31	0.31	0.30	0.31	0.31
Ni	0.00	0.01	0.00	0.00	0.00	0.00	0.00
TOTAL	3.01	3.00	3.00	3.00	3.00	3.01	3.00
ENDMEMBER %							
Fo	83.15	83.15	83.95	83.99	84.30	84.37	84.24
Fa	16.51	15.50	15.66	15.61	15.32	15.26	15.47
Mo	0.34	0.35	0.39	0.40	0.38	0.37	0.29

Table 7.2 Composition of cumulus olivines from a feldspathic peridotite xenolith (KBGX1).

Clinopyroxene

Clinopyroxene is a major constituent of all the cumulate xenolith types, either as a cumulus or interstitial (intercumulus) phase. The range of clinopyroxene compositions recorded is large, ranging from diopside and salite, through diopsidic-augite, augite, to ferroaugite. The compositional trend is shown on the Di-Hd-En-Fs quadrilateral in *Figure 7.8a*. The pyroxenes of the cumulate xenoliths parallel the trend defined by the pyroxenes of the Skaergaard Intrusion (Brown, 1957, Brown & Vincent, 1963; Wager & Brown, 1968). This reinforces the proposal that the parent magmas to the LSSC were tholeiitic in nature, and underwent low pressure 'gabbroic' fractionation, at least, prior to emplacement within the upper crust. This range in compositions is not only seen within the suite of xenolith types, but also within individual cumulate crystals, as shown in *Figure 7.8b*. This zonation is extreme, showing a similar iron enrichment as the pyroxenes of the Layered Series of the Skaergaard Intrusion (Brown, 1957; Wager & Brown, 1968).

The majority of the clinopyroxenes contain an excess of aluminium after allocation of Al to the tetrahedral site (*Figure 7.9a*). The pyroxenes are in fact enriched in Al at any given Si content when compared with those from the Group I and Group II host magmas. The highest Al contents occur in the iron-rich rims of certain cumulus pyroxenes.

Titanium contents vary from 0.005 to 0.024 CPFU, and are, for the most part, positively correlated with degree of fractionation (decreasing Mg#), as shown in *Figure 7.9b*. The interstitial clinopyroxenes from the feldspathic peridotites are, however, enriched in Ti at a relatively constant low Mg#. The iron-rich rims to some of the cumulus clinopyroxenes (Mg# 0.76-0.44), although having high Ti contents (0.015-0.024 CPFU) show a decrease in the rate of Ti enrichment with degree of fractionation. Titanium shows a similar 'curvi-linear' relationship with total Al content (*Figure 7.9d*), and a negative correlation with Si (*Figure 7.9e*).

These relationships between Al, Ti and Si are similar to those seen in the groundmass clinopyroxenes of the Group I and II magmas (see Chapter 2.2). The Al content of calcic-pyroxene is a reflection of the silica activity of the magma (Brown, 1957), and the conditions under which the pyroxene crystallized (Binns *et al.*, 1970), with high Al (and

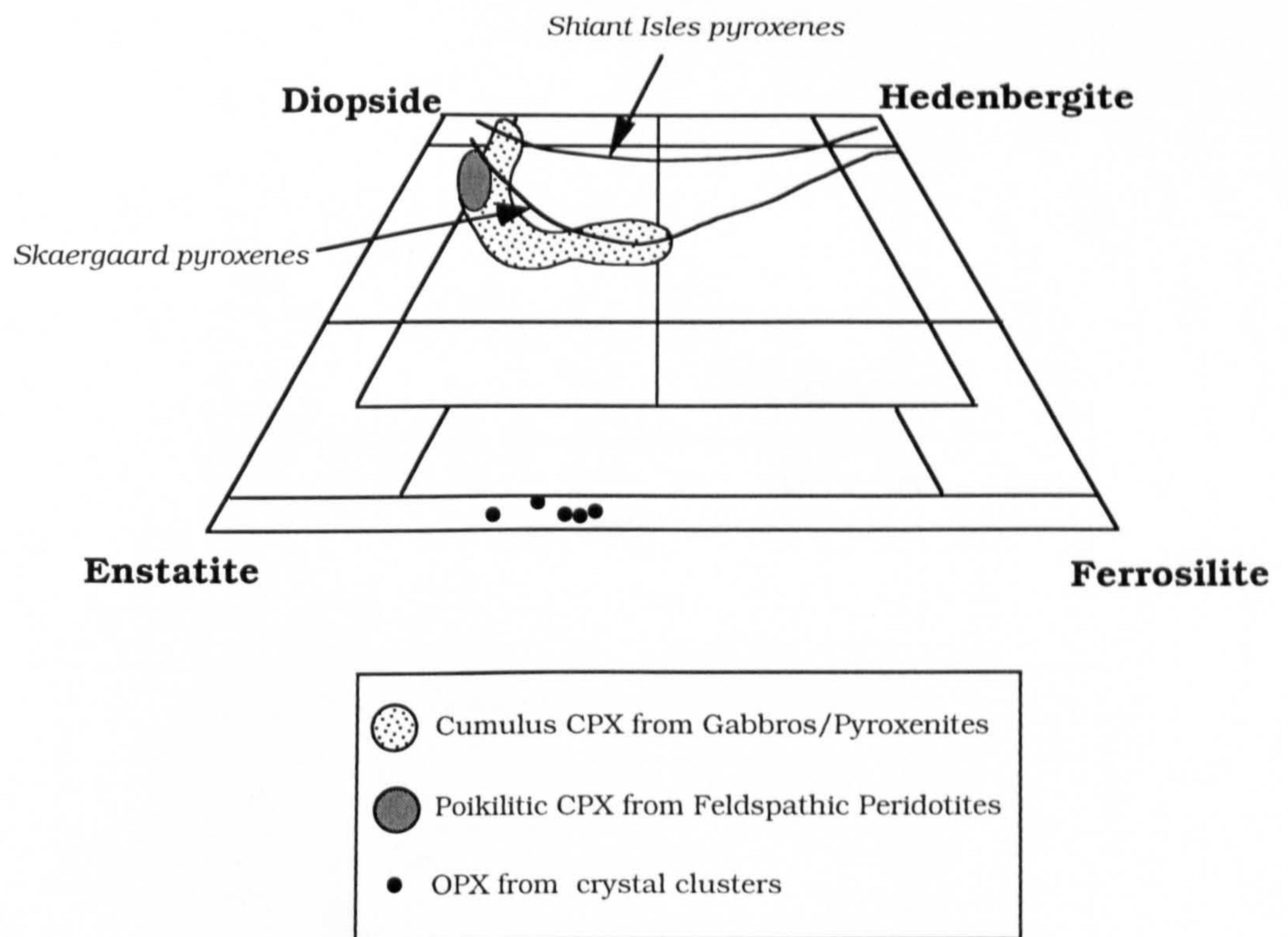


FIGURE 7.8a Pyroxene compositions within gabbroic cumulate xenoliths and crystal clusters found in members of the LSSC.

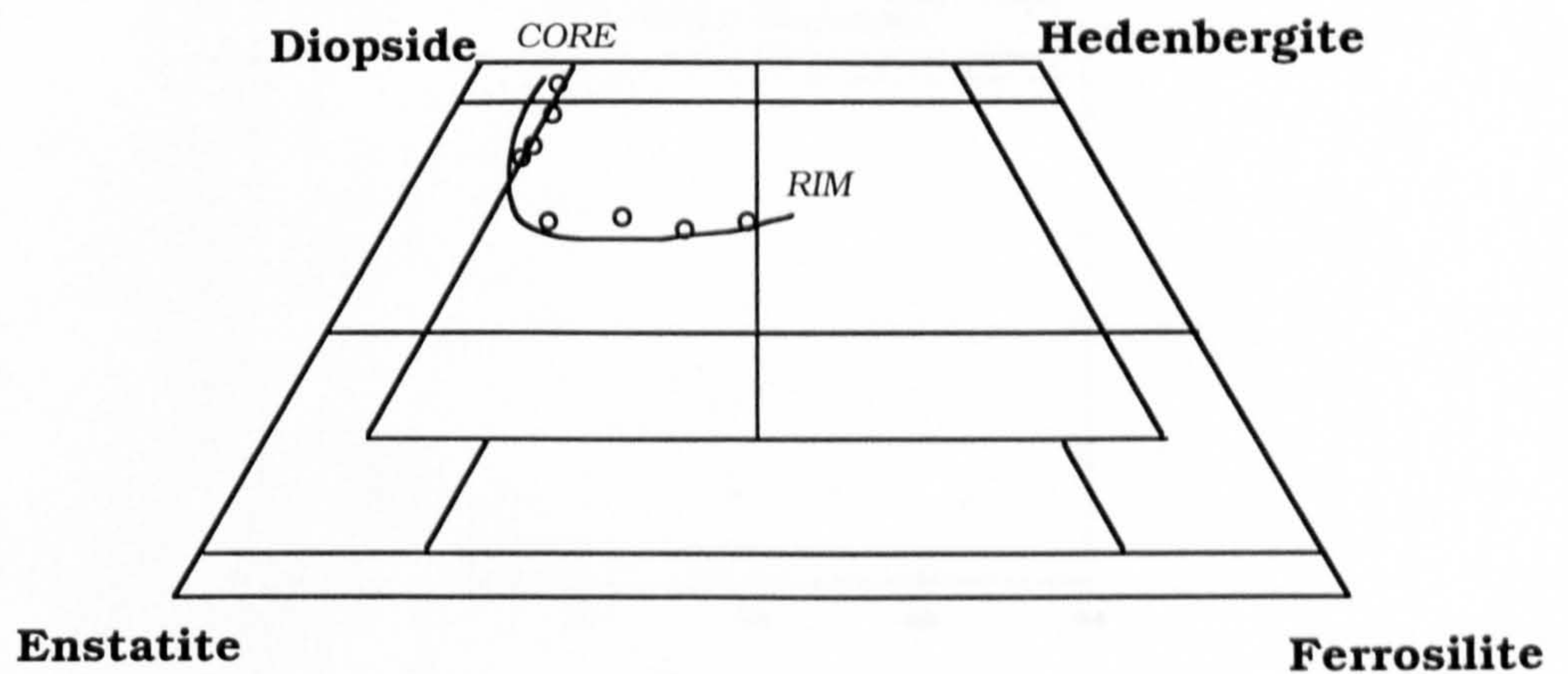


FIGURE 7.8b Compositional zoning within single clinopyroxene crystals found in clinopyroxene-plagioclase cumulate xenoliths.

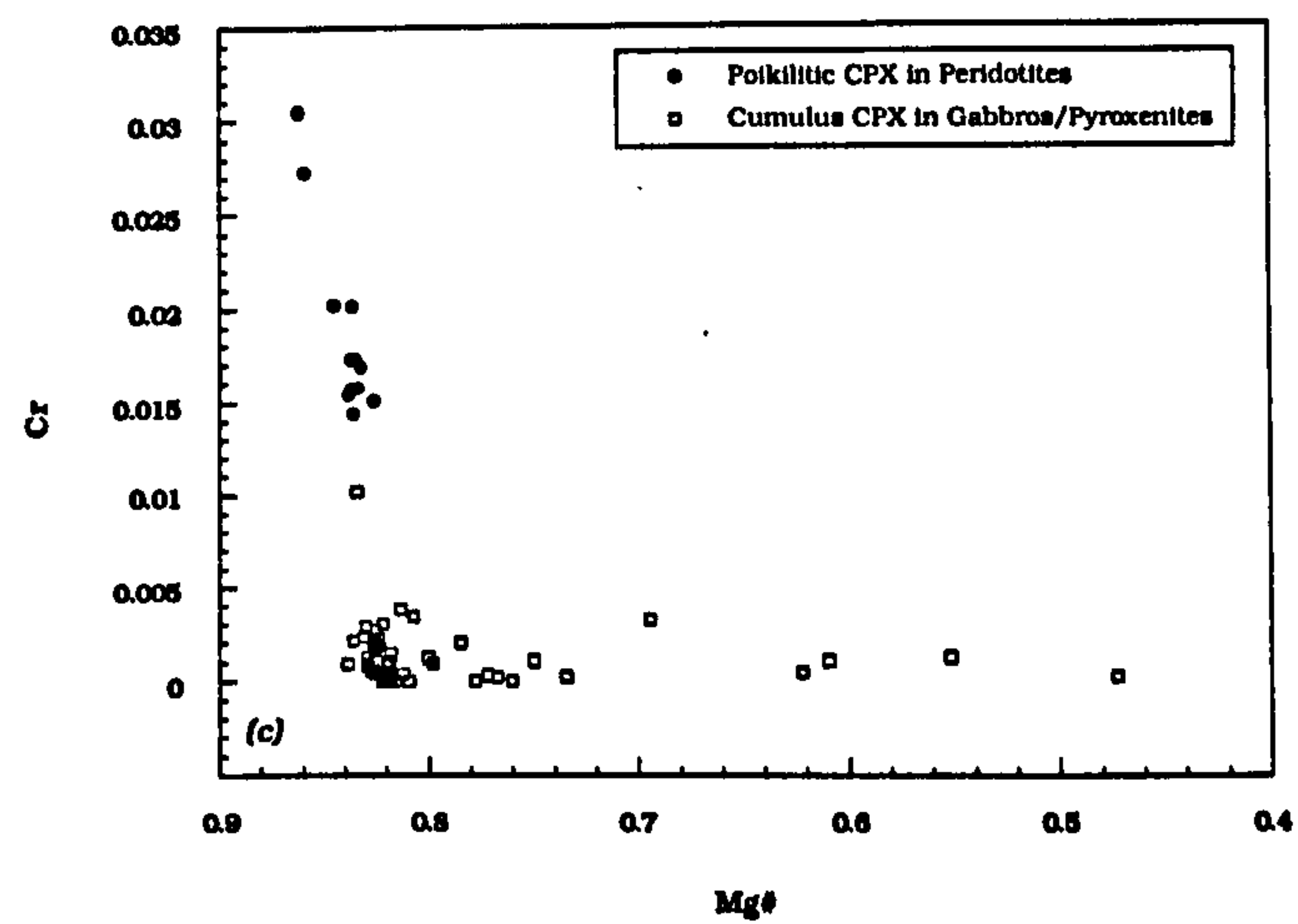
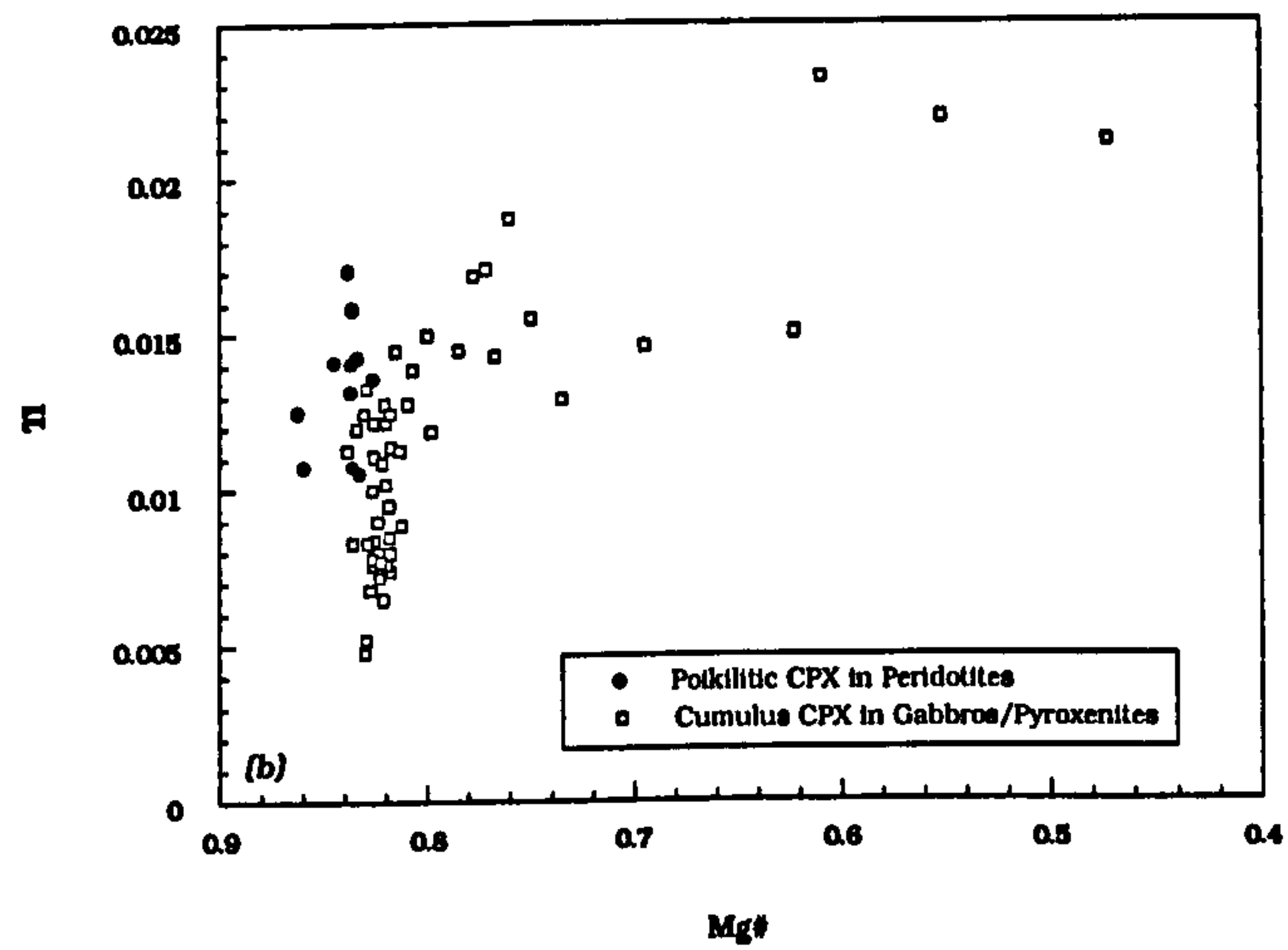
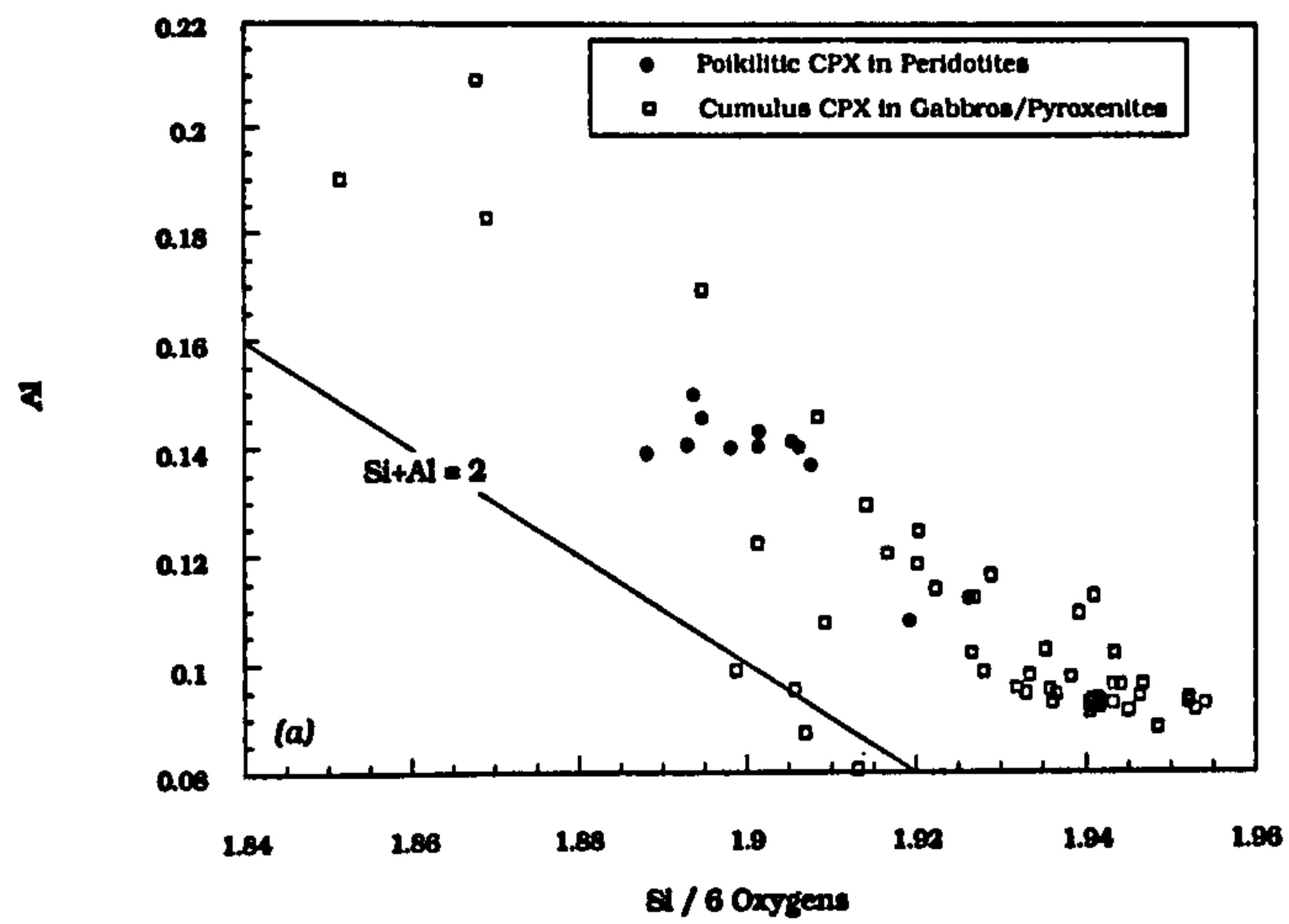


FIGURE 7.9 Cation variations in cumulus and interstitial clinopyroxene from gabbroic cumulate xenoliths. Cations calculated on the basis of 6 oxygens per formula unit.

(a) Al - Si

(b) Ti - Mg#

(c) Cr - Mg#

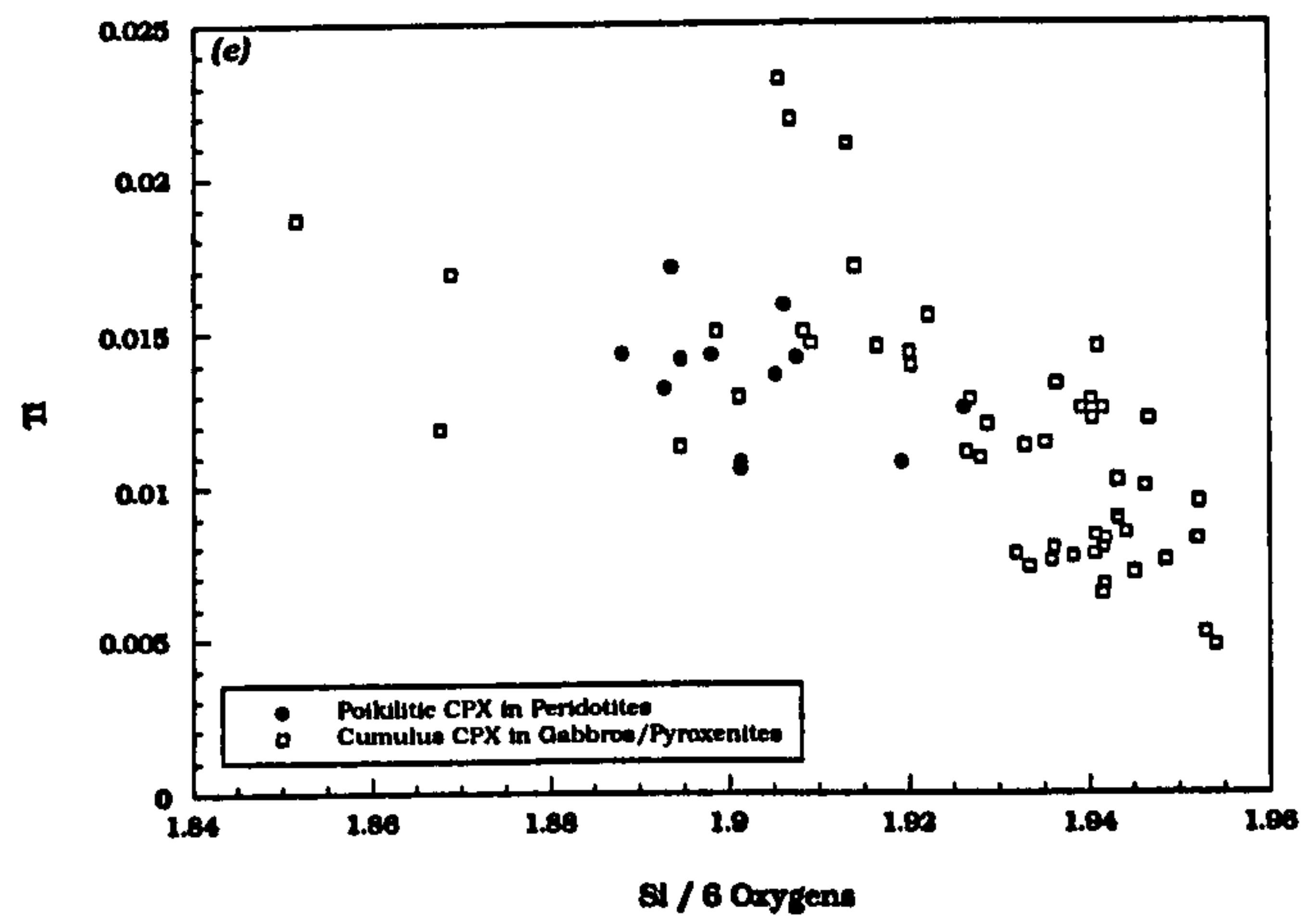
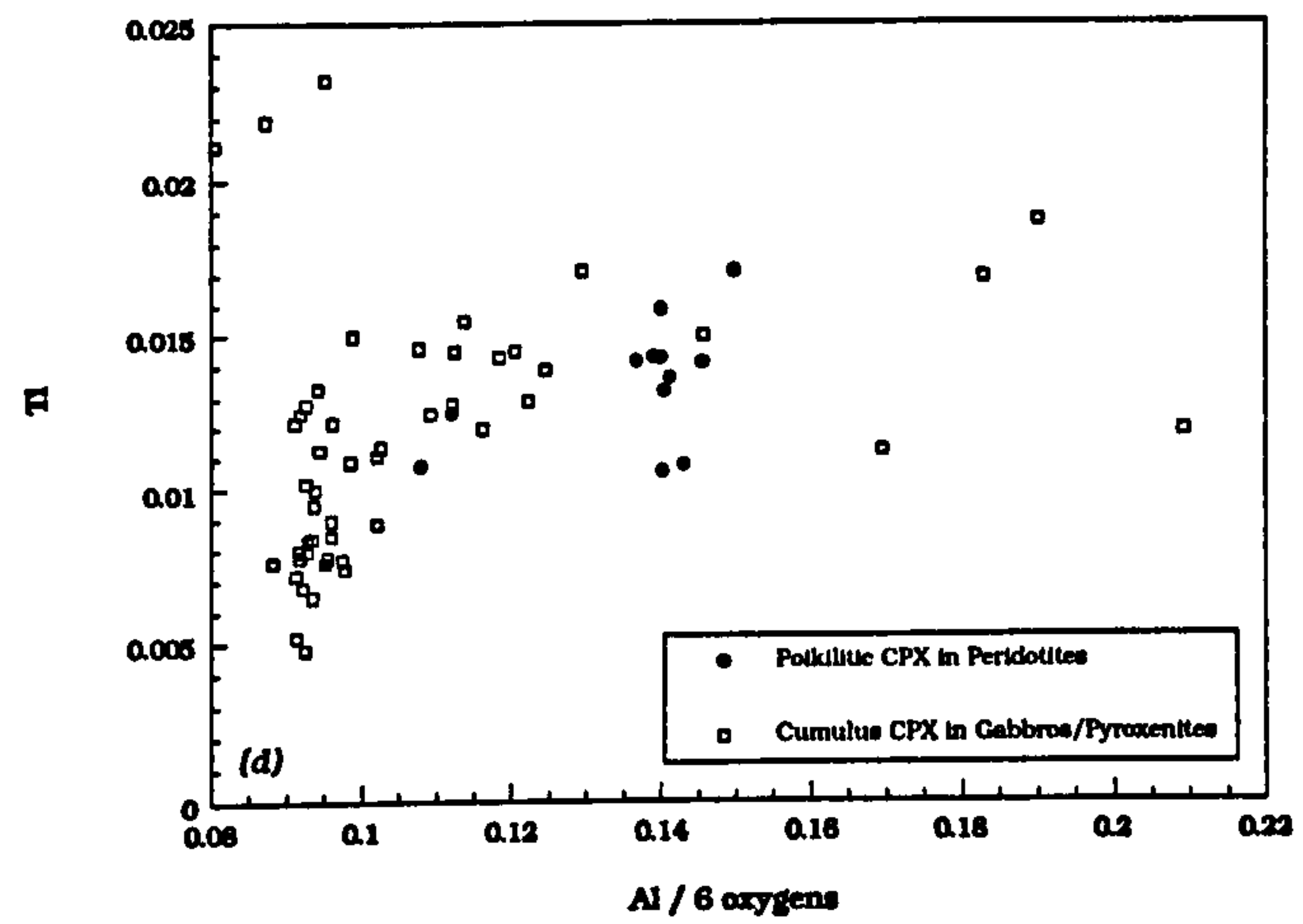


FIGURE 7.9 Cation variations in cumulus and interstitial clinopyroxene from gabbroic cumulate xenoliths. Cations calculated on the basis of 6 oxygens per formula unit.

(d) Ti - Al

(e) Ti - Si

Ti) contents being associated with low Si activities and elevated pressures. As such, the relationships shown (*Figures 7.9a-e*) are what would be expected in pyroxenes from early-formed cumulates. The Ti correlations also show that neither magnetite nor ilmenite were liquidus phases.

Chromium shows a strongly bi-modal correlation with degree of fractionation (*Figure 7.9c*). The poikilitic pyroxenes within the peridotites, have high Cr contents at between 0.013 and 0.028 CPFU, at relatively constant Mg# (0.82-0.86). The cumulus pyroxenes from the gabbros and the pyroxenite have Cr contents generally below 0.005 CPFU. The Cr content remains at this low value with decreasing Mg#. The interstitial pyroxenes associated with the feldspathic peridotites are also the least evolved of all those analysed, having an Mg# of 0.82-0.86. This is unusual, in that it should be the cumulus pyroxenes which have the highest Mg#, since these most likely represent near liquidus compositions (some cumulus pyroxenes do have Mg# at 0.83). Using the equations of Duke (1976) which can be used to calculate the Fe-Mg ratios of mafic melts in equilibrium with olivine and Ca-clinopyroxene, it can be shown that the interstitial pyroxenes apparently crystallized from a more magnesian liquid than the coexisting cumulus olivine :-

$$\text{Mol (Fe/Mg)}_{\text{olivine}} = 0.3970 \quad \{7.1\}$$

$$\text{Mol (Fe/Mg)}_{\text{clinopyroxene}} = 0.2071 \quad \{7.2\}$$

Where,

Mol Fe/Mg = measured molecular Fe/Mg ratio

$$\log \frac{(x_{Fe}^{Ol})}{(x_{Mg}^{Ol})} = -0.523 + \log \frac{(x_{Fe}^{Liq})}{(x_{Mg}^{Liq})} \quad \{7.3\}$$

$$\log \frac{(x_{Fe}^{Cpx})}{(x_{Mg}^{Cpx})} = -0.564 + 0.755 \log \frac{(x_{Fe}^{Liq})}{(x_{Mg}^{Liq})} \quad \{7.4\}$$

Where,

X_{Fe}^{Ol} = mole fraction of Fa in olivine

X_{Mg}^{Ol} = mole fraction of Fo in olivine

X_{Fe}^{Cpx} = mole fraction of Fs in clinopyroxene

X_{Mg}^{Cpx} = mole fraction of En in clinopyroxene

X_{Fe}^{Liq} = mole fraction of FeO in liquid

X_{Mg}^{Liq} = mole fraction of MgO in liquid

Therefore for the olivine and clinopyroxene in the peridotites,

$$\text{Mol (Fe/Mg)}_{\text{liq}^{\text{ol}}} = 1.32 \quad \{7.5\}$$

$$\text{Mol (Fe/Mg)}_{\text{liq}^{\text{cpx}}} = 0.693 \quad \{7.6\}$$

Similar observations have been made on peridotites from the lower part of the Eastern Layered Series of the Rum Intrusion (Faithfull, 1985). It has been suggested that migration of interstitial liquids in the cumulus pile can cause re-equilibration of certain minerals, particularly olivine and chrome-spinel, in both the Rum and Skye layered igneous complexes (Faithfull, 1985; Tait, 1985; Palacz & Tait, 1985; Claydon & Bell, 1992). Faithfull (1985) suggested that such melt movements may be responsible for the anomalous clinopyroxene compositions, although sub-solidus re-equilibration between olivine and clinopyroxene may also be an important process.

SAMPLE	Feldspathic Peridotite KBGX1		Pyroxenite KBGX2		Gabbro KBHYX1	
ANALYSIS No.	Interstitial	Fine Grained	Cumulus CORE	Cumulus RIM	Cumulus	Fine Grained
SiO ₂	51.35	49.81	49.53	49.16	52.35	50.15
TiO ₂	0.39	0.83	0.66	0.72	0.28	0.85
Al ₂ O ₃	3.47	4.36	4.31	1.76	2.19	3.06
Cr ₂ O ₃	0.58	0.24	0.00	0.01	0.06	0.03
Fe ₂ O ₃	0.38	2.58	3.12	2.60	1.35	2.12
MgO	16.35	14.77	13.66	10.34	16.32	13.65
CaO	20.00	20.42	22.98	16.60	21.80	17.63
FeO	5.75	6.16	4.87	18.21	4.95	12.35
Na ₂ O	0.26	0.35	0.25	0.30	0.19	0.30
K ₂ O	0.01	0.01	0.00	0.04	0.01	0.03
TOTAL	98.55	99.53	99.40	99.74	99.49	100.17
FORMULA BASED ON 6 OXYGENS						
Si	1.91	1.85	1.85	1.91	1.93	1.89
Al	0.09	0.15	0.15	0.08	0.07	0.11
Al	0.06	0.05	0.04	0.00	0.03	0.03
Fe(iii)	0.01	0.07	0.09	0.08	0.04	0.06
Fe(ii)	0.18	0.19	0.15	0.59	0.15	0.39
Ti	0.01	0.02	0.02	0.02	0.01	0.02
Ca	0.80	0.82	0.92	0.69	0.86	0.71
Mg	0.91	0.82	0.76	0.60	0.90	0.77
Cr	0.02	0.01	0.00	0.00	0.00	0.00
Na	0.02	0.03	0.02	0.02	0.01	0.02
K	0.00	0.00	0.00	0.01	0.00	0.00
TOTAL	4.00	4.00	4.00	4.01	4.00	4.00
ENDMEMBER %						
Wo	42.34	44.61	50.20	36.72	45.08	38.11
En	48.16	44.89	41.51	31.83	46.94	41.05
Fs	9.5	10.5	8.29	31.44	7.98	20.84

Table 7.3 Intercumulus and cumulus clinopyroxene compositions from the various ultramafic xenolith types.

Plagioclase

Plagioclase occurs in all of the ultramafic xenolith types, and is very often a cumulus phase. Cumulus plagioclase is generally a highly calcic labradorite (An₇₀ - An₈₈), and crystals show a range of zoning styles. Plagioclase compositions are shown in the An-Ab-Or ternary (*Figure 7.10*), and representative analyses are given in *Table 7.4*. The most common zoning style is that of an unzoned to gently, normally zoned inner core making up the bulk of the crystal, with an outer rim showing strong, continuous normal zoning, especially where the crystal is in contact with interstitial liquid (*Figure 7.11*). The cores of some crystals record evidence of a previous stage of resorption. Certain crystals exhibit well-developed oscillatory zoning, again with an unzoned or continuously zoned core, and strongly zoned margins (*Figure 7.12*). Finally, some crystals display a patchily zoned core, often rich in inclusions of glass and other minerals, with strongly zoned margins (*Figure 7.13*). Several crystals from each zoning style have been examined with the electron probe, in order to reveal the extent of the zoning. The chemical extent of the zoning from a simply zoned plagioclase with a resorbed core is shown in *Figure 7.14*.

Zoning in igneous plagioclase is a very common phenomenon, and is controlled mainly by changes in the growth rate of individual crystals, and by the diffusion rate of ions at the crystal/liquid interface (Sibley *et al.*, 1976). Oscillatory zoning is thought to result from the recurrent supersaturation of the melt in anorthite adjacent to individual crystals, possibly in response to shearing motions of the crystals within the magma (Vance, 1962; Anderson, 1984). The patchily-zoned, inclusion-rich, cores common in many igneous feldspars are thought to have crystallized in gas-saturated environments during periods of relatively high supersaturation (Anderson, 1984).

Plagioclase crystals similarly zoned to those from the LSSC cumulates, have been described from the Skaergaard Intrusion (Maaløe, 1976), and the Rum Intrusion (Henderson & Suddaby, 1971; Young, 1984). Young (1984) suggested that complex zoning of some of the Rum plagioclase crystals was due to the penetration of newly emplaced primitive magma into the crystal mush on the intrusion floor. Therefore, the presence of complex zoning in some of the plagioclases from the LSSC xenoliths supports the theory that the migration of melts through the crystal pile may have re-equilibrated cumulus olivine

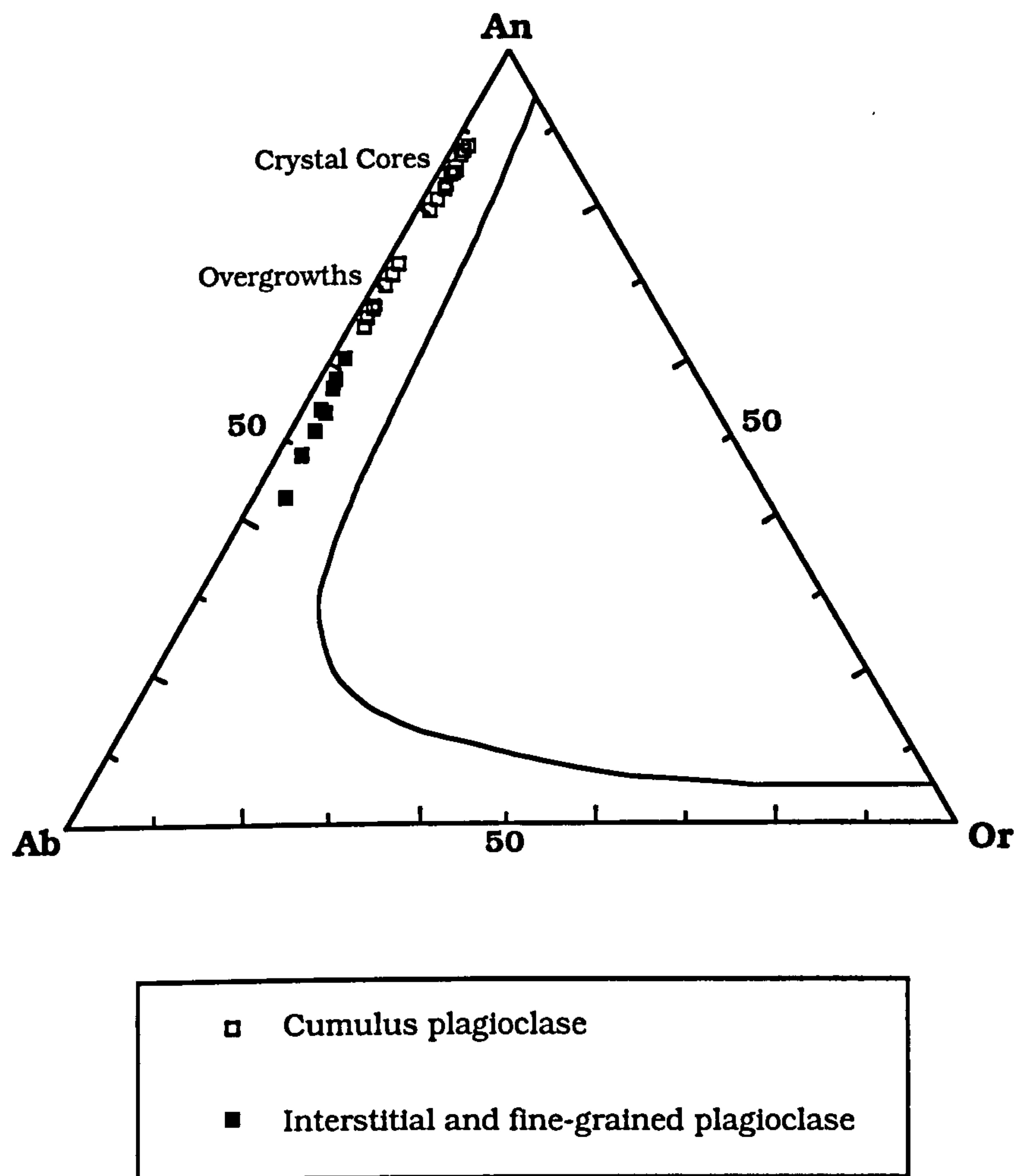


FIGURE 7.10 Plagioclase compositions in the ternary Anorthite-Albite-Orthoclase projection at 2kbar water pressure (after Tuttle & Bowen, 1958), for cumulus and interstitial feldspars from the gabbroic xenoliths.

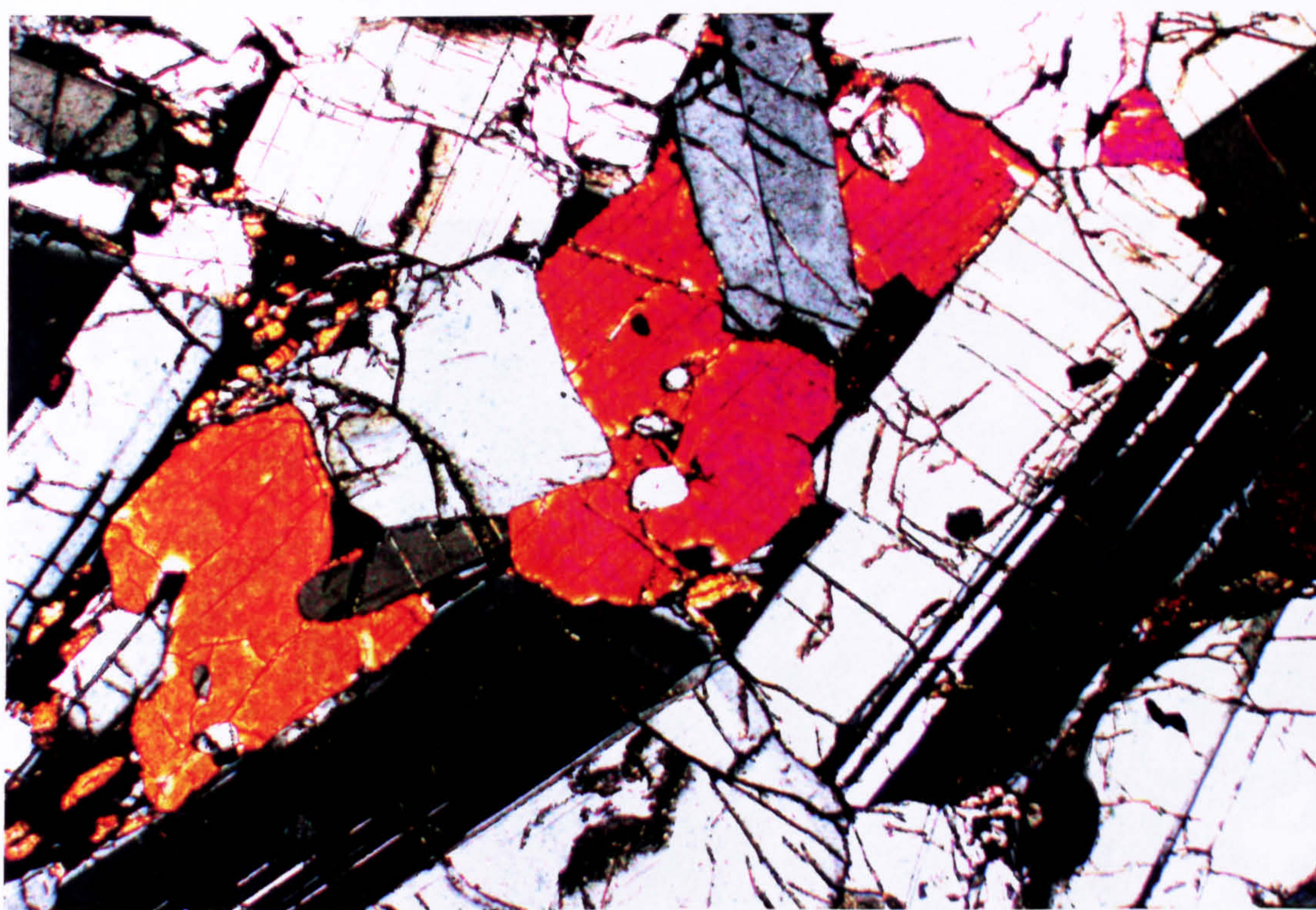
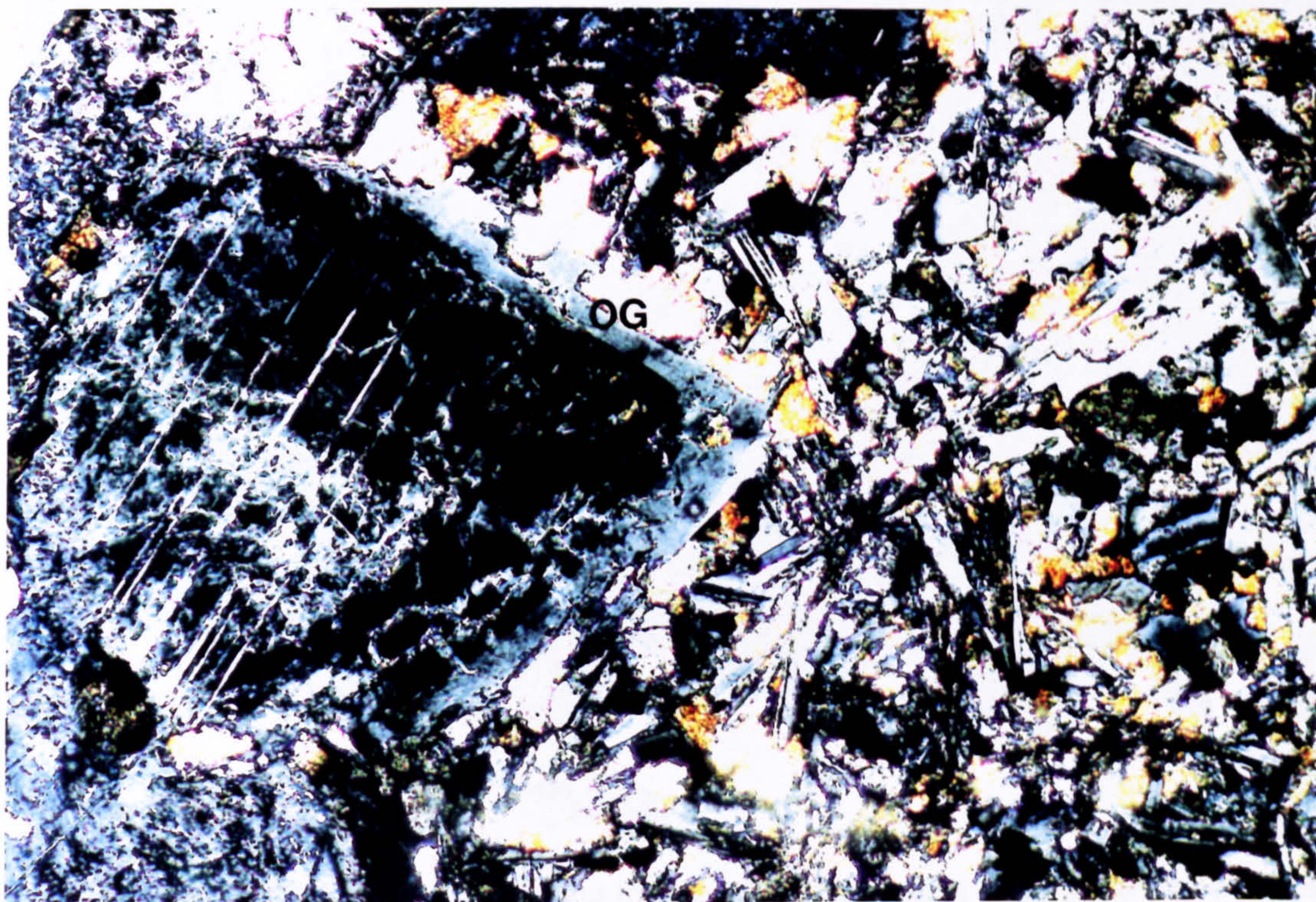


FIGURE 7.11

Cumulus plagioclase from gabbroic cognate xenoliths showing overgrowth textures (OG). These are particularly well developed where the plagioclase is in contact with fine-grained interstitial material. Overgrowth rims are often strongly normally zoned. (xpl; Field of view 0.8x1.2mm (upper) Field of view 2x3mm (lower); Samples KBGX1 (upper) and KBHYX4).

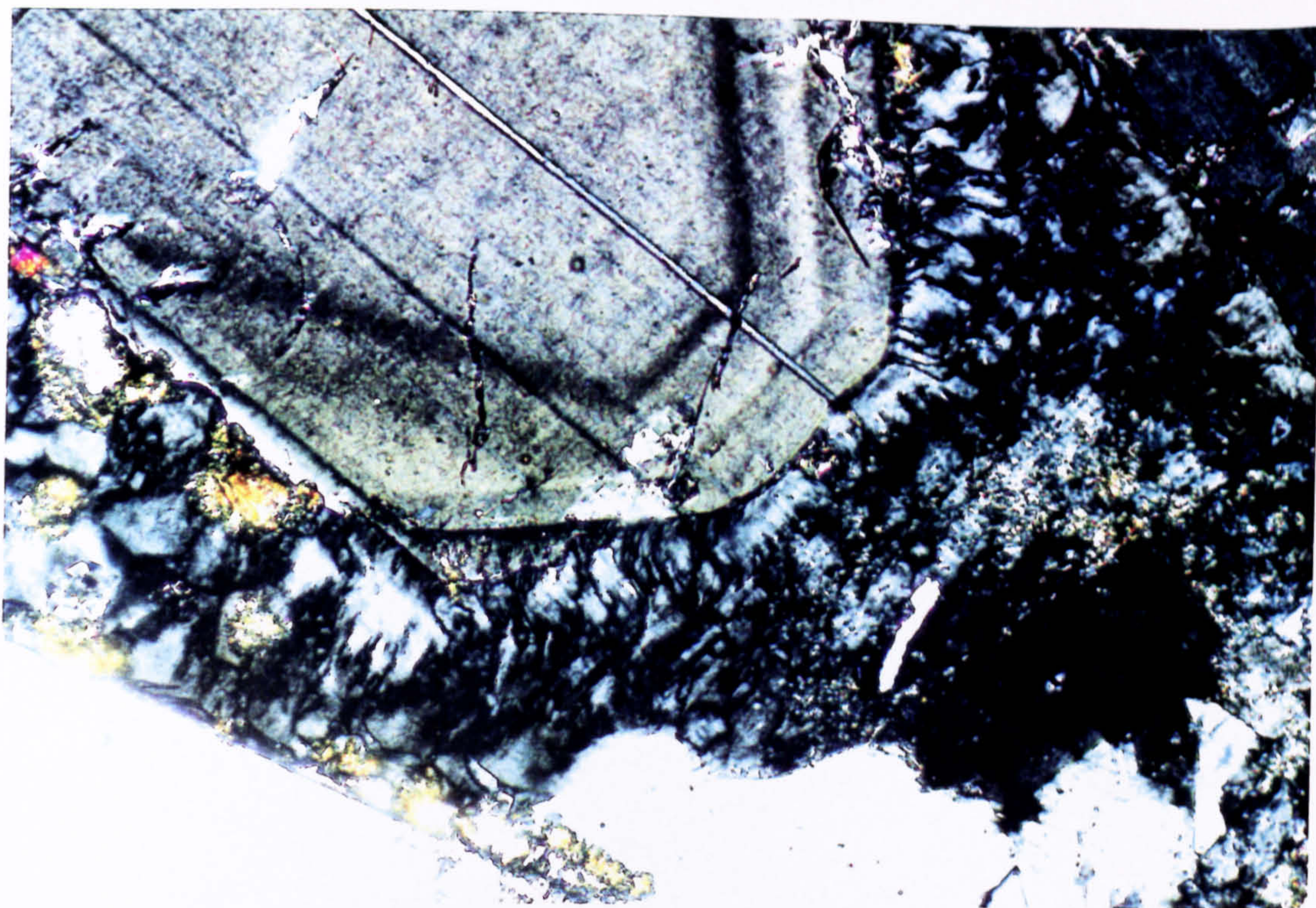


FIGURE 7.12

Oscillatory zoning in cumulus plagioclase from a gabbroic cognate xenolith. Interstitial material consists of altered plagioclase and clinopyroxene. (xpl; Field of view 0.8x1.2mm; Sample KBHYX3).

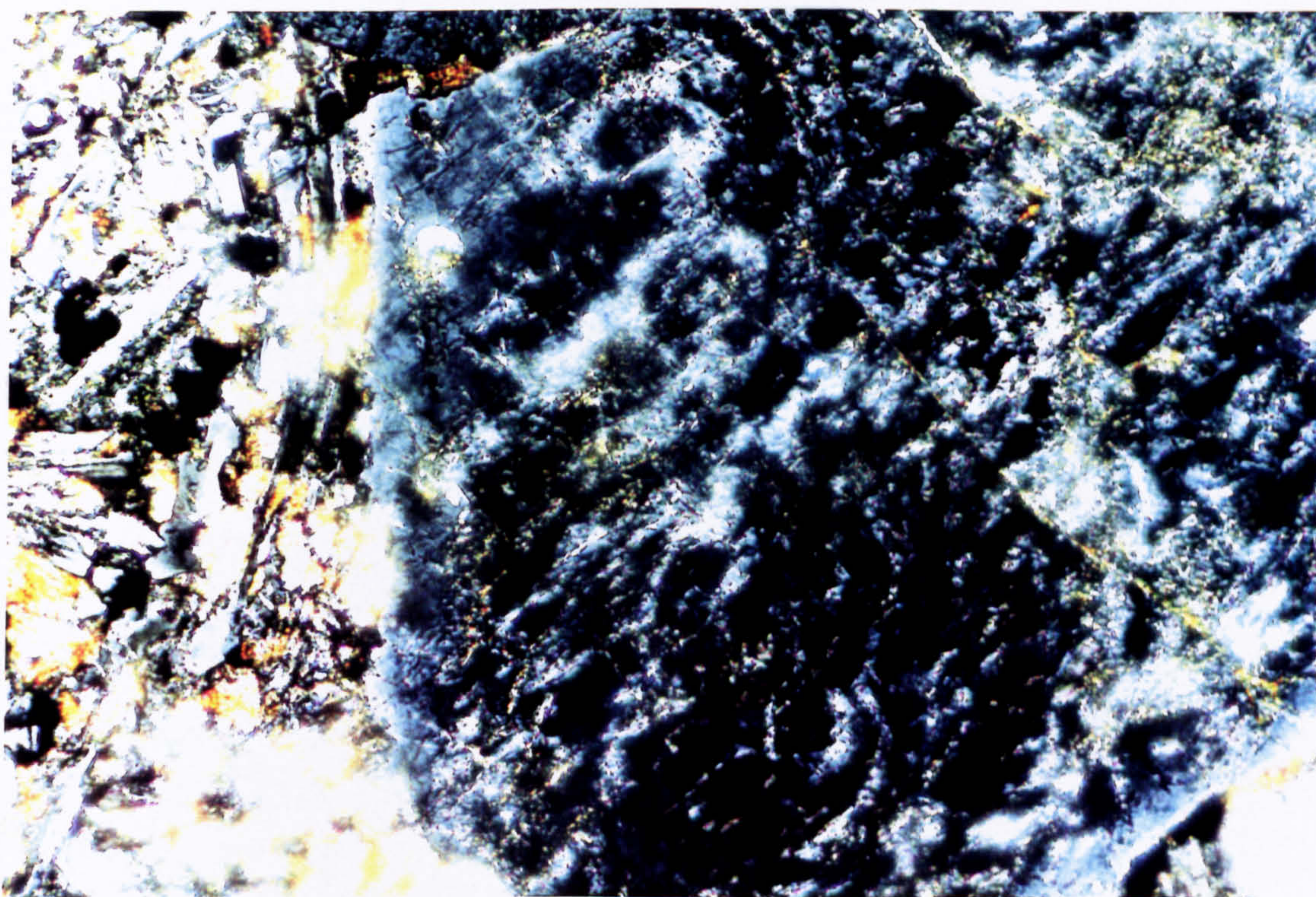


FIGURE 7.13

Complex, patchy zoning in cumulus plagioclase from a gabbroic cognate xenolith. Plagioclase is quite heavily altered to sericite. Interstitial material consists of fine grained plagioclase and clinopyroxene. (xpl; Field of view 0.8x1.2mm; Sample KBHYX3).

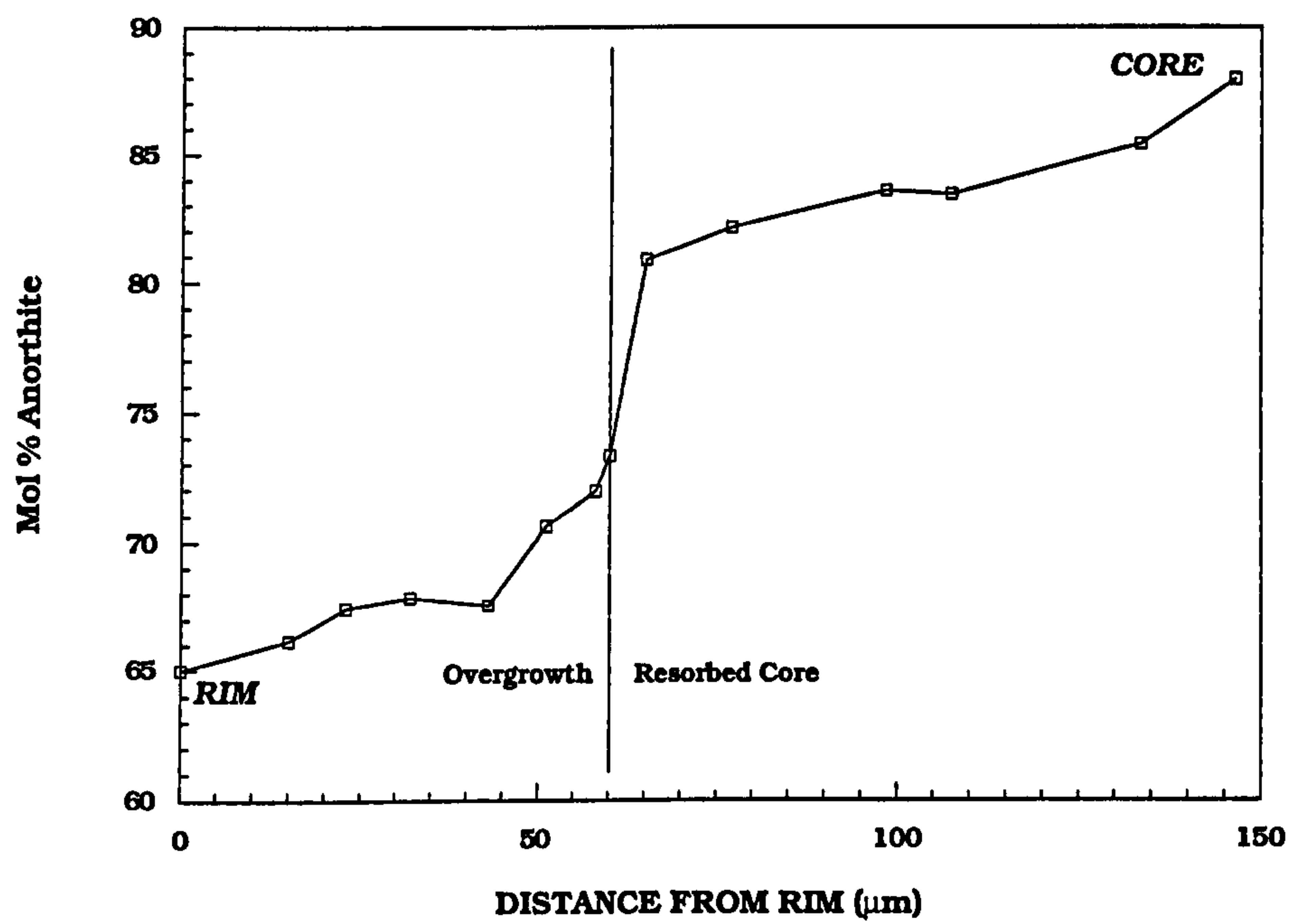


FIGURE 7.14 An example of zoning in cumulus plagioclase from a gabbroic cumulate xenolith (KBHYX4).

compositions in the peridotites.

Interstitial plagioclases from the clinopyroxene-rich xenoliths are generally slightly less calcic (An_{63} - An_{47}), and those from the scoriaceous inclusions are strongly zoned from An_{57} to An_{45} , core to rim.

SAMPLE	Feldspathic Peridotite KBGX1		Pyroxenite KBGX2		Gabbro KBHYX1		Anorthosite KIFX1
ANALYSIS No.	Cumulus	Fine Grained	Inter- Cumulus RIM	Inter- Cumulus RIM	Cumulus CORE	Cumulus RIM	Cumulus CORE
SiO ₂	44.77	53.31	53.38	57.83	46.36	49.84	46.68
TiO ₂	0.00	0.05	0.06	0.07	0.03	0.00	0.09
Al ₂ O ₃	35.32	29.35	28.20	25.36	34.01	31.74	33.27
FeO*	0.42	0.86	0.75	0.76	0.51	0.82	0.46
CaO	18.06	10.94	12.49	8.98	16.56	13.81	17.60
Na ₂ O	1.35	4.86	4.28	6.14	2.17	3.57	1.52
K ₂ O	0.03	0.31	0.21	0.61	0.06	0.14	0.10
TOTAL	99.94	99.68	99.36	99.75	99.68	99.91	99.70
FORMULA ON BASIS OF 32 OXYGENS							
Si	8.28	9.70	9.76	10.44	8.57	9.12	8.63
Ti	0.00	0.01	0.01	0.01	0.00	0.00	0.01
Al	7.70	6.29	6.08	5.40	7.41	6.85	7.25
Fe (ii)	0.06	0.13	0.12	0.12	0.08	0.13	0.07
Ca	3.58	2.13	2.45	1.74	3.28	2.71	3.49
Na	0.48	1.72	1.52	2.15	0.78	1.27	0.55
K	0.01	0.07	0.05	0.14	0.01	0.03	0.02
TOTAL	20.11	20.04	19.97	19.99	20.12	20.10	20.02
ENDMEMBER %							
Ab	11.86	43.77	37.79	53.37	19.07	31.59	13.45
Or	0.17	1.84	1.24	3.48	0.34	0.79	0.55
An	87.97	54.39	60.97	43.15	80.59	67.62	85.99

Table7.4 Cumulus, intercumulus and fine-grained plagioclase compositions from the various types of ultramafic xenolith.

Spinel

Spinel occurs only within the olivine cumulates and is found as inclusions within cumulus olivines, in embayments in individual olivine crystals, and within interstitial clinopyroxene and plagioclase. The spinel is considered to be an early cumulus phase. It is a chrome-spinel, with Cr contents varying between 33 and 42 wt% Cr₂O₃. Individual crystals show no zoning, and no exsolution features are evident. Representative Cr-spinel analyses are documented in *Table 7.5*. Spinel compositions are also shown in *Figure 7.15a*, projected on to the basal plane of the spinel prism, which documents the change in $\text{Fe}^{2+}/(\text{Fe}^{2+}+\text{Mg})$ relative to $\text{Cr}/(\text{Cr}+\text{Al})$, and in *Figure 7.15b* which documents the variation of $\text{Fe}^{2+}/(\text{Fe}^{2+}+\text{Mg})$ with $\text{Fe}^{3+}/(\text{Fe}^{3+}+\text{Cr}+\text{Al})$. These diagrams show that the cumulus spinels found as inclusions in olivine crystals define a trend of increasing $\text{Cr}/(\text{Cr}+\text{Al})$, with little change in $\text{Fe}^{2+}/(\text{Fe}^{2+}+\text{Mg})$. However, the spinels found dispersed through the intercumulus silicate phases (plagioclase and clinopyroxene), show a trend of increasing $\text{Fe}^{2+}/(\text{Fe}^{2+}+\text{Mg})$, with little change in the $\text{Cr}/(\text{Cr}+\text{Al})$ ratio. *Figure 7.15c* is a triangular plot of the tri-valent cations found in naturally occurring spinels (Cr^{3+} , Al^{3+} , Fe^{3+}). The Cr-spinels of the feldspathic peridotite xenoliths define a trend of increasing Al/Cr ratio with little change in Fe^{3+} . This trend has also been identified within spinels of the Eastern Layered Series of the Rum Intrusion (Henderson, 1975; Henderson & Wood, 1981), from the Ben Buie layered gabbro, Isle of Mull (Henderson & Wood, 1981), and within the Cuillin Peridotite Series, Isle of Skye (Claydon, 1990; Bell & Claydon, 1992). These studies have documented *two* divergent trends in Cr-spinel compositions. Henderson (1975) postulated that the 'Al-trend' documented above, was due to the reaction of the initial Cr-rich spinel reacting with olivine and plagioclase, or a melt rich in the plagioclase component, and making the spinels over to more Al-rich compositions. The 'Fe-trend' of more Fe^{3+} -rich spinels came about where the spinels were able to react with *trapped* intercumulus melt over a considerable temperature interval (Henderson, 1975; Henderson & Wood, 1981). The spinels found as inclusions in early formed cumulus olivine were thought to be the initial spinel which crystallized from the melt, and that their inclusion into early cumulus olivine prevented their reaction with the magma (Henderson, 1975). However, work by Scowen *et al.* (1991) has shown that olivine is very

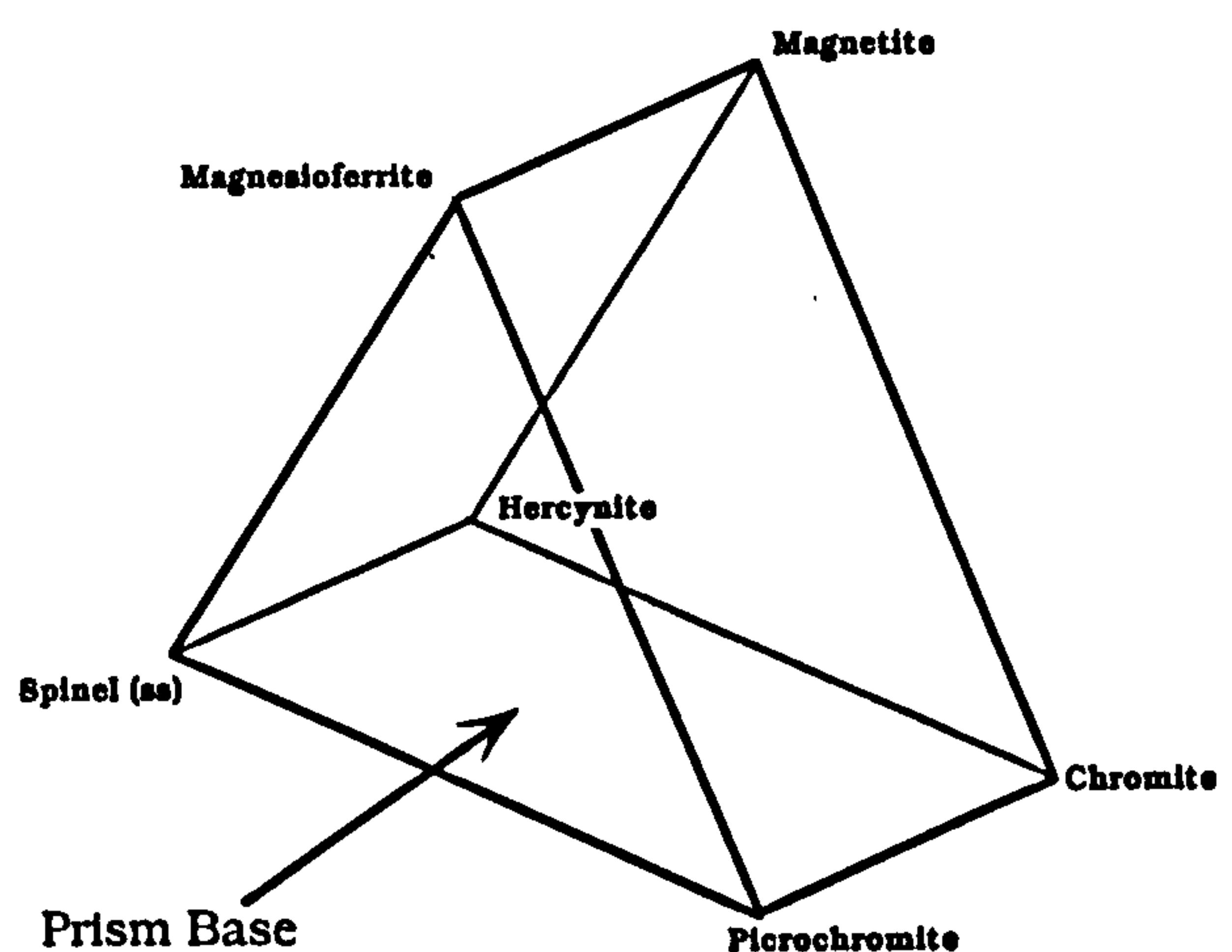
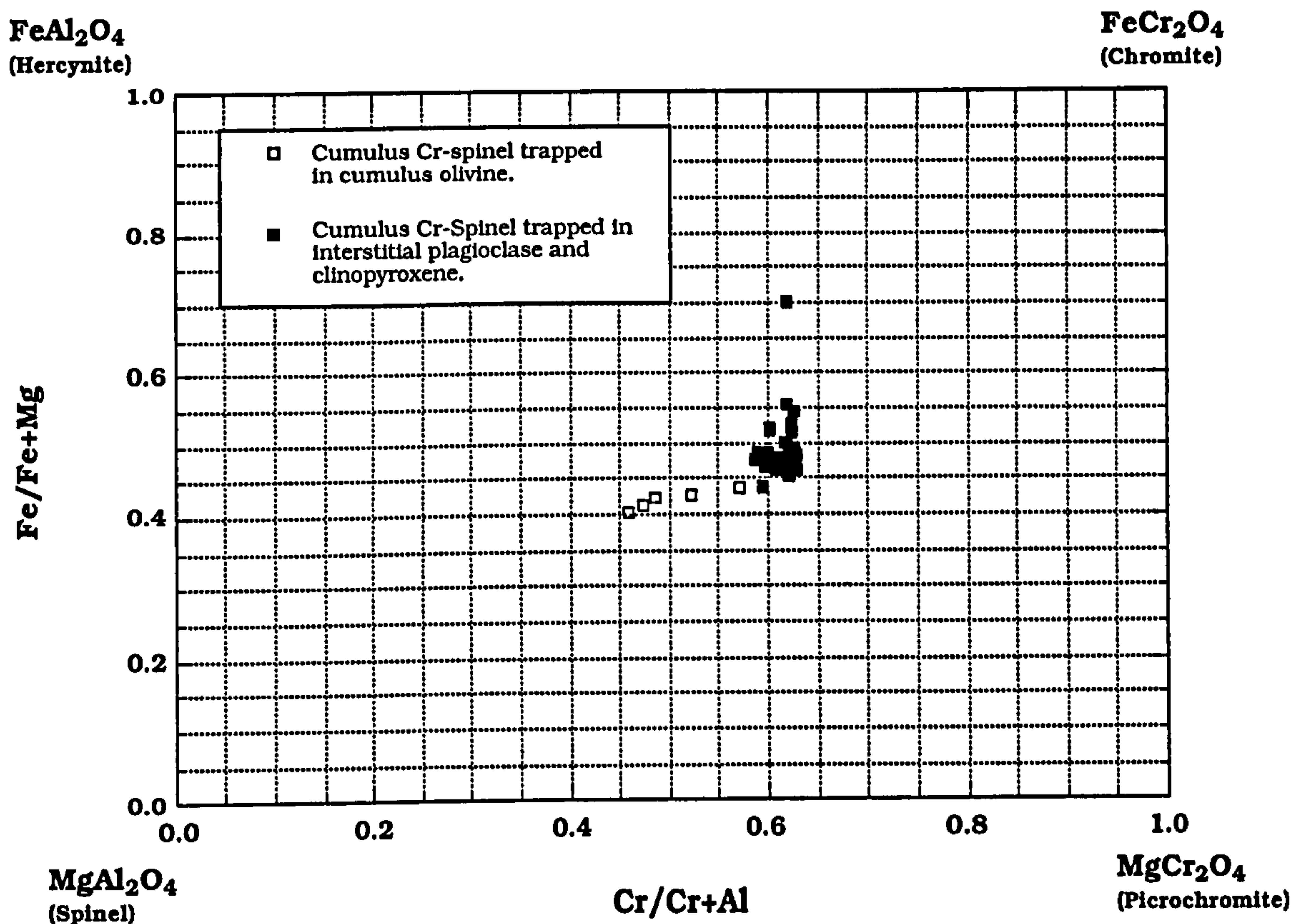


FIGURE 7.15a Variation of Fe/(Fe+Mg) with Cr/(Cr+Al) for chrome-rich spinel inclusions in cumulus olivine, and intercumulus plagioclase and clinopyroxene, from feldspathic peridotite xenoliths. Inset shows relationship of diagram to the spinel prism.

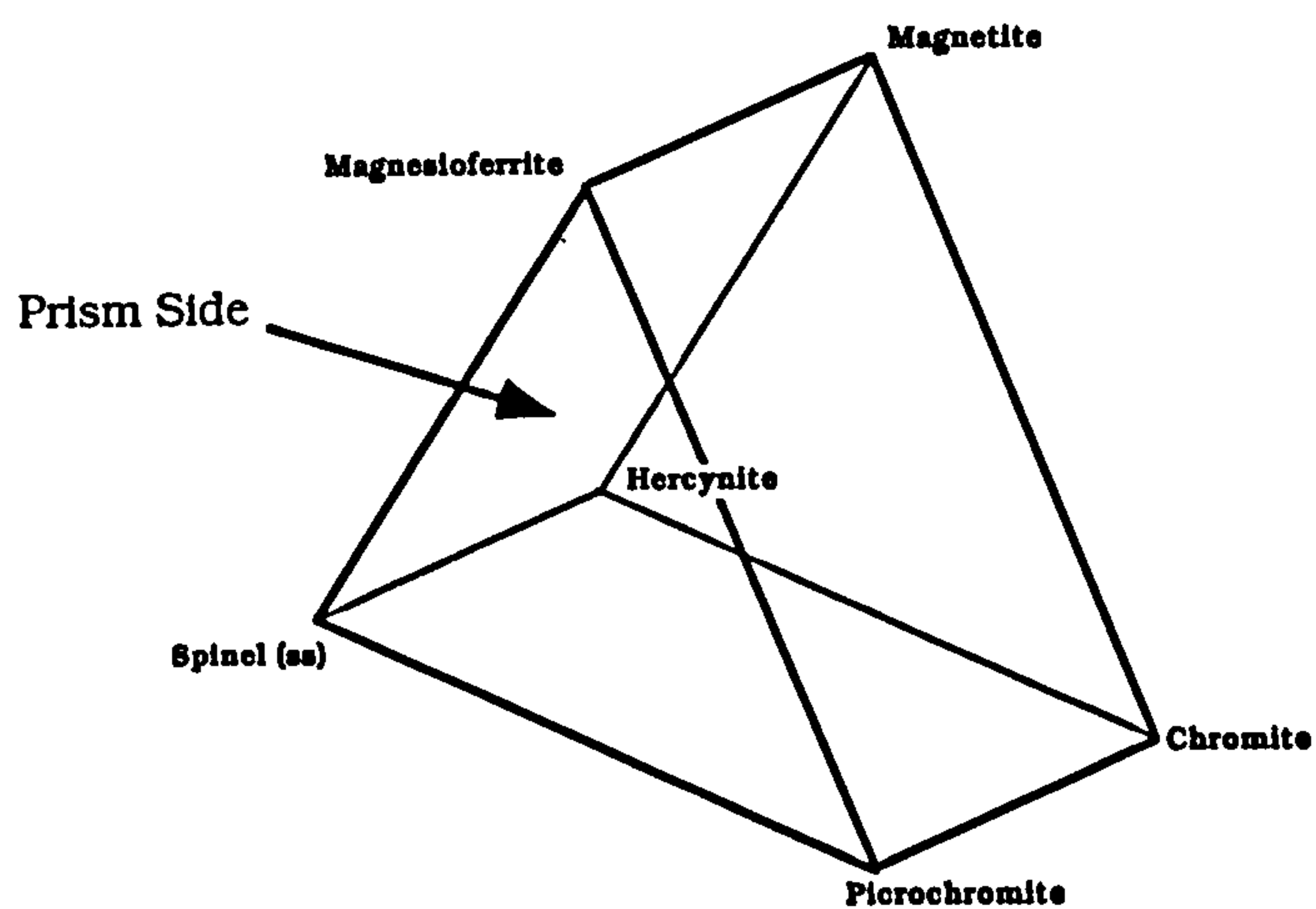
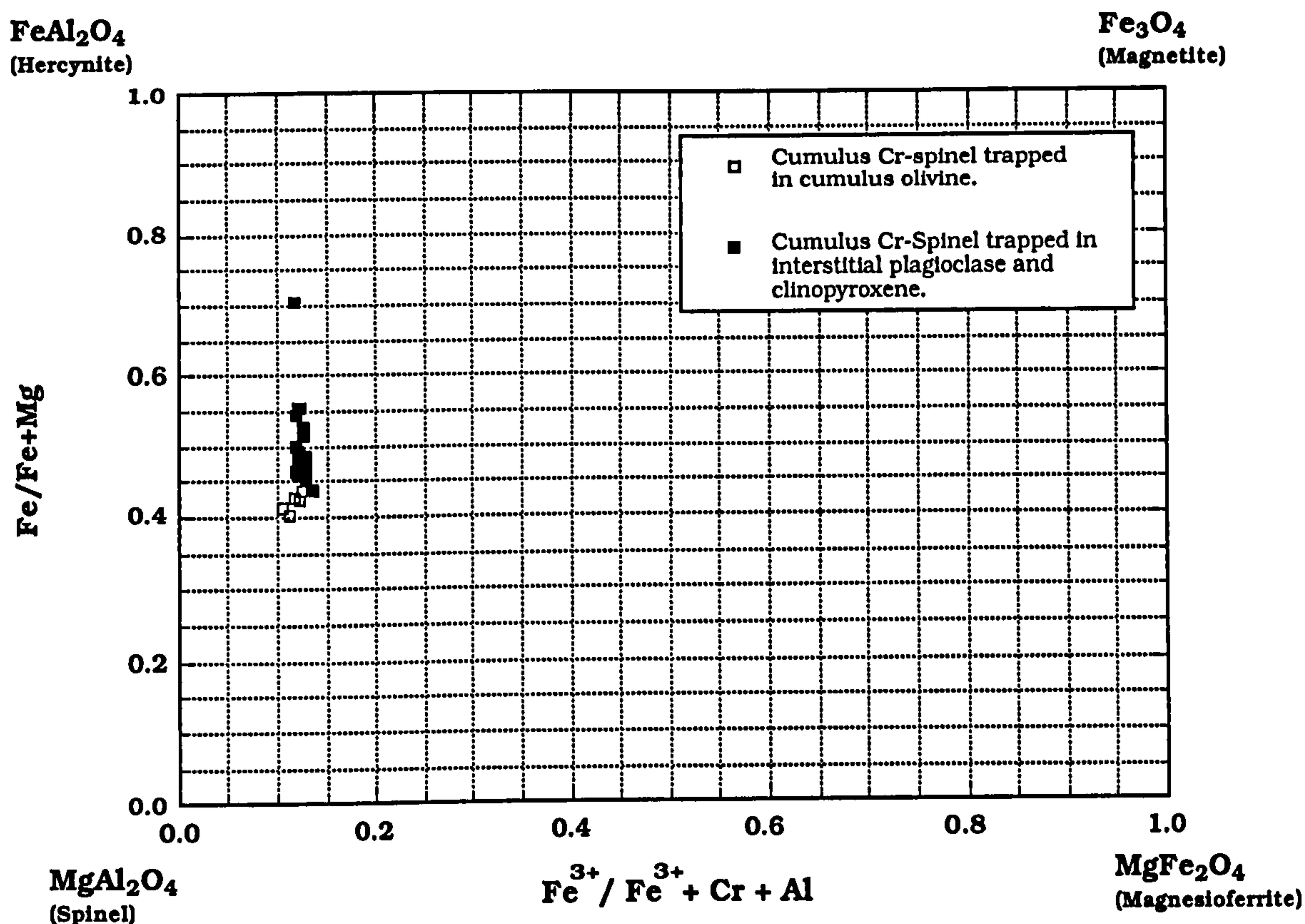


FIGURE 7.15b Variation of Fe/(Fe+Mg) with Fe(III) / (Fe(III) + Cr + Al) for chrome-rich spinel inclusions in cumulus olivine, and intercumulus plagioclase and clinopyroxene, from feldspathic peridotite xenoliths. Inset shows relationship of diagram to the spinel prism.

□ Cumulus Cr-Spinel
trapped in cumulus
olivine.

■ Cumulus Cr-Spinel
trapped in interstitial
plagioclase and
clinopyroxene.

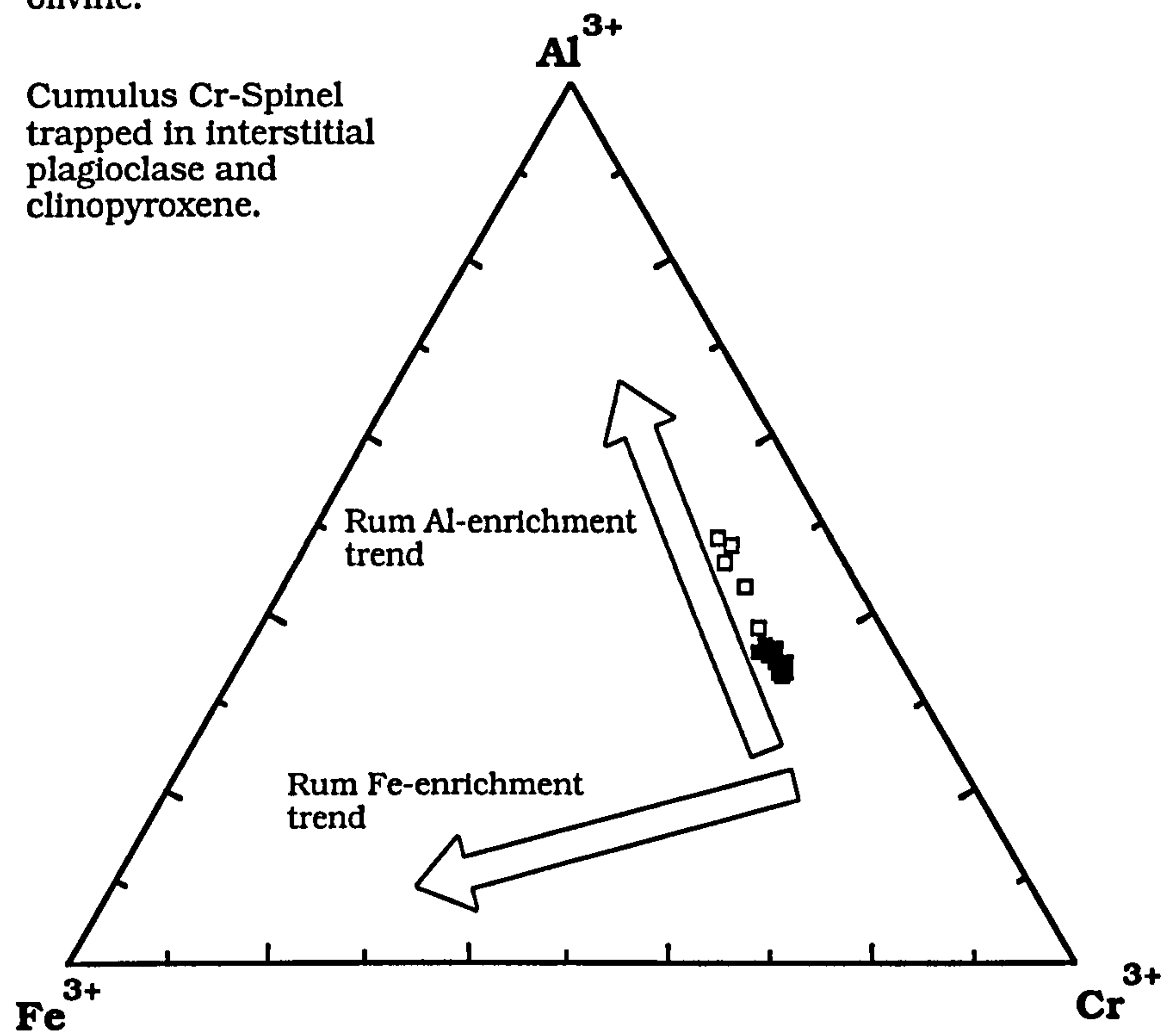


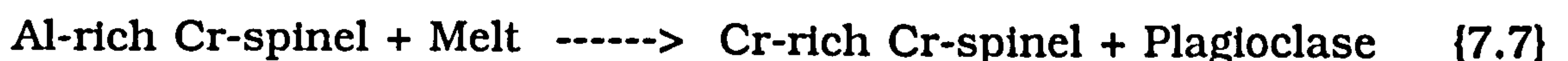
FIGURE 7.15c Variation of the tri-valent cations (Cr, Fe, Al) in Cr-spinels included in cumulus olivine, and interstitial plagioclase and clinopyroxene from olivine-plagioclase cumulate xenoliths. Al- and Fe-enrichment trends from Henderson (1975).

poor at retaining Cr-spinel compositions due to the ease with which cations can diffuse through the olivine structure. Those spinels completely encapsulated by plagioclase are more likely to maintain their magmatic compositions since diffusion of cations through plagioclase is thought to be very difficult (Scowen *et al.*, 1991).

Within the peridotitic xenoliths, those spinels completely enclosed by cumulus olivine, have the highest Al and Mg contents (see *Figure 7.15d*), coupled with the lowest Ti concentrations. This is consistent with a high temperature, magmatic origin (*cf.* Henderson & Suddaby, 1971; Dunham & Wilkinson, 1985; Claydon, 1990). Those spinels found in embayments in cumulus olivine, and within interstitial clinopyroxene and plagioclase are enriched in Cr relative to Mg and Al. Experimental studies by Hill & Roeder (1974), and Fisk & Bence (1980) suggest that the chemistry of spinels crystallizing from basaltic liquids is controlled mainly by the temperature, pressure and oxygen fugacity (fO_2) of the system. Hill & Roeder (1974) observed that with decreasing fO_2 the spinel crystallizes with increasing $Mg/(Mg+Fe)$ and Al, and Fisk & Bence (1980) suggested that high-Al spinels crystallize at elevated pressures.

However, many studies have emphasized the importance of post-cumulus and sub-solidus reactions and re-equilibration between spinels and silicate phases (Henderson & Suddaby, 1971; Henderson, 1975; Cameron, 1975; Roeder *et al.*, 1979; Henderson & Wood, 1981; Scowen *et al.*, 1991; Bell & Claydon, 1992).

The textural features of the Cr-spinels and silicate phases in the peridotitic xenoliths suggest that the compositional variation seen in the Cr-spinels from the peridotitic xenoliths are the result of post-cumulus reactions, rather than an artefact of the crystallization history of the magma. The intercumulus spinels, are more Fe-, Ti- and Cr-enriched. It has been suggested, from similar relationships found in spinels from Rum and Muck basaltic lavas (Ridley, 1977) and for spinels from the Cuillin Peridotite Series (Bell & Claydon, 1992), that the initial Al-rich spinel reacts with the melt to give a more Cr-rich spinel, via a reaction such as:



This is essentially the reverse of the reaction proposed by Henderson (1975) to account for the 'Al-trend' of the Rum peridotite spinels.

Ridley (1977) suggests that the interaction of early-formed Al-enriched spinel with a cooling silicate melt results from a peritectic reaction in which the spinel loses Al during the crystallization of plagioclase, with a concomitant increase in Fe and Ti. This was supported by the work of Dunham & Wilkinson (1985) who considered that the spinels became more Cr-enriched and Al-depleted after the onset of plagioclase crystallization.

Utilizing the geothermometry equation of Fabriès (1979), based upon the mole fractions of Fe and Mg in coexisting olivines and spinels and the relative concentrations of the trivalent cations in the spinels, produces temperature estimates of between 1300°C and 800°C, with the Al- and Mg-rich spinels resulting in the highest temperatures :

$$T(K) = \frac{4250\alpha + 1343}{\ln K_D + 1.825\alpha + 0.571} \quad \{7.8\}$$

Where,

$$\alpha = \text{Cr}^{3+} / \text{Cr}^{3+} + \text{Al}^{3+} + \text{Fe}^{3+} \quad \{7.9\}$$

and

$$K_D = \left(\frac{X_{\text{Mg}}^{\text{ol}}}{X_{\text{Fe}}^{\text{ol}}} \right) * \left(\frac{X_{\text{Fe}}^{\text{sp}}}{X_{\text{Mg}}^{\text{sp}}} \right) \quad \{7.10\}$$

These temperatures are consistent with the hypothesis suggested that it is the most Al-and Mg-rich spinels, rather than the most Cr-rich, which represent the first spinels to crystallize. However, it must be stressed that such empirical calibrations are subject to problems, especially when post-cumulus and subsolidus re-equilibration of both spinel and olivine is a major possibility (Roeder *et al.*, 1979; Fabriès, 1979; Bell & Claydon, 1992).

SAMPLE	Cumulus Cr-Spinels trapped in cumulus olivine			Cumulus Cr-Spinel trapped in interstitial plagioclase and clinopyroxene			
ANALYSIS No.	Cr-Spinel 22	Cr-Spinel 24	Cr-Spinel 4	Cr-Spinel 12	Cr-Spinel 17	Cr-Spinel 23	Cr-Spinel 32
SiO₂	0.01	0.06	0.05	0.09	0.10	0.09	0.11
TiO₂	1.22	1.08	0.78	1.35	1.66	1.32	1.42
Al₂O₃	22.59	26.16	25.49	17.37	17.83	16.98	19.85
Cr₂O₃	36.71	33.20	34.34	42.00	40.78	42.26	39.29
Fe₂O₃	9.75	9.71	8.93	9.58	10.27	9.85	10.24
MgO	12.29	13.02	12.74	10.39	11.11	10.71	11.98
FeO	16.36	15.81	16.03	18.56	17.47	17.93	16.53
TOTAL	98.94	99.04	98.35	99.34	99.23	99.14	99.42
FORMULA BASED ON 32 OXYGENS							
Si	0.03	0.02	0.01	0.02	0.03	0.02	0.03
Ti	0.23	0.20	0.15	0.26	0.32	0.26	0.27
Al	6.63	7.53	7.40	5.26	5.36	5.15	5.88
Cr	7.23	6.41	6.69	8.53	8.23	8.60	7.81
Fe(III)	1.83	1.79	1.66	1.85	1.97	1.91	1.94
Mg	4.53	4.74	4.68	3.98	4.23	4.11	4.49
Fe(II)	3.41	3.23	3.30	3.99	3.73	3.86	3.48
TOTAL	23.87	23.92	23.89	23.89	23.87	23.90	23.89
Fe/Fe+Mg	0.43	0.41	0.41	0.50	0.47	0.48	0.44
Cr/Cr+Al	0.52	0.46	0.48	0.62	0.61	0.63	0.57

Table 7.5 Cumulus Cr-Spinel compositions from feldspathic peridotite xenolith (KBGX1).

7.4 Whole-rock Geochemistry

One sample of each xenolith type has been analysed for bulk-rock major-, trace- and rare-earth-element concentrations, and two for Sr and Nd isotope geochemistry. *Table 7.6* is a tabulation of these data. Since all the xenoliths are fragments of cumulate rocks, bulk-rock compositions are controlled mainly by the proportions of olivine, plagioclase and pyroxene. For example, the olivine cumulate has high MgO and Ni contents, the xenoliths with cumulus plagioclase have high Sr values, and those rich in clinopyroxene have high V and Sc contents. The olivine-rich xenolith also has the highest Cr contents (731ppm), which is most likely due to the presence of minor Cr-spinel, and also the high Cr content of the interstitial clinopyroxene of these early-formed cumulates; the interstitial clinopyroxene has Cr contents at between 0.014 and 0.032 CPFU. Later-formed, olivine-free cumulates have lower Cr contents, since the liquid would have been effectively depleted in Cr through the removal of early-precipitated Cr-spinel. The olivine-rich xenoliths also have high LOI values (6.7), indicating a high degree of alteration.

All xenolith types are depleted in the full range of incompatible elements when compared with the host Group I and Group II sheets. All xenolith types have flat to LREE-enriched rare-earth-element patterns, with the plagioclase cumulates having positive Eu anomalies (*Figure 7.16*). Those xenoliths with abundant clinopyroxene, typically have the highest total REE contents. However, the anorthosite shows the greatest LREE enrichment. Similar LREE enrichment in plagioclase has been found in anorthosites from the Eastern Layered Series of the Rum intrusion (Henderson & Gijbels, 1976; Palacz & Tait, 1985). The feldspathic peridotite has the lowest total REE content due to the dilution effect caused by the abundant olivine, which contains little in the way of REE.

The xenoliths have $^{87}\text{Sr}/^{86}\text{Sr}_i$ ranging from 0.708163 in the pyroxene cumulate, to 0.709226 in the anorthosite, and $^{143}\text{Nd}/^{144}\text{Nd}_i$ values of 0.511899 in the pyroxene cumulate, and 0.511929 in the anorthosite. Both initial Sr and Nd isotope ratios fall within the ranges of the Group I basalts and basaltic andesites (*Figure 7.17*). The initial Sr values are more similar to the basalts of Group I rather than the more evolved rocks. Therefore, these less evolved specimens of Group I may still be

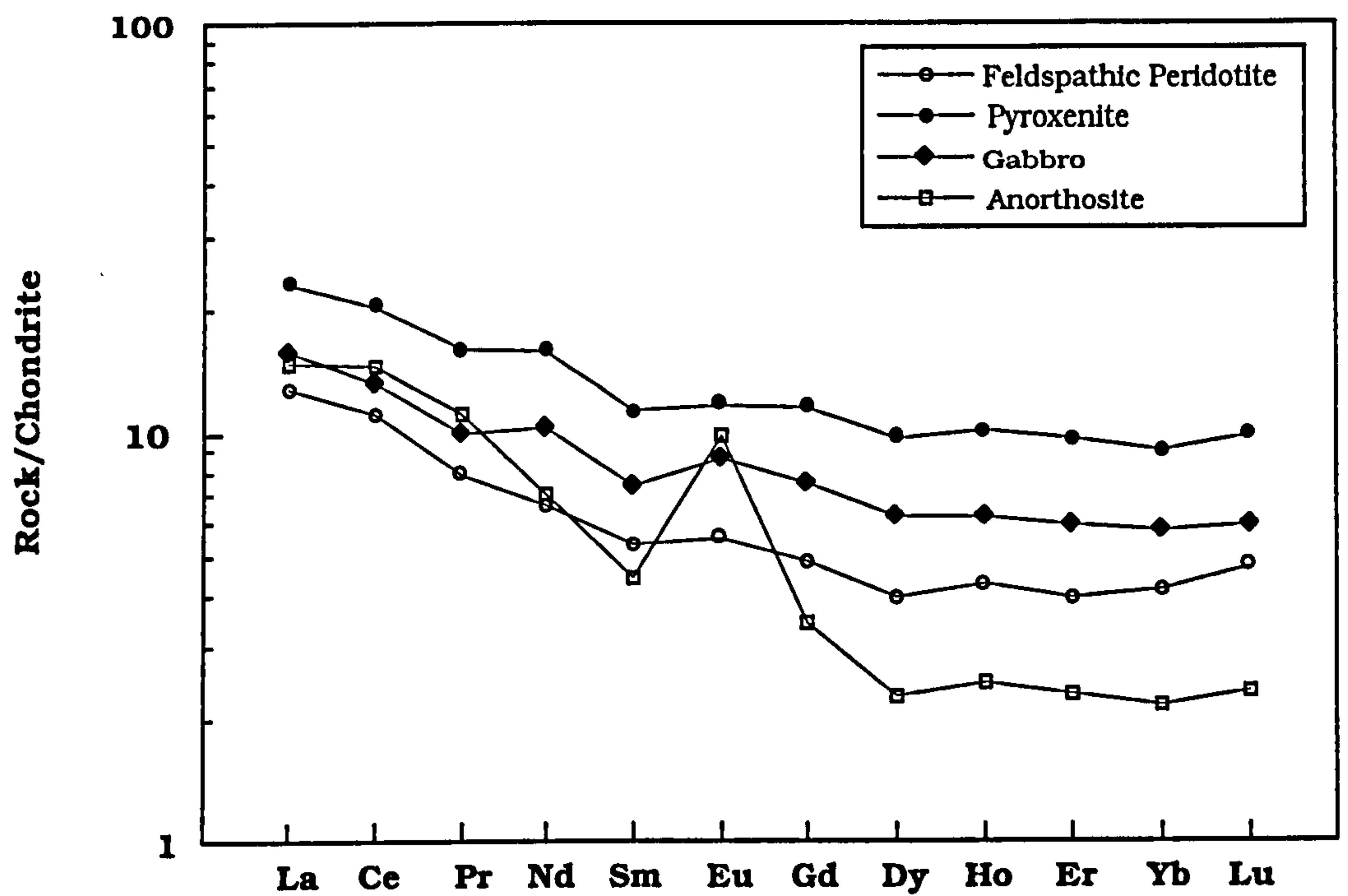


FIGURE 7.16 Chondrite normalized REE profiles for the gabbroic xenoliths of the LSSC

Feldspathic Peridotite = Olivine + Plagioclase cumulate

Pyroxenite = Clinopyroxene cumulate

Gabbro = Plagioclase + Clinopyroxene cumulate

Anorthosite = Plagioclase cumulate

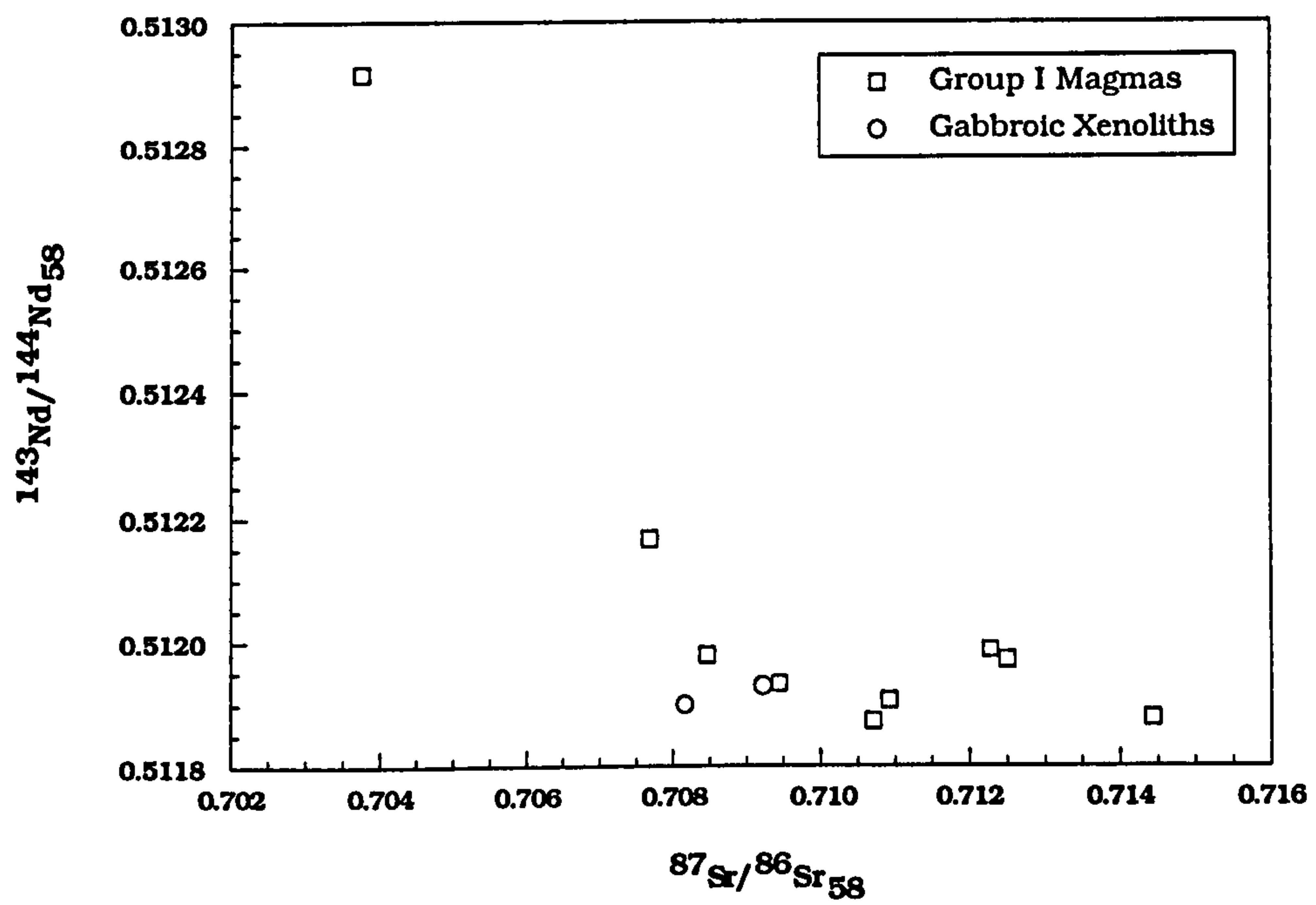


FIGURE 7.17 $^{143}\text{Nd}/^{144}\text{Nd}_i$ vs. $^{87}\text{Sr}/^{86}\text{Sr}_i$ for the gabbroic xenoliths compared to the Group I magmas. Isotope ratios age corrected to 58Ma.

capable of precipitating ultrabasic cumulates. The initial Nd isotope values of both the cumulates and the majority of the Group I magmas scatter around 0.51190 to 0.51120, suggesting that contamination of the Group I magmas occurred relatively early in their evolution, and that Nd isotopic values were buffered by the Nd isotope values of the contaminants.

	Feldspathic Peridotite KBGX1	Pyroxenite KBGX2	Gabbro KBHYX1	Anorthosite KIFX1
MAJOR ELEMENTS IN Wt%				
SiO ₂	42.50	51.50	50.82	46.20
TiO ₂	0.27	0.58	0.40	0.13
Al ₂ O ₃	8.24	10.50	16.31	30.26
Fe ₂ O ₃ *	11.05	7.84	5.58	2.17
MnO	0.17	0.15	0.10	0.02
MgO	26.88	11.05	8.06	0.77
CaO	3.81	14.54	14.79	13.95
Na ₂ O	0.51	1.94	1.97	2.34
K ₂ O	0.12	0.69	1.00	1.05
P ₂ O ₅	0.02	0.04	0.03	0.02
LOI	6.73	1.17	1.08	2.67
TOTAL	100.30	100.00	100.14	99.59
TRACE ELEMENTS IN PPM				
Nb	1.3	1.3	1.2	1.4
Zr	26.0	47.5	32.3	25.9
Y	7.2	18.0	11.5	3.4
Sr	54.2	169.1	328.9	809.6
Rb	4.5	17.5	23.0	20.3
Th	0.2	0.0	0.0	0.0
Pb	0.0	3.4	4.1	6.3
Zn	75.5	70.2	45.1	27.7
Cu	13.1	36.8	17.0	59.9
Ni	805.9	72.4	22.3	84.9
Cr	731.1	273.6	171.6	24.7
V	86.6	273.0	189.1	30.8
Ba	42.8	530.7	693.6	784.8
Sc	19.8	78.9	50.7	5.4
La	3.03	5.46	3.75	3.50
Ce	6.82	12.41	8.09	8.86
Pr	0.75	1.51	0.95	1.05
Nd	3.08	7.35	4.78	3.27
Sm	0.81	1.73	1.13	0.67
Eu	0.32	0.68	0.50	0.57
Gd	0.99	2.37	1.54	0.74
Dy	1.00	2.47	1.58	0.58
Ho	0.24	0.57	0.35	0.14
Er	0.65	1.58	0.98	0.38
Yb	0.70	1.54	0.98	0.37
Lu	0.12	0.25	0.15	0.06
⁸⁷ Sr/ ⁸⁶ Sr _i		0.708163		0.709226
¹⁴³ Nd/ ¹⁴⁴ Nd _i		0.511899		0.511929

Table 7.6 Whole-rock compositions of the gabbroic xenoliths.

7.5 Origin and Significance of the Gabbroic Xenoliths

The lack of a high-pressure mineral assemblage (for example, no chrome-diopside or garnet), and the cumulate textures of these xenoliths, precludes them from representing fragments of mantle material. As the host sheets have passed through Pre-Cambrian basement rocks, Mesozoic sedimentary rocks and Palaeocene lavas, it seems unlikely that the xenoliths are accidental inclusions of pre-existing gabbroic rocks. It is therefore considered most likely that the xenoliths are indeed cognate to the LSSC magmas, and represent early-formed precipitates.

The presence of gabbroic xenoliths within members of the LSSC, provides perhaps some of the best evidence that fractional crystallization of the parent magmas was occurring within the Loch Scridain magma chamber(s). The xenoliths provide some evidence as to the early evolution of the Loch Scridain magmas, with knowledge of mineral and bulk-rock compositions enabling a few constraints to be put on the nature of the parent magma(s) of the LSSC.

The presence of near-monomineralic xenoliths with markedly different major cumulus phases (olivine, plagioclase, or clinopyroxene) suggests that a magma chamber, similar to those now represented by the Rum and Skye ultrabasic layered intrusions, was involved in the formation of the LSSC. The parent magma(s) for these intrusions has been argued to be basaltic (Brown, 1956), picritic (Huppert & Sparks, 1980), and eucritic with suspended olivine crystals (Gibb, 1976). Kitchen (1985) suggested that the parental magma for the Rum Intrusion was more alkaline in nature, rather than tholeiitic, on the evidence of alkaline segregation veins found in some of the peridotites. The cumulus phases found in the Loch Scridain xenoliths are similar in composition to those found in both the Rum and Skye ultrabasic rocks, although the olivines do not extend to such high Fo contents, and the cumulus plagioclases are generally less calcic (Faithfull, 1985; Tait, 1985; Palacz & Tait, 1985; Claydon & Bell, 1992). Olivine of composition Fo₈₅ typical of that found in the olivine-bearing xenoliths would be in equilibrium with a basic liquid with 9-10 wt% MgO (Roeder & Emslie, 1970). This composition is basaltic rather than picritic or ultrabasic, although there is some evidence that olivine compositions are easily re-equilibrated through post-cumulus

processes (Faithfull, 1985; Tait, 1985; Palacz & Tait, 1985; Claydon & Bell, 1992).

Bulk-rock Cr and Ni contents of the olivine and pyroxene cumulates are also more consistent with a basaltic parent; Cr contents reach over 6000ppm and Ni over 1900ppm in some of the Rum peridotites (Tait, 1985). The abundant cumulus clinopyroxene also points to a basaltic parent magma (Gibb, 1976; Claydon & Bell, 1992). These pyroxenes are all hypersthene normative, and define an iron-enrichment trend identical to those from the Skaergaard Intrusion. The parent magma for the LSSC gabbroic xenoliths is therefore likely to have been tholeiitic in nature; this again suggests that they may be cognate with the host sheets. The similarity in initial Sr and Nd isotopic values between the gabbroic xenoliths and the more-basic members of Group I also provides strong evidence for a cognate origin for the xenoliths.

The presence of cognate cumulates within a suite of essentially aphyric magmas enables some constraints to be placed upon the temperature of crystallization of the early-formed products. Application of the Kudo-Weill plagioclase thermometer (Kudo & Weill, 1970; Mathez, 1973), yields dry, liquidus temperatures of between 1300°C for cumulus plagioclase from the feldspathic peridotites, and 1250°C for cumulus plagioclase from the gabbros. Temperatures for cumulus clinopyroxene vary from 1250°C (gabbros) to 850°C (pyroxenites) (Kretz, 1982). These temperatures are entirely consistent with down-temperature crystallization of olivine, followed by plagioclase, then clinopyroxene, from a tholeiitic basalt magma.

CHAPTER 8

THE PETROGENESIS OF THE LSSC

8.1 The Magmatic History of the BTVP

It is now widely accepted that large continental flood basalt provinces develop where mantle plumes impact at the base of the lithosphere (Richards *et al.*, 1989; Campbell & Griffiths, 1990; Carlson, 1991; Wilson, 1993a). Basaltic magmatism in such areas is due to the decompressive melting of upwelling asthenosphere (Klein & Langmuir, 1987; McKenzie & Bickle, 1988). Magmatism in western Britain, Iceland and Greenland during the Tertiary is believed to be no exception (White, 1988), the mantle plume arriving off the east Greenland coast (as it is now). This plume is now situated under Iceland (White & McKenzie, 1989; Thirlwall *et al.*, 1994). Morton *et al.* (1995) provide evidence from rocks from the Rockall Trough that basaltic magmatism started in the area during the Late Cretaceous, implying that activity in the North Atlantic Igneous Province took place at least 7Ma before the postulated arrival of the Icelandic plume at 62Ma. In the case of the Palaeogene magmatism in the BTVP, Thompson & Gibson (1991) argue that lithospheric stretching of the Sea of the Hebrides area occurred during the Mesozoic, creating a local lithospheric "thinspot", which then acted as a focus for the later magmatism.

During extension, the lithosphere is stretched and thinned by a factor β (the ratio of initial to final surface area). Asthenospheric mantle will rise adiabatically to fill the 'space' created, and may begin to melt if it crosses its solidus. If stretching occurs at a slow rate, heat will be conducted away from the upwelling asthenosphere and no melt will be produced (Fitton *et al.*, 1991). However, if stretching takes place over a shorter time scale, then asthenospheric upwelling will outstrip conductive heat loss and melting will occur. *Figure 8.1a* shows the effects of various degrees of stretching (β) on convective geotherms for normal mantle potential temperatures ($T_p=1280^\circ\text{C}$), and *Figure 8.1b* for anomalously hot mantle ($T_p=1480^\circ\text{C}$) in a convective mantle plume (McKenzie & Bickle, 1988; Fitton *et al.*, 1991). (T_p is the temperature the mantle would have if it were allowed to rise adiabatically to the

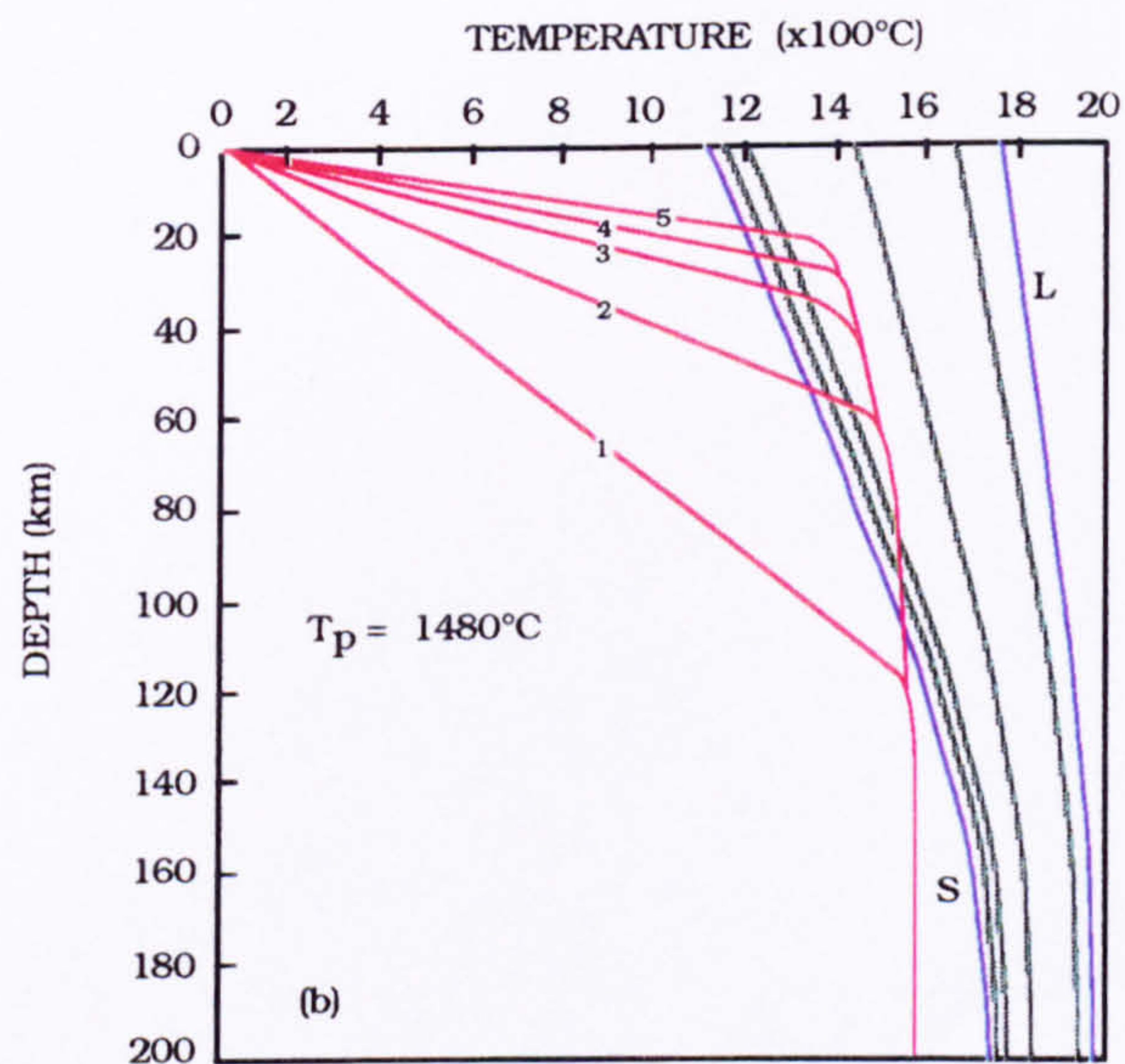
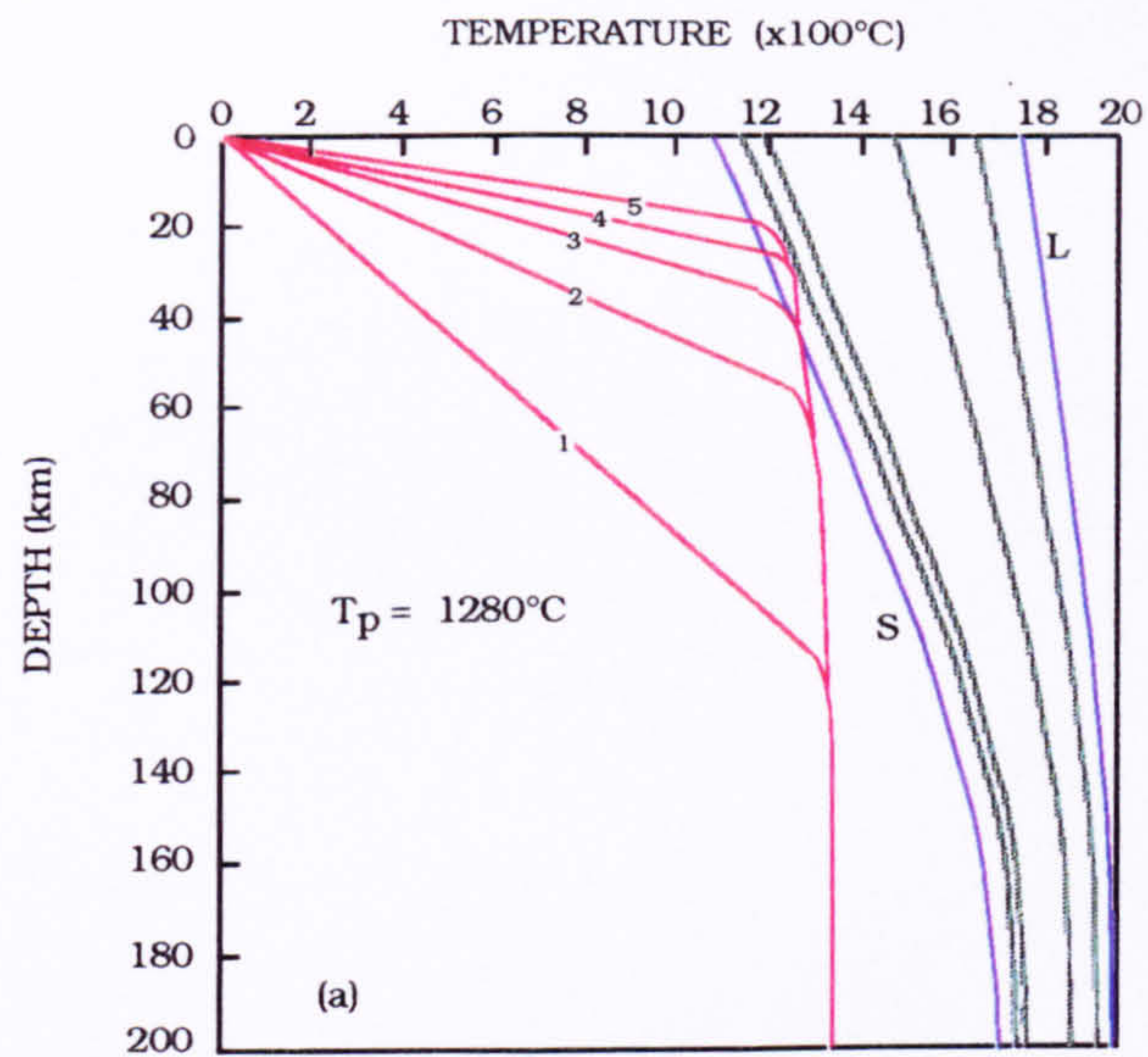


FIGURE 8.1 (a) Geotherms for the mantle with a potential temperature (T_p) of 1280°C , and a mechanical boundary layer thickness of 100km , calculated from the equations of McKenzie & Bickle (1988), for stretching factors (β) of 1, 2, 3, 4 and 5. The curves labelled S and L are the solidus and liquidus for anhydrous peridotite. Intermediate (green) curves represent 15, 24.5, 43.8, and 70% melting.

(b) As for 8.1(a) but for a mantle potential temperature of 1480°C , appropriate for a mantle plume.

After Fitton *et al.* (1991).

surface without melting). The amount of melt produced is governed by the amount by which the geotherm oversteps the solidus. This is depicted in *Figures 8.1c* and *8.1d*, which show the cumulative amount of melt produced and the average depth of melting, respectively, for normal and anomalously hot asthenosphere. It is possible to draw several important conclusions from these diagrams (Fitton *et al.*, 1991):

- (a) Mantle of normal T_p will not produce significant amounts of melt until β approaches 3.
- (b) The presence of a plume beneath an un-rifted continental lithosphere is unlikely to produce much magma unless the lithosphere becomes thinned by thermal erosion.
- (c) Large volumes of magma are only likely to be generated in the continental environment if rifting accompanies the impingement of a mantle plume, unless the mantle T_p is in excess of 1480°C.
- (d) As β increases at all values of T_p , the average depth of melting moves to shallower levels in the mantle as the amount of melt increases.
- (e) Melting of anhydrous peridotite is concentrated within the thermal boundary layer in all cases, that is around the point of inflection in the geotherm. Melts from this region will have the chemical and isotopic characteristics of the asthenosphere, but can interact with the lithosphere on their way to the surface.

Since the impact site of the Iceland plume is considered to have been some 600km away from the BTVP, under eastern Greenland (White & McKenzie, 1989; Thirlwall *et al.*, 1994), it would seem unlikely that a T_p of 1480°C could have been achieved beneath the BTVP (Bell *et al.*, 1994). White & McKenzie (1989) suggest that beneath broad swells found around mantle plumes, the T_p is generally ~ 100°C hotter than under normal oceanic lithosphere (1280°C), suggesting that the mantle T_p under the BTVP during Tertiary times may have been of the order of 1380°C. As such, relatively high stretching factors (β in excess of 3) would be required to produce the voluminous basalt sequences found on Skye and Mull. Evidence for regional extension and thinning takes the form of extensive dyke swarms throughout the area (Speight *et al.*, 1982).

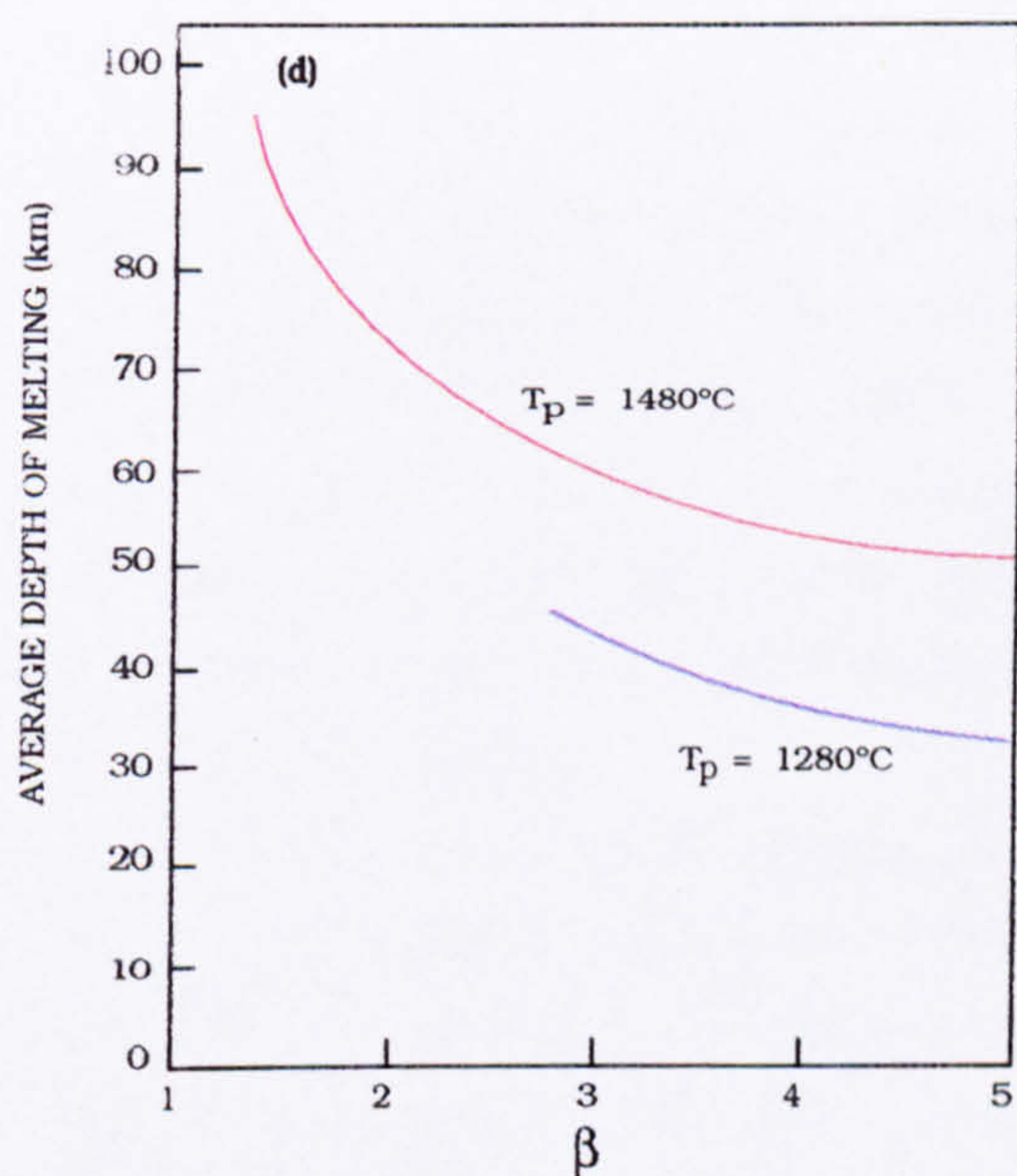
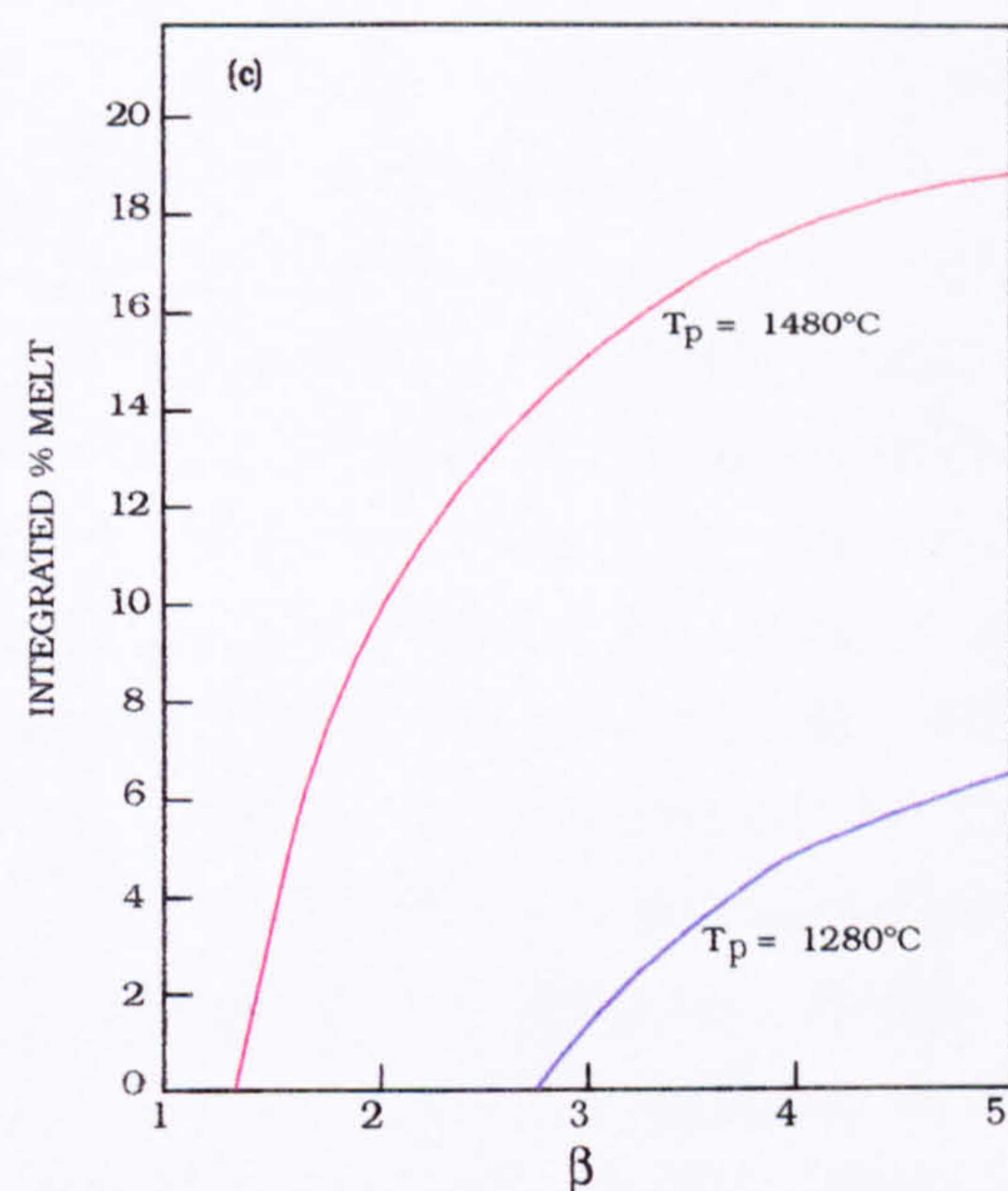


FIGURE 8.1 (c) Integrated (cumulative) percentage of melt generated by the geotherm oversteps on the solidus in Figures 8.1(a) and 8.1(b) as a function of β of normal (1280°C) and plume (1480°C) potential temperatures (T_p).

(d) Average depth of melting as a function of β .

After Fitton *et al.* (1991).

The trace-element and isotopic geochemistry of the SMLS and Mull Plateau Group lavas require an asthenospheric source region which was depleted relative to Bulk Earth (Beckinsale *et al.*, 1978; Morrison *et al.*, 1980; Thompson & Morrison, 1988; Kerr 1995). Kerr (1995) suggests that the Mull Plateau Group was generated from 7 to 11% partial melting of a depleted *garnet* (\pm spinel) lherzolite source, and that the later Central Mull Tholeiites (similar to the Skye PM basalt type) represent between 13-17% further partial melting of a depleted *spinel* lherzolite source. This implies that the *depth* of melting decreased with time. Similar conclusions have been suggested for the SMLS and PM basalt types of Skye (Morrison *et al.*, 1980; Thompson & Morrison, 1988; Bell *et al.*, 1994). The depletion of the mantle source prior to the extraction of the early Plateau Group magmas is thought to be due to the extraction of small degree melts in the Permo-Carboniferous (Morrison *et al.*, 1980; Thompson & Morrison, 1988). Some of these melts "froze" within parts of the upper mantle, and later contributed to the *enrichment* of a few flows within the Plateau sequences (Kerr, 1993). The extraction of the Plateau Group magmas would have further depleted the mantle source prior to its further melting and the production of the tholeiitic PM basalt type magmas (Thompson *et al.*, 1980; Bell *et al.*, 1994; Kerr, 1995). However, if the PM basalts represent higher degree melts as a consequence of higher β factors at a given T_p , then they will be more depleted than the earlier SMLS magmas, irrespective of the degree of depletion attributable to the extraction of the SMLS.

The declining influence, with time, of deeper, garnet-bearing, sources, suggests that as the BTVP magmatic system developed, melting occurred at progressively shallower depths in response to lithospheric thinning (Kerr, 1995). This is in accord with the suggestion of Ellam (1992) that the thickness of the lithosphere, and therefore the extent of thinning, acts as an important control on basalt chemistry.

In the Hebrides, Speight *et al.* (1982) calculated, from aggregate dyke thicknesses at their present level, that extension rarely exceeds 10% ($\beta=1.1$), and more often than not, is closer to 5%. This provides a problem with the generation of voluminous flood basalts, even given the possibility of previous lithospheric thinning (Thompson & Gibson, 1991). Olson (1988) calculated that plumes can "significantly erode the lithosphere" on a time-scale of ~ 10 Ma, provided that small-scale convection is considered. Kerr (1993) therefore considered that a

previously thinned lithosphere (Thompson & Gibson, 1991), coupled with the processes of lithospheric extension and erosion by the mantle plume, allowed the generation of the voluminous flood basalt sequences in the BTVP, and that as the processes continued, the depth of melting decreased, and the degree of melting increased producing the later tholeiitic magmas.

This progression in depth and degree of partial melting would have affected the passage of magma through the crust, and as a result would influence the position of magma ponding, and the style and amount of crustal contamination and fractional crystallization, which affected the bulk of the magmas produced (Bell *et al.*, 1994).

8.2 A Petrogenetic Model for the LSSC

The LSSC displays a large elemental and isotopic diversity. This is the product of a complex magmatic history involving the simultaneous action of a number of magmatic processes. Although each magma group of the LSSC has seen a complex history, it has been possible to elucidate which processes have been dominant in the production of each individual group.

The geochemistry of the LSSC is, on the whole, influenced by the fact that basic magmas ponded within and interacted with the upper crust. The basalts and basaltic andesites of Group I show coherent trends on major- and trace-element Harker diagrams, indicating that fractional crystallization played an important role in their petrogenesis, a fact supported by the presence of gabbroic cumulate xenoliths within these rocks. The high degree of incompatible-element enrichment, however, requires that crustal contamination of the basic magmas also occurred. This contamination resulted in extreme Sr and Nd isotope ratios being imparted on the Group I rocks. Good correlations between trace-element ratios, isotopic ratios, and degree of fractionation for the Group I rocks, provide strong evidence in support of high-level AFC processes being the major control over their evolution (DePaolo, 1981; Wilson, 1989). However, the strong decoupling between major- and trace-elements, and even between different incompatible trace-elements, during fractional crystallization, requires that magma recharge and RTF processes also played a significant part in their petrogenesis (O'Hara, 1977; O'Hara & Mathews, 1981; Cox, 1988).

These processes imply that the basic magmas ponded within the crust; phase relationships suggest that this last occurred between 1-3kbar, corresponding to a maximum depth of ~10km.

The Group III rhyolites, with their strongly incompatible-element-enriched compositions and high initial Sr isotope ratios, represent partial melts extracted from the crust. Their peraluminous major-element geochemistry requires that the parent rocks were sediments or metasediments, and the Moine metasedimentary succession provides an ideal source. These silicic magmas coexisted with basic magmas since the two were commonly emplaced as composite sheets. Mixing between silicic and basic magmas in various proportions most likely gave rise to the andesites and porphyritic dacites of Group II. All magma groups underwent substantial amounts of fractional crystallization, involving olivine, plagioclase and Ca-clinopyroxene in the most basic magmas, and plagioclase, Ca-clinopyroxene and low-Ca pyroxene in the more evolved rocks. The silicic magmas fractionated plagioclase, low-Ca pyroxene, and possibly apatite and zircon.

It is envisaged that these processes occurred more-or-less concurrently within a plexus of small magma chambers or sill complexes within the upper crust (Cox, 1980; Dickin *et al.*, 1984; Morrison *et al.*, 1985).

8.3 The LSSC and its Magmatic Plumbing System

The geochemistry of the LSSC (*i.e.* phase relationships, major-element, trace-element and isotopic characteristics) requires that the initial parental melts ponded within the *upper crust*. The distinctly tholeiitic nature of the suite (Chapter 3), and the depleted character of the least-evolved, least-contaminated magmas (Chapter 4 and 5), suggests that the parent basic magmas were of Preshal More type. This is supported by the timing of emplacement of the LSSC towards the end of the development of Centre 1 of the Mull Central Igneous Complex (Musset, 1986; Dagley *et al.*, 1987), well after the extrusion of the Plateau Group lavas, and is consistent with the magmatic development of the BTVP as a whole, as discussed in Section 8.1. The presence of gabbroic cumulate xenoliths within many of the sheets (Chapter 7) suggests that discrete magma storage reservoirs developed within the crust. This is also a requirement for the process of combined

assimilation and fractional crystallization, by which the majority of the Group I magmas evolved. The possible form of these reservoirs is discussed below.

It has been shown that turbulent flow of hot basic magma within conduits is a very effective way to assimilate crustal material (Huppert & Sparks, 1985; Kille *et al.*, 1986; Kerr *et al.*, 1995). The process of assimilation during turbulent ascent (ATA) (Moorbath & Thompson, 1980; Thompson *et al.*, 1982, 1986; Huppert & Sparks, 1985) has been suggested to account for the contamination of the Mull Plateau Group lavas (Kerr *et al.*, 1995). Significantly, such a process will lead to the hottest, most magnesian magmas becoming the most contaminated.

The turbulent flow of magma in sill or dyke-like conduits will also be an efficient mechanism for the breaking-off of wall-rock xenoliths, for their transport into connected magma chambers, and for the continuous mixing of silicic partial melts from the wall-rocks into the body of the magma. Once a magma reservoir is filled with hot basic magma, both wall-rocks and xenoliths can be melted, and fractional crystallization can occur.

The presence of relatively long-lived magma reservoirs, and their continual recharge with fresh, hot basic magma (Chapter 3 and 4), will also facilitate the segregation of significant amounts of silicic magma, generated by partial melting of the country-rocks. Such silicic melts will tend to pond at the roof of the magma reservoirs due to density and viscosity differences, leading to a chemically stratified magma column (*cf.* Sparks, 1988; Bell & Pankhurst, 1993). The Group III rhyolites probably represent silicic magmas emplaced from the tops of such stratified magma reservoirs, the emplacement possibly induced by basic magma recharge at the base.

This model can also account for the Group II andesites and dacites. These magmas most likely evolved via the mixing of silicic crustal melts with small amounts of basic magma (Chapters 3, 4 and 5) within a zone of hybridization between the stratified silicic and basic magmas in the chamber. That all three magma groups of the LSSC contain phenocrysts, is further evidence for the establishment of relatively long-lived crustal magma reservoirs, and the stable stratification of basic, intermediate and silicic magma types.

An alternative to the "classic" magma chamber plumbing system is one whereby primary magmas are stored in deep sill complexes near the

base of the crust (Cox, 1980). Cox (1980) considers that the characteristic phenocryst assemblage of CFB provinces, being dominated by plagioclase, suggests that they have been involved in relatively low-pressure crystal fractionation equilibria. This supports the theory that the basalts evolved from more magnesian primary magmas (Cox, 1980, Thompson *et al.*, 1986; Wilson, 1989). The preferred model of Cox (1980) is where dense picritic primary magmas pond in sill complexes at the Moho, where they undergo fractional crystallization until their densities are reduced sufficiently to regain buoyancy and continue to rise. In such a system, significant volumes of gabbroic and ultramafic cumulates can be underplated to the base of the crust. Sill complexes also provide the ideal, large surface area environment for the contamination of basic magmas (Pattchet, 1980). Once fractionated sufficiently, the now basaltic magmas will rise through the crust, where they may pond again in upper sill complexes and undergo further fractional crystallization and crustal contamination (Cox, 1980, Thompson *et al.*, 1986; Wilson, 1989). The least-evolved members of the LSSC are similar to the depleted PM basalts of Skye. These magmas appear to have avoided ponding at the base of the crust, unlike the SMLS magmas which fractionated first at high pressures (Thompson *et al.*, 1972, 1980). The fact that the LSSC magmas did not pond at these deeper levels suggests that the degree of extension at this time was large.

Therefore, a possible model for the magmatic plumbing system of the LSSC, is one of a network of poorly connected conduits and small sill-like bodies, some of which may have been relatively long-lived, others more ephemeral. In such a system, *turbulent flow* in the feeder conduits will have supplied the base of the magma chamber with crustal xenoliths and would have mixed small-volume crustal melts with the basic magma as it ascended. This generally *active* magmatic plumbing system provides the ideal environment for the assimilation of country-rock material. Once the sill complex filled, the basic magma would have evolved via a process of combined assimilation and fractional crystallization (AFC). Silicic magmas would be generated, and would tend to pond at the top of the magma reservoir. Mixing between these rhyolitic and basic melts could occur. The entire system would be self-perpetuating, as long as fresh batches of basic magma were injected into the sill complex. As shown in Chapter 7, the gabbroic xenoliths are slightly contaminated, with this contamination probably

occurring at an early stage. This, coupled with the fact that the LSSC evolved at low pressures, and appears to have been contaminated with material derived solely from the Moine metasediments, implies that the sill complex was situated within the Moine. The Moine is potentially very "thin-skinned", especially in the west, and the site of initial magma ponding and fractionation was therefore probably only just within the Moine metasedimentary succession. Further contamination could have occurred during the turbulent emplacement of the sheets to a higher level, as exemplified by the Group I basic sheet at Traigh Bhàn na Sgurra (Chapter 6). *Figure 8.2* shows a schematic diagram for the proposed magmatic plumbing system for the LSSC. Also shown are how, and where, the individual magmatic processes which affected the geochemistry of the different LSSC magmas. *Figure 8.2* also shows that the interaction of individual crustal xenoliths with the basic magma may also be a very important process. These interactions are discussed fully in Chapter 9 and 10. A similarly complex magmatic plumbing system has been proposed for the evolution of the early plateau lava succession on Skye and Mull (Dickin *et al.*, 1984; Morrison *et al.*, 1985; Scarrow & Cox, 1995). High-level sill complexes such as this would therefore appear to be ideal for the fractionation of large volumes of basic magma, and its interaction with the continental crust.

8.4 A Few Conclusions

The preceding description and discussion of the geochemical characteristics and petrogenesis of the LSSC, has shown that no one individual magmatic process can account for the variation seen within the suite. Each batch of magma probably saw a complex series of mixing and fractionation processes before its final emplacement within the crust. The scenario of basic magmas passing through and ponding within old continental crust is not, however, unique to the BTVP. What is unusual about the LSSC perhaps, is the preservation of a suite of basic to silicic minor intrusions *with* their associated cumulate and crustal xenoliths. The Group I *basic* magmas are also unusual, in that they have extreme incompatible-element enrichment and extreme Sr and Nd isotope signatures. Such characteristics are rare for continental tholeiitic basalts (Thompson *et al.*, 1986; Wilson, 1989). It

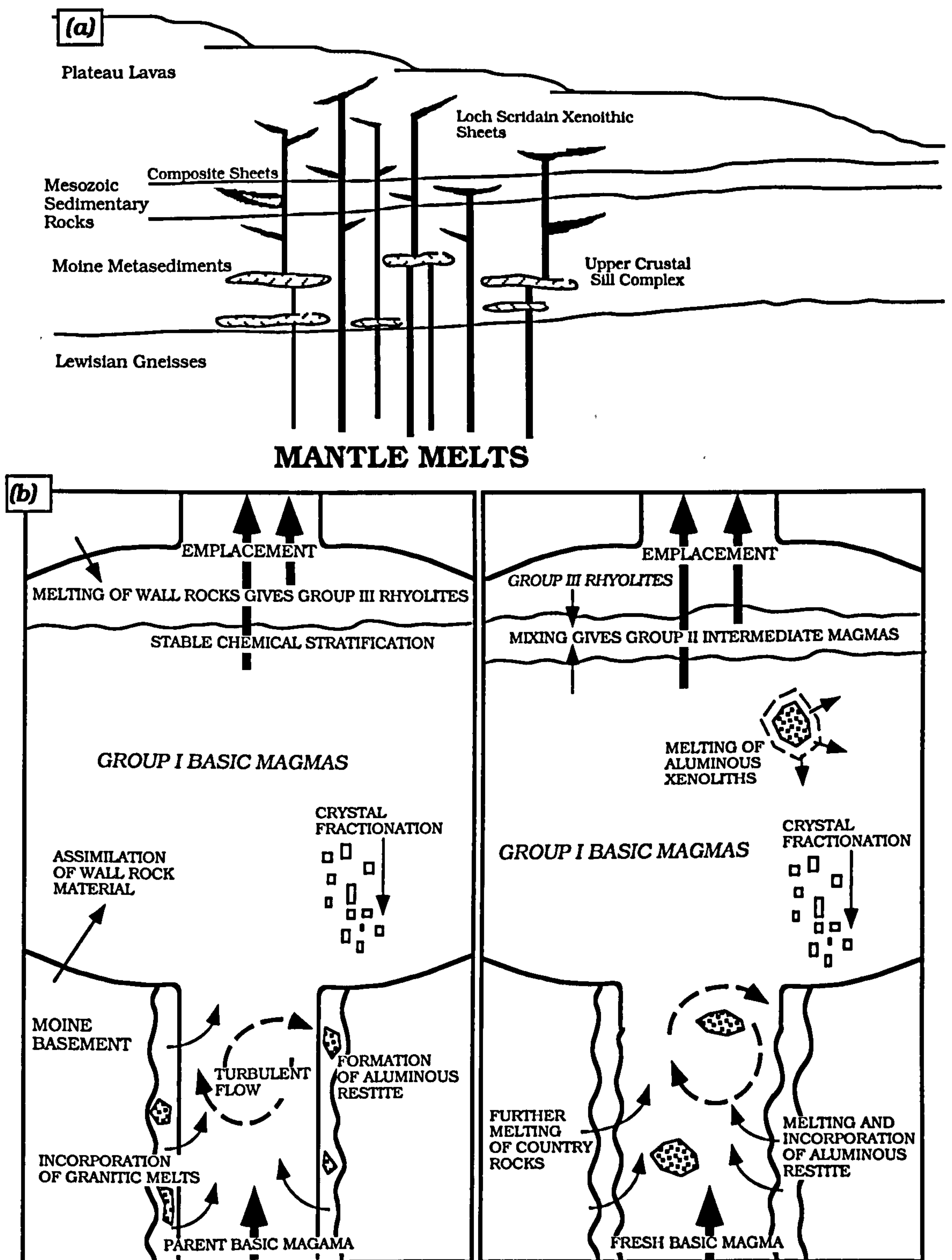


FIGURE 8.2 (a) Schematic diagram showing the proposed structure of the LSSC magmatic plumbing system; and (b) the evolution of the various magma groups within upper crustal sill complexes. Processes of magma/xenolith interaction are discussed fully in Chapters 9 and 10. No vertical scale implied in either diagram.

has been the unusually good physical preservation of the LSSC, and its extreme geochemistry that has enabled the documentation of how, when and where the "competing" magmatic processes may actually occur. This study also highlights the complex nature of magmatic systems, and shows that although it is often possible to pinpoint the *dominant* magmatic process involved in the petrogenesis of a particular group of volcanic rocks, it is also very probable that other processes also played a part. Such complex magmatic histories are very possibly the norm in continental environments. The implications for basic magma/crustal xenolith interactions are further discussed in Chapters 10 and 11.

CHAPTER 9

THE CRUSTAL XENOLITHS

9.1 Introduction

The most conspicuous feature of the LSSC is the number of sheets which contain abundant xenoliths of crustal origin. They were first described by Thomas (1922) and Bailey *et al.* (1924), when the original mapping of the island was completed. The xenoliths and their petrogenesis have also been discussed by Kille (1987).

The xenoliths occur mainly within the holocrystalline and hypocrySTALLINE sheets of Groups I and II, and often occur in such profusion that it is difficult to see the host basaltic rocks. They occur either in xenolith-rich pods and lenses, or as single, isolated blocks, always located towards the top margin of each sheet. Individual xenoliths vary in size from a few centimetres across, to large rafts several metres long, although the majority fall into the 10-50cm size range.

The following discussion provides a detailed description of the various xenolith types, their mineralogy and mineral chemistry, incorporating major-element, trace-element and isotopic characteristics where appropriate. A limited number of bulk-rock analyses are also presented. This information is used to elucidate the high temperature metamorphic history of the xenoliths, and therefore shed some light on their origins.

The petrogenesis of the LSSC has been shown to be strongly influenced by assimilation of upper-crustal material (Chapters 3, 4, 5 and 7). The preservation of crustal xenoliths, at various stages of reaction with the host magma, enables the physical processes involved in assimilation to be explored.

9.2 Mineralogy and Mineral Chemistry

The crustal xenoliths of the LSSC can be subdivided into two broad groups :-

- (a) Siliceous xenoliths
- (b) Aluminous xenoliths

Each group can be further sub-divided on the basis of mineralogy, structures, textures, and probable origins. Both siliceous and aluminous xenoliths can be found within the same sheet. The mineralogy and mineral chemistry of each group and sub-group will be treated separately. Although it is difficult not to discuss aspects of the petrogenesis of the xenoliths as their characteristics are described, consideration of their mode of formation, and of the processes of magma-xenolith interactions is deferred until Chapter 10.

Siliceous Xenoliths

Xenoliths containing a significant proportion of modal quartz (> 40%), fall into three major categories :-

(a) Sandstones and conglomerates

This group consists of rocks which are derived from the local Mesozoic sedimentary succession. This consists of a sequence of grits, sandstones, shales and limestones, the total thickness of which (Triassic - Cretaceous) does not exceed 270m, although the full sequence is never preserved in one section in its entirety (Lee & Bailey, 1925). These xenolith types are found in sheets which intrude the Mesozoic strata, and also within sheets which intrude the overlying Palaeocene lavas.

The basic portion of the composite sheet at Rudh' a' Chromain [NM 521202] contains numerous small quartzose xenoliths derived from the Carsaig Sandstone (Middle Lias), into which the sheet is partly intruded. In its un-metamorphosed state, this sandstone consists of angular and sub-rounded grains of quartz with minor oligoclase and microcline. The grain size is of the order of 150µm (see *Figure 9.1a*).

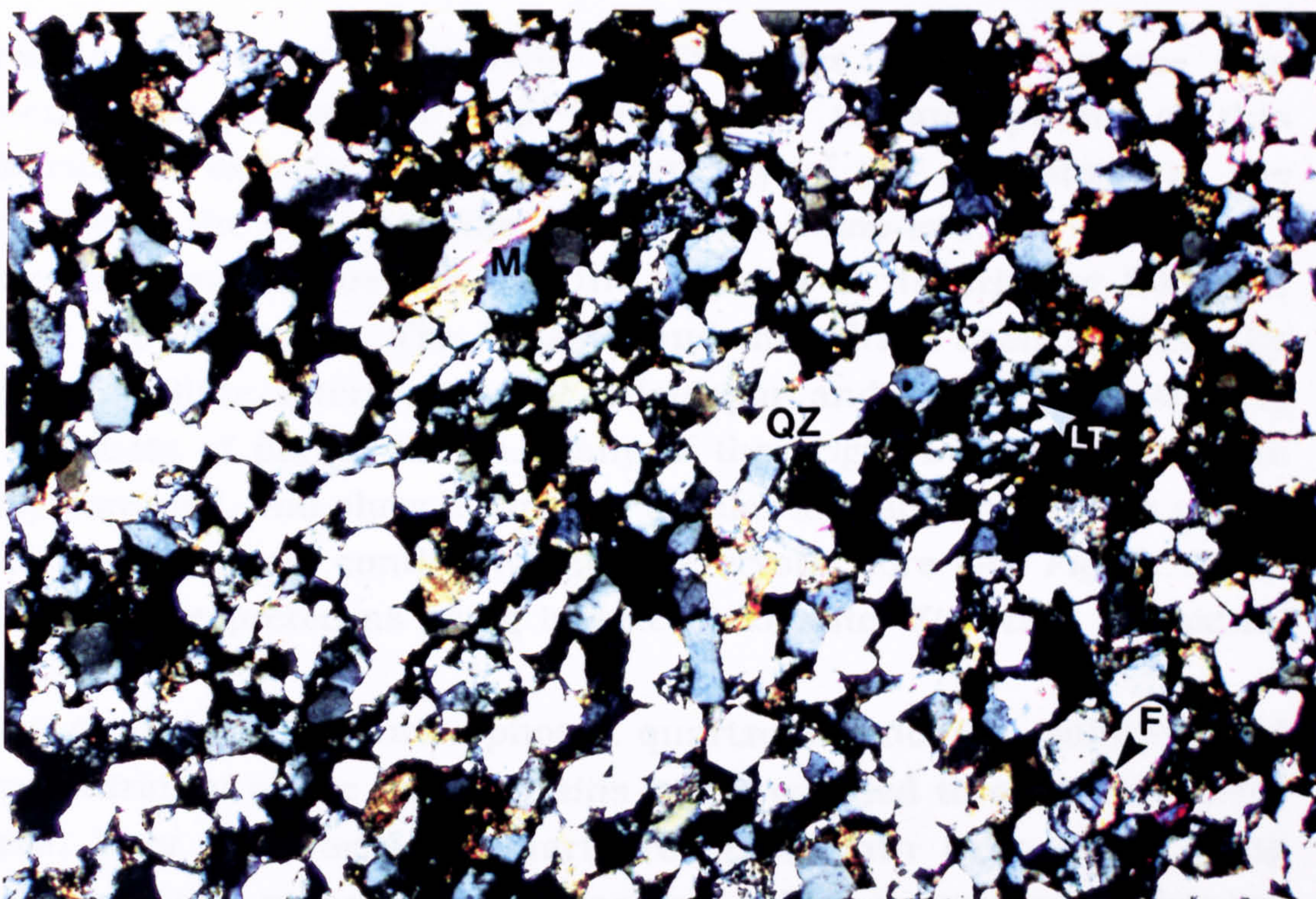


FIGURE 9.1a Unmetamorphosed Jurassic sandstone from Rudh' a' Chromain [NM 521202]. Rock consists of sub-angular quartz grains (QZ), with minor lithic grains (LT), feldspar (F) and mica (M). (xpl; Field of view 2x3mm; Sample R0).

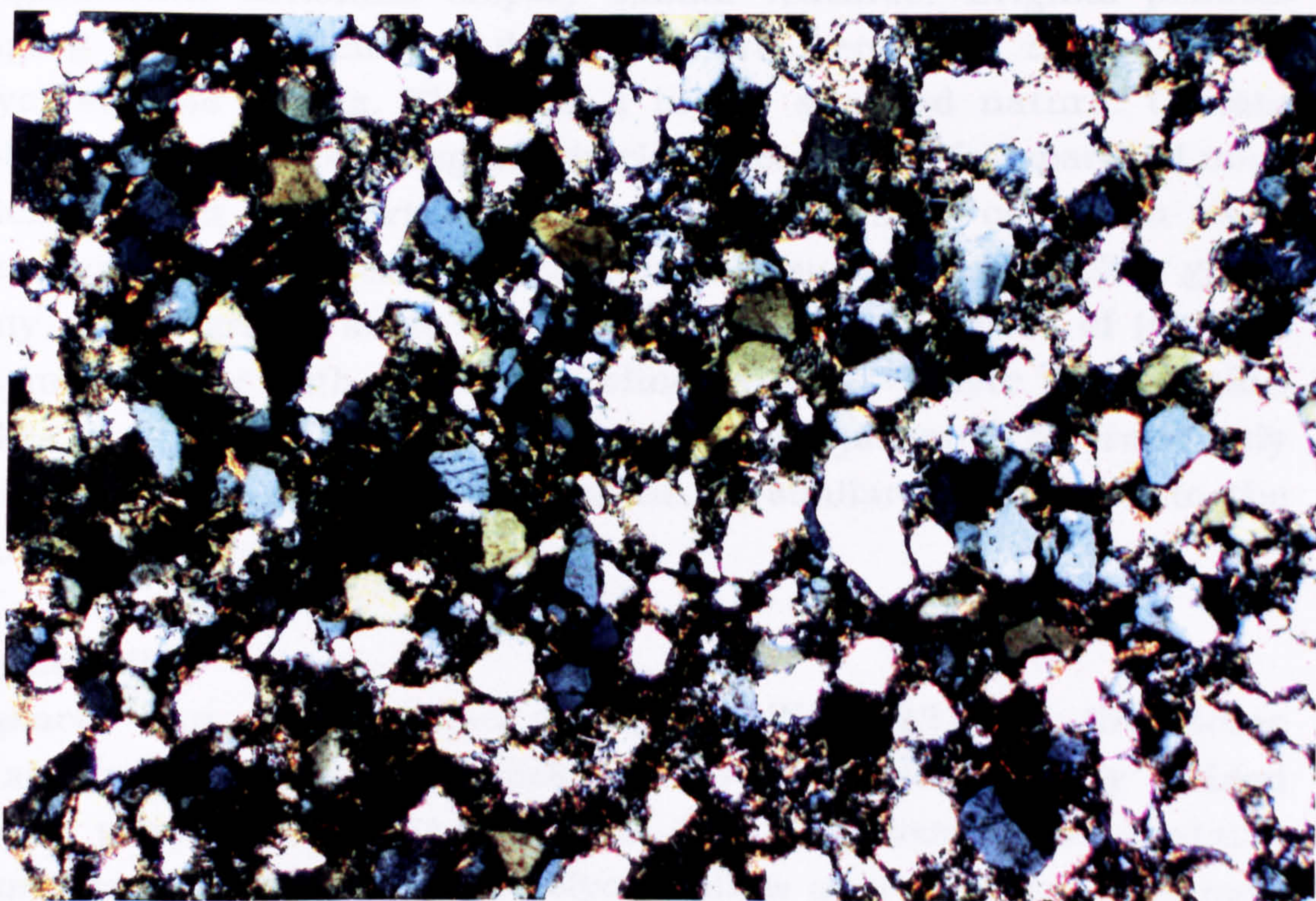


FIGURE 9.1b Jurassic sandstone in contact with composite sheet at Rudh' a' Chromain. Rock shows effects of high temperature metamorphism, with the breakdown of the micas and some of the feldspar. Quartz grains are often fringed with small tabular crystals of inverted tridymite. (xpl; Field of view 2x3mm; Sample R1)

Occasional grains of muscovite, Fe-Ti oxides, and zircon are also present. The progressive high-temperature metamorphism of this rock can be examined if the petrography of the sandstone at the contact with the sheet and the xenoliths are compared.

The contact sandstone has lost the majority of its primary feldspar, and all the muscovite. The feldspar and mica have been replaced by cryptocrystalline intergrowths of K-feldspar and quartz representing the products of partial fusion. Many of the original quartz grains are highly corroded, and show a fringe of tabular and acicular quartz grains which are in optical continuity with the crystal core (see *Figure 9.1b*). These are interpreted as being inverted tridymite. Zircon is a residual phase.

In the more highly metamorphosed quartzose xenoliths, solution and recrystallization of the quartz grains has proceeded to an even greater degree. Very little original quartz remains, with each grain being enveloped in a mosaic of interlocking tabular inverted tridymite, generally in optical continuity with the crystal core. In places, clusters of tabular tridymite occur. Interstitial melt pockets are represented by microcrystalline intergrowths of K-feldspar and quartz. Patches of slightly coarser oligoclase (and sanidine ?) also occur.

Conglomeratic xenoliths display similar features. Original pebbles ranging up to 15cm in diameter, are generally composed of polycrystalline quartz. This has a highly strained nature. Certain pebbles, and the supporting matrix clearly contained feldspar and mica which allowed the partial melting of the rock to occur. In such instances, individual relict quartz grains are surrounded by clear glass. Many quartz grains show envelopes of radiating clusters of inverted tridymite, along with needles of clinopyroxene. Where the xenolith makes contact with the host basalt, it is jacketed by randomly oriented, coarse-grained clinopyroxene, of similar composition to the groundmass pyroxene.

(b) Quartzites

In places (*e.g.* Traigh Bhàn na Sgurra [NM 423185]), the Moine metasedimentary basement rocks consist of relatively finely bedded impure psammites and semipelites. The succession also contains numerous large lenses of pure polycrystalline quartz. These rocks have furnished the LSSC with numerous xenoliths, and can be found within sheets all over the Loch Scridain district. Most of these xenoliths form

rectangular to irregularly-shaped blocks up to 50cm across (*Figure 9.2*). Mineralogically, the quartzites consist of almost 100% quartz of coarse (2-5cm), irregularly-shaped interlocking grains, which have a highly strained nature. There is minor muscovite and feldspar (< 1%). The lack of abundant, easily fusible phases to act as a flux (feldspar or mica), means that the xenoliths have not been altered by high temperature metamorphism. Alternatively, the pure quartzite xenoliths may represent Mesozoic sediments that have had granitic melts removed to leave a pure quartzose restite. However, the highly strained nature of the quartz grains in these xenoliths supports the contention that they are from the Moine metasedimentary succession. At the contact between the xenolith and the host basalt, a zone rich in coarse-grained clinopyroxene has developed within the basalt.

(c) Quartzo-feldspathic schists

A small number of banded quartzo-feldspathic schist xenoliths (*Figure 9.3*) have been found in sheets which intrude both the Moine metasedimentary succession, and the overlying Palaeocene lavas (*e.g.* Kilfinichen Bay [NM484280], Killunaig [NM 496258], Traigh Bhàn na Sgurra [NM 423185]). They consist of bands of quartz and feldspar, and darker bands which were presumably originally of biotite. However, no mica can be seen in hand-specimen. In thin-section, the rock is dominated by quartz, together with subordinate microcline and oligoclase. The quartz grains are highly corroded with irregular shapes, and show a strained undulose extinction. Much of the original feldspar is intact, but where it is in contact with quartz, small (0.5-1 mm) pools of melt have developed. These melt pockets have crystallized into fan spherulites of feldspar, which are often nucleated on remnant feldspar grains (*Figure 9.4*). Original biotites in the xenolith have been completely decomposed, being replaced with breakdown products such as spinel, ilmenite/magnetite, and rutile. The spinel, and Fe-Ti oxide phases take the form of minute (1-4 μ m) octahedra. The rutile is acicular, often with a dendritic structure. It has similar dimensions to the spinel and Fe-Ti oxides. Chlorite is also present. However, in contrast to the Fe-Ti oxide phases, chlorite is a low temperature alteration product of mica, associated with the passage of hydrothermal fluids through the rock. As with other quartz-rich xenoliths, a corona of medium-grained (1-3mm) clinopyroxene has developed at the magma-xenolith interface.



FIGURE 9.2

Xenolith of quartzite in basaltic sheet at Port Mor [NM 435239]. These common xenoliths are believed to come from the Moine metasedimentary succession. Hand lens 5cm long.

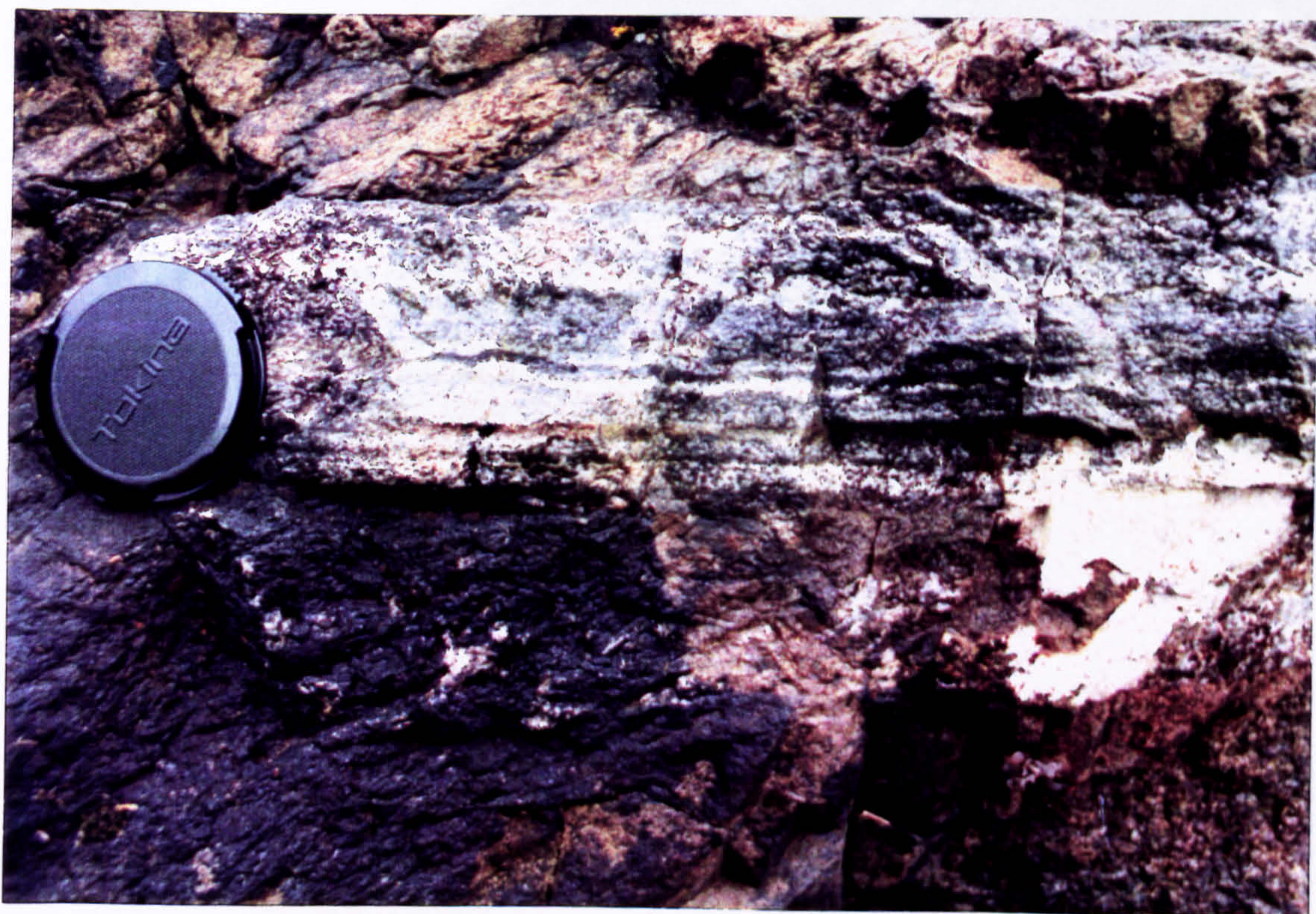


FIGURE 9.3

Xenolith showing schistose banding, from Kilfinichen Bay [NM 484280]. Lens cap 5cm across.

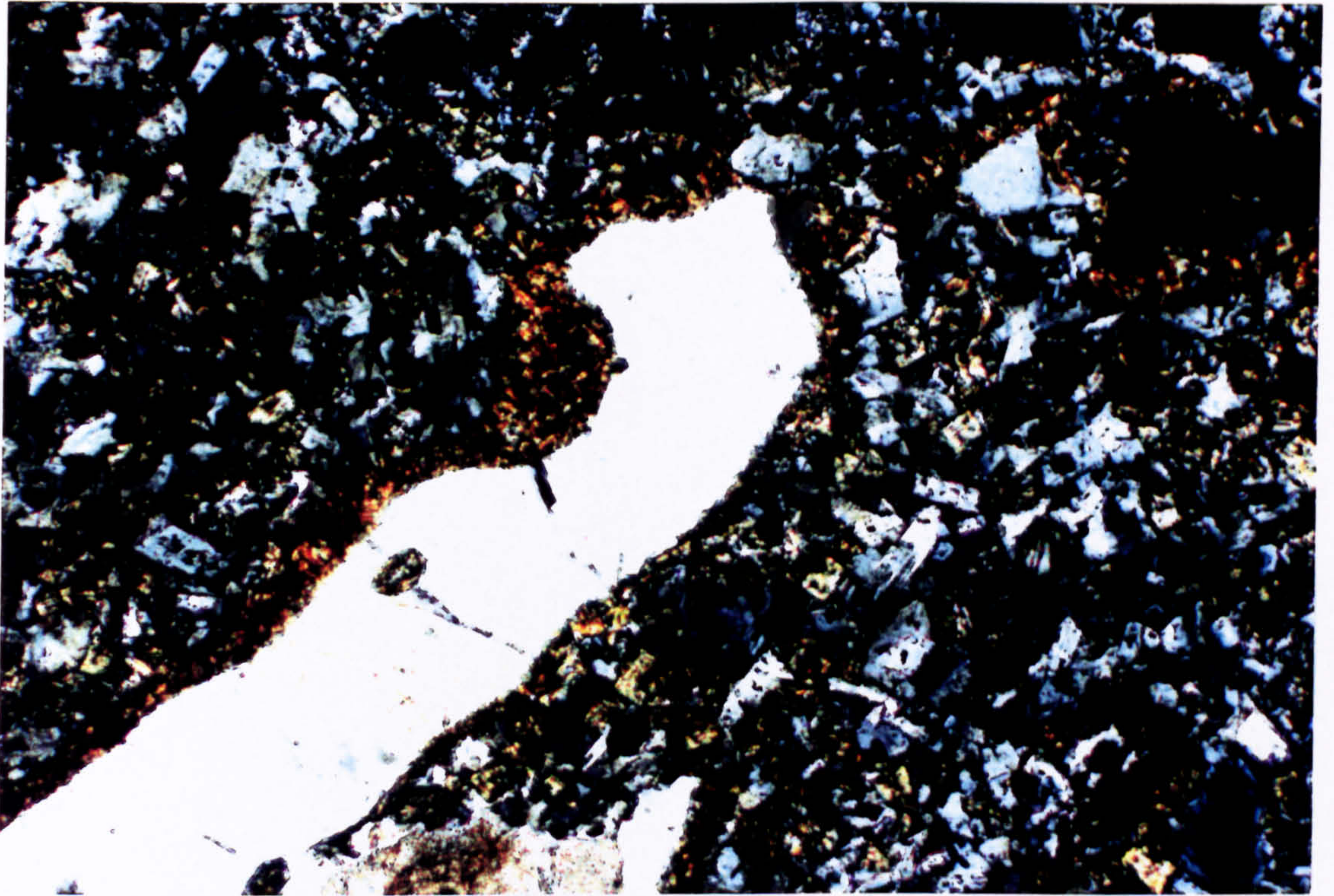


FIGURE 9.4

The effects of high temperature metamorphism on a Moine pelitic schist, from the contact zone of the basaltic sheet at Traigh Bhan na Sgurra [NM 423185]. Quartz grains are highly corroded and are set in a matrix of finely crystallized K-feldspar and quartz. This fine-grained material represents the melts formed via the breakdown of micas and some feldspar. (xpl; Field of view 2x3mm; Sample SOBC)

(d) Possible granite xenoliths

A small number of coarse-grained (2-5mm) plagioclase-quartz-alkali feldspar xenoliths have been identified (*e.g.* Port Mor [NM 435239]). The quartz grains are strongly corroded and embayed, and show undulose extinction indicative of strain. Feldspar is dominantly plagioclase of oligoclase composition, although un-twinned K-feldspar is also common. Feldspar crystals also have corroded crystal outlines. Separating most individual crystals are thin films of what was originally melt. This has quenched into numerous fan spherulites of K-feldspar and plagioclase. The melt also contains vesicles, now filled with fibrous silica. The origin of these xenoliths is ambiguous. The only large, exposed granite body in the vicinity is the late-Caledonian Ross of Mull granite. This body is of comparable mineralogy, being rich in plagioclase. The granite is however, also rich in quite coarse-grained (1-2mm) biotite and hornblende, yet there is no trace of these phases, or their high temperature alteration products, in the xenoliths. The Ross of Mull granite intrudes Moine metasedimentary rocks, both of which structurally sit to the west of the Loch Assapol Fault (see *Figure 1.2*). The Loch Assapol Fault is thought to have been active during the Tertiary (B.R. Bell, *pers. comm.*). Moine metasedimentary rocks underlie the Palaeocene volcanic rocks, and it is assumed that Lewisian amphibolite and granulite facies gneisses underlie the Moine metasediments. It is difficult to argue that the Port Mor sheet could not have picked-up Ross of Mull granite xenoliths due to structural problems, particularly if the granite margins were gently inclined outwards. However, the strained nature of the quartz grains, the dominance of plagioclase over K-feldspar, and the lack of evidence for former biotite and hornblende crystals would suggest that this particular granite did not furnish the LSSC with xenoliths. The xenoliths possibly represent fragments of either an unseen granitic body, thoroughly re-crystallized pegmatitic rocks from the Moine, or Lewisian amphibolite/granulite facies gneiss.

The pyrometamorphic features exhibited by the quartz-rich xenoliths are commonly-reported phenomena. Wyllie (1961) reported inverted tridymite from partially fused Torridonian sandstone xenoliths in a picrite sill from the island of Soay, NW Scotland. Tridymite has also

been described from siliceous xenoliths in basalt lavas from Surtsey (Sigurdson, 1968), and from xenoliths in basalt lavas from Auckland (Searle, 1962a,b). These reports together with the present study, reinforce the importance of interstitial fluxing material in the development of liquids from minerals with high-melting points. Where quartz grains are tightly packed together, no interstitial melt can develop, and therefore no tridymite fringes can crystallize on cooling. In such cases, the quartz grains themselves rarely invert to tridymite due to the sluggish nature of this transition, and due to the fact that liquids enriched in volatiles, which enhance tridymite crystallization, have no access to the quartz grains (Tuttle & Bowen, 1958).

The composition of glasses from a selection of quartzose xenoliths from the LSSC, along with comparative analyses reported from other suites, is given in *Figure 9.5*. A representative sample of the analyses are shown in *Table 9.1*. Element totals of these analyses are highly variable due to the difficulties associated with the analysis of glasses on an electron-probe. To minimise the loss of alkalis on analysis, count-times for K and Na were reduced, and the electron beam size was increased to 10 μ m.

The initial melts formed at quartz-feldspar crystal interfaces will plot near to the minimum in the system Ab-Or-Qtz (Tuttle & Bowen, 1958; Thompson, 1981; Vielzeuf & Holloway, 1988). As equilibrium melting continues, the proportion of liquid will increase and change in composition along the cotectic, as quartz and feldspar dissolve. Once all the feldspar is consumed, assuming the rock initially contained more quartz than feldspar, the composition of the melt will become progressively enriched in silica, until all the solid has melted, and the composition of the liquid is that of the original "bulk xenolith". All the glasses analysed, plot well within the silica field of the Ab-Or-Qtz system, indicating that all the feldspar and much of the quartz has melted, confirming the petrographic evidence. Kille (1987), in his study of the LSSC xenoliths, reported even more silica-enriched glasses. However, similar compositions have not been found by this study. Such liquids will precipitate tridymite (or quartz, or cristobalite, depending upon the temperature and pressure) until the liquid reaches the cotectic. Tridymite would then be joined by feldspar, and both would crystallize together while the liquid composition changed along the field boundary towards the minimum, until the liquid quenched as a glass on emplacement. However, very few of the quartz-

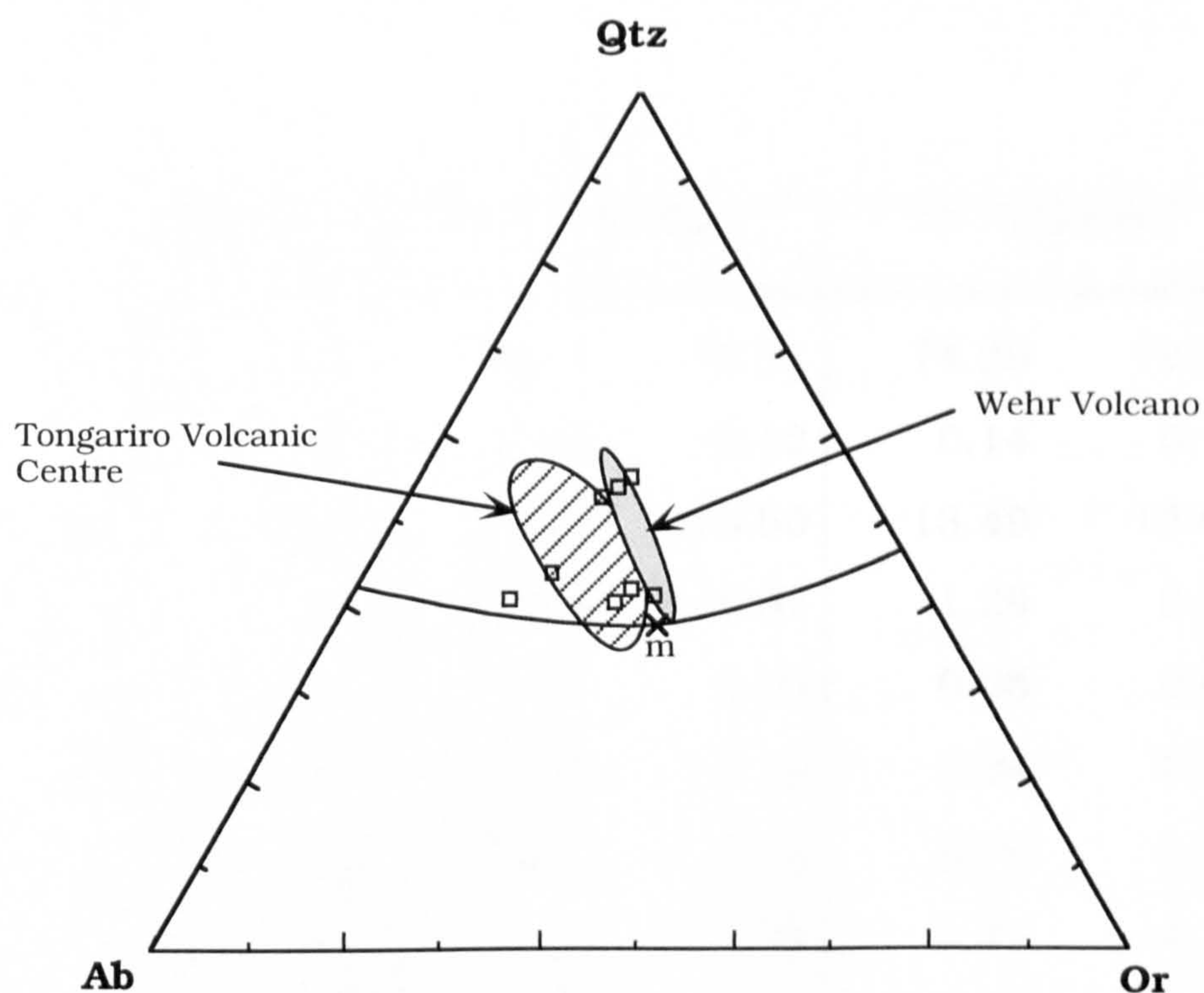


FIGURE 9.5 Normative Qtz-Ab-Or for siliceous glasses from quartz-rich crustal xenoliths, associated with mica breakdown and, melting at quartz-feldspar grain boundaries (*open squares*). 1 kbar, anhydrous liquidus surface and ternary minimum (m) after Tuttle & Bowen (1958). Also shown are fields occupied by siliceous glasses from pelitic xenoliths from the Wehr Volcano, Germany (Grapes, 1986), and from metasedimentary xenoliths from the Tongariro Volcanic Centre, New Zealand (Graham, 1987).

rich xenoliths from the LSSC contain quenched glass, much of the interstitial liquid being represented by a microcrystalline mixture of quartz and feldspar.

Sample :	PB1 - Banded Schist		PQS1 - Sandstone		R2 - Sandstone	
SiO ₂	73.21	76.37	78.11	73.31	74.29	70.42
TiO ₂	0.34	0.16	0.04	0.12	0.14	0.14
Al ₂ O ₃	13.63	12.39	11.51	13.50	13.49	13.65
FeO	2.40	1.66	0.86	0.97	1.29	0.84
MnO	0.00	0.01	0.01	0.03	0.05	0.00
MgO	0.13	0.53	0.23	0.19	0.24	0.38
CaO	0.32	3.30	0.21	0.78	0.76	1.41
Na ₂ O	3.22	2.35	2.15	1.78	1.71	4.11
K ₂ O	6.37	2.00	3.34	5.53	5.51	3.48
TOTAL	99.62	98.77	96.46	96.21	97.48	94.43

Table 9.1 Representative glass analyses from siliceous xenoliths from the LSSC, associated with the melting at quartz-feldspar grain boundaries. All analyses carried out using a Cameca SX50 electron microprobe at the Department of Geology & Applied Geology, Glasgow University. Machine conditions for analyses of glasses are outlined in Appendix I. Samples PB1 and PQS1 from Port Mor [NM 435239], sample R2 from Rudh' a' Chromain [NM 521202].

Coarse-grained pyroxene coronas at contacts between quartzose xenoliths and their host basaltic magmas are another well-documented and understood phenomenon. The heat required to melt and assimilate minerals that would only precipitate at a later stage of cooling (*i.e.* quartz in undersaturated basaltic magma) is gained by the precipitation of phases with which the magma is currently saturated (Bowen, 1928). During experimental work, Sato (1975) found a complex zonation of reaction products around quartz xenocrysts in basalts and andesites. Around the unfused quartz a zone of glass and Ca-

rich pyroxene was formed, followed by a zone composed completely of Ca-rich pyroxene. It was also shown that alkalis and Al were preferentially concentrated close to the xenocryst, diffusing against their concentration gradients, producing a low-melting point liquid through reaction with the quartz. This suggests that the presence of clinopyroxene reaction-rims is due to the high (Na+K)/Al ratios being set-up by diffusion in the contact zone around siliceous xenoliths. This increases the chemical potential of CaO in the liquid causing clinopyroxene, rather than orthopyroxene to crystallize (Sato, 1975). Plagioclase rarely appears within these coronas, even if the magma is saturated with this phase and precipitating it elsewhere. This relation is possibly due to the relative diffusion rates of the components of mafic minerals and plagioclase (McBirney, 1979). Similar pyroxene coronas around quartz xenocrysts and xenoliths have been reported from the Loch Uisg granophyre, Mull (Bailey *et al.*, 1924), from xenoliths in basalt lavas from Auckland (Searle, 1962a,b) and New Zealand (Graham, 1987), and many other occurrences are reviewed by Holgate (1954), and McBirney (1979).

Aluminous Xenoliths

The most striking, and certainly the most enigmatic, of the xenolith types, are the aluminous varieties. They are found in sheets of Groups I and II type, which intrude the Moine metasedimentary succession, the Mesozoic sedimentary rocks, and the overlying Palaeocene lavas. They occur in close association with the Moine pure quartzite xenoliths, and also with xenoliths of Mesozoic derivation. Since both the pure quartzites and the aluminous xenoliths are invariably found together, in sheets from all over the Loch Scridain district, important structural constraints can be placed upon the ultimate origins of the aluminous xenoliths. This is returned to in Chapter 10.

The aluminous xenoliths can be divided into three major groups, on the basis of the mineral assemblage present :

- (a) Mullite buchites
- (b) Cordierite (mullite) buchites
- (c) Plagioclase-corundum-spinel assemblages

Representative whole-rock, glass and mineral analyses are given throughout the text. Full listing of rock and mineral analyses can be found in Appendix II and Appendix IV, respectively.

(a) Mullite buchites

The mullite buchites are glassy rocks, which range in colour from dark-grey, through lilac, to almost pure white. They form irregularly-shaped masses, which vary in size from a few centimetres across, to large rafts several metres in length (*Figure 9.6*). Apart from the occasional crystal of corundum, no individual mineral phases can be identified in hand-specimen. The rocks are frequently vesiculated, the vesicles being filled primarily with zeolite.

In thin-section, the mullite buchites consist of a pale or dark glass containing a mass of randomly oriented needles of mullite ($3\text{Al}_2\text{O}_3 \cdot 2\text{SiO}_2$). The mullite closely resembles sillimanite ($\text{Al}_2\text{O}_3 \cdot \text{SiO}_2$), and it was originally mis-identified as such by Bailey *et al.* (1924). Bowen *et al.* (1924) provided the first chemical analysis of the Mull "sillimanite". The mullite needles generally have dimensions in the order of $50 \times 2\mu\text{m}$, although 'exceptional' specimens can reach $200\mu\text{m}$ in length. Representative electron-probe microanalyses of mullite



FIGURE 9.6

Aluminous mullite buchite xenoliths in the basaltic sheet at Traigh Bhan na Sgurra [NM 423185]. Mullite buchites show a great variety of colour, from almost pure white, through pale lilac to dark grey. Hammer shaft 60cm long.

crystals are given in *Table 9.2*. Most analyses correspond closely to the ideal formula, although the majority of crystals contain appreciable amounts of TiO₂ (0.4-1.4 wt%) and FeO* (~ 0.3 wt%).

Cameron (1976a) has examined the mullite buchites from the LSSC, as well as similar rocks from other areas, but of different paragenesis. Cameron (1976a) also found co-existing sillimanite within a few of the Mull buchites. This work on the Mull buchites, and other rocks containing both mullite and sillimanite, suggests that these two phases can co-exist stably over a wide range of temperatures, which points to the presence of a miscibility gap between the two phases (Cameron, 1976a).

Sample :	KIFX1 - Central Buchite		PM2 - Unzoned Mullite Buchite			KBAX1 - Cordierite Buchite	
SiO ₂	27.78	28.47	27.45	28.05	28.08	30.06	30.52
TiO ₂	1.19	1.22	1.41	1.35	1.31	0.53	0.84
Al ₂ O ₃	69.68	69.34	69.79	69.00	69.56	68.12	67.81
FeO	0.30	0.36	0.33	0.35	0.34	0.53	0.51
MgO	0.39	0.43	0.36	0.40	0.39	0.18	0.19
CaO	0.03	0.11	0.05	0.01	0.03	0.03	0.02
Na ₂ O	0.27	0.26	0.33	0.31	0.26	0.10	0.09
TOTAL	99.64	100.18	99.71	99.46	99.98	99.54	99.98
FORMULA ON THE BASIS OF 13 OXYGENS							
Si	1.99	2.03	1.97	2.01	2.01	2.15	2.17
Ti	0.06	0.07	0.08	0.07	0.07	0.05	0.05
Al	5.88	5.82	5.89	5.84	5.85	5.74	5.68
Fe(ii)	0.02	0.02	0.03	0.02	0.02	0.04	0.03
Mg	0.02	0.03	0.03	0.02	0.02	0.01	0.01
Ca	0.00	0.01	0.00	0.00	0.00	0.00	0.00
Na	0.04	0.04	0.05	0.05	0.04	0.02	0.01
TOTAL	8.03	8.01	8.04	8.02	8.02	7.97	7.95

Table 9.2 Electron probe microanalyses of mullite from three aluminous xenoliths. KIFX1 is a zoned mullite buchite - plagioclase xenolith from Killunaig [NM 496258], PM2 is a buchite without a plagioclase rim from Port Mor [NM 435239], and KBAX1 is a cordierite (mullite) buchite from Kilfinichen Bay [NM 484280].

Electron-probe analyses of the glass between the mullite crystals are presented in *Table 9.3*, along with a bulk-rock analysis of a mullite buchite. Both glass and bulk-rock compositions are alumina-rich, suggesting possible derivation from a clay-rich sediment or metasediment. However, the variation in K contents between the whole-rock and the glasses is striking, with the glasses containing up to six times more K. This may be due to the dilution effect of the numerous mullite needles which would have been analysed in the whole-rock sample. Simple mass-balance calculation suggests that at least 80% of the whole-rock must consist of K-free mullite crystals, which is very often the case.

One sample examined (PL1) contains residual plagioclase. The feldspar clot has a strongly corroded margin, and individual crystals have a strained appearance, with kinked twin planes (*Figure 9.7*). The plagioclase is of andesine composition.

(b) Cordierite (mullite) buchites

The cordierite-bearing buchites are much rarer than the mullite buchites described above. They are jet black, vitreous rocks, which again form irregularly shaped masses, up to a metre in the maximum dimension. Unlike the paler-coloured mullite buchites, the cordierite buchites are friable rocks and often highly fractured.

In thin-section, the cordierite buchites consist of dense mats of mullite needles, along with numerous tiny crystals of cordierite, and rarer anhedral of tridymite.

The cordierite generally has the form of minute (10-20 μ m), occasionally twinned, square shaped crystals, which occur either singly, or in clusters of many individuals (*Figure 9.8*). Representative analyses of cordierite are presented in *Table 9.4*. The cordierite is a Mg-rich variety (Mg# ~ 0.56), of similar composition to those found, for example, in contact metamorphosed phyllites (Smith, 1965; Kitchen, 1984), and from pelitic xenoliths in volcanic rocks (Pedersen, 1979; Grapes, 1986).

Mullite analyses from a cordierite buchite are presented in *Table 9.2*. These mullites are significantly enriched in Fe, and depleted in Ti, when compared to the mullites from a "normal" mullite buchite. The mullites from the cordierite buchite are also slightly enriched in Si and depleted in Al.

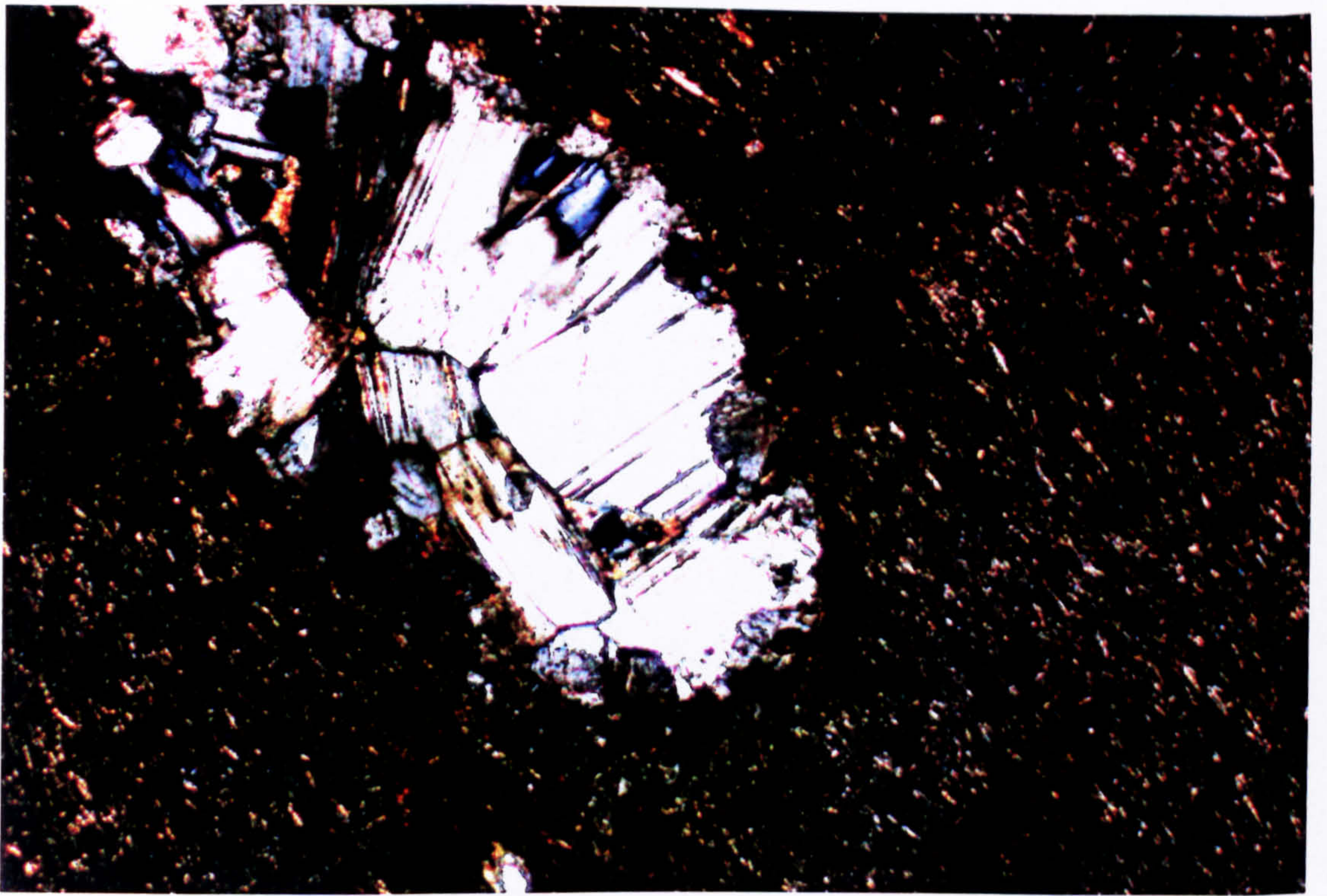


FIGURE 9.7 Residual plagioclase in a mullite buchite. Matrix consists of a dense mat of minute mullite needles, very little fresh glass is present. (xpl; Field of view 2x3mm; Sample PL1).

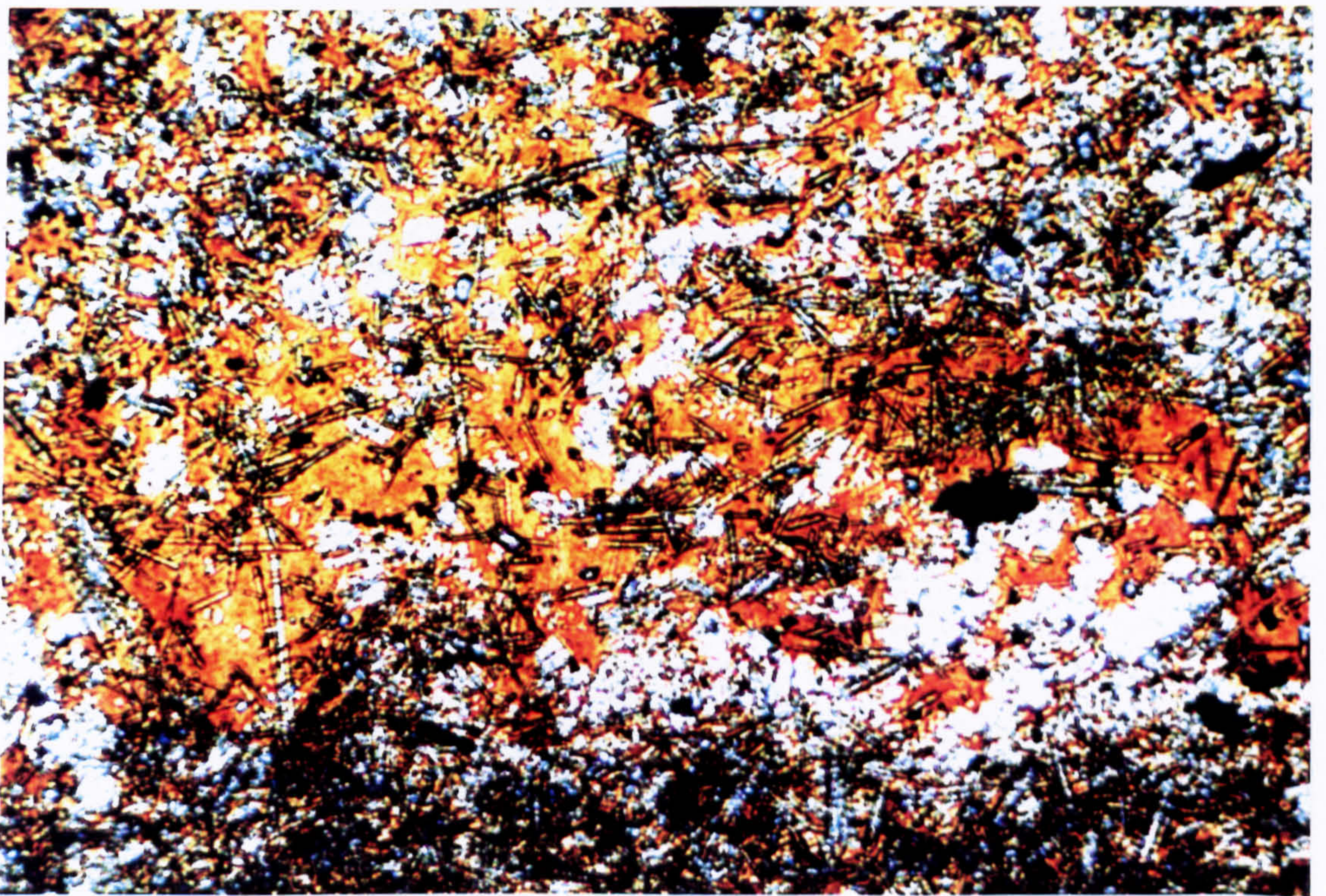


FIGURE 9.8 Tiny cubes of cordierite and needles of mullite set in a clear brown glass. (ppl; Field of view 0.8x1.2mm; Sample KBAX1).

The mullite and cordierite crystals are set in a dark glass, which often has a reddish tinge in thin-section. Analyses of the glass, and of a bulk-rock cordierite buchite, are given in *Table 9.5*. Again, both glasses and the whole-rock are rich in alumina, although not to the same extent as the mullite buchites. The whole-rock is enriched in MgO and FeO* relative to the 'normal' mullite buchite. The whole-rock and glasses from the cordierite buchite are also richer in SiO₂ and K₂O. Bailey *et al.* (1924) suggested that the cordierite buchites may have resulted from the mixing between an aluminous liquid (*i.e.* normal mullite buchite) and Fe-rich basaltic magma, and that this may have enabled the resulting liquids to precipitate cordierite, and Fe-rich mullite. However, with the benefit of whole-rock and glass analyses, this hypothesis seems difficult to substantiate on the terms of mass-balance. Cordierite has been found as a residual phase after partial melting of pelitic source-rocks, in both laboratory experiments (*e.g.* Green, 1976) and in natural examples (*e.g.* Gribble, 1968, 1970). It is suggested, therefore, that the cordierite buchites formed from aluminous liquids which were naturally enriched in FeO and MgO. Such liquids may have been generated from a more biotite-rich protolith. However, since they contain more SiO₂ and K₂O than the normal mullite buchites, the cordierite buchites most likely represent liquids produced at an *earlier* stage of partial fusion, when only relatively small amounts of granitic liquid had been removed from the protolith. There is a complete gradation between the mullite buchites and the cordierite-rich buchites. Occasionally the two lithologies coexist within the same xenolith, with the cordierite buchite occurring towards the edge of the xenolith.

Sample:	PMAX2	----- Glasses in KIFX2 -----			
SiO₂	54.68	49.85	50.08	56.30	56.69
TiO₂	2.73	1.81	1.98	3.33	2.80
Al₂O₃	30.75	29.03	29.17	21.49	23.08
FeO	1.11	1.56	1.67	1.11	2.03
MnO	0.01	0.08	0.01	0.04	0.01
MgO	0.50	1.88	1.87	0.57	1.52
CaO	0.49	0.74	0.76	2.35	2.16
Na₂O	2.21	0.32	0.32	1.79	3.66
K₂O	1.61	8.89	8.72	8.90	5.38
P₂O₅	0.04	-	-	-	-
TOTAL	94.13	94.15	94.56	95.88	97.32
Nb	52.2	-	-	-	-
Zr	829.6	-	-	-	-
Sr	275.2	-	-	-	-
Rb	66.5	-	-	-	-
Ba	391.1	-	-	-	-
Cr	206.6	-	-	-	-
V	224.9	-	-	-	-

Table 9.3 Major-element and partial trace-element analysis of a mullite buchite (PMAX2). Major-elements in wt%, trace-elements in ppm determined by XRF. All iron determined as Fe₂O₃. Glasses from KIFX2 analyses by electron probe. All iron determined as FeO. Sample PMAX2 from Port Mor [NM 435239], and KIFX2 from Killunaig [NM 496258].

Sample : Cordierites from cordierite/mullite buchite KBAX1				
SiO ₂	47.48	47.27	47.25	47.46
TiO ₂	0.08	0.13	0.08	0.02
Al ₂ O ₃	32.76	33.13	33.17	32.74
FeO	9.88	10.25	9.93	9.46
MnO	0.01	0.00	0.05	0.00
MgO	7.13	7.23	7.18	7.48
CaO	0.02	0.05	0.05	0.05
Na ₂ O	0.13	0.15	0.14	0.10
K ₂ O	0.23	0.20	0.26	0.28
TOTAL	97.72	98.42	98.09	97.59
FORMULA ON THE BASIS OF 18 OXYGENS				
Si	4.96	4.92	4.93	4.96
Ti	0.01	0.01	0.01	0.00
Al	4.04	4.06	4.08	4.03
Fe(ii)	0.86	0.89	0.87	0.83
Mn	0.00	0.00	0.00	0.00
Mg	1.11	1.12	1.12	1.16
Ca	0.00	0.01	0.01	0.01
Na	0.03	0.03	0.03	0.02
K	0.03	0.03	0.04	0.04
TOTAL	11.04	11.07	11.06	11.05

Table 9.4 Representative electron probe microanalyses of cordierite from cordierite/mullite buchite xenolith KBAX1, from Kilfinichen Bay [NM 484280]. All iron determined as FeO. Low totals in wt% columns are due to the presence of water within the cordierite structure.

Sample	KBAX1	----- Glasses in KBAX1 -----			
SiO ₂	56.88	65.08	64.70	65.10	64.85
TiO ₂	1.42	1.93	2.01	2.00	2.05
Al ₂ O ₃	23.84	15.52	15.50	15.19	15.30
FeO	4.70	4.24	4.37	3.82	4.15
MnO	0.02	0.02	0.00	0.00	0.02
MgO	1.56	0.30	0.31	0.20	0.26
CaO	0.98	0.78	0.82	0.89	0.78
Na ₂ O	3.14	4.30	4.30	4.56	4.40
K ₂ O	1.31	1.91	1.85	1.79	1.65
P ₂ O ₅	0.05	-	-	-	-
TOTAL	93.90	94.08	93.86	93.54	93.46
Nb	26.6	-	-	-	-
Zr	646.2	-	-	-	-
Sr	200.4	-	-	-	-
Rb	103.8	-	-	-	-
Ba	855.2	-	-	-	-
Cr	99.9	-	-	-	-
V	133.8	-	-	-	-

Table 9.5 Major-element and partial trace-element analysis of a cordierite buchite (KBAX1), from Kilfinichen Bay [NM 484280]. Major-elements in wt%, trace-elements in ppm determined by XRF. All iron determined as Fe₂O₃. Glasses from KBAX1 analyses by electron probe. All iron determined as FeO.

(c) Plagioclase-corundum-spinel assemblages

The plagioclase-corundum-spinel bearing rocks occur in close association with the mullite buchites. Although single xenoliths composed entirely of this assemblage can be found, it is more common to find these minerals forming a rim around a core of mullite buchite. No xenoliths with *partial* rims have been found. Individual xenoliths range up to 1 metre across (*Figure 9.9*).

In hand-specimen the plagioclase rims often have a very striking appearance. The plagioclase crystals have idiomorphic shapes, particularly where in contact with the buchitic core, and are invariably a strong lilac colour (*Figure 9.10*). Towards the margin with the host basalt, the plagioclase has a uniform vitreous black or dark-green colour. At the contact with the buchite, the plagioclase is often studded with numerous small crystals of corundum. This has a distinct dark-blue colour (sapphire). Corundum crystals are generally only about 1mm across, although they occasionally reach 3-4mm. Spinel is also present as black, rounded crystals, concentrated mainly towards the contact with the host basalt.

In thin-section the plagioclase rims show many textural features which indicate their mode of formation. The following discussion describes the mineral phases found as inclusions within the plagioclase first (*e.g.* corundum, spinel, mullite), since many of the textural features found in the plagioclase relate to these. *Figure 9.11* shows a *schematic* scale-diagram of a section through a zoned mullite buchite-plagioclase xenolith. All the textural features described in the text are labelled on the diagram, and the labelled numbers refer to the figure numbers of photomicrographs displaying that particular texture.

Corundum

Corundum occasionally occurs within the mullite buchite core of the zoned xenoliths, but is more commonly found within the plagioclase rim, immediately adjacent to the buchite (see *Figure 9.11*). However, wherever it occurs, it is always surrounded by *mullite-free* glass, or *mullite-free* plagioclase. It frequently appears to have crystallized close to basaltic melt-pockets. In thin-section, the corundum often shows euhedral crystals, with six-sided prisms being the most common (*Figure 9.12*). Crystals are also a bladed habit. However, the corundum is also commonly highly skeletal, particularly when included in

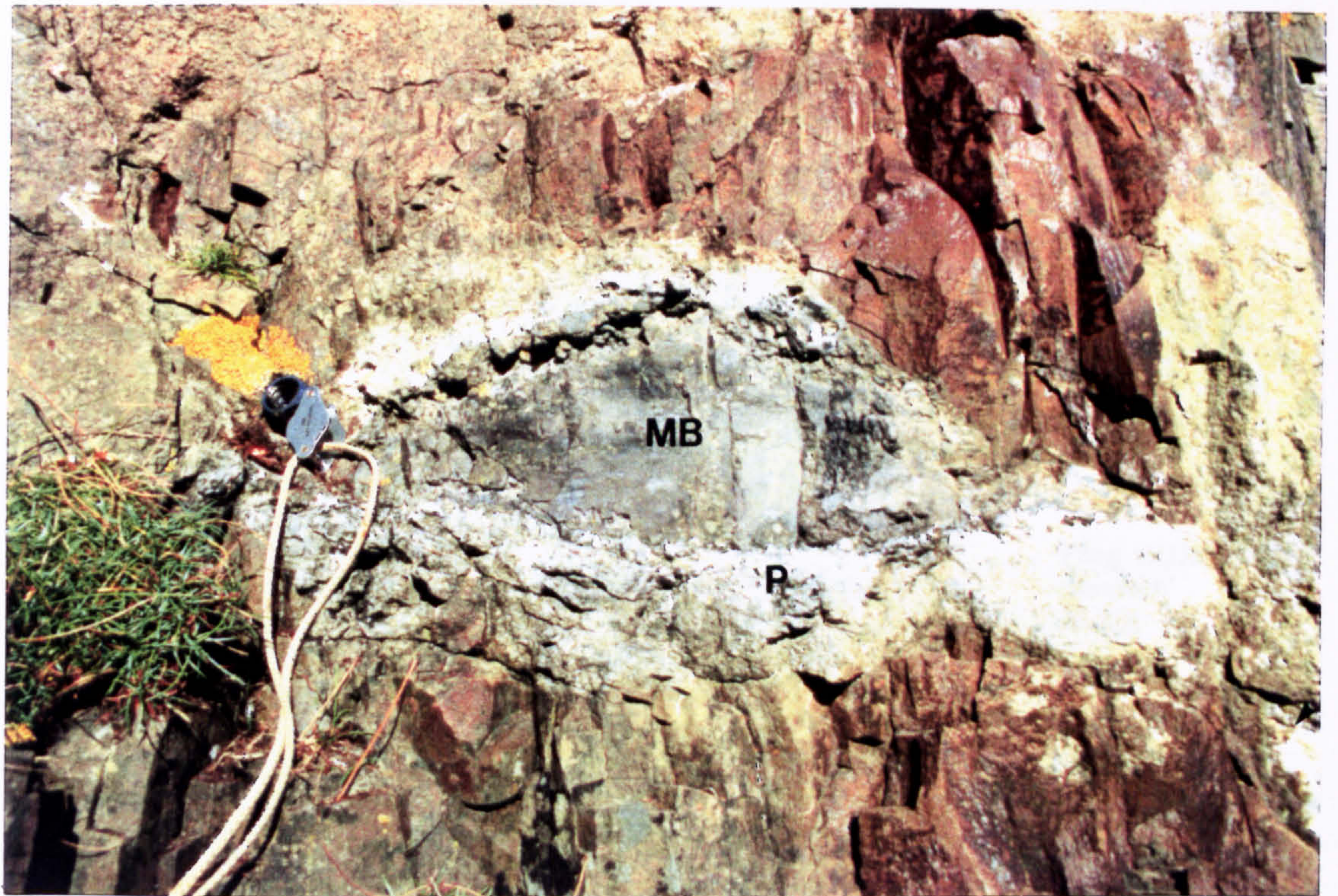


FIGURE 9.9

Mullite buchite xenolith (MB) with plagioclase reaction rim (P), in basaltic sheet at Kilfinichen Bay [NM 484280]. Hand lens approx. 5cm long.

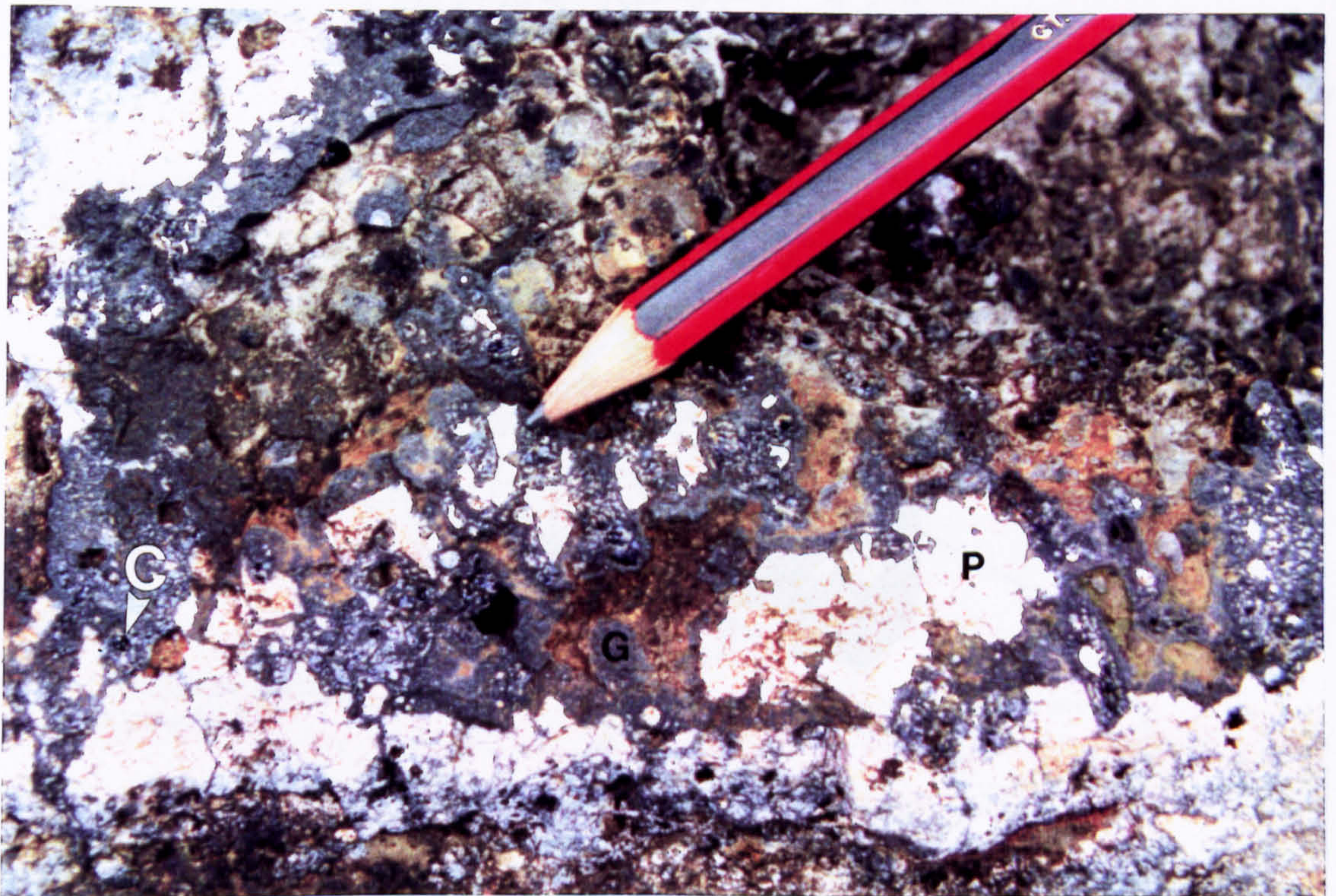


FIGURE 9.10

Close-up of the plagioclase reaction rim around a mullite buchite xenolith. Shows idiomorphic plagioclase laths (P) surrounded by glass (G) at the centre of the xenolith. Small studs of corundum (C) are just visible. Basaltic sheet at Kilfinichen Bay [NM 484280].

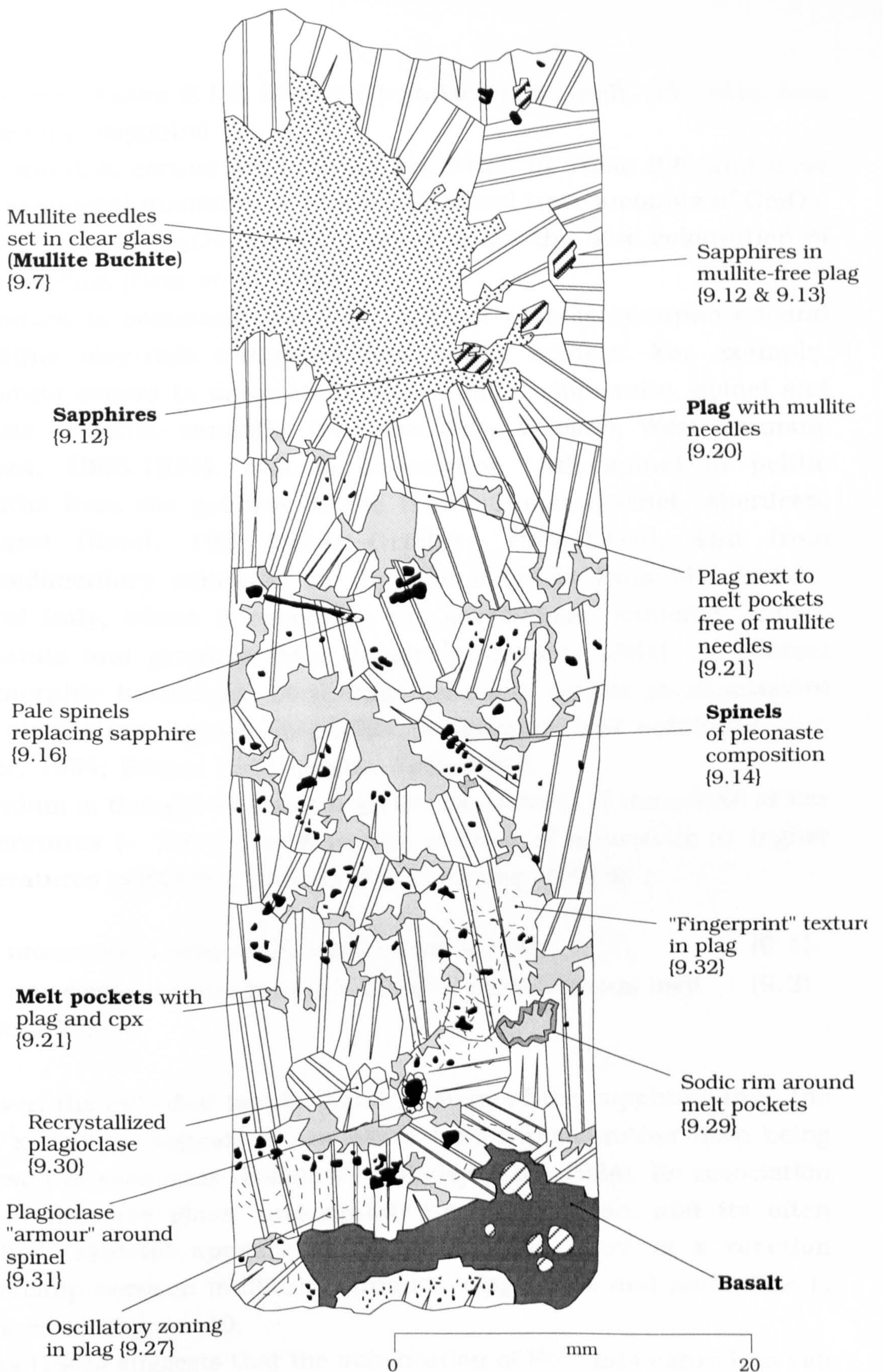


FIGURE 9.11

Diagrammatic section through a zoned mullite buchite - plagioclase aluminous xenolith (sample PMFX1 from Port Mor [NM 433239]), showing the major textural features described in the text. Figures in brackets refer to figure numbers depicting that particular texture.

plagioclase (*Figure 9.13*). In plane-polarised-light (ppl), the corundum is pale blue (sapphire).

Representative corundum analyses are listed in *Table 9.6*, and most show significant quantities of Fe_2O_3^* , TiO_2 and trace amounts of Cr_2O_3 . The presence of Fe_2O_3 and TiO_2 accounts for the blue colouration of the corundum (Deer *et al.*, 1992).

Corundum is commonly found in contact pyrometamorphosed and xenolithic clay-rich sediments and pelitic schists. For example, corundum occurs in association with mullite, sillimanite, spinel and ilmenite in pelitic xenoliths from the Wehr Volcano, West Germany (Grapes, 1986,1991), and in association with spinel in pelitic xenoliths from the gabbros of the Haddo House district, Aberdeen, Scotland (Read, 1931,1935; Gribble, 1968,1970), and from metasedimentary xenoliths in rhyolitic magmas from Mt. Amiata, Central Italy, where it occurs in the assemblage: sanidine, spinel, sillimanite and graphite (van Bergen & Barton, 1984). In contact metamorphic hornfelses, corundum generally occurs in association with plagioclase, spinel, magnetite, sillimanite and cordierite (*e.g.* Barker, 1964; Evans, 1964; Smith, 1965,1969).

Corundum is thought to result from the breakdown of muscovite at low temperatures ($\sim 700^\circ\text{C}$), or from the melting of muscovite at higher temperatures ($>1000^\circ\text{C}$), according to reactions such as :



(Grapes, 1986)

However, the euhedral tabular habit of many of the sapphires from the LSSC xenoliths suggests it has grown from a melt, rather than being the result of solid state reactions (*cf.* Bailey *et al.*, 1924). Its association with mullite-free glass, and mullite-free plagioclase, and its often resorbed, skeletal appearance, suggests that there is a reaction relationship between mullite, corundum, plagioclase and melt. This is discussed in Chapter 10.

Grapes (1986) suggests that the substitution of Fe^{3+} into corundum can be correlated with conditions of high oxidation state and high temperature, with low Fe-Ti corundums developing in reducing conditions and at high temperatures. Under such conditions, Smith (1965) found that ilmenite or rutile was very often exsolved from

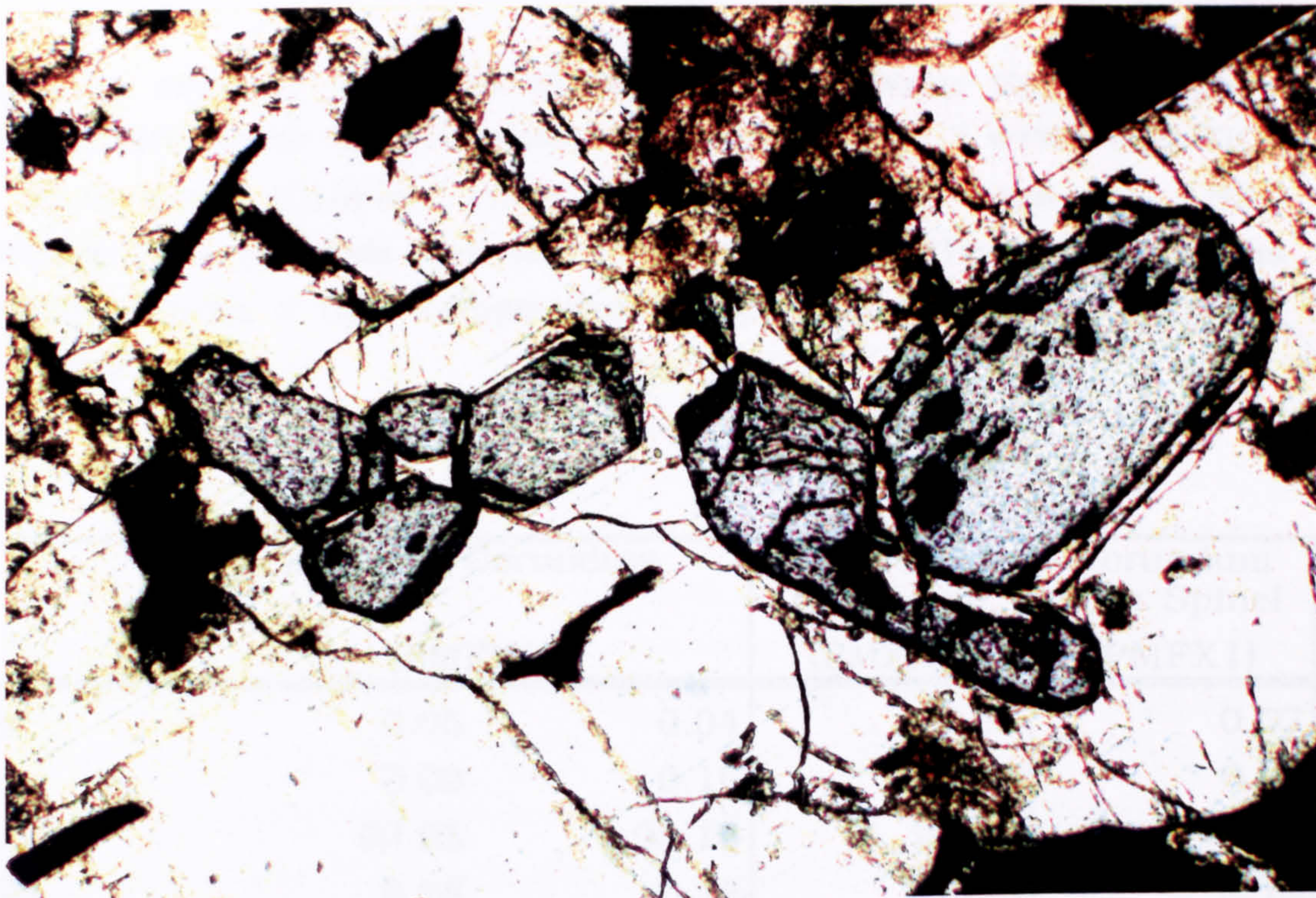


FIGURE 9.12

Euhedral corundum crystals surrounded by mullite-free plagioclase. From near the glassy core of a plagioclase-rimmed mullite buchite. Plagioclase is, in places altered to sericite. (ppl; Field of view 2x3mm; Sample PMFX1).



FIGURE 9.13

Skeletal corundum crystals surrounded by, and intergrown with, mullite-free plagioclase. Dark areas are melt pockets containing quench plagioclase and pyroxene. From near the glassy core of a plagioclase-rimmed mullite buchite (ppl; Field of view 2x3mm; Sample PMFX1).

corundum crystals. The corundums from the Wehr Volcano pelitic xenoliths are much more enriched in Fe₂O₃ (up to 7 wt%), and TiO₂ (up to 2 wt%) (Grapes, 1986,1991) than those from the LSSC xenoliths. This suggests that the corundums from the Mull xenoliths crystallized from a high temperature melt, under relatively reducing conditions.

	Euhedral Corundum (PMFX1)		Skeletal Corundum (PMFX1)	Corundum with Spinel (PMFX1)
SiO ₂	0.05	0.04	0.08	0.07
TiO ₂	0.09	0.16	0.29	0.18
Al ₂ O ₃	98.25	98.10	97.90	97.87
Cr ₂ O ₃	0.25	0.18	0.16	0.15
FeO	0.41	0.35	0.27	0.47
TOTAL	99.05	98.82	98.69	98.74
FORMULA ON THE BASIS OF 6 OXYGENS				
Si	0.00	0.00	0.00	0.00
Ti	0.00	0.00	0.01	0.01
Al	3.98	3.98	3.98	3.98
Cr	0.01	0.01	0.00	0.00
Fe	0.01	0.01	0.01	0.01
TOTAL	4.00	4.00	4.00	4.00

Table 9.6 Representative electron probe analyses of corundums from aluminous xenoliths. All corundums included in plagioclase.

Spinel

Crystals of spinel occur throughout the plagioclase rims, although their abundance is greater towards the contact with the host basaltic magma.

The spinel occurs as small euhedral octahedra (<0.5 mm), and larger rounded and irregularly shaped crystals generally no more than 2mm in length. Skeletal growth is common, with crystals often displaying hollow cores, infilled with plagioclase (*Figure 9.14a*). Some crystals have cracked surfaces, down which the spinel is being altered to a reddish-brown material. However, the extent of the alteration is not great, extending only a few μm each side of the crack (*Figure 9.14b*). The spinels vary greatly in colour, the most common colours being deep olive-green and dark brown. However, some spinels have a deep purple colour, and those nearest the basalt contact are very often opaque (*Figure 9.15a-b*). As with the corundum, spinel is always included in plagioclase which is free of mullite crystals, although a close association with basaltic melt-pockets is not always apparent, with many spinels being found in the middle of large plagioclase laths. Many spinels occur in close association with sapphire (*Figure 9.16a*), with the spinel appearing to replace the corundum. In these examples, the spinels have a very pale brown to yellow colour. This alteration from sapphire to spinel appears to be associated with the influx of basaltic magma into the xenolith, via cracks in the plagioclase-rim, since those parts of the sapphire crystals undergoing replacement lie adjacent to basaltic melt pockets (*Figure 9.16b*). In certain xenoliths, individual crystals of spinel are armoured by finely crystalline plagioclase (see *Figure 9.31*). The plagioclase is extremely fresh and unzoned. This texture suggests that a reaction relationship between spinel and basaltic melt exists, in which plagioclase is the product. Pedersen (1978, 1979) has described similar spinel-sapphire and spinel-plagioclase associations in reconstituted shale xenoliths from Disko Island, West Greenland.

The composition of the spinels is very limited, with all spinels analysed being an Mg-rich pleonaste. They are relatively Cr_2O_3 -poor (<0.4 wt%). Spinel compositions are shown in *Figure 9.17a* plotted within a modified (MgCr_2O_4 - FeCr_2O_4 free) multicomponent spinel prism (after Grapes, 1986). The limited compositional range of the spinels can be best seen in *Figures 9.17b* and *9.17c*, which plot the

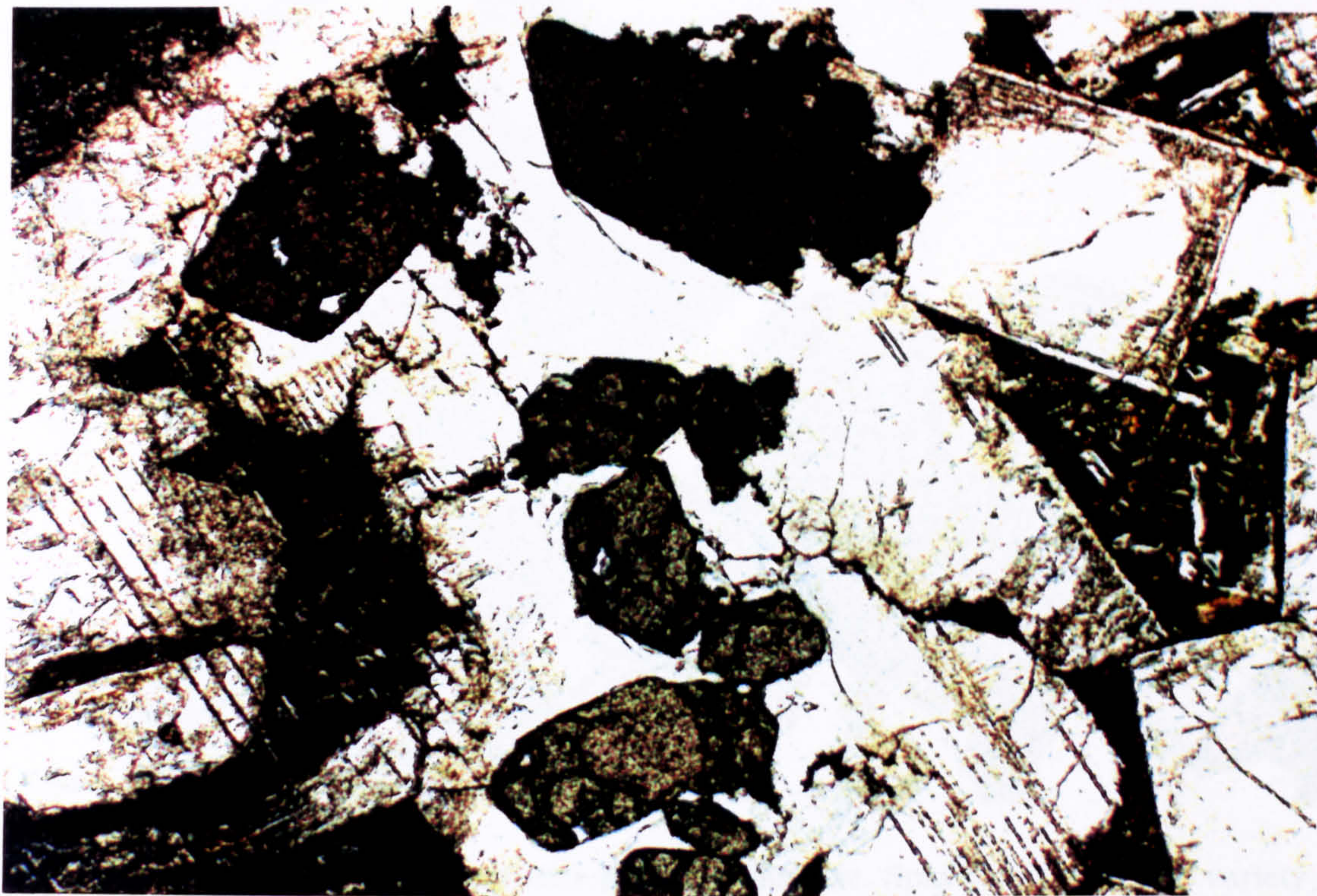


FIGURE 9.14a Euhedral spinel (pleonaste) crystals set in mullite-free, plagioclase. Plagioclase is some-what altered to sericite around the crystal margins. Plagioclase laths have isolated pockets of quenched plagioclase and clinopyroxene. (xpl; Field of view 2x3mm; Sample PMFX1).

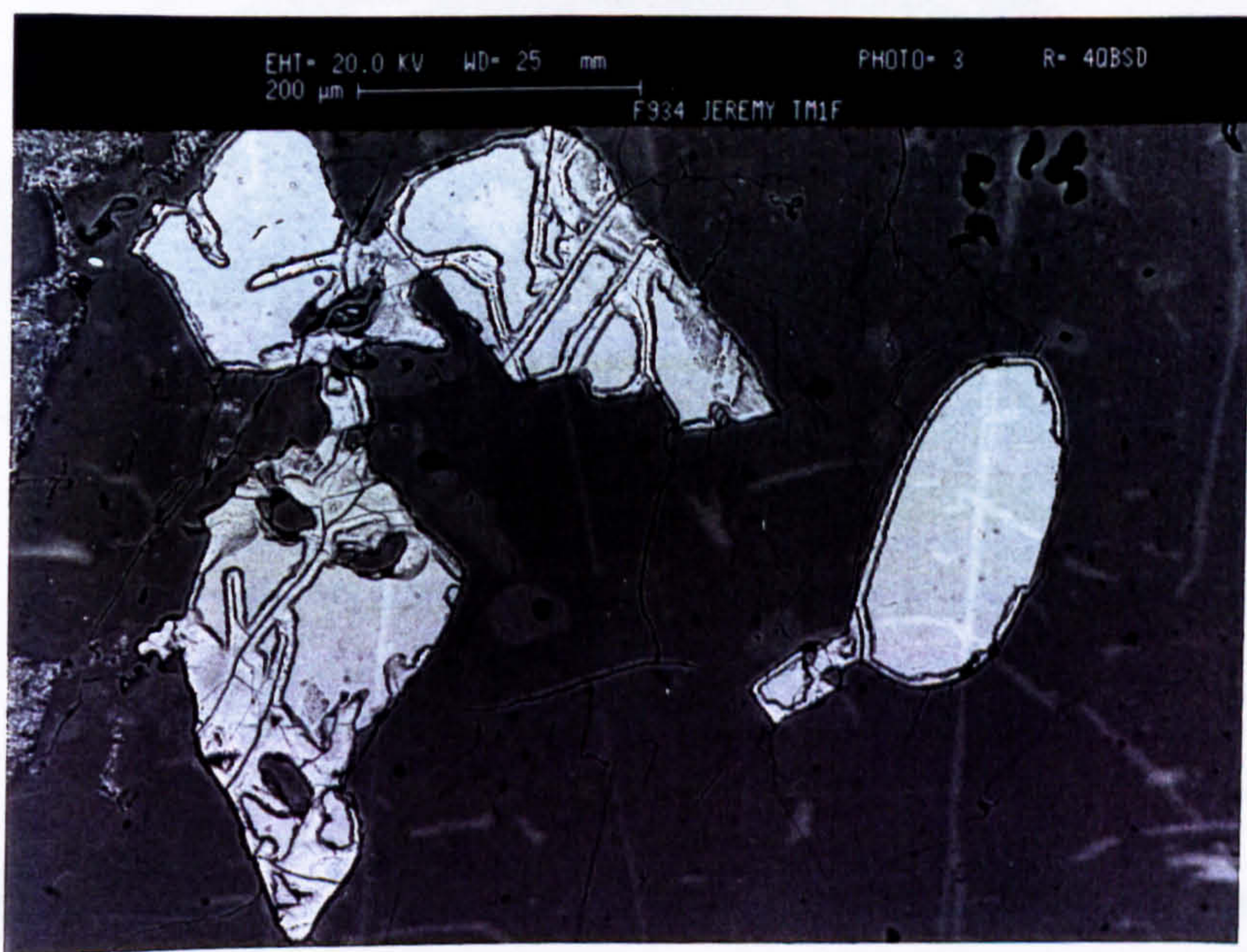


FIGURE 9.14b Back-scattered SEM image of resorbed and altered spinels set in plagioclase. Spinel is altering around the crystal margins and down cracks. (Sample TM1F).

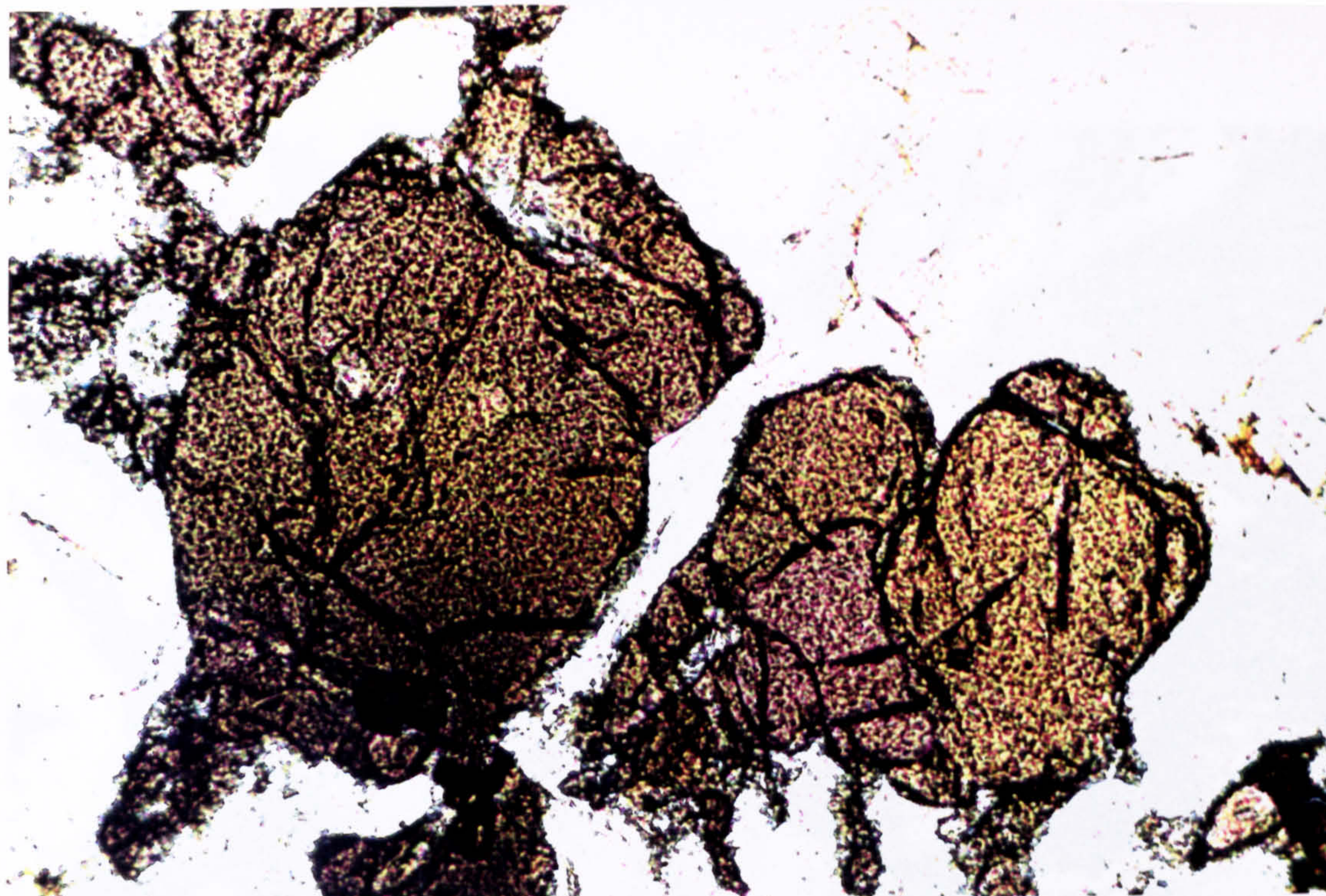


FIGURE 9.15a

Anhedral spinels set in plagioclase. Spinel shows a wide variety of colours within individual crystals and throughout individual specimens. Brown and purple spinels are most common towards the centre of the plagioclase rim. (ppl; Field of view 0.8x1.2mm; Sample PMFX1).

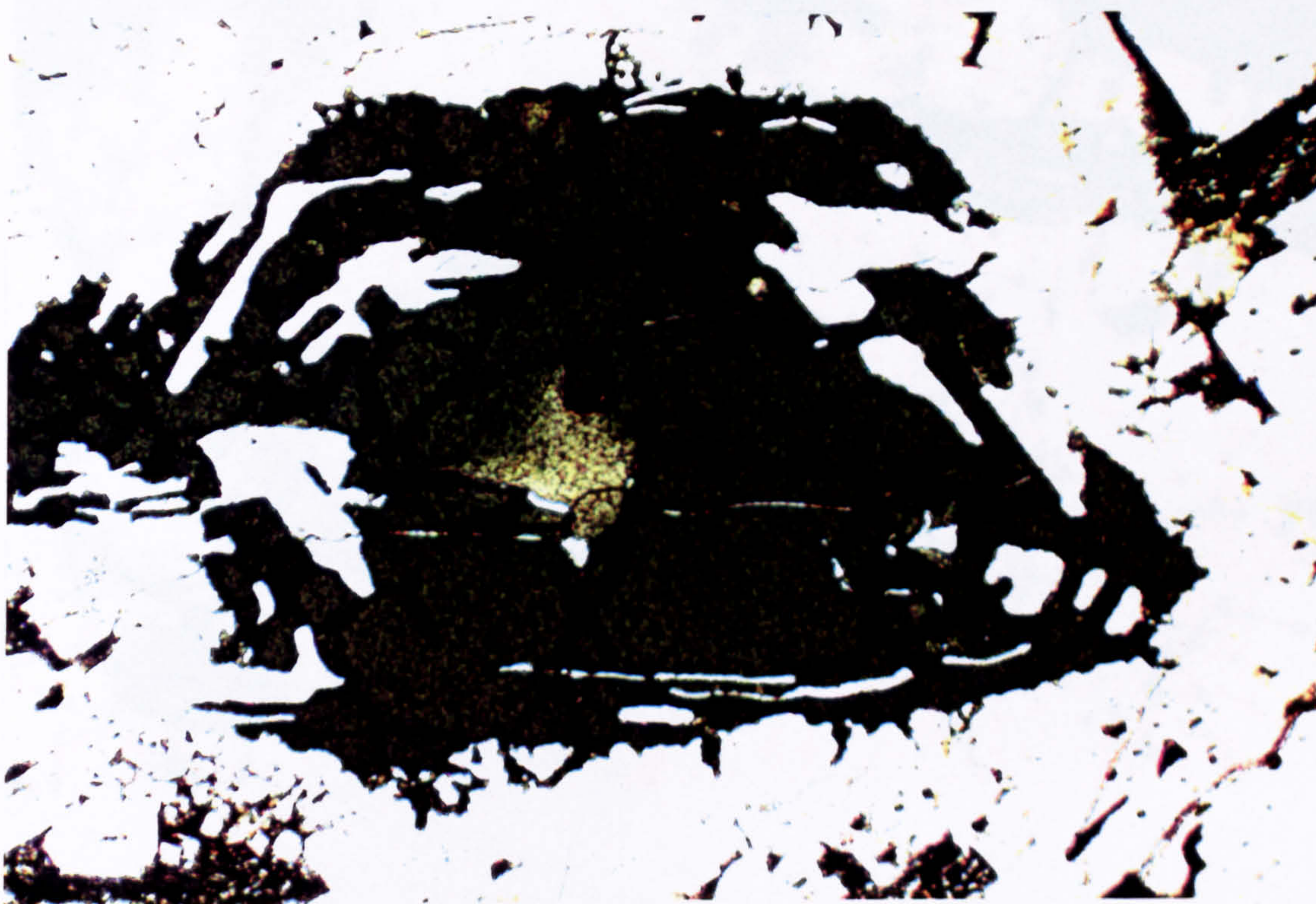


FIGURE 9.15b

Skeletal green spinel set in plagioclase. Colour of the spinels cannot be simply linked to spinel chemistry, although the darkest spinels generally contain the most iron, and the palest spinels the most aluminium. Spinel is enclosed by fine grained plagioclase which has a highly calcic composition (~An₈₆). Skeletal appearance of spinel and fine grained nature of surrounding plagioclase is thought to be due to a reactionary relationship between the spinel and the aluminous liquid. (ppl; Field of view 0.8x1.2mm; Sample TM1F)

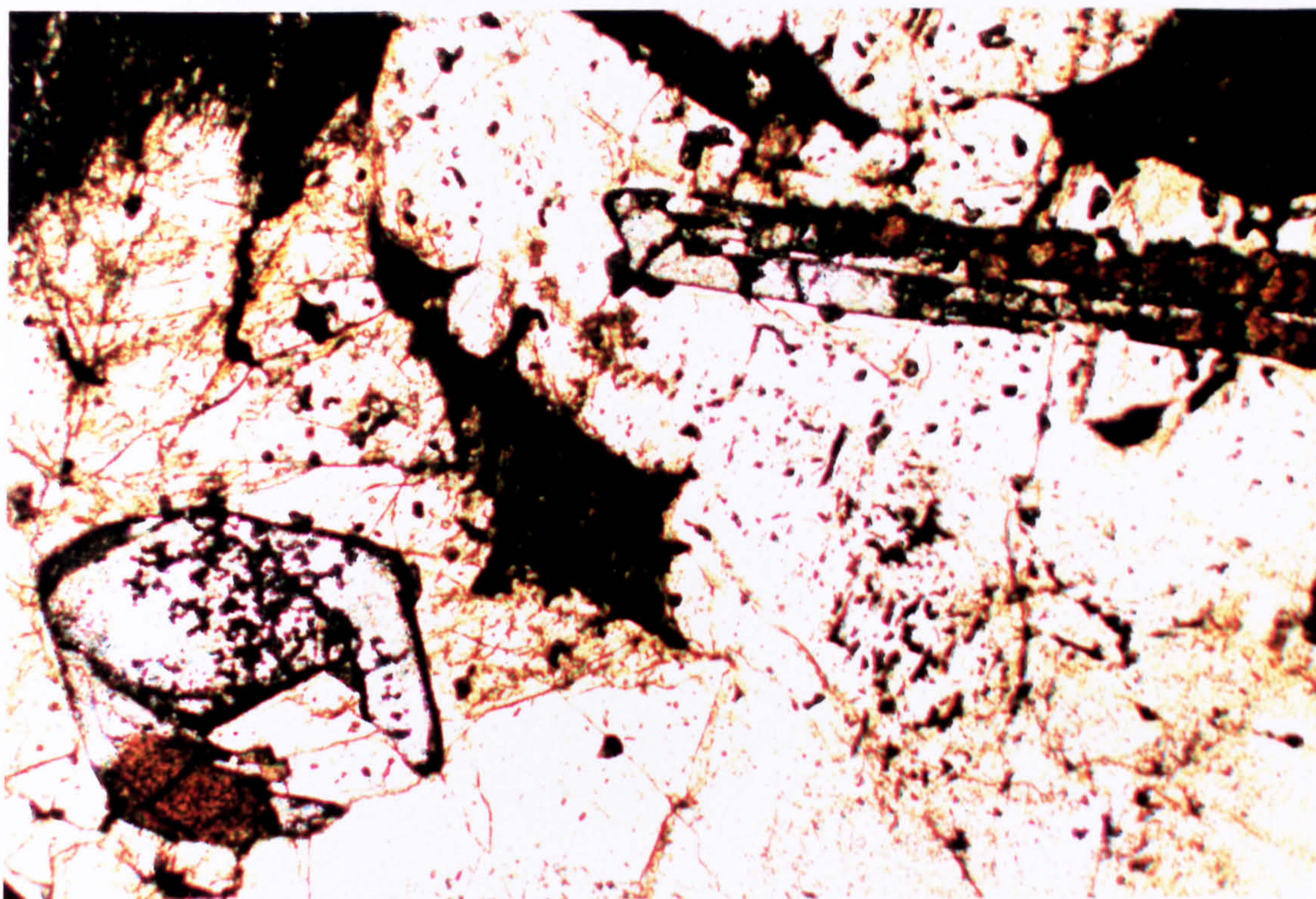
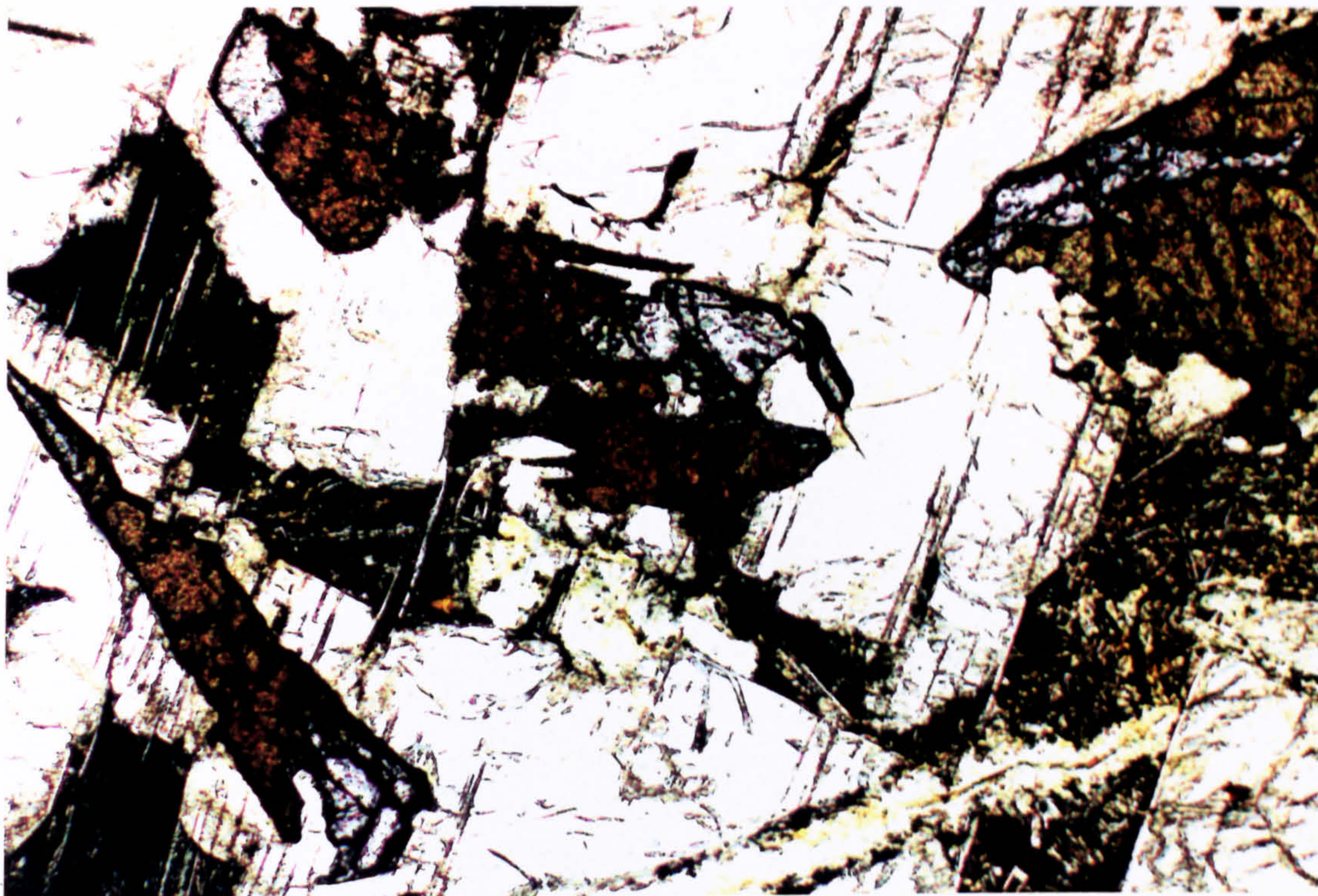


FIGURE 9.16a -b

Pale coloured spinels being formed via the alteration of corundum (pale blue colour). Corundums alter to spinels adjacent to basaltic melt pockets. (ppl; Field of view 2x3mm; Sample PMFX1).

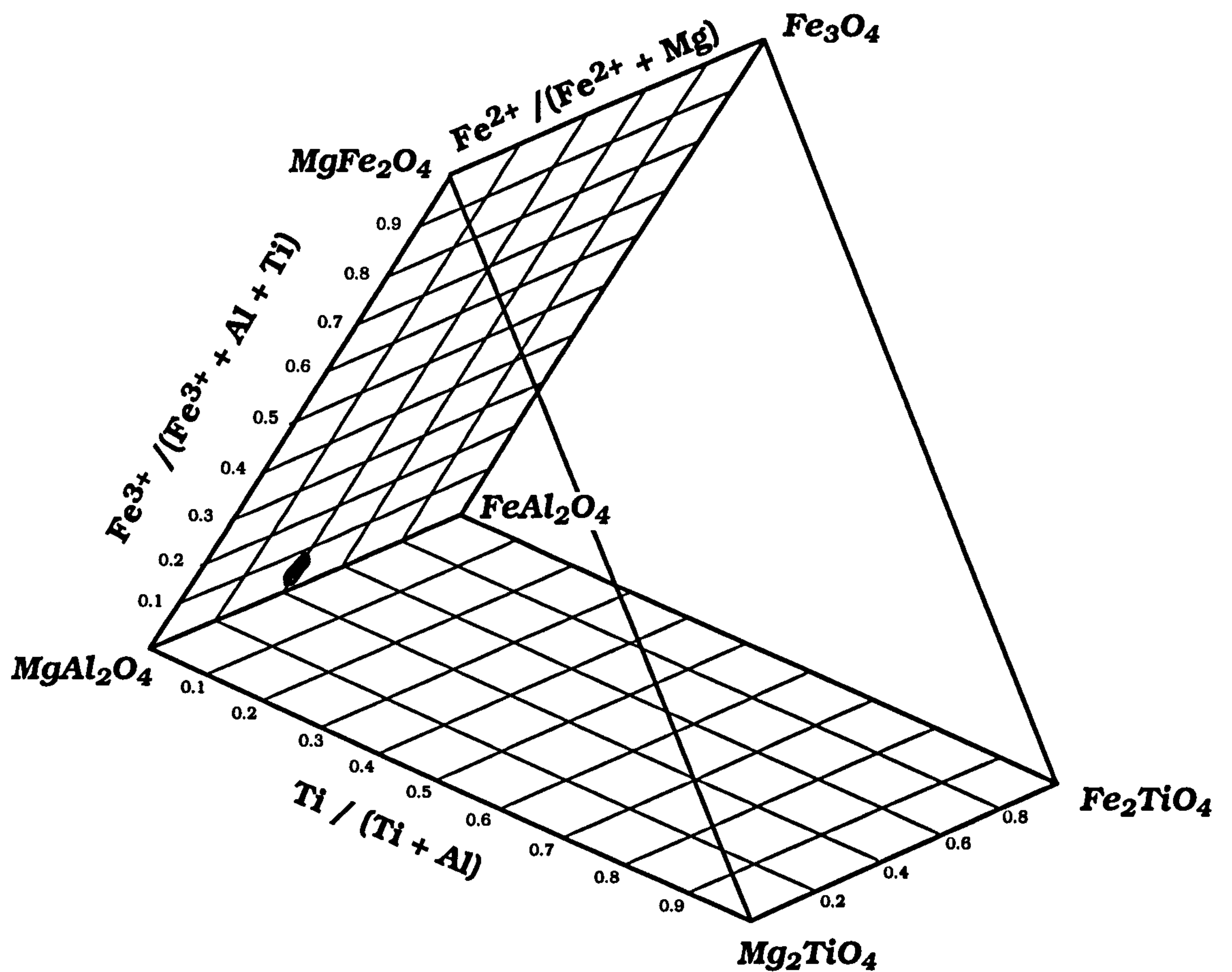


FIGURE 9.17a Composition of pleonaste-rich spinels in LSSC pelitic xenoliths plotted within a modified (MgCr_2O_4 - FeCr_2O_4 free) multicomponent spinel prism (after Grapes, 1986).

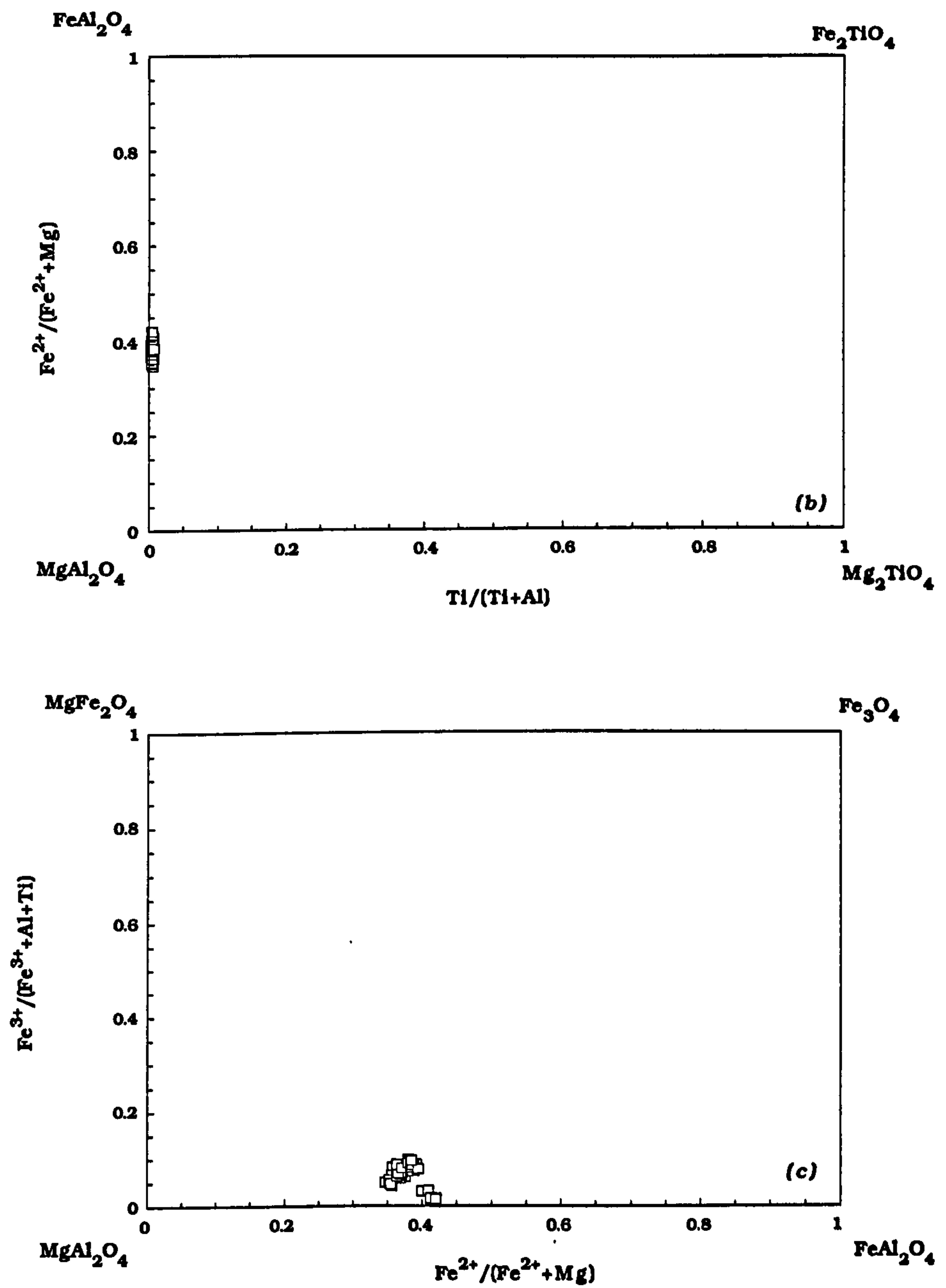


FIGURE 9.17 (b) Base of modified spinel prism, for pleonaste from aluminous xenolith PMFX1.

(c) "Ti-free" side of modified spinel prism.

After Grapes (1986)

base and 'Ti-free' side of the prism shown in *Figure 9.17a*. Individual spinel crystals are usually unzoned. However, where the spinel appears to be replacing corundum chemical zonation exists, with the spinel closest to the remnant corundum being enriched in Al_2O_3 and FeO. Representative electron-probe analyses of spinels are presented in *Table 9.7*.

Despite the restricted overall range of spinel compositions, there is a systematic variation in spinel compositions within any one xenolith, between those crystals nearest the contact with the host basalt, compared to those nearer the central buchitic core. *Figures 9.18a-d* record the variation of wt% Al_2O_3 , MgO, Fe_2O_3 and FeO in spinels with distance in mm to the basalt contact, from one particular xenolith (PMFX1, from Port Mor [NM 433239]). All the plots show well constrained trends, with the spinels nearer the buchite core being Al- and Mg-rich, and those at the basalt contact being significantly Fe-enriched. The greatest absolute variations are seen in Al_2O_3 , which ranges from 60 - 65 wt%, and Fe_2O_3 , which ranges from 1 - 7 wt%. MgO and FeO, however, only vary within 1.5 wt% between the basalt and buchite contacts. The spinels found at the very centre of the xenolith, adjacent to the glassy core are those associated with, and replacing the sapphire crystals (*Figure 9.16*) These spinels have the highest Al_2O_3 and FeO contents, whilst being relatively MgO and Fe_2O_3 poor. They also have the lowest Cr_2O_3 contents (<0.1 wt%). The chemical trend of these spinels is toward the MgO-rich compositions, as shown by one zoned crystal which has its highest MgO and Fe_2O_3 contents away from the remnant corundum, and its highest Al_2O_3 and FeO contents where it is directly adjacent to the corundum. Smith (1965) found very similar chemical gradients in the spinels from pyrometamorphosed phyllites adjacent to a dolerite plug at Sithean Slough, south west Scotland.

Extensive solid-solution exists between naturally occurring spinels (Deer *et al.*, 1992), with the most common ionic substitutions occurring in pleonaste-rich spinels being :



This type of substitution can be verified if the variation of these ion pairs is examined. *Figures 9.19a-b* show the variation of Al_2O_3 with

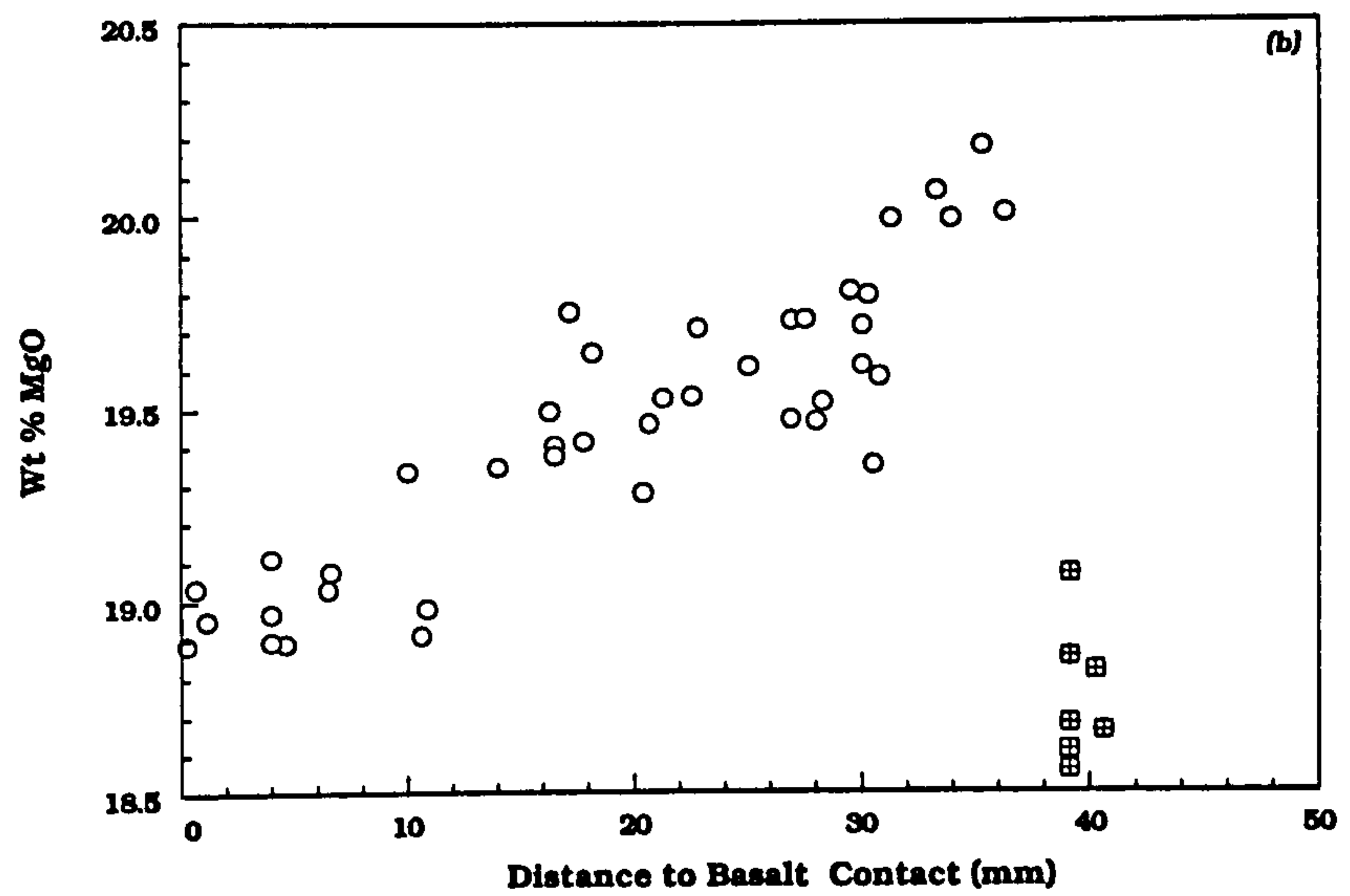
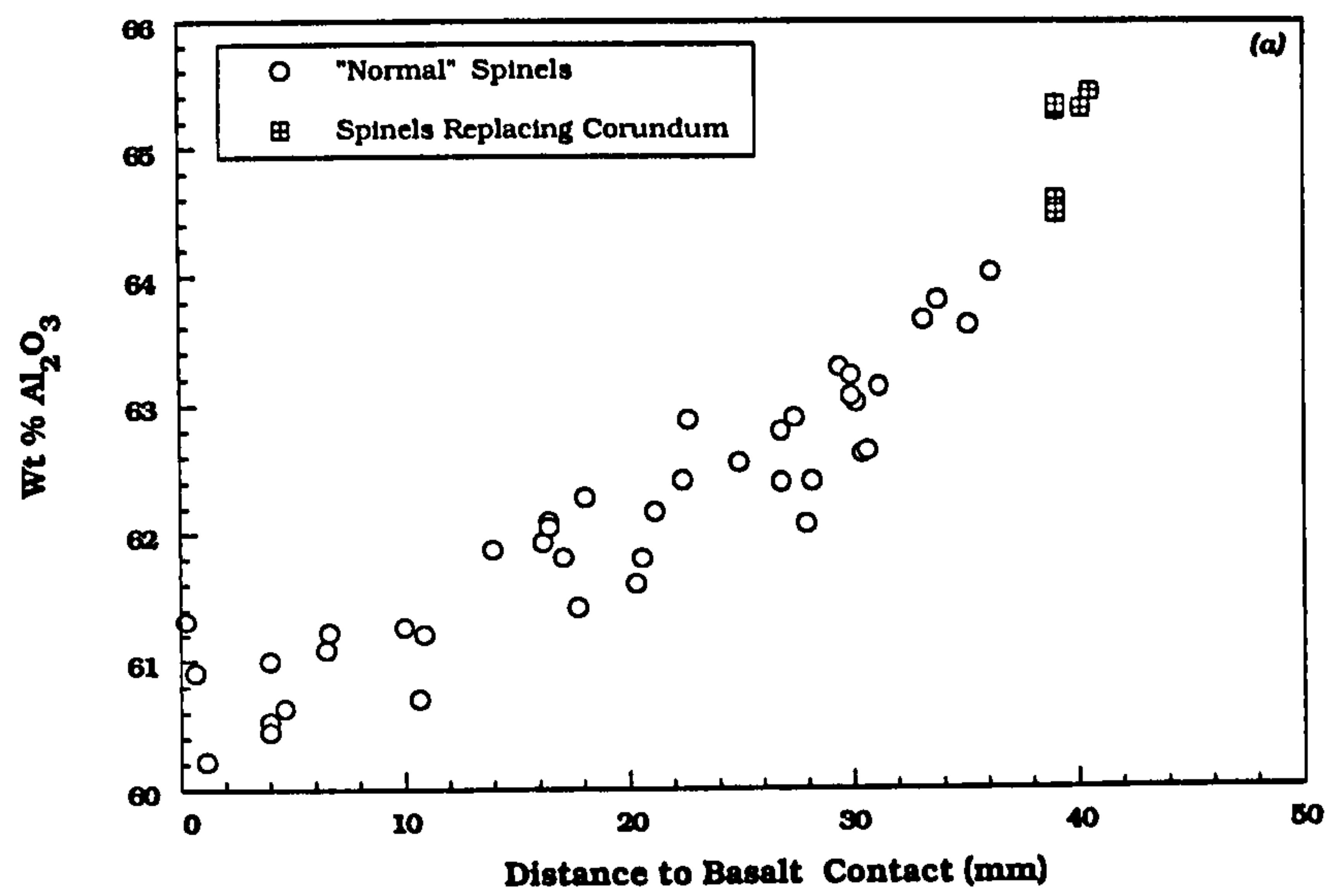


FIGURE 9.18 (a) Wt% Al_2O_3 vs. Distance to basalt contact for pleonastes from aluminous xenolith PMFX1.

(b) Wt% MgO vs. Distance to basalt contact.

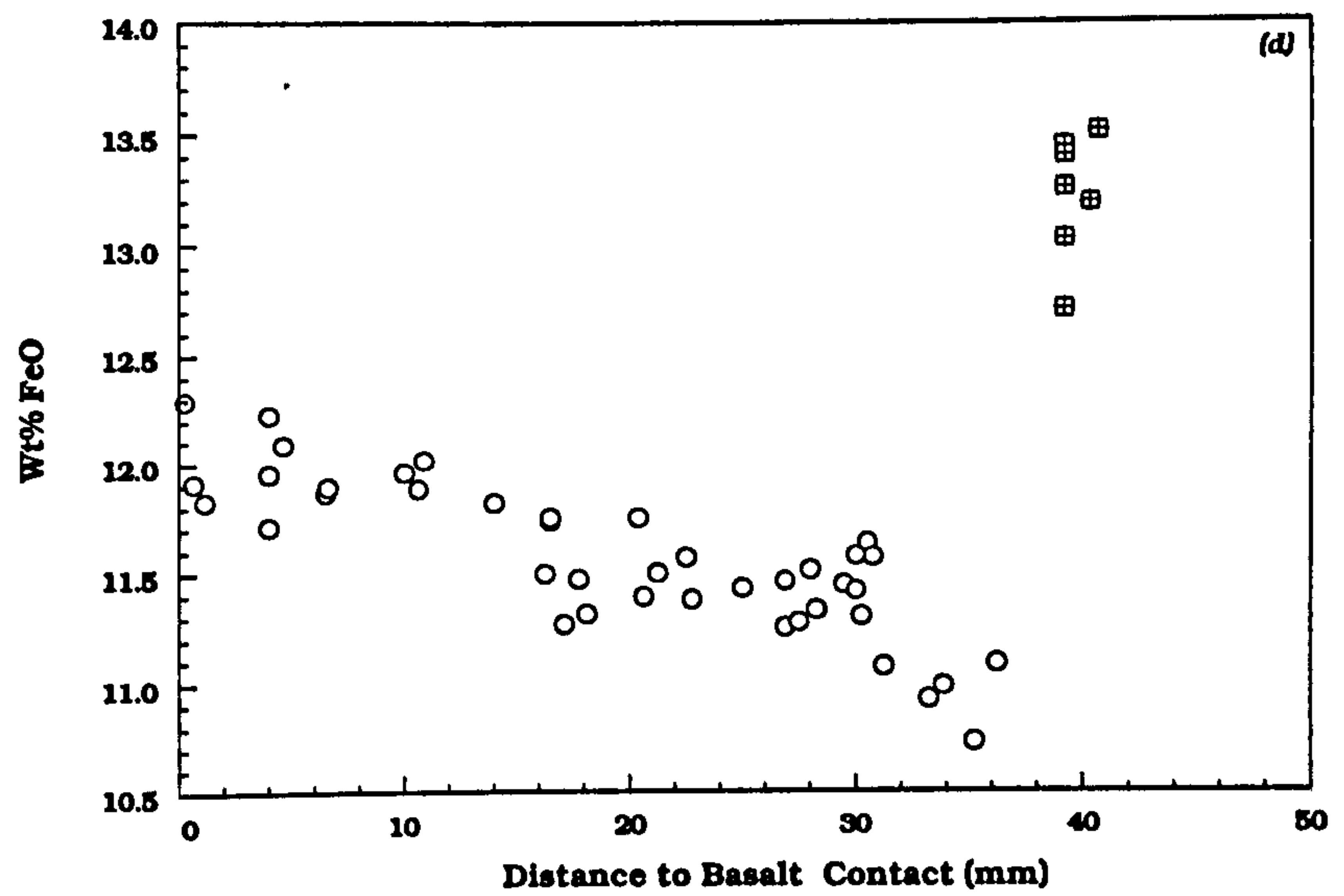
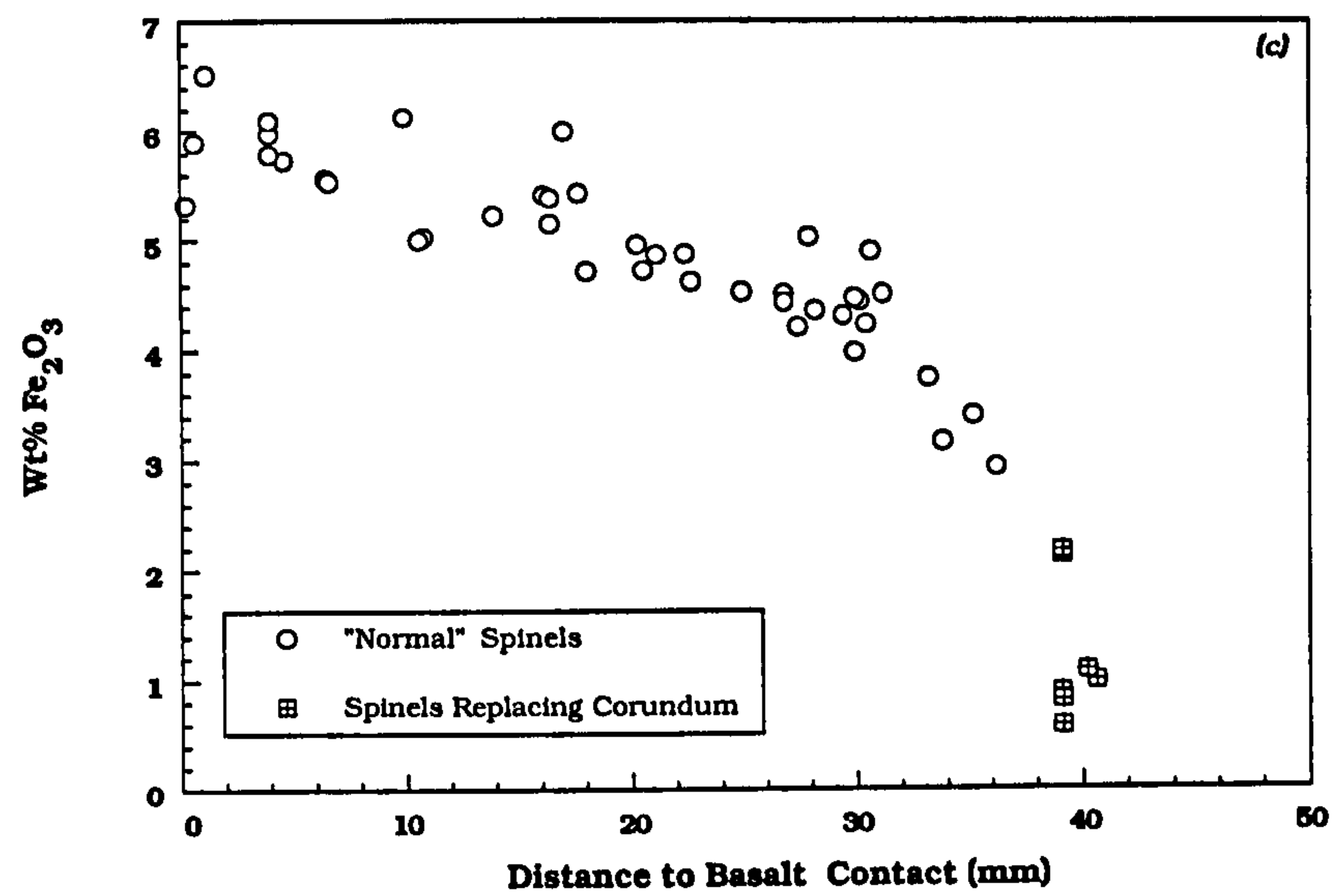


FIGURE 9.18 (c) Wt% Fe_2O_3 vs. Distance to basalt contact for pleonastes from aluminous xenolith PMFX1.

(d) Wt% FeO vs. Distance to basalt contact.

Fe₂O₃, and MgO with FeO, for spinels from xenolith PMFX1. The good correlations between these ion pairs suggests that these were indeed the substitutions which took place. The spatial controls on the compositional variation seen in spinels from xenoliths of this type suggest that they resulted from interaction between the basic magma and the Al-rich buchites.

Spinel compositions from aluminous xenolith PMFX1							
SiO ₂	0.09	0.09	0.06	0.06	0.06	0.06	0.05
TiO ₂	0.30	0.22	0.30	0.31	0.22	0.35	0.43
Al ₂ O ₃	60.44	62.64	63.28	65.29	61.00	61.32	61.33
Cr ₂ O ₃	0.81	0.16	0.12	0.11	0.50	0.40	0.36
Fe ₂ O ₃	6.58	4.89	4.30	0.90	5.96	5.32	5.83
MgO	19.24	19.59	19.81	18.61	18.97	18.89	19.25
FeO	11.78	11.58	11.45	13.45	12.23	12.29	11.84
NiO	0.05	0.09	0.00	0.02	0.00	0.03	0.08
TOTAL	99.29	99.24	99.31	98.74	98.94	98.66	99.17
FORMULA ON THE BASIS OF 32 OXYGENS							
Si	0.02	0.02	0.01	0.01	0.01	0.01	0.01
Ti	0.05	0.04	0.05	0.05	0.03	0.05	0.07
Al	14.76	15.15	15.25	15.77	14.93	15.02	14.94
Cr	0.13	0.03	0.02	0.02	0.08	0.07	0.06
Fe(III)	1.03	0.76	0.66	0.14	0.93	0.83	0.91
Mg	5.94	5.99	6.04	5.68	5.87	5.85	5.94
Fe(II)	2.04	1.99	1.96	2.31	2.12	2.14	2.05
Ni	0.01	0.01	0.00	0.00	0.00	0.01	0.01
TOTAL	23.98	23.98	23.98	23.98	23.98	23.97	23.98

Table 9.7 Representative spinel analyses from aluminous xenolith PMFX1, from Port Mor [NM 433239]. All spinels are included in plagioclase from rim of xenolith. All iron determined as FeO, then proportioned to Fe₂O₃ and FeO assuming stoichiometry.

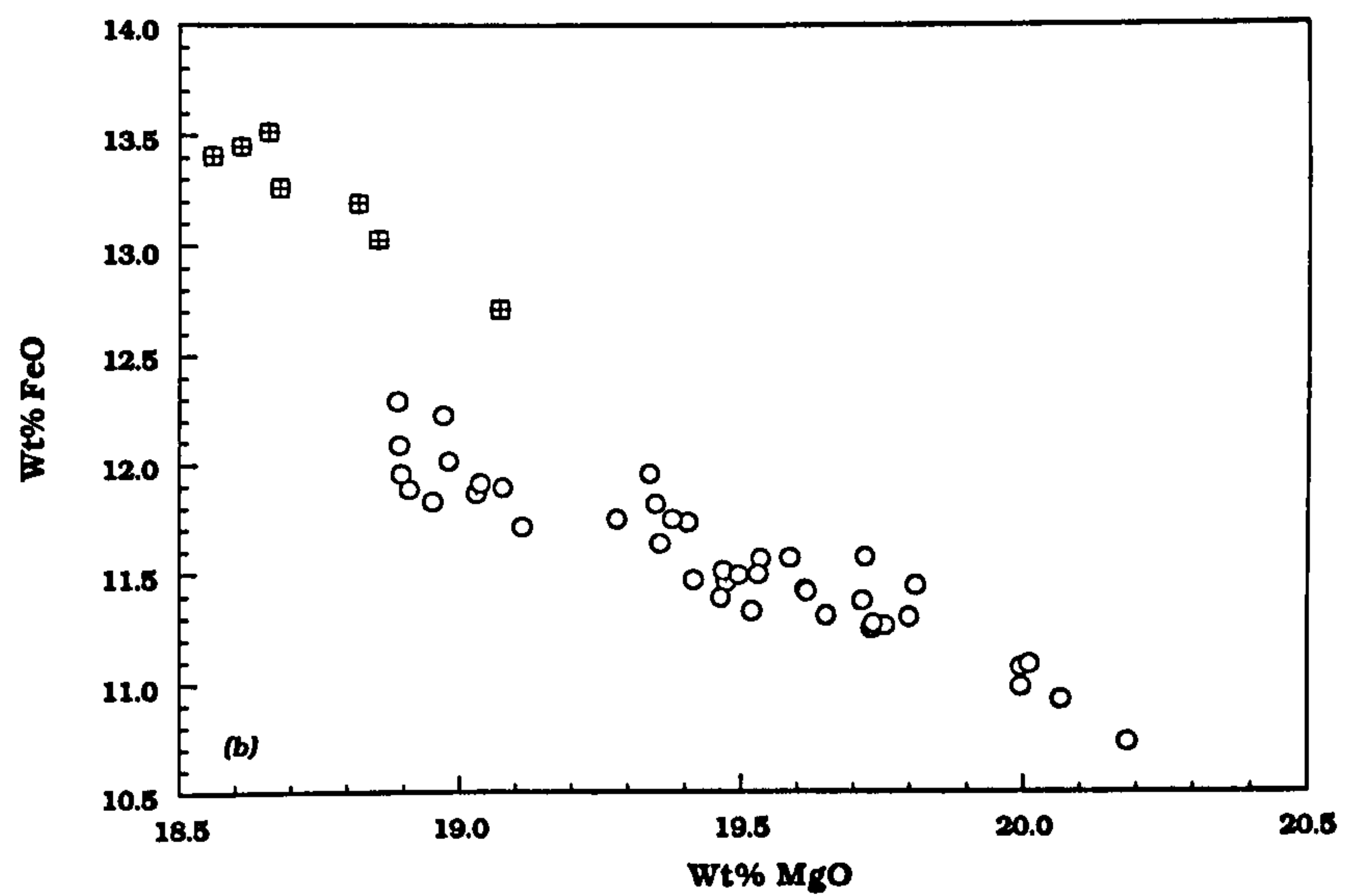
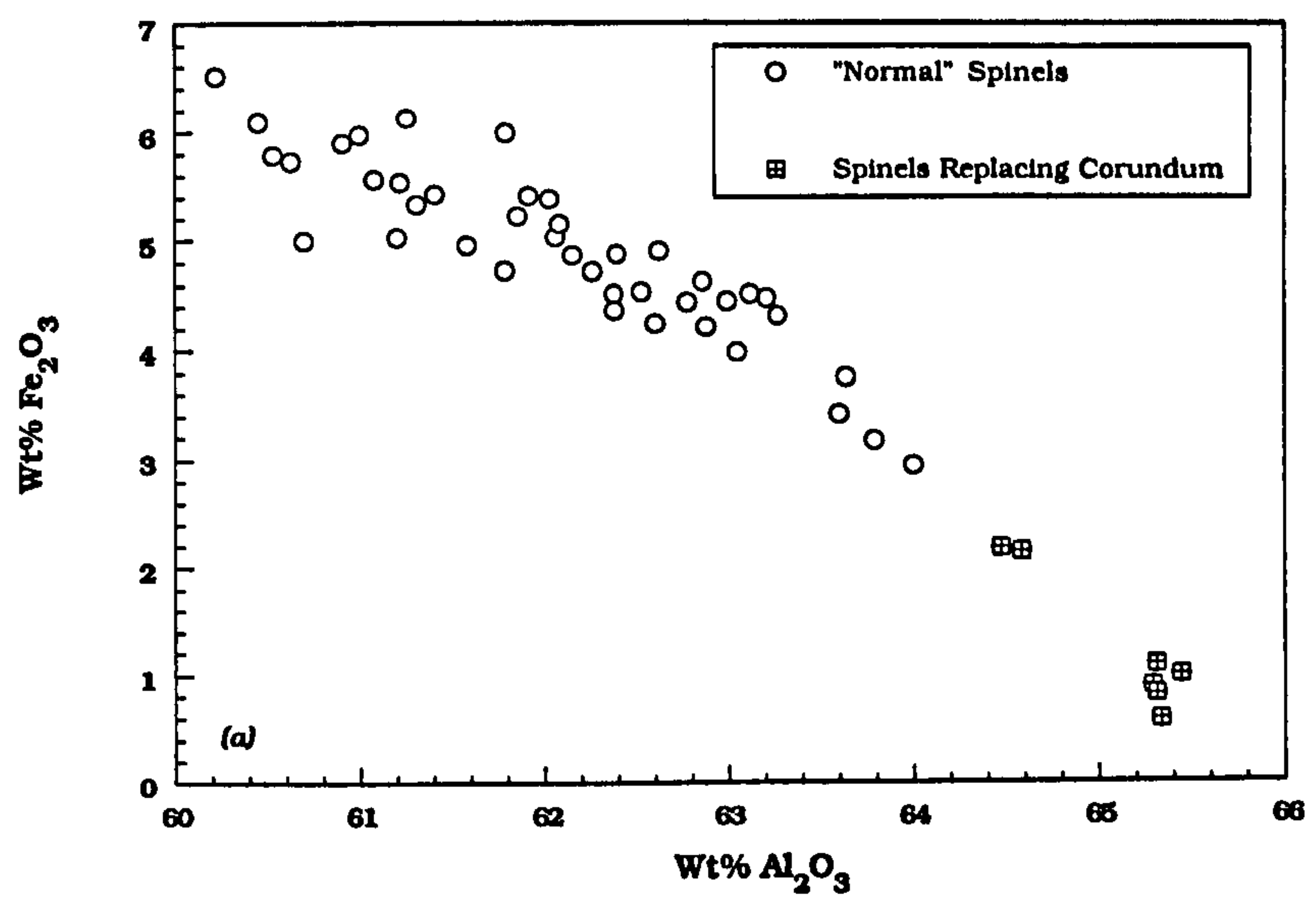
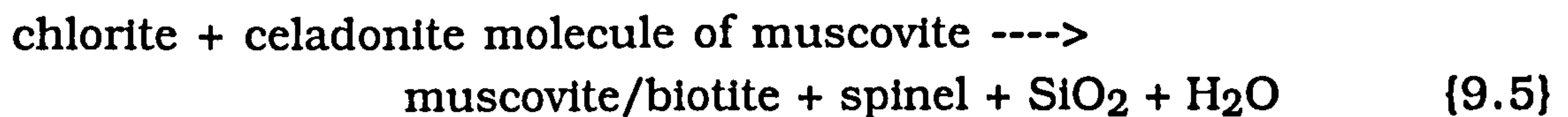
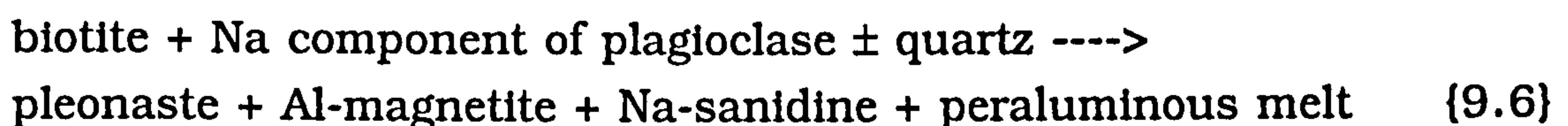


FIGURE 9.19 (a) Wt% Al_2O_3 vs. Wt% Fe_2O_3 for pleonastes from aluminous xenolith PMFX1.
(b) Wt% FeO vs. Wt% MgO .

Like corundum, spinel is a ubiquitous phase associated with contact metamorphism of pelitic rocks. During the first stages of metamorphism, spinels are formed through the reaction between chlorite and the celadonite portion of muscovite (Grapes, 1986):



At higher temperatures, spinels are produced through the breakdown or melting of biotite (Grapes, 1986) :



However, as with the corundums, due to their large size (up to 2mm) and euhedral shape, most of the spinels in the LSSC xenoliths are thought to have crystallized from a melt.

Melson & Switzer (1966) have shown that the Fe contents of spinels found in reconstituted shale xenoliths from basaltic volcanics of Disko Island, West Greenland, were controlled by the oxygen fugacity ($f\text{O}_2$) of the enclosing magma. The basalts in contact with the xenoliths from Disko were highly reducing due to the presence of large amounts of graphite. This led to low $f\text{O}_2$ (~ -13.5 to -15.5 $-\log_{10}\text{atm}$), and low Fe contents in the spinels (Pedersen, 1981). The system in these xenoliths was reducing enough to commonly produce native iron nodules (Melson & Switzer, 1966; Pedersen, 1978, 1979). Pedersen (1978, 1979) has also shown that although the majority of the spinels are stoichiometric, some from the centres of xenoliths are cation-deficient, and have a non-stoichiometric character. Many of the spinels have also suffered partial reaction with the host magma (Pedersen, 1978, 1979). The spinels from the LSSC aluminous xenoliths are typically not as enriched in Al_2O_3 and MgO when compared to some of the spinels from the Disko xenoliths; the latter commonly contain up to 76.0 wt% Al_2O_3 , 21.8 wt% MgO and only 1.6 wt% FeO (Melson & Switzer, 1966; Pedersen, 1978, 1979). Although small graphite xenoliths have been found within the LSSC (Bailey *et al.*, 1924), the difference in the spinel compositions suggests that conditions in the LSSC were not as reducing during the period of xenolith formation.

Mullite

Needles of mullite occur included in plagioclase towards the centre of the zoned xenoliths. The mullite has the same dimensions as that in the buchite core, and is randomly oriented within the plagioclase crystals (*Figure 9.20a*). In places mullite needles can be seen projecting from the edge of the plagioclase crystal into the glassy centre of the xenolith. This confirms that the mullite was one of the first phases to crystallize from the aluminous melt (*cf.* Cameron, 1976), and shows that it has not exsolved from a plagioclase enriched in Al and Si (*cf.* Sturt, 1970). Thomas *et al.* (1922) considered that the plagioclase in the rims grew at the expense of the already crystallized mullite crystals. The mullite acted as the source of Al, and Ca was derived through diffusion from the host basaltic magma. However, later experimental work by Osborn & Muan (1960) has shown there to be a simple cotectic relationship between mullite and anorthite in the system $\text{CaO-SiO}_2\text{-Al}_2\text{O}_3$. Towards the basalt contact, the mullite inclusions appear to be dissolving, until the plagioclase immediately adjacent to the basalt contact is free of mullite. It is more likely, therefore, that plagioclase and mullite precipitated almost simultaneously, and that the dissolution of the mullite was in response to a reheating event.

Most of the plagioclase crystals which contain mullite have continuous or discontinuous zones around the edge of the feldspar, which is free of included mullite (*Figure 9.20b*). This suggests that the plagioclase has undergone a period of resorption and re-crystallization (*cf.* Thomas *et al.*, 1922). This feature will be considered further when the composition of the plagioclase is discussed.

Melt Pockets

Pockets of quenched 'basaltic' melt are trapped between the plagioclase laths throughout the feldspar rims of the buchitic xenoliths. These consist of microlites of plagioclase and clinopyroxene, along with subordinate Fe-Ti oxides, K-feldspar and glass (*Figure 9.21*). The composition of the plagioclase and pyroxene crystals varies systematically between different melt pockets according to the position of the melt pocket relative to the outer contact with the basalt, and the inner contact with the mullite buchite. The plagioclase varies from ~ An₆₀ to An₄₀, and the pyroxene from ~ Wo₃₀En₄₀Fs₃₀

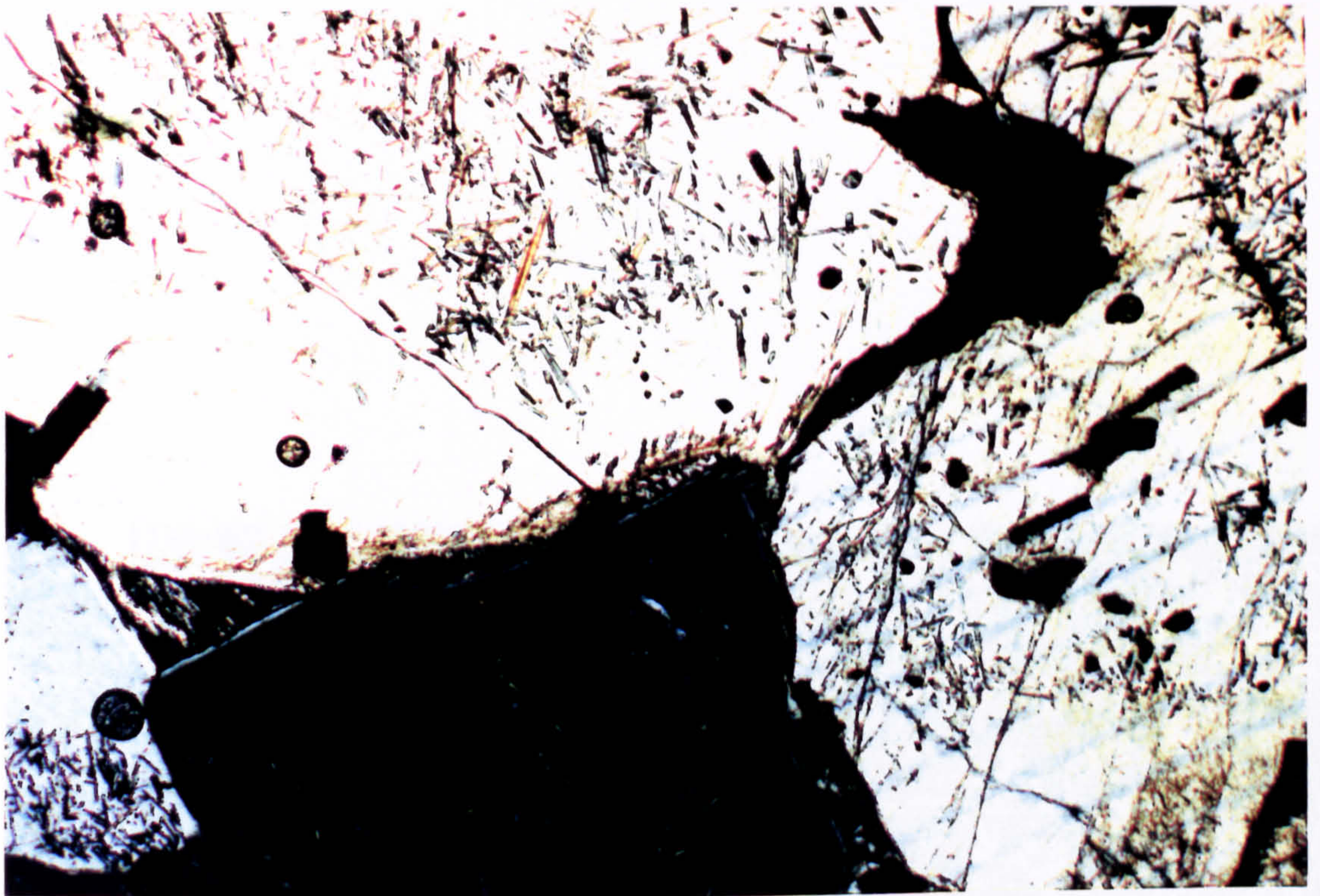


FIGURE 9.20a Plagioclase crystals adjacent to the mullite buchite core of aluminous xenoliths contain numerous inclusions of mullite. (xpl; Field of view 2x3mm; Sample PMFX1)

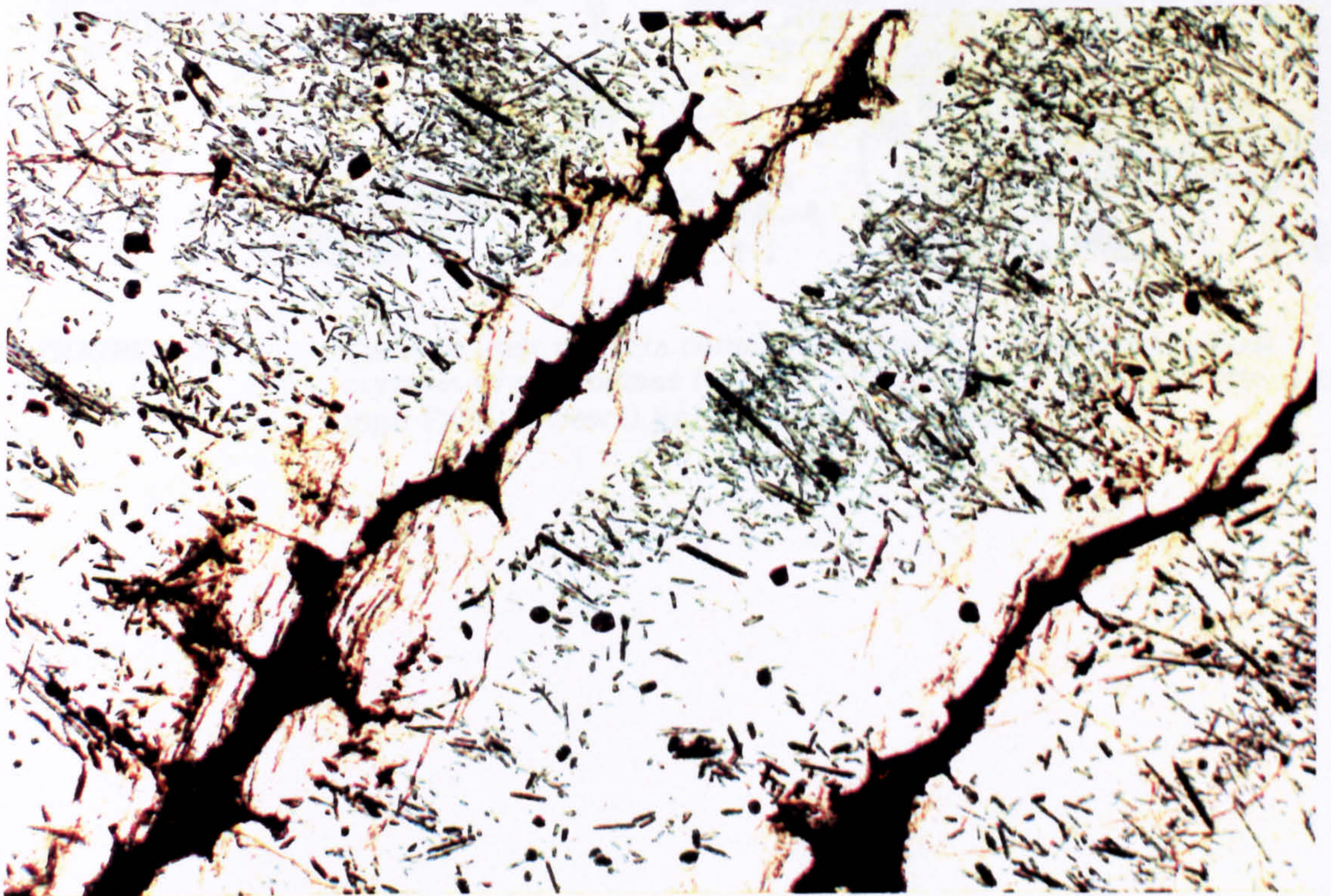


FIGURE 9.20b Where basaltic melts have penetrated into the plagioclase rim down cracks and in melt pockets, the surrounding plagioclase becomes free of mullite inclusions. (ppl; Field of view 2x3mm; Sample PMFX1).



FIGURE 9.21

Basaltic melt pockets consist of quenched needle and hollow crystals of plagioclase (~An₅₀), clinopyroxene and dendritic rutile. (ppl; Field of view 0.8x1.2mm; Sample PMFX1)

(ferroaugite) to $\text{Wo}_8\text{En}_{42}\text{Fs}_{50}$ (ferropigeonite), as shown in *Figures 9.22a-b*, with the less calcic pyroxene and plagioclase in melt pockets closest to the mullite buchite core of the xenoliths. Individual plagioclase and pyroxene crystals are occasionally slightly zoned. Since the melt pockets have proved too small for separation for major- and trace-element analysis (individual melt pockets have been analysed for Rb-Sr and Sm-Nd isotope ratios, see Chapter 10), crude estimates for the bulk composition of the melt pockets have been obtained using area-analysis on an SEM. *Figures 9.23a-c* show a selection of the major-element variations of melt-pockets from xenolith PMFX1. Despite the obvious limitations of such analyses, these graphs show that the overall trend in composition of the melt-pockets from the edge to the centre of the xenoliths, is broadly from basalt to basaltic-andesite, which explains the changes in plagioclase and pyroxene composition.

It is believed that the melt-pockets represent basaltic magma which made its way down cracks in the plagioclase rim, and mixed with a little of the 'resident' aluminous liquid. The melts nearer the xenolith cores have been more extensively mixed with xenolithic material, hence the more evolved compositions. This will be returned to in Chapter 10.

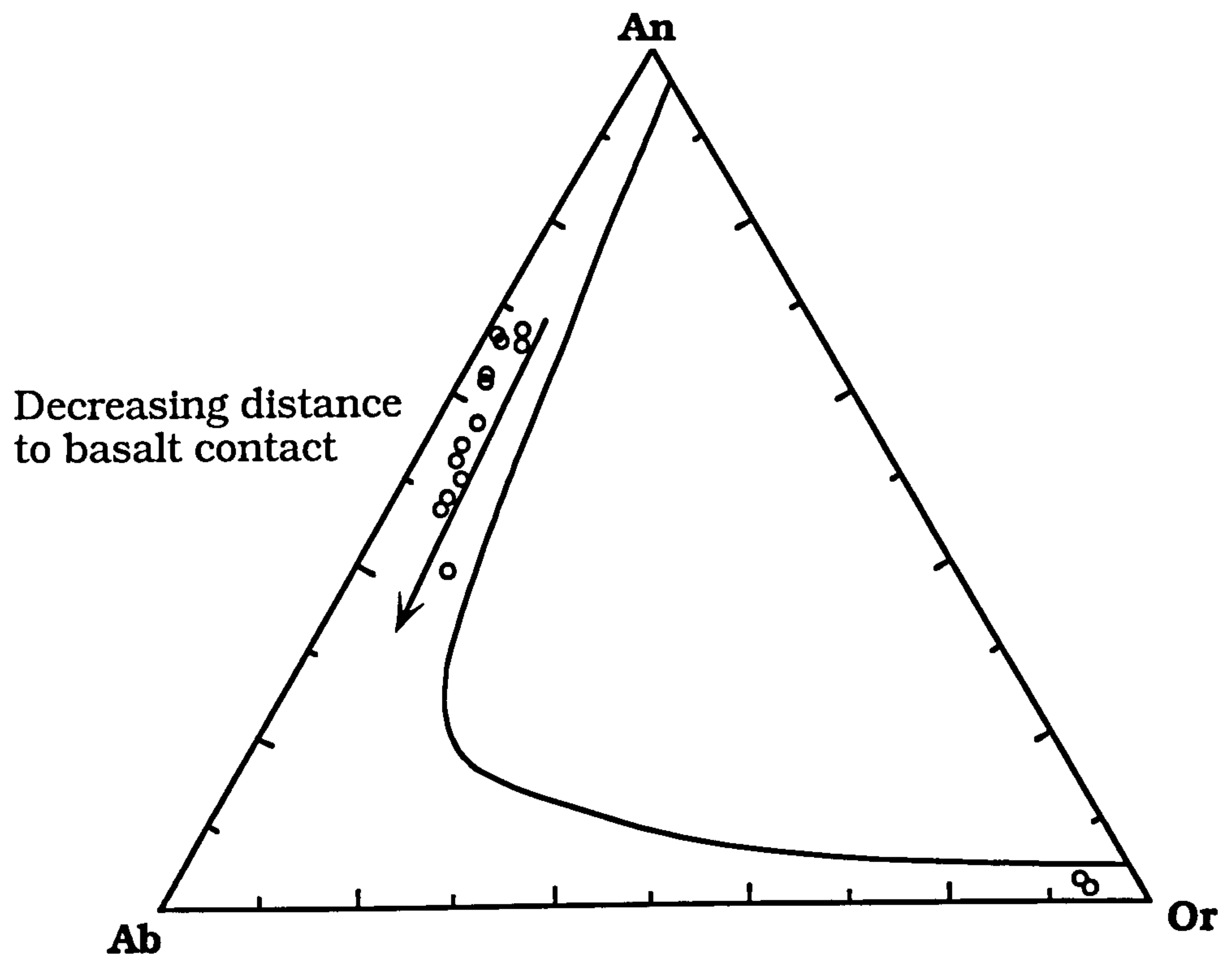


FIGURE 9.22 (a) Feldspar compositions from melt-pockets in aluminous xenolith PMFX1, plotted in the system Anorthite-Albite-Orthoclase at 2kbar water pressure. Note that both plagioclase and alkali-feldspar occur. The more calcic plagioclase occurs in melt pockets closer to the contact with the host basalt.

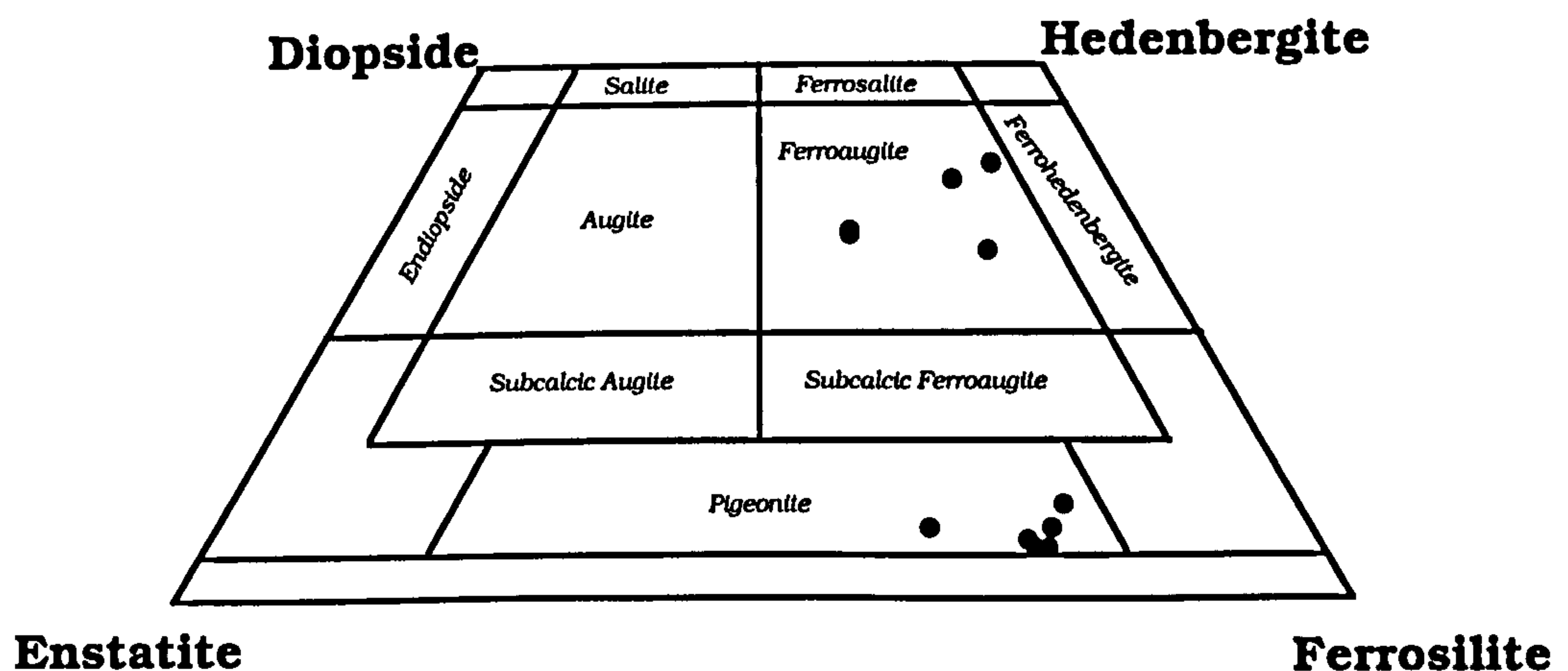


FIGURE 9.22 (b) Compositions of fine-grained pyroxene from melt-pockets in aluminous xenolith PMFX1, plotted in the pyroxene quadrilateral Di-En-Fs-Hd. Ferropigeonite compositions occur in melt-pockets closest to the buchite core of the xenolith.

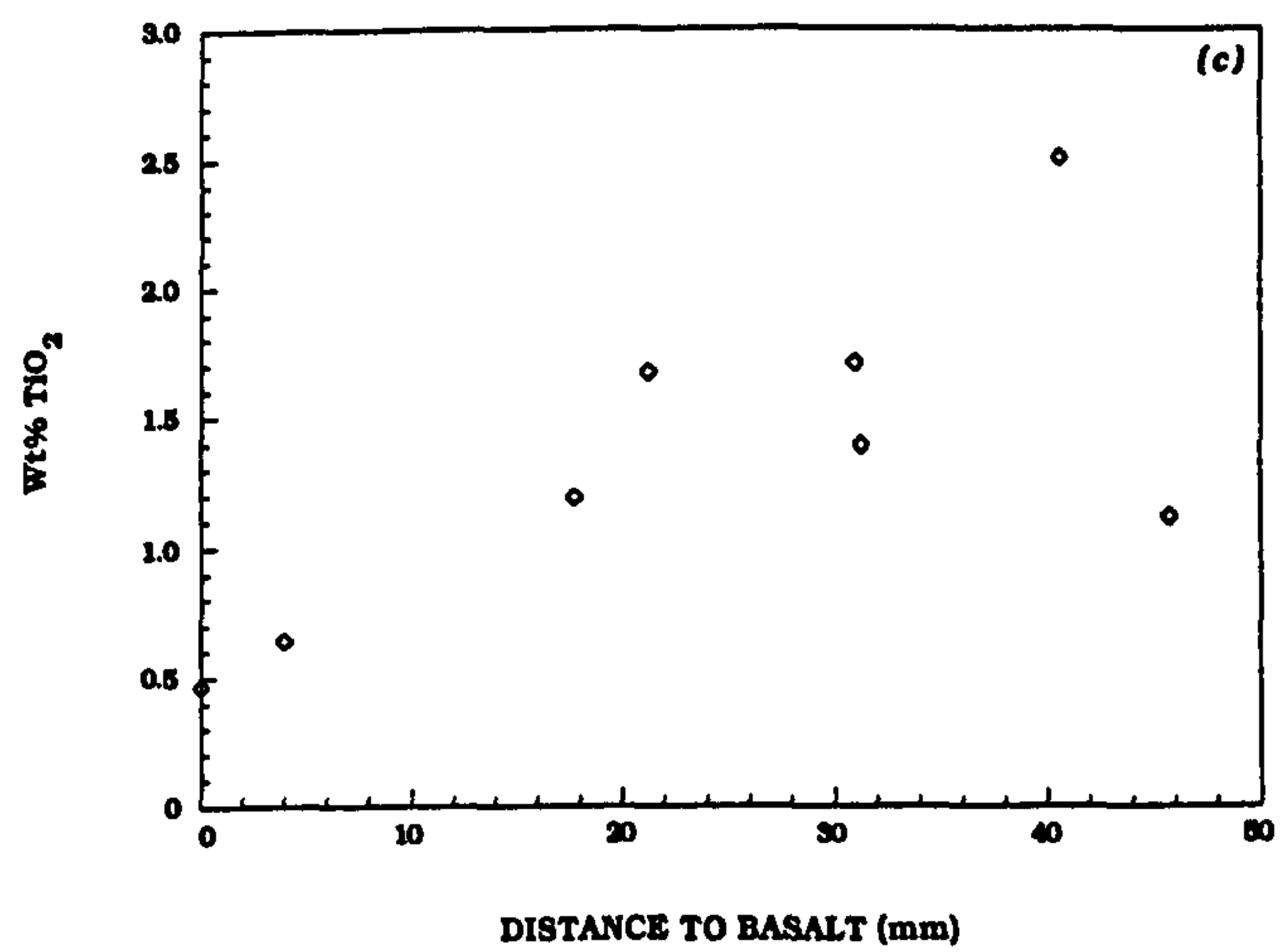
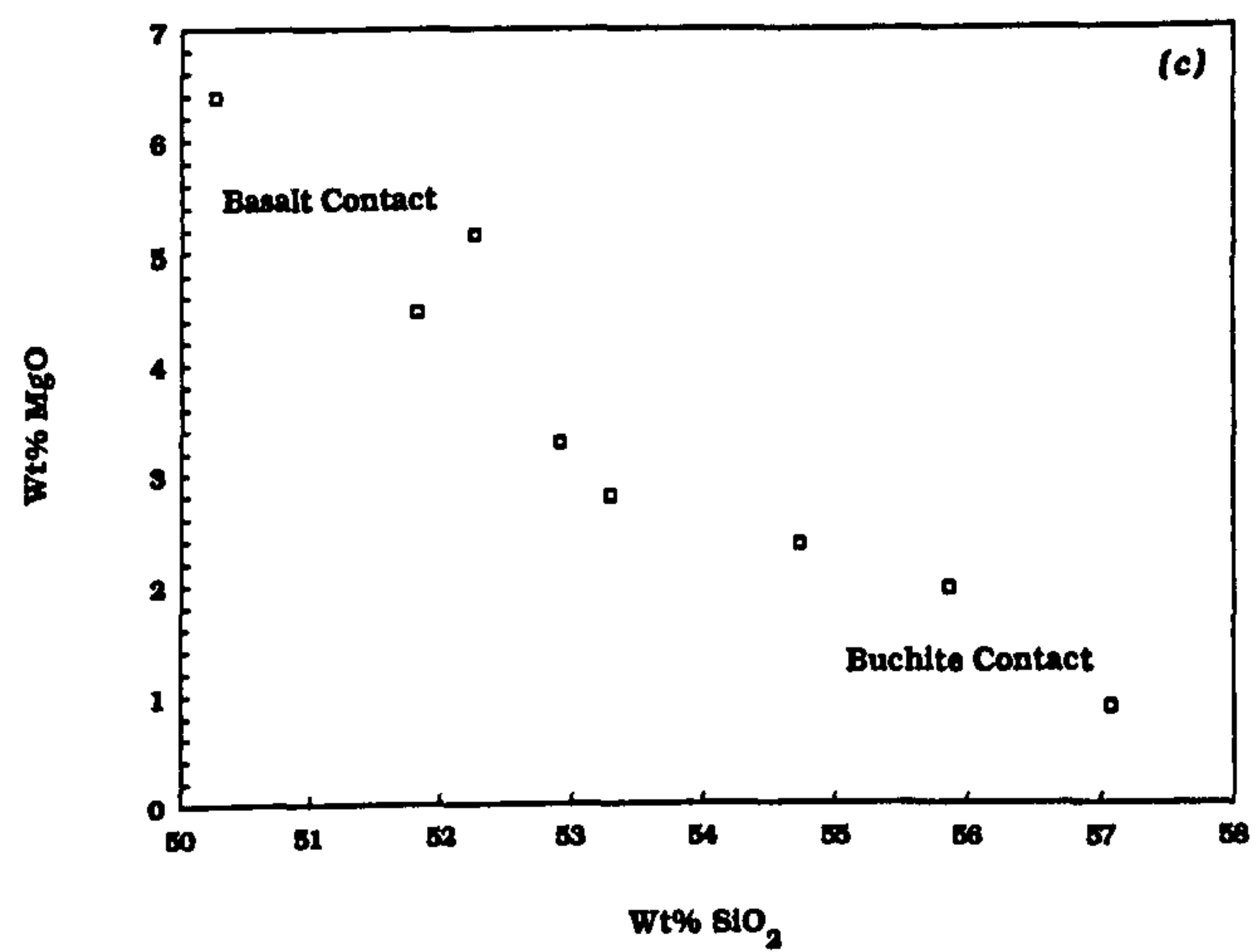
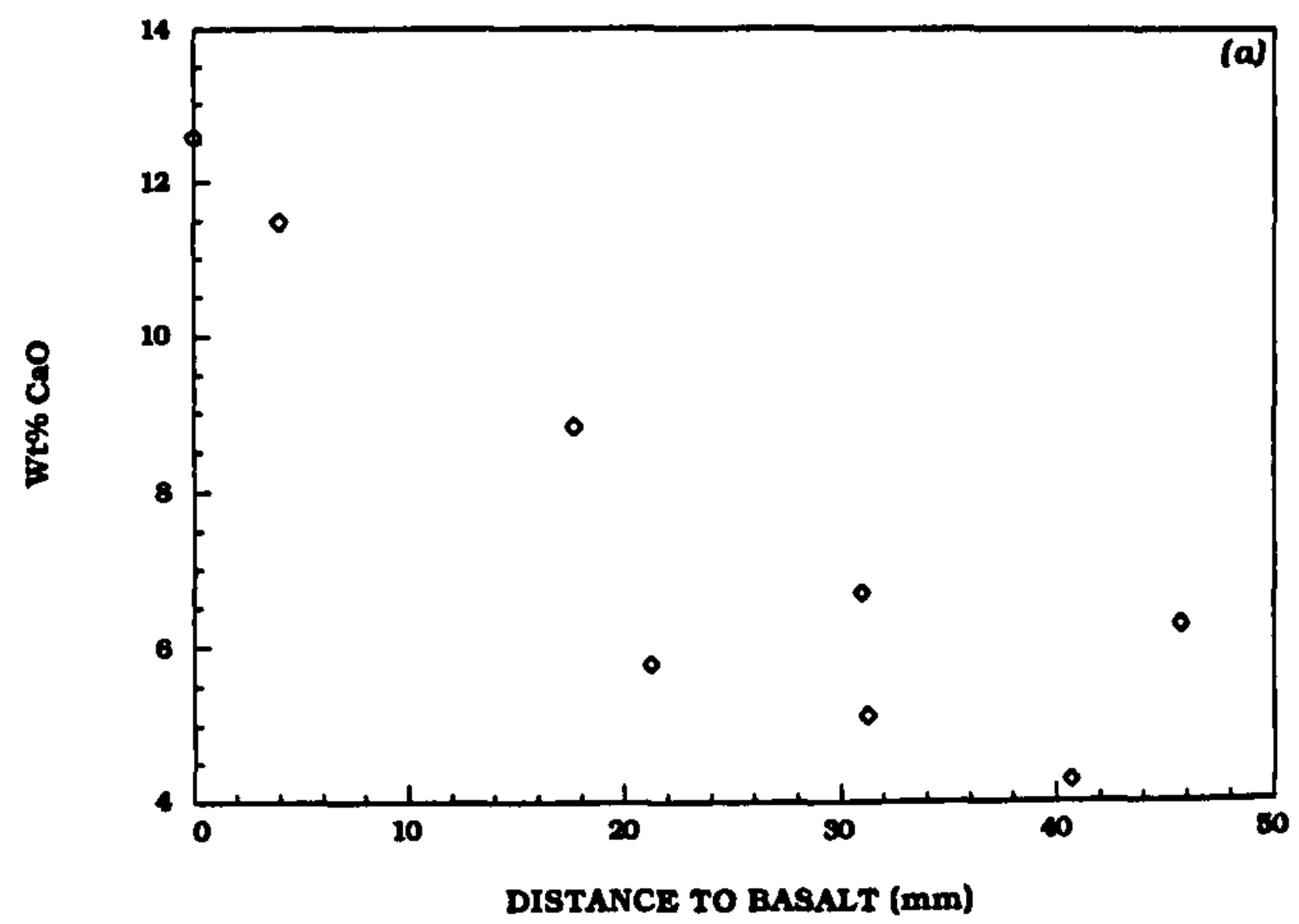


FIGURE 9.23a-c Variation in composition of melt pockets in aluminous xenolith (PMFX1) with distance to the contact with basalt.

Plagioclase

Plagioclase forms the bulk of the palisade around the aluminous buchite xenoliths (*Figure 9.11*). However, it must be stressed that not all mullite buchites have reaction rims. The plagioclase displays a variety of textures, indicative of a complex growth history. Those textures which relate to the initial growth of the feldspar rims will be described first, followed by those which indicate that the feldspar has suffered re-heating events.

Towards the core of the xenoliths, the plagioclase forms large (5-8mm), idiomorphic plates, often completely surrounded by aluminous glass (*Figure 9.24*). However, the crystals further towards the contact with the basaltic magma have obviously mutually interfered whilst growing, resulting in a mosaic of large plagioclase laths. The plagioclase laths adjacent to the central mullite buchite tend to grow with their long-axes (therefore twin planes) perpendicular to the buchitic core. Further towards the host magma contact, the plagioclase is of a smaller grain-size (1-3mm), and the crystals are more randomly oriented (*Figure 9.25*).

The composition of the plagioclase varies greatly, from An₈₇ to An₆₀, the most calcic plagioclase generally being found nearer the enclosing basalt, and forming reaction caps around spinel and corundum (see *Table 9.8*). The range in plagioclase compositions is shown in the Ab-An-Or ternary diagram of *Figure 9.26*. Many crystals show well developed oscillatory zoning (*Figure 9.27*), especially where in contact with the host magma. The extent of the oscillatory zoning can be of the order of 20 mol% variation in the An content of the plagioclase (see *Table 9.8*), which is almost the complete spectrum of plagioclase compositions seen. Examples of zoning profiles are shown in *Figure 9.28*. The zoning suggests that the plagioclase initially grew from a melt, rather than being a restite phase after the partial melting of the protolith (cf. van Bergen & Barton, 1984; Ripley & Alawi, 1988; Grapes, 1986,1991). The zoning of plagioclase is less well-developed adjacent to the buchitic core of the xenoliths. However, this textural evidence suggests that the majority of the plagioclase grew inwards from the interface between the aluminous liquids and the basaltic magma, with only minor growth in the opposite direction.

Where basaltic melts have found a way into the plagioclase rim, the liquid has precipitated mullite-free feldspar, which is in optical



FIGURE 9.24

Large euhedral plagioclase laths towards the centre of the plagioclase rim. Alteration of the plagioclase is typically to sericite. (ppl; Field of view 2x3mm; Sample PMFX1).

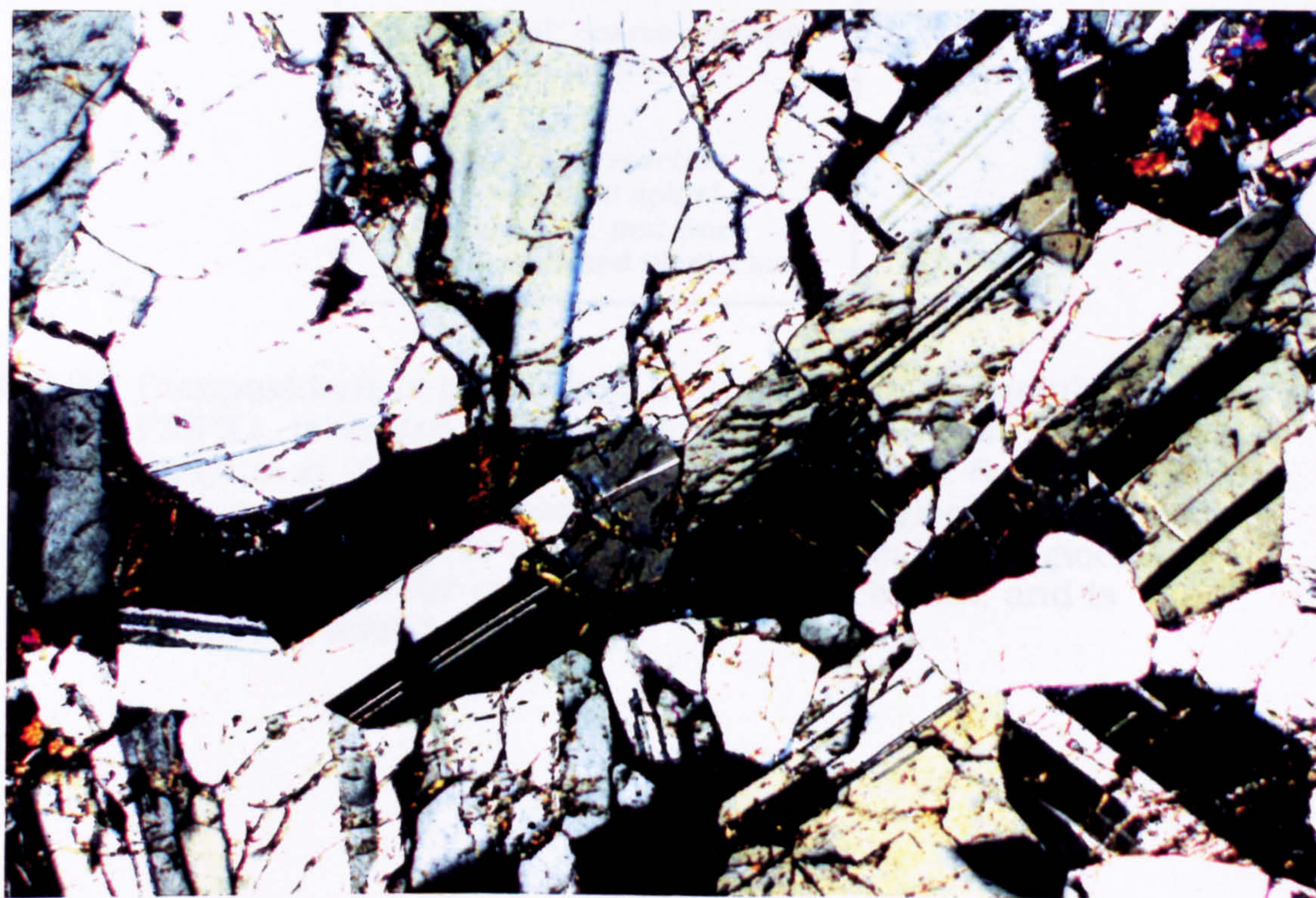


FIGURE 9.25

Towards the contact with the host basalt, the plagioclase is of a smaller grain size. (xpl; Field of view 2x3mm; Sample PMFX1).

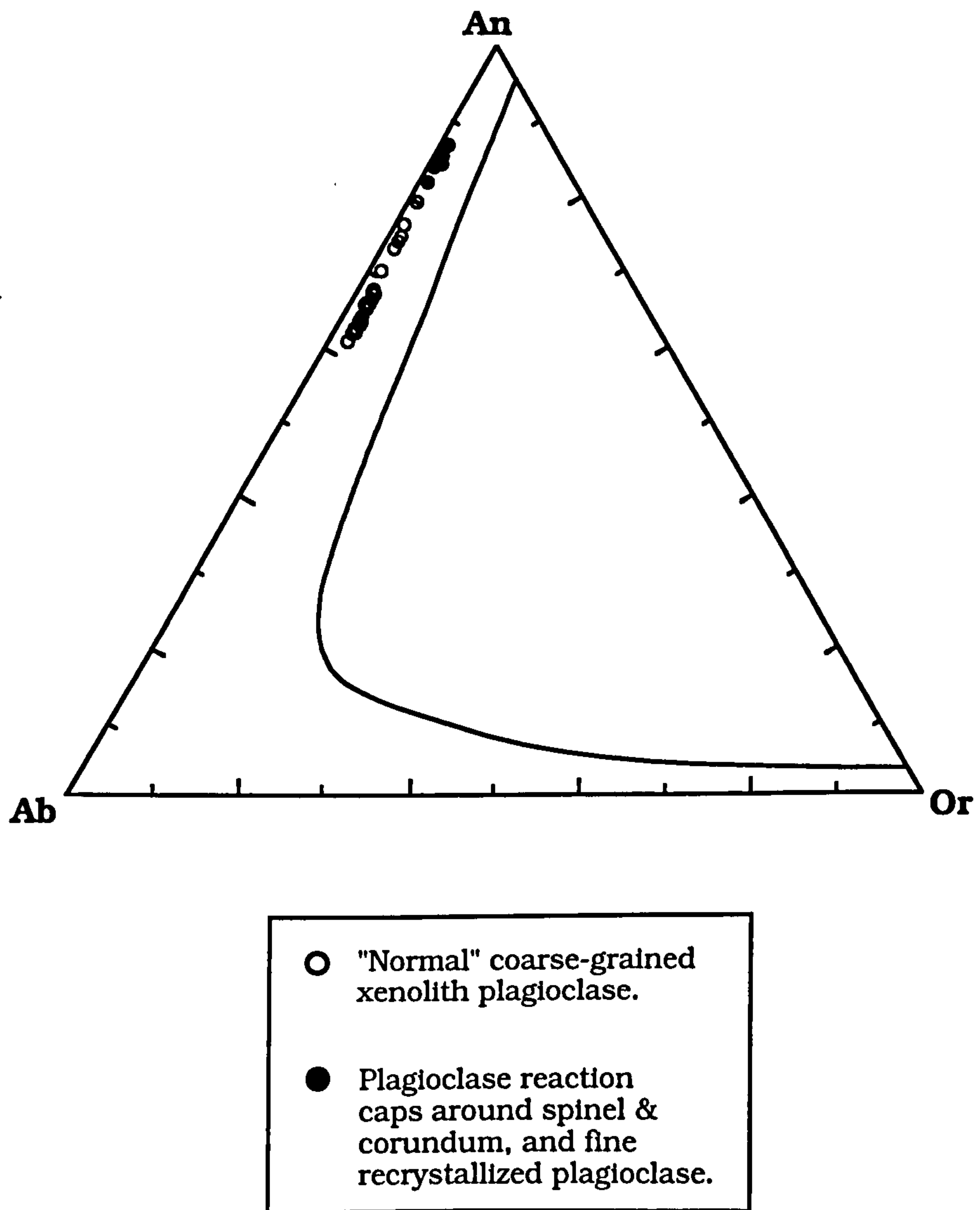


FIGURE 9.26 Compositions of plagioclase from aluminous xenolith PMFX1, projected in the ternary Anorthite-Albite-Orthoclase diagram at 2kbar water pressure (after Tuttle & Bowen, 1958). The more sodic compositions are from plagioclase next to the mullite buchite core of the xenolith. The calcic plagioclase occurs next to the contact with the host basalt, and is oscillatory zoned An_{62} - An_{82} .

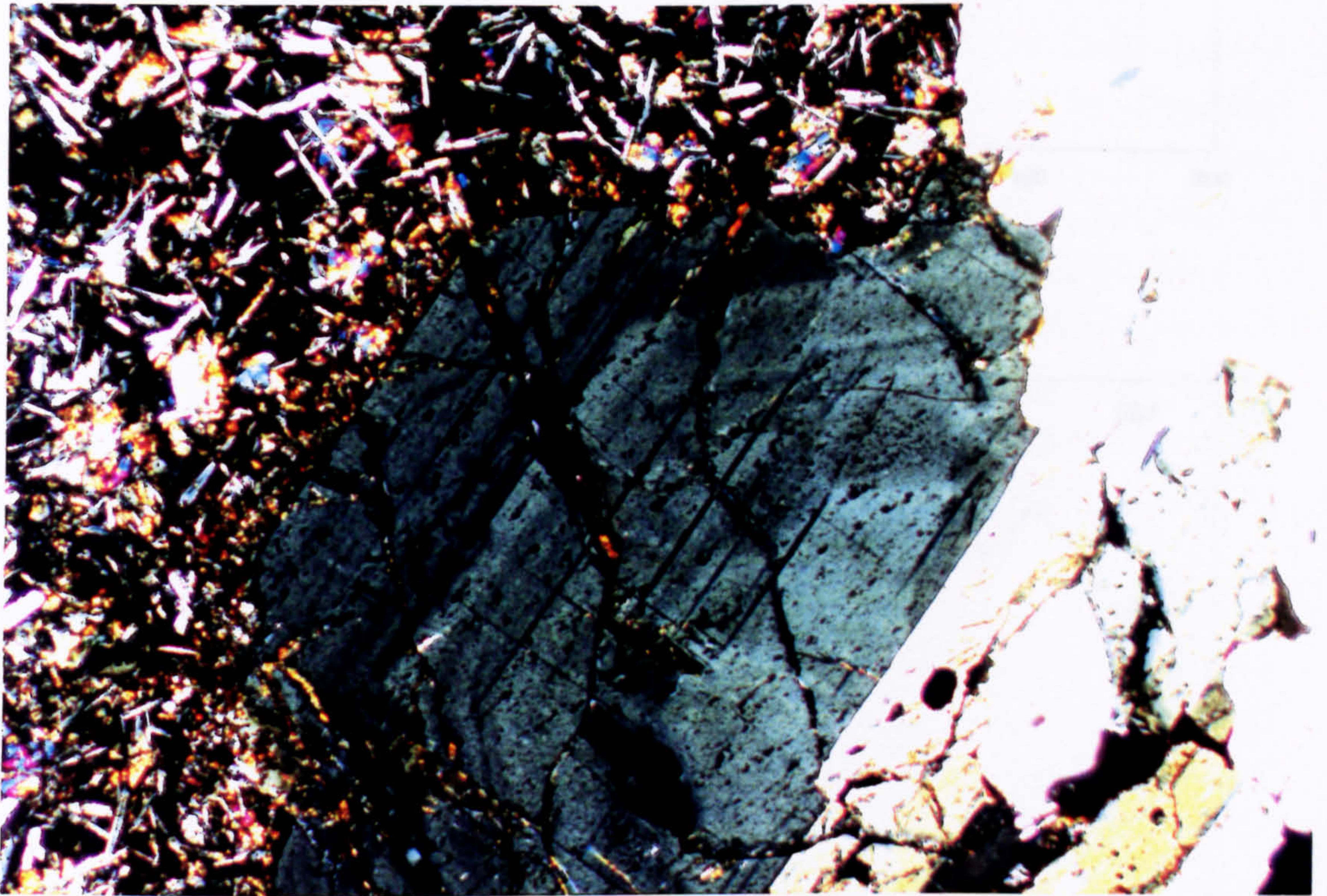


FIGURE 9.27

Where they contact the host basalt, the xenolith plagioclase often displays well developed oscillatory zoning (An₈₃ to An₆₄). (xpl; Field of view 2x3mm; Sample TM1F).

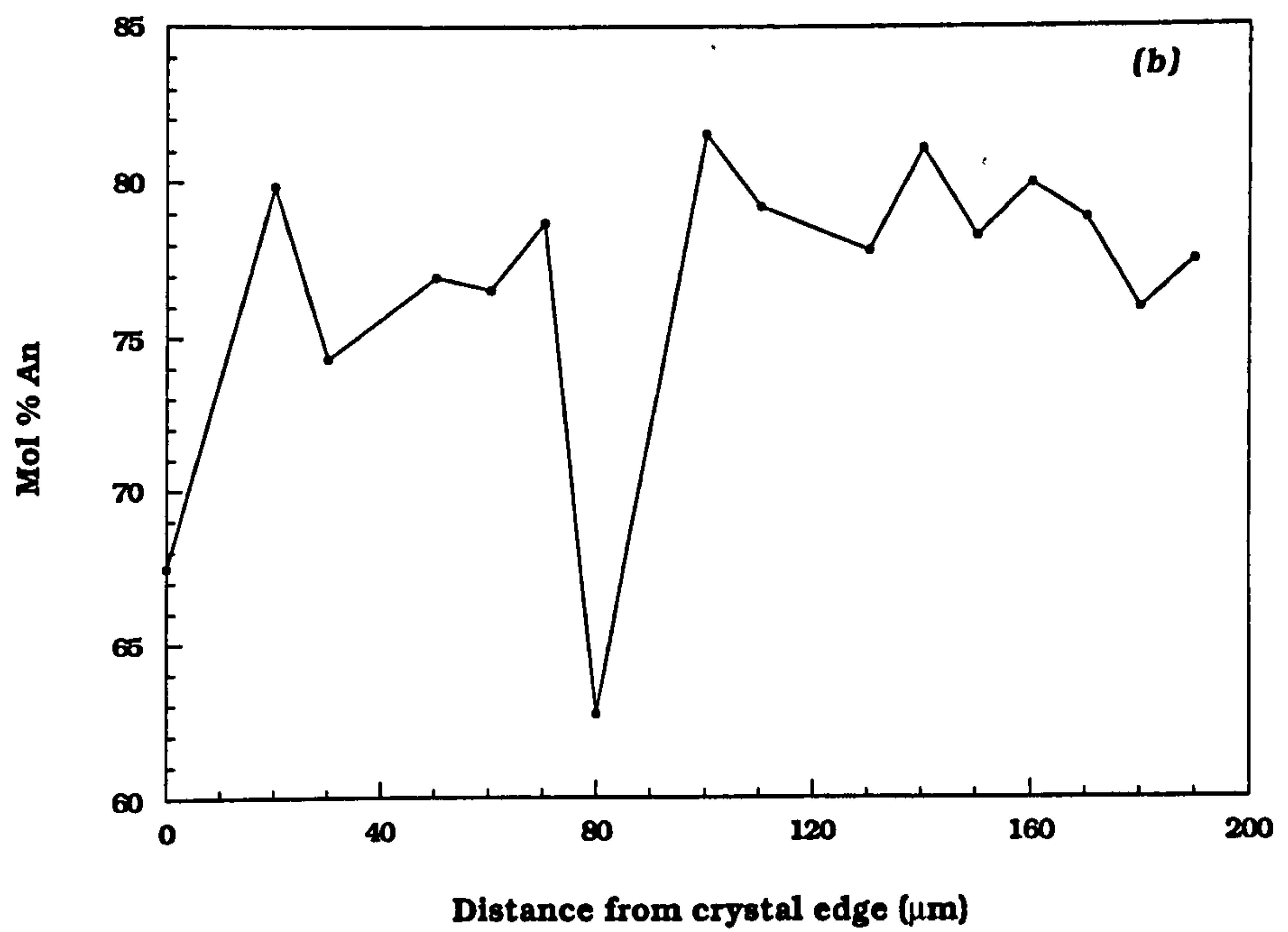
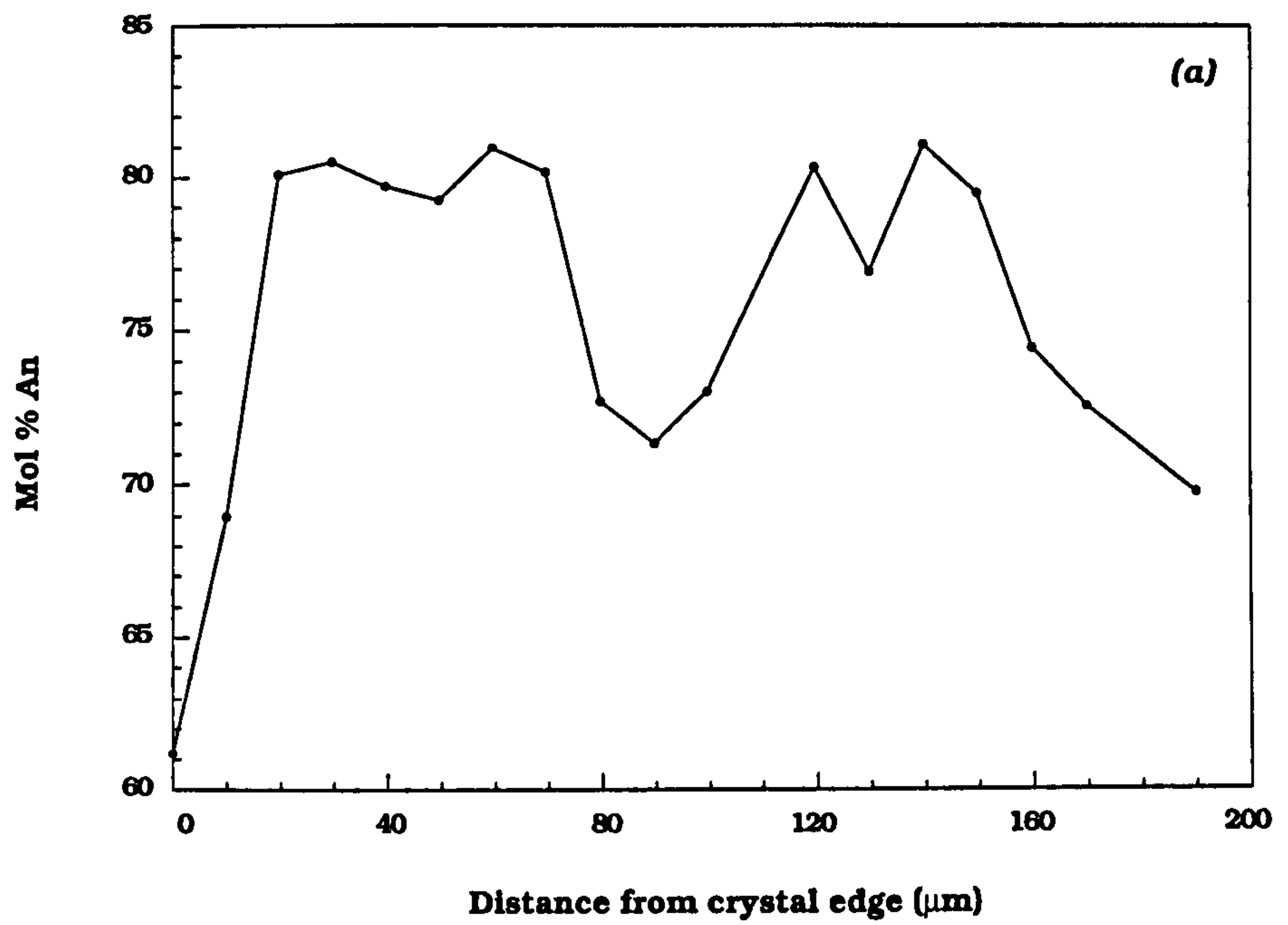


FIGURE 9.28 Examples of oscillatory zoning profiles in plagioclase from aluminous xenolith PMFX1. All crystals occur next to the contact with the host basalt.

continuity with the mullite-bearing plagioclase. This has occurred around basalt melt-pockets and cracks. The mullite-free plagioclase is of a slightly more calcic composition than the original, and it commonly shows normal zoning (see *Figure 9.20b*). Where in contact with melt-pockets, and at the contact with the host basalt, the plagioclase has a narrow overgrowth of a similar composition to the quench-feldspar within the basaltic melt (*Figure 9.29*). This is typically of a more sodic composition (see *Table 9.8*).

The plagioclase in many xenoliths has, in places, been extensively recrystallized, particularly near the basalt contact (*Figure 9.11*). Zones of fine-grained plagioclase crystals occur enclosed within large plates of 'original' feldspar (*Figure 9.30*). The new plagioclase is typically more calcic (An₈₂ to An₈₇) than its host (see *Table 9.8*). Included crystals of spinel and corundum also occasionally show an armour of this fine-grained plagioclase (*Figure 9.31*). Again this plagioclase is more calcic (An₈₂ to An₈₆) than the enclosing coarse-grained plagioclase. It is believed that this plagioclase formed after the spinel reacted with the liquid. This would explain the often skeletal and resorbed appearance of some of the spinel crystals. This point is returned to in Chapter 10.

The plagioclase nearest the enclosing basalt (*Figure 9.11*) often has a very distinctive 'fingerprint' texture, indicative of re-heating (*Figures 9.32a-c*) (e.g. Kaczor *et al.*, 1988; Johannes & Holtz, 1992; Philpotts & Asher, 1993). The experiments of Johannes (1978) and Johannes & Holtz (1992) show that during the melting of plagioclase in the systems Ab-An-H₂O and Qtz-Ab-An-H₂O at between 1atm and P_{H₂O}=5kbar, the Ab and An components are effectively separated, with the Ab component, along with K and Fe, being partitioned into the melt. New An-rich plagioclase forms at the edges of the melting crystals:



If melting is to continue, there must be a further increase in temperature to enable the melting of the more calcic plagioclase. This increase in temperature must be at an equal or faster rate than the rate of diffusion of NaSi-CaAl within the melting edge of the crystal (Grapes, 1986). Johannes (1978) found that the average composition of plagioclase became more calcic at temperatures above the solidus as

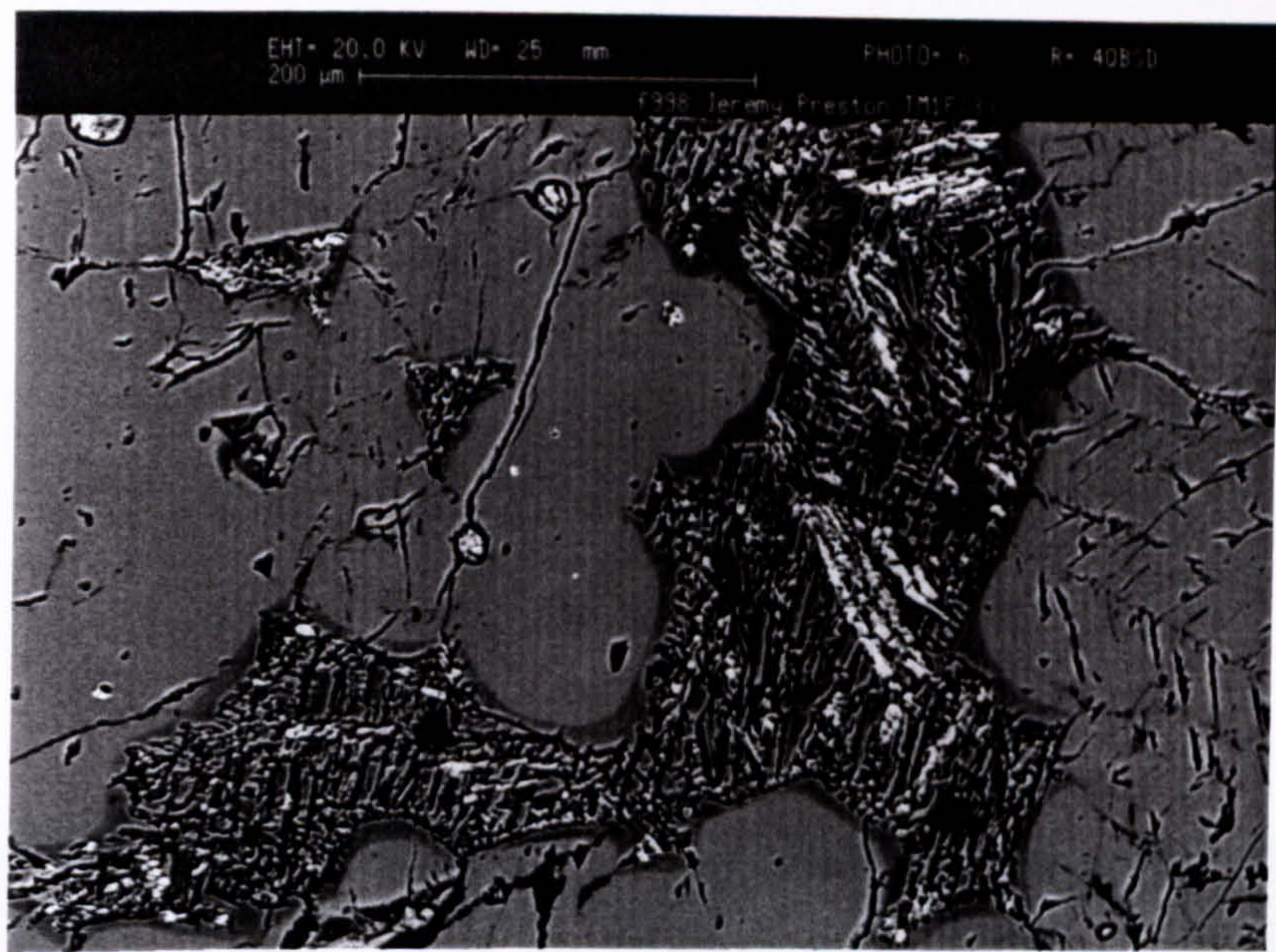


FIGURE 9.29

Back scattered SEM image of a basaltic melt pocket surrounded by large laths of plagioclase. The xenolith plagioclase has an overgrowth of a more sodic composition (dark coloured rim), which is of a similar composition to the plagioclase in the melt pocket. (Sample TM1F).

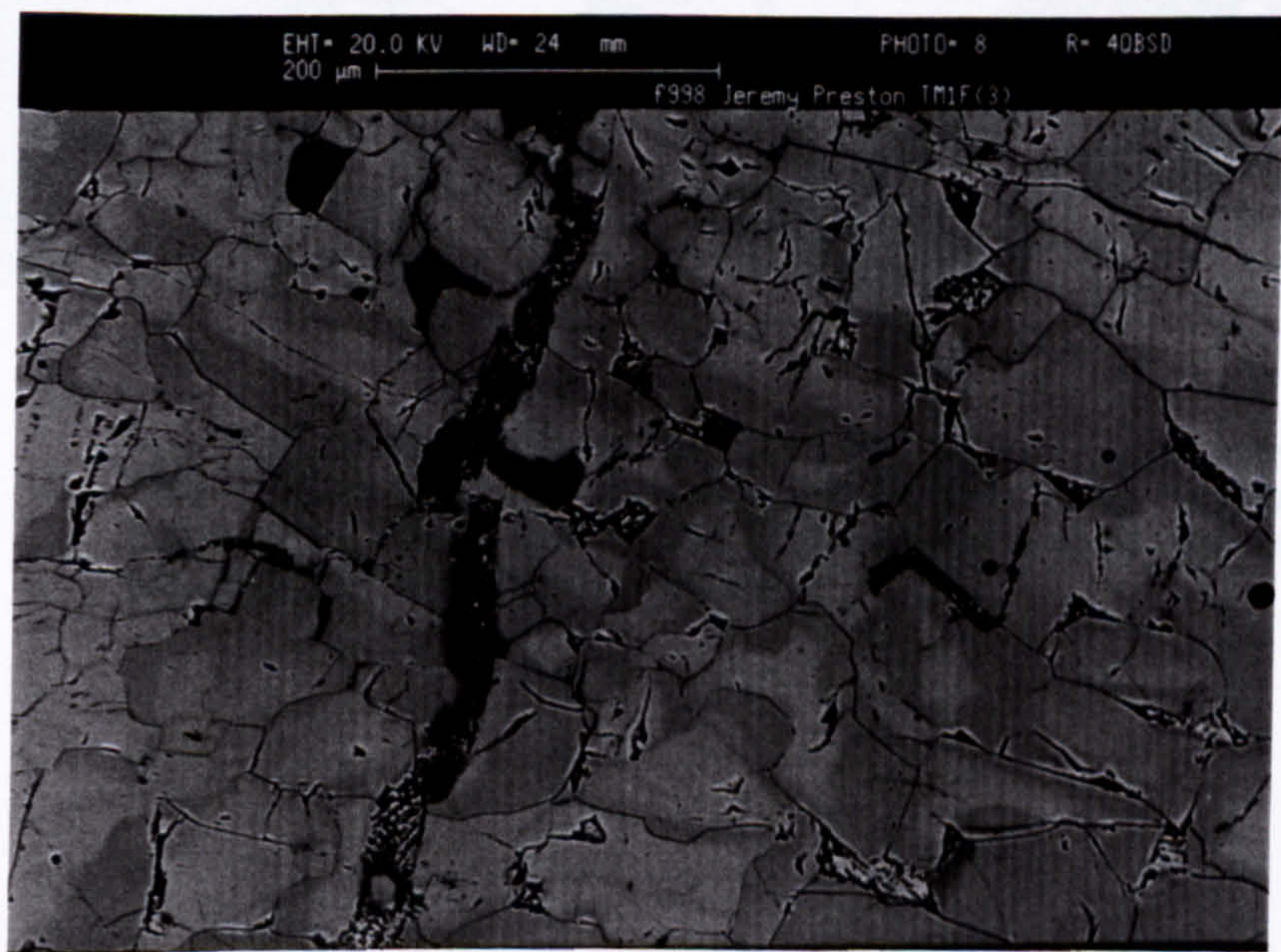


FIGURE 9.30

Back scattered SEM image showing complex zoning patterns in fine recrystallized xenolith plagioclase. Darker zones are of a more sodic composition. Zones of fine grained plagioclase occur within the centres of large individual plagioclase laths. (Sample TM1F).



FIGURE 9.31

Fine recrystallized plagioclase "armour" around a resorbed spinel (SP). Texture suggests a reaction relationship between spinel and plagioclase. Plagioclase is of a highly calcic composition (An₈₇). (xpl; Field of view 2x3mm; Sample TM1F).

temperature increased, or with increasing time at the same temperature, and that the change was greater for a more calcic starting composition. This suggests that the melting of plagioclases with compositions intermediate between pure albite and anorthite is a complex process. It was also discovered that melting is especially fast parallel to the α -axis (Johannes, 1978; Grapes, 1986). The 'fingerprint' texture noted above from the LSSC xenoliths is an excellent example of this melting process occurring within a natural system. *Figures 9.32b-c* are back-scattered electron images of this texture, showing variation in the mean atomic mass of the plagioclase, with brighter areas on the image corresponding to material with a higher mean atomic mass. *Figure 9.32b* clearly shows the separation of the plagioclase into Ab-rich crystals (medium grey), with An-rich rims (light-grey), surrounded by K-Na-rich glass (dark grey). *Figure 9.32c* shows the incipient melting of plagioclase. Here no melt has developed, and the plagioclase has separated into An- and Ab-rich zones, which are parallel to the long axis of the crystal. The bright crystals in this image are of clinopyroxene and Fe-Ti oxide inclusions.

The textural evidence preserved in the mullite buchite-plagioclase xenolith suite suggests that the original plagioclase from the rims, crystallized initially from a melt. The compositional characteristics of this melt will be discussed in Chapter 10 when the possible consequences of xenolith-magma interactions will be examined. The xenoliths then underwent a reheating event, and the plagioclase nearest the outer margins of the xenoliths started to melt, possibly via the process outlined above. The xenoliths were then carried into the site of emplacement, where rapid cooling preserved the glassy core of the xenoliths, and quenched the basaltic liquid in the melt-pockets.

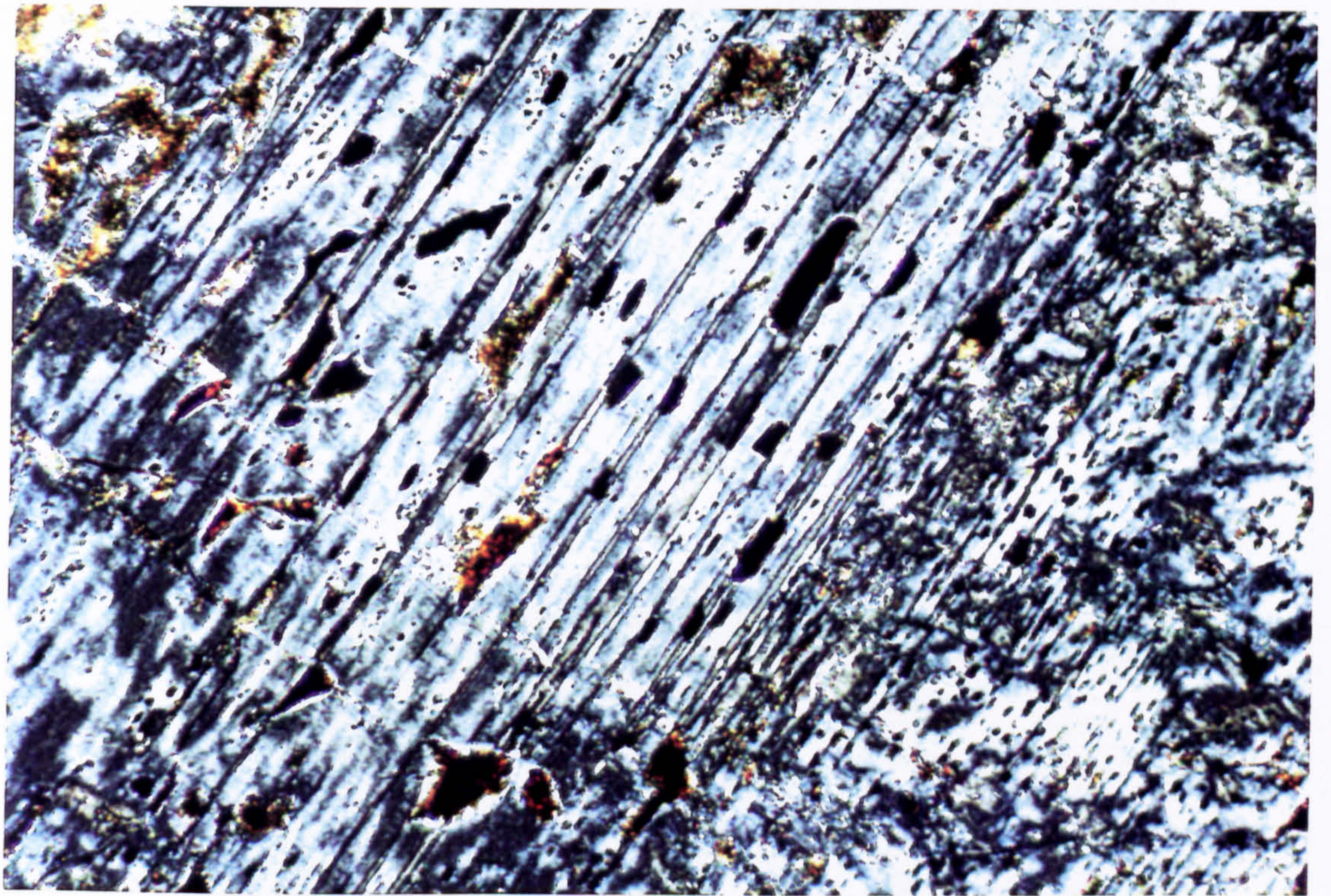


FIGURE 9.32a

Complex "fingerprint" zoning texture in xenolith plagioclase close to the contact with the host basalt. (xpl; Field of view 0.8x1.2mm; Sample PMFX1)

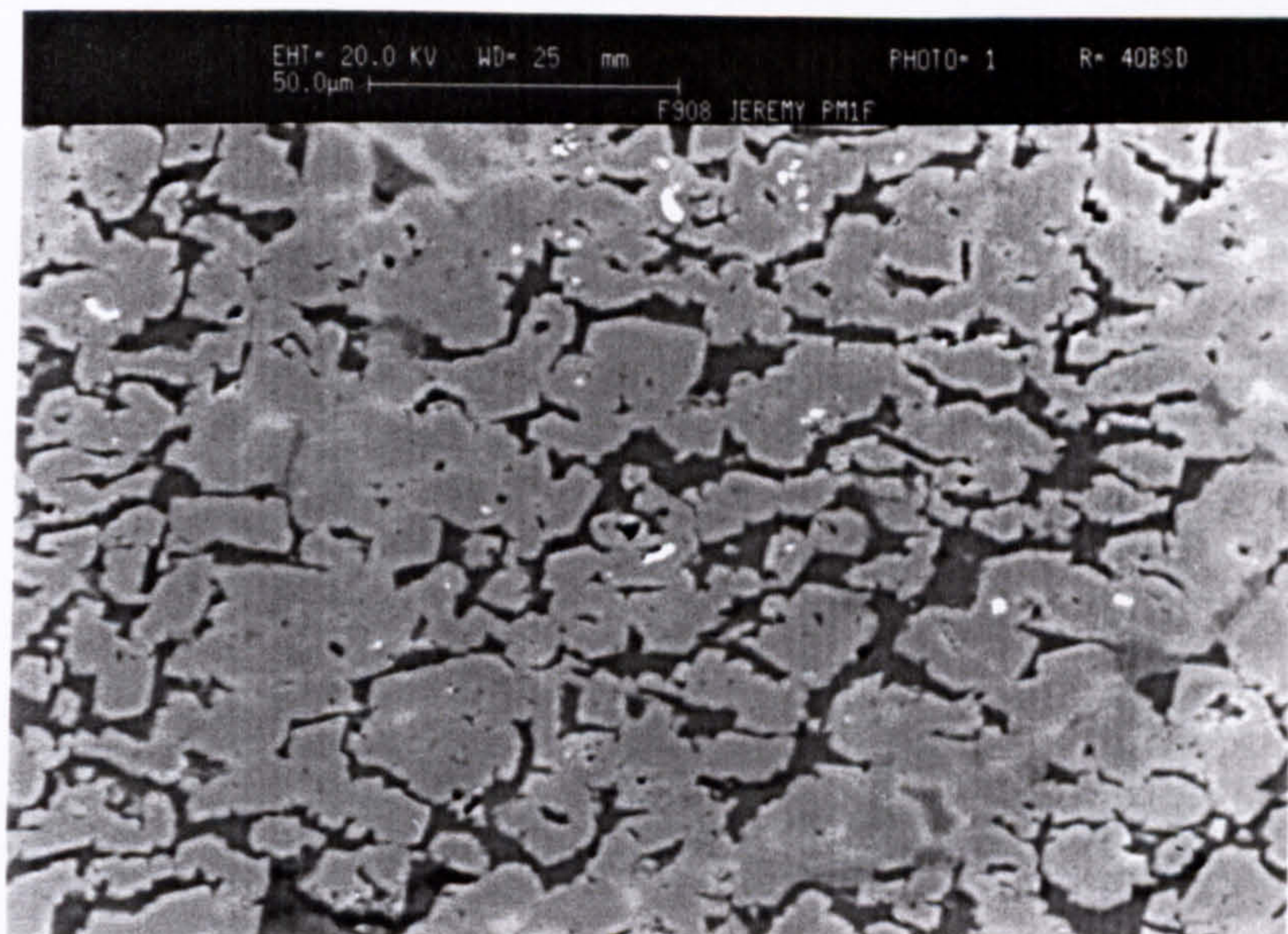


FIGURE 9.32c

Back scattered SEM image of the fingerprint texture. Extensive melting of the plagioclase has occurred and large pools of melt have developed within the plagioclase crystal.

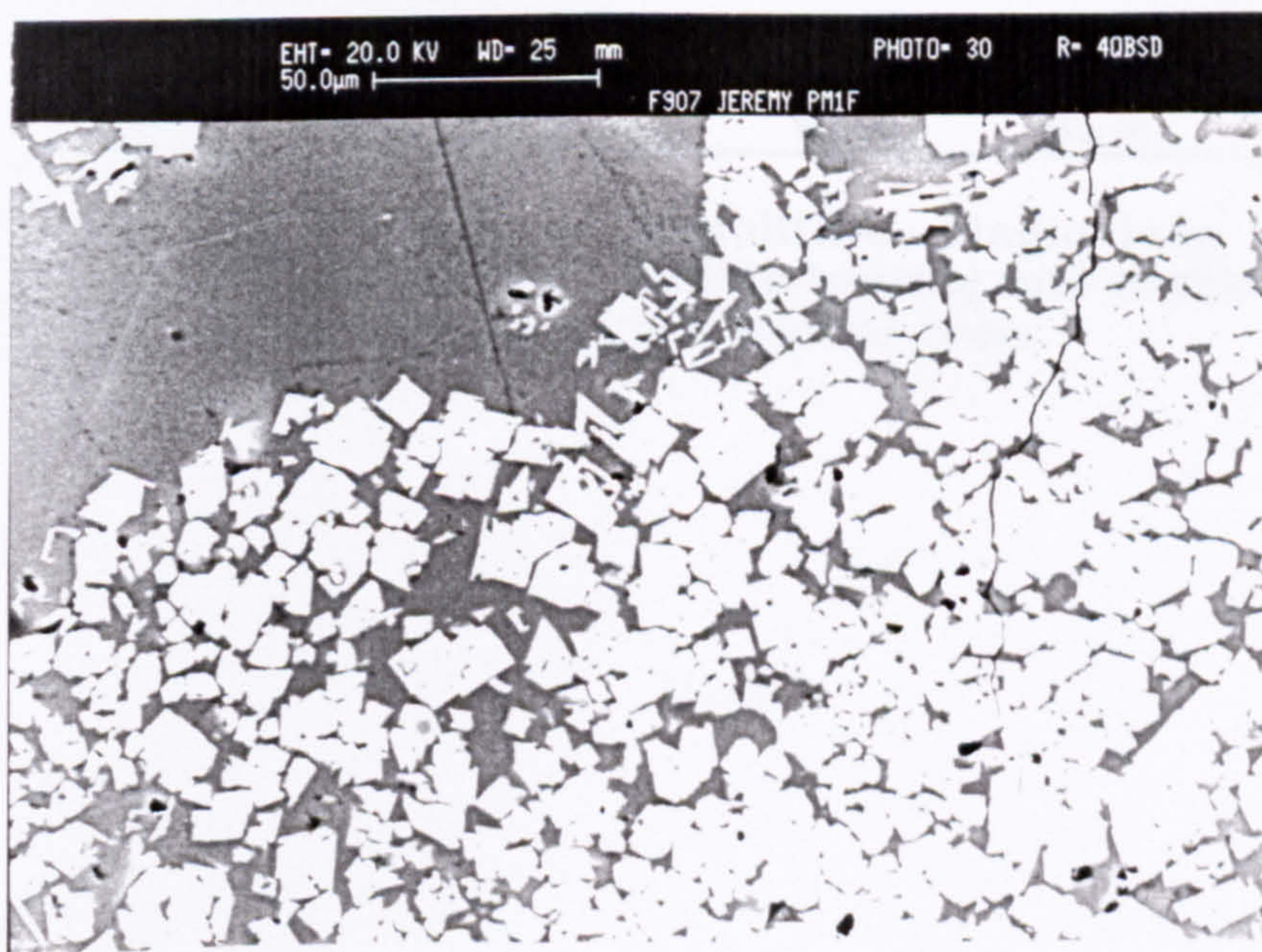


FIGURE 9.32b

Fingerprint texture is the result of melting of the plagioclase (Kazor *et al.*, 1988; Johannes & Holtz, 1992; Philpotts & Asher, 1992), and the redistribution of the Ab and An components. Figure shows a back scattered SEM image of the texture, with An-rich plagioclase (lightest grey) forming at the melting edge of the more albitic crystals (mid grey). Interstitial material (dark grey) is K-rich melt. (Sample PM1F).

Plagioclase adjacent to mullite buchite core						
Mullite-bearing				Mullite-free		
SiO ₂	50.61	50.41	50.81	50.55	50.88	50.82
TiO ₂	0.14	0.20	0.22	0.29	0.20	0.24
Al ₂ O ₃	31.89	32.18	31.96	31.97	32.01	32.30
FeO*	0.16	0.18	0.24	0.11	0.18	0.08
CaO	12.20	12.50	12.53	12.51	12.68	12.53
Na ₂ O	3.95	4.02	4.14	3.99	4.04	3.99
K ₂ O	0.35	0.33	0.34	0.37	0.35	0.37
TOTAL	99.30	99.83	100.24	99.79	100.33	100.32
FORMULA ON BASIS OF 32 OXYGENS						
Si	9.25	9.18	9.22	9.21	9.23	9.20
Ti	0.02	0.03	0.03	0.04	0.03	0.03
Al	6.87	6.91	6.84	6.86	6.84	6.89
Fe (ii)	0.02	0.03	0.04	0.02	0.03	0.01
Ca	2.39	2.44	2.44	2.44	2.46	2.43
Na	1.40	1.42	1.46	1.41	1.42	1.40
K	0.08	0.08	0.08	0.09	0.08	0.09
TOTAL	20.04	20.09	20.10	20.07	20.08	20.06
ENDMEMBER %						
Ab	36.14	36.08	36.67	35.79	35.82	35.73
Or	2.11	1.94	1.99	2.16	2.02	2.18
An	61.75	61.97	61.34	62.05	62.16	62.09

Table 9.8 Compositional range of xenolithic plagioclase from aluminous xenolith PMFX1. Mullite-bearing and mullite-free plagioclase from adjacent to the buchite core.

Zoned plagioclase adjacent to basalt contact, showing range of compositions.					"Fingerprint" textured plagioclase	
	RIM		CORE			
SiO ₂	51.52	48.86	46.16	48.14	47.22	50.05
TiO ₂	0.03	0.07	0.06	0.00	0.06	0.16
Al ₂ O ₃	30.40	32.35	34.23	32.89	34.56	32.07
FeO*	1.11	0.82	0.51	0.66	0.36	0.33
CaO	12.45	14.11	16.19	14.77	15.89	13.38
Na ₂ O	4.17	3.36	2.13	2.97	2.39	3.70
K ₂ O	0.28	0.22	0.14	0.19	0.15	0.27
TOTAL	99.95	99.78	99.41	99.62	100.64	99.96
FORMULA ON BASIS OF 32 OXYGENS						
Si	9.41	8.98	8.55	8.86	8.62	9.13
Ti	0.00	0.01	0.01	0.00	0.01	0.02
Al	6.54	7.00	7.47	7.14	7.43	6.90
Fe (ii)	0.17	0.13	0.08	0.10	0.06	0.05
Ca	2.43	2.78	3.21	2.91	3.11	2.62
Na	1.48	1.20	0.77	1.06	0.84	1.31
K	0.06	0.05	0.03	0.05	0.04	0.06
TOTAL	20.09	20.14	20.11	20.12	20.10	20.09
ENDMEMBER %						
Ab	37.13	29.71	19.10	26.40	21.18	32.83
Or	1.61	1.25	0.80	1.11	0.90	1.55
An	61.26	69.04	80.10	72.50	77.93	65.62

Table 9.8 cont. Compositional range of xenolithic plagioclase from aluminous xenolith PMFX1. Oscillatory zoned plagioclase at basalt contact, and "fingerprint" textured plagioclase.

Feldspar from melt-pockets in aluminous xenolith PMFX1						
	Plag	K-spar	Plag	K-spar	Plag	Xenolith Plag Overgrowth
SiO ₂	52.83	65.40	53.34	65.14	55.02	55.40
TiO ₂	0.04	0.00	0.06	0.08	0.13	0.14
Al ₂ O ₃	29.28	18.10	28.74	17.63	27.69	26.53
FeO*	0.93	0.12	0.72	0.25	0.68	0.33
CaO	11.28	0.00	11.02	0.04	9.68	10.30
Na ₂ O	4.46	0.03	4.65	0.34	5.15	5.47
K ₂ O	0.50	15.47	0.45	14.58	0.79	0.59
TOTAL	99.31	99.12	98.98	98.07	99.15	98.76
FORMULA ON BASIS OF 32 OXYGENS						
Si	9.66	12.11	9.77	12.16	10.03	10.14
Ti	0.01	0.00	0.01	0.01	0.02	0.02
Al	6.31	3.95	6.20	3.88	5.95	5.72
Fe (ii)	0.14	0.02	0.11	0.04	0.10	0.05
Ca	2.21	0.00	2.16	0.01	1.89	2.02
Na	1.58	0.01	1.65	0.12	1.82	1.94
K	0.12	3.65	0.11	3.47	0.18	0.14
TOTAL	20.03	19.75	20.01	19.69	19.99	20.02
ENDMEMBER %						
Ab	40.45	0.31	42.15	3.40	46.73	47.34
Or	2.99	99.69	2.70	96.37	4.71	3.36
An	56.56	0.00	55.15	0.23	48.56	49.31

Table 9.8 cont. Compositional range of xenolithic feldspar from aluminous xenolith PMFX1. Melt-pocket plagioclase and k-feldspar, and plagioclase overgrowths in melt-pockets.

Plagioclase from Aluminous xenolith TM1F							
	Host Plag	Plagioclase reaction caps around spinel			Fine-grained recrystallized plagioclase		
SiO ₂	47.15	46.91	47.14	45.86	46.94	45.89	46.89
TiO ₂	0.06	0.04	0.02	0.04	0.03	0.04	0.03
Al ₂ O ₃	32.74	33.01	33.03	33.60	32.61	33.93	33.03
FeO*	0.55	0.54	0.48	0.53	0.47	0.44	0.45
CaO	16.85	17.12	17.08	18.10	16.97	18.06	17.21
Na ₂ O	2.02	1.93	1.86	1.47	1.99	1.36	1.87
K ₂ O	0.10	0.10	0.09	0.07	0.11	0.09	0.09
TOTAL	99.46	99.64	99.69	99.67	99.13	99.81	99.56
FORMULA ON BASIS OF 32 OXYGENS							
Si	8.73	8.68	8.71	8.51	8.73	8.49	8.68
Ti	0.01	0.01	0.00	0.01	0.01	0.01	0.00
Al	7.15	7.20	7.19	7.35	7.14	7.40	7.21
Fe (ii)	0.08	0.08	0.07	0.08	0.07	0.07	0.07
Ca	3.34	3.39	3.38	3.60	3.38	3.58	3.41
Na	0.72	0.69	0.67	0.53	0.72	0.49	0.67
K	0.02	0.02	0.02	0.02	0.03	0.02	0.02
TOTAL	20.06	20.08	20.04	20.09	20.07	20.06	20.06
ENDMEMBER %							
Ab	17.69	16.87	16.38	12.79	17.42	11.90	16.31
Or	0.57	0.55	0.52	0.40	0.61	0.54	0.49
An	81.74	82.58	83.10	86.81	81.98	87.56	83.20

Table 9.8 cont. Compositional range of xenolithic feldspar from aluminous xenolith TM1F, from Torr Morr [NM 414240]. Plagioclase reaction caps around spinels, and fine-grained recrystallized plagioclase found in the centres of larger plagioclase laths.

9.3 Concluding Remarks

The descriptions of the siliceous and aluminous xenoliths presented above show that the interaction and reaction of a xenolith with basic magma is a very complex, multi-stage process. The evidence for these processes is best preserved within the aluminous xenoliths. Assuming that the mullite buchites represent liquid products of partial melting of either a pelitic sediment or metasediment, *after* one or more silicic melt has been extracted (cf. Cameron, 1976), the Al-rich liquids would possibly remain relatively separate from the surrounding basalt magma due to viscosity and density differences (e.g. Grasset & Albarède, 1994); they may also have been chemically immiscible (e.g. Holgate, 1954). In such a system, extreme chemical gradients would exist, down which components could diffuse. The aluminous liquids precipitated mullite, and at the interface between the basic magma and the xenolithic liquid, plagioclase precipitated. Plagioclase and mullite may have precipitated simultaneously more-or-less continuously. It is thought that the crystallization of corundum and spinel was in response to the introduction of small amounts of basic magma into the semi-crystallized plagioclase rim, mixing with resident aluminous liquid in the melt pockets. Evidence for this multi-step crystallization and mixing process is partly deduced from the Sr and Nd isotope geochemistry of the plagioclase rims and associated melt-pockets, which is discussed in Chapter 10. However, one problem which is difficult to resolve is why some mullite buchites *do not* have reaction rims of plagioclase. It is possible that *all* the aluminous liquids reacted with basic magma and precipitated plagioclase rims, and some xenoliths lost the rims due to mechanical attrition. However, no mullite buchites with *partial* plagioclase rims have been found. Alternatively, the fact that some buchites do not have plagioclase rims may be a consequence of the time required to precipitate large amounts of coarse-grained plagioclase, compared with the residence time of the magma in the processing chamber prior to emplacement. These complex interactions provide ample opportunity for the contamination of the surrounding basic magmas. Each step of the process should leave its own unique geochemical fingerprint on the magma being contaminated. It may be possible to decipher these processes by looking at the small-scale geochemical (trace-element

and isotopic) variations within the xenoliths and their enclosing magmas. Chapter 10 discusses these processes, and examines their implications for the geochemical modelling of contamination processes in suites of basaltic-rhyolitic volcanic rocks.

CHAPTER 10

THE INTERACTION OF CRUSTAL XENOLITHS AND BASIC MAGMA

10.1 Introduction

In Chapters 3, 4 and 5, it was determined that the basic magmas of the LSSC had interacted extensively with upper-crustal lithologies. Evidence for this is not only preserved by the presence of numerous crustal xenoliths, but also within the whole-rock trace-element and isotope geochemistry of the suite. The evolution of the basic magmas can be modelled via a process of combined assimilation and fractional crystallization (AFC; DePaolo, 1981), coupled with a limited amount of magma recharge (RTF; O'Hara, 1977; O'Hara & Mathews, 1981). However, the textural and geochemical evidence preserved within the zoned plagioclase-mullite buchite xenoliths described in Chapter 9, strongly suggests that the process of interaction between the xenoliths and basic magma is far more complex than the simple models of magma contamination may suggest (*cf.* DePaolo, 1981; Fodor *et al.*, 1985; Devey & Cox, 1987; Bell *et al.*, 1994.) The following discussion examines: a) the possible origins of the crustal xenoliths; b) mechanisms of partial melt extraction; c) the small-scale evidence for the processes of magma/xenolith interaction preserved within the mullite/cordierite buchites and the zoned plagioclase-mullite buchite xenoliths; and, d) the possible wider implications of such processes to the contamination of basic magmas within the continental crust.

10.2 Origins of the crustal xenoliths

The majority of the crustal xenoliths found in the LSSC are not derived from the immediate vicinity of the intrusions, at their present crustal level. Due to the fact that they have apparently suffered less in the way of dissolution and reaction with the basic magma, the quartz-rich xenoliths generally have recognisable protoliths. Most of the quartz-rich and banded xenoliths appear to have been derived from the Moine metasedimentary succession, and sandstones and conglomerates from the Mesozoic sediments. What is unclear, however, is the ultimate origin the mullite/cordierite buchite, and plagioclase-mullite buchite xenoliths. The aluminous xenoliths show the best evidence for extensive interaction and reaction with basic magma, and deducing the origins of these rocks is important to the understanding of the contamination processes which affected the LSSC basic magmas.

Many different protoliths have been suggested for the aluminous xenoliths, with most theories being based upon trying to match bulk-rock compositions of possible protoliths to that of the xenoliths:

- (a) Highly aluminous fireclay (Thomas, 1922);
- (b) Aluminous bole (Agrell & Langley, 1958);
- (c) Jurassic shale (Cameron, 1979; Kille, 1987);
- (d) Moine pelitic schist (Cameron, 1979; Thompson *et al.*, 1986);
- (e) Lewisian amphibolite or granulite facies gneiss.

The highly aluminous nature of the glasses, and of the crystalline phases which make up these xenoliths, is consistent with their derivation from clay-rich sediment, or its metamorphic equivalent (*cf.* Thomas, 1922; Gribble & O'Hara, 1967; Kille, 1987). Unfortunately, the bulk compositions of the aluminous xenoliths do not match any of the listed possible protoliths. However, if prior to the formation of the aluminous liquids, one or more low temperature, broadly granitic melts were removed from the system, compositions approaching those of the mullite buchites could result (*e.g.* Smith, 1965; Wöner *et al.*, 1982; van Bergen & Barton, 1984; Graham, 1987; Grapes, 1986; Grunder, 1992). This was possibly not taken into account by Thomas *et al.* (1922) who considered that the aluminous xenoliths resembled a "highly aluminous fireclay". Agrell & Langley (1958) suggested an

aluminous bole as the protolith of these xenoliths. Such lithologies may be represented on Mull as lateritized ash and claystone layers which occur within the Palaeocene lava succession. However, such rocks are likely to be greatly enriched in iron when compared to the aluminous xenoliths.

Jurassic shales, exposed on the south coast of Mull, also provide a possible protolith. These were dismissed by Kille (1987) however, on the basis of their higher MgO, Fe₂O₃ and K₂O/Na₂O values. From the data of Burke *et al.* (1982) it is evident that marine carbonates in the Jurassic would have present day ⁸⁷Sr/⁸⁶Sr values of around 0.7068 to 0.7077. The ⁸⁷Sr/⁸⁶Sr ratios of Jurassic shales could therefore range from these low values up to values in excess of 0.720 depending upon the amount and source of detrital material (mica and feldspar) (*e.g.* Dasch, 1969; McCulloch & Wasserburg, 1978; Haszeldine *et al.*, 1992). These studies assumed that the Sr and Nd isotope ratios of detrital grains are not affected by sedimentary transport, deposition or diagenesis. However, it has been shown recently that the REE can be mobilised during low-temperature sandstone diagenesis (Bouch *et al.*, 1995). Bouch *et al.* 1995 showed that detrital apatite grains in lower Jurassic sandstones from the North Sea, possessed overgrowths of LREE-enriched francolite (carbonate fluor-apatite). It was suggested that REE mobilization during sandstone diagenesis may be on a scale greater than that of sampling. Initial Sr isotope ratios of plagioclase which crystallized from the aluminous liquids are in the order of 0.713 to 0.715. The aluminous liquids *could* therefore have resulted from the partial melting of a Jurassic shale, followed by the complete melting of the restite.

However, the largest problem with all of the above possible protoliths is that mullite buchites can be found within sheets which intrude the Moine metasediments, which are structurally *below* the Mesozoic and Palaeocene rocks. The only other possible starting materials therefore lie within the Moine rocks themselves (Cameron, 1976; Thompson *et al.*, 1986), or unseen rocks below these, such as Dalradian rocks which lie south of the Great Glen Fault, or Lewisian gneiss which probably underlies the whole region.

The Lewisian exposed in the Hebridean area is composed primarily of granitic orthogneiss and metabasites, although metasediments are represented in some areas (*e.g.* Fettes *et al.*, 1992). The orthogneisses would be suitable for providing granitic melts for the contamination of

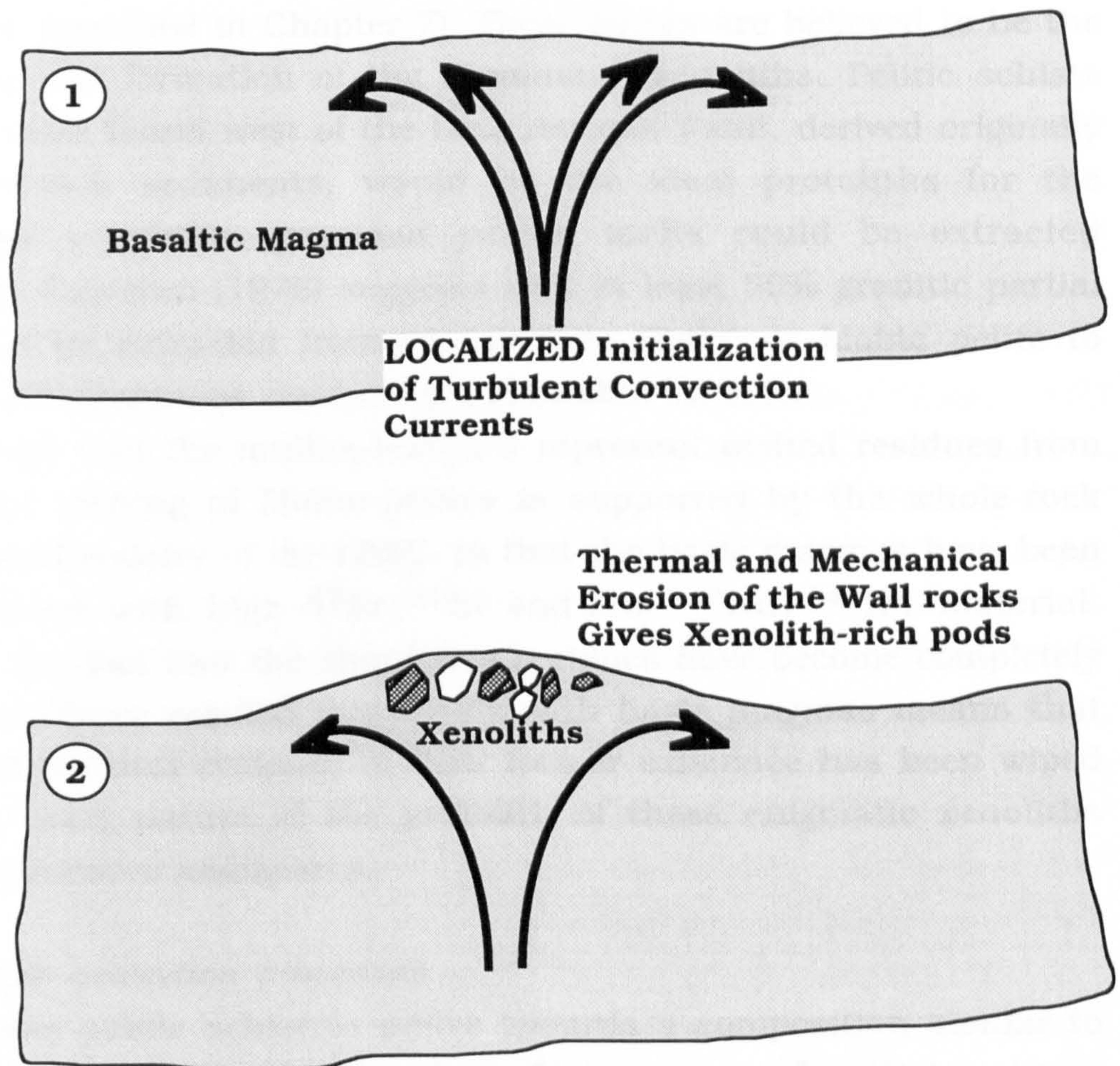


FIGURE 10.1 Schematic diagram showing the possible evolution of the xenolith-rich pods and lenses found in the Group I basaltic andesite sheet at Traigh Bhàn na Sgurra. Localized thermal and mechanical erosion of the wall rocks is caused by turbulent flow and convection currents. Xenoliths are therefore formed *in situ*.

the basic magmas. However, the partial melting of such lithologies is unlikely to leave highly aluminous restites.

The Moine succession exposed south and west of the Loch Assapol Fault on the Ross of Mull (*Figure 1.2*), contains garnetiferous pelites and semipelites, which locally contain kyanite and staurolite (the Shiaba and Assapol Groups; Holdsworth *et al.*, 1987). At Traigh Bhàn na Sgurra, where a thick Group I sheet cuts such lithologies, mullite buchite and quartzite xenoliths can be found in xenolith-rich pods and lenses (as described in Chapter 7). These lenses are believed to be the sites of *in situ* formation of the aluminous xenoliths. Pelitic schists such as those found west of the Loch Assapol Fault, derived originally from clay-rich sediments, would be the ideal protoliths for the aluminous xenoliths, provided partial melts could be extracted efficiently. Cameron (1976) suggests that at least 50% granitic partial melt must be extracted from an "average shale" or Moine pelite to produce the aluminous residues of the mullite buchites.

The concept that the mullite-buchites represent melted residues from the partial melting of Moine pelites is supported by the whole-rock isotope geochemistry of the LSSC, in that the basic magmas have been contaminated with high $^{87}\text{Sr}/^{86}\text{Sr}$ and low $^{143}\text{Nd}/^{144}\text{Nd}$ material. However, the fact that the aluminous residues have become completely molten and have reacted extensively with basic magmas means that any direct textural evidence of their former existence has been wiped out. The exact nature of the protolith of these enigmatic xenoliths remains somewhat ambiguous.

Partial melt extraction processes

For a Moine pelitic schist to evolve towards a composition similar to the LSSC aluminous xenoliths through a process of partial melting, requires that the melts are efficiently extracted. The first partial melts to form will be broadly granitic in composition (*e.g.* Barker, 1964; Brown & Fyfe, 1970; Thompson, 1981), however these will evolve as the residue becomes more and more refractory. The following discussion briefly examines, some of the concepts involved in the melt extraction process, and how this is often related to the concurrent deformation of the rocks involved.

Partial melting of rock occurs first at the grain boundaries between the reactant phases (Mehnert *et al.*, 1973). The melt pockets enlarge as melting proceeds, and these will eventually coalesce to form an

interconnected network of melt channels along the grain boundaries. Once this has occurred, the source is permeable and melt can migrate (Maaløe, 1985); this is the first percolation threshold (FPT) of Vigneresse *et al.* (1991). At around 26 to 40% partial melting, the solid matrix of the rock will break down, and the melt plus solid can flow as a magma and escape through buoyant rise (Arzi, 1978; van der Molen & Paterson, 1979; Sawyer, 1994); this is termed the second percolation threshold (SPT). During the process of diapiric uprise, the melt may segregate from its restite (Sawyer, 1994).

Within the mantle it is widely accepted that melt segregation is driven by buoyancy (Nicolas, 1989), and occurs when the FPT is reached at around 2% partial melting. Within the crust, melt segregation can occur below the SPT as long as deformation accompanies partial melting. Field studies have suggested that certain granite bodies have been derived from between 10% and 15% partial melting of their source rocks (*e.g.* Le Fort, 1981; Crawford & Windley, 1990), and experimental studies (*e.g.* Dell'Angelo & Tullis, 1988) have shown it is possible to extract as little as 5% melt from a slowly deformed rock. This latter study also demonstrated that between the FPT and the SPT, the matrix crystals become decoupled and surrounded by a thin film of melt; magma flow is in response to the applied stresses, rather than buoyancy, and probably occurs by a grain-boundary sliding process (Dell'Angelo & Tullis, 1988).

Within the crust, melt migration will only occur if there is a low-pressure site for the melt to migrate into. These sites may be present in different beds, layers, or folds, or within dilatancy structures such as shear bands, tension gashes, and boudins (Platt & Vissers, 1980).

Within a crustal xenolith in contact with flowing basic magma, similar processes of partial melt extraction probably occur. Again, melting will start at mineral grain interfaces; within pelitic rocks this is likely to involve initially the breakdown of hydrous phases such as biotite and muscovite (*e.g.* Wöner *et al.*, 1982; Grapes, 1986, 1991), followed by the melting of feldspar grains at quartz-feldspar crystal boundaries (Tuttle & Bowen, 1958; Thompson, 1981; Vielzeuf & Holloway, 1988). During syntaxis, xenolith boundaries are modified by diffusion processes which include both crystal-liquid exchange where residual crystals contact the host liquid, and liquid-liquid interdiffusion where partial melt channels meet the host magma (Green 1994). If the xenolith suffers extensive partial melting, its rigidity and mechanical

integrity will be greatly reduced (Arzi, 1978). As a result of this, unstable portions of the xenolith margin will be dislodged and entrained within the magma as it moves past the xenolith. This disaggregation will reduce xenolith size, and expose the interior of the xenolith to reaction with the magma. During this process, partial melts may be intermingled with the host magma on a very small scale (μm), and the two liquids are rapidly and efficiently homogenized due to the large area of mutual contact (Green, 1994). Such processes are likely to be most efficient where the magma flows in conduits, and the flowing magma exerts shear stresses upon the xenolith (Huppert & Sparks, 1989; Green, 1994). At Traigh Bhàn na Sgurra, the basaltic sheet has only interacted extensively with the wall rocks on a very localized scale. The presence of chilled margins is highly variable, and where no chill has developed, the country-rocks have been partially melted in a zone up to 50cm from the contact. Xenoliths also occur in sporadic pods and lenses at the top of the sheet. It is believed that these features are the result of highly localized turbulent flow (*e.g.* Kille *et al.*, 1986), and of the setting up of small convection currents within the magma (*Figure 10.1*).

10.3 Magma-xenolith interactions within the LSSC

The LSSC is remarkable, particularly within the BTVP, in that it preserves numerous crustal xenoliths in all stages of reaction with their host magmas. The xenoliths are also derived from a wide range of protoliths. The xenoliths which preserve the most detailed information concerning xenolith-magma interaction are those which started-off with a reactive mineral assemblage, such as a garnetiferous mica schist from the Moine metasedimentary succession. It has already been suggested that such rocks may represent the protoliths to the aluminous xenoliths. However, such xenoliths only represent the final stages of reaction with basic magma. Very few relatively unmodified pelitic schists have been found within the LSSC xenolith suite. Therefore, the initial stages of high temperature metamorphism (pyrometamorphism; Smith, 1969) can be best seen where pelitic schists have undergone contact metamorphism against a thick basaltic sheet. This can be seen at Traigh Bhàn na Sgurra (described in Chapter 7), where the pelitic schists of the Moine succession have been extensively, but very locally, pyrometamorphosed in a wide zone

up to 50cm from the contact with a thick Group I sheet.

The pelitic schists in the contact with the Traigh Bhàn na Sgurra sheet show many features of progressive partial melting, similar to those described by Grapes (1986, 1991) from pelitic xenoliths in magmas from the Wehr Volcano, Germany. One xenolithic sample of a "relatively" unmodified pelitic schist from the LSSC has been examined and shows identical features to those found in the contact metamorphosed pelites, and other glassy xenoliths contain variable amounts of residual phases (*e.g.* quartz and feldspar). The *preservation* of xenoliths in the early stages of partial melting is probably controlled by the residence time of the xenoliths within the basic magma, assuming the temperature of the system remains constant. Once emplaced as a sheet within the crust, the basic magma is likely to solidify quite rapidly, thus preventing the further dissolution of xenoliths. The final stages of xenolith syntexis are displayed by the completely glassy mullite and cordierite buchites. The buchites represent the restites of partial melting of a pelitic source rock, which has then been completely melted. Such a process would require a large input of heat since the restite phases are likely to have been very refractory. As a result these rocks must have had a long residence time in the basaltic magma prior to emplacement. Some of these aluminous liquids have gone one stage further by *reacting* with the basic magma to form the crystalline rims. All stages of syntexis and reaction are therefore represented within the country-rocks and xenoliths associated with the LSSC.

(a) The initial stages of pyrometamorphism

During progressive contact metamorphism, pelitic rocks would normally undergo striking changes in texture and mineral assemblage. Passing from low to high grade, pelitic rocks would generally experience a coarsening of the grain-size, and the growth of porphyroblastic minerals in the succession: chlorite, biotite, cordierite, andalusite, sillimanite (Mason, 1978; Yardley, 1989). If the rock already possesses a regional-metamorphic fabric, such recrystallization is likely to overprint the fabric already in existence. However, if the rock passes very quickly to high grade, these progressive stages of contact metamorphism are likely to be missed out. There will be little or no grain-size coarsening, and the rock is likely to preserve some vestige of its original fabric. Such conditions

are likely to be met where the country-rocks are heated quickly to very high temperatures, but also where the heat is dissipated relatively rapidly. Therefore, where relatively thick basic sheets cut pelitic country-rocks, such as in the sheet at Traigh Bhàn na Sgurra, the thermal conditions might be appropriate for the relatively rapid partial melting of the country-rock, rather than the production of a contact metamorphic "aureole".

At between 30 and 40cm away from the contact between the Moine pelitic schists and the Traigh Bhàn na Sgurra sheet, the pelites locally show the first signs of partial melting. The first melts can be found associated with decomposed biotite and muscovite, indicating that partial melting accompanied mica dehydration (*cf.* Green, 1994). Muscovite goes through an initial stage of dehydroxylation, and at higher temperatures it melts to produce corundum, mullite/sillimanite and a peraluminous melt (Reactions 9.1 and 9.2) (Grapes, 1986). Biotite breakdown also begins with a dehydroxylation and oxidation process involving the loss of H₂O and alkalis, and the oxidation of Fe²⁺, resulting in the formation of Fe-oxides (Addison *et al.*, 1969; Vedder & Wilkins, 1969). If rapid heating occurs, biotite may begin to melt without passing through this initial stage. The reaction has already been quoted in Chapter 9 (Reaction 9.6), and involves the formation of pleonaste, magnetite, Na-rich sanidine, and a peraluminous melt (Grapes, 1986).

Reactions similar to these can be seen to be occurring within the partially melted pelitic schists of the Moine at Traigh Bhàn na Sgurra. An unmetamorphosed pelitic schist from Traigh Bhàn na Sgurra is shown in *Figure 10.2a*. In a partially melted specimen (*Figure 10.2b*), original biotite crystals have been replaced by numerous tiny crystals of spinel and Fe-Ti oxides (~4µm), set in K-feldspar (*cf.* Green, 1994). Pools of recrystallized melt also occur adjacent to the decomposed biotite. These are assumed to be the sites of former muscovite crystals, since, in the unmodified rock, biotite and muscovite are generally found adjacent to each other.

At higher degrees of partial melting, melt starts to form at quartz-feldspar crystal interfaces. Edges of feldspar crystals take on a distinct "streaky" appearance which tends to blend in with the surrounding recrystallized melt. Internally, the feldspars have a mottled texture similar to the "fingerprint" texture described from the plagioclase rims of the aluminous buchites in Chapter 9. Quartz grains occasionally

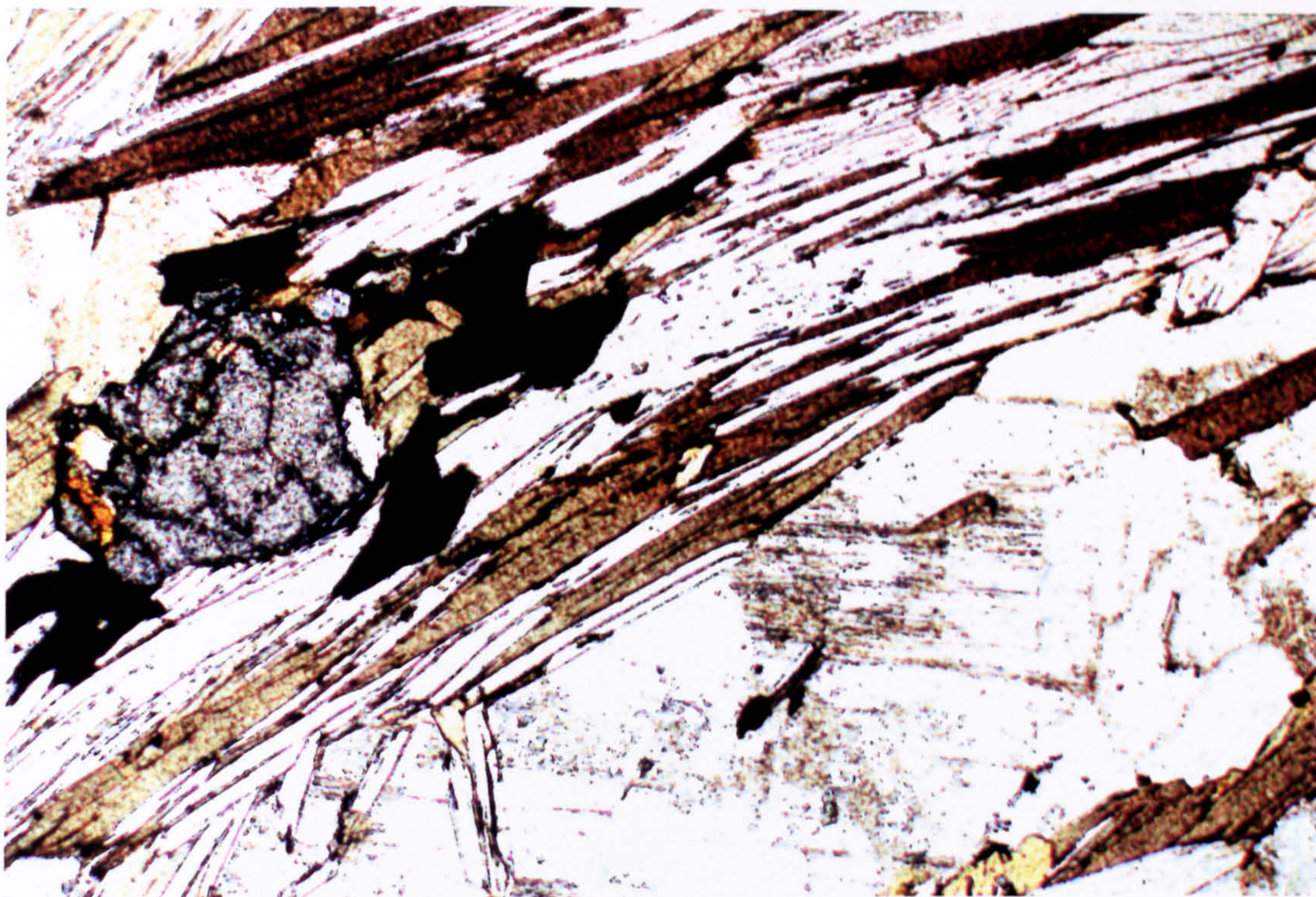


FIGURE 10.2a

Unmetamorphosed Moine pelitic schist, composed of bands of quartz and feldspar, interspersed with biotite and muscovite, and the occasional porphyroblast of garnet. (ppl; Field of view 2x3mm; Sample SOM3)

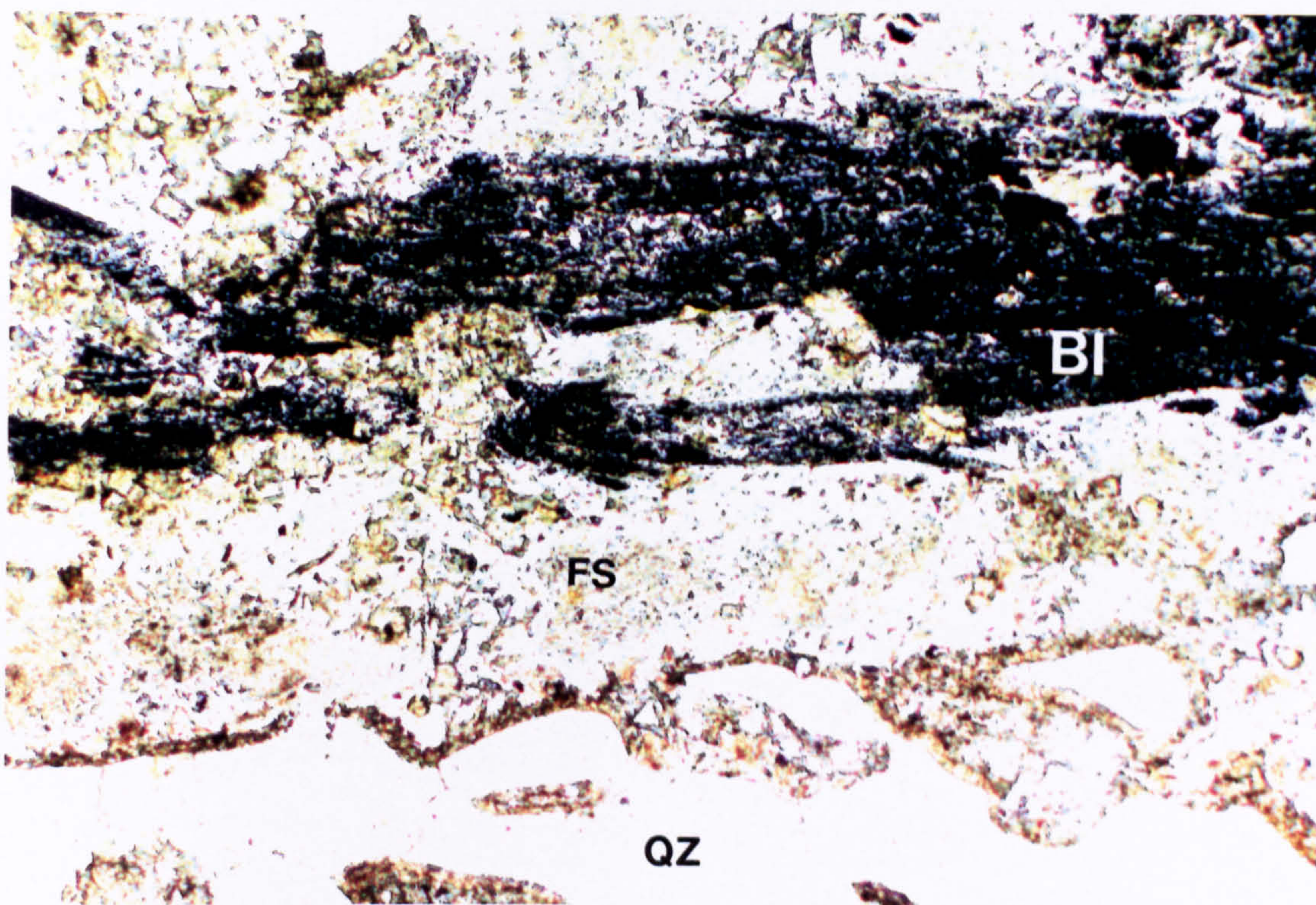


FIGURE 10.2b

The effects of partial melting on a Moine pelitic schist. Quartz (QZ) becomes highly corroded, and feldspar (FS) starts to recrystallize. Biotite (BI) breaks down to spinels, magnetite and rutile, set in peraluminous melt. Garnet is similarly decomposed. (ppl; Field of view 2x3mm; sample SOBC).

have fringes of inverted tridymite. At this stage garnet porphyroblasts have also decomposed to a mixture of spinel, magnetite and feldspar. Biotite may also be formed through garnet breakdown with the addition of potassium (Grapes, 1991). Biotite may also crystallize from the peraluminous melts generated from the melting of muscovite and the original biotite (Grapes, 1986). Evidence for growth of *new* biotite crystals can be found in the contact pelites from Traigh Bhàn na Sgurra. These often contain small euhedral "crystals" of chlorite/mica intergrowths, which are possibly the retrogressed remnants of new biotite. Retrogression to chlorite would have been in response to the passage of late, low temperature fluids through the rocks. In Chapter 7 evidence for the hydrothermal alteration of the sheet at Traigh Bhàn na Sgurra was presented. Such fluid movement would have undoubtedly affected the country-rocks immediately adjacent to the sheet. Mullite has also been identified within these contact rocks

The mineral compositions of biotite, muscovite, plagioclase and garnet from an unmodified pelitic schists are given in *Table 10.1a*. In contrast, *Table 10.1b* lists the composition of restite phases (plagioclase and spinel) from the pyrometamorphosed contact pelitic schist, along with analyses of the feldspar which has crystallized from the produced melt. The spinel associated with the breakdown of biotite is significantly enriched in Fe when compared to the spinels associated with the crystallization of the aluminous melts of the mullite buchites (see *Table 9.7*). This is probably due to the Fe-rich nature of the original biotite. Restitic plagioclase is distinctly more calcic than the original plagioclase (An₄₂ compared with An₂₀). The melts generated in the contact pelites are peraluminous, near minimum granitic compositions, very similar to the Group III rhyolites. These have generally crystallized to a microcrystalline mixture of K-feldspar and quartz. Also shown in *Table 10.1b* is an analysis of what appears to be chlorite which is probably replacing small euhedral biotite. Again this is very Fe-rich. However, the high alkali contents of this phase suggests that the biotite has only partially retrogressed, and that some vestige of biotite is still present.

	BIOTITE	MUSCOVITE	GARNET	PLAGIOCLASE
SiO ₂	35.53	46.01	37.09	62.26
TiO ₂	2.44	0.47	0.01	0.05
Al ₂ O ₃	18.04	34.33	20.84	24.07
MgO	8.35	0.87	2.11	n.d.
CaO	0.01	0.00	2.24	5.90
MnO	0.14	0.04	5.87	n.d.
FeO	22.34	1.71	31.89	0.01
Fe ₂ O ₃	n.d.	n.d.	0.21	n.d.
Cr ₂ O ₃	n.d.	n.d.	0.03	n.d.
Na ₂ O	0.16	0.88	n.d.	8.13
K ₂ O	9.16	10.32	n.d.	0.11
F	0.24	0.20	n.d.	n.d.
Cl	0.01	0.00	n.d.	n.d.
TOTAL	96.42	94.82	100.29	100.53
Formula Units (24 O,OH,F,Cl)	(24 O,OH,F,Cl)	(24 Oxygens)	(8 Oxygens)	
Si	5.43	6.19	6.00	2.75
Ti	0.28	0.05	0.00	0.00
Al	3.25	5.44	3.97	1.25
Mg	1.90	0.17	0.51	-
Ca	0.00	0.00	0.39	0.28
Mn	0.02	0.01	0.80	-
Fe ⁱⁱ	2.86	0.19	4.31	0.00
Fe ⁱⁱⁱ	-	-	0.03	-
Cr	-	-	0.00	-
Na	0.05	0.23	-	0.70
K	1.79	1.77	-	0.01
TOTAL	15.58	14.05	16.01	4.98

Table 10.1a Mineral compositions of biotite, muscovite, garnet and feldspar from a Moine pelitic schist from Traigh Bhàn na Sgurra. n.d. = not determined.

	SPINEL	PLAGIOCLASE	K-FELDSPAR	MELT	"CHLORITE"
SiO ₂	0.11	58.84	64.33	76.08	39.29
TiO ₂	0.59	0.01	0.10	0.17	0.07
Al ₂ O ₃	62.99	25.97	19.60	14.87	28.64
MgO	13.00	n.d.	n.d.	0.01	4.23
CaO	n.d.	7.76	0.57	1.03	0.64
MnO	0.17	n.d.	n.d.	0.03	0.10
FeO	21.75	0.08	0.17	0.06	13.64
Fe ₂ O ₃	0.96	n.d.	n.d.	n.d.	n.d.
Cr ₂ O ₃	0.11	n.d.	n.d.	n.d.	n.d.
Na ₂ O	n.d.	5.22	4.45	5.47	0.28
K ₂ O	n.d.	0.89	9.89	3.22	1.03
TOTAL	99.68	98.78	99.12	100.94	87.92
FORUMLA UNITS (32 O)					
		(32 O)	(32 O)		(36 O, OH)
Si	0.08	10.60	11.77	-	7.40
Ti	0.09	0.00	0.01	-	0.01
Al	15.57	5.51	4.23	-	6.36
Mg	3.43	-	-	-	1.19
Ca	-	1.50	0.11	-	0.13
Mn	0.03	-	-	-	0.02
Fe ⁱⁱ	4.49	0.01	0.03	-	2.15
Fe ⁱⁱⁱ	0.20	-	-	-	-
Cr	0.01	-	-	-	-
Na	-	1.82	1.58	-	0.10
K	-	0.21	2.31	-	0.25
TOTAL	23.91	19.67	20.04	-	17.59

Table 10.1b Compositions of restite phases, melt recrystallization phases, and a peraluminous melt, from a partially melted Moine pelitic schist from Traigh Bhàn na Sgurra. Spinel is associated with the breakdown of primary biotite. Plagioclase is a restite composition. K-feldspar has crystallized from a melt such as the composition shown. The chlorite is thought to be the result of retrogression of biotite which also crystallized from the melt. n.d. = not determined.

(b) Production of the mullite buchites

The process of melt production from crustal xenoliths will continue provided the temperature of the magma does not fall. Melting could also continue under conditions of falling temperature if fluid were added to the system. Melts will become more siliceous as more quartz is consumed. Within the LSSC, *extraction* of these granitic partial melts appears to have been very efficient since very few partially digested xenoliths have been found which contain peraluminous glasses or the crystalline equivalent. As the melts are extracted, the residue will become progressively enriched in refractory elements such as Al, Ca, Ti and Mg, whilst becoming impoverished in elements such as Si, K, Na, Rb and Ba (Smith, 1965, 1969; MacRae & Nesbitt, 1980). The refractory phases associated with such chemical changes at low pressure include Ca-plagioclase, spinel, corundum and aluminosilicates (*e.g.* Read, 1931; Smith, 1965; Gribble & O'Hara, 1967; Gardien *et al.*, 1995). These phases are found within the crystalline rims of the aluminous xenoliths. However, here they are considered to have crystallized from a melt rather than being restite phases, due to the often euhedral shapes of the crystals, and the oscillatory zoning displayed by the plagioclase. The LSSC *xenolith* suite contains very little evidence for a truly restitic origin of these mineral assemblages. However, spinel, Ca-plagioclase and mullite can be found within the pyrometamorphosed contact Moine pelites from Traigh Bhàn na Sgurra, as described previously.

Within the LSSC the fusion of the crustal xenoliths has gone a stage further than is seen in the contact metamorphosed pelites, in that the majority of the xenoliths have become completely molten at some stage. The formation of these xenoliths may have occurred in one of two ways; a) the wall rocks of the magma conduit became completely molten *before* the xenoliths were plucked-off, or b); the xenoliths were disaggregated from the wall-rocks *prior* to complete fusion. Of these two possibilities, the second case would appear to be more likely. As the wall-rocks of the magma conduit started to melt, the granitic liquids produced would be continually swept into the main body of the magma, especially if the magma flow was turbulent. It is envisaged that the aluminous liquid would not have sufficient cohesion to be form xenoliths. However, if the xenoliths were completely melted, *after* inclusion into the magma, the aluminous liquids may

remain isolated due to density and viscosity differences, and possibly chemical immiscibility.

Where complete fusion has occurred, the xenoliths consist of a mass of tiny mullite needles and/or cubes of cordierite set in aluminous glass, as described in Chapter 9. Due to their euhedral shape, it is considered that these phases have also crystallized from the liquid, rather than representing "true" restite phases (cf. Cameron, 1976; Kille, 1987). Occasionally, these glassy xenoliths contains unfused, residual quartz grains. These quartz grains are often fringed by tabular crystals of inverted tridymite.

The production of these highly aluminous liquids however provides a major problem. Upon examination of the relevant phase diagrams which contain the probable residual phases involved in the melting process (*i.e.* plagioclase, spinel, mullite, corundum), it can be seen that the temperatures involved in such systems appear prohibitively high. Figures 10.3, 10.4 and 10.5 show the systems FeO-SiO₂-Al₂O₃, CaO-SiO₂-Al₂O₃ and MgO-SiO₂-Al₂O₃ respectively (Osbourn & Muan, 1960). Temperatures within these systems range up to, and exceed, 2000°C, well in excess of the 1000-1200°C associated with the liquidus temperatures of normal basaltic magmas. However, the experiments carried out to produce these phase diagrams were conducted at 1atm pressure and under anhydrous conditions (Osbourn & Muan, 1960). The effect of adding water to a system is usually to lower the liquidus temperatures of the phases involved, provided that the mineral phases are anhydrous. The effect of confining pressure is to alter the size of the stability fields of the phases involved, and therefore, to alter which phases can coexist stably (Ehlers, 1972). Since the majority of the mullite buchites contain vesicles (now filled with silica and zeolites), it is possible that the xenoliths still contained some dissolved fluids, associated with the final breakdown of the hydrous phases. Since the mullite buchites are TiO₂-rich (up to 4 wt%), biotite (or rutile ?) may have been residual after the initially extraction of granitic partial melts. Biotite would have therefore contributed H₂O to the system on the melting of the restite, thus lowering the liquidus temperature. The presence of biotite in the restite may also explain the high K₂O contents of the mullite buchite glasses noted in Chapter 9. It is therefore considered possible that the complete fusion of an aluminous restite could be conducted at normal basaltic magma liquidus temperatures. In addition, it is possible that

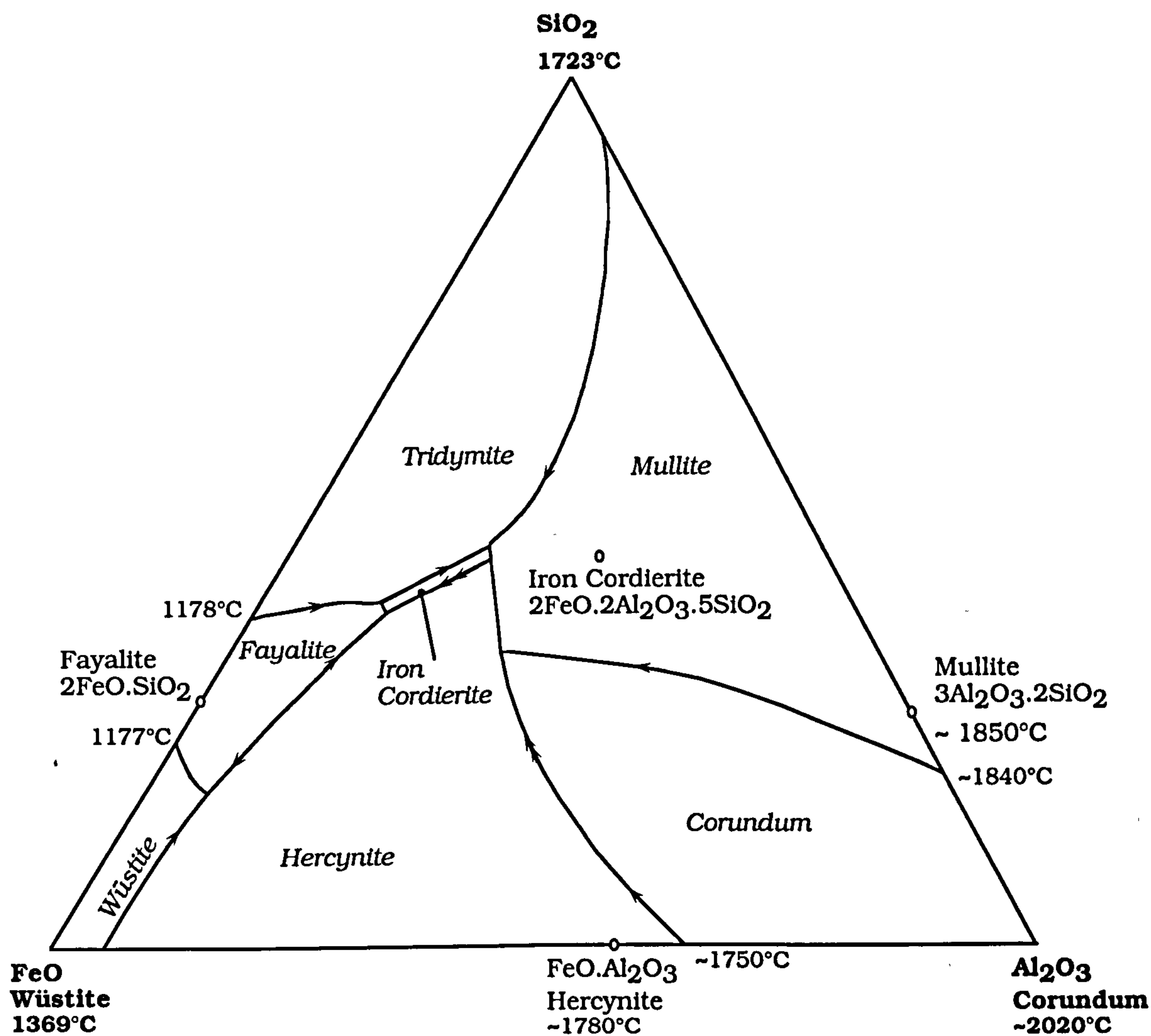


FIGURE 10.3 Liquidus surfaces in the system FeO-SiO₂-Al₂O₃ at a pressure of 1atm. Double arrows indicate resorptional relationships. (after Osborn & Muan, 1960)

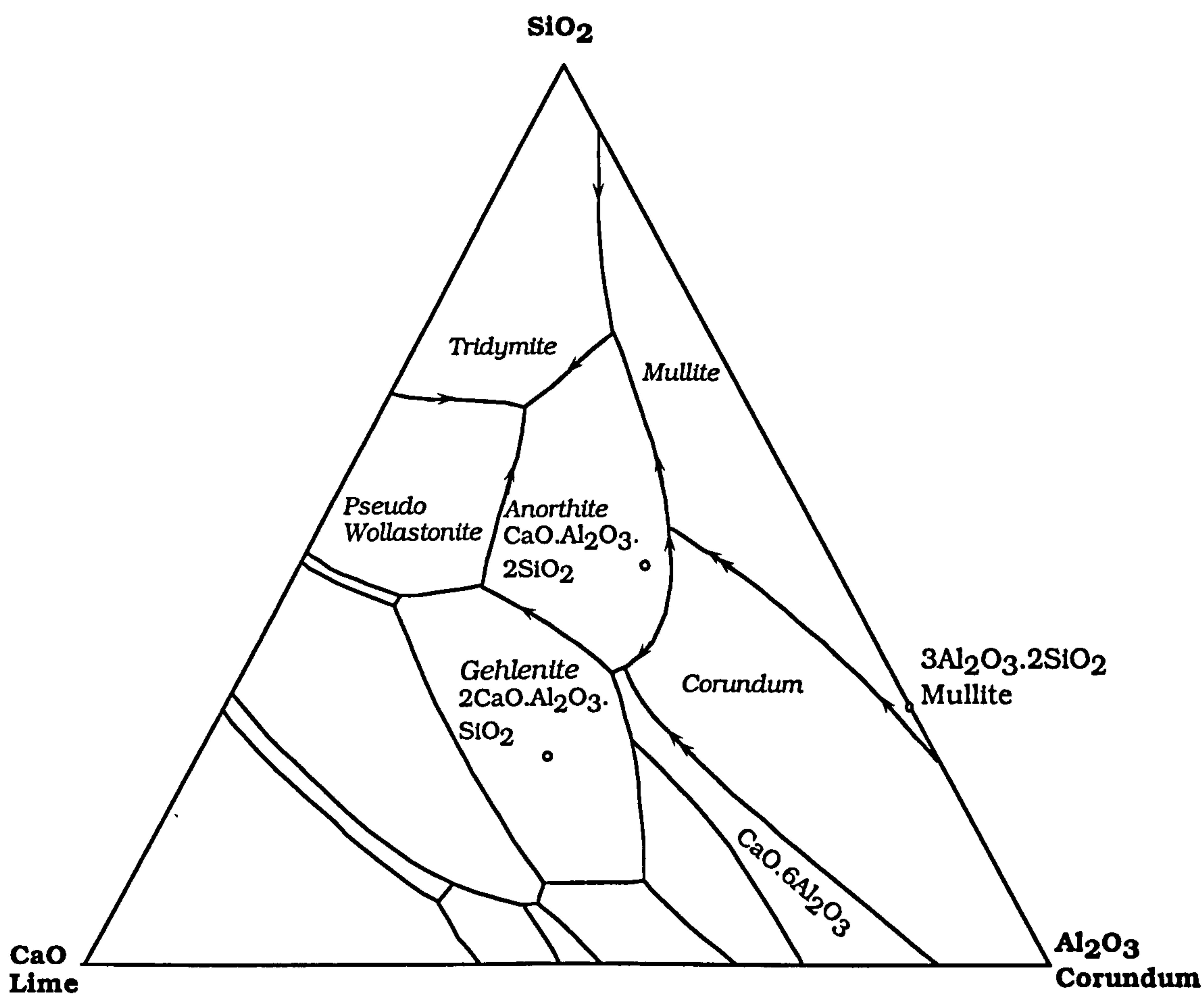


FIGURE 10.4a Liquidus surfaces in the system $\text{CaO-SiO}_2\text{-Al}_2\text{O}_3$ at a pressure of 1 atm. Double arrows represent resorptional relationships. (after Osborn & Muan, 1960)

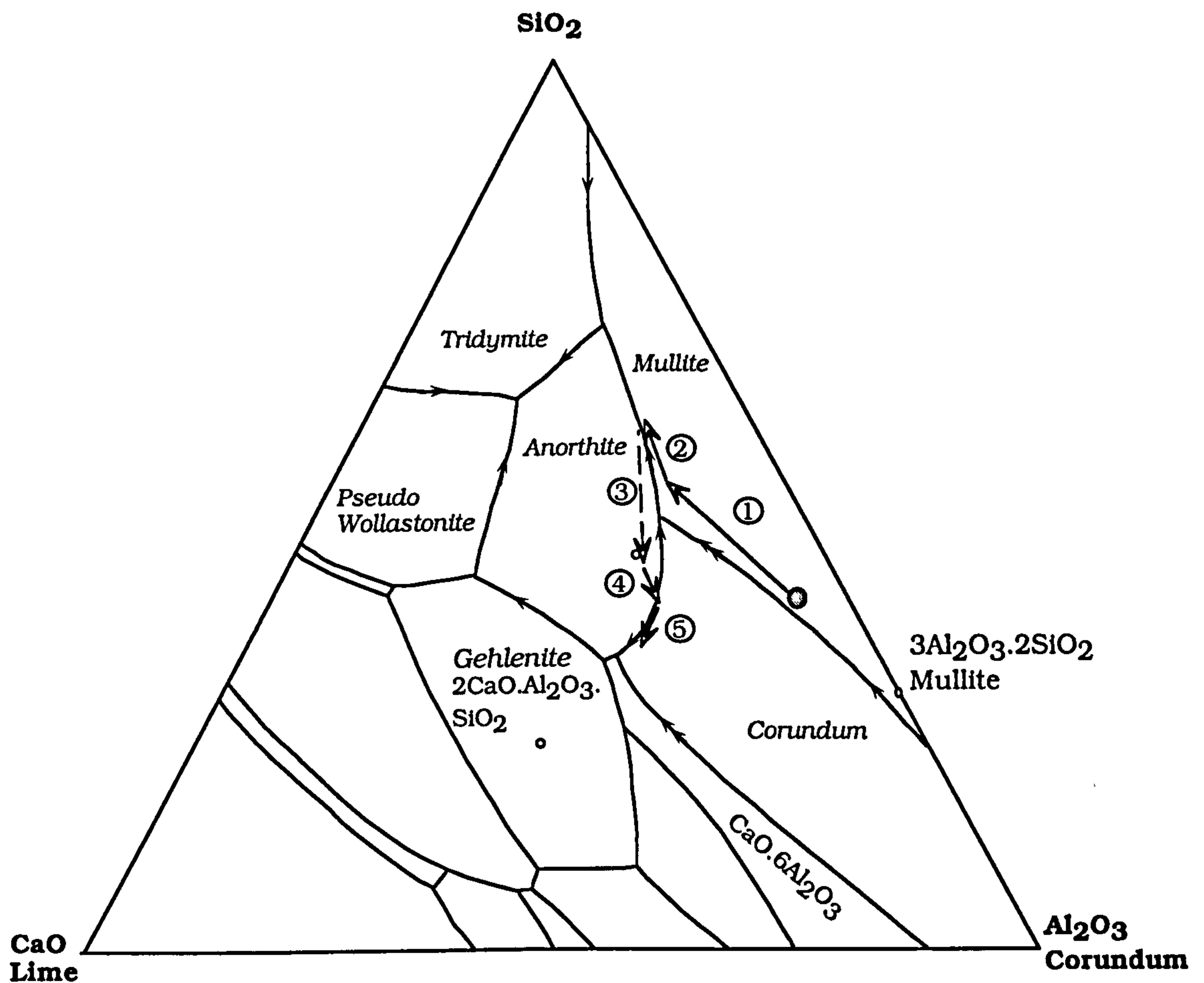


FIGURE 10.4b Liquidus surfaces in the system CaO-SiO₂-Al₂O₃ at a pressure of 1atm (after Osborn & Muan, 1960), showing a possible crystallization path of an aluminous xenolith.

● = Hypothetical starting composition

- (1) Crystallization of mullite
- (2) Crystallization of mullite + anorthite down cotectic
- (3) Mixing with small amount of basalt moves composition into anorthite field.
- (4) Crystallization of anorthite towards anorthite/corundum cotectic.
- (5) Crystallization of anorthite + corundum down cotectic.

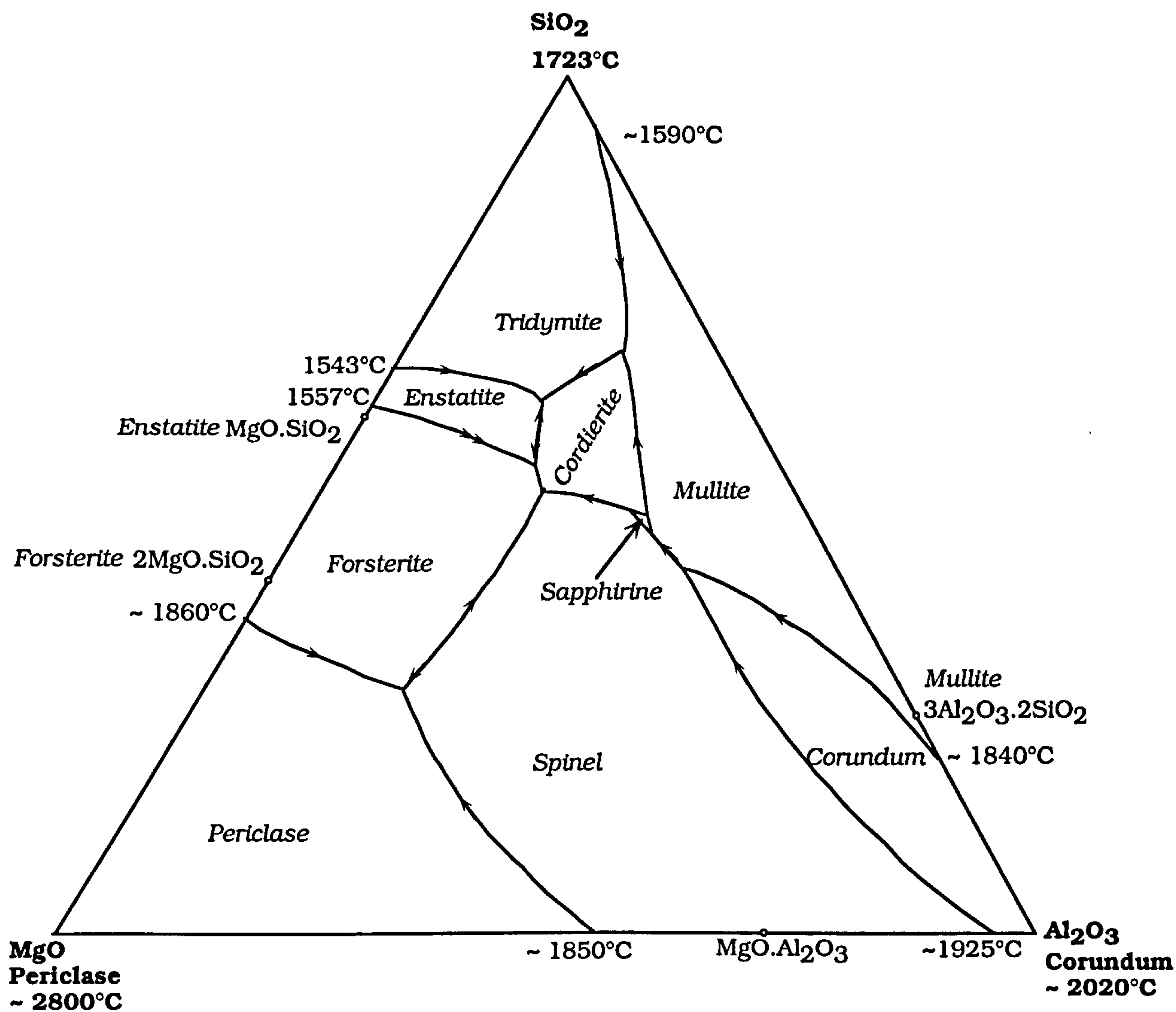


FIGURE 10.5 Liquidus surfaces in the system MgO-SiO₂-Al₂O₃ at a pressure of 1atm. Double arrows represent resorptional relationships. (after Osborn & Muan, 1960)

since the LSSC basic magmas may have been generated in an environment of high extension (high β factor, Chapter 8) and of higher than normal mantle T_p , they may have reached high crustal levels in a slightly superheated condition due to rapid decompression. This could also help to overcome the problem of melting refractory residues.

(c) The crystallization of the plagioclase-spinel-corundum rims

The phase relationships shown in *Figures 10.3 to 10.5* are also pertinent to the question of how the mullite buchites interacted with enclosing basaltic magma during the crystallization of the plagioclase rims. All the phases which appear in these rims occur within the three depicted ternary systems and, as such, crystallization histories and crystal-liquid reactions can be predicted and related to the textures found within the rims.

Since the glassy cores to the zoned mullite buchite-plagioclase xenoliths contain mainly mullite (\pm corundum), and also since it is thought that some of the mullite buchites may not have developed reaction rims due to short residence times in the basaltic magma, the mullite must have been the first to crystallize from the melt (*cf.* Cameron, 1976). This would mean that the liquid had a composition that lies within the mullite primary phase volume on the relevant phase diagrams. Upon cooling the liquid would evolve away from mullite, towards the field of anorthite (in the system $\text{CaO-SiO}_2\text{-Al}_2\text{O}_3$), hercynite (in the system $\text{FeO-SiO}_2\text{-Al}_2\text{O}_3$), and cordierite (in the system $\text{MgO-SiO}_2\text{-Al}_2\text{O}_3$). If the system were MgO- and FeO-rich, the mullite/cordierite buchites could be the result of simple down temperature equilibrium crystallization. The amount of MgO and FeO in the system would be controlled mainly by the modal amount and composition of the mafic minerals in the protolith. Alternatively, liquids capable of crystallizing cordierite could result from the slightly more extensive mixing of basaltic magma with the aluminous liquids (*cf.* Bailey *et al.*, 1924; Thomas, 1922).

Within the zoned mullite buchite-plagioclase xenoliths, textural evidence suggests that plagioclase was the next phase to crystallize. Anorthite would precipitate simultaneously with mullite, and the liquid would evolve towards the silica primary phase volume, where tridymite would join the crystallizing assemblage (in the system $\text{CaO-SiO}_2\text{-Al}_2\text{O}_3$). Since tridymite (or quartz) is not a phase found within the crystalline

rims, there must have been a shift in liquid composition to enable the crystallization of corundum and spinel (see crystallization paths in *Figure 10.4b*).

Corundum and spinel are frequently texturally associated with melt-pockets. It is suggested therefore, that the mixing of small amounts of basaltic magma with the aluminous liquid on a very localized scale, in isolated melt pockets was sufficient to shift liquid compositions into new primary phase volumes (see crystallization paths in *Figure 10.4b*). These hybrid liquids crystallized corundum and/or spinel, and plagioclase. Since the liquids had evolved away from the mullite primary phase volume, the plagioclase that crystallized in the melt pockets, along with the spinel and corundum, was free of mullite inclusions. The melt pockets eventually had compositions capable of crystallizing plagioclase and minor pigeonite.

The mixing of basic magma and aluminous liquids probably took place after a considerable amount of the plagioclase rim had crystallized. This would have insured that the melt pockets remained relatively isolated, and that the hybrid liquids could evolve along separate crystallization paths.

Many of the specific textures within the crystalline rims can be explained in terms of crystallization, mineral-liquid and mineral-mineral reactions within the ternary phase diagrams depicted, and also within the pseudo-quaternary system forsterite-diopside-anorthite-silica (*Figures 10.6a* and *10.6b*). For example, corundum occasionally occurs within the central glassy portion of the zoned xenoliths. Here the glass is completely free of mullite needles, suggesting that the mullite reacted with the liquid to form corundum. Within the system $\text{CaO-SiO}_2\text{-Al}_2\text{O}_3$ (*Figure 10.4b*), corundum has a reaction relationship with the liquid along the lower portion of the mullite-corundum field boundary (Ehlers, 1972), with the following reaction occurring :-



This reaction involves the loss of heat from the system (i.e. "down temperature"). The reverse reaction must therefore require to input of heat, possibly through the mixing of fresh basaltic magma with the xenolithic liquids.

The fine-grained plagioclase "armour" found around many of the

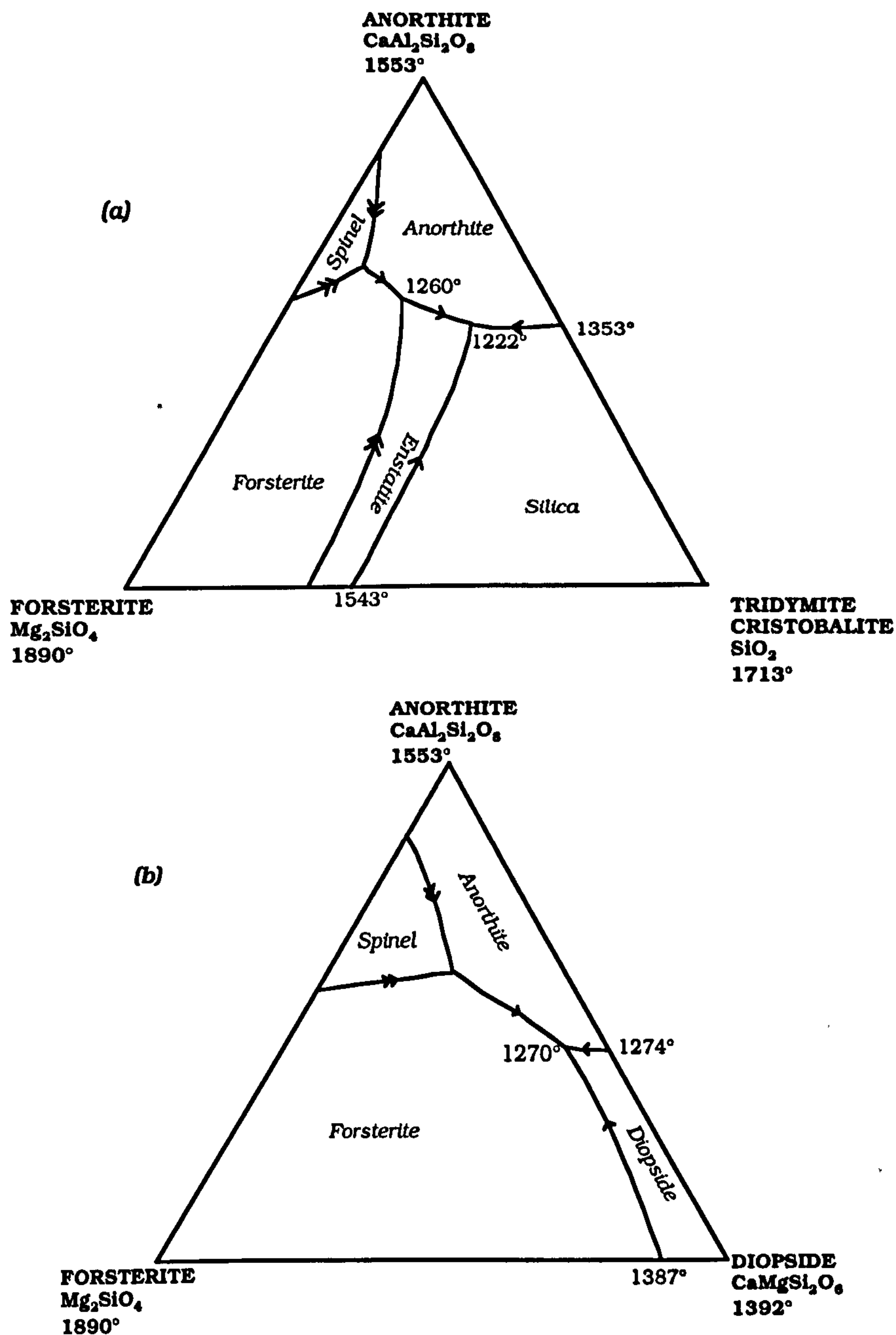


FIGURE 10.6

a) Liquidus projection for the system forsterite-anorthite-silica at 1 atm pressure (after Andersen, 1915) .

b) Liquidus projection for the system forsterite-diopside-anorthite at 1 atm pressure (after Osborn & Tait, 1952).

These ternary systems are part of the pseudo-quaternary system forsterite-diopside-anorthite-silica. The spinel field in these diagrams appears even though this compound cannot be represented in these systems as an end-member compound. Spinel has a reactionary relationship with the liquid, in which anorthite and forsterite are the products. The texture of finely crystallized Ca-plagioclase around skeletal pleonaste in many of the LSSC aluminous xenoliths suggests that a similar reaction between spinel and liquid may have occurred in the xenolith system.

skeletal spinels in the plagioclase rims (*Figure 9.30*) also suggests that the spinel has reacted with the liquid. Within the pseudo-quaternary system forsterite-diopside-anorthite-silica (*Figures 10.6a* and *10.6b*) there is a large stability field for spinel, even though this compound cannot be represented as a pure end-member in these diagrams. Spinel has a reaction relationship with the liquid, resulting in the precipitation of plagioclase (Osborn & Tait, 1952).

Although the composition of the aluminous liquids is not strictly applicable to this system, the texture shown in *Figure 9.30* suggests that a similar relationship between spinel and liquid existed (*cf.* Pedersen, 1978).

(d) Geochemical evidence for complex magma/xenolith interactions

Further evidence for these complex crystallization histories and magma/xenolith interactions and reactions can be found in the trace-element and isotope geochemistry of the zoned aluminous xenoliths.

Figure 10.7 is a chondrite-normalized REE diagram for the components of a mullite buchite-plagioclase xenolith. REE analyses from the crustal xenoliths are presented in Appendix II. Shown are the REE profiles of the buchitic core, the plagioclase-corundum-(\pm spinel) assemblage directly adjacent to the core, the plagioclase-spinel-(\pm corundum) assemblage directly adjacent to the host magma from one of the zoned xenoliths, and a profile of the host magma. All profiles are strongly LREE-enriched. The buchitic core has LREE abundances at between 70 and 40 times chondritic, and HREE at between 40 and 50 times chondritic ($(\text{Ce/Yb})_n = 1.77$). It also possesses a very deep negative Eu anomaly ($\text{Eu/Eu}^* = 0.052$). The plagioclase immediately adjacent to the core has LREE abundances between 250 and 70 times chondritic, and HREE abundances between 60 and 20 times chondritic ($(\text{Ce/Yb})_n = 12.88$). Surprisingly, it also has a deep negative Eu anomaly ($\text{Eu/Eu}^* = 0.166$). In contrast, the plagioclase nearer the host basalt has REE abundances between 70 and 3 times chondritic, exhibiting a relatively smooth profile ($(\text{Ce/Yb})_n = 13.53$), with no Eu anomaly. The REE profile for the host basalt is typical for an evolved member of Group I, with LREE-enrichment ($(\text{Ce/Yb})_n = 6.5$), and a slight negative Eu anomaly ($\text{Eu/Eu}^* = 0.75$).

The REE are generally incompatible with respect to plagioclase crystallization. The one exception is Eu, which is progressively

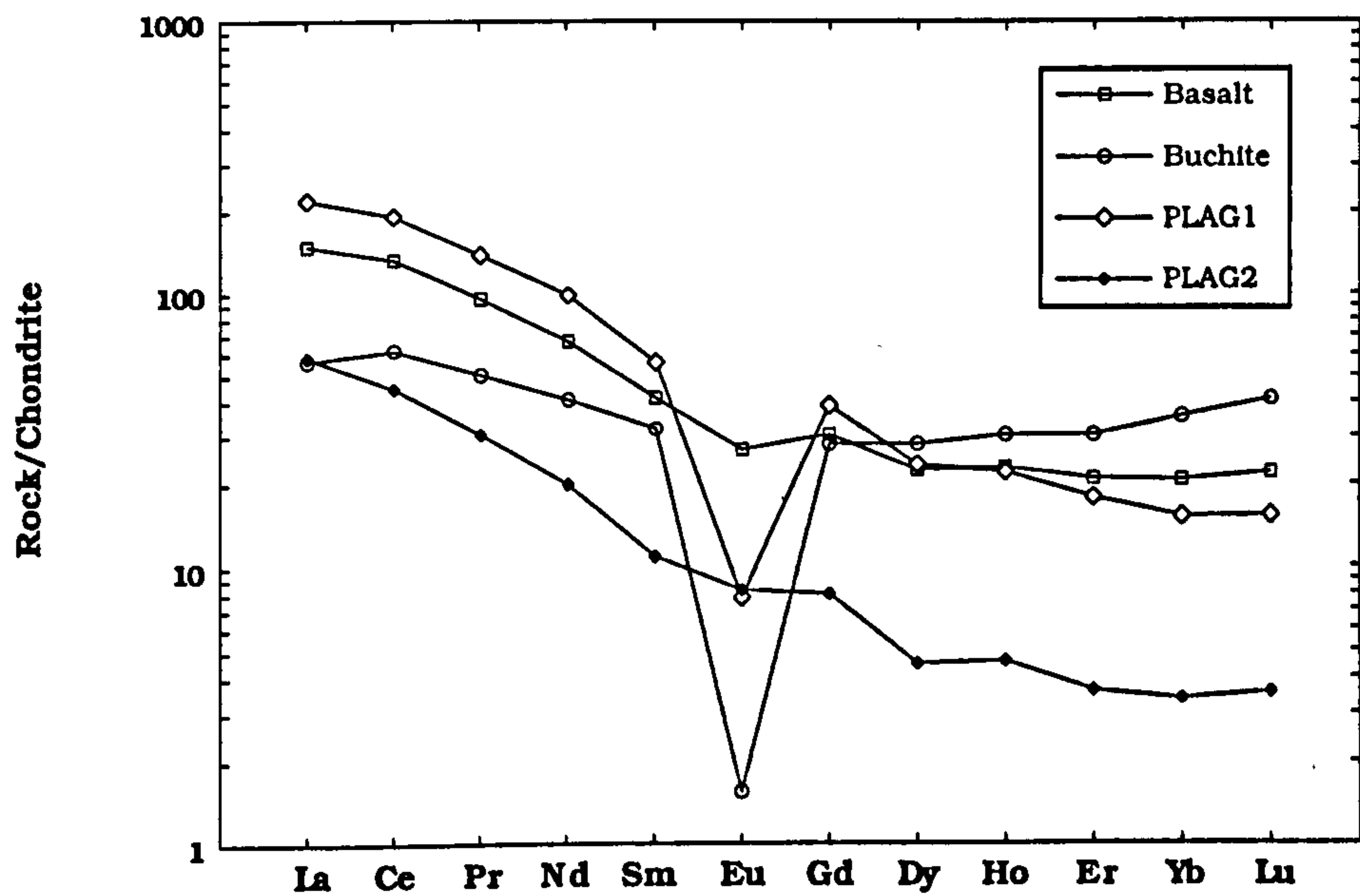


FIGURE 10.7 Chondrite normalized REE profiles for components of a zoned mullite buchite - plagioclase aluminous xenolith.
 PLAG 1 = Plagioclase next to buchite core
 PLAG 2 = Plagioclase next to basalt contact

partitioned into the plagioclase as the oxygen fugacity of the system decreases (Drake & Weill, 1975). The first plagioclase to crystallize from a liquid, in this case the aluminous buchite, would be expected to have low total REE contents, and possibly a positive Eu anomaly. The liquid will become enriched in the full range of the REE except Eu which will become progressively depleted in the melt. Later plagioclase to crystallize may well have a negative Eu anomaly due to the previous depletion of this element. The total amount of the REE in the plagioclase will increase as their concentration in the melt increases (provided that the distribution coefficients for the REE in plagioclase remain constant through this process). However, due to their incompatibility, the concentration of REE in the melt should always be greater than that in the plagioclase crystallizing from it. It is therefore surprising that the plagioclase adjacent to the mullite buchite has a greater concentration of the REE than the glassy core. This can be explained by the fact that the buchites contain numerous needles of mullite, which are effectively microphenocrysts. These will have the effect of diluting the trace-element concentrations of the analysed rock. The mullite-buchites, as analysed, therefore do not represent true liquid compositions. Taking this into account, however, the REE profiles from the zoned xenoliths are consistent with the theory of crystallization outlined above. They also suggest that the plagioclase rim started to crystallize at the contact between the aluminous liquid and the enclosing basalt, although oscillatory zoning within the plagioclase at the contact suggests limited "outward" growth.

A diagrammatic section through a zoned plagioclase-mullite buchite xenolith (PMFX1) is shown in *Figure 10.8* (as seen in Chapter 9, *Figure 9.11*). This xenolith has been analysed in detail for Sr and Nd isotope ratios, and these values are depicted on the figure. Full Sr and Nd analyses are presented in Appendix II. Assuming that the protolith for the aluminous xenoliths is a Moine pelitic schist, any melts derived from this source would be expected to have high $(^{87}\text{Sr}/^{86}\text{Sr})_{58}$ and low $(^{143}\text{Nd}/^{144}\text{Nd})_{58}$. The plagioclase which crystallized from the aluminous liquids in xenolith PMFX1 has an elevated $^{87}\text{Sr}/^{86}\text{Sr}_i$ at between 0.7136 and 0.7147 (*Figure 10.8*) which is, in part, consistent with the derivation of the aluminous liquids from the Moine metasediments. However, since the Sr isotope values for two analysed Moine pelites are both in excess of 0.7283, it is possible that the

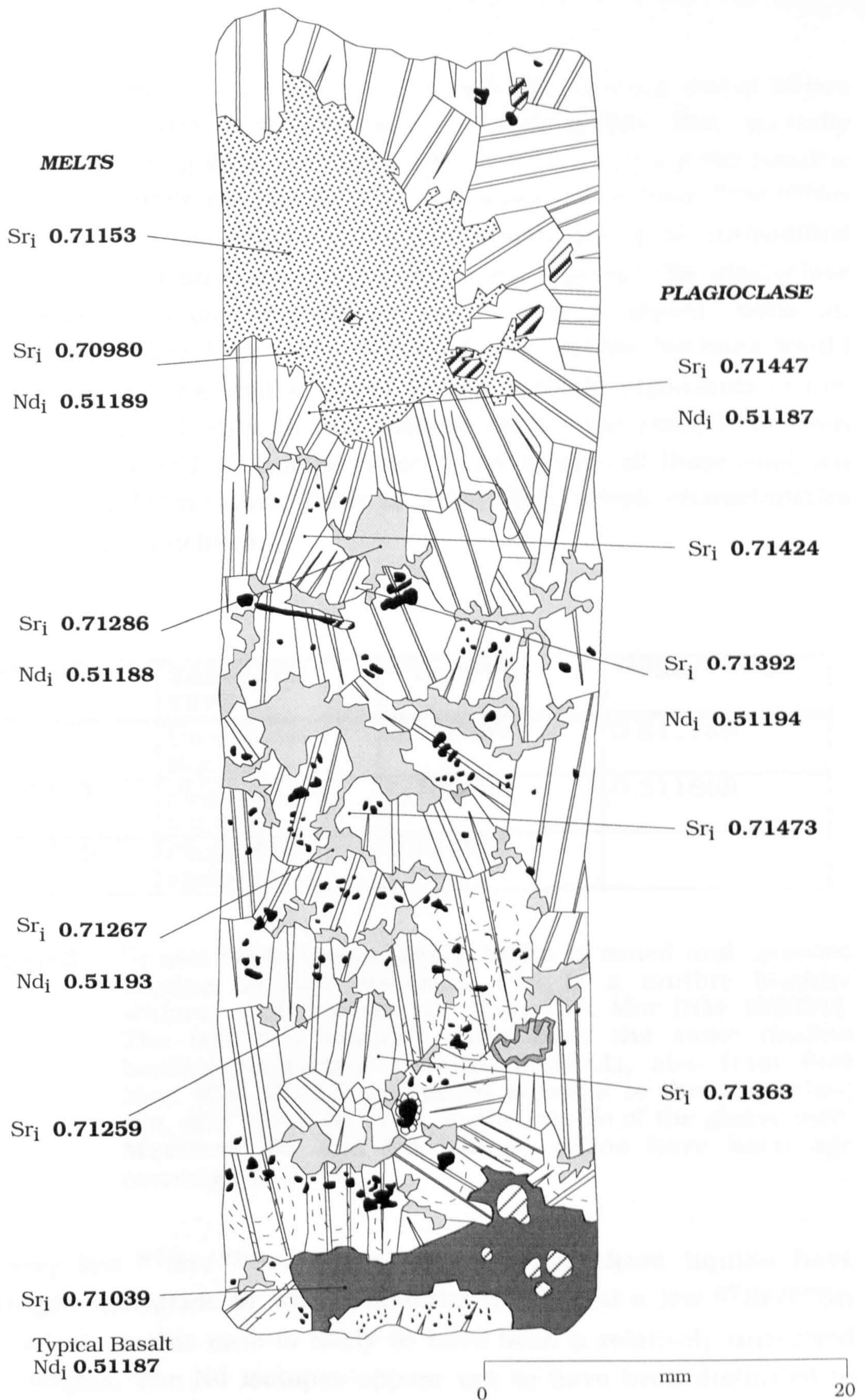


FIGURE 10.8 Diagrammatic section through aluminous xenolith PMFX1 showing position of sample points, and $^{87}\text{Sr}/^{86}\text{Sr}_i$ and $^{143}\text{Nd}/^{144}\text{Nd}_i$ ratios of plagioclase, mullite buchite and melt pockets. Isotope ratios age corrected to 58Ma. See Figure 9.11 for key to diagram.

aluminous liquid had exchanged Sr isotopes to a certain extent *before* the plagioclase rim started to grow. If Moine pelites were partially melting, interacting with, and concurrently contaminating the basaltic magma, the aluminous liquids would be expected to have $^{87}\text{Sr}/^{86}\text{Sr}_i$ values which lie somewhere between the extremes of an unmodified Moine pelite and an uncontaminated basalt magma. The plagioclase may therefore have crystallized from such a liquid, with an intermediate $^{87}\text{Sr}/^{86}\text{Sr}_i$ value. Therefore, the mullite buchites would be expected to have similar upper crustal isotopic signatures. Three mullite buchites, both with and without plagioclase rims, have been analysed for Sr and Nd isotope ratios. Surprisingly, all those analysed have low $^{87}\text{Sr}/^{86}\text{Sr}_i$ values. Table 10.2 lists the isotopic characteristics of three mullite buchites.

SAMPLE No.	XENOLITH TYPE	$^{87}\text{Sr}/^{86}\text{Sr}_i$	$^{143}\text{Nd}/^{144}\text{Nd}_i$
PL1	Un-rimmed Buchite	0.707397	0.511789
MULL BUCH	Plagioclase rimmed	0.709803	0.511888
MUL GLASS	Plagioclase rimmed	0.711525	-

Table 10.2 Sr and Nd isotopic characteristics of zoned and unzoned mullite buchite xenoliths. PL1 is a mullite buchite without a plagioclase rim from Port Mor [NM 435239]. The last two samples come from the same mullite buchite-plagioclase xenolith (PMFX1), also from Port Mor. MUL GLASS was taken adjacent to the plagioclase rim, and MULL BUCH from the middle of the glassy core. Measured Sr and Nd isotope ratios have been age corrected to 58Ma.

The very low $^{87}\text{Sr}/^{86}\text{Sr}_i$ ratios suggest that these liquids have exchanged radiogenic Sr with a material which had a low $^{87}\text{Sr}/^{86}\text{Sr}_i$ ratio, which in this case is likely to have been a relatively unevolved basic magma. The Nd isotopes appear not to have been disturbed to any great extent, in that they are almost identical to values measured from Moine pelitic schists from Traigh Bhàn na Sgurra.

The intermediate initial Sr isotope ratios of the plagioclase implies that they grew before the Sr isotope ratio of the central glass was reset

to its present day value. The Sr isotope ratios of plagioclase is less likely to be reset in such a manner (Gilotti & Casserly, 1994). It is suggested, therefore, that a basic magma partially melted Moine pelites to produce an aluminous restite. This was then completely fused. During this process, the basalt would have become concurrently contaminated with the extracted granitic partial melts, some of which segregated to form the Group III sheets, and also exchanged Sr isotopes with the aluminous liquids, resulting in the basalt and aluminous liquids having very similar "intermediate" $^{87}\text{Sr}/^{86}\text{Sr}_i$ values. The subsequent reaction of the aluminous liquids and enclosing basic magma resulted in the precipitation of the plagioclase rims. The plagioclase would acquire the same intermediate $^{87}\text{Sr}/^{86}\text{Sr}_i$ value. Small amounts of basaltic magma infiltrated the plagioclase rims via cracks in the plagioclase framework, mixed with the resident aluminous liquids, and caused the precipitation of spinel, corundum and further plagioclase within the melt pockets. Melting textures within the plagioclase rims suggest that the xenoliths experienced a reheating event, possibly caused by the influx of fresh basic magma into the magma storage area. It is suggested that this "new" magma was uncontaminated (*i.e.* low $^{87}\text{Sr}/^{86}\text{Sr}_i$), and that diffusion of Sr through the partially crystallized melt pockets (tracer diffusion; Baker, 1989, 1991), caused the partial resetting of the $^{87}\text{Sr}/^{86}\text{Sr}_i$ values of these melt pockets, and the complete resetting of the $^{87}\text{Sr}/^{86}\text{Sr}_i$ values of the aluminous liquids at the core of the xenoliths. The $^{87}\text{Sr}/^{86}\text{Sr}_i$ values of the melt pockets were only *partially* reset due to the fact that crystallization of plagioclase had effectively "tied up" much of the Sr in these isolated pockets. The melt pockets as analysed therefore consist of plagioclase microlites with a high $^{87}\text{Sr}/^{86}\text{Sr}_i$, and pyroxene and residual glass with a low $^{87}\text{Sr}/^{86}\text{Sr}_i$, resulting in a "bulk" melt pocket analysis which lies between these two values. Gilotti & Casserly (1994) have shown that Sr diffusion rates in plagioclase depend upon the composition of the plagioclase, and upon the temperature, with rates in anorthite being approximately 10^4 times slower than those in albite at the same temperature. The resetting of $^{87}\text{Sr}/^{86}\text{Sr}_i$ values within the reaction rims implies that tracer diffusion (Baker, 1989, 1991) probably took place via liquid-liquid contact rather than through plagioclase crystals.

The major-element geochemistry of the melt pockets was introduced in Chapter 9, and it was noted that the compositions became more

"evolved" towards the centre of the xenolith. *Figures 10.9a-c* show the variation diagrams of CaO, TiO₂ and MgO versus SiO₂, respectively, for the melt pockets, the host basalt, and the mullite buchite. Given the errors involved in the analysis of the melt pockets, these diagrams define reasonable mixing trends between the basalt and the mullite buchite. However, the evolution of the zoned mullite buchite-plagioclase xenoliths outlined above requires that at least two different basic magmas, presumably from the same source, with different ⁸⁷Sr/⁸⁶Sr_i values, were involved in the process.

(e) Post-crystallization magma-xenolith interactions

The mullite buchite-plagioclase xenoliths show textural and geochemical evidence for extensive post-crystallization interaction with the enclosing basic magmas. The plagioclase adjacent to the host magma has started to remelt, resulting in the fingerprint texture described in Chapter 9. The mobilization of the albitic portion of the plagioclase provides another source of contamination of the host magmas. This process must have involved an increase in temperature of the system, suggesting that fresh, hot basic magma was introduced. Magma recharge has been suggested as a possible mechanism for the decoupling of certain trace-elements during fractionation of the LSSC basic magmas (Chapter 4). The textures preserved in the zoned xenoliths lend weight to this argument. The mixing of new, possibly uncontaminated, basic magma into the system could also have been responsible for the partial resetting of the Sr isotope values of the xenoliths, as outlined above.

Evidence for late stage magma/xenolith interactions is also preserved in the spinel chemistry of the reaction rims. As documented in *Figures 9.18a-d*, there are well defined trends in MgO, Al₂O₃, Fe₂O₃ and FeO with respect to the position of the spinel relative to the basalt contact. *Figure 10.10a* shows a schematic diagram of how the distance measurements were calculated. Although the xenolith used is asymmetric, in that the glassy core is not exactly at the centre, the measurements of the compositions of those spinels nearest the buchite which occur on the top side of the xenolith, reveal that the composition of these spinels is more like those nearer the basalt contact. This indicates that the basalt contact was the controlling factor on spinel chemistry. Had the xenolith crystallized in a symmetrical fashion, spinels of similar chemistry would be arranged in

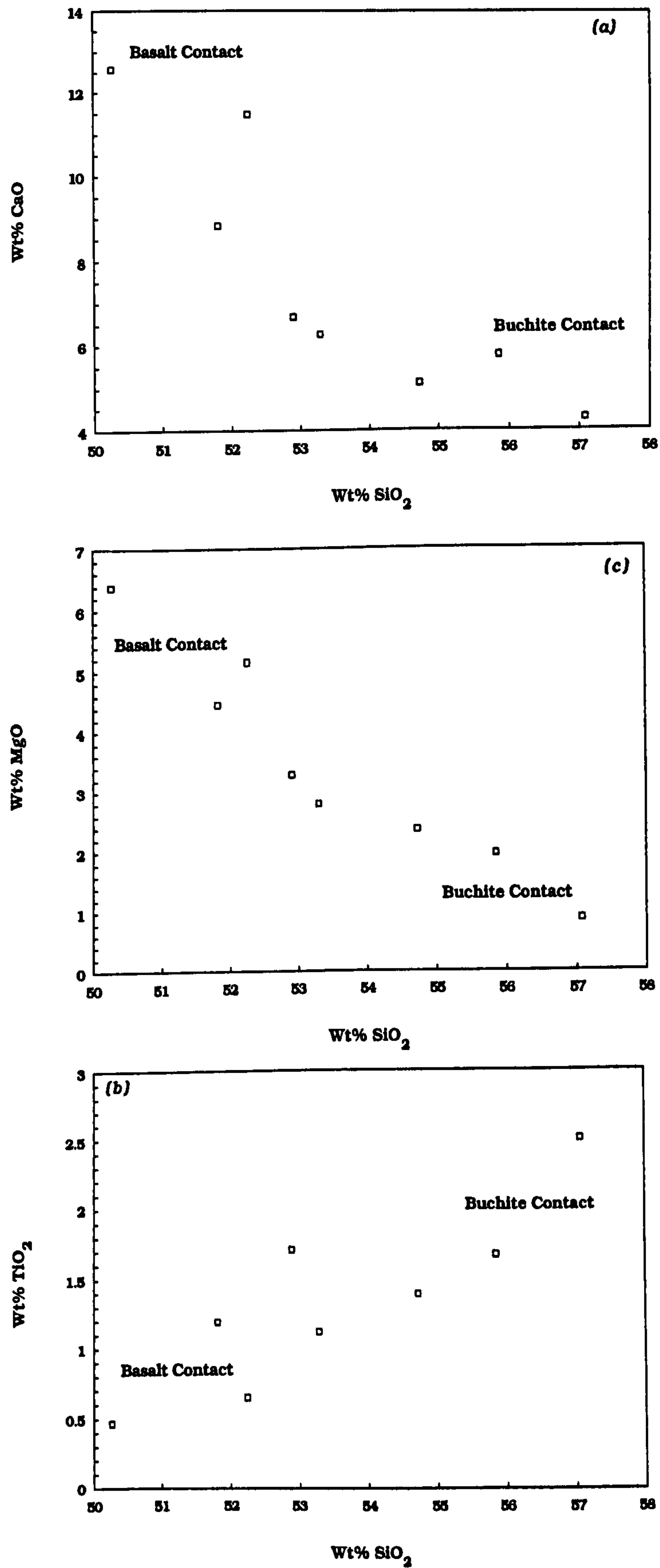


FIGURE 10.9 (a) Variation in CaO vs. SiO₂ for melt pockets in aluminous xenolith PMFX1

(b) Variation in TiO₂ vs. SiO₂

(c) Variation in MgO vs. SiO₂

concentric zones as shown in *Figure 10.10*. Since this is not the case, the variation in spinel chemistry can be explained in one of two ways:-

- a) The xenolith crystallized in an asymmetric fashion. The extreme difference in composition between the enclosing basalt and the aluminous melt would have set up chemical gradients, especially in MgO, FeO and Al₂O₃, to which the crystallizing spinels responded, resulting in the smooth profiles shown (*Figures 9.18a-d*). The chemical gradients on the "narrow" side of the xenolith would have been "telescoped" into a shorter distance, resulting in anomalously Fe-rich spinels closer to the core of the xenolith (See *Figure 10.10b*).
- b) The spinel chemistry is the result of late-stage re-equilibration with the host magma. The "equilibrium" spinels would appear to be the most MgO- and Al₂O₃-rich, since the sapphire-->spinel reactions appear to be producing spinels of this composition (see *Figure 9.18a* and *9.18b*). These spinels were made-over to more Fe-rich compositions due to the presence of Fe-rich basaltic magma at the outer margin. This re-equilibration may be linked to the mixing of basaltic melts and aluminous liquids within the intra-plagioclase melt pockets (cf. Pedersen, 1978).

Of the two hypotheses, the second is considered more likely. If the first were the case, spinels of the entire compositional range would be expected within the "narrow" portion of the plagioclase rim. Since this is not the case, it is suggested that post-crystallization re-equilibration of the spinels produced the trends seen. It has been shown that spinel chemistry is easily reset through late-stage, post-magmatic processes (Roeder *et al.*, 1979; Fabriès, 1979; Dunham & Wilkinson, 1985; Bell & Claydon, 1992). However, Scowen *et al.* (1991) have shown that spinels included in plagioclase crystals are more likely to preserve their magmatic compositions. This would appear to negate the possibility of late-stage re-equilibration of the spinels. However, it is considered that the influx of hot basic magma into the partly crystalline plagioclase rim along fractures and grain boundaries, into the interstitial melt pockets, may be sufficient to alter the spinel chemistry, particularly where the spinels sit close to the melt pocket.

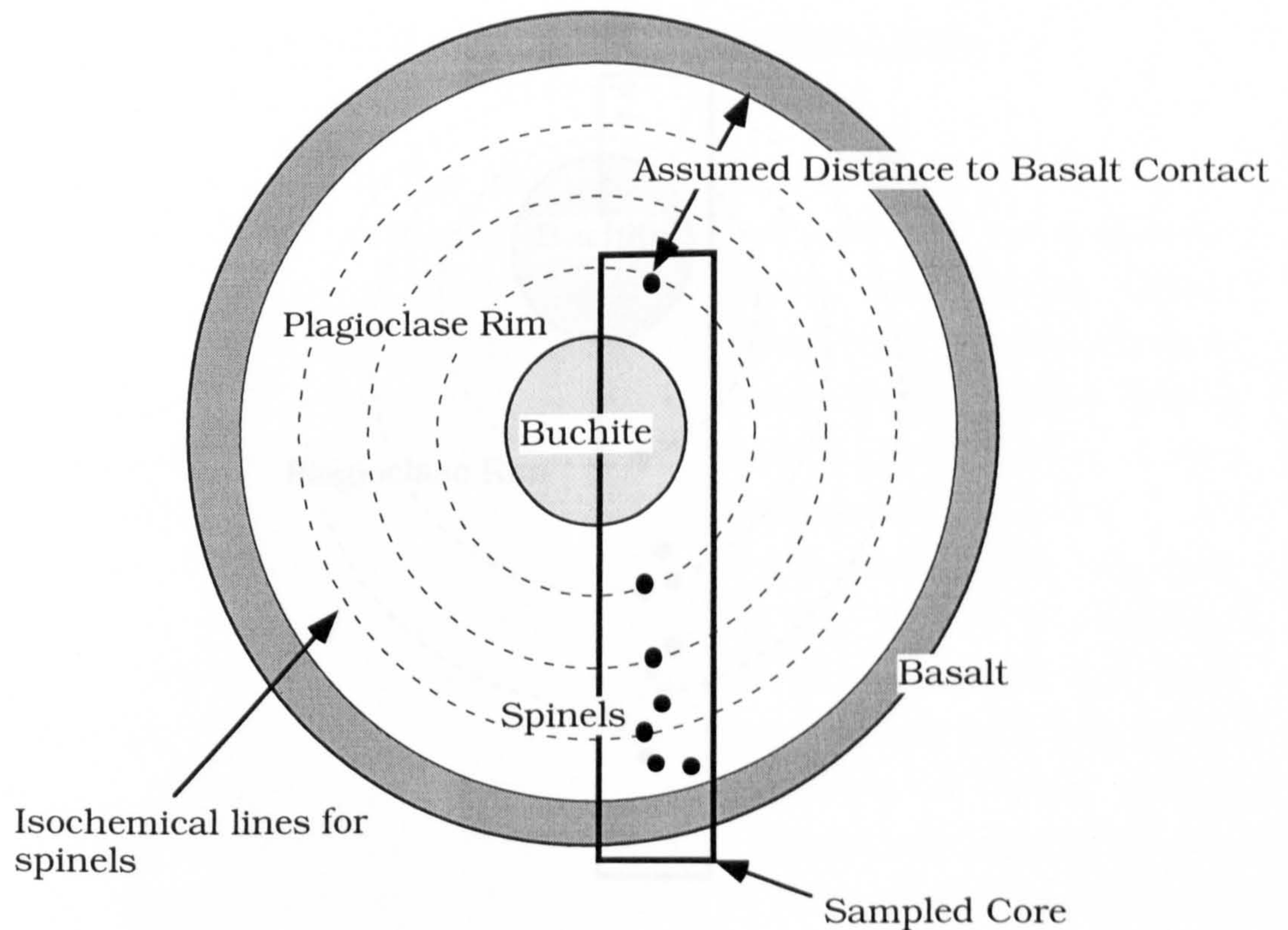


FIGURE 10.10a Measurement of distance from basalt contact for spinels in a zoned mullite buchite-plagioclase xenolith. The distance measurements were made assuming the xenolith was symmetrical about the central glassy core when the rim grew. If this were the case, then those spinels at the top of the now asymmetric xenolith would have the same chemistry as those the same distance from the contact from the bottom of the xenolith, as shown in the diagram. Since these spinels are more similar to ones nearer the basalt contact, it is considered more likely that the spinel chemistry was controlled by the basalt contact *after* their initial crystallization.

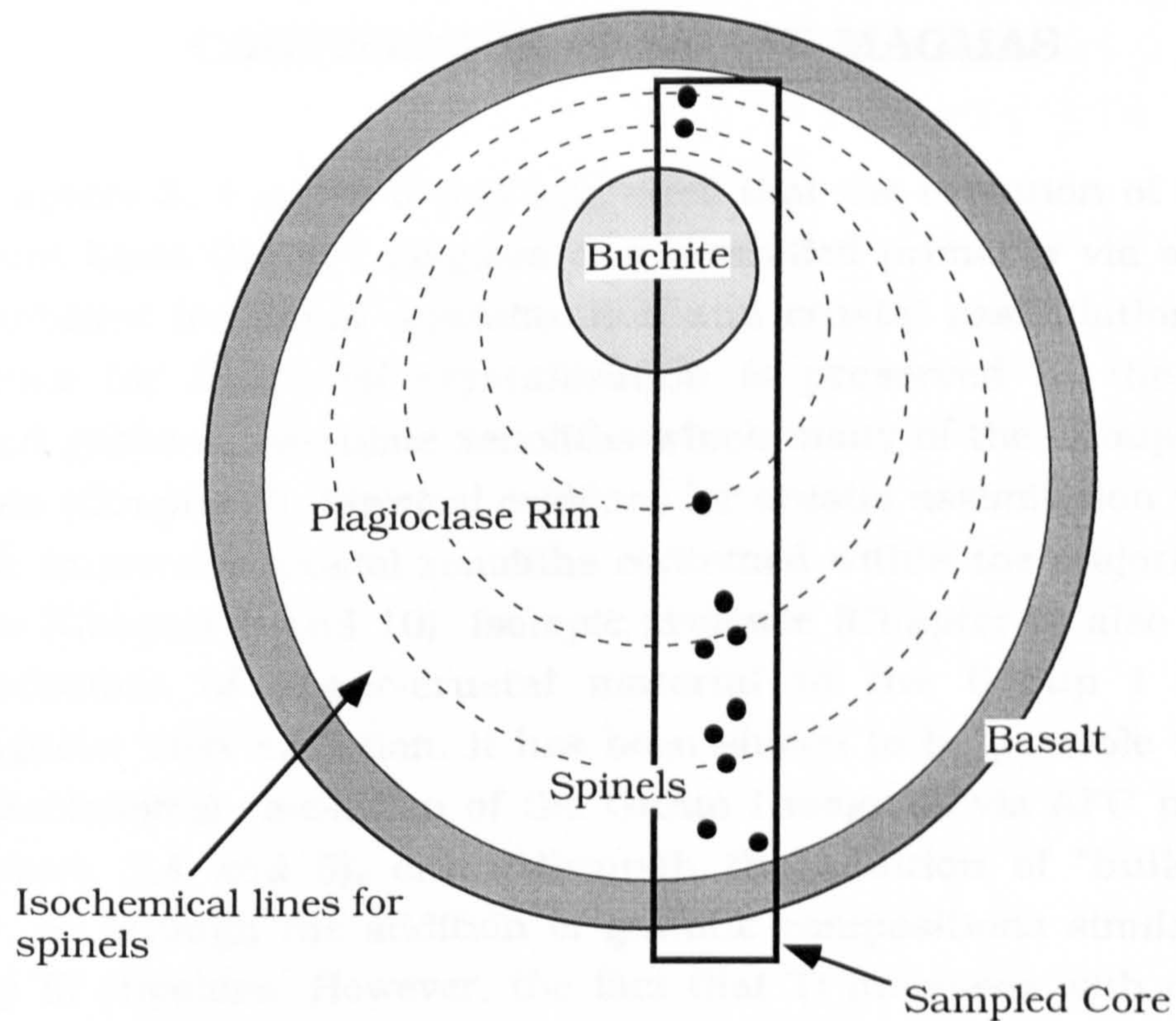


FIGURE 10.10b

If xenoliths had crystallized in an asymmetric fashion, and the spinel chemistry was controlled by the presence of steep geochemical gradients, then spinels on the "narrow" side would be expected to have similar compositions to those nearest the basalt contact on the other side of the xenolith, as shown in the diagram. However, spinels of the *entire* compositional spectrum would also be expected on the narrow side of the xenolith. Since this is *not* the case, it is considered more likely that spinel chemistry was controlled by the nearness to the basalt contact *after* their initial crystallization.

CHAPTER 11

FINAL CONCLUSIONS : THE SIGNIFICANCE OF MAGMA- XENOLITH INTERACTION TO THE CONTAMINATION OF CONTINENTAL BASALTIC MAGMAS

In Chapters 3, 4 and 5 it was suggested that the evolution of the Loch Scridain basic Group I magmas was controlled primarily via a process of combined fractional crystallization and crustal assimilation. Direct evidence for fractional crystallization is preserved in the coarse-grained gabbroic cumulate xenoliths which many of the Group I sheets contain (Chapter 7). Physical evidence for crustal assimilation is shown by the numerous crustal xenoliths contained within the majority of the sheets (Chapter 9 and 10). Isotopic evidence (Chapter 5) also requires the addition of upper-crustal material to the Group I magmas throughout their evolution. It has been shown to be possible to *model* the geochemical evolution of the Group I magmas via AFC processes (Chapters 3,4 and 5), either through the addition of "bulk" Moine pelite, or through the addition of granitic compositions similar to the Group III rhyolites. However, the fact that Ti increases with degree of fractionation through Group I, and that these rocks do not contain cumulative titanomagnetite, requires that the basic magmas have also interacted extensively with Ti-enriched partial melts from the basement rocks (*i.e.* the mullite buchites). The geochemical trends displayed by certain compatible trace-elements (*e.g.* Ni and Cr) suggest that magma recharge processes may also have been operating. The evolution of Group II intermediate magmas has been demonstrated to be due to the mixing of rhyolitic magmas derived from the partial melting of basement rocks, with small amounts of the regionally available basic magma. Group III rhyolites were derived from the extraction of "near-minimum", granitic melts from the basement Moine pelitic schists.

The discussion in Chapters 9 and 10 highlights the complex nature of magma-xenolith interactions. The evolution of the mullite buchite-plagioclase xenoliths has provided the most valuable information

concerning these interactions. A schematic summary diagram of their evolution is presented in *Figure 11.1*.

Most experimental studies into the processes of melting and assimilation of xenoliths have failed to take into account the possibility of *reaction* between the magma and the xenolith at some stage in the dissolution process (e.g. Maury & Bizouard, 1974; McLeod & Sparks, 1995). However, many *field* studies have highlighted the complexities of xenolith-magma interaction, and the possible mechanisms for magma contamination (Maury *et al.*, 1978; Pedersen, 1978; Tindle & Pearce, 1983; van Bergen & Barton, 1984).

The crustal xenoliths of the LSSC have "gone one step further", in that the residue from the early partial melting process has become completely molten, interacted with the enclosing basic magma, and precipitated a rim of refractory crystalline phases. These further stages of interaction add new dimensions to fingerprinting the effects of xenolith dissolution on magma geochemistry. The individual processes of xenolith-magma interaction should leave their own unique trace-element and isotopic fingerprints. In the case of the LSSC, it appears that Ti is an excellent tracer for these processes. However, in a suite of basaltic rocks which may have suffered concurrent fractional crystallization, magma mixing, and magma recharge, the effects of these different contamination events may be difficult to decipher.

Grunder (1992) provides isotopic evidence, from volcanic rocks from eastern Nevada, for complex contamination processes. Certain members from early in the volcanic sequence have suffered contamination with granitic partial melts extracted from the basement lithologies. Later rocks have been contaminated through interaction with the restite formed by the earlier partial melting event. This two-stage contamination process has the effect of decoupling Sr and Nd isotope behaviour during magma-crust interaction. The first stage in contamination caused the largest change in the Nd isotope composition of the magma, since the first melts produced in the partial melting process will be greatly enriched in Nd. The later stages of contamination drastically altered the Sr isotope characteristics of the magma with little change in the Nd isotope ratios. This is due to the fact that the restite from the early partial melting phase is dominated by plagioclase, and is therefore a very effective sink for Sr. The overall effect is similar to bulk assimilation, albeit in two stages. This de-coupling of Sr and Nd isotopes is potentially a very important

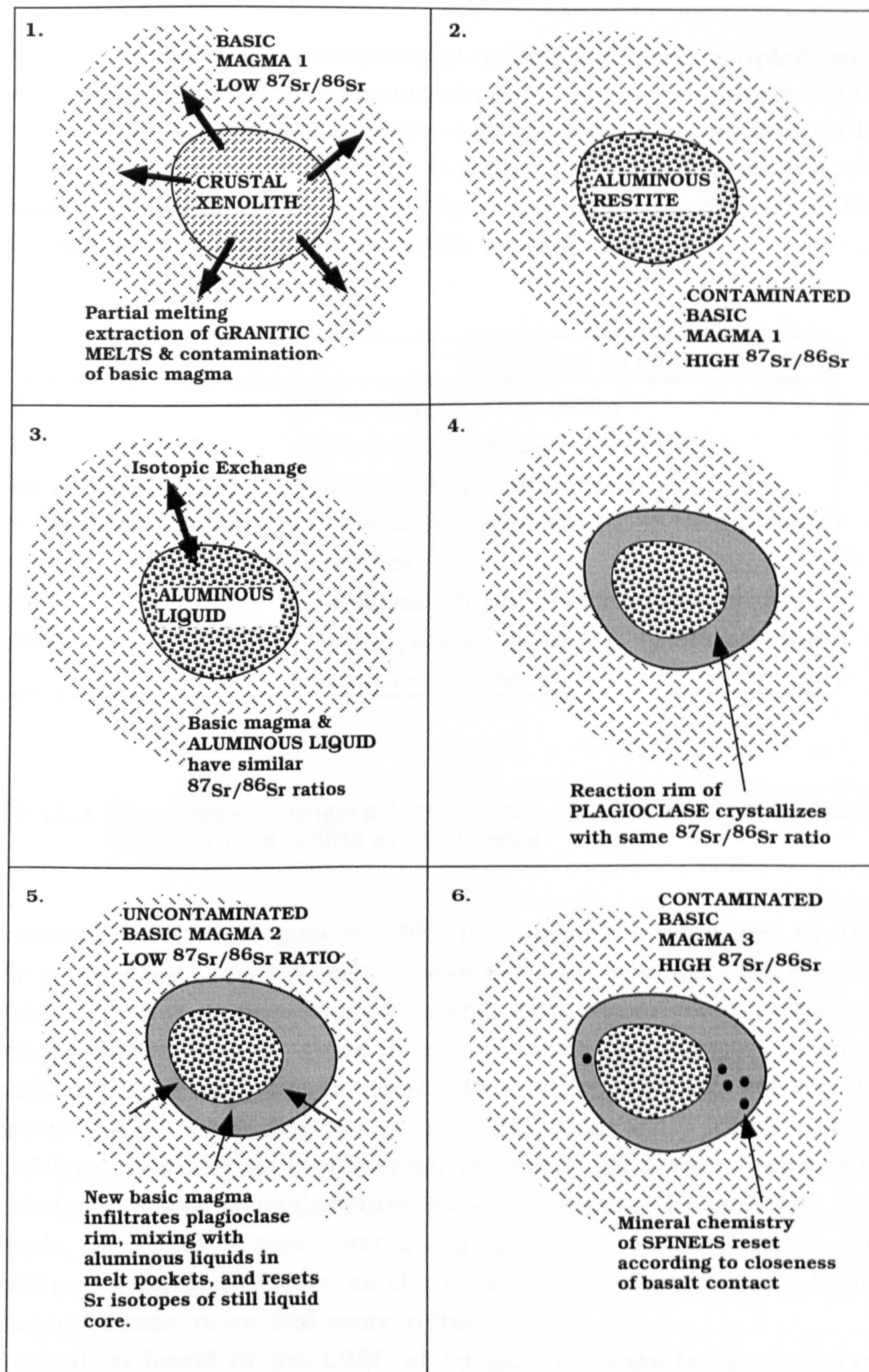


FIGURE 11.1 Schematic Diagrams showing the evolution of a mullite buchite-plagioclase xenolith, as deduced from textural information, mineral chemistry and mineral Sr isotope characteristics. Starting material is a typical peltic schist from the Moine metasedimentary succession.

fingerprint of magma contamination processes, and coupled with trace-element information, the contamination history of a magma suite which does not contain direct evidence in the form of xenoliths can be assessed. *Table 11.1* shows a list of some of the 'most useful' trace-element fingerprints, and where they are partitioned during the interaction of basic magmas with pelitic crustal rocks.

ELEMENT	"WHERE IT GOES"
K	Minimum granitic melts
Ti	Aluminous residues
Nd (isotope ratios)	Mainly into granitic melts
Sr (isotope ratios)	If residual plagioclase -> aluminous residues
Zr	If residual zircon -> aluminous residues
REE	Minimum granitic melts, 'unless residual zircon or sphene

Table 11.1 Geochemical fingerprints during the interaction of basic magmas with pelitic crustal rocks.

The complexities of magma-xenolith interactions highlighted by the study of the LSSC xenolith suite, imply that the most commonly used models of crustal contamination (*i.e.* AFC, bulk assimilation), although sound in theory, may be gross oversimplifications compared to what actually occurs. These models assume that certain components remain constant (*e.g.* composition of the contaminant, fractionating assemblage, distribution coefficients). In reality, all these components are likely to evolve in conjunction with the magmas in question. For example, the partial melts extracted from the country-rocks and xenoliths are likely to evolve as the rocks from which they are being extracted become more and more refractory.

The situation found in the LSSC of basaltic magmas being emplaced into old continental crust is hardly unique (*e.g.* Carlson *et al.*, 1981; Cox & Hawkesworth, 1985; Devey & Cox, 1987; Graham, 1987; Lightfoot *et al.*, 1990). There is very little of exception in terms of the magma chemistry, the thermal regime, or the tectonic setting of the

LSSC. The fact that the LSSC is not extraordinary in most aspects, suggests that the magmatic processes which have occurred are likely to be very common. However, the LSSC does possess much more extreme initial Sr isotopic characteristics than other CFB suites (Bellieni *et al.*, 1984; Cox & Hawkesworth, 1985; Wilson, 1989; Brewer *et al.*, 1992). This suggests that the LSSC magmas have seen more in the way of interaction with the continental crust. Compared to CFB provinces such as the Paraná or the Deccan, the LSSC is a very small magmatic system. The great interaction of the LSSC basic magmas with the continental crust may therefore be a consequence of the scale of the magmatism (*i.e.* small amounts of magma interacting with large amounts of crust).

What is unusual, however, is the excellent preservation of a suite of crustal xenoliths which record the complex processes of xenolith-magma interaction. Moreover, what is also exceptional, and *difficult to explain*, is why typical tholeiitic basic magmas, which are very unlikely to have contained significant superheat, have been able to completely melt and interact with refractory restites. What must therefore be addressed, is *why* the LSSC has preserved such a complete record of the processes of fractional crystallization and crustal contamination. One possibility is that the magmatic plumbing system for the LSSC provided the ideal environment for the formation and preservation of the xenolith suite. It has been suggested (Chapter 8) that the magma storage reservoirs for the LSSC consisted of a network of interconnected sills and dykes (*cf.* Cox, 1980; Dickin *et al.*, 1984; Morrison *et al.*, 1985). As new magma is fed into this system, the uppermost parts of the sills and dykes will become inflated, increasing the stress on the wall rocks, and thus propagating new fissures (Lister *et al.*, 1991). Fissure propagation will be encouraged if zones of weakness already exist within the crustal lithologies (*e.g.* bedding planes). Sigurdsson & Sparks (1978) have shown that basaltic magmas from Iceland may have moved up to 70km laterally from the central magma storage reservoirs, through a network of crustal fissures, prior to eruption or emplacement. Since there is little geophysical evidence for large magma chambers under the Loch Scridain district (Bott & Tandrigoda, 1987), it is possible that the major magma storage reservoir for the LSSC was under the Central Complex, and that the LSSC was emplaced forcibly from a central location. However, there is little evidence for a consistent flow direction within the LSSC (*e.g.*

Kille, 1987). It seems unlikely that the suite should have such a limited distribution, unless major faults (Moine Thrust ?) extended westward from the Central Complex. There is consistent isotopic evidence that the Mull Plateau Group Lavas have been contaminated with Lewisian granulite facies material (*e.g.* Morrison *et al.*, 1985; Thompson *et al.*, 1986; Kerr *et al.*, 1994). The LSSC, however, would appear to have been only contaminated with Moine material (Morrison *et al.*, 1985; Thompson *et al.*, 1986; this study). Thompson *et al.* (1986) analysed one sheet from the LSSC for Pb isotopes. It was found that the $^{206}\text{Pb}/^{204}\text{Pb}$ value was high (18.6). Lewisian material has lower $^{206}\text{Pb}/^{204}\text{Pb}$ values at between 14 and 17 (Dickin, 1981). Moine metasediments have $^{206}\text{Pb}/^{204}\text{Pb}$ values in excess of 18 (Thompson *et al.*, 1986). This geochemical evidence lends some weight to the lateral movement of magma theory. Unfortunately there is no geochemical evidence concerning the crustal contamination of basic rocks from the Mull Central Complex. If the gabbros and basic cone-sheets from the Mull Central Complex were also contaminated with Moine material, rather than Lewisian, the lateral (and upward) movement of magma from a central position may be a distinct possibility. Such a plumbing system would possibly provide the ideal scenario for the mechanical disintegration of the country-rock, the entrainment of xenoliths, and their dissolution *into*, and reaction *with* the basic magma. It is also probable that the continual availability of fresh basic magma played an important role in the formation of the suite, in terms of supplying heat for the thermal erosion of the wall rocks and for the dissolution of xenoliths. Alternatively, the LSSC may represent the only surface expression of magmas which have risen *rapidly* through the lower crust from a separate magmatic complex which lies under the Loch Scridain district, and subsequently ponded and fractionated within the upper crust (*i.e.* within the Moine).

What ever the actual plumbing system for the LSSC consists of, the very fact that a particularly normal suite of basaltic rocks have interacted with the crust in this way should breed caution when interpreting the contamination history of other continental basaltic magmas where the preservation of crustal xenoliths is not as good, or indeed absent.

REFERENCES

- Addison, C.C., Addison, W.E., Neal, G.H. & Sharp, J.H.** (1969). Dehydroxylation and rehydroxylation, oxidation and reduction of micas. *American Mineralogist*, **54**, 482-509.
- Agrell, S.O. & Langley, J.M.** (1958). The dolerite plug at Tievebullagh, near Cushendall, Co. Antrim. *Proceedings of the Royal Irish Academy*, **59**, 93-127.
- Albaredé, F.** (1992). How deep do common basaltic magmas form and differentiate? *Journal of Geophysical Research*, **97**, No. B7, 10997-11009.
- Anderson, E.M. & Radley, E.G.** (1916). The pitchstones of Mull and their genesis. *Quarterly Journal of the Geological Society, London*, **71**, No. 2, 205-216.
- Arculus, R.J. & Wills, K.J.A.** (1980). The petrology of plutonic blocks and inclusions from the Lesser Antilles island arc. *Journal of Petrology*, **21**, No. 4, 743-799.
- Arzi, A.A.** (1978). Critical phenomena in the rheology of partially melted rocks. *Tectonophysics*, **44**, 173-184.
- Bailey, D.K.** (1982). Mantle metasomatism - Continuing chemical change within the Earth. *Nature*, **296**, 525-530.
- Bailey, E.B., Clough, C.T., Wright, W.B., Richey, J.E. & Wilson, G.V.** (1924). *Tertiary and Post-Tertiary geology of Mull, Loch Aline, and Oban.*, 1 edn. H.M.S.O., Edinburgh.
- Baker, D.R.** (1989). Tracer versus trace element diffusion : Diffusional decoupling of Sr concentration from Sr isotope composition. *Geochimica et Cosmochimica Acta*, **53**, 3015-3023.
- Baker, D.R.** (1991). Interdiffusion of hydrous dacitic and rhyolitic melts and the efficacy of rhyolite contamination of dacitic enclaves. *Contributions to Mineralogy and Petrology*, **106**, 462-473.
- Bamford, D., Nunn, K., Prodehl, C. & Jacob, B.** (1977). LISP III : Upper crustal structure of Northern Britain. *Journal of the Geological Society, London*, **133**, 481-488.
- Barker, F.** (1964). Reaction between mafic magmas and pelitic schist, Cortland, New York. *American Journal of Science*, **262**, 614-634.
- Beckisale, R.D., Pankhurst, R.J., Skelhorn, R.R. & Walsh, J.N.** (1978). Geochemistry and petrogenesis of the Early Tertiary lava pile of the Isle of Mull, Scotland. *Contributions to Mineralogy and Petrology*, **66**, 415-427.
- Bell, B.R.** (1983). Significance of ferrodioritic liquids in magma mixing processes. *Nature*, **306**, 323-327.
- Bell, B.R. & Claydon, R.V.** (1992). The cumulus and post-cumulus evolution of chrome-spinels in ultrabasic intrusions : Evidence from the Cuillin Igneous Complex, Isle of Skye, Scotland. *Contributions to Mineralogy and Petrology*, **112**, 242-253.
- Bell, B.R. & Pankhurst, R.J.** (1993). Sr-isotope variations in a composite sill : Crystal-liquid processes and the origin of the Skye granites. *Journal of the Geological Society, London*, **150**, 121-124.
- Bell, B.R., Claydon, R.V. & Rogers, G.** (1994). The petrology and geochemistry of cone-sheets from the Cuillin igneous complex, Isle of Skye : Evidence for combined assimilation and fractional crystallization during lithospheric extension. *Journal of Petrology*, **35**, No. 4, 1055-1094.

Bellieni, G., Brotzu, P., Comin-Chiaramonti, P., Ernesto, M., Melfi, A., Pacca, I.G. & Piccirillo, E.M. (1984). Flood basalt to rhyolite suites in the Southern Paraná Plateau (Brazil) : Palaeomagnetism, petrogenesis and geodynamic implications. *Journal of Petrology*, **25**, No. 3, 579-618.

Bellieni, G., Comin-Chiaramonti, P., Marques, L.S., Melfi, A.J., Nardy, A.J.R., Papatrechas, C., Piccirillo, E.M., Roisenberg, A. & Stolfa, D. (1986). Petrogenetic aspects of acid and basaltic lava from the Paraná Plateau (Brazil) : Geological, mineralogical and petrological relationships. *Journal of Petrology*, **27**, No. 3, 915-944.

Binns, R.A. (1969). High-pressure megacrysts in basaltic lavas near Armidale, New South Wales. *American Journal of Science*, **267-A**, 33-49.

Binns, R.A., Duggan, M.B. & Wilkinson, J.F.G. (1970). High pressure megacrysts in alkaline lavas from northeastern New South Wales. *American Journal of Science*, **269**, 132-168.

Bott, M.H.P. & Tandrigoda, T.A. (1987). Interpretation of the gravity and magnetic anomalies over the Mull Tertiary intrusive complex, NW Scotland. *Journal of the Geological Society, London*, **91**, 17-28.

Bouch, J.E., Hole, M.J., Trewin, N.H. & Morton, A.C. (1995). Low-temperature aqueous mobility of the rare-earth elements during sandstone diagenesis. *Journal of the Geological Society, London*, **152**, 895-898.

Bowen, N.L. (1913). The melting phenomena of the plagioclase feldspars. *American Journal of Science*, **34**, 577-599.

Bowen, N.L. (1922). The behaviour of inclusions in igneous magmas. *Journal of Geology*, **30**, 513-570.

Bowen, N.L. (1928). *The Evolution of the Igneous Rocks*. Princeton University Press, New Jersey, 334 pp.

Bowen, N.L., Greig, J.W. & Zies, E.G. (1924). Mullite, a silicate of alumina. *Journal of the Washington Academy of Science*, **14**, 183.

Brewer, T.S., Hergt, J.M., Hawkesworth, C.J., Rex, D. & Storey, B.C. (1992). Coats Land dolerites and the generation of Antarctic continental flood basalts. In: Storey, B.C., Alabaster, T. & Pankhurst, R.J. (eds.), *Magmatism and the Causes of Continental Break-up*. Geological Society Special Publication No. 68, 185-208.

Brooks, C.K. (1976). The Fe₂O₃/FeO ratio of basalt analyses : An appeal for a standardised procedure. *Bulletin of the Geological Society of Denmark*, **25**, 117-120.

Brown, G.C. & Fyfe, W.S. (1970). The production of granitic melts during ultrametamorphism. *Contributions to Mineralogy and Petrology*, **28**, 310-318.

Brown, G.M. (1956). The layered ultrabasic rocks of Rhum, Inner Hebrides. *Philosophical Transactions of the Royal Society of London*, **B240**, 1-53.

Brown, G.M. (1957). Pyroxenes from the early and middle stages of fractionation of the Skaergaard intrusion, East Greenland. *Mineralogical Magazine*, **31**, 511-543.

Brown, G.M. & Vincent, E.A. (1963). Pyroxenes from the late stages of fractionation of the Skaergaard intrusion, East Greenland. *Journal of Petrology*, **4**, No. 2, 175-197.

Bulst, D.S. (1958). The bostonite of Rudh' a' Chromain, Carsaig, Mull. *Geological Magazine*, **115**, No. 6, 463-464.

- Buist, D.S.** (1959). The composite sill of Rudh' an Elreannaich, Skye. *Geological Magazine*, **96**, No. 3, 246-252.
- Buist, D.S.** (1961). The composite sill of Rudh' a' Chromain, Carsaig, Mull. *Geological Magazine*, **98**, No. 1, 67-76.
- Burke, W.H., Denison, R.E., Hetherington, E.A., Koepnick, R.B., Nelson, N.F. & Otto, J.B.** (1982). Variation of seawater $^{87}\text{Sr}/^{86}\text{Sr}$ throughout Phanerozoic time. *Geology*, **10**, 516-519.
- Cameron, E.N.** (1975). Postcumulus and subsolidus equilibration of chromite and coexisting silicates in the Eastern Bushveld Complex. *Geochimica et Cosmochimica Acta*, **39**, 1021-1033.
- Cameron, W.E.** (1976a). Coexisting sillimanite and mullite. *Geological Magazine*, **113**, No. 6, 497-592.
- Cameron, W.E.** (1976b). Exsolution in 'stoichiometric' mullite. *Nature*, **264**, 736-738.
- Campbell, I.H.** (1985). The difference between oceanic and continental tholeiites : A fluid dynamic explanation. *Contributions to Mineralogy and Petrology*, **91**, 37-43.
- Campbell, I.H. & Turner, J.S.** (1986). The influence of viscosity on fountains in magma chambers. *Journal of Petrology*, **27**, 1-30.
- Campbell, I.H. & Turner, J.S.** (1987). A laboratory investigation of assimilation at the top of a basaltic magma chamber. *Journal of Geology*, **95**, 155-172.
- Campbell, I.H. & Griffiths, R.W.** (1990). Implications of mantle plume structure for the evolution of flood basalts. *Earth Science and Planetary Letters*, **99**, 79-83.
- Carlson, R.W.** (1991). Physical and chemical evidence on the cause and source characteristics of flood basalt volcanism. *Australian Journal of Earth Sciences*, **38**, 525-544.
- Carlson, R.W., Lugmair, G.W. & MacDougall, J.D.** (1981). Columbia River Volcanism : The question of mantle heterogeneity or crustal contamination. *Geochimica et Cosmochimica Acta*, **45**, 2483-2499.
- Carmichael, I.S.E.** (1960a). The feldspar phenocrysts of some Tertiary acid glasses. *Mineralogical Magazine*, **32**, No. 251, 587-608.
- Carmichael, I.S.E.** (1960b). The pyroxenes and olivines from some Tertiary acid glasses. *Journal of Petrology*, **1**, No. 3, 309-336.
- Carmichael, I.S.E.** (1963). The occurrence of magnesian pyroxenes and magnetite in porphyritic acid glasses. *Mineralogical Magazine*, **33**, 394-403.
- Carmichael, I.S.E.** (1964). The petrology of Thingmull, a Tertiary volcano in Eastern Iceland. *Journal of Petrology*, **5**, No. 3, 435-460.
- Carter, S.R., Evensen, N.M., Hamilton, P.J. & O'Nions, R.K.** (1978). Continental volcanics derived from enriched and depleted source regions : Nd- and Sr-isotope evidence. *Earth and Planetary Science Letters*, **37**, 401-408.
- Chappel, B.W. & White, A.J.R.** (1974). Two contrasting granite types. *Pacific Geology*, **8**, 173-174.
- Chappell, B.W. & White, A.J.R.** (1992). I- and S-type granites in the Lachlan Fold Belt. *Transactions of the Royal Society of Edinburgh : Earth Sciences*, **83**, 1-26.

- Chayes, F.** (1964). Variance-covariance relations in some published Harker diagrams of volcanic suites. *Journal of Petrology*, **5**, No. 2, 219-237.
- Cigolini, C. & Kudo, A.M.** (1987). Xenoliths in recent basaltic andesite flows from Arenal Volcano, Costa Rica :Inference on the composition of the lower crust. *Contributions to Mineralogy and Petrology*, **96**, 381-390.
- Claydon, R.V.** (1990). *A petrological study of mafic hypabyssal and ultramafic plutonic rocks of the Cuillin Igneous Complex, Isle of Skye, Scotland*, Unpublished PhD Thesis, University of Glasgow.
- Claydon, R.V. & Bell, B.R.** (1992). The structure and petrology of ultrabasic rocks in the southern part of the Cuillin Igneous Complex, Isle of Skye. *Transactions of the Royal Society of Edinburgh*, **83**, 635-653.
- Coish, R.A. & Taylor, L.A.** (1979). The effects of cooling rate on texture and pyroxene chemistry in DSDP Leg 34 basalt : A microprobe study. *Earth Science and Planetary Letters*, **42**, 389-398.
- Colson, R.O., McKay, G.A. & Taylor, L.A.** (1988). Temperature and composition dependencies of trace element partitioning : Olivine/melt and low Ca-pyroxene/melt. *Geochimica et Cosmochimica Acta*, **52**, 539-553.
- Conrad, W.K. & Kay, R.W.** (1984). Ultramafic and mafic inclusions from Adak Island : Crystallization history, and implications for the nature of primary magmas and crustal evolution in the Aleutian Arc. *Journal of Petrology*, **25**, No. 1, 88-125.
- Cox, K.G.** (1980). A model for flood basalt vulcanism. *Journal of Petrology*, **21**, No. 4, 629-650.
- Cox, K.G.** (1988). Numerical modelling of a randomized RTF magma chamber : A comparison with continental flood basalt sequences. *Journal of Petrology*, **29**, No. 3, 681-697.
- Cox, K.G. & Bell, J.D.** (1972). A crystal fractionation model for the basaltic rocks of the New Georgia Group, British Solomon Islands. *Contributions to Mineralogy and Petrology*, **37**, 1-13.
- Cox, K.G. & Hawkesworth, C.J.** (1985). Geochemical stratigraphy of the Deccan Traps at Mahabaleswar, Western Ghats, India, with implications for open system magmatic processes. *Journal of Petrology*, **26**, No. 2, 355-377.
- Cox, K.G. & Mitchell, C.** (1988). Importance of crystal settling in the differentiation of Deccan Trap basaltic magmas. *Nature*, **333**, 447-449.
- Cox, K.G., Macdonald, R. & Hornung, G.** (1967). Geochemical and petrographic provinces in the Karoo basalts of southern Africa. *American Mineralogist*, **52**, 1451-1474.
- Cox, K.G., Bell, J.D. & Pankhurst, R.P.** (1979). *The Interpretation of Igneous Rocks*. Unwin Hyman, London, 450 pp.
- Crawford, M.B. & Windley, B.F.** (1990). Leucogranites of the Himalaya/Karakoram : Implications for magmatic evolution within collisional belts and the study of collision-related leucogranite petrogenesis. *Journal of Volcanological and Geothermal Research*, **44**, No. 1-19,
- Czamanske, G.K. & Moore, J.G.** (1977). Composition and phase chemistry of sulfide globules in basalt from the Mid-Atlantic Ridge rift valley near 37deg N lat. *Geological Society of America Bulletin*, **88**, 587-599.

- Dagley, P., Musset, A.E. & Skelhorn, R.R.** (1987). Polarity, stratigraphy and duration of the Tertiary igneous activity of Mull, Scotland. *Journal of the Geological Society, London*, **144**, 985-996.
- Dasch, E.J.** (1969). Strontium isotopes in weathering profiles, deep-sea sediments, and sedimentary rocks. *Geochimica et Cosmochimica Acta*, **33**, 1521-1552.
- Deer, W.A., Howie, R.A. & Zussman, J.** (1992). *An Introduction to the Rock-Forming Minerals.*, 2nd edn. John Wiley & Sons, New York, 696 pp.
- Dell'Angelo, L.N. & Tullis, J.** (1988). Experimental deformation of partially melted granitic aggregates. *Journal of Metamorphic Geology*, **6**, 495-516.
- DeLong, S.E., Hodges, F.N. & Arculus, R.J.** (1975). Ultramafic and mafic inclusions, Kanga Island, Alaska, and the occurrence of alkaline rocks in island arcs. *Journal of Geology*, **83**, 721-736.
- Dempster, T.J., Hutton, D.H.W., Harrison, T.N., Brown, P.E. & Jenkin, G.R.T.** (1991). Textural evolution of the rapakivi granites, south Greenland - Sr, O and H isotopic investigations. *Contributions to Mineralogy and Petrology*, **107**, 459-471.
- DePaolo, D.J.** (1981). Trace element and isotopic effects of combined wallrock assimilation and fractional crystallization. *Earth and Planetary Science Letters*, **53**, 189-202.
- DePaolo, D.J. & Wasserburg, G.J.** (1976a). Inferences about magma sources and mantle structure from variations of $^{143}\text{Nd}/^{144}\text{Nd}$. *Geophysical Research Letters*, **3**, 743-746.
- DePaolo, D.J. & Wasserburg, G.J.** (1976b). Nd isotopic variations and petrogenetic models. *Geophysical Research Letters*, **3**, 249-252.
- DePaolo, D.J. & Wasserburg, G.J.** (1979). Petrogenetic mixing models and Nd-Sr isotopic patterns. *Geochimica et Cosmochimica Acta*, **43**, 615-627.
- Devey, C.W. & Cox, K.G.** (1987). Relationships between crustal contamination and crystallization in continental flood basalt magmas with special reference to the Deccan Traps of the Western Ghats, India. *Earth and Planetary Science Letters*, **84**, 59-68.
- Dickin, A.P.** (1981). Isotope geochemistry of Tertiary igneous rocks from the Isle of Skye, N.W. Scotland. *Journal of Petrology*, **22**, No. 2, 155-189.
- Dickin, A.P. & Exley, R.A.** (1981). Isotopic and geochemical evidence for magma mixing in the petrogenesis of the Coire Uaigneach granophyre, Isle of Skye, N.W. Scotland. *Contributions to Mineralogy and Petrology*, **76**, 98-108.
- Dickin, A.P. & Jones, N.W.** (1983a). Isotopic evidence for the age and origin of pitchstones and felsites, Isle of Elgg, NW Scotland. *Journal of the Geological Society, London*, **140**, 691-700.
- Dickin, A.P. & Jones, N.W.** (1983b). Relative elemental mobility during hydrothermal alteration of a basic sill, Isle of Skye, N.W. Scotland. *Contributions to Mineralogy and Petrology*, **82**, 147-153.
- Dickin, A.P., Moor bath, S. & Welke, H.J.** (1981). Isotope, trace element and major element geochemistry of Tertiary igneous rocks, Isle of Arran, Scotland. *Transactions of the Royal Society of Edinburgh*, **72**, 159-170.
- Dickin, A.P., Brown, J.L., Thompson, R.N., Halliday, A.N. & Morrison, M.A.** (1984). Crustal contamination and the granite problem in the British Tertiary Volcanic Province. *Philosophical Transactions of the Royal Society of London, Ser A* **310**, 755-780.

- Dickin, A.P., Henderson, C.M.B. & Gibb, F.G.F.** (1984). Hydrothermal Sr contamination of the Dippin sill, Isle of Arran, Western Scotland. *Mineralogical Magazine*, **48**, 311-322.
- Donaldson, C.H.** (1977). Petrology of anorthite-bearing gabbroic anorthosite dykes in northwest Skye. *Journal of Petrology*, **18**, No. 4, 595-620.
- Douce, A.E.P.** (1995). Experimental generation of hybrid silicic melts by reaction of high-Al basalt with metamorphic rocks. *Journal of Geophysical Research*, **100**, No. B8, 15623-15639.
- Drake, M.J. & Weill, D.F.** (1975). Partitioning of Sr, Ba, Ca, Y, Eu^{2+} , Eu^{3+} and other REE between plagioclase feldspar and magmatic liquid : An experimental study. *Geochimica et Cosmochimica Acta*, **39**, 689-712.
- Drysdale, D.J.** (1979). A note on sheath and core structure in the Mull pitchstones. *Geological Magazine*, **116**, No. 2, 99-104.
- Duke, J.M.** (1976). Distribution of the period four transition elements among olivine, calcic clinopyroxene and mafic silicate liquids : Experimental results. *Journal of Petrology*, **17**, 499-521.
- Duncan, A.R.** (1987). The Karoo igneous province - A problem area for inferring tectonic setting from basalt geochemistry. *Journal of Volcanological and Geothermal Research*, **32**, 13-34.
- Dunham, A.C. & Wilkinson, F.C.F.** (1985). Sulphide droplets and the Unit 11/12 chromite band, Rhum : A mineralogical study. *Geological Magazine*, **122**, No. 5, 539-548.
- Ehlers, E.G.** (1972). *The Interpretation of Geological Phase Diagrams*. W.H. Freeman & Company, San Francisco, 280 pp.
- Ellam, R.M.** (1992). Lithospheric thickness as a control on basalt geochemistry. *Geology*, **20**, 153-156.
- Elliot, D.H.** (1992). Jurassic magmatism and tectonism associated with Gondwanaland break-up : an Antarctic perspective. In: Storey, B.C., Alabaster, T. & Pankhurst, R.J. (eds.), *Magmatism and the Causes of Continental Break-up*. Geological Society Special Publication No. 68, 165-184.
- Engel, A.E.J., Engel, C.G. & Havens, R.G.** (1965). Chemical characteristics of oceanic basalts and the upper mantle. *Geological Society of America Bulletin*, **76**, 719-734.
- Esson, J., Dunham, A.C. & Thompson, R.N.** (1975). Low alkali, high calcium olivine tholeiite lavas from the Isle of Skye, Scotland. *Journal of Petrology*, **16**, No. 2, 488-497.
- Evans, B.W.** (1964). Fractionation of elements in the pelitic hornfelses of the Cashel-Lough Wheelaun intrusion, Connemara, Eire. *Geochimica et Cosmochimica Acta*, **28**, 127-156.
- Evans, B.W. & Moore, J.G.** (1968). Mineralogy as a function of depth in the pre-historic Makaopuhi tholeiitic lava lake, Hawaii. *Contributions to Mineralogy and Petrology*, **17**, 85-115.
- Fabriès, J.** (1979). Spinel-olivine geothermometry in Peridotites from ultrabasic complexes. *Contributions to Mineralogy and Petrology*, **69**, 329-336.
- Faithfull, J.W.** (1985). The Lower Eastern Layered Series of Rhum. *Geological Magazine*, **122**, No. 5, 459-468.
- Faure, G.** (1986). *Principles of Isotope Geology*, 2nd edn. John Willey & Sons, New York, 589 pp.

- Fettes, D.J., Mendum, J.R., Smith, D.I. & Watson, J.V. (1992).** *Geology of the Outer Hebrides. Memoir for 1:100000 geological sheets, Lewis and Harris, Uist and Barra.* British Geological Survey, London,
- Fisk, M.R. & Bence, A.E. (1980).** Experimental crystallization of chrome spinel in FAMOUS basalt 567-1-1. *Earth and Planetary Science Letters*, **48**, 111-123.
- Fitton, J.D. & Dunlop, H.M. (1985).** The Cameroon line, West Africa, and its bearing on the origin of oceanic and continental alkali basalts. *Earth and Planetary Science Letters*, **72**, 23-38.
- Fitton, J.D., James, D. & Leeman, W.P. (1991).** Basic magmatism associated with Late Cenozoic extension in the Western United States : Compositional variations in space and time. *Journal of Geophysical Research*, **96**, No. 8B, 13693-13711.
- Fodor, R.V. (1987).** Low- and high-TiO₂ flood basalts of southern Brazil : Origin from picritic parentage and a common mantle source. *Earth and Planetary Science Letters*, **84**, 423-430.
- Fodor, R.V., Corwin, C. & Roisenberg, A. (1985).** Petrology of Serra Geral (Paraná) continental flood basalts, Southern Brazil: Crustal contamination, source material, and South Atlantic magmatism. *Contributions to Mineralogy and Petrology*, **91**, 54-65.
- Fodor, R.V., Corwin, C. & Sial, A.N. (1985).** Crustal signatures in the Serra Geral flood-basalt province, southern Brazil : O- and Sr- isotope evidence. *Geology*, **13**, 763-765.
- Fournet, (1846).** *Géologie Lyonnais.* De Barret, Lyon, 744 pp.
- Francis, D. (1986).** The pyroxene paradox in MORB glasses - a signature of picritic parental magmas ? *Nature*, **319**, 586-589.
- Gamble, R.P. & Taylor, L.A. (1980).** Crystal/liquid partitioning in augite : Effects of cooling rate. *Earth Science and Planetary Letters*, **47**, 21-33.
- Gardien, V., Thompson, A.B., Grujic, D. & Ulmer, P. (1995).** Experimental melting of biotite + plagioclase + quartz ± muscovite assemblages and the implication for crustal melting. *Journal of Geophysical Research*, **100**, No. B8, 15581-15591.
- Gibb, F.G.F. (1968).** Flow differentiation in the xenolithic ultrabasic dykes of the Cuillins and the Strathaird Peninsula, Isle of Skye, Scotland. *Journal of Petrology*, **9**, No. 3, 411-443.
- Gibb, F.G.F. (1969).** Cognate xenoliths in the Tertiary ultrabasic dykes of south-west Skye. *Mineralogical Magazine*, **37**, 504-514.
- Gibb, F.G.F. (1973).** The zoned clinopyroxenes of the Shiant Isles sill, Scotland. *Journal of Petrology*, **14**, No. 2, 203-230.
- Gibb, F.G.F. (1976).** Ultrabasic rocks of Rhum and Skye : The nature of the parent magma. *Journal of the Geological Society, London*, **132**, 209-222.
- Giletti, B.J. & Casserly, J.E.D. (1994).** Strontium diffusion kinetics in plagioclase feldspars. *Geochimica et Cosmochimica Acta*, **58**, No. 18, 3785-3793.
- Graham, I.J. (1987).** Petrography and origin of metasedimentary xenoliths in lavas from Tongariro Volcanic Centre. *New Zealand Journal of Geology and Geophysics*, **30**, 139-157.
- Grapes, R.H. (1986).** Melting and thermal reconstitution of pelitic xenoliths, Wehr Volcano, East Eifel, West Germany. *Journal of Petrology*, **27**, No. 2, 343-396.

- Grapes, R.H.** (1991). Aluminous alkali feldspar-bearing xenoliths and the origin of sanidinite, East Eifel, Germany. *Neues Jahrbuch für Mineralogie Abhandlungen*, No. 3, 129-144.
- Grasset, O. & Albarède, F.** (1994). Hybridization of mingling magmas with different densities. *Earth and Planetary Science Letters*, **121**, 327-332.
- Green, N.L.** (1994). Mechanism for middle to upper crustal contamination : Evidence from continental-margin magmas. *Geology*, **22**, 231-234.
- Green, T.H.** (1976). Experimental generation of cordierite- or garnet-bearing granitic liquids from pelitic compositions. *Geology*, 85-88.
- Gribble, C.D.** (1968). The cordierite-bearing rocks of the Haddo House and Arnage districts, Aberdeenshire. *Contributions to Mineralogy and Petrology*, **17**, 315-330.
- Gribble, C.D.** (1970). The role of partial fusion in the genesis of certain cordierite-bearing rocks. *Scottish Journal of Geology*, **6**, No. 1, 75-82.
- Gribble, C.D. & O'Hara, M.J.** (1967). Interaction of basic magma with pelitic materials. *Nature*, **214**, No. 5094, 1198-1201.
- Grove, T.L. & Baker, M.B.** (1984). Phase equilibrium controls on the tholeiitic versus calc-alkaline differentiation trends. *Journal of Geophysical Research*, **89**, No. B5, 3253-3274.
- Grove, T.L., Gerlach, D.C. & Sando, T.W.** (1982). Origin of calc-alkaline series lavas at Medicine Lake volcano by fractionation, assimilation and mixing. *Contributions to Mineralogy and Petrology*, **80**, 160-182.
- Grunder, A.L.** (1992). Two-stage contamination during crustal assimilation : Isotope evidence from volcanic rocks in eastern Nevada. *Contributions to Mineralogy and Petrology*, **112**, 219-229.
- Hall, A.** (1987). *Igneous Petrology*. Longman Scientific & Technical, Harlow, 573 pp.
- Hallimond, A.F.** (1914). Optically uniaxial augite from Mull. *Mineralogical Magazine*, **17**, 97-99.
- Harker, A.** (1904). *The Tertiary Igneous Rocks of Skye*. Geological Survey, Scotland,
- Harris, C.** (1983). The petrology of lavas and associated plutonic inclusions of Ascension Island. *Journal of Petrology*, **24**, No. 4, 424-470.
- Hart, S.R.** (1988). Heterogeneous mantle domains : Signatures, genesis and mixing chronologies. *Earth and Planetary Science Letters*, **90**, 273-296.
- Haszeldine, R.S., Brint, J.F., Fallick, A.E., Hamilton, P.S. & Brown, S.** (1992). Open and restricted hydrologies in Brent Group diagenesis : North Sea. In: Morton, A.C., Haszeldine, R.S., Giles, M.R. & Brown, S. (eds.), *Geology of the Brent Group*. **Geological Society Special Publication No. 61**, Geological Society, London,
- Hawkesworth, C. & Ellam, R.** (1989). Chemical fluxes and wedge replenishment rates along recent destructive plate margins. *Geology*, **17**, 46-49.
- Hawkesworth, C.J., Erlank, A.J., Marsh, J.S., Menzies, M.A. & Van Calsteren, P.W.C.** (1983). Evolution of the continental lithosphere : Evidence from volcanics and xenoliths in Southern Africa. In: Hawkesworth, C.J. & Norry, M.J. (eds.), *Continental Basalts and Mantle Xenoliths*. Shiva Publishing, Nantwich,

- Hawkesworth, C.J., Gallagher, K., Kelley, S., Mantovani, M., Peate, D.W., Regelous, M. & Rogers, N.W.** (1992). Paraná magmatism and the opening of the South Atlantic. In: Storey, B.C., Alabaster, T. & Pankhurst, R.J. (eds.), *Magmatism and the Causes of Continental Break-up*. Geological Society Special Publication No. 68, 221-240.
- Hawkesworth, C.J., Rogers, N.W., Van Clasteren, P.W.C. & Menzies, M.A.** (1984). Mantle enrichment processes. *Nature*, **311**, 331-335.
- Henderson, P.** (1975). Reaction trends shown by chrome-spinels of the Rhum layered intrusion. *Geochimica et Cosmochimica Acta*, **39**, 1035-1044.
- Henderson, P. & Gijbels, R.** (1976). Trace element indicators of the genesis of the Rhum layered intrusion, Inner Hebrides. *Scottish Journal of Geology*, **12**, No. 4, 325-333.
- Henderson, P. & Suddaby, P.** (1971). The nature and origin of the chrome-spinel of the Rhum layered intrusion. *Contributions to Mineralogy and Petrology*, **33**, 21-31.
- Henderson, P. & Wood, R.J.** (1981). Reaction relationships of chrome-spinels in igneous rocks - Further evidence from the layered intrusions of Rhum and Mull, Inner Hebrides, Scotland. *Contributions to Mineralogy and Petrology*, **78**, 225-229.
- Hergt, J.M., Chappell, B.W., Faure, G. & Mesing, T.M.** (1989). The geochemistry of Jurassic dolerites from Portal Peak, Antarctica. *Contributions to Mineralogy and Petrology*, **102**, 298-305.
- Hergt, J.M., Peate, D.W. & Hawkesworth, C.J.** (1991). The petrogenesis of Mesozoic Gondwana Low-Ti flood basalts. *Earth and Planetary Science Letters*, **105**, 134-148.
- Hill, R. & Roeder, P.** (1974). The crystallization of spinel from basaltic liquid as a function of oxygen fugacity. *Journal of Geology*, **82**, 709-729.
- Holdsworth, R.E., Harris, A.L. & Roberts, A.M.** (1987). The stratigraphy, structure and regional significance of the Moine rocks of Mull, Argyllshire, W. Scotland. *Geological Journal*, **22**, 83-107.
- Holgate, N.** (1954). The role of liquid immiscibility in igneous petrogenesis. *Journal of Geology*, **62**, 439-480.
- Holland, J.G. & Brown, G.M.** (1972). Hebridean tholeiitic magmas : A geochemical study of the Ardnamurchan cone-sheets. *Contributions to Mineralogy and Petrology*, **37**, 139-160.
- Hooper, P.R. & Hawkesworth, C.J.** (1993). Isotopic and geochemical constraints on the origin and evolution of the Columbia River Basalt. *Journal of Petrology*, **34**, No. 6, 1203-1246.
- Humphris, S.E., Morrison, M.A. & Thompson, R.N.** (1978). Influence of rock crystallization history upon subsequent lanthanide mobility during hydrothermal alteration of basalts. *Chemical Geology*, **23**, 125-137.
- Hunter, R.H. & Sparks, R.S.J.** (1987). The differentiation of the Skaergaard Intrusion. *Contributions to Mineralogy and Petrology*, **95**, 451-461.
- Huppert, H.E. & Sparks, R.S.J.** (1980). The fluid dynamics of a basaltic magma chamber replenished by an influx of hot dense ultrabasic liquid. *Contributions to Mineralogy and Petrology*, **75**, 279-289.
- Huppert, H.E. & Sparks, R.S.J.** (1985). Cooling and contamination of mafic and ultramafic magmas during ascent through continental crust. *Earth and Planetary Science Letters*, **74**, 371-386.

Huppert, H.E. & Sparks, R.S.J. (1989). Chilled margins in igneous rocks. *Earth and Planetary Science Letters*, **92**, 397-405.

Irvine, T.N. (1967). Chromian spinels as a petrological indicator. Part 2. Petrologic applications. *Canadian Journal of Earth Sciences*, **4**, 71-103.

Jaques, A.L. & Green, D.H. (1980). Anhydrous melting of peridotite at 0-15 kbar pressure, and the genesis of tholeiitic basalts. *Contributions to Mineralogy and Petrology*, **73**, 287-310.

Johannes, W. (1978). Melting of plagioclase in the system Ab-An-H₂O and Qtz-Ab-An-H₂O at P(H₂O)=5kbars, an equilibrium problem. *Contributions to Mineralogy and Petrology*, **66**, 295-303.

Johannes, W. & Holtz, F. (1992). Melting of plagioclase in granite and related systems : Composition of coexisting phases and kinetic observations. *Transactions of the Royal Society of Edinburgh : Earth Sciences*, **83**, 417-422.

Kaczor, S.M., Hanson, G.N. & Peterman, Z.E. (1988). Disequilibrium melting of granite at the contact with a basic plug : A geochemical and petrographic study. *Journal of Geology*, **96**, 61-78.

Kerr, A.C. (1993). Elemental evidence for an enriched small-fraction-melt input into Tertiary Mull basalts, Western Scotland. *Journal of the Geological Society, London*, **150**, 763-769.

Kerr, A.C. (1994). Lithospheric thinning during the evolution of continental large igneous provinces : A case study from the North Atlantic Tertiary province. *Geology*, **22**, 1027-1030.

Kerr, A.C. (1995a). The geochemistry of the Mull-Morvern Tertiary lava succession, NW Scotland : An assessment of mantle sources during plume-related volcanism. *Chemical Geology*, **122**, 43-58.

Kerr, A.C. (1995b). The melting processes and composition of the North Atlantic (Iceland) plume : Geochemical Evidence from the Early Tertiary basalts. *Journal of the Geological Society, London*, **152**, 975-978.

Kerr, A.C., Kempton, P.D. & Thompson, R.N. (1995). Crustal assimilation during turbulent magma ascent (ATA); new isotopic evidence from the Mull Tertiary lava succession, N.W. Scotland. *Contributions to Mineralogy and Petrology*, **119**, 142-154

Kille, I.C. (1987). *The minor Tertiary intrusions around Loch Scridain, Isle of Mull*. Unpublished PhD Thesis, Imperial College, London,

Kille, I.C., Thompson, R.N., Morrison, M.A. & Thompson, R.F. (1986). Field evidence for turbulence during flow of basalt magma through conduits from South-West Mull. *Geological Magazine*, **123**, No. 6, 693-697.

King, B.C. (1982). Composite intrusions : Association of acid and basic magma. : Part 7 (The Tertiary) Chapter 32. In: Sutherland, D.S. (ed.), *The Igneous Rocks of the British Isles*. John Wiley & Sons Ltd., 441-447.

Kitchen, D.E. (1984). Pyrometamorphism and the contamination of basaltic magma at Tieveragh, Co. Antrim. *Journal of the Geological Society, London*, **141**, 733-745.

Kitchen, D.E. (1985). The parental magma on Rhum : Evidence from alkaline segregations and veins in the peridotites from Salisbury's dam. *Geological Magazine*, **122**, No. 5, 529-537.

- Klein, E.M. & Langmuir, C.H.** (1987). Global correlations of ocean ridge basalt chemistry with axial depth and crustal thickness. *Journal of Geophysical Research*, **92**, No. B8, 8089-8115.
- Kretz, R.** (1982). Transfer and exchange equilibria in a portion of the pyroxene quadrilateral as deduced from natural and experimental data. *Geochimica et Cosmochimica Acta*, **46**, 411-421.
- Kudo, A.M. & Weill, D.** (1970). An igneous plagioclase geothermometer. *Contributions to Mineralogy and Petrology*, **25**, 52-65.
- Kuno, H.** (1950). Petrology of Hakone Volcano and the adjacent areas, Japan. *Geological Society of America Bulletin*, **61**, 957-1020.
- Kuno, H.** (1955). Ion substitution in the diopside-ferropigeonite series of clinopyroxenes. *American Mineralogist*, **40**, 70-93.
- Kushiro, I.** (1960). Si-Al relation in clinopyroxenes from igneous rocks. *American Journal of Science*, **258**, 548-554.
- Langmuir, C.H., R.D., V.J., Hanson, G.N. & Hart, S.R.** (1978). A general mixing equation with applications to Icelandic basalts. *Earth and Planetary Science Letters*, **37**, 393-400.
- Le Bas, M.J., Le Maitre, R.E., Streckeisen, A. & Zanettin, B.** (1986). A chemical classification of volcanic rocks based on the total alkali-silica diagram. *Journal of Petrology*, **27**, No. 3, 745-750.
- Le Fort, P.** (1981). Manaslu leucogranite : A collision signature of the Himalaya. A model for its genesis and emplacement. *Journal of Geophysical Research*, **86**, 10545-10568.
- Lee, G.W. & Bailey, E.B.** (1925). *Pre-Tertiary Geology of Mull, Loch Aline and Oban.*, 1 edn. H.M.S.O., Edinburgh, 140 pp.
- Leshner, C.E.** (1990). Decoupling of chemical and isotopic exchange during magma mixing. *Nature*, **344**, 235-237.
- Lightfoot, P.C., Naldrett, A.J., Gorbachev, N.S., Doherty, W. & Fedorenko, V.A.** (1990). Geochemistry of the Siberian trap of the Noril'sk area, USSR, with implications for the relative contributions of crust and mantle to flood basalt magmatism. *Contributions to Mineralogy and Petrology*, **104**, 631-644.
- Lister, J.R., Campbell, I.H. & Kerr, R.C.** (1991). The eruption of komatiites and picrites in preference to primitive basalts. *Earth and Planetary Science Letters*, **105**, 343-352.
- Lofgren, G.E.** (1974). An experimental study of plagioclase morphology : Isothermal crystallization. *American Journal of Science*, **274**, 243-273.
- Ludden, J.N. & Thompson, G.** (1978). Behaviour of rare earth elements during submarine weathering of tholeiitic basalts. *Nature*, **274**, 147-149.
- Lyle, P. & Preston, J.** (1993). Geochemistry and volcanology of the Tertiary basalts of the Giant's Causeway area, Northern Ireland. *Journal of the Geological Society, London*, **150**, 109-120.
- Lyon, T.D.B., Gillen, C. & Bowes, D.R.** (1975). Rb-Sr isotopic studies near the major Precambrian junction, between Scourie and Loch Laxford, northwest Scotland. *Scottish Journal of Geology*, **11**, 333-337.
- Maaløe, S.** (1976). The zoned plagioclase of the Skaergaard intrusion, East Greenland. *Journal of Petrology*, **17**, No. 3, 398-419.

- Maaløe, S.** (1985). *Principles of igneous petrology*. Springer-Verlag, Berlin, 374 pp.
- MacRae, N.D. & Nesbitt, H.W.** (1980). Partial melting of common metasedimentary rocks : A mass balance approach. *Contributions to Mineralogy and Petrology*, **75**, 21-26.
- Mantovani, M.S.M., Marques, L.S., De Sousa, M.A., Civetta, L., Atalla, L. & Innocenti, F.** (1985). Trace element and strontium isotope constraints on the Origin and evolution of Paraná continental flood basalts of Santa Catarina State (Southern Brazil). *Journal of Petrology*, **26**, No. 1, 187-209.
- Mason, R.** (1978). *Petrology of the Metamorphic Rocks*. Allen & Unwin, London, 254 pp.
- Mathez, E.A.** (1973). Refinement of the Kudo-Weill plagioclase geothermometer and its application to basaltic rocks. *Contributions to Mineralogy and Petrology*, **41**, 61-72.
- Mattey, D.P., Gibson, I.L., Marriner, G.F. & Thompson, R.N.** (1977). The diagnostic geochemistry, relative abundance, and spatial distribution of high-calcium, low-alkali olivine tholeiite dykes in the Lower Tertiary regional swarm of the Isle of Skye, NW Scotland. *Mineralogical Magazine*, **41**, 273-285.
- Maury, R.C. & Bizouard, H.** (1974). Melting of acid xenoliths into a basanite : An approach to the possible mechanisms of crustal contamination. *Contributions to Mineralogy and Petrology*, **48**, 275-286.
- Maury, R.C., Didier, J. & Lameyre, J.** (1978). Comparative magma/xenolith relationships in some volcanic and plutonic rocks from the French Massif Central. *Contributions to Mineralogy and Petrology*, **66**, 401-408.
- McBirney, A.R.** (1979). Effects of assimilation. In: (eds.), *The Evolution of Igneous Rocks : Fiftieth Anniversary Perspective*. Princeton University Press, 307-338.
- McBirney, A.R. & Hunter, R.H.** (1995). The cumulate paradigm reconsidered. *Journal of Geology*, **103**, 114-122.
- McCulloch, M.T. & Wasserburg, G.J.** (1978). Sm-Nd and Rb-Sr chronology of continental crust formation. *Science*, **200**, 1003-1011.
- McDonough, W.F., Sun, S., Ringwood, A.E., Jagoutz, E. & Hofmann, A.W.** (1991). K, Rb and Cs in the earth and moon and the evolution of the earth's mantle. *Geochimica et Cosmochimica Acta*, **Ross Taylor Symposium volume**,
- McKenzie, D.P. & Bickle, M.J.** (1988). Partial melt distributions from inversion of rare earth element concentrations. *Journal of Petrology*, **32**, 1021-1091.
- McLeod, P.S. & Sparks, R.S.J.** (1995). (Conf. Abs.) *Melting and assimilation of xenoliths*. Conference on Magmatic Processes, Sheffield University , 27 pp.
- Mehnert, K.R., Büsch, W. & Schneider, G.** (1973). Initial melting at grain boundaries of quartz and feldspar in gneisses and granulites. *Neues Jahrbuch für Mineralogie Monatshefte*, **4**, No. 165-183,
- Melson, W.G. & Switzer, G.** (1966). Plagioclase-spinel-graphite xenoliths in metallic iron-bearing basalts, Disko Island, Greenland. *American Mineralogist*, **51**, 664-676.
- Menzies, M., Seyfried, W. & Blanchard, D.** (1979). Experimental evidence of rare earth element mobility in greenstones. *Nature*, **282**, 398-399.
- Menzies, M.A.** (1983). Mantle ultramafic xenoliths in alkaline magmas : Evidence for mantle heterogeneity modified by magmatic activity. In: Hawkesworth, C.J. & Norry, M.J. (eds.), *Continental Basalts and Mantle Xenoliths*. Shiva Publishing, Nantwich, 92-110.

Moorbath, S. & Bell, J.D. (1965). Strontium isotope abundance studies and Rb-Sr age determinations on Tertiary igneous rocks from the Isle of Skye, north west Scotland. *Journal of Petrology*, **6**, 37-66.

Moorbath, S. & Thompson, R.N. (1980). Strontium isotope geochemistry and petrogenesis of the Early Tertiary lava pile of the Isle of Skye, Scotland, and other basic rocks of the British Tertiary Province : An example of magma-crust interaction. *Journal of Petrology*, **21**, No. 2, 295-321.

Moorbath, S. & Welke, H. (1969). Lead isotope studies on igneous rocks from the Isle of Skye, north west Scotland. *Earth and Planetary Science Letters*, **5**, 217-230.

Morrison, A.D. & Reay, A. (1995). Geochemistry of Ferrar dolerite sills and dykes at Terra Cotta Mountain, south Victoria Land, Antarctica. *Antarctic Science*, **7**, No. 1, 73-85.

Morrison, M.A. (1977). *Igneous and metamorphic geochemistry of Mull lavas*. Unpublished PhD Thesis, London,

Morrison, M.A. (1978). The use of "immobile" trace elements to distinguish the palaeotectonic affinities of metabasalts : Applications to the Palaeocene basalts of Mull and Skye, Northwest Scotland. *Earth and Planetary Science Letters*, **39**, 417-426.

Morrison, M.A., Thompson, R.N., Gibson, I.L. & Marriner, G.F. (1980). Lateral chemical heterogeneity in the Palaeocene upper mantle beneath the Scottish Hebrides. *Philosophical Transactions of the Royal Society of London, Ser A* **297**, 229-244.

Morrison, M.A., Thompson, R.N. & Dickin, A.P. (1985). Geochemical evidence for complex magmatic plumbing during development of a continental volcanic centre. *Geology*, **13**, 581-584.

Morton, A.C., Hitchen, K., Ritchie, J.D., Hine, N.M., Whitehouse, M. & Carter, S.G. (1995). Late Cretaceous basalts from Rosemary Bank, Northern Rockall Trough. *Journal of the Geological Society, London*, **152**, 947-952.

Munha, J., Palacios, T., MacRae, N.D. & Mata, J. (1990). Petrology of ultramafic xenoliths from Madeira island. *Geological Magazine*, **127**, No. 6, 543-566.

Musset, A.E. (1986). ^{40}Ar - ^{39}Ar step-heating ages of the Tertiary igneous rocks of Mull, Scotland. *Journal of the Geological Society, London*, **143**, 887-896.

Nakamura, N. (1974). Determination of REE, Ba, Fe, Mg, Na and K in carbonaceous and ordinary chondrites. *Geochimica et Cosmochimica Acta*, **38**, 757-773.

Nathan, H.D. & Van Kirk, C.K. (1978). A model of magmatic crystallization. *Journal of Petrology*, **19**, 66-94.

Nicholson, H. & Latin, D. (1992). Olivine tholeiites from Krafla, Iceland : Evidence for variations in melt fraction within a plume. *Journal of Petrology*, **1106**-1124.

Nicolas, A. (1989). *Structures of ophiolites and dynamics of ocean lithosphere*. Kluwer Academic Publishers, Dordrecht, 367 pp.

O'Hara, M.J. (1968). The bearing of phase equilibria studies on the origin and evolution of basic and ultrabasic rocks. *Earth Science Reviews*, **4**, 69-133.

O'Hara, M.J. (1977). Geochemical evolution during fractional crystallization of a periodically refilled magma chamber. *Nature*, **266**, 503-507.

O'Hara, M.J. & Mathews, R.E. (1981). Geochemical evolution in an advancing, periodically replenished, periodically tapped, continuously fractionating magma chamber. *Journal of the Geological Society, London*, **138**, 237-277.

Olson, P. (1988). Plume formation and lithospheric erosion : A comparison of laboratory and numerical experiments. *Journal of Geophysical Research*, **93**, 15065-15084.

Osborn, E.F. & Muan, A. (1960). *Phase equilibrium diagrams of oxide systems*. The American Ceramic Society and the Edward Orton Jr. Ceramic Foundation, Columbus, Ohio,

Osborn, E.F. & Tait, D.B. (1952). The system diopside-forsterite-anorthite. *American Journal of Science, Bowen Volume*, 413-433.

Palacz, Z.A. & Tait, S.R. (1985). Isotopic and geochemical investigation of unit 10 from the Eastern Layered Series of the Rhum Intrusion, Northwest Scotland. *Geological Magazine*, **122**, No. 5, 485-490.

Pankhurst, R.J., Walsh, J.N., Beckinsale, R.D. & Skelhorn, R.R. (1978). Isotopic and other geochemical evidence for the origin of the Loch Uisg granophyre, Isle of Mull, Scotland. *Earth and Planetary Science Letters*, **38**, 355-363.

Patchett, P.J. (1980). Thermal effects of basalt on continental crust and crustal contamination of magmas. *Nature*, **283**, 559-561.

Pearce, J.A. (1983). Role of the sub-continental lithosphere in magma genesis at active continental margins. In: Hawkesworth, C.J. & Norry, M.J. (eds.), *Continental Basalts and Mantle Xenoliths*. Shiva, Nantwich, 230-249.

Pedersen, A.K. (1978). Non-stoichiometric magnesian spinels in shale xenoliths from a native iron-bearing andesite at Asuk, Disko, Central West Greenland. *Contributions to Mineralogy and Petrology*, **67**, 331-340.

Pedersen, A.K. (1979). A shale buchite xenolith with Al-armalcolite and native iron in a lava from Asuk, Disko, Central West Greenland. *Contributions to Mineralogy and Petrology*, **69**, 83-94.

Pedersen, A.K. (1981). Armalcolite-bearing Fe-Ti oxide assemblages in graphite-equilibrated salic volcanic rocks with native iron from Disko, Central West Greenland. *Contributions to Mineralogy and Petrology*, **77**, 307-324.

Petrini, R., Civetta, L., Piccirillo, E., M., Bellieni, G., Comin-Chiaramonti, P., Marques, L.S. & Melfi, A.J. (1987). Mantle heterogeneity and crustal contamination in the genesis of low-Ti continental flood basalts from the Paraná Plateau (Brazil): Sr-Nd isotope and geochemical evidence. *Journal of Petrology*, **28**, 701-726.

Philpotts, A.R. & Asher, P.M. (1993). Wallrock melting and reaction effects along the Higganum diabase dike in Connecticut : Contamination of a continental flood basalt feeder. *Journal of Petrology*, **34**, No. 5, 1029-1058.

Platt, J.P. & Vissers, R.L.M. (1980). Extensional structures in anisotropic rocks. *Journal of Structural Geology*, **2**, 397-410.

Potts, G.J., Hunter, R.H., Harris, A.L. & Fraser, F.M. (1995). Late-orogenic extensional tectonics at the NW margin of the Calidonides in Scotland. *Journal of the Geological Society, London*, **152**, 907-910.

Powell, R. (1984). Inversion of the assimilation and fractional crystallization (AFC) equations; characterization of contaminants from isotope and trace element relationships in volcanic suites. *Journal of the Geological Society, London*, **141**, 449-452.

- Read, H.H.** (1931). On corundum-spinel xenoliths in the gabbro of Haddo House, Aberdeenshire. *Geological Magazine*, **68**, 446-453.
- Read, H.H.** (1935). The gabbros and associated xenolithic complexes of the Haddo House district, Aberdeenshire. *Quarterly Journal of the Geological Society, London*, **91**, 591-638.
- Reiners, P.W., Nelson, B.K. & Ghiorso, M.S.** (1995). Assimilation of felsic crust by basaltic magma : Thermal limits and extents of crustal contamination of mantle-derived magmas. *Geology*, **23**, No. 3, 563-566.
- Richard, P., Shimizu, N. & Allegre, C.J.** (1976). $^{143}\text{Nd}/^{144}\text{Nd}$, a natural tracer : An application to oceanic basalts. *Earth and Planetary Science Letters*, **31**, 269-278.
- Richards, M.A., Duncan, R.A. & Courtillot, V.E.** (1989). Flood basalts and hotspot tracks : Plume heads and tails. *Science*, **246**, 103-107.
- Ridley, W.I.** (1973). The petrology of volcanic rocks from the Small Isles of Invernesshire. *Report of the Institute of Geological Sciences*, **73/10**, .
- Ridley, W.I.** (1977). The crystallization trends of spinels in Tertiary basalts from Rhum and Muck and their petrogenetic significance. *Contributions to Mineralogy and Petrology*, **64**, 243-255.
- Ripley, E.M. & Alawi, J.A.** (1988). Petrogenesis of pelitic xenoliths at the Babbitt Cu-Ni deposit, Duluth Complex, Minnesota, USA. (abstr). *Lithos*, **21**, 143-159.
- Roeder, P.L. & Emslie, R.F.** (1970). Olivine-liquid equilibrium. *Contributions to Mineralogy and Petrology*, **29**, 275-289.
- Roeder, P.L., Campbell, I.H. & Jamieson, H.E.** (1979). A re-evaluation of the olivine-spinel geothermometer. *Contributions to Mineralogy and Petrology*, **68**, 325-334.
- Rollinson, H.R.** (1993). *Using Geochemical Data : Evaluation, Presentation, Interpretation*. John Wiley & Sons, New York, 352 pp.
- Sato, H.** (1975). Diffusion coronas around quartz xenocrysts in andesite and basalt from the Tertiary Volcanic Region in northeaster Shikoku, Japan. *Contributions to Mineralogy and Petrology*, **50**, 49-64.
- Saunders, A.D., Storey, M., Kent, R.W. & Norry, M.J.** (1992). Consequences of plume-lithosphere interactions. In: Storey, B.C., Alabaster, T. & Pankhurst, R.J. (eds.), *Magmatism and the Causes of Continental Break-up*. Geological Society Special Publication No. 68, 41-60.
- Sawyer, E.W.** (1994). Melt segregation in the continental crust. *Geology*, **22**, 1019-1022.
- Scarrow, J.H. & Cox, K.G.** (1995). Basalt generated by decompressive adiabatic melting of a mantle plume : A case study from the Isle of Skye, NW Scotland. *Journal of Petrology*, **36**, No. 1, 3-22.
- Scowen, P.A.H., Roeder, P.L. & Helz, R.T.** (1991). Re-equilibration of chromite within Kilauea Iki lava lake, Hawaii. *Contributions to Mineralogy and Petrology*, **107**, 8-20.
- Searle, E.J.** (1962a). Quartzose xenoliths and pyroxene aggregates in the Auckland basalts. *New Zealand Journal of Geology and Geophysics*, **5**, 130-140.
- Searle, E.J.** (1962b). Xenoliths and metamorphosed rocks associated with the Auckland basalts. *New Zealand Journal of Geology and Geophysics*, **5**, 384-403.

- Seewald, J.S. & Seyfried, W.E. (1990).** The effect of temperature on metal mobility in sub-seafloor hydrothermal systems : Constraints from basalt alteration experiments. *Earth and Planetary Science Letters*, **101**, 388-403.
- Shibata, T., S.E., D. & Walker, D. (1979).** Abyssal tholeiites from the Oceanographer fracture zone. I. Petrology and fractionation. *Contributions to Mineralogy and Petrology*, **70**, 89-102.
- Sibley, D.F., Vogel, T.A., Walker, B.M. & Byerly, G. (1976).** The origin of oscillatory zoning in plagioclase : A diffusion and growth controlled model. *American Journal of Science*, **276**, 275-284.
- Siders, M.A. & Elliot, D.H. (1985).** Major and trace element geochemistry of the Kirkpatrick basalt, Mesa Range, Antarctica. *Earth and Planetary Science Letters*, **72**, 54-64.
- Sigurdsson, H. (1968).** Petrology of acid xenoliths from Surtsey. *Geological Magazine*, **105**, No. 5, 440-453.
- Sigurdsson, H. & Sparks, S.R.J. (1978).** Lateral magma flow within rifted Icelandic crust. *Nature*, **274**, 126-130.
- Simkin, T. (1967).** Flow differentiation in the picritic sills of North Skye. In: Wyllie, P.J. (ed.), *Ultramafic and Related Rocks*. John Wiley & Sons, 64-69.
- Smith, D.G.W. (1965).** The chemistry and mineralogy of some emery-like rocks from Sithean Sluaigh, Strachur, Argyllshire. *American Mineralogist*, **50**, 1982-2023.
- Smith, D.G.W. (1969).** Pyrometamorphism of phyllites by a dolerite plug. *Journal of Petrology*, **10**, No. 1, 20-55.
- Smith, D.G.W. & Lindsley, D.H. (1971).** Stable and metastable augite crystallization trends in a single basalt flow. *American Mineralogist*, **56**, 225-233.
- Sparks, R.S.J. (1988).** Petrology and geochemistry of the Loch Ba ring dyke, Mull (NW Scotland) : An example of the extreme differentiation of tholeiitic magmas. *Contributions to Mineralogy and Petrology*, **100**, 446-461.
- Speight, J.M., Skelhorn, R.R., Sloan, T. & Knaap, R.J. (1982).** The dyke swarms of Scotland. : Part 7 (The Tertiary) Chapter 33. In: Sutherland, D.S. (ed.), *The Igneous Rocks of the British Isles*. John Wiley & Sons Ltd., 449-459.
- Stamatelopoulous-Seymour, K. & Vlassopoulos, D. (1992).** Magma mixing at Nisyros volcano, as inferred from incompatible trace-element systematics. *Journal of Volcanology and Geothermal Research*, **50**, 273-299.
- Sturt, B.A. (1970).** Exsolution during metamorphism with particular reference to feldspar solid solutions. *Mineralogical Magazine*, **37**, No. 291, 815-832.
- Sun, S.-S. & McDonough, W.F. (1989).** Chemical and isotopic systematics of oceanic basalts : Implications for mantle composition and processes. In: Saunders, A.D. & Norry, M.J. (eds.), *Magmatism in the Ocean Basins*. Geological Society Special Publications No. 42, 313-345.
- Sun, S.-S., Nesbitt, R.W. & Sharaskin, A.Y. (1979).** Geochemical characteristics of mid-ocean ridge basalts. *Earth and Planetary Science Letters*, **44**, 119-138.
- Sutherland, D.S. (1982).** *Igneous Rocks of the British Isles*. John Wiley & Sons Ltd. 645pp
- Thirwall, M.F. & Jones, N.W. (1983).** Isotope geochemistry and contamination mechanics of Tertiary lavas from Skye, Northwest Scotland. In: Hawkesworth, C.J. &

Norry, M.J. (eds.), *Continental Basalts and Mantle Xenoliths*. Shiva Publishing, Cheshire, 186-250.

Thirwall, M.F., Upton, B.G.J. & Jenkins, C. (1994). Interaction between continental lithosphere and the Iceland plume - Sr-Nd-Pb isotope geochemistry of Tertiary basalts, NE Greenland. *Journal of Petrology*, **35**, No. 3, 839-879.

Thomas, H.H. (1922). On certain xenolithic Tertiary minor intrusions in the Island of Mull (Argyllshire). *Quarterly Journal of the Geological Society (London)*, **78**, 229-260.

Thompson, A.B. (1982). Dehydration melting of pelitic rocks and the generation of H₂O-undersaturated granitic liquid. *American Journal of Science*, **282**, 1567-1595.

Thompson, R.N. (1981). Thermal aspects of the origin of Hebridean Tertiary acid magmas. 1. An experimental study of partial fusion of Lewisian gneisses and Torridonian sediments. *Mineralogical Magazine*, **44**, 161-170.

Thompson, R.N. (1982). Geochemistry and magma genesis. : Part 7 (The Tertiary) Chapter 34. In: Sutherland, D.S. (ed.), *The Igneous Rocks of the British Isles*. John Wiley & Sons Ltd., 461-477.

Thompson, R.N. & Gibson, S.A. (1991). Subcontinental mantle plumes, hotspots and pre-existing thinspots. *Journal of the Geological Society, London*, **148**, 973-977.

Thompson, R.N. & Morrison, M.A. (1988). Asthenospheric and lower-lithospheric mantle contributions to continental extensional magmatism : An example from the British Tertiary Province. *Chemical Geology*, **68**, 1-15.

Thompson, R.N., Esson, J. & Dunham, A.C. (1972). Major element chemical variation in the Eocene lavas of the Isle of Skye, Scotland. *Journal of Petrology*, **13**, No. 2, 219-253.

Thompson, R.N., Gibson, I.L., Marriner, G.F., Matthey, D.P. & Morrison, M.A. (1980). Trace-element evidence of multistage mantle fusion and polybaric fractional crystallization in the Palaeocene lavas of Skye, NW Scotland. *Journal of Petrology*, **21**, No. 2, 265-293.

Thompson, R.N., Dickin, A.P., Gibson, I.L. & Morrison, M.A. (1982). Elemental fingerprints of isotopic contamination of Hebridean Palaeocene mantle-derived magmas by Archaean sial. *Contributions to Mineralogy and Petrology*, **79**, 159-168.

Thompson, R.N., Morrison, M.A., Dickin, A.P. & Hendry, G.L. (1983). Continental flood basalts...Arachnids rule Ok ? In: Hawkesworth, C.J. & Norry, M.J. (eds.), *Continental Basalts and Mantle Xenoliths*. Shiva Publishing, Cheshire, 159-185.

Thompson, R.N., Morrison, M.A., Dickin, A.P., Gibson, I.L. & Harmon, R.S. (1986). Two contrasting styles of interaction between basic magmas and continental crust in the British Tertiary Volcanic Province. *Journal of Geophysical Research*, **91**, No. B6, 5985-5997.

Tilley, C.E. & Muir, I.D. (1962). The Hebridean plateau magma type. *Transactions of the Edinburgh Geological Society*, **19**, 208-215.

Tindle, A.G. & Pearce, J.A. (1983). Assimilation and partial melting of continental crust : Evidence from the mineralogy and geochemistry of autoliths and xenoliths. *Lithos*, **16**, 185-202.

Tuttle, O.F. & Bowen, N.L. (1958). Origin of granite in the light of experimental studies in the system NaAlSi₃O₈-KAlSi₃O₈-SiO₂-H₂O. *Geological Society of America Memoirs*, **74**,

van Bergen, M.J. & Barton, M. (1984). Complex interaction of aluminous metasedimentary xenoliths and siliceous magma; An example from Mt. Amiata (Central Italy). *Contributions to Mineralogy and Petrology*, **86**, 374-385.

- van Breemen, O. & Hawkesworth, C.J.** (1980). Sm-Nd isotopic study of garnets and their metamorphic host rocks. *Transactions of the Royal Society of Edinburgh*, **71**, 97-102.
- van der Molen, I. & Paterson, M.S.** (1989). Experimental deformation of partly melted granite. *Contributions to Mineralogy and Petrology*, **70**, 299-318.
- Vance, J.A.** (1962). Zoning in igneous plagioclase : Normal and oscillatory zoning. *American Journal of Science*, **260**, 746-760.
- Vedder, W. & Wilkins, R.W.T.** (1969). Dehydroxylation and rehydroxylation, oxidation and reduction of micas. *American Mineralogist*, **54**, 484-509.
- Vielzeuf, D. & Holloway, J.R.** (1988). Experimental determination of the fluid-absent melting relations in the pelitic system - Consequences for crustal differentiation. *Contributions to Mineralogy and Petrology*, **98**, 257-276.
- Vigneresse, J.L., Cuney, M. & Barbey, P.** (1991). Deformation assisted crustal melts, segregation and transfer. *Geological Association of Canada - Mineralogical Association of Canada Abstracts.*, **16**, A128.
- Wager, L.R. & Brown, G.M.** (1968). *Layered Igneous Rocks*. Oliver & Boyd, Edinburgh and London, 588 pp.
- Wager, L.R., Brown, G.M. & Wadsworth, W.J.** (1960). Types of igneous cumulate. *Journal of Petrology*, **1**, No. 1, 73-85.
- Walker, D., Shibata, T. & DeLong, S.E.** (1979). Abyssal tholeiites from the Oceanographer fracture zone II. Phase equilibria and mixing. *Contributions to Mineralogy and Petrology*, **70**, 111-125.
- Walker, G.P.L.** (1970). The distribution of amygdale minerals in Mull and Morvern (western Scotland). In: Murty, T.V. & Rao, S.S. (eds.), *Studies in Earth Sciences. West Commemorative Volume*,
- Walsh, J.N., Beckinsale, R.D., Skelhorn, R.R. & Thorpe, R.S.** (1979). Geochemistry and petrogenesis of Tertiary granitic rocks from the Isle of Mull, Northwest Scotland. *Contributions to Mineralogy and Petrology*, **71**, 99-116.
- Walsh, J.N., Buckley, F. & Barker, J.** (1981). The simultaneous determination of the rare earth elements in rocks using inductively coupled plasma source spectrometry. *Chemical Geology*, **33**, 141-153.
- Weaver, B.L.** (1991). The origin of ocean island basalt end-member compositions : Trace-element and isotopic constraints. *Earth and Planetary Science Letters*, **104**, 381-397.
- White, R.S.** (1988). A hot-spot model for early Tertiary volcanism in the North Atlantic. In: Morton, A.C. & Parson, L.M. (eds.), *Early Tertiary Volcanism and the Opening of the NE Atlantic*. **39**, Geological Society of London Special Publication, 1-13.
- White, R.S. & McKenzie, D.P.** (1989). Magmatism at rift zones : The generation of volcanic continental margins and flood basalts. *Journal of Geophysical Research*, **94**, 7685-7729.
- Whitney, J.A.** (1988). The origin of granite : The role and source of water in the evolution of granitic magmas. *Geological Society of America Bulletin*, **100**, 1886-1897.
- Wilson, M.** (1989). *Igneous Petrogenesis*. Unwin Hyman, London, 466 pp.
- Wilson, M.** (1993a). Geochemical signatures of oceanic and continental basalts : A key to mantle dynamics ? *Journal of the Geological Society, London*, **150**, 977-990.

- Wilson, M.** (1993b). Magmatic differentiation. *Journal of the Geological Society, London*, **150**, 611-624.
- Wörner, G., Schmincke, H.-U. & Schreyer, W.** (1982). Crustal xenoliths from the Quarternary Wehr volcano. *Neues Jahrbuch für Mineralogie Abhandlungen*, **144**, No. 1, 29-55.
- Wyllie, P.J.** (1961). Fusion of Torridonian sandstones by a picrite sill in Soay (Hebrides). *Journal of Petrology*, **2**, No. 1, 1-37.
- Yardley, B.W.D.** (1989). *An Introduction to Metamorphic Petrology*. Longman, London, 248 pp.
- Yoder, H.S. & Tilley, C.E.** (1962). Origin of basalt magmas : An experimental study of natural and synthetic rock systems. *Journal of Petrology*, **3**, 342-532.
- Young, I.M.** (1984). Mixing of supernatant and interstitial fluids in the Rhum layered intrusion. *Mineralogical Magazine*, **48**, 345-350.
- Zindler, A., Hart, S.R., Frey, F.A. & Jakobsson, S.P.** (1979). Nd and Sr isotope ratios and rare earth element abundances in Reykjanes Peninsula Basalts : Evidence for mantle heterogeneity beneath Iceland. *Earth and Planetary Science Letters*, **45**, 249-262.

"Rocks, like everything else, are subject to change, and so are our views on them."

Loewinson-Lessing (1936)

APPENDIX

APPENDIX I

Analytical techniques

(a) Sample collection and preparation

Several samples were collected from each of the 30 sheets examined (see Appendix III for sample names and brief descriptions). Only the freshest material was collected, with at least 2-3 kg of sample being collected to be able to give representative material for whole-rock major- and trace-element analysis, as well as Sr and Nd isotope analysis. Samples from crustal xenoliths were either collected as complete specimens where possible, or with a 5cm diameter powered corer to preserve xenolith/magma relationships. All samples were slabbed to obtain totally unweathered material prior to crushing for analysis and thin-section preparation. Thin-sections were obtained from the majority of the samples as a screen to sample freshness; excessively altered samples were excluded from further analysis at this point.

Initial preparation of samples for whole-rock chemical analysis, consisted of passing the samples through a jaw crusher, followed by powdering in an agate Tema mill to produce a grain size of approximately 140 μ m. Samples for XRF trace-element analysis were further reduced in an agate ball mill to a grain size of 58 μ m.

(b) Electron probe, BSE and CL studies

In the electron probe microanalyser, under high vacuum a beam of high-energy electrons is focused on to an area of about $1\text{-}2\mu\text{m}^2$ of a polished sample. Those electrons which penetrate the specimen to a depth of $\sim 1\text{-}2\mu\text{m}$ excite the atoms of the sample to give off X-rays with energies and wavelengths specific to the elements which make up the material in the volume analysed. The X-rays are detected and measured by wavelength spectrometers fitted with diffracting crystals of appropriate d spacings, enabling all elements above atomic number $Z=4$ to be analysed. The intensities of these characteristic X-rays are proportional to the amounts of the elements present, and are compared with the intensities obtained from standard materials. In producing the final analysis, matrix absorption, secondary fluorescence, background and dead-time must all be taken into account.

All of the electron probe analyses, were taken by a sun workstation-controlled Cameca SX-50 electron probe microanalyser (at Glasgow University) fitted with four wavelength spectrometers. The typical generating conditions of the electron probe were 15 kV and 20 nA, with 10s counting time on the peak and 5s on each the positive and negative backgrounds. The beam size for analysis was typically $1\text{-}3\mu\text{m}$. The vacuum was typically 4×10^{-5} Pa in the chamber and 4×10^{-6} Pa at the electron gun. Standards comprised a series of pure elements and compound standards supplied by Cameca and Micro analysis Consultants Ltd. Where alkali loss during analysis was found to be a problem (*e.g.* with the mica and glass analyses), count times on K and Na were reduced to 5s, and the beam size increased to 5 or $10\mu\text{m}$.

Material from the crustal xenoliths was examined using both backscattered electron and cathodoluminescence imaging to investigate and highlight specific textural relationships.

A scanning electron microscope works by firing a narrow beam of high-energy electrons at a suitably prepared specimen, under high vacuum. Upon striking the surface of the specimen, some electrons are reflected or *back-scattered* from a thin surface layer, about $1\mu\text{m}$ deep. These back-scattered electrons (BSE) are easily detected and their intensities measured. The proportion of the incident electrons back-scattered from a specimen is a function of the mean atomic number of the small part of the specimen being irradiated by the electron beam.

This information is gathered by detector, and can be used to produce a grey-scale image of mean atomic number of the specimen. Secondary electrons (SE) are also produced at the point of impact of the electron beam. These electrons are those which were initially bound to the atoms of the specimens but were given enough energy to escape. These electrons can be used to give information concerning the topography of the specimen.

Backscattered electron studies were carried out using a Cambridge Stereoscan 360 electron microscope, with 4 quadrant BSE detector (SI-N type). Mineral modes were calculated by first collecting an x-ray spectrum from a selected *area* of the specimen, and displaying a backscattered electron image. Image-analysis software was then used to give "false colours" to the separate mineral species, the number of colours being selected by the user. The software is then able to calculate the area occupied by (therefore the mode) each mineral species. In order to get meaningful results, several analyses were made from each specimen, and the results averaged

In a cathodoluminescence microscope, a narrow beam of electrons is fired at the specimen under vacuum. On striking the surface of the specimen, some of the energy from the original electron beam may be converted into visible light. Only certain elements (usually trace-elements) will produce this effect. For example, the plagioclases from the rims of the aluminous xenoliths glow with a pale blue colour. It is believed this is due to the high Ti contents of the plagioclase. Cathodoluminescence studies were carried out using a Technosyn model 8200 MK2 with autohold, at typical operating conditions of 20 kV, 200 μ A, and a vacuum of approximately 0.05 torr.

(c) X-Ray Fluorescence

The X-ray fluorescence technique operates by firing of high-energy X-rays at the sample under vacuum. This excites the constituent elements of the sample to emit their own characteristic secondary X-rays. These are detected, and the intensity of the individual X-rays is proportional to the concentration of the element in the sample.

Whole rock major- and trace-element analyses were carried out using a Philips PW 1480 automatic x-ray fluorescence spectrometer in the Department of Geology and Geophysics in the University of Edinburgh. The spectrometer was equipped with a La heavy absorber and an on-line PC for data processing. Several samples were analysed in triplicate as a test of instrument accuracy and precision. The mean and standard deviation of major- and trace-element analyses of one such triplicate sample are given below.

Oxide	Mean $\pm \sigma$ (wt%)	Trace Element	Mean $\pm \sigma$ (ppm)
SiO ₂	54.88 \pm 0.47	Nb	7.4 \pm 0.2
TiO ₂	0.957 \pm 0.001	Zr	133.4 \pm 0.3
Al ₂ O ₃	14.76 \pm 0.13	Y	32.4 \pm 0.1
Fe ₂ O ₃	10.96 \pm 0.048	Sr	224.4 \pm 0.5
MnO	0.178 \pm 0.001	Rb	18.4 \pm 0.1
MgO	5.67 \pm 0.06	Th	6.5 \pm 0.35
CaO	9.02 \pm 0.017	Pb	6.5 \pm 0.25
Na ₂ O	2.63 \pm 0.09	Zn	11.0 \pm 1.8
K ₂ O	1.247 \pm 0.005	Cu	28.0 \pm 0.3
P ₂ O ₅	0.116 \pm 0.002	Ni	12.6 \pm 0.7
		Cr	40.3 \pm 0.9
		Ce	42.4 \pm 6.5
		Nd	19.6 \pm 0.6
		La	20.2 \pm 0.4
		V	273.7 \pm 0.05
		Ba	298.9 \pm 1.7
		Sc	46.2 \pm 1.4

The accuracy and precision of the analyses are comparable to those quoted by Fitton and Dunlop (1985) and Thirlwall *et al.* (1994). The preparation method is described by Fitton and Dunlop (1985) and is summarised below:

Major elements analyses

Samples were made into fused glass discs from 0.9-1.0g of dried sample and 4.5-5.0g of Spectroflux 105 (containing lithium carbonate, lithium tetraborate and lanthanum oxide).

Trace elements analyses

Samples were prepared as pressed pellets, containing 6g of the rock powder and 4 drops of Mowiol, covered by 1 tablespoon of Boric acid powder.

Loss on ignition

The samples were dried overnight in a oven at 110°C, weighted out into crucibles and mixed with about 5 times its weight of flux. The mixture was ignited at 1100°C for 20 minutes, and then placed on a cool block for about 5 minutes. After this, the samples were re-weighted and the loss on ignition (LOI) was calculated:

$$\text{LOI} = [\text{wt (sample + crucible + flux)}_0 - \text{wt (sample + crucible + flux)}_t] / \text{wt (sample)},$$

where: 0 and t, refer to wt. before and after ignition, respectively.

(d) ICP-MS and ICP-AES (Rare earth elements determination)

The Inductively Coupled Plasma technique of trace-element analysis operates by the ionisation of a liquid sample in an exceedingly hot (~11,000°C) argon plasma. In the Atomic Emission Spectrometry (AES) technique, the ions in the liquid sample are excited to emit light with characteristic wavelengths. Diffraction gratings are commonly used to separate the various wavelengths. The intensity of the light is measured and compared to a set of calibration standards to give the element concentration. In the Mass Spectrometry (MS) method, the liquid sample is again ionised within a high temperature plasma. However, the ions produced are then transferred to the attached mass spectrometer, detected and measured. This technique has greater accuracy, precision and lower detection limits than ICP-AES.

ICP-MS

About 0.1g of whole-rock samples, and 0.04-0.05g mineral separates from the crustal xenolith samples were weighted out into PTFE beakers. All samples were mixed with 5ml hydrofluoric acid (40%) and 5ml nitric acid (conc.) and placed on a hot plate at 80°C for 24 hours.

The contents were allowed to evaporate to dryness at 200°C on the hot plate, and then 25ml of 2% nitric acid was added to those samples which had completely dissolved. The samples were then slightly heated on a hot plate and transferred by a filtration process to a volumetric flask. A USGS standard (BHVO-1), 2 blanks, and some duplicate samples were prepared in the same fashion.

For the REE analyses, a VG plasma Quad PQ2 Turbo plus (Fisons Instruments Elemental Analysis) ICP-MS at SURRC, East Kilbride was used. Measured masses were : ^{138}Ba , ^{139}La , ^{140}Ce , ^{141}Pr , ^{143}Nd , ^{146}Nd , ^{147}Sm , ^{150}Nd , ^{151}Eu , ^{157}Gd , ^{159}Tb , ^{162}Dy , ^{165}Ho , ^{166}Er , ^{169}Tm , ^{174}Yb , ^{175}Lu .

ICP-AES

Certain samples were analysed for the REE at the Department of Geology at Royal Holloway University, London. The method used is that of Walsh *et al.*, (1981), and is outlined below.

About 0.5g of rock powder was weighed accurately into a platinum crucible. One standard and one blank were also prepared with each batch of 6 samples. To each crucible 12ml of HF/HNO₃ mixture was added from a safe dispenser. The samples were digested to dryness on

a sand bath, which took about 4 to 5 hours. Once digested they were allowed to cool. 5ml of conc. HCl and a little distilled water were then added to each sample, and then the crucibles were heated on the sand bath for a short while until each crucible was 3/4 full. Once all the residue has dissolved the crucibles were taken off the sand bath and allowed to cool.

Each sample was filtered into a 100ml beaker using a number 43 ashless filter paper, washing the filter paper with distilled water several times. The filtrate was not allowed to exceed 50ml.

The filter papers were then folded into silver crucibles which had been cleaned with HCl and distilled water. The crucibles were placed in a furnace, and ashed at 800°C, starting at around 200°C and taking the temperature in 100°C steps. After cooling, several pellets of sodium hydroxide were added to each sample. The crucibles were put back into the furnace for a further 30 minutes at 800°C. The crucibles were removed one at a time, a swirled until the mixture solidified in a homogeneous way. After the samples had cooled, 5ml of distilled water was added to digest the cake, followed by 5ml of HCl after approximately 30 minutes. The correct portion was added to the filtered samples, and the total solution made up to 100ml with distilled water. The samples were then ready for separation of the REE on standard cation exchange columns.

The columns were pre-washed with 600ml of 4M HCl. The samples were then added to the column. The samples were eluted with 500ml of 1.7M HCl. This portion was discarded. The columns were then eluted with 600ml of 4M HCl, which was collected. The columns were then rinsed with 200ml of dilute HCl.

The samples were evaporated on a sand bath until approximately 15ml of fluid remained. This was transferred to a clean 50ml beaker, and then taken down to dryness. The sample was cooled and covered with cling film.

Prior to running on the ICP, a small hole was punched in the cling film, and 5ml of 10% HNO₃ was added through the hole. The beakers were then placed in a microwave and heated for 10 seconds to make sure all the solid had dissolved. The samples were allowed to cool and then transferred to small washed tubes

Analyses of an "in-house" artificial liquid standard and one basaltic or granitic rock standard were made with each batch of six samples, and the USGS basalt standard BHVO-1 was also analysed. The mean and

the USGS basalt standard BHVO-1 was also analysed. The mean and standard deviation of 11 analyses of one of these liquid samples is quoted below, along with the analysed and recommended values for the BHVO-1 USGS standard.

	Repeat Analyses Mean \pm σ (ppm)	BHVO-1 Analysed	BHVO-1 Recommended
La	95.60 \pm 0.81	14.74	15.8 \pm 1.3
Ce	200.82 \pm 0.77	38.72	39 \pm 4
Pr	19.25 \pm 0.79	5.04	5.7 \pm 0.4
Nd	93.92 \pm 0.77	21.28	25.2 \pm 2.0
Sm	18.94 \pm 0.80	5.32	6.2 \pm 0.3
Eu	9.48 \pm 0.69	1.91	2.06 \pm 0.08
Gd	18.99 \pm 0.80	5.84	6.4 \pm 0.5
Dy	9.79 \pm 0.79	4.36	5.2 \pm 0.3
Ho	9.40 \pm 0.78	0.90	0.99 \pm 0.08
Er	9.42 \pm 0.72	2.13	2.4 \pm 0.2
Yb	9.61 \pm 0.75	1.79	2.02 \pm 0.2
Lu	9.33 \pm 0.77	0.28	0.29 \pm 0.026

Accuracy and Precision of the ICP-AES analyses performed at Royal Holloway University, London.

(e) Strontium and Neodymium Isotope Analysis

In a mass spectrometer, the solid sample is loaded on to a metal filament. Under vacuum, a high current is passed through the filament which causes the ionisation of the sample. The ions are accelerated away from the filament by using high voltage plates. The ions stream away, and are focused into a narrow beam by the use of further high voltage plates. The flight path of the ion beam is deflected into a curve using two large magnets. The amount of curvature given to the path of any one ion will depend upon the mass of the ion in question. The ions are detected at the end of the flight tube, where they are counted. The strength of the magnetic field controls which elements reach the detectors, and therefore the mass spectrometer can scan through a range of elemental masses.

Sample dissolution, column chemistry and machine conditions are essentially identical to those summarised in Dempster *et al.*, (1991).

Sample Dissolution :

Approximately 0.1g of sample was placed in PFA Teflon screw-top beakers (Savillex), and dissolved in 10mls 40% HF and 1ml 14M HNO₃, being placed on a hot plate overnight. The beakers were removed, cooled, and then the solution was dried down under clean air flow lamps. The residue was then dissolved in 3 mls 14M HNO₃ overnight on a hot plate, and dried down as before. The residue was next dissolved in 8 mls 6M HCl overnight on a hot plate. After cooling, a weighed aliquot of about 1/3 the volume of the solution was taken, to which was added weighed quantities of ¹⁴⁵Nd and ¹⁴⁹Sm spikes for isotope dilution determination of Sm and Nd concentrations. The remaining 2/3 aliquot was used for the determination of the isotopic composition of both Sr and Nd. ⁸⁷Rb and ⁸⁴Sr spikes were also added to this solution for the determination of Rb and Sr concentrations by isotope dilution analysis. Both solutions were dried down and the final residues each taken up in 2 mls 2.5M HCl.

Column chemistry (Separation of Rb, Sr and REE)

Sr, Rb and the REE were separated using standard cation exchange chromatography techniques. The sample was transferred to a centrifuge tube and any residue was centrifuged off. The solution was then loaded onto a preconditioned cation exchange column containing 10 mls Bio-Rad AG50W x 8, 200-400 mesh resin. The sample was

washed in with 2 * 1 ml 2.5M HCl. For samples where Rb and Sr were to be collected 29 mls 2.5M HCl were eluted, followed by collection of Rb in 7 mls 2.5M HCl; this was then evaporated to dryness. 10 mls 2.5M HCl was then eluted. The Sr fraction was collected with a further 10 mls 2.5M HCl, and evaporated to dryness. Sr blanks were less than 1 ng. For Sm and Nd spiked samples the Sr fraction did not need to be collected, and so 56 mls 2.5M HCl were eluted.

The REE were separated by further eluting 20 mls 2.5M HCl and 10 mls 3M HNO₃. The next 26 mls 3M HNO₃ were collected, and evaporated to dryness.

Initially Sm and Nd were isolated from Ba and the other REE using 3 columns. This was later superseded by a single "micro column" technique for the removal of Ba, followed by a further column to separate the REE.

Column Chemistry (Initial Ba clean-up)

The residue from the REE fraction from the Sr columns was dissolved in 1 ml of a solution of 75% CH₃COOH - 25% 5M HNO₃ (hereafter called 75/25). This was loaded onto a column containing 8ml of Bio-Rad AG1 x8, 200-400 mesh anion exchange resin which had been preconditioned with 5 mls of a solution of 90% CH₃COOH - 10% 5M HNO₃ (90/10). The sample was washed in with 2 * 1 ml 90/10 solution, and then eluted with 50 mls 90/10 solution. The REE's were collected with 15 mls 0.05M HNO₃, and evaporated to dryness.

Column Chemistry (Sm-Nd separation)

The residue from column 1 was dissolved in 1 ml of "orange cocktail". This cocktail consisted of 75% CH₃OH - 25% orange cocktail mix; the mix is made of 1336 mls H₂O + 406 mls CH₃COOH + 256 mls 5M HNO₃. The sample was loaded onto a column containing 8 ml of Bio-Rad AG1 x8, 200-400 mesh anion exchange resin which had been preconditioned with 5 mls "orange cocktail". This column was encased in a water jacket through which water kept at 25°C by a thermostatically-controlled water bath was circulated. The sample was washed in with 2 * 1 ml "orange cocktail", and eluted with 10 mls "orange cocktail". For spiked samples the next 17 mls "orange cocktail" were collected which contained the Sm fraction; this was evaporated to dryness. A further 12 mls "orange cocktail" were then eluted. For unspiked samples 29 mls "orange cocktail" were eluted.

The next 29 mls "orange cocktail" containing the Nd fraction were then collected, and the solution evaporated to dryness.

Column Chemistry (Final Ba clean-up)

The residue from the Nd fraction from column 2 (both spiked and unspiked) was dissolved in 1 ml 75/25 solution, and loaded onto a column containing 5 ml of Bio-Rad AG1 x8, 200-400 mesh anion exchange resin which had been preconditioned with 3 mls 90/10 solution. The sample was washed in with 2 * 1 ml of 90/10 solution and eluted with 15 mls 90/10 solution. The Nd was collected with 10 mls 0.05M HNO₃, and evaporated to dryness. Sm and Nd blanks were less than 0.2 ng.

Column Chemistry ("Micro-column" Ba clean-up)

Certain samples were put through Teflon "micro-columns" to remove the Ba, after the separation of the REE. This single column method replaced the two column Ba clean-up procedure at the SURRC, late in 1994. The procedure is as follows. The columns used consist of acid-cleaned 2ml columns supplied by the Sr-Spec resin manufacturer, into which is placed 2mls of Eichrom Sr-Spec resin. This is pre-treated with 2mls 3M HNO₃. The sample is dissolved and loaded in 1ml 3M HNO₃, and a further 2x 3mls 3M HNO₃ is added and collected. The columns are then washed with 2x 35mls 3M HNO₃.

Mass Spectrometry (Rb)

Rb samples were run on single collector VG MM30 thermal ionisation mass spectrometer. Rb samples were dissolved in a few ml of RO H₂O in a glass spitzer, loaded onto a Ta side filament of an outgassed triple Ta filament assembly, and carefully dried down so as to avoid the sample bubbling up on the filament. Beams were managed to give a peak intensity of about 5 pA ⁸⁷Rb. Peak intensities were corrected for zero and dynamic memory.

Mass Spectrometry (Sr)

Sr samples were run on a single collector VG 54E thermal ionisation mass spectrometer. Sr samples were dissolved in 1ml 1M H₃PO₄ and were loaded onto a single outgassed Ta filament. A small current is passed through the filament to dry the sample which is then increased slowly until the H₃PO₄ fumes off and the filament glows dull red. Sr

beams were managed to give an intensity of 1.5 pA ^{86}Sr . Peak intensities were corrected for zero, dynamic memory and Rb interference (if necessary). The $^{87}\text{Sr}/^{86}\text{Sr}$ ratio was corrected for mass fractionation using $^{86}\text{Sr}/^{88}\text{Sr} = 0.1194$. Repeat analysis of NBS 987 Sr standard gave $^{87}\text{Sr}/^{86}\text{Sr} = 0.710236 \pm 19$ (2s.d.).

Mass Spectrometry (Nd)

Nd analyses were performed on a VG Sector 54-30 thermal ionisation mass spectrometer with 8 Faraday collectors. Nd samples were dissolved in water and loaded on the Ta side filaments of an outgassed triple filament assembly with a Re centre filament. The sample was dried very carefully at 0.5A. For Nd isotopic composition runs beams were managed to give a ^{144}Nd intensity of 10pA with a centre filament current of 4 A. Data were acquired in multi-dynamic mode (to avoid inter-collector gain calibration uncertainties) using a 5 collector peak jumping routine. The data were collected in 12 blocks of 10 cycles/block, giving 120 ratios in total. Each cycle comprised 4 sequences; after each sequence the magnet was switched to place a different isotope into any given collector. The integration time for each sequence within a cycle was 5 seconds with a 2 second wait time between each sequence to allow the magnet to settle. $^{143}\text{Nd}/^{144}\text{Nd}$ ratios were corrected for mass fractionation using $^{146}\text{Nd}/^{144}\text{Nd} = 0.7219$. Peak intensities were corrected for background and the ^{144}Nd peak was corrected for Sm interference. During the course of this study the JM Nd standard gave $^{143}\text{Nd}/^{144}\text{Nd} = 0.511500 \pm 10$ (2s.d.). For Nd isotope dilution runs the ^{143}Nd beam intensity was 0.5 pA. The analyses were performed in static mode, with 3 blocks of 10 cycles being collected. The integration time for each cycle was 5 seconds. Peak intensities are corrected for zero and Sm interference (where necessary).

Mass Spectrometry (Sm)

Sm analyses were also performed on the Sector 54-30 instrument. Loading techniques were the same as those for Nd. Sm beams were managed to give a ^{149}Sm beam intensity of 0.5 pA. The analyses were performed in static mode, with 3 blocks of 10 cycles being collected. The integration time for each cycle was 5 seconds. Peak intensities are corrected for background. Measured Sm/Nd ratios are considered to be better than 0.15% (2 s.d.).



(courtesy Australian Geologist)

APPENDIX II

The following tables consist of the whole-rock major- and trace-element XRF analyses of Group I, II and III sheets, gabbroic xenoliths, crustal xenoliths, and Moine pelitic schists and quartzites. All analyses were carried out using a Philips PW 1480 automatic x-ray fluorescence spectrometer in the Department of Geology and Geophysics at the University of Edinburgh. Also shown are the REE analyses carried out by ICP-AES, in the Department of Geology at Royal Holloway University, London. The Sr and Nd isotope analyses were carried out using VG semi- and fully-automatic mass-spectrometers at the SURRC, East Kilbride. All Sr and Nd isotope data are quoted as initial ratios, age-corrected to 58Ma. Full details of the Sr and Nd isotope analysis results (*i.e.* measured isotopic ratios, 2σ errors, age-corrected isotope ratios) are given in separate tables which follow the major listings. CIPW Norms calculated assuming a $\text{Fe}^{3+}/\text{Fe}^{2+}$ ratio of 0.15 (Brookes, 1976). All analytical procedures are summarised in Appendix I. Sample numbers and descriptions are given in Appendix III.

GROUP I BASALTS AND BASALTIC ANDESITES

SAMPLE:	ARB1	KBB4	KIB1	PGB5	PGB6	PGB9	PGB10
SiO ₂	59.30	53.60	53.28	56.91	57.29	50.31	56.18
TiO ₂	0.95	1.23	0.94	1.26	1.26	0.89	1.19
Al ₂ O ₃	14.49	14.43	14.64	14.48	14.66	14.96	14.46
Fe ₂ O ₃ *	8.30	11.38	11.29	9.55	9.28	11.15	9.83
MnO	0.13	0.17	0.18	0.15	0.17	0.18	0.14
MgO	4.84	5.29	6.30	4.29	4.18	7.75	4.52
CaO	6.40	5.49	9.36	7.06	6.83	11.80	8.06
Na ₂ O	2.88	4.80	2.98	2.78	2.98	2.59	2.70
K ₂ O	2.20	1.99	0.83	1.96	1.60	0.33	1.59
P ₂ O ₅	0.15	0.14	0.10	0.16	0.16	0.07	0.14
LOI	0.49	0.77	0.43	1.38	1.43	0.33	1.22
TOTAL	99.65	98.52	99.90	98.60	98.41	100.04	98.82
Mg#	0.37	0.32	0.36	0.31	0.31	0.41	0.32
Nb	11.0	16.2	4.1	10.0	9.7	2.3	8.4
Zr	199.8	296.8	105.1	176.8	168.7	65.8	156.2
Y	33.5	40.2	25.7	29.8	29.2	24.9	27.9
Sr	215.7	219.4	276.3	289.5	273.8	205.4	278.5
Rb	73.5	105.0	22.6	40.7	43.4	6.2	44.8
Th	8.1	12.1	4.6	7.3	5.0	2.6	6.1
Pb	12.6	18.1	5.3	9.0	8.6	2.6	9.5
Zn	93.0	99.3	103.5	110.7	99.4	90.8	162.7
Cu	47.0	13.0	42.6	30.5	31.7	105.4	38.2
Ni	34.7	6.4	23.1	17.8	19.1	76.0	22.1
Cr	152.7	18.7	68.0	76.4	82.1	351.8	89.7
V	172.3	202.9	298.6	263.1	262.1	295.8	261.2
Ba	559.7	807.3	312.6	546.9	451.6	183.1	458.2
Sc	31.2	22.3	43.0	35.2	33.6	51.2	35.6
La	27.55			37.44		5.97	
Ce	62.42			50.45		13.92	
Pr	6.97			6.14		1.71	
Nd	25.18			24.71		8.36	
Sm	5.23			5.10		2.20	
Eu	1.31			1.55		0.95	
Gd	5.41			5.62		3.19	
Dy	4.92			5.04		3.53	
Ho	1.13			0.96		0.82	
Er	2.99			2.99		2.31	
Yb	3.07			2.82		2.30	
Lu	0.50			0.45		0.37	
⁸⁷ Sr/ ⁸⁶ Sr	0.715405			0.714436		0.70769	
¹⁴³ Nd/ ¹⁴⁴ Nd	0.511876			0.511877		0.512167	
CIPW NORMS							
Ap	0.36	0.32	0.23	0.38	0.36	0.17	0.33
Il	1.81	2.34	1.79	2.40	2.40	1.70	2.27
Mt	1.58	2.17	2.15	1.82	1.77	2.12	1.87
Or	13.00	11.77	4.91	11.56	9.46	1.97	9.40
Ab	24.36	40.60	25.21	23.52	25.21	21.90	22.84
An	20.11	11.93	24.11	21.25	21.89	28.19	22.63
Di	8.76	11.94	17.89	10.53	9.10	24.46	13.61
Hy	17.43	4.67	20.64	16.34	16.45	11.92	15.86
Ol	0.00	11.79	0.00	0.00	0.00	6.63	0.00
C	0.00	0.00	0.00	0.00	0.00	0.00	0.00
Qtz	11.52	0.00	2.00	9.99	10.97	0.00	9.16
TOTAL	98.93	97.53	98.92	97.77	97.61	99.07	97.96

GROUP I BASALTS AND BASALTIC ANDESITES

SAMPLE:	PM2B1	ORB1	ORB2	RCB1	RCB2	RCB3	SFB2
SiO ₂	53.06	54.28	48.29	54.06	54.31	54.41	54.02
TiO ₂	0.95	0.97	1.40	1.16	1.18	1.18	0.99
Al ₂ O ₃	14.43	14.71	13.75	14.29	14.34	14.54	14.66
Fe ₂ O ₃ *	10.90	10.84	15.37	11.62	11.57	11.68	11.21
MnO	0.17	0.18	0.25	0.18	0.17	0.17	0.20
MgO	6.54	5.50	6.29	5.06	5.22	4.91	5.78
CaO	10.05	9.16	11.53	8.39	8.54	8.08	8.74
Na ₂ O	2.78	2.58	2.76	2.91	2.99	3.02	2.94
K ₂ O	0.98	1.35	0.15	1.35	1.39	1.44	1.40
P ₂ O ₅	0.11	0.12	0.11	0.14	0.15	0.15	0.12
LOI	0.23	0.77	0.53	0.75	0.44	0.52	0.47
TOTAL	99.97	99.68	99.89	99.16	99.86	99.58	100.06
Mg#	0.38	0.34	0.29	0.30	0.31	0.30	0.34
Nb	5.4	7.3	2.0	7.4	7.9	7.8	7.3
Zr	114.3	134.5	84.6	145.4	145.5	156.6	132.9
Y	28.3	31.4	43.3	35.1	34.7	35.4	32.0
Sr	225.0	212.1	120.8	222.4	225.7	214.3	201.6
Rb	26.8	42.5	3.9	42.6	43.4	43.4	31.2
Th	3.2	6.7	3.5	7.4	5.7	6.6	6.1
Pb	5.1	7.0	1.4	8.1	6.4	6.9	7.6
Zn	121.8	109.0	117.9	104.0	147.9	109.9	99.6
Cu	65.1	23.3	179.7	32.3	31.0	31.9	29.9
Ni	48.7	12.1	49.0	14.3	14.1	14.8	11.2
Cr	206.7	39.3	73.1	42.8	47.6	43.3	34.6
V	270.5	256.4	364.0	209.0	301.2	299.1	274.4
Ba	356.6	783.9	151.6	455.0	403.8	477.3	425.2
Sc	44.8	41.1	51.3	43.2	41.1	45.7	44.4
La			2.77	19.32	19.34		
Ce			8.63	44.04	43.89		
Pr			1.36	5.01	4.99		
Nd			8.66	19.30	19.20		
Sm			3.22	4.31	4.31		
Eu			1.37	1.28	1.28		
Gd			5.33	4.96	4.91		
Dy			6.03	4.95	4.90		
Ho			1.44	1.15	1.13		
Er			3.98	3.12	3.06		
Yb			3.91	3.13	3.09		
Lu			0.63	0.50	0.50		
⁸⁷ Sr/ ⁸⁶ Sr			0.703756	0.712282	0.71256		
¹⁴³ Nd/ ¹⁴⁴ Nd			0.512916	0.511986	0.51197		
CIPW NORMS							
Ap	0.26	0.27	0.25	0.33	0.34	0.35	0.28
Il	1.81	1.85	2.66	2.21	2.25	2.24	1.89
Mt	2.08	2.06	2.92	2.21	2.20	2.22	2.13
Or	5.76	7.95	0.86	7.98	8.22	8.49	8.27
Ab	23.52	21.82	23.34	24.62	25.29	25.55	24.87
An	24.01	24.58	24.68	21.93	21.59	21.87	22.67
Di	20.68	16.63	26.48	15.58	16.44	14.34	16.46
Hy	19.32	18.58	6.89	18.69	18.56	18.96	19.86
Ol	0.00	0.00	10.47	0.00	0.00	0.00	0.00
C	0.00	0.00	0.00	0.00	0.00	0.00	0.00
Gtz	1.60	4.99	0.00	4.60	3.95	4.54	2.66
TOTAL	99.02	98.74	98.55	98.15	98.86	98.56	99.09

GROUP I BASALTS AND BASALTIC ANDESITES

SAMPLE:	SFB3	SOB1	TILE1	TMB1	TMB2	TMB3	PMBASE
SiO ₂	55.32	54.86	52.38	54.37	51.27	52.63	50.93
TiO ₂	1.16	0.98	0.99	0.96	1.01	0.99	1.04
Al ₂ O ₃	14.60	14.78	14.77	14.66	14.53	15.05	15.16
Fe ₂ O ₃ *	10.08	10.60	11.19	10.89	11.67	11.06	10.82
MnO	0.16	0.18	0.18	0.18	0.18	0.21	0.21
MgO	4.62	5.59	7.30	5.58	7.01	6.43	7.10
CaO	8.37	8.76	10.66	9.04	10.92	9.60	11.40
Na ₂ O	2.82	2.73	2.92	2.53	2.77	2.64	2.98
K ₂ O	0.85	1.25	0.73	1.25	0.67	1.06	0.57
P ₂ O ₅	0.20	0.12	0.11	0.12	0.11	0.12	0.11
LOI	2.04	0.43	0.15	0.33	0.26	0.61	0.31
TOTAL	98.17	99.85	101.23	99.57	100.14	99.79	100.31
Mg#	0.31	0.35	0.40	0.34	0.38	0.37	0.40
Nb	9.0	7.0	4.5	6.7	3.8	7.6	3.9
Zr	148.7	136.9	96.2	132.2	94.0	133.1	89.4
Y	29.2	31.5	27.4	31.8	27.9	32.5	28.6
Sr	410.9	214.1	224.3	211.3	226.1	223.9	226.1
Rb	49.4	44.1	18.1	41.9	12.7	18.3	12.2
Th	6.0	7.0	2.3	5.8	3.5	6.2	3.4
Pb	9.9	7.7	4.8	7.1	3.2	6.8	2.6
Zn	110.0	95.5	144.0	108.4	103.4	111.8	83.7
Cu	31.5	25.8	71.6	23.7	73.7	27.7	77.1
Ni	18.1	11.5	52.8	12.2	52.3	11.9	58.9
Cr	77.0	39.2	232.6	35.9	224.0	41.2	242.9
V	276.7	258.4	295.5	254.4	297.7	273.8	321.0
Ba	504.2	362.7	288.8	356.3	280.1	297.2	270.7
Sc	32.5	44.8	47.9	38.7	45.2	47.6	49.1
La	21.05		10.96	17.15			8.72
Ce	47.78		25.10	39.37			21.01
Pr	5.41		2.92	4.46			2.58
Nd	20.58		14.49	17.40			11.44
Sm	4.29		2.99	3.87			2.78
Eu	1.29		1.11	1.14			1.11
Gd	4.58		3.83	4.41			3.80
Dy	4.22		3.97	4.40			3.89
Ho	0.95		0.91	1.01			0.90
Er	2.55		2.52	2.75			2.50
Yb	2.58		2.54	2.79			2.44
Lu	0.42		0.41	0.45			0.39
⁸⁷ Sr/ ⁸⁶ Sr			0.709445	0.710713			0.708464
¹⁴³ Nd/ ¹⁴⁴ Nd			0.511932	0.511872			0.511979
CIPW NORMS							
Ap	0.47	0.28	0.25	0.27	0.25	0.28	0.25
Il	2.20	1.87	1.88	1.82	1.92	1.88	1.98
Mt	1.92	2.02	2.13	2.07	2.22	2.11	2.36
Or	5.00	7.39	4.33	7.39	3.97	6.28	3.39
Ab	23.85	23.09	24.70	21.40	23.43	22.33	25.20
An	24.67	24.37	25.02	24.94	25.22	26.07	26.28
Di	12.87	15.11	22.29	15.84	23.24	17.12	24.22
Hy	16.88	19.23	16.52	19.27	15.27	21.01	8.54
Ol	0.00	0.00	3.14	0.00	3.60	0.00	7.23
C	0.00	0.00	0.00	0.00	0.00	0.00	0.00
Qtz	9.43	5.56	0.00	5.62	0.00	1.75	0.00
TOTAL	97.29	98.93	100.25	98.63	99.12	98.83	99.45

GROUP I BASALTS AND BASALTIC ANDESITES

SAMPLE:	PM+50	PM+100	PM+200	PM+380
SiO ₂	53.69	53.88	53.42	52.59
TiO ₂	0.95	0.96	0.94	0.98
Al ₂ O ₃	14.54	14.50	14.35	14.41
Fe ₂ O ₃ *	10.54	10.42	10.53	11.11
MnO	0.17	0.16	0.17	0.17
MgO	6.39	6.13	6.33	6.84
CaO	9.69	9.65	9.45	10.00
Na ₂ O	2.81	2.89	2.69	2.62
K ₂ O	1.06	1.09	1.10	0.89
P ₂ O ₅	0.11	0.11	0.11	0.11
LOI	0.24	0.35	0.48	0.19
TOTAL	99.95	99.80	99.09	99.71
Mg#	0.38	0.37	0.38	0.38
Nb	5.5	6.0	5.4	4.4
Zr	120.3	123.2	123.6	107.8
Y	28.8	28.5	28.5	28.0
Sr	224.7	227.3	227.4	223.5
Rb	29.6	31.1	32.0	23.6
Th	2.9	4.6	3.9	3.9
Pb	3.0	6.4	7.1	4.6
Zn	99.6	107.3	98.6	99.1
Cu	63.4	60.8	59.6	67.7
Ni	45.0	44.5	46.9	50.0
Cr	199.5	192.3	189.4	206.6
V	270.9	265.3	262.3	281.5
Ba	397.1	394.4	488.0	354.9
Sc	42.5	42.6	46.0	46.1
La			14.85	
Ce			33.94	
Pr			3.85	
Nd			15.48	
Sm			3.47	
Eu			1.13	
Gd			4.15	
Dy			4.16	
Ho			0.96	
Er			2.62	
Yb			2.66	
Lu			0.43	
⁸⁷ Sr/ ⁸⁶ Sr			0.710796	
¹⁴³ Nd/ ¹⁴⁴ Nd			0.511906	
CIPW NORMS				
Ap	0.25	0.26	0.26	0.25
Il	1.81	1.83	1.79	1.86
Mt	2.30	2.27	2.29	2.42
Or	6.24	6.44	6.48	5.23
Ab	23.77	24.45	22.75	22.16
An	23.94	23.36	23.83	24.94
Di	19.25	19.56	18.33	19.68
Hy	18.71	17.71	18.99	20.30
Ol	0.00	0.00	0.00	0.00
C	0.00	0.00	0.00	0.00
Qtz	2.80	3.03	3.45	1.93
TOTAL	99.07	98.91	98.17	98.77

GROUP I BASALTS AND BASALTIC ANDESITES

SAMPLE:	SOBS1B	SOBS1M	SOBS1T	SOBS2B	SOBS2+ 100	SOBS2+ 200	SOBS2T
SiO ₂	54.48	54.31	54.17	54.76	54.54	54.65	54.69
TiO ₂	0.93	0.91	0.93	0.97	0.95	0.98	0.96
Al ₂ O ₃	14.49	14.36	14.64	14.84	14.66	14.74	14.60
Fe ₂ O ₃ *	10.70	10.29	11.08	10.67	10.70	10.64	10.69
MnO	0.18	0.18	0.17	0.16	0.19	0.18	0.16
MgO	5.98	5.89	6.22	5.95	5.97	5.84	5.81
CaO	9.29	9.13	9.58	8.34	8.63	7.66	7.87
Na ₂ O	2.63	2.55	2.62	2.84	2.93	3.43	4.51
K ₂ O	1.15	1.15	1.05	1.19	1.28	1.62	1.39
P ₂ O ₅	0.11	0.11	0.11	0.12	0.16	0.12	0.13
LOI	0.26	0.86	0.30	0.62	0.48	0.69	0.46
TOTAL	100.20	99.74	100.88	100.46	100.49	100.55	101.27
Mg#	0.36	0.36	0.36	0.36	0.36	0.35	0.35
Nb	6.4	6.7	6.1	7.3	7.1	6.9	7.0
Zr	127.8	128.4	120.9	131.7	127.3	133.6	131.3
Y	30.4	29.8	30.4	31.2	30.7	31.6	30.6
Sr	202.0	202.3	198.9	206.5	214.0	273.5	227.7
Rb	39.4	39.6	36.4	41.7	46.6	59.0	49.0
Th	5.5	4.9	5.1	5.0	5.3	5.1	5.6
Pb	6.0	6.9	7.0	6.0	8.2	5.5	5.3
Zn	84.8	83.2	83.9	125.2	93.3	94.7	104.7
Cu	45.3	32.3	33.0	26.1	29.5	26.2	25.1
Ni	14.4	12.8	11.9	10.5	12.7	11.5	11.3
Cr	38.3	35.7	35.7	42.0	38.0	39.2	43.8
Ce	45.0	38.1	35.5	45.8	43.1	47.8	42.5
Nd	17.6	16.7	18.4	20.9	14.6	23.9	18.2
La	19.3	18.2	17.6	19.5	19.8	20.5	16.3
V	253.3	250.1	261.7	274.0	257.7	257.9	263.8
Ba	322.8	299.0	334.0	339.4	381.6	412.4	355.7
Sc	42.9	43.7	42.6	45.0	43.6	44.6	43.4
⁸⁷ Sr/ ⁸⁶ Sr			0.715125				
¹⁴³ Nd/ ¹⁴⁴ Nd			0.512031				

GROUP I BASALTS AND BASALTIC ANDESITES

SAMPLE:	SOBS3B	SOBS3T	SOBS4B	SOBS4M	SOBS4T	SOBT1	SOBT2
SiO ₂	54.71	54.52	54.58	54.50	54.67	54.54	54.67
TiO ₂	0.94	0.94	0.93	0.96	0.95	0.95	0.94
Al ₂ O ₃	14.75	14.60	14.54	14.64	14.62	14.88	14.74
Fe ₂ O ₃ *	10.76	10.79	10.73	10.86	10.62	10.66	10.53
MnO	0.16	0.18	0.18	0.18	0.19	0.19	0.18
MgO	5.81	5.83	6.12	6.09	6.00	5.88	5.99
CaO	8.13	8.44	8.75	8.97	8.91	9.21	8.13
Na ₂ O	3.16	2.90	2.65	2.61	2.58	2.73	3.11
K ₂ O	1.29	1.27	1.24	1.16	1.19	1.52	1.47
P ₂ O ₅	0.12	0.11	0.11	0.12	0.11	0.11	0.11
LOI	0.44	0.44	0.36	0.36	0.64	0.53	0.42
TOTAL	100.27	100.02	100.19	100.45	100.48	101.20	100.30
Mg#	0.35	0.35	0.36	0.36	0.36	0.36	0.36
Nb	6.8	6.6	6.8	6.5	6.9	6.8	6.7
Zr	129.0	128.3	130.2	127.4	129.5	126.4	130.9
Y	30.5	29.8	30.9	31.1	30.7	30.0	30.4
Sr	214.5	231.2	202.2	207.0	202.1	206.1	236.6
Rb	43.7	46.0	43.3	40.3	41.5	40.1	53.2
Th	6.5	6.4	6.0	6.5	6.9	6.0	6.3
Pb	6.8	7.5	5.8	6.6	6.7	8.3	8.1
Zn	136.2	108.5	90.5	116.7	93.2	150.8	100.3
Cu	26.9	26.2	29.7	25.4	30.1	53.8	23.0
Ni	10.7	10.7	11.3	10.3	11.9	12.3	11.9
Cr	42.6	44.5	38.2	34.0	39.3	39.0	42.3
Ce	32.2	42.6	37.4	39.7	39.2	42.5	48.7
Nd	17.8	19.4	18.1	17.1	14.1	18.3	24.7
La	19.5	20.4	19.7	23.3	18.0	20.7	17.8
V	263.8	262.9	258.1	250.1	258.7	272.2	267.4
Ba	377.3	364.7	406.8	343.1	352.9	312.7	429.8
Sc	44.8	48.0	43.7	44.3	44.9	45.3	48.8
⁸⁷ Sr/ ⁸⁶ Sr		0.714512					0.714838
¹⁴³ Nd/ ¹⁴⁴ Nd		0.512031					0.512024

GROUP I BASALTS AND BASALTIC ANDESITES

SAMPLE:	SOBT3
SiO ₂	54.89
TiO ₂	0.98
Al ₂ O ₃	14.85
Fe ₂ O ₃ *	10.47
MnO	0.18
MgO	5.64
CaO	8.83
Na ₂ O	2.70
K ₂ O	1.25
P ₂ O ₅	0.12
LOI	0.45
TOTAL	100.35
Mg#	0.35
Nb	11.5
Zr	204.4
Y	50.1
Sr	198.8
Rb	68.3
Th	10.3
Pb	11.5
Zn	132.4
Cu	20.0
Ni	7.6
Cr	17.7
Ce	71.9
Nd	33.9
La	31.6
V	306.7
Ba	539.4
Sc	41.7
⁸⁷ Sr/ ⁸⁶ Sr	
¹⁴³ Nd/ ¹⁴⁴ Nd	

GROUP II ANDESITES AND PORPHYRITIC DACITES

SAMPLE:	CUPI1	KBB1 +100	KBB1 +50	KBB3	KBB5	KMB1	PCRPI1
SiO ₂	64.84	65.77	65.17	61.88	63.97	66.43	64.84
TiO ₂	1.11	1.05	1.04	1.02	1.02	1.00	1.13
Al ₂ O ₃	13.21	14.45	14.20	14.09	14.31	13.38	13.29
Fe ₂ O ₃ *	8.05	7.45	7.23	8.15	7.61	6.48	8.42
MnO	0.13	0.12	0.10	0.13	0.15	0.09	0.14
MgO	1.01	1.80	1.72	2.64	2.08	1.37	1.12
CaO	3.27	3.09	3.12	4.79	3.53	2.49	2.92
Na ₂ O	3.96	2.93	3.04	3.70	3.15	3.16	3.23
K ₂ O	2.62	3.40	3.42	1.61	3.33	3.83	3.57
P ₂ O ₅	0.30	0.18	0.18	0.17	0.18	0.21	0.30
LOI	1.46	0.86	0.74	2.11	0.74	1.56	1.08
TOTAL	99.97	101.10	99.96	100.28	100.06	100.01	100.05
Mg#	0.11	0.19	0.19	0.24	0.21	0.17	0.12
Nb	18.3	16.3	15.9	13.9	15.9	16.5	18.3
Zr	366.7	288.4	289.1	254.3	277.4	303.9	368.0
Y	56.9	41.3	40.6	37.6	29.1	41.8	69.8
Sr	218.9	231.5	228.8	278.6	234.1	156.2	207.3
Rb	108.8	110.7	112.7	82.5	108.0	100.8	108.9
Th	10.7	10.3	11.0	9.1	10.5	10.2	10.4
Pb	19.4	19.0	19.5	17.2	17.4	17.6	17.7
Zn	111.2	93.9	97.3	116.8	118.4	103.2	137.8
Cu	12.1	12.5	12.9	21.3	13.5	14.4	16.3
Ni	6.5	5.6	6.9	12.2	6.0	6.0	8.0
Cr	2.2	19.7	19.0	49.5	27.9	23.0	2.2
V	45.0	196.5	196.5	211.6	192.3	103.1	47.1
Ba	999.2	847.8	752.7	689.7	751.1	934.0	935.2
Sc	20.2	23.3	19.6	24.1	22.3	20.4	19.4
La	48.16					41.45	54.55
Ce	108.75					94.03	121.26
Pr	12.44					10.40	13.63
Nd	45.79					36.78	50.58
Sm	9.19					7.32	10.26
Eu	2.18					1.54	2.26
Gd	9.35					7.08	10.91
Dy	8.46					6.11	9.81
Ho	1.93					1.39	2.26
Er	5.07					3.61	5.96
Yb	5.11					3.71	5.98
Lu	0.83					0.61	0.99
⁸⁷ Sr/ ⁸⁶ Sr	0.715742					0.714106	0.71573
¹⁴³ Nd/ ¹⁴⁴ Nd	0.511839					0.511846	0.51183
CIPW NORMS							
Ap	0.71	0.43	0.42	0.39	0.41	0.49	0.71
Il	2.10	2.00	1.99	1.94	1.94	1.90	2.15
Mt	1.53	1.43	1.38	1.55	1.45	1.23	1.60
Or	15.50	20.24	20.22	9.48	19.69	22.64	21.09
Ab	33.49	24.98	25.78	31.30	26.65	26.73	27.32
An	10.52	14.25	14.35	17.09	15.06	10.99	11.21
Di	3.20	0.00	0.00	4.68	1.09	0.00	1.10
Hy	9.97	12.96	12.38	13.59	13.32	10.54	11.81
Ol	0.00	0.00	0.00	0.00	0.00	0.00	0.00
C	0.00	0.02	0.01	0.00	0.00	0.00	0.00
Qtz	20.78	23.30	22.07	17.44	19.06	23.37	21.24
TOTAL	97.80	99.60	98.60	97.46	98.66	97.88	98.23

GROUP II ANDESITES AND PORPHYRITIC DACITES

SAMPLE:	PCRPI2	PGB7	PGB8	TIP11	TVPI1
SiO ₂	64.34	65.83	64.16	60.70	64.63
TiO ₂	1.09	1.07	0.92	0.94	1.11
Al ₂ O ₃	13.10	14.22	14.12	15.14	13.33
Fe ₂ O ₃ *	8.17	7.01	6.69	7.68	8.35
MnO	0.13	0.11	0.11	0.12	0.11
MgO	1.03	1.39	1.92	3.01	0.91
CaO	3.15	2.91	3.83	5.00	2.91
Na ₂ O	3.32	3.05	3.34	3.69	3.23
K ₂ O	3.47	3.51	2.08	1.43	3.52
P ₂ O ₅	0.30	0.18	0.19	0.18	0.30
LOI	1.53	1.44	2.78	2.07	1.09
TOTAL	99.63	100.72	100.14	99.97	99.49
Mg#	0.11	0.17	0.22	0.28	0.10
Nb	17.5	8.1	15.9	14.2	18.2
Zr	358.6	149.7	280.7	246.0	365.8
Y	54.9	31.6	39.4	37.2	57.1
Sr	210.0	207.4	281.7	307.2	207.7
Rb	106.4	42.2	109.8	105.9	106.3
Th	10.9	6.2	10.6	9.7	10.6
Pb	16.8	8.2	17.9	15.8	17.8
Zn	128.4	114.7	90.8	116.4	132.3
Cu	12.2	37.0	13.1	11.8	13.6
Ni	5.7	22.5	8.0	10.3	4.9
Cr	6.4	78.8	37.5	69.8	5.2
V	47.9	362.8	107.6	149.6	49.3
Ba	933.1	422.5	795.1	749.8	929.3
Sc	20.5	44.6	22.0	25.9	26.7
La		20.85		37.92	48.66
Ce		47.41		85.30	108.81
Pr		5.31		9.37	12.13
Nd		19.90		33.47	44.70
Sm		4.27		6.58	9.07
Eu		1.33		1.60	2.16
Gd		4.71		6.41	9.12
Dy		4.55		5.57	8.32
Ho		1.04		1.27	1.89
Er		2.83		3.33	4.98
Yb		2.87		3.42	5.01
Lu		0.46		0.56	0.81
⁸⁷ Sr/ ⁸⁶ Sr				0.716794	0.715803
¹⁴³ Nd/ ¹⁴⁴ Nd				0.511844	0.511807
CIPW NORMS					
Ap	0.70	0.42	0.44	0.43	0.71
Il	2.07	2.05	1.76	1.79	2.12
Mt	1.56	1.34	1.27	1.46	1.59
Or	20.46	20.85	12.27	8.45	20.76
Ab	28.08	25.94	28.25	31.22	27.32
An	10.61	13.34	17.39	20.52	11.49
Di	2.64	0.00	0.32	2.57	0.84
Hy	10.51	11.25	12.18	15.08	11.29
Ol	0.00	0.00	0.00	0.00	0.00
C	0.00	0.01	0.00	0.00	0.00
Qtz	20.77	23.47	22.90	15.72	21.57
TOTAL	97.39	98.68	96.78	97.23	97.67

GROUP III RHYOLITES

SAMPLE:	PGF1	RCF1	RCF2	RCF3	RCF4
SiO ₂	71.80	70.13	70.38	71.61	65.95
TiO ₂	0.66	0.73	0.73	0.71	0.80
Al ₂ O ₃	12.23	12.17	12.19	12.24	12.34
Fe ₂ O ₃ *	4.91	5.26	5.52	5.04	6.63
MnO	0.08	0.09	0.05	0.03	0.09
MgO	0.39	0.68	0.80	0.85	1.39
CaO	1.47	1.97	1.48	1.14	2.87
Na ₂ O	3.23	2.76	2.89	2.72	2.48
K ₂ O	4.31	4.15	4.08	4.20	3.53
P ₂ O ₅	0.17	0.19	0.19	0.19	0.18
LOI	0.65	1.58	1.70	1.16	2.80
TOTAL	99.90	99.71	100.01	99.89	99.06
Mg#	0.07	0.11	0.13	0.14	0.17
Nb	17.9	17.9	17.9	17.8	16.3
Zr	364.2	355.5	351.6	357.5	318.3
Y	49.2	48.4	47.5	46.1	45.4
Sr	122.1	132.3	98.2	90.7	140.2
Rb	154.4	136.4	131.1	137.0	117.4
Th	12.0	11.4	12.6	11.5	10.3
Pb	24.0	22.2	21.8	23.2	20.6
Zn	133.4	89.2	88.0	97.6	139.3
Cu	9.1	10.7	11.1	10.6	17.5
Ni	4.2	3.6	4.0	4.1	7.7
Cr	0.0	0.0	1.1	0.0	11.7
V	14.6	23.4	28.6	23.3	67.4
Ba	914.1	866.8	876.7	816.2	822.3
Sc	14.6	17.7	17.1	19.1	17.9
La	47.55	48.05		46.03	41.94
Ce	108.25	109.90		104.83	94.92
Pr	12.23	12.33		11.78	10.25
Nd	43.28	43.58		41.38	35.28
Sm	8.31	8.53		8.16	7.39
Eu	1.34	1.41		1.40	1.36
Gd	7.86	8.17		7.87	7.45
Dy	7.04	7.04		7.00	6.25
Ho	1.59	1.58		1.59	1.45
Er	4.18	4.13		4.19	3.79
Yb	4.24	4.19		4.30	4.00
Lu	0.68	0.68		0.70	0.68
⁸⁷ Sr/ ⁸⁶ Sr	0.720319	0.717169		0.719059	0.717622
¹⁴³ Nd/ ¹⁴⁴ Nd	0.511853	0.511886		0.511862	0.511862
CIPW NORMS					
Ap	0.40	0.45	0.44	0.44	0.41
Il	1.25	1.39	1.41	1.38	1.52
Mt	0.93	1.00	1.06	0.98	1.31
Or	25.45	24.50	24.30	25.22	20.84
Ab	27.32	23.35	24.64	23.38	20.98
An	6.14	8.51	6.17	4.51	12.11
Di	0.04	0.00	0.00	0.00	0.82
Hy	6.54	7.64	8.26	7.81	11.67
Ol	0.00	0.00	0.00	0.00	0.00
C	0.00	0.00	0.02	0.03	0.00
Qtz	30.77	30.83	31.55	34.57	26.60
TOTAL	98.84	97.67	97.84	98.32	96.26

GABBROIC AND CRUSTAL XENOLITHS

SAMPLE:	KBGX1	KBGX2	KBHYX1	KIFX1	PMQX1	PMAX2	KBAX1
SiO ₂	42.50	51.50	50.82	46.20	96.03	54.68	56.88
TiO ₂	0.27	0.58	0.40	0.13	0.06	2.73	1.42
Al ₂ O ₃	8.24	10.50	16.31	30.26	0.77	30.75	23.84
Fe ₂ O ₃ *	11.05	7.84	5.58	2.17	1.20	1.11	4.70
MnO	0.17	0.15	0.10	0.02	0.01	0.01	0.02
MgO	26.88	11.05	8.06	0.77	0.22	0.50	1.56
CaO	3.81	14.54	14.79	13.95	0.65	0.49	0.98
Na ₂ O	0.51	1.94	1.97	2.34	0.03	2.21	3.14
K ₂ O	0.12	0.69	1.00	1.05	0.07	1.61	1.31
P ₂ O ₅	0.02	0.04	0.03	0.02	0.02	0.04	0.05
LOI	6.73	1.17	1.08	2.67	1.13	4.78	4.75
TOTAL	99.64	99.53	99.80	99.59	100.18	98.92	98.64
Mg#	0.71	0.58	0.59	0.26	0.15	0.31	0.25
Nb	1.3	1.3	1.2	1.4	0.0	52.2	26.6
Zr	26.0	47.5	32.3	25.9	10.7	829.6	646.2
Y	7.2	18.0	11.5	3.4	2.1	43.3	54.8
Sr	54.2	169.1	328.9	809.6	14.2	275.2	200.4
Rb	4.5	17.5	23.0	203.0	2.3	66.5	103.8
Th	0.2	0.0	0.0	0.0	0.0	32.9	18.8
Pb	0.0	3.4	4.1	6.3	9.2	2.5	15.8
Zn	75.5	70.2	45.1	27.7	25.5	28.3	91.2
Cu	13.1	36.8	17.0	59.9	21.5	4.1	6.5
Ni	805.9	72.4	22.3	84.9	8.7	3.8	6.9
Cr	731.1	273.6	171.6	24.7	9.0	206.6	99.9
V	86.6	273.0	189.1	30.8	9.4	224.9	133.8
Ba	42.8	530.7	693.6	784.8	198.0	391.1	855.2
Sc	19.8	78.9	50.7	5.4	0.0	33.0	23.3
La	3.03	5.46	3.75	3.50		40.95	40.86
Ce	6.82	12.41	8.09	8.86		83.50	98.17
Pr	0.75	1.51	0.95	1.05		9.84	11.05
Nd	3.08	7.35	4.78	3.27		35.08	40.09
Sm	0.81	1.73	1.13	0.67		7.11	7.57
Eu	0.32	0.68	0.50	0.57		0.18	1.09
Gd	0.99	2.37	1.54	0.74		7.16	7.21
Dy	1.00	2.47	1.58	0.58		6.31	6.56
Ho	0.24	0.57	0.35	0.14		1.46	1.45
Er	0.65	1.58	0.98	0.38		3.86	3.66
Yb	0.70	1.54	0.98	0.37		4.14	3.58
Lu	0.12	0.25	0.15	0.06		0.74	0.58
⁸⁷ Sr/ ⁸⁶ Sr		0.708163		0.709226	0.71093		
¹⁴³ Nd/ ¹⁴⁴ Nd		0.511929		0.511899			
CIPW NORMS							
Ap	0.06	0.10	0.06				
Il	0.51	1.10	0.76				
Mt	6.45	4.55	3.24				
Or	0.73	4.08	5.91				
Ab	4.34	16.40	16.66				
An	18.83	17.88	32.68				
Di	0.00	42.74	32.08				
Hy	31.87	10.67	5.31				
Ol	30.12	0.83	2.03				
C	0.01	0.00	0.00				
Qtz	0.00	0.00	0.00				
TOTAL	92.91	98.36	98.72				

MOINE METASEDIMENTARY ROCKS

SAMPLE:	SOM1	SOM2	SOM3	SOM4	SOM5	SOM6
SiO ₂	63.10	67.90	61.10	58.40	95.01	62.59
TiO ₂	0.90	0.77	1.01	0.98	0.04	0.92
Al ₂ O ₃	16.61	14.85	17.82	18.58	2.78	18.07
Fe ₂ O ₃ *	6.19	5.04	7.19	8.08	0.51	6.70
MnO	0.13	0.08	0.11	0.09	0.03	0.08
MgO	1.83	1.56	2.14	2.61	0.06	1.95
CaO	3.04	2.23	1.92	1.62	0.23	1.19
Na ₂ O	4.75	4.67	4.87	3.20	1.00	2.51
K ₂ O	1.95	1.89	3.71	4.34	0.52	3.97
P ₂ O ₅	0.25	0.13	0.27	0.35	0.00	0.18
LOI	0.54	0.81	1.45	1.73	0.35	1.87
TOTAL	99.28	99.93	101.59	99.99	100.54	100.03
Nb	18.7	15.9	20.6	21.6	1.0	20.7
Zr	252.7	267.6	263.0	196.1	37.2	243.9
Y	45.1	36.7	46.9	47.4	3.2	39.1
Sr	415.3	429.1	275.0	302.1	35.6	229.9
Rb	101.9	97.6	145.5	176.1	16.4	135.2
Th	14.5	11.8	15.8	16.0	0.0	15.3
Pb	32.8	27.5	23.3	29.2	4.9	24.4
Zn	93.0	78.9	101.5	131.9	16.5	101.8
Cu	7.0	7.9	32.8	8.3	2.3	50.1
Ni	28.3	21.4	30.7	41.6	2.7	33.9
Cr	50.6	35.4	57.7	73.9	0.5	67.9
V	108.1	86.1	124.4	122.2	9.7	123.1
Ba	450.9	514.5	981.5	904.5	173.0	991.6
Sc	16.5	15.6	19.9	21.4	1.3	21.5
La	64.83	45.55				
Ce	165.98	101.52				
Pr	16.57	11.48				
Nd	57.38	40.35				
Sm	10.46	7.28				
Eu	2.06	1.55				
Gd	8.93	6.45				
Dy	7.31	5.40				
Ho	1.62	1.20				
Er	4.19	3.12				
Yb	4.42	3.16				
Lu	0.72	0.51				
⁸⁷ Sr/ ⁸⁶ Sr	0.728383					
¹⁴³ Nd/ ¹⁴⁴ Nd	0.510457					

Group I Basalts & Basaltic andesites

SAMPLE	SOBS1top	SOBS3top	SOBT2	PMBASE	PM+200	RCB1	RCB2	TILE1	ORB2	PGB9	ARB1	TMB1
Rb (ppm)	36.40	46.00	53.20	12.20	32.00	42.60	43.40	18.10	3.90	6.20	73.50	41.90
Sr (ppm)	198.90	231.20	236.60	226.10	227.40	222.40	225.70	224.30	120.80	205.40	215.70	211.30
Rb/Sr	0.18	0.20	0.22	0.05	0.14	0.19	0.19	0.08	0.03	0.03	0.34	0.20
87Rb/86Sr	0.530087	0.576270	0.651283	0.156187	0.407434	0.554671	0.556840	0.233603	0.093407	0.087366	0.987065	0.574129
87Sr/86Sr	0.715562	0.714987	0.715375	0.708593	0.711257	0.712739	0.713019	0.709637	0.703833	0.707762	0.716219	0.711186
2 sigma	24	24	20	28	53	14	12	36	89	37	12	12
(87Sr/86Sr)I	0.715125	0.714512	0.714838	0.708464	0.710921	0.712282	0.712560	0.709445	0.703756	0.707690	0.715405	0.710713
E Sr58	151.79	143.09	147.72	57.23	92.11	111.43	115.37	71.15	-9.61	46.24	155.76	89.15
Sm (ppm)	3.63	3.83	3.96	2.78	3.47	4.31	4.31	2.99	3.22	2.6172	5.23	3.87
Nd (ppm)	15.63	16.66	17.25	11.44	15.48	19.3	19.2	14.49	8.66	8.5041	25.18	17.4
Sm/Nd	0.23	0.23	0.23	0.24	0.22	0.22	0.22	0.21	0.37	0.31	0.21	0.22
147Sm/144Nd	0.140388	0.138966	0.138768	0.146892	0.135497	0.134989	0.135692	0.124732	0.224810	0.186041	0.125549	0.134440
143Nd/144Nd	0.512084	0.512084	0.512078	0.512040	0.511958	0.512040	0.512021	0.511990	0.513011	0.512238	0.511924	0.511924
2 sigma	9	7	8	8	35	6	7	6	6	7	7	7
(143Nd/144Nd)I	0.512031	0.512031	0.512025	0.511984	0.511906	0.511989	0.511970	0.511943	0.512926	0.512167	0.511876	0.511872
E Nd58	-10.39	-10.38	-10.50	-11.30	-12.82	-11.21	-11.59	-12.11	7.07	-7.73	-13.41	-13.48

87/86Sr UR (58Ma) 0.704433
143Nd/144Nd CHUR (58Ma) 0.512563

Group II Andesites & Porphyritic Dacites

	Group II Andesites & Porphyritic Dacites						
	SAMPLE	CUP11	PCRPI1	TIPI1	PGB5	TVPI1	KMB1
Rb (ppm)		108.80	108.90	105.90	40.70	106.30	100.80
Sr (ppm)		218.90	207.30	307.20	289.50	207.70	156.20
Rb/Sr		0.50	0.53	0.34	0.14	0.51	0.65
87Rb/86Sr		1.439865	1.521842	0.998717	0.407186	1.482653	1.869234
87Sr/86Sr		0.716928	0.716984	0.717617	0.714771	0.717025	0.715646
2 sigma		10	44	22	23	39	14
(87Sr/86Sr)1		0.715742	0.715730	0.716794	0.714436	0.715803	0.714106
E Sr58		160.54	160.37	175.48	142.00	161.42	137.32
Sm (ppm)		6.42	10.26	6.58	5.1017	9.07	7.32
Nd (ppm)		31.84	50.58	33.47	24.709	44.7	36.78
Sm/Nd		0.20	0.20	0.20	0.21	0.20	0.20
147Sm/144Nd		0.121878	0.122611	0.118832	0.124804	0.122648	0.120300
143Nd/144Nd		0.511885	0.511877	0.511891	0.511924	0.511854	0.511917
2 sigma		7	6	7	6	12	128
(143Nd/144Nd)1		0.511839	0.511830	0.511846	0.511877	0.511807	0.511871
E Nd58		-14.14	-14.31	-14.00	-13.40	-14.75	-13.50

87/86Sr UR (58Ma) 0.704433
143Nd/144Nd CHUR (58Ma) 0.512563

Group III Rhyolites

	Group III Rhyolites				
	PGF1	RCF1	RCF3	RCF4	
	154.40	136.40	137.00	117.40	
	122.10	132.30	90.70	140.20	
	1.26	1.03	1.51	0.84	
	3.665577	2.987500	4.378198	2.426459	
	0.723339	0.719631	0.722666	0.719621	
	11	14	12	21	
	0.720319	0.717169	0.719059	0.717622	
	225.52	180.81	207.63	187.23	
	8.31	8.53	8.16	7.39	
	43.28	43.58	41.38	35.28	
	0.19	0.20	0.20	0.21	
	0.116059	0.118311	0.119197	0.126614	
	0.511897	0.511886	0.511907	0.511907	
	7	6	6	6	
	0.511853	0.511841	0.511862	0.511859	
	-13.86	-14.09	-13.69	-13.74	

Gabbroic Xenoliths

	Gabbroic Xenoliths		
	KFX1	KBGX2	
	20.30	17.50	
	809.60	169.10	
	0.03	0.10	
	0.072584	0.299551	
	0.709286	0.708410	
	14	12	
	0.709226	0.708163	
	68.05	52.96	
	0.55388	1.73	
	2.595	7.35	
	0.21	0.24	
	0.129017	0.142276	
	0.511948	0.511983	
	12	6	
	0.511899	0.511929	
	-12.96	-12.38	

Moine Pelites

	Moine Pelites	
	SOM1	SOBCc
	101.90	100.00
	413.40	400.00
	0.25	0.25
	0.714913	0.725158
	0.728972	0.729985
	20	14
	0.728383	0.729388
	339.99	354.26
	10.46	9.46
	57.38	50.79
	0.18	0.19
	0.110185	0.112582
	0.511785	0.511803
	6	3
	0.511743	0.511760
	-16.00	-15.67

Plagioclase, Melt pockets & Glass from Aluminous Xenoliths

SAMPLE	MPOCK1	MPOCK2	PLAG MB	PLAG MP2	MULL BUC	PL1	PMQX1	MUL GLASS	MELT INCL	PLAG 1	PLAG 2	PLAG 3	DOL TOP	DOL BOT
Rb (ppm)	49.02	39.15	8.49	45.00	70.31	66.50	2.30	66.50	39.00	17.65	19.38	14.36	26.00	25.92
Sr (ppm)	135.90	173.76	323.89	284.16	103.90	275.20	14.20	275.20	227.00	462.8	451.21	470.13	225.00	223.60
Rb/Sr	0.36	0.23	0.03	0.16	0.68	0.24	0.16	0.24	0.17	0.04	0.04	0.03	0.12	0.12
87Rb/86Sr	1.044615	0.652473	0.075918	0.458645	1.959323	0.699409	0.468947	0.699692	0.497520	0.110454	0.124401	0.088459	0.334552	0.335600
87Sr/86Sr	0.713721	0.713212	0.714536	0.714294	0.711417	0.707973	0.710930	0.712102	0.712997	0.714329	0.714832	0.713699	0.710654	0.710344
2 sigma	12	10	13	11	12	12		19	17	26	24	26	16	21
(87Sr/86Sr)H	0.712861	0.712674	0.714473	0.713917	0.709803	0.707397	0.710544	0.711525	0.712587	0.714238	0.714730	0.713626	0.710378	0.710067
E Sr58	119.64	117.00	142.53	134.63	76.23	42.08	86.75	100.69	115.76	139.19	146.17	130.51	84.40	79.99
Sm (ppm)	4.73	4.31	6.89	2.59	3.08	7.1	-	-	-	-	-	-	-	-
Nd (ppm)	27.68	32.8	29.39	28.51	12.786	35	-	-	-	-	-	-	-	-
Sm/Nd	0.17	0.13	0.23	0.09	0.24	0.20	-	-	-	-	-	-	-	-
147Sm/144Nd	0.103291	0.079428	0.141705	0.054913	0.145608	0.122616	-	-	-	-	-	-	-	-
143Nd/144Nd	0.511926	0.511956	0.511922	0.511956	0.511943	0.511836	-	-	-	-	-	-	-	-
2 sigma	16	8	9	6	7	11	-	-	-	-	-	-	-	-
(143Nd/144Nd)H	0.511887	0.511926	0.511868	0.511935	0.511888	0.511789	-	-	-	-	-	-	-	-
E Nd58	-13.20	-12.44	-13.57	-12.26	-13.18	-15.10	-	-	-	-	-	-	-	-

87/86Sr UR (58Ma) 0.704433
143Nd/144Nd CHUR (58Ma) 0.512563

APPENDIX III

The following tables lists the samples collected from the Group I, II and III sheets of the LSSC, and the associated crustal and cumulate xenoliths. The sample numbers, brief descriptions, and the locality name and grid reference are listed.

SAMPLE No.	SAMPLE DESCRIPTION	LOCATION	GRID REF.
PM2	Core mullite buchite	Port Mor	NM 43523
PM3	Rim mullite buchite		
PM4	Dolerite contact with PM3		
PM5 - PM9	Dolerite away from contact PM3		
PB1	Banded schistose xenolith		
PB2	Banded schistose xenolith		
PQ1	Quartzite xenolith		
PQ2	Quartzite xenolith		
PL1	Mullite buchite		
PQS1	Sandstone xenolith		
PMCG1	Plagioclase/sapphire xenolith	Port Mor	NM 435239
PMCG2	As PMCG1 plus contact basalt		
P1	Sandstone xenolith		
PM1F(1-3)	Plagioclase/spinel xenolith		
PM1A	Mullite buchite		
PCON1	Conglomeritic xenolith		
PMAX1(1)	Cores through mullite buchite PM2		
PMAX1(2)	(1) From Edge; (2) From centre;		
PMAX1(3)	(3) Slant through contact with dolerite.		
PMAX2(1)	Cores through mullite buchite PL1		
PMAX2(2)	from the centre towards the dolerite		
PMAX2(3)	contact. Plus cores PMB4-PMB8.		
PMAX2(4)			
PMB4	Dolerite 4cm from contact with PMAX2		
PMB5	Dolerite 7cm from contact with PMAX2		
PMB6	Dolerite 15cm from contact with PMAX2		
PMB7	Dolerite 19cm from contact with PMAX2		
PMB8	Dolerite 83cm from contact with PMAX2		

SAMPLE No.	SAMPLE DESCRIPTION	LOCATION	GRID REF.
PMFX1(1)	Cores through anorthitic xenolith PMCG1 from centre towards the dolerite contact. Plus cores PMB1-PMB3 Dolerite 6cm from contact with PMFX1 Dolerite 19cm from contact with PMFX1 Dolerite 40cm from contact with PMFX1 Cores through quartzite xenolith. Plus cores PMB9-PMB12. Dolerite 4cm from contact with PMQX1 Dolerite 10cm from contact with PMQX1 Dolerite 14cm from contact with PMQX1 Dolerite 23cm from contact with PMQX1 Sequence of dolerite from the base of the sheet to the top.	Port Mor	NM 435239
PMFX1(2)			
PMFX1(3)			
PMB1			
PMB2			
PMB3			
PMQX1(1)			
PMQX1(2)			
PMB9			
PMB10			
PMB11			
PMB12			
PMBASE	Dolerite	Port Mor	NM 433239
PM+50			
PM+110			
PM+200			
PM+270			
PM+380			
PM2B1			
KBB1	Dolerite Dolerite - chilled margin Dolerite - glassy with microphenocrysts of plagioclase Dolerite Loose block - anorthite crystals in dark glass Loose block - Mullite Buchite with anorthite rim Loose block - Mullite Buchite with anorthite rim Loose block - Mullite Buchite with anorthite rim Loose block - Mullite Buchite with anorthite rim Loose block - Mullite Buchite banded glass Mullite Buchite xenolith with anorthite rim	Kilfinichen Bay	NM 484280
KBB2			
KBB3			
KBB4			
KBLF1			
KBLF2			
KBLF3			
KBLF3			
KBLF4			
KBLF5			
KBFX1			

SAMPLE No.	SAMPLE DESCRIPTION	LOCATION	GRID REF.
KBAX1(a) KBAX1(b) KBGX1 KBGX2 KBGX3 KBGX4 KBGX5 KBGNX1 KBHXY1-5 KBB5	Grey mullite buchite Black vitreous cordierite buchite Gabbroic cognate xenolith Light coloured gabbroic xenolith KBGX1 plus contact with dolerite of sheet Coarse grained gabbroic xenolith Coarse grained gabbroic xenolith Gneissose xenolith - banded Gabbroic cognate xenoliths many with large, green pyroxene crystals visible in hand specimen. Dolerite	Kilfinichen Bay	NM 484280
TILE1 TIP11	Dolerite margin to composite sheet Glassy andesite - centre to composite sheet	Tirolan	NM 480275
ARB1 ARB2	Dolerite from centre of sheet Dolerite from centre of sheet	Ardtun Peninsula	NM 375238
KIAX1 KIFX1 KIAX2 KIFX2 KIGX1 KIB1	Porphyritic dacite (glassy) with plagioclase and pyroxene phenocrysts Anorthosite cumulate xenolith Porphyritic dacite (glassy) Mullite buchite with anorthitic rim Gabbroic cognate xenolith Dolerite	Killunaig	NM 496258
PCFX1	Amygdaloidal mullite buchite	Port na Cloidheig	NM 475253

SAMPLE No.	SAMPLE DESCRIPTION	LOCATION	GRID REF.
R0	Sandstone	Rudh' a' Chromain	NM 521202
R1	Sandstone from dolerite contact		
R2	Quartzitic xenolith		
R5	Rhyolite from centre of composite sheet		
R6	Mullite buchite xenolith		
R8	Anorthitic xenolith		
R9	Dolerite from basic margin of sheet		
R10	Anorthitic xenolith		
R11	Contact between dolerite and bostonite		
RCCHILL	Chilled doerite-sandstone contact		
RCGX1	Cognate xenolith in hybrid felsite	Rudh' a' Chromain	NM 521202
RCB1	Dolerite - central portion of lower margin		
RCB2	Dolerite - central portion of upper margin		
RCB3	Dolerite - separate sheet		
RCF1	Porphyritic rhyolite adjacent to lower margin		
RCF2	Aphyric rhyolite from central sheet (upper)		
RCF3	Aphyric rhyolite from central sheet (lower)		
RCF4	Dark grey, porphyritic hybridized rhyolite		
RCGX1	Gabbroic xenolith in hybrid rhyolite		
RCBOS	Monzonite sheet		
TM1F(1-3)	Plagioclase/spinel xenolith	Torr Mor	NM 414240
TMB2	Dolerite from centre of sheet		
TMB1	Dolerite from centre of sheet		
TMB3	Dolerite from centre of sheet		

SAMPLE No.	SAMPLE DESCRIPTION	LOCATION	GRID REF.
SFB1	Dolerite from centre of xenolithic sheet	Sgeir an Fheilidh	NM 513262
SFB2	Dolerite from centre of xenolithic sheet		NM 513262
SFB3	Dolerite from centre and margin of sheet		NM 513262
ORB1	Dolerite from centre of sheet	Ormsaig	NM 445239
ORB2	Dolerite from centre of sheet		NM 441240
SOB1	Dolerite from centre of sheet	Traigh Bhàn na Sgurra	NM 423185
SOBC1	Contact between dolerite and baked pelite		
SOM1	Medium-grained gnt-bio-qtz schist		
SOM2	Fine-grained biotite-quartz schist		
SOM3	Coarse biotite-quartz schist		
SOM4	Mica rich schist		
SOM5	Coarse psammite		
SOM6	Garnet-mica schist		
SOBS1Base	Section 1 - 3 dolerite samples through sheet		
SOBS1Mid			
SOBS1Top			
SOBS2Base			
SOBS2+1m	Section 2 - 4 dolerite samples through sheet		
SOBS2+2m			
SOBS2Top			
SOBS3Base			
SOBS3Mid	Section 3 - 3 dolerite samples through sheet		
SOBS3Top			
SOBS4Base			
SOBS4Mid			
SOBS4Top	Section 4 - 3 dolerite samples through sheet		
SOBT1			
SOBT2			
SOBT3			
SOBT4	Transect of four samples taken from the centre of the sheet between the four sections		

SAMPLE No.	SAMPLE DESCRIPTION	LOCATION	GRID REF.
KMB1	Dolerite - augite phyric	Killiemore	NM 509295
CUPI1	Porphyritic dacite (glassy) with plagioclase and pyroxene phnocrysts	Culliemore	NM 445277
TVPI1	Porphyritic dacite (glassy)	Tavool	NM 436273
TVB1	Dolerite		NM 432272
PCRPI1	Porphyritic dacite (glassy)	Port na Croise	NM 425264
PCRPI2	Coarser porphyritic dacite from centre of sheet, with phenocrysts of plagioclase and pyroxene set in fine-grained matrix.		
PGB1	Dolerite from centre of sheet	Pennyghael	NM 520267
PGF1	Rhyolite		NM 525275
PGB2	Dolerite from centre of sheet		NM 515265
PGB3-4	Dolerite from centre of sheet		NM 513264
PGB5	Dolerite/Glassy andesite		NM 512264
PGB6	Dolerite from centre of sheet		NM 512264
PGB7	Dolerite from centre of sheet		NM 512264
PGB8	Glassy andesite associated with PGB7 & PGB9		NM 512264
PGB9	Xenolithic dolerite associated with PGB8		NM 512264
PGB10	Dolerite from centre of sheet		NM 512264

APPENDIX IV

The following data tables consist of *selected, representative* mineral analysis performed on the Cameca SX50 at the Department of Geology and Applied Geology, Glasgow University. The data tables are arranged in the following order :

- (i) Plagioclase, pyroxene and Fe-Ti oxide analyses from Group I, II and III sheets.
- (ii) Olivine, plagioclase, pyroxene and Cr-spinel analyses from the gabbroic cumulate xenoliths.
- (iii) Plagioclase, spinel, mullite, cordierite, corundum, and glass analyses from the aluminous xenoliths.
- (iv) Plagioclase, muscovite, biotite and garnet analyses from a Moine pelitic schist.
- (v) K-feldspar, plagioclase, and spinel analyses from a partially melted Moine pelitic schist.

FELDSPAR ANALYSIS SHEET

SAMPLE TILE1 - Fine Grained Basaltic Andesite

POINT No.	Groundmass Plagioclase									
	Plag1	Plag2	Plag3	Plag4	Plag5	Plag6	Plag7	Plag8	Plag9	Plag10
SiO2	50.77	51.81	54.62	49.38	49.29	49.97	51.03	52.83	49.69	51.19
TiO2	0.07	0.16	0.07	0.13	0.15	0.08	0.02	0.05	0.08	0.04
Al2O3	30.86	30.60	28.22	31.72	32.00	31.29	30.15	29.70	31.64	30.86
FeO*	1.09	1.34	1.20	1.13	1.04	1.08	1.14	1.15	1.40	1.02
CaO	13.13	11.70	9.23	13.57	13.22	13.49	13.10	10.40	12.29	12.40
Na2O	3.67	4.73	5.69	3.67	3.74	3.90	3.91	5.23	4.57	4.15
K2O	0.22	0.29	0.51	0.14	0.18	0.20	0.25	0.39	0.25	0.20
TOTAL	99.82	100.63	99.54	99.74	99.63	100.02	99.60	99.76	99.92	99.86

FORMULA BASED ON 32 OXYGENS

Si	9.29	9.40	9.93	9.07	9.06	9.16	9.37	9.62	9.12	9.35
Ti	0.01	0.02	0.01	0.02	0.02	0.01	0.00	0.01	0.01	0.01
Al	6.65	6.54	6.05	6.87	6.93	6.76	6.52	6.38	6.84	6.64
Fe (ii)	0.17	0.20	0.18	0.17	0.16	0.17	0.18	0.18	0.22	0.16
Ca	2.57	2.27	1.80	2.67	2.60	2.65	2.58	2.03	2.42	2.43
Na	1.30	1.66	2.01	1.31	1.33	1.39	1.39	1.85	1.62	1.47
K	0.05	0.07	0.12	0.03	0.04	0.05	0.06	0.09	0.06	0.05
TOTAL	20.16	20.32	20.28	20.25	20.26	20.29	20.22	20.31	20.43	20.21
ENDMEMBER %										
Ab	33.17	41.57	51.16	32.59	33.49	33.98	34.58	46.55	39.64	37.30
Or	1.31	1.66	2.99	0.80	1.07	1.12	1.47	2.28	1.41	1.16
An	65.52	56.77	45.85	66.61	65.43	64.89	63.95	51.16	58.95	61.54

FELDSPAR ANALYSIS SHEET

SAMPLE TILE1 - Fine Grained Basaltic Andesite

POINT No.	core	pnt2	pnt3	pnt4	Plagioclase Xenocryst					rim
					pnt5	pnt6	pnt7	pnt8	pnt9	
SiO2	45.58	46.05	46.10	46.15	46.04	45.86	45.17	45.22	45.12	47.25
TiO2	0.05	0.00	0.01	0.06	0.06	0.00	0.00	0.03	0.04	0.04
Al2O3	35.30	34.84	35.03	35.08	35.32	34.99	35.79	35.54	35.70	33.95
FeO*	0.47	0.43	0.51	0.50	0.61	0.53	0.58	0.56	0.58	0.71
CaO	16.71	16.41	16.17	16.33	16.44	16.44	16.94	16.70	17.07	15.51
Na2O	1.93	2.16	2.20	2.23	2.08	2.13	1.91	1.94	1.89	2.55
K2O	0.06	0.04	0.07	0.08	0.06	0.07	0.06	0.04	0.06	0.17
TOTAL	100.10	99.94	100.09	100.42	100.61	100.02	100.46	100.04	100.45	100.19

FORMULA BASED ON 32 OXYGENS

Si	8.39	8.48	8.48	8.46	8.43	8.45	8.30	8.34	8.30	8.67
Ti	0.01	0.00	0.00	0.01	0.01	0.00	0.00	0.00	0.01	0.01
Al	7.66	7.56	7.59	7.58	7.62	7.59	7.75	7.72	7.74	7.34
Fe (ii)	0.07	0.07	0.08	0.08	0.09	0.08	0.09	0.09	0.09	0.11
Ca	3.30	3.24	3.18	3.21	3.22	3.24	3.33	3.30	3.36	3.05
Na	0.69	0.77	0.79	0.79	0.74	0.76	0.68	0.69	0.67	0.91
K	0.01	0.01	0.02	0.02	0.01	0.02	0.01	0.01	0.01	0.04
TOTAL	20.13	20.13	20.13	20.15	20.13	20.15	20.17	20.15	20.17	20.12
ENDMEMBER %										
Ab	17.26	19.22	19.70	19.72	18.60	18.99	16.91	17.31	16.60	22.67
Or	0.34	0.23	0.39	0.44	0.34	0.43	0.36	0.23	0.33	0.99
An	82.40	80.55	79.91	79.84	81.06	80.58	82.73	82.46	83.06	76.34

FELDSPAR ANALYSIS SHEET

TILE1 - Fine Grained Basaltic Andesite

POINT No.	core	pnt2	Plagioclase Phenocryst				rim
			pnt3	pnt4	pnt5	pnt6	
SiO2	48.05	48.55	47.76	48.48	48.93	48.82	51.88
TiO2	0.09	0.02	0.00	0.09	0.03	0.06	0.02
Al2O3	33.44	33.24	33.93	33.40	33.06	33.10	30.01
FeO*	0.45	0.44	0.36	0.42	0.37	0.55	1.17
CaO	14.48	13.78	15.06	14.47	13.93	14.34	11.34
Na2O	3.09	3.22	3.02	3.24	3.36	3.30	4.74
K2O	0.23	0.23	0.21	0.19	0.22	0.18	0.36
TOTAL	99.83	99.48	100.35	100.27	99.89	100.34	99.51

FORMULA BASED ON 32 OXYGENS

Si	8.82	8.91	8.73	8.85	8.95	8.91	9.50
Ti	0.01	0.00	0.00	0.01	0.00	0.01	0.00
Al	7.23	7.19	7.31	7.19	7.12	7.12	6.48
Fe (ii)	0.07	0.07	0.06	0.06	0.06	0.08	0.18
Ca	2.85	2.71	2.95	2.83	2.73	2.80	2.22
Na	1.10	1.15	1.07	1.15	1.19	1.17	1.68
K	0.05	0.05	0.05	0.04	0.05	0.04	0.08
TOTAL	20.13	20.09	20.17	20.14	20.11	20.13	20.14

ENDMEMBER %

Ab	27.51	29.29	26.30	28.51	30.03	20.07	42.16
Or	1.34	1.40	1.22	1.09	1.27	1.03	2.09
An	71.16	69.31	72.49	70.41	68.70	69.89	55.75

FELDSPAR ANALYSIS SHEET

SAMPLE Basalt - PMBASE

POINT No.	Groundmass Plagioclase										
	Plag 1	Plag 2	Plag 3	Plag 4 core	Plag 4 rim	Plag 5 core	Plag 5 rim	Plag 6 core	Plag 6 rim	Plag 7	Plag 8
SiO2	53.26	50.88	53.41	51.37	51.28	52.61	54.93	49.63	52.30	53.60	52.07
TiO2	0.04	0.00	0.07	0.05	0.12	0.03	0.05	0.08	0.00	0.10	0.12
Al2O3	29.44	31.53	29.18	31.23	30.83	29.59	28.58	32.31	29.92	29.64	30.38
FeO*	0.94	1.11	1.01	0.94	0.84	1.20	0.87	0.72	0.88	0.98	1.00
CaO	10.83	12.44	10.53	12.44	12.39	10.99	9.68	13.60	11.30	10.85	11.57
Na2O	4.97	4.22	5.12	4.09	4.15	4.88	5.70	3.51	4.72	5.11	4.88
K2O	0.40	0.26	0.42	0.28	0.30	0.42	0.44	0.19	0.30	0.35	0.36
TOTAL	99.89	100.43	99.74	100.42	99.91	99.72	100.25	100.03	99.42	100.65	100.37

FORMULA BASED ON 32 OXYGENS

Si	9.68	9.25	9.72	9.32	9.35	9.60	9.91	9.07	9.56	9.67	9.46
Ti	0.01	0.00	0.01	0.01	0.02	0.00	0.01	0.01	0.00	0.01	0.02
Al	6.30	6.76	6.26	6.68	6.63	6.36	6.08	6.96	6.44	6.30	6.50
Fe (ii)	0.14	0.17	0.15	0.14	0.13	0.18	0.13	0.11	0.13	0.15	0.15
Ca	2.11	2.42	2.05	2.42	2.42	2.15	1.87	2.66	2.21	2.10	2.25
Na	1.75	1.49	1.81	1.44	1.47	1.73	1.99	1.24	1.67	1.79	1.72
K	0.09	0.06	0.10	0.07	0.07	0.10	0.10	0.04	0.07	0.08	0.08
TOTAL	20.09	20.15	20.10	20.08	20.08	20.12	20.09	20.09	20.09	20.10	20.18

ENDMEMBER %

Ab	44.31	37.47	45.67	36.69	37.07	43.45	50.24	31.47	42.29	45.06	42.37
Or	2.37	1.52	2.47	1.67	1.76	2.46	2.56	1.10	1.76	2.04	2.07
An	53.32	61.01	51.86	61.64	61.17	54.09	47.19	67.44	55.95	52.90	55.55

FELDSPAR ANALYSIS SHEET

SAMPLE Basalt - PMBASE

POINT No.	Plagioclase Phenocryst					Core	Plagioclase Xenocryst					rim	
	pnt 2	pnt 3	pnt 4	pnt 5	rim		Core	pnt 2	pnt 3	pnt 4	pnt 5		pnt 6
SiO2	52.25	52.87	52.23	51.96	51.11	51.97	45.92	48.11	46.27	45.90	46.90	45.79	54.69
TiO2	0.16	0.15	0.00	0.06	0.11	0.01	0.01	0.09	0.01	0.06	0.06	0.00	0.04
Al2O3	30.50	30.00	30.20	30.61	31.37	29.96	35.47	33.38	34.69	35.45	34.54	35.26	28.95
FeO*	0.50	0.43	0.43	0.43	0.36	1.01	0.51	0.80	0.54	0.52	0.49	0.53	0.82
CaO	11.64	11.16	11.44	11.42	12.24	11.40	16.92	14.78	16.29	16.68	15.80	17.01	9.64
Na2O	4.53	4.49	4.35	4.43	4.16	4.52	2.11	2.92	2.23	1.93	2.19	1.91	5.50
K2O	0.45	0.49	0.51	0.42	0.26	0.31	0.03	0.15	0.07	0.08	0.05	0.04	0.48
TOTAL	100.05	99.58	99.16	99.34	99.61	99.17	100.96	100.23	100.10	100.62	100.02	100.53	100.12

FORMULA BASED ON 32 OXYGENS

Si	9.49	9.61	9.55	9.49	9.32	9.53	8.39	8.81	8.51	8.60	8.40	9.87
Ti	0.02	0.02	0.00	0.01	0.02	0.00	0.00	0.01	0.00	0.01	0.00	0.01
Al	6.53	6.43	6.51	6.59	6.74	6.47	7.64	7.20	7.52	7.47	7.62	6.16
Fe (II)	0.08	0.07	0.07	0.07	0.05	0.15	0.08	0.12	0.08	0.07	0.08	0.12
Ca	2.26	2.17	2.24	2.23	2.39	2.24	3.31	2.90	3.21	3.10	3.34	1.86
Na	1.60	1.58	1.54	1.57	1.47	1.61	0.75	1.04	0.79	0.78	0.68	1.93
K	0.10	0.11	0.12	0.10	0.06	0.07	0.01	0.03	0.02	0.01	0.01	0.11
TOTAL	20.08	20.00	20.02	20.05	20.06	20.07	20.17	20.12	20.13	20.05	20.13	20.06
ENDMEMBER %												
Ab	40.25	40.87	39.50	40.23	37.48	41.01	18.39	26.11	19.74	20.01	16.85	49.39
Or	2.64	2.93	3.04	2.50	1.57	1.83	0.17	0.88	0.43	0.29	0.25	2.84
An	57.11	56.19	57.46	57.27	60.96	57.17	81.44	73.01	79.83	79.70	82.90	47.78

FELDSPAR ANALYSIS SHEET

SAMPLE Basalt - PM+50

POINT No.	Plag 1	Plag 2	Plag 3	Plag 4	Groundmass Plagioclase			Plag 7	Plag 8	Plag 9	Plag 10
					Plag5	Plag 6 core	Plag 6 rim				
SiO2	49.78	49.98	50.18	49.21	50.16	50.82	50.79	49.99	50.74	53.10	50.50
TiO2	0.06	0.08	0.12	0.07	0.02	0.05	0.13	0.09	0.06	0.23	0.07
Al2O3	31.07	32.59	31.24	32.50	31.13	31.66	31.84	30.22	31.19	29.69	32.05
FeO*	0.87	0.85	1.08	0.85	0.83	0.68	0.70	2.36	1.12	1.14	0.85
CaO	12.46	13.68	13.01	13.84	12.54	13.03	13.36	13.04	12.47	11.01	13.48
Na2O	4.07	3.47	3.84	3.37	4.10	3.90	3.69	3.47	4.17	4.72	3.76
K2O	0.31	0.19	0.28	0.19	0.28	0.29	0.28	0.27	0.29	0.50	0.24
TOTAL	98.62	100.83	99.74	100.01	99.07	100.43	100.79	99.45	100.04	100.39	100.95

FORMULA BASED ON 32 OXYGENS

Si	9.22	9.06	9.20	9.00	9.24	9.23	9.20	9.25	9.26	9.62	9.14
Ti	0.01	0.01	0.02	0.01	0.00	0.01	0.02	0.01	0.01	0.03	0.01
Al	6.78	6.96	6.75	7.01	6.76	6.78	6.79	6.59	6.71	6.34	6.84
Fe (ii)	0.13	0.13	0.17	0.13	0.13	0.10	0.11	0.36	0.17	0.17	0.13
Ca	2.47	2.66	2.56	2.71	2.47	2.54	2.59	2.58	2.44	2.14	2.61
Na	1.46	1.22	1.36	1.19	1.47	1.37	1.29	1.25	1.48	1.66	1.32
K	0.07	0.04	0.06	0.04	0.07	0.07	0.07	0.06	0.07	0.12	0.06
TOTAL	20.15	20.08	20.12	20.10	20.14	20.09	20.07	20.10	20.14	20.07	20.11

ENDMEMBER %

Ab	36.49	31.08	34.23	30.23	36.59	34.53	32.75	31.99	37.07	42.40	33.10
Or	1.80	1.10	1.62	1.10	1.67	1.69	1.66	1.65	1.68	2.98	1.39
An	61.71	67.82	64.15	68.68	61.75	63.78	65.60	66.36	61.25	54.63	65.51

FELDSPAR ANALYSIS SHEET

SAMPLE Basalt - PM+200

POINT No.	Groundmass Plagioclase									
	Plag 1 core	Plag 1 rim	Plag 2	Plag 3	Plag 4 core	Plag 4 rim	Plag 5	Plag 6	Plag 7	Plag 8
SiO2	50.24	51.84	52.49	50.55	51.03	51.40	51.29	51.43	51.28	50.26
TiO2	0.06	0.00	0.09	0.02	0.00	0.01	0.11	0.02	0.07	0.00
Al2O3	31.53	30.10	30.63	32.06	31.10	31.42	31.54	31.46	31.41	30.34
FeO*	0.47	1.45	0.84	0.61	0.54	0.75	0.60	0.72	0.90	2.17
CaO	14.01	11.91	11.90	13.30	13.26	12.73	13.13	13.09	12.72	12.67
Na2O	3.55	3.90	4.51	3.81	3.86	4.01	3.88	3.94	4.14	3.69
K2O	0.18	0.30	0.38	0.23	0.27	0.33	0.18	0.22	0.25	0.24
TOTAL	100.04	99.50	100.83	100.58	100.06	100.65	100.73	100.88	100.78	99.37

FORMULA BASED ON 32 OXYGENS

Si	9.17	9.49	9.47	9.17	9.30	9.31	9.28	9.29	9.28	9.28
Ti	0.01	0.00	0.01	0.00	0.00	0.00	0.01	0.00	0.01	0.00
Al	6.78	6.49	6.52	6.85	6.68	6.70	6.72	6.70	6.70	6.60
Fe (ii)	0.07	0.22	0.13	0.09	0.08	0.11	0.09	0.11	0.14	0.34
Ca	2.74	2.33	2.30	2.59	2.59	2.47	2.54	2.53	2.47	2.51
Na	1.26	1.38	1.58	1.34	1.36	1.41	1.36	1.38	1.45	1.32
K	0.04	0.07	0.09	0.05	0.06	0.08	0.04	0.05	0.06	0.06
TOTAL	20.08	19.99	20.09	20.10	20.07	20.08	20.05	20.07	20.11	20.11

ENDMEMBER %

Ab	31.10	36.54	39.80	33.69	33.95	35.63	34.46	34.84	36.54	34.02
Or	1.05	1.85	2.19	1.36	1.56	1.93	1.08	1.26	1.47	1.45
An	67.85	61.61	58.02	64.95	64.49	62.44	64.47	63.90	61.99	64.53

FELDSPAR ANALYSIS SHEET

SAMPLE Basalt - PM+380

POINT No.	Groundmass Plagioclase							
	Plag 1	Plag 2	Plag 3	Plag 4	Plag 5	Plag 6	Plag 7	Plag 8
SiO2	51.27	50.20	50.80	52.42	50.90	51.68	50.61	52.43
TiO2	0.07	0.00	0.10	0.08	0.10	0.06	0.05	0.01
Al2O3	31.08	31.70	31.56	30.38	31.38	31.56	31.17	30.67
FeO*	0.85	0.84	0.80	0.79	0.85	0.71	0.72	0.71
CaO	12.19	12.99	12.77	11.61	12.87	12.56	13.94	12.23
Na2O	4.32	3.92	4.11	4.55	3.87	4.12	3.37	4.54
K2O	0.30	0.24	0.23	0.36	0.28	0.27	0.17	0.33
TOTAL	100.08	99.89	100.36	100.19	100.24	100.96	100.04	100.92

FORMULA BASED ON 32 OXYGENS

Si	9.34	9.18	9.23	9.51	9.26	9.32	9.24	9.46
Ti	0.01	0.00	0.01	0.01	0.01	0.01	0.01	0.00
Al	6.67	6.83	6.76	6.50	6.73	6.71	6.71	6.52
Fe (ii)	0.13	0.13	0.12	0.12	0.13	0.11	0.11	0.11
Ca	2.38	2.54	2.49	2.26	2.51	2.43	2.73	2.36
Na	1.53	1.39	1.45	1.60	1.36	1.44	1.19	1.59
K	0.07	0.06	0.05	0.08	0.06	0.06	0.04	0.08
TOTAL	20.12	20.13	20.12	20.07	20.07	20.07	20.02	20.11

ENDMEMBER %

Ab	38.40	34.80	36.29	40.61	34.64	36.65	30.15	39.43
Or	1.74	1.42	1.35	2.13	1.62	1.60	1.00	1.88
An	59.86	63.78	62.37	57.25	63.74	61.75	68.85	58.69

FELDSPAR ANALYSIS SHEET

SAMPLE Basalt - PGB9

POINT No.	Groundmass Plagioclase									
	Plag 1	Plag 2	Plag 3	Plag 4	Plag 5	Plag 6	Plag 7	Plag 8	Plag 9	Plag 10
SiO2	50.32	48.69	49.54	53.24	49.49	50.94	54.19	52.36	52.46	49.39
TiO2	0.09	0.05	0.07	0.08	0.05	0.05	0.00	0.11	0.09	0.00
Al2O3	30.99	31.87	31.67	29.45	31.73	30.42	28.46	29.86	29.62	32.02
FeO*	1.02	1.13	0.94	1.09	1.18	1.04	0.86	0.87	1.01	0.80
CaO	12.17	13.58	12.86	10.57	13.12	11.71	8.69	11.04	11.03	13.54
Na2O	4.38	3.53	3.77	5.28	3.69	4.59	5.94	4.86	4.99	3.69
K2O	0.29	0.15	0.21	0.40	0.28	0.27	0.57	0.33	0.35	0.19
TOTAL	99.26	98.99	99.06	100.11	99.53	99.02	98.72	99.42	99.55	99.64

FORMULA BASED ON 32 OXYGENS

Si	9.26	9.02	9.14	9.67	9.10	9.38	9.92	9.57	9.58	9.07
Ti	0.01	0.01	0.01	0.01	0.01	0.01	0.00	0.02	0.01	0.00
Al	6.72	6.96	6.88	6.30	6.88	6.60	6.14	6.43	6.38	6.93
Fe (ii)	0.16	0.17	0.15	0.16	0.18	0.16	0.13	0.13	0.15	0.12
Ca	2.40	2.69	2.54	2.06	2.59	2.31	1.70	2.16	2.16	2.66
Na	1.56	1.27	1.35	1.86	1.32	1.64	2.11	1.72	1.77	1.31
K	0.07	0.03	0.05	0.09	0.07	0.06	0.13	0.08	0.08	0.04
TOTAL	20.18	20.15	20.11	20.15	20.14	20.16	20.14	20.10	20.14	20.14

ENDMEMBER %

Ab	38.80	31.69	34.20	46.39	33.19	40.83	53.44	43.50	44.12	32.69
Or	1.69	0.87	1.26	2.33	1.64	1.56	3.40	1.92	2.03	1.08
An	59.50	67.43	64.53	51.28	65.17	57.61	43.17	54.58	53.86	66.23

FELDSPAR ANALYSIS SHEET

SAMPLE Basaltic-andesite KIB1

POINT No.	Groundmass Plagioclase									
	Plag 1 core	Plag1 rim	Plag 2	Plag 3	Plag 4	Plag 5	Plag 6	Plag7	Plag 8 core	Plag 8 rim
SiO2	49.44	52.26	50.43	49.56	49.41	50.65	51.09	52.27	49.80	50.77
TiO2	0.03	0.14	0.07	0.09	0.12	0.10	0.08	0.05	0.04	0.02
Al2O3	31.18	29.43	30.95	31.02	31.28	31.27	30.89	29.79	31.47	30.22
FeO*	0.90	1.17	1.05	1.12	0.92	0.99	1.02	1.28	0.71	1.25
CaO	13.14	10.66	11.61	12.83	12.81	12.47	12.37	11.27	13.44	11.71
Na2O	3.84	5.13	4.82	3.88	4.13	4.08	4.29	4.76	3.77	4.55
K2O	0.19	0.36	0.33	0.22	0.24	0.28	0.26	0.40	0.16	0.29
TOTAL	98.73	99.15	99.26	98.73	98.90	99.84	100.01	99.83	99.38	98.80

FORMULA BASED ON 32 OXYGENS

Si	9.16	9.59	9.28	9.18	9.14	9.26	9.32	9.54	9.16	9.38
Ti	0.00	0.02	0.01	0.01	0.02	0.01	0.01	0.01	0.01	0.00
Al	6.81	6.37	6.71	6.77	6.82	6.74	6.64	6.41	6.82	6.58
Fe (ii)	0.14	0.18	0.16	0.17	0.14	0.15	0.16	0.20	0.11	0.19
Ca	2.61	2.10	2.29	2.55	2.54	2.44	2.42	2.20	2.65	2.32
Na	1.38	1.83	1.72	1.39	1.48	1.44	1.52	1.68	1.34	1.63
K	0.05	0.09	0.08	0.05	0.06	0.06	0.06	0.09	0.04	0.07
TOTAL	20.15	20.16	20.25	20.14	20.20	20.11	20.13	20.14	20.12	20.17

ENDMEMBER %

Ab	34.23	45.57	42.08	34.89	36.32	36.55	37.98	42.29	33.37	40.55
Or	1.12	2.13	1.91	1.31	1.40	1.67	1.52	2.35	0.92	1.70
An	64.65	52.30	56.01	63.80	62.28	61.78	60.50	55.36	65.71	57.75

FELDSPAR ANALYSIS SHEET

SAMPLE Basaltic-andesite KIB1

POINT No.	Groundmass plagioclase		Plagioclase phenocryst					
	Plag 9	Plag 10	core	pnt2	pnt3	pnt4	pnt5	rim
SiO2	50.27	51.98	49.23	49.87	49.23	48.79	49.70	49.98
TiO2	0.12	0.05	0.01	0.02	0.00	0.05	0.00	0.08
Al2O3	30.88	29.95	32.51	32.17	32.09	32.58	31.52	31.33
FeO*	1.07	1.33	0.62	0.65	0.56	0.73	0.78	0.95
CaO	12.11	11.14	13.97	13.76	13.60	13.62	13.22	12.91
Na2O	4.44	4.87	3.32	3.56	3.67	3.46	3.84	4.05
K2O	0.28	0.34	0.17	0.15	0.20	0.14	0.22	0.25
TOTAL	99.16	99.67	99.82	100.18	99.35	99.36	99.29	99.55

FORMULA BASED ON 32 OXYGENS

Si	9.26	9.51	9.01	9.09	9.06	8.98	9.15	9.18
Ti	0.02	0.01	0.00	0.00	0.00	0.01	0.00	0.01
Al	6.71	6.46	7.02	6.91	6.96	7.07	6.84	6.78
Fe (ii)	0.16	0.20	0.09	0.10	0.09	0.11	0.12	0.15
Ca	2.39	2.18	2.74	2.69	2.68	2.69	2.61	2.54
Na	1.59	1.72	1.18	1.26	1.31	1.23	1.37	1.44
K	0.07	0.08	0.04	0.03	0.05	0.03	0.05	0.06
TOTAL	20.19	20.16	20.09	20.09	20.14	20.11	20.14	20.16

ENDMEMBER %

Ab	39.25	43.28	29.77	31.59	32.41	31.20	34.00	35.66
Or	1.63	1.96	1.02	0.88	1.15	0.85	1.31	1.46
An	59.12	54.76	69.20	67.53	66.44	67.96	64.70	62.89

FELDSPAR ANALYSIS SHEET

SAMPLE Basaltic-andesite KIB1

POINT No.	core	pnt2	Plagioclase xenocryst				rim	Plagioclase inclusion in pyrite
			pnt3	pnt4	pnt5	pnt6		
SiO2	48.14	48.05	48.43	47.99	48.34	48.16	51.71	50.43
TiO2	0.00	0.03	0.15	0.02	0.03	0.16	0.05	0.05
Al2O3	33.20	33.70	32.71	33.00	32.98	32.95	30.52	30.82
FeO*	0.66	0.57	0.67	0.73	0.63	0.67	0.95	1.57
CaO	14.60	14.64	14.15	14.39	14.30	14.56	11.78	12.12
Na2O	3.16	2.97	3.24	3.20	3.17	3.31	4.57	4.35
K2O	0.17	0.12	0.11	0.13	0.15	0.18	0.33	0.27
TOTAL	99.94	100.08	99.47	99.47	99.61	100.00	99.91	99.61

FORMULA BASED ON 32 OXYGENS

Si	8.84	8.79	8.91	8.85	8.89	8.84	9.43	9.27
Ti	0.00	0.00	0.02	0.00	0.00	0.02	0.01	0.01
Al	7.18	7.27	7.09	7.17	7.15	7.13	6.56	6.68
Fe (ii)	0.10	0.09	0.10	0.11	0.10	0.10	0.14	0.24
Ca	2.87	2.87	2.79	2.84	2.82	2.86	2.30	2.39
Na	1.13	1.05	1.16	1.14	1.13	1.18	1.62	1.55
K	0.04	0.03	0.03	0.03	0.04	0.04	0.08	0.06
TOTAL	20.16	20.11	20.11	20.15	20.12	20.18	20.13	20.19
ENDMEMBER %								
Ab	27.87	26.68	29.12	28.49	28.39	28.86	40.45	38.76
Or	1.01	0.73	0.66	0.77	0.89	1.02	1.94	1.60
An	71.12	72.59	70.22	70.74	70.72	70.11	57.61	59.64

FELDSPAR ANALYSIS SHEET

SAMPLE PCRPI1 - Porphyritic Dacite (Sheet Margin)				SAMPLE PCRPI2 - Porphyritic Dacite (Sheet Centre)								
Plagioclase Phenocrysts				Groundmass Feldspar								
POINT No.	Plag 1 core	Plag 1 rim	Plag 2 core	Plag 2 rim	Plag 3 core	Plag 3 rim	POINT No.	Plag 1	Plag 2	K-Spar	Plagioclase Phenocryst	
											core	rim
SiO2	56.39	57.01	56.56	55.59	56.49	54.79	SiO2	58.26	57.08	63.88	56.03	54.90
TiO2	0.13	0.14	0.08	0.14	0.12	0.02	TiO2	0.04	0.02	0.05	0.06	0.14
Al2O3	27.37	25.98	27.39	27.77	27.16	28.43	Al2O3	26.12	26.83	19.82	27.77	28.07
FeO*	0.65	0.94	0.55	0.66	0.52	0.62	FeO*	0.67	0.61	0.29	0.46	1.44
CaO	9.15	8.05	9.05	9.49	8.97	9.92	CaO	7.43	8.09	0.33	9.46	9.97
Na2O	5.46	6.07	5.56	5.49	5.67	5.21	Na2O	5.95	6.44	4.15	5.69	4.99
K2O	0.71	0.76	0.70	0.62	0.73	0.57	K2O	0.64	0.70	10.21	0.65	0.53
TOTAL	99.86	98.95	99.89	99.76	99.65	99.56	TOTAL	99.12	99.76	98.71	100.12	100.04

FORMULA BASED ON 32 OXYGENS

Si	10.17	10.37	10.19	10.06	10.20	9.94	Si	11.75	10.09	9.94
Ti	0.02	0.02	0.01	0.02	0.02	0.00	Ti	0.01	0.01	0.02
Al	5.82	5.57	5.81	5.92	5.78	6.08	Al	4.30	5.89	5.99
Fe (ii)	0.10	0.14	0.08	0.10	0.08	0.09	Fe (ii)	0.04	0.07	0.22
Ca	1.77	1.57	1.75	1.84	1.74	1.93	Ca	0.07	1.82	1.93
Na	1.91	2.14	1.94	1.93	1.99	1.83	Na	1.48	1.99	1.75
K	0.16	0.18	0.16	0.14	0.17	0.13	K	2.39	0.15	0.12
TOTAL	19.94	19.99	19.95	20.00	19.97	20.00	TOTAL	20.03	20.02	19.98

ENDMEMBER %

Ab	49.74	55.11	50.46	49.27	51.06	47.09	Ab	56.61	50.16	46.03
Or	4.22	4.53	4.20	3.67	4.30	3.37	Or	4.08	3.76	3.21
An	46.03	40.36	45.34	47.06	44.64	49.54	An	39.31	46.07	50.76

FELDSPAR ANALYSIS SHEET

SAMPLE TIPI1 - Porphyritic Dacite

POINT No.	Groundmass Plagioclase									
	Plag1 Core	Plag1 Rim	Plag2	Plag3	Plag4	Plag5 Core	Plag5 Rim	Plag6	Plag7	Plag8
SiO2	50.36	52.54	49.77	51.53	53.02	49.97	50.45	50.81	50.08	51.15
TiO2	0.04	0.06	0.00	0.13	0.10	0.02	0.10	0.00	0.02	0.04
Al2O3	32.35	30.18	32.67	31.30	28.83	32.31	32.14	31.19	32.12	31.01
FeO*	0.57	0.73	0.64	0.73	0.85	0.58	0.64	0.66	0.65	0.85
CaO	13.42	11.29	13.17	12.14	9.69	13.24	13.01	11.78	13.29	12.08
Na2O	3.60	4.63	3.73	4.11	5.43	3.65	3.60	3.48	3.78	3.98
K2O	0.34	0.42	0.34	0.44	0.70	0.27	0.32	1.16	0.30	0.83
TOTAL	100.69	99.85	100.32	100.40	98.63	100.03	100.26	99.08	100.24	99.95

FORMULA BASED ON 32 OXYGENS

Si	9.13	9.55	9.06	9.34	9.75	9.11	9.17	9.34	9.13	9.34
Ti	0.01	0.01	0.00	0.02	0.01	0.00	0.01	0.00	0.00	0.01
Al	6.91	6.47	7.01	6.69	6.25	6.94	6.89	6.76	6.90	6.67
Fe (ii)	0.09	0.11	0.10	0.11	0.13	0.09	0.10	0.10	0.10	0.13
Ca	2.61	2.20	2.57	2.36	1.91	2.59	2.53	2.32	2.59	2.36
Na	1.27	1.63	1.32	1.45	1.94	1.29	1.27	1.24	1.34	1.41
K	0.08	0.10	0.08	0.10	0.17	0.06	0.07	0.27	0.07	0.19
TOTAL	20.08	20.07	20.13	20.07	20.16	20.09	20.04	20.03	20.12	20.12

ENDMEMBER %

Ab	32.04	41.56	33.22	37.02	48.30	32.79	32.73	32.34	33.39	35.55
Or	2.01	2.47	2.02	2.61	4.12	1.58	1.90	7.09	1.75	4.90
An	65.95	55.96	64.76	60.37	47.58	65.64	65.36	60.57	64.85	59.55

FELDSPAR ANALYSIS SHEET

SAMPLE TIPI1 - Porphyritic Dacite

POINT No.	Groundmass Plagioclase		Plagioclase Phenocryst					
	Plag9	Plag10	core	pnt 2	pnt 3	pnt 4	pnt 5	rim
SiO2	50.25	50.57	51.58	51.78	51.09	51.33	51.01	57.61
TiO2	0.13	0.00	0.06	0.10	0.09	0.09	0.06	0.34
Al2O3	31.49	31.36	31.51	31.02	31.87	31.52	31.54	26.70
FeO*	0.52	0.67	0.30	0.39	0.31	0.24	0.54	1.02
CaO	12.40	12.46	12.14	12.23	12.23	12.16	12.24	7.54
Na2O	4.03	4.26	4.18	4.32	4.23	4.12	4.22	5.71
K2O	0.37	0.46	0.49	0.51	0.55	0.52	0.43	0.89
TOTAL	99.20	99.78	100.27	100.36	100.37	99.96	100.03	99.80

FORMULA BASED ON 32 OXYGENS

Si	9.23	9.25	9.35	9.39	9.27	9.33	9.29	10.36
Ti	0.02	0.00	0.01	0.01	0.01	0.01	0.01	0.05
Al	6.81	6.76	6.73	6.63	6.81	6.75	6.77	5.66
Fe (ii)	0.08	0.10	0.05	0.06	0.05	0.04	0.08	0.15
Ca	2.44	2.44	2.36	2.37	2.38	2.37	2.39	1.45
Na	1.44	1.51	1.47	1.52	1.49	1.45	1.49	1.99
K	0.09	0.11	0.11	0.12	0.13	0.12	0.10	0.20
TOTAL	20.11	20.18	20.07	20.10	20.13	20.07	20.12	19.86

ENDMEMBER %

Ab	36.22	37.18	37.30	37.86	37.26	36.86	37.44	54.60
Or	2.21	2.65	2.88	2.96	3.21	3.04	2.50	5.57
An	61.57	60.17	59.82	59.18	59.52	60.10	60.07	39.83

FELDSPAR ANALYSIS SHEET

SAMPLE Rhyolite - PGF1

POINT No.	G	G	P	P	P	P	P	P
SiO2	65.10	65.50	64.45	65.94	65.08	65.70	65.62	66.05
TiO2	0.00	0.00	0.17	0.00	0.00	0.02	0.02	0.00
Al2O3	21.53	21.84	22.33	21.66	22.16	21.89	21.62	21.58
FeO*	0.02	0.02	0.01	0.02	0.00	0.00	0.06	0.04
CaO	1.81	1.88	2.43	1.64	2.26	1.72	1.62	1.73
Na2O	6.86	6.35	6.45	6.30	7.04	5.71	7.20	7.13
K2O	0.06	0.07	0.06	0.05	0.09	0.05	0.14	0.11
TOTAL	95.37	95.66	95.90	95.60	96.63	95.08	96.27	96.64

FORMULA BASED ON 32 OXYGENS

Si	11.78	11.79	11.62	11.85	11.66	11.84	11.78	11.80
Ti	0.00	0.00	0.02	0.00	0.00	0.00	0.00	0.00
Al	4.59	4.63	4.74	4.59	4.68	4.65	4.57	4.54
Fe (ii)	0.00	0.00	0.00	0.00	0.00	0.00	0.01	0.01
Ca	0.35	0.36	0.47	0.32	0.43	0.33	0.31	0.33
Na	2.40	2.22	2.25	2.19	2.44	2.00	2.50	2.47
K	0.01	0.02	0.01	0.01	0.02	0.01	0.03	0.03
TOTAL	19.14	19.01	19.12	18.96	19.23	18.83	19.20	19.17

ENDMEMBER %

Ab	86.84	85.41	82.36	87.04	84.30	85.37	87.97	87.38
Or	0.47	0.63	0.47	0.46	0.71	0.47	1.09	0.92
An	12.68	13.95	17.17	12.50	14.99	14.17	10.93	11.69

PYROXENE ANALYSIS SHEET

SAMPLE Basaltic andesite - ARB1

POINT No.	Cpx1	Cpx 2	Cpx 3	Cpx 4	Cpx 5	Cpx 6 core	Cpx 6 rim	Cpx 7	Cpx 8	Cpx 9	Cpx 10
SiO2	53.30	53.13	52.49	53.18	53.46	51.21	50.23	53.15	51.30	52.59	50.86
TiO2	0.18	0.17	0.27	0.21	0.27	0.40	0.61	0.14	0.33	0.36	0.50
Al2O3	1.77	1.96	2.01	2.01	1.82	2.27	2.06	1.84	3.63	1.73	1.53
Cr2O3	0.35	0.41	0.31	0.29	0.59	0.10	0.05	0.38	0.11	0.24	0.00
Fe2O3	1.54	1.08	2.02	0.93	1.42	1.50	1.62	2.60	0.93	0.78	1.77
MgO	26.50	26.12	24.04	24.74	26.74	15.97	14.12	26.39	23.76	24.01	18.28
CaO	3.26	3.23	5.00	4.39	3.00	16.74	17.40	3.30	3.60	4.45	8.22
MnO	0.37	0.38	0.48	0.45	0.37	0.29	0.35	0.36	0.40	0.35	0.53
FeO	11.92	12.38	13.07	13.40	11.98	10.64	11.94	11.74	14.14	14.17	17.36
Na2O	0.04	0.05	0.05	0.04	0.07	0.16	0.18	0.06	0.03	0.04	0.05
K2O	0.00	0.00	0.00	0.00	0.00	0.01	0.01	0.02	0.00	0.00	0.00
TOTAL	99.23	98.92	99.74	99.66	99.72	99.29	98.56	99.99	98.23	98.70	99.10

FORMULA BASED ON 6 OXYGENS

Si	1.93	1.93	1.92	1.94	1.93	1.92	1.92	1.92	1.90	1.94	1.93
Al	0.07	0.07	0.08	0.06	0.07	0.08	0.08	0.08	0.10	0.06	0.07
Al	0.01	0.02	0.01	0.02	0.01	0.02	0.01	0.00	0.06	0.01	0.00
Fe(III)	0.04	0.03	0.06	0.03	0.04	0.04	0.05	0.07	0.03	0.02	0.05
Fe(II)	0.36	0.38	0.40	0.41	0.36	0.33	0.38	0.35	0.44	0.44	0.55
Ti	0.00	0.00	0.01	0.01	0.01	0.01	0.02	0.00	0.01	0.01	0.01
Mn	0.01	0.01	0.01	0.01	0.01	0.01	0.01	0.01	0.01	0.01	0.02
Ca	0.13	0.13	0.20	0.17	0.12	0.67	0.71	0.13	0.14	0.18	0.33
Mg	1.43	1.42	1.31	1.34	1.44	0.89	0.80	1.42	1.31	1.32	1.03
Cr	0.01	0.01	0.01	0.01	0.02	0.00	0.00	0.01	0.00	0.01	0.00
Na	0.00	0.00	0.00	0.00	0.00	0.01	0.01	0.00	0.00	0.00	0.00
K	0.00	0.00	0.00	0.00	0.00	0.00	0.00	0.00	0.00	0.00	0.00
TOTAL	4.00	4.00	4.00	4.00	4.00	4.00	4.00	4.00	4.00	4.00	4.00

ENDMEMBER %

Wo	6.55	6.52	10.20	8.84	6.02	35.24	37.30	6.67	7.51	9.04	17.26
En	74.14	73.36	68.21	69.36	74.63	46.78	42.13	74.23	68.85	67.91	53.41
Fs	19.31	20.12	21.59	21.79	19.35	17.97	20.57	19.11	23.65	23.04	29.32
Mg#	0.78	0.78	0.74	0.76	0.78	0.70	0.65	0.77	0.74	0.74	0.63

PYROXENE ANALYSIS SHEET

SAMPLE Basaltic andesite - TILE1

POINT No.	Groundmass clinopyroxene									
	Cpx 1	Cpx 2	Cpx 3	Cpx 4	Cpx 5	Cpx 6	Cpx 7	Cpx 8	Cpx 9	Cpx 10
SiO2	49.96	49.77	49.20	48.66	49.19	48.82	49.38	49.55	49.47	49.95
TiO2	0.39	0.50	0.68	0.51	0.63	0.71	0.50	0.61	0.80	0.63
Al2O3	4.64	4.85	5.97	5.72	6.01	4.79	4.67	5.98	5.19	4.69
Cr2O3	0.23	0.18	0.26	0.28	0.33	0.08	0.09	0.36	0.24	0.29
Fe2O3	1.84	1.85	1.41	2.42	1.20	2.72	1.56	0.73	1.52	1.66
MgO	18.53	16.11	15.93	15.18	15.01	14.25	16.16	17.31	16.06	16.91
CaO	14.84	18.93	19.07	19.65	19.77	19.60	14.54	16.39	18.68	17.41
MnO	0.28	0.18	0.09	0.21	0.13	0.26	0.32	0.21	0.16	0.26
FeO	6.74	5.77	5.37	5.01	5.66	7.02	10.05	6.76	6.03	6.41
Na2O	0.22	0.21	0.23	0.26	0.26	0.25	0.25	0.21	0.24	0.24
K2O	0.00	0.02	0.03	0.00	0.10	0.02	0.17	0.01	0.01	0.03
TOTAL	97.67	98.37	98.24	97.90	98.31	98.52	97.70	98.11	98.39	98.47

FORMULA BASED ON 6 OXYGENS

Si	1.87	1.86	1.84	1.83	1.84	1.84	1.87	1.84	1.85	1.86
Al	0.13	0.14	0.16	0.17	0.16	0.16	0.13	0.16	0.15	0.14
Al	0.07	0.07	0.10	0.08	0.11	0.06	0.08	0.11	0.08	0.07
Fe(III)	0.05	0.05	0.04	0.07	0.03	0.08	0.04	0.02	0.04	0.05
Fe(II)	0.21	0.18	0.17	0.16	0.18	0.22	0.32	0.21	0.19	0.20
Ti	0.01	0.01	0.02	0.01	0.02	0.02	0.01	0.02	0.02	0.02
Mn	0.01	0.01	0.00	0.01	0.00	0.01	0.01	0.01	0.00	0.01
Ca	0.59	0.76	0.76	0.79	0.79	0.79	0.59	0.65	0.75	0.69
Mg	1.03	0.90	0.89	0.85	0.84	0.80	0.91	0.96	0.89	0.94
Cr	0.01	0.01	0.01	0.01	0.01	0.00	0.00	0.01	0.01	0.01
Na	0.02	0.02	0.02	0.02	0.02	0.02	0.02	0.01	0.02	0.02
K	0.00	0.00	0.00	0.00	0.01	0.00	0.02	0.00	0.00	0.00
TOTAL	4.00	4.00	4.00	4.00	4.01	4.00	4.02	4.00	4.00	4.00

ENDMEMBER %

Wo	32.19	41.16	41.91	43.82	43.76	43.45	32.21	35.70	40.75	37.73
En	55.93	48.73	48.72	47.10	46.22	43.94	49.83	52.44	48.72	50.98
Fs	11.89	10.11	9.37	9.08	10.02	12.61	17.96	11.86	10.53	11.29
Mg#	0.80	0.79	0.81	0.79	0.80	0.73	0.72	0.81	0.79	0.79

PYROXENE ANALYSIS SHEET

SAMPLE Basalt - PMBASE

POINT No.	Groundmass clinopyroxene							
	CPX1	CPX2 CORE	CPX2 RIM	CPX3	CPX4	CPX5	CPX6	CPX7 CORE
							CPX7 RIM	CPX8
SiO2	51.13	51.14	51.54	51.74	51.20	51.04	51.40	51.26
TiO2	0.52	0.43	0.47	0.47	0.61	0.51	0.44	0.43
Al2O3	3.47	2.76	1.58	3.76	3.60	2.67	3.39	3.64
Cr2O3	0.43	0.06	0.05	0.48	0.22	0.00	0.21	0.61
Fe2O3	1.24	2.41	0.58	0.76	1.09	1.85	1.30	1.31
MgO	17.91	17.18	17.27	18.68	17.31	16.24	17.47	18.01
CaO	17.32	17.12	12.45	16.57	17.92	17.80	17.90	16.96
MnO	0.22	0.23	0.43	0.16	0.26	0.30	0.20	0.20
FeO	6.38	7.83	14.16	6.67	6.68	8.41	6.64	6.53
Na2O	0.20	0.20	0.15	0.19	0.22	0.21	0.19	0.22
K2O	0.00	0.00	0.01	0.01	0.00	0.02	0.02	0.00
TOTAL	98.81	99.37	98.69	99.49	99.10	99.04	99.16	99.17
							100.00	98.56

FORMULA BASED ON 6 OXYGENS

Si	1.89	1.90	1.95	1.90	1.89	1.91	1.90	1.89
Al	0.11	0.10	0.05	0.10	0.11	0.09	0.10	0.11
Al	0.04	0.02	0.02	0.06	0.05	0.03	0.05	0.05
Fe(III)	0.03	0.07	0.02	0.02	0.03	0.05	0.04	0.04
Fe(II)	0.20	0.24	0.45	0.20	0.21	0.26	0.21	0.20
Ti	0.01	0.01	0.01	0.01	0.02	0.01	0.01	0.01
Mn	0.01	0.01	0.01	0.00	0.01	0.01	0.01	0.01
Ca	0.69	0.68	0.50	0.65	0.71	0.71	0.71	0.67
Mg	0.99	0.95	0.97	1.02	0.95	0.91	0.96	0.99
Cr	0.01	0.00	0.00	0.01	0.01	0.00	0.01	0.02
Na	0.01	0.01	0.01	0.01	0.02	0.01	0.01	0.02
K	0.00	0.00	0.00	0.00	0.00	0.00	0.00	0.00
TOTAL	4.00	4.00	4.00	4.00	4.00	4.00	4.00	4.00

ENDMEMBER %

Wo	36.55	36.18	26.01	34.61	37.80	37.72	37.65	35.88
En	52.57	50.51	50.20	54.26	50.78	47.87	51.11	52.99
Fs	10.88	13.31	23.79	11.13	11.43	14.41	11.24	11.13
Mg#	0.81	0.75	0.68	0.82	0.80	0.74	0.80	0.81
							0.80	0.80

PYROXENE ANALYSIS SHEET

SAMPLE Basalt - PM+50

POINT No.

Groundmass clinopyroxene

	CPX1	CPX2	CPX3	CPX4	CPX5	CPX6	CPX7	CPX8
SiO2	51.66	51.68	50.86	51.89	49.27	51.37	52.11	51.90
TiO2	0.27	0.45	0.57	0.29	0.79	0.43	0.41	0.43
Al2O3	2.38	2.89	2.52	2.62	3.42	3.33	2.30	2.96
Cr2O3	0.08	0.11	0.00	0.51	0.00	0.19	0.00	0.30
Fe2O3	2.12	1.26	1.31	1.44	2.89	1.66	0.59	1.44
MgO	18.38	17.09	17.17	18.79	14.35	17.55	17.95	19.10
CaO	15.98	18.69	13.35	16.88	14.37	17.99	15.26	15.83
MnO	0.26	0.18	0.32	0.23	0.34	0.23	0.31	0.20
FeO	7.83	6.58	12.49	5.92	14.14	6.13	10.00	7.00
Na2O	0.15	0.22	0.17	0.22	0.24	0.24	0.18	0.20
K2O	0.00	0.01	0.00	0.00	0.01	0.00	0.00	0.00
TOTAL	99.12	99.16	98.76	98.80	99.81	99.13	99.10	99.35

FORMULA BASED ON 6 OXYGENS

Si	1.91	1.91	1.92	1.92	1.87	1.90	1.94	1.91
Al	0.09	0.09	0.08	0.08	0.13	0.10	0.06	0.09
Al	0.02	0.04	0.03	0.03	0.02	0.04	0.04	0.03
Fe(iii)	0.06	0.04	0.04	0.04	0.08	0.05	0.02	0.04
Fe(ii)	0.24	0.20	0.39	0.18	0.45	0.19	0.31	0.21
Ti	0.01	0.01	0.02	0.01	0.02	0.01	0.01	0.01
Mn	0.01	0.01	0.01	0.01	0.01	0.01	0.01	0.01
Ca	0.63	0.74	0.54	0.67	0.58	0.71	0.61	0.62
Mg	1.02	0.94	0.96	1.03	0.81	0.97	0.99	1.05
Cr	0.00	0.00	0.00	0.01	0.00	0.01	0.00	0.01
Na	0.01	0.02	0.01	0.02	0.02	0.02	0.01	0.01
K	0.00	0.00	0.00	0.00	0.00	0.00	0.00	0.00
TOTAL	4.00	4.00	4.00	4.00	4.00	4.00	4.00	4.00

ENDMEMBER %

Wo	33.39	39.14	28.26	35.30	31.49	37.99	31.60	31.60
En	53.41	49.80	50.55	54.66	43.73	51.53	51.72	51.72
Fs	13.19	11.06	21.18	10.04	24.77	10.48	16.68	16.68
Mg#	0.77	0.80	0.69	0.82	0.60	0.80	0.75	0.80

PYROXENE ANALYSIS SHEET

SAMPLE Basalt - PM+200

POINT No.	Groundmass clinopyroxene							
	CPX1	CPX2	CPX3 CORE	CPX3 RIM	CPX4	CPX5	CPX6	CPX7 CPX8 CORE CPX8 RIM
SiO2	51.75	52.80	51.29	49.89	51.10	51.95	50.77	51.50 51.67 51.72
TiO2	0.59	0.28	0.69	0.62	0.55	0.45	0.67	0.32 0.44 0.54
Al2O3	2.98	1.26	2.89	2.70	2.55	2.60	2.81	3.17 2.79 2.75
Cr2O3	0.09	0.03	0.04	0.00	0.00	0.54	0.02	0.73 0.21 0.03
Fe2O3	0.97	0.15	1.37	2.83	1.73	0.54	1.88	1.01 1.21 0.37
MgO	17.40	19.36	16.30	14.31	14.92	18.11	16.18	18.00 18.02 16.72
CaO	17.65	13.89	18.77	17.58	19.12	17.77	17.64	17.54 17.52 17.86
MnO	0.17	0.27	0.23	0.38	0.22	0.14	0.29	0.17 0.25 0.18
FeO	7.60	10.15	7.58	10.50	9.16	6.49	8.69	6.15 6.67 8.57
Na2O	0.20	0.14	0.22	0.27	0.24	0.18	0.19	0.21 0.15 0.19
K2O	0.02	0.00	0.01	0.01	0.00	0.00	0.00	0.01 0.00 0.00
TOTAL	99.42	98.32	99.38	99.09	99.59	98.76	99.15	98.81 98.92 98.95

FORMULA BASED ON 6 OXYGENS

Si	1.91	1.97	1.91	1.89	1.91	1.92	1.90	1.91 1.91 1.93
Al	0.09	0.03	0.09	0.11	0.09	0.08	0.10	0.09 0.09 0.07
Al	0.04	0.02	0.03	0.01	0.03	0.04	0.02	0.04 0.03 0.05
Fe(III)	0.03	0.00	0.04	0.08	0.05	0.01	0.05	0.03 0.03 0.01
Fe(II)	0.23	0.32	0.24	0.33	0.29	0.20	0.27	0.19 0.21 0.27
Ti	0.02	0.01	0.02	0.02	0.02	0.01	0.02	0.01 0.01 0.02
Mn	0.01	0.01	0.01	0.01	0.01	0.00	0.01	0.01 0.01 0.01
Ca	0.70	0.55	0.75	0.71	0.77	0.70	0.71	0.70 0.69 0.71
Mg	0.96	1.08	0.90	0.81	0.83	1.00	0.90	0.99 0.99 0.93
Cr	0.00	0.00	0.00	0.00	0.00	0.02	0.00	0.02 0.01 0.00
Na	0.01	0.01	0.02	0.02	0.02	0.01	0.01	0.01 0.01 0.01
K	0.00	0.00	0.00	0.00	0.00	0.00	0.00	0.00 0.00 0.00
TOTAL	4.00	4.00	4.00	4.00	4.00	4.00	4.00	4.00 4.00 4.00

ENDMEMBER %

Wo	36.84	28.37	39.48	38.23	40.50	36.92	37.40	36.92 36.50 37.25
En	50.50	55.01	47.71	43.30	43.98	52.33	47.73	52.69 52.23 48.51
Fs	12.66	16.61	12.81	18.47	15.52	10.75	14.87	10.39 11.27 14.24
Mg#	0.79	0.77	0.77	0.66	0.71	0.82	0.74	0.82 0.81 0.77

PYROXENE ANALYSIS SHEET

SAMPLE Basalt - PM+380

POINT No.	Groundmass clinopyroxene						
	CPX1	CPX2	CPX3	CPX4	CPX5	CPX6	CPX7
SiO2	53.77	53.32	52.28	51.34	51.80	51.25	51.45
TiO2	0.24	0.21	0.50	0.51	0.47	0.40	0.48
Al2O3	1.33	1.70	3.10	3.72	3.21	3.71	3.67
Cr2O3	0.10	0.16	0.23	0.33	0.12	0.61	0.34
Fe2O3	0.16	0.86	0.90	0.97	0.74	0.43	0.57
MgO	21.72	20.78	19.31	18.01	17.67	17.88	17.30
CaO	11.77	12.85	15.12	17.21	17.43	16.96	18.01
MnO	0.34	0.32	0.22	0.19	0.16	0.18	0.25
FeO	9.93	9.28	8.02	6.50	7.35	6.80	6.74
Na2O	0.10	0.18	0.19	0.21	0.22	0.23	0.22
K2O	0.00	0.01	0.02	0.01	0.00	0.00	0.01
TOTAL	99.46	99.66	99.91	98.99	99.16	98.47	99.05

FORMULA BASED ON 6 OXYGENS

Si	1.96	1.95	1.91	1.89	1.91	1.90	1.90
Al	0.04	0.05	0.09	0.11	0.09	0.10	0.10
Al	0.02	0.02	0.04	0.06	0.05	0.06	0.06
Fe(iii)	0.00	0.02	0.02	0.03	0.02	0.01	0.02
Fe(ii)	0.30	0.28	0.25	0.20	0.23	0.21	0.21
Ti	0.01	0.01	0.01	0.01	0.01	0.01	0.01
Mn	0.01	0.01	0.01	0.01	0.00	0.01	0.01
Ca	0.46	0.50	0.59	0.68	0.69	0.67	0.71
Mg	1.18	1.13	1.05	0.99	0.97	0.99	0.95
Cr	0.00	0.00	0.01	0.01	0.00	0.02	0.01
Na	0.01	0.01	0.01	0.02	0.02	0.02	0.02
K	0.00	0.00	0.00	0.00	0.00	0.00	0.00
TOTAL	4.00	4.00	4.00	4.00	4.00	4.00	4.00

ENDMEMBER %

Wo	23.53	26.08	31.23	36.24	36.41	35.86	37.89
En	60.43	58.70	55.48	52.76	51.35	52.61	50.62
Fs	16.04	15.22	13.30	11.00	12.24	11.54	11.49
Mg#	0.79	0.79	0.80	0.81	0.80	0.82	0.81

PYROXENE ANALYSIS SHEET

SAMPLE : Porphyritic dacite : PCRPI1 (sheet margin)				SAMPLE Porphyritic dacite - PCRPI2 (sheet interior)			
POINT No.	CPX Phenocrysts		core	POINT No. Phenocrysts		core	Groundmass
	core	core		CPX1	CPX2	CPX3	CPX1
SiO2	48.76	49.02	48.71	48.79	SiO2	49.76	49.83
TiO2	0.41	0.34	0.41	0.41	TiO2	0.32	0.38
Al2O3	0.80	0.72	0.73	0.77	Al2O3	0.76	0.76
Cr2O3	0.04	0.04	0.01	0.01	Cr2O3	0.00	0.00
Fe2O3	2.12	1.74	2.74	1.60	Fe2O3	2.25	2.26
MgO	13.51	14.13	13.93	13.88	MgO	14.19	13.90
CaO	4.62	3.65	3.75	4.09	CaO	3.49	4.18
FeO	28.25	28.90	28.66	28.45	FeO	29.74	29.57
Na2O	0.09	0.03	0.06	0.05	Na2O	0.07	0.05
K2O	0.00	0.01	0.01	0.01	K2O	0.00	0.00
TOTAL	98.62	98.58	99.02	98.07	TOTAL	100.58	100.62
							99.63

FORMULA BASED ON 6 OXYGENS

FORMULA BASED ON 6 OXYGENS				FORMULA BASED ON 6 OXYGENS			
Si	1.94	1.95	1.93	1.95	Si	1.94	1.95
Al	0.04	0.03	0.03	0.04	Al	0.04	0.03
Al	0.00	0.00	0.00	0.00	Al	0.00	0.00
Fe(III)	0.06	0.05	0.08	0.05	Fe(III)	0.07	0.05
Fe(II)	0.94	0.96	0.95	0.95	Fe(II)	0.97	1.00
Ti	0.01	0.01	0.01	0.01	Ti	0.01	0.01
Ca	0.20	0.16	0.16	0.17	Ca	0.15	0.15
Mg	0.80	0.84	0.82	0.83	Mg	0.83	0.81
Cr	0.00	0.00	0.00	0.00	Cr	0.00	0.00
Na	0.01	0.00	0.00	0.00	Na	0.00	0.00
K	0.00	0.00	0.00	0.00	K	0.00	0.00
TOTAL	4.00	4.00	4.00	4.00	TOTAL	4.00	4.00
							4.13

ENDMEMBER %

Wo	10.16	7.96	8.25	8.97	Wo	7.51	8.97
En	41.34	42.85	42.58	42.34	En	42.50	41.50
Fs	48.50	49.19	49.16	48.69	Fs	49.99	49.53
Mg#	0.44	0.45	0.44	0.45	Mg#	0.44	0.44
							0.37

PYROXENE ANALYSIS SHEET

SAMPLE Porphyritic andesite - TPI1

POINT No.	Cpx 1 Core	Cpx1 Rim	Groundmass Pyroxene								
			Cpx 2	Cpx 3	Cpx 4	Cpx 5	Cpx 6	Cpx 7	Cpx 8	Cpx 9	Cpx 10
SiO2	50.79	50.43	51.07	52.46	52.13	52.62	52.80	52.04	53.00	52.08	52.94
TiO2	0.27	0.50	0.41	0.22	0.34	0.17	0.23	0.40	0.13	0.37	0.18
Al2O3	1.35	1.45	1.36	1.67	1.53	1.71	1.59	1.27	1.82	1.40	1.41
Cr2O3	0.08	0.00	0.05	0.17	0.10	0.16	0.16	0.09	0.14	0.13	0.08
Fe2O3	2.37	1.08	2.46	2.03	1.24	1.54	0.33	1.25	1.34	2.11	1.99
MgO	20.21	18.58	20.88	25.48	23.85	25.14	24.74	22.66	25.47	23.14	25.02
CaO	1.84	2.25	2.11	1.45	1.58	1.60	1.45	1.79	1.57	1.71	1.54
MnO	0.59	0.52	0.55	0.37	0.43	0.35	0.39	0.52	0.37	0.45	0.41
FeO	21.77	23.98	20.76	15.20	17.59	15.83	16.71	19.09	15.59	18.57	16.19
Na2O	0.04	0.06	0.04	0.02	0.01	0.00	0.05	0.05	0.02	0.02	0.06
K2O	0.01	0.01	0.01	0.00	0.01	0.01	0.01	0.01	0.01	0.02	0.01
TOTAL	99.32	98.87	99.70	99.07	98.83	99.13	98.48	99.17	99.46	100.00	99.82

FORMULA BASED ON 6 OXYGENS

Si	1.93	1.94	1.92	1.93	1.94	1.93	1.95	1.94	1.94	1.93	1.94
Al	0.06	0.06	0.06	0.07	0.06	0.07	0.05	0.06	0.06	0.06	0.06
Al	0.00	0.00	0.00	0.00	0.01	0.01	0.02	0.00	0.02	0.00	0.00
Fe(iii)	0.07	0.03	0.07	0.06	0.03	0.04	0.01	0.04	0.04	0.06	0.05
Fe(ii)	0.69	0.77	0.65	0.47	0.55	0.49	0.52	0.60	0.48	0.58	0.50
Ti	0.01	0.01	0.01	0.01	0.01	0.00	0.01	0.01	0.00	0.01	0.00
Mn	0.02	0.02	0.02	0.01	0.01	0.01	0.01	0.02	0.01	0.01	0.01
Ca	0.07	0.09	0.09	0.06	0.06	0.06	0.06	0.07	0.06	0.07	0.06
Mg	1.14	1.06	1.17	1.40	1.32	1.38	1.37	1.26	1.39	1.28	1.37
Cr	0.00	0.00	0.00	0.01	0.00	0.00	0.00	0.00	0.00	0.00	0.00
Na	0.00	0.00	0.00	0.00	0.00	0.00	0.00	0.00	0.00	0.00	0.00
K	0.00	0.00	0.00	0.00	0.00	0.00	0.00	0.00	0.00	0.00	0.00
TOTAL	4.00	4.00	4.00	4.00	4.00	4.00	4.00	4.00	4.00	4.00	4.00

ENDMEMBER %

Wo	3.88	4.77	4.41	2.96	3.24	3.25	2.95	3.68	3.17	3.51	3.12
En	59.31	54.77	60.78	72.26	67.94	71.08	69.93	64.83	71.63	66.02	70.60
Fs	36.81	40.46	34.81	24.78	28.82	25.67	27.12	21.48	25.20	30.47	26.28
Mg#	0.60	0.57	0.62	0.73	0.69	0.72	0.72	0.67	0.73	0.67	0.71

PYROXENE ANALYSIS SHEET

SAMPLE Basaltic andesite - KBB3

POINT No.	Glomerocryst OPX				OPX Phenocrysts		core		rim		Groundmass CPX		core		core	
					core	rim	core		core	rim	core	rim	core		core	
SiO2	51.12	50.79	51.05		50.09	51.62	53.73		52.64		53.59	51.69	53.12		52.26	
TiO2	0.33	0.42	0.41		0.36	0.40	0.22		0.36		0.08	0.25	0.19		0.25	
Al2O3	1.48	1.42	1.78		2.44	1.83	1.04		1.46		1.40	1.25	1.73		1.51	
Cr2O3	0.00	0.00	0.01		0.03	0.03	0.14		0.10		0.36	0.04	0.41		0.06	
Fe2O3	2.01	2.01	1.86		2.51	0.95	1.30		1.06		2.21	1.55	1.87		1.64	
MgO	19.70	20.22	20.25		20.42	21.82	24.97		23.21		26.88	22.20	26.26		23.90	
CaO	1.01	0.97	0.92		0.81	1.58	2.52		2.23		3.24	2.77	3.37		2.97	
MnO	0.62	0.68	0.55		0.47	0.42	0.39		0.40		0.35	0.48	0.40		0.48	
FeO	24.31	23.10	23.46		22.13	20.55	16.28		18.49		11.43	18.21	11.82		15.74	
Na2O	0.02	0.01	0.02		0.02	0.04	0.01		0.03		0.07	0.04	0.07		0.01	
K2O	0.00	0.00	0.01		0.02	0.00	0.00		0.00		0.01	0.01	0.01		0.01	
TOTAL	100.60	99.62	100.32		99.31	99.26	100.60		99.98		99.62	98.48	99.25		98.84	

FORMULA BASED ON 6 OXYGENS

Si	1.93	1.93	1.92		1.90	1.94	1.95		1.94		1.94	1.94	1.93		1.94	
Al	0.07	0.06	0.08		0.10	0.06	0.04		0.06		0.06	0.06	0.07		0.06	
Al	0.00	0.00	0.00		0.01	0.02	0.00		0.01		0.00	0.00	0.00		0.00	
Fe(iii)	0.06	0.06	0.05		0.07	0.03	0.04		0.03		0.06	0.04	0.05		0.05	
Fe(ii)	0.77	0.73	0.74		0.70	0.64	0.49		0.57		0.35	0.57	0.36		0.49	
Ti	0.01	0.01	0.01		0.01	0.01	0.01		0.01		0.00	0.01	0.01		0.01	
Mn	0.02	0.02	0.02		0.02	0.01	0.01		0.01		0.01	0.02	0.01		0.02	
Ca	0.04	0.04	0.04		0.03	0.06	0.10		0.09		0.13	0.11	0.13		0.12	
Mg	1.11	1.14	1.14		1.16	1.22	1.35		1.28		1.45	1.24	1.42		1.32	
Cr	0.00	0.00	0.00		0.00	0.00	0.00		0.00		0.01	0.00	0.01		0.00	
Na	0.00	0.00	0.00		0.00	0.00	0.00		0.00		0.00	0.00	0.00		0.00	
K	0.00	0.00	0.00		0.00	0.00	0.00		0.00		0.00	0.00	0.00		0.00	
TOTAL	4.00	4.00	4.00		4.00	4.00	4.00		4.00		4.00	4.00	4.00		4.00	

ENDMEMBER %

Wo	2.11	2.03	1.92		1.73	3.26	5.01		4.53		6.50	5.74	6.82		6.08	
En	57.24	59.01	58.89		60.62	62.84	69.11		65.53		75.04	64.01	73.88		68.01	
Fs	40.64	38.96	39.19		37.65	33.90	25.89		29.94		18.46	30.25	19.30		25.91	
Mg#	0.57	0.59	0.59		0.60	0.65	0.72		0.68		0.78	0.67	0.78		0.71	

MAGNETITE ANALYSIS SHEET

SAMPLE		PMBASE			PM+200			PGB9			ARB1		
POINT No.	Magnt1	Magnt2	Magnt3	Magnt1	Magnt2	Magnt3	Magnt1	Magnt2	Magnt3	Magnt1	Magnt2	Magnt3	
TiO2	16.82	18.02	16.92	18.00	19.09	18.75	15.85	17.25	17.53	19.52	19.93	19.31	
Cr2O3	0.00	0.05	0.03	0.08	0.01	0.03	0.13	0.23	0.06	0.00	0.05	0.05	
Fe2O3	33.19	30.36	32.52	31.68	29.00	29.19	37.01	34.10	33.89	27.68	26.61	27.45	
MnO	2.17	2.49	2.46	1.24	1.38	1.36	1.46	1.95	1.96	2.11	2.11	2.23	
FeO	42.99	43.58	42.61	45.41	45.99	45.49	43.74	44.49	44.81	45.41	45.70	44.85	
TOTAL	95.16	94.51	94.53	96.41	95.47	94.82	98.20	98.02	98.26	94.72	94.39	93.89	
FORMULA BASED ON 32 OXYGENS													
Ti	4.03	4.34	4.08	4.25	4.54	4.50	3.68	4.01	4.06	4.68	4.79	4.67	
Cr	0.00	0.01	0.01	0.02	0.00	0.01	0.03	0.06	0.01	0.00	0.01	0.01	
Fe(iii)	7.95	7.31	7.84	7.48	6.91	7.00	8.60	7.93	7.86	6.64	6.40	6.64	
Mn	0.58	0.68	0.67	0.33	0.37	0.37	0.38	0.51	0.51	0.57	0.57	0.61	
Fe(ii)	11.44	11.66	11.41	11.92	12.17	12.13	11.30	11.50	11.55	12.11	12.22	12.06	
TOTAL	24.00	24.00	24.00	24.00	24.00	24.00	24.00	24.00	24.00	24.00	24.00	24.00	

MAGNETITE ANALYSIS SHEET

SAMPLE Basaltic Andesite - SFB2

POINT No.	Magnt 1	Magnt 2	Magnt 3	Magnt 4	Magnt 5	Magnt 6	Magnt 7
SiO2	0.26	0.22	0.23	0.26	0.19	0.19	0.20
TiO2	24.24	23.65	23.77	22.95	23.68	23.79	24.42
Al2O3	1.38	1.80	1.40	2.00	2.09	1.80	1.33
Cr2O3	0.05	0.04	0.04	0.06	0.04	0.03	0.05
Fe2O3	42.27	42.94	43.16	43.39	43.05	43.36	42.77
MgO	0.00	0.00	0.00	0.00	0.00	0.00	0.00
MnO	6.53	6.02	6.33	5.86	5.79	6.41	6.17
FeO	23.87	24.72	24.31	24.93	25.47	24.69	24.61
ZnO	0.48	0.37	0.43	0.49	0.29	0.31	0.31
TOTAL	98.60	99.38	99.25	99.45	100.31	100.28	99.53

FORMULA BASED ON 32 OXYGENS

Si	0.07	0.06	0.07	0.07	0.05	0.05	0.05
Ti	5.16	5.00	5.04	4.85	4.97	4.99	5.16
Al	0.46	0.60	0.46	0.66	0.69	0.59	0.44
Cr	0.01	0.01	0.01	0.01	0.01	0.01	0.01
Fe(iii)	9.00	9.09	9.16	9.18	9.03	9.11	9.05
Mg	0.00	0.00	0.00	0.00	0.00	0.00	0.00
Mn	1.57	1.43	1.51	1.39	1.37	1.52	1.47
Fe(ii)	5.65	5.81	5.73	5.86	5.94	5.76	5.79
Zn	0.10	0.08	0.09	0.10	0.06	0.06	0.06
TOTAL	22.03	22.09	22.08	22.14	22.12	22.10	22.03

MAGNETITE ANALYSIS SHEET

SAMPLE Basaltic Andesite - RCB1

POINT No.	Mgnt 1	Mgnt 2	Mgnt 3	Mgnt 4	Mgnt 5	Mgnt 6	Mgnt 6
SiO2	0.21	0.74	0.24	0.17	0.23	0.26	0.18
TiO2	22.25	21.34	21.77	22.25	21.83	23.42	21.97
Al2O3	1.76	1.90	1.68	2.10	1.32	1.26	1.94
Cr2O3	0.05	0.08	0.07	0.06	0.06	0.00	0.07
Fe2O3	44.70	44.03	45.39	44.47	45.50	44.34	44.68
MgO	0.04	0.07	0.00	0.00	0.00	0.00	0.01
MnO	0.93	0.84	0.88	0.84	0.94	1.00	1.00
FeO	30.16	29.86	30.49	30.63	30.78	30.33	30.01
ZnO	0.27	0.35	0.11	0.00	0.12	0.03	0.19
TOTAL	100.09	98.86	100.52	100.52	100.66	100.61	99.86

FORMULA BASED ON 32 OXYGENS

Si	0.06	0.21	0.07	0.05	0.06	0.07	0.05
Ti	4.71	4.55	4.60	4.69	4.62	4.93	4.66
Al	0.58	0.64	0.56	0.69	0.44	0.42	0.65
Cr	0.01	0.02	0.01	0.01	0.01	0.00	0.02
Fe(iii)	9.46	9.40	9.60	9.38	9.64	9.34	9.48
Mg	0.02	0.03	0.00	0.00	0.00	0.00	0.01
Mn	0.22	0.20	0.21	0.20	0.23	0.24	0.24
Fe(ii)	7.09	7.08	7.17	7.18	7.25	7.10	7.08
Zn	0.06	0.07	0.02	0.00	0.02	0.01	0.04
TOTAL	22.21	22.21	22.24	22.21	22.27	22.11	22.22

MAGNETITE ANALYSIS SHEET

SAMPLE	PCRPI1	KBB5				KBB3			
POINT No.	Magnt1	Magnt2	Magn Phen 2		Magn Phen 3		Gmass Mag1	Gmass Mag2	
TiO2	17.25	21.09	14.69	15.19	15.27	17.46	16.82		
Cr2O3	0.22	0.02	0.00	0.08	0.00	0.03	0.03		
Fe2O3	48.41	22.13	38.90	36.73	37.36	34.28	33.64		
MnO	0.36	0.78	0.38	0.37	0.42	0.40	0.40		
FeO	29.28	47.10	43.54	43.50	43.84	46.42	44.87		
TOTAL	95.53	91.11	97.51	95.87	96.89	98.59	95.75		
FORMULA BASED ON 32 OXYGENS									
Ti	3.93	5.25	3.44	3.62	3.60	4.03	4.00		
Cr	0.05	0.01	0.00	0.02	0.00	0.01	0.01		
Fe(iii)	11.03	5.51	9.12	8.75	8.81	7.92	8.01		
Mn	0.09	0.22	0.10	0.10	0.11	0.11	0.11		
Fe(ii)	7.42	13.02	11.34	11.52	11.48	11.93	11.87		
TOTAL	22.53	24.00	24.00	24.00	24.00	24.00	23.99		

OLIVINE ANALYSIS SHEET

SAMPLE Cognate Xenolith - KBGX1 (Feldspathic Peridotite) - Cumulus Olivine

POINT No.	Olivine 1	Olivine 2	Olivine 3	Olivine 3 Core	Olivine 3 Rim	Olivine 4	Olivine 5	Olivine 6	Olivine 7	Olivine 8	Olivine 9	Olivine 10	Olivine 11	Olivine 12
SiO2	39.43	39.61	39.82	39.35	39.35	39.35	39.22	39.58	39.41	39.54	39.44	39.12	39.47	39.33
TiO2	0.03	0.08	0.07	0.00	0.00	0.00	0.12	0.00	0.00	0.04	0.02	0.07	0.00	0.03
Al2O3	0.05	0.02	0.08	0.02	0.02	0.03	0.05	0.04	0.04	0.03	0.07	0.04	0.02	0.08
Cr2O3	0.03	0.04	0.09	0.03	0.03	0.05	0.01	0.03	0.03	0.07	0.05	0.01	0.07	0.04
MgO	44.40	44.38	43.92	44.57	44.38	44.12	44.90	44.68	44.49	44.63	44.12	44.52	44.73	44.43
CaO	0.26	0.26	0.27	0.29	0.29	0.28	0.27	0.21	0.28	0.30	0.29	0.28	0.28	0.25
MnO	0.18	0.24	0.22	0.23	0.24	0.23	0.21	0.26	0.26	0.23	0.25	0.25	0.21	0.21
FeO	15.71	15.70	16.13	14.82	14.71	14.29	14.48	14.62	14.25	14.82	14.49	14.79	15.04	14.73
NiO	0.09	0.25	0.21	0.18	0.19	0.17	0.16	0.07	0.15	0.23	0.12	0.15	0.20	0.25
TOTAL	100.18	100.58	100.81	99.57	99.19	98.52	99.43	99.50	98.90	99.88	98.84	99.23	100.02	99.36

FORMULA BASED ON 4 OXYGENS

Si	0.99	0.99	1.00	0.99	1.00	1.00	0.99	1.00	1.00	1.00	1.00	0.99	0.99	1.00
Ti	0.00	0.00	0.00	0.00	0.00	0.00	0.00	0.00	0.00	0.00	0.00	0.00	0.00	0.00
Al	0.00	0.00	0.00	0.00	0.00	0.00	0.00	0.00	0.00	0.00	0.00	0.00	0.00	0.00
Cr	0.00	0.00	0.00	0.00	0.00	0.00	0.00	0.00	0.00	0.00	0.00	0.00	0.00	0.00
Mg	1.67	1.66	1.64	1.68	1.68	1.67	1.69	1.68	1.68	1.67	1.67	1.68	1.68	1.68
Ca	0.01	0.01	0.01	0.01	0.01	0.01	0.01	0.01	0.01	0.01	0.01	0.01	0.01	0.01
Mn	0.00	0.01	0.00	0.00	0.01	0.01	0.00	0.01	0.01	0.00	0.01	0.01	0.00	0.00
Fe(ii)	0.33	0.33	0.34	0.31	0.31	0.30	0.31	0.31	0.30	0.31	0.31	0.31	0.32	0.31
Ni	0.00	0.00	0.00	0.00	0.00	0.00	0.00	0.00	0.00	0.00	0.00	0.00	0.00	0.01
TOTAL	3.01	3.00	3.00	3.00	3.00	3.00	3.01	3.00	3.00	3.00	3.00	3.01	3.01	3.00

ENDMEMBER %

Fo	83.15	83.15	82.63	83.95	83.99	84.30	84.37	84.24	84.45	83.96	84.11	83.97	83.82	84.03
Fa	16.51	16.50	17.01	15.66	15.61	15.32	15.26	15.47	15.18	15.64	15.49	15.65	15.80	15.63
Mo	0.34	0.35	0.36	0.39	0.40	0.38	0.37	0.29	0.38	0.40	0.40	0.39	0.37	0.34

FELDSPAR ANALYSIS SHEET

SAMPLE RCGX1 - Gabbroic xenolith in hybrid rhyolite

SAMPLE KIFX1 - Cumulate plagioclase in anorthosite

POINT No.	Plag1	Plag2	Plag3	Plag4	Plag5	POINT No.	Plag1	Plag2	Plag3	Plag4	Plag5
SiO2	44.34	44.66	43.22	45.89	45.37	SiO2	50.28	49.04	47.79	46.95	47.04
TiO2	0.09	0.04	0.06	0.02	0.00	TiO2	0.07	0.05	0.09	0.09	0.05
Al2O3	36.40	35.13	36.45	34.97	35.30	Al2O3	30.51	31.78	32.30	32.80	33.00
FeO*	0.72	0.66	0.69	0.68	0.66	FeO*	0.49	0.49	0.62	0.58	0.43
CaO	17.48	16.37	17.12	15.97	16.46	CaO	15.07	16.15	16.83	17.49	17.39
Na2O	1.42	2.05	1.69	2.30	2.02	Na2O	3.06	2.27	1.87	1.64	1.59
K2O	0.08	0.13	0.09	0.14	0.13	K2O	0.20	0.13	0.09	0.10	0.12
TOTAL	100.53	99.04	99.32	99.98	99.93	TOTAL	99.68	99.92	99.59	99.65	99.62

FORMULA BASED ON 32 OXYGENS

Si	8.16	8.33	8.06	8.46	8.37	Si	9.23	9.00	8.83	8.69	8.70
Ti	0.01	0.01	0.01	0.00	0.00	Ti	0.01	0.01	0.01	0.01	0.01
Al	7.89	7.72	8.01	7.59	7.68	Al	6.60	6.87	7.03	7.15	7.19
Fe (ii)	0.11	0.10	0.11	0.11	0.10	Fe (ii)	0.07	0.07	0.10	0.09	0.07
Ca	3.44	3.27	3.42	3.15	3.26	Ca	2.97	3.18	3.33	3.47	3.44
Na	0.51	0.74	0.61	0.82	0.72	Na	1.09	0.81	0.67	0.59	0.57
K	0.02	0.03	0.02	0.03	0.03	K	0.05	0.03	0.02	0.02	0.03
TOTAL	20.14	20.19	20.24	20.17	20.16	TOTAL	20.02	19.97	19.99	20.03	20.00

ENDMEMBER %

Ab	12.74	18.32	15.11	20.51	18.01	Ab	26.56	20.15	16.66	14.40	14.13
Or	0.48	0.75	0.53	0.82	0.75	Or	1.12	0.75	0.54	0.59	0.70
An	86.78	80.93	84.35	78.67	81.24	An	72.32	79.10	82.80	85.01	85.18

FELDSPAR ANALYSIS SHEET

SAMPLE Gabbroic Cognate Xenolith - KBGX1

POINT No.	Cumulus Plagioclase									
	Plag1	Plag2	Plag3	Plag4	Plag5	Plag6	Plag7	Plag8	Plag9	Plag10
SiO2	47.07	47.19	47.49	47.22	47.22	47.08	47.13	47.38	47.23	47.02
TiO2	0.00	0.00	0.01	0.00	0.03	0.00	0.01	0.04	0.02	0.02
Al2O3	32.61	32.16	32.18	32.21	32.32	32.62	32.15	32.26	32.26	32.38
FeO*	0.42	0.49	0.43	0.43	0.39	0.47	0.50	0.49	0.43	0.45
CaO	17.42	16.92	16.91	17.13	17.17	17.08	17.01	17.19	17.19	17.29
Na2O	1.72	1.89	2.03	1.89	1.80	1.74	1.83	1.84	1.83	1.87
K2O	0.08	0.06	0.08	0.08	0.07	0.09	0.06	0.08	0.06	0.06
TOTAL	99.31	98.72	99.12	98.97	98.99	99.09	98.69	99.29	99.01	99.08

FORMULA BASED ON 32 OXYGENS

Si	8.73	8.80	8.82	8.79	8.78	8.75	8.79	8.79	8.78	8.74
Ti	0.00	0.00	0.00	0.00	0.00	0.00	0.00	0.00	0.00	0.00
Al	7.13	7.06	7.04	7.06	7.08	7.14	7.07	7.05	7.07	7.10
Fe (ii)	0.06	0.08	0.07	0.07	0.06	0.07	0.08	0.08	0.07	0.07
Ca	3.46	3.38	3.36	3.42	3.42	3.40	3.40	3.42	3.43	3.45
Na	0.62	0.68	0.73	0.68	0.65	0.63	0.66	0.66	0.66	0.67
K	0.02	0.02	0.02	0.02	0.02	0.02	0.02	0.02	0.01	0.01
TOTAL	20.02	20.02	20.04	20.03	20.01	20.01	20.01	20.02	20.02	20.05

ENDMEMBER %

Ab	15.06	16.74	17.76	16.57	15.89	15.49	16.26	16.17	16.06	16.29
Or	0.45	0.38	0.45	0.48	0.40	0.55	0.37	0.49	0.34	0.35
An	84.49	82.88	81.79	82.95	83.71	83.97	83.37	83.34	83.60	83.36

FELDSPAR ANALYSIS SHEET

SAMPLE Gabbroic Cognate Xenolith - KBHYX1

POINT No.	Cumulate Plagioclase			Fine-grained	
	Plag 1	Plag 2 Core	Plag 2 Rim	Plag 3	Plag 1 Core Plag 2 Rim
SiO2	45.55	46.36	49.84	45.47	52.57 53.90
TiO2	0.05	0.03	0.00	0.02	0.05 0.03
Al2O3	35.02	34.01	31.74	35.36	29.71 28.79
FeO*	0.52	0.50	0.82	0.53	0.93 1.28
CaO	17.44	16.56	13.81	17.59	11.84 10.53
Na2O	1.65	2.16	3.57	1.62	4.74 5.22
K2O	0.07	0.06	0.14	0.06	0.29 0.41
TOTAL	100.28	99.68	99.91	100.64	100.14 100.16

FORMULA BASED ON 32 OXYGENS

Si	8.38	8.57	9.12	8.34	9.56 9.78
Ti	0.01	0.00	0.00	0.00	0.01 0.00
Al	7.60	7.41	6.85	7.65	6.37 6.15
Fe (ii)	0.08	0.08	0.13	0.08	0.14 0.19
Ca	3.44	3.28	2.71	3.46	2.31 2.05
Na	0.59	0.78	1.27	0.58	1.67 1.84
K	0.02	0.01	0.03	0.01	0.07 0.09
TOTAL	20.11	20.12	20.10	20.12	20.12 20.11

ENDMEMBER %

Ab	14.59	19.07	31.59	14.24	41.32 46.18
Or	0.40	0.34	0.79	0.34	1.69 2.38
An	85.01	80.59	67.62	85.43	57.00 51.44

FELDSPAR ANALYSIS SHEET

SAMPLE Gabbroic Cognate Xenolith - KBHYX1

CUMULUS PLAGIOCLASE 13 POINT SCAN

POINT No.	rim	pnt1	pnt2	pnt3	pnt4	pnt5	pnt6	pnt7	pnt8	pnt9	pnt10	pnt11	pnt12	core
SiO2	52.07	51.76	51.45	51.17	51.30	50.75	50.33	49.74	48.02	47.52	47.35	47.31	46.60	46.10
TiO2	0.05	0.06	0.02	0.02	0.05	0.05	0.00	0.04	0.04	0.06	0.06	0.03	0.02	0.00
Al2O3	29.16	29.24	29.48	29.68	29.62	29.81	30.38	30.77	31.87	32.14	32.58	32.38	32.91	33.36
FeO*	0.79	0.76	0.67	0.72	0.63	0.68	0.57	0.57	0.53	0.47	0.70	0.54	0.55	0.45
CaO	13.57	13.63	14.08	14.03	13.98	14.27	14.80	15.27	16.53	16.97	16.98	17.25	17.65	18.27
Na2O	3.92	3.75	3.64	3.56	3.60	3.20	3.11	3.00	2.11	1.98	1.80	1.85	1.64	1.36
K2O	0.17	0.15	0.18	0.18	0.17	0.13	0.12	0.11	0.06	0.08	0.07	0.07	0.05	0.03
TOTAL	99.73	99.35	99.53	99.36	99.33	98.90	99.30	99.51	99.16	99.24	99.55	99.42	99.42	99.57

FORMULA BASED ON 32 OXYGENS

Si	9.53	9.50	9.44	9.41	9.43	9.37	9.27	9.16	8.90	8.82	8.76	8.77	8.65	8.55
Ti	0.01	0.01	0.00	0.00	0.01	0.01	0.00	0.00	0.01	0.01	0.01	0.00	0.00	0.00
Al	6.29	6.33	6.38	6.43	6.41	6.49	6.59	6.68	6.96	7.03	7.10	7.07	7.20	7.29
Fe (ii)	0.12	0.12	0.10	0.11	0.10	0.11	0.09	0.09	0.08	0.07	0.11	0.08	0.09	0.07
Ca	2.66	2.68	2.77	2.76	2.75	2.82	2.92	3.01	3.28	3.37	3.37	3.42	3.51	3.63
Na	1.39	1.34	1.29	1.27	1.28	1.15	1.11	1.07	0.76	0.71	0.65	0.66	0.59	0.49
K	0.04	0.04	0.04	0.04	0.04	0.03	0.03	0.03	0.01	0.02	0.02	0.02	0.01	0.01
TOTAL	20.04	20.01	20.03	20.03	20.02	19.97	20.01	20.04	20.00	20.03	20.01	20.03	20.05	20.05
ENDMEMBER %														
Ab	34.00	32.96	31.51	31.11	31.47	28.66	27.37	26.05	18.68	17.36	16.03	16.18	14.33	11.85
Or	0.99	0.87	1.04	1.04	0.96	0.75	0.68	0.65	0.36	0.48	0.41	0.38	0.26	0.18
An	65.01	66.17	67.45	67.85	67.57	70.59	71.95	73.30	80.95	82.16	83.57	83.43	85.41	87.97

PYROXENE ANALYSIS SHEET

SAMPLE Gabbroic Cognate Xenolith - KBGX1

POINT No.	Interstitial Polkilitic Pyroxene				Fine Grained CPX5
	CPX1	CPX2	CPX3	CPX4 CORE	CPX4 RIM
SiO2	51.35	51.29	51.39	51.90	51.92
TiO2	0.39	0.42	0.53	0.55	0.41
Al2O3	3.47	3.81	3.40	3.05	2.97
Cr2O3	0.58	0.60	0.95	0.43	0.91
Fe2O3	0.38	1.80	0.35	0.65	0.49
MgO	16.35	16.33	16.19	16.86	17.08
CaO	20.00	21.37	20.72	19.94	19.92
FeO	5.75	4.04	5.15	5.64	5.20
Na2O	0.26	0.25	0.30	0.27	0.28
K2O	0.01	0.00	0.00	0.02	0.01
TOTAL	98.55	99.92	98.98	99.31	99.18

FORMULA BASED ON 6 OXYGENS

Si	1.91	1.88	1.90	1.91	1.91
Al	0.09	0.12	0.10	0.09	0.09
Al	0.06	0.05	0.05	0.05	0.04
Fe(iii)	0.01	0.05	0.01	0.02	0.01
Fe(ii)	0.18	0.12	0.16	0.17	0.16
Ti	0.01	0.01	0.01	0.02	0.01
Ca	0.80	0.84	0.82	0.79	0.79
Mg	0.91	0.89	0.89	0.93	0.94
Cr	0.02	0.02	0.03	0.01	0.03
Na	0.02	0.02	0.02	0.02	0.02
K	0.00	0.00	0.00	0.00	0.00
TOTAL	4.00	4.00	4.00	4.00	4.00

ENDMEMBER %

Wo	42.34	45.24	43.85	41.72	41.73
En	48.16	48.09	47.65	49.06	49.77
Fs	9.50	6.68	8.51	9.22	8.50
Mg#	0.83	0.84	0.84	0.83	0.84
					0.76

PYROXENE ANALYSIS SHEET

SAMPLE Gabbroic Cognate Xenolith - KBGX1

POINT No.	Interstitial Poikilitic Pyroxene											
	CPX 6	CPX 7	CPX 8	CPX 9	CPX 10	CPX 11	CPX 12	CPX 13	CPX 14	CPX 15	CPX 16	CPX 17
SiO2	51.99	52.23	51.46	51.45	51.17	51.65	51.42	51.27	51.47	51.11	51.51	51.44
TiO2	0.39	0.45	0.62	0.39	0.51	0.49	0.38	0.48	0.51	0.51	0.57	0.51
Al2O3	2.48	2.58	3.46	3.28	3.34	3.25	3.22	3.23	3.22	3.19	3.21	3.13
Cr2O3	0.94	1.05	0.53	0.49	0.54	0.52	0.58	0.59	0.59	0.54	0.69	0.69
Fe2O3	0.84	0.00	1.15	1.29	1.40	0.88	1.38	1.77	1.42	2.07	0.48	0.66
MgO	17.28	17.31	16.30	16.24	16.58	16.60	16.53	16.62	16.65	16.52	16.31	16.37
CaO	20.36	20.08	21.20	21.23	20.55	20.20	20.55	20.70	20.40	20.98	20.73	20.84
MnO	0.17	0.08	0.12	0.09	0.12	0.10	0.12	0.17	0.22	0.14	0.10	0.13
FeO	4.27	4.92	4.55	4.50	4.49	5.41	4.67	4.17	4.57	4.01	5.24	4.75
Na2O	0.26	0.26	0.25	0.25	0.25	0.26	0.26	0.27	0.29	0.23	0.25	0.26
K2O	0.00	0.00	0.00	0.00	0.00	0.00	0.01	0.00	0.01	0.01	0.00	0.01
TOTAL	98.97	98.95	99.63	99.21	98.93	99.38	99.12	99.27	99.37	99.32	99.09	98.77

FORMULA BASED ON 6 OXYGENS

Si	1.92	1.93	1.89	1.90	1.89	1.91	1.90	1.89	1.90	1.89	1.91	1.91
Al	0.08	0.07	0.11	0.10	0.11	0.09	0.10	0.11	0.10	0.11	0.09	0.09
Al	0.03	0.04	0.04	0.04	0.04	0.05	0.04	0.03	0.04	0.03	0.05	0.04
Fe(III)	0.02	0.00	0.03	0.04	0.04	0.02	0.04	0.05	0.04	0.06	0.01	0.02
Fe(II)	0.13	0.15	0.14	0.14	0.14	0.17	0.14	0.13	0.14	0.12	0.16	0.15
Ti	0.01	0.01	0.02	0.01	0.01	0.01	0.01	0.01	0.01	0.01	0.02	0.01
Mn	0.01	0.00	0.00	0.00	0.00	0.00	0.00	0.01	0.01	0.00	0.00	0.00
Ca	0.81	0.79	0.84	0.84	0.82	0.80	0.81	0.82	0.81	0.83	0.82	0.83
Mg	0.95	0.95	0.89	0.89	0.92	0.91	0.91	0.92	0.92	0.91	0.90	0.90
Cr	0.03	0.03	0.02	0.01	0.02	0.02	0.02	0.02	0.02	0.02	0.02	0.02
Na	0.02	0.02	0.02	0.02	0.02	0.02	0.02	0.02	0.02	0.02	0.02	0.02
K	0.00	0.00	0.00	0.00	0.00	0.00	0.00	0.00	0.00	0.00	0.00	0.00
TOTAL	4.00	4.00	4.00	4.00	4.00	4.00	4.00	4.00	4.00	4.00	4.00	4.00

ENDMEMBER %

Wo	42.02	41.77	44.60	44.78	43.51	42.44	43.45	43.83	43.12	44.44	43.56	43.94
En	49.62	50.11	47.72	47.66	48.87	48.52	48.64	48.99	48.97	48.70	47.69	48.03
Fs	8.36	8.12	7.68	7.57	7.62	9.04	7.91	7.18	7.91	6.86	8.76	8.03
Mg#	0.86	0.86	0.84	0.84	0.84	0.83	0.83	0.84	0.84	0.83	0.84	0.85

PYROXENE ANALYSIS SHEET

SAMPLE Gabbroic Cognate Xenolith KBGX2

POINT No.	CORE	CUMMULATE CLINOPYROXENE - 9 POINT SCAN							
		PNT2	PNT3	PNT4	PNT5	PNT6	PNT7	PNT8	RIM
SiO2	49.53	50.16	51.49	52.44	50.74	51.45	50.16	49.46	49.16
TiO2	0.66	0.60	0.54	0.27	0.43	0.46	0.53	0.75	0.72
Al2O3	4.31	4.16	3.33	2.25	4.82	2.81	2.21	1.92	1.76
Cr2O3	0.00	0.00	0.04	0.01	0.03	0.01	0.01	0.04	0.01
Fe2O3	3.12	2.43	1.02	1.32	1.76	2.37	3.39	2.62	2.60
MgO	13.66	13.84	14.85	16.77	15.79	16.80	14.07	12.33	10.34
CaO	22.98	23.06	22.22	20.71	20.48	17.34	16.98	16.40	16.60
FeO	4.87	4.86	5.69	5.47	5.53	8.70	12.17	15.49	18.21
Na2O	0.25	0.31	0.31	0.23	0.25	0.23	0.31	0.27	0.30
K2O	0.00	0.00	0.00	0.00	0.00	0.00	0.01	0.02	0.04
TOTAL	99.40	99.43	99.49	99.46	99.83	100.18	99.85	99.32	99.73

FORMULA BASED ON 6 OXYGENS

Si	1.85	1.87	1.91	1.93	1.87	1.90	1.90	1.91	1.91
Al	0.15	0.13	0.09	0.07	0.13	0.10	0.10	0.09	0.08
Al	0.04	0.05	0.05	0.03	0.08	0.02	0.00	0.00	0.00
Fe(iii)	0.09	0.07	0.03	0.04	0.05	0.07	0.10	0.08	0.08
Fe(ii)	0.15	0.15	0.18	0.17	0.17	0.27	0.39	0.50	0.59
Ti	0.02	0.02	0.02	0.01	0.01	0.01	0.02	0.02	0.02
Ca	0.92	0.92	0.88	0.82	0.81	0.69	0.69	0.68	0.69
Mg	0.76	0.77	0.82	0.92	0.87	0.93	0.79	0.71	0.60
Cr	0.00	0.00	0.00	0.00	0.00	0.00	0.00	0.00	0.00
Na	0.02	0.02	0.02	0.02	0.02	0.02	0.02	0.02	0.02
K	0.00	0.00	0.00	0.00	0.00	0.00	0.00	0.00	0.01
TOTAL	4.00	4.00	4.00	4.00	4.00	4.00	4.00	4.00	4.00

ENDMEMBER %

Wo	50.20	50.01	46.96	42.87	43.80	36.50	36.88	35.93	36.72
En	41.51	41.76	43.65	48.29	46.98	49.20	42.49	37.58	31.83
Fs	8.29	8.23	9.39	8.84	9.23	14.30	20.63	26.49	31.44
Mg#	0.76	0.78	0.80	0.82	0.80	0.73	0.62	0.55	0.47

PYROXENE ANALYSIS SHEET

SAMPLE Gabbroic Cognate Xenolith KBGX2

POINT No.	CORE	CUMMULATE CLINOPYROXENE - 13 POINT SCAN											
		PNT 2	PNT 3	PNT 4	PNT 5	PNT 6	PNT 7	PNT 8	PNT 9	PNT 10	PNT 11	PNT 12	RIM
SiO2	52.30	53.21	52.49	52.89	52.51	53.16	53.36	53.24	53.24	51.44	52.09	51.94	50.07
TiO2	0.40	0.53	0.46	0.32	0.41	0.24	0.35	0.31	0.46	0.41	0.62	0.56	0.81
Al2O3	2.35	2.61	2.59	2.36	2.36	2.17	2.17	2.17	2.14	3.90	2.99	2.61	2.12
Cr2O3	0.01	0.00	0.00	0.01	0.00	0.02	0.04	0.09	0.08	0.13	0.01	0.04	0.03
Fe2O3	1.31	0.29	0.87	0.32	0.75	1.00	0.00	0.79	0.49	1.18	1.06	0.98	2.35
MgO	16.45	16.26	16.35	16.38	16.41	16.77	16.66	16.96	17.05	16.15	16.22	15.97	13.15
CaO	21.46	20.77	20.89	20.82	20.98	21.09	20.72	20.91	20.90	20.48	19.35	18.82	17.70
MnO	0.20	0.20	0.18	0.18	0.14	0.13	0.14	0.17	0.13	0.15	0.18	0.27	0.27
FeO	4.98	6.29	6.07	6.46	5.83	5.59	6.57	5.69	5.74	5.54	7.59	8.62	12.89
Na2O	0.20	0.42	0.22	0.21	0.23	0.25	0.24	0.23	0.22	0.25	0.29	0.25	0.28
K2O	0.00	0.03	0.00	0.01	0.00	0.00	0.01	0.00	0.01	0.00	0.01	0.00	0.01
TOTAL	99.67	100.61	100.12	99.97	99.62	100.42	100.25	100.56	100.44	99.63	100.40	100.03	99.69

FORMULA BASED ON 6 OXYGENS

Si	1.93	1.94	1.93	1.94	1.94	1.94	1.95	1.94	1.94	1.89	1.91	1.92	1.91
Al	0.07	0.06	0.07	0.06	0.06	0.06	0.05	0.06	0.06	0.11	0.09	0.08	0.09
Al	0.03	0.05	0.04	0.05	0.04	0.03	0.05	0.03	0.03	0.06	0.04	0.04	0.00
Fe(iii)	0.04	0.01	0.02	0.01	0.02	0.03	0.00	0.02	0.01	0.03	0.03	0.03	0.07
Fe(ii)	0.15	0.19	0.19	0.20	0.18	0.17	0.20	0.17	0.17	0.17	0.23	0.27	0.41
Ti	0.01	0.01	0.01	0.01	0.01	0.01	0.01	0.01	0.01	0.01	0.02	0.02	0.02
Mn	0.01	0.01	0.01	0.01	0.00	0.00	0.00	0.01	0.00	0.00	0.01	0.01	0.01
Ca	0.85	0.81	0.82	0.82	0.83	0.83	0.81	0.82	0.82	0.81	0.76	0.75	0.72
Mg	0.90	0.88	0.89	0.90	0.90	0.91	0.91	0.92	0.93	0.89	0.89	0.88	0.75
Cr	0.00	0.00	0.00	0.00	0.00	0.00	0.00	0.00	0.00	0.00	0.00	0.00	0.00
Na	0.01	0.03	0.02	0.02	0.02	0.02	0.02	0.02	0.02	0.02	0.02	0.02	0.02
K	0.00	0.00	0.00	0.00	0.00	0.00	0.00	0.00	0.00	0.00	0.00	0.00	0.00
TOTAL	4.00	4.00	4.00	4.00	4.00	4.00	4.00	4.00	4.00	4.00	4.00	4.00	4.00

ENDMEMBER %

Wo	44.34	42.86	43.06	42.66	43.27	43.13	42.16	42.61	42.47	43.21	40.32	39.23	38.24
En	47.30	46.68	46.89	46.71	47.11	47.72	47.18	48.07	48.22	47.41	47.03	46.31	39.55
Fs	8.36	10.47	10.05	10.62	9.62	9.14	10.66	9.32	9.31	9.38	12.65	14.46	22.21
Mg#	0.83	0.82	0.81	0.81	0.82	0.82	0.82	0.83	0.83	0.81	0.77	0.75	0.61

PYROXENE ANALYSIS SHEET

SAMPLE Gabbroic Cognate Xenolith - KBHYX1

POINT No.	Cumulative			Interstitial		Fine Grained		
	CPX1	CPX2	CPX3	CPX1	CPX2	CPX3	CPX1	CPX2
SiO2	52.35	52.26	52.46	52.24	52.58	52.54	50.15	49.95
TiO2	0.28	0.39	0.27	0.31	0.25	0.33	0.85	0.90
Al2O3	2.19	2.27	2.19	2.22	2.24	2.17	3.06	3.94
Cr2O3	0.06	0.10	0.01	0.08	0.04	0.06	0.03	0.00
Fe2O3	1.35	1.29	1.27	1.30	1.29	1.86	2.12	1.80
MgO	16.32	16.32	16.56	15.83	16.37	16.55	13.65	14.32
CaO	21.80	21.60	21.08	21.70	21.44	21.65	17.63	19.44
FeO	4.95	5.13	5.34	5.53	5.35	4.98	12.35	9.11
Na2O	0.19	0.19	0.22	0.26	0.24	0.19	0.30	0.21
K2O	0.01	0.02	0.03	0.00	0.00	0.01	0.03	0.00
TOTAL	99.49	99.56	99.43	99.48	99.80	100.35	100.17	99.68

FORMULA BASED ON 6 OXYGENS

[illegible]

ENDMEMBER %

	W ₀	45.08	44.72	43.65	45.17	44.31	44.58	38.11	41.83
En		46.94	46.99	47.71	45.83	47.06	47.42	41.05	42.86
Fs		7.98	8.30	8.63	8.99	8.63	8.00	20.84	15.31
Mg#		0.83	0.82	0.82	0.81	0.82	0.82	0.63	0.70

SPINEL ANALYSIS SHEET

SAMPLE KBGX1 - Feldspathic Peridotite - Cr-Spinel inclusions in cumulus olivine and plagioclase

POINT No.	Cr-Spinel 1	Cr-Spinel 2	Cr-Spinel 3	Cr-Spinel 4	Cr-Spinel 5	Cr-Spinel 6	Cr-Spinel 7	Cr-Spinel 8
SiO2	0.08	0.07	0.11	0.04	0.07	0.09	0.05	0.06
TiO2	1.35	1.28	1.14	0.78	1.23	0.89	1.23	1.60
Al2O3	18.40	17.24	18.03	25.49	17.68	24.10	16.52	18.52
Cr2O3	40.81	41.95	40.13	34.33	40.59	34.09	40.18	39.43
Fe2O3	9.77	9.64	10.49	8.93	9.99	10.21	9.33	10.29
MgO	11.25	11.23	10.72	12.74	11.17	12.41	6.01	10.96
FeO	17.48	17.15	18.08	16.02	17.06	16.27	24.93	17.77
TOTAL	99.14	98.57	98.71	98.35	97.79	98.06	98.24	98.63

FORMULA BASED ON 32 OXYGENS

Si	0.02	0.02	0.03	0.01	0.02	0.02	0.01	0.02
Ti	0.26	0.25	0.22	0.15	0.24	0.17	0.25	0.31
Al	5.50	5.21	5.44	7.40	5.37	7.06	5.20	5.57
Cr	8.19	8.50	8.13	6.69	8.27	6.70	8.49	7.95
Fe(iii)	1.87	1.86	2.02	1.66	1.94	1.91	1.88	1.97
Mg	4.26	4.29	4.10	4.68	4.29	4.60	2.39	4.17
Fe(ii)	3.71	3.68	3.87	3.30	3.68	3.38	5.57	3.79
TOTAL	23.80	23.80	23.81	23.89	23.81	23.83	23.80	23.78
Fe/Fe+Mg	0.47	0.46	0.49	0.41	0.46	0.42	0.70	0.48
Cr/Cr+Al	0.60	0.62	0.60	0.47	0.61	0.49	0.62	0.59

SPINEL ANALYSIS SHEET

SAMPLE KBGX1 - Feldspathic Peridotite - Cr-Spinel inclusions in cumulus olivine and plagioclase

POINT No.	Cr-Spinel 9	Cr-Spinel 10	Cr-Spinel 11	Cr-Spinel 12	Cr-Spinel 13	Cr-Spinel 14	Cr-Spinel 15	Cr-Spinel 16
SiO2	0.11	0.07	0.10	0.09	0.13	0.07	0.08	0.10
TiO2	1.32	1.34	1.35	1.35	1.34	1.36	1.66	1.70
Al2O3	17.29	16.72	17.14	17.37	17.87	17.40	18.21	18.51
Cr2O3	41.75	42.11	41.67	42.00	40.17	41.74	40.61	39.68
Fe2O3	9.96	10.20	9.90	9.58	10.21	9.57	9.92	10.30
MgO	11.25	10.76	9.21	10.39	9.96	10.41	11.03	10.75
FeO	17.00	17.74	20.48	18.56	19.10	18.40	17.63	18.10
TOTAL	98.69	98.94	99.85	99.34	98.78	98.95	99.13	99.15

FORMULA BASED ON 32 OXYGENS

Si	0.03	0.02	0.03	0.02	0.03	0.02	0.02	0.03
Ti	0.26	0.26	0.26	0.26	0.26	0.26	0.32	0.33
Al	5.24	5.08	5.22	5.26	5.44	5.29	5.48	5.57
Cr	8.48	8.59	8.50	8.53	8.20	8.51	8.19	8.01
Fe(iii)	1.93	1.98	1.92	1.85	1.99	1.86	1.90	1.98
Mg	4.31	4.14	3.54	3.98	3.84	4.00	4.20	4.09
Fe(ii)	3.65	3.83	4.42	3.99	4.13	3.97	3.76	3.86
TOTAL	23.89	23.90	23.89	23.89	23.89	23.90	23.87	23.87
Fe/Fe+Mg	0.46	0.48	0.55	0.50	0.52	0.50	0.47	0.49
Cr/Cr+Al	0.62	0.63	0.62	0.62	0.60	0.62	0.60	0.59

MULLITE ANALYSIS SHEET

SAMPLE KIFX2 - Buchite Core to zoned xenolith

POINT No.	1	2	3	4	5	6	7	8	9	10
SiO2	27.78	28.47	27.45	28.05	28.08	27.44	28.30	27.98	28.73	28.04
TiO2	1.19	1.22	1.41	1.35	1.31	1.44	1.15	1.35	1.32	1.34
Al2O3	69.68	69.34	69.79	69.00	69.56	69.80	69.14	69.89	68.86	69.83
FeO	0.30	0.36	0.33	0.35	0.34	0.41	0.37	0.47	0.39	0.26
MgO	0.39	0.43	0.36	0.40	0.39	0.41	0.40	0.40	0.37	0.40
CaO	0.03	0.11	0.05	0.01	0.03	0.03	0.06	0.04	0.02	0.10
Na2O	0.27	0.26	0.33	0.31	0.26	0.31	0.28	0.31	0.30	0.30
TOTAL	99.64	100.18	99.71	99.46	99.98	99.84	99.69	100.43	99.99	100.27

FORMULA BASED ON 13 OXYGENS

Si	1.99	2.03	1.97	2.01	2.01	1.97	2.03	1.99	2.05	2.00
Ti	0.06	0.07	0.08	0.07	0.07	0.08	0.06	0.07	0.07	0.07
Al	5.88	5.82	5.89	5.84	5.85	5.89	5.83	5.86	5.79	5.86
Fe(ii)	0.02	0.02	0.02	0.02	0.02	0.02	0.02	0.03	0.02	0.02
Mg	0.02	0.03	0.02	0.02	0.02	0.02	0.02	0.02	0.02	0.02
Ca	0.00	0.01	0.01	0.00	0.00	0.00	0.01	0.00	0.00	0.01
Na	0.04	0.04	0.05	0.05	0.04	0.05	0.04	0.05	0.05	0.05
TOTAL	8.02	8.01	8.03	8.02	8.02	8.03	8.02	8.03	8.01	8.02

MULLITE ANALYSIS SHEET

SAMPLE KBAX1 - Mullite in Cordierite Buchite

POINT No.	1	2	3	4	5	6	7	8	9	10
SiO2	30.52	29.65	29.99	29.87	29.98	29.68	30.06	29.81	29.94	32.64
TiO2	0.84	0.92	0.98	0.94	0.99	0.88	0.53	0.98	1.01	0.66
Al2O3	67.81	68.89	68.35	68.20	68.32	67.97	68.12	68.73	68.54	66.35
FeO	0.51	0.39	0.47	0.49	0.49	0.54	0.53	0.58	0.52	0.38
MgO	0.19	0.16	0.17	0.19	0.19	0.18	0.18	0.16	0.19	0.16
CaO	0.02	0.00	0.02	0.02	0.01	0.00	0.03	0.01	0.01	0.03
Na2O	0.09	0.11	0.10	0.10	0.08	0.11	0.10	0.12	0.12	0.08
TOTAL	99.98	100.12	100.07	99.82	100.05	99.36	99.54	100.39	100.32	100.29

FORMULA BASED ON 13 OXYGENS

Si	2.17	2.11	2.13	2.13	2.13	2.12	2.15	2.11	2.12	2.30
Ti	0.04	0.05	0.05	0.05	0.05	0.05	0.03	0.05	0.05	0.03
Al	5.68	5.77	5.72	5.73	5.72	5.74	5.73	5.74	5.73	5.52
Fe(ii)	0.03	0.02	0.03	0.03	0.03	0.03	0.03	0.03	0.03	0.02
Mg	0.01	0.01	0.01	0.01	0.01	0.01	0.01	0.01	0.01	0.01
Ca	0.00	0.00	0.00	0.00	0.00	0.00	0.00	0.00	0.00	0.00
Na	0.01	0.02	0.02	0.02	0.01	0.02	0.02	0.02	0.02	0.01
TOTAL	7.95	7.97	7.96	7.96	7.96	7.97	7.97	7.97	7.97	7.91

FELDSPAR ANALYSIS SHEET

SAMPLE Aluminous xenolith - TM1F - Plagioclase reaction caps around spinel, and fine-grained plagioclase

POINT No.	Plagioclase reaction caps around spinel and corundum										Fine-grained re-crystallized plagioclase																		
	SiO2	TiO2	Al2O3	FeO*	CaO	Na2O	K2O	TOTAL	99.118	99.156	99.587	99.356	99.136	99.471	99.489	99.639	99.692	99.671	99.141	99.267	99.133	99.809	99.561						
	46.194	0.069	33.024	0.588	17.503	1.683	0.057		47.988	0.034	31.726	0.522	16.505	2.278	0.105		46.400	46.997	46.820	46.975	46.982	46.910	47.136	45.861	46.911	46.408	46.944	45.886	46.893
																	0.020	0.021	0.054	0.013	0.050	0.036	0.016	0.035	0.014	0.042	0.034	0.040	0.025
																	33.202	32.755	32.678	32.970	32.766	33.008	33.032	33.601	32.757	33.140	32.612	33.931	33.031
																	0.498	0.475	0.465	0.468	0.525	0.535	0.478	0.534	0.435	0.495	0.471	0.444	0.451
																	17.597	17.131	17.180	17.076	17.137	17.120	17.080	18.097	16.967	17.352	16.974	18.059	17.212
																	1.778	1.881	1.831	1.867	1.970	1.933	1.860	1.474	1.970	1.755	1.993	1.356	1.865
																	0.093	0.095	0.110	0.102	0.060	0.096	0.089	0.069	0.088	0.076	0.105	0.093	0.085
																	99.587	99.356	99.136	99.471	99.489	99.639	99.692	99.671	99.141	99.267	99.133	99.809	99.561

FORMULA BASED ON 32 OXYGENS

Si	8.605	8.902	8.604	8.715	8.704	8.698	8.705	8.680	8.706	8.509	8.715	8.623	8.725	8.492	8.679
Ti	0.010	0.005	0.003	0.003	0.007	0.002	0.007	0.005	0.002	0.005	0.002	0.006	0.005	0.006	0.003
Al	7.250	6.936	7.256	7.158	7.160	7.195	7.155	7.198	7.190	7.347	7.171	7.257	7.144	7.401	7.205
Fe (ii)	0.092	0.081	0.077	0.074	0.072	0.072	0.081	0.083	0.074	0.083	0.068	0.077	0.073	0.069	0.070
Ca	3.493	3.280	3.496	3.403	3.422	3.388	3.402	3.394	3.380	3.597	3.377	3.454	3.380	3.581	3.413
Na	0.608	0.819	0.639	0.676	0.660	0.670	0.708	0.693	0.666	0.530	0.710	0.632	0.718	0.486	0.669
K	0.014	0.025	0.022	0.023	0.026	0.024	0.014	0.023	0.021	0.016	0.021	0.018	0.025	0.022	0.020
TOTAL	20.071	20.047	20.096	20.052	20.051	20.049	20.071	20.075	20.040	20.086	20.063	20.067	20.070	20.056	20.059
ENDMEMBER %															
Ab	14.77	19.86	15.37	16.48	16.06	16.42	17.16	16.87	16.38	12.79	17.28	15.40	17.42	11.90	16.31
Or	0.33	0.60	0.53	0.55	0.63	0.59	0.34	0.55	0.52	0.40	0.50	0.44	0.61	0.54	0.49
An	84.90	79.53	84.10	82.97	83.30	82.99	82.50	82.58	83.10	86.81	82.22	84.16	81.98	87.56	83.20

FELDSPAR ANALYSIS SHEET

SAMPLE Aluminous xenolith PMFX1C1 & C2

POINT No.	Mullite Bearing			Mullite Free			Composition range of zoned plagioclase				Fingerprint Texture	
SiO2	50.61	50.41	50.81	50.55	50.88	50.82	51.52	48.86	46.16	48.14	47.22	50.05
TiO2	0.14	0.20	0.22	0.29	0.20	0.24	0.03	0.07	0.06	0.00	0.06	0.16
Al2O3	31.89	32.18	31.96	31.97	32.01	32.30	30.40	32.35	34.23	32.89	34.56	32.07
FeO*	0.16	0.18	0.24	0.11	0.18	0.08	1.11	0.81	0.51	0.66	0.36	0.33
CaO	12.20	12.50	12.53	12.51	12.68	12.53	12.45	14.11	16.19	14.77	15.89	13.38
Na2O	3.95	4.02	4.14	3.99	4.04	3.99	4.17	3.36	2.13	2.97	2.39	3.70
K2O	0.35	0.33	0.34	0.37	0.35	0.37	0.27	0.22	0.14	0.19	0.15	0.27
TOTAL	99.30	99.83	100.24	99.79	100.33	100.32	99.95	99.78	99.41	99.62	100.63	99.96

FORMULA BASED ON 32 OXYGENS

Si	9.25	9.18	9.22	9.21	9.22	9.20	9.40	8.97	8.55	8.86	8.62	9.13
Ti	0.02	0.03	0.03	0.04	0.03	0.03	0.00	0.01	0.01	0.00	0.01	0.02
Al	6.87	6.91	6.84	6.86	6.84	6.89	6.54	7.00	7.47	7.14	7.43	6.90
Fe (II)	0.02	0.03	0.04	0.02	0.03	0.01	0.17	0.13	0.08	0.10	0.05	0.05
Ca	2.39	2.44	2.44	2.44	2.46	2.43	2.43	2.78	3.21	2.91	3.11	2.62
Na	1.40	1.42	1.46	1.41	1.42	1.40	1.48	1.20	0.77	1.06	0.84	1.31
K	0.08	0.08	0.08	0.08	0.08	0.09	0.06	0.05	0.03	0.04	0.04	0.06
TOTAL	20.03	20.08	20.10	20.06	20.08	20.06	20.09	20.14	20.11	20.12	20.10	20.09

ENDMEMBER %

Ab	36.14	36.08	36.67	35.79	35.82	35.73	37.13	29.71	19.10	26.40	21.18	32.83
Or	2.11	1.94	1.99	2.16	2.02	2.18	1.61	1.25	0.80	1.11	0.90	1.55
An	61.75	61.97	61.34	62.05	62.16	62.09	61.26	69.04	80.10	72.50	77.93	65.62

FELDSPAR ANALYSIS SHEET

SAMPLE Plagioclase-mullite buchite xenolith (PMFX1) - Plagioclase in melt pockets

POINT No.	Plag	Melt Pocket 1		Plag	Melt Pocket 2		Plag	Melt Pocket 3		Xenolith OG
		K-Spar			Plag	K-Spar		Plag		
SiO2		52.83	65.40		54.55	53.34	65.14	53.35	55.02	55.40
TiO2		0.04	0.00		0.02	0.06	0.08	0.11	0.13	0.14
Al2O3		29.28	18.10		28.41	28.74	17.63	28.53	27.69	26.53
FeO*		0.93	0.12		0.44	0.72	0.25	0.56	0.68	0.33
CaO		11.28	0.00		9.94	11.02	0.04	11.14	9.68	10.30
Na2O		4.46	0.03		5.16	4.65	0.34	4.54	5.15	5.47
K2O		0.50	15.47		0.56	0.45	14.58	0.44	0.79	0.59
TOTAL		99.31	99.12		99.09	98.98	98.07	98.69	99.15	98.76

FORMULA BASED ON 32 OXYGENS

Si	9.66	12.11	9.93	9.77	12.16	9.79	10.03	10.14
Ti	0.01	0.00	0.00	0.01	0.01	0.02	0.02	0.02
Al	6.31	3.95	6.10	6.20	3.88	6.17	5.95	5.72
Fe (ii)	0.14	0.02	0.07	0.11	0.04	0.09	0.10	0.05
Ca	2.21	0.00	1.94	2.16	0.01	2.19	1.89	2.02
Na	1.58	0.01	1.82	1.65	0.12	1.62	1.82	1.94
K	0.12	3.65	0.13	0.11	3.47	0.10	0.18	0.14
TOTAL	20.03	19.75	19.99	20.00	19.69	19.97	19.99	20.02

ENDMEMBER %

Ab	40.45	0.31	46.83	42.15	3.40	41.34	46.73	47.34
Or	2.99	99.69	3.31	2.70	96.37	2.66	4.71	3.36
An	56.56	0.00	49.85	55.15	0.23	56.00	48.56	49.31

CORDIERITE ANALYSIS SHEET

SAMPLE KBAX1 - Cordierite Buchite

POINT No.	Cord 1	Cord 2	Cord 3	Cord 4	Cord 5	Cord 6	Cord 7	Cord 8	Cord 9	Cord 10
SiO2	47.48	47.43	47.39	47.45	47.49	47.67	47.15	47.25	47.44	47.27
TiO2	0.08	0.20	0.16	0.02	0.06	0.12	0.11	0.08	0.13	0.13
Al2O3	32.76	32.89	33.06	32.74	32.83	32.88	33.22	33.17	33.20	33.13
MgO	7.13	7.20	7.20	7.47	7.10	7.03	7.28	7.18	7.21	7.23
CaO	0.02	0.03	0.01	0.05	0.00	0.07	0.01	0.05	0.03	0.05
MnO	0.01	0.00	0.03	0.00	0.04	0.15	0.03	0.05	0.06	0.00
FeO	9.88	10.00	10.22	9.46	10.49	9.03	9.72	9.93	10.12	10.25
Na2O	0.13	0.15	0.09	0.10	0.11	0.42	0.13	0.13	0.10	0.15
K2O	0.23	0.22	0.23	0.28	0.19	0.47	0.21	0.26	0.21	0.20
TOTAL	97.72	98.12	98.40	97.58	98.30	97.84	97.87	98.09	98.51	98.42

FORMULA BASED ON 18 OXYGENS

Si	4.96	4.94	4.93	4.96	4.95	4.97	4.92	4.93	4.93	4.92
Ti	0.01	0.02	0.01	0.00	0.00	0.01	0.01	0.01	0.01	0.01
Al	4.04	4.04	4.05	4.03	4.03	4.04	4.09	4.08	4.06	4.06
Mg	1.11	1.12	1.12	1.16	1.10	1.09	1.13	1.12	1.12	1.12
Ca	0.00	0.00	0.00	0.01	0.00	0.01	0.00	0.01	0.00	0.01
Mn	0.00	0.00	0.00	0.00	0.00	0.01	0.00	0.00	0.01	0.00
Fe (ii)	0.86	0.87	0.89	0.83	0.91	0.79	0.85	0.87	0.88	0.89
Na	0.03	0.03	0.02	0.02	0.02	0.08	0.03	0.03	0.02	0.03
K	0.03	0.03	0.03	0.04	0.02	0.06	0.03	0.03	0.03	0.03
TOTAL	11.04	11.05	11.06	11.05	11.05	11.07	11.06	11.06	11.05	11.07
Mg#	0.56	0.56	0.56	0.58	0.55	0.58	0.57	0.56	0.56	0.56

CORUNDUM ANALYSIS SHEET

SAMPLE Aluminous xenolith - PMFX1		Corundums Being Replaced by Spinel			
POINT No.	Euhedral Corundums				
SiO2	0.01	0.08	0.04	0.05	0.07
TiO2	0.21	0.29	0.16	0.09	0.18
Al2O3	97.94	97.90	98.10	98.25	97.87
Cr2O3	0.19	0.16	0.18	0.25	0.15
FeO*	0.24	0.27	0.35	0.41	0.47
TOTAL	98.58	98.69	98.82	99.05	98.74
					98.43

FORMULA BASED ON 6 OXYGENS

Si	0.00	0.00	0.00	0.00	0.00
Ti	0.01	0.01	0.00	0.00	0.00
Al	3.98	3.98	3.98	3.98	3.98
Cr	0.01	0.00	0.00	0.01	0.00
Fe (ii)	0.01	0.01	0.01	0.01	0.01
TOTAL	4.00	4.00	4.00	4.00	4.00

SPINEL ANALYSIS SHEET

SAMPLE Aluminous xenolith - PMFX1

POINT No.	Spin1	Spin2	Spin3	Spin4	Spin5	Spin6	Spin7	Spin8	Spin9	Spin10	Spin11	Spin12
SiO2	0.06	0.09	0.07	0.09	0.06	0.08	0.10	0.05	0.03	0.06	0.09	0.05
TiO2	0.26	0.30	0.24	0.22	0.30	0.29	0.26	0.31	0.26	0.41	0.32	0.31
Al2O3	61.08	60.44	62.79	62.64	63.28	63.01	63.22	65.29	64.59	64.48	65.44	62.09
Cr2O3	0.90	0.81	0.11	0.15	0.12	0.14	0.12	0.11	0.19	0.19	0.14	0.29
Fe2O3	5.24	6.58	4.43	4.89	4.30	4.44	4.46	0.90	2.15	2.18	0.99	5.14
MgO	19.19	19.24	19.73	19.59	19.81	19.80	19.72	18.61	19.07	18.85	18.66	19.40
FeO	11.66	11.78	11.25	11.58	11.45	11.30	11.58	13.45	12.72	13.03	13.52	11.74
NiO	0.11	0.05	0.02	0.09	0.00	0.05	0.07	0.02	0.00	0.10	0.05	0.06
TOTAL	98.40	99.24	98.62	99.15	99.31	99.06	99.45	98.72	99.00	99.20	99.16	99.03

FORMULA BASED ON 32 OXYGENS

Si	0.01	0.02	0.01	0.02	0.01	0.02	0.02	0.01	0.01	0.01	0.02	0.01
Ti	0.04	0.05	0.04	0.03	0.05	0.04	0.04	0.05	0.04	0.06	0.05	0.05
Al	14.97	14.76	15.23	15.15	15.25	15.22	15.22	15.77	15.58	15.54	15.74	15.08
Cr	0.15	0.13	0.02	0.03	0.02	0.02	0.02	0.02	0.03	0.03	0.02	0.05
Fe(iii)	0.82	1.03	0.69	0.75	0.66	0.68	0.69	0.14	0.33	0.33	0.15	0.80
Mg	5.95	5.94	6.05	5.99	6.04	6.05	6.00	5.69	5.82	5.75	5.68	5.96
Fe(ii)	2.03	2.04	1.94	1.99	1.96	1.94	1.98	2.31	2.18	2.23	2.31	2.02
Ni	0.02	0.01	0.00	0.01	0.00	0.01	0.01	0.00	0.00	0.02	0.01	0.01
TOTAL	23.98	23.98	23.98	23.98	23.98	23.98	23.98	23.98	23.98	23.97	23.98	23.98
Fe/Fe+Mg	0.32	0.34	0.30	0.31	0.30	0.30	0.31	0.30	0.30	0.31	0.30	0.32
Cr/Cr+Al	0.01	0.01	0.00	0.00	0.00	0.00	0.00	0.00	0.00	0.00	0.00	0.00

SPINEL ANALYSIS SHEET

SAMPLE Aluminous xenolith - PMFX1

POINT No.	Spin13	Spin14	Spin15	Spin16	Spin17	Spin18	Spin19	Spin20	Spin21	Spin22	Spin23	Spin24
SiO2	0.06	0.08	0.09	0.03	0.04	0.06	0.06	0.04	0.04	0.06	0.08	0.06
TiO2	0.31	0.26	0.26	0.27	0.34	0.22	0.29	0.35	0.40	0.35	0.44	0.36
Al2O3	61.26	62.04	62.41	62.87	62.54	61.00	61.80	62.17	60.91	61.32	60.22	61.23
Cr2O3	0.68	0.18	0.22	0.10	0.36	0.50	0.14	0.32	0.27	0.40	0.37	0.27
Fe2O3	6.12	5.37	4.86	4.61	4.52	5.96	5.98	4.85	5.90	5.32	6.51	5.53
MgO	19.34	19.38	19.53	19.71	19.61	18.97	19.75	19.53	19.04	18.89	18.95	19.08
FeO	11.96	11.75	11.57	11.38	11.43	12.23	11.27	11.50	11.91	12.29	11.83	11.89
NiO	0.00	0.10	0.05	0.06	0.07	0.00	0.02	0.01	0.07	0.03	0.01	0.06
TOTAL	99.73	99.06	98.94	98.98	98.84	98.94	99.30	98.76	98.48	98.63	98.41	98.41

FORMULA BASED ON 32 OXYGENS

Si	0.01	0.02	0.02	0.01	0.01	0.01	0.01	0.01	0.01	0.01	0.02	0.01
Ti	0.05	0.04	0.04	0.04	0.05	0.03	0.04	0.05	0.06	0.05	0.07	0.06
Al	14.86	15.07	15.14	15.21	15.16	14.93	14.98	15.12	14.94	15.02	14.82	15.00
Cr	0.11	0.03	0.04	0.02	0.06	0.08	0.02	0.05	0.05	0.07	0.06	0.04
Fe(iii)	0.95	0.83	0.75	0.71	0.70	0.93	0.93	0.75	0.92	0.83	1.02	0.87
Mg	5.93	5.95	5.99	6.03	6.02	5.87	6.06	6.01	5.91	5.85	5.90	5.91
Fe(ii)	2.06	2.02	1.99	1.95	1.97	2.12	1.94	1.98	2.07	2.14	2.07	2.07
Ni	0.00	0.02	0.01	0.01	0.01	0.00	0.00	0.00	0.01	0.00	0.00	0.01
TOTAL	23.98	23.98	23.98	23.98	23.98	23.98	23.98	23.98	23.97	23.97	23.96	23.97
Fe/Fe+Mg	0.34	0.32	0.31	0.31	0.31	0.34	0.32	0.31	0.34	0.34	0.34	0.33
Cr/Cr+Al	0.01	0.00	0.00	0.00	0.00	0.01	0.00	0.00	0.00	0.00	0.00	0.00

XENOLITH GLASS ANALYSES

SAMPLE KIFX2 - Glass from Mullite Buchite

POINT No.	GLS1	GLS2	GLS3	GLS4	GLS5	GLS6
SiO2	49.85	50.08	49.97	50.03	56.30	56.69
TiO2	1.81	1.98	1.93	2.38	3.33	2.80
Al2O3	29.03	29.17	29.60	28.86	21.49	23.08
FeO*	1.56	1.67	1.69	1.70	1.11	2.03
MgO	1.88	1.87	1.89	1.80	0.57	1.52
MnO	0.08	0.01	0.05	0.05	0.04	0.01
CaO	0.74	0.76	0.67	0.64	2.35	2.16
Na2O	0.32	0.32	0.32	0.43	1.79	3.66
K2O	8.89	8.72	8.57	8.52	8.90	5.38
TOTAL	94.15	94.56	94.68	94.41	95.88	97.32

SAMPLE KBAX1 - Glass from Cordierite Buchite

POINT No.	GLS1	GLS2	GLS3	GLS4
SiO2	64.85	64.70	65.08	65.10
TiO2	2.05	2.01	1.93	2.00
Al2O3	15.30	15.50	15.52	15.19
FeO*	4.15	4.37	4.24	3.82
MgO	0.26	0.31	0.30	0.20
MnO	0.02	0.00	0.00	0.00
CaO	0.78	0.82	0.78	0.89
Na2O	4.40	4.30	4.30	4.56
K2O	1.65	1.85	1.91	1.79
TOTAL	93.46	93.86	94.06	93.54

MICA ANALYSIS SHEET

SAMPLE Moine Pelitic Schist - SOM1

POINT No.	Biotite1	Biotite 2	Biotite 3	Biotite 4	Muscovite 1	Muscovite 2	Muscovite 3	Muscovite 4
SiO2	34.79	35.57	35.52	35.53	45.56	46.04	46.01	45.85
TiO2	1.88	1.88	2.39	2.44	0.89	0.75	0.47	0.71
Al2O3	17.64	18.72	18.08	18.04	34.11	35.13	34.24	34.10
MgO	6.88	7.78	7.47	8.35	0.93	0.78	0.87	0.97
CaO	0.00	0.02	0.00	0.01	0.06	0.00	0.00	0.01
MnO	0.15	0.05	0.05	0.14	0.00	0.02	0.04	0.00
FeO	23.24	19.79	20.67	22.34	1.37	1.51	1.71	1.70
Na2O	0.14	0.16	0.14	0.16	0.77	0.86	0.87	0.78
K2O	8.91	9.13	9.14	9.16	9.73	9.93	10.32	10.41
F	0.35	0.33	0.40	0.24	0.16	0.00	0.20	0.00
Cl	0.02	0.02	0.00	0.01	0.01	0.00	0.00	0.02
TOTAL	93.99	93.47	93.87	96.42	93.59	95.03	94.73	94.54

FORMULA BASED ON 24 O, OH, F and Cl

Si	5.50	5.54	5.54	5.43	6.18	6.14	6.19	6.18
Ti	0.22	0.22	0.28	0.28	0.09	0.08	0.05	0.07
Al	3.28	3.44	3.32	3.25	5.45	5.52	5.44	5.41
Mg	1.62	1.81	1.74	1.90	0.19	0.16	0.17	0.19
Ca	0.00	0.00	0.00	0.00	0.01	0.00	0.00	0.00
Mn	0.02	0.01	0.01	0.02	0.00	0.00	0.00	0.00
Fe (ii)	3.07	2.57	2.70	2.86	0.16	0.17	0.19	0.19
Na	0.04	0.05	0.04	0.05	0.20	0.22	0.23	0.20
K	1.80	1.82	1.82	1.79	1.68	1.69	1.77	1.79
TOTAL	15.56	15.45	15.45	15.58	13.95	13.98	14.04	14.04
Mg#	0.35	0.41	0.39	0.40	0.55	0.48	0.47	0.50

GARNET ANALYSES

PLAGIOCLASE ANALYSES

SAMPLE Moine Pelitic Schist - SOM1

SAMPLE Moine Pelitic Schist - SOM1

POINT No.	Garn 1	Garn 2	Garn 3
SiO2	37.09	37.18	36.83
TiO2	0.01	0.05	0.01
Al2O3	20.84	20.82	20.81
Cr2O3	0.03	0.04	0.00
Fe2O3	0.21	0.34	0.22
MgO	2.11	2.55	2.30
CaO	2.24	3.86	3.52
MnO	5.87	2.48	2.81
FeO	31.89	32.74	33.10

TOTAL	100.29	100.07	99.61
--------------	---------------	---------------	--------------

FORMULA BASED ON 24 OXYGENS

Si	5.99	5.99	5.97
Al	3.97	3.95	3.98
Fe(iii)	0.03	0.04	0.03
Fe(ii)	4.31	4.41	4.49
Ti	0.00	0.01	0.00
Mn	0.80	0.34	0.39
Ca	0.39	0.67	0.61
Mg	0.51	0.61	0.56
Cr	0.00	0.01	0.00

TOTAL	16.00	16.01	16.02
--------------	--------------	--------------	--------------

ENDMEMBER %

Uv	0.09	0.14	0.00
An	0.67	1.11	0.69
Gr	5.67	9.75	9.43
Py	8.45	10.17	9.20
Sp	13.38	5.61	6.39
Al	71.74	73.22	74.29

POINT No.	Plag 1	Plag 2	Plag 3
-----------	--------	--------	--------

SiO2	60.50	62.26	64.29
TiO2	0.03	0.05	0.04
Al2O3	23.31	24.07	23.10
FeO*	0.04	0.01	0.02
CaO	5.04	5.90	4.19
Na2O	9.19	8.13	9.10
K2O	0.80	0.11	0.10
TOTAL	98.92	100.53	100.84

FORMULA BASED ON 32 OXYGENS

Si	10.93	10.98	11.25
Ti	0.00	0.01	0.01
Al	4.96	5.00	4.76
Fe (ii)	0.01	0.00	0.00
Ca	0.98	1.11	0.78
Na	3.22	2.78	3.09
K	0.19	0.03	0.02

TOTAL	20.29	19.91	19.92
--------------	--------------	--------------	--------------

ENDMEMBER %

Ab	73.49	70.91	79.27
Or	4.23	0.65	0.56
An	22.28	28.44	20.16

SPINEL ANALYSES

FELDSPAR ANALYSES

SAMPLE	Melting Pelite - SOBC	SAMPLE	Melting Pelite - SOBCc
POINT No.	Spinel's Replacing Biotite	POINT No.	K-feldspar associated with Recrystallization of Melts
SiO2	0.11	0.14	0.37
TiO2	0.59	0.74	0.58
Al2O3	62.99	60.56	61.45
Cr2O3	0.11	0.01	0.07
Fe2O3	0.96	1.71	1.25
MgO	13.00	9.47	10.71
MnO	0.17	0.14	0.18
FeO	21.75	26.70	24.99
ZnO	0.04	0.15	0.10
TOTAL	99.67	99.47	99.60
FORMULA BASED ON 32 OXYGENS		FORMULA BASED ON 32 OXYGENS	
Si	0.02	0.03	0.08
Ti	0.09	0.12	0.09
Al	15.69	15.53	15.57
Cr	0.02	0.00	0.01
Fe(iii)	0.15	0.28	0.20
Mg	4.09	3.07	3.43
Mn	0.03	0.03	0.03
Fe(ii)	3.84	4.86	4.49
Zn	0.01	0.02	0.02
TOTAL	23.95	23.94	23.93
Fe/Fe+Mg	33.29	25.53	30.41
Cr/Cr+Al	16.69	16.53	16.57
ENDMEMBER %		ENDMEMBER %	
Ab	41.45	39.50	40.33
Or	55.06	57.68	58.68
An	3.49	2.82	0.99
K-feldspar associated with Biotite Breakdown		K-feldspar associated with Biotite Breakdown	
SiO2	64.89	64.33	67.54
TiO2	0.09	0.10	0.03
Al2O3	19.62	19.60	18.89
FeO*	0.10	0.17	0.02
CaO	0.71	0.57	0.19
Na2O	4.68	4.45	4.30
K2O	9.45	9.89	9.51
TOTAL	99.54	99.12	100.48
K-feldspar associated with Biotite Breakdown		K-feldspar associated with Biotite Breakdown	
Si	11.80	11.77	12.08
Ti	0.01	0.01	0.00
Al	4.20	4.23	3.98
Fe (ii)	0.02	0.03	0.00
Ca	0.14	0.11	0.04
Na	1.65	1.58	1.49
K	2.19	2.31	2.17
TOTAL	20.01	20.04	19.76
K-feldspar associated with Biotite Breakdown		K-feldspar associated with Biotite Breakdown	
Si	11.79	11.76	11.76
Ti	0.01	0.01	0.02
Al	4.25	4.25	4.25
Fe (ii)	0.01	0.01	0.02
Ca	0.13	0.13	0.13
Na	1.37	1.37	1.19
K	2.42	2.42	2.63
TOTAL	19.97	19.97	20.00
K-feldspar associated with Biotite Breakdown		K-feldspar associated with Biotite Breakdown	
Si	35.04	30.11	30.11
Al	61.63	66.62	66.62
Fe	3.33	3.27	3.27